REINFORCED CONCRETE COUPLING BEAMS WITH HIGH-STRENGTH STEEL BARS

By

Alexander S. Weber-Kamin

Rémy D. Lequesne

Andrés Lepage

A Report on Research Sponsored by

Charles Pankow Foundation

ACI Foundation's Concrete Research Council

Concrete Reinforcing Steel Institute

Structural Engineering and Engineering Materials
SM Report No. 143
August 2020
(Second Printing)

THE UNIVERSITY OF KANSAS CENTER FOR RESEARCH, INC.
2385 Irving Hill Road, Lawrence, Kansas 66045-7563

REINFORCED CONCRETE COUPLING BEAMS WITH HIGH-STRENGTH STEEL BARS

By

Alexander S. Weber-Kamin

Rémy D. Lequesne

Andrés Lepage

A Report on Research Sponsored by

Charles Pankow Foundation

ACI Foundation's Concrete Research Council

Concrete Reinforcing Steel Institute

Structural Engineering and Engineering Materials
SM Report No. 143
THE UNIVERSITY OF KANSAS CENTER FOR RESEARCH, INC.
LAWRENCE, KANSAS
August 2020
(Second Printing)

ABSTRACT

The use of high-strength steel bars in reinforced concrete coupling beams has the potential to reduce reinforcement congestion and support more efficient design and construction methods. A series of tests was conducted to investigate the effects of high-strength reinforcement on coupling beam behavior.

Eleven large-scale coupling beam specimens were tested under fully reversed cyclic displacements of increasing magnitude. The main variables of the test program included: yield stress of the primary longitudinal reinforcement (Grades 80, 100, and 120 [550, 690, and 830]), span-to-depth (aspect) ratio (1.5, 2.5, and 3.5), and layout of the primary longitudinal reinforcement (diagonal [D] and parallel [P]). All beams had the same nominal concrete compressive strength (8,000 psi [55 MPa]) and cross-sectional dimensions (12 by 18 in. [310 by 460 mm]). Beams were designed for target shear stresses of $8\sqrt{f_c'}$ psi ($0.67\sqrt{f_c'}$ MPa) for D-type beams and $6\sqrt{f_c'}$ psi ($0.5\sqrt{f_c'}$ MPa) for P-type beams. Transverse reinforcement was Grade 80 (550) in all but one beam, which had Grade 120 (830) reinforcement.

The test program is documented by presenting the details of specimen construction, test setup, instrumentation, and loading protocol. Documentation of test data includes material properties, cyclic force-deformation response, progression of damage, calculated and measured strengths, initial stiffness, and measured reinforcement strains. Analysis of test data includes hysteretic energy, changes in beam length and depth, components of chord rotation, and the development of an equation for estimating chord rotation capacity.

ACKNOWLEDGMENTS

This report was prepared as a doctoral dissertation by Alexander Weber-Kamin under the direction of Professor Andrés Lepage (Chair).

Primary financial support for the experimental program was provided by the Charles Pankow Foundation, the ACI Foundation's Concrete Research Council, and the Concrete Reinforcing Steel Institute. Additional support was provided by Commercial Metals Company, MMFX Technologies Corporation, Harris Rebar, Midwest Concrete Materials, Nucor Corporation, and The University of Kansas through the Department of Civil, Environmental and Architectural Engineering and the School of Engineering.

Grateful acknowledgment is made to the Industry Champions, David Fields (principal at MKA, Seattle) and Ramón Gilsanz (partner at GMS, New York) and the Advisory Panel, Dominic Kelly (principal at SGH, Boston) and Conrad Paulson (principal at WJE, Los Angeles), for their ideas and constructive criticism.

Appreciation is due to a number of dedicated students and technicians who were involved in the construction of specimens and test programs.

TABLE OF CONTENTS

LIST OF TABLES

LIST OF FIGURES

CHAPTER 1: INTRODUCTION

1.1 Background and Motivation

Reinforced concrete structural walls are a common lateral force resisting system used in medium to high-rise construction. Structural walls resist lateral forces and limit building drift during earthquakes or high wind events. Perforations in a structural wall to accommodate windows, doors, and other building components may lead to the structural wall acting as a series of independent, smaller structural walls, which reduces the stiffness and strength of the lateral force resisting system. Coupling beams are used to couple the actions of structural walls, restoring much of the lost stiffness and strength while retaining the openings necessary for building use. The transfer of forces between structural wall segments by coupling beams results in wall axial tension and compression forces that form a moment couple in response to overturning loads.

The geometry of the coupled wall system amplifies interstory wall drifts into higher coupling beam deformations. The high shear and deformation demands placed on reinforced concrete coupling beams require special reinforcement detailing. This detailing is aimed at preventing shear strength and stiffness reductions when the coupling beam is subjected to repeated inelastic loading cycles that would compromise the lateral strength and stiffness of the reinforced concrete coupled wall system.

The amount and detailing of reinforcement required in concrete coupling beams typically causes reinforcement congestion and increases construction costs. Reducing the quantity or size of the coupling beam diagonal and transverse reinforcement by using high-strength reinforcement is one way to reduce reinforcement congestion and construction costs. The ACI Building Code (ACI 318-14)[6] limits the nominal yield stress of the primary longitudinal reinforcement in special

seismic systems to 60 ksi (420 MPa) and transverse confining reinforcement to 100 ksi (690 MPa). These limitations are due to paucity of experimental data from specimens constructed with high-strength reinforcement. Typical problems associated with the use of high-strength steel in reinforced concrete, such as width of cracks, are not a concern in members primarily designed to resist inelastic cyclic deformations. Therefore, it is reasonable to suggest that high-strength steel reinforcement can function as diagonal reinforcement in coupling beams.

The ACI Building Code[6] requires the use of diagonal reinforcement in coupling beams with aspect ratios (ℓ_n/h) less than two and nominal shear stresses greater than $4\sqrt{f_c'}$ psi ($0.33\sqrt{f_c'}$ MPa). Coupling beams with aspect ratios not less than four are required to be designed as a beam of a special moment frame. The Code permits coupling beams with aspect ratios between two and four to be designed as either diagonally-reinforced or as special moment frame beams. Diagonal bars in slender beams (with aspect ratios greater than two) have a small angle relative to the longitudinal axis of the beam, requiring large amounts of diagonal reinforcement to resist the shear demand. Slender coupling beams may therefore especially benefit from the use of high-strength reinforcement. The effect of using high-strength reinforcing bars on the behavior of coupling beams needs to be evaluated for a representative range of aspect ratios.

1.2 Research Objectives

This study was undertaken to investigate the use of high-strength steel as reinforcement in diagonally-reinforced and special moment frame coupling beams. The expected impact of this work is to reduce reinforcement congestion and, as a result, lower construction costs of robust and more efficient reinforced concrete buildings.

The test results presented in this report may be useful as a basis for comparisons between coupling beams reinforced with Grades 80, 100, and 120 (550, 690, and 830) steel bars. They may also be useful for developing and calibrating models for use in design and analysis of systems with high-strength reinforcement.

CHAPTER 2: LITERATURE REVIEW

This chapter presents summaries of selected research related to cyclic loading of reinforced concrete coupling beams with conventional and high-strength reinforcement. This literature review indicates that the strength and deformation capacity of coupling beams are primarily affected by the ratio of length to depth (aspect ratio) of the beam, magnitude of shear and axial load on the beam, layout and strength of the primary reinforcement, and distribution of transverse and confining reinforcement.

2.1 General Observations on Coupling Beams

Coupling beams are used to connect structural walls so they behave as a structural unit with increased strength and stiffness[104]. Architectural and structural demands typically result in coupling beams with short spans. The deformation, or drift, of the coupled structural walls under lateral loading causes the coupling beams to undergo high shear demands and deformations, called chord rotation. This chord rotation may be significantly greater than the interstory drift ratios distorting the connected walls. Coupling beams are crucial for transferring shear forces between coupled structural walls and maintaining adequately high stiffness and shear strength during inelastic cyclic deformations. Ideal energy dissipation performance would be seen as stable inelastic deformation or hysteretic loops with increasingly large area[27,45]. However, the frequent use of low aspect ratios lead to shear dominant deformations and difficulty achieving a design with stable energy dissipation through large deformations.

A coupling beam member in a structure subjected to earthquake induced forces will experience a combination of flexural and shear loading. For short and deep coupling beams, shear deformations dominate the response, though large flexural deformations are also expected[105,106].

Therefore, it is reasonable to assume that the behavior of short coupling beams after cracking will not be explained by classical beam theory[43,109,111]. The special moment frame reinforcement layout, prescribed in Chapter 18 of ACI 318-14[6], places the primary reinforcement parallel to the longitudinal axis and the transverse reinforcement perpendicular to the longitudinal axis. The transverse reinforcement controls diagonal cracking and resists shear forces. This special moment frame reinforcement layout (also simply referred to as a "moment frame beam" in this chapter) tolerates flexural yielding but is prone to sliding shear failures for beams with low span-to-depth ratios ($\ell_n/h < 4$), such as those that occurred in the McKinley Tower in Anchorage during the 1964 Great Alaska Earthquake[90].

Luisoni et al.[71] and Paulay and Binney[33,92] were the first researchers to test beam specimens with intersecting groups of diagonal bars, called diagonally-reinforced coupling beams. The diagonal reinforcement can be expected to provide the primary shear resistance of the beams, at low aspect ratios, as shown by a truss analogy of forces in the beam. The contribution to shear strength provided by the diagonal reinforcement is proportional to the reinforcement angle of inclination (with respect to the beam longitudinal axis) and inversely proportional to the aspect ratio (ℓ_n/h). Diagonal reinforcement in beams has been shown to delay sliding shear.

The diagonally-reinforced beams in the current study include aspect ratios of 1.5, 2.5, and 3.5, which correspond to reinforcement angles of inclination of approximately 23, 15, and 10 degrees. For these angles, the force components transverse to the longitudinal axis of the beam were 40, 26, and 17% of the total force in each group of diagonal bars, respectively. This reduction in efficiency requires increasing reinforcement ratios for higher aspect ratios to achieve the same shear resistance. Harries et al.[58] note that this leads to constructability issues in

diagonally-reinforced beams where high aspect ratio and high shear resistance are practically mutually exclusive.

Building drift imposes a uniform distribution of shear across the length of the coupling beam by deflecting one end relative to the other, placing the coupling beam under double curvature. This uniform shear will induce a linear moment distribution with zero moment at midspan and maximum moments at the beam-wall interface. A short coupling beam under double curvature may develop one diagonal strut and one diagonal tie along the beam span.

Crushing of the concrete surrounding the primary reinforcement of coupling beams is likely to occur during inelastic cyclic deformations. Therefore, most calculations of coupling beam strength ignore the contribution of concrete to the shear resistance due to concrete crushing, grinding of aggregate at the crack interface, imperfect interlock at the failure plane due to disconnected fragments, and accumulation of plastic strain in reinforcing steel[31,32,34,38,99,115].

Paulay and Binney[33,92] described the role of concrete in diagonally-reinforced coupling beams subjected to inelastic cyclic loading as "relatively minor." The groups of diagonal bars reinforcing the beams were expected to carry the majority of the shear through diagonal tension and compression.

The design equation for diagonally-reinforced coupling beams, ACI 318-14 Section 18.10.7.4(a)[6], relies on the diagonal bars to resist shear and flexure and neglects the contribution of concrete. However, the concrete plays a major role, when properly confined, in delaying the buckling of the primary longitudinal reinforcement[92,115]. Additionally, the concrete compression forces after crack closure may lead to an increased internal lever arm of the tension reinforcement.

2.2 Effect of High-Strength Steel Reinforcement

ASTM A370-17[18] defines the yield point of steel as "the first stress in a material, less than the maximum obtainable stress, at which an increase in strain occurs without an increase in stress." High-strength steel is typically defined as having yield stress in excess of 80 ksi (550 MPa). It is not uncommon for high-strength reinforcement to display a stress-strain "round-house" curve without a well-defined yield point. ASTM A370 alternatively defines yield as the "stress at which a material exhibits a specified limiting deviation from the proportionality of stress to strain" to account for materials without a clearly defined yield point. The "specified limiting deviation" for most structural specifications is identified by either the 0.2% Offset Method or the Extension Under Load (EUL) Method. The 0.2% Offset Method identifies the yield point of "round-house" materials as the intersection between the stress-strain curve of the tested material with a straight line from a point of zero stress and 0.2% strain and a slope equal to Young's Modulus of the material (E_s). The EUL Method identifies the yield stress of the material as the stress at a given strain, typically 0.35%. EUL Method findings are used as an additional check for minimum yield strengths in certain high-strength steels.

Reinforced concrete structures with high-strength reinforcement comes with design challenges such as strain compatibility between the steel and concrete and reduced ultimate strain of steel. Some of the first member-based testing of high-strength steel in reinforced concrete were in the 1930s and 1940s with Richart and Brown[97] and Germundsson[52]. Richart and Brown tested a series of circular columns with longitudinal reinforcement having a yield stress of up to 96 ksi (660 MPa). The strains of the column longitudinal reinforcement exceeded yielding under the applied axial loads if the column cores were adequately confined. Germundsson[52] tested three square columns, designed using ACI 501-36T[10]. The first specimen was reinforced with

undeformed, square Grade 40 (275) reinforcing bars with a reinforcement ratio of 2.6%. The second was reinforced with undeformed, round Grade 75 (520) reinforcing bars with a reinforcement ratio of 6.3%. Both specimens were reinforced with approximately the same longitudinal steel area to achieve approximately the same maximum allowable axial load per ACI 501-36T[10]. The column with higher strength reinforcement had a smaller cross section. The third specimen had a Grade 33 (230) W14x211 (W360x314) wide flange steel section with a reinforcement ratio of 16%. The reinforcing bars were arranged in a circle concentrically around the column centers and confined with spiral transverse reinforcement despite the square column cross-section, which led to spalling of the unconfined corners. The conclusions drawn emphasized the economy of high-strength reinforcement to build columns that could have smaller cross sections, require less reinforcement, and facilitates standardization of design and construction details.

The Research and Development Laboratories of the Portland Cement Association (PCA) published a series of studies involving high-strength reinforcement from 1961 to 1966. In Part 1, Hognestad[61] identifies additional design considerations associated with reducing the area of steel reinforcement by using high-strength reinforcement; namely, member stiffness, durability and crack widths, and strain compatibility. However, Hognestad describes many of the benefits that use of high-strength steel can bring to reinforced concrete: “the reduction in steel area which accompanies an increase in f_y often facilitates concrete placement by eliminating steel congestion. Steel reduction may also permit a reduction in width of major girders, which in turn also reduces dead loads.” High-strength reinforcement can now be produced economically as the increased costs due to steel alloys and advanced steel production techniques are offset by the reduced reinforcement congestion as well as reduced handling costs from having to store, ship, and place

less material. These factors have resulted in increased interest in high-strength steel in reinforced concrete structures.

The ACI Code has progressively adapted to reflect the increased acceptance of high-strength steel. The 1936 ACI Code[10] limited the allowable compressive stress in the longitudinal reinforcement of spirally-reinforced columns to not greater than 40% of the yield stress and not to exceed 30 ksi (210 MPa), which did not allow the effective use of a yield stress in excess of 75 ksi (520 MPa). The 1963 ACI Building Code[2] limited the yield stress of longitudinal column reinforcement to 75 ksi (520 MPa), which, in 1971, was increased to 80 ksi (550 MPa) for non-seismic applications. The limit remained 60 ksi (420 MPa) for seismic applications.

Todeschini et al.[113] tested nineteen columns with Grade 75 (520) reinforcement without a distinct yield plateau in eccentric axial loading. The specimens were cast with nominal concrete strengths of 3500, 5000, or 7500 psi (25, 35, or 50 MPa), load eccentricities of 0, 1.5, 3.5, or 5.5 in. (0, 38, 89, or 140 mm), and reinforcement ratios of 1.0, 3.3, or 5.0%. One of the specimens was constructed using reinforcement with distinct stress-strain behavior characterized by a “flat yield plateau”. All specimen failures were initiated by concrete crushing. Buckling of the longitudinal reinforcement occurred in some specimens but was preceded by concrete crushing. The strain in the concrete associated with peak stress was generally less than the yield strain of the reinforcement. Strains in the concrete exceeding the strain associated with peak stress resulted in decreased concrete force. However, the specimens carried increasing load as the reinforcement had not yielded.

Starting in the 1970's, significant research aimed to understand the seismic behavior of concrete members with conventional and high-strength transverse reinforcement. Experiments[39,79,108,115] were conducted to evaluate the effects of confining reinforcement on limiting concrete compressive strain, bar buckling, and member ductility. It was found that conventional and high-strength reinforcement enhanced axial strength, delayed bar buckling, and improved flexural ductility.

A major effort in the 1980s and 1990s was led by Japanese researchers (as documented by Aoyama[14]) on the use of high-strength reinforcement with yield strengths in excess of 80 ksi (550 MPa). A summary of 105 beam tests was reported by Otani et al.[86], suggesting that the use of high-strength reinforcement was commonplace in Japanese construction before the turn of the century.

More recently, Kwan and Zhao[65] cyclically tested six normal-strength concrete coupling beams with Grade 75 (520) primary reinforcement. One specimen was diagonally-reinforced while the other five were moment frame beams. Specimens were constructed with aspect ratios of 1.17, 1.40, 1.75, or 2.0. Chord rotation capacities ranged from 3.6 to 5.7% and were generally proportional to aspect ratio. The diagonally-reinforced specimen had a more stable force-deformation curve than the moment frame beams, with buckling of the diagonal bars controlling the mode of failure. Moment frame beams typically failed by sliding shear at beam ends.

Rautenberg et al.[95] reported test results of four columns under fully reversed cyclic loading with a column width of 9 in. (230 mm), depth of 12 in. (310 mm), and aspect ratio of 5.0. Two specimens were reinforced with Grade 60 (420) reinforcement and two specimens were

reinforced with Grade 120 (830) reinforcement. The specimens were subjected to $0.1f_c'A_g$ or $0.2f_c'A_g$ axial load during the cyclic loading. The product of the longitudinal reinforcement ratio and longitudinal reinforcement yield stress, ρf_y, was nearly identical for all specimens, which resulted in nearly identical strength for a given axial load. Transverse reinforcement Grade 60 (420) was provided and satisfied detailing requirements of ACI 318-08[5]. All specimens exhibited similar deformation capacities. Similar conclusions were drawn by other researchers regarding beams[110,112], columns[96,101,102], slender walls[62], and squat walls[42].

Yotakhong[117] tested four beams, three specimens with high-strength reinforcement and one with normal-strength reinforcement. One of the specimens with high-strength reinforcement was tested under cyclic loading, the other three were tested under static loading conditions. The failure mode of all beams was ductile, though the specimens with high-strength reinforcement had higher strength given that all beams had the same reinforcement ratio.

Tavallali et al.[110] tested seven beams in fully reversed cyclic loading with a beam width of 16 in. (410 mm), depth of 10 in. (250 mm), and aspect ratio of 4.8. The reinforcement for the specimens was a combination of four variables: Grade 60 or 100 (420 or 690) longitudinal reinforcing bars, Grade 60 (420) transverse reinforcement at 2 or 4-in. (50 or 100-mm) spacing, bottom reinforcement area equal to 50 or 100% of the top reinforcement, and whether high-performance fiber reinforced concrete (HPFRC) was used or not. Beams with Grade 100 (690) reinforcement had drift ratio capacities in excess of 5%, which was comparable to the deformation capacities of similar beams reinforced with Grade 60 (420) bars.

Huq et al.[62] tested six large-scale "T-shaped" slender walls in fully reversed cyclic loading with low axial and shear stresses. The walls were reinforced with Grade 60, 100, or 120 (420, 690,

or 830) bars with an approximately constant ρf_y targeting the same nominal strength. Test results indicated that walls designed for similar flexural strengths achieved similar strength and deformation capacity (drift ratios in excess of 3.0%) if the primary reinforcement had a tensile-to-yield stress ratio (f_t/f_{ym}) greater than 1.18 and ultimate strain (ε_{su}) greater than 6%. Buckling of the bars was observed in loading cycles prior to fracture in specimens reinforced with bars that met the f_t/f_{ym} and ε_{su} thresholds (T1, T3, T4, and T6). Specimens reinforced with bars that did not meet the f_t/f_{ym} and ε_{su} thresholds (T2 and T5) had lower deformation capacities (drift ratios of 1.8 to 2.4%) and a higher concentration of damage at the wall base that led to fracture of the primary bars without prior buckling.

Cheng et al.[42] tested five squat wall specimens in cyclic loading with Grade 60 or 115 (420 or 785) reinforcing bars with approximately constant ρf_y for horizontal and vertical reinforcement, except that Grade 60 (420) reinforcement was used as boundary element confinement in all specimens. Deformation capacity for the two types of specimen was similar though crack widths were larger and initial lateral stiffness was lower for specimens with Grade 115 (760) reinforcement.

Ghannoum and Slavin[53,54] conducted steel bar tests to compare the low-cycle fatigue behavior of high-strength reinforcing bars with that of benchmark Grade 60 (420) bars. The test program considered three yield strengths (Grades 60, 80, or 100 [420, 550, or 690]), three bar diameters (No. 5, 8, or 11 [16, 25, or 36]), and two reinforcing bar manufacturing processes. Monotonic axial tension loading tests to failure were used to generate the monotonic stress-strain relationship of the reinforcement. A total of 206 fully reversed cyclic tests were conducted on the combinations of material strengths, bar diameters, manufacturing processes, unsupported lengths,

and loading history. Findings showed that Grade 60 (420) reinforcement carried more cycles to failure than Grades 80 or 100 (550 or 690) reinforcement and exhibited lower variability in fatigue life compared with the higher grade reinforcement. Measurements of surface strain in the buckled regions were up to five times the average bar strain in the buckled region leading to significantly shorter fatigue life after buckling of the reinforcement. Findings showed that reducing the spacing of transverse reinforcement of high-strength longitudinal reinforcement compared with conventional reinforcement reduced the degree of buckling and increased low-cycle fatigue life. Buckling of the longitudinal reinforcement was observed but uncommon in unsupported lengths less than $4d_b$. Therefore, the authors recommended reducing the ACI 318-14 spacing limit of transverse reinforcement in members of special moment frames from $6d_b$ for conventional longitudinal reinforcement to spacing between $4d_b$ and $5d_b$ for high-strength longitudinal reinforcement, in agreement with previous recommendations by others[83,96,110]. Spacing less than $4d_b$ to $5d_b$ was not expected to provide additional improvement of fatigue life.

Zhong and Deierlein[119] integrated multiple experimental studies with computational simulations to evaluate high-strength reinforcement design requirements for cyclic loading. The authors also presented a concise summary of the behavioral effects of high-strength reinforcement as:

1. High-strength reinforcement tends to have a lower tensile-to-yield stress ratio compared with conventional reinforcement, which may reduce the spread of plasticity and induce localization of plastic strains.
2. High-strength reinforcement tends to have lower fracture toughness compared with conventional reinforcement, which may lead to premature fracture under cyclic loading.

3. Smaller bar sizes with higher strength may be used in design to achieve the same strength as larger bar sizes with lower strength. However, this would require closer transverse reinforcement spacing or lead to earlier bar buckling. Smaller reinforcement diameters will also lead to deterioration of bond, leading to reduced member strength and stiffness but may mitigate the effects of lower tensile-to-yield stress ratio of high-strength reinforcement on the localization of plastic strains.
4. Overall drift demand in structures was positively correlated with steel grade due to reduced steel area and, therefore, reduced member stiffness.

Members with the same cross-section, similar reinforcement layout, and designed for similar strength using high-strength reinforcement will be more flexible than members with conventional reinforcement, potentially leading to increased building drift with reduced ductility demands.[66]

2.3 Experimental Studies on Reinforced Concrete Beams

Paulay[90,91] tested twelve reinforced concrete coupling beams with aspect ratios of 1.0, 1.3, and 2.0 under cyclic and monotonic loading as part of a study investigating coupled shear wall behavior following the 1964 Great Alaska Earthquake. Beam widths were consistently 6 in. (150 mm). Beam depths were 39, 31, and 24 in. (990, 790, and 610 mm). Beam clear spans were 40, 40, and 48 in. (1020, 1020, and 1220 mm), respectively. Test results documented the inadequacy of moment frame beams, with the primary reinforcement parallel to the beam longitudinal axis, for coupling beams with aspect ratios between 1.0 and 2.0. The ultimate shear capacity for the tested specimens was less than that predicted by conventional reinforced concrete flexural theory. Crushing of the concrete combined with sliding shear or diagonal tension failure was a common mode of failure. This led to the conclusion that reinforcement parallel to the beam

longitudinal axis and hoops were not effective in preventing both sliding shear and diagonal splitting. Acceptable levels of ductility were only possible at low shear stresses.

Additionally, results from experiments by Paulay[90,91] demonstrated that strain profile assumptions based on the conventional truss analogy were incorrect in short beams undergoing fully reversed cyclic loading. After flexural yielding of beams with an aspect ratio between 1.4 and 2.0, strain readings from stirrups indicated that the transverse reinforcement carried about 80% of the shear across the "major cracks" connecting opposite corners of the beam. Dowel action of the flexural reinforcement accounted for the remainder of the shear capacity of the beam. The authors reasoned that flexural reinforcement could not be relied upon to carry compression forces because the plastic elongation due to flexural tensile yielding did not completely recover in subsequent cycles. Ultimately, Paulay emphasized the inadequacy of short moment frame beams under high shear stress and inelastic cyclic loading, prompting further study into alternative reinforcement layouts.

Brown and Jirsa[38] tested 12 doubly-reinforced moment frame beams, acting as cantilevers, under monotonic and cyclic loading. Variables included two span lengths (30 and 60 in. [760 and 1520 mm]) and one beam depth (12 in. [310 mm]) that resulted in beams with equivalent aspect ratios of 5.0 and 10.0. The primary longitudinal reinforcement was either two No. 6 (19) or two No. 8 (25) bars (top and bottom), with a yield stress of 46 ksi (310 MPa). Transverse reinforcement consisted of No. 3 (10) stirrups spaced at 2, 4, or 5 in. (50, 100, or 130 mm). Reinforcement layout and loading history were consistent between beams with different longitudinal bar sizes so the applied shear was higher in the specimens with No. 8 (25) reinforcement, which resisted fewer cycles than the beams reinforced with No. 6 (19) reinforcement. Sliding shear was the controlling failure mode for all beams, typically occurring after yielding of the longitudinal reinforcement and

the formation of large flexural cracks near the support. For a target shear stress, reducing the stirrup spacing, increasing the confinement of the concrete core, and increasing the aspect ratio are all associated with an increased deformation capacity. These findings support those of Agrawal et al.[11] and Paulay[90,91].

Using diagonal reinforcement to resist shear in beams was discussed as early as 1909 by Morsch[76] in the truss analogy of shear resistance in beams. Later research[55,77] expanded upon the concept but some of the first applications of diagonal reinforcement in coupling beams were Luisoni et al.[71] and Binney and Paulay[33,92].

Luisoni et al.[71] constructed three ⅒-scale specimens consisting of two shear walls connected by ten diagonally-reinforced coupling beams undergoing monotonic loading to failure. One specimen was tested with a concentrated load at the top (Model 1), the other two specimens used a distributed load apparatus that simulated earthquake loading from the weight of the building floors (Models 2 and 3). The secondary longitudinal reinforcement for all coupling beams was developed. The diagonal reinforcing bars in Model 1 were bent near the beam ends so they were parallel to the longitudinal reinforcement and developed into the walls as straight bars. The diagonal reinforcing bars in Models 2 and 3 were straight but developed into the walls as hooked bars. Model 1, with the concentrated load at the top, displayed greater distribution of cracking than Models 2 and 3 where cracking was localized at the base of the shear wall in tension. Test results closely matched calculated stresses but not calculated displacements.

Binney and Paulay[33,92] were the first researchers to test large-scale diagonally-reinforced coupling beams. The test program included three diagonally-reinforced beams and one conventionally-reinforced or moment frame beam. All four beams were subjected to fully reversed

cyclic loading to compare the effects of reinforcement orientation and aspect ratio on behavior. The conventionally-reinforced beam and two of the diagonally-reinforced beams had aspect ratios of 1.3. The remaining diagonally-reinforced beam had an aspect ratio of 1.0. This study[33] selected diagonally-oriented reinforcement to address the shortcomings of short moment frame beams identified by earlier studies[90,91]. Tensile forces were observed along the entire length of the longitudinal reinforcement of a specimen, with the moment frame beam exhibiting similar behavior to the moment frame beams tested by Paulay[90,91].

The primary shear resistance of the diagonally-reinforced beams studied by Luisoni et al.[71] and Binney and Paulay[33,92] was provided by two groups of diagonal reinforcing bars that intersected at the beam midspan. This reinforcement layout follows the same profile as the moment demand induced by double curvature or antisymmetric bending, with constant shear along the beam span. Symmetric diagonal reinforcement gives equal diagonal tension and compression capacity after the concrete contribution to shear strength degrades with large inelastic cyclic loading, provided the compression reinforcement does not prematurely buckle. The calculated shear strength based only on the contribution of the diagonal reinforcement was shown to be less than the measured strength of short coupling beams (aspect ratios of 2 or less).

The diagonally-reinforced beams of Binney and Paulay[33,92] demonstrated that diagonal reinforcement prevented diagonal tension and sliding shear failures, ensured ductile behavior by forcing yielding of the diagonal reinforcement to govern strength, and exhibited superior deformation capacity and reduced hysteretic pinching compared with the moment frame beams. The failure of diagonally-reinforced beams was initiated by bar buckling near the beam ends. The short embedment length of the secondary longitudinal reinforcement into the end blocks was associated with damage localization at the beam-block interfaces.

Bertero et al.[32] cyclically tested seven cantilever beams with shear span-to-depth ratios of 2.7 (equivalent to a beam undergoing double curvature with an aspect ratio of 5.4). The test program considered two types of reinforcement layout, one typical of moment frame beams with primary flexural reinforcement parallel to the longitudinal axis of the beam and the other with a rhomboidal layout. The rhomboidal reinforcement layout (referred to in the paper[32] as "inclined bracing bars") consisted of longitudinal reinforcement bent near the beam ends (but within the clear span) at approximately 45 degrees while the reinforcement remained parallel at midspan, see Figure 1 in Reference 32. The rhomboidal layout was intended to achieve similar improvement to deformation capacity as diagonally-reinforced beams by preventing sliding shear at the beam ends. The testing protocol[32] was noteworthy because five of the seven specimens were tested to failure with fully reversed cyclic loading. The remaining two specimens were monotonically loaded to failure, returned to their initial position, repaired through epoxy injection, and then cyclically tested to failure. One of the main findings of this study[32] was that the use of a rhomboidal reinforcement layout allowed stable hysteresis and minimized the degradation of stiffness.

Irwin and Ord[63] tested six small-scale coupling beams. Their findings also showed that diagonally-reinforced coupling beams exhibit improved ductility, strength, and hysteresis compared with moment frame beams under similar loading conditions. However, the specimens tested by Irwin and Ord[63] were reinforced with smooth welded wire and the beams were 2.4-in. (60-mm) long, 0.47-in. (12-mm) wide, and 0.49- to 0.79-in. (12.5- to 20-mm) deep (corresponding to aspect ratios of 3 to 4.8). Scaling effects limit the applicability of their findings.

Barney et al.[31] tested eight 1/3-scale coupling beams with various reinforcement layouts (conventional, diagonal, or rhomboidal) with aspect ratios of 2.5 or 5.0 and shear stresses varying

between 3.5 and $11\sqrt{f_c'}$ psi (0.3 and $0.9\sqrt{f_c'}$ MPa). The rhomboidal reinforcement layout consisted of primary longitudinal reinforcement bent near the beam ends to intersect in the hinging regions while being parallel through midspan. A rhomboidal layout was viewed as a possible alternative to a diagonal layout to prevent sliding shear failures near the beam ends. However, a rhomboidal layout caused more construction difficulties than a diagonal one. Barney et al.[31] observed that conventionally-reinforced beams (or moment frame beams) with aspect ratios less than 3.0 typically failed by sliding shear near the beam ends, independent of the amount of transverse reinforcement. Inclined longitudinal reinforcement, by means of rhomboidal or diagonal bars, prevented sliding shear. Failure of beams with inclined longitudinal reinforcement was initiated by inelastic buckling of the inclined bars. Chord rotation associated with peak force varied between 2 and 5% with low values corresponding to conventionally-reinforced beams and high values to diagonally-reinforced beams. Barney et al.[31] noted that for beams with aspect ratios of 5.0, the improvement obtained by using full-length diagonals was relatively small. This study [31] also emphasized that improved inelastic performance of conventionally-reinforced beams was obtained by increasing the size of the confined concrete core.

Tegos and Penelis[111] cyclically tested 24 specimens (21 columns and 3 beams), with a 7.9-in. (200-mm) square section. Test variables included three reinforcement layouts (conventional, diagonal, or rhomboidal), three aspect ratios (2.0, 3.0, or 4.0), yield stresses from 46 to 70 ksi (320 to 485 MPa), and axial load from 0.0 to $0.35f'_cA_g$. Diagonal shear cracking and sliding shear failure modes were not observed in beams with diagonal or rhomboidal reinforcement layout. Instead, buckling of the compression reinforcement caused the primary shear strength loss in beams with inclined reinforcement layouts, leading to superior chord rotation capacity and hysteretic energy dissipation compared with beams with conventional reinforcement layout.

Specimens with diagonal or rhomboidal reinforcement layout and with the same axial load retained their strength for chord rotations of 4%, whereas noticeable strength loss occurred below chord rotations of 2% for the corresponding specimen with conventional reinforcement.

Kuramoto et al.[64] tested 15 columns under reversed cyclic loading. All columns were square with 7.9-in. (200-mm) sides and had an aspect ratio of 2.0. Test variables included reinforcement layout (conventional or diagonal), axial loads (0.10, 0.29, or 0.42 $f'_c\ A_g$), transverse reinforcement yield stress (49 or 292 ksi [340 or 2010 MPa]), and transverse reinforcement ratio (0.0055 to 0.011 $s\ b_w$). The reinforcement layouts of the columns in this study[64] were either conventional or a combination of diagonal and conventional. All columns had 10 No. 3 (10) developed reinforcing bars evenly distributed around the square cross-section. However, 4 of the 10 bars crossed at midspan for the diagonally reinforced columns rather than remaining parallel throughout the column span, like the conventionally reinforced columns. The columns with a conventional layout displayed hysteretic loops with much lower energy dissipation and deformation capacities than similarly loaded beams with the diagonal layout. Generally, deformation capacity was inversely proportional to the level of axial loading (in terms of $f'_c\ A_g$) and proportional to the quantity of transverse reinforcement (in terms of $\rho_t\ f_{yt}$). Test results[64] validated the general findings of previous research that diagonally-reinforced frame members have higher chord rotation capacity and higher shear strength than similarly loaded conventionally-reinforced frame members.

Tassios et al.[109] cyclically tested 10 rectangular beam specimens with five reinforcement layouts: conventional, diagonal, rhomboidal (similar to other studies[31,111]), long dowels, or short dowels. The dowels were planned to control the sliding failure at the beam-wall interface. All

beams had a clear span of 19.7 in. (500 mm), width of 5.1 in. (130 mm), and a depth of 11.8 or 19.7 in. (300 or 500 mm), resulting in aspect ratios of 1.0 or 1.67. The test setup used a single actuator that allowed rotation of one of the end blocks. No restraint to axial elongation was applied. The crack pattern and the mode of failure differed for each beam based on the reinforcement layout and aspect ratio. The specimens with an aspect ratio of 1.0 and conventional, diagonal, or rhomboidal reinforcement layouts exhibited cracks along the main diagonals. The specimens with an aspect ratio of 1.67, regardless of reinforcement layout, developed flexure-shear cracks near the beam ends. Vertical sliding cracks were observed in all of the specimens but the presence of dowels controlled the opening of cracks near the beam ends. The beams with conventional reinforcement behaved in a brittle manner with "intense cracking and considerable strength and stiffness degradation" though their ductility and energy dissipation were superior to those exhibited by the dowel-reinforced specimens. Test results[109] once again confirmed the higher overall performance of the diagonally-reinforced coupling beams. The performance superiority of both the diagonal and rhomboidal layout was more evident for beams with lower aspect ratios.

Monti and Nuti[75] studied the nonlinear cyclic behavior of reinforcing bars (including buckling) to develop an analytical model of the nonlinear stress-strain behavior that could be applied at a member level analysis. Specimens consisted of reinforcing bars with a yield stress of 64 ksi (440 MPa). Three unsupported length-to-bar diameter ratios were considered (s/d_b = 5, 8, or 11) for three bar diameters (0.63, 0.79, or 0.94 in. [16, 20, or 24 mm]) and six loading histories (one monotonic tensile to yielding, two "random", two nonsymmetrical, and one symmetrical about zero strain). The selected values of s/d_b correspond to typical tie spacing used in construction. Test results showed that reinforcement undergoing monotonic compression showed decreasing ultimate stresses with increasing s/d_b. Only the specimens with s/d_b = 5

approximated the monotonic tensile behavior to ultimate strain. Specimens with s/d_b = 8 or 11 showed greater divergence from the monotonic tensile curve beyond yielding. Buckling of the reinforcement occurred immediately after yielding in specimens with s/d_b = 11. Expansion of the hysteretic curves (isotropic hardening) was observed in the cyclic testing of bars with s/d_b = 5 but contraction of the hysteretic curves (isotropic softening) was observed in both bars with s/d_b = 8 or 11. Monti and Nuti[75] developed an analytical model incorporating four parameters that can be determined from a monotonic tensile test. The model provided similar results compared with other more complicated models [49,74].

Bristowe et al. [36] cyclically tested four reinforced concrete coupling beams with no axial restraint. Specimens were moment frame beams with conventional steel reinforcement and used either normal-strength concrete (4.4 ksi [30 MPa]) or high-strength concrete (10.2 ksi [70 MPa]]), and were either ductile or nominally ductile, as defined by the CSA Standard[46]. The loading protocol consisted of monotonically displacing one end of the specimen parallel to the other fixed end until yielding, "when a significant drop in stiffness is observed," then applying three cycles of increasing positive and negative displacement increments. The authors reported that the high-strength concrete specimens dissipated more energy than the normal-strength concrete specimens, which was attributed to the increased concrete strength. However, the high-strength specimens also had transverse reinforcement more closely spaced than their companion normal-strength specimens, which contributed to better confinement. The higher concrete strength also reduced the normalized shear stresses.

Breña et al.[35] investigated the effects of low reinforcement density in a coupling beam, typical of 1950s design (without diagonal bars), undergoing reversed cyclic loading. A single beam, 9-in. (229-mm) wide and 41-in. (1040-mm) deep, was tested with an aspect ratio of 1.46.

The beam longitudinal reinforcement ratio (ρ) was 0.31% and the transverse reinforcement ratio (ρ_t) was 0.2%. Diagonal cracks within the coupling beam occurred when the shear in the beam was more than "twice the level calculated using ACI 318-95 procedures for determining the concrete contribution to shear." Limited damage was exhibited prior to failure with cracking starting near midspan and growing diagonally toward the corners of the beam. Imminent failure of the beam could not be inferred from crack observations. Immediately after the formation of the critical diagonal crack, the transverse reinforcement fractured. The brittle mode of failure was attributed to the small amount of transverse reinforcement in the coupling beam.

Xiao et al.[116] cyclically tested six high-strength concrete beams (compressive strength exceeding 10 ksi [69 MPa]) with Grade 70 (480) reinforcement. Comparison specimens were not cast using "normal-strength" concrete. The testing protocol consisted of applying one cycle of positive and negative displacement increments to first yielding of the beam followed by three cycles of positive and negative multiples of the yield displacement (1, 1.5, 2, 3, 4, and 6). Three specimens had aspect ratios of 3.0 and three had aspect ratios of 4.0. Primary reinforcement was parallel to the longitudinal axis in all specimens but the arrangement varied. The test matrix included one specimen for each aspect ratio with a conventional reinforcement layout of three No. 6 (19) as primary layers of flexural reinforcement and another specimen with the same reinforcement plus additional secondary layers of two No. 6 (19) inset approximately 3 in. (7.5 cm) from the primary layers of the beam. In addition, one specimen for each aspect ratio had four No. 6 (19) reinforcing bars as primary layers and two No. 6 (19) reinforcing bars distributed evenly on both sides of the beam (between primary layers). Measured peak shear stress ranged from 3.7 to $7.8\sqrt{f_c'}$ psi (0.31 to $0.65\sqrt{f_c'}$ MPa). All beams exhibited pinched hysteretic curves. The beams with single layers reached an ultimate chord rotation of 4.6 and 3.6% for aspect ratios of 4.0 and

3.0, respectively. The beams with an additional layer of reinforcement reached 3.6 and 3.2% chord rotation for aspect ratios of 4.0 and 3.0, respectively. The beams with evenly distributed reinforcement exhibited broader hysteretic curves, higher applied shear stresses, and reached 5.0 and 4.4% ultimate chord rotation for aspect ratios of 4.0 and 3.0, respectively. The ultimate chord rotation for this study[116] was based on the last completed cycle to a targeted multiple of the yield displacement for each specimen, typically a multiple of 5 or 6, where a large reduction of shear strength (in excess of 20%) was observed. Generally, increasing aspect ratio and a distributed reinforcement layout was positively correlated with increased deformation capacity. The ultimate chord rotations reached by beams with aspect ratios of 3.0 were 15 to 25% lower than those with an aspect ratio of 4.0. However, narrower hysteretic curves were not as evident in the beams with aspect ratios of 3.0 as the beams with aspect ratios of 4.0.

Rodriguez and Botero[98] further studied the effect of loading history on reinforcement buckling in large strain reversals. Specimens were made from reinforcing bars conforming to ASTM A706[20] with minimum yield strength of 60 ksi (420 MPa) and four unsupported length-to-bar diameter ratios were considered (s/d_b = 2.5, 4, 6, or 8). Original reinforcing bar diameters were 1.25 in. (32 mm) but the tested specimens were machined to a 0.63 in. (16 mm) diameter. Findings supported the results of Monti and Nuti[75] though buckling of the specimens with s/d_b = 2.5 and 4 was possible at large strain reversals. Other relevant studies[1,29,30,37,60,72,73,87,107] have addressed low-cycle fatigue and inelastic buckling of reinforcing bars.

Galano and Vignoli[51] tested 15 coupling beams with aspect ratios of 1.5. All beams had a clear span of 23.6 in. (600 mm), width of 5.9 in. (150 mm), and a depth of 15.7 in. (400 mm). The main variables of the tests were the loading history (monotonic or cyclic) and the reinforcement

layout (conventional, rhomboidal, or diagonal with or without group confinement). Group confinement refers to confined groups of diagonal bars with limited transverse reinforcement at the beam periphery. Test results showed that beams with diagonal or rhomboidal layout behaved better than beams with conventional layout. Energy dissipation was similar for beams with inclined reinforcement but diagonally-reinforced beams reached higher strength than rhomboidally-reinforced beams. Chord rotation capacity was reported for monotonic loading, with the highest values for beams with a rhomboidal layout (8.4%), followed by diagonal layout with group confinement (6.5%), without group confinement (6.2%), and conventional layout (5.1%). However, for the same reinforcement area in each group of inclined bars (diagonal or rhomboidal layout), the rhomboidal layout resulted in approximately 20% lower strength than beams with diagonal layout.

Lim et al.[69] tested six coupling beams with aspect ratios ranging from 3.0 to 4.0 with diagonal, conventional, or hybrid reinforcement layout. The hybrid reinforcement layout combined the detailing of a diagonally-reinforced beam (using full-section confinement and reduced amount of diagonal reinforcement) with that of a special moment frame column. Although the beams were axially restrained, the resultant axial load was set to zero by two actuators. All beams were 19.7-in. (500-mm) deep. Four beams with an aspect ratio of 3.0 had a width of 11.8 in. (300 mm) and two beams with an aspect ratio of 4.0 had a width of 15.7 in. (400 mm). The hybrid reinforcement layout reached a chord rotation capacity of approximately 6%, lower than the diagonally-reinforced beams, which reached approximately 7%.

Choi et al. [44] presented a novel coupling beam design called a “Double-Beam Coupling Beam” (DBCB) as part of a series of five coupling beams tested in cyclic loading without axial restraint. A DBCB consists of a single monolithically-cast coupling beam with transverse

reinforcement around two groups of parallel (longitudinal) bars separated by a sacrificial, unreinforced concrete layer between the two groups of bars. Three thicknesses of sacrificial layers were tested (0.25, 1, and 2 in. [6, 25, and 50 mm]). This arrangement, similar to two parallel conventional beams, was designed so the two groups would separate under reversed cyclic loading, effectively doubling the beam aspect ratio. All five beams were 6-in. (152-mm) wide and 15-in. (381-mm) deep. Four beams had a clear span of 36 in. (914 mm) and one of 49.5 in. (1260 mm) for aspect ratios of 2.4 and 3.3, respectively. Longitudinal reinforcement ratio, $A_s/b_w\ h$, ranged between 5.9 to 8%. The amount of transverse reinforcement differed along the beam span, 0.037 $s\ b_w$ to 0.049 $s\ b_w$ near beam ends and 0.018 $s\ b_w$ to 0.029 $s\ b_w$ near midspan. The test results showed that DBCB specimens reached chord rotation capacities between 6 and 11%, except for the beam with an unreinforced concrete layer of 0.25 in. (6.3 mm), which did not fully separate and the overall beam section failed in shear at 2% chord rotation.

2.4 Stiffness and Deformation Capacity

Performance-based seismic design resources provide guidelines for the nonlinear modeling of structural walls and coupling beams; such as effective stiffness and a generalized force-deformation envelope.

ACI 369-17[8] and ASCE 41-17[16] provide effective stiffness values for reinforced concrete components, including coupling beams. Both documents[8,16] allow the use of flexural rigidity and shear rigidity based on $0.3E_cI_g$ and $0.4E_cA_w$, respectively, which correspond to 30 and 100% of stiffness values based on gross section properties (the coefficient of 0.4 corresponds to a Poisson ratio of 0.25). These values are based on recommendations by Elwood et al.[47] and take into account the deformations associated with strain penetration (bond slip) into the member end

anchorages. Based on calibration of tests of reinforced concrete columns, Haselton et al.[59] proposed a general equation to account for member axial load, concrete compressive strength, and aspect ratio, resulting in flexural rigidity ranging from $0.2E_cI_g$ to $0.6E_cI_g$, with shear rigidity of $0.4E_cA_w$.

ATC-72[28] makes reference to several design codes [5,15,84] for estimates of the secant stiffness to the yield point of coupling beams. ACI 318-08[5] prescribes effective flexural rigidity of $0.35E_cI_g$, while ASCE/SEI 41-06[15] prescribes $0.5E_cI_g$, later modified to $0.3E_cI_g$ in its supplement No. 1[15]. The effective flexural rigidity given in ACI 318 and ASCE 41 apply to coupling beams with conventional or diagonal reinforcement layouts. The effective flexural rigidity in the New Zealand Standard NZS 3101:1995[84] is defined based on the layout of the longitudinal reinforcement (conventional or diagonal), the expected ductility demand, and the aspect ratio of the beam. For a low ductility demand of 1.25, the effective flexural rigidity calculated using NZS 3101:1995 ranges from $0.34E_cI_g$ to $0.56E_cI_g$ for aspect ratios from 1 to 4. For a high ductility demand of 6, it ranges from $0.09E_cI_g$ to $0.21E_cI_g$ for aspect ratios from 1 to 4.

The 2017 Tall Buildings Initiative Guidelines for Performance-Based Seismic Design of Tall Buildings[93] recommends calculating the effective flexural rigidity of coupling beams with conventional or diagonal reinforcement layouts as the minimum of either $0.07(l_n/h)E_cI_g$ or $0.3E_cI_g$ and shear rigidity is calculated as $0.4E_cA_g$. These recommendations were based on the work of Naish[82], Vu et al.[114], and Motter et al.[78].

2.5 ACI Building Code Design Requirements

The ACI Building Code (ACI 318-14)[6] has three sets of requirements for designing coupling beams that are dependent on nominal shear stress and aspect ratio: 1) coupling beams

with aspect ratios of 4.0 or higher must be designed with special moment frame detailing; 2) coupling beams with aspect ratios of 2.0 or less and factored shear force exceeding $4\sqrt{f_c'}b_w h$ psi ($0.33\sqrt{f_c'}b_w h$ MPa) must be designed with diagonal reinforcement; and 3) coupling beams with intermediate aspect ratios, between 2.0 and 4.0, may be designed with diagonal reinforcement or with special moment frame detailing. These requirements are intended to ensure ductile behavior of the coupling beam by recognizing the increased dominance of flexural actions and reduced effectiveness of diagonal reinforcement in beams with higher aspect ratios.

Added to the ACI Building Code in 1999[3], diagonal reinforcement has become a commonly selected reinforcement layout for coupling beams because it results in superior deformation capacity. According to the ACI Building Code, the diagonal bars are required to resist the entire shear and assumed to provide sufficient flexural strength. The nominal shear strength is calculated using ACI 318-14 Section 18.10.7.4(a)[6], $V_n = 2A_{vd}f_y \sin\alpha \leq 10\sqrt{f_c', \text{psi}}\, b_w h$ ($0.83\sqrt{f_c', \text{MPa}}\, b_w h$) where A_{vd} is the area of reinforcement in each group of diagonal bars, f_y is the specified yield stress, and α is the angle of inclination of the bars with respect to the longitudinal axis of the beam. The value of V_n is limited to a maximum shear force of $10\sqrt{f_c', \text{psi}}\, b_w h$ ($0.83\sqrt{f_c', \text{MPa}}\, b_w h$), based on test results[31] that demonstrated adequate ductility at shear forces near that level in diagonally-reinforced coupling beams. The ACI Building Code[6] requires that each group of diagonal bars consists of at least four bars in two or more layers and that they be placed in a rectangular arrangement. Bar groups must also be symmetric and every diagonal reinforcing bar must have sufficient embedment length to develop $1.25f_y$ in tension at the beam-wall interface.

The amount of conventional grade diagonal bars required to withstand high shear stresses, approaching $10\sqrt{f_c'}$ psi ($0.83\sqrt{f_c'}$ MPa), leads to reinforcement congestion and construction difficulties in diagonally-reinforced coupling beams with aspect ratios exceeding 2.0. Harries et al.[58] presented a review of ACI 318-05[4] code-compliant diagonally-reinforced coupling beams with aspect ratios of 1, 2, 3, and 4, concrete compressive strengths of 5,000 and 8,000 psi (34 and 55 MPa), and nominal shear stresses of approximately 6, 10, and $14\sqrt{f_c'}$ psi (0.5, 0.83, and $1.17\sqrt{f_c'}$ MPa). Many of the hypothetical coupling beams with high shear stresses and high aspect ratios were impractical to construct.

Increasing the maximum permissible specified yield stress of reinforcement from 60 ksi (420 MPa) offers a way to alleviate reinforcement congestion and construction costs by reducing the quantity of reinforcing bars. Alternatively, diagonally-reinforced coupling beams, which can resist shear stresses in excess of $10\sqrt{f_c'}$ psi ($0.83\sqrt{f_c'}$ MPa), is feasible with high-strength reinforcement[12]. The ACI Building Code[6] limits the nominal yield stress of longitudinal reinforcement in seismic applications to 60 ksi (420 MPa) due to insufficient experimental data. However, recent experimental work, discussed in Section 2.2: Effect of High-Strength Steel Reinforcement, indicates that structural members reinforced with high-strength reinforcement exhibit adequate deformation capacities when subjected to inelastic cyclic loading.

The ACI Building Codes from 1999[3] (the introduction of diagonally-reinforced coupling beams in ACI 318) to 2005[4] required separate confinement around each group of diagonal bars to confine concrete in the compression strut and delay buckling of the diagonal bars. This requirement remained unchanged until ACI 318-08[5] added the option to confine the entire cross-section. The alternative of full-section confinement simplified construction and was shown

by Naish et al.[80,81] to provide slightly improved behavior compared with confinement of each group of diagonal bars. The improved behavior associated with full-section confinement was further supported by the findings of Lim et al.[69].

The ACI Building Code[6] recommends terminating all secondary longitudinal reinforcement with a short embedment into the walls so it will not increase the flexural strength of the coupling beam. This is intended to avoid higher than expected shear demands on the coupling beam. Relatively few studies have been conducted that directly compare the effects of developed versus non-developed secondary longitudinal reinforcement. Non-developed (cutoff) secondary longitudinal reinforcement have been associated with damage localized at the beam-wall interface[68,80]. Concentration of deformations at the beam-wall interface are less pronounced by developing the secondary reinforcement[13,65].

The test program of the present study was conducted starting in the fall of 2014 and ended in the summer of 2018. For this reason, most references to ACI 318 point to ACI 318-14[6]. Design provisions in ACI 318-19[7] for coupling beams (Section 18.10.7) are identical to those in ACI 318-14 except that Section 20.2.2.4 in ACI 318-19 allows the use of f_y up to 100 ksi (690 MPa) in longitudinal and transverse reinforcement of coupling beams. Transverse reinforcement spacing is limited to a maximum spacing of 6, 5, and $4d_b$ of the smallest diagonal bars Grades 60, 80, and 100 (420, 550, and 690), respectively.

CHAPTER 3: EXPERIMENTAL PROGRAM

3.1 Specimens

3.1.1 Design and Detailing

Eleven large-scale coupling beam specimens were subjected to pseudo-static cyclic displacements of increasing magnitude. Details of the specimens are listed in Table 1 and shown in Figures 1 through 23. The approximately ½-scale specimens had nominally the same beam cross section, with a height (h) of 18 in. (460 mm) and a width (b_w) of 12 in. (310 mm); clear span lengths (ℓ_n) of 27, 45, or 63 in. (690, 1140, or 1600 mm), resulting in aspect ratios (ℓ_n/h) of 1.5, 2.5, or 3.5 (which are similar to the range of aspect ratios commonly used in practice); either Grade 80, 100, or 120 (550, 690, or 830) reinforcing bars; and either diagonal (D-type) or special moment frame (P-type) reinforcement.

Each specimen consisted of a coupling beam that framed into top and bottom blocks. The end blocks had dense reinforcement cages near the connection with the coupling beam to emulate structural wall boundary elements. The coupling beams were tested rotated 90 degrees from the horizontal for convenience. All reinforcement in the end blocks was Grade 60 (420) except for the coupling beam reinforcement embedded into the end blocks.

Specimens, such as D120-3.5 or P80-2.5, were named using the following rules: the first letter indicates whether it has diagonal (D) or parallel (P) primary longitudinal reinforcement (see Figure 1), followed by a number that represents the reinforcement grade (in ksi), and the last number (separated by a dash) indicates the coupling beam aspect ratio (clear span-to-overall height ratio, ℓ_n/h).

One D-type coupling beam was constructed for each combination of aspect ratio (1.5, 2.5, or 3.5) and diagonal bar grade (Grade 80, 100, or 120 [550, 690, or 830]), for a total of nine specimens with D-type reinforcement layout. D-type specimens were designed to have a nominal shear stress of approximately $8\sqrt{f_c'}$ psi ($0.67\sqrt{f_c'}$ MPa) based on f_c' of 8,000 psi (55 MPa). The targeted shear stress is near the maximum design stress of $10\sqrt{f_c'}$ psi ($0.71\sqrt{f_c'}$ MPa) permitted by the ACI Building Code[6] for diagonally-reinforced coupling beams. Beam shear strength (V_n) was calculated using ACI 318-14 Section 18.10.7.4(a)[6] (shown in Equation 3.1) with nominal f_y:

$$V_n = 2A_{vd} f_y \sin\alpha \qquad \text{Equation 3.1}$$

The product of yield stress and reinforcement ratio, ρf_y, was approximately constant for a given beam aspect ratio so the amount of diagonal reinforcement was inversely proportional to its yield stress. Transverse reinforcement was provided in accordance with ACI 318-14 Section 18.10.7.4(d)[6] using Equation 3.2, see below for additional details. The transverse reinforcement was Grade 80 (550) for all beams except D120-2.5, which had Grade 120 (830) transverse reinforcement.

Two P-type coupling beams were constructed with an aspect ratio of 2.5 and either Grade 80 or 100 (550 or 690) longitudinal reinforcement. The target shear stress for the P-type beams was approximately $6\sqrt{f_c'}$ psi ($0.5\sqrt{f_c'}$ MPa). This shear stress was based on the beam reaching its probable flexural strength at both ends. Probable flexural strength was calculated using a rectangular stress block for concrete in compression with f_c' of 8,000 psi (55 MPa), linear strain distribution, and elasto-plastic stress-strain behavior for the reinforcement with a maximum stress of $1.25f_y$ in the longitudinal tension reinforcement. The maximum design shear stress permitted

by the Code for beams with special moment frame reinforcement is $6\sqrt{f_c'}$ psi ($0.5\sqrt{f_c'}$ MPa). Transverse reinforcement was provided such that 0.75 times the nominal shear strength of a P-type coupling beam exceeded the shear demand associated with probable flexural strength at both ends of the beam. All of the shear strength was based on strength attributed to the transverse reinforcement, with zero strength attributed to the concrete.

The coupling beams described in Table 1 are similar to those tested by Naish et al.[81], which included diagonally-reinforced beams with aspect ratios of 2.4 and 3.3, Grade 60 (420) reinforcement, and confinement for the entire beam cross section. The similarities between the beams allow the use of those tested by Naish et al.[81] as control beams with Grade 60 (420) reinforcement; the scope of this study was therefore focused on beams with higher-grade reinforcement. However, there were some differences in the designs that caused the beams in this study to be subjected to more demanding conditions. First, the design shear stresses for D-type beams in this study were 10% to 70% higher than the design shear stresses used by Naish et al.[81], where nominal shear stresses of $7.3\sqrt{f_c'}$ psi ($0.61\sqrt{f_c'}$ MPa) and $4.8\sqrt{f_c'}$ psi ($0.40\sqrt{f_c'}$ MPa) were used for diagonally-reinforced beams with aspect ratios of 2.4 and 3.3, respectively; and second, the volumetric ratios of transverse reinforcement for D-type beams in this study were approximately 20% lower (but still compliant with the ACI Building Code[6]) than those used by Naish et al.[81] Regarding the P-type beams, the amount of primary longitudinal and transverse reinforcement in this study was similar to the one beam tested by Naish et al.[81], except for the amount of secondary longitudinal reinforcement placed near beam mid-depth, which was $0.003b_w h$ for Naish et al.[81] and zero for this study.

The specimens in this study are also similar to those described in Ameen et al[12] and Poudel et al.[94], which included diagonally-reinforced coupling beams with an aspect ratio of 1.9, Grades 60 and 120 (420 and 830) reinforcement, full-section confinement, and several coupling beams with developed secondary longitudinal reinforcement. However, the design shear stresses in Ameen et al.[12] and Poudel et al.[94] were purposely in the range of 10 to $14\sqrt{f_c'}$ psi (0.83 to $1.2\sqrt{f_c'}$ MPa), approximately 20% to 80% higher than the design shear stresses of the D-type beams in this study. Another difference was that coupling beams in this study were free to elongate axially whereas some of the beams tested by Ameen et al.[12] and Poudel et al.[94] were restrained axially. This may have caused those beams to exhibit higher strengths and lower chord rotation capacities. The beam depths in these studies were 18 in. (460 mm) but the beam width in these studies[12,94] was 10 in. (250 mm) rather than the 12 in. (310 mm) used in this study. The 20% increase in width was not expected to affect results and allowed more options when selecting transverse reinforcement for concrete confinement.

The coupling beams had No. 6 (19) or No. 7 (22) Grade 80, 100, or 120 (550, 690, or 830) steel bars as primary longitudinal reinforcement. D-type specimens were constructed with two groups of diagonal reinforcing bars intersecting near midspan of the coupling beam with an angle of inclination between 10 and 23 degrees depending on the aspect ratio. P-type specimens were constructed with parallel longitudinal reinforcing bars, three bars near each of the extreme fibers of the beam cross section. The design data in Table 1 include the quantity and minimum straight embedment length (ℓ_e) of the primary longitudinal reinforcement of the coupling beams into the top and bottom blocks. The dimensions of the specimens are shown in Figures 2 through 23.

Transverse reinforcement, in the form of closed hoops and crossties oriented parallel to both strong and weak axes, was used in all D-type beams to provide full-section confinement. For D-type beams, the transverse reinforcement was not considered when calculating the shear strength in accordance with ACI 318-14 Section 18.10.7.4(a)[6] (shown in Equation 3.1). Instead, it met the requirements of ACI 318-14 Section 18.10.7.4(d)[6] (shown in Equation 3.2). All D-type beams had No. 3 (10) Grade 80 (550) transverse reinforcement except D120-2.5, where No. 3 (10) Grade 120 (830) was used. Each layer of transverse reinforcement in D-type beams consisted of a closed hoop with seismic hooks (135 degrees), one crosstie along the beam depth, and two crossties along the beam width. All crossties had one end with a 135 degree hook and the other with a 90 degree hook, as permitted by ACI 318-14[6]. Beam cross sections for the D-type beams are shown in Figures 2 through 19. The longitudinal spacing of each layer of transverse reinforcement in the D-type beams was 3 in. (76 mm). For both transverse directions of the cross-sectional area of D-type beams, the amount of transverse reinforcement provided closely matched the amount required ACI 318-14 Section 18.10.7.4(d)[6]:

$$A_{sh} \geq \quad [0.09\ s\ b_c\ f_c'/f_{yt}\ ;\ \ 0.3\ s\ b_c \left(\frac{A_g}{A_{ch}} - 1\right) f_c'/f_{yt}] \qquad \text{Equation 3.2}$$

Beam cross sections for P-type beams are shown in Figures 21 and 23, where the transverse reinforcement was designed such that 0.75 times the nominal shear strength (V_n) exceeded the shear force associated with the probable flexural strength ($V_e = v_e b_w d$) acting at both ends of the beam ($0.75V_n \geq V_e$). The shear strength attributed to the concrete was zero. The provided spacing of transverse reinforcement for P80-2.5 and P100-2.5 was 3.5 in. (89 mm) and 3 in. (76 mm), respectively, which satisfied ACI 318-14 Section 18.6.4.4[6].

Following recommendations by NIST GCR 14-917-30[83], the maximum spacing of transverse reinforcement for both D-type and P-type beams was limited to $5d_b$ for beams with Grade 80 (550) longitudinal reinforcement and $4d_b$ for beams with Grade 100 or 120 (690 or 830) longitudinal reinforcement.

D-type specimens had ten secondary longitudinal No. 3 (10) bars distributed around the perimeter of the beam such that each secondary longitudinal bar was supported by either a crosstie or a corner of a hoop. These bars were Grade 80 (550) for all specimens except for D120-2.5, where all transverse and longitudinal reinforcement were Grade 120 (830). Consistent with the detailing recommended in the ACI Building Code[6] commentary, the secondary longitudinal reinforcement was terminated 2 in. (51 mm) into the top and bottom blocks for all specimens except D120-2.5. The No. 3 (10) longitudinal bars in D120-2.5 were extended into the end blocks a length sufficient to develop a stress of $1.25f_y$. This deviation, along with the Grade 120 (830) transverse reinforcement, was done to explore whether developing the secondary longitudinal reinforcement and providing excess transverse reinforcement (by means of higher f_{yt}) would cause improved deformation capacity by inhibiting the concentration of damage at the interfaces between the beam and end blocks.

3.1.2 Materials

3.1.2.1 Concrete

Ready-mix concrete with a maximum aggregate size of 0.5 in. (13 mm), provided by a local supplier, was used to cast the specimens. The specified compressive strength (f'_c) was 8,000 psi (55 MPa). The measured compressive and tensile strengths of concrete (f_{cm} and f_{ct} in Table 2) were obtained from tests of 6 by 12 in. (150 by 300 mm) standard concrete cylinders

following ASTM C39[23] and C496[25]. Slump of the plastic concrete was obtained in accordance with ASTM C143[21]. Slump measurements and concrete mixture proportions are shown in Table 3.

3.1.2.2 Reinforcing Steel

Deformed steel reinforcing bars were used for all reinforcement. Mill certifications for reinforcing bars used as Grade 80 and 100 (550 and 690) showed compliance with ASTM A615[19] Grades 80 and 100 (550 and 690). Mill certifications for reinforcing bars used as Grade 120 (830) showed compliance with ASTM A1035[17] Grade 120 (830). Mechanical properties of reinforcing bars (Table 4) used in the beams were obtained from tensile tests in accordance with ASTM A370[18]. Figure 24 shows sample tensile test results of the six types of reinforcing bars used in the coupling beams.

Reinforcement used to construct the top and bottom blocks was Grade 60 (420) and complied with ASTM A615[19] Grade 60 (420).

3.1.3 Construction

Photos taken during various stages of specimen construction are shown in Figures B.1 through B.8 of Appendix B. The specimens were cast monolithically with formwork for the top and bottom blocks lying flat on the laboratory floor. The coupling beam concrete was supported with elevated wood formwork because the width of the beam was narrower than the width of the end blocks. Construction of each specimen included the assembly of reinforcing bar cages, installation of strain gauges on selected reinforcing bars, assembly of wooden formwork, and placement of the concrete. After casting, specimens and cylinders were covered with wet burlap

and plastic sheets until formwork removal three to five days after casting. Specimens were kept in a climate-controlled laboratory from casting to testing.

3.2 Test Setup

The test setup is shown in Figures 25 through 27. The bottom block of each specimen was bolted to the laboratory strong floor with two unbonded 2.5-in. (64-mm) diameter high-strength threaded rods passing through the bottom block and the 36-in. (914-mm) thick strong floor. Two hydraulic actuators acting in parallel were used to load the specimens. The actuators each have a stroke length of 40 in. (1020 mm) and a force capacity of 220 kips (980 kN). The two actuators were connected to the strong wall and the specimen by means of vertically oriented HP steel sections. Actuator elevations are indicated in Table 5 and illustrated in Figures 28 through 30. One of the HP sections was connected to the top block of the specimen with two hollow structural steel (HSS) sections (acting as a spacer) transmitting compression when the actuators pushed the specimen and six unbonded 2.25-in. (57-mm) diameter high-strength threaded rods transmitting tension when the actuators pulled the specimen. Additional steel fixtures were used to externally brace the HP section against out-of-plane motions. Mirrored steel (attached to the HP section), nylon pads (attached to the external bracing system), and white lithium grease (between the mirrored steel and nylon pads) were used to minimize friction between the HP section and the external bracing.

3.3 Instrumentation

Several instruments were used to record specimen response during the tests: one linear variable differential transformer (LVDT) and load cell integral to each actuator; two LVDTs attached to the top block; an infrared non-contact position measurement system; and strain gauges

attached to reinforcing bars. Actuator load cell data were used to report the applied shear throughout the tests. LVDT data are not reported because they are redundant with data from the infrared position measurement system.

3.3.1 Linear Variable Differential Transformers

Movement of the top block was recorded with two LVDTs (Figure 31). The data were used to validate the measurements made with the infrared position measurement system. These LVDTs were attached to the top block face opposite to the actuators, horizontally centered with respect to the thickness of the top block. They were located approximately 24 and 36 in. (610 and 910 mm) above the bottom of the top block.

3.3.2 Infrared Non-Contact Position Measurement System

The motion capture system recorded the positions of optical markers attached to the surface of each specimen (63, 83, or 94 markers for beams with aspect ratios of 1.5, 2.5 or 3.5) and three optical markers attached to a rigid stand on the laboratory floor. The markers emit infrared light pulses that are detected by the infrared camera system. The spatial coordinates of the markers were triangulated and recorded throughout the tests. The markers were arranged in a 4-in. (100-mm) square grid over one face of the coupling beam and part of the top and bottom blocks, as shown in Figure 32.

Figure 33 identifies the row, column, and layer of markers. Horizontal rows were numbered from -1 to n_r+2 (top to bottom) as each aspect ratio of beam had a different number of rows of markers, n_r. Rows -1 and n_r+2 were only used to verify data from neighboring rows 0 and n_r+1 and were not present in beams with an aspect ratio of 3.5. Vertical columns of markers

were numbered from 0 to 6 (right to left as viewed from laboratory north, see Figure 27). The grid of optical markers was divided into "layers" of four markers in two adjacent rows, arranged in a rectangle bounded by the two extreme columns of markers. Layers were numbered from the top to the bottom of the beam, based on the lower row number bounding the layer. The grid of optical markers was also divided into "stations" of four adjacent markers, arranged in a 4-in. (100-mm) square (as shown in the shaded area of Figure 33).

3.3.3 Strain Gauges

Several 120-ohm electrical resistance strain gauges were applied to selected reinforcing bars prior to casting. D-type specimens were instrumented with at least 31 strain gauges and P-type specimens with at least 22. Figures 34 and 35 generically show locations where a strain gauge was used in at least one specimen. Tables 6 and 7 indicate the strain gauge locations for each specimen and identify gauges that malfunctioned. Strain gauges on diagonal reinforcement (D in D-type beams) and developed longitudinal reinforcement (P in P-type beams and H in D120-2.5) were rated for 15% strain (150 millistrain) to allow strain measurements near fracture elongation of reinforcement. The remaining strain gauges were rated for 5% strain (50 millistrain).

3.4 Loading Protocol

Specimens were subjected to a series of reversed cyclic displacements following the protocol described in Table 8 and shown in Figure 36, patterned after the protocol recommended in FEMA 461[48]. Several small cycles were imposed prior to testing (without exceeding 10% of V_{nm}) to facilitate tightening of the threaded rods connecting the bottom block to the strong floor and the top block to the actuators. Force-based control was used for the first few cycles of loading. Displacement-based control was used starting at 0.5% chord rotation for beams with aspect ratios

of 1.5 and 2.5. A chord rotation of 0.75% was used for beams with an aspect ratio of 3.5. Testing continued until the beam residual strength was nearly 20% of the peak strength, provided instability was not a concern.

The weight of all fixtures (HP sections, spacer sections, steel plates, and actuators) eccentrically attached to the specimen (Figure 25) caused a permanent moment of approximately 42 ft-kips (57 m-kN) prior to loading. At the start of the test, an equal and opposite moment was applied using the actuators.

Forces or displacements assigned to each actuator were adjusted throughout the test to minimize the relative rotation between top and bottom blocks (i.e., the difference between the top block rotation and the bottom block rotation). This was done to ensure that double-curvature was imposed on the coupling beam, resulting in an inflection point near beam midspan. The loading rates are given in Table 8 for coupling beams with aspect ratios of 1.5 and 2.5; coupling beams with an aspect ratio of 3.5 were tested at twice the given rates.

CHAPTER 4: EXPERIMENTAL RESULTS

4.1 Measured Shear versus Chord Rotation

Chord rotation (CR) of the coupling beam is defined as the displacement of the top block relative to the bottom block divided by the beam clear span and corrected for the average rotation of the top and bottom blocks:

$$CR = \frac{\delta_{top} - \delta_{bot}}{l_n} - \frac{\theta_{top} + \theta_{bot}}{2} \qquad \text{Equation 4.1}$$

Figure 37 shows the generalized deformed shape of a coupling beam with displacement and rotational components identified. The chord rotation represents the average of the relative rotation at each end of the coupling beam. Figure 37 corresponds to a specimen elevation view from laboratory north with the top block displacement (δ_{top}) and bottom block displacement (δ_{bot}) positive when moving eastward (away from the laboratory strong wall). Figure 37 also shows positive top block rotation (θ_{top}) and bottom block rotation (θ_{bot}) as counterclockwise rotation when viewed from laboratory north.

Displacements and rotations were calculated from measurements obtained with the infrared non-contact position measurement system (Section 3.3.2) and checked with data from redundant LVDTs (Section 3.3.1). The infrared markers were offset from the edges of the top and bottom blocks by approximately 2.5 in. (64 mm) to reduce the probability of losing a marker early in the test (due to concrete spalling) near the beam-block interface. This offset was accounted for when evaluating Equation 4.1.

4.2 Specimen Response and Observations

The eleven specimens described in Chapter 3 were subjected to the loading protocol discussed in Section 3.4. Table 9 summarizes the deformation capacity and maximum applied shear for each coupling beam. The maximum applied shear is also shown in terms of stress normalized by the square root of the concrete compressive strength at the time of testing (f_{cm} in Table 2). General observations during testing of each specimen are summarized in Sections 4.2.1 through 4.2.11.

The measured force-deformation relationships for each coupling beam are plotted in Figures 38 through 48 in terms of shear versus chord rotation and discussed in this chapter. A shear-chord rotation envelope for each coupling beam was developed in accordance with ASCE 41-17[16] Section 7.6.3 (item 1.1) by connecting the maximum displacement of the first cycle of each loading step. The envelopes thus generated were superimposed on the measured shear-chord rotation data in Figures 49 through 59. Coordinates of the breakpoints for the envelopes are listed in Tables 11 through 14.

Two definitions were used herein for deformation capacity or chord rotation capacity in Table 9. The first, called Deformation Capacity A, was defined as the average of the maximum chord rotations reached in each loading direction while sustaining 80% of the maximum applied shear in each loading direction. The second, called Deformation Capacity B, was defined as the average of the maximum chord rotations in each loading direction where the envelope of the shear versus chord rotation curve (formed by connecting the maximum chord rotation of the first cycle of each loading step) intersects with 80% of the maximum applied shear in each loading direction.

Both definitions of chord rotation capacity are provided because the distinctions may appeal to designers and researchers differently. Deformation Capacity A is a more stringent appraisal of chord rotation capacity and represents chord rotations the coupling beam was actually subjected to. Deformation Capacity B, which is based on an envelope drawn according to ASCE 41-17[16], is based on the assumption that force-deformation relationships are represented by linear interpolations between measured values. Deformation Capacity B is less sensitive to loading protocol than Deformation Capacity A and is also always greater than or equal to Deformation Capacity A. Deformation capacity in this report refers to Deformation Capacity B unless otherwise noted.

The deformation capacity of each D-type beam is shown in Figure 60, organized by aspect ratio (ℓ_n/h) and measured yield stress (f_{ym}) of the diagonal reinforcement. Deformation capacity for D-type beams is positively correlated to aspect ratio and negatively correlated to the yield stress of the diagonal reinforcement for the nine D-type beams considered. The deformation capacity of D120-2.5 deviates from the trend shown by the beams with aspect ratios of 2.5. This may be attributable to the higher $\rho_t f_{yt}$ provided throughout the beam span and/or developing (for $1.25f_y$) the secondary longitudinal reinforcement into the end blocks, which helped distribute the damage away from the beam-block interfaces.

4.2.1 D80-1.5

Measured shear force is plotted versus chord rotation in Figure 38 for D80-1.5. The coupling beam completed both cycles to 6% chord rotation (Step 10 of the loading protocol in Table 8) before strength notably diminished. The second excursion to -6% reached a shear of approximately 80% of the strength after at least one bar fractured. This resulted in a deformation

capacity of 6.9% (as reported in Table 9). One cycle to 8% chord rotation (Step 11 in Table 8) was completed before the test was terminated. Strength loss was initiated by buckling of diagonal bars, which fractured in subsequent loading cycles.

4.2.2 D100-1.5

Measured shear force is plotted versus chord rotation in Figure 39 for D100-1.5. This coupling beam completed both cycles to 4% chord rotation (Step 9) before multiple bar fractures occurred during the first cycle to 6% and strength diminished rapidly. This resulted in a deformation capacity of 5.3% (as reported in Table 9). One excursion to +8% chord rotation (Step 11) was attempted but aborted at approximately +6.1% due to stability concerns from the numerous bar fractures during the previous loading cycle. Strength loss was initiated by buckling of the diagonal bars followed by bar fractures in subsequent cycles.

4.2.3 D120-1.5

Measured shear force is plotted versus chord rotation in Figure 40 for D120-1.5. The coupling beam completed both cycles to 3% chord rotation (Step 8) and the first excursion to 4%. However, a deviation from the testing protocol occurred during the first excursion to -4% (Step 9). The deviation was due to operator error in reading instrumentation data. The coupling beam was displaced through -4.9% before fracturing all reinforcing bars in one group of diagonal bars near the top end of the beam. The sudden bar fractures caused a large increase in top block rotation, resulting in a large increase in chord rotation to -8.1%. There was no prior evidence of bar buckling or fracture. The test resumed with cycles to 4% and 6% chord rotations (Steps 9 and 10). The deformation capacity was 5.2% based on the definition of Deformation Capacity B (as reported in Table 9).

Reinforcing bar fractures near -5% suggest that the beam would not have completed Step 10 if the deviation from the loading protocol had not occurred. Failure was imminent regardless of the testing protocol, most likely due to the relatively low value of uniform elongation of the Grade 120 (830) diagonal bars, ε_{su} = 5.2%. It was observed after testing that all four reinforcing bars in one of the diagonal-bar groups had fractured near the top of the coupling beam.

4.2.4 D80-2.5

Measured shear force is plotted versus chord rotation in Figure 41 for D80-2.5. The coupling beam completed two cycles to 6% chord rotation (Step 10) and half of a cycle to 8% chord rotation before strength diminished by more than 20%. This resulted in a deformation capacity of 7.6% (as reported in Table 9). One cycle to 10% chord rotation (Step 12) was completed before the test was terminated. Strength loss was due to fracture of diagonal bars near the ends of the coupling beam (during first excursion to a chord rotation of -8%) after they were observed to have buckled in the prior half cycle.

4.2.5 D100-2.5

Measured shear force is plotted versus chord rotation for D100-2.5 in Figure 42. The coupling beam reached chord rotations of -4.7%[a] and +6% in each loading direction before a 20% loss of strength, resulting in a deformation capacity of 6% (as reported in Table 9). Loading continued until nearly two cycles at 8% chord rotation (Step 11) were completed. Strength loss was caused by fracture of one set of diagonal bars near the top end of the coupling beam (during

[a] A chord rotation of 4% was targeted.

the first excursion to a chord rotation of -6%) after they were observed to have buckled in the prior half cycle.

4.2.6 D120-2.5

Measured shear force is plotted versus chord rotation for D120-2.5 in Figure 43. The deformation capacity of the coupling beam was 6.9% (as reported in Table 9). Beam strength began to diminish in the first cycle to 6% with bar fractures occurring during the first excursion to +6%. Loading continued until completion of two cycles to 8% (Step 11). Strength loss was associated with hoop opening and bar buckling followed by bar fracture in both diagonal groups near the bottom end of the coupling beam. Several longitudinal No. 3 bars also fractured. D120-2.5 had longitudinal No. 3 bars extended into the end blocks for a length sufficient to develop 1.25 times the specified yield stress of the bar at the face of the end blocks. This may have contributed to achieving a maximum shear stress of $15\sqrt{f_c'}$ psi ($1.25\sqrt{f_c'}$ MPa). For other D-type beams, maximum shear stress ranged between 10 and $14\sqrt{f_c'}$ psi (0.83 and $1.17\sqrt{f_c'}$ MPa) (see Table 9).

4.2.7 D80-3.5

Measured shear force is plotted versus chord rotation in Figure 44 for D80-3.5. The coupling beam completed one cycle to 8% chord rotation (Step 11). Bar fracture was observed during the first excursion to -8% resulting in a strength loss of nearly 20%. This resulted in a deformation capacity of 8.6% (as reported in Table 9). Testing continued through one cycle of 10% (Step 12). A second excursion to +10% chord rotation was attempted but aborted due to numerous bar fractures. Strength loss was due to buckling of diagonal bars (during first cycle to a chord rotation of 8%) followed by fracture of diagonal bars near the ends of the coupling beam.

4.2.8 D100-3.5

Measured shear force is plotted versus chord rotation in Figure 45 for D100-3.5. The coupling beam completed one cycle to 6% chord rotation (Step 10). During the second excursion to +6%, bar fractures caused a strength loss of nearly 20%. This resulted in a deformation capacity of 6.8% (as reported in Table 9). Testing continued through one cycle of 10% (Step 12). Fractures of diagonal bars near the ends of the coupling beam occurred during the second excursion to +6% after they were observed to have buckled during the first cycle to 6%. Large out-of-plane single-curvature deformations (2.7% of the beam clear span) occurred during the second cycle to 6% chord rotation (due to an excessive initial gap with the out-of-plane bracing system).

4.2.9 D120-3.5

Measured shear force is plotted versus chord rotation in Figure 46 for D120-3.5. The coupling beam completed one cycle to 6% chord rotation (Step 10) with bar fractures occurring during the first excursion to -6% with a strength loss of nearly 20%. This resulted in a deformation capacity of 6.7% (as reported in Table 9). Testing continued through two cycles of 8% (Step 11). Strength loss was due to buckling (during the first cycle to 6%) followed by fracture of diagonal bars near the ends of the coupling beam (during the second cycle to 6%).

Continuous data from the position tracking marker system are unavailable after the second 3% cycle (end of Step 8) due to a recording error of the primary data acquisition system. However, shear-chord rotation coordinates were also recorded each time the test was paused with a separate secondary recording system that used optical character recognition to capture in real-time the display of the primary data acquisition system. These discrete data are shown in Figure 46 as hollow points connected with dotted lines.

4.2.10 P80-2.5

Test results are plotted for P80-2.5 in terms of measured shear force versus chord rotation in Figure 47. The deformation capacity of the coupling beam was 3.9% (as reported in Table 9). Although strength began to diminish during the second cycle to a chord rotation of 3%, the first excursion to +4% reached a shear that was greater than 80% of the strength in the positive loading direction. Loading continued until cycles targeting 6% chord rotation (Step 10) were completed. Bar fracture was not observed during the test. Strength loss was due to shear strength decay, with damage concentrated near the ends of the coupling beam.

4.2.11 P100-2.5

Test results are plotted for P100-2.5 in terms of measured shear force versus chord rotation in Figure 48. The chord rotation capacity of the coupling beam was 4.1% (as reported in Table 9). The first cycle to 3% was the last cycle to exceed 80% of the strength in the positive loading direction. The second excursion to a chord rotation of -3% reached a shear nearly equal to 80% of the strength in the negative loading direction, while the first excursion to -4% exceeded the 80% threshold. Loading continued until two cycles to 6% chord rotation (Step 10) had been completed. Bar fracture was not observed during the test. Strength loss was due to shear strength decay associated with damage near the ends of the coupling beam.

4.3 ASCE 41 Envelopes

Figures 61 through 65 show the shear-chord rotation envelopes of the tested beams grouped by aspect ratio (ℓ_n/h of 1.5, 2.5, or 3.5) and reinforcement layout (D- or P-type beams). The plots also include the generalized force-deformation curve for modeling coupling beams as defined in

ASCE 41-17 Table 10-19[16]. The coordinates of points A through E are based on Figure 10-1(b) [16] (shown in Figure 66), which depend on parameters *c*, *d*, and *e* in Table 10-19[16]. For D-type beams, Table 10-19[16] gives $c = 0.8$, $d = 0.03$, and $e = 0.05$. For P-type beams with conforming transverse reinforcement and shear stresses greater than or equal to $6\sqrt{f_c'}\, b_w d$ psi ($0.5\sqrt{f_c'}\, b_w d$ MPa), Table 10-19[16] gives $c = 0.5$, $d = 0.02$, and $e = 0.04$. Parameters *c*, *d*, and *e* correspond, respectively, to the residual strength ratio (or shear at points D and E in relation to point B); the deformation at peak force (or chord rotation at point C); and the maximum deformation before total loss of strength (or chord rotation at point E). In ASCE 41-17[16], point B is generally associated with the calculated member strength based on the measured yield strength of reinforcement f_{ym}, whereas point C is generally based on $1.25 f_{ym}$.

For D-type beams, the ordinate of point B in Figures 61 through 63 was determined based on the target design shear stress of $8\sqrt{f_c'}$ psi ($0.67\sqrt{f_c'}$ MPa), as indicated by the average v_e in Table 1, and the ordinate of point C was based on $10\sqrt{f_c'}$ psi ($0.83\sqrt{f_c'}\ MPa$), or 5/4 of the ordinate of point B.

For P-type beams, the ordinate of point C in Figure 64 was determined based on the target design shear stress of $6\sqrt{f_c'}$ psi ($0.5\sqrt{f_c'}\ MPa$), as indicated by v_e in Table 1, and the ordinate of point B was based on $4.8\sqrt{f_c'}$ psi ($0.40\sqrt{f_c'}$ MPa), or 4/5 of the ordinate of point C.

The slope from points A to B (initial stiffness) was calculated based on ASCE 41-17 Table 10-5[16] using a flexural rigidity of $E_c I_{eff}$, where $I_{eff} = 0.3 I_g$, and a shear rigidity of $G_c A_{eff}$, where $A_{eff} = 1.0 A_w$. The initial slope of the shear versus chord rotation curve (in units of force/rad) is given by

$$K = \left(\frac{l_n^2}{12E_cI_{eff}} + \frac{1}{G_cA_{eff}}\right)^{-1}$$ Equation 4.2

Figures 61 through 64 show Point B was not enclosed by the envelopes of any of the coupling beams, which indicates that the calculated stiffness based on ASCE 41-17[16] was greater than the measured stiffness. Beam stiffness is discussed in more detail in Section 4.6.

Figures 61 through 64 show that envelopes from the measured test data of each coupling beam exceeded the chord rotation capacity (defined by point E) that ASCE 41-17[16] assigns to coupling beams that are compliant with ACI 318-14[6].

Figure 64 shows that the shear strength exhibited by P100-2.5 was greater than the shear force at point C though the shear strength of P80-2.5 was not. This can be attributed to the different design strengths of the P-type beams. The design shear stresses of P80-2.5 and P100-2.5 were 5.2 and $6.4\sqrt{f_c'}$ psi (0.43 and $0.53\sqrt{f_c'}$ MPa), respectively. When the shear force applied to each P-type beam is normalized by the shear force associated with the nominal flexural strength (M_{nm}), as shown in Figure 65, both P-type beams exceeded the normalized shear at point B, which is shown as ±1.0, indicating that both beams exceeded their nominal strength. However, neither P-type beam reached a peak that exceeded the normalized shear at point C, which is shown as ±1.25. This indicates that an acceptable upper bound for the shear demand in P-type coupling beams may be determined using $1.25M_{nm}$.

4.4 Progression of Damage

The condition of the specimens (viewed from the south) during the last cycle to target chord rotations of 2, 4, 6, 8, and 10% (if reached by the specimen) are shown in Figures C.1 through

C.109 of Appendix C. The locations of necked and fractured bars were recorded after each test, as shown in Figures 67 through 77. Table 10 shows the cycle where bar fracture was first observed and the number of bars that were fractured in each reinforcing bar group, as observed after completing the test.

The first flexural cracks in each test were frequently observed during the first cycle to 0.2% chord rotation. Flexural and shear cracks continued to develop until testing ceased but most cracks initiated before 2% chord rotation, afterwards cracks primarily widened and lengthened.

Flexural cracking was observed on both 12-in. (310-mm) faces of the coupling beam. When these cracks penetrated through the 18-in. (460-mm) depth of the coupling beam, some remained perpendicular to the beam longitudinal axis but they frequently developed into inclined flexure-shear cracks. Generally, flexural cracks became inclined toward the compression zone at the nearest support.

All specimens had flexural cracks extending across the 18-in. (460-mm) beam depth at both ends of the coupling beam early in the tests. These cracks tended to become wide as deformations concentrated near the face of the top and bottom blocks. These deformations are attributed to elongation and slip of the longitudinal (diagonal and parallel) reinforcement inside the end blocks, also referred to as strain penetration.

Inclined (shear) cracks formed along the 18-in. (460-mm) face of the beam, primarily developing from the tips of horizontal (flexural) cracks. Most inclined cracks were oriented at approximately 45 degrees from the beam longitudinal axis. Corner to corner cracks only occurred in the beams with an aspect ratio of 1.5, see cracks on D80-1.5 (Figure C.1) or D120-1.5 (Figure C.20). The spacing of inclined cracks was fairly even near midspan of the beams.

Most of the fractured diagonal reinforcement was observed to buckle during the half cycle prior to fracturing. For example, buckling of reinforcing bars in the bottom west bar group of D80-1.5 was observed at -6% chord rotation (shown in Figure C.8) followed by bar fracture en route to +8% chord rotation (shown in Figure C.9). This type of buckling-induced fracture may be due to the bar exceeding a "critical bending strain" from high curvature demands on the bar during buckling. Barcley and Kowalsky[30] showed that the magnitude of the imposed strain due to buckling influences the tensile strain capacity of reinforcing bars tested under cyclic loading. Buckling, necking, or fracture was not observed for the primary longitudinal reinforcement in the P-type beams. However, at chord rotations in excess of 4%, the primary longitudinal reinforcement deformed laterally near the coupling beam ends as a result of concentrated shear deformations (also referred to as sliding shear), see Figure C.95 for P80-2.5 and Figure C.103 for P100-2.5.

One beam end exhibited more damage than the other in most specimens. Differences between beam ends were least pronounced in D80-1.5, D80-2.5, D120-2.5, and D80-3.5, which are shown near final loading steps in Figures C.2, C.29, C.51, and C.61. This list consists of the three D-type specimens with Grade 80 (550) primary reinforcement and the single D-type Grade 120 (830) specimen with developed No. 3 (10) secondary longitudinal reinforcement. The more symmetrical behavior in the Grade 80 (550) beams may be due to reduced occurrence of buckling. It is likely that fewer Grade 80 (550) diagonal bars buckled because spacing of transverse reinforcement in all D-type beams was identical (3 in. [76 mm]) with $s/d_b \leq 4$. The likelihood of buckling for Grade 80 (550) bars was reduced due to lower stress demands (associated with their lower yield stress). The bar diameter of Grade 80 (550) diagonal reinforcement was equal to or greater than the bar diameter of Grade 100 or 120 (690 or 830) diagonals.

The development of the No. 3 (10) longitudinal reinforcement in D120-2.5 likely contributed to the more symmetric observed damage because it forced beam deformations to be less concentrated at the beam ends. During chord rotation cycles to 6%, specimens D100-1.5 and D120-1.5 (Figures C.12 and C.21) with secondary longitudinal reinforcement terminating at 2 in. (51 mm) into the end blocks had damage concentrated near the beam ends. During chord rotation cycles to 6%, D100-2.5 (Figure C.41) had concrete loss due to crushing or spalling extending approximately 3 to 4 in. (76 and 100 mm) away from the end blocks. The damage at the bottom end was primarily localized in the bottom east corner, corresponding to the compression zone for positive chord rotations. The damage to the top end was distributed through the entire 18-in. (460-mm) beam depth. In contrast, D120-2.5 at chord rotations of -6% (Figure C.51) had visible damage to its concrete through the beam depth at both ends and extended up to 8 in. (200 mm) away from the end blocks and into the beam span.

4.5 Calculated and Measured Strengths of Beams

Table 15 shows the maximum measured and calculated strengths for each beam and the measured-to-calculated strength ratio. The calculated shear strength of the D-type beams, V_{nm}, was obtained by substituting measured yield stress, f_{ym}, into Equation 3.1, which corresponds to the nominal strength of a diagonally-reinforced coupling beam according to ACI 318-14 Section 18.10.7.4(a)[6]. The developed No. 3 (10) longitudinal bars in D120-2.5 were not considered in the calculated strength as the ACI 318 equation neglects developed longitudinal reinforcement in diagonally-reinforced coupling beams.

The calculated strength of the P-type beams, V_{nm}, corresponds to the shear stress associated with the nominal flexural strength acting at both ends of the beam for a tensile bar stress of $1.0f_{ym}$,

a concrete compressive strength of f_{cm}, and including the contribution of reinforcement in compression. Values of f_{cm} and f_{ym} were taken from Tables 2 and 4.

The average ratio of measured-to-calculated strength was 1.48 for D-type beams and 1.15 for P-type beams. The higher average ratio for D-type beams may be because the calculated strength, V_{nm}, depends only on the diagonal reinforcement and neglects the contribution of the transverse reinforcement to the shear strength and the concrete to the flexural strength of the beams (the participation of concrete in compression will tend to increase the internal lever arm and therefore increase the beam flexural strength). These results are consistent with those from other studies[12,67,81,94]. The ratios for the D-type beams ranged from 1.28 to 1.68, excluding D120-2.5, which had a ratio of 1.90 partly due to developing the No. 3 (10) bars (secondary longitudinal reinforcement) into the end blocks. All of the measured-to-calculated strength ratios for D120 beams were greater than those of D80 and D100 beams with the same aspect ratio.

For D-type beams, the average measured-to-calculated strength ratio would reduce from 1.48 to 1.18 if the strength is estimated using $1.25f_{ym}$ instead of $1.0f_{ym}$. Alternative calculations based on probable flexural strength (using $1.25f_{ym}$) and accounting for the projected area (normal to the longitudinal axis) of steel may also reduce the average measured-to-calculated strength ratio to a value closer to 1.0. This is further examined in other work[12,67,94].

4.6 Stiffness

Secant stiffness (K_S) refers to the slope of a line drawn from a point at the origin of the force-deformation envelope to any other point on the envelope. Secant stiffness was calculated with Equation 4.3. This definition of stiffness is based on deformations determined using chord

rotation times clear span length ($CR\ l_n$). For each of the coordinates (CR, V) presented in Tables 11 through 14, the corresponding K_s were tabulated.

$$K_S = \frac{V}{CR\ \ell_n} \qquad \text{Equation 4.3}$$

Shear-chord rotation envelope data, shown in Tables 11 through 14, were used to estimate the initial stiffness (K_e) and the corresponding effective moment of inertia (I_{eff}) for each of the coupling beams. The initial stiffness was defined as the secant stiffness associated with a shear equal to $0.75V_{max}$. Two initial stiffness values were determined for each coupling beam, one for each loading direction. This definition of initial stiffness, recommended by Park[88], was selected because it is simple and it was observed that tangential stiffness visibly decreased beyond a shear of $0.75\ V_{max}$. Chord rotations (CR_{75}) associated with $0.75\ V_{max}$ are listed in Tables 11 through 14 and identified with a diamond in the envelopes of shear versus chord rotation in Figures 78 through 81.

Values of K_e in the positive loading direction ranged from 990 kips/in. (173 kN/mm) for D80-1.5 to 167 kips/in. (29 kN/mm) for D120-3.5. Although similar stiffness values were expected for both loading directions, minor differences were observed. Values of K_e in the negative loading direction were within 7% of its positive loading counterpart for beams with aspect ratios of 2.5 and 3.5 but a difference of up to 22% was observed for beams with aspect ratios of 1.5. The greater difference for beams with aspect ratios of 1.5 was in part due to the lower displacement associated with $0.75V_{max}$. of beams with a clear span of 27 in. (690 mm). Note that a chord rotation of CR_{75}= -0.55%, as seen in Table 11 for D80-1.5, corresponds to a displacement (corrected for relative rotation of the end blocks) of -0.15 in. (3.8 mm).

Values of K_e were negatively correlated to both beam aspect ratio and primary reinforcement grade. The average values of K_e for the D-type beams with an aspect ratio of 1.5, 2.5, and 3.5 were 922, 362, and 206 kips/in. (161, 63, and 36 kN/mm), respectively. For P-type beams with an aspect ratio of 2.5, the average value of K_e was 277 kips/in. (49 kN/mm).

Comparisons among beams grouped by grade of the primary reinforcement show that K_e was inversely proportional to reinforcement grade. This observation is consistent with the coupling beam test data reported by Ameen[12]. Average values of K_e for D-type beams Grade 80 (550) were approximately 15% greater than K_e for D-type beams Grade 100 (690) and approximately 40% greater than K_e for D-type beams Grade 120 (830). Average values of K_e for P80-2.5 were approximately 20% greater than K_e for P100-2.5.

An effective moment of inertia (I_{eff}) for both loading directions was calculated using Equation 4.4, which attributes all deformations to flexure. Values of I_{eff} are plotted in Figures 82 and 83 as the ratio of I_{eff} to either the gross moment of inertia (I_g) or transformed uncracked moment of inertia (I_{tr}). For D-type beams, the value of I_{tr} accounts for the projected area of the diagonal bars ($A_{vd}\cos\alpha$) and the net area of concrete.

$$I_{eff} = \frac{0.75\, V_{max}\, \ell_n^2}{12\, E_c\, CR_{75}} \qquad \text{Equation 4.4}$$

The effective moments of inertia normalized by I_g and I_{tr} in Figures 82 and 83 have similar trends. Aspect ratio (ℓ_n/h) and I_{eff}/I_g were positively correlated for D-type beams, with average values of 0.05, 0.09, and 0.14 for ℓ_n/h of 1.5, 2.5, and 3.5, respectively. The average I_{eff}/I_g for P-type beams was approximately 0.07. The positive correlation of I_{eff}/I_g and I_{eff}/I_{tr} to ℓ_n/h may

in part be due to the more important role of shear deformations in the behavior of beams with low ℓ_n/h. In other words, I_{eff}/I_g was lower for beams with higher shear deformations than for those with lower shear deformations. The negative correlations between reinforcement grade and both I_{eff}/I_g and I_{eff}/I_{tr} are attributed to the amount of longitudinal reinforcement in the beams, which was inversely proportional to the steel grade. Beams with ℓ_n/h of 3.5, namely, D80-3.5, D100-3.5, and D120-3.5, had I_{eff}/I_{tr} of 0.13, 0.11, and 0.095 and I_{eff}/I_g of 0.17, 0.14, and 0.12, respectively. The trend was less pronounced in D-type beams with ℓ_n/h of 2.5, but this was expected because D120-2.5 had the secondary longitudinal reinforcement developed into the end blocks, which may have increased the cracked stiffness of the beam.

4.7 Hysteretic Energy Dissipation

The shear versus chord rotation data were used to calculate the hysteretic energy dissipation index, E_h, based on Equation 4.5.

$$E_h = \frac{1}{2\pi}\left(\frac{W^+}{D_m^+ V_m^+} + \frac{W^-}{D_m^- V_m^-}\right) \qquad \text{Equation 4.5}$$

The value of E_h represents the equivalent viscous damping factor of a linear-elastic system capable of dissipating energy W^+ and W^- for each loading cycle under steady-state oscillation[85]. Figure 84 shows the variables involved in Equation 4.5. For a symmetrical hysteresis loop, Equation 4.5 in this study simplifies to Equation 3.1 in reference 85.

Figure 85 shows the energy dissipation index for D-type beams with an aspect ratio of 1.5. The area under the shear-chord rotation curve to calculate W corresponds to the second cycle of loading to chord rotations of 1 through 6% (Steps 5 through 10 in Table 8). The plotted data show that E_h is inversely proportional to the grade of reinforcement or yield stress (f_y) of the diagonal

bars. Figure 86 shows E_h versus the normalized chord rotation to account for f_y. The normalized curves show very similar slopes, an indication that the area enclosed by a hysteresis loop (for a given chord rotation) is inversely proportional to f_y. For a target chord rotation (in excess of yielding), higher f_y implies higher yield deformation and consequently lower ductility and plastic deformation with a reduced area under the force-deformation curve. Similar findings were reported by Ameen et al.[12]

The energy dissipation index for D-type beams with aspect ratios of 2.5 and 3.5 are shown in Figures 87 through 90. The curves show similar trends to those in Figures 85 and 86. Values of E_h varied between 0.1 and 0.3 for chord rotations between 3 and 5%. Lower values of E_h were generally associated with higher grade of reinforcement (f_y) and higher aspect ratio (ℓ_n/h).

The energy dissipation index for P-type beams with aspect ratio of 2.5 are shown in Figures 91 and 92. General trends were similar to those shown in Figures 85 through 90. Figures 91 and 92 show values of E_h between 0.1 and 0.2 for chord rotations between 2 and 4%, with lower values of E_h generally associated with higher grade of reinforcement (f_y).

4.8 Residual Chord Rotation

Damage to the tested beams can be indicated by the residual chord rotation, defined as the chord rotation associated with zero shear after unloading from the peak chord rotation of a given cycle. Figures 93 through 103 show the ratio of the residual chord rotation to the preceding peak chord rotation versus chord rotation. Values of residual chord rotation resulting from loading steps 1 through 4 (nominal chord rotations below 1%, see Table 8) were omitted from the plots because low values of chord rotation are more sensitive to measurement errors. In addition, residual chord rotations are nearly zero prior to yielding of the primary longitudinal reinforcement. Figures 93

through 103 show values from the first and second cycles of each loading step. Residual chord rotations for first cycles were generally greater than those for second cycles.

Figure 104 shows the residual chord rotation for D-type beams with an aspect ratio of 1.5. The zero-shear chord rotations were taken from the hysteresis loops associated with second cycles of loading for chord rotations between 1 and 6% (Steps 5 through 10 in Table 8). Data in Figure 104 indicate that zero-shear chord rotations were generally higher for beams with lower grade of reinforcement. Figure 105 shows the residual chord rotation versus the normalized chord rotation based on f_{ym} of the diagonal bars. All three normalized curves show similar slope, which is an indication that the unloading stiffness (for beams targeting the same strength) is negatively correlated with the yield stress of the primary longitudinal reinforcement for chord rotations below 6%. This is likely due to the lower reinforcement ratio in beams with higher strength bars. Similar findings were reported by Ameen et al.[12]. Figures 106 through 109 show the residual chord rotations during the second cycles for D-type beams with aspect ratios of 2.5 and 3.5. The plots show similar trends to those observed in Figures 104 and 105. The zero-shear chord rotations in Figures 104 through 109 were between 20 and 60% of the peak chord rotation reached at the end of Step 9 (nominal chord rotation of 4%). Residual chord rotations were generally inversely proportional to primary reinforcement yield stress and aspect ratio.

Figures 110 and 111 show residual chord rotation data for P-type beams with an aspect ratio of 2.5. The curves indicate similar trends to those observed in D-type beams. Zero-shear chord rotation values between 40 and 60% of the peak rotation were attained at the end of Step 8 (nominal chord rotation of 3%), versus 30 and 40% attained by D-type beams with the same aspect ratio of 2.5. Thus, D-type beams consistently showed lower residual chord rotations than P-type beams, an outcome closely related to the higher force levels reached by D-type beams.

4.9 Beam Elongation

The elongation of the coupling beams are plotted in Figures 112 through 133 as a function of chord rotation and shear. Beam elongation is defined as the change in beam length divided by the initial beam length. Two symbols in Figures 112 through 129 identify the peak chord rotations reached before ("O") and after ("X") the first observed bar fracture for D-type beams. Elongation was calculated as the change of distance between the middle marker on the top block and the middle marker on the bottom block (Column 3 at Rows 0 and Row $n_r + 1$, in Figure 33) divided by the initial distance (measured before the test). Both marker rows were attached to their respective block, nominally 2.5 in. (64 mm) from the beam-block interface.

The beam elongation versus chord rotation relationships exhibited a V-shaped curve with elongation occurring in both loading directions and typically increasing with increased chord rotation until the cycle where bar fracture or a 20% strength loss occurred. Maximum beam elongation values were generally inversely proportional to reinforcement grade and aspect ratio.

Elongation of the beams was primarily due to yielding of the reinforcing bars and unrecovered plastic strains. Reduction of elongation with increased chord rotations only occurred after fracture of diagonal bars and/or buckling of the opposite diagonal bars, and in some cases followed by concrete crushing.

Beam elongations curves for D80-1.5 are shown in Figures 112 and 113. During cycles to chord rotations of 4%, the maximum elongation reached 2.3%. Elongation increased to approximately 3% during the loading steps targeting a chord rotation of 6%. The elongation of the beam reduced to approximately 2% during the first excursion to a chord rotation +8% following the first observed fracture of several diagonal bars in the previous cycle. The peak elongation for

D80-1.5 of approximately 4.2% occurred when approaching a chord rotation of -8%. Figure 113 shows that strength was nearly constant while beam elongation increased from 0.3 to 3%.

Figure 114 shows the beam elongation versus chord rotation for D100-1.5. The beam reached approximately 2% elongation during the first loading cycle to 4% chord rotation. This specimen reached a peak beam elongation of nearly 3.5% during the cycles to 6% chord rotation, where bar fracture occurred. Figure 115 shows that beam elongations between 0.4 and 0.6% occurred near the maximum shear of approximately ±250 kips (1110 kN). A gradual decrease in strength occurred for beam elongations between 0.6 and 2%.

Figure 116 shows that for chord rotations not exceeding 4%, D120-1.5 reached a beam elongation of 2%, which is similar to D100-1.5 but slightly less than D80-1.5. For chord rotations exceeding 4%, D120-1.5 reached values between 3 and 4% after bar fracture occurred. Figure 117 shows nearly constant strength for beam elongations between 0.5 and 2%.

Specimen D80-2.5, shown in Figures 118 and 119, exhibited a beam elongation of approximately 1.2% at 4% chord rotation progressing to an elongation of nearly 1.8% at 6% chord rotations, while the applied shear was near maximum values. During the first excursion to a chord rotation of -8%, where bar fracture occurred, beam elongation reached 2.7%. Elongation reduced to 0.2% when loading in the opposite direction, given that the fractured bars had no resistance to closing of the concrete cracks. Figure 119 shows nearly constant strength in both loading directions while elongation increased from 0.25 to 1.8%.

Specimen D100-2.5, shown in Figures 120 and 121, exhibited a beam elongation of approximately 1.3% during the first excursion to a chord rotation of +4%, while resisting approximately 90% of the maximum applied shear. During the first cycle to 6% chord rotation,

the occurrence of bar fracture increased beam elongation to 2.4% in the negative loading direction and reduced to 0.3% elongation in the positive loading direction. Figure 121 shows strength reducing for elongations exceeding 1%.

Specimen D120-2.5, shown in Figures 122 and 123, reached a beam elongation of 1.1% through the first cycle to a chord rotation of 4%. The first bar fractures of the diagonal reinforcement were observed during the first cycle to a chord rotation of 6%. The maximum and minimum elongations of 3 and -0.2% occurred during the cycles to chord rotations of 8%. The developed Grade 120 (830) secondary longitudinal reinforcement in D120-2.5 may have decreased the beam elongation of this specimen compared with other D-type beams. At chord rotations of 4%, D120-2.5 had the lowest maximum elongation of the three D-type beams with an aspect ratio of 2.5 (elongation maxima of 1.2, 1.3, and 1.0% for D80-2.5, D100-2.5, and D120-2.5, respectively).

Specimen D80-3.5, shown in Figures 124 and 125, exhibited nearly 1% beam elongation during the cycles to chord rotations of 4%. The first bar fracture was observed during the first cycle to a chord rotation of 8% reaching a beam elongation of nearly 1.4%. After several bars fractured in both groups of diagonals, elongation reduced to -0.3% during the cycle to 10% chord rotation. Figure 125 shows nearly constant strength (in each loading direction) for beam elongations between 0.2 and 1.4%.

Specimen D100-3.5, shown in Figures 126 and 127, reached a beam elongation of nearly 0.9% for a chord rotation of 4%. Maximum elongation approached 1.5% during the cycles to a chord rotation of 6% where the first bar fracture was observed. The minimum elongation of -0.9%

was observed at a chord rotation of +8% after multiple bars fractured in both groups of diagonals. Figure 127 shows a gradual decrease in strength for beam elongations ranging from 0.25 to 1.4%.

Specimen D120-3.5, shown in Figures 128 and 129, exhibited approximately 0.9% beam elongation during cycles to 4% chord rotation. The elongation reached nearly 1.5% during the first cycle to 6%, where the applied shear reached near peak values in both loading directions. The maximum elongation of 2.2% occurred during the second cycle to a chord rotation of 8% after several bars fractured. Continuous beam elongation data for chord rotations exceeding 3% were not available for this specimen due to a recording error of the primary data acquisition system, refer to Section 4.2.9. Figure 129 shows strength reducing after elongations exceeding 0.9%, similar to D100-3.5.

The above observations on beam elongations of D-type beams clearly indicate that at chord rotations of 4%, maximum beam elongations were inversely proportional to aspect ratio. Elongation maxima of 2.3, 1.3, and 0.9% were obtained for beams with aspect ratios of 1.5, 2.5, and 3.5, respectively.

Specimens P80-2.5 and P100-2.5, shown in Figures 130 through 133, exhibited approximately 1% beam elongation at chord rotations of 3 and 4%. The elongations of 1% in P80-2.5 and P100-2.5 at chord rotations of 3% was approximately 10 to 20% higher than the elongations of D80-2.5 and D100-2.5 for the same chord rotation. Beyond a chord rotation of 4%, after severe strength loss, both P-type beams exhibited reduced elongations in both loading directions. The observed maximum elongations of 1% reached at chord rotations of 3 and 4% in the P-type beams were less than the maximum elongations in any of the D-type beams for chord

rotations of 6% or higher. This was likely due to the occurrence of bar buckling and bar fracture associated with the higher chord rotations reached by D-type beams.

4.10 Changes in Beam Depth

The normalized beam depths of all specimens for target chord rotations between 0.75 and 4% (Steps 4 through 9 in Table 8) are plotted in Figures 134 through 155. The plotted data are based on the position of markers at the end of the first cycles. The normalized beam depth was calculated as the average distance between the edge markers for two consecutive rows (defining a layer) divided by the average initial distance between the edge markers for each of the rows. Typically, the outer markers were located in Columns 1 and 5 (Figure 33) but inner columns were used (for both rows defining the layer) when marker malfunction or disconnection occurred. Replacement markers were selected from the pair of most widely spaced markers remaining on the same row. The normalized beam depths calculated with the replacement markers are shown as filled symbols in Figures 134 through 155.

Changes in beam depth (measured by the normalized beam depth) for D80-1.5, D100-1.5, and D120-1.5 did not exceed 0.3% at chord rotations of approximately 3%. Maximum values typically occurred in layers near the beam-block interfaces (Layers 1 and n_r-1, where n_r=7 for beams with an aspect ratio of 1.5), as shown in Figures 134 through 139. Beam D80-1.5 exhibited larger changes in beam depth than other beams with an aspect ratio of 1.5. Maximum values approached 0.6% during the cycle to 4% chord rotation and near midspan values ranged from 0.2 to 0.3% during the cycles targeting chord rotations between 2 and 4%. The other specimens, D100-1.5 and D120-1.5, had a maximum change of beam depths near midspan of nearly 0.2%.

Figures 140 through 143 show that changes in beam depth for D80-2.5 and D100-2.5 did not exceed 0.8% at chord rotations of approximately 4% with maximum changes in depth occurring in the first two layers away from the beam-block interfaces. The change in depth at midspan for both beams was nearly 0.2%.

The change of depth of D120-2.5 was the largest observed in all D-type beams. The maximum change in beam depth of D120-2.5 was approximately 1.4%, occurring in the second layer away from the beam-block interfaces, as shown in Figures 144 and 145 for the cycles targeting chord rotations of 4%. The higher values in D120-2.5 may be attributable to having developed secondary longitudinal reinforcement, which reduced rotations at the beam-block interface and distributed damage into the beam span.

Figures 146 through 149 show that maximum changes in beam depth of D80-3.5 typically did not exceed 0.4%, whereas values of 0.6% were reached in D100-3.5 with maximum values typically occurring in the first two layers away from the beam-block interfaces. Maximum change of depth near midspan typically did not exceed 0.2%, with an exception for D100-3.5 at chord rotations exceeding 3%, which may be explained by the use of replacement markers at that location.

D120-3.5 had slightly larger change in beam depth than D80-3.5 or D100-3.5 with values reaching 0.7 to 0.8% for target a chord rotations of 3%, as shown in Figures 150 and 151. Optical marker data were not available beyond a chord rotation of 3% due to the error in the recording system described in Section 4.2.9.

Figures 152 through 155 show the changes in beam depth of P80-2.5 and P100-2.5. For chord rotations of 2%, changes of depth for both beams were approximately the same, between

0.7 and 0.8%. The largest changes in depth typically occurred in the layers near the beam-block interfaces, where plastic curvature demands were expected. Such large changes in beam depth are consistent with the shear-related damage observed during testing and expected in the P-type beams. As chord rotations approached ±3%, markers near the bottom beam-block interface stopped functioning for P80-2.5 but those in P100-2.5 showed changes in beam depth between 3.5 and 4.2%. Midspan changes of beam depth reached approximately 0.3% in P80-2.5 and 0.4% in P100-2.5 at chord rotations of 3%.

4.11 Components of Chord Rotation

Position data from the optical markers attached to the surface of each specimen were processed to quantify the beam deformations attributable to flexural rotation, beam-end rotation, shear, and sliding at the beam ends. As shown in Figures 32 and 33, the markers were arranged in a 4-in. (100-mm) square grid pattern over one side of each specimen and included part of the top and bottom blocks.

Figure 33 identifies the vertical columns of markers, numbered from 0 to 6 (right to left as viewed from laboratory north, see Figure 27), and horizontal rows, numbered from -1 to n_r+2 (top to bottom) as each aspect ratio of beam had a different number of rows (n_r) of markers. Rows -1 and n_r+2 were only used to verify data from neighboring rows 0 and n_r+1 and were not present in beams with an aspect ratio of 3.5. The grid of optical markers was divided into rectangular "layers" bounded by the two outermost markers in consecutive rows. The layer number was based on the lower value of row number bounding the layer (Layer n_r is bounded by Rows n_r and n_r+1).

The grid of optical markers was also divided into "stations", which were defined by four adjacent markers. Each station consisted of a 4-in. (100-mm) square (as shown in the shaded area

of Figure 33). The angles at the corners of each station were identified in calculations as A, B, C, or D, as shown in the general deformed shape of a station in Figure 156.

4.11.1 Flexural and Beam-End Rotations

Flexural rotations for each beam are shown in Figures 158 through 179. The data in the Figures were calculated for each of the layers of each specimen as the difference between rotations of the two consecutive rows of markers. For a given row of markers, rotation was calculated based on the vertical displacements of the two outermost markers in the row:

$$\theta_i = \frac{\Delta y_{i,5} - \Delta y_{i,1}}{\ell_i} - \frac{\Delta y_{i+1,5} - \Delta y_{i+1,1}}{\ell_{i+1}} \qquad \text{Equation 4.6}$$

Where θ_i is the flexural rotation of layer i, Δy is the change in vertical position (y-axis coordinate) from the initial position of the marker identified by the subscripts as row and column, and ℓ_i is the initial horizontal distance along the x-axis between the markers in Columns 1 and 5 (Figure 33) on Rows i or $i + 1$. Position data from markers in Column 2 replaced Column 1 in the case of marker malfunction or detachment. Similarly, data from markers in Column 4 replaced Column 5, as needed. Cases where the markers in either Column 1 or 5 were replaced are identified in Figures 158 through 179 with solid symbols.

Rotations occurring in Layers 0 and n_r, each bounded by a row of markers on the beam span and an end block, are herein referred to as beam-end rotation and calculated with Equation 4.7, which includes strain penetration into the end blocks and flexural rotation into the beam span.

$$\theta_{be,top} = \frac{\Delta y_{0,5} - \Delta y_{0,1}}{\ell_0} - \frac{\Delta y_{1,5} - \Delta y_{1,1}}{\ell_1} \quad \text{Equation 4.7a}$$

$$\theta_{be,bot} = \frac{\Delta y_{n_r,5} - \Delta y_{n_r,1}}{\ell_{n_r}} - \frac{\Delta y_{n_r+1,5} - \Delta y_{n_r+1,1}}{\ell_{n_r+1}} \quad \text{Equation 4.7b}$$

The calculated flexural rotations in Figures 158 through 179 are plotted at midheight of each layer with the y-axis identifying the distance above and below the beam midspan. The plotted values are taken at the peak chord rotation of the first cycle to target chord rotations between 0.75 and 4% (Steps 4 through 9 in Table 8).

The maximum observed flexural rotations in Figures 158 through 179 were observed in Layers 0 and n_r, the layers containing the beam-block interface (as shown in Figure 33), which include strain penetration. For target chord rotations between 3 and 4%, maximum flexural rotations occurred in D-type beams with an aspect ratio of 3.5. For beams with the same aspect ratio, maximum flexural rotations generally occurred in beams with higher strength reinforcement.

Figures 176 through 179 show that maximum flexural rotations for P-type beams, at chord rotations of 3%, were between 0.011 and 0.018 radians for P80-2.5 and P100-2.5, respectively, both less than flexural rotations in D80-2.5 and D100-2.5. Maximum flexural rotations in D120-2.5 were less than half of those in D80-2.5 and D100-2.5, very likely due to having developed the secondary longitudinal reinforcement into the supports of D120-2.5, which reduced the concentration of rotation at the beam-block interfaces.

The maximum flexural rotations of the layers adjacent to the beam-end interface, Layers 1 and $n_r - 1$, were between 0.005 and 0.014 radians for D-type beams and between 0.003 and 0.008 for P-type beams. The maximum flexural rotation for the remaining layers of the beam span, Layers 2 through $n_r - 2$ did not exceed 0.005 radians for both D and P-type beams.

In general, flexural rotations (including strain penetration) were higher for D-type beams than P-type beams. Flexural rotations had a tendency to increase with higher aspect ratio and higher strength reinforcement.

4.11.2 Shear

Shear deformations were calculated within the beam span using optical marker data. Shear distortion of each station was calculated throughout the tests using the positions of the four corner markers that define the station with four sides (h_t, v_r, h_b, and v_l) and four angles (A, B, C, and D), as shown in Figure 156).

Angles A, B, C and D were calculated using Equations 4.8 through 4.11, as a function of distances between station markers as illustrated in Figure 156.

$$A = \cos^{-1}\left(\frac{h_t^2 + v_l^2 - d_2^2}{2h_t v_l}\right) \quad \text{Equation 4.8}$$

$$B = \cos^{-1}\left(\frac{h_t^2 + v_r^2 - d_1^2}{2h_t v_r}\right) \quad \text{Equation 4.9}$$

$$C = \cos^{-1}\left(\frac{h_b^2 + v_r^2 - d_2^2}{2h_b v_r}\right) \quad \text{Equation 4.10}$$

$$D = \cos^{-1}\left(\frac{h_b^2 + v_l^2 - d_1^2}{2h_b v_l}\right) \quad \text{Equation 4.11}$$

The general deformed shape of a station (Figure 156) can be decomposed into three distinct deformation components that cause changes in the angles at each corner of the station: flexural rotation θ, shear distortion γ, and expansion ψ (as shown in Figure 157). The change in angle at each corner of a station was set equal to the sum of the three components of angular change, as shown in Equations 4.12 through 4.15, where $\Delta A, \Delta B, \Delta C,$ and ΔD are the change in angle at each of the four corners of a distorted station from the initial condition at the start of the test.

$$\Delta A = +\theta/_2 - \gamma' - \psi \quad \text{Equation 4.12}$$

$$\Delta B = -\theta/_2 + \gamma' - \psi \quad \text{Equation 4.13}$$

$$\Delta C = -\theta/_2 - \gamma' + \psi \quad \text{Equation 4.14}$$

$$\Delta D = +\theta/_2 + \gamma' + \psi \quad \text{Equation 4.15}$$

The shear distortion γ' of each station was then calculated with Equation 4.16, which represents the average of γ' solved from Equation 4.12 through Equation 4.15. This approach for calculating shear distortion assumes uniform curvature within each station.

$$\gamma' = {}^1/_4\,(-\Delta A + \Delta B - \Delta C + \Delta D) \quad \text{Equation 4.16}$$

The shear distortion of a layer was calculated using Equation 4.17a, which represents a weighted average of the shear distortions calculated for the four stations comprising one layer. If one of the markers in the two outer stations malfunctioned, the data from the two middle stations were used (Equation 4.17b). In Equation 4.17, subscript i indicates the layer number, subscript j indicates the station number, and ℓ_j is the width of the station (nominally 4 in. [102 mm]).

$$\gamma_i = \frac{\sum_{j=1}^{4} \gamma'_{i,j}\,\ell_j}{\sum_{j=1}^{4} \ell_j} \quad \text{Equation 4.17a}$$

$$\gamma_i = \frac{\sum_{j=2}^{3} \gamma'_{i,j}\,l_j}{\sum_{j=2}^{3} \ell_j} \quad \text{Equation 4.17b}$$

Figures 180 through 201 show the shear distortion per layer, γ_i, along the beam span for both loading directions. Instances where shear distortion was calculated using Equation 4.17b are identified with solid symbols. The shear distortion for a given layer is plotted at the distance from midspan associated with the midheight of the layer. In each figure, shear distortions are plotted for

chord rotations targeting 0.75% to 4% (Steps 4 through 9 in Table 8) determined at the peak chord rotation during the first cycle to the target chord rotation. Shearing at the end layers (within the beam span), Layers 0 and n_r, is addressed as sliding in Section 4.11.3.

The maximum observed shear distortions in Figures 180 through 201 were generally observed in Layers 1, 2, $n_r - 2$, or $n_r - 1$, which are the first layers away from those used for calculating sliding in Section 4.11.3. The plots show that for target chord rotations not exceeding 3%, maximum shear distortions were between 0.5 and 1% for D-type beams with Grade 80 or 100 (550 or 690) reinforcement. D-type beams with Grade 120 (830) reinforcement reached maximum shear distortions between 1 and 2%. For P-type beams, maximum shear distortions reached 2% in P80-2.5 and 2.5% in P100-2.5. These observations support that higher shear distortions occurred in P-type beams compared with D-type beams, consistent with measured changes in beam depth. In addition, beams with lower longitudinal reinforcement ratio (diagonal or parallel), which are associated with higher grade of reinforcement, showed higher shear distortions. Finally, shear distortions tended to increase with aspect ratio, perhaps because the diagonal bars were less effective at resisting shear deformations with a reduced angle of inclination (α).

4.11.3 Sliding

Sliding at the top or bottom of the beam is defined herein as the relative movement (in the direction of loading) between one beam end and the adjacent end block and corrected for in-plane rotation of the end block. Sliding (at the top or bottom) was calculated as the difference between horizontal displacements of the row of optical markers located on one end block and the first row of markers (within the beam span) closest to the end block. Sliding at the top of the beam is based

on displacements of markers bounding Layer 0. Similarly, the markers bounding Layer n_r were used for calculating sliding at the bottom of the beam.

This definition of sliding includes the effects of shear distortion between the face of the end block and the first row of markers (within the beam span) ignoring the effects of expansion (see Figure 157). Sliding was calculated using Equation 4.18, where $\Delta_{sl,top}$ and $\Delta_{sl,bot}$ are sliding at the beam-block interfaces (top and bottom); Δx is the change in horizontal position (x-axis coordinate) from the initial position of the markers indexed by subscripts of row and column; θ_y and θ_z are rotations about the y and z axes; subscripts 0, 1, n_r, and $n_r + 1$ refer to the row numbers shown in Figure 33; and the coefficients 2.5, 1.5, and 5 in. (64, 38, and 127 mm) refer to the nominal y-axis distance from the beam end to the first row of markers on the end block (Rows 0 or $n_r + 1$), the nominal y-axis distance from the beam end to the first row of markers on the beam (Rows 1 or n_r), and the nominal z-axis distance between the rows of markers on the beam and the markers on the end blocks, respectively. These equations were derived assuming that rotations at rows 1 and n_r were uniform for 1.5 in. (38 mm) into the beam span and concentrated at the beam-block interface. Similarly, rotations at Row 0 and $n_r + 1$ were uniform for 2.5 in. (64 mm) into the end block and concentrated at the beam-block interface.

$$\Delta_{sl,top} = \left[\Delta x_{0,3} - (2.5\ in.)\theta_{z,0}\right] - \left[\Delta x_{1,3} + (1.5\ in.)\theta_{z,1}\right] - (5\ in.)\theta_{y,0} \quad \text{Equation 4.18a}$$

$$\Delta_{sl,bot} = \left[\Delta x_{n_r,3} - (1.5\ in.)\theta_{z,n_r}\right] - \left[\Delta x_{n_r+1,3} + (2.5\ in.)\theta_{z,n_r+1}\right] + (5\ in.)\theta_{y,n_r+1} \quad \text{Equation 4.18b}$$

Figures 202 through 223 show sliding versus chord rotation for all beams. The Figures show sliding with a nearly linear response for chord rotations below 2% and a nonlinear response for higher chord rotations.

Up to a chord rotation of 3%, in both positive and negative loading directions, none of the specimens exhibited sliding greater than ±0.1 in. (±2.5 mm). The overall maximum sliding exceeded ±0.15 in. (±3.8 mm) in every D-type beam with an aspect ratio of 1.5 or 2.5 except D120-2.5. Calculated sliding in D120-2.5 reached ±0.05 in. (±1.3 mm) at chord rotations of 4%, which may be attributable to the developed secondary longitudinal reinforcement, which reduced beam-end rotations and therefore may have reduced the potential for sliding near the beam end. The D-type beams with an aspect ratio of 3.5 never exhibited sliding greater than ±0.1 in. (±2.5 mm), which may be attributable to the large area of longitudinal (diagonal) bars in the more slender beams; even if the shallow inclination angle makes the diagonal bars less effective in the more slender beams, the large area of reinforcement crossing the interface may help limit the sliding deformations. For P-type beams, maximum sliding values were in the vicinity of ±0.1 in. (±2.5 mm) for chord rotations of 3%.

4.11.4 Contribution of Chord Rotation Components

Based on the calculated deformation components described previously (Sections 4.11.1 through 4.11.3), the contributions of the four primary components to the total chord rotation (flexural rotation, beam-end rotation, shear deformation, and sliding) were calculated for the first cycle of chord rotations targeting 0.75% to 4% (Steps 4 through 9 in Table 8). Values were linearly interpolated between chord rotations of -0.75 and +0.75% and skipped if data were not available due to marker malfunction. Figures 224 through 234 show the calculated cumulative contributions of the four deformation components versus chord rotation for each beam.

The total chord rotation due to flexure, CR_f, was calculated with Equation 4.19, where θ_i is based on Equation 4.6 for the flexural rotation of layer i and d_i is the y-axis distance between

the beam midspan and the midheight of layer *i* (refer to Figure 33). This distance d_i was negative for layers above beam midspan. This calculation assumes curvature is uniformly distributed within each layer.

$$CR_f = \frac{\sum_{i=1}^{n_r-1} \theta_i \, d_i}{\ell_n} \qquad \text{Equation 4.19}$$

The total chord rotation due to beam-end rotation, CR_{be}, at the top and bottom blocks was calculated with Equation 4.20. It was assumed that beam-end rotations are lumped at the beam ends.

$$CR_{be} = \frac{\theta_{be,bot}(+\ell_n/2) + \theta_{be,top}(-\ell_n/2)}{\ell_n} = \frac{\theta_{be,bot} - \theta_{be,top}}{2} \qquad \text{Equation 4.20}$$

The total chord rotation due to shear distortion, CR_v, was calculated with Equation 4.21, the sum of the product of average shear distortion for a given layer, γ_i, and the height of the layer, h_i, for Layers 1 through $n_r - 1$ divided by l_n.

$$CR_v = \frac{\sum_{i=1}^{n_r-1} \gamma_i \, h_i}{\ell_n} \qquad \text{Equation 4.21}$$

The total chord rotation due to sliding at the beam-block interface, CR_{sl}, was calculated using Equation 4.22, the sum of total sliding at the bottom and top beam-block interfaces divided by l_n.

$$CR_{sl} = \frac{\Delta_{sl,bot} + \Delta_{sl,top}}{\ell_n} \qquad \text{Equation 4.22}$$

Figures 224 through 234 show that for D-type beams, beam-end rotation, CR_{be}, was the largest component of chord rotation with contributions ranging between 35 and 90% at chord rotations between 3 and 4%. For P-type beams, beam-end rotation was also the largest component

of chord rotation, with contributions ranging between 35 and 50% at chord rotations between 1 and 2%. The contributions of beam-end rotation were larger for D-type beams than for P-type beams, as exemplified by beams with an aspect ratio of 2.5. At chord rotations of 2%, beam-end rotation contributions were as high as 80% for D-type beams with cutoff bars, 50% for D-type beams with developed bars, and 40% for P-type beams. For chord rotations between 3 and 4%, the contributions of beam-end rotation in D-type beams were larger for beams with lower aspect ratio. For beams with an aspect ratio of 1.5, beam-end rotation contributions ranged between 40 and 80%, whereas for those with an aspect ratio of 3.5, values ranged between 40 and 65%.

The contribution of flexure (CR_f) to chord rotation was proportional to aspect ratio while that of shear distortion (CR_v) was inversely proportional to aspect ratio. At chord rotations between 3 and 4%, beams with an aspect ratio of 1.5 had flexure contributions to chord rotation of up to 20% and shear distortion contributions of 5 to 20%. Beams with an aspect ratio of 3.5 had flexure contributions of up to 40% and shear distortion contributions of 5 to 15%. Compared with D-type beams, P-type beams had much larger contributions to chord rotation from shear distortion and similar contributions from flexural rotation. At 2% chord rotation, shear distortion accounted for approximately 40% of chord rotation in P-type beams while flexural rotation accounted for less than approximately 20% of chord rotation.

The contribution of sliding (CR_{sl}) at chord rotations of 3 to 4% in D-type beams with an aspect ratio of 1.5 ranged between 5 and 25%. The sliding contributions were negligible in beams with an aspect ratio of 3.5. The contribution of sliding in the P-type beams (similar to D-type beams) was the lowest of all four deformation components with up to 15% contribution for chord rotations between 1 and 2%.

Specimen D120-2.5 had the only beam with developed secondary longitudinal reinforcement. This difference in detailing caused a change in the relative contributions of deformation components to total chord rotation compared with other D-type beams. For chord rotations between 3 and 4%, beam-end rotation remained the largest contributor to chord rotation (40 to 50%), while the contribution of shear distortion was similar to that of flexure (20 to 30%). The developed secondary longitudinal bars resulted in lower concentration of rotations (due to flexure and strain penetration) near the beam-block interface, causing greater damage within the beam span in the form of flexure and shear distortions The contribution due to sliding was less than 5% in D120-2.5.

CHAPTER 5: MEASURED REINFORCEMENT STRAINS

Reinforcing bars were instrumented with electrical resistance strain gauges as described in Section 3.3.3 and listed in Tables 6 and 7. All strain gauge data are reported assuming zero strain in the reinforcement at the start of the tests. The layout of strain gauges is shown in Figures 34 and 35. Measured strain data versus chord rotation are shown in Figures 235 through 598 with a sketch of the specimen reinforcement and the location (circled) of the strain gauge providing the plotted data. The Figures are sorted by specimen identification followed by strain gauge identification: D for Diagonal bars in D-type beams; P for primary Parallel bars in P-type beams; S for closed Stirrups; H for secondary Horizontal longitudinal bars in D-type beams; and T for Transverse crossties. Bars with H gauges were in the horizontal position during casting.

Figures 599 through 640 show the envelope of measured strains at the peak chord rotation of each loading step, where envelope strains for one loading direction may have been taken from a different cycle than the one used in the other direction. It is important to note that higher strains may have been measured during a cycle that did not define the peak chord rotation for a loading step (which involves two cycles). Each of these Figures contain data from all gauges of one type in a single specimen (for D-type beams: gauges D, S, H, or T; for P-type beams: gauges P, S, or T). For example, Figure 599 shows strain maxima measured with D strain gauges in D80-1.5 at discrete points corresponding to the peak chord rotation of each loading step. The text labels in Figures 599 through 640 identify which strain gauge corresponds to each curve shown. The text labels were vertically translated to avoid overlap. The ends of each curve have an “x” indicating the chord rotation when the gauge became inoperable and an open circle identifies the overall maximum strain (in each loading direction) recorded for the reported gauge type. Figures 599

through 640 also include a heavier black line to represent the overall strain envelope for that gauge type in that specimen. To facilitate comparisons among specimens, the overall envelopes are grouped in Figures 641 through 655 based on reinforcement layout (D- or P-type) and aspect ratio (1.5, 2.5, or 3.5). For example, Figure 641 shows the envelopes of strains measured with D strain gauges in D-type beams with an aspect ratio of 1.5.

In the following sections, strain gauge data are occasionally used as a basis for stating that the reinforcement yielded at a certain point during the test. For the purpose of this discussion, strains in excess of 0.3, 0.4, and 0.5% (3, 4, and 5 millistrain) are taken to be indicative of yielding for Grades 80, 100, and 120 (550, 690, and 830) reinforcement, respectively. More precise statements regarding the initiation of yielding are not made for several reasons: 1) effects of concrete shrinkage on bar strains at the start of the test are neglected, 2) strain gauges measure bar strains at discrete locations that may not coincide with the location of maximum strain, and 3) stress-strain curves for high-strength reinforcement do not generally show a well-defined yield plateau.

A change in slope in the strain versus chord rotation curves is apparent for beams with Grade 80 (550) reinforcement, which shows a well-defined yield plateau in Figure 24. This is evident in Figures 364 and 366 for gauges D12 and D14 in D80-2.5. However, a more gradual change in slope occurred in Figures 420 and 421 for gauges D5 and D6 in D120-2.5 with Grade 120 (830) reinforcement, which lacked a well-defined yield plateau in Figure 24.

Continuous strain gauge data are not shown for D120-3.5 in Figures 524 through 554 after the second 3% cycle (end of Step 8 in Table 8) due to a recording error that occurred with the primary data acquisition system. The plots of strain gauge data versus chord rotation shown in

Figures 524 through 554 show the strain for each gauge with the corresponding chord rotation recorded by a backup system based on optical character recognition (OCR) activated each time the test was paused. The strain data synchronized with the recordings of the OCR system are shown with dashed lines and bounded by open circles.

5.1 Diagonal Reinforcement

The strain envelopes in Figures 641, 645, and 649 show the maximum strains measured on the diagonal reinforcement with D gauges in the D-type specimens. The location of the gauges are shown in Figure 34. Consistent patterns are not discernible between the maximum strain measured with the D strain gauges and either reinforcement grade or aspect ratio. However, for chord rotations less than 3%, specimens with Grade 120 (830) reinforcement tended to have lower strains than other specimens, particularly more noticeable for D120-2.5, which had the secondary longitudinal reinforcement (No. 3 [10] bars) developed into the end blocks.

Strain values consistent with yielding were observed in D gauges at both beam-block interfaces. Beams with primary reinforcement of higher grade and higher aspect ratio (ℓ_n/h) experienced yielding at higher chord rotations. Maximum strain values were consistently measured in D gauges located at the beam-block interfaces (D5, D6, D11, D12, D13, and D14, see Figure 34).

Figures 641, 645, and 649 show that the maximum strain in diagonal bars exceeded 4% (40 millistrain) in all specimens before a chord rotation of 5%, with strains occasionally approaching 9%. The highest strains generally occurred at chord rotations between 3 and 6%, with the higher chord rotations typically occurring in beams with an aspect ratio of 1.5. In loading cycles where beam strength was decreasing, the reported maximum strain in diagonal bars appears to

decrease. This is largely because gauges became inoperable where damage was most severe (and strains were highest) but also because the loss of strength generally coincided with a change in mechanism; flexural tension strain demands tend to decrease after diagonal bars buckle or fracture. The envelopes (Figures 641, 645, and 649) therefore included working gauges with strains relatively low corresponding to high chord rotations and low residual strength.

Figure 656 shows the maximum measured strain in the diagonal bars of D-type beams during any of the cycles of Steps 5 through 9 (nominal chord rotations of 1 through 4%, see Table 8). Based on the limited test data, an estimate of maximum strain (ε_{max}) for D-type beams with aspect ratios of 1.5, 2.5, or 3.5 may be defined by $\varepsilon_{max} = 2\,CR$, which gives 8% strain for $CR =$ 4%. In contrast, for D120-2.5 with developed secondary longitudinal reinforcement, Figure 656 shows that the maximum strain in the diagonal bars is bounded by $\varepsilon_{max} = CR$, for CR between 1 and 4%.

5.2 Parallel Primary Reinforcement

The envelopes of strains measured with P gauges on the primary reinforcement (parallel to the beam longitudinal axis) in P-type specimens, are shown in Figure 653. The overall maximum measured strains were approximately 5% (50 millistrain) for P80-2.5 and 3% for P100-2.5, both considerably greater than the strain associated with yielding. The strains in P80-2.5 were similar in magnitude to the strains measured with D gauges in D-type specimens whereas the maximum strains in P100-2.5 were lower. This may be due to the absence of a yield plateau in the Grade 100 (690) reinforcement of P100-2.5 or simply because gauges P5 and P6 malfunctioned and strain maxima were not recorded.

Strains measured with P gauges at the beam-block interfaces (P5, P6, P11, and P12, see Figure 35) all exceeded 1% with a maximum of 3.5% at or below chord rotations of 2%, see Figures 635 and 638. Strain gauge P6 in P80-2.5 (Figure 635) recorded the maximum strains throughout the chord rotation history, but gauge P6 malfunctioned in P100-2.5 and P5 became inoperable early in the test (Figure 638). The highest measured strains generally occurred at chord rotations higher than those corresponding to the maximum shear (see open circles at CR_{100} in Figure 653).

Figure 657 shows the maximum strain in the primary longitudinal reinforcement of P-type beams during any of the cycles of Steps 5 through 9 (nominal chord rotations of 1 through 4%, see Table 8). Based on the limited test data, an estimate of maximum strain (ε_{max}) for P-type beams with an aspect ratio of 2.5 may be defined by $\varepsilon_{max} = 1.5\,CR$, which gives 4.5% strain for $CR = 3\%$.

5.3 Parallel Secondary Reinforcement

Figure 34 shows the location of the H strain gauges on the secondary longitudinal reinforcement (parallel to the beam longitudinal axis) in D-type specimens. The strain envelopes for these gauges are shown in Figures 643, 647, and 651. All of the parallel secondary reinforcement in D-type specimens was Grade 80 (550), and only extended 2 in. (51 mm) into the end blocks, except for the secondary reinforcement in D120-2.5, which was Grade 120 (830) and extended nominally 17 in. (430 mm) into the end blocks.

The maximum strains measured with H gauges in D-type beams were highly variable, with maximum values recorded in gauges located approximately at one-third of the beam span (except for D120-2.5). Beams with an aspect ratio of 1.5 were the only ones with maximum strains (for H

gauges) generally below yielding, strains well in excess of yielding were recorded in all other D-type beams.

Strain gauges at the beam-block interfaces of D120-2.5 recorded maximum values near 1.3% (13 millistrain, refer to gauges H1 and H2 in Figure 621), clearly indicating yielding of the reinforcement. High strain demands were expected in the H gauges of D120-2.5 due to the 17-in. (430-mm) embedment of the secondary longitudinal reinforcement into the end blocks.

5.4 Transverse Reinforcement

The strain envelopes for S gauges on the closed stirrups are shown in Figures 642, 646, 650, and 654 and those for T gauges on crossties are shown in Figures 644, 648, 652, and 655. The locations of S and T gauges are shown in Figures 34 and 35. Grade 80 (550) transverse reinforcement was used in all beams except D120-2.5, which had Grade 120 (830) transverse reinforcement.

The maximum strains recorded by S gauges in D-type beams, for chord rotations less than 3%, were generally below 0.3% (3 millistrain), except in D120-2.5. The recorded strains from the closed stirrups in D120-2.5 were greater than those recorded in D80-2.5 and D100-2.5, which indicates that the developed secondary longitudinal reinforcement had an effect on distributing damage into the beam span, with increased expansion of the concrete core and higher strains in the closed stirrups. However, in D120-2.5, strains remained below 0.5% through chord rotations of 6% in both loading directions, indicating that the Grade 120 closed stirrups may not have yielded, though recorded strains exceeded 0.3% in several of the S gauges in D120-2.5. Therefore, providing $\rho_t f_{yt}$ greater than required by ACI 318-14[6] seemed to be effective and avoided yielding of the transverse reinforcement. The maximum strains of S gauges in P-type beams (Figure 654)

show strains approaching 0.4% for chord rotations in excess of 3%, showing that the closed stirrups likely yielded. Yielding of the transverse reinforcement in the P-type beams was expected based on the magnitude of the measured shear distortions and changes in beam depths (Section 4.10).

Crossties were instrumented (T gauges) in both D-type and P-type beams. The strain versus chord rotation envelopes (Figures 644, 648, 652, and 655) were very similar in both loading directions. For chord rotations less than 3%, maximum strains in T gauges were generally below 0.3% except for the single instrumented crosstie (T1) in P80-2.5, which approached 0.4%. Measured strains in T gauges did not appear to be correlated with the grade of the primary longitudinal reinforcement or aspect ratio (ℓ_n/h).

CHAPTER 6: CHORD ROTATION CAPACITY OF COUPLING BEAMS

6.1 Description of Database

A database was assembled that contains results from tests of 52 diagonally-reinforced coupling beams. The database expands the list of specimens assembled by Ameen et al.[12] and Lequesne[67] with data recently available[41,89,118] including the nine D-type beams tested as part of this study. The database contains beams that meet these criteria: 1) the beam was diagonally reinforced; 2) sufficient information was available describing the specimens; and 3) the concrete did not contain fiber reinforcement. Details of the beams are provided in Tables 17 or 18, depending on whether the specimen was included or excluded, respectively, in subsequent analyses to derive a best-fit equation for chord rotation capacity. Reasons to exclude a beam from subsequent analyses are documented in Table 18. Footnotes for both Tables 17 and 18 are explained in Table 19.

Using the envelope of the shear versus chord rotation data, the chord rotation capacity of a beam was defined as the average of the chord rotations (in each loading direction) that correspond to the post-peak shear equal to 80% of the peak. If a specimen was not tested to failure, the chord rotation capacity assigned to a loading direction was taken as the maximum imposed chord rotation if the specimen retained more than 80% of its strength. Measured values of chord rotation capacity are as reported by the given reference if insufficient data were provided to determine chord rotation capacities consistent with the above definition.

Of the 52 diagonally-reinforced coupling beams, 32 had all longitudinal reinforcement terminated near the beam-wall interface while other beams had all longitudinal reinforcement developed into the end blocks. Thirty-five of the 52 beams had full-section confinement with hoops

around the beam perimeter (with cover). The other 27 beams had "diagonal confinement" with hoops around each diagonal group of bars and light transverse reinforcement around the beam perimeter (with cover).

The 33 beams in Table 17 were used as a basis for subsequent analyses aimed at identifying the most influential parameters on deformation capacity and deriving a best-fit equation for chord rotation capacity. These beams satisfy the following selection criteria: 1) rectangular cross-section (not integral with a slab); 2) least cross-sectional dimension not less than 5 in. (125 mm); 3) ratio of transverse reinforcement spacing to diagonal bar diameter (s/d_b) less than or equal to 8; 4) applied axial force (or force induced by axial restraint) not exceeding $0.15A_g f_{cm}$; and 5) loading protocol with fully reversed cycles of increasing displacements. Test variables represented by a limited number of beams in the database, such as beams integral with a slab or high axial forces, were omitted from the analysis because they have been identified in previous studies[12,13,65,81,94] to affect chord rotation capacity. Table 18 describes the 19 beams that were not in compliance with the selection criteria and were excluded from the database analysis.

Table 20 lists the range of values for the main database variables in three groups of beams: those included or excluded in the statistical analysis and those part of this study. All D-type beams of this study were part of the group included in the analysis. The values in Table 20 indicate that most D-type beams in this study were within the range of values of the included group. The main variables include beam width (b_w), beam depth (h), aspect ratio (l_n/h), measured average concrete compressive strength (f_{cm}), measured yield stress (f_{ym}) of the diagonal reinforcement, hoop spacing-to-bar diameter ratio (s/d_b), normalized hoop spacing-to-bar diameter ratio ($[s/d_b]\sqrt{f_{ym}/60\ ksi}$), normalized shear stress ($v_{max}/\sqrt{f_{cm}}$), and chord rotation capacity

(CR_{cap}). The hoop spacing-to-diagonal bar diameter ratio (s/d_b) was normalized by the measured yield stress of the diagonal bar because the transverse reinforcement provides bracing to the diagonal bars and the Euler buckling equation indicates that buckling stress is inversely proportional to the square of s/d_b.

6.2 Analysis of Trends

Using data from Table 17, a linear regression in the form of Equation 6.1 was conducted to help identify the influence of parameters X_i on the beam chord rotation capacity. The selected parameters X_i were ℓ_n/h, f_{cm}, f_{ym} of the diagonal reinforcement, s/d_b, $(s/d_b)\sqrt{f_{ym}/60\ ksi}$, $A_{sh,provided}/A_{sh,required}$, and $v_{max}/\sqrt{f_{cm}}$. Table 21 shows the equation coefficients c_0 and c_1, the coefficient of determination r^2, and the coefficient of variation *CV* resulting from the linear regression for the selected variables. Coefficients c_0 and c_1 informed initial values for later multivariate regression analysis. Higher values of r^2 and lower values of *CV* indicate high correlation of the selected variable with chord rotation capacity.

$$CR_{cap} = c_0 + c_1 X_i \qquad \text{Equation 6.1}$$

Figures 658 through 673 show pairs of plots for each of the eight parameters that were selected for evaluation. The first plot within each pair shows chord rotation capacity versus the selected parameter. Beams with secondary longitudinal bars not developed (or cutoff) into the end blocks are shown with triangles while beams with developed secondary longitudinal reinforcement are shown with circles. The first plot within each pair from Figures 660 through 673 further separates the data based on the beam aspect ratio, with filled symbols for beams with aspect ratios

equal to or greater than 2.0 and hollow symbols for aspect ratios less than 2.0. The second plot within each pair identifies the Specimen Number from Table 17. The coordinates in the Figure for the symbol containing the Specimen Number were slightly tweaked to reduce overlap and improve readability.

Figures 658 and 659 show a moderate positive correlation (r^2 = 0.40; CV = 0.18) between chord rotation capacity and aspect ratio (ℓ_n/h). Figures 658 does not reveal a different trend for triangles than circles, which correspond to beams with cutoff and developed secondary longitudinal reinforcement, respectively.

Figures 660 through 663 show the correlations between measured concrete compressive strength (f_{cm}) or yield stress of the diagonal bars (f_{ym}) and chord rotation capacity. The plotted data show a poor correlation with chord rotation capacity, which was slightly proportional to f_{cm} (r^2 = 0.14; CV = 0.22) and slightly inversely proportional to f_{ym} (r^2 = 0.07; CV = 0.22).

The two pairs of plots in Figures 664 through 667 show chord rotation capacity plotted against hoop spacing-to-diagonal bar diameter ratio (s/d_b) and the normalized hoop spacing-to-diagonal bar diameter ratio ($[s/d_b]\sqrt{f_{ym}/60\ ksi}$). Both parameters show strong correlations to chord rotation capacity (r^2 = 0.63 and 0.66; CV = 0.15 and 0.14, respectively). Some of this correlation might be a result of the dataset, as specimens with s/d_b < 4 frequently had ℓ_n/h > 2 and specimens with s/d_b > 4 frequently had ℓ_n/h < 2. This is evident based on the distribution of solid and hollow symbols in Figures 664 through 667. A multivariate analysis that considers both s/d_b and ℓ_n/h, described later, will better capture these combined trends.

Figures 668 through 671 show poor correlation ($r^2 \leq 0.05$; $CV \geq 0.22$) between chord rotation capacity and $A_{sh,provided}/A_{sh,required}$ (perpendicular to beam width or depth). These results may be because 29 of the 33 beams in Table 17 complied with the Code[6] giving $A_{sh,provided}/A_{sh,required} \geq 1.0$. In addition, strain maxima in transverse reinforcement are likely below yielding, as shown for D-type beams in Section 5.4.

Figures 672 and 673 show that there is poor correlation (r^2 = 0.08; CV = 0.22) between chord rotation capacity and normalized shear stress ($v_{max}/\sqrt{f_{cm}}$). This is consistent with observations in this and previous studies[12,41,69] that the chord rotation capacity of well-detailed, diagonally-reinforced coupling beams is not sensitive to the shear stress.

6.3 Best-Fit Equation for Chord Rotation

A multivariate regression analysis was done on data from the 33 specimens listed in Table 17 using the parameters with the highest correlation to chord rotation capacity, ℓ_n/h and $(s/d_b)\sqrt{f_{ym}/60\ ksi}$, in a form similar to prior research (Eq. 5.2 [12]) to develop Equation 6.2, which was further simplified into Equation 6.3, after rounding. Equation 6.3 is similar to Eq. 5.2[12], which uses the same parameters but had coefficients of 9.75, 0.78, and -1.2 (compared with 9, 1, and -1 selected for Equation 6.3). Equation 6.4 is an oversimplification of Equation 6.3 after adopting a value of 6 for the normalized hoop spacing-to-diagonal bar diameter ratio ($[s/d_b]\sqrt{f_{ym}/60\ ksi}$). This value closely corresponds to the maximum value permitted by the Code[6]. All further discussion of calculated chord rotation capacity refers to Equation 6.3.

$$CR_{est} = 9.471 + 0.700\,\frac{l_n}{h} - 0.958\frac{s}{d_b}\sqrt{\frac{f_{ym}}{60\ ksi}}$$ Equation 6.2

$$r^2 = 0.771 \qquad CV = 0.111$$

$$CR_{est} = 9 + \frac{l_n}{h} - \frac{s}{d_b}\sqrt{\frac{f_{ym}}{60\ ksi}} \geq 3\%$$ Equation 6.3

$$r^2 = 0.764 \qquad CV = 0.116$$

$$CR_{est} = 3 + \frac{l_n}{h} \geq 3\%$$ Equation 6.4

$$r^2 = 0.402 \qquad CV = 0.182$$

A lower limit of chord rotation equal to 3% is proposed for the best-fit equations as it is unlikely that a well-detailed, diagonally-reinforced coupling beam would exhibit a chord rotation capacity less than 3%. All of the specimens listed in Table 17 exhibited a chord rotation capacity of at least 3%. As shown in Table 20, this analysis included diagonally-reinforced coupling beams with $1.0 \leq l_n/h \leq 3.5$, $2.3 \leq s/d_b \leq 6.0$, $2.5 \leq (s/d_b)\sqrt{f_{ym}/60\ ksi} \leq 6.2$, and 63 ksi $\leq f_{ym} \leq$ 128 ksi (434 to 883 MPa). Practical limits when using Equation 6.3 may be set to ℓ_n/h between 1 and 4, s/d_b between 2 and 6, and f_{ym} between 60 and 130 ksi (420 and 900 MPa). It is safe to assume $\ell_n/h = 3.5$ for $l_n/h > 3.5$ but there is insufficient data to assume Equations 6.2 through 6.4 apply for $\ell_n/h < 1.0$. Similarly, it is safe to assume $s/d_b = 2.0$ for values less than 2.0 while values of s/d_b greater than 6 are not Code[6] compliant.

Although not explicitly required in the limits given above for applying Equations 6.2 through 6.4, it is essential for diagonal bars to meet the minimum mechanical properties of ASTM A706[20], especially those related to ε_{su}, ε_{sf}, and f_t/f_y. Current versions of ASTM A706[20] do not specify minimum values for ε_{su}, though ACI 318-19[7] does.

Figure 674 shows the measured chord rotation capacity versus the calculated chord rotation capacity using Equation 6.3 for the beams included in Table 17. Values above a 45-degree line correspond to measured chord rotation capacities greater than those calculated by Equation 6.3. The two dashed lines represent the mean plus or minus one standard deviation. These lines were obtained by multiplying the trend line values by one plus or minus the coefficient of variation (a factor of 1 ± 0.116). Inspection of Figure 674 indicates that when adopting 2 standard deviations or 0.78 times the mean, only one specimen of 33 would have a measured-to-calculated ratio less than 1.0.

Figure 675 shows the relationship between measured and calculated chord rotation capacity using data from Figure 674 with additional specimens, represented by diamonds, that were part of the database but excluded from the best-fit analysis (listed in Table 18). The 3% chord rotation minimum was applied to the calculated chord rotation capacity of several specimens from Table 18 (Specimen Numbers 35, 36, 39, and 52)[51,65,118].

Figure 676 shows the same points as in Figure 675 with increased symbol size and label corresponding to the Specimen Number shown in Table 17 or 18. Positions of the symbols and numerical labels were slightly tweaked to increase readability by reducing overlap.

Figures 677 and 678 show the measured-to-calculated chord rotation capacity ratio versus l_n/h and $(s/d_b)\sqrt{f_{ym}/60\ ksi}$, respectively, for specimens shown in Table 17. The dashed lines

indicate a width of two standard deviations centered on the trend line. Both Figures show the trend line of the ratios is approximately centered on 1.0 for the range of parameters considered.

CHAPTER 7: SUMMARY AND CONCLUSIONS

Experimental data are reported for eleven large-scale reinforced concrete coupling beams subjected to reversed cyclic displacements. This research was conducted to investigate the use of high-strength reinforcement in diagonally-reinforced (D-type) and moment frame (P-type) coupling beams. Variables included nominal yield stress of the primary longitudinal reinforcement (80, 100, and 120 ksi [550, 690, and 830 MPa]), span-to-depth (aspect) ratio (1.5, 2.5, and 3.5), and layout of primary longitudinal reinforcement (diagonal [D] and parallel [P]). All beams had the same nominal concrete compressive strength (8,000 psi [55 MPa]) and cross-sectional dimensions (12 by 18 in. [310 by 460 mm]). The D-type beams were designed for a target shear strength of $8\sqrt{f_c', \text{psi}}\, b_w h$ ($0.67\sqrt{f_c', \text{MPa}}\, b_w h$) and the P-type beams for $6\sqrt{f_c', \text{psi}}\, b_w d$ ($0.5\sqrt{f_c', \text{MPa}}\, b_w d$). All transverse and secondary longitudinal reinforcement were Grade 80 (550) except in D120-2.5, which had all Grade 120 (830) reinforcement, an aspect ratio of 2.5, and developed secondary longitudinal reinforcement into supports. A summary of the test data is listed in Table 16. The main findings and observations from this study are summarized as follows:

1. Chord rotation capacities of D-type beams with Grade 100 or Grade 120 (690 or 830) diagonal reinforcement and secondary longitudinal bars cutoff near the wall face were similar, with average deformation capacities of approximately 5, 6, and 7% for beams with aspect ratios of 1.5, 2.5, and 3.5, respectively. Deformation capacity was based on the average chord rotation (for positive and negative loading directions) corresponding to 20% loss of strength. These deformation capacities exceeded the minimum chord rotation capacities in ASCE 41-17[16] for diagonally-reinforced coupling beams.

2. Beam D120-2.5 exhibited a chord rotation capacity of 6.9% compared with 6.0% for D100-2.5. The improved deformation capacity of D120-2.5 was attributed to the combined effects of 1) extending the non-diagonal longitudinal reinforcement into the end blocks to develop $1.25f_y$, which reduced localized rotations (and therefore diagonal bar strain demands) at the beam-wall interface and 2) using 50% more transverse reinforcement (in terms of $\rho_t f_{yt}$) than other D-type beams. Beam D120-2.5 also reached a strength of $15\sqrt{f_{cm}, \text{psi}}\, b_w h$ ($1.25\sqrt{f_{cm}, \text{MPa}}\, b_w h$) approximately 75% higher than the usable strength (ϕV_n) permitted in ACI 318-14[6].
3. D-type beams with Grade 80 (550) diagonal reinforcement exhibited approximately 25% higher chord rotation capacities, on average, than their Grade 100 or Grade 120 (690 or 830) counterparts. The increased rotation capacity of the beams with Grade 80 (550) diagonal bars may be attributed to their lower ratio of f_y to s/d_b, where f_y is the yield stress of the diagonal bar, d_b is the diameter of the diagonal bar, and s is the spacing of the hoops, which delayed buckling of the Grade 80 (550) diagonal bars during testing.
4. Chord rotation capacities of P-type beams with Grade 80 or Grade 100 (550 or 690) longitudinal reinforcement were similar, with an average chord rotation capacity of approximately 4% for beams with an aspect ratio of 2.5 and shear stresses near $6\sqrt{f_{cm}}$ psi ($0.5\sqrt{f_{cm}}$ MPa).
5. D-type beams with secondary longitudinal reinforcement not developed into supports exhibited concentrated rotations near the beam-block interface, with up to 90% of chord rotation attributable to beam-end rotation. Beam D120-2.5 with developed secondary longitudinal reinforcement had more distributed damage throughout the beam span. For this study, the combination of this difference in damage and the use of 50% more transverse

reinforcement (in terms of $\rho_t f_{yt}$) than other D-type beams resulted in higher deformation capacity for the beam with developed secondary longitudinal reinforcement.

6. Measured strength of D-type beams was 30 to 90% higher than the calculated nominal shear strength (V_n for a diagonally-reinforced coupling beam based on f_{ym}). Therefore, the expected strength of diagonally-reinforced coupling beams was underestimated if based only on the contribution of the diagonal reinforcement. The highest overstrength occurred in D120-2.5, which extended the secondary longitudinal reinforcement into the end blocks to develop $1.25f_y$.
7. Measured strength of P-type beams was 10 to 20% higher than the calculated nominal flexural strength (M_n based on f_{cm} and f_{ym}). Therefore, the probable flexural strength (based on $1.25f_y$) was conservative for determining the required shear reinforcement for these beams.
8. For the coupling beams of this study, the initial stiffness associated with the secant to 75% of the maximum shear (on the ascending branch of the shear-chord rotation envelope) was consistently lower than the recommended value in ASCE 41-17[16]. The effective moment of inertia (I_{eff}) corresponding to the initial stiffness varied between 0.04 I_g to 0.17 I_g, with the lower coefficients for beams with aspect ratios of 1.5 and higher coefficients for beams with aspect ratios of 3.5. These values of I_{eff} account for the effects of shear deformations and bar slip (or strain penetration into supports). For beams designed to achieve similar strength (with constant ρf_y), the initial stiffness was inversely proportional to the reinforcement grade.
9. Hysteretic energy dissipation was negatively correlated to aspect ratio and yield stress of the primary reinforcement for coupling beams designed to achieve similar strength (with constant ρf_y). The energy dissipation index (E_h), during the second cycle to 3% chord rotation, ranged from approximately 0.15 to 0.25 for D-type beams with an aspect ratio of 1.5, and from 0.1 to

0.2 for beams with an aspect ratio of 3.5. The high end of these values were for beams with Grade 80 (550) reinforcement and the low end for beams with Grade 120 (830) reinforcement. Values of E_h for D-type beams were nearly twice of those for P-type beams with the same aspect ratio and reinforcement grade.

10. Residual chord rotations (or chord rotations associated with zero shear) were generally inversely proportional to the beam aspect ratio and the yield stress of the primary longitudinal reinforcement. During the cycles to chord rotations between 1 and 4%, D-type beams consistently showed lower residual chord rotations than P-type beams, an outcome closely related to the higher force levels reached by D-type beams.
11. Maximum beam elongation values (based on optical marker data) were generally inversely proportional to aspect ratio and yield stress of the primary longitudinal reinforcement. At chord rotations approaching 4%, elongation maxima of 2.3, 1.3, and 0.9% were determined for beams with aspect ratios of 1.5, 2.5, and 3.5, respectively. The maximum beam elongation in P-type beams was approximately 1% at chord rotations of 3 and 4%, lower than those in D-type beams, including D120-2.5.
12. Changes in beam depth (based on optical marker data) were generally larger at the beam-block interfaces or adjacent layers. The maximum observed change in beam depth, at chord rotations near 4%, was between 0.4 and 0.8% for D-type beams (excluding D120-2.5, which reached 1.4% with developed secondary longitudinal reinforcement). For D-type beams, changes in beam depth were nearly insensitive to beam aspect ratio and yield stress of the primary longitudinal reinforcement. P-type beams exhibited larger changes in beam depth than in D-type beams, reaching approximately 4% at chord rotations approaching 4%. The larger change in beam depth in D120-2.5 and the P-type beams are consistent with the greater extent of damage observed

within the span of these beams relative to D-type beams with secondary bars terminated near the wall face.

13. Beam-end rotation was consistently the component with the largest contribution but nearly insensitive to the yield stress of the primary longitudinal reinforcement. During the cycles to chord rotations between 2 and 3%, the contributions of beam-end rotation in D-type beams were inversely proportional to the beam aspect ratio, with contributions as high as 80% for beams with an aspect ratio of 1.5 and 65% for beams with an aspect ratio of 3.5. The contributions of beam-end rotation in P-type beams (with an aspect ratio of 2.5) were as high as 40%.
14. Strain gauge measurements from diagonal bars of nine D-type beams showed maximum strains of 8% at a chord rotation of 4%, with lower maxima occurring in D120-2.5, which extended the secondary longitudinal reinforcement into the end blocks to develop $1.25f_y$. Strain gauge data from the two P-type beams showed that maximum strains in the primary longitudinal bars reached 4.5% at a chord rotation of 3%.
15. Using a database of 33 specimens, a best fit equation was developed to estimate the chord rotation capacity (CR_{est}) of diagonally-reinforced coupling beams:

$$CR_{est} = 9 + \frac{l_n}{h} - \frac{s}{d_b}\sqrt{\frac{f_{ym}}{60\ ksi}} \geq 3\%$$

The beam aspect ratio and the normalized hoop spacing-to-bar diameter ratio were chosen from parameters in the database because they were found to have the strongest correlation with chord rotation capacity of well-detailed diagonally-reinforced coupling beams. The equation applies for

ℓ_n/h between 1 and 4, s/d_b between 2 and 6, and f_{ym} between 60 and 130 ksi (420 and 900 MPa). For $\ell_n/h = 2$ and $(s/d_b)\sqrt{f_{ym}/60\ ksi} = 6$, $CR_{est} = 5\%$.

REFERENCES

1. Abdalla, J.A., Hawileh, R.A., Oudah, F., and Abdelrahman, K. (2009). "Energy-Based Prediction of Low-Cycle Fatigue Life of BS 460B and BS B500B Steel Bars." Materials & Design, 30(10), 4405-4413.

2. ACI 318 (1963). "Building Code Requirements for Reinforced Concrete (ACI 318-63)." American Concrete Institute, Detroit, Michigan.

3. ACI 318 (1999). "Building Code Requirements for Structural Concrete (ACI 318-99) and Commentary (ACI 318R-99)." American Concrete Institute, Farmington Hills, Michigan.

4. ACI 318 (2005). "Building Code Requirements for Structural Concrete (ACI 318-05) and Commentary (ACI 318R-05)." American Concrete Institute, Farmington Hills, Michigan.

5. ACI 318 (2008). "Building Code Requirements for Structural Concrete (ACI 318-08) and Commentary (ACI 318R-08)." American Concrete Institute, Farmington Hills, Michigan.

6. ACI 318 (2014). "Building Code Requirements for Structural Concrete (ACI 318-14) and Commentary (ACI 318R-14)." American Concrete Institute, Farmington Hills, Michigan.

7. ACI 318 (2019). "Building Code Requirements for Structural Concrete (ACI 318-19) and Commentary (ACI 318R-19)." American Concrete Institute, Farmington Hills, Michigan.

8. ACI 369 (2017). "Standard Requirements for Seismic Evaluation and Retrofit of Existing Concrete Buildings (ACI 369.1-17) and Commentary." American Concrete Institute, Farmington Hills, Michigan.

9. ACI 408 (2003). "Bond and Development of Straight Reinforcing Bars in Tension (ACI 408R-03)." American Concrete Institute, Farmington Hills, Michigan.

10. ACI 501 (1936). "Building Regulations for Reinforced Concrete (ACI 501-36T)." ACI Journal Proceedings, 32(2), 407-447.

11. Agrawal, G.L., Tulin, L.G., and Gersite, K.H. (1965). "Response of Doubly Reinforced Concrete Beams to Cyclic Loading." ACI Journal Proceedings, 62(7), 823-836.

12. Ameen, S., Lequesne, R.D., and Lepage, A. (2020). "Diagonally-Reinforced Concrete Coupling Beams with High-Strength Steel Bars." SM Report No. 138, University of Kansas Center for Research, Inc., Lawrence, Kansas.

13. Ameen, S., Lequesne, R.D., Lepage, A., Weber-Kamin, A.S., and Huq, M.S. (2017). "Behavior of Diagonally-Reinforced Concrete Coupling Beams with High-Strength Steel Bars." 16th World Conference on Earthquake Engineering (16WCEE). Santiago, Chile.

14. Aoyama, H. (2001). "Design of Modern High-Rise Reinforced Concrete Structures." Imperial College Press, London, United Kingdom.

15. ASCE 41 (2006). “Seismic Evaluation and Retrofit of Existing Buildings (ASCE/SEI 41-06).” American Society of Civil Engineers, Reston, Virginia.

16. ASCE 41 (2017). “Seismic Evaluation and Retrofit of Existing Buildings (ASCE/SEI 41-17).” American Society of Civil Engineers, Reston, Virginia.

17. ASTM A1035 (2016). “Standard Specification for Deformed and Plain, Low-Carbon, Chromium, Steel Bars for Concrete Reinforcement (ASTM A1035/1035M-16b).” ASTM International, West Conshohocken, Pennsylvania.

18. ASTM A370 (2017). “Standard Test Methods and Definitions for Mechanical Testing of Steel Products (ASTM A370-17).” ASTM International, West Conshohocken, Pennsylvania.

19. ASTM A615 (2016). “Standard Specification for Deformed and Plain Carbon-Steel Bars for Concrete Reinforcement (A615-16/A615M-16).” ASTM International, West Conshohocken, Pennsylvania.

20. ASTM A706 (2016). “Standard Specification for Deformed and Plain Low-Alloy Steel Bars for Concrete Reinforcement (ASTM A706/A706M-16).” ASTM International, West Conshohocken, Pennsylvania.

21. ASTM C143 (2015). “Standard Test Method for Slump of Hydraulic-Cement Concrete (ASTM C143/C143M-15a).” ASTM International, West Conshohocken, Pennsylvania.

22. ASTM C33 (2016). “Standard Specification for Concrete Aggregates (ASTM C33/C33M-16).” ASTM International, West Conshohocken, Pennsylvania.

23. ASTM C39 (2017). “Standard Test Method for Compressive Strength of Cylindrical Concrete Specimens (ASTM C39/C39M-17a).” ASTM International, West Conshohocken, Pennsylvania.

24. ASTM C494 (2016). “Standard Specification for Chemical Admixtures for Concrete (ASTM C494/C494M-16).” ASTM International, West Conshohocken, Pennsylvania.

25. ASTM C496 (2011). “Standard Test Method for Splitting Tensile Strength of Cylindrical Concrete Specimens (ASTM C496/C496M-11).” ASTM International, West Conshohocken, Pennsylvania.

26. ASTM E8 (2016). “Standard Test Methods for Tension Testing of Metallic Materials (ASTM E8/E8M-16a).” ASTM International, West Conshohocken, Pennsylvania.

27. ATC 40 (1996). “Seismic Evaluation and Retrofit of Concrete Buildings (ATC-40).” California Seismic Safety Commission, Report SSC 96-01, Applied Technology Council, Redwood City, California.

28. ATC 72-1 (2010). “Modeling and Acceptance Criteria for Seismic Design and Analysis of Tall Buildings.” Applied Technology Council, Redwood City, California.

29. Barbosa, A.R., Trejo, D., Nielson, D., Mazerei, V., and Tibbits, C. (2017). “High Strength Reinforcing Steel Bars: Low–Cycle Fatigue Behavior (FHWA-OR-RD-17-09).” Oregon State University, Corvallis, Oregon.

30. Barcley, L. and Kowalsky, M. (2019). “Critical Bending Strain of Reinforcing Steel and the Buckled Bar Tension Test.” ACI Materials Journal, 116(3), 53-61.

31. Barney, G.B., Shiu, K.N. Rabbat, B.G., Fiorato, A.E., Russell, H.G., and Corley, W.G. (1980). “Behavior of Coupling Beams Under Load Reversals.” Portland Cement Association Bulletin RD068.01B, Skokie, Illinois.

32. Bertero, V.V., Popov, E.P., and Wang, T.Y. (1974). “Hysteretic Behavior of Reinforced Concrete Flexural Members with Special Web Reinforcement.” Report No. EERC 74-9, Earthquake Engineering Research Center, University of California, Berkeley.

33. Binney, J.R. (1972). “Diagonally Reinforced Coupling Beams.” MS Thesis, University of Canterbury, Christchurch, New Zealand.

34. Biskinis, D.E., Roupakias, G.K., and Fardis, M.N. (2004). “Degradation of Shear Strength of Reinforced Concrete Members with Inelastic Cyclic Displacements.” ACI Structural Journal, 101(6), 773-783.

35. Breña, S.F., Unal, A.M., and Wood, S.L. (1998). “Seismic Response of Lightly-Reinforced Coupling Beams.” 6th U.S. National Conference on Earthquake Engineering (6NCEE). Seattle, Washington.

36. Bristowe, S., Cook, W., and Mitchell, D. (1997). Influence of High-Strength Concrete on the Seismic Response of Coupling Beams. Proceedings of the Canadian Society for Civil Engineering Conference, Vol. 4, 319-328.

37. Brown, J. and Kunnath, S.K. (2004). “Low-Cycle Fatigue Failure of Reinforcing Steel Bars.” ACI Materials Journal, 101(6), 457-466.

38. Brown, R.H. and Jirsa, J.O. (1971). “Reinforced Concrete Beams Under Load Reversals.” ACI Journal Proceedings, 68(5), 380-390.

39. Budek, A.M., Priestley, M.J.N., and Lee, C.O. (2002). “Seismic Design of Columns with High-Strength Wire and Strand as Spiral Reinforcement.” ACI Structural Journal, 99(5), 660-670.

40. Canbolat, B.A., Parra-Montesinos, G.J., and Wight, J.K. (2005). “Experimental Study on Seismic Behavior of High-Performance Fiber-Reinforced Cement Composite Coupling Beams.” ACI Structural Journal, 102(1), 159-166.

41. Cheng, M.-Y., Gitomarsono, J., and Zeng, H.-Y. (2019). “Cyclic Test of Diagonally Reinforced Concrete Coupling Beam with Different Shear Demand.” ACI Structural Journal, 116(6), 241-250.

42. Cheng, M.-Y., Hung, S.-C., Lequesne, R.D., and Lepage, A. (2016). "Earthquake-Resistant Squat Walls Reinforced with High-Strength Steel." ACI Structural Journal, 113(5), 1065-1076.

43. Choi, K.-K. and Park, H.-G. (2010). "Evaluation of Inelastic Deformation Capacity of Beams Subjected to Cyclic Loading." ACI Structural Journal, 107(5), 507-515.

44. Choi, Y., Hajyalikhani, P., and Chao, S.-H. (2018). "Seismic Performance of Innovative Reinforced Concrete Coupling Beam – Double-Beam Coupling Beam." ACI Structural Journal, 115(1), 113-125.

45. Coull, A. (1974). "Stiffening of Coupled Shear Walls Against Foundation Movement." Structural Engineer, 52(1), 23-26.

46. CSA A23.3 (1994). "Design of Concrete Structures (CSA A23.3-94)." Canadian Standards Association, Toronto, Canada.

47. Elwood, K.J., Matamoros, A.B., Wallace, J.W., Lehman, D.E., Heintz, J.A., Mitchell, A.D., Moore, M.A., Valley, M.T., Lowes, L.N., Comartin, C.D., and Moehle, J.P. (2007). "Update to ASCE/SEI 41 Concrete Provisions." Earthquake Spectra, 23(3), 493-523.

48. FEMA 461 (2007). "Interim Testing Protocols for Determining the Seismic Performance Characteristics of Structural and Nonstructural Components (FEMA 461)." Applied Technology Council, Redwood City, California.

49. Filippou, F.C, Popov, E.P., and Bertero, V.V.(1983). "Effects of Bond Deterioration on Hysteretic Behavior of Reinforced Concrete Joints." Report No. UCB/EERC-83/19, Earthquake Engineering Research Center, University of California, Berkeley, California.

50. Fortney, P.J., Rassati, G.A. and Shahrooz, B.M. (2008). "Investigation on Effect of Transverse Reinforcement on Performance of Diagonally-Reinforced Coupling Beams." ACI Structural Journal, 105(6), 781-788.

51. Galano, L. and Vignoli, A. (2000). "Seismic Behavior of Short Coupling Beams with Different Reinforcement Layouts." ACI Structural Journal, 97(6), 876-885.

52. Germundsson, T. (1941). "Columns with High Yield Point Reinforcement Designed under the ACI Code." ACI Journal Proceedings, Vol. 37, 569-576.

53. Ghannoum, W.M. and Slavin, C.M. (2015). "Defining Structurally Acceptable Properties of High-Strength Steel Bars through Material and Column Testing – Part I: Material Testing Report." CPF Research Grant Agreement #05-14, Charles Pankow Foundation, Vancouver, Washington.

54. Ghannoum, W.M. and Slavin, C.M. (2016). "Low-Cycle Fatigue Performance of High-Strength Steel Reinforcing Bars." ACI Materials Journal, 113(6), 803-814.

55. Godfrey, E. (1920). “Reinforcement for Diagonal Tension in Reinforced Concrete Beams.” Concrete, 17(1), 15-20.

56. Gonzalez, E. (2001). “Seismic Response of Diagonally Reinforced Slender Coupling Beams.” MS Thesis, The University of British Columbia, Vancouver, British Columbia, Canada.

57. Han, S.W., Lee, C.S., Shin, M., and Lee, K. (2015). “Cyclic Performance of Precast Coupling Beams with Bundled Diagonal Reinforcement.” Engineering Structures, Vol. 93, 142-151.

58. Harries, K.A., Fortney, P.J., Shahrooz, B.M., and Brienen, P.J. (2005). “Practical Design of Diagonally-Reinforced Concrete Coupling Beams – Critical Review of ACI 318 Requirements.” ACI Structural Journal, 102(6), 876-882.

59. Haselton, C.B., Liel, A.B., Taylor-Lange, S.C., and Deierlein, G.G. (2008). “Beam-Column Element Model Calibrated for Predicting Flexural Response Leading to Global Collapse of RC Frame Buildings (PEER Report 2007/03).” Pacific Earthquake Engineering Research Center, University of California, Berkeley, California.

60. Hawileh, R.A., Abdalla, J.A., Oudah, F., and Abdelrahman, K. (2010). “Low-Cycle Fatigue Life Behaviour of BS 460B and BS B500B Steel Reinforcing Bars.” Fatigue & Fracture of Engineering Materials & Structures, 33(7), 397-407.

61. Hognestad, E. (1961). “High Strength Bars as Concrete Reinforcement. Part 1 – Introduction to a Series of Experimental Reports.” Journal of the PCA Research and Development Laboratories, 3(3), 23-29.

62. Huq, M.S., Burgos, A.E., Lequesne, R.D., and Lepage, A. (2018). “High-Strength Steel Bars in T-Shaped Concrete Walls.” 11th U.S. National Conference on Earthquake Engineering, Los Angeles, California.

63. Irwin, A.W. and Ord, A.E.C. (1976). “Cyclic Load Tests on Shear Wall Coupling Beams.” Proceedings of the Institution of Civil Engineers, 61(2), 331-342.

64. Kuramoto, H., Minami, K., and Wakabayashi, M. (1988). “Deformation Capacity of Diagonally Reinforced Concrete Short Columns Subject to High Axial Compressive Stress.” 9th World Conference on Earthquake Engineering (9WCEE), Tokyo-Kyoto, Japan.

65. Kwan, A.K.H. and Zhao, Z.-Z. (2002). "Cyclic Behavior of Deep Reinforced Concrete Coupling Beams.” Proceedings of the Institution of Civil Engineers - Structures and Buildings, 152(3), 283-293.

66. Lepage, A., Tavallali, H., Pujol, S., and Rautenberg, J.M. (2012). “High-Performance Steel Bars and Fibers as Concrete Reinforcement for Seismic-Resistant Frames.” Advances in Civil Engineering, Hindawi Publishing Corporation.

67. Lequesne, R.D. (2011). “Behavior and Design of High-Performance Fiber-Reinforced Concrete Coupling Beams and Coupled-Wall Systems.” PhD Dissertation, University of Michigan, Ann Arbor, Michigan.

68. Lequesne, R.D., Parra-Montesinos, G.J., and Wight, J.K. (2013). “Seismic Behavior and Detailing of High-Performance Fiber-Reinforced Concrete Coupling Beams and Coupled Wall Systems.” ASCE Journal of Structural Engineering, 139(8), 1362-1370.

69. Lim, E., Hwang, S.-J., Cheng, C.-H., and Lin, P.-Y. (2016). “Cyclic Tests of Reinforced Concrete Coupling Beam with Intermediate Span-Depth Ratio.” ACI Structural Journal, 113(3), 515-524.

70. Lim, E., Hwang, S.-J., Wang, T.-W., and Chang, Y.-H. (2016). “An Investigation on the Seismic Behavior of Deep Reinforced Concrete Coupling Beams.” ACI Structural Journal, 113(2), 217-226.

71. Luisoni, C.J., Somenson, H.M., and Ungaro, M.A. (1970). “Experimental Verification of the Elastic and Plastic Calculus of a Shear Wall.” XIV Jornadas Sudamericanas de Ingeniería Estructural y IV Simposio Panamericano de Estructuras, Buenos Aires, Argentina, Vol. 5, 230-286. (In Spanish).

72. Mander, J.B., Panthaki, F.D., and Kasalanati, A. (1994). “Low-Cycle Fatigue Behavior of Reinforcing Steel.” ASCE Journal of Materials in Civil Engineering, 6(4), 453-468.

73. Mau, S.T. and El-Mabsout, M. (1989). "Inelastic Buckling of Reinforcing Bars." ASCE Journal of Engineering Mechanics, 115(1), 1-17.

74. Menegotto, M. and Pinto, P.E. (1973). "Method of Analysis for Cyclically Loaded Reinforced Concrete Plane Frames Including Changes in Geometry and Non-Elastic Behavior of Elements Under Combined Normal Force and Bending Moment." Symposium on Resistance and Ultimate Deformability of Structures Acted on by Well Defined Reported Loads, Proceedings of IABSE, Vol. 11, 15-22.

75. Monti, G. and Nuti, C. (1992). “Nonlinear Cyclic Behavior of Reinforcing Bars Including Buckling.” ASCE Journal of Structural Engineering, 118(12), 3268-3284.

76. Morsch, E. (1909). “Concrete-Steel Construction.” English Translation by E. P. Goodrich, The Engineering News Publishing Company, New York.

77. Morsch, E. (1927). “Zur Frage Der Schubsicherung der Eisenbetonbalken (The Problem of Diagonal Shear Reinforcement of Reinforced Concrete Beams).” Der Bauingenieur, 8(16), 277-283. (In German).

78. Motter, C.J., Fields, D.C., Hooper, J.D., Klemencic, R., and Wallace, J.W. (2017). “Steel-Reinforced Concrete Coupling Beams. II: Modeling.” ASCE Journal of Structural Engineering, 143(3), 04016192.

79. Muguruma, H. and Watanabe, F. (1990). “Ductility Improvement of High-Strength Concrete Columns with Lateral Confinement.” ACI Special Publication, SP-121, 47-60.

80. Naish, D. (2010). “Testing and Modeling of Reinforced Concrete Coupling Beams.” PhD Dissertation, University of California, Los Angeles, California.

81. Naish, D., Fry, A., Klemencic, R., and Wallace, J. (2013). “Reinforced Concrete Coupling Beams – Part I: Testing.” ACI Structural Journal, 110(6), 1057-1066.

82. Naish, D., Fry, A., Klemencic, R., and Wallace, J. (2013). “Reinforced Concrete Coupling Beams – Part II: Modeling.” ACI Structural Journal, 110(6), 1067-1075.

83. NIST GCR 14-917-30 (2014). “Use of High-Strength Reinforcement in Earthquake-Resistant Concrete Structures.” National Institute of Standards and Technology, Gaithersburg, Maryland.

84. NZS 3101 (1995). “Concrete Structures Standard (NZS 3101:1995).” Standards New Zealand, Wellington, New Zealand.

85. Otani, S. (1981). “Hysteresis Models of Reinforced Concrete for Earthquake Response Analysis.” The University of Tokyo Journal of the Faculty of Engineering, 36(2), 125-159.

86. Otani, S., Nagai, S., and Aoyama, H. (1996). “Load-Deformation Relationship of High-Strength Reinforced Concrete Beams.” ACI Special Publication, SP-162, 35-52.

87. Pantazopoulou, S.J. (1998). ‘‘Detailing for Reinforcement Stability in RC Members.’’ ASCE Journal of Structural Engineering, 124(6), 623-632.

88. Park, R. (1988). “State-of-the-Art Report: Ductility Evaluation from Laboratory and Analytical Testing”, 9th World Conference on Earthquake Engineering (9WCEE), Tokyo-Kyoto, Japan.

89. Park, W.-S., Kang, T.H.-K., Kim, S., and Yun, H.-Y. (2020). “Seismic Performance of Moderately Short Concrete Coupling Beams with Various Reinforcements.” ACI Structural Journal, 117(3), 141-154.

90. Paulay, T. (1969). “The Coupling of Shear Walls.” PhD Dissertation, University of Canterbury, Christchurch, New Zealand.

91. Paulay, T. (1971). “Coupling Beams of Reinforced Concrete Shear Walls.” ASCE Journal of the Structural Division, 97(3), 843-862.

92. Paulay, T. and Binney, J.R. (1974). “Diagonally Reinforced Coupling Beams of Shear Walls.” ACI Special Publication, SP-42, 579-598.

93. PEER TBI (2017). “Guidelines for Performance-Based Seismic Design of Tall Buildings (PEER Report 2017/06).” Pacific Earthquake Engineering Research Center, Tall Buildings Initiative, University of California, Berkeley, California.

94. Poudel, A., Lequesne, R.D., and Lepage, A. (2018). “Diagonally-Reinforced Concrete Coupling Beams: Effects of Axial Restraint.” SL Report 18-3. University of Kansas Center for Research, Inc., Lawrence, Kansas.

95. Rautenberg, J.M., Pujol, S., Tavallali, H., and Lepage, A. (2012). “Reconsidering the Use of High-Strength Reinforcement in Concrete Columns.” Engineering Structures, Vol. 37, 135-142.

96. Rautenberg, J.M., Pujol, S., Tavallali, H., and Lepage, A. (2013). “Drift Capacity of Concrete Columns Reinforced with High-Strength Steel.” ACI Structural Journal, 110(2), 307-317.

97. Richart, F.E. and Brown, R.L. (1934). “An Investigation of Reinforced Concrete Columns.” Bulletin No. 267, University of Illinois Experiment Station, Urbana, Illinois.

98. Rodriguez, M.E., Botero, J.C., and Villa, J. (1999). “Cyclic Stress-Strain Behavior of Reinforcing Steel Including Effect of Buckling.” ASCE Journal of Structural Engineering, 125(6), 605-612.

99. Scribner, C.F. and Wight, J.K. (1980). “Strength Decay in RC Beams under Load Reversals.” ASCE Journal of the Structural Division, 106(4), 861-876.

100. Shiu, K.N., Barney, G.B., Fiorato, A.E., and Corley W.G. (1978) “Reversing Load Tests of Reinforced Concrete Coupling Beams.” Proceedings of the Central American Conference on Earthquake Engineering, San Salvador, El Salvador.

101. Sokoli D. and Ghannoum W.M. (2016). “High-Strength Reinforcement in Columns under High Shear Stresses.” ACI Structural Journal, 113(3), 605-614.

102. Sokoli, D., Limantono, A., and Ghannoum, W.M. (2017). “Defining Structurally Acceptable Properties of High-Strength Steel Bars through Material and Column Testing - Part II: Column Testing Report.” CPF Research Grant Agreement #05-14, Charles Pankow Foundation, Vancouver, Washington.

103. Sonobe, Y., Kanakubo, T., Fujisawa, M., Fukuyama, H., Tanigaki, M., and Okamoto, T. (1995). “Structural Performance of Concrete Beams Reinforced with Diagonal FRP Bars.” Non-Metallic (FRP) Reinforcement for Concrete Structures, Proceedings of the Second International RILEM Symposium (FRPRCS-2), Ghent, Belgium.

104. Stafford Smith, B. and Coull, A. (1991). “Tall Building Structures: Analysis and Design.” John Wiley and Sons, Inc., New York.

105. Subedi, N.K. (1990). “Ultimate Strength Analysis of Reinforced Concrete Coupling Beams.” The Structural Engineer, 68(3), 45-50.

106. Subedi, N.K. (1991). “RC Coupled Shear Wall Structures. I: Analysis of Coupling Beams.” ASCE Journal of Structural Engineering, 117(3), 667-680.

107. Suda, K., Murayama, Y., Ichinomiya, T., and Shimbo, H. (1996). ‘‘Buckling Behavior of Longitudinal Reinforcing Bars in Concrete Columns Subjected to Reversed Lateral Loading.’’ 11th World Conference on Earthquake Engineering (11WCEE), Acapulco, Mexico.

108. Sugano, S., Nagashima, T., Kimura, H., Tamura, A., and Ichikawa, A. (1990). “Experimental Studies on Seismic Behavior of Reinforced Concrete Members of High Strength Concrete.” ACI Special Publication, SP-121, 61-87.

109. Tassios, T.P., Moretti, M., and Bezas, A. (1996). “On the Behavior and Ductility of Reinforced Concrete Coupling Beams of Shear Walls.” ACI Structural Journal, 93(6), 711-720.

110. Tavallali, H., Lepage, A., Rautenberg, J.M., and Pujol, S. (2014). “Concrete Beams Reinforced with High-Strength Steel Subjected to Displacement Reversals.” ACI Structural Journal, 111(5), 1037-1048.

111. Tegos, I.A. and Penelis, G.G. (1988). “Seismic Resistance of Short Columns and Coupling Beams Reinforced with Inclined Bars.” ACI Structural Journal, 85(1), 82-88.

112. To, D.V. and Moehle, J.P. (2017). “Seismic Performance Characterization of Beams with High-Strength Reinforcement.” CPF Research Grant Agreement #04-14, Charles Pankow Foundation, Vancouver, Washington.

113. Todeschini, C.E., Bianchini, A.C., Kesler, C.E. (1964). “Behavior of Concrete Columns Reinforced with High Strength Steels.” ACI Journal Proceedings, 61(6), 701-716.

114. Vu, N.S., Li, B., and Beyer, K. (2014). “Effective Stiffness of Reinforced Concrete Coupling Beams.” Engineering Structures, Vol. 76, 371-382.

115. Wight, J.K. and Sozen, M.A. (1975). “Strength Decay of RC Columns Under Shear Reversals.” ASCE Journal of the Structural Division, 101(5), 1053-1065.

116. Xiao, Y., Esmaeily-Ghasemabadi, A., and Wu, H. (1999). “High-Strength Concrete Short Beams Subjected to Cyclic Shear.” ACI Structural Journal, 96(3), 392-399.

117. Yotakhong, P. (2003). “Flexural Performance of MMFX Reinforcing Rebars in Concrete Structures.” MS Thesis, North Carolina State University, Raleigh, North Carloina.

118. Yun, H.D., Kim, S.W., Jeon, E., Ji, S.K., Park, W.S. (2007). “Seismic Performance of Shear Dominant Coupling Beams Using High-Performance Fiber-Reinforced Cement-Based Composites.” 8th Pacific Conference on Earthquake Engineering (8PCEE), Singapore.

119. Zhong, K. and Deierlein, G.G. (2019). “Low-Cycle Fatigue Effects on the Seismic Performance of Concrete Frame and Wall Systems with High Strength Reinforcing Steel.” CPF Research Grant #02-16, Charles Pankow Foundation, Vancouver, Washington.

TABLES

Table 1 – Design data for coupling beam specimens [a]
(1 in. = 25.4 mm, 1 ksi = 1,000 psi = 6.89 MPa)

Coupling Beam [b]				Primary Longitudinal Reinforcement							Transverse Reinforcement			
Id.	v_e	$\frac{\ell_n}{h}$	ℓ_n	f_y	n	d_b	ℓ_e [c]	A_{vd}	α	A_s	Weak Axis [d]	Strong Axis [e]	f_{yt}	s
	$\sqrt{f'_c}$, psi		in.	ksi		in.	in.	in.^{2}	degrees	in.^{2}	in.^{2}	in.^{2}	ksi	in.
D80-1.5	8.4	1.5	27	80	6	0.75	21	2.64	22.7	-	0.44	0.33	80	3
D100-1.5	8.8	1.5	27	100	5	0.75	27	2.20	22.7	-	0.44	0.33	80	3
D120-1.5	8.4	1.5	27	120	4	0.75	34	1.76	22.7	-	0.44	0.33	80	3
D80-2.5	8.0	2.5	45	80	9	0.75	21	3.96	14.2	-	0.44	0.33	80	3
D100-2.5	7.8	2.5	45	100	7	0.75	27	3.08	14.2	-	0.44	0.33	80	3
D120-2.5	8.0	2.5	45	120	6	0.75	34	2.64	14.2	-	0.44	0.33	120	3
D80-3.5	7.8	3.5	63	80	9	0.875	24	5.40	10.0	-	0.44	0.33	80	3
D100-3.5	7.3	3.5	63	100	9	0.75	27	3.96	10.3	-	0.44	0.33	80	3
D120-3.5	7.8	3.5	63	120	8	0.75	34	3.52	10.3	-	0.44	0.33	80	3
P80-2.5	5.2	2.5	45	80	3	0.75	21	-	-	1.32	0.22	0.33	80	3.5
P100-2.5	6.4	2.5	45	100	3	0.75	27	-	-	1.32	0.22	0.33	80	3

[a] For notation and definitions, see APPENDIX A: NOTATION.

[b] All specimens have $f'_c = 8{,}000$ psi, $h = 18\ in.$, $b_w = 12\ in.$, and $c_c = 0.75\ in.$ to No. 3 (10) transverse reinforcement. Specimen Id. starts with D for cases with diagonal reinforcement and P for cases with parallel reinforcement, see Figure 1.

[c] Minimum straight embedment length based on ACI 408R-03 Eq. 4.11(a)[9] using $\phi = \omega = \alpha = \beta = \lambda = 1$, $(c\ \omega + K_{tr})/d_b = 4$, $1.25 f_y$ psi, and $f'_c = 8{,}000$ psi. Grade 80 (550) No. 3 (10) longitudinal reinforcing bars were terminated approximately 2 in. into the top and bottom blocks consistent with the detailing recommendations in the ACI Building Code[6] commentary, except for Grade 120 (830) No. 3 (10) longitudinal reinforcing bars in D120-2.5 with a minimum straight embedment length of 17 in. into the top and bottom blocks.

[d] Transverse reinforcement along the 12-in. width of the coupling beam; four legs of No. 3 (10) bars at spacing *s* for D-type beams and two legs of No. 3 (10) bars for P-type beams.

[e] Transverse reinforcement along the 18-in. depth of the coupling beam; three legs of No. 3 (10) bars at spacing *s*.

Table 2 – Measured compressive and tensile strengths of concrete [a] (1,000 psi = 6.89 MPa)

Coupling Beam Identification	Cast Date	Test Date	Age (days)	f_{cm} [b] (psi)	f_{ct} [c] (psi)
D80-1.5	3 Nov 17	1 May 18	179	7,600	710
D100-1.5	3 Nov 17	9 Apr 18	157	8,200	720
D120-1.5	3 Nov 17	31 May 18	209	7,600	610
D80-2.5	16 Jun 17	3 Oct 17	109	8,400	620
D100-2.5	30 Jun 17	29 Nov 17	152	8,000	790
D120-2.5	18 Aug 17	6 Mar 18	200	7,800	760
D80-3.5	26 Jul 17	19 Jun 18	328	7,800	660
D100-3.5	26 Jul 17	6 Jul 18	345	7,900	650
D120-3.5	18 Aug 17	25 Jul 18	341	8,200	660
P80-2.5	16 Jun 17	10 Nov 17	147	8,300	790
P100-2.5	30 Jun 17	12 Dec 17	165	7,500	790

[a] For notation and definitions, see APPENDIX A: NOTATION.

[b] Tested in accordance with ASTM C39[23], average of two tests of 6 by 12 in. (150 by 310 mm) cylinders.

[c] Tested in accordance with ASTM C496[25], average of two tests of 6 by 12 in. (150 by 310 mm) cylinders.

Table 3 – Concrete mixture proportions
(1 lb = 4.45 N, 1 gal = 128 oz = 3.79 L, 1 in. = 25.4 mm, 1 yd^3 = 0.764 m^3)

Constituent Materials	Unit	Date of Casting				
		16 Jun 17	30 Jun 17	26 Jul 17	18 Aug 17	3 Nov 17
		Coupling Beam Identification				
		D80-2.5, P80-2.5	D100-2.5, P100-2.5	D80-3.5, D100-3.5	D120-2.5, D120-3.5	D80-1.5, D100-1.5, D120-1.5
Water	gal/yd^3	34	34	34	35	33
Cementitious Material (*CM*)						
Cement, Type I/II	lb/yd^3	647	647	645	668	662
Fly Ash, Type C	lb/yd^3	149	158	148	157	149
Fine Aggregate [a]	lb/yd^3	1740	1725	1674	1714	1720
Coarse Aggregate [a]	lb/yd^3	1180	1184	1194	1178	1177
Admixtures [b]						
Set Retarder	oz/yd^3	32	32	32	32	32
Rheology Modifier	oz/yd^3	48	48	48	48	48
Water Reducer	oz/yd^3	56	56	56	56	56
Water/*CM*		0.36	0.35	0.36	0.35	0.34
Initial Slump [c]	in.	9.0	10.5	9.0	9.5	9.0
Ticket Number [d]		20079637	20080213	20081466	20082382	20085070

[a] Maximum aggregate size of 0.5 in. Aggregate compliant with ASTM C33[22].

[b] Concrete arrived at laboratory with tabulated amounts of admixtures. Supplemental water-reducing admixture was added in the laboratory to achieve a minimum 20-in. spread before casting. Admixtures compliant with ASTM C494[24].

[c] Slump measured in accordance with ASTM C143[21] when concrete arrived at laboratory.

[d] Batch ticket number for ready-mix concrete supplied by Midwest Concrete Materials.

Table 4 – Reinforcing steel properties [a] (1 in. = 25.4 mm, 1 ksi = 6.89 MPa)

Coupling Beam Identification	Bar Size	Nominal Bar Diameter	Yield Stress [b]		Tensile Strength [b]	f_t/f_{ym}	Uniform Elongation [c]	Fracture Elongation [d]
	No.	d_b in.	f_{ym} ksi	f_{ytm} ksi	f_t ksi		ε_{su} %	ε_{sf} %
D80-1.5 D80-2.5 P80-2.5	3 (10)	0.375		89	113		9.7	12.9
	6 (19)	0.75	83		110	1.33	9.2	13.3
D80-3.5	3 (10)	0.375		89	113		9.7	12.9
	7 (22)	0.875	84		114	1.36	10.0	16.4
D100-1.5 D100-2.5 D100-3.5 P100-2.5	3 (10)	0.375		89	113		9.7	12.9
	6 (19)	0.75	108		125	1.16	6.8	9.8
D120-1.5 D120-3.5	3 (10)	0.375		89	113		9.7	12.9
	6 (19)	0.75	116		163	1.41	5.2	9.9
D120-2.5	3 (10)	0.375	133	133	173	1.30	4.5	6.3
	6 (19)	0.75	116		163	1.41	5.2	9.9

[a] For notation and definitions, see APPENDIX A: NOTATION.

[b] Tested in accordance with ASTM A370[18].

[c] Corresponds to strain at peak stress, in accordance with ASTM E8[26], based on 8-in. gauge length

[d] Calculated strain corresponding to zero stress on a line with slope equal to modulus of elasticity and passing through the fracture point, based on 8-in. gauge length.

Table 5 – Specimen and actuator nominal elevations relative to strong floor (1 in. = 25.4 mm)

$\frac{l_n}{h}$	Top of Bottom Block (in.)	Bottom of Top Block (in.)	Actuator A Centerline (in.)	Actuator B Centerline (in.)
1.5	39.5	66.5	21	87
2.5	36.5	81.5	45	87
3.5	36.5	99.5	51	130

Table 6 – List of strain gauges on primary and secondary longitudinal reinforcement

			Coupling Beam Identification										
			D80-1.5	D100-1.5	D120-1.5	D80-2.5	D100-2.5	D120-2.5	D80-3.5	D100-3.5	D120-3.5	P80-2.5	P100-2.5
Primary Reinforcement	Diagonal	D1	X	X	X	X	X	X	X	O	X		
		D2	X	O	X	O	X	X	X	X	X		
		D3	X	X	X	X	X	X	X	O	X		
		D4	X	X	X	X	X	X	X	X	X		
		D5	X	X	X	X	O	X	X	X	X		
		D6	X	X	X	X	X	X	X	X	X		
		D7	X	X	X	X	X	X	X	X	X		
		D8	X	X	X	X	X	X	O	X	X		
		D9	O	X	X	O	X	O	X	X	X		
		D10	X	X	X	X	X	X	X	X	X		
		D11	X	X	X	X	O	X	X	X	X		
		D12	X	X	X	X	O	X	X	X	X		
		D13	X	X	O	O	X	X	X	X	X		
		D14	X	X	X	X	X	X	X	X	X		
	Parallel [a]	P1										X	X
		P2										X	O
		P3										X	X
		P4										X	X
		P5										X	X
		P6										X	O
		P7										X	X
		P8										X	O
		P9										X	X
		P10										X	X
		P11										X	X
		P12										X	X
Secondary Reinforcement	Parallel [b]	H1	X	O	O	X	X	X	X	X	X		
		H2	X	O	X	X	O	X	O	X	X		
		H3	X	X	X	X	O	X	O	X	X		
		H4	X	X	X	X	X	X	X	O	X		
		H5	X	X	O	X	X	O	X	O	X		
		H6	X	X	X		X	O	X	X			
		H7		X	X				O	X			
		H8		O	X				X				
		H9	X	X	O								
		H10		X	X								
		H11	X	O	X								
		H12	X	X									
		H13	X										
		H14	X										

"X" indicates strain gauge is present.
"O" indicates strain gauge is present but data not available due to instrument malfunction.

[a] No. 6 (19) reinforcement placed parallel to the longitudinal axis of the P-type beams.

[b] No. 3 (10) reinforcement placed parallel to the longitudinal axis of the D-type beams.

Table 7 – List of strain gauges on transverse reinforcement

Transverse Reinforcement		Coupling Beam Identification										
		D80-1.5	D100-1.5	D120-1.5	D80-2.5	D100-2.5	D120-2.5	D80-3.5	D100-3.5	D120-3.5	P80-2.5	P100-2.5
Closed Stirrups	S1	O	O	X	O	X	O	O	O	O	X	X
	S2	X	X	X	X	X	X	X	X	X	X	X
	S3	X	X	X	X	X	X	X	X	X	O	X
	S4	X	X	X	X	X	X	X	X	X	O	X
	S5	X	X	X	X	O	X	X	X	X	X	X
	S6	X	O	X	X	X	X	X	X	X	X	X
	S7	X	X	X	X	X	X	X	X	X	X	X
	S8	X	X	X	X	X	X	X	X	X	X	X
	S9	X	X	X	X	X	X	X	O	X	X	X
	S10						X					
	S11						X					
	S12						X					
	S13						X					
	S14						X					
	S15						X					
	S16						X					
	S17						X					
	S18						O					
Crossties	T1	X	X	O	X	X	X	X	X	X	X	X
	T2	X	X	O	X	X	X	X	X	X		
	T3	X	X	X	O	X	X	X	X	X		
	T4	X	X	X								
	T5		X	X								
	T6			X								

"X" indicates strain gauge is present.
"O" indicates strain gauge is present but data not available due to instrument malfunction.

Table 8 – Loading protocol (1 in. = 25.4 mm)

Step [a]	Chord Rotation [b] %	Loading Rate in./s [c]
1	0.20	0.01
2	0.30	0.01
3	0.50	0.01
4	0.75	0.01
5	1.00	0.02
6	1.50	0.02
7	2.00	0.02
8	3.00	0.03
9	4.00	0.03
10	6.00	0.04
11	8.00	0.04
12	10.00	0.04

[a] Two cycles of loading per step, following recommendations in FEMA 461[48], see Figure 36.

[b] Based on the relative lateral displacement between end blocks divided by the beam clear span (excluding contributions due to sliding of the specimen and rotation of the end blocks).

[c] Loading rate of coupling beams with aspect ratios of 1.5 and 2.5. Coupling beams with an aspect ratio of 3.5 were tested at twice these rates.

Table 9 – Coupling beam maximum shear stress and deformation capacity [a]
(1,000 psi = 6.89 MPa, 1 kip = 4.45 kN)

Coupling Beam Id.	Maximum Applied Shear V_{max} kips	Maximum Applied Shear Stress v_{max} $\sqrt{f_{cm}}$, psi	Deformation Capacity A [b] %	Deformation Capacity B [c] %
D80-1.5	254	13.5	6.1	6.9
D100-1.5	257	13.1	4.9	5.3
D120-1.5	264	14.0	4.6	5.2
D80-2.5	220	11.1	7.1	7.6
D100-2.5	220	11.4	5.4	6.0
D120-2.5	286	15.0	6.6	6.9
D80-3.5	219	11.5	8.3	8.6
D100-3.5	196	10.2	6.3	6.8
D120-3.5	216	11.0	6.5	6.7
P80-2.5	91	5.0	3.6	3.9
P100-2.5	110	6.4	3.6	4.1

[a] For notation and definitions, see APPENDIX A: NOTATION.

[b] The average of the chord rotations reached in each loading direction before strength diminished to less than 80% of the maximum applied shear.

[c] The average of the maximum chord rotations in each loading direction where the envelope of the shear versus chord rotation curve (formed by connecting the maximum chord rotation of the first cycle of each loading step) intersects 80% of the maximum applied shear.

Table 10 – Chord rotation cycle and bar location where bar fracture was observed

Coupling Beam Id.	Cycle where Bar Fracture was First Observed [a]	Number of Fractured Bars Observed After Testing Divided by Total Bars in Each Group or Layer Located at:			
		Bottom Tension [b]	Bottom Compression [c]	Top Tension [b]	Top Compression [c]
D80-1.5	–6B	4 / 6	1 / 6	1 / 6	4 / 6
D100-1.5	–6A	5 / 5	0 / 5	1 / 5	2 / 5
D120-1.5	–4A	1 / 4	0 / 4	1 / 4	4 / 4
D80-2.5	–8A	2 / 9	2 / 9	0 / 9	9 / 9
D100-2.5	–6A	0 / 7	0 / 7	0 / 7	7 / 7
D120-2.5 [d]	+6A	2 / 6	2 / 6	0 / 6	1 / 6
D80-3.5	–8A	3 / 9	0 / 9	8 / 9	3 / 9
D100-3.5	+6B	2 / 9	8 / 9	3 / 9	3 / 9
D120-3.5	–6A	3 / 8	1 / 8	8 / 8	1 / 8
P80-2.5		0 / 3	0 / 3	0 / 3	0 / 3
P100-2.5		0 / 3	0 / 3	0 / 3	0 / 3

[a] The notation in this column refers to the displacement direction (+ or –) , target chord rotation in percent, and first (A) or second (B) cycle to that target chord rotation.

[b] The bar group (or layer) that would be in tension during the positive loading direction (i.e., near bottom west side or top east side).

[c] The bar group (or layer) that would be in compression during the positive loading direction (i.e., near bottom east side or top west side).

[d] The secondary longitudinal reinforcement in D120-2.5 consisted of No. 3 (10) Grade 120 (830) steel bars, which were developed into the end blocks. Based on strain gauge data, these bars were first observed to fracture at approximately +4% chord rotation during the first cycle to +6% chord rotation. Inspection after testing confirmed that 5 of the 10 No. 3 (10) bars had fractured (1 near the top block and 4 near the bottom block, see Figure 72).

Table 11 – Force-deformation envelope for D-type coupling beams with aspect ratio of 1.5 (1 kip = 4.45 kN, 1 in. = 25.4 mm)

Target Chord Rot.	D80-1.5				D100-1.5				D120-1.5			
	Actual Chord Rot.	Shear		Secant Stiffness	Actual Chord Rot.	Shear		Secant Stiffness	Actual Chord Rot.	Shear		Secant Stiffness
CR	CR [a]	V	V / V_{max} [b]	K_S	CR [a]	V	V / V_{max} [b]	K_S	CR [a]	V	V / V_{max} [b]	K_S
%	%	kips		kips / in.	%	kips		kips / in.	%	kips		kips / in.
-10												
-8	-8.23	-31.75	0.13	14					-8.56	-31.43	0.12	14
-6	-6.07	-226.30	0.95	138	-6.61	-151.45	0.59	85				
-4	-4.09	-235.70	0.99	213	-4.24	-216.96	0.84	190	-4.88	-237.76	0.91	180
-3	-3.01	-235.67	0.99	290	-3.08	-241.74	0.94	291	-3.20	-261.53	1.00	303
-2	-1.90	-229.89	0.96	448	-2.05	-246.26	0.96	445	-2.06	-254.64	0.97	458
-1.5	-1.54	-223.37	0.93	537	-1.74	-257.10	1.00	547	-1.60	-246.66	0.94	571
	-1.44	-228.92	0.96	589								
-1	-1.12	-238.91	1.00	790	-1.04	-238.81	0.93	850	-1.05	-209.23	0.80	738
-.75	-0.78	-221.76	0.93	1053	-0.78	-202.63	0.79	962	-0.77	-177.18	0.68	852
-.5	-0.51	-171.53	0.72	1246	-0.52	-168.44	0.66	1200	-0.52	-138.50	0.53	986
-.3	-0.31	-124.27	0.52	1485	-0.32	-123.83	0.48	1433	-0.31	-92.79	0.35	1109
-.2	-0.21	-96.21	0.40	1697	-0.22	-103.48	0.40	1742	-0.20	-68.89	0.26	1276
0	0.00	1.37	0.01	0	0.00	3.83	0.02	0	0.00	2.37	0.01	0
.2	0.20	80.68	0.32	1494	0.22	82.98	0.33	1397	0.21	71.26	0.27	1257
.3	0.30	103.95	0.41	1283	0.31	99.00	0.39	1183	0.31	91.17	0.35	1089
.5	0.50	150.30	0.59	1113	0.51	142.57	0.57	1035	0.52	120.71	0.46	860
.75	0.75	197.28	0.78	974	0.77	185.55	0.74	892	0.76	157.36	0.60	767
1	0.99	229.39	0.90	858	1.01	223.96	0.89	821	1.02	189.37	0.72	688
1.5	1.48	248.17	0.98	621	1.47	251.72	1.00	634	1.52	231.26	0.88	563
2	2.12	254.24	1.00	444	2.03	240.36	0.95	439	2.08	254.60	0.96	453
	2.69	252.05	0.99	347								
3	2.98	251.50	0.99	313	2.95	241.39	0.96	303	2.99	264.11	1.00	327
4	3.87	248.72	0.98	238	3.99	229.06	0.91	213	4.16	243.43	0.92	217
					5.60	218.95	0.87	145	5.44	192.14	0.73	131
6	6.11	246.22	0.97	149	6.04	185.41	0.74	114	6.09	141.53	0.54	86
8	8.22	170.00	0.67	77	8.30	20.79	0.08	9				
10												
$-0.75\ V_{max}$ [c]	-0.55	-179	0.75	1207	-0.70	-193	0.75	1016	-0.93	-196	0.75	777
$+0.75\ V_{max}$ [c]	0.71	191	0.75	990	0.79	189	0.75	887	1.11	198	0.75	656

[a] The actual chord rotation, CR, associated with the peak force for each loading step. CR is the measured displacement of the top block relative to the bottom block divided by the coupling beam clear span, ℓ_n, and corrected for relative rotation of the end blocks.

[b] V_{max} is the maximum measured shear force in the respective loading direction.

[c] The interpolated chord rotation at the intersection of $0.75\ V_{max}$ (before V_{max}) and the shear-chord rotation envelope.

Table 12 – Force-deformation envelope for D-type coupling beams with aspect ratio of 2.5 (1 kip = 4.45 kN, 1 in. = 25.4 mm)

Target Chord Rot.	D80-2.5				D100-2.5				D120-2.5			
	Actual Chord Rot.	Shear		Secant Stiffness	Actual Chord Rot.	Shear		Secant Stiffness	Actual Chord Rot.	Shear		Secant Stiffness
CR	CR [a]	V	V / V_{max} [b]	K_S	CR [a]	V	V / V_{max} [b]	K_S	CR [a]	V	V / V_{max} [b]	K_S
%	%	kips		kips / in.	%	kips		kips / in.	%	kips		kips / in.
-10	-10.01	-20.96	0.10	5								
-8	-7.91	-131.70	0.60	37	-7.99	-46.15	0.21	13	-8.35	-119.57	0.42	32
-6	-5.91	-216.84	0.99	82	-6.04	-127.65	0.58	47	-6.42	-243.63	0.86	84
-4	-3.85	-215.74	0.98	125	-4.67	-216.89	0.99	103	-4.30	-283.51	1.00	146
-3	-3.11	-220.13	1.00	157					-3.15	-272.27	0.96	192
-2	-2.03	-213.19	0.97	233	-2.48	-220.12	1.00	197	-2.04	-241.03	0.85	263
-1.5	-1.51	-201.65	0.92	297	-1.50	-207.61	0.94	308	-1.56	-217.28	0.77	310
-1	-0.99	-170.95	0.78	384	-0.98	-167.82	0.76	381	-1.00	-162.48	0.57	361
-.75	-0.70	-144.26	0.66	458	-0.75	-138.02	0.63	409	-0.74	-134.47	0.47	404
-.5	-0.47	-108.58	0.49	513	-0.50	-101.22	0.46	450	-0.53	-105.53	0.37	442
-.3	-0.28	-80.44	0.37	638	-0.29	-73.03	0.33	560	-0.31	-65.09	0.23	467
-.2	-0.23	-72.21	0.33	698	-0.19	-60.27	0.27	705	-0.20	-40.35	0.14	448
0	0.00	0.00	0.00	0	0.00	0.00	0.00	0	0.01	2.10	0.01	467
.2	0.23	63.45	0.29	613	0.20	58.02	0.27	645	0.20	40.13	0.14	446
.3	0.38	92.87	0.43	543	0.33	76.62	0.36	516	0.31	64.96	0.23	466
.5	0.48	106.54	0.49	493	0.54	102.19	0.48	421	0.61	116.76	0.41	425
.75	0.76	142.91	0.66	418	0.81	144.25	0.67	396	0.77	138.26	0.48	399
1	0.98	166.18	0.76	377	1.04	170.74	0.80	365	1.01	168.12	0.59	370
1.5	1.89	212.34	0.97	250	1.45	203.97	0.95	313	1.50	216.83	0.76	321
2	2.06	193.89	0.89	209	2.16	214.25	1.00	220	2.10	251.95	0.88	267
3	2.92	209.56	0.96	159	3.06	210.68	0.98	153	3.15	277.43	0.97	196
4	3.94	207.45	0.95	117	4.02	194.51	0.91	108	4.29	285.94	1.00	148
									5.80	271.60	0.95	104
6	6.00	217.95	1.00	81	6.01	191.05	0.89	71	6.68	251.57	0.88	84
8	8.17	180.68	0.83	49	8.12	124.04	0.58	34	9.11	94.56	0.33	23
10												
$-0.75\ V_{max}$ [c]	-0.92	-165	0.75	398	-0.96	-165	0.75	382	-1.50	-213	0.75	313
$+0.75\ V_{max}$ [c]	0.96	163	0.75	380	0.95	161	0.75	375	1.47	214	0.75	323

[a] The actual chord rotation, CR, associated with the peak force for each loading step. CR is the measured displacement of the top block relative to the bottom block divided by the coupling beam clear span, ℓ_n, and corrected for relative rotation of the end blocks.

[b] V_{max} is the maximum measured shear force in the respective loading direction.

[c] The interpolated chord rotation at the intersection of $0.75\ V_{max}$ (before V_{max}) and the shear-chord rotation envelope.

Table 13 – Force-deformation envelope for D-type coupling beams with aspect ratio of 3.5 (1 kip = 4.45 kN, 1 in. = 25.4 mm)

Target Chord Rot.	D80-3.5				D100-3.5				D120-3.5			
	Actual Chord Rot.	Shear		Secant Stiffness	Actual Chord Rot.	Shear		Secant Stiffness	Actual Chord Rot.	Shear		Secant Stiffness
CR	CR [a]	V	V / V_{max} [b]	K_S	CR [a]	V	V / V_{max} [b]	K_S	CR [a]	V	V / V_{max} [b]	K_S
%	%	kips		kips / in.	%	kips		kips / in.	%	kips		kips / in.
-10	-10.29	-53.91	0.25	8	-10.25	-38.06	0.20	6				
-8	-8.24	-182.26	0.84	35	-8.09	-102.84	0.54	20	-7.91	-93.00	0.43	19
-6	-6.04	-217.50	1.00	57	-6.35	-180.91	0.94	45	-6.38	-184.10	0.85	46
-4	-4.13	-209.83	0.96	81	-4.12	-186.92	0.97	72	-4.08	-215.70	1.00	84
-3	-3.09	-207.46	0.95	107	-3.10	-191.73	1.00	98	-3.01	-214.54	0.99	113
-2	-2.16	-204.24	0.94	150	-2.11	-189.19	0.99	142	-1.97	-191.87	0.89	155
-1.5	-1.56	-195.04	0.90	198	-1.58	-175.56	0.92	176	-1.58	-172.44	0.80	173
-1	-1.08	-164.62	0.76	242	-1.05	-134.79	0.70	204	-1.03	-129.45	0.60	199
-.75	-0.77	-125.98	0.58	260	-0.76	-106.16	0.55	222	-0.77	-105.13	0.49	217
-.5	-0.51	-95.35	0.44	297	-0.51	-77.91	0.41	242	-0.51	-78.48	0.36	244
-.3	-0.30	-66.42	0.31	351	-0.31	-55.74	0.29	285	-0.31	-55.70	0.26	285
-.2	-0.22	-46.14	0.21	333	-0.22	-45.86	0.24	331	-0.20	-40.57	0.19	322
0	0.00	-0.16	0.00	0	0.00	1.63	0.01	0	0.00	0.06	0.00	0
.2	0.22	49.87	0.23	360	0.26	52.65	0.27	321	0.23	43.16	0.20	298
.3	0.34	71.92	0.33	336	0.31	57.99	0.30	297	0.33	57.05	0.27	274
.5	0.51	95.47	0.44	297	0.53	86.95	0.44	260	0.53	79.80	0.38	239
.75	0.78	130.92	0.60	266	0.77	114.71	0.59	236	0.78	104.60	0.49	213
1	1.08	166.34	0.76	244	1.02	139.32	0.71	217	1.02	126.60	0.60	197
1.5	1.55	196.19	0.90	201	1.57	177.08	0.90	179	1.55	161.65	0.76	166
2	2.03	206.40	0.95	161	2.02	187.53	0.96	147	2.07	182.77	0.86	140
3	3.13	212.97	0.98	108	3.16	195.99	1.00	98	3.04	211.46	1.00	110
4	4.16	211.81	0.97	81	4.36	189.27	0.97	69	4.14	212.40	1.00	81
6	5.96	219.40	1.00	57	6.20	184.12	0.94	47	6.53	191.10	0.90	46
8	8.28	211.74	0.97	41	8.11	94.05	0.48	18	8.48	62.12	0.29	12
10	10.20	84.96	0.39	13	10.25	34.29	0.17	5				
$-0.75\ V_{max}$ [c]	-1.07	-163	0.75	243	-1.17	-144	0.75	195	-1.44	-162	0.75	178
$+0.75\ V_{max}$ [c]	1.06	165	0.75	245	1.14	147	0.75	206	1.52	159	0.75	167

[a] The actual chord rotation, CR, associated with the peak force for each loading step. CR is the measured displacement of the top block relative to the bottom block divided by the coupling beam clear span, ℓ_n, and corrected for relative rotation of the end blocks.

[b] V_{max} is the maximum measured shear force in the respective loading direction.

[c] The interpolated chord rotation at the intersection of $0.75\ V_{max}$ (before V_{max}) and the shear-chord rotation envelope.

Table 14 – Force-deformation envelope for P-type coupling beams with aspect ratio of 2.5 (1 kip = 4.45 kN, 1 in. = 25.4 mm)

Target Chord Rot.	P80-2.5				P100-2.5			
	Actual Chord Rot.	Shear		Secant Stiffness	Actual Chord Rot.	Shear		Secant Stiffness
CR	CR [a]	V	V / V_{max} [b]	K_S	CR [a]	V	V / V_{max} [b]	K_S
%	%	kips		kips / in.	%	kips		kips / in.
-10								
-8								
-6	-6.03	-16.81	0.19	6	-6.53	-29.39	0.27	10
-4	-4.06	-39.15	0.44	21	-4.02	-96.44	0.89	53
-3	-3.04	-77.09	0.86	56	-3.23	-106.60	0.98	73
-2	-1.98	-89.56	1.00	101	-2.05	-108.48	1.00	118
-1.5	-1.50	-87.17	0.97	129	-1.46	-104.53	0.96	159
-1	-1.01	-82.07	0.92	181	-0.99	-95.65	0.88	215
-.75	-0.84	-80.11	0.89	212	-0.73	-82.75	0.76	252
-.5	-0.47	-66.10	0.74	313	-0.50	-67.15	0.62	298
-.3	-0.35	-58.97	0.66	374	-0.29	-50.74	0.47	389
-.2	-0.19	-42.31	0.47	495	-0.23	-44.38	0.41	429
0	0.00	0.00	0.00	0	0.00	0.00	0.00	0
.2	0.18	42.34	0.47	523	0.23	41.34	0.38	399
.3	0.31	52.68	0.58	378	0.35	51.10	0.47	324
.5	0.55	73.64	0.81	298	0.58	63.98	0.58	245
.75	0.82	84.79	0.94	230	0.77	83.49	0.76	241
1	1.00	84.80	0.94	188	1.09	98.78	0.90	201
1.5	1.58	88.92	0.98	125	1.76	109.85	1.00	139
2	1.93	88.61	0.98	102	2.11	107.52	0.98	113
3	2.86	90.58	1.00	70	3.18	106.76	0.97	75
4	4.09	80.15	0.88	44	4.10	76.02	0.69	41
6	7.09	30.53	0.34	10	6.15	48.95	0.45	18
8								
10								
$-0.75\ V_{max}$ [c]	-0.50	-67	0.75	299	-0.71	-81	0.75	255
$+0.75\ V_{max}$ [c]	0.48	68	0.75	311	0.76	82	0.75	242

[a] The actual chord rotation, CR, associated with the peak force for each loading step. CR is the measured displacement of the top block relative to the bottom block divided by the coupling beam clear span, ℓ_n, and corrected for relative rotation of the end blocks.

[b] V_{max} is the maximum measured shear force in the respective loading direction.

[c] The interpolated chord rotation at the intersection of $0.75\ V_{max}$ (before V_{max}) and the shear-chord rotation envelope.

Table 15 – Coupling beam measured and calculated strengths [a]
(1,000 psi = 6.89 MPa, 1 kip = 4.45 kN)

Coupling Beam Id.	Measured		Calculated			Measured-to-Calculated Ratio [b]
	V_{max} kips	v_{max} $\sqrt{f_{cm}}$, psi	V_{nm} kips	$2M_{nm}/l_n$ kips	v_{nm} $\sqrt{f_{cm}}$, psi	
D80-1.5	254	13.5	169	-	9.0	1.50
D100-1.5	257	13.1	183	-	9.4	1.40
D120-1.5	264	14.0	158	-	8.4	1.68
D80-2.5	220	11.1	161	-	8.1	1.36
D100-2.5	220	11.4	163	-	8.4	1.35
D120-2.5	286	15.0	150	-	7.9	1.90
D80-3.5	219	11.5	158	-	8.3	1.39
D100-3.5	196	10.2	153	-	8.0	1.28
D120-3.5	216	11.0	146	-	7.5	1.48
P80-2.5	91	5.0	-	77	4.3	1.18
P100-2.5	110	6.4	-	99	5.8	1.11

[a] For notation and definitions, see APPENDIX A: NOTATION.

[b] The average of measured-to-calculated ratios is 1.43 for D-type beams (excluding D120-2.5, which had secondary longitudinal reinforcement developed into the end blocks) and 1.15 for P-type beams.

Table 16 – Summary of test data [a]
(1 ksi = 1000 psi = 6.89 MPa)

Coupling Beam Id.	Reinforcement Type	$\frac{\ell_n}{h}$	f_{cm}	f_{ym}	f_{ytm}	v_{max} [b]	v_{nm} [c]	Measured Chord Rotation Capacity [d]	ASCE 41-17 Chord Rotation Capacity [e]
			psi	ksi	ksi	$\sqrt{f_{cm}}$, psi	$\sqrt{f_{cm}}$, psi	%	%
D80-1.5	Diagonal	1.5	7,600	83	89	13.5	9.0	6.9	5.0
D100-1.5	Diagonal	1.5	8,200	108	89	13.1	9.4	5.3	5.0
D120-1.5	Diagonal	1.5	7,600	116	89	14.0	8.4	5.2	5.0
D80-2.5	Diagonal	2.5	8,400	83	89	11.1	8.1	7.6	5.0
D100-2.5	Diagonal	2.5	8,000	108	89	11.4	8.4	6.0	5.0
D120-2.5	Diagonal	2.5	7,800	116	133	15.0	7.9	6.9	5.0
D80-3.5	Diagonal	3.5	7,800	84	89	11.5	8.3	8.6	5.0
D100-3.5	Diagonal	3.5	7,900	108	89	10.3	8.0	6.8	5.0
D120-3.5	Diagonal	3.5	8,200	116	89	11.0	7.5	6.7	5.0
P80-2.5	Parallel	2.5	8,300	83	89	5.0	4.3	3.9	4.0 [f]
P100-2.5	Parallel	2.5	7,500	108	89	6.4	5.8	4.1	4.0 [f]

[a] For notation and definitions, see APPENDIX A: NOTATION.

[b] Shear stress associated with maximum applied shear V_{max}.
For D-type beams, $v_{max} = V_{max}/(b_w h)$.
For P-type beams, $v_{max} = V_{max}/(b_w d)$.

[c] For D-type beams, $v_{nm} = (2A_{vd}\, f_{ym} \sin\alpha)/(b_w h)$.
For P-type beams, $v_{nm} = (2M_{nm}/\ell_n)/(b_w d)$.

[d] The average of the maximum chord rotations in each loading direction where the envelope curve (formed by connecting the maximum chord rotation of the first cycle of each loading step) intersects with 80% of the maximum applied shear.

[e] Chord rotation capacity from ASCE 41-17[16] Table 10-19 corresponding to the maximum chord rotation associated with the residual strength defined by segment D-E in ASCE 41-17[16] Figure 10-1(b). It is important to note that the measured chord rotation capacity (see footnote d) corresponds to a residual strength greater than those used in ASCE 41-17[16], where the residual strength is defined as 80% of the strength at point B in Figure 10-1(b)[16] (instead of point C, which represents the maximum).

[f] The reported ASCE 41-17[16] chord rotation capacity is taken from Table 10-19[16] and corresponds to a residual strength of 50% of the strength at point B in Figure 10-1(b)[16]. In contrast, the measured chord rotation capacity (see footnote d) corresponds to the chord rotation associated with a post-peak strength of 80% of the maximum applied shear.

Table 17 – Database of diagonally-reinforced coupling beams included in derivation of best-fit equation for chord rotation capacity [a]
(1 in. = 25.4 mm, 1 ksi = 1000 psi = 6.89 MPa, 1 kip = 4.45 kN)

Specimen Number			1	2	3	4	5	6	7	8	9	10	11	12	13	14	15	16
Reference			Ameen et al. (2020)[12]					Canbolat et al. (2005)[40]	Cheng et al. (2019)[41]						Fortney et al. (2008)[50]	Gonzalez (2001)[56]	Lim et al. (2016)[69]	
Specimen Id.			CB1	CB2	CB2D	CB2AD [f]	CB3D	1	D1.5_L [f]	D1.5_H [f]	D1.5_H2 [f]	D2.5_L [f]	D2.5_H [f]	D3.5_L [f]	DCB-2	K [f]	CB30-DA	CB30-DB
Beam Properties	b_w	in.	10.0	10.0	10.0	10.0	10.0	7.9	11.0	11.0	11.0	11.0	11.0	11.0	10.0	12.0	11.8	11.8
	h	in.	18.0	18.0	18.0	18.0	18.0	23.6	19.0	19.0	19.0	19.0	19.0	19.0	12.0	17.5	19.7	19.7
	Confinement [b]		Full	Full	Full	Full	Full	Diag.	Full	Full	Full	Full	Full	Full	Diag.	Diag.	Diag.	Full
	$b_c \perp b_w$ [c]	in.	8.5	8.5	8.5	8.5	8.5	4.6	9.0	9.0	9.0	9.0	9.0	9.0	5.0	7.7	5.5	10.2
	$b_c \perp h$ [c]	in.	16.5	16.5	16.5	16.5	16.5	4.6	17.0	17.0	17.0	17.0	17.0	17.0	4.3	4.6	4.9	16.5
	ℓ_n	in.	34.0	34.0	34.0	34.0	34.0	23.6	28.0	28.0	28.0	47.0	47.0	67.0	36.0	48.0	59.1	59.1
	ℓ_n/h		1.89	1.89	1.89	1.89	1.89	1.00	1.47	1.47	1.47	2.47	2.47	3.53	3.00	2.74	3.00	3.00
	f_{cm}	psi	6000	7200	6300	5650	6200	5950	4400	6600	7000	4700	5100	6800	8000	5150	5750	5550
Diagonal Reinforcement	Quantity	ea. diag.	6	4	4	4	6	4	4	8	4	4	6	4	4	4	4	4
	α	degrees	18.0	18.0	18.0	18.0	18.0	36.0	20.9	20.9	18.5	9.0	12.5	8.9	12.8	12.3	8.8	8.8
	d_b	in.	0.88	0.75	0.75	0.75	0.75	0.50	0.75	0.75	1.13	1.13	1.13	1.13	0.88	1.18	1.27	1.27
	f_{ym}	ksi	63.0	128	128	128	128	65.0	69.5	66.2	66.8	70.8	70.8	66.8	69.2	67.4	67.4	67.4
Parallel Reinforcement	Quantity	total	8	8	8	8	8	10	6	6	6	6	6	6	12	4	4	10
	d_b	in.	0.38	0.38	0.38	0.38	0.38	0.25	0.50	0.50	0.50	0.50	0.50	0.50	0.25	0.44	0.50	0.38
	f_{ym}	ksi	69.0	69.0	69.0	69.0	69.0	65.0	64.1	61.9	61.9	64.1	64.1	61.9	66.9	67.4	63.9	68.9
	Condition [d]		Cut.	Cut.	Devel.	Devel.	Devel.	Devel.	Cut.	Cut.	Cut.	Cut.	Cut.	Cut.	Cut.	Devel.	Devel.	Devel.
Transverse Reinforcement	d_b	in.	0.38	0.38	0.38	0.38	0.38	0.25	0.50	0.50	0.50	0.50	0.50	0.50	0.25	0.44	0.38	0.38
	f_{ytm}	ksi	68.0	68.0	68.0	68.0	68.0	65.0	125	120	120	125	125	120	66.9	67.4	68.9	68.9
	s	in.	3.0	3.0	3.0	3.0	3.0	3.0	4.3	4.3	4.3	4.5	4.5	4.3	2.0	4.0	5.9	3.9
	s/d_b		3.4	4.0	4.0	4.0	4.0	6.0	5.8	5.8	3.8	4.0	4.0	3.8	2.3	3.4	4.6	3.1
	$(s/d_b)\sqrt{f_{ym}/60\text{ ksi}}$		3.5	5.8	5.8	5.8	5.8	6.2	6.2	6.1	4.1	4.3	4.3	4.1	2.5	3.6	4.9	3.3
	$\frac{A_{sh,provided}}{s\,b_c} \perp b_w$ [e]		0.009	0.009	0.009	0.009	0.009	0.006	0.010	0.010	0.010	0.010	0.010	0.010	0.010	0.007	0.007	0.008
	$\frac{A_{sh,provided}}{s\,b_c} \perp h$ [e]		0.009	0.009	0.009	0.009	0.009	0.006	0.008	0.008	0.008	0.008	0.008	0.008	0.012	0.012	0.008	0.007
	$\frac{A_{sh,provided}}{A_{sh,required}} \perp b_w$ [e]		1.09	0.91	1.03	1.15	1.05	0.77	3.24	2.08	1.96	2.92	2.69	2.01	0.93	1.04	0.90	1.14
	$\frac{A_{sh,provided}}{A_{sh,required}} \perp h$ [e]		1.12	0.93	1.07	1.19	1.08	0.77	2.57	1.65	1.55	2.32	2.14	1.60	1.09	1.75	1.01	0.94
V_m	–	kips	184	192	194	234	268	95	209	347	378	173	238	166	90	221	150	157
	+	kips	182	207	204	228	275	106	221	356	401	178	238	163	93	206	151	164
v_{max}	$\frac{V_{max}}{b_w h\sqrt{f_{cm},\text{ psi}}}$		13.2	13.6	14.3	17.3	19.4	7.4	15.9	21.0	22.9	12.4	15.9	9.6	8.7	14.7	8.6	9.5
CR_{cap}	–	%	6.30	4.50	5.30	5.50	5.00	2.50	4.50	5.20	5.00	6.50	5.90	6.00	10.00	6.60	6.50	8.30
	+	%	8.00	5.60	5.30	5.10	6.30	3.50	5.10	5.50	5.30	6.10	7.20	6.50	10.00	8.20	6.15	7.50
	Avg.	%	7.15	5.05	5.30	5.30	5.65	3.00	4.80	5.35	5.15	6.30	6.55	6.25	10.00	7.40	6.33	7.90
Axial Restraint			No	No	No	Yes	No	No	Yes	Yes	Yes	Yes	Yes	Yes	No	Yes	No	No

a-f See Table 19 for key to footnotes.

Table 17 – Continued [a]

Specimen Number			17	18	19	20	21	22	23	24	25	26	27	28	29	30	31	32	33
Reference			Lim et al. (2016)[70]		Naish et al. (2013)[81]			Sonobe et al. (1995)[103]	Tassios et al. (1996)[109]		This Study								
Specimen Id.			CB10-1	CB20-1	CB24D	CB24F	CB33F	NX7L	CB-2A	CB-2B	D80-1.5	D100-1.5	D120-1.5	D80-2.5	D100-2.5	D120-2.5	D80-3.5	D100-3.5	D120-3.5
Beam Properties	b_w	in.	9.8	11.8	12.0	12.0	12.0	9.4	5.1	5.1	12.0	12.0	12.0	12.0	12.0	12.0	12.0	12.0	12.0
	h	in.	19.7	19.7	15.0	15.0	18.0	13.8	19.7	11.8	18.0	18.0	18.0	18.0	18.0	18.0	18.0	18.0	18.0
	Confinement [b]		Full	Full	Diag.	Full	Full	Full	Diag.	Diag.	Full	Full	Full	Full	Full	Full	Full	Full	Full
	$b_c \perp b_w$ [c]	in.	8.3	10.2	8.6	9.5	9.5	6.7	2.4	2.4	10.5	10.5	10.5	10.5	10.5	10.5	10.5	10.5	10.5
	$b_c \perp h$ [c]	in.	16.5	16.5	3.3	13.5	16.5	11.0	2.4	2.4	16.5	16.5	16.5	16.5	16.5	16.5	16.5	16.5	16.5
	ℓ_n	in.	19.7	39.4	36.0	36.0	60.0	38.6	19.7	19.7	27.0	27.0	27.0	45.0	45.0	45.0	63.0	63.0	63.0
	ℓ_n/h		1.00	2.00	2.40	2.40	3.33	2.80	1.00	1.67	1.50	1.50	1.50	2.50	2.50	2.50	3.50	3.50	3.50
	f_{cm}	psi	5000	7550	6850	6850	6850	4600	4150	3800	7600	8200	7600	8400	8000	7800	7800	7900	8200
Diagonal Reinforcement	Quantity	ea. diag.	4	4	6	6	6	4	4	4	6	5	4	9	7	6	9	9	8
	α	degrees	26.0	16.0	15.7	15.7	12.3	13.8	36.9	19.4	22.7	22.7	22.7	14.2	14.2	14.2	10.0	10.3	10.3
	d_b	in.	1.00	1.13	0.88	0.88	0.88	0.63	0.38	0.38	0.75	0.75	0.75	0.75	0.75	0.75	0.88	0.75	0.75
	f_{ym}	ksi	70.4	67.6	70.0	70.0	70.0	76.6	73.1	73.1	83.0	108	116	83.0	108	116	84.0	108	116
Parallel Reinforcement	Quantity	total	10	10	10	10	12	4	8	8	10	10	10	10	10	10	10	10	10
	d_b	in.	0.38	0.50	0.25	0.38	0.38	0.63	0.25	0.25	0.38	0.38	0.38	0.38	0.38	0.38	0.38	0.38	0.38
	f_{ym}	ksi	70.4	72.8	70.0	70.0	70.0	76.6	40.7	40.7	89.0	89.0	89.0	89.0	89.0	133	89.0	89.0	89.0
	Condition [d]		Devel.	Devel.	Cut.	Cut.	Cut.	Devel.	Devel.	Devel.	Cut.	Cut.	Cut.	Cut.	Cut.	Devel.	Cut.	Cut.	Cut.
Transverse Reinforcement	d_b	in.	0.50	0.50	0.38	0.38	0.38	0.24	0.25	0.25	0.38	0.38	0.38	0.38	0.38	0.38	0.38	0.38	0.38
	f_{ytm}	ksi	67.9	72.8	70.0	70.0	70.0	134	40.7	40.7	89.0	89.0	89.0	89.0	89.0	133	89.0	89.0	89.0
	s	in.	3.9	3.9	2.5	3.0	3.0	3.2	2.0	2.0	3.0	3.0	3.0	3.0	3.0	3.0	3.0	3.0	3.0
	s/d_b		3.9	3.5	2.9	3.4	3.4	5.0	5.3	5.3	4.0	4.0	4.0	4.0	4.0	4.0	3.4	4.0	4.0
	$(s/d_b)\sqrt{f_{ym}/60\text{ ksi}}$		4.3	3.7	3.1	3.7	3.7	5.6	5.8	5.8	4.7	5.4	5.6	4.7	5.4	5.6	4.1	5.4	5.6
	$\frac{A_{sh,provided}}{s\,b_c} \perp b_w$ [e]		0.020	0.016	0.010	0.012	0.012	0.004	0.018	0.018	0.010	0.010	0.010	0.010	0.010	0.010	0.010	0.010	0.010
	$\frac{A_{sh,provided}}{s\,b_c} \perp h$ [e]		0.013	0.013	0.027	0.011	0.011	0.002	0.018	0.018	0.009	0.009	0.009	0.009	0.009	0.009	0.009	0.009	0.009
	$\frac{A_{sh,provided}}{A_{sh,required}} \perp b_w$ [e]		2.95	1.68	1.17	1.31	1.31	1.33	1.99	2.17	1.36	1.26	1.36	1.23	1.29	1.98	1.33	1.31	1.26
	$\frac{A_{sh,provided}}{A_{sh,required}} \perp h$ [e]		1.97	1.39	3.07	1.23	1.26	0.80	1.99	2.17	1.16	1.07	1.16	1.05	1.10	1.68	1.13	1.11	1.07
V_m	–	kips	315	241	150	171	115	82	54	30	239	257	262	220	220	283	218	192	216
	+	kips	325	230	159	151	124	81	63	38	254	252	264	218	214	286	219	196	212
v_{max}	$\frac{V_{max}}{b_w h\sqrt{f_{cm},\text{ psi}}}$		23.8	11.9	10.7	11.5	7.1	9.3	9.7	10.2	13.5	13.1	14.0	11.1	11.4	15.0	11.5	10.2	11.0
CR_{cap}	–	%	5.70	7.50	8.60	9.00	8.00	5.10	4.40	5.00	6.40	4.70	5.40	6.90	5.30	6.70	8.40	6.90	6.60
	+	%	6.00	7.90	8.90	10.00	8.10	6.80	4.50	5.10	7.30	5.80	5.00	8.30	6.60	7.00	8.80	6.70	6.80
	Avg.	%	5.85	7.70	8.75	9.50	8.05	5.95	4.45	5.05	6.85	5.25	5.20	7.60	5.95	6.85	8.60	6.80	6.70
Axial Restraint			No	No	No	No	No	No	No	No	No	No	No	No	No	No	No	No	No

[a-f] See Table 19 for key to footnotes.

Table 18 – Database of diagonally-reinforced coupling beams excluded from derivation of best-fit equation for chord rotation capacity [a]
(1 in. = 25.4 mm, 1 ksi = 1000 psi = 6.89 MPa, 1 kip = 4.45 kN)

Specimen Number			34	35	36	37	38	39	40	41	42	43	44	45	46	47	48	49	50	51	52
Reference			Fortney et al. (2008)[50]	Galano and Vignoli (2000)[51]		Han et al. (2015)[57]		Kwan and Zhao (2002)[65]	Naish et al. (2013)[81]				Park et al. (2020)[89]		Paulay and Binney (1974)[92]			Poudel et al. (2018)[94]	Shiu et al. (1978)[100]		Yun et al. (2007)[118]
Specimen Id.			DCB-1 [g]	P07	P12	SD-2.0	SD-3.5	CCB11	CB33D	CB24F-RC	CB24F-PT	CB24F-1/2-PT	CCB	CCBWC	316 [h]	317 [h]	395 [h]	CB1A	C6 [h]	C8 [h]	PCB-DC
Beam Properties	b_w	in.	10.0	5.9	5.9	9.8	9.8	4.7	12.0	12.0	12.0	12.0	7.9	7.9	6.0	6.0	6.0	10.0	4.0	4.0	7.9
	h	in.	14.0	15.7	15.7	20.7	11.8	23.6	18.0	15.0	15.0	15.0	11.8	11.8	31.0	31.0	39.0	18.0	6.7	6.7	23.6
	Confinement [b]		Diag.	Full	Diag.	Full	Full	Diag.	Diag.	Full	Full	Full	Full	Full	Full	Diag.	Diag.	Full	Full	Full	Full
	$b_c \perp b_w$ [c]	in.	5.0	4.8	3.2	7.9	7.9	2.4	8.6	9.5	9.5	9.5	6.3	6.3	3.5	3.5	3.5	8.5	3.5	3.5	6.6
	$b_c \perp h$ [c]	in.	4.3	13.4	3.2	18.8	9.9	3.3	3.3	13.5	13.5	13.5	10.2	10.2	28.0	5.3	5.3	16.5	6.2	6.2	22.3
	ℓ_n	in.	36.0	23.6	23.6	41.3	41.3	27.6	60.0	36.0	36.0	36.0	23.6	23.6	40.0	40.0	40.0	34.0	16.7	33.3	23.6
	ℓ_n/h		2.57	1.50	1.50	2.00	3.50	1.17	3.33	2.40	2.40	2.40	2.00	2.00	1.29	1.29	1.03	1.89	2.50	5.00	1.00
	f_{cm}	psi	5550	7850	6050	6400	6400	5500	6850	7300	7250	7000	9650	9650	4800	7350	5150	6400	2600	3450	7250
Diagonal Reinforcement	Quantity	ea. diag.	4	4	4	4	4	6	6	6	6	6	8	8	4	4	4	6	2	2	2
	α	degrees	13.0	23.9	23.9	20.4	8.9	32.0	12.3	15.7	15.7	15.7	17.0	17.0	29.5	29.5	37.5	18.0	18.0	9.1	30.0
	d_b	in.	1.00	0.38	0.38	0.88	1.00	0.32	0.88	0.88	0.88	0.88	0.39	0.39	0.88	0.88	0.88	0.88	0.38	0.38	0.63
	f_{ym}	ksi	62.6	82.2	82.2	63.5	64.1	75.0	70.0	70.0	70.0	70.0	69.5	69.5	41.8	44.4	37.6	64.0	59.2	62.8	68.7
Parallel Reinforcement	Quantity	total	4	6	6	14	10	8	12	10	10	10	14	14	4	4	4	8	4	4	8
	d_b	in.	0.75	0.25	0.25	0.50	0.50	0.32	0.25	0.38	0.38	0.38	0.24	0.24	0.50	0.25	0.25	0.38	0.20	0.20	0.63
	f_{ym}	ksi	60.7	82.2	82.2	73.4	73.4	75.0	70.0	70.0	70.0	70.0	60.6	60.6	46.8	44.4	37.6	69.0	71.4	71.0	68.7
	Condition [d]		Devel.	Devel.	Devel.	Cut.	Cut.	Devel.	Cut.	Cut.	Cut.	Cut.	Devel.	Devel.	Cut.	Cut.	Cut.	Cut.	Cut.	Cut.	Devel.
Transverse Reinforcement	d_b	in.	0.38	0.25	0.25	0.50	0.50	0.32	0.38	0.38	0.38	0.38	0.24	0.24	0.25	0.25	0.25	0.38	0.20	0.20	0.24
	f_{ytm}	ksi	60.6	82.2	82.2	73.4	73.4	50.2	70.0	70.0	70.0	70.0	60.6	60.6	44.4	44.4	37.6	68.0	71.4	71.0	42.2
	s	in.	3.0	5.0	3.5	4.7	4.3	2.4	2.5	3.0	3.0	6.0	2.0	2.0	4.8	4.4	4.4	3.0	1.3	1.3	5.9
	s/d_b		3.0	13.3	9.3	5.4	4.3	7.6	2.9	3.4	3.4	6.9	5.1	5.1	5.4	5.0	5.0	3.4	3.5	3.5	9.4
	$(s/d_b)\sqrt{f_{ym}/60\text{ ksi}}$		3.1	15.6	12.5	5.5	4.4	8.4	3.1	3.7	3.7	7.4	5.5	5.5	4.5	4.3	4.0	3.5	3.7	3.9	10.0
	$\frac{A_{sh,provided}}{s\,b_c} \perp b_w$ [e]		0.015	0.004	0.008	0.017	0.018	0.027	0.010	0.012	0.012	0.006	0.014	0.007	0.006	0.006	0.006	0.009	0.013	0.013	0.002
	$\frac{A_{sh,provided}}{s\,b_c} \perp h$ [e]		0.017	0.001	0.008	0.014	0.019	0.019	0.027	0.011	0.011	0.005	0.011	0.004	0.001	0.004	0.004	0.009	0.007	0.007	0.001
	$\frac{A_{sh,provided}}{A_{sh,required}} \perp b_w$ [e]		1.78	0.42	1.16	2.12	2.31	2.69	1.17	1.23	1.24	0.64	0.98	0.49	0.61	0.43	0.52	1.02	4.02	3.02	0.14
	$\frac{A_{sh,provided}}{A_{sh,required}} \perp h$ [e]		2.09	0.15	1.16	1.78	2.46	1.97	3.07	1.16	1.17	0.60	0.75	0.30	0.08	0.43	0.51	1.05	2.28	1.71	0.04
V_m	–	kips	124	52	53	251	113	74	118	190	200	180	92	88	124	120	120	244	13	6	128
	+	kips	142	56	56	245	114	78	121	191	212	190	93	85	151	130	146	240	13	8	158
v_{max}	$\frac{V_{max}}{b_w h\sqrt{f_{cm},\text{ psi}}}$		13.6	6.8	7.8	15.5	12.3	9.4	6.8	12.4	13.8	12.6	10.2	9.7	11.7	8.2	8.7	16.9	9.6	5.1	10.0
CR_{cap}	–	%	4.50	4.50	3.20	5.20	9.90	5.30	6.00	10.30	8.60	8.20	3.30	3.20	0.90	6.20	1.00	7.30	6.10	6.60	1.59
	+	%	4.60	5.00	4.00	6.20	10.10	5.40	6.90	10.50	9.10	8.40	4.50	3.00	6.10	3.80	5.80	7.30	6.10	6.60	1.41
	Avg.	%	4.55	4.75	3.60	5.70	10.00	5.35	6.45	10.40	8.85	8.30	3.90	3.10	3.50	5.00	3.40	7.30	6.10	6.60	1.50
Axial Restraint			No	Yes	Yes	Yes	Yes	No	No	No	No	No	Yes	Yes	No	No	No	Yes	No	No	Yes
Reason for Exclusion [i]			1	2, 3	2, 3	3	3	7	4	5	5	5	3	3	6	6	6	3	7	7	2

[a-i] See Table 19 for key to footnotes.

Table 19 – Key to footnotes in Tables 17 and 18

Footnotes	
a	For notation and definitions, see Appendix A: NOTATION.
b	"Diag." refers to confinement of each diagonal element, as permitted in ACI 318-14 18.10.7.4(c)[6]. "Full" refers to confinement of the entire beam cross-section, as permitted in ACI 318-14 18.10.7.4(d)[6].
c	"b_c" refers to the cross-sectional dimension of the member core measured to outside edges of the transverse reinforcement composing area A_{sh}: for a beam with full-section confinement, $b_c = b_w - 2c_c$ or $h - 2c_c$; for a beam with diagonal group confinement, b_c is the side dimension of the confined concrete core for the diagonal bar group.
d	"Cut." refers to secondary longitudinal reinforcement not developed into supports. "Devel." refers to secondary longitudinal bars developed into the supports.
e	"⊥ to b_w" refers to transverse reinforcement placed perpendicular to beam width. "⊥ to h" refers to transverse reinforcement perpendicular to beam height. A_g/A_c was assumed equal to 1.3, which simplified ACI 318-14 Eq. 18.10.7.4[6] to $A_{sh,required} = 0.09\, sb_c\, f_{cm}/f_{ytm}$.
f	Axial force due to restraint did not exceed $0.15A_g f_{cm}$.
g	Confinement deviated from detailing based on ACI 318-14 18.10.7.4(c or d)[6]: For Specimen Number 34[50], diagonal confinement was used but not equally spaced along the beam span.
h	Data refer to the smallest diagonal bar diameter for cases where diagonal reinforcement was not symmetric [92,100].
i	Reasons for exclusion: 1 - Diagonal bars irregularly confined throughout beam span; 2 - s/d_b >8.0; 3 - Axial force exceeded $0.15A_g f_{cm}$ or beam axially restrained without reported axial force; 4 - Insufficient test data to define post-peak force-deformation envelope; 5 - Beam built integral with a slab; 6 - No systematic loading protocol; 7 - Small-scale beam with least cross-sectional dimension < 5 in. (127 mm).

Table 20 – Range of values for main variables in the database for diagonally-reinforced coupling beams [a]
(1 in. = 25.4 mm, 1 ksi = 1000 psi = 6.89 MPa)

Group		b_w	h	$\frac{\ell_n}{h}$	f_{cm}	f_{ym} [b]	$\frac{s}{d_b}$	$\frac{s}{d_b}\sqrt{\frac{f_{ym}}{60ksi}}$	v_{max} [c]	Chord Rotation Capacity [d]
		in.	in.		psi	psi			$\sqrt{f_{cm}}$, psi	%
Included	Minimum	5.1	11.8	1.0	3800	63000	2.3	2.5	7.1	3.0
	Average	10.8	17.9	2.2	6450	85300	4.1	4.8	13.0	6.4
	Maximum	12.0	23.6	3.5	8400	128000	6.0	6.2	23.8	10.0
This Study [e]	Minimum	12.0	18.0	1.5	7600	83000	3.4	4.1	10.2	5.2
	Average	12.0	18.0	2.5	7950	102400	3.9	5.1	12.3	6.7
	Maximum	12.0	18.0	3.5	8400	116000	4.0	5.6	15.0	8.6
Excluded	Minimum	4.0	6.7	1.0	2600	37600	2.9	3.1	5.1	1.5
	Average	8.1	18.1	2.1	6450	64600	5.5	5.9	10.6	5.7
	Maximum	12.0	39.0	5.0	9650	82200	13.3	15.6	16.9	10.4

[a] For notation and definitions, see APPENDIX A: NOTATION.
[b] Measured yield stress of diagonal reinforcement.
[c] Shear stress associated with maximum applied shear, $v_{max} = V_{max}/(b_w h)$.
[d] The average of the maximum chord rotations in each loading direction where the envelope curve (shear versus chord rotation) intersects with 80% of the maximum applied shear.
[e] All D-type beams in this study also belong to the included group.

Table 21 – Summary data for single variable linear regression of chord rotation capacity versus selected parameters [a]
(1 in. = 25.4 mm, 1 ksi = 1000 psi = 6.89 MPa)

Selected Parameter [b]	Name	$\frac{\ell_n}{h}$	f_{cm}	f_{ym} [c]	$\frac{s}{d_b}$	$\frac{s}{d_b}\sqrt{\frac{f_{ym}}{60\ ksi}}$	$\frac{A_{sh,provided}}{A_{sh,required}}$ [d]		$\frac{v_{max}}{\sqrt{f_{cm}}}$
							$\perp$ to b_w	$\perp$ to h	
	Unit	$\frac{\text{in.}}{\text{in.}}$	ksi	ksi	$\frac{\text{in.}}{\text{in.}}$	$\frac{\text{in.}}{\text{in.}}$	$\frac{\text{in.}^2}{\text{in.}^2}$		
	c_0	3.65	3.68	7.88	12.32	12.16	7.26	6.43	7.80
	c_1	1.24	0.43	-16.9	-1.45	-1.19	-0.53	0.011	-0.10
	r^2	0.40	0.14	0.07	0.63	0.66	0.05	2E-5	0.08
	CV	0.18	0.22	0.22	0.15	0.14	0.22	0.24	0.22

[a] For notation and definitions, see APPENDIX A: NOTATION.
[b] A single variable linear regression was conducted in the form $CR_{cap} = c_0 + c_1 X_i$, where X_i is the variable of interest and c_0 and c_1 are the regression coefficients.
[c] Measured yield stress of diagonal reinforcement.
[d] "$\perp$ to b_w" refers to transverse reinforcement placed perpendicular to beam width.
"$\perp$ to h" refers to transverse reinforcement placed perpendicular to beam height.

FIGURES

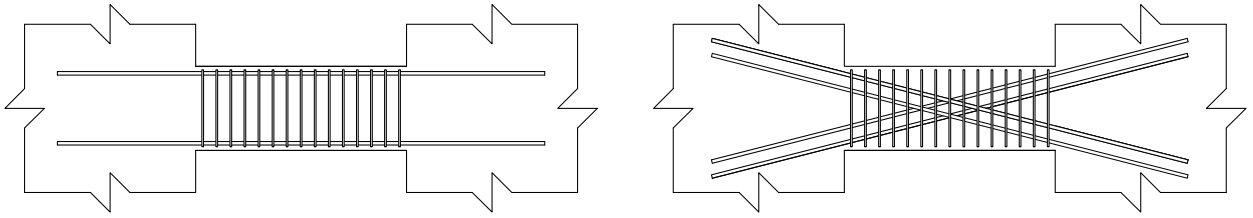

(a)P-type beam (b)D-type beam

Figure 1 – Reinforcement layout types, parallel (P) and diagonal (D)

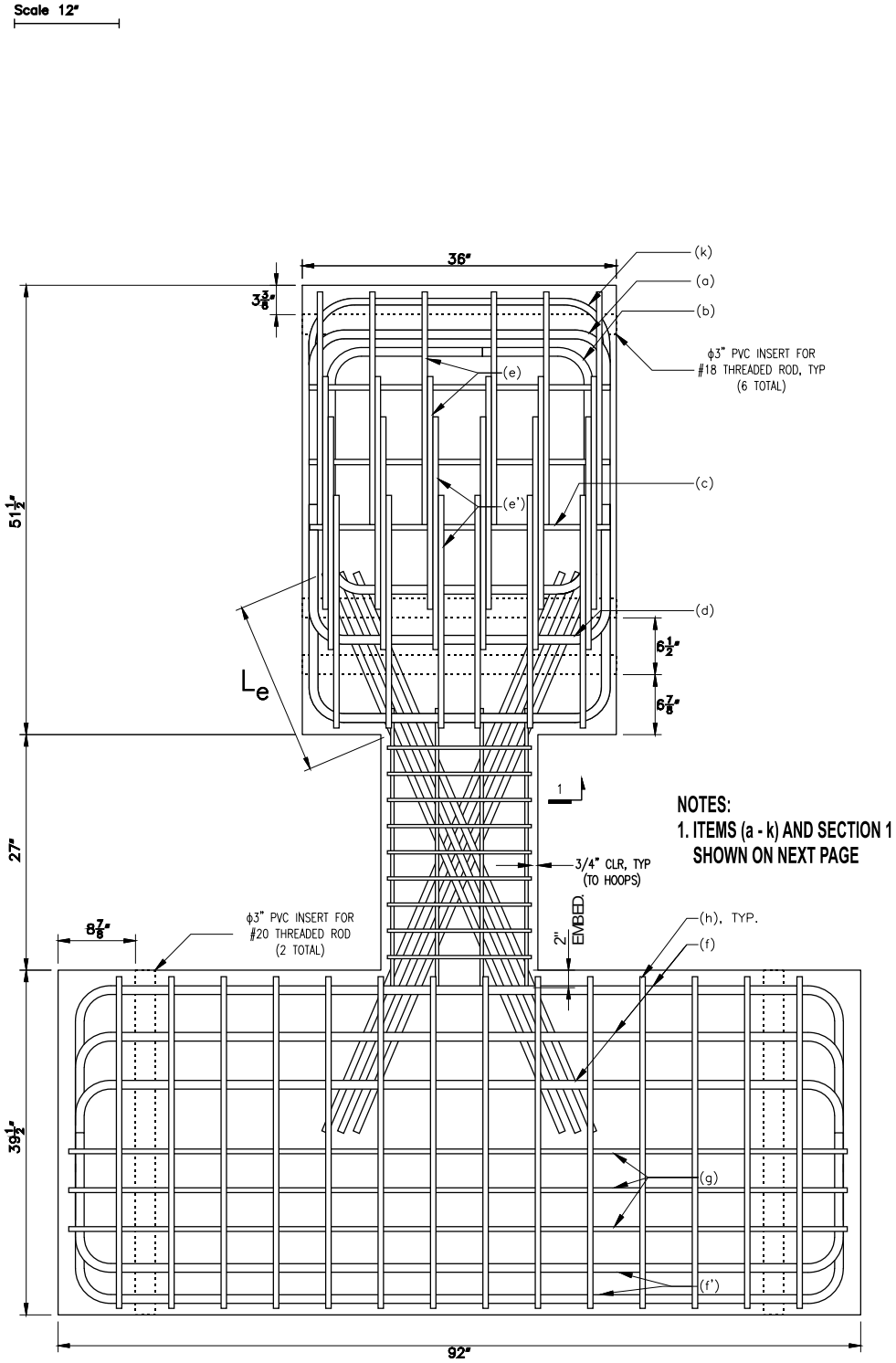

Figure 2 – Elevation view of D80-1.5 (1 in. = 25.4 mm)

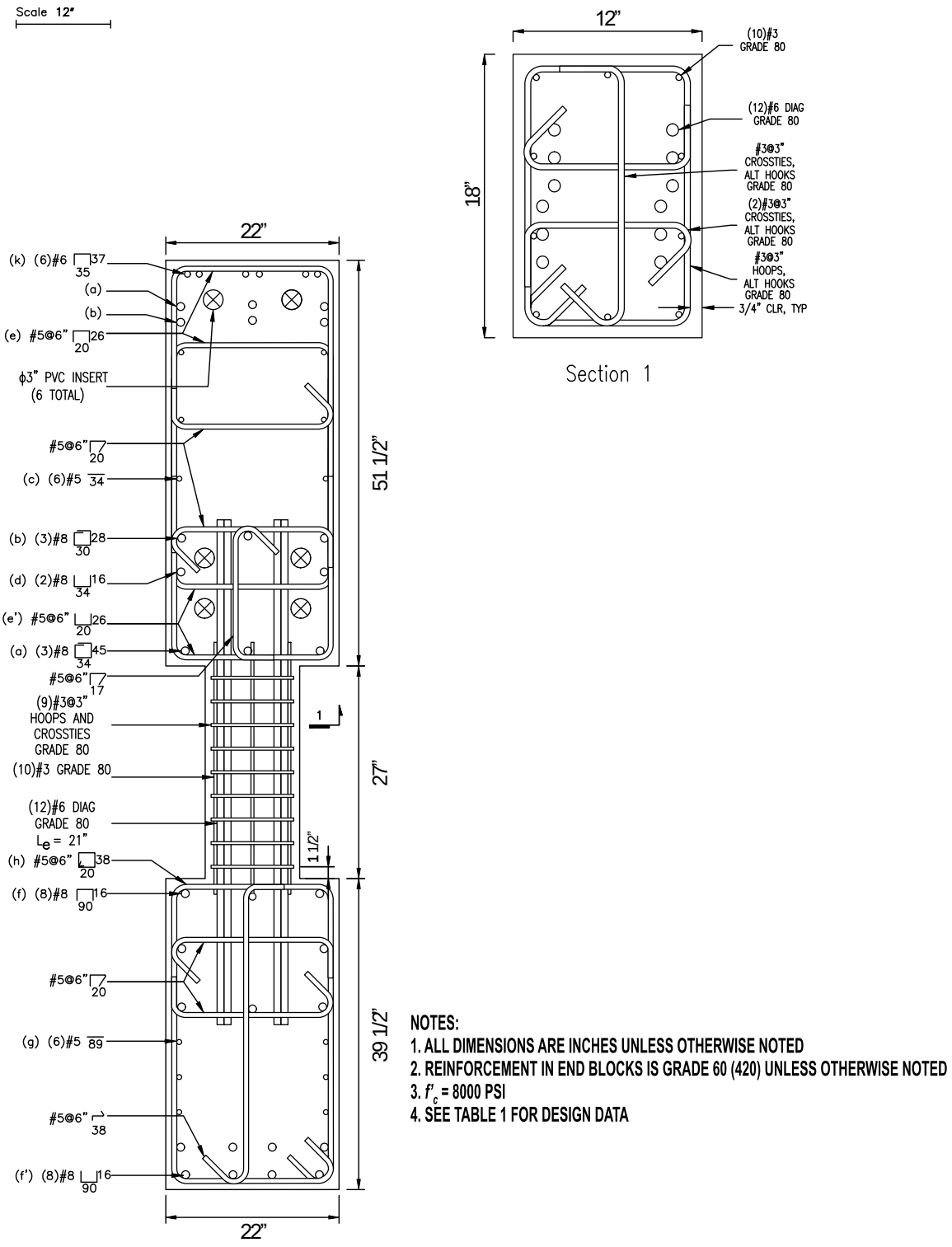

Figure 3 – Reinforcement details of D80-1.5 (1 in. = 25.4 mm, 1 ksi = 1,000 psi = 6.89 MPa)

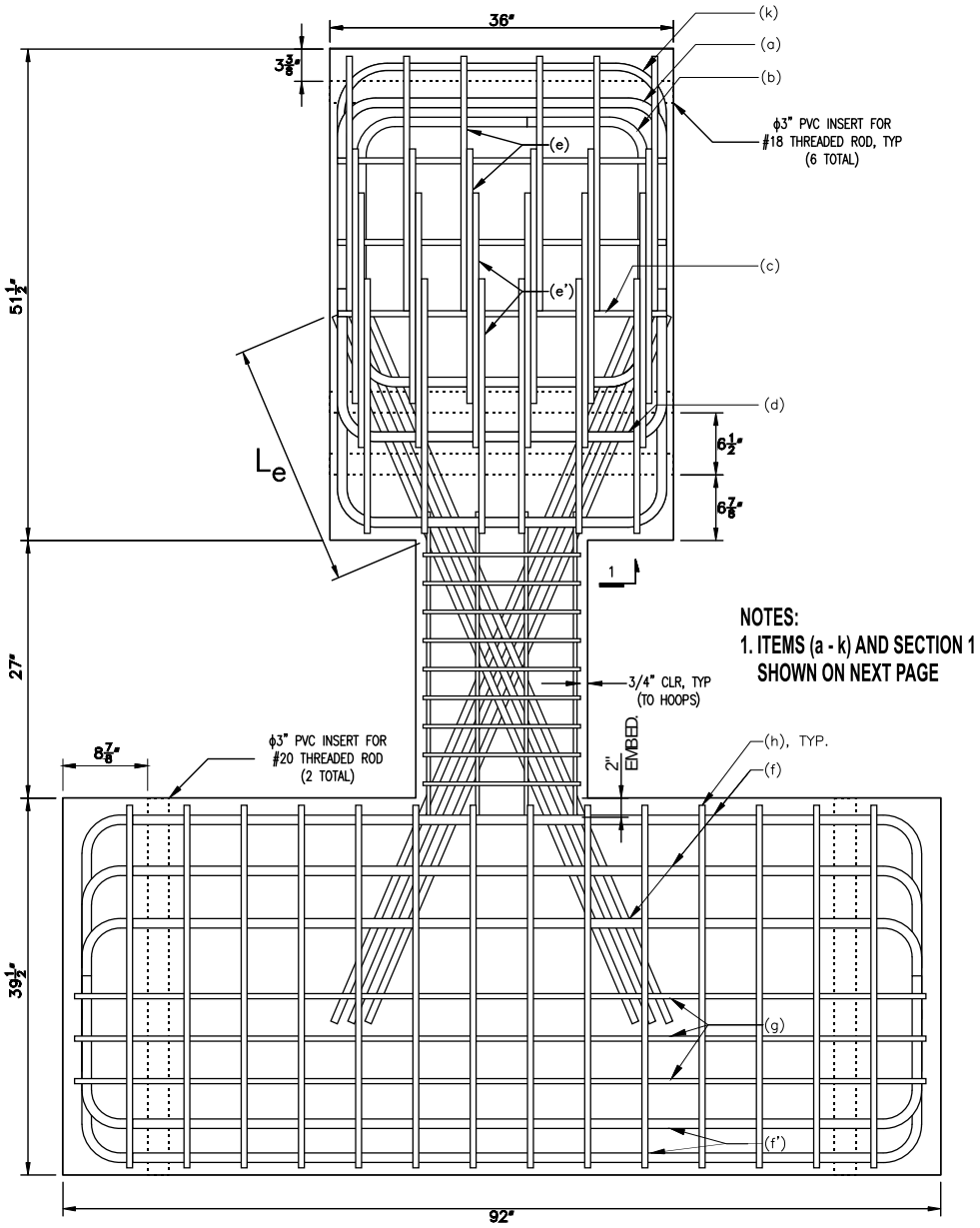

Figure 4 – Elevation view of D100-1.5 (1 in. = 25.4 mm)

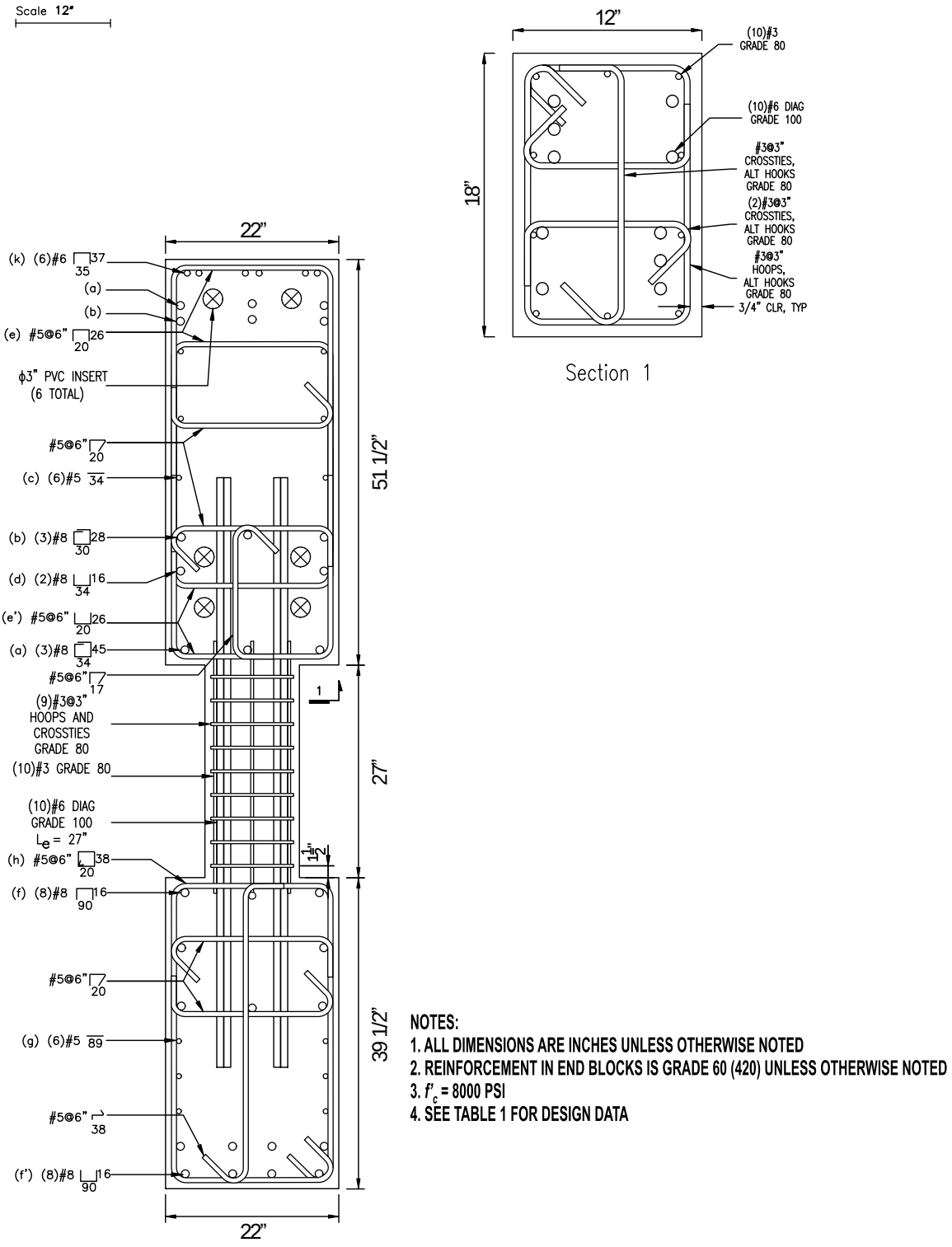

Figure 5 – Reinforcement details of D100-1.5 (1 in. = 25.4 mm, 1 ksi = 1,000 psi = 6.89 MPa)

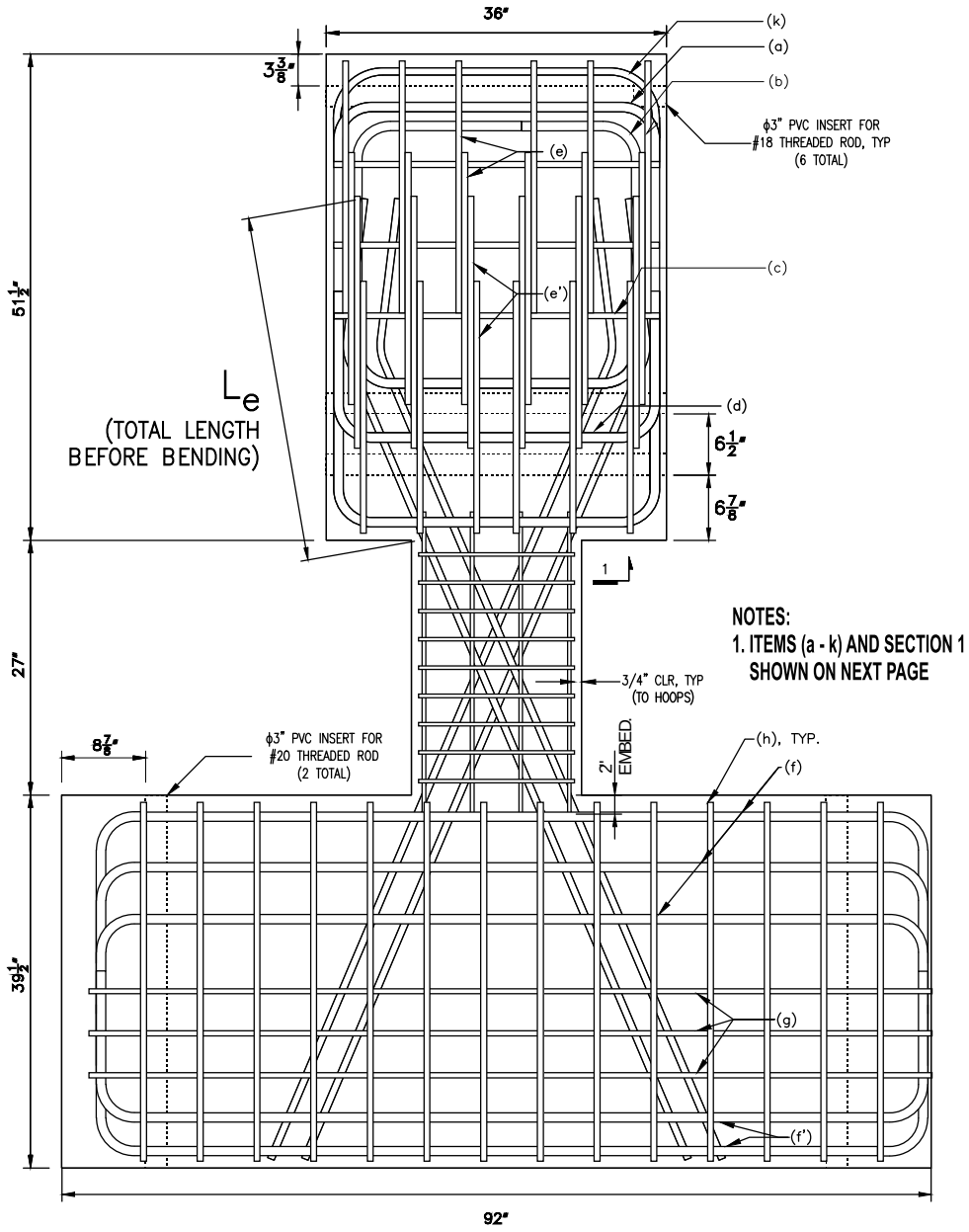

Figure 6 – Elevation view of D120-1.5 (1 in. = 25.4 mm)

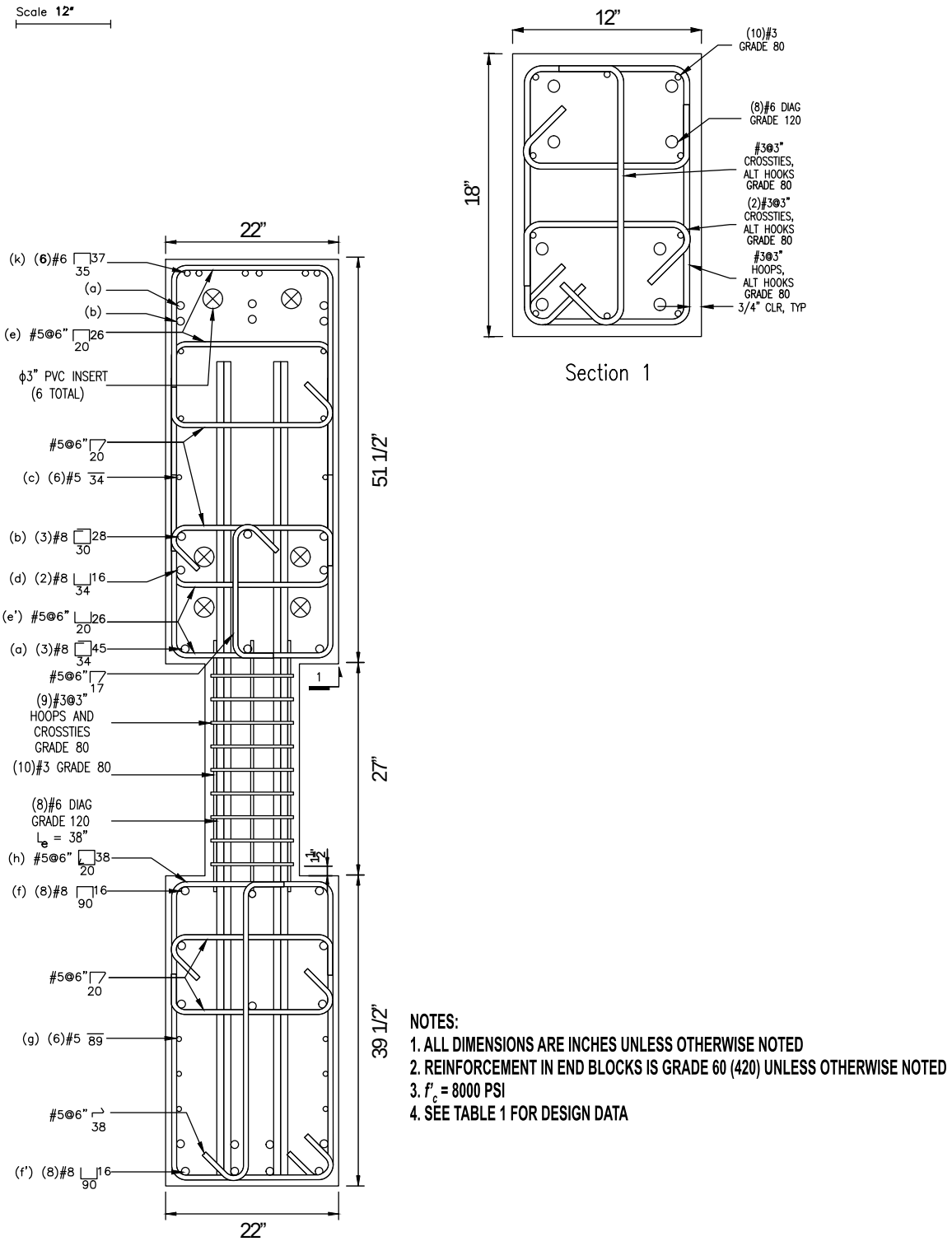

Figure 7 – Reinforcement details of D120-1.5 (1 in. = 25.4 mm, 1 ksi = 1,000 psi = 6.89 MPa)

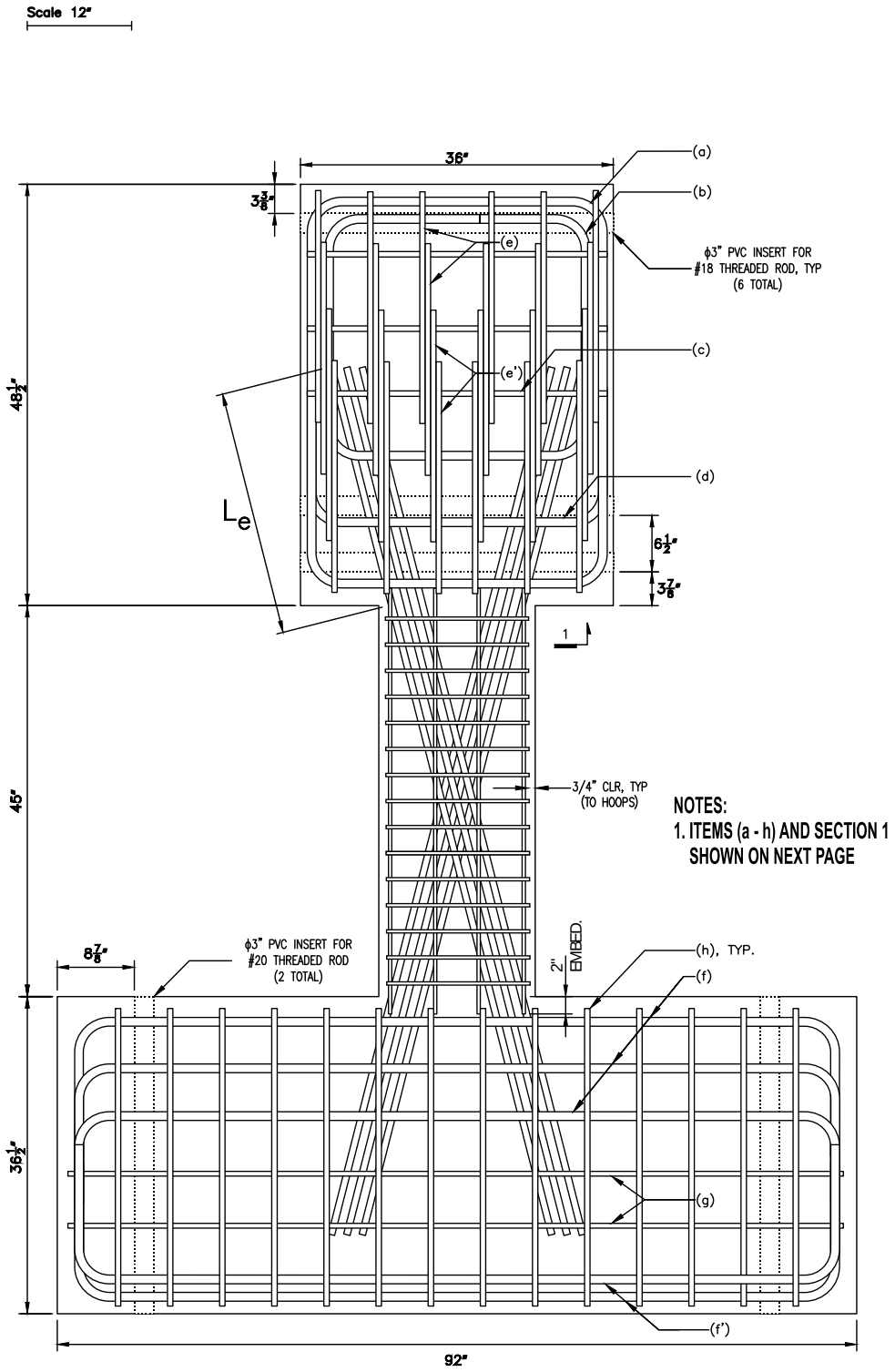

Figure 8 – Elevation view of D80-2.5 (1 in. = 25.4 mm)

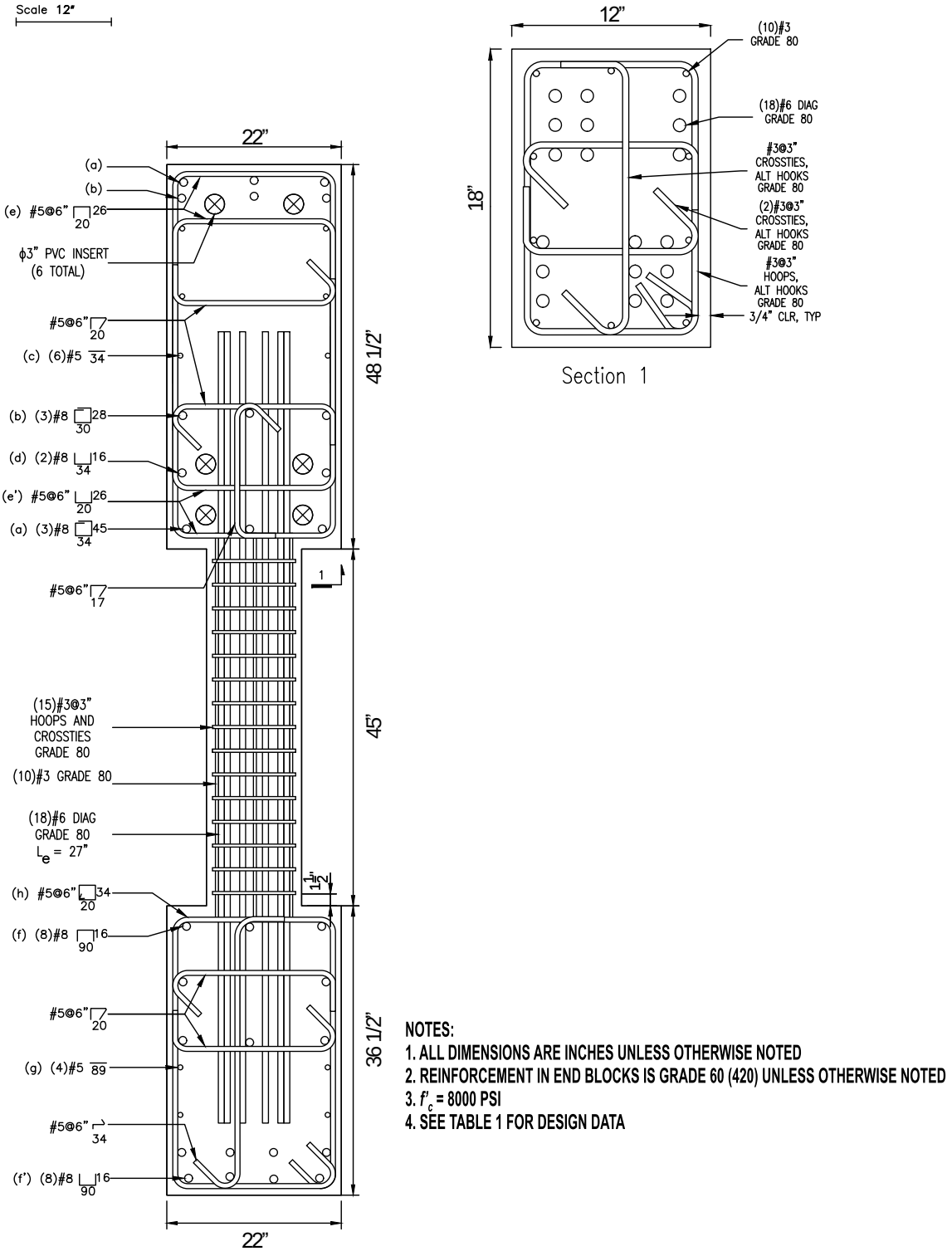

Figure 9 – Reinforcement details of D80-2.5 (1 in. = 25.4 mm, 1 ksi = 1,000 psi = 6.89 MPa)

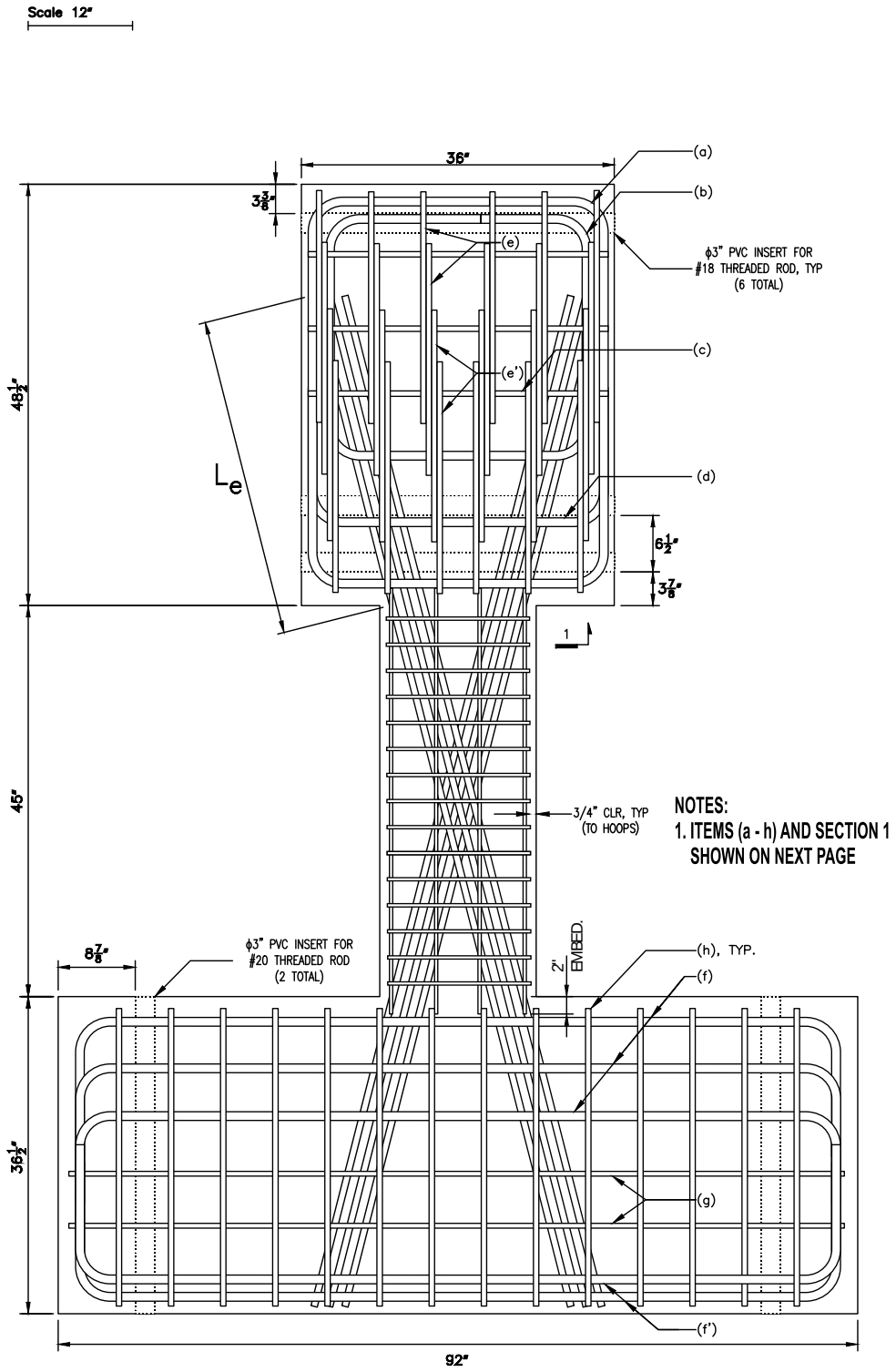

Figure 10 – Elevation view of D100-2.5 (1 in. = 25.4 mm)

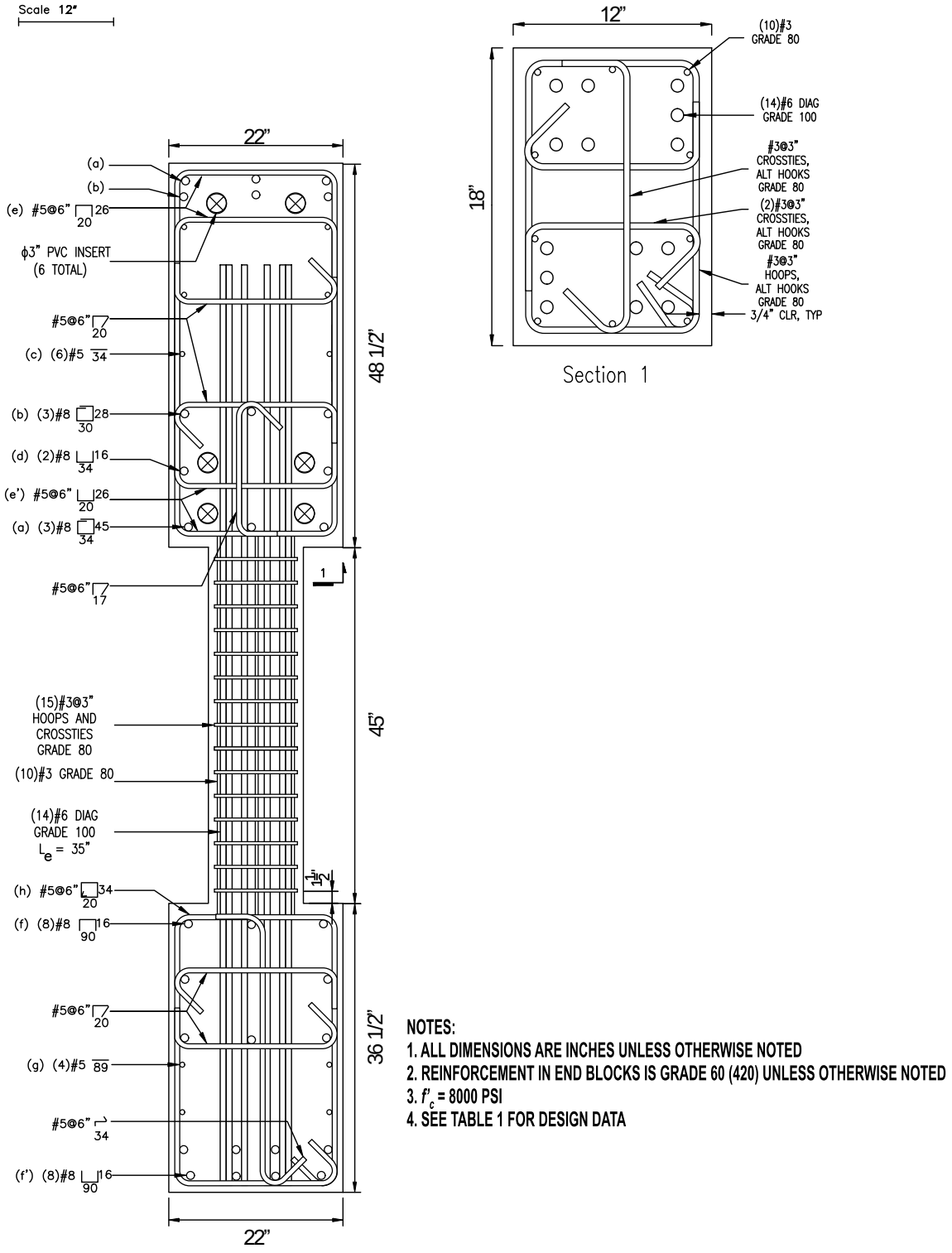

Figure 11 – Reinforcement details of D100-2.5 (1 in. = 25.4 mm, 1 ksi = 1,000 psi = 6.89 MPa)

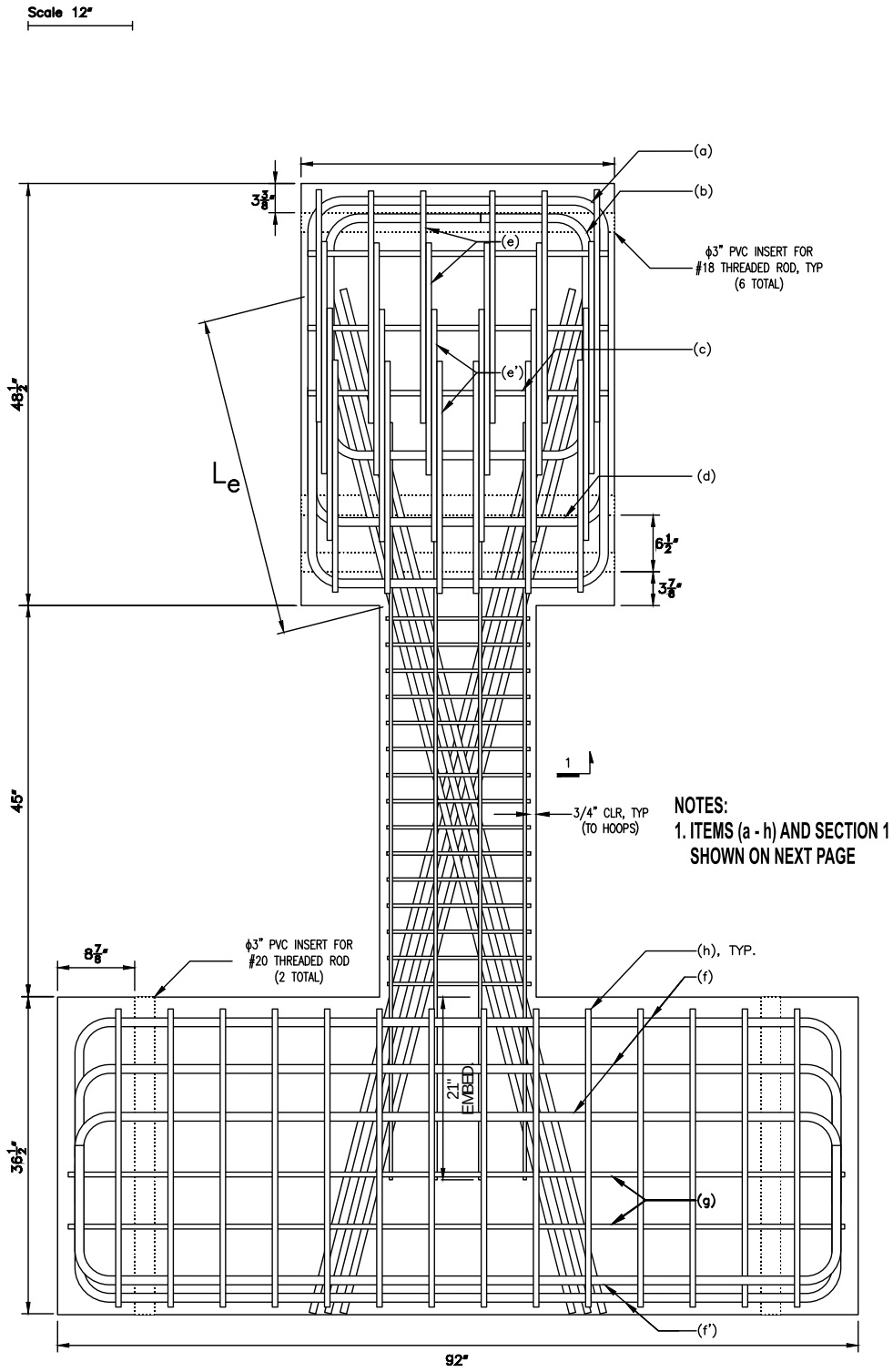

Figure 12 – Elevation view of D120-2.5 (1 in. = 25.4 mm)

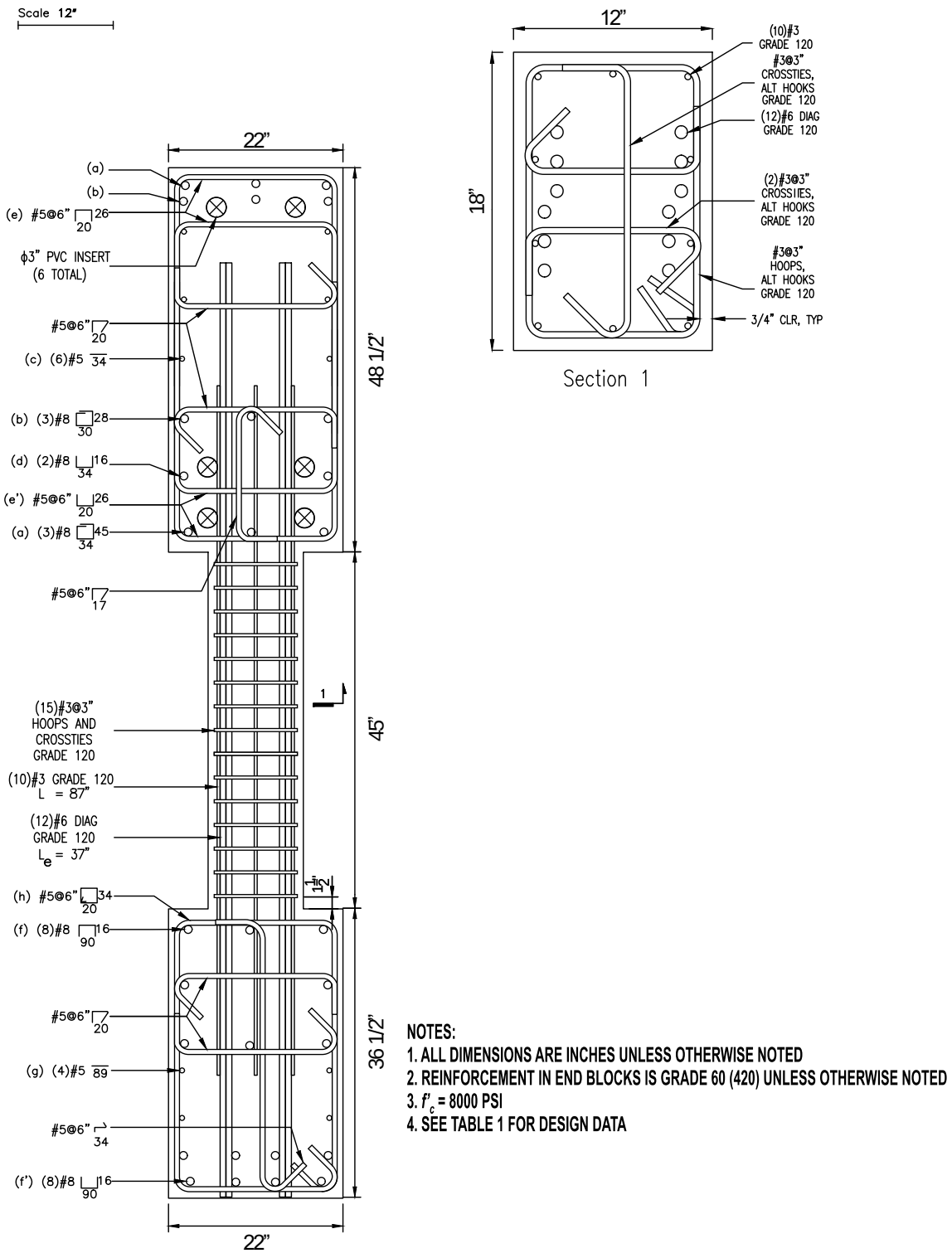

Figure 13 – Reinforcement details of D120-2.5 (1 in. = 25.4 mm, 1 ksi = 1,000 psi = 6.89 MPa)

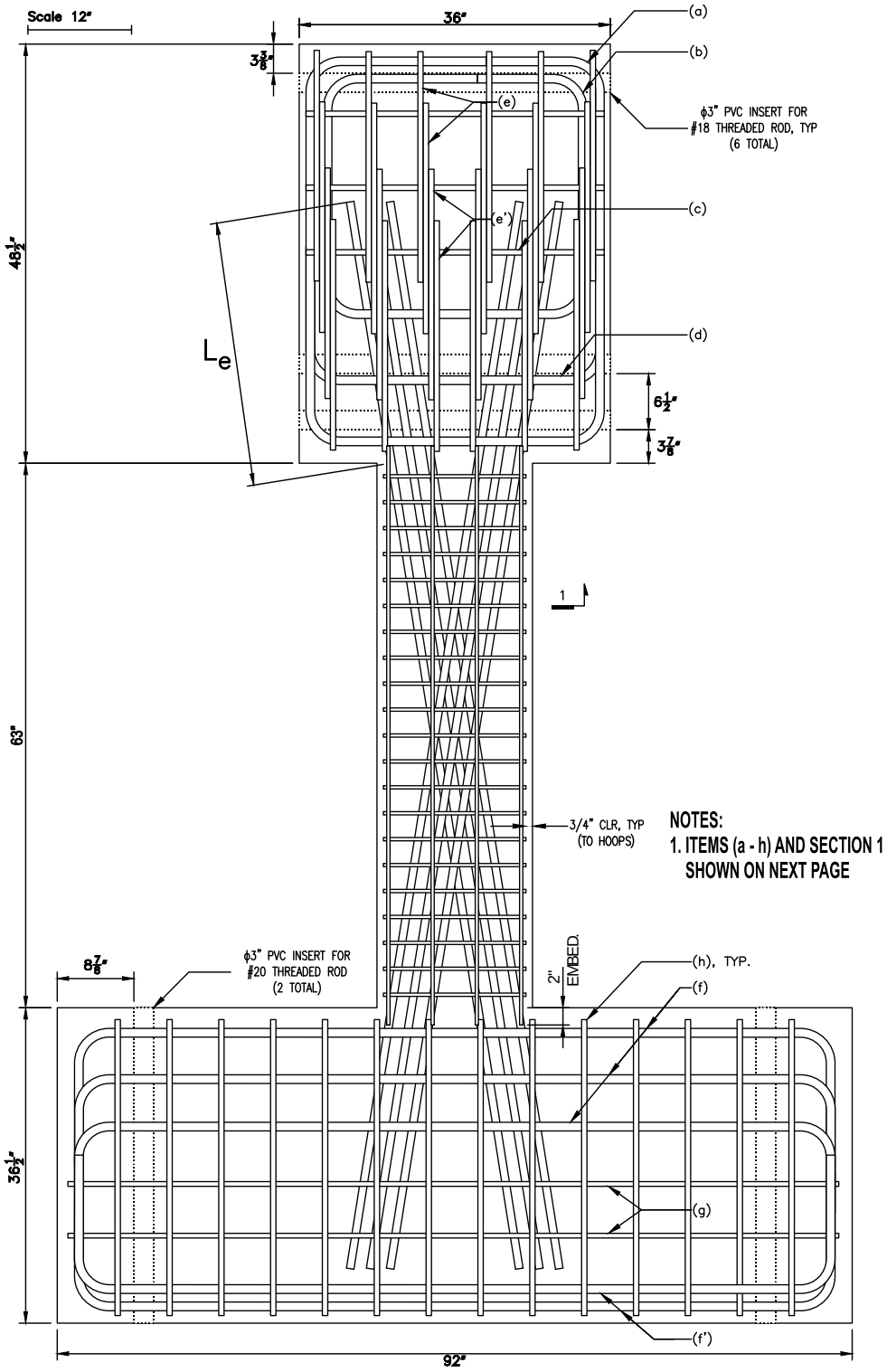

Figure 14 – Elevation view of D80-3.5 (1 in. = 25.4 mm)

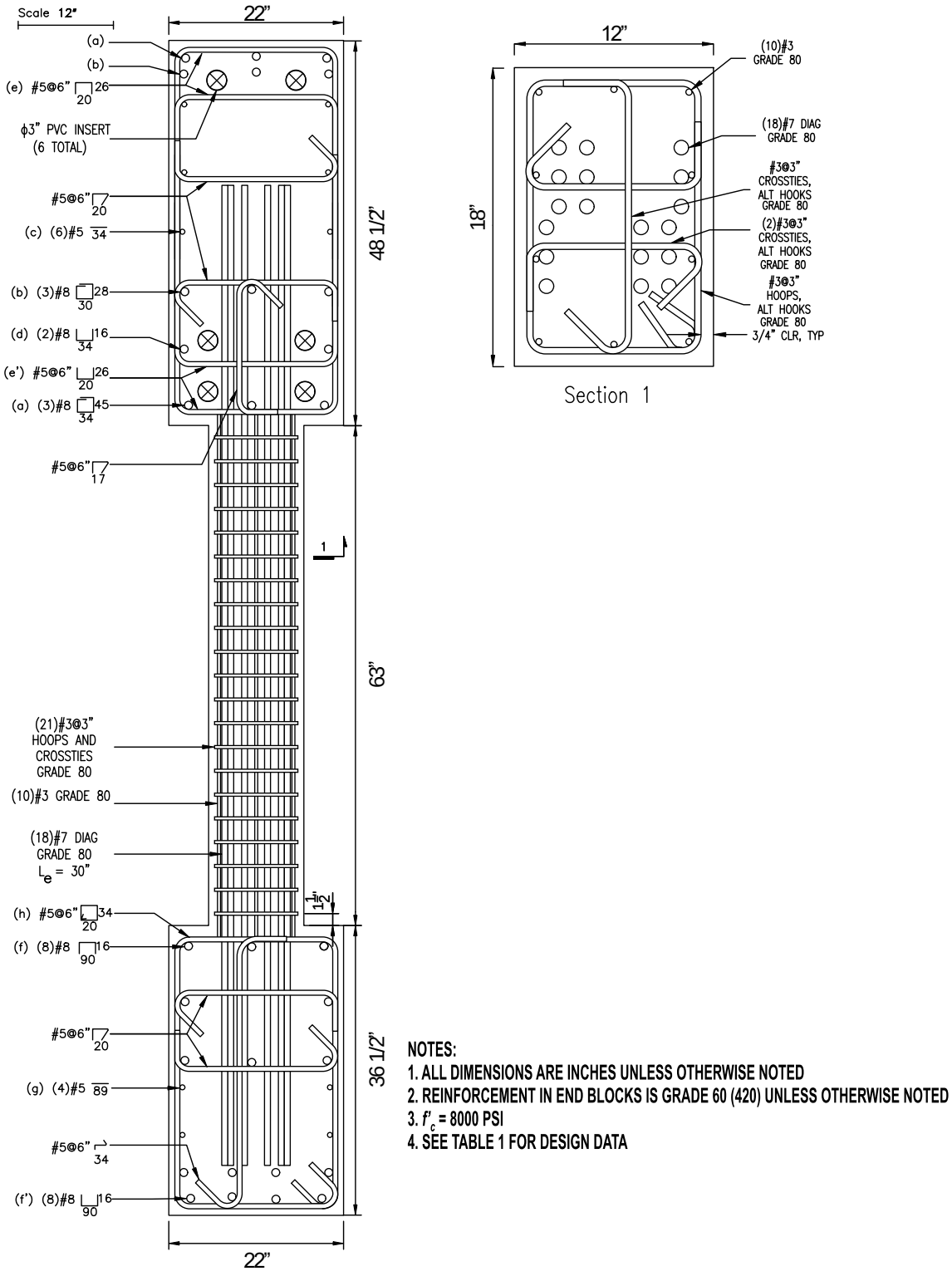

Figure 15 – Reinforcement details of D80-3.5 (1 in. = 25.4 mm, 1 ksi = 1,000 psi = 6.89 MPa)

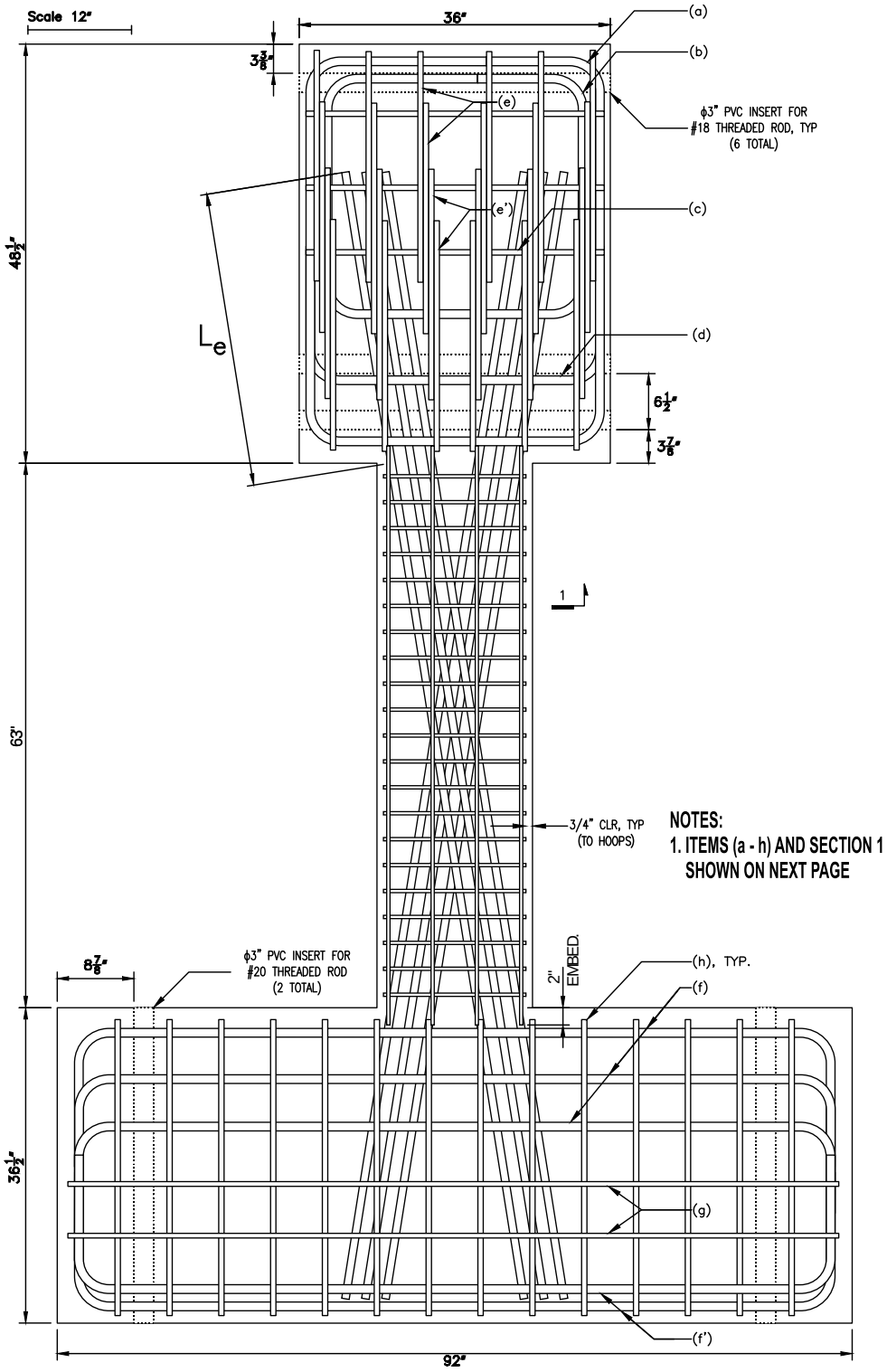

Figure 16 – Elevation view of D100-3.5 (1 in. = 25.4 mm)

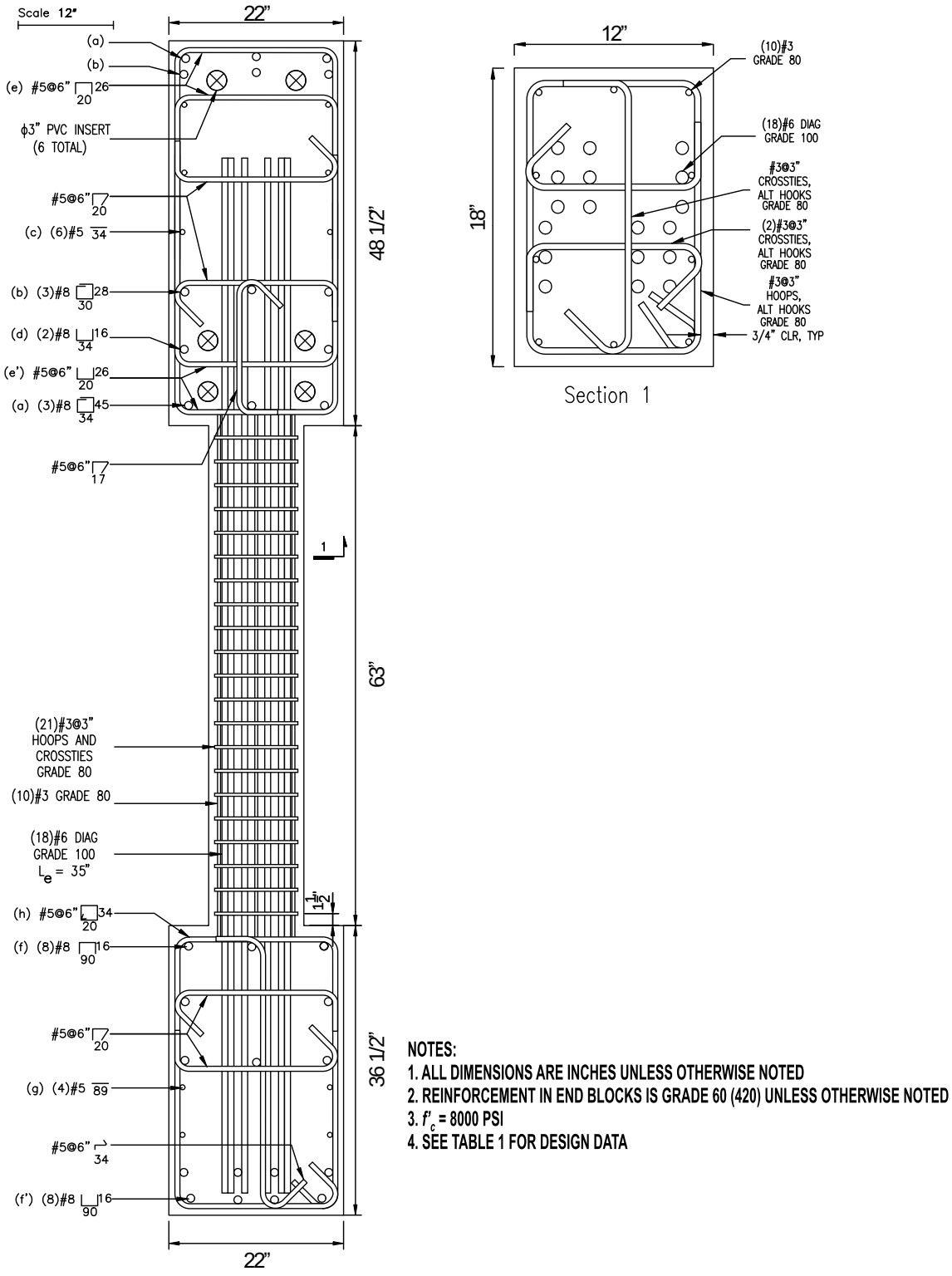

Figure 17 – Reinforcement details of D100-3.5 (1 in. = 25.4 mm, 1 ksi = 1,000 psi = 6.89 MPa)

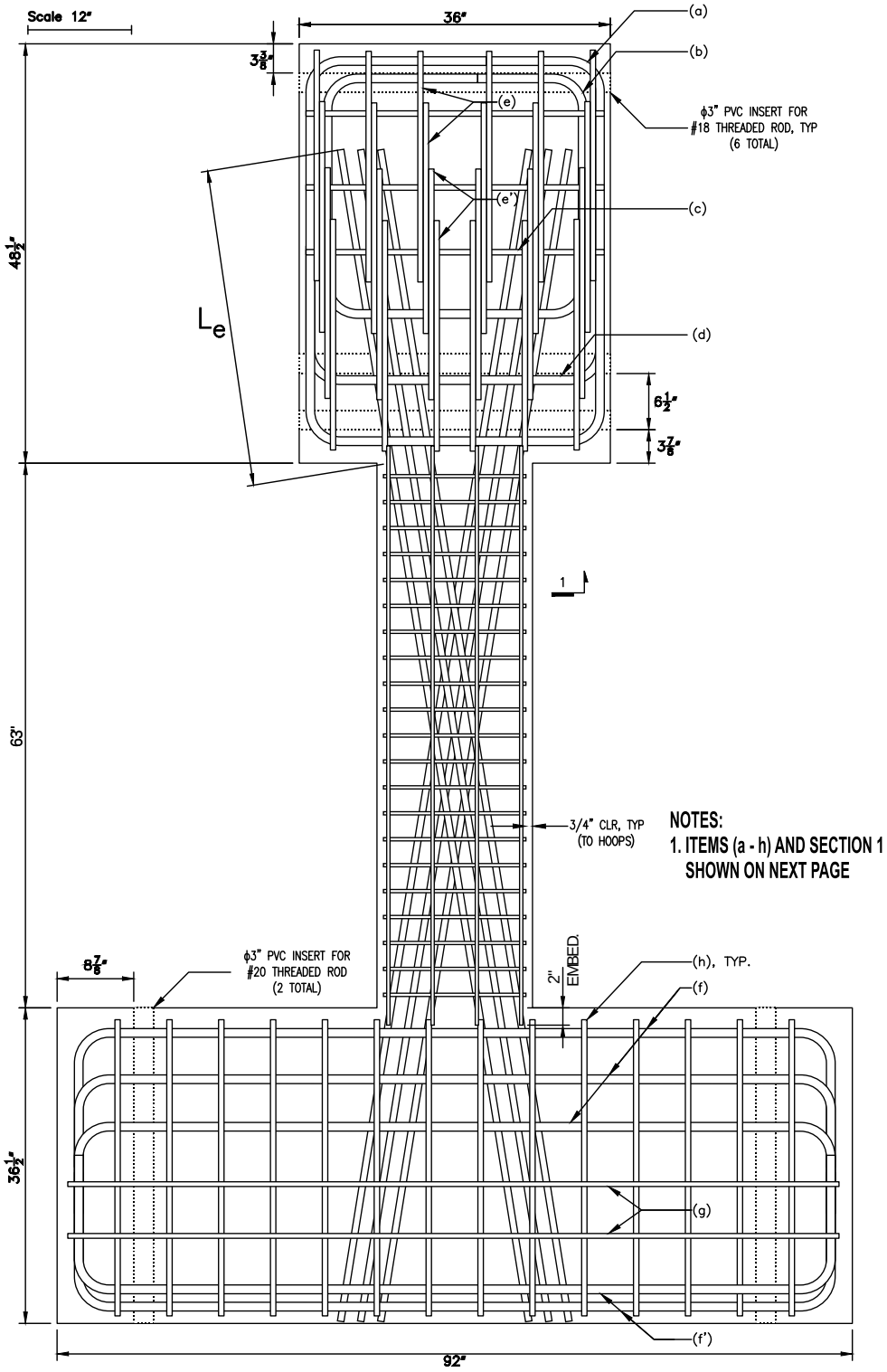

Figure 18 – Elevation view of D120-3.5 (1 in. = 25.4 mm)

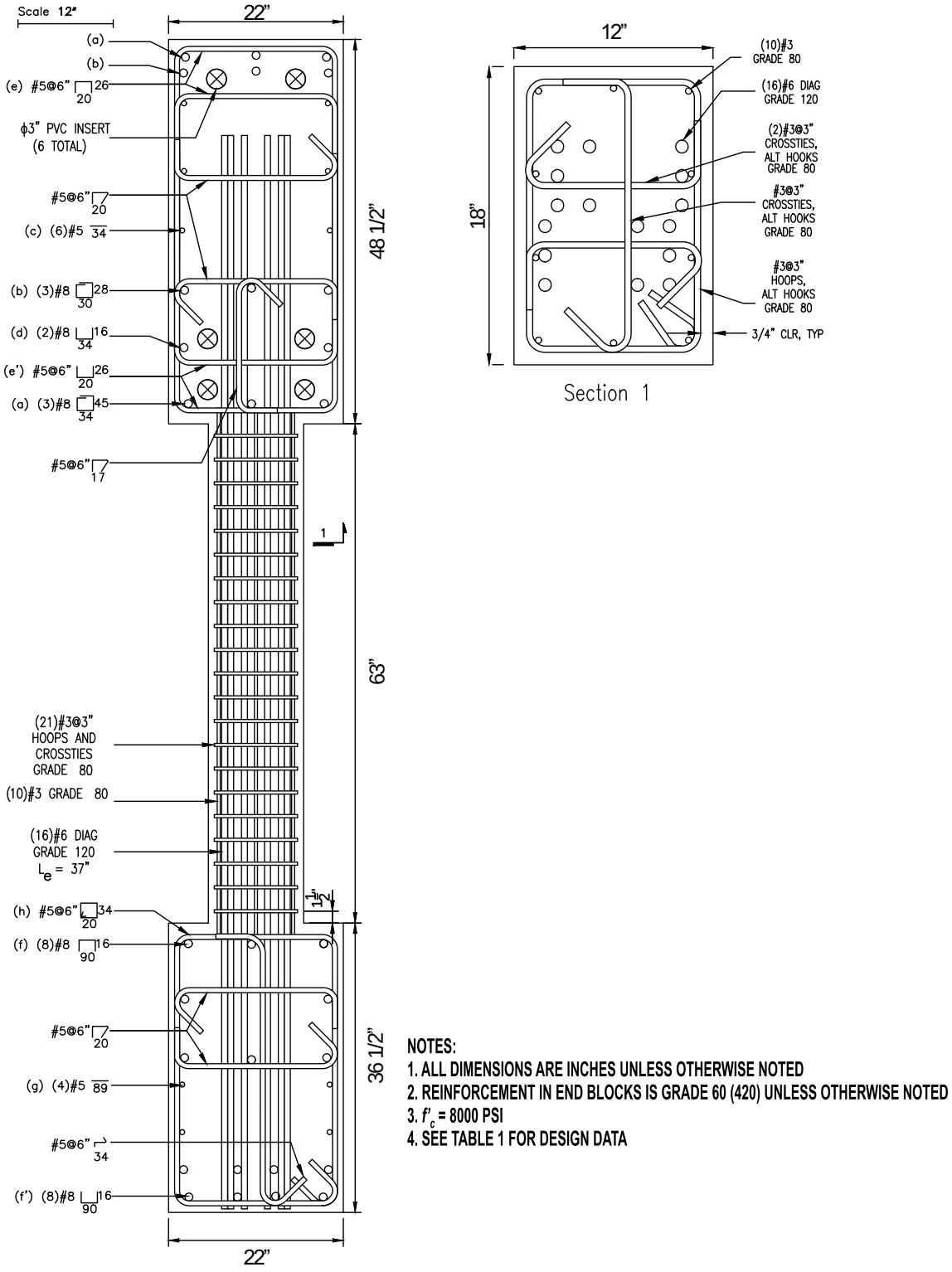

Figure 19 – Reinforcement details of D120-3.5 (1 in. = 25.4 mm, 1 ksi = 1,000 psi = 6.89 MPa)

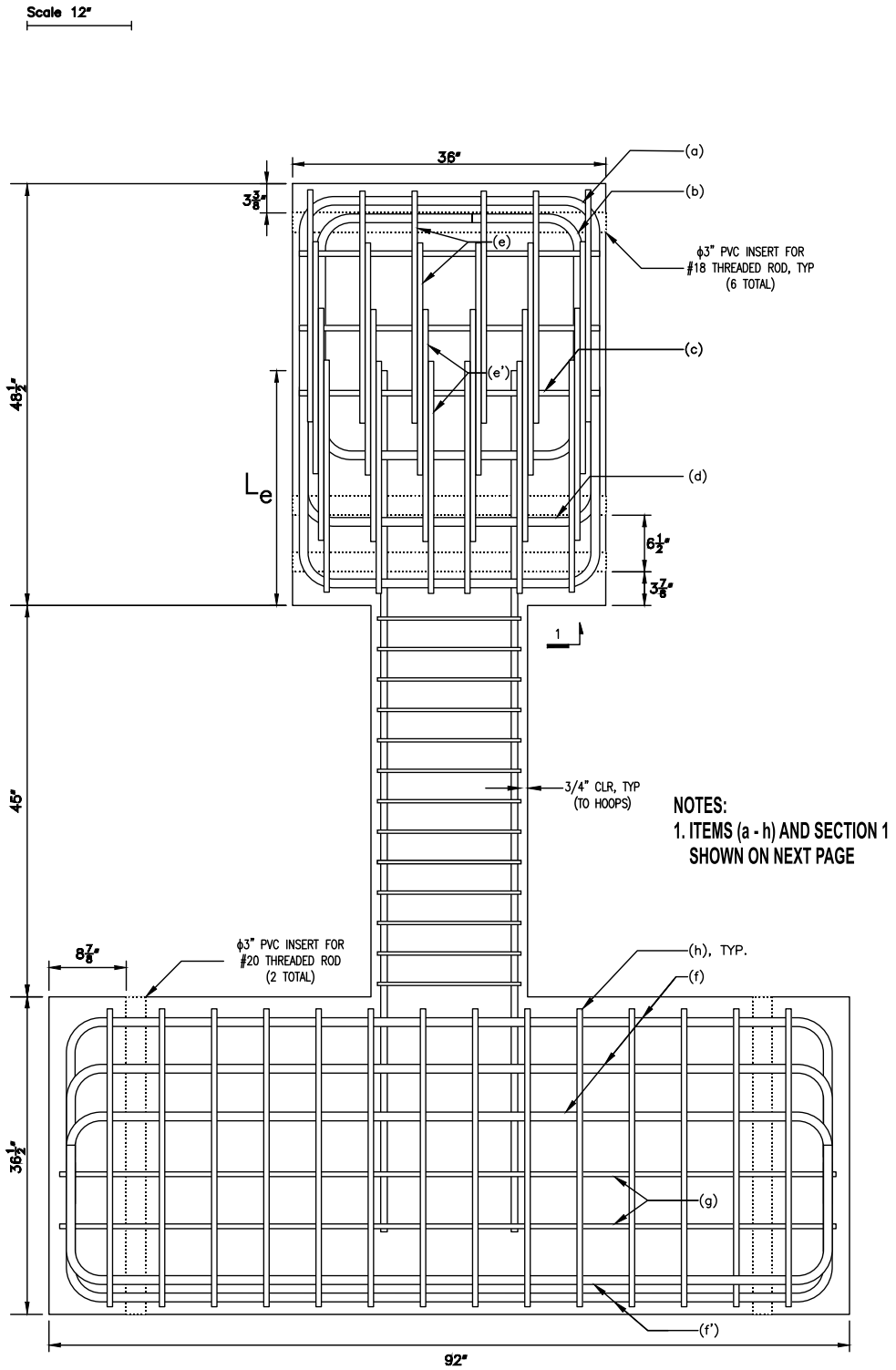

Figure 20 – Elevation view of P80-2.5 (1 in. = 25.4 mm)

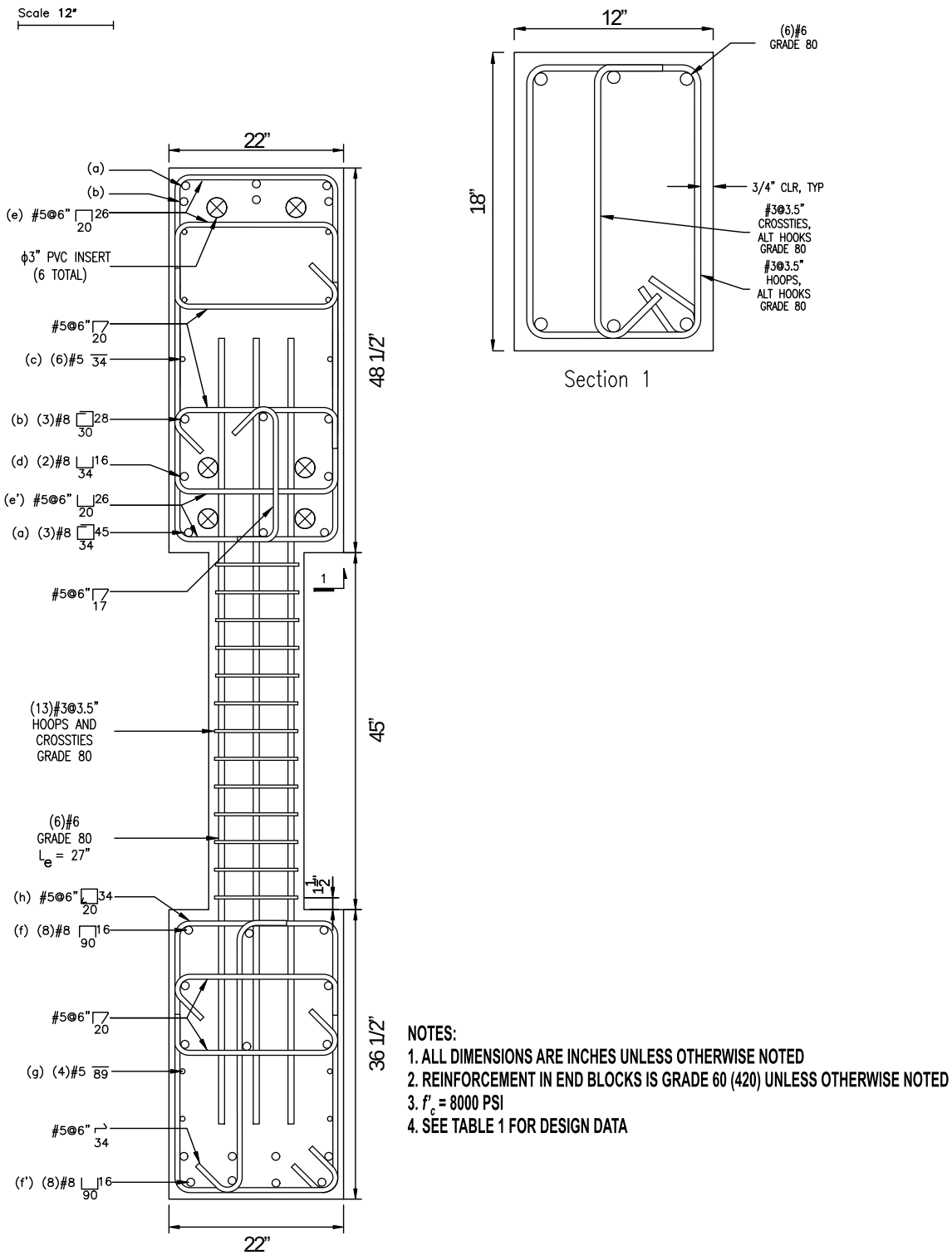

Figure 21 – Reinforcement details of P80-2.5 (1 in. = 25.4 mm, 1 ksi = 1,000 psi = 6.89 MPa)

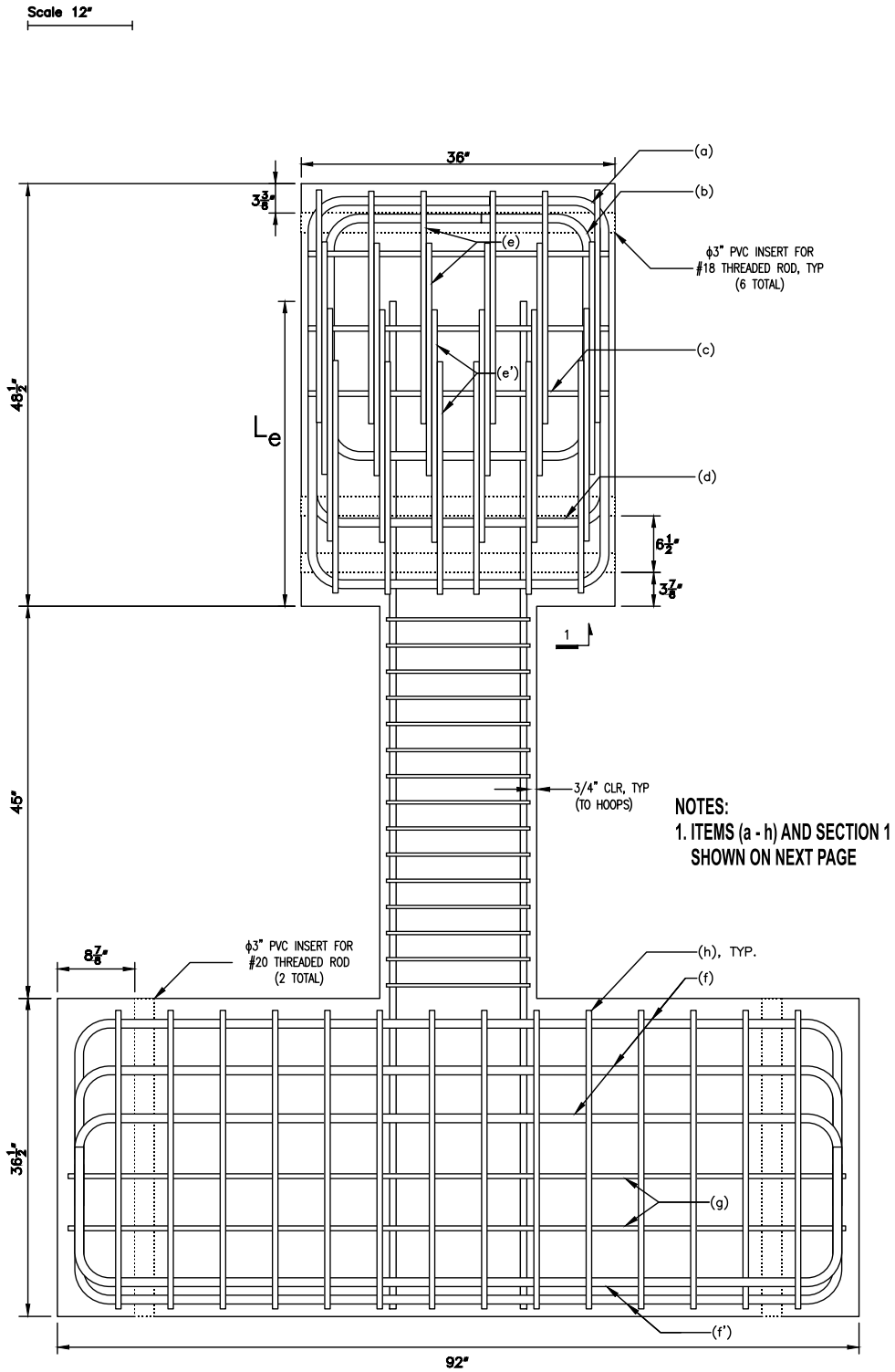

Figure 22 – Elevation view of P100-2.5 (1 in. = 25.4 mm)

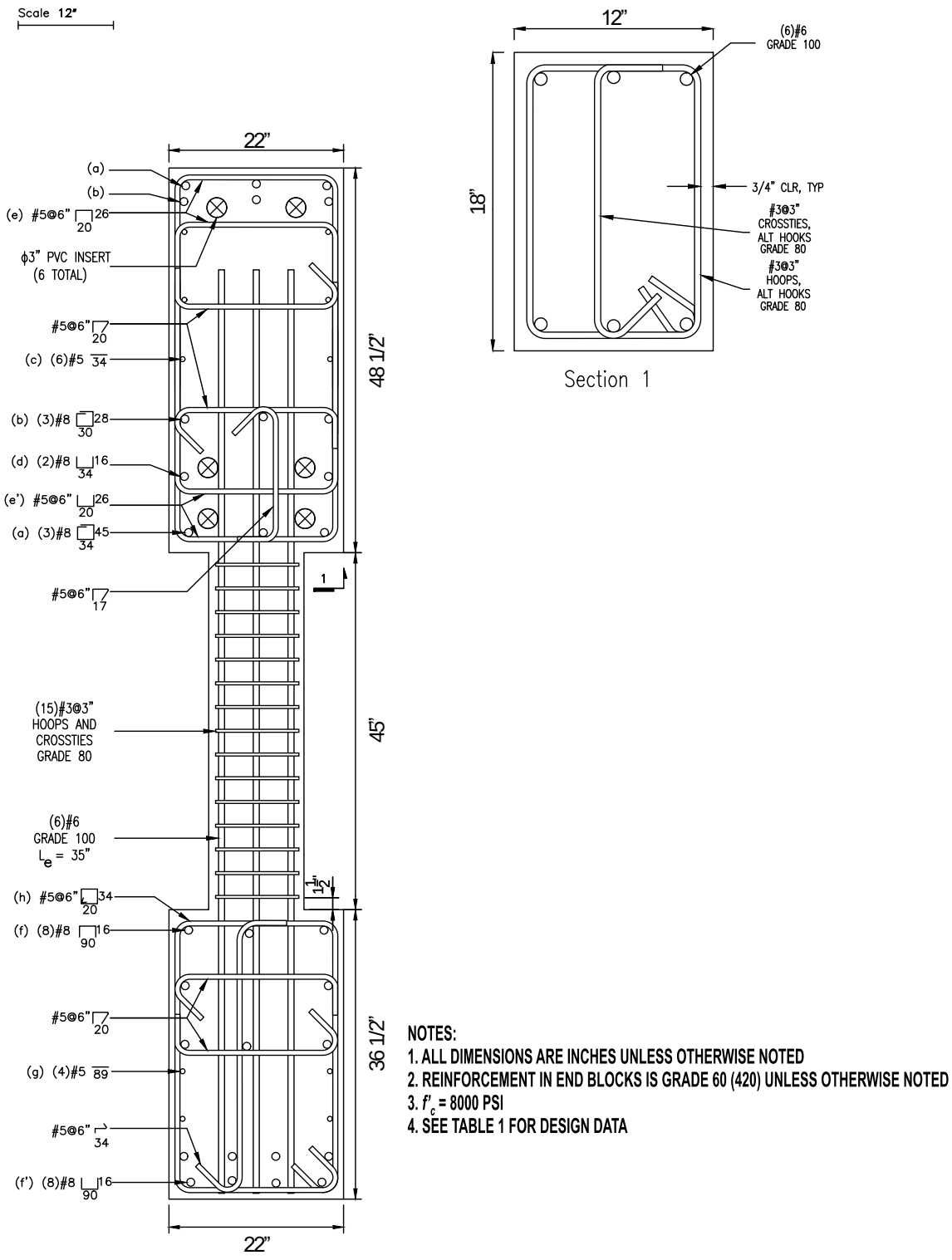

Figure 23 – Reinforcement details of P100-2.5 (1 in. = 25.4 mm, 1 ksi = 1,000 psi = 6.89 MPa)

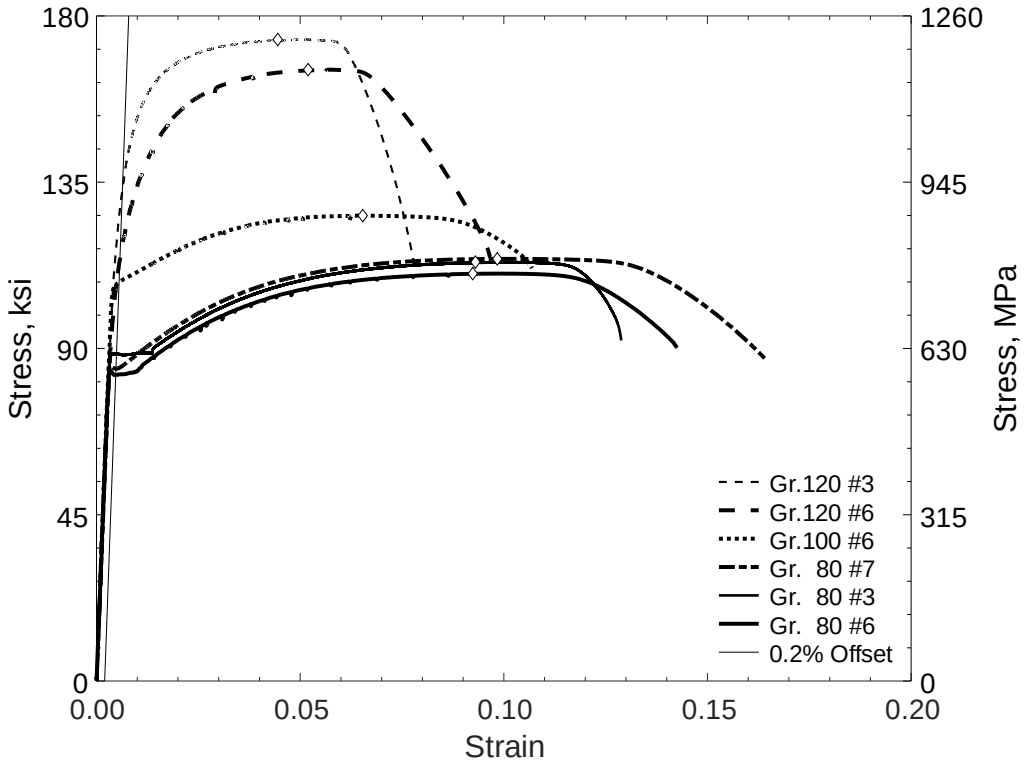

Figure 24 – Measured stress versus strain for reinforcement

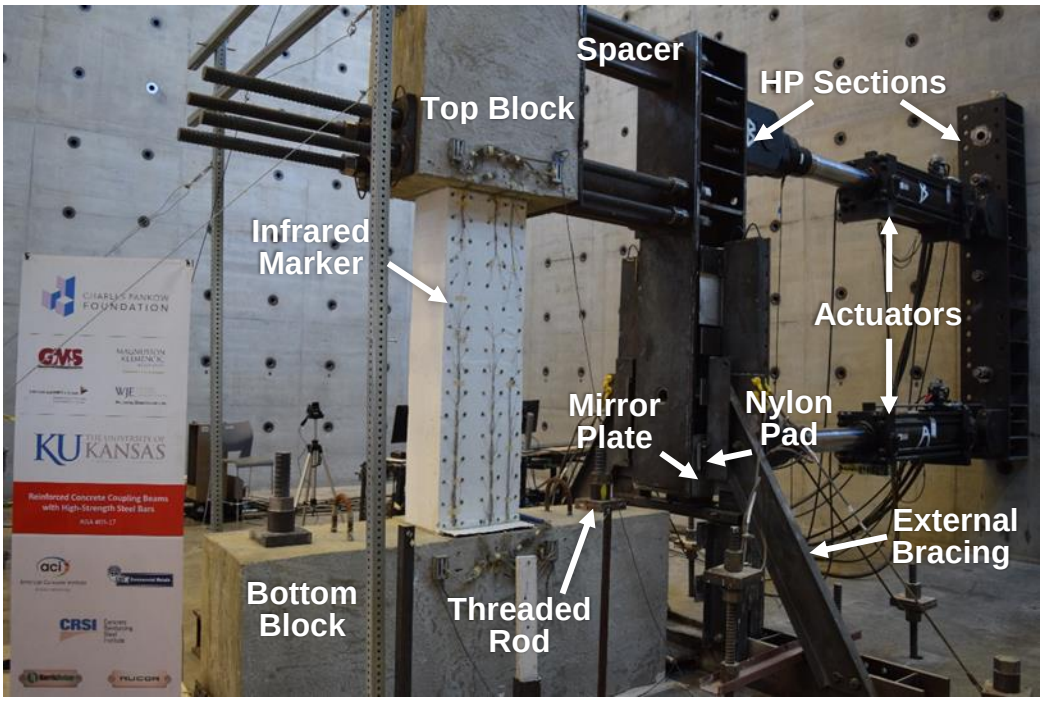

Figure 25 – Test setup, view from northeast

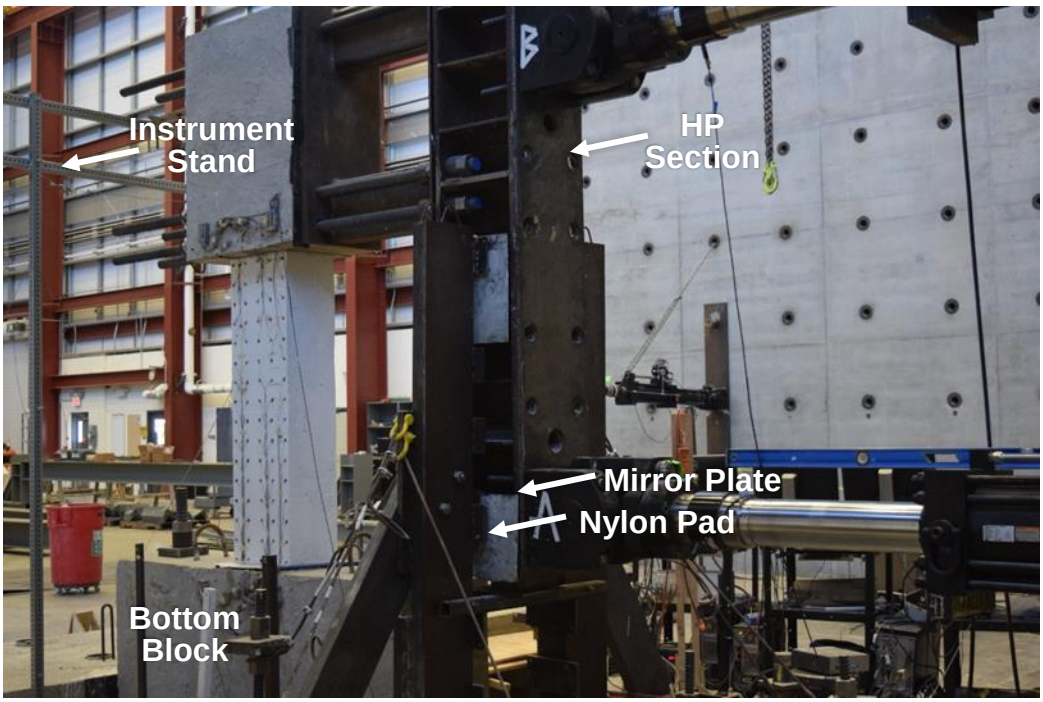

Figure 26 – Test setup, view from northwest

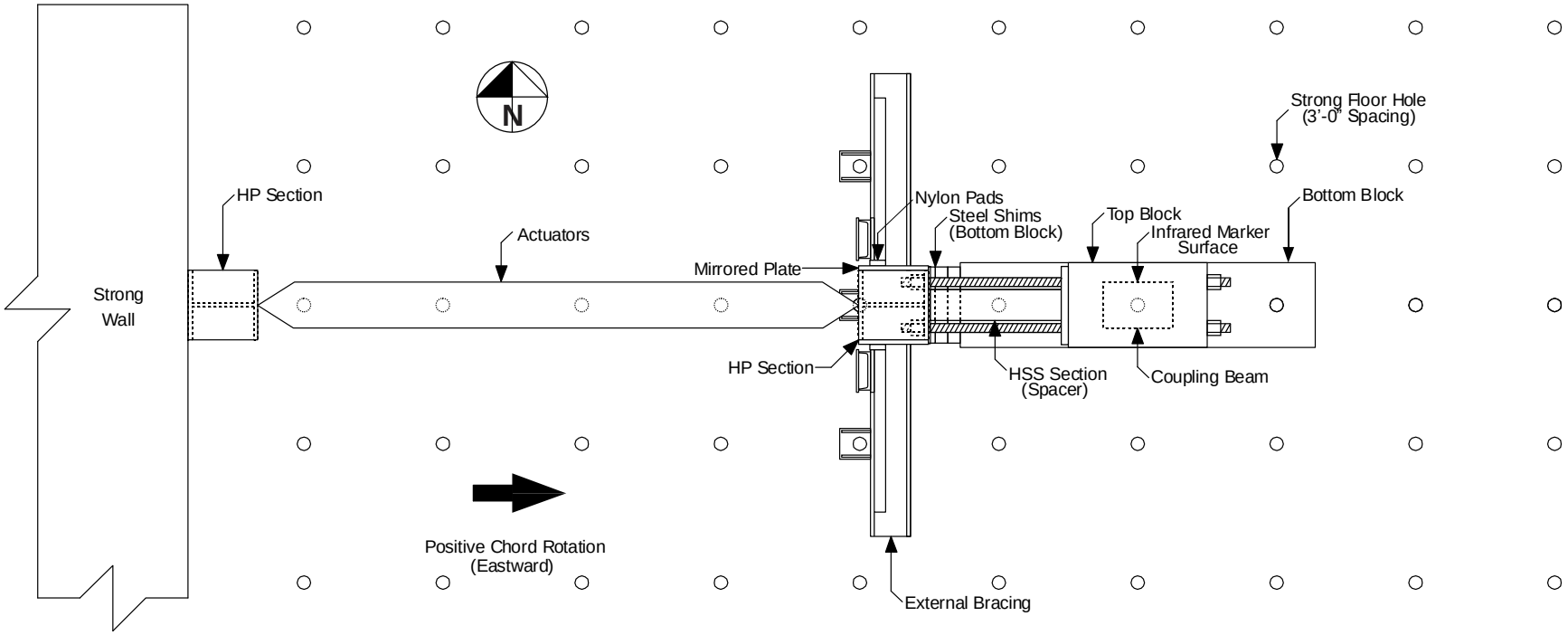

Figure 27 – Test setup, plan view

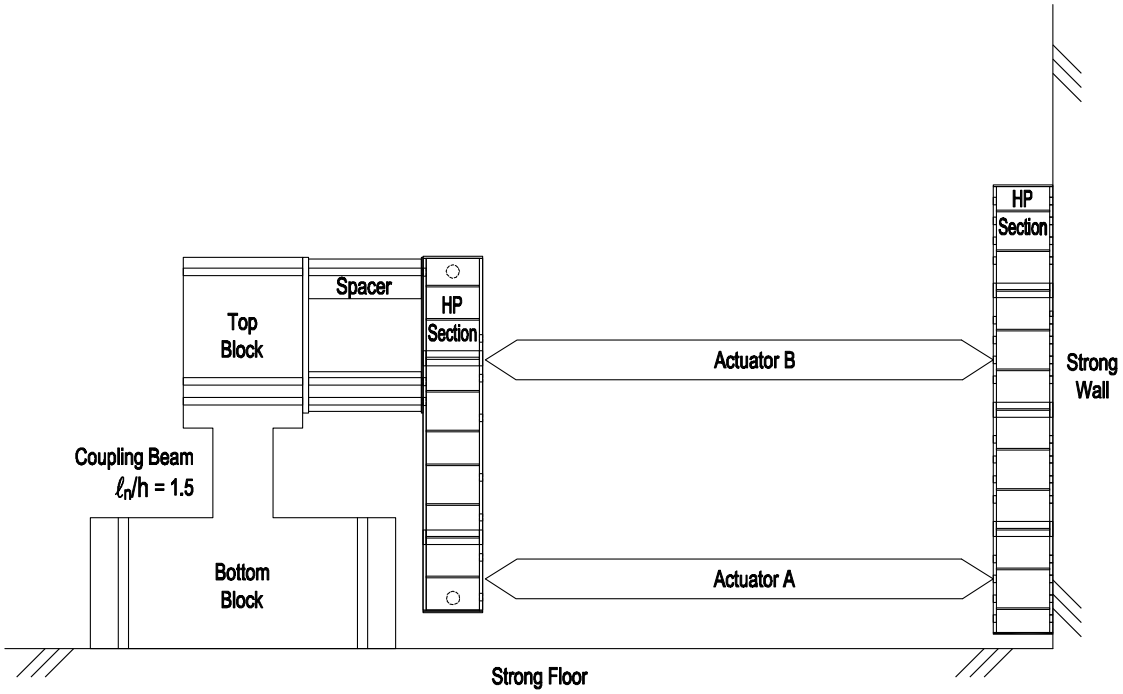

Figure 28 – Test setup schematics for coupling beams with aspect ratio of 1.5 [a]

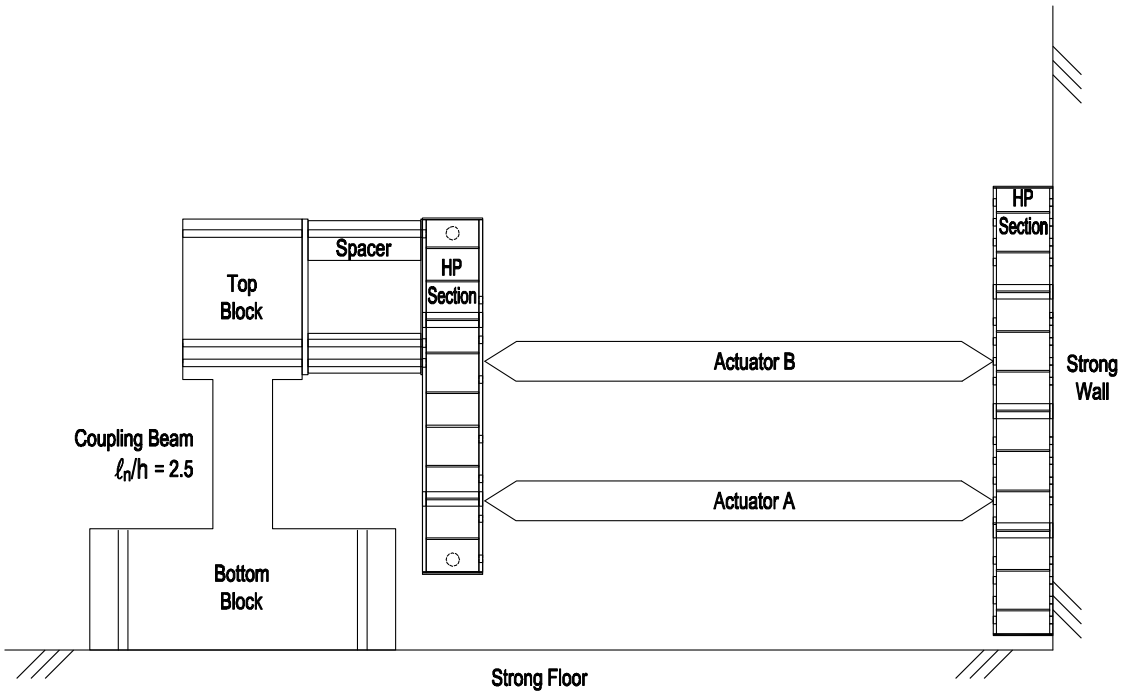

Figure 29 – Test setup schematics for coupling beams with aspect ratio of 2.5 [a]

[a] External bracing omitted for clarity. For actuator and coupling beam elevations, see Table 5.

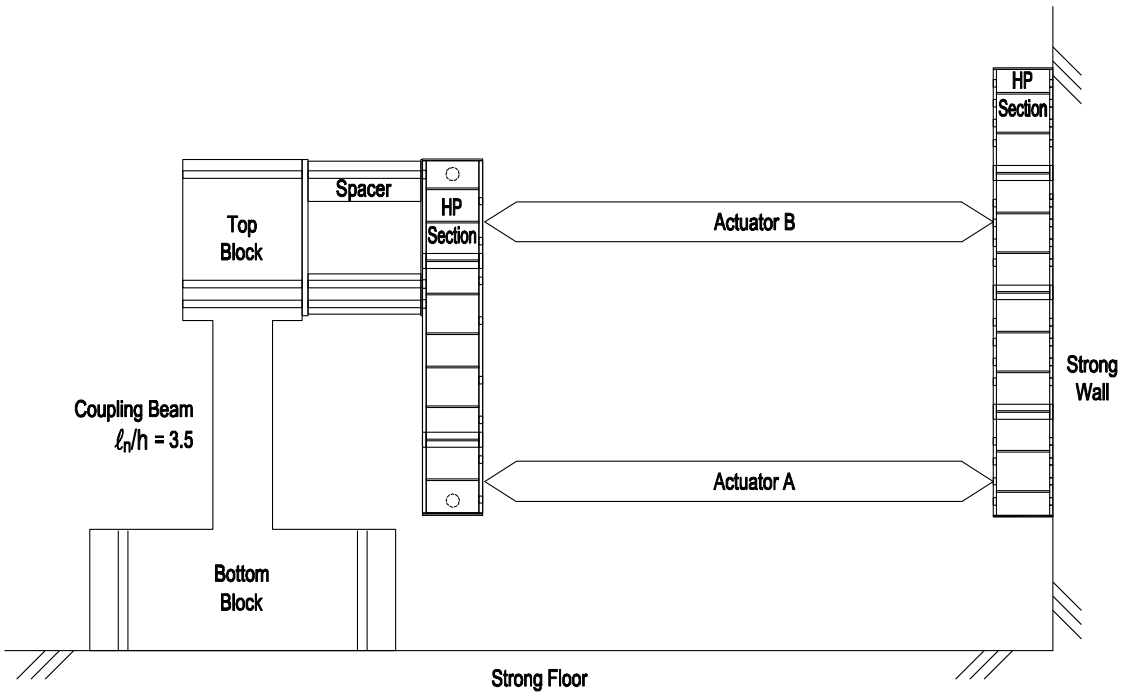

Figure 30 – Test setup schematics for coupling beams with aspect ratio of 3.5 [a]

[a] External bracing omitted for clarity. For actuator and coupling beam elevations, see Table 5.

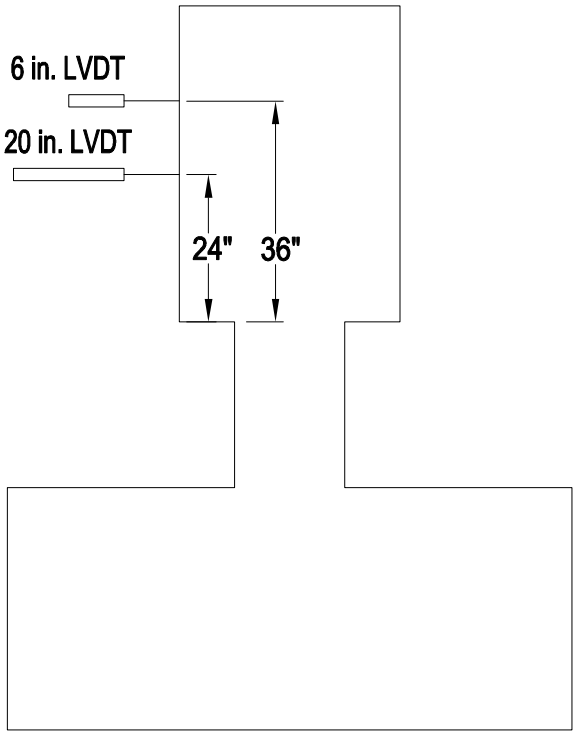

Figure 31 – LVDT locations (1 in. = 25.4 mm)

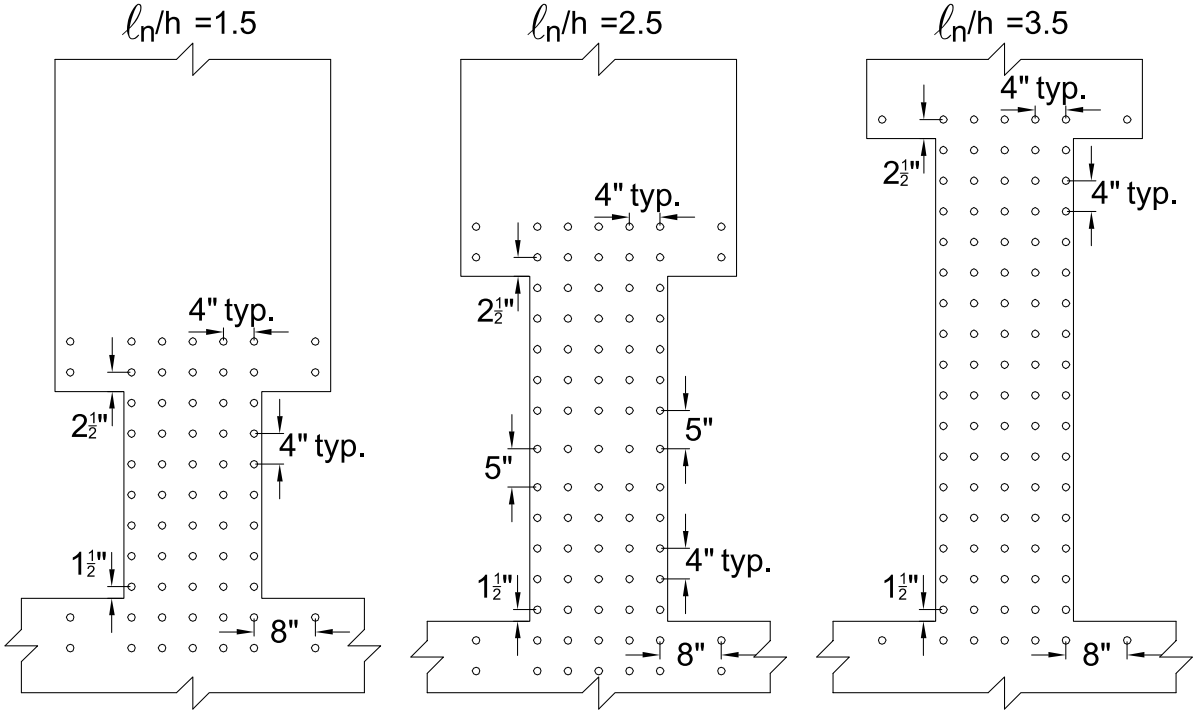

Figure 32 – Infrared marker positions (1 in. = 25.4 mm)

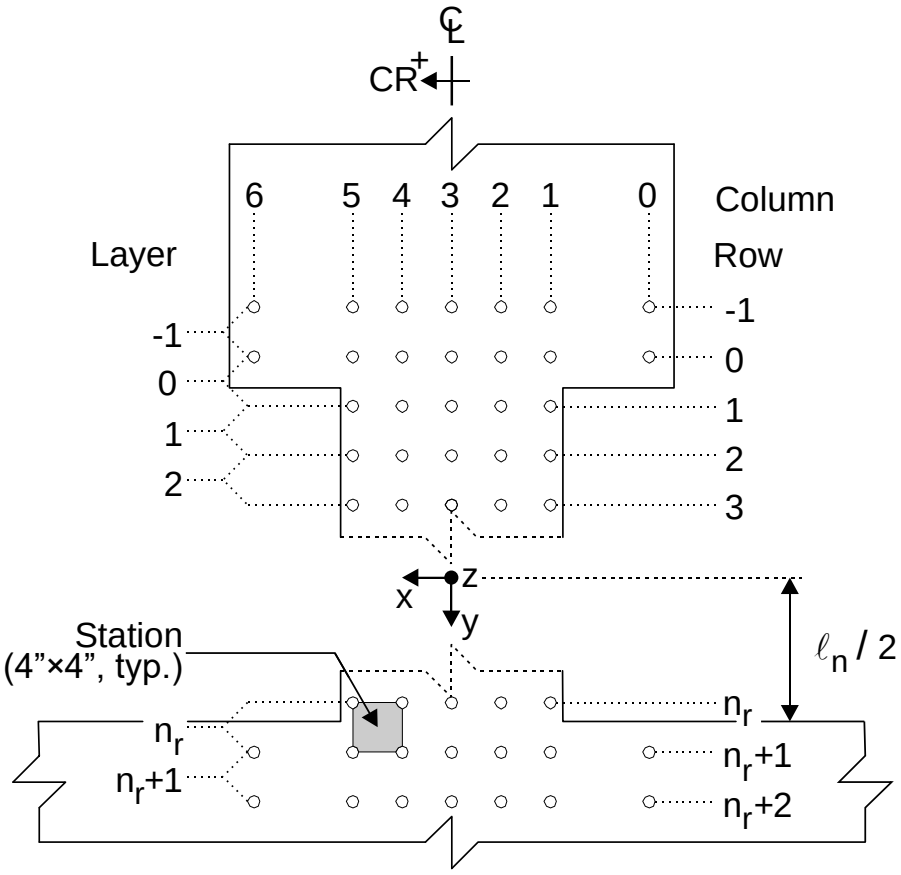

Figure 33 – Infrared marker identification by row, column, and layer (1 in. = 25.4 mm)

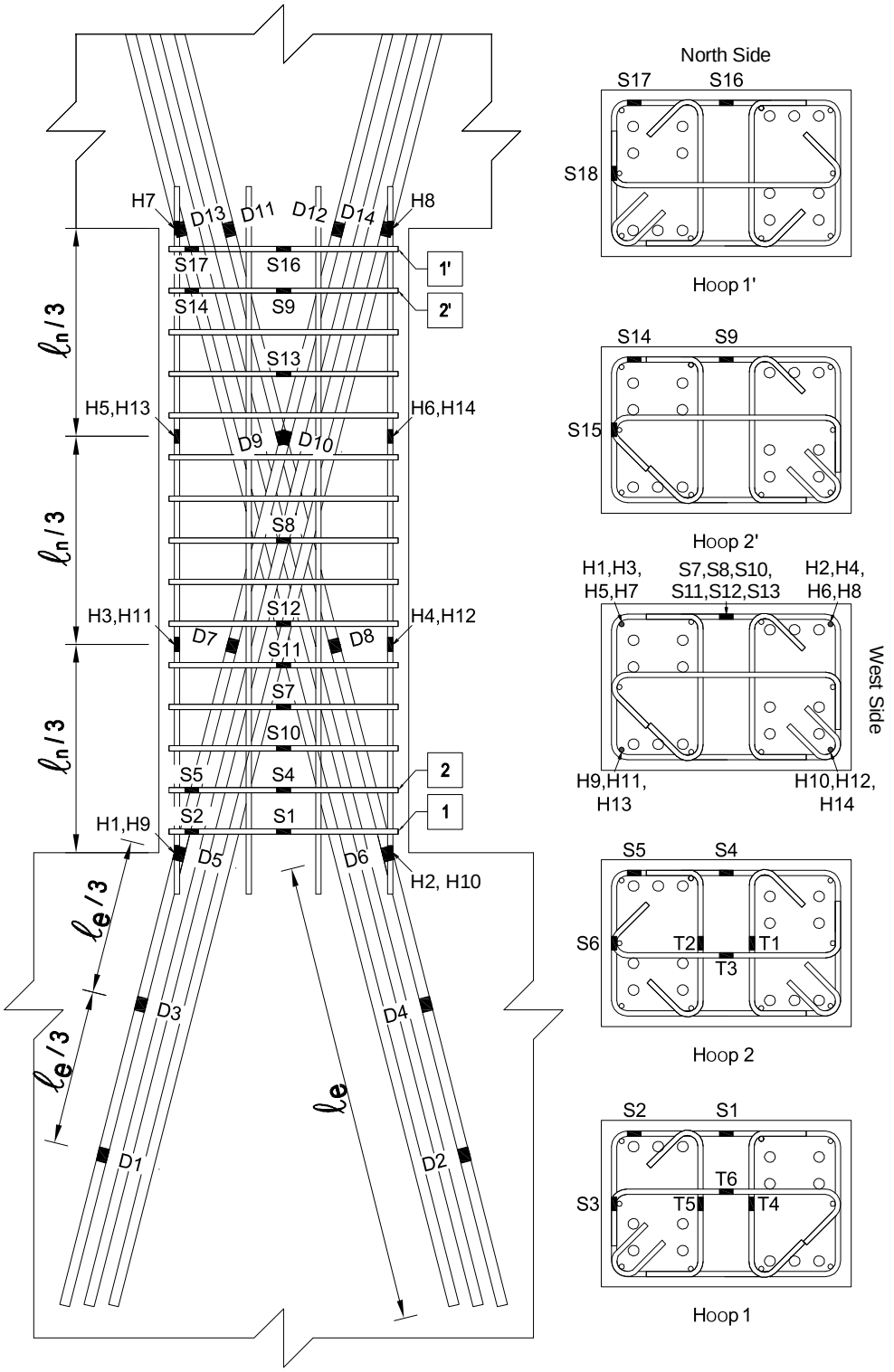

Figure 34 – Strain gauge layout (view from north), D-type specimens

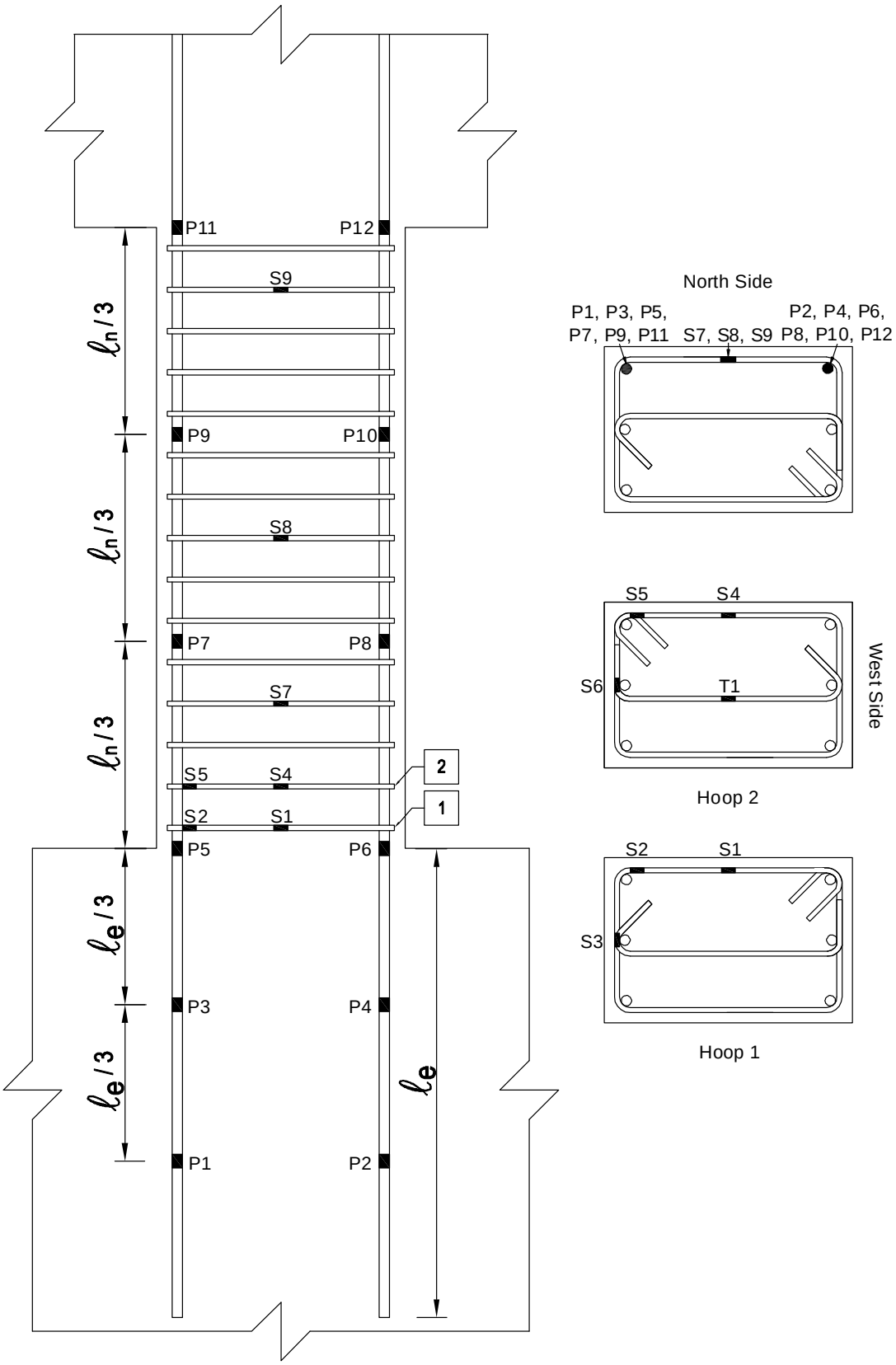

Figure 35 – Strain gauge layout (view from north), P-type specimens

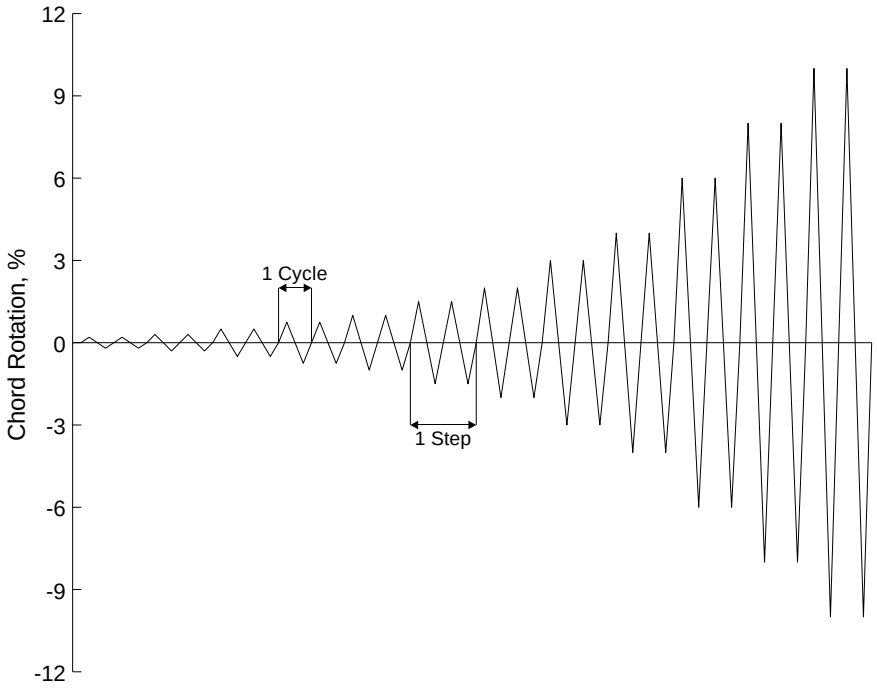

Figure 36 – Loading protocol [a]

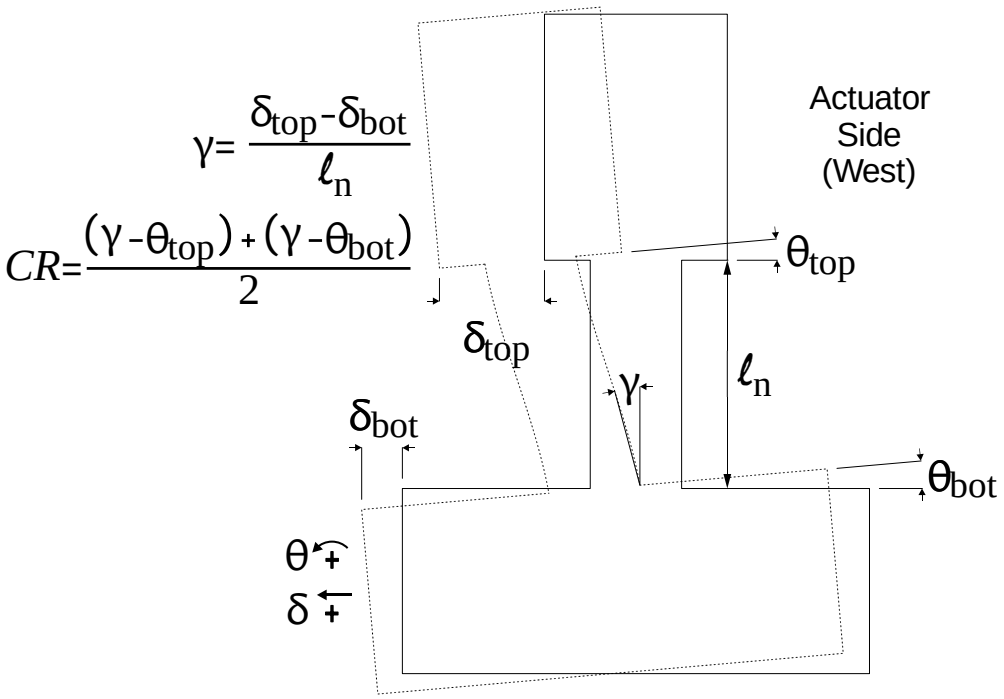

Figure 37 – General deformed shape of specimen, view from north [b]

[a] Values listed in Table 8.

[b] Positive displacement corresponds to actuator extension toward laboratory east.

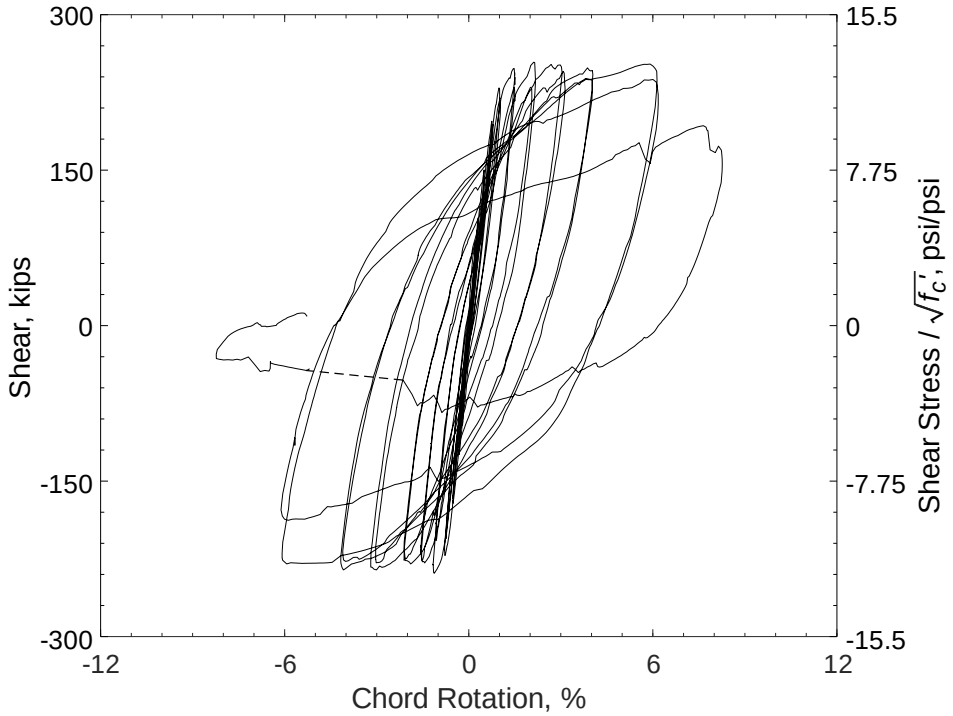

Figure 38 – Shear versus chord rotation for D80-1.5
(1,000 psi = 6.89 MPa, 1 kip = 4.45 kN)

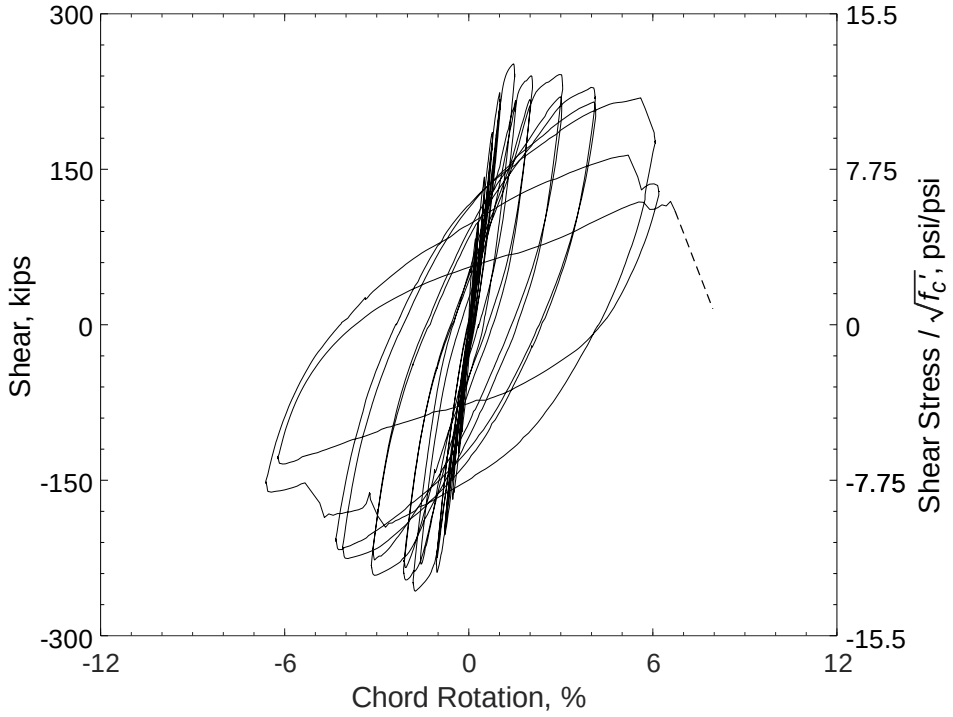

Figure 39 – Shear versus chord rotation for D100-1.5
(1,000 psi = 6.89 MPa, 1 kip = 4.45 kN)

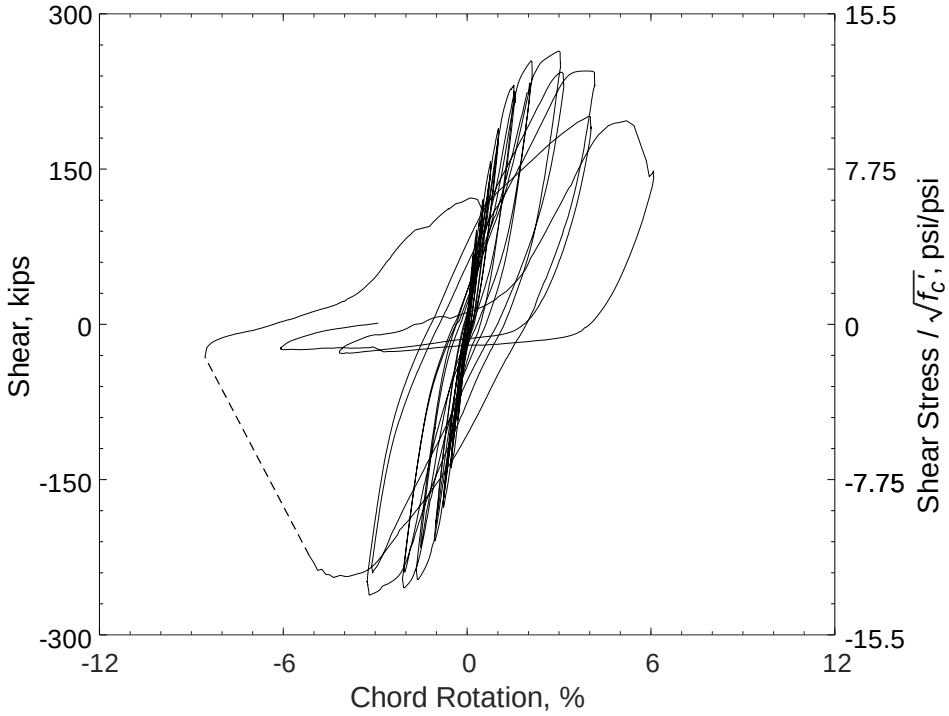

Figure 40 – Shear versus chord rotation for D120-1.5
(1,000 psi = 6.89 MPa, 1 kip = 4.45 kN)

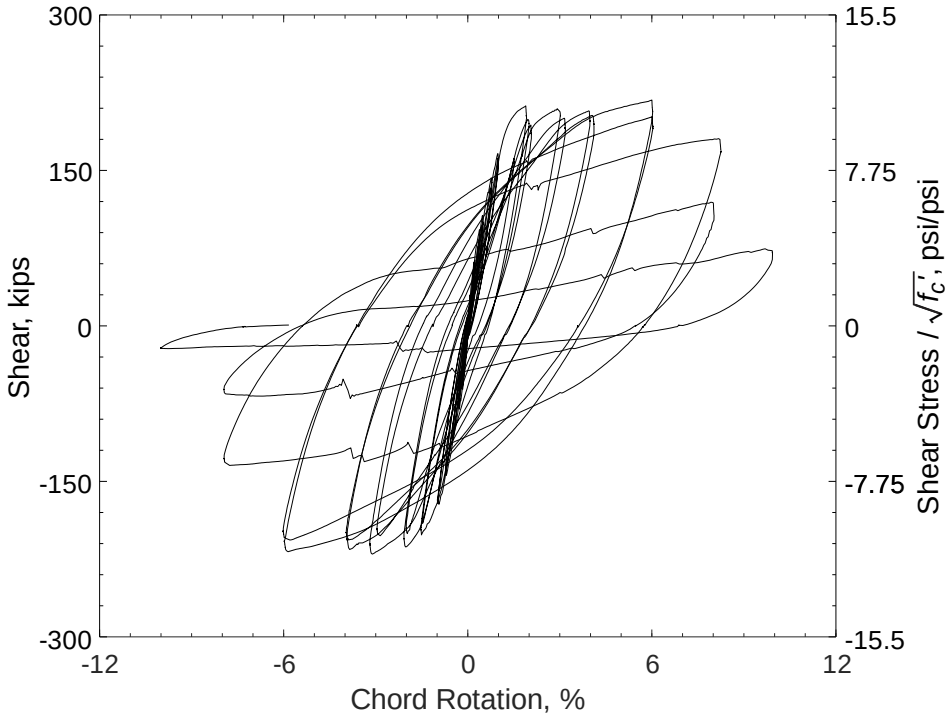

Figure 41 – Shear versus chord rotation for D80-2.5
(1,000 psi = 6.89 MPa, 1 kip = 4.45 kN)

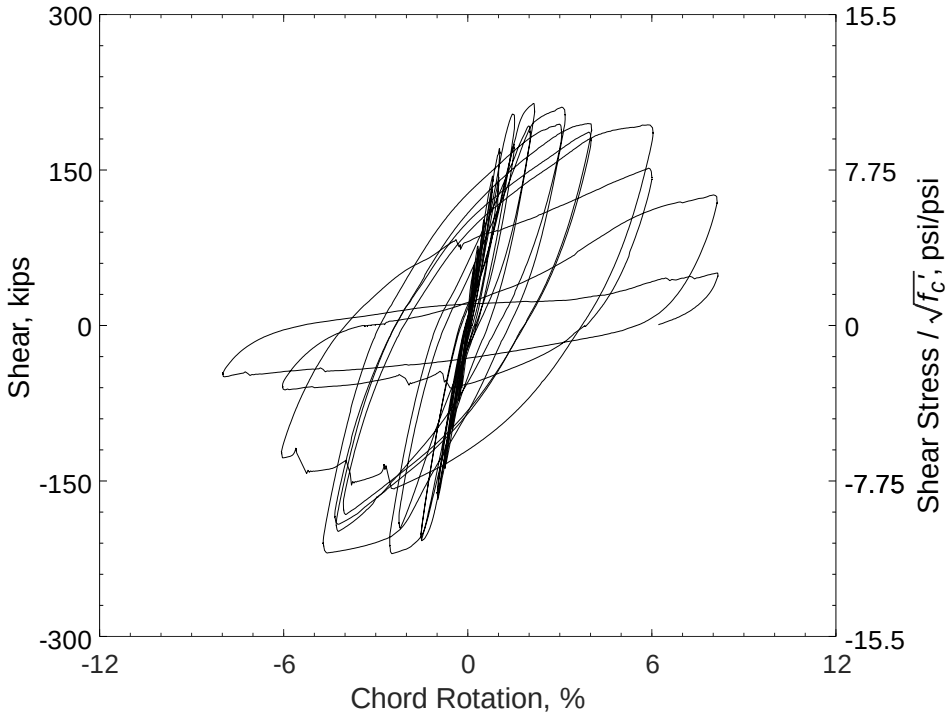

Figure 42 – Shear versus chord rotation for D100-2.5
(1,000 psi = 6.89 MPa, 1 kip = 4.45 kN)

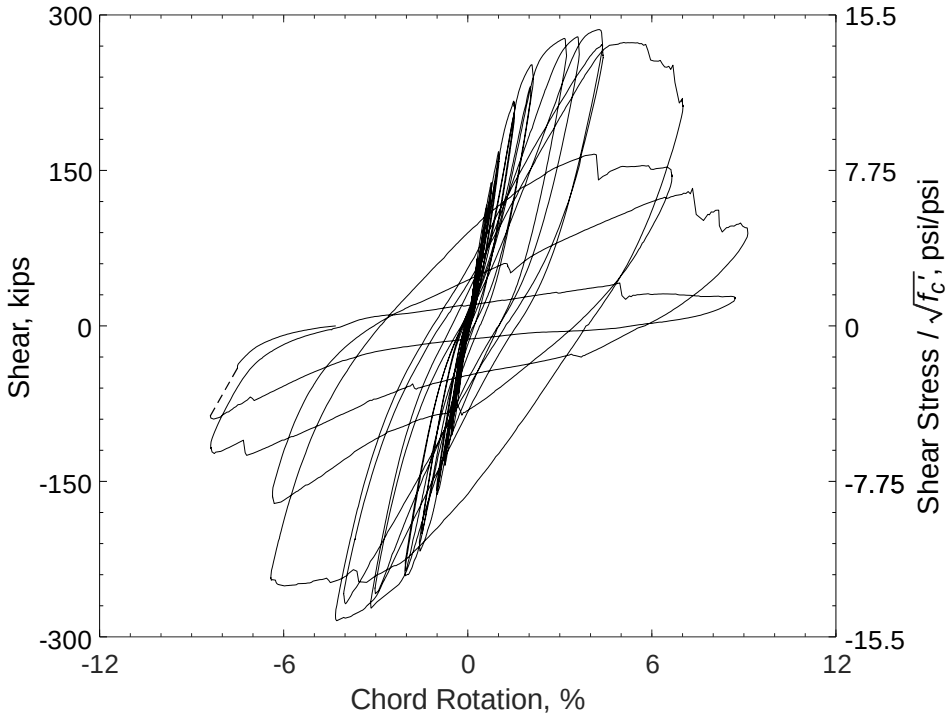

Figure 43 – Shear versus chord rotation for D120-2.5
(1,000 psi = 6.89 MPa, 1 kip = 4.45 kN)

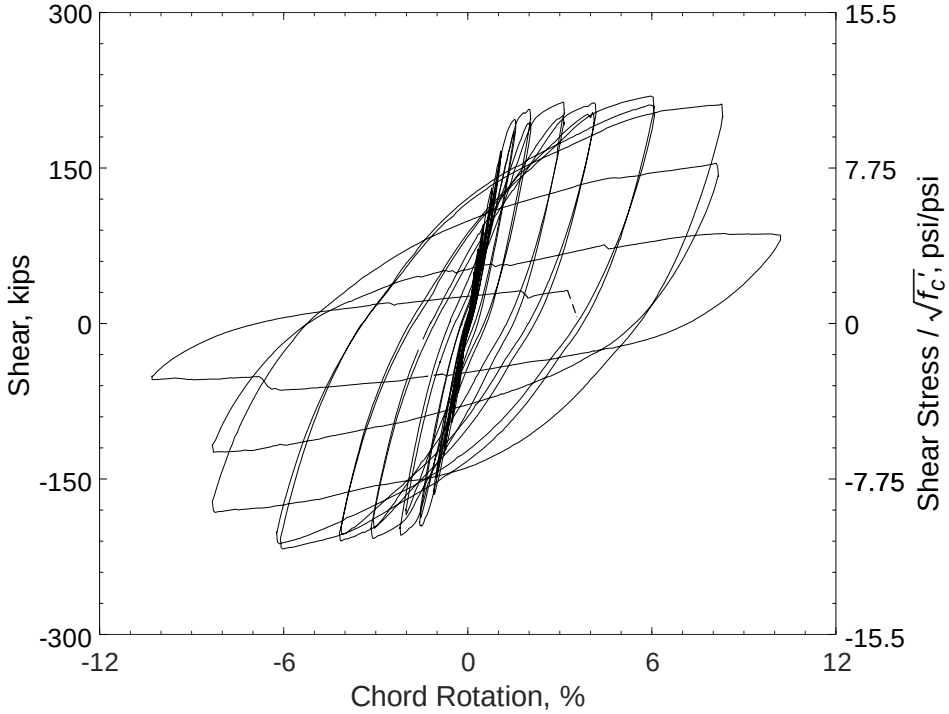

Figure 44 – Shear versus chord rotation for D80-3.5
(1,000 psi = 6.89 MPa, 1 kip = 4.45 kN)

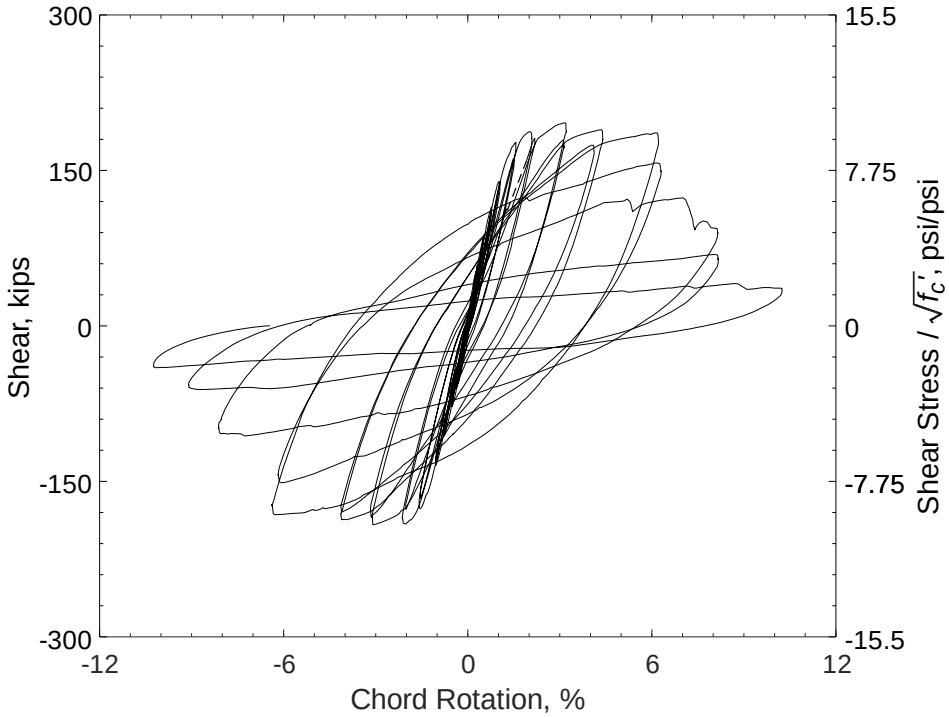

Figure 45 – Shear versus chord rotation for D100-3.5
(1,000 psi = 6.89 MPa, 1 kip = 4.45 kN)

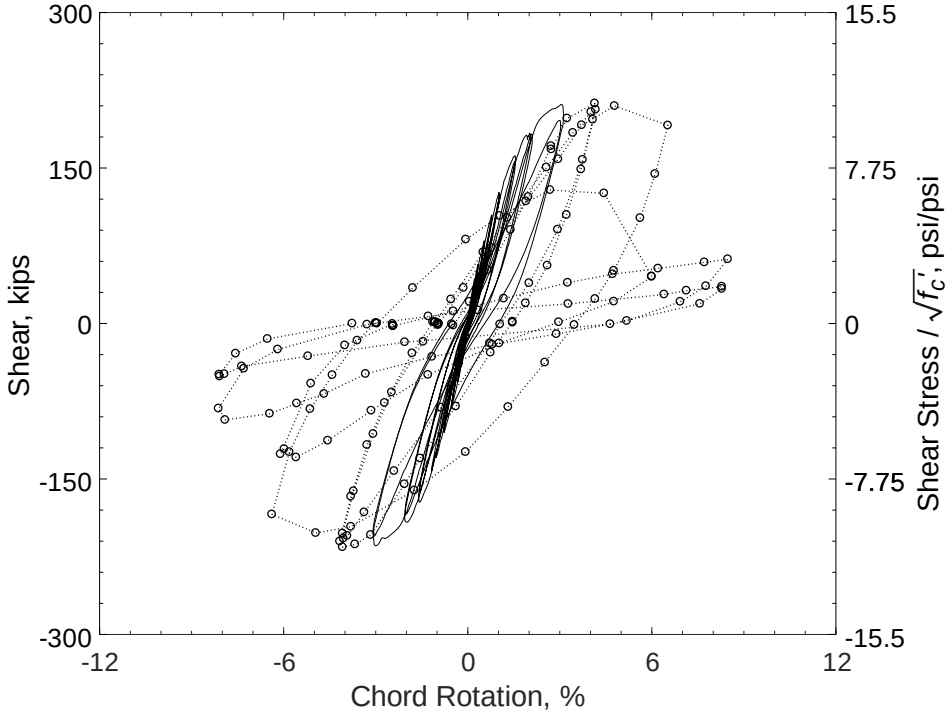

Figure 46 – Shear versus chord rotation for D120-3.5
(1,000 psi = 6.89 MPa, 1 kip = 4.45 kN)

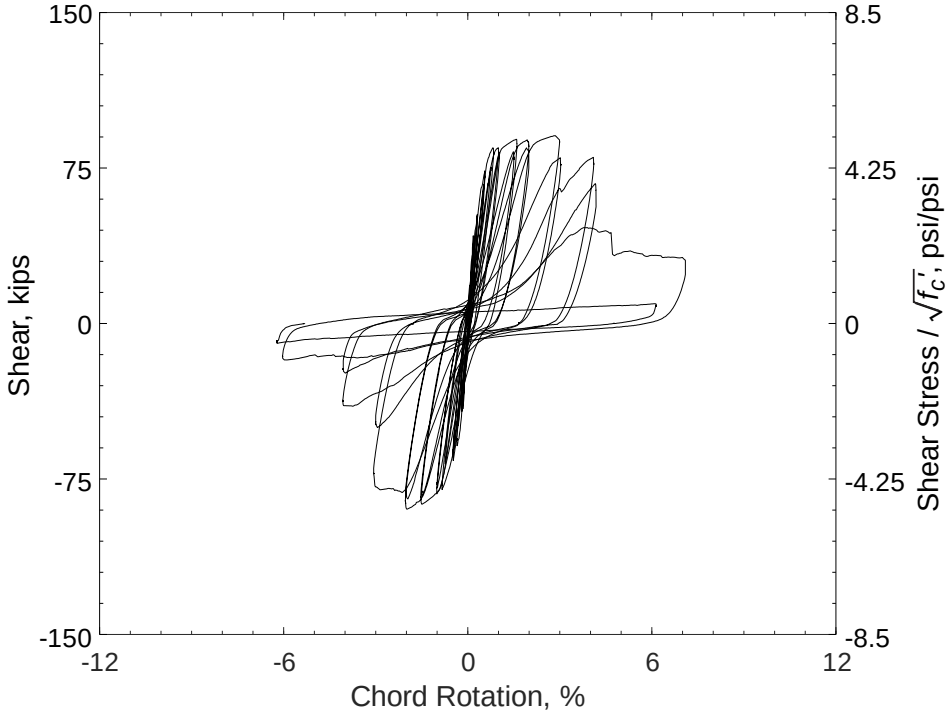

Figure 47 – Shear versus chord rotation for P80-2.5
(1,000 psi = 6.89 MPa, 1 kip = 4.45 kN)

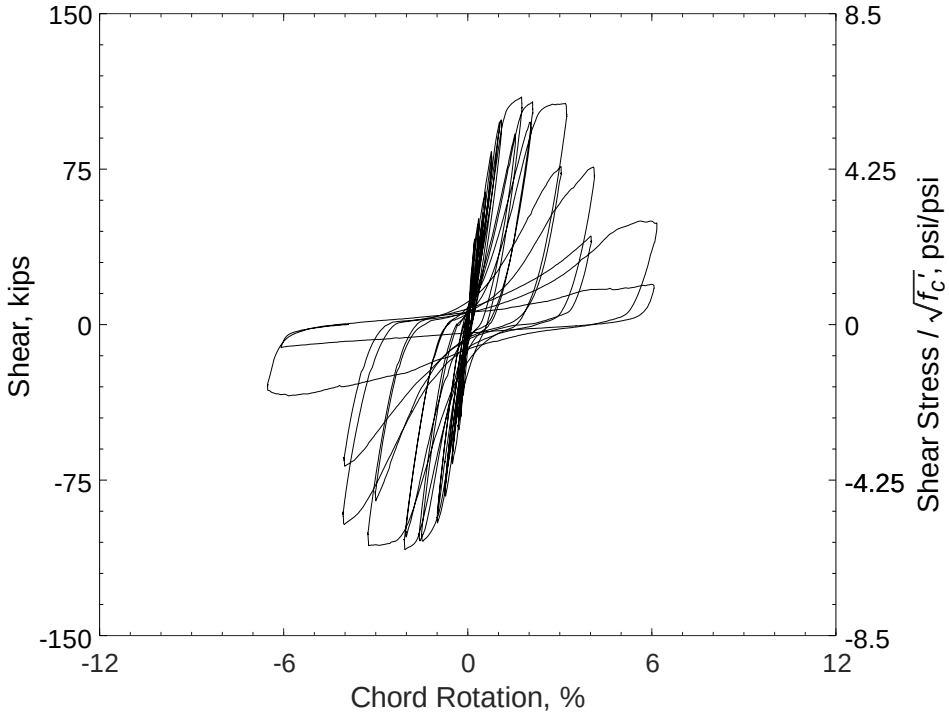

Figure 48 – Shear versus chord rotation for P100-2.5
(1,000 psi = 6.89 MPa, 1 kip = 4.45 kN)

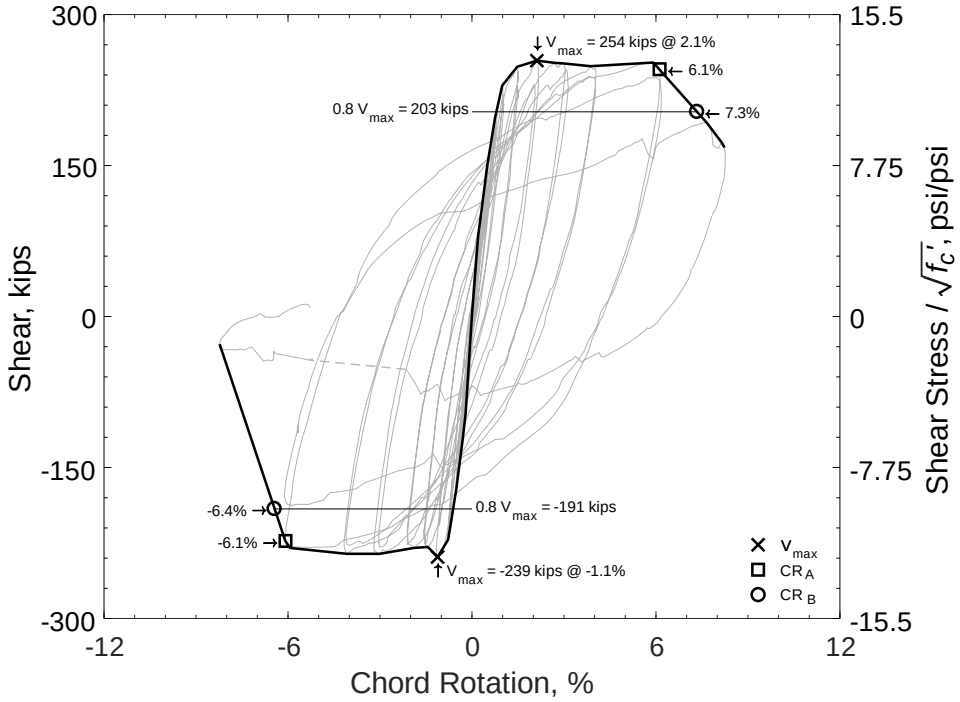

Figure 49 – Shear versus chord rotation envelope for D80-1.5
(1,000 psi = 6.89 MPa, 1 kip = 4.45 kN)

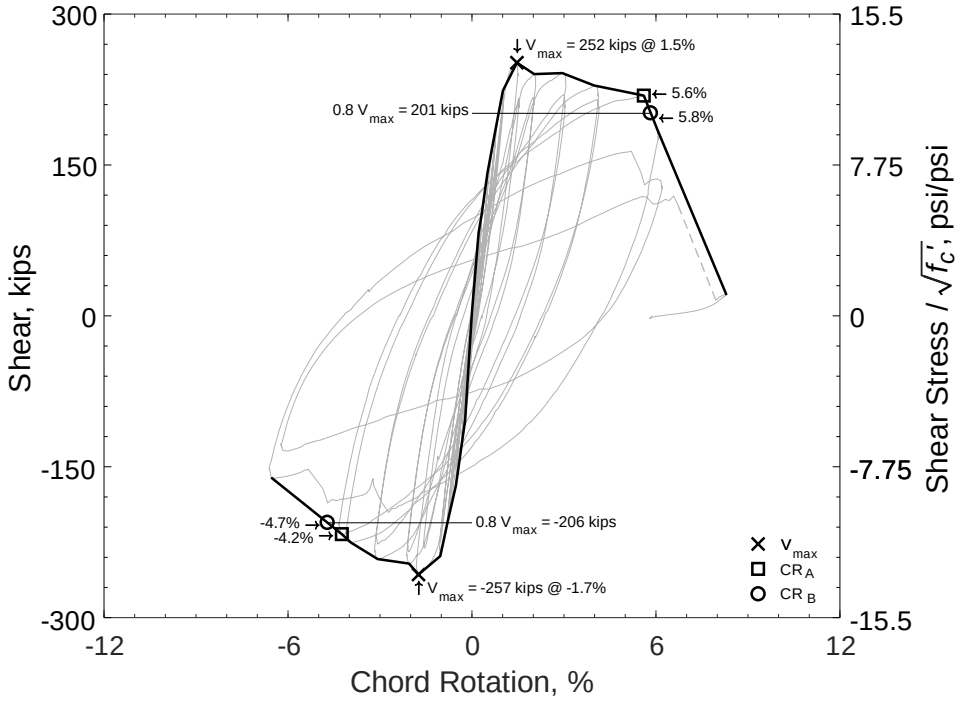

Figure 50 – Shear versus chord rotation envelope for D100-1.5
(1,000 psi = 6.89 MPa, 1 kip = 4.45 kN)

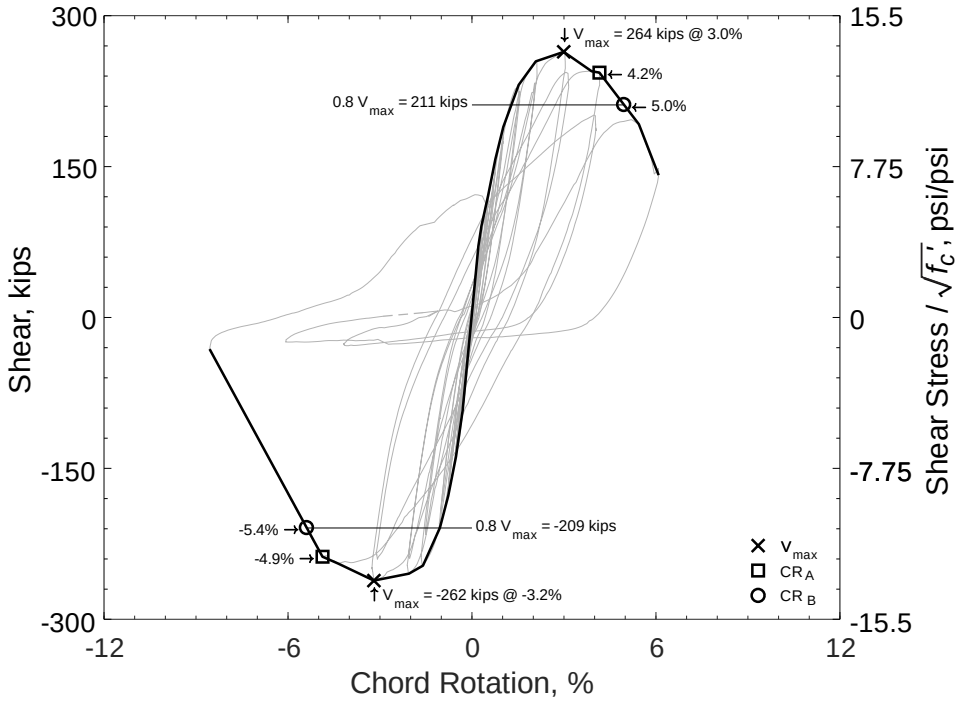

Figure 51 – Shear versus chord rotation envelope for D120-1.5
(1,000 psi = 6.89 MPa, 1 kip = 4.45 kN)

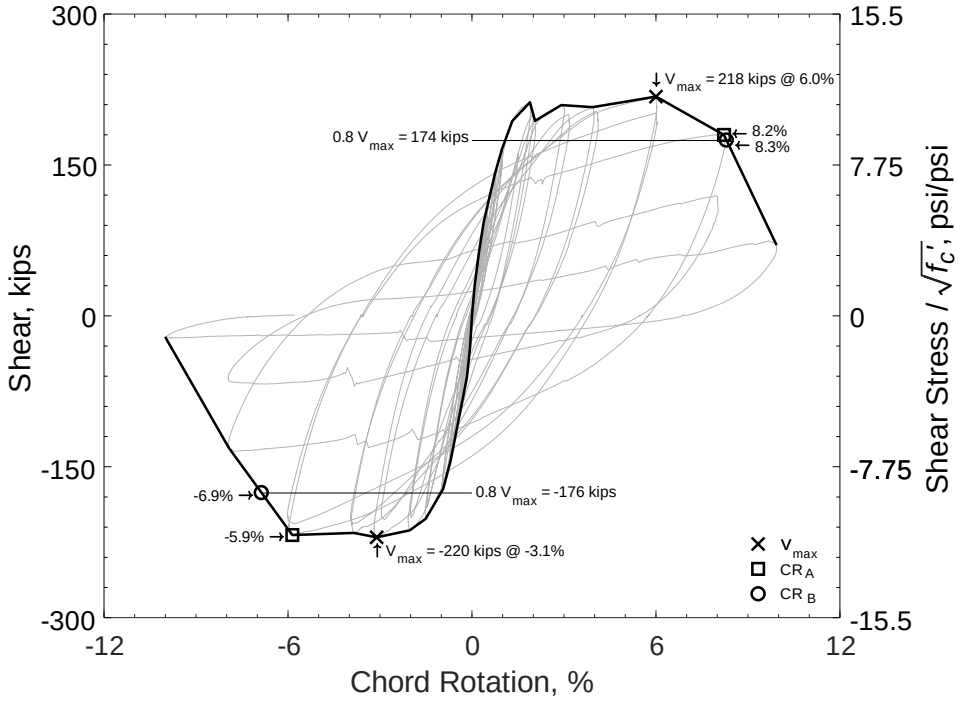

Figure 52 – Shear versus chord rotation envelope for D80-2.5
(1,000 psi = 6.89 MPa, 1 kip = 4.45 kN)

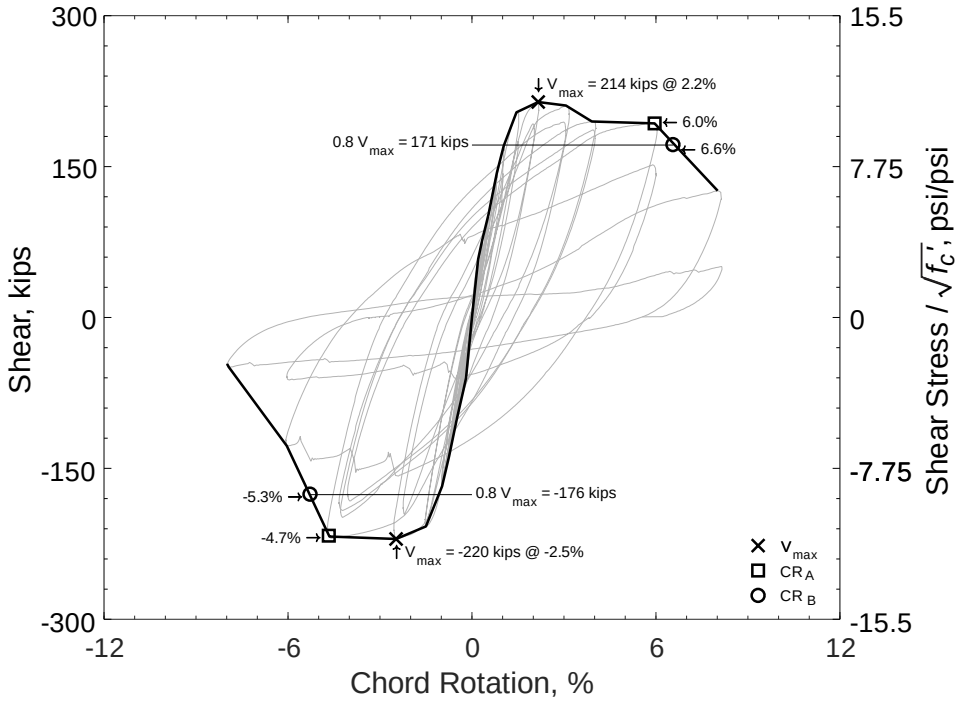

Figure 53 – Shear versus chord rotation envelope for D100-2.5
(1,000 psi = 6.89 MPa, 1 kip = 4.45 kN)

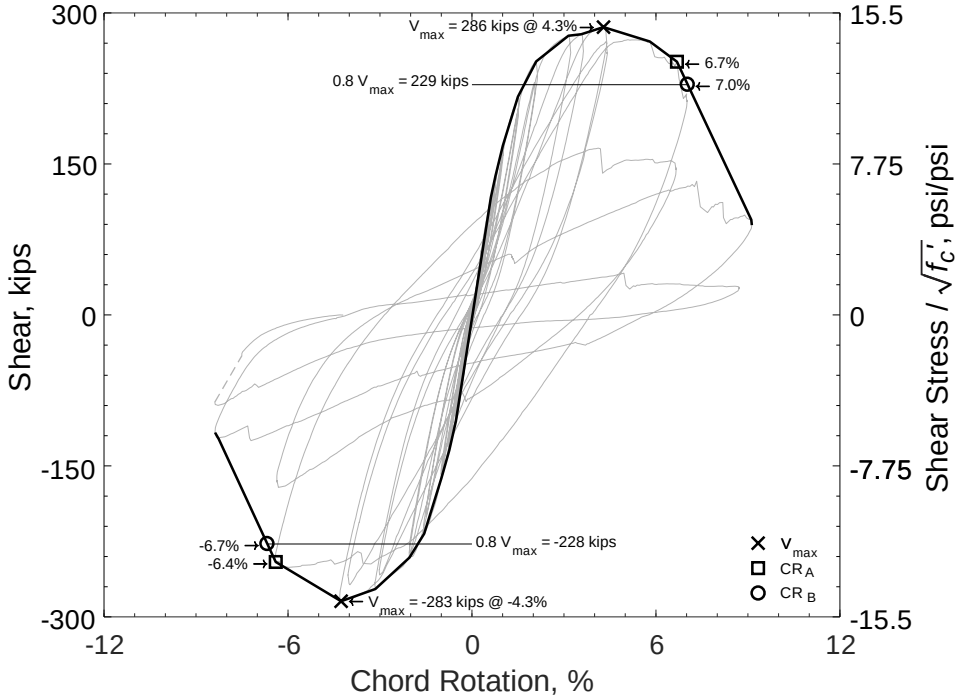

Figure 54 – Shear versus chord rotation envelope for D120-2.5
(1,000 psi = 6.89 MPa, 1 kip = 4.45 kN)

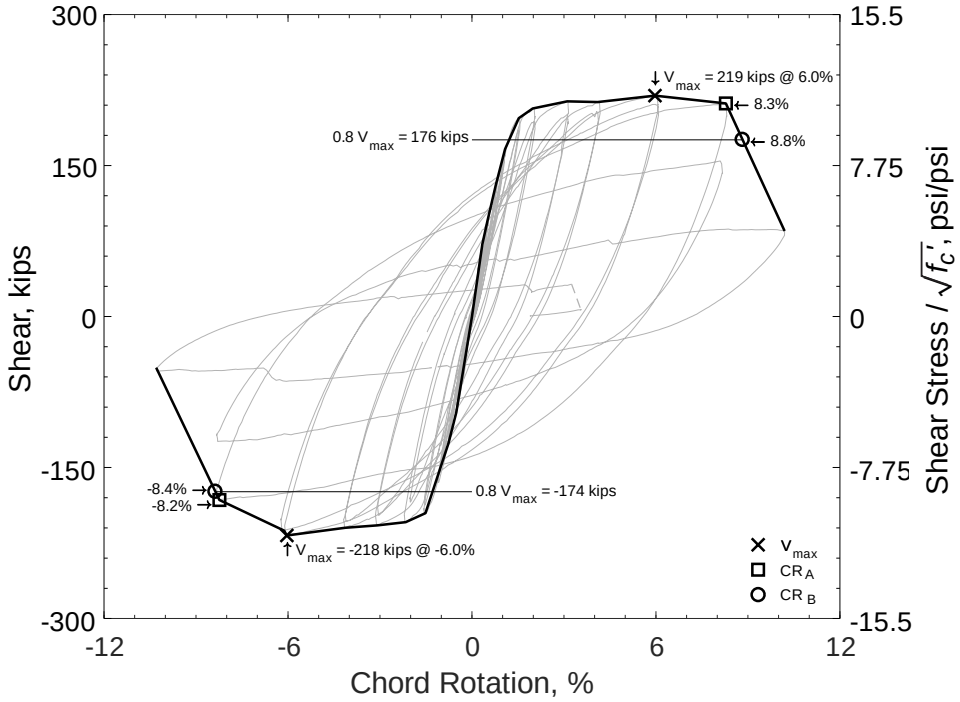

Figure 55 – Shear versus chord rotation envelope for D80-3.5
(1,000 psi = 6.89 MPa, 1 kip = 4.45 kN)

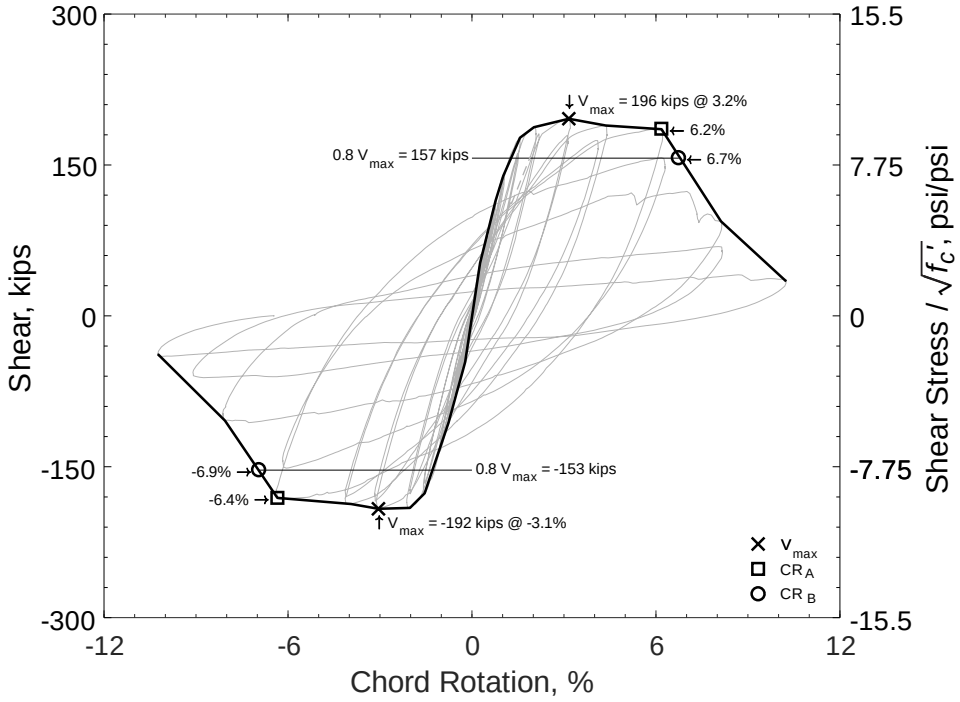

Figure 56 – Shear versus chord rotation envelope for D100-3.5
(1,000 psi = 6.89 MPa, 1 kip = 4.45 kN)

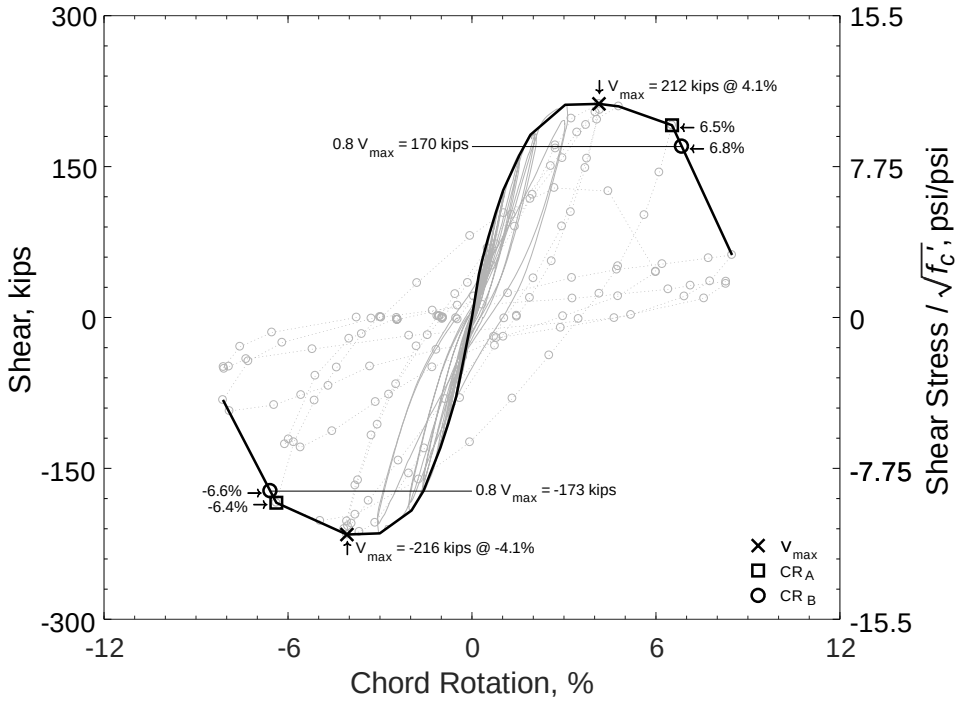

Figure 57 – Shear versus chord rotation envelope for D120-3.5
(1,000 psi = 6.89 MPa, 1 kip = 4.45 kN)

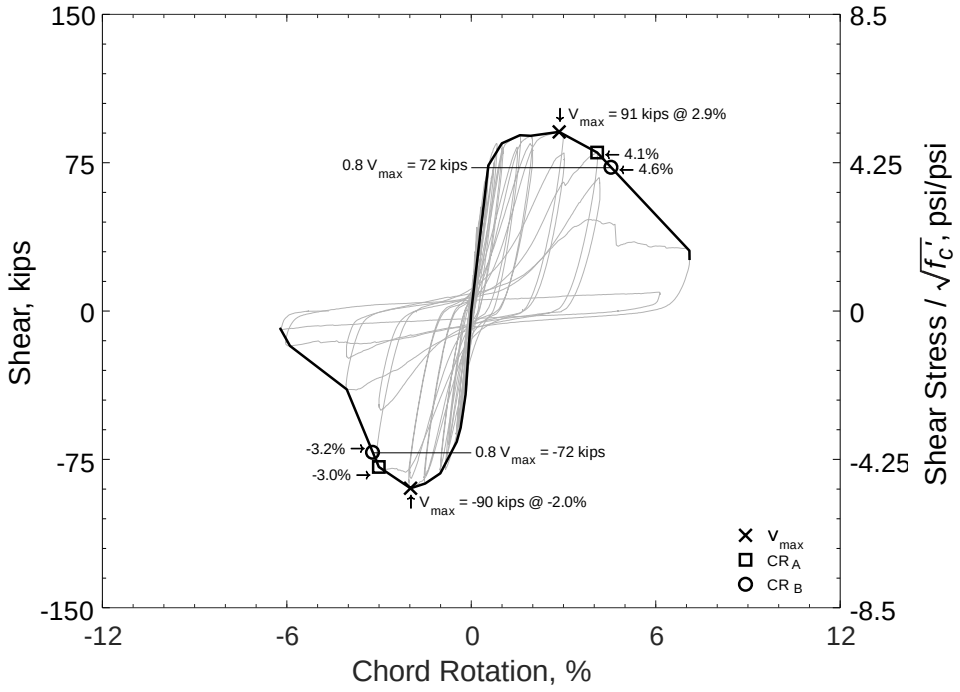

Figure 58 – Shear versus chord rotation envelope for P80-2.5
(1,000 psi = 6.89 MPa, 1 kip = 4.45 kN)

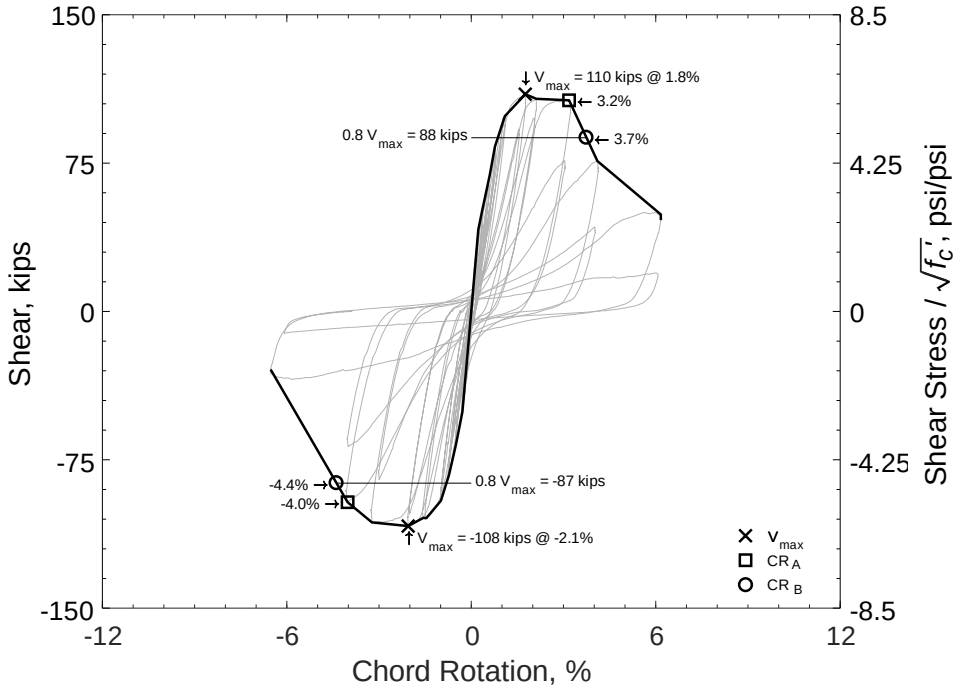

Figure 59 – Shear versus chord rotation envelope for P100-2.5
(1,000 psi = 6.89 MPa, 1 kip = 4.45 kN)

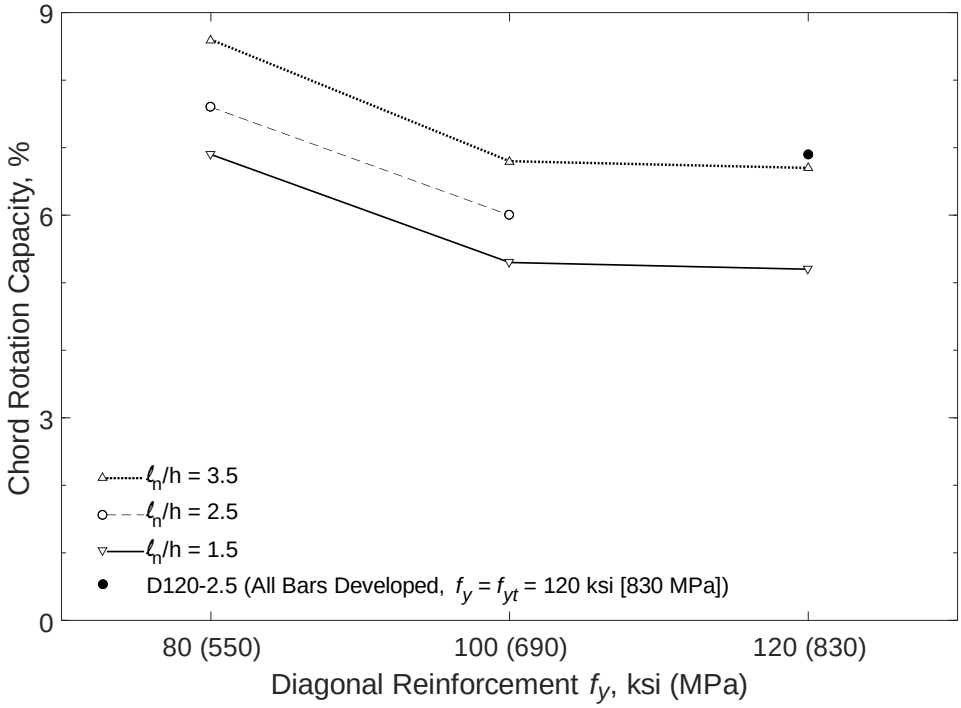

Figure 60 – Chord rotation capacity versus grade of primary reinforcement for D-type coupling beams (1,000 psi = 6.89 MPa)

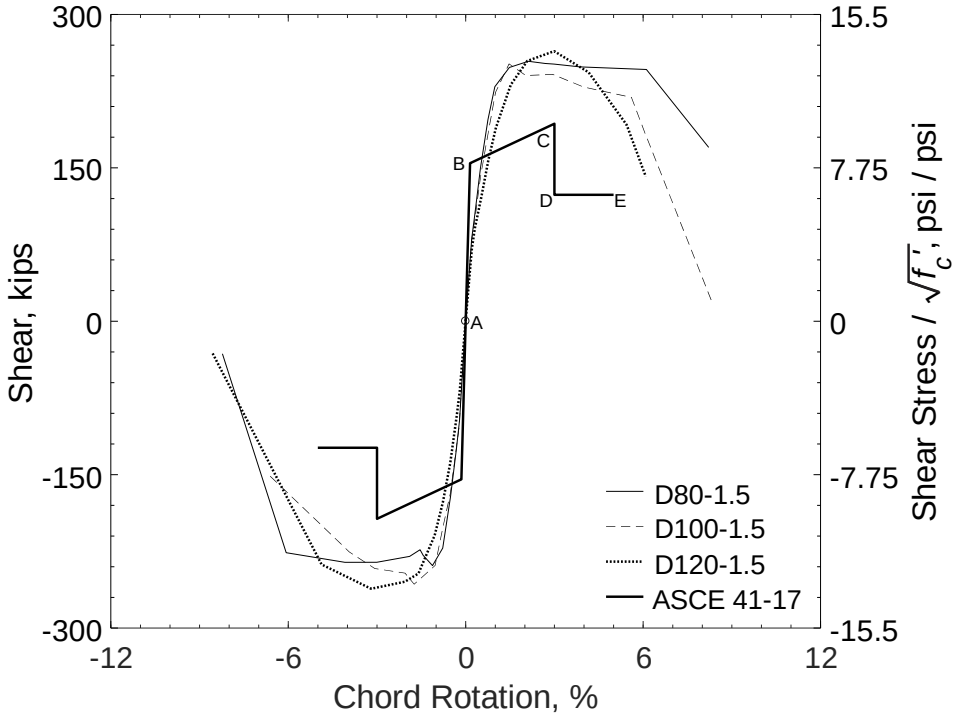

Figure 61 – Shear versus chord rotation envelopes for D-type beams (aspect ratio of 1.5) compared with ASCE 41-17[16] envelope (1,000 psi = 6.89 MPa, 1 kip = 4.45 kN)

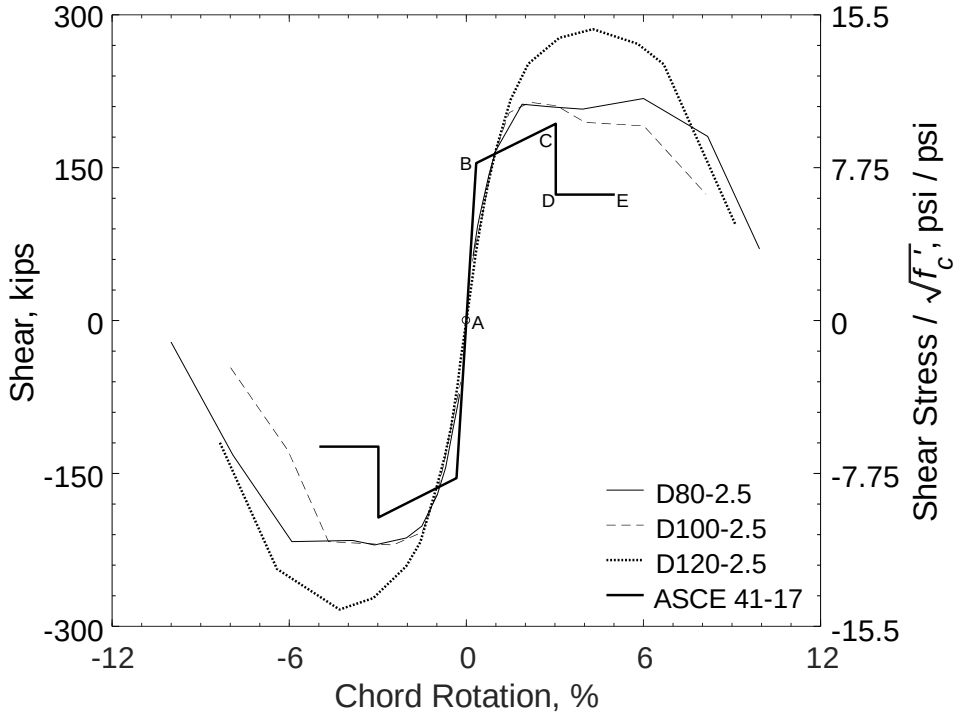

Figure 62 – Shear versus chord rotation envelopes for D-type beams (aspect ratio of 2.5) compared with ASCE 41-17[16] envelope (1,000 psi = 6.89 MPa, 1 kip = 4.45 kN)

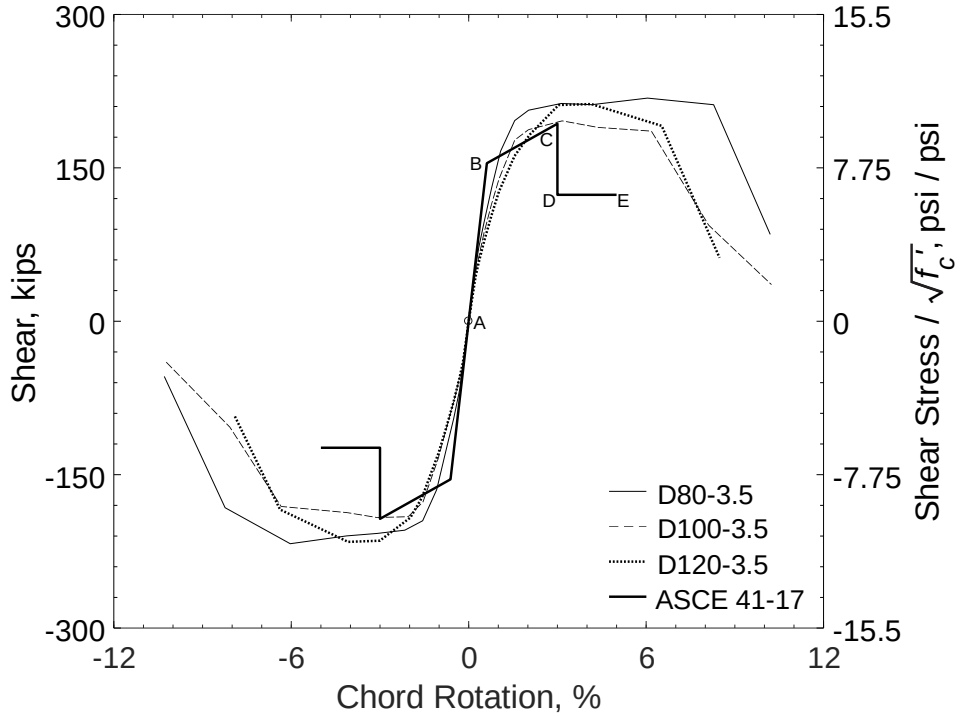

Figure 63 – Shear versus chord rotation envelopes for D-type beams (aspect ratio of 3.5) compared with ASCE 41-17[16] envelope (1,000 psi = 6.89 MPa, 1 kip = 4.45 kN)

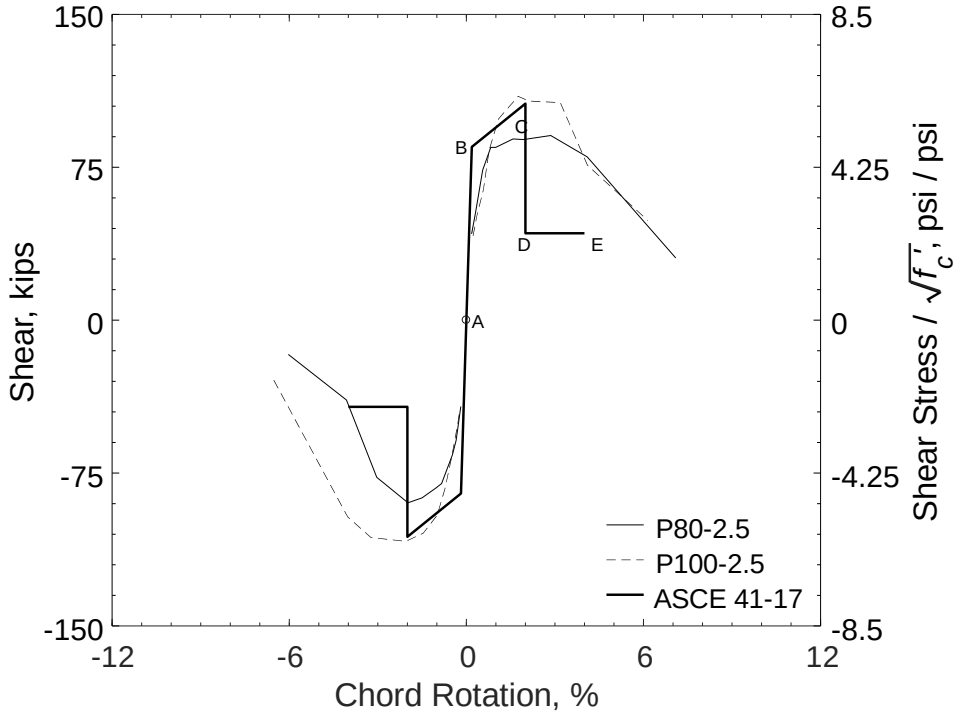

Figure 64 – Shear versus chord rotation envelopes for P-type beams (aspect ratio of 2.5) compared with ASCE 41-17[16] envelope (1,000 psi = 6.89 MPa, 1 kip = 4.45 kN)

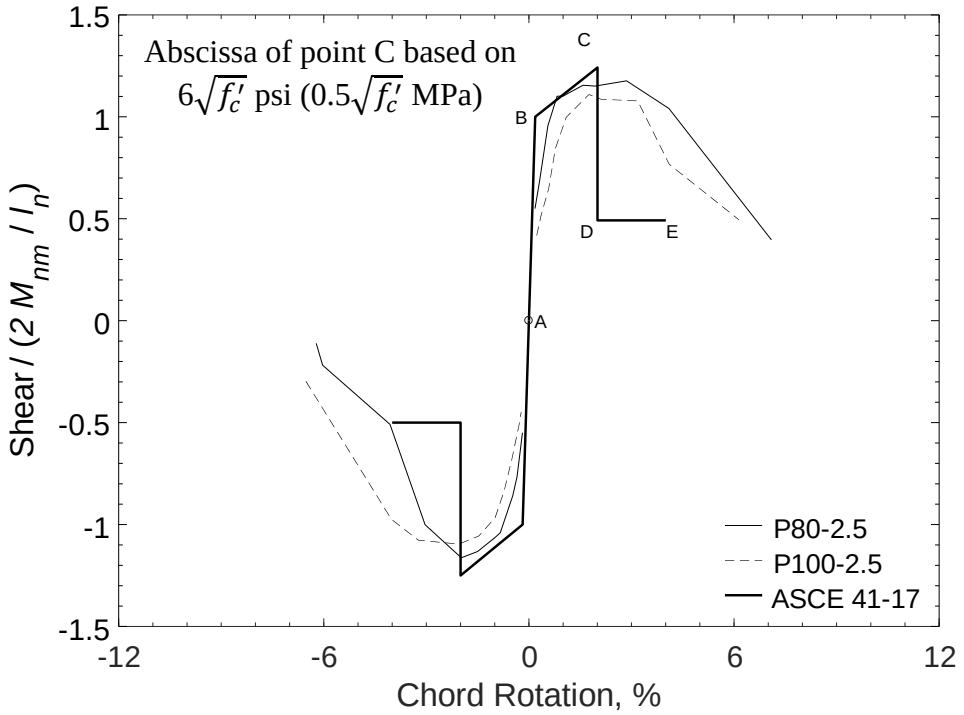

Figure 65 – Normalized shear versus chord rotation envelopes for P-type beams (aspect ratio of 2.5) compared with ASCE 41-17[16] envelope (1,000 psi = 6.89 MPa, 1 kip = 4.45 kN)

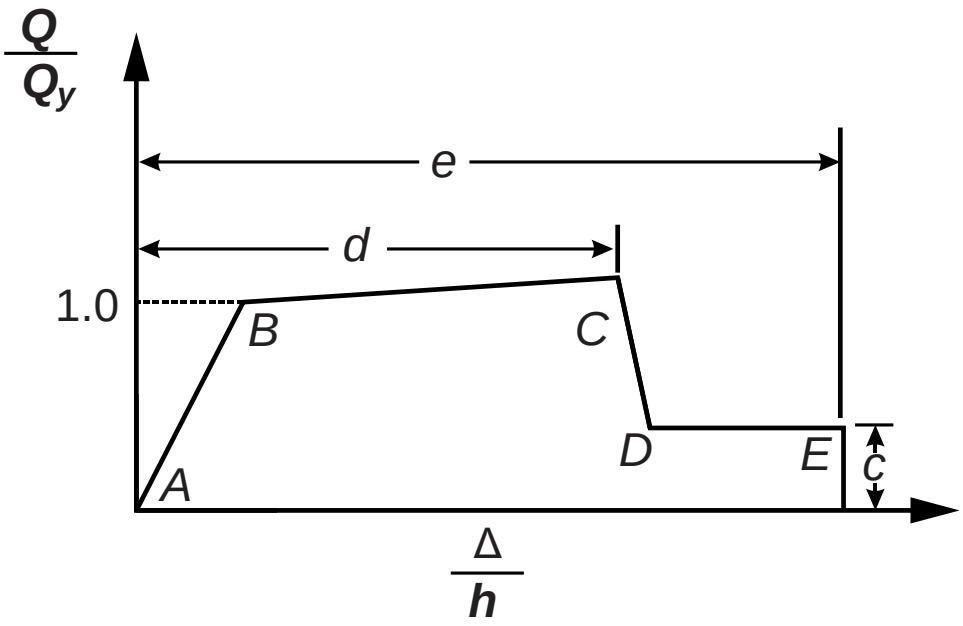

Figure 66 – Generalized force-deformation relationship for diagonally-reinforced concrete coupling beams (taken from ASCE 41-17[16] Figure 10-1(b))

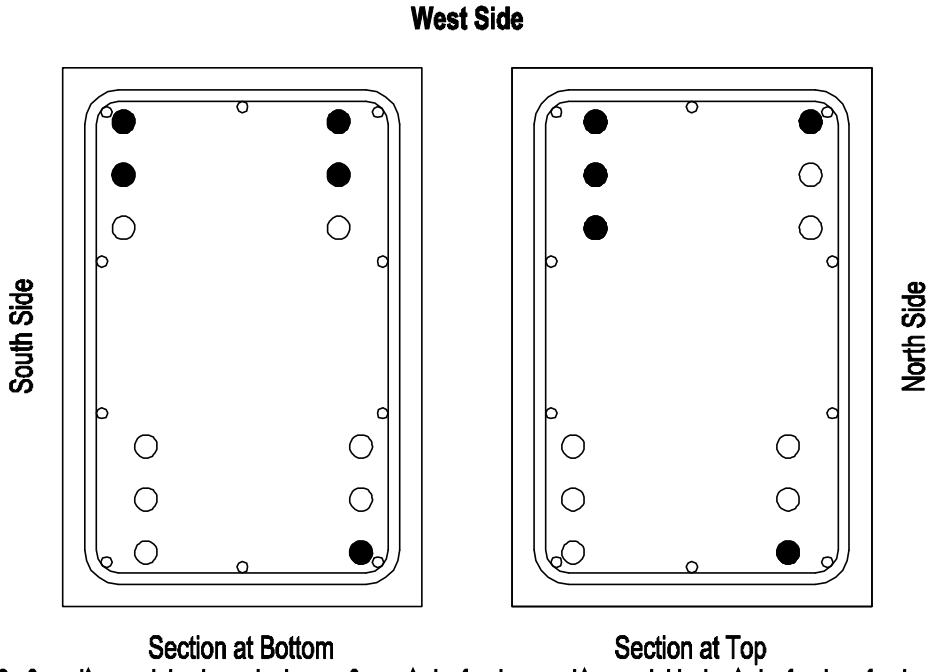

Figure 67 – Reinforcing bar fracture locations, D80-1.5

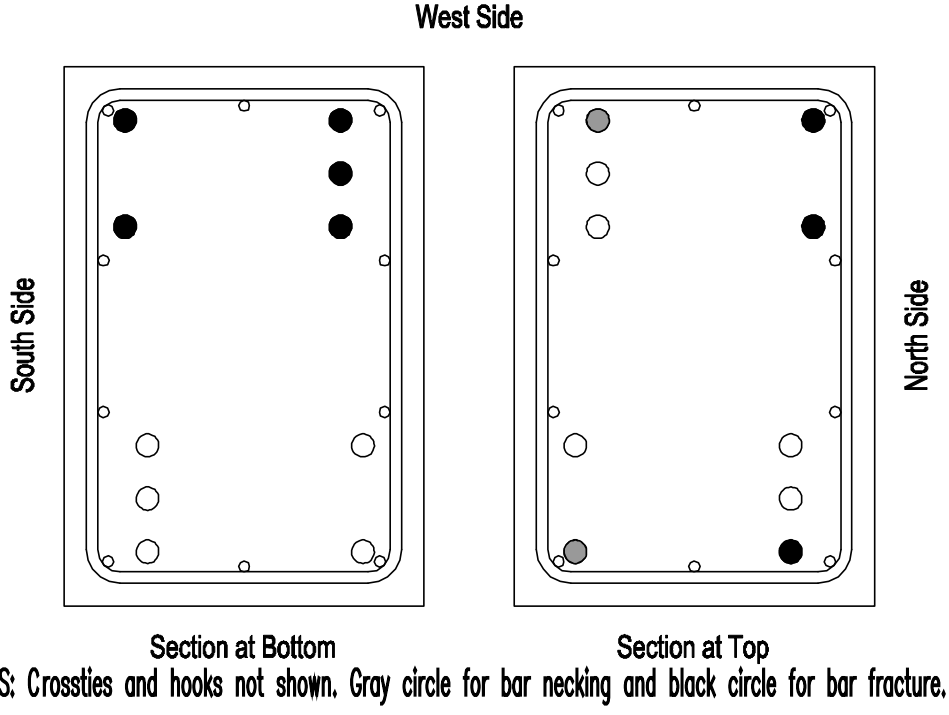

Figure 68 – Reinforcing bar fracture locations, D100-1.5

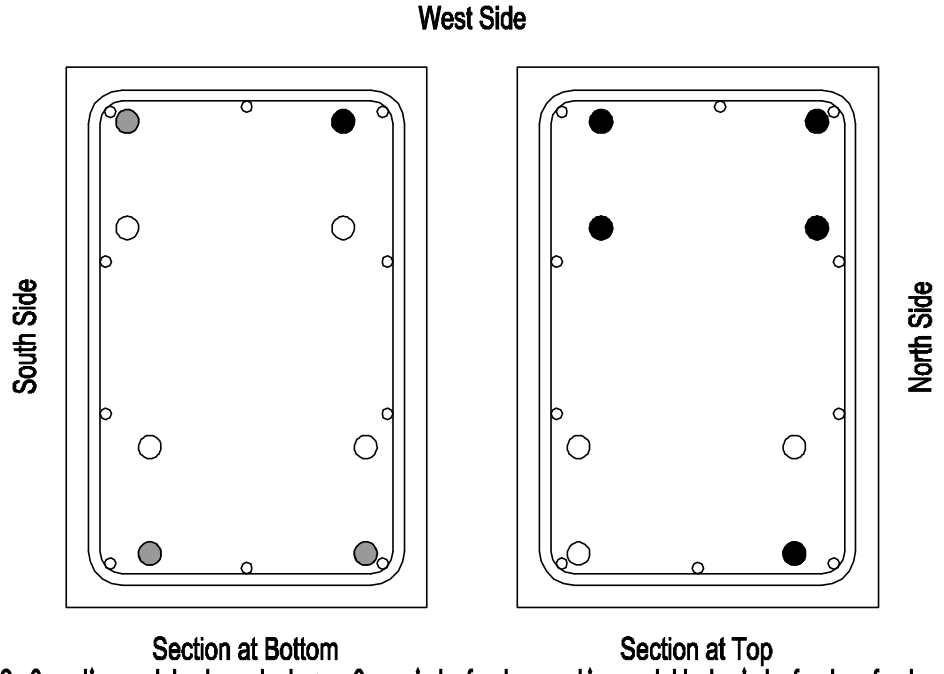

Figure 69 – Reinforcing bar fracture locations, D120-1.5

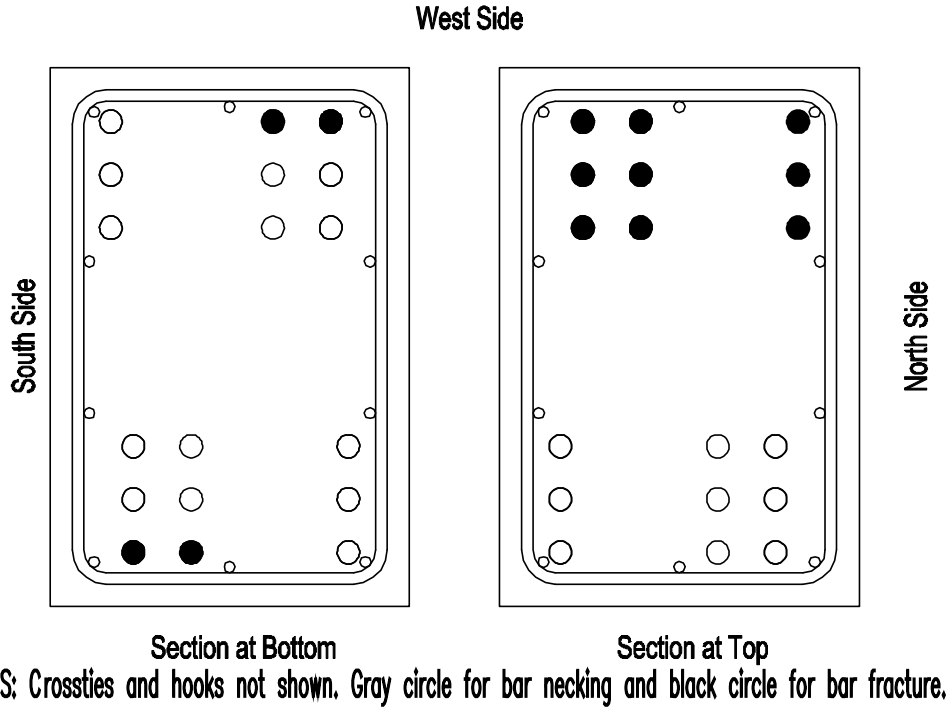

Figure 70 – Reinforcing bar fracture locations, D80-2.5

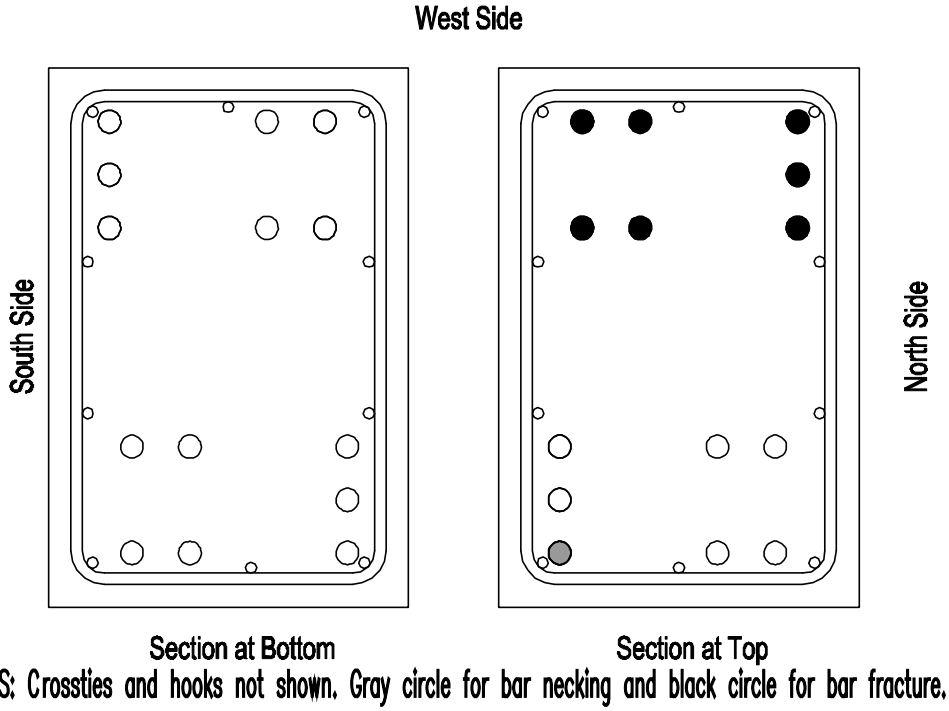

Figure 71 – Reinforcing bar fracture locations, D100-2.5

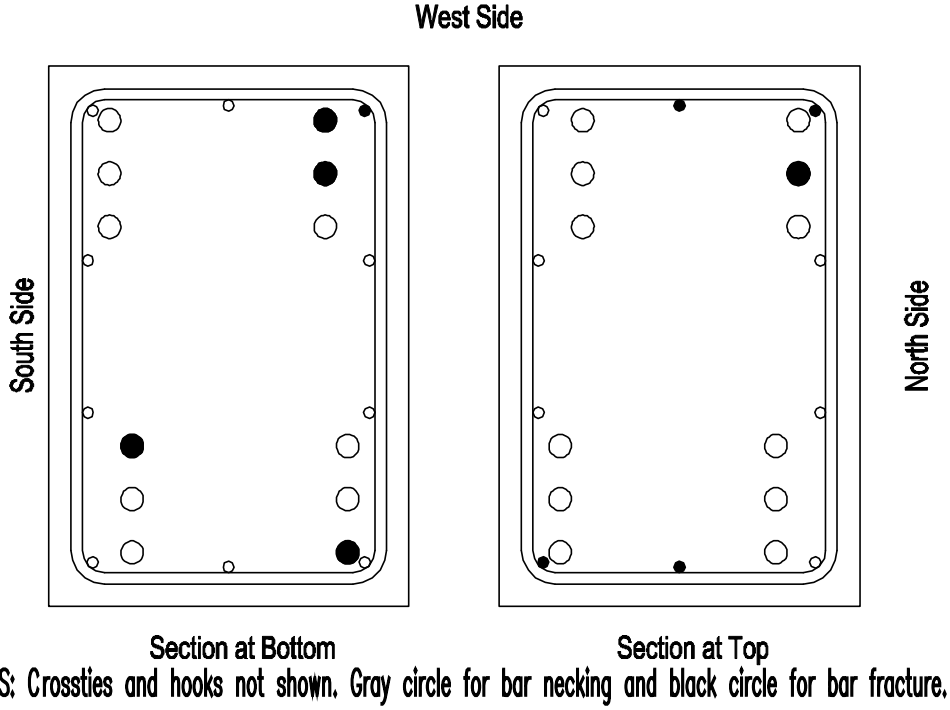

Figure 72 – Reinforcing bar fracture locations, D120-2.5

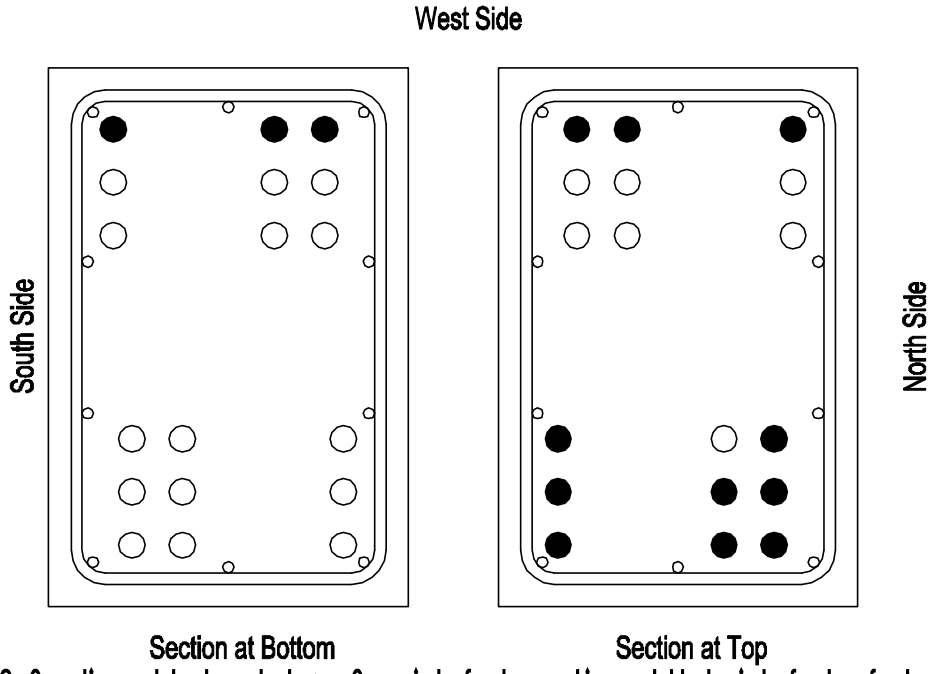

Figure 73 – Reinforcing bar fracture locations, D80-3.5

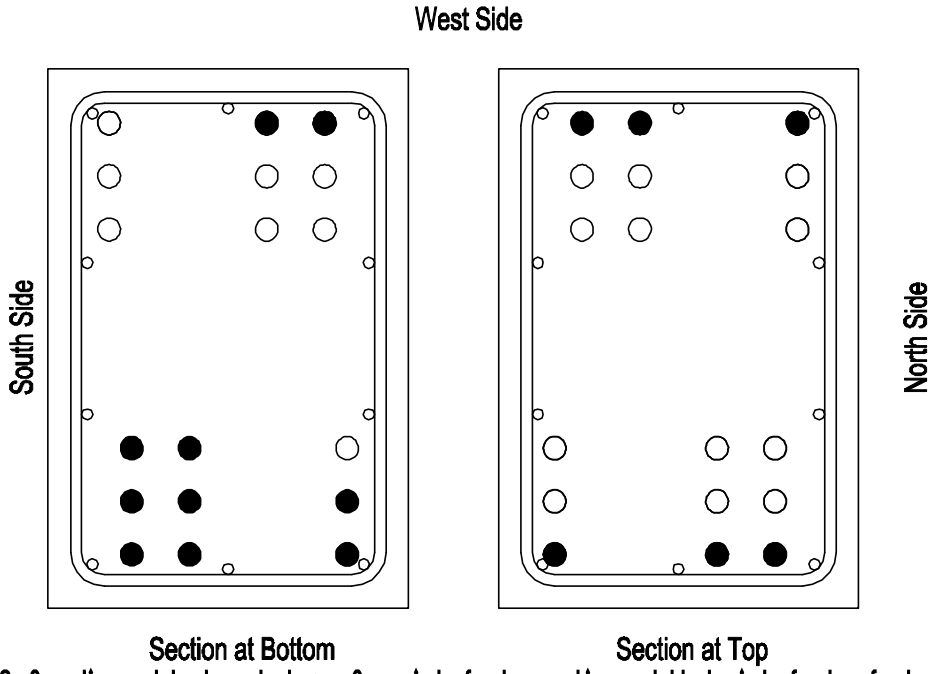

Figure 74 – Reinforcing bar fracture locations, D100-3.5

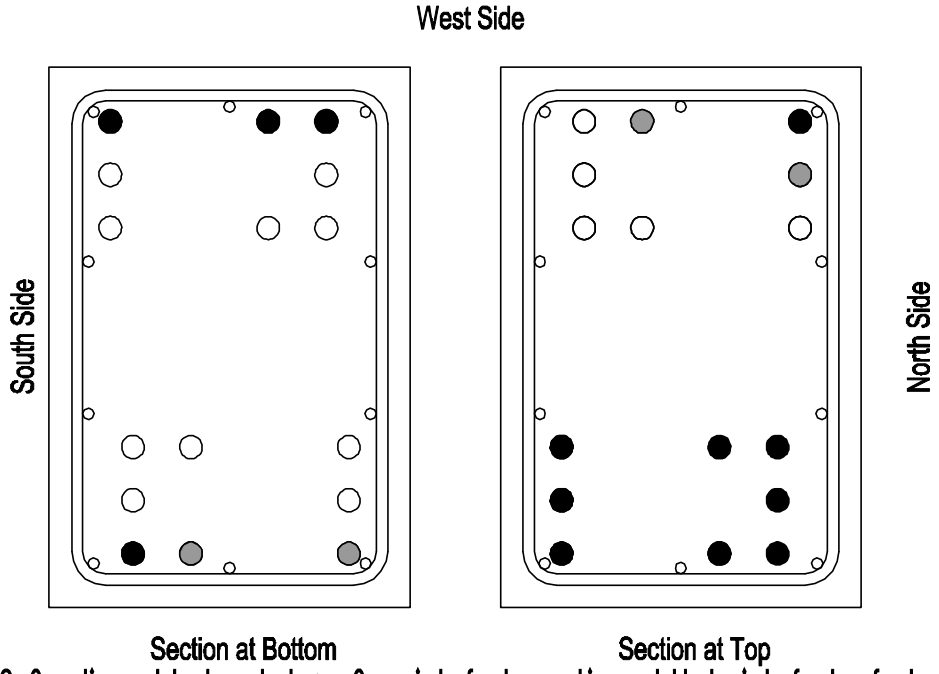

Figure 75 – Reinforcing bar fracture locations, D120-3.5

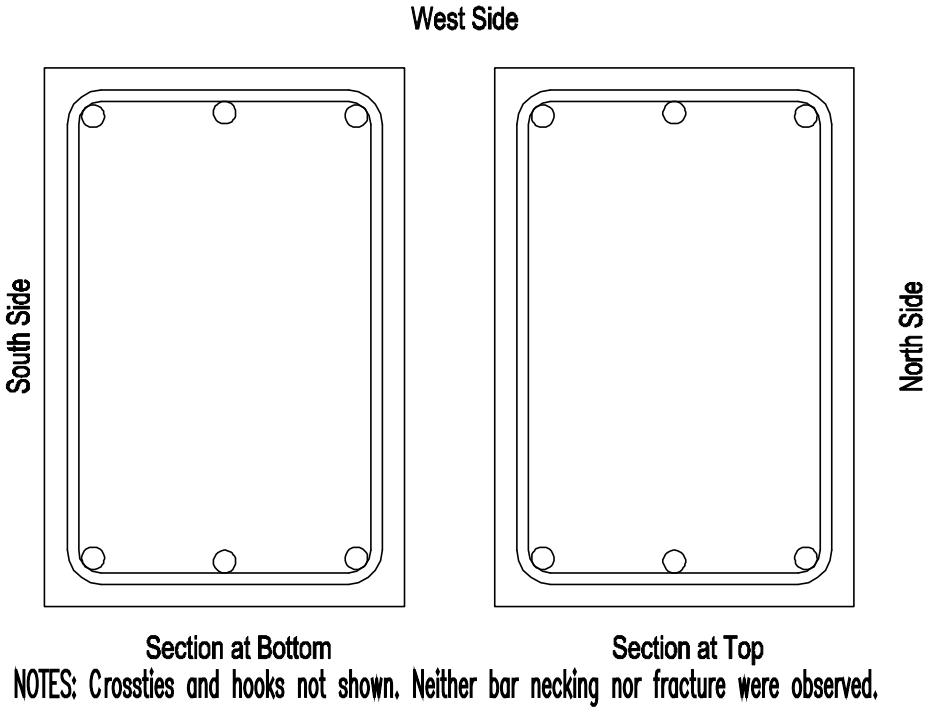

Figure 76 – Reinforcing bar fracture locations, P80-2.5

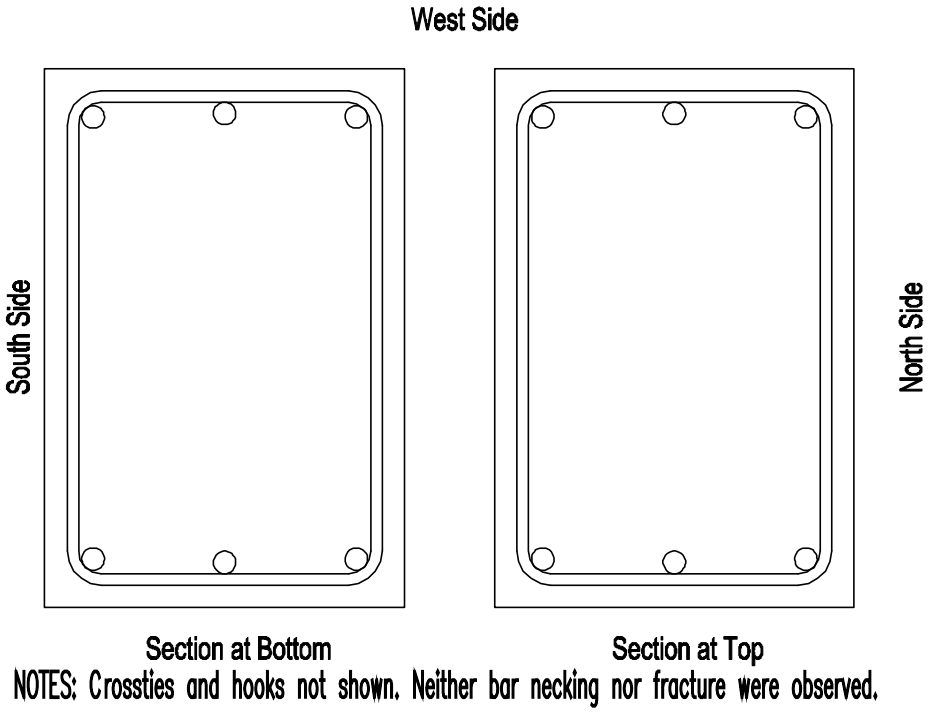

Figure 77 – Reinforcing bar fracture locations, P100-2.5

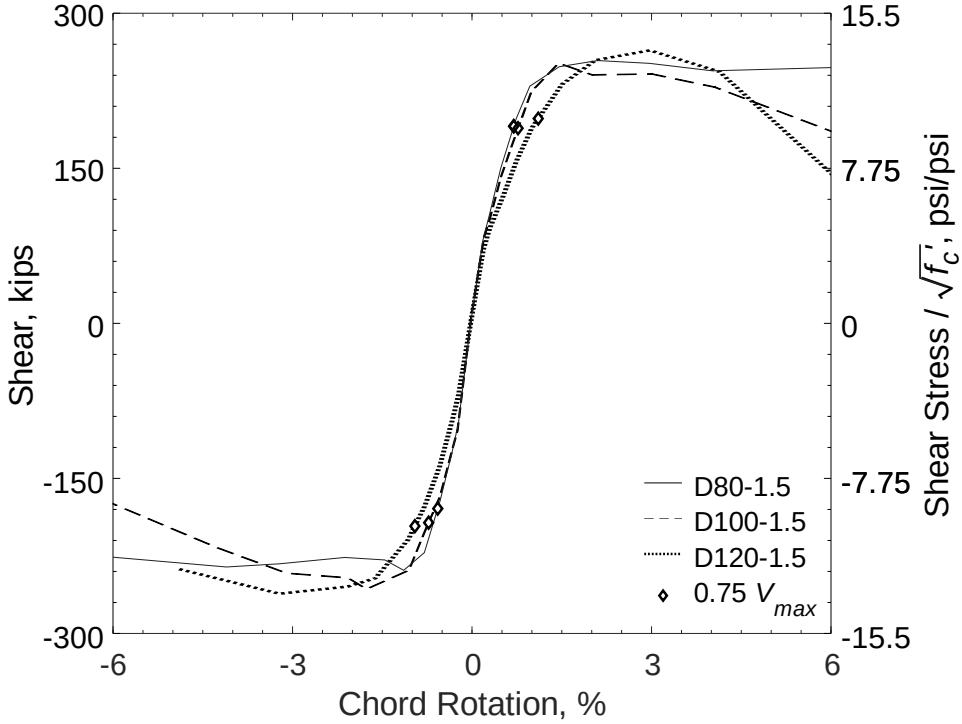

Figure 78 – Shear versus chord rotation envelopes for D80-1.5, D100-1.5, and D120-1.5 identifying $0.75V_{max}$

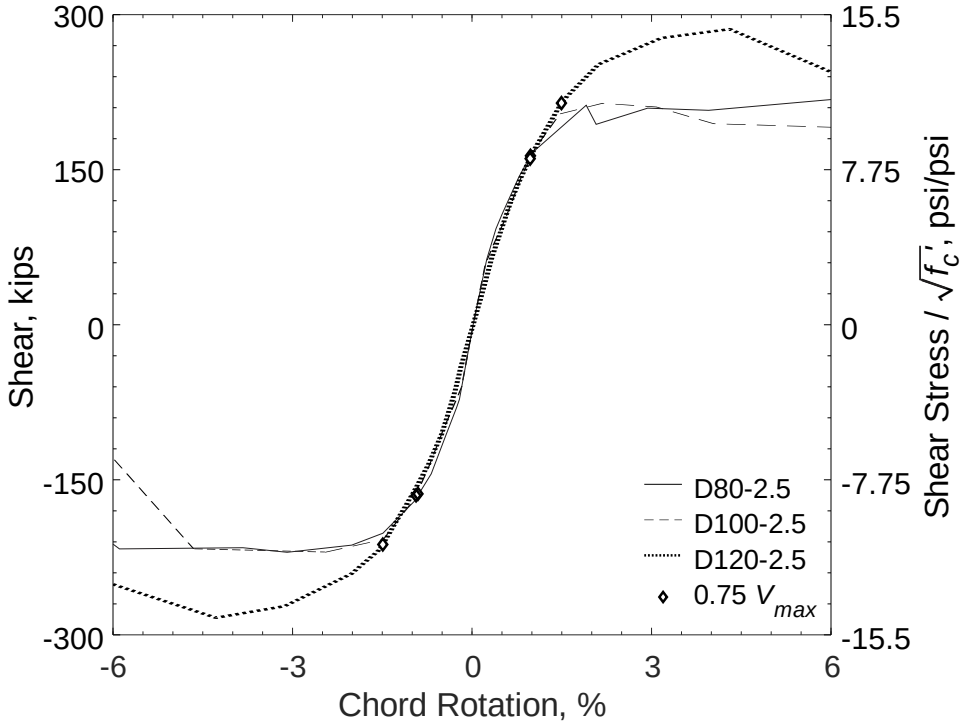

Figure 79 – Shear versus chord rotation envelopes for D80-2.5, D100-2.5, and D120-2.5 identifying $0.75V_{max}$

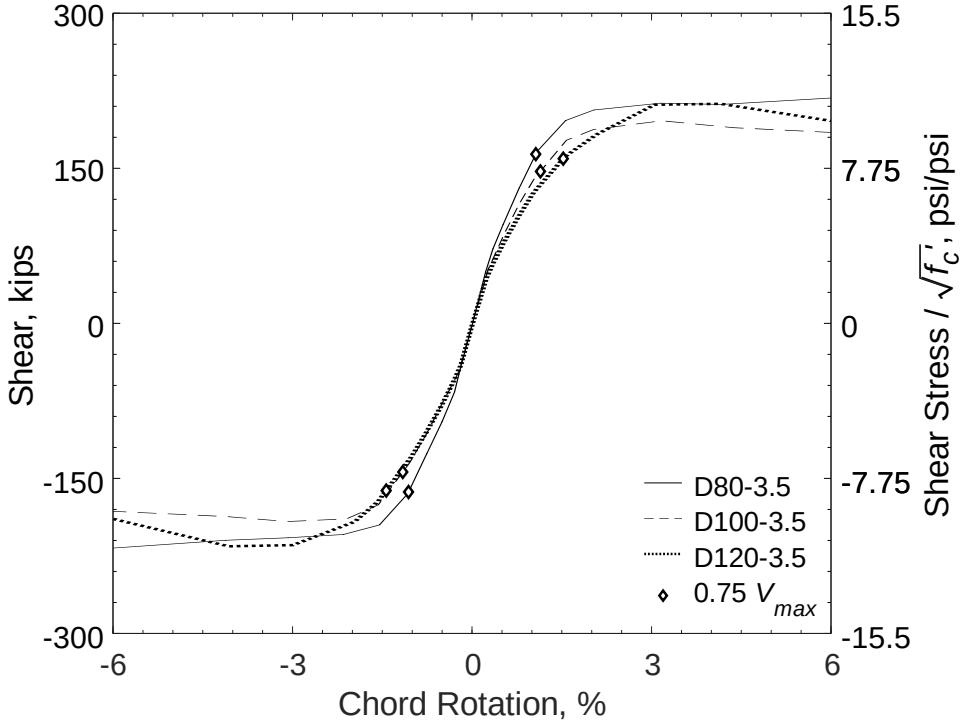

Figure 80 – Shear versus chord rotation envelopes for D80-3.5, D100-3.5, and D120-3.5 identifying $0.75V_{max}$

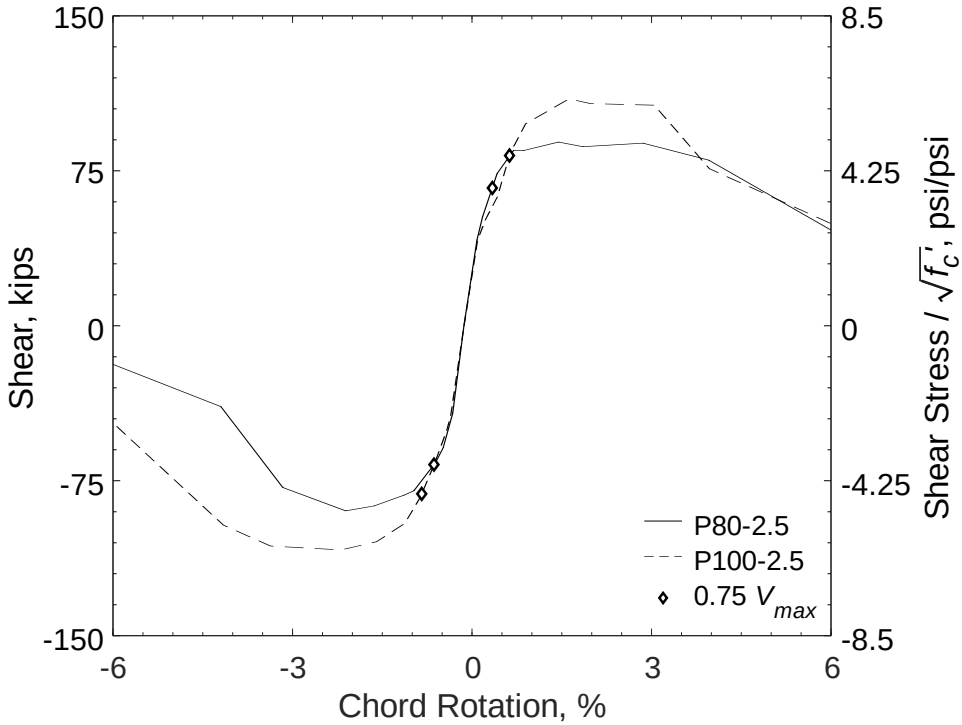

Figure 81 – Shear versus chord rotation envelopes for P80-2.5 and P100-2.5 identifying $0.75V_{max}$

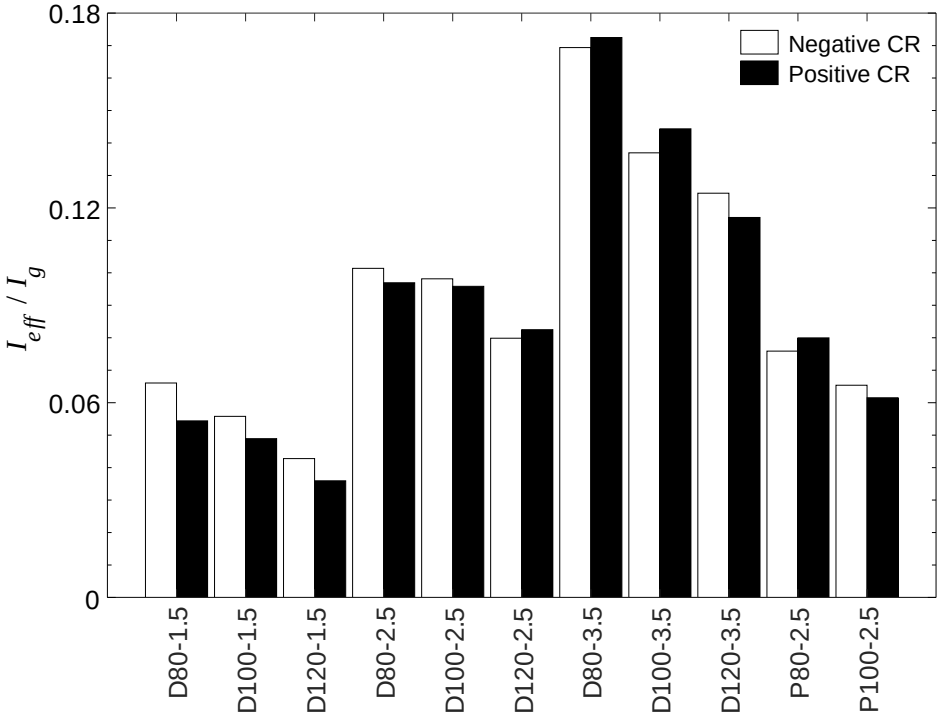

Figure 82 – Effective moment of inertia, I_{eff}, normalized by gross moment of inertia, I_g

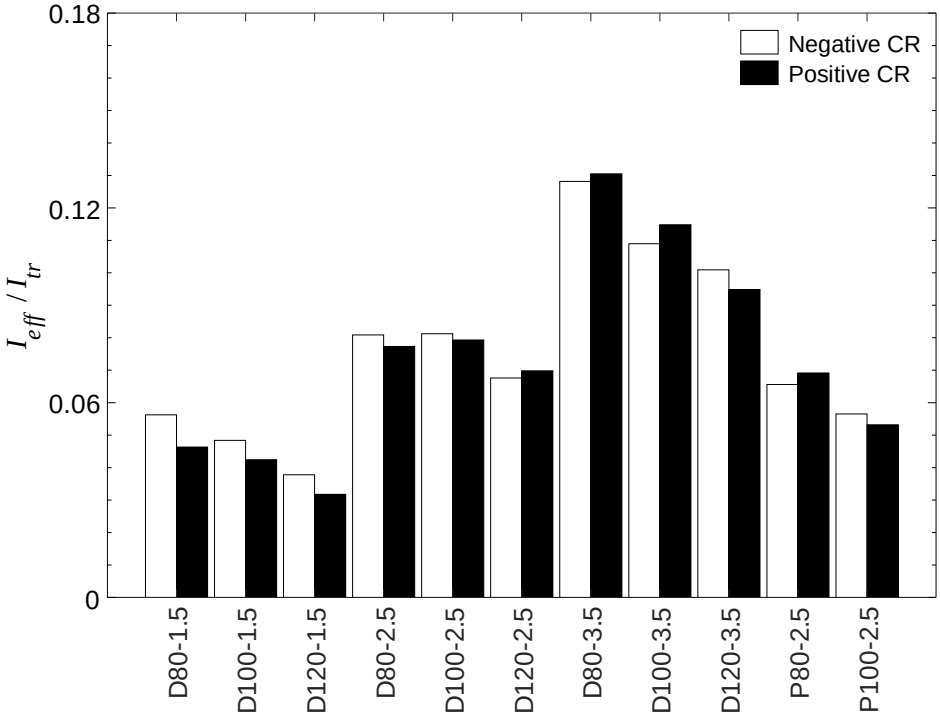

Figure 83 – Effective moment of inertia, I_{eff}, normalized by transformed uncracked moment of inertia, I_{tr}

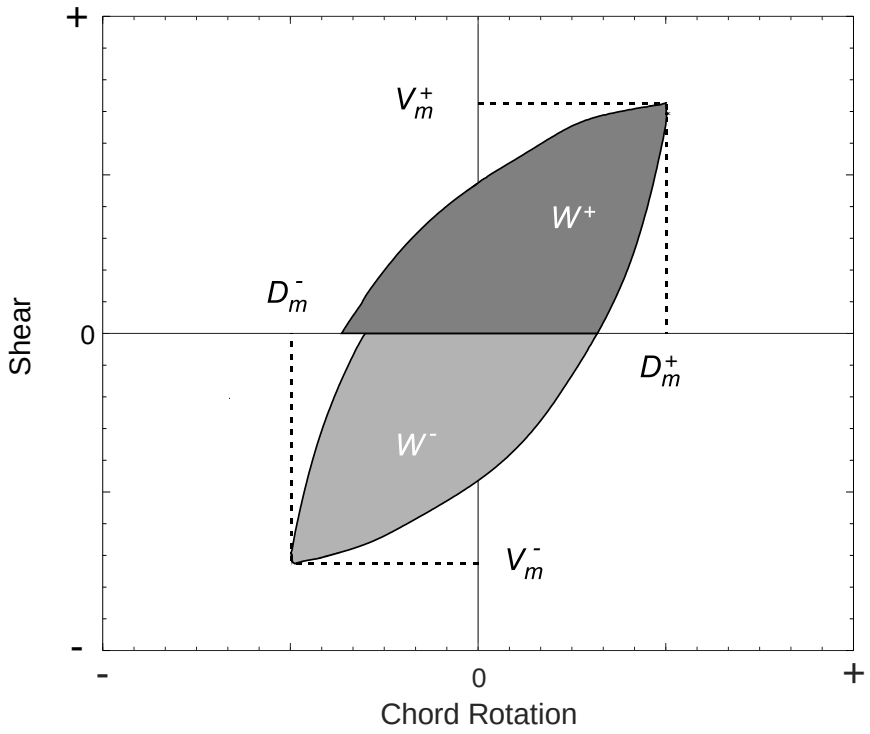

Figure 84 – Variables involved in determining the energy dissipation index, E_h, based on Equation 4.5

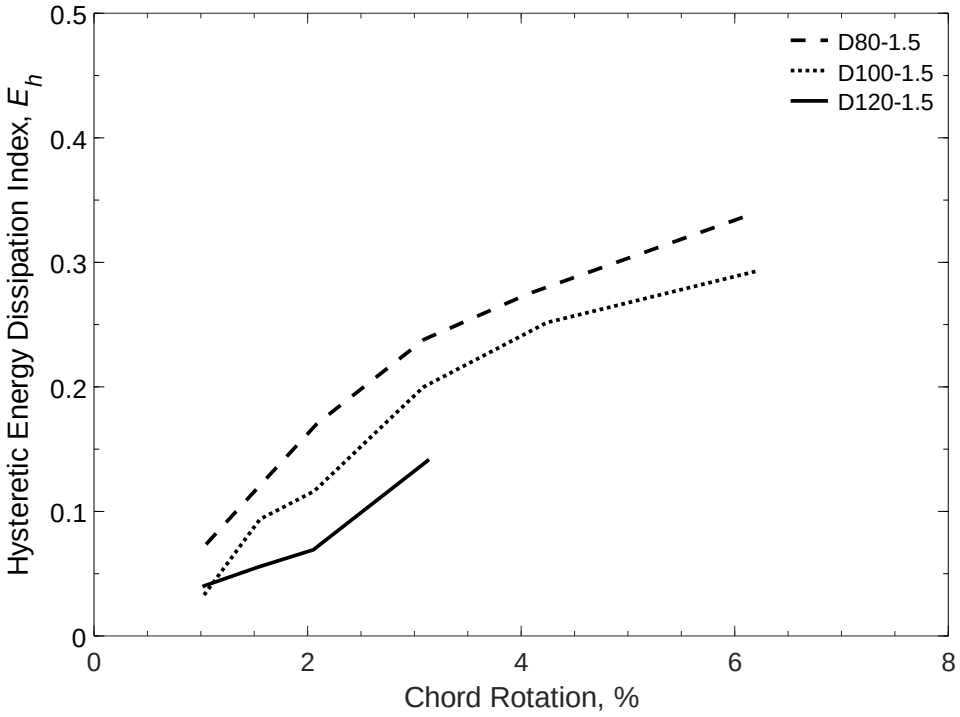

Figure 85 – Energy dissipation index (second cycle) versus chord rotation, D-type beams (aspect ratio of 1.5)

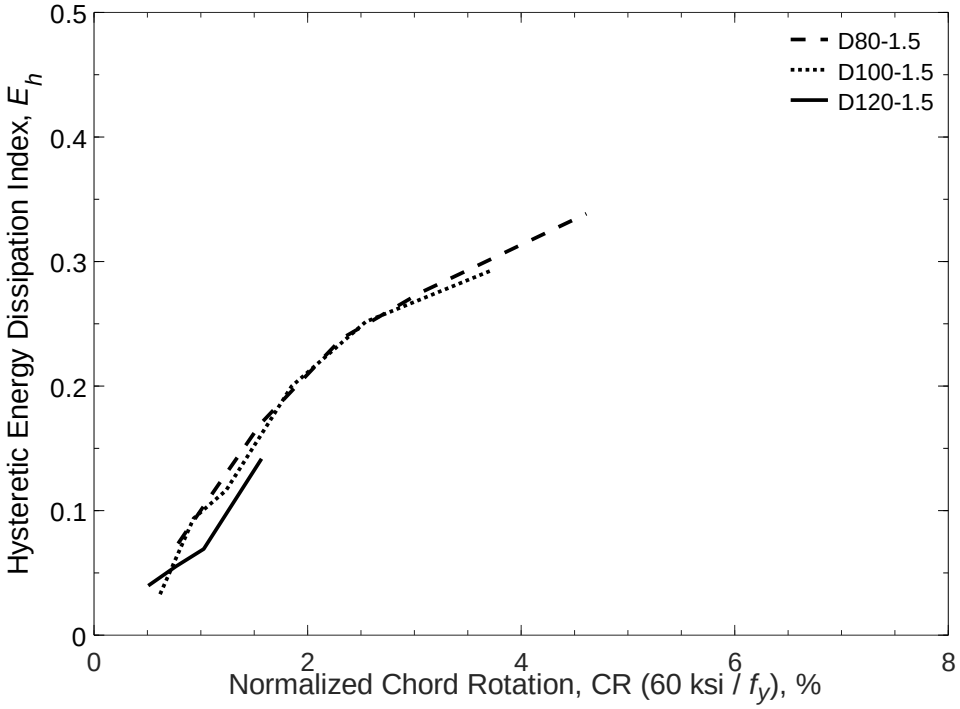

Figure 86 – Energy dissipation index (second cycle) versus normalized chord rotation, D-type beams (aspect ratio of 1.5)

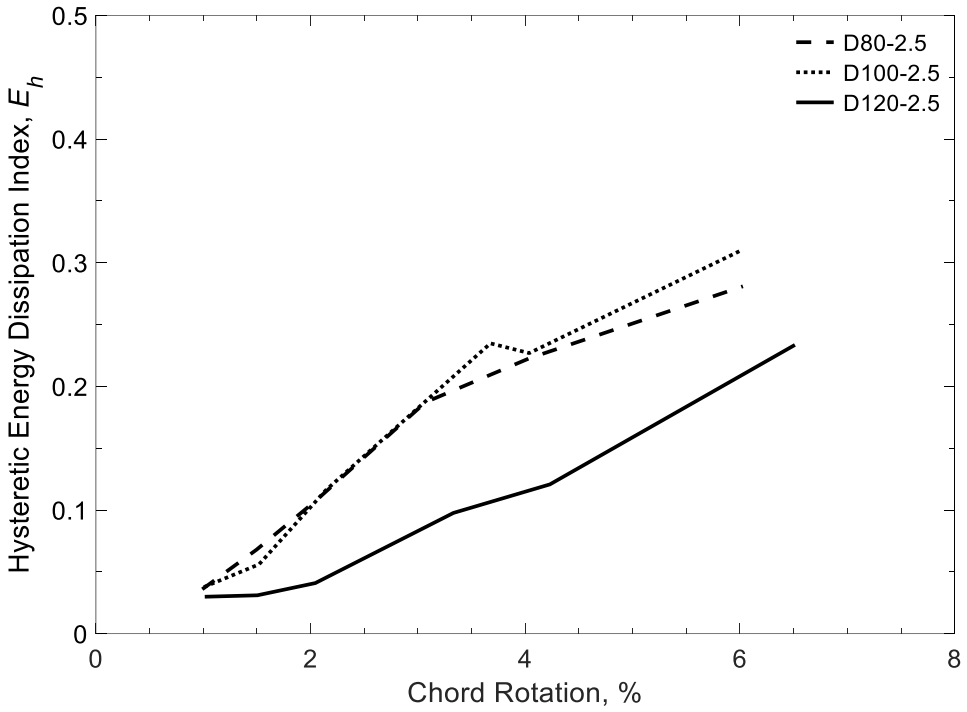

Figure 87 – Energy dissipation index (second cycle) versus chord rotation, D-type beams (aspect ratio of 2.5)

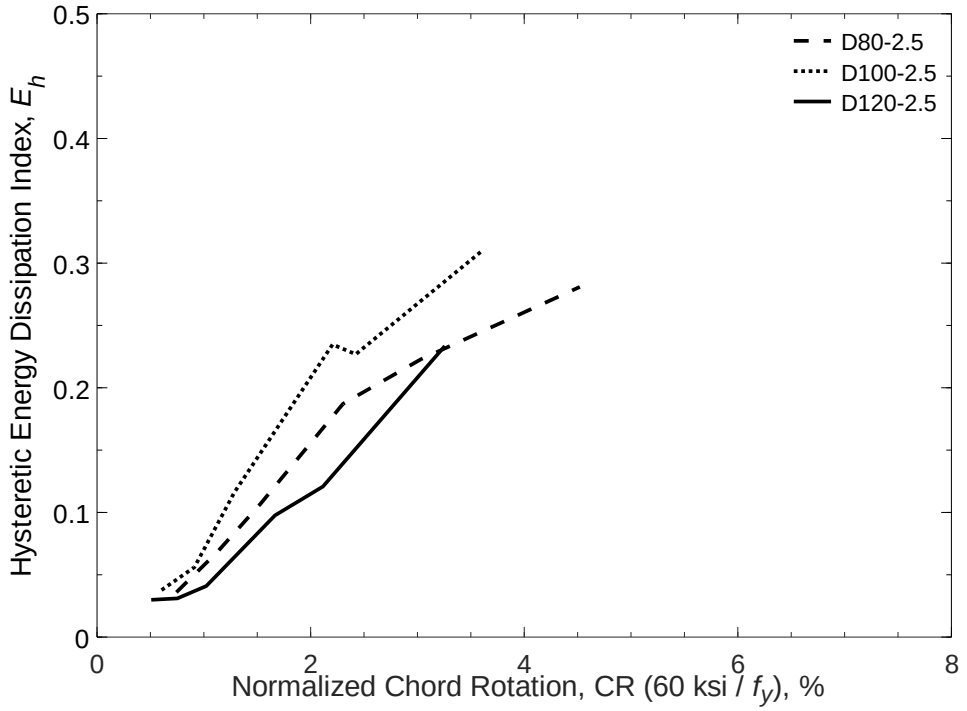

Figure 88 – Energy dissipation index (second cycle) versus normalized chord rotation, D-type beams (aspect ratio of 2.5)

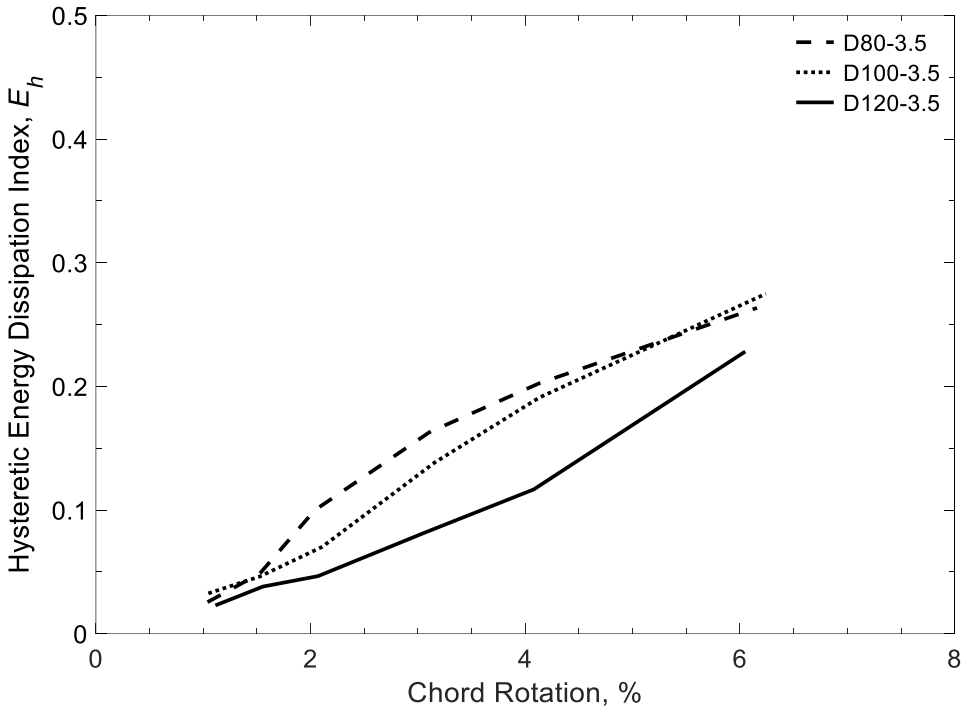

Figure 89 – Energy dissipation index (second cycle) versus chord rotation, D-type beams (aspect ratio of 3.5)

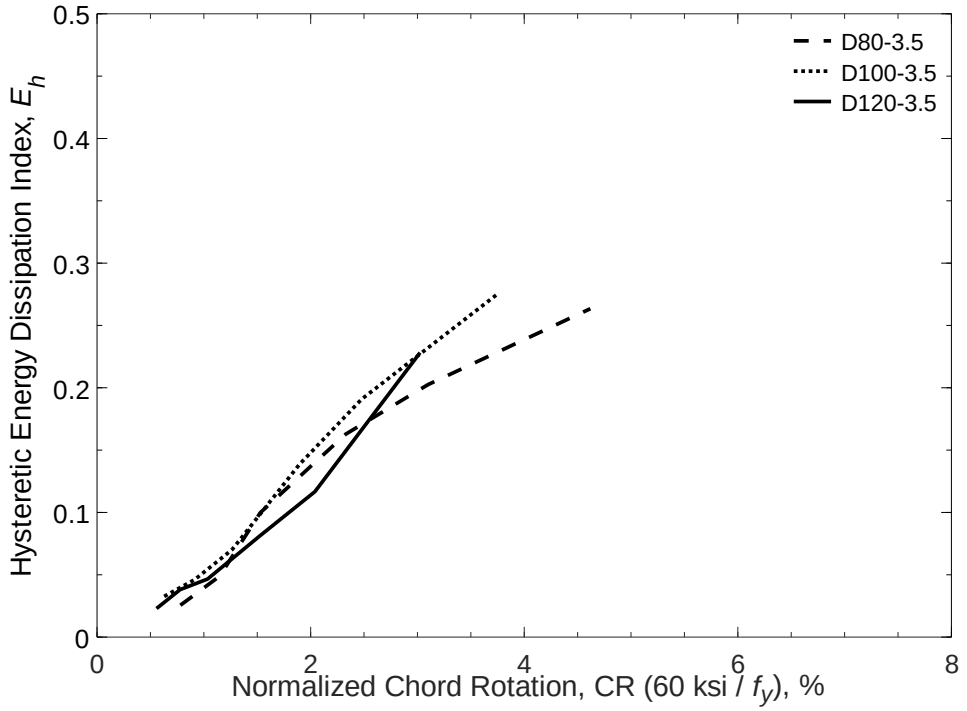

Figure 90 – Energy dissipation index (second cycle) versus normalized chord rotation, D-type beams (aspect ratio of 3.5)

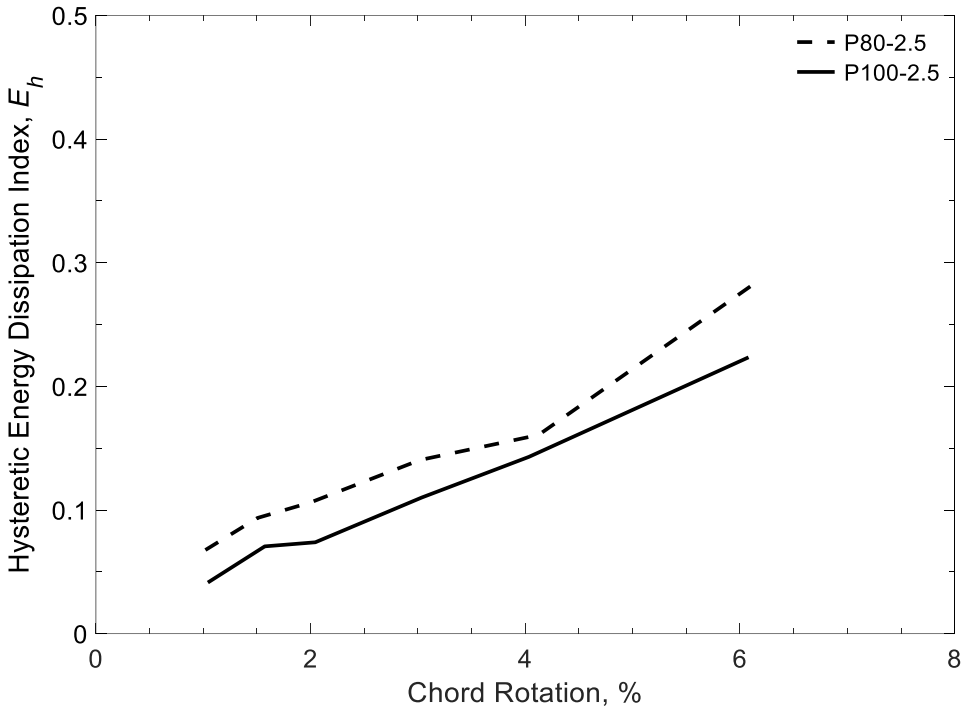

Figure 91 – Energy dissipation index (second cycle) versus chord rotation, P-type beams (aspect ratio of 2.5)

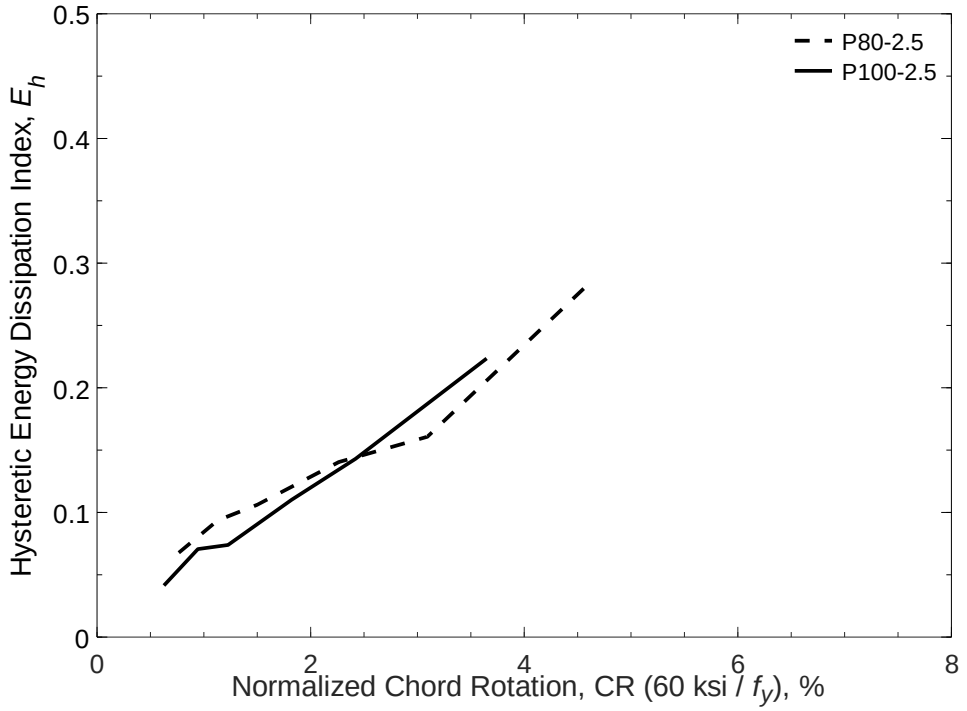

Figure 92 – Energy dissipation index (second cycle) versus chord rotation, P-type beams (aspect ratio of 2.5)

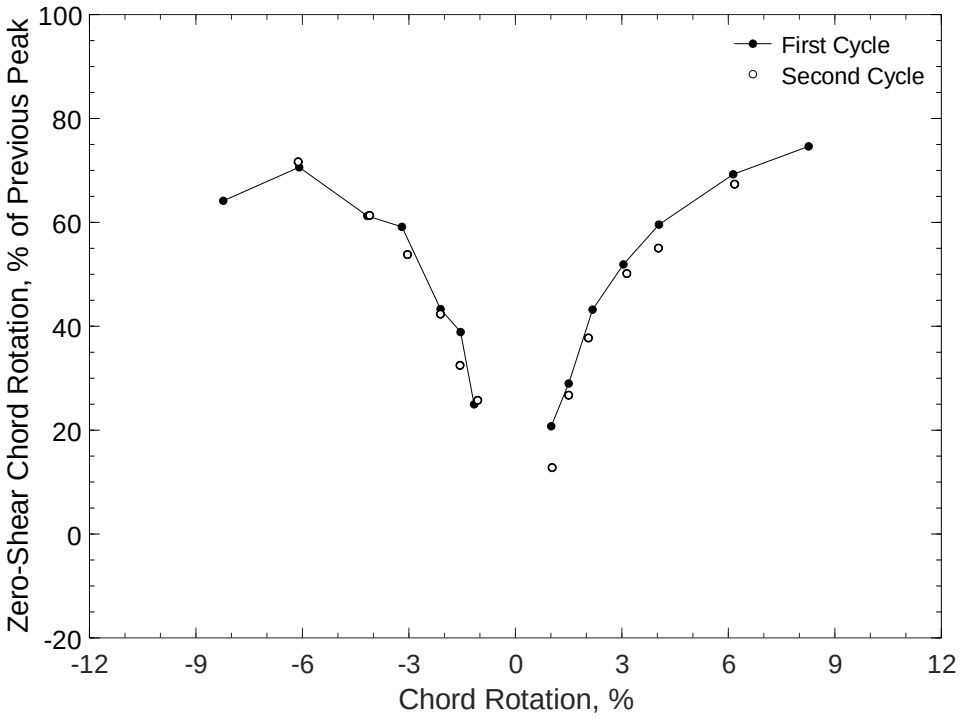

Figure 93 – Zero-shear chord rotation versus peak chord rotation, D80-1.5

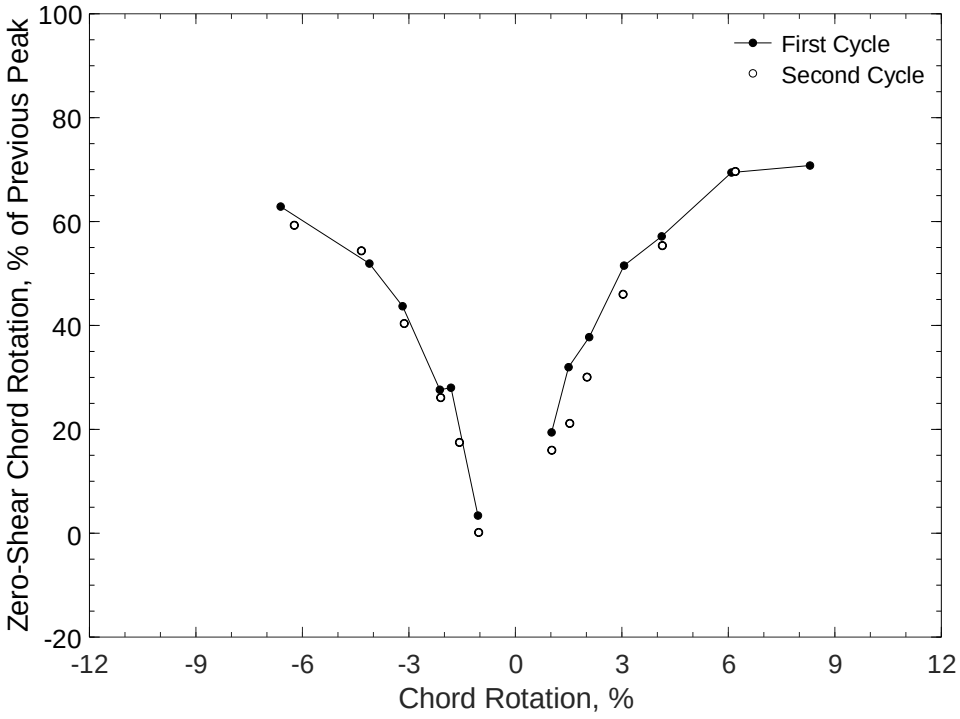

Figure 94 – Zero-shear chord rotation versus peak chord rotation, D100-1.5

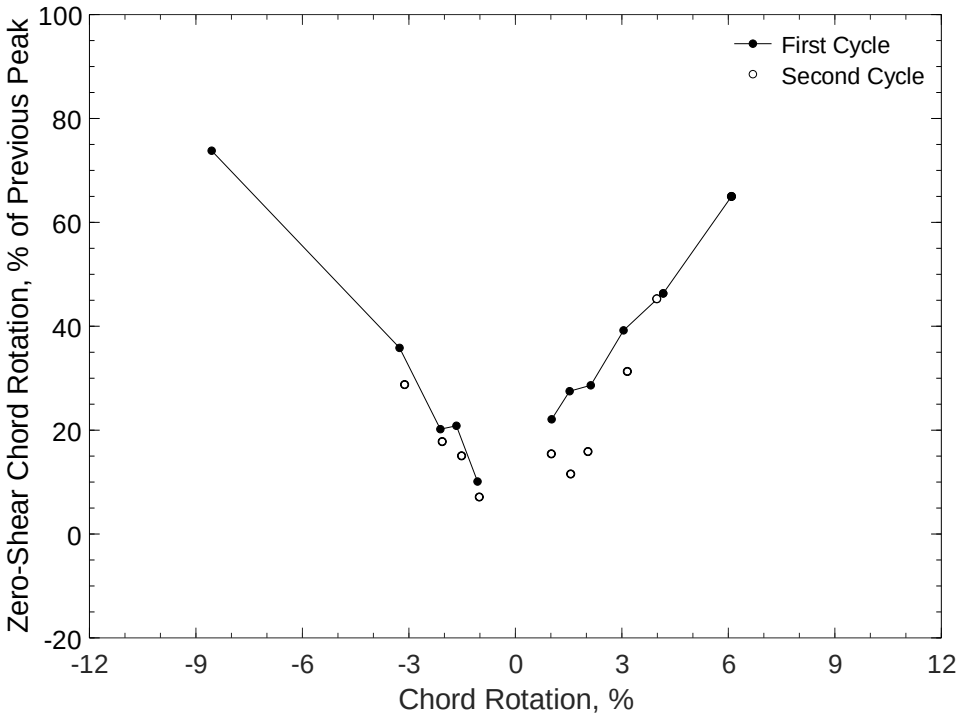

Figure 95 – Zero-shear chord rotation versus peak chord rotation, D120-1.5

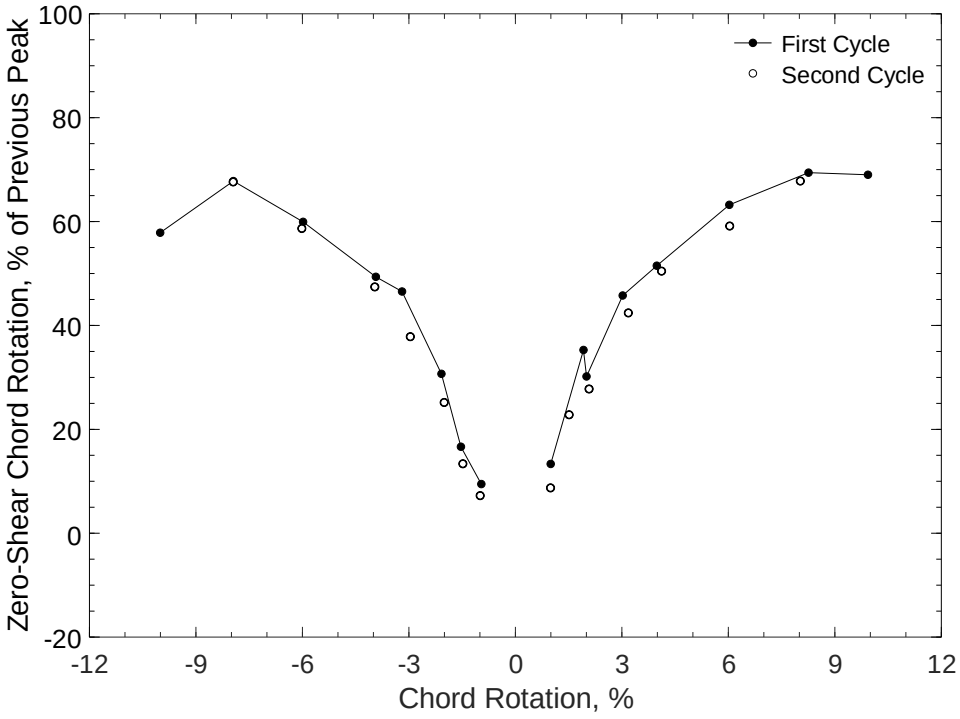

Figure 96 – Zero-shear chord rotation versus peak chord rotation, D80-2.5

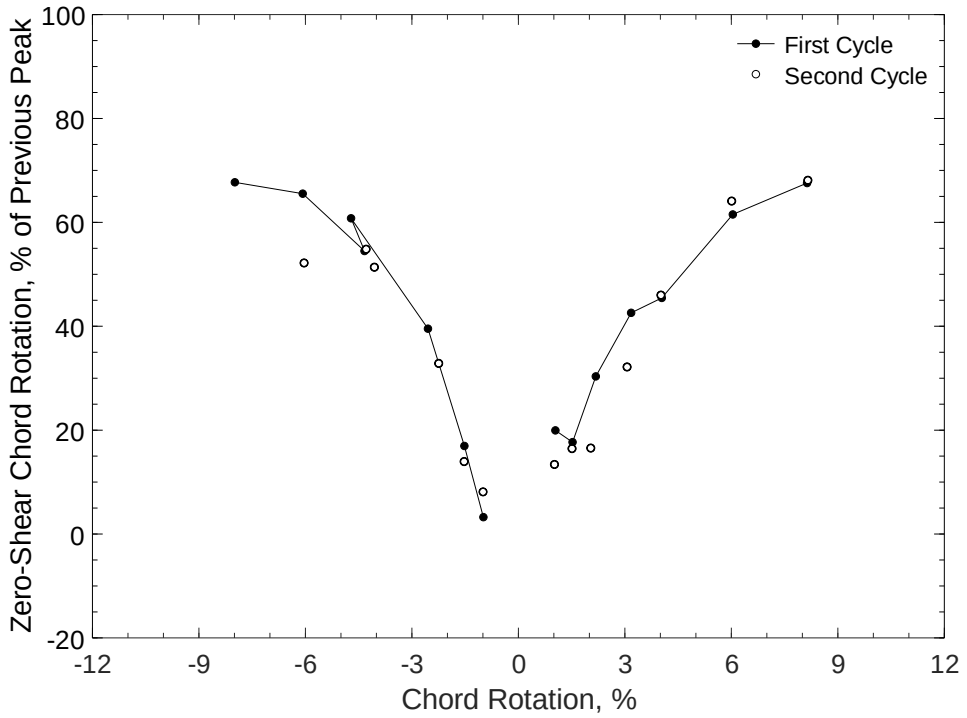

Figure 97 – Zero-shear chord rotation versus peak chord rotation, D100-2.5

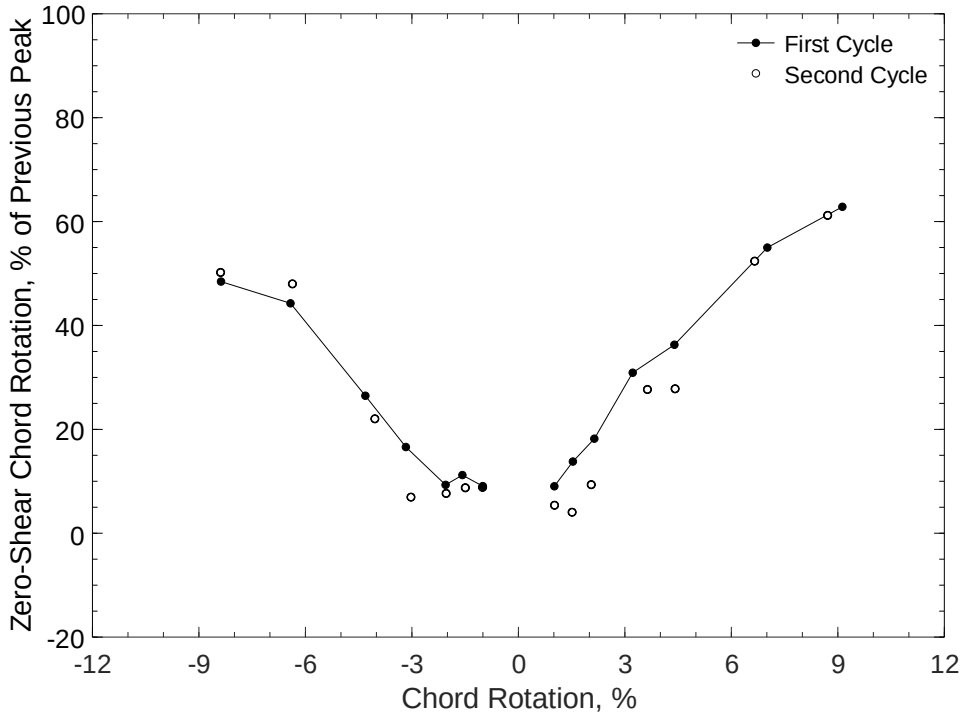

Figure 98 – Zero-shear chord rotation versus peak chord rotation, D120-2.5

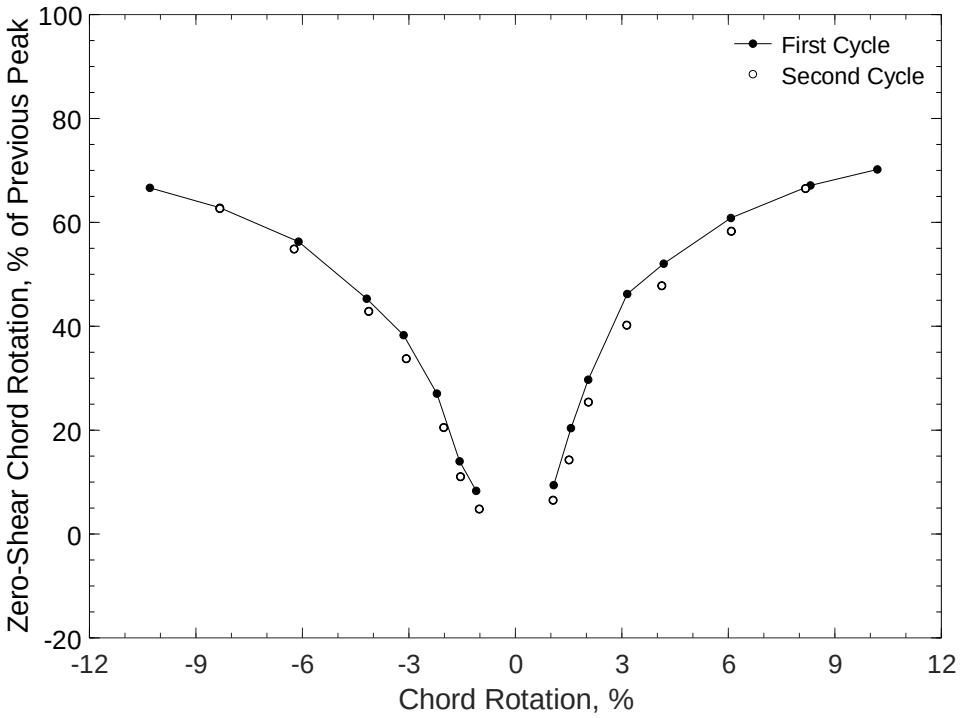

Figure 99 – Zero-shear chord rotation versus peak chord rotation, D80-3.5

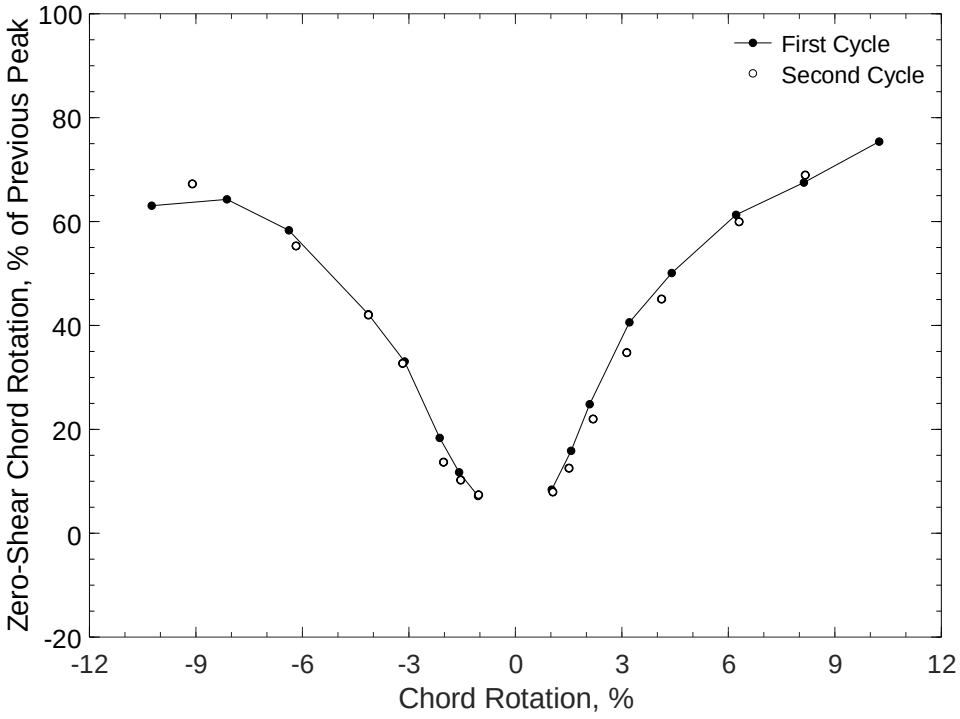

Figure 100 – Zero-shear chord rotation versus peak chord rotation, D100-3.5

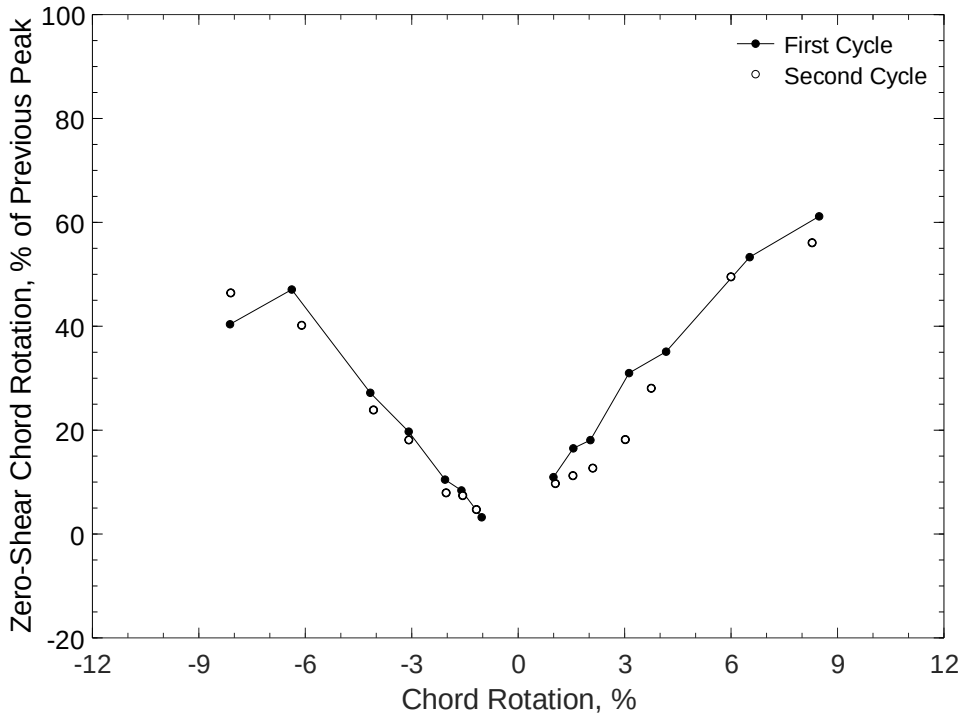

Figure 101 – Zero-shear chord rotation versus peak chord rotation, D120-3.5

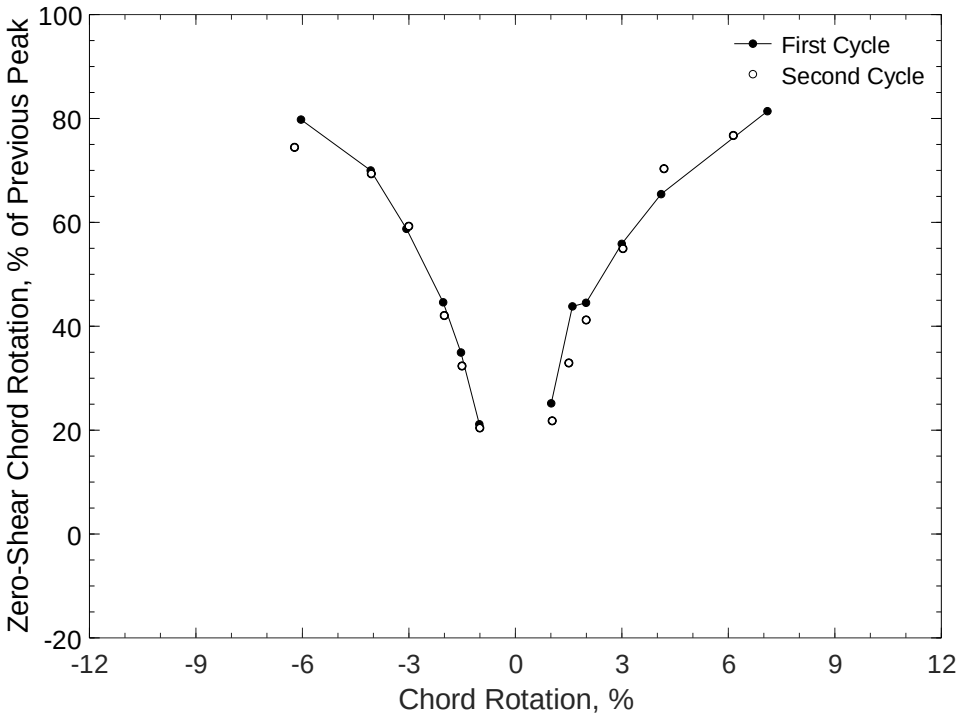

Figure 102 – Zero-shear chord rotation versus peak chord rotation, P80-2.5

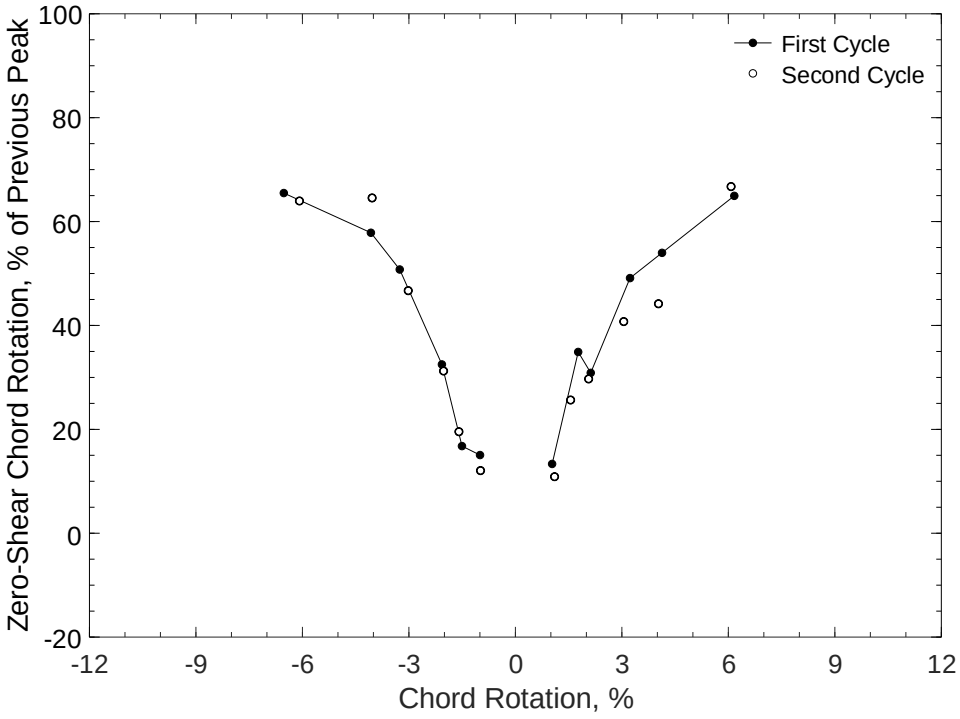

Figure 103 – Zero-shear chord rotation versus peak chord rotation, P100-2.5

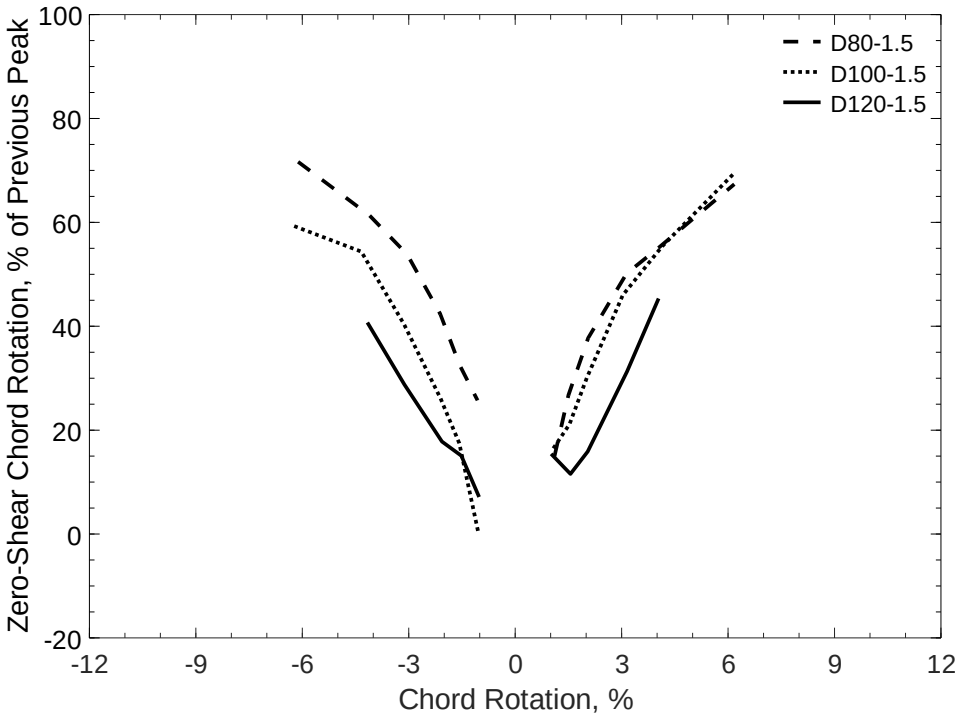

Figure 104 – Zero-shear chord rotation versus peak chord rotation (second cycle), D-type beams (aspect ratio of 1.5)

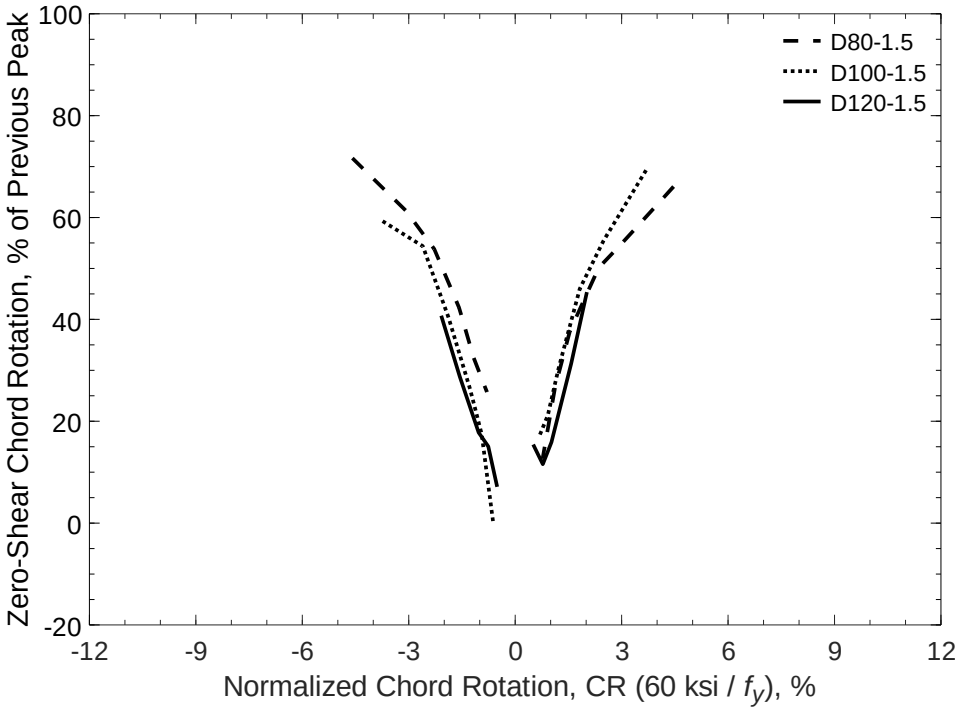

Figure 105 – Zero-shear chord rotation versus normalized peak chord rotation (second cycle), D-type beams (aspect ratio of 1.5)

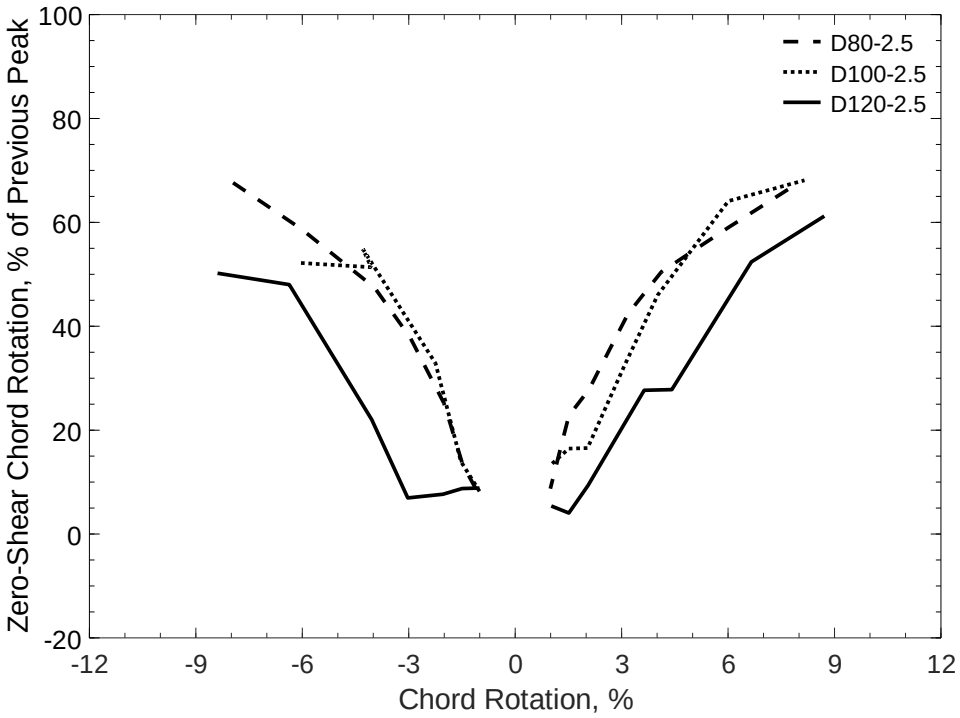

Figure 106 – Zero-shear chord rotation versus peak chord rotation (second cycle), D-type beams (aspect ratio of 2.5)

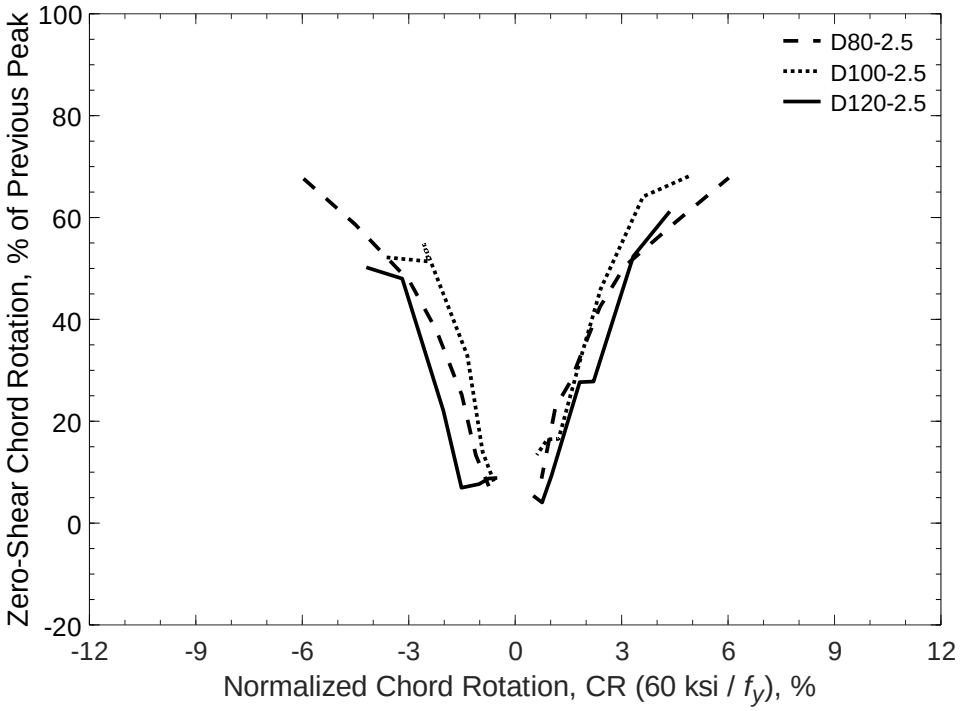

Figure 107 – Zero-shear chord rotation versus normalized peak chord rotation (second cycle), D-type beams (aspect ratio of 2.5)

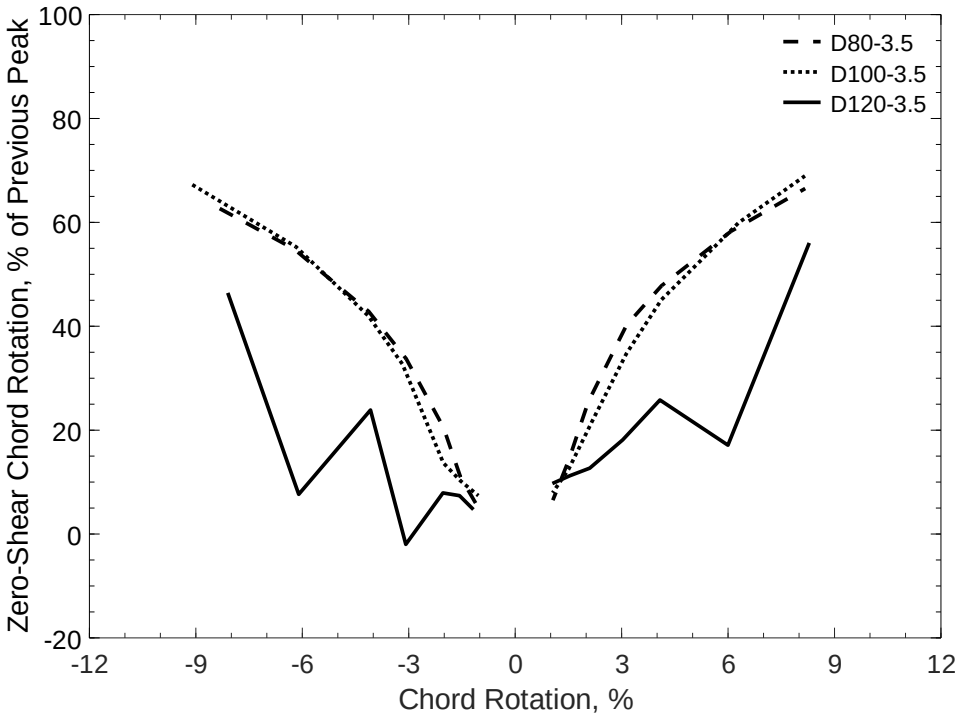

Figure 108 – Zero-shear chord rotation versus peak chord rotation (second cycle), D-type beams (aspect ratio of 3.5)

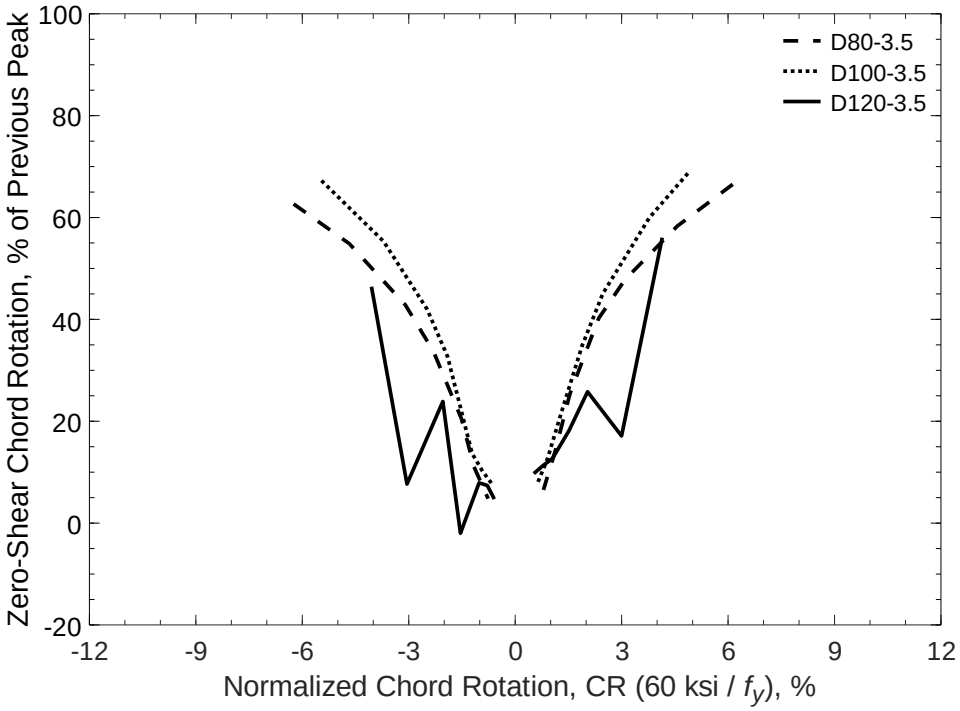

Figure 109 – Zero-shear chord rotation versus normalized peak chord rotation (second cycle), D-type beams (aspect ratio of 3.5)

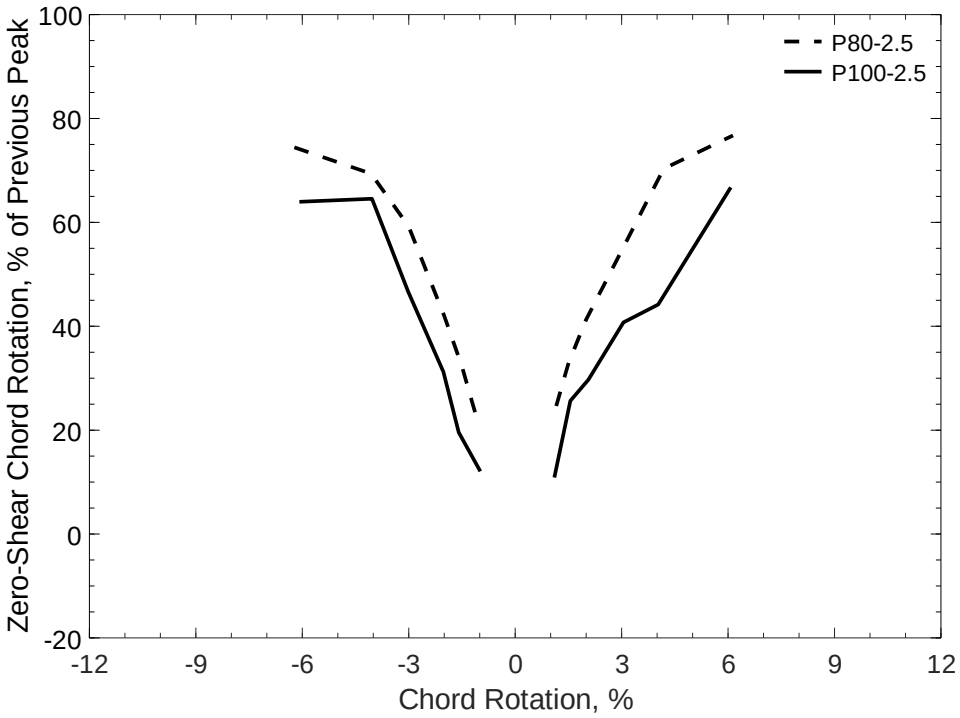

Figure 110 – Zero-shear chord rotation versus peak chord rotation (second cycle), P-type beams (aspect ratio of 2.5)

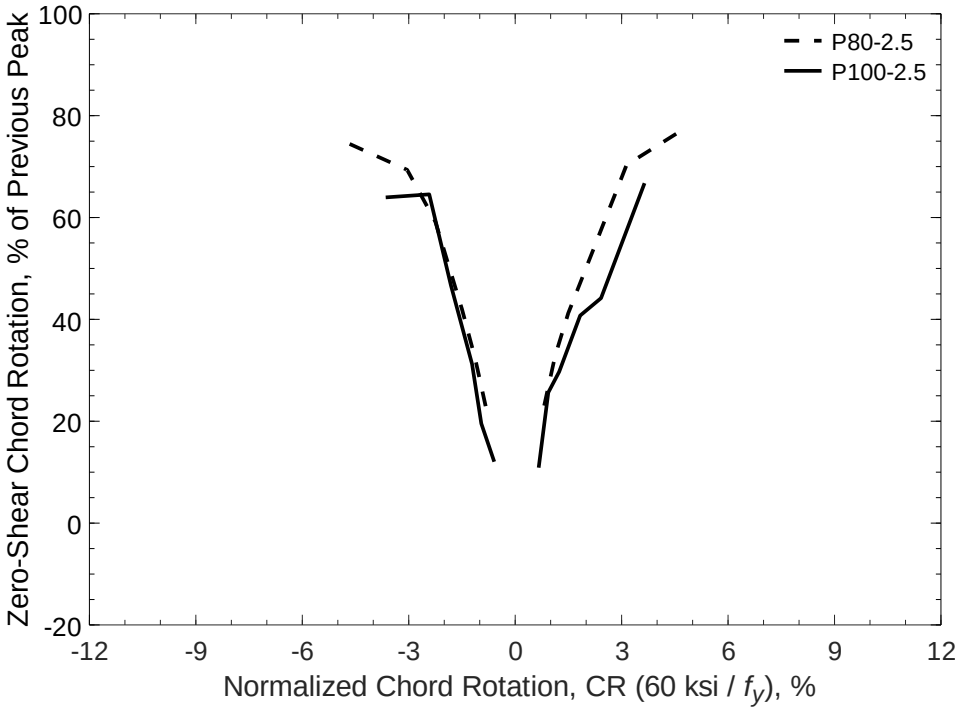

Figure 111 – Zero-shear chord rotation versus normalized peak chord rotation (second cycle), P-type beams (aspect ratio of 2.5)

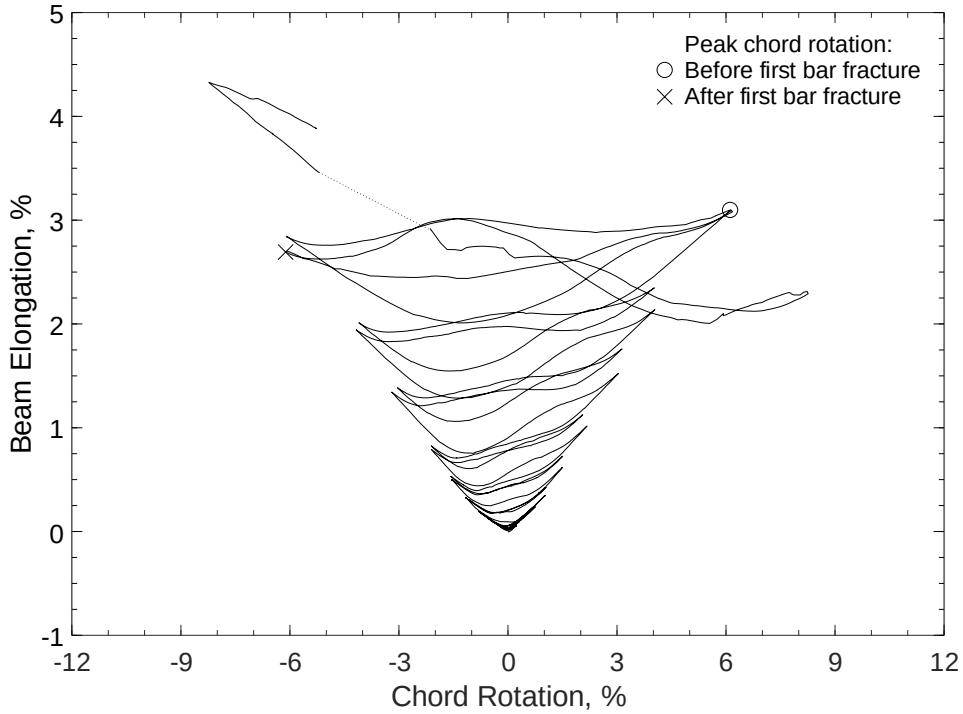

Figure 112 – Beam elongation versus chord rotation, D80-1.5

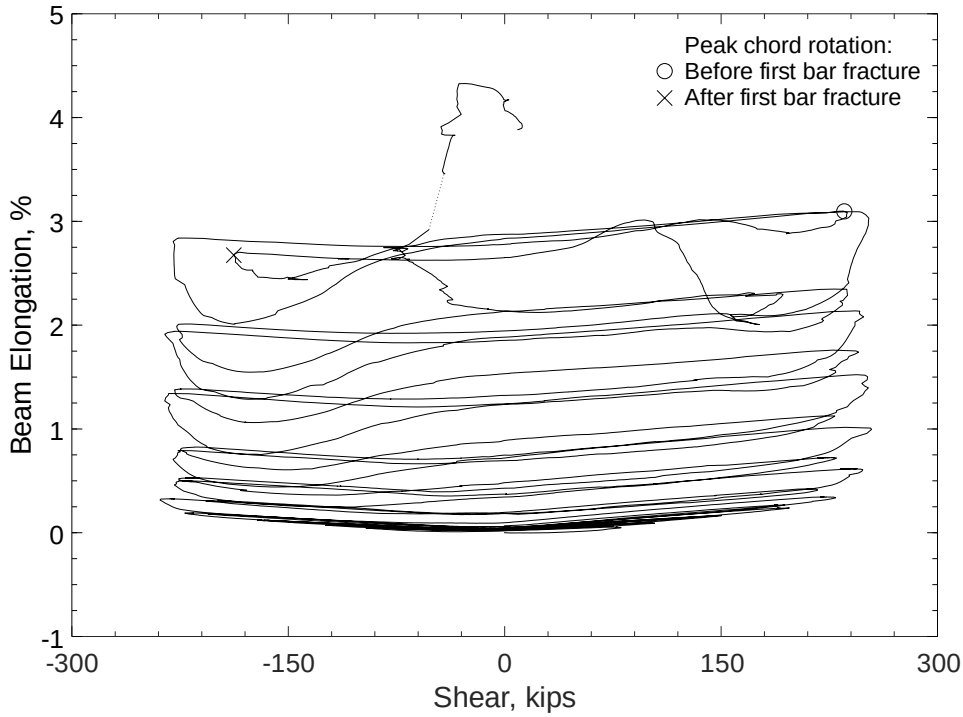

Figure 113 – Beam elongation versus shear, D80-1.5

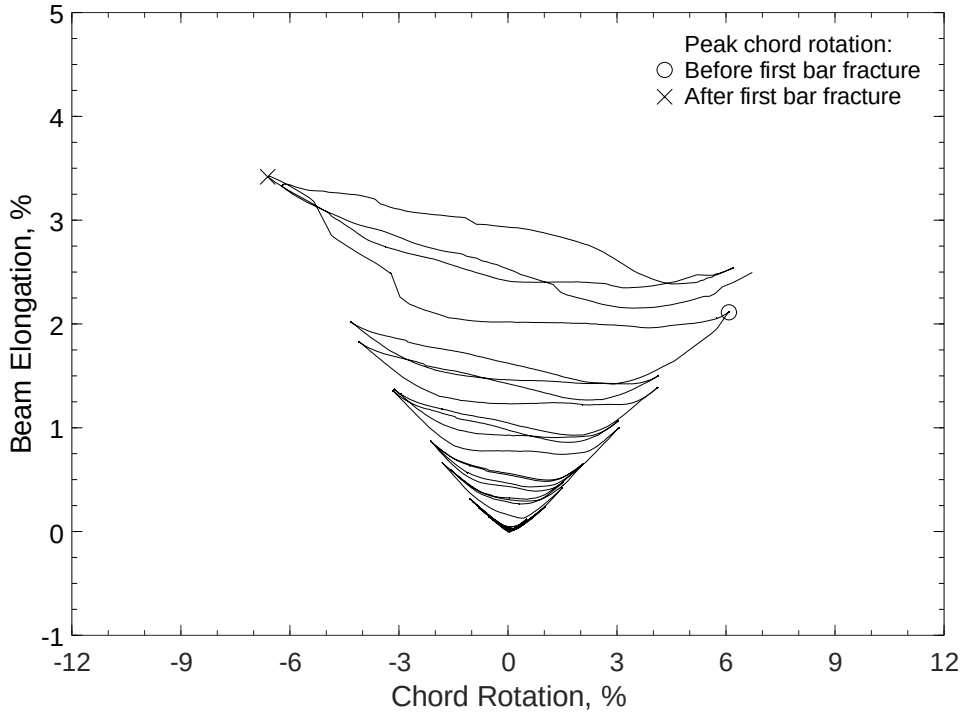

Figure 114 – Beam elongation versus chord rotation, D100-1.5

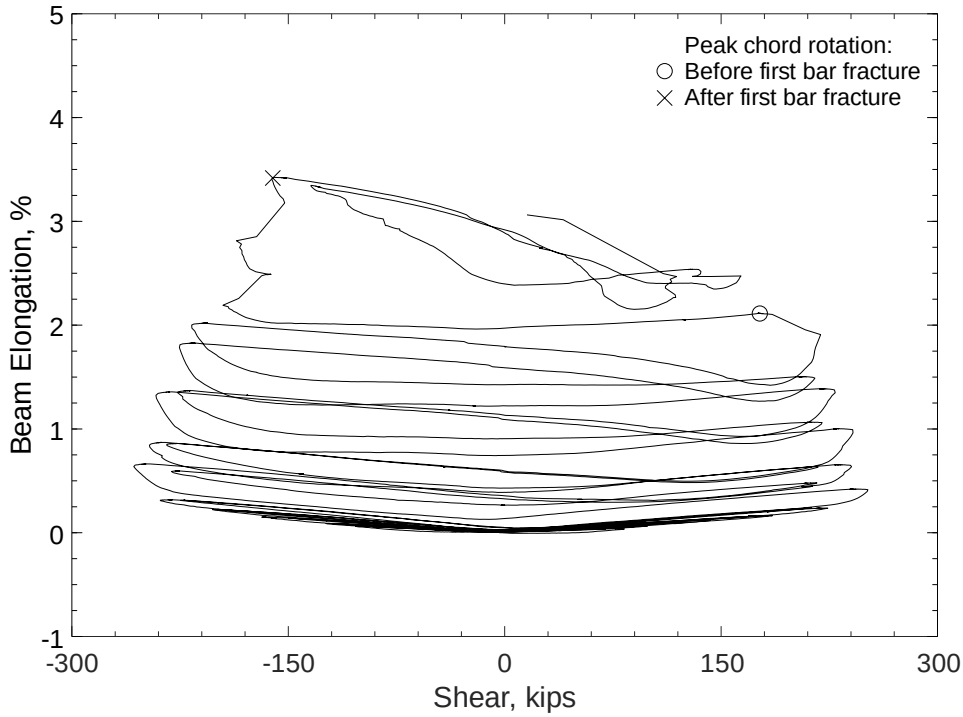

Figure 115 – Beam elongation versus shear, D100-1.5

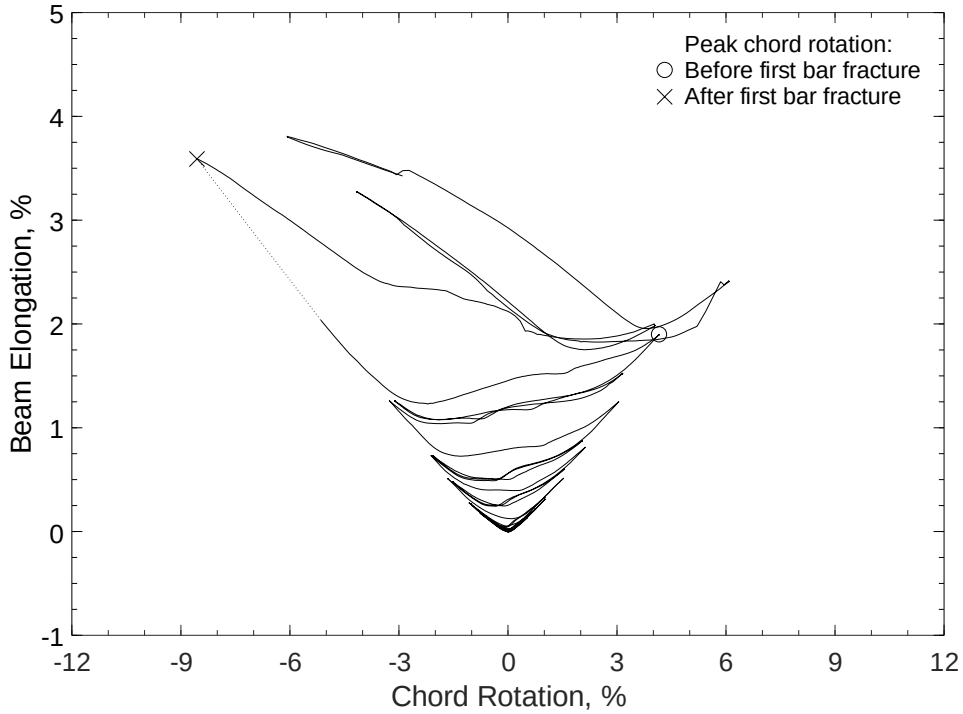

Figure 116 – Beam elongation versus chord rotation, D120-1.5

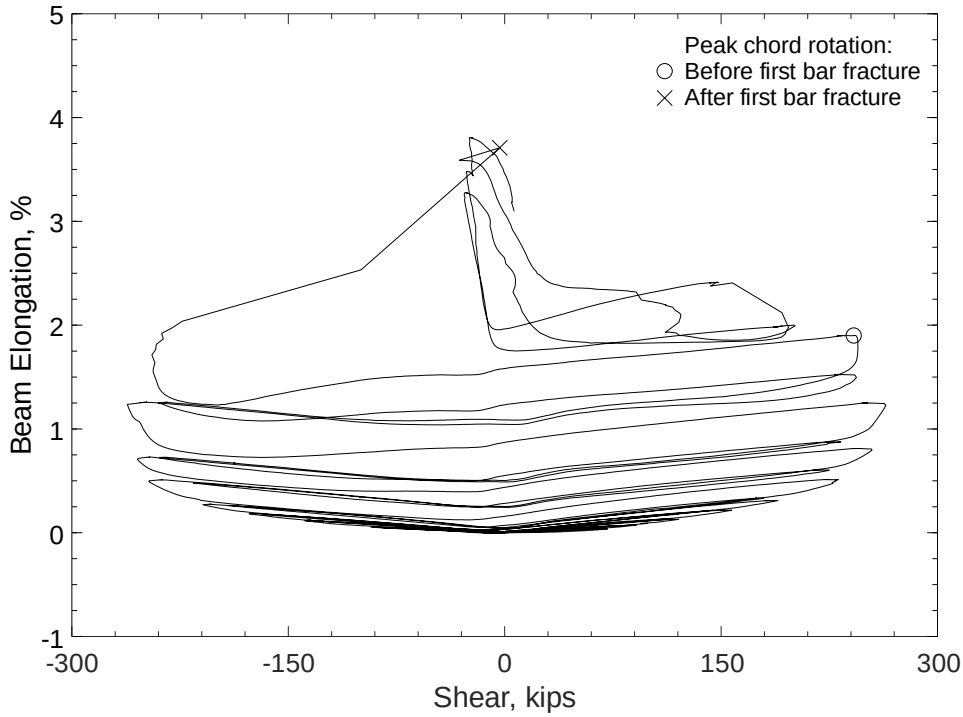

Figure 117 – Beam elongation versus shear, D120-1.5

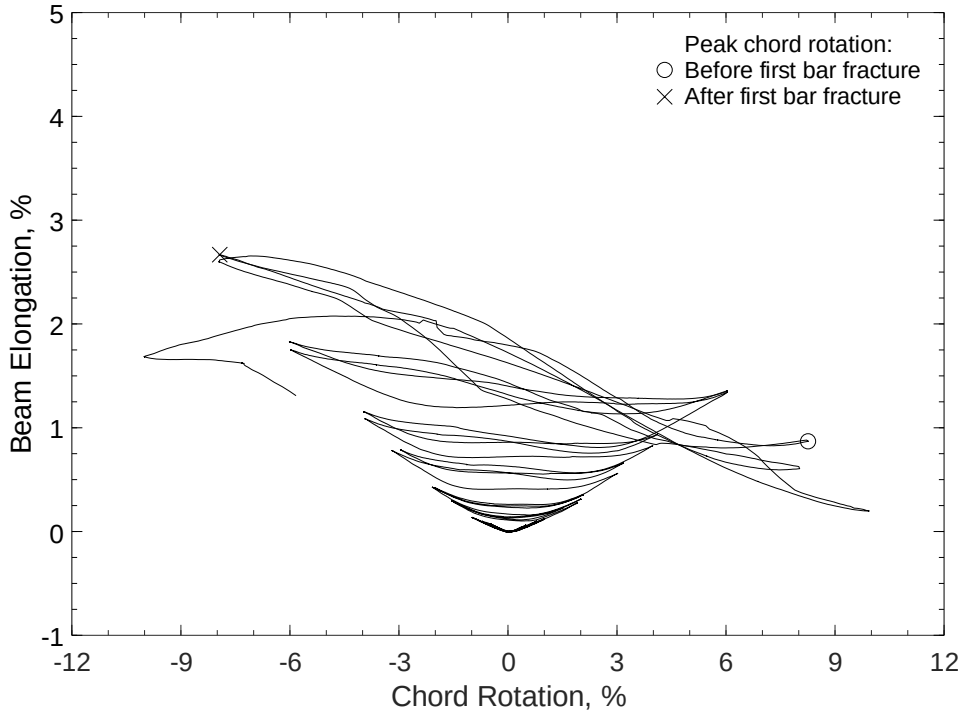

Figure 118 – Beam elongation versus chord rotation, D80-2.5

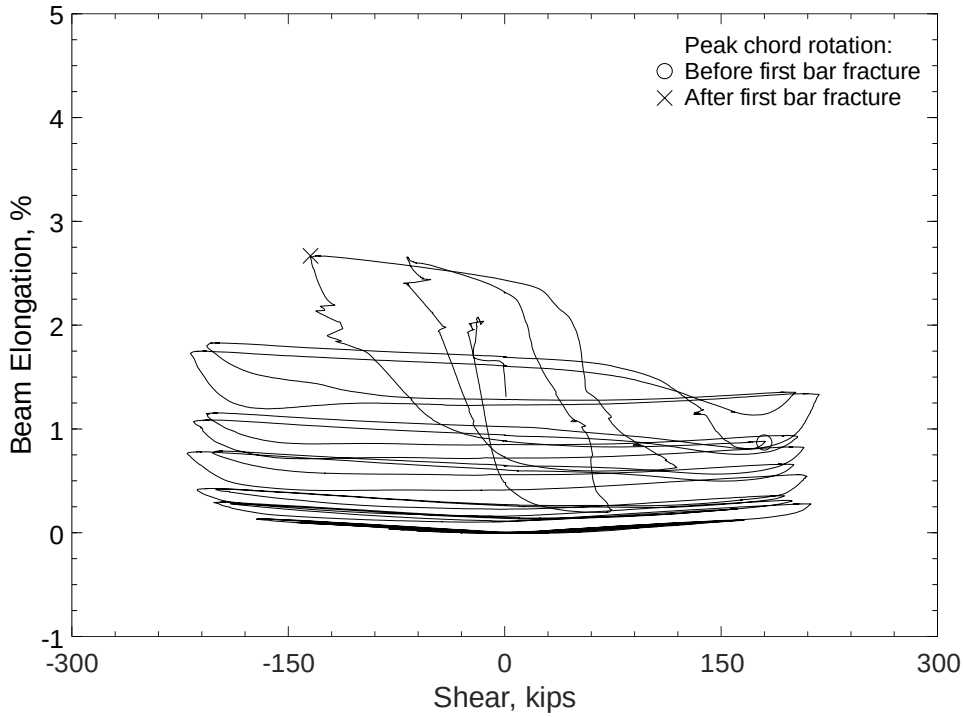

Figure 119 – Beam elongation versus shear, D80-2.5

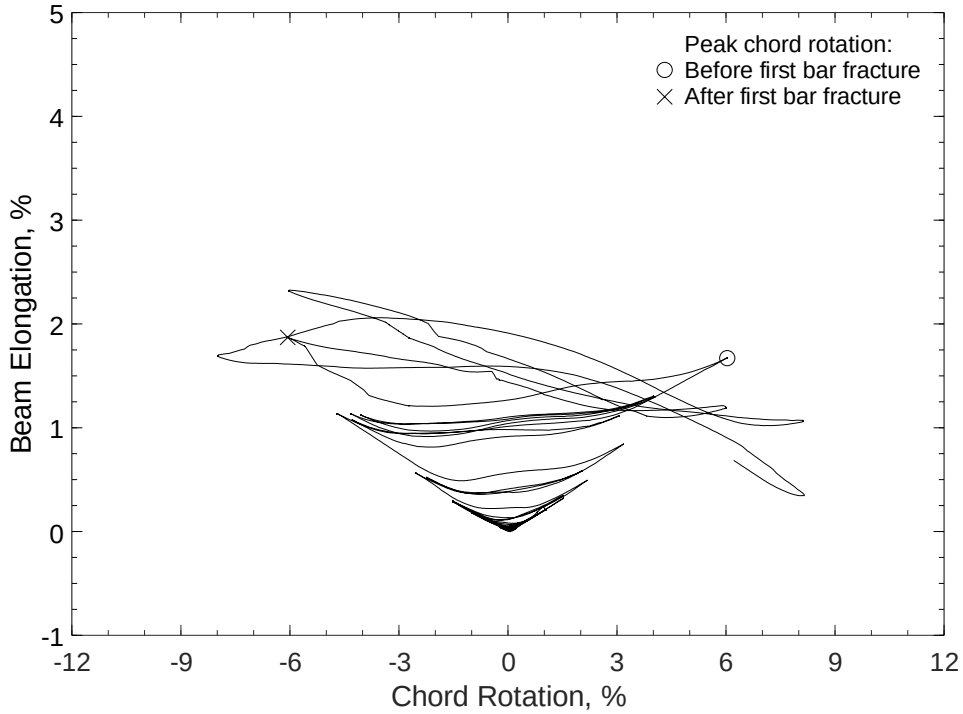

Figure 120 – Beam elongation versus chord rotation, D100-2.5

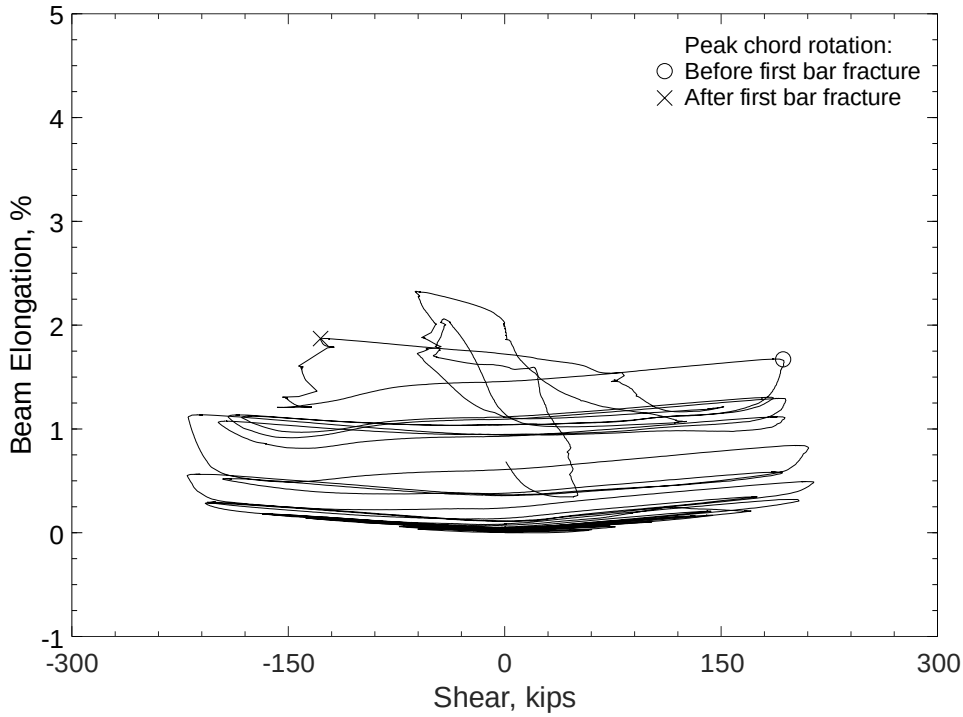

Figure 121 – Beam elongation versus shear, D100-2.5

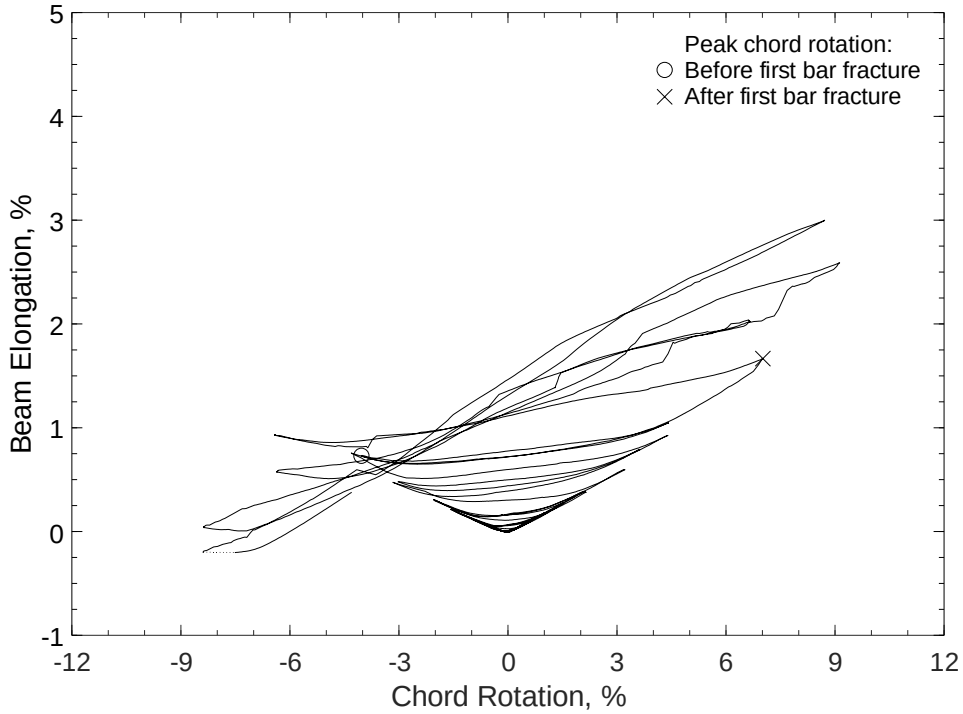

Figure 122 – Beam elongation versus chord rotation, D120-2.5

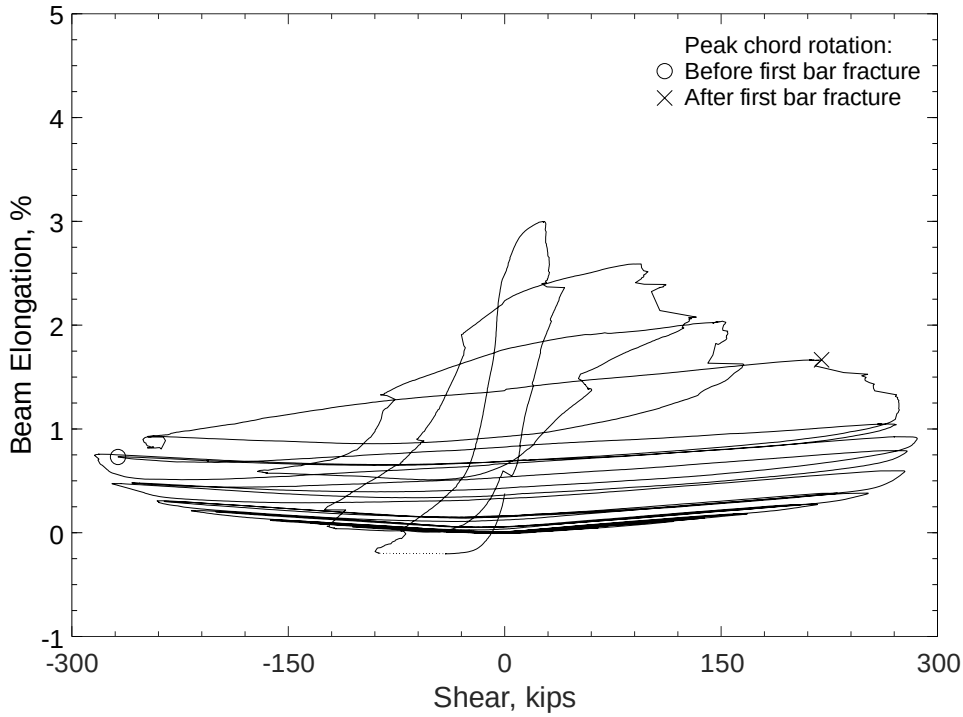

Figure 123 – Beam elongation versus shear, D120-2.5

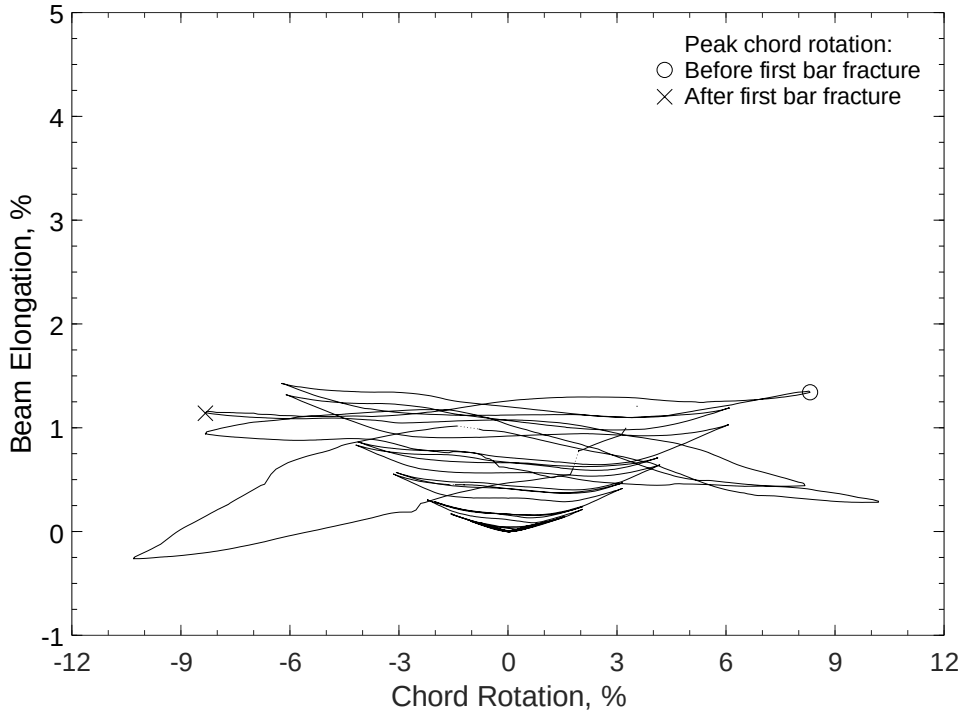

Figure 124 – Beam elongation versus chord rotation, D80-3.5

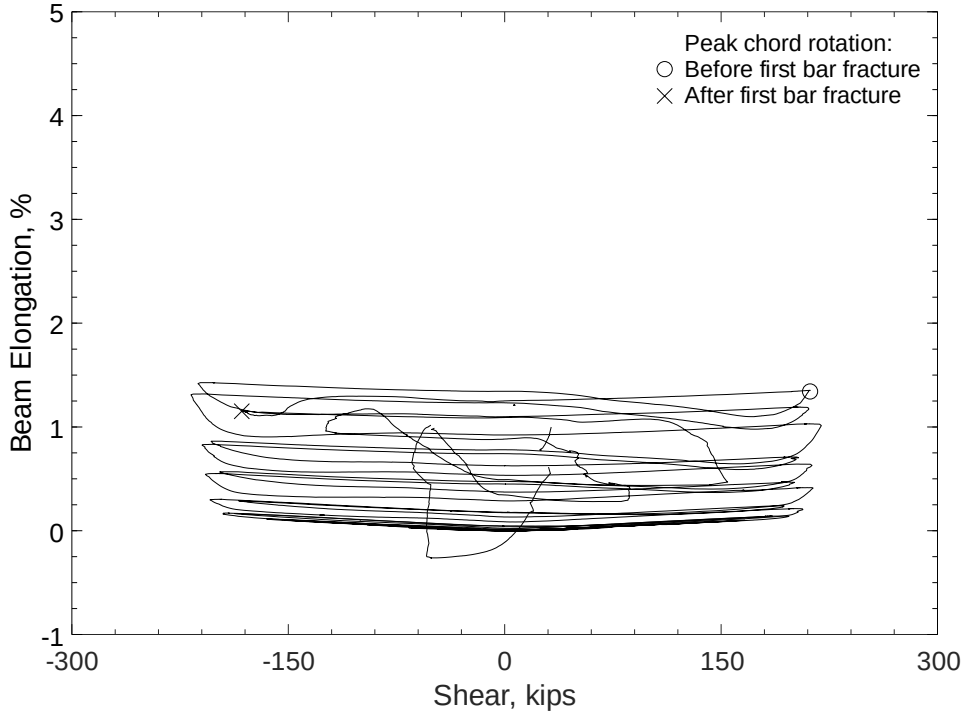

Figure 125 – Beam elongation versus shear, D80-3.5

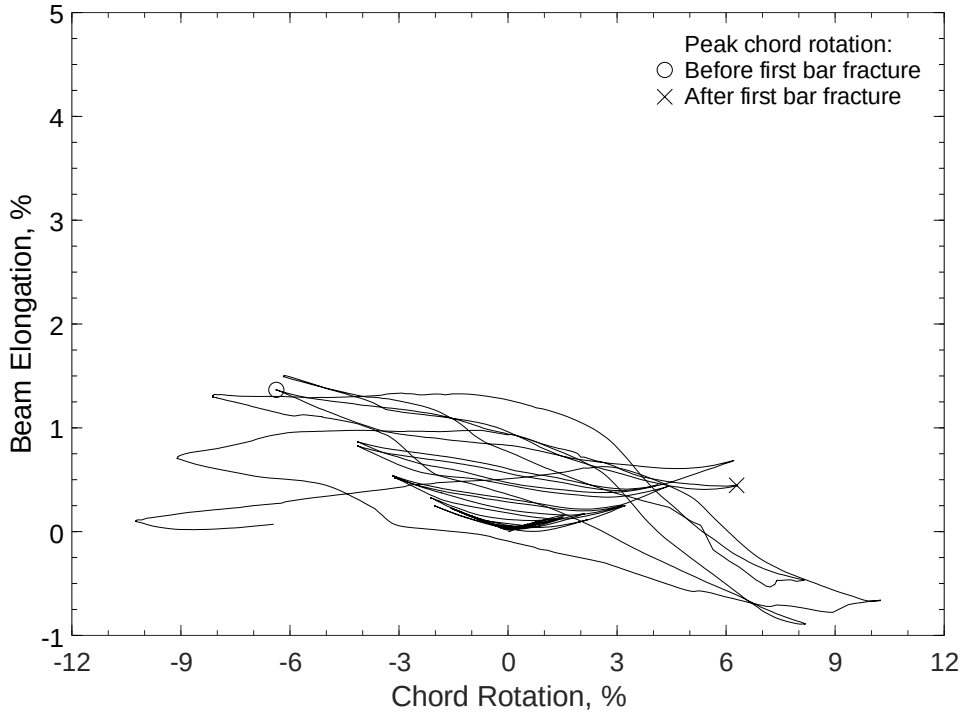

Figure 126 – Beam elongation versus chord rotation, D100-3.5

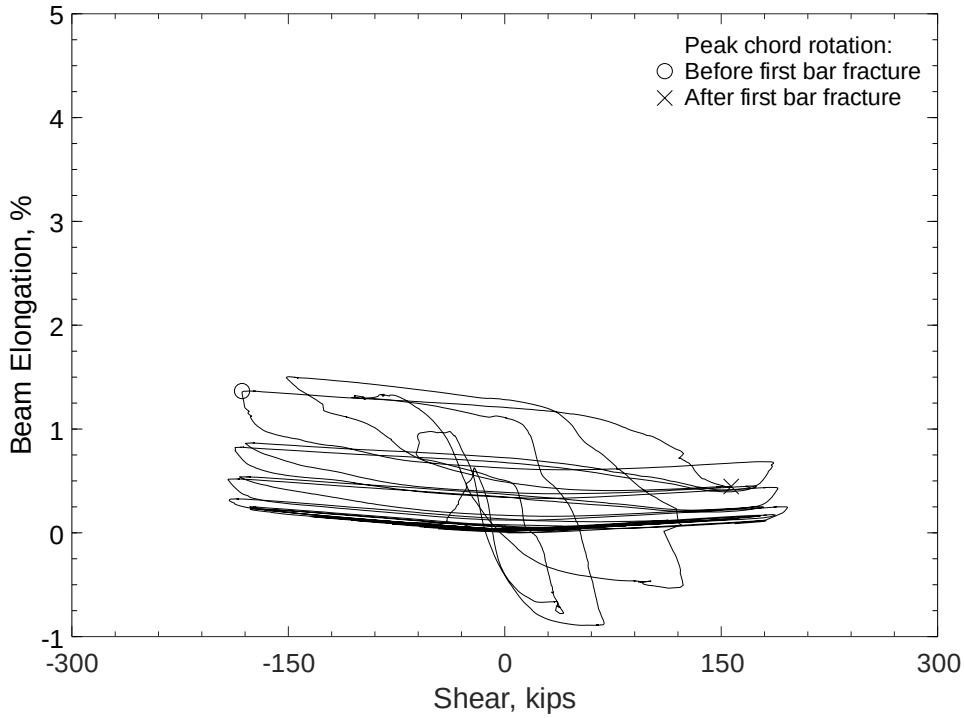

Figure 127 – Beam elongation versus shear, D100-3.5

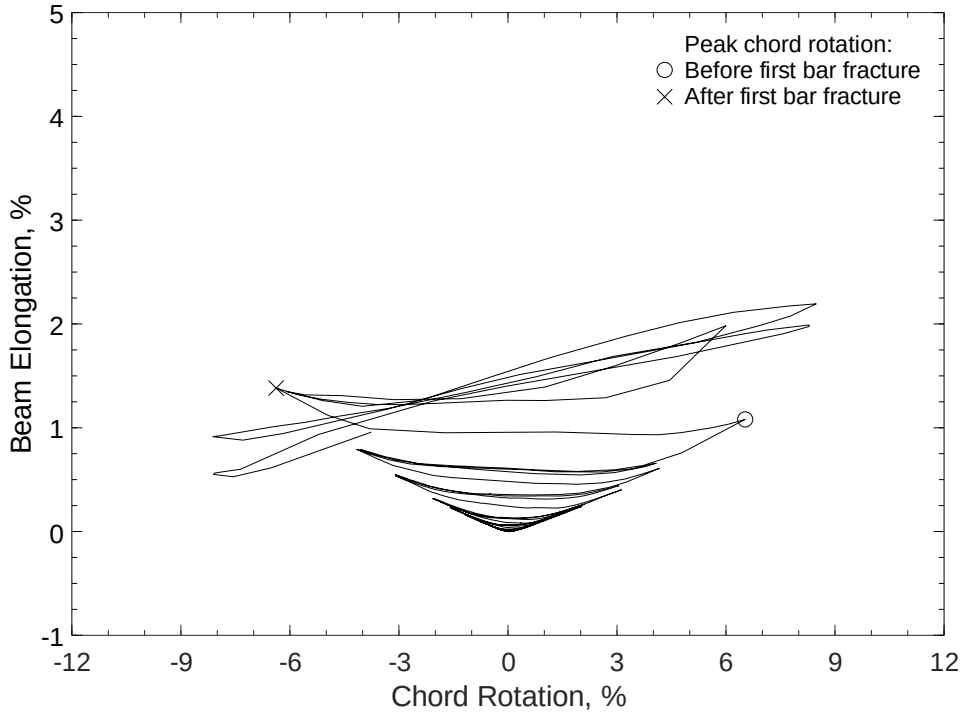

Figure 128 – Beam elongation versus chord rotation, D120-3.5

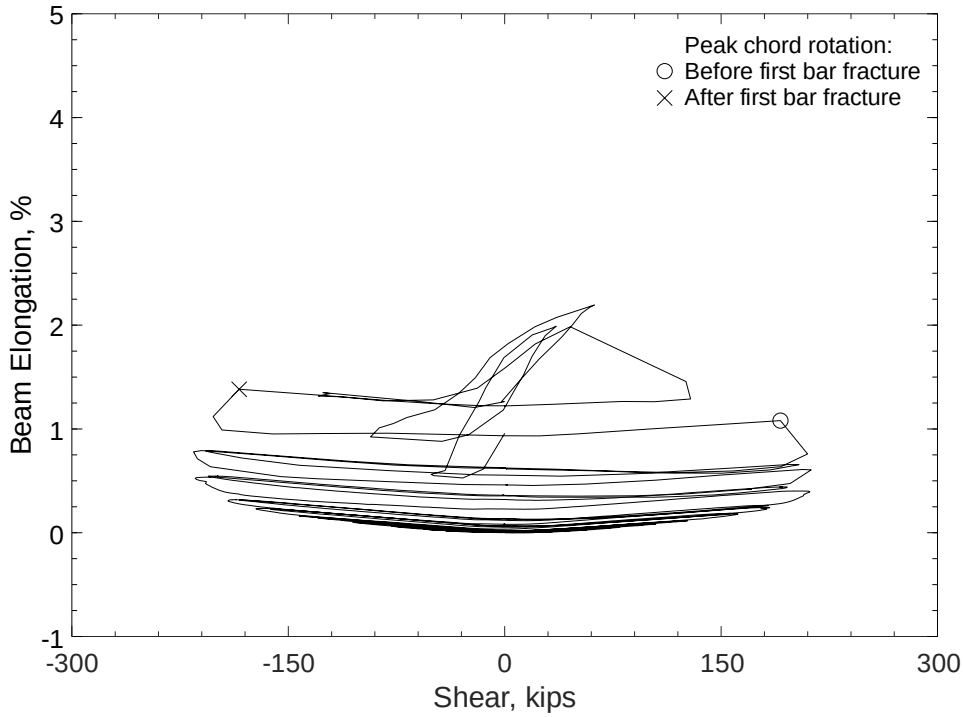

Figure 129 – Beam elongation versus shear, D120-3.5

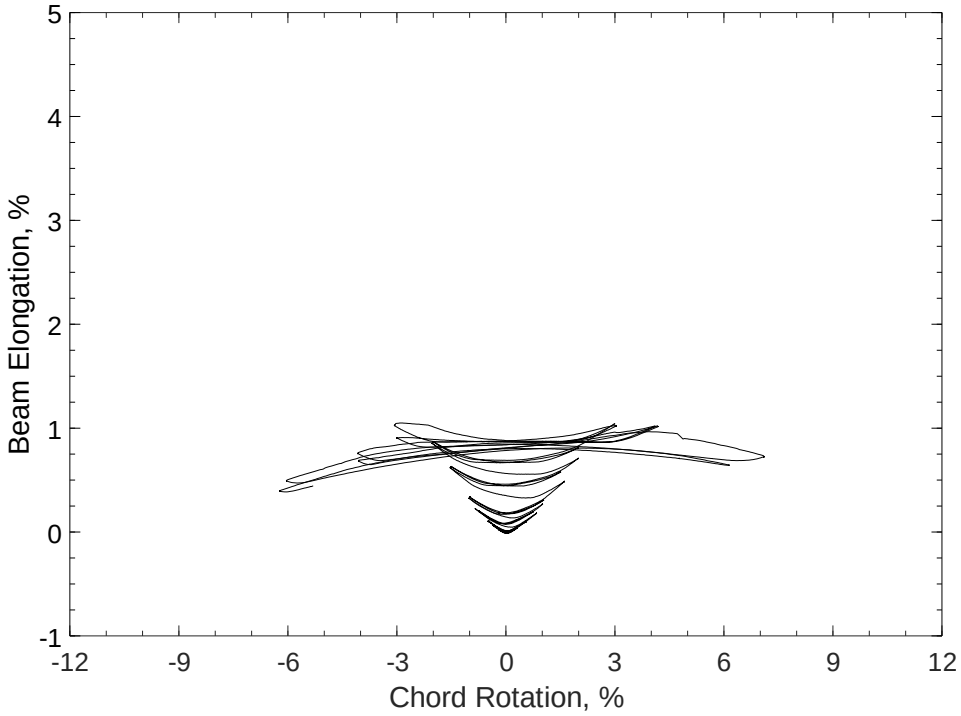

Figure 130 – Beam elongation versus chord rotation, P80-2.5

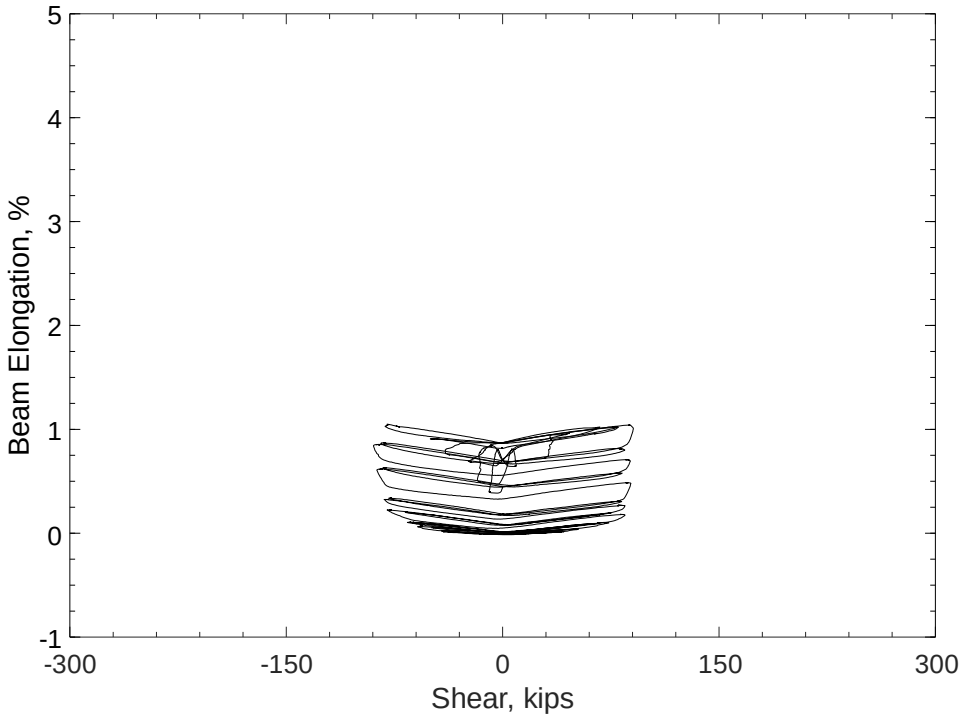

Figure 131 – Beam elongation versus shear, P80-2.5

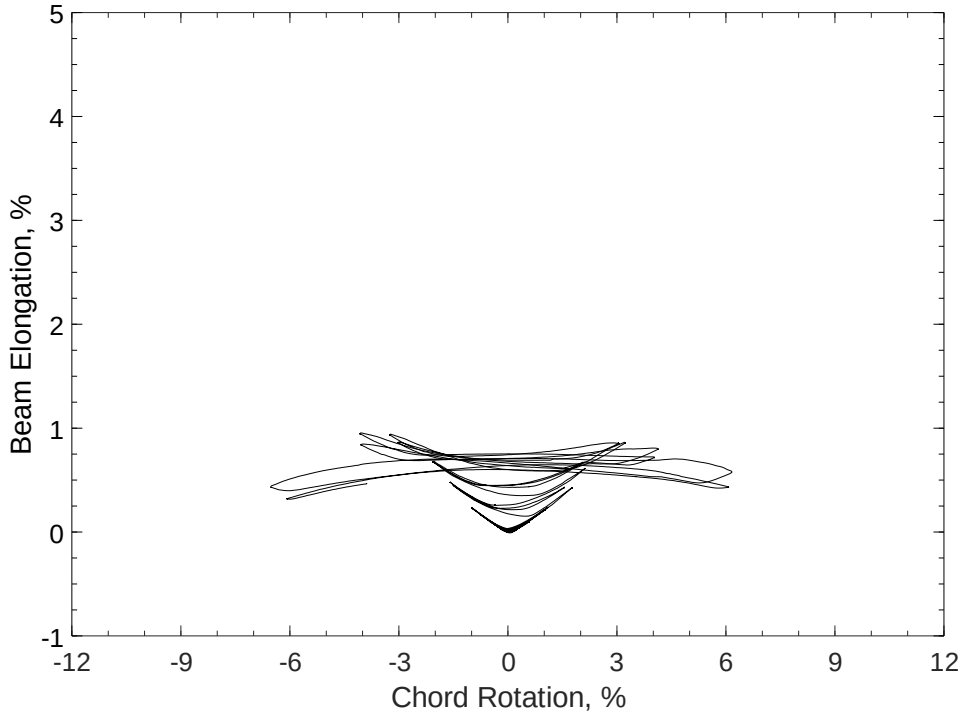

Figure 132 – Beam elongation versus chord rotation, P100-2.5

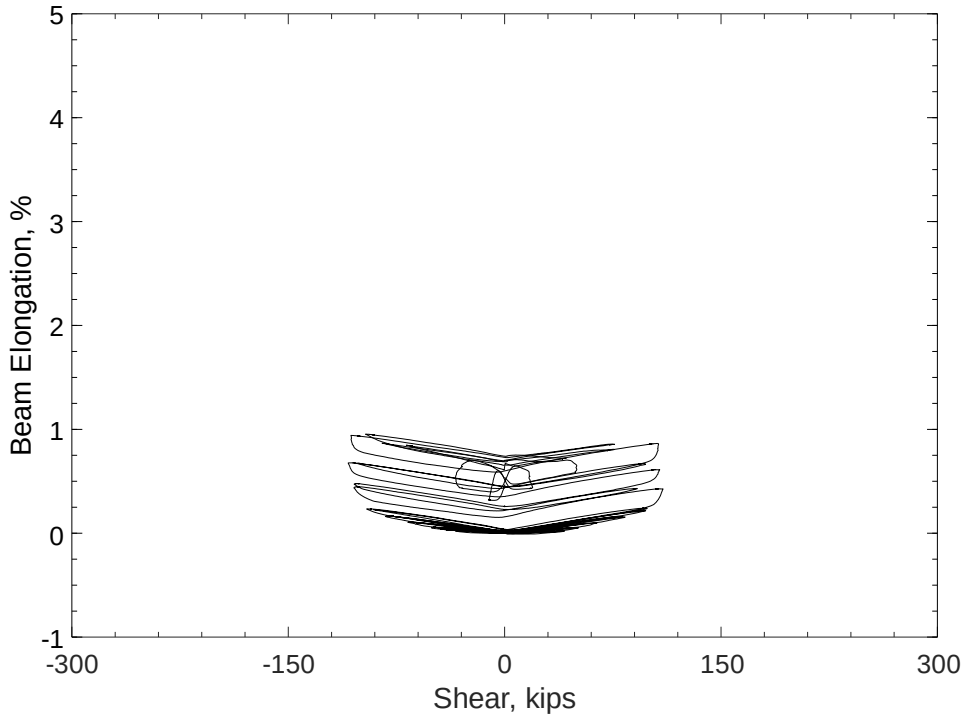

Figure 133 – Beam elongation versus shear, P100-2.5

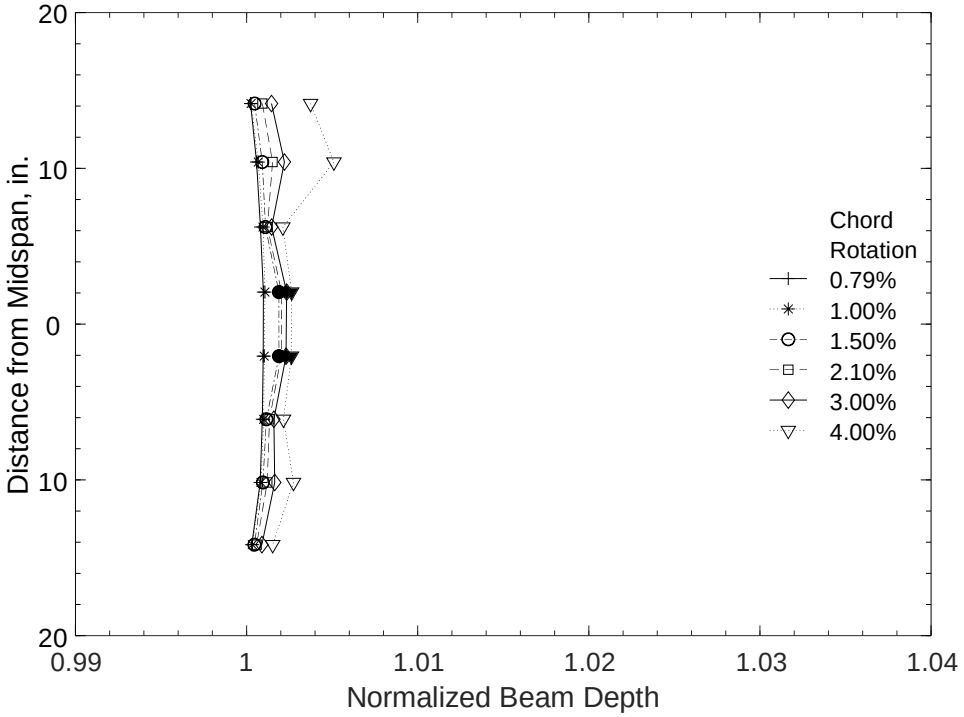

Figure 134 – Normalized beam depth at positive chord rotations, D80-1.5 (1 in. = 25.4 mm)

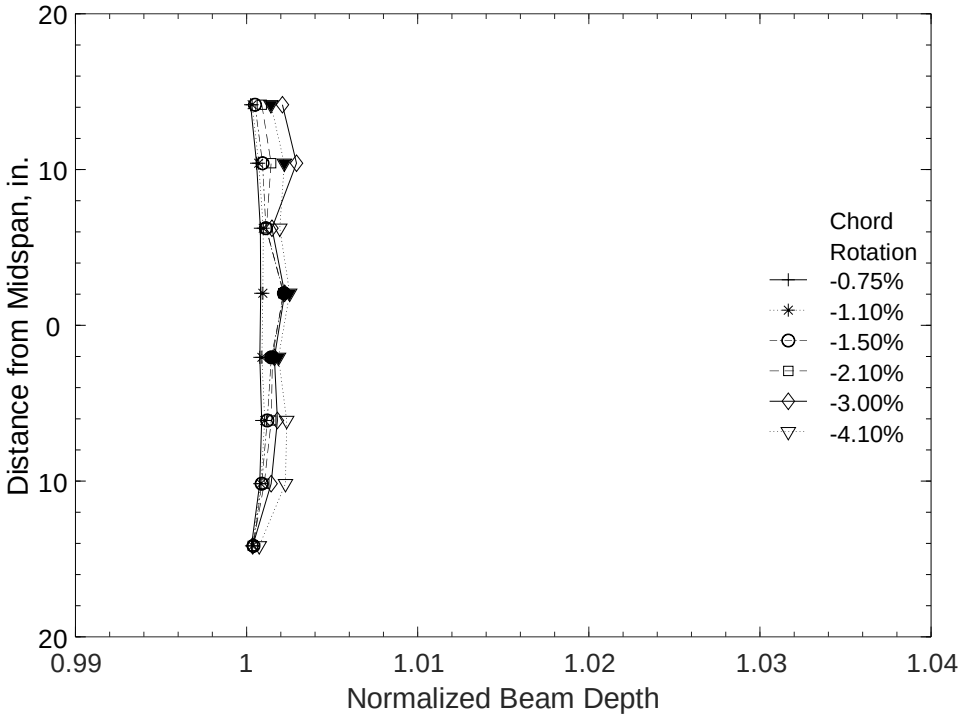

Figure 135 – Normalized beam depth at negative chord rotations, D80-1.5 (1 in. = 25.4 mm)

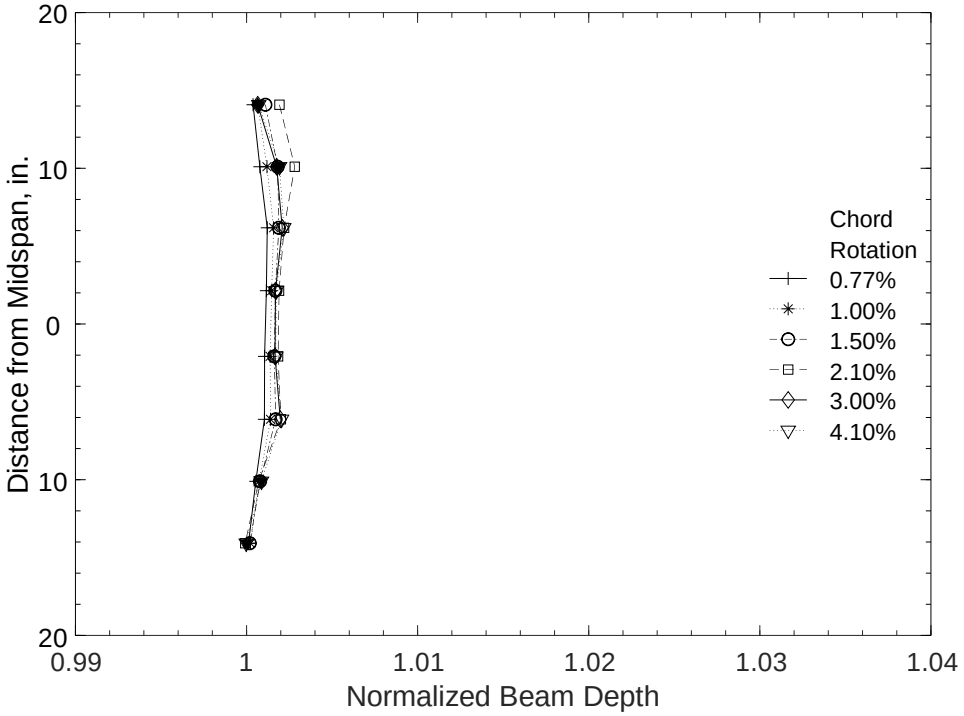

Figure 136 – Normalized beam depth at positive chord rotations, D100-1.5 (1 in. = 25.4 mm)

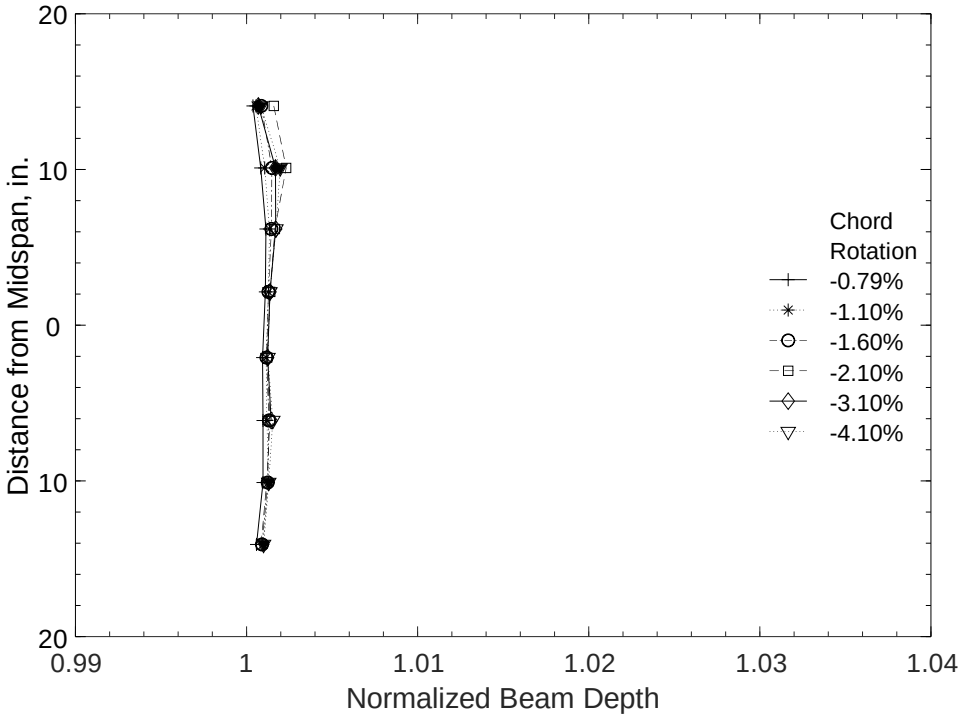

Figure 137 – Normalized beam depth at negative chord rotations, D100-1.5 (1 in. = 25.4 mm)

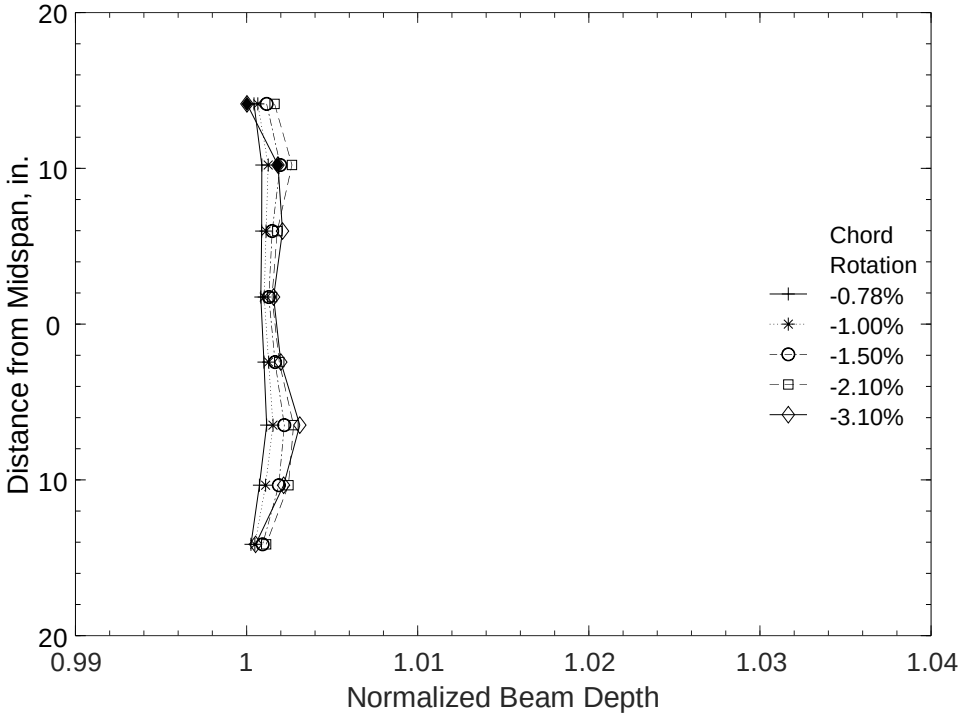

Figure 138 – Normalized beam depth at positive chord rotations, D120-1.5 (1 in. = 25.4 mm)

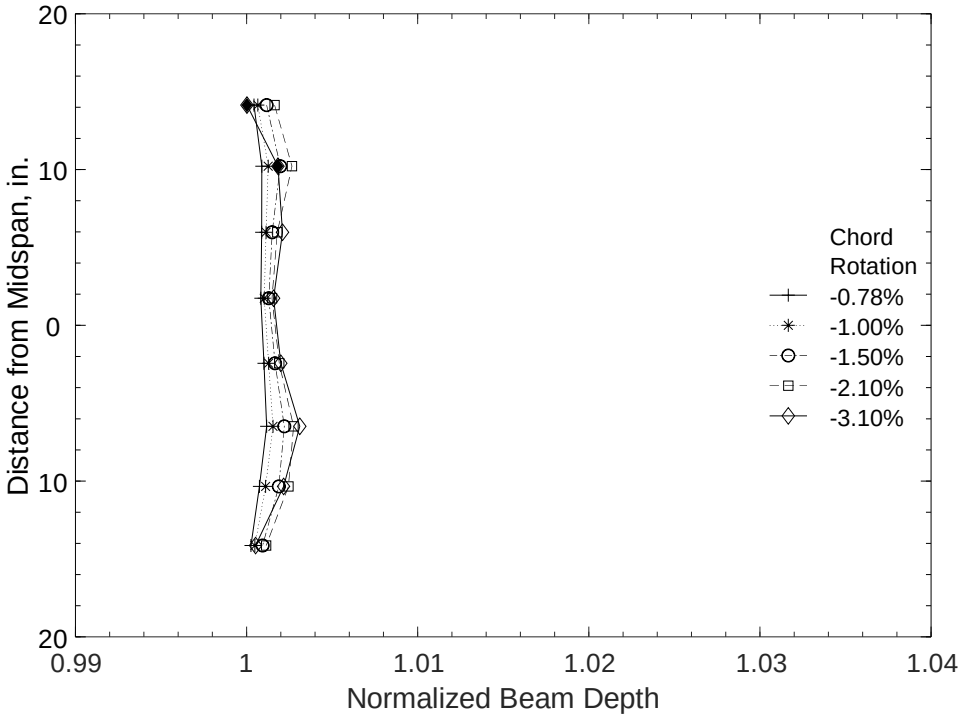

Figure 139 – Normalized beam depth at negative chord rotations, D120-1.5 (1 in. = 25.4 mm)

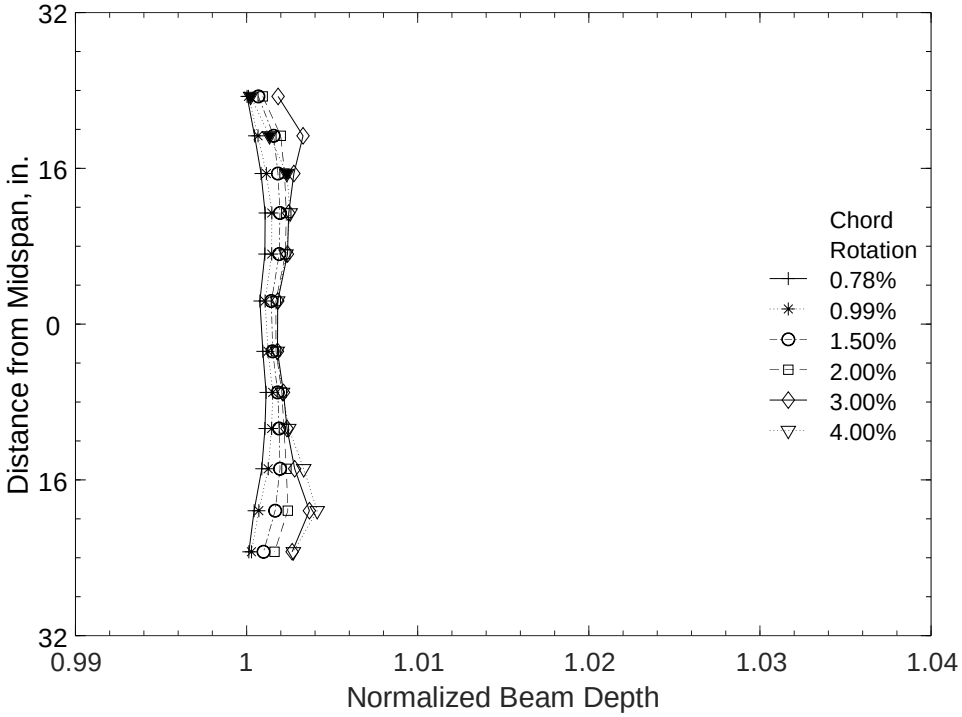

Figure 140 – Normalized beam depth at positive chord rotations, D80-2.5 (1 in. = 25.4 mm)

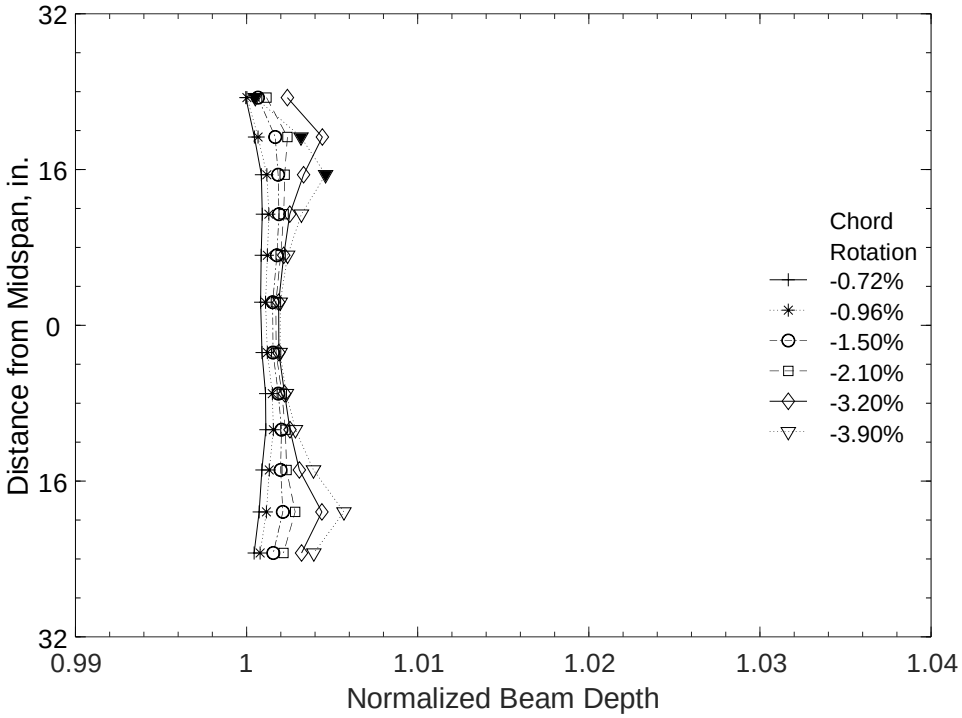

Figure 141 – Normalized beam depth at negative chord rotations, D80-2.5 (1 in. = 25.4 mm)

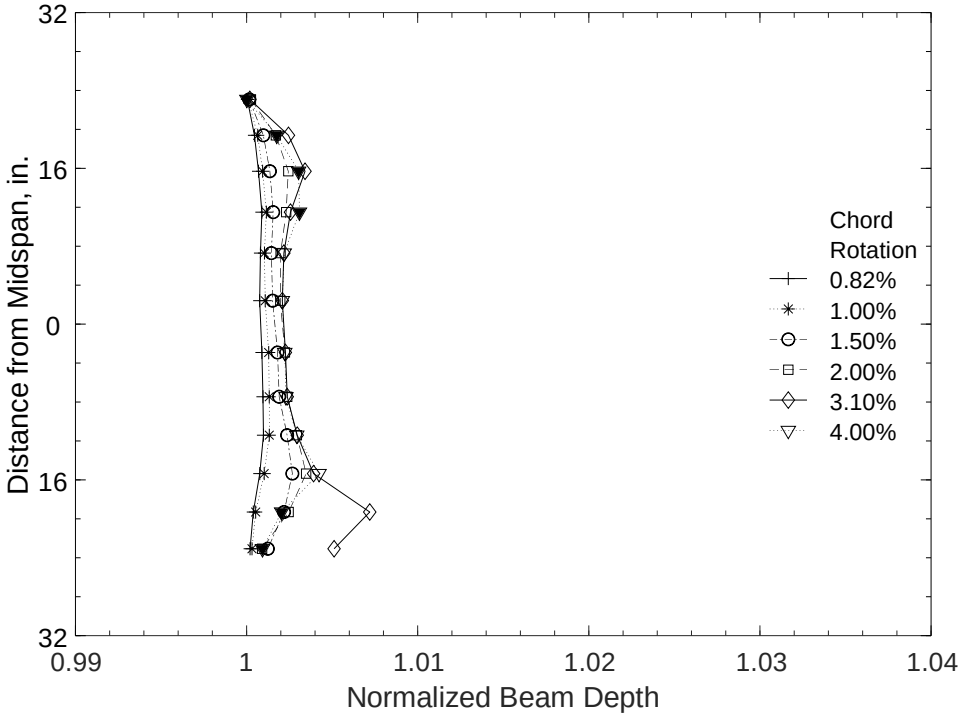

Figure 142 – Normalized beam depth at positive chord rotations, D100-2.5 (1 in. = 25.4 mm)

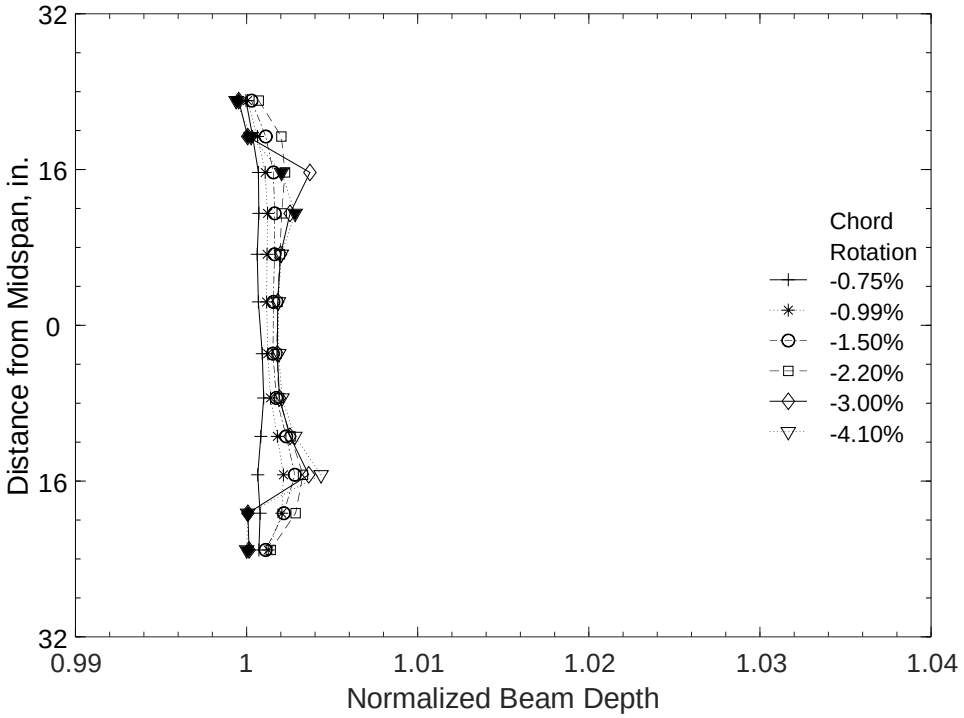

Figure 143 – Normalized beam depth at negative chord rotations, D100-2.5 (1 in. = 25.4 mm)

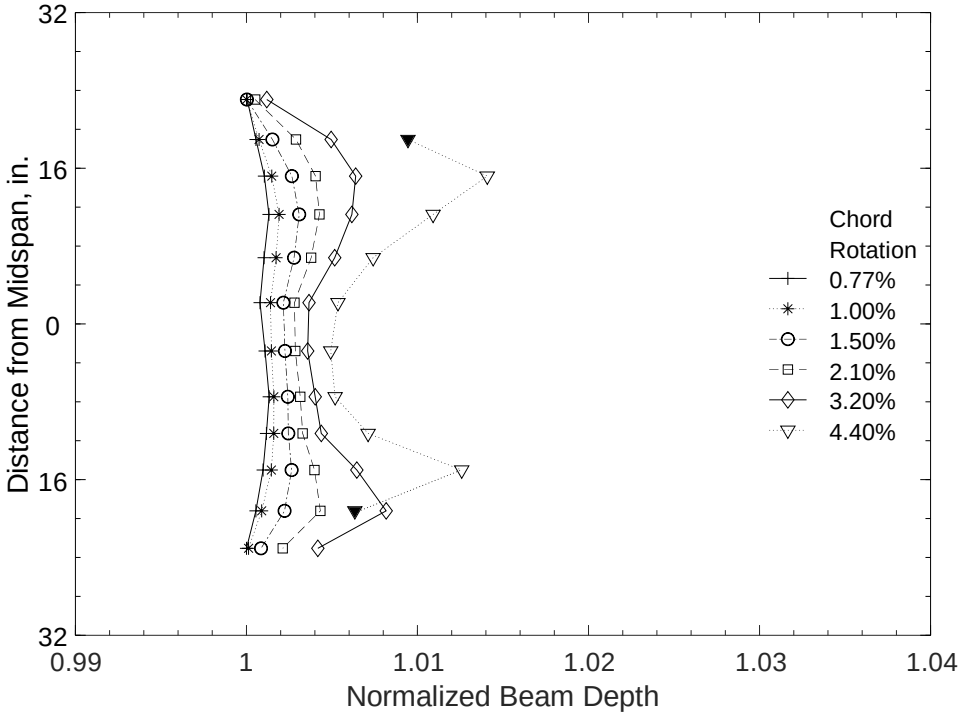

Figure 144 – Normalized beam depth at positive chord rotations, D120-2.5 (1 in. = 25.4 mm)

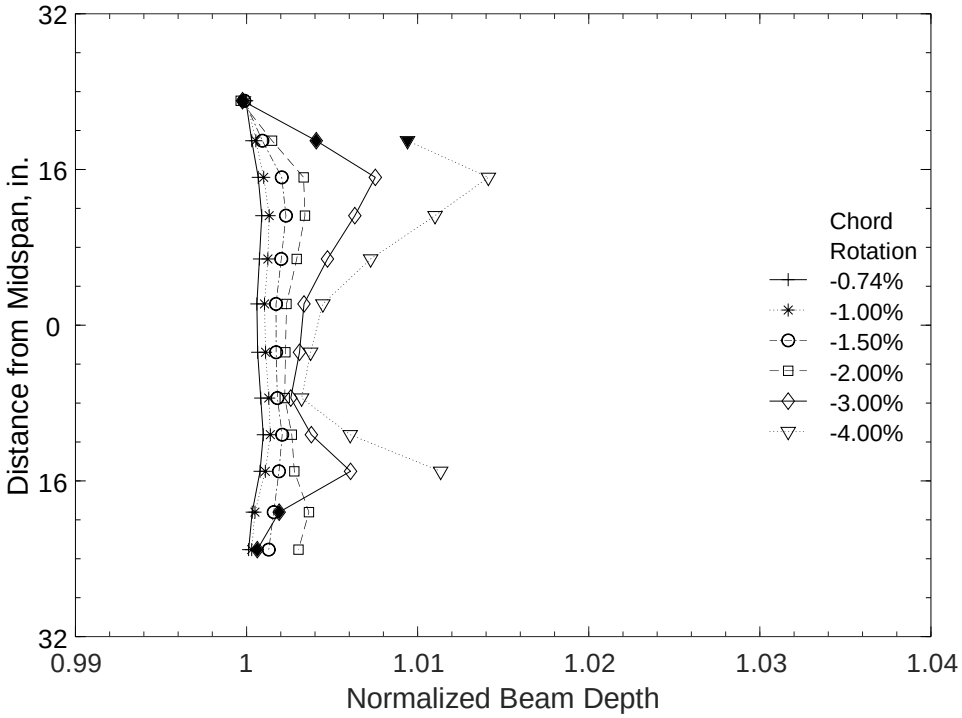

Figure 145 – Normalized beam depth at negative chord rotations, D120-2.5 (1 in. = 25.4 mm)

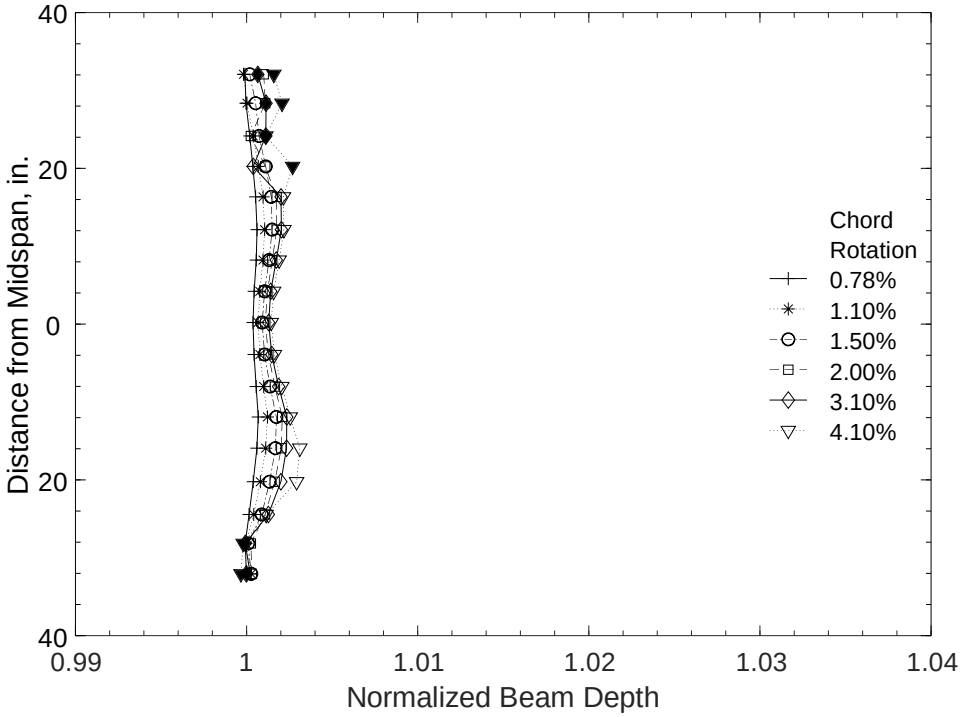

Figure 146 – Normalized beam depth at positive chord rotations, D80-3.5 (1 in. = 25.4 mm)

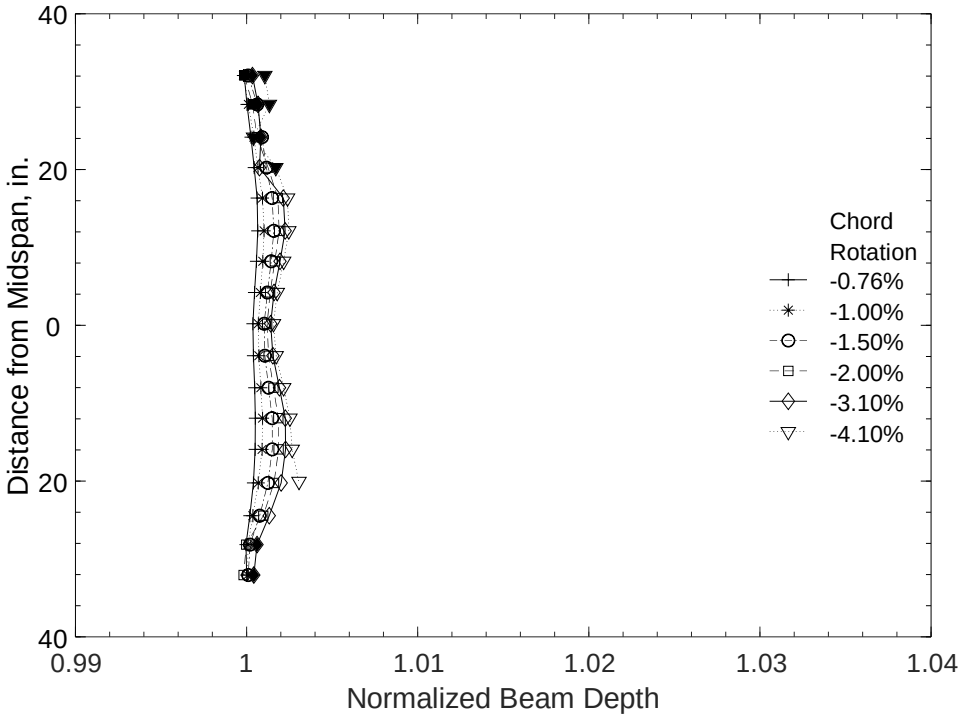

Figure 147 – Normalized beam depth at negative chord rotations, D80-3.5 (1 in. = 25.4 mm)

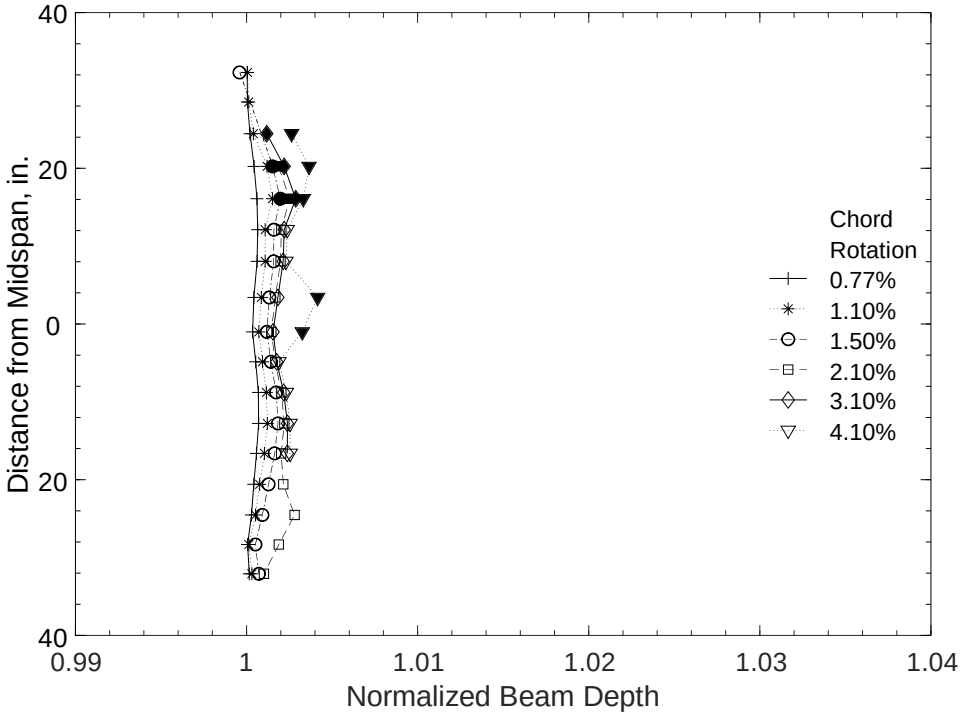

Figure 148 – Normalized beam depth at positive chord rotations, D100-3.5 (1 in. = 25.4 mm)

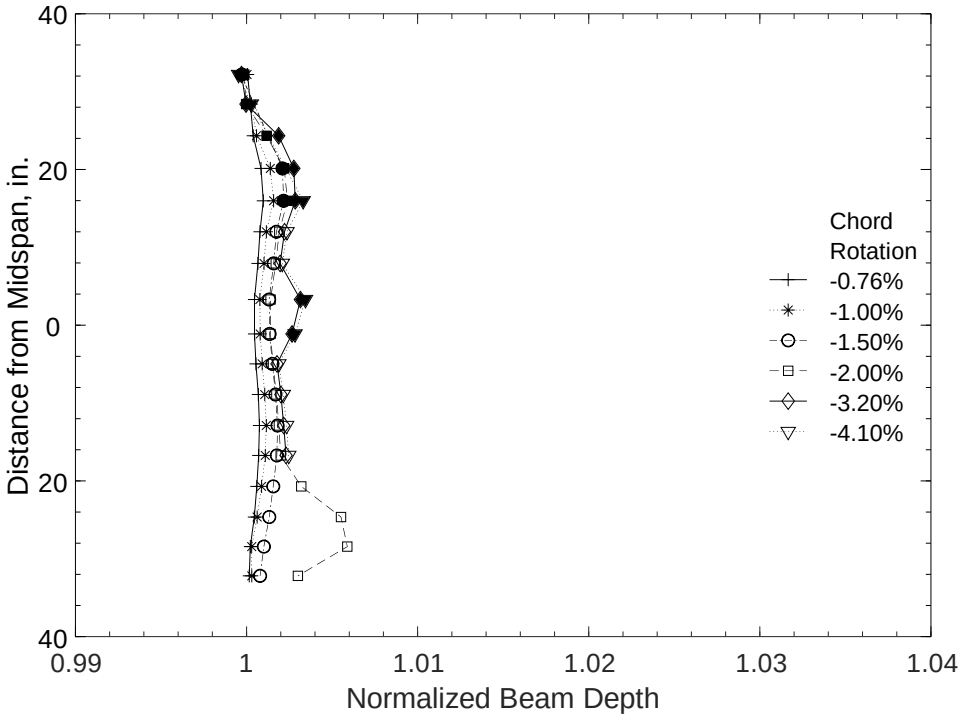

Figure 149 – Normalized beam depth at negative chord rotations, D100-3.5 (1 in. = 25.4 mm)

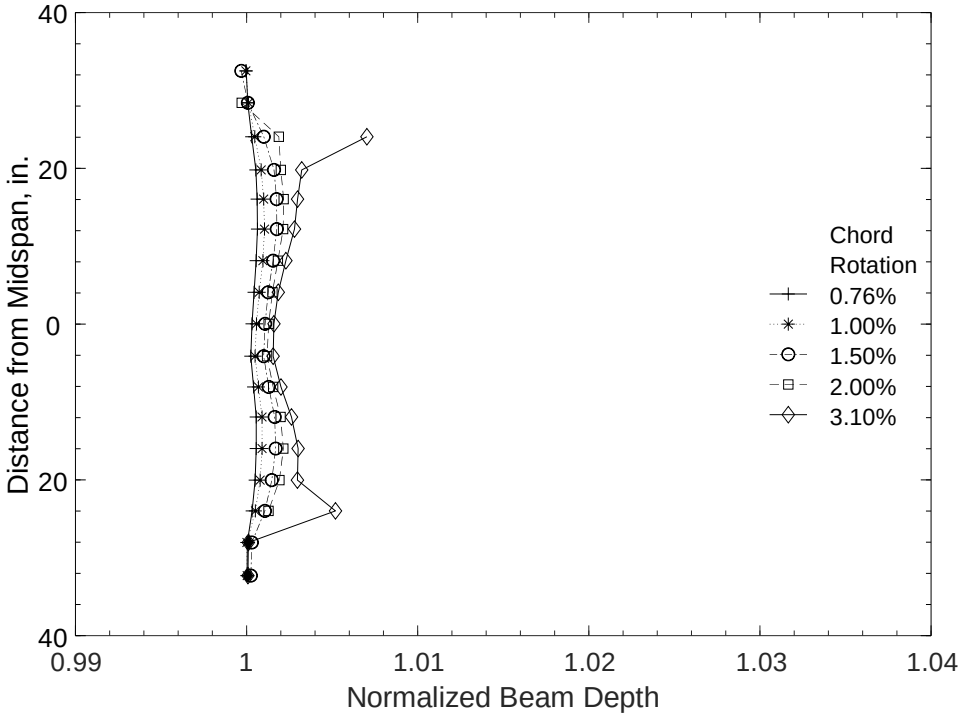

Figure 150 – Normalized beam depth at positive chord rotations, D120-3.5 (1 in. = 25.4 mm)

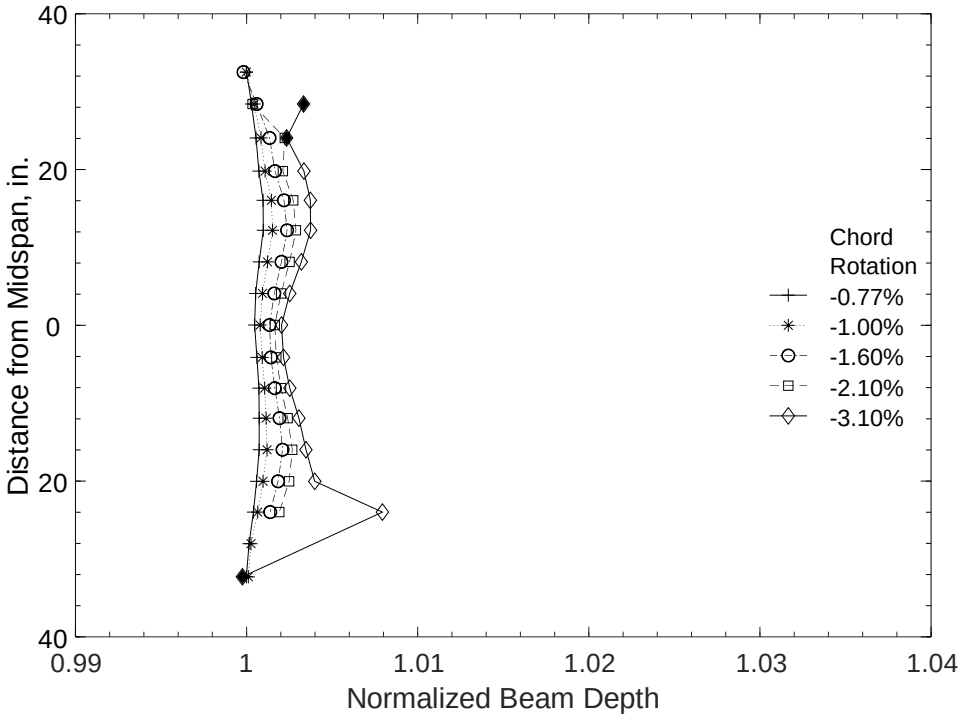

Figure 151 – Normalized beam depth at negative chord rotations, D120-3.5 (1 in. = 25.4 mm)

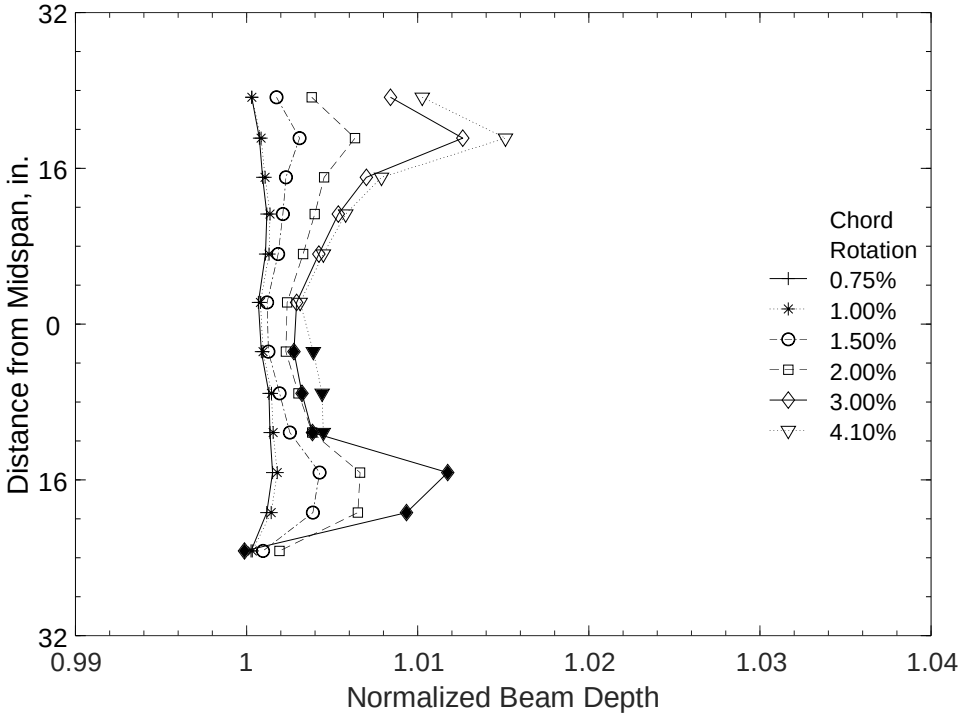

Figure 152 – Normalized beam depth at positive chord rotations, P80-2.5 (1 in. = 25.4 mm)

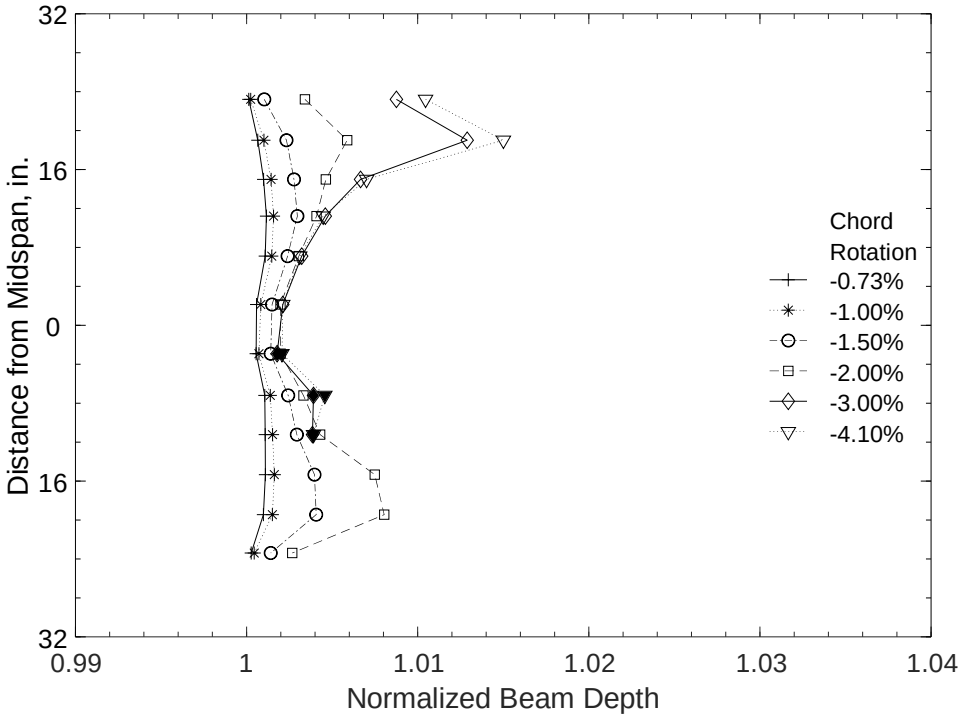

Figure 153 – Normalized beam depth at negative chord rotations, P80-2.5 (1 in. = 25.4 mm)

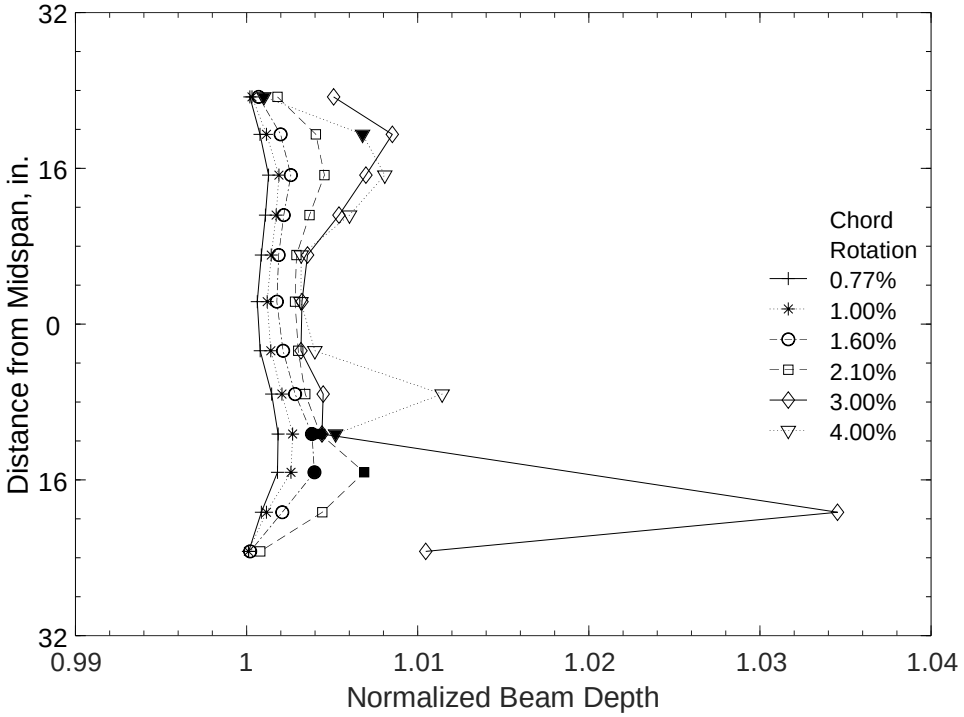

Figure 154 – Normalized beam depth at positive chord rotations, P100-2.5 (1 in. = 25.4 mm)

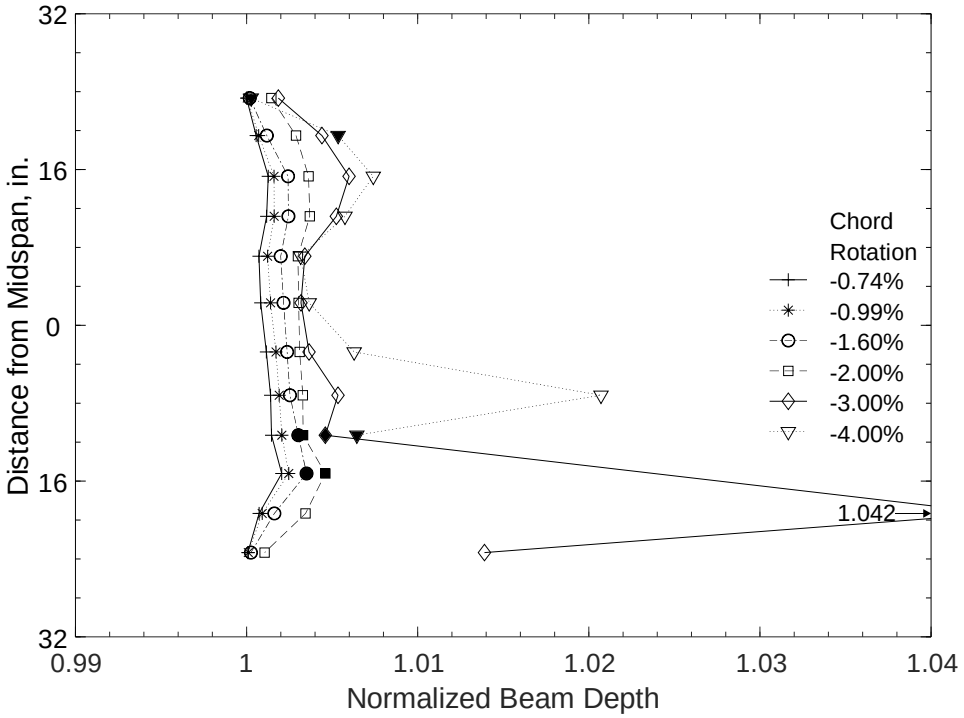

Figure 155 – Normalized beam depth at negative chord rotations, P100-2.5 (1 in. = 25.4 mm)

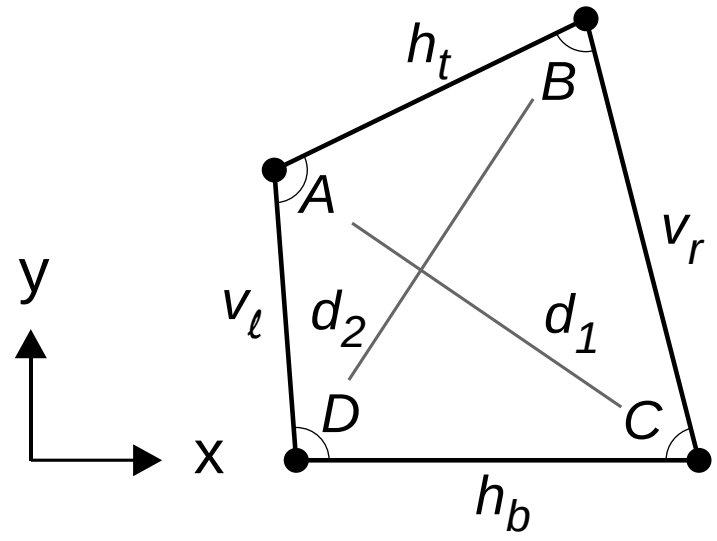

Figure 156 – General deformed shape of a station

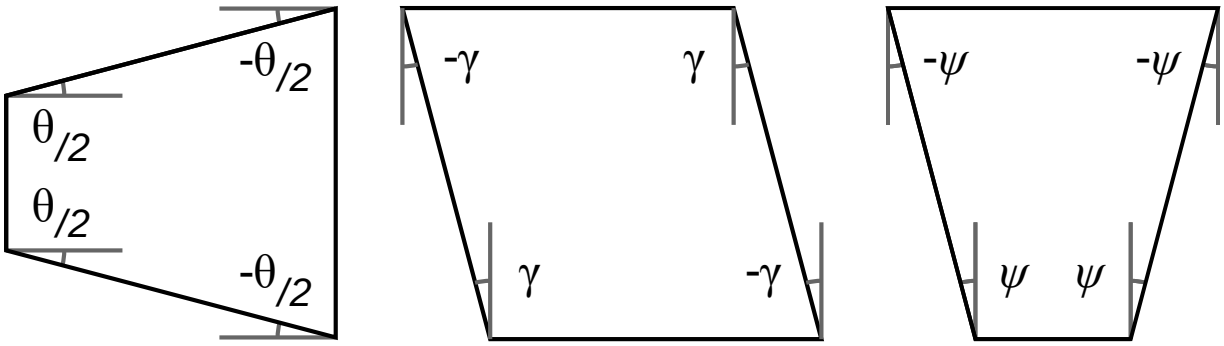

Flexure Shear Expansion

Figure 157 – Components of angular change of a station

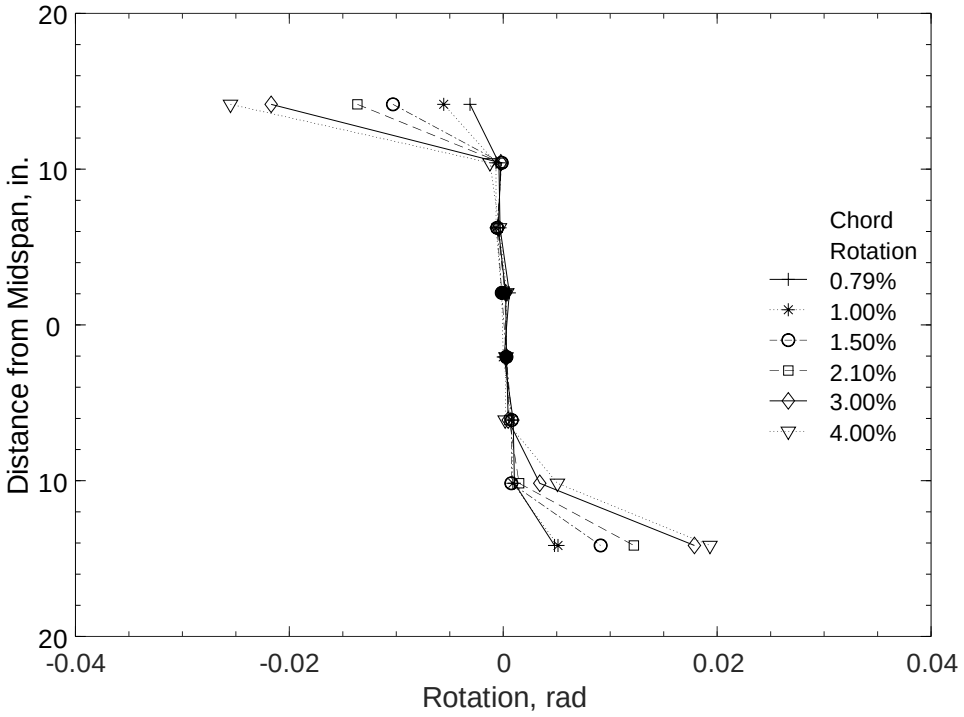

Figure 158 – Calculated flexural rotation (including strain penetration) at positive chord rotations, D80-1.5 (1 in. = 25.4 mm)

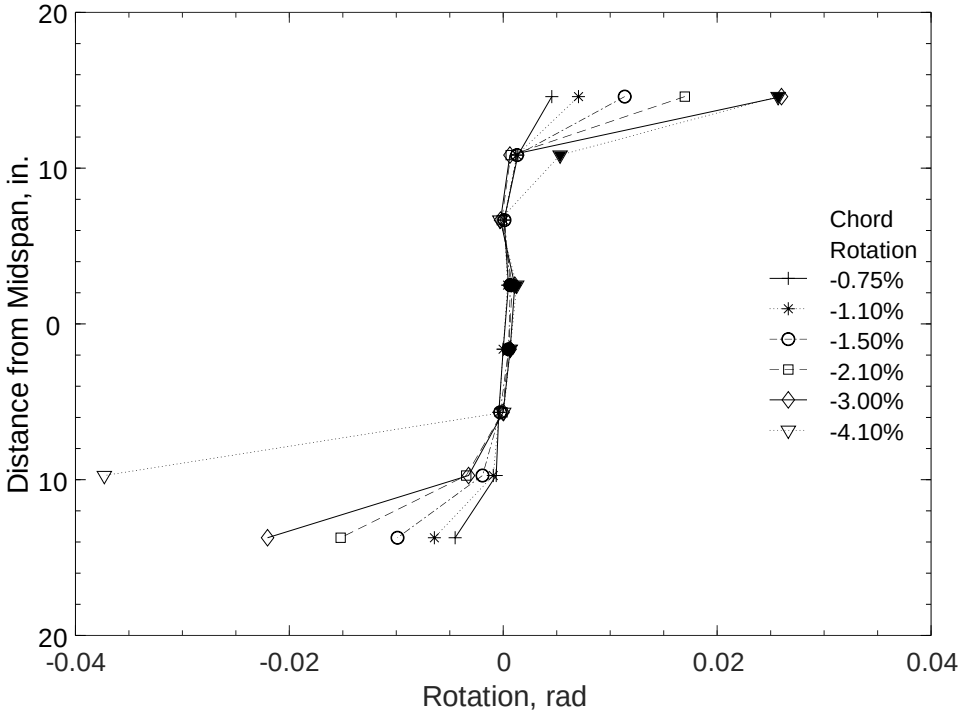

Figure 159 – Calculated flexural rotation (including strain penetration) at negative chord rotations, D80-1.5 (1 in. = 25.4 mm)

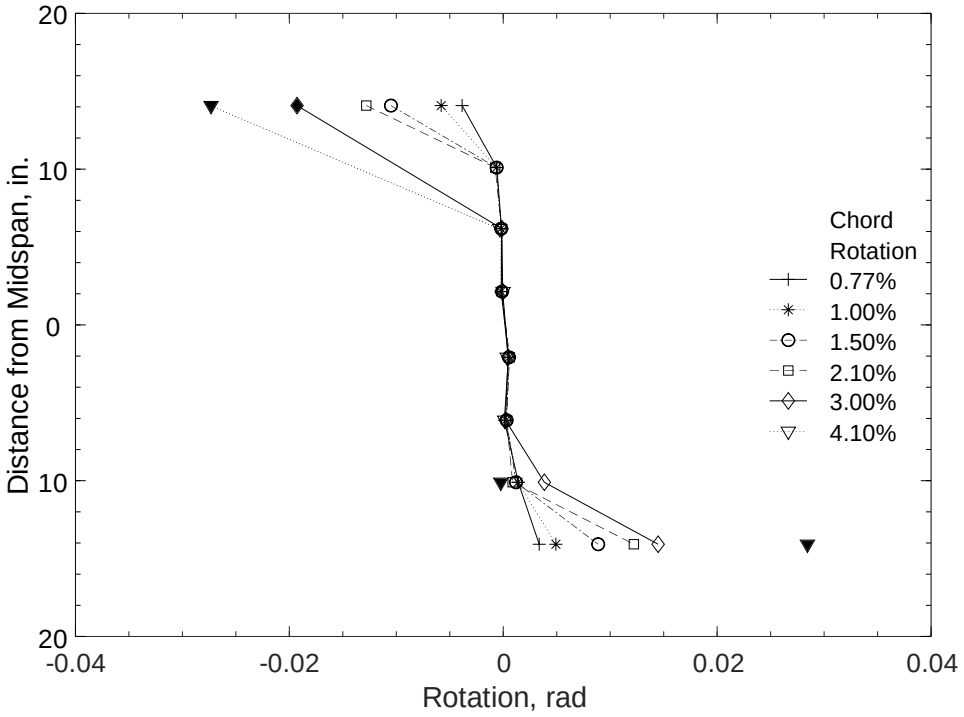

Figure 160 – Calculated flexural rotation (including strain penetration) at positive chord rotations, D100-1.5 (1 in. = 25.4 mm)

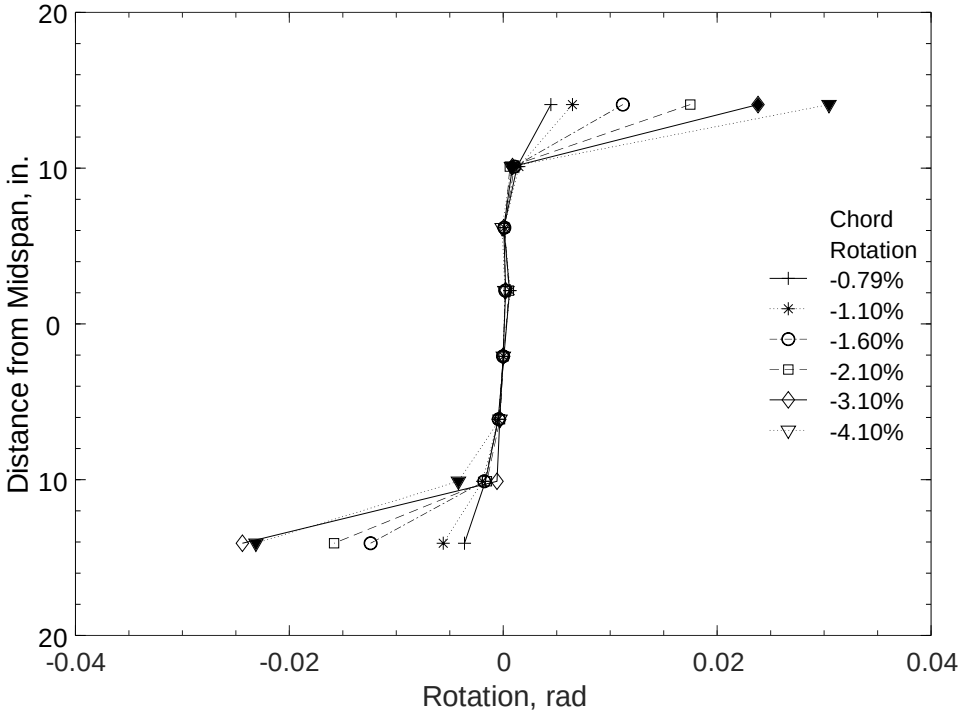

Figure 161 – Calculated flexural rotation (including strain penetration) at negative chord rotations, D100-1.5 (1 in. = 25.4 mm)

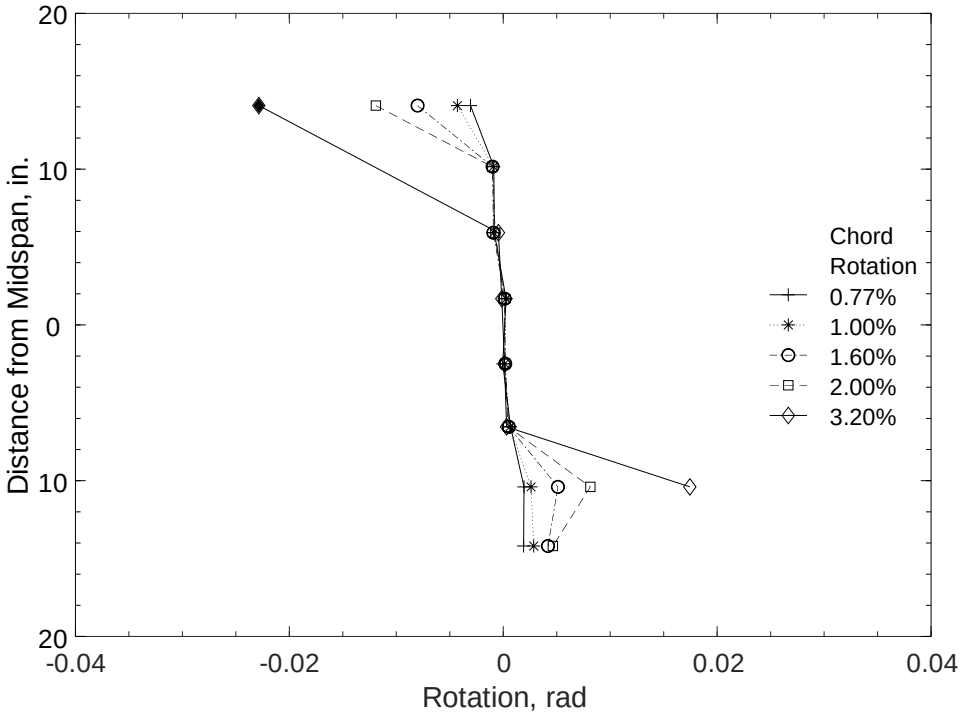

Figure 162 – Calculated flexural rotation (including strain penetration) at positive chord rotations, D120-1.5 (1 in. = 25.4 mm)

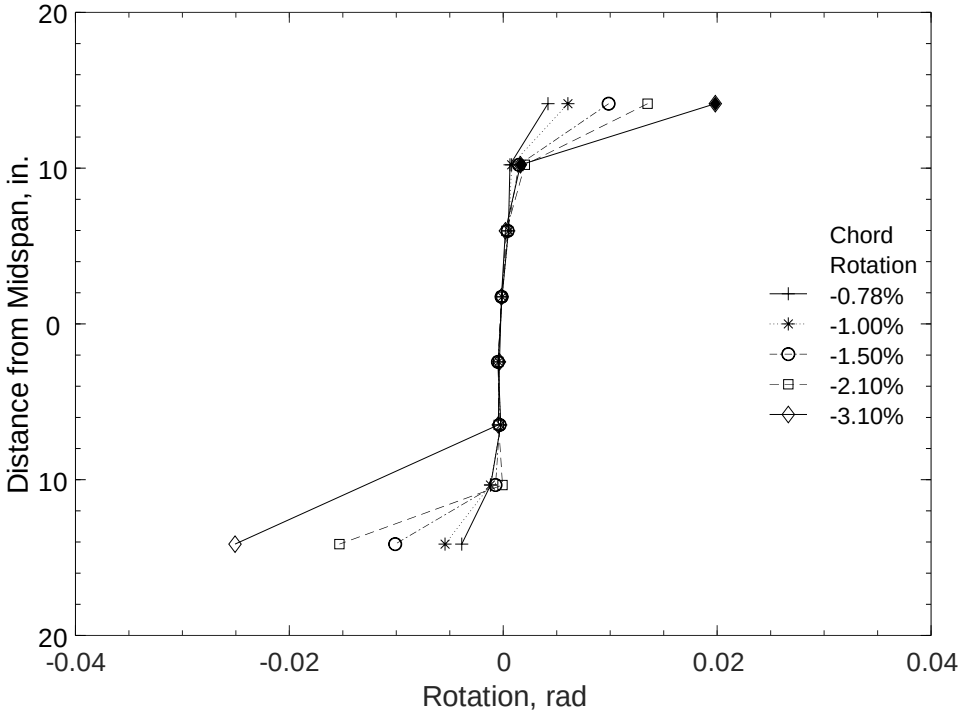

Figure 163 – Calculated flexural rotation (including strain penetration) at negative chord rotations, D120-1.5 (1 in. = 25.4 mm)

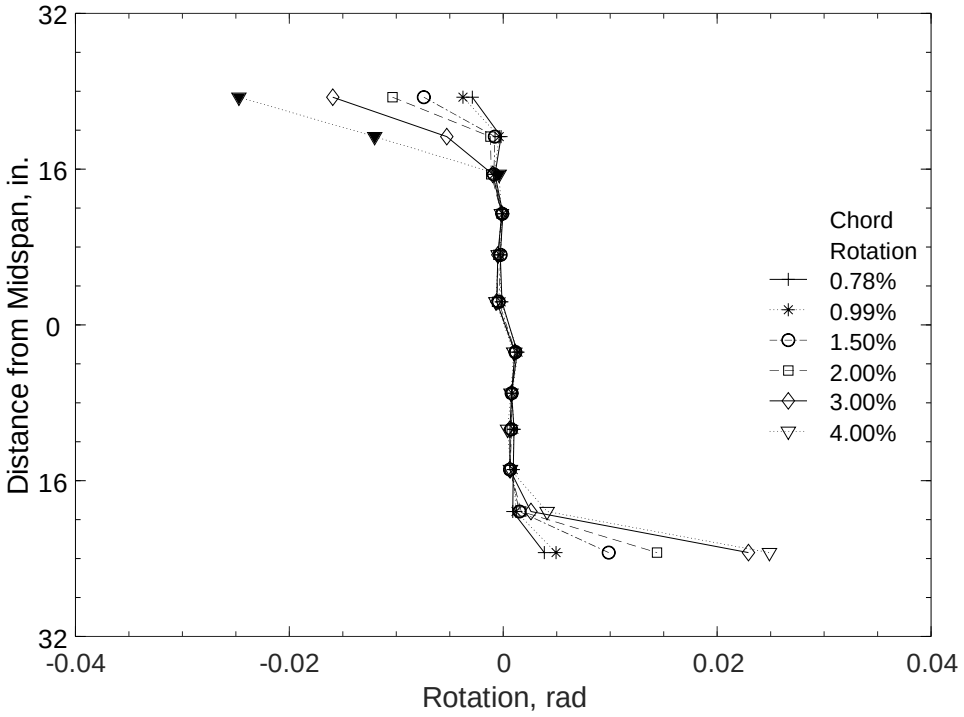

Figure 164 – Calculated flexural rotation (including strain penetration) at positive chord rotations, D80-2.5 (1 in. = 25.4 mm)

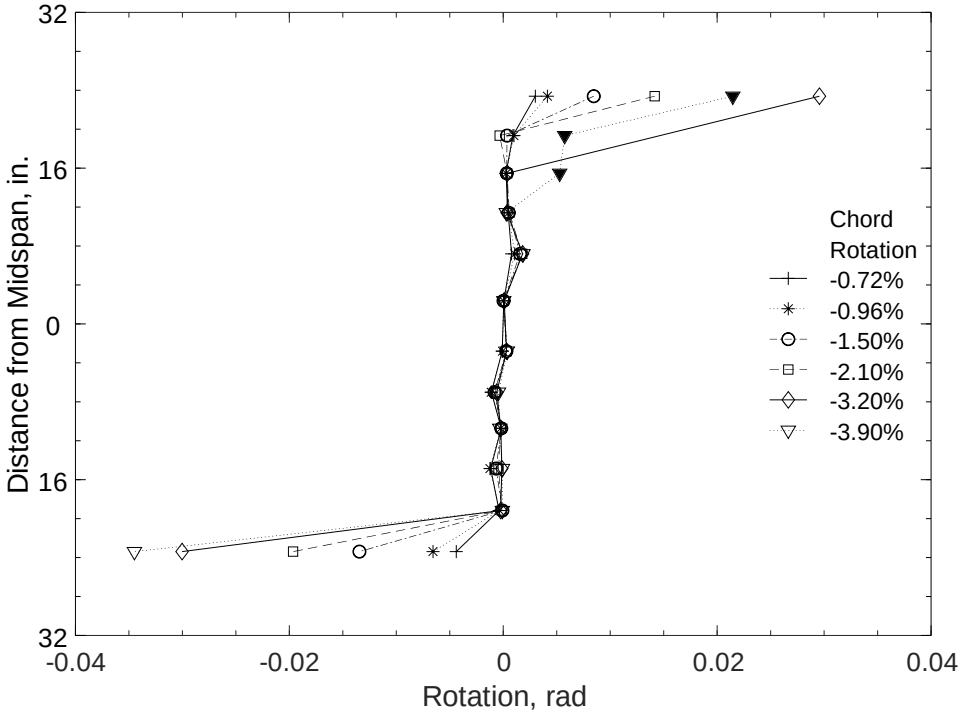

Figure 165 – Calculated flexural rotation (including strain penetration) at negative chord rotations, D80-2.5 (1 in. = 25.4 mm)

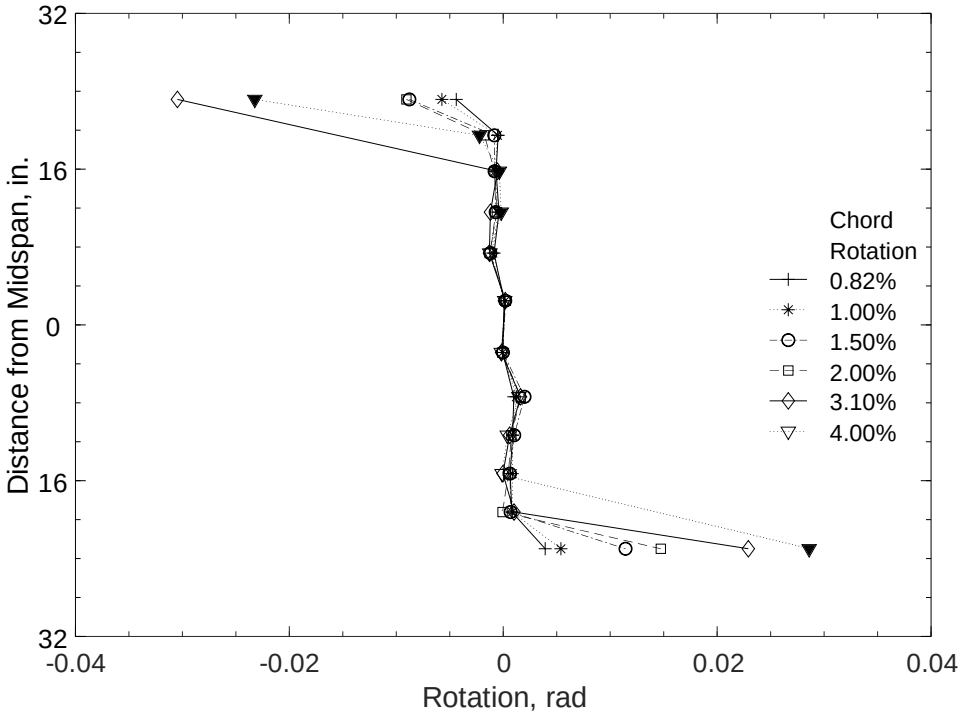

Figure 166 – Calculated flexural rotation (including strain penetration) at positive chord rotations, D100-2.5 (1 in. = 25.4 mm)

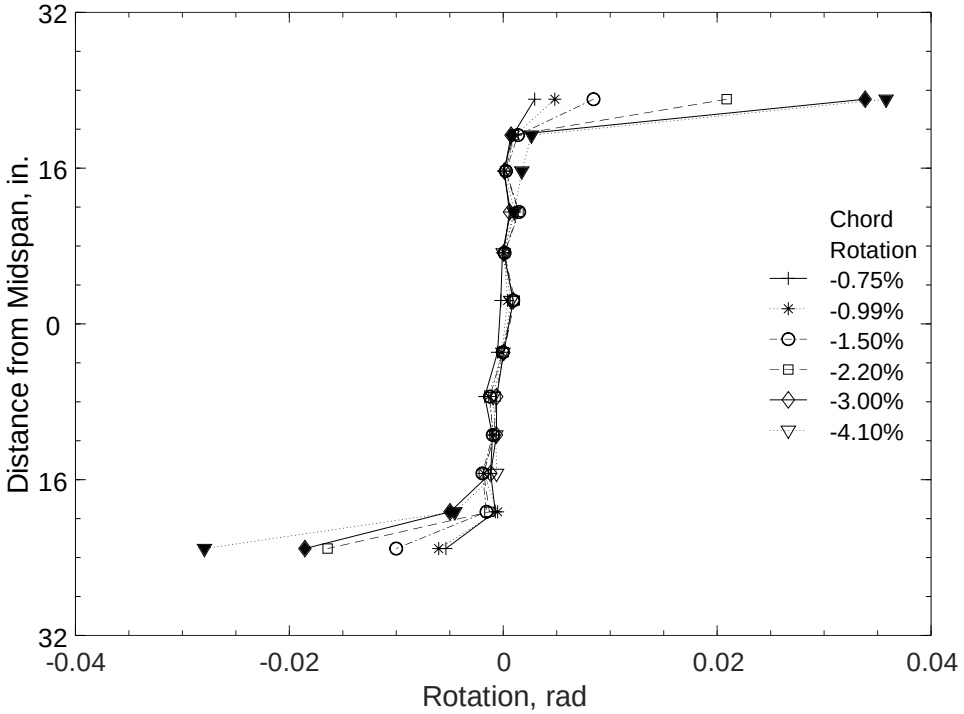

Figure 167 – Calculated flexural rotation (including strain penetration) at negative chord rotations, D100-2.5 (1 in. = 25.4 mm)

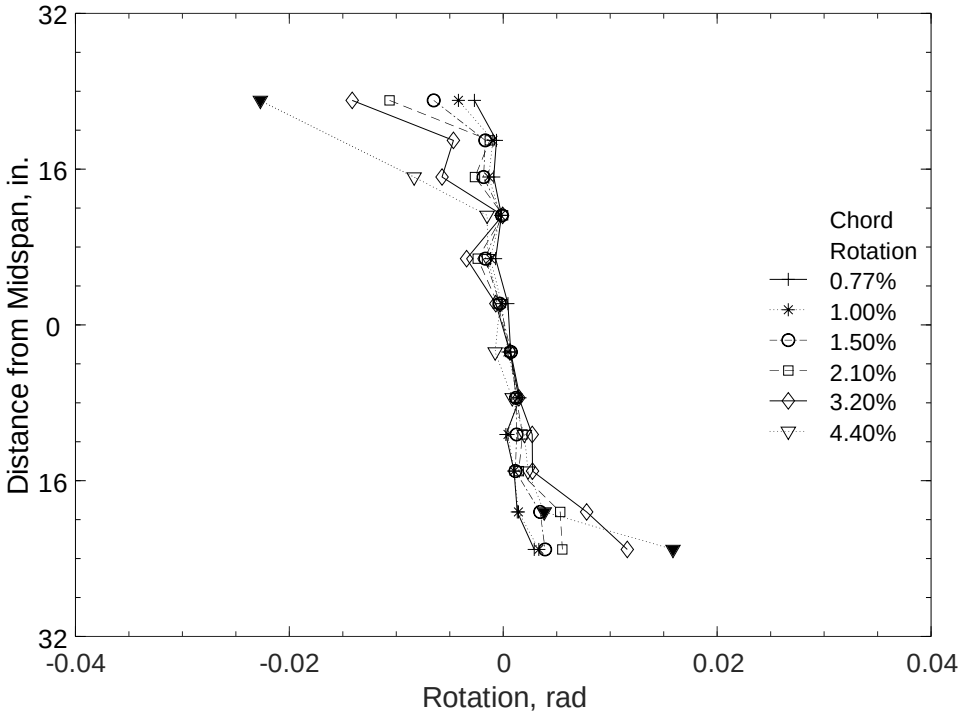

Figure 168 – Calculated flexural rotation (including strain penetration) at positive chord rotations, D120-2.5 (1 in. = 25.4 mm)

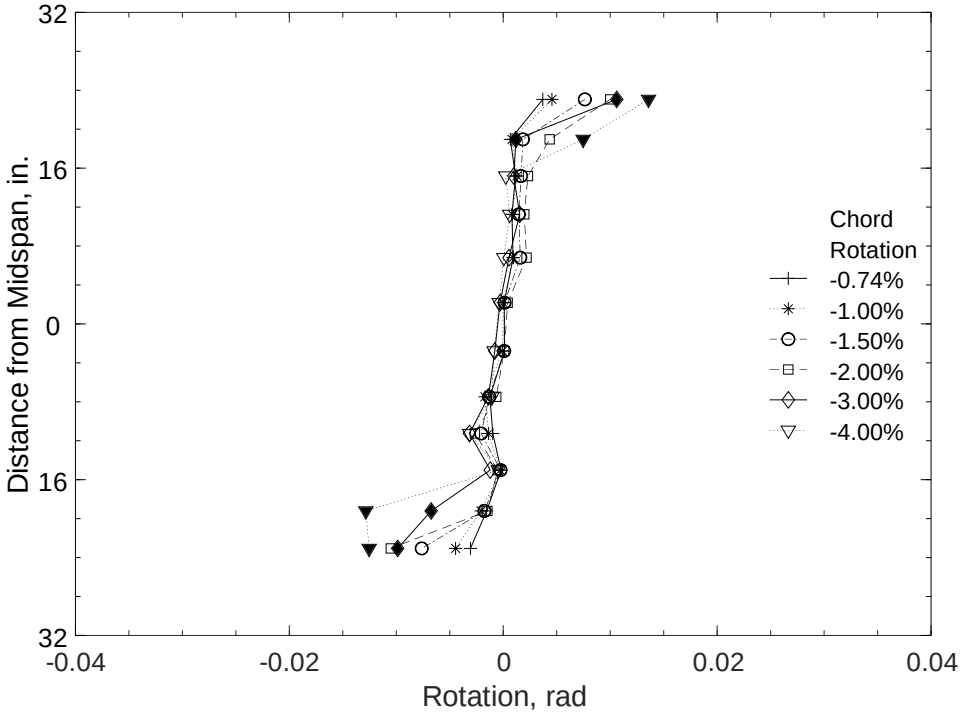

Figure 169 – Calculated flexural rotation (including strain penetration) at negative chord rotations, D120-2.5 (1 in. = 25.4 mm)

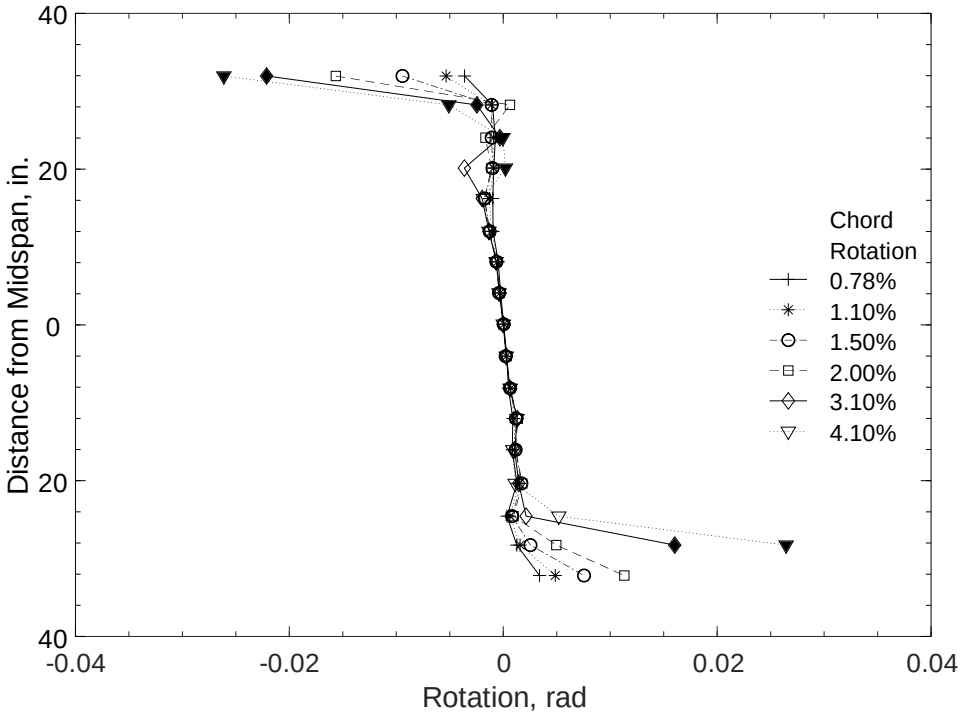

Figure 170 – Calculated flexural rotation (including strain penetration) at positive chord rotations, D80-3.5 (1 in. = 25.4 mm)

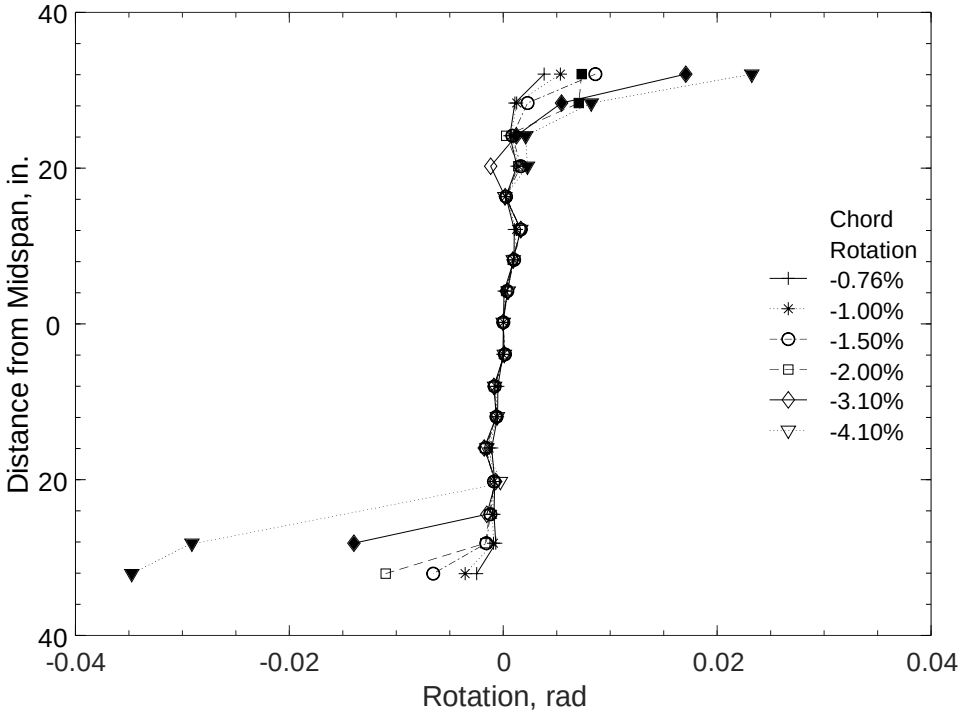

Figure 171 – Calculated flexural rotation (including strain penetration) at negative chord rotations, D80-3.5 (1 in. = 25.4 mm)

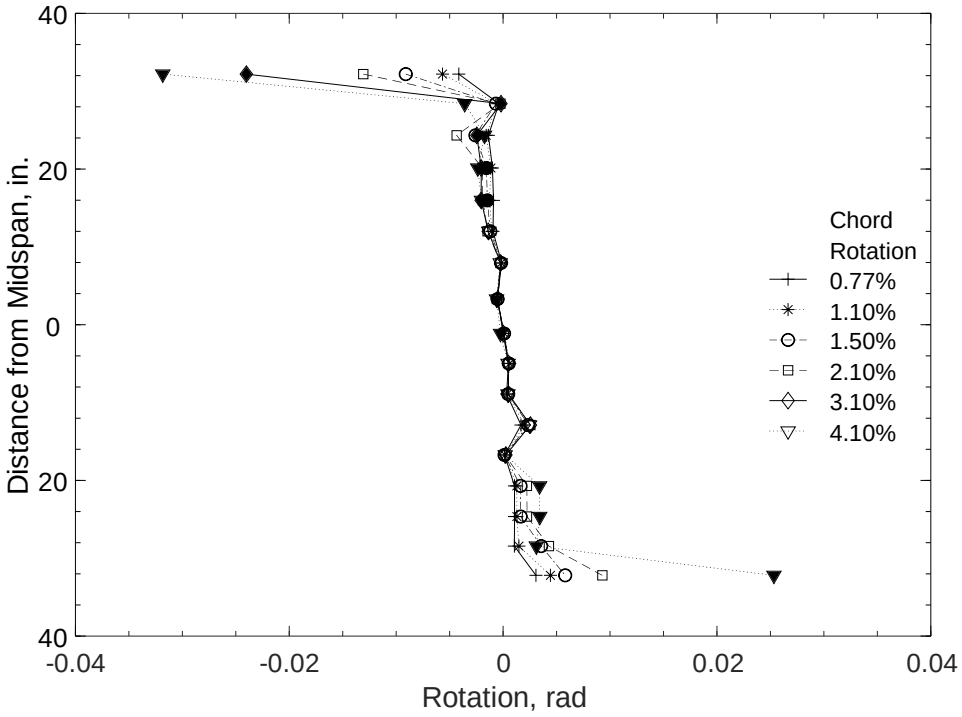

Figure 172 – Calculated flexural rotation (including strain penetration) at positive chord rotations, D100-3.5 (1 in. = 25.4 mm)

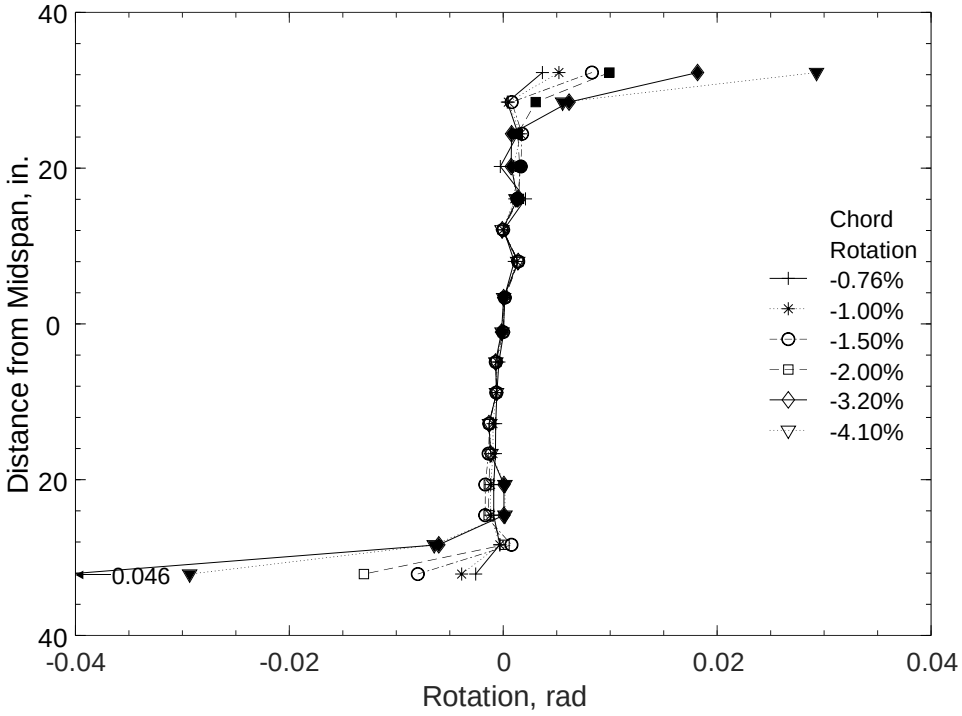

Figure 173 – Calculated flexural rotation (including strain penetration) at negative chord rotations, D100-3.5 (1 in. = 25.4 mm)

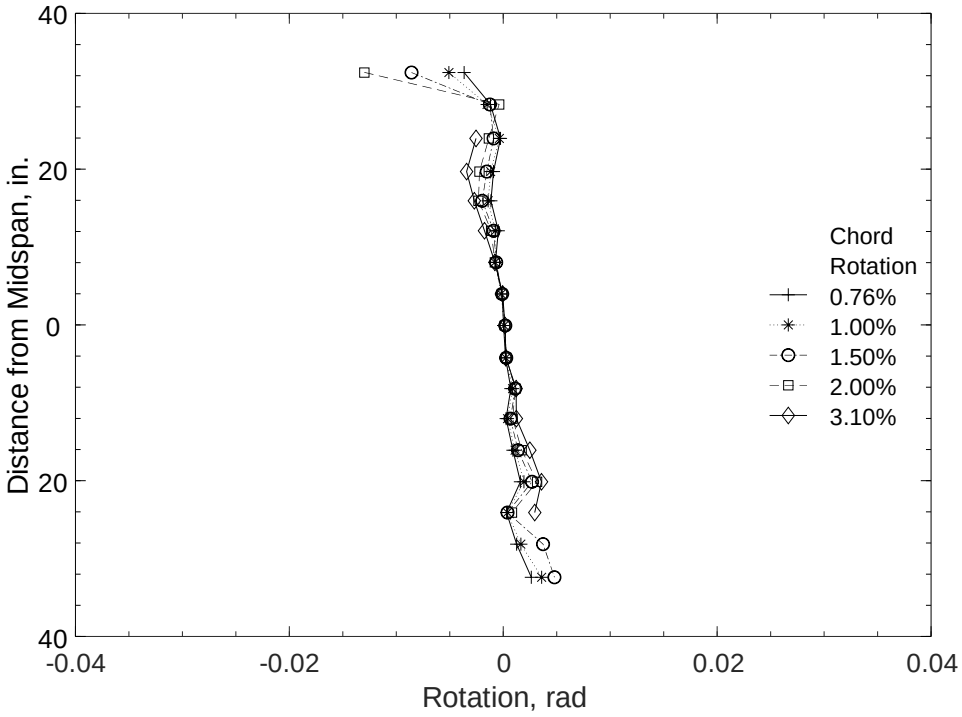

Figure 174 – Calculated flexural rotation (including strain penetration) at positive chord rotations, D120-3.5 (1 in. = 25.4 mm)

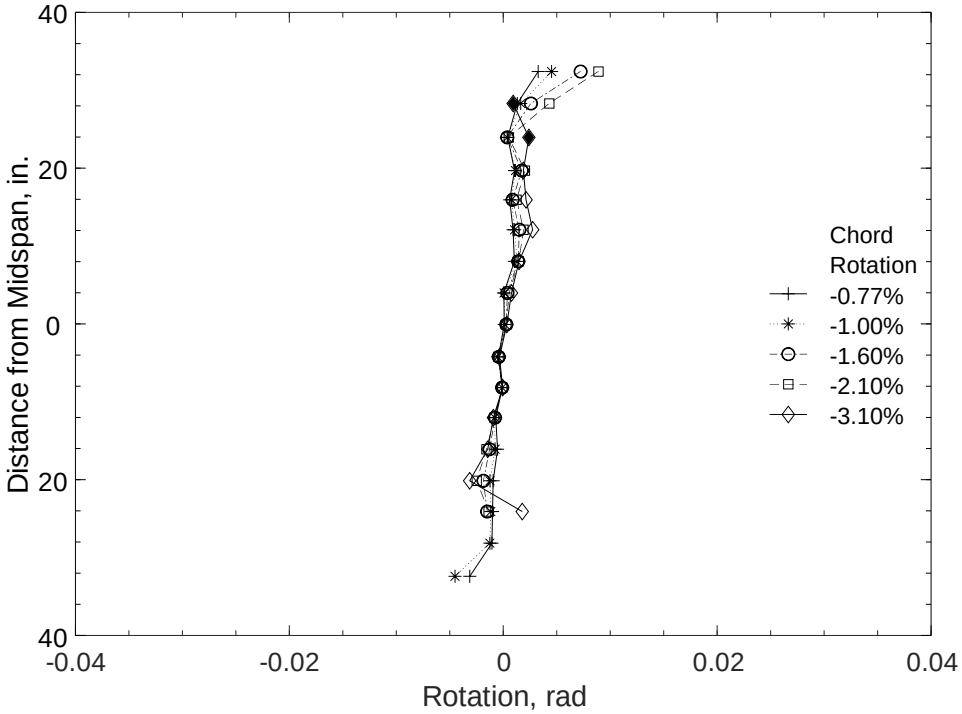

Figure 175 – Calculated flexural rotation (including strain penetration) at negative chord rotations, D120-3.5 (1 in. = 25.4 mm)

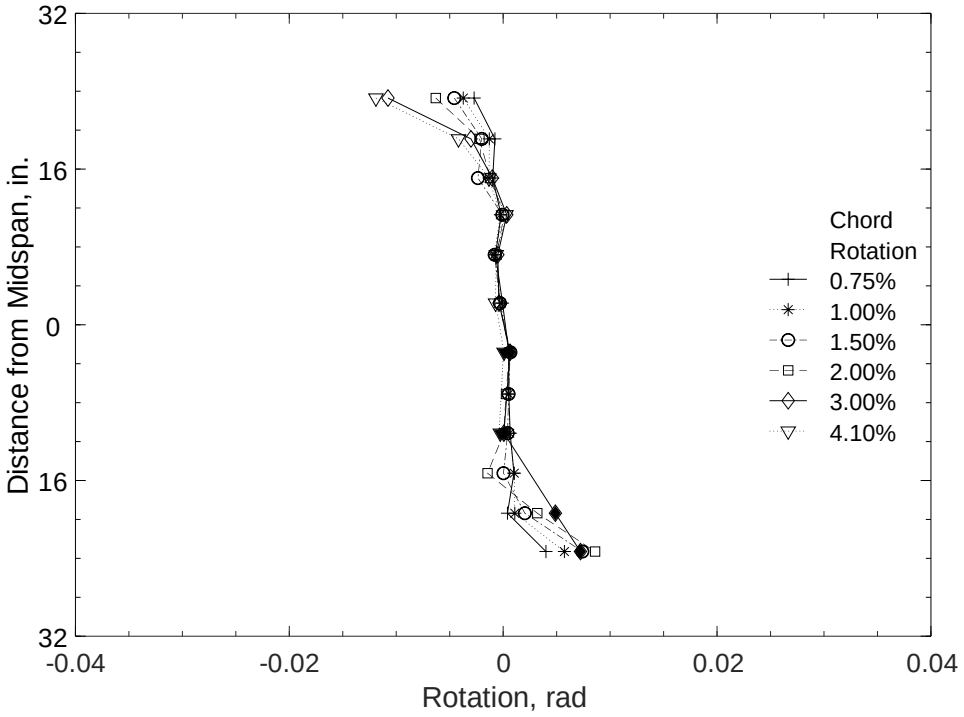

Figure 176 – Calculated flexural rotation (including strain penetration) at positive chord rotations, P80-2.5 (1 in. = 25.4 mm)

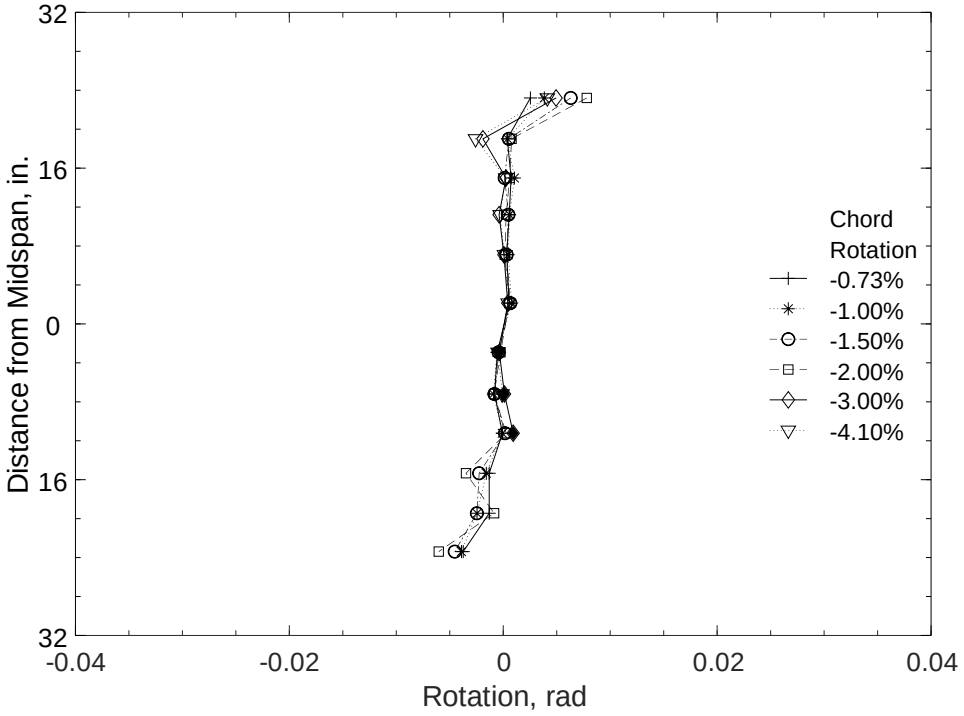

Figure 177 – Calculated flexural rotation (including strain penetration) at negative chord rotations, P80-2.5 (1 in. = 25.4 mm)

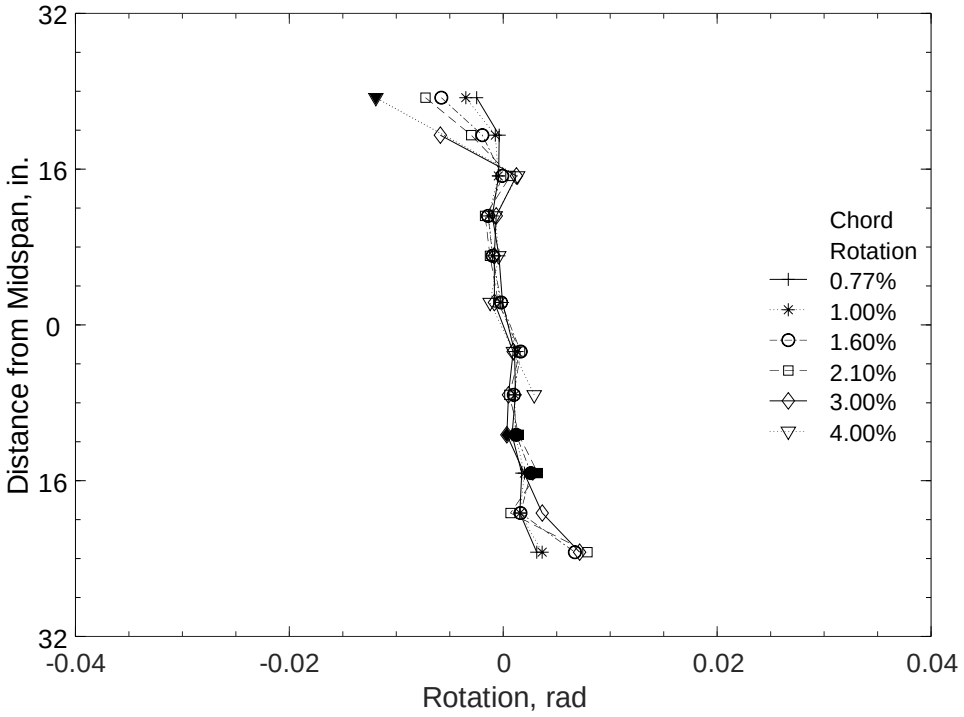

Figure 178 – Calculated flexural rotation (including strain penetration) at positive chord rotations, P100-2.5 (1 in. = 25.4 mm)

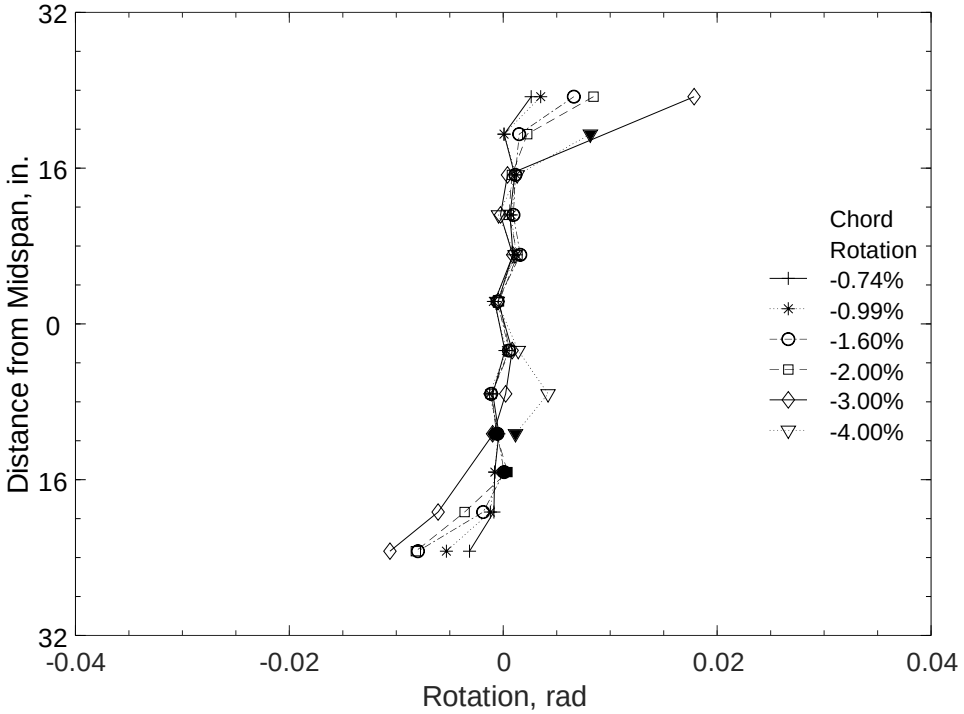

Figure 179 – Calculated flexural rotation (including strain penetration) at negative chord rotations, P100-2.5 (1 in. = 25.4 mm)

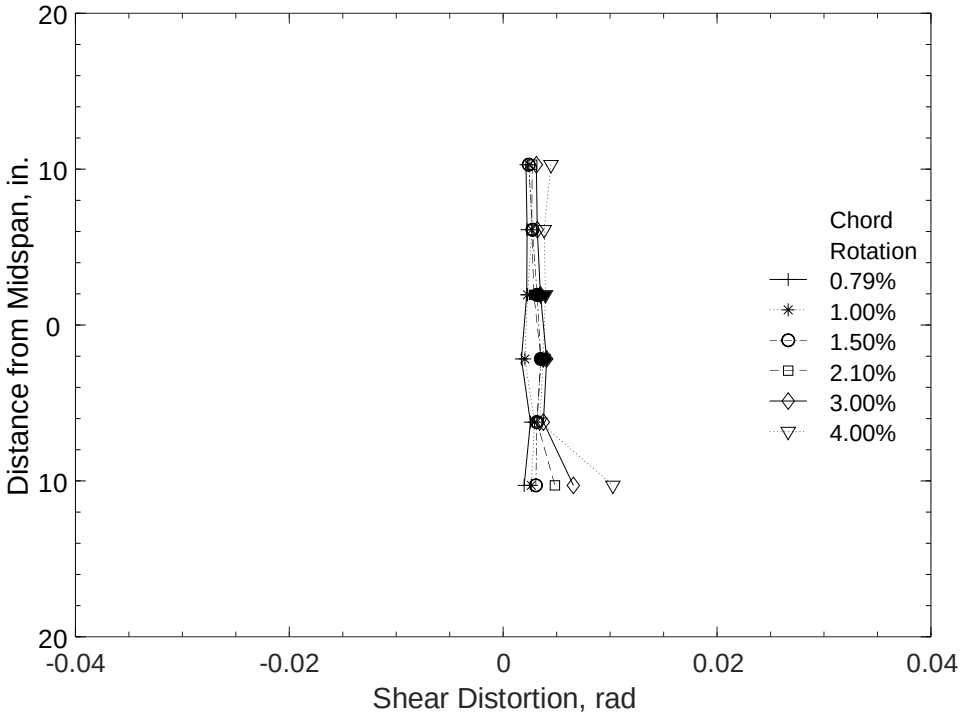

Figure 180 – Calculated shear distortion at positive chord rotations, D80-1.5 (1 in. = 25.4 mm)

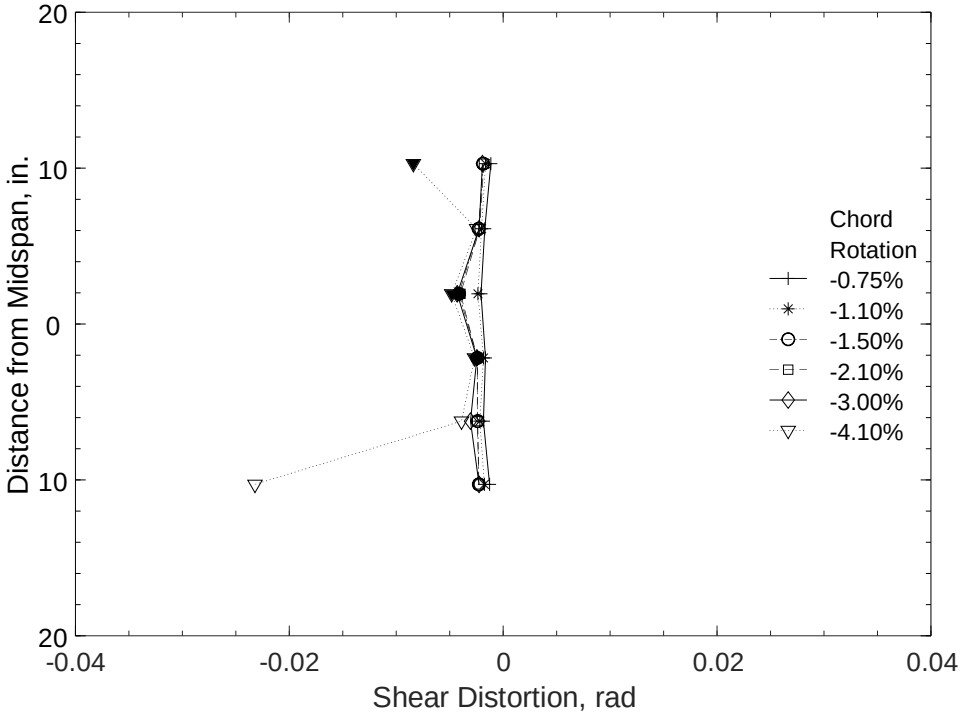

Figure 181 – Calculated shear distortion at negative chord rotations, D80-1.5 (1 in. = 25.4 mm)

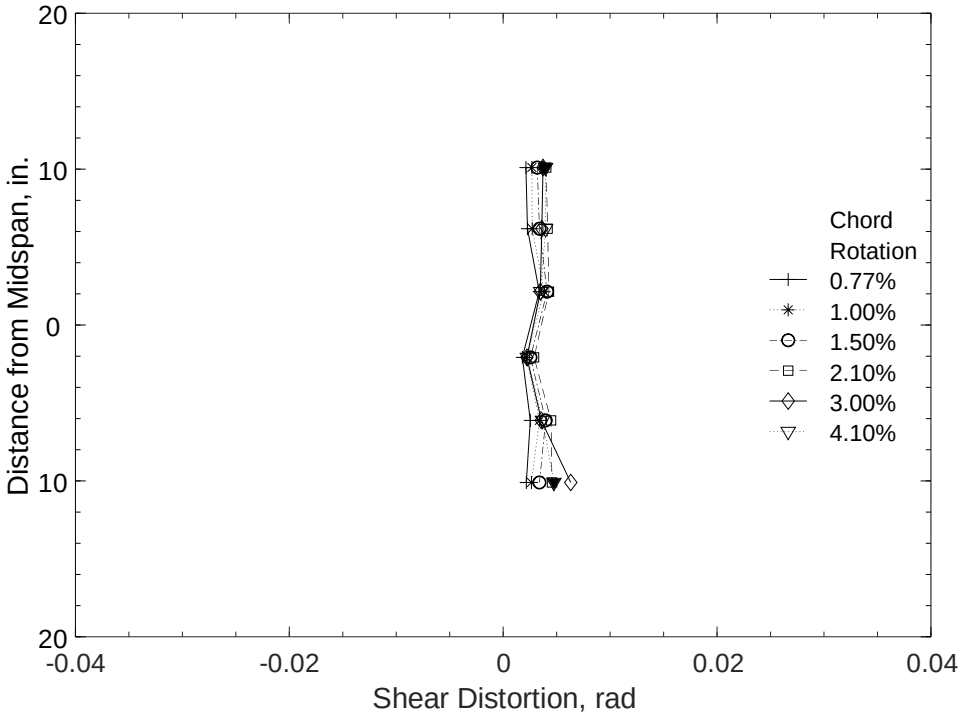

Figure 182 – Calculated shear distortion at positive chord rotations, D100-1.5 (1 in. = 25.4 mm)

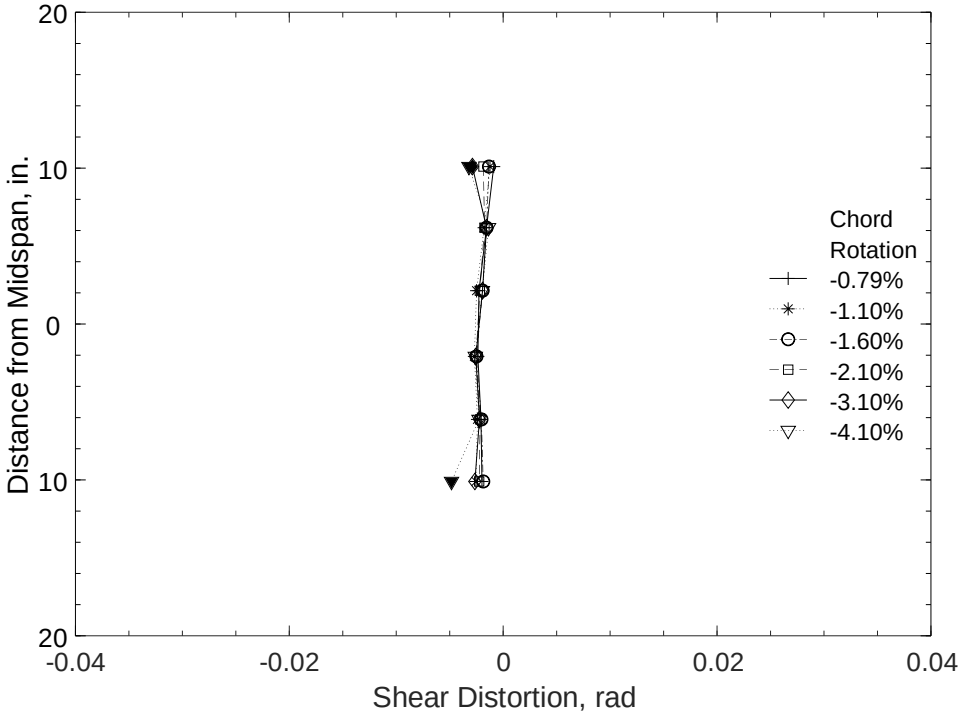

Figure 183 – Calculated shear distortion at negative chord rotations, D100-1.5 (1 in. = 25.4 mm)

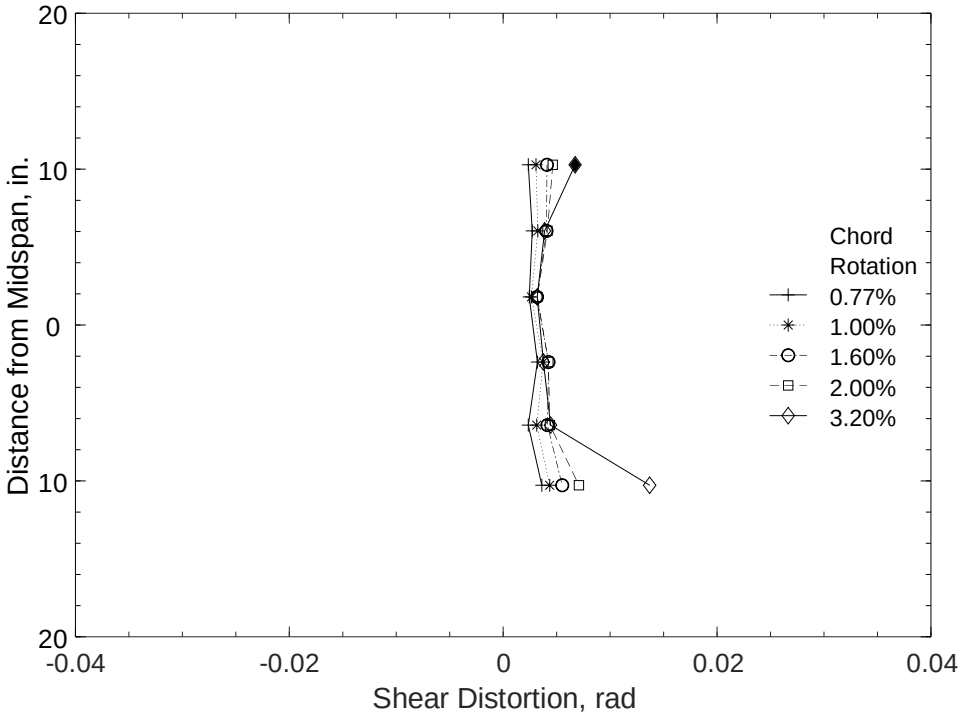

Figure 184 – Calculated shear distortion at positive chord rotations, D120-1.5 (1 in. = 25.4 mm)

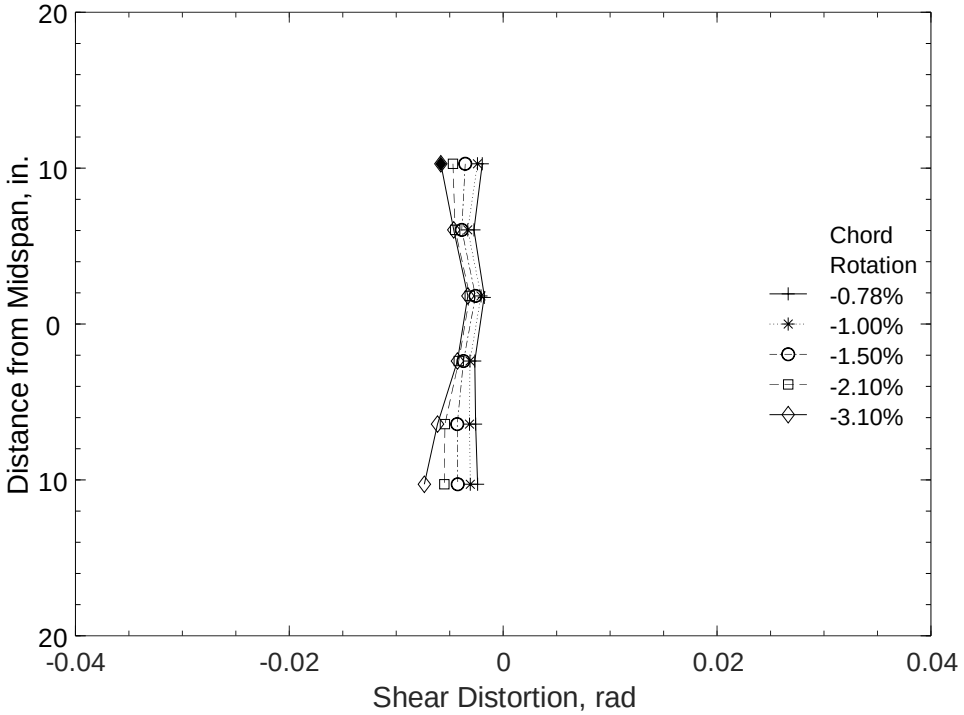

Figure 185 – Calculated shear distortion at negative chord rotations, D120-1.5 (1 in. = 25.4 mm)

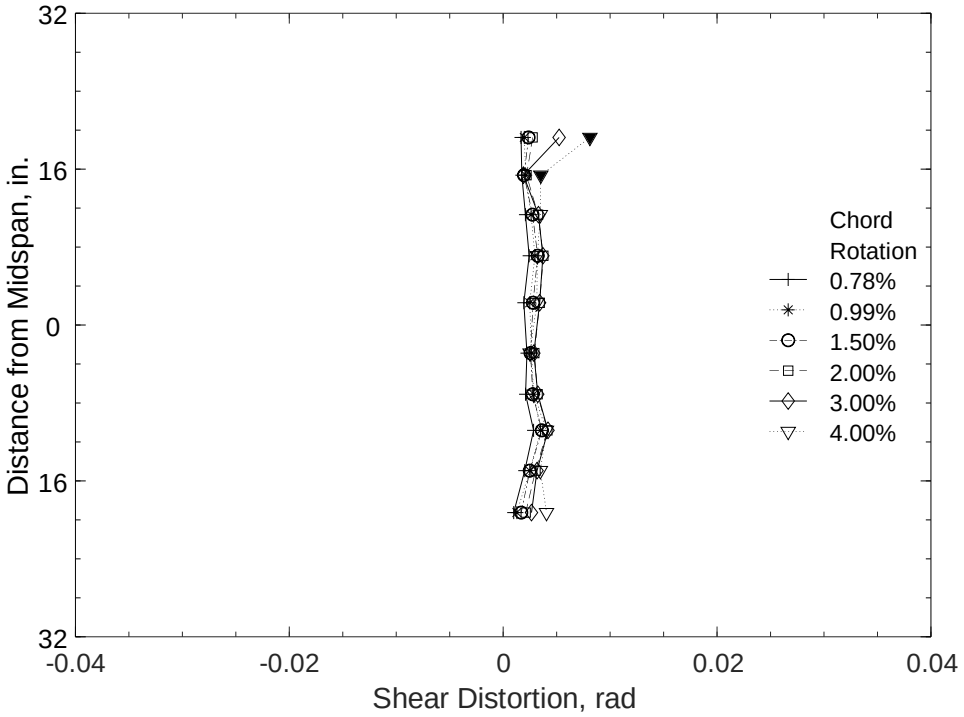

Figure 186 – Calculated shear distortion at positive chord rotations, D80-2.5 (1 in. = 25.4 mm)

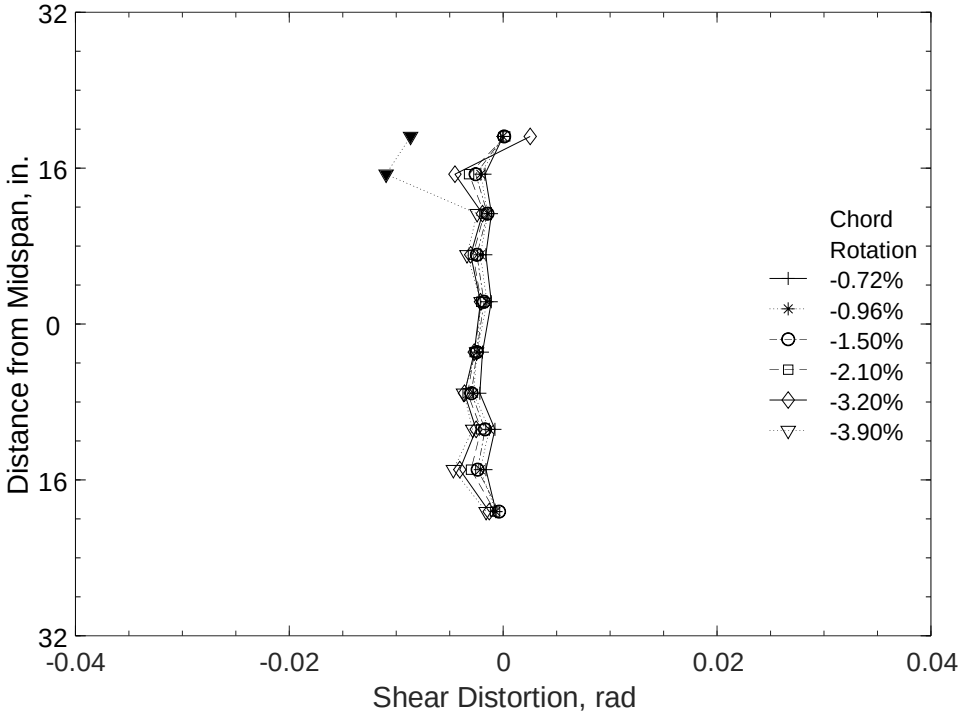

Figure 187 – Calculated shear distortion at negative chord rotations, D80-2.5 (1 in. = 25.4 mm)

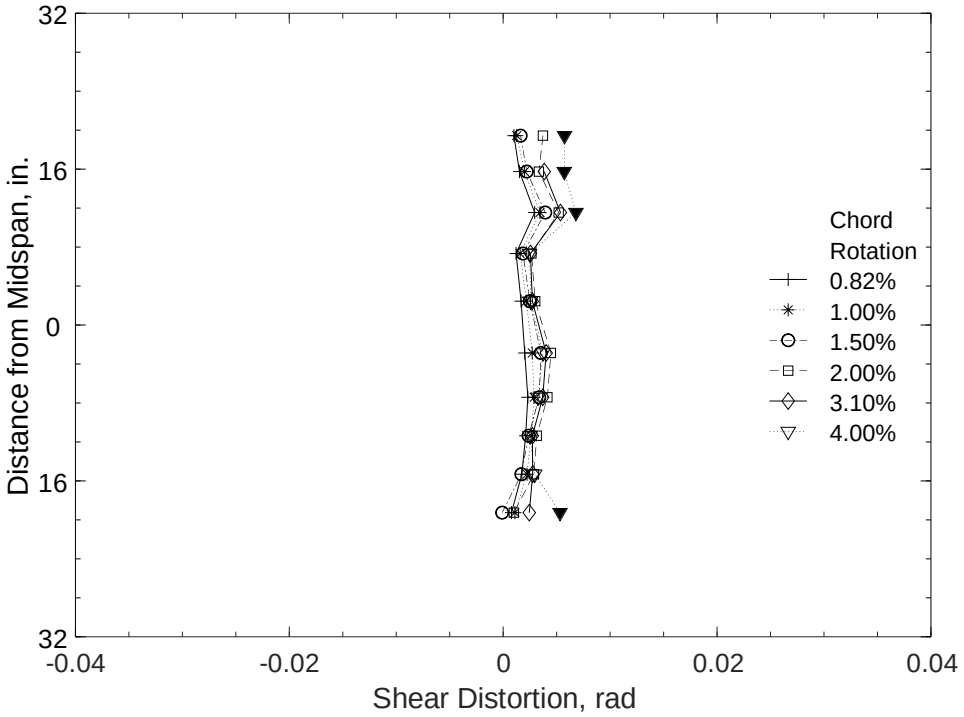

Figure 188 – Calculated shear distortion at positive chord rotations, D100-2.5 (1 in. = 25.4 mm)

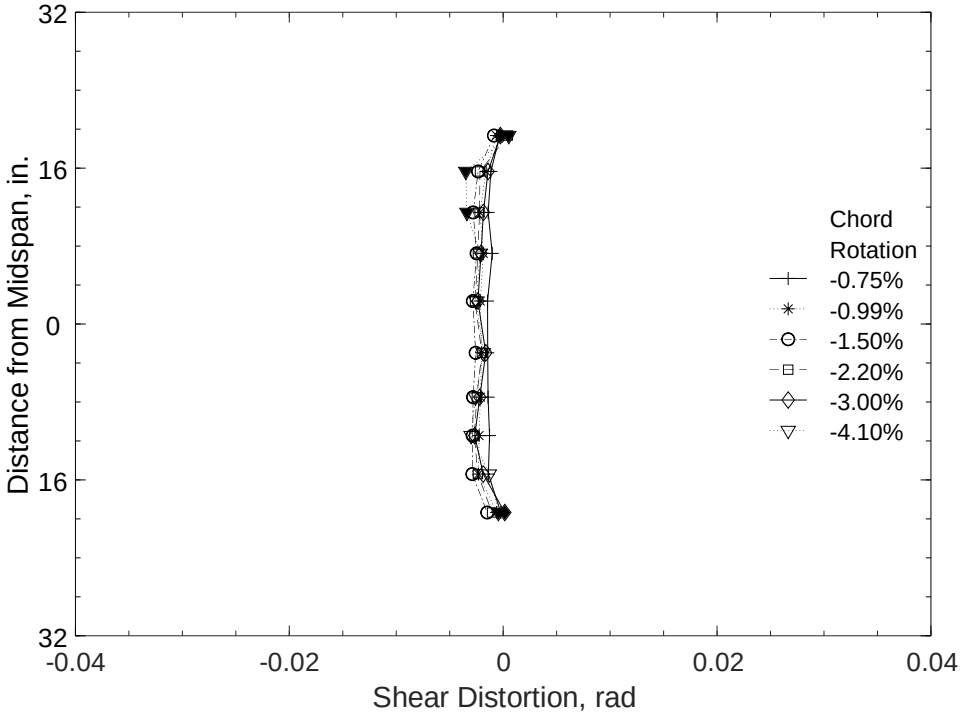

Figure 189 – Calculated shear distortion at negative chord rotations, D100-2.5 (1 in. = 25.4 mm)

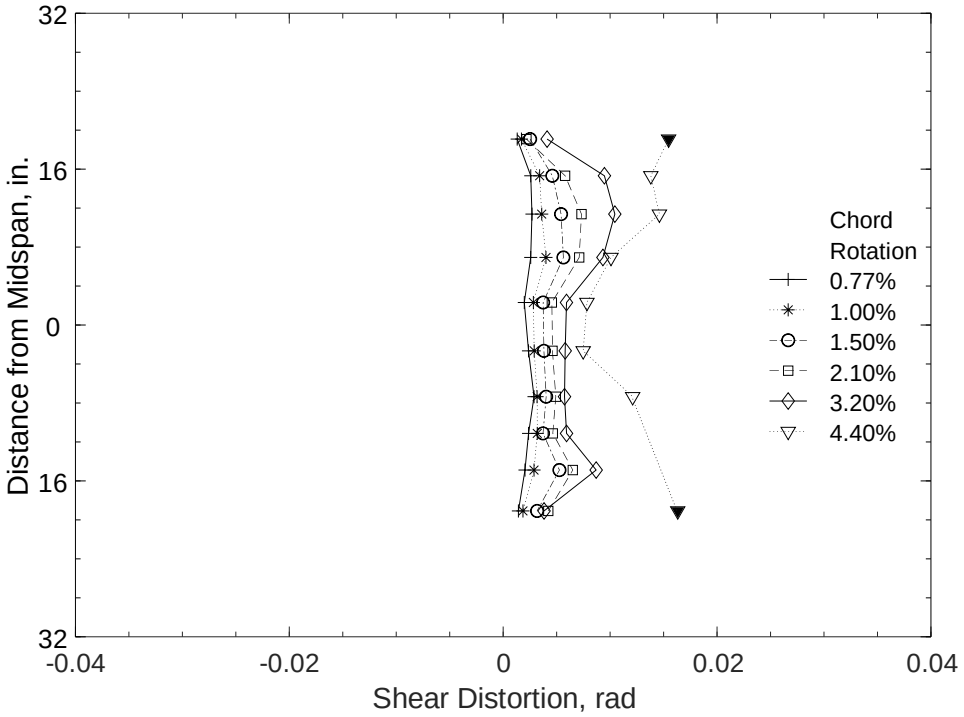

Figure 190 – Calculated shear distortion at positive chord rotations, D120-2.5 (1 in. = 25.4 mm)

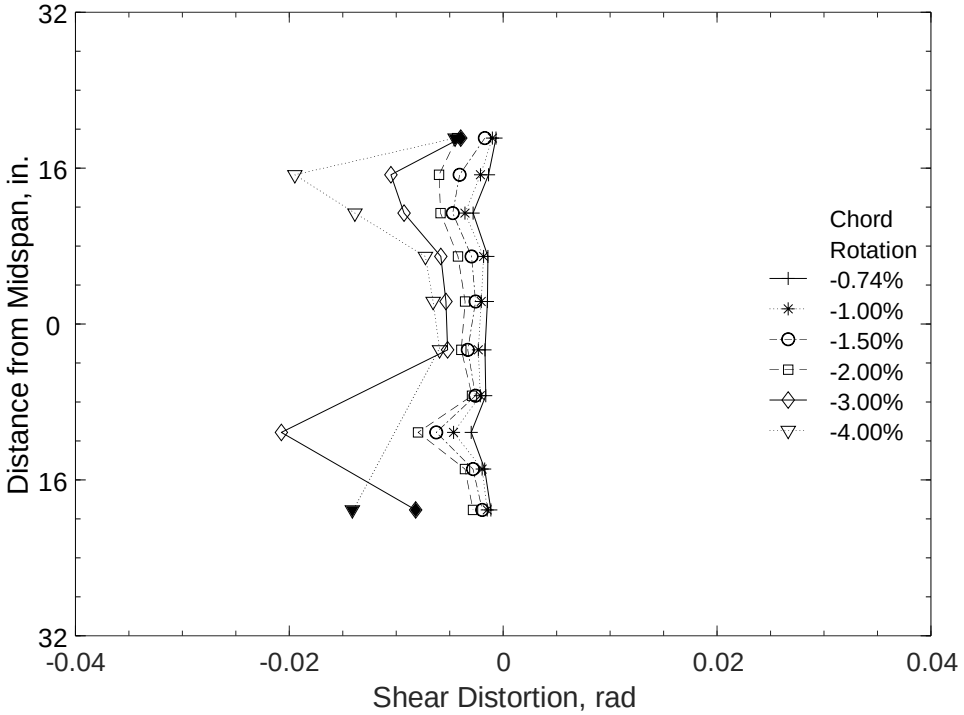

Figure 191 – Calculated shear distortion at negative chord rotations, D120-2.5 (1 in. = 25.4 mm)

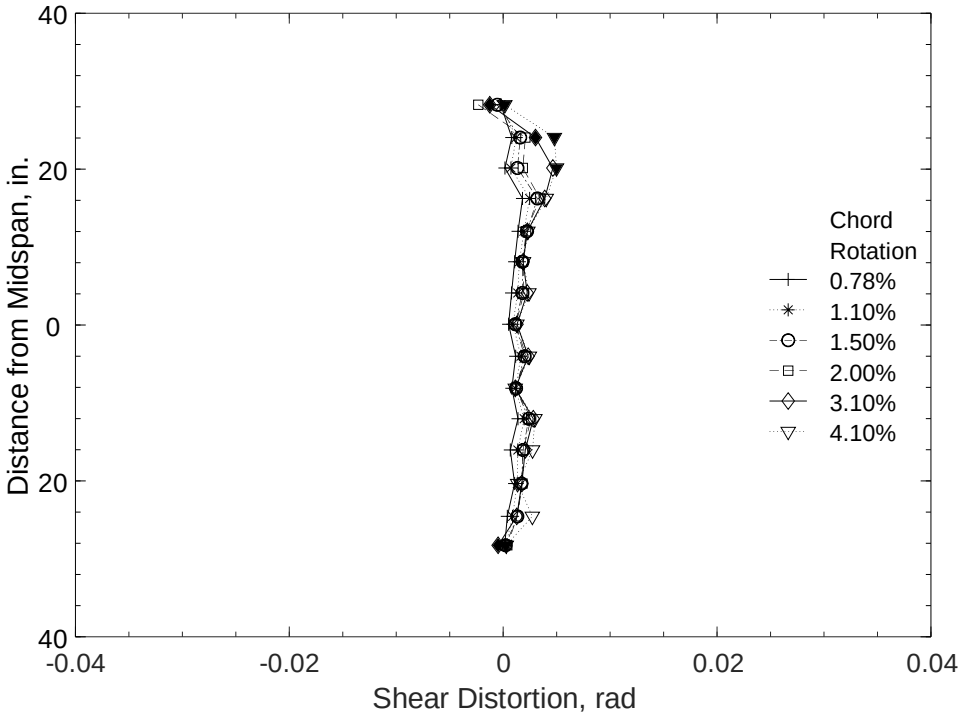

Figure 192 – Calculated shear distortion at positive chord rotations, D80-3.5 (1 in. = 25.4 mm)

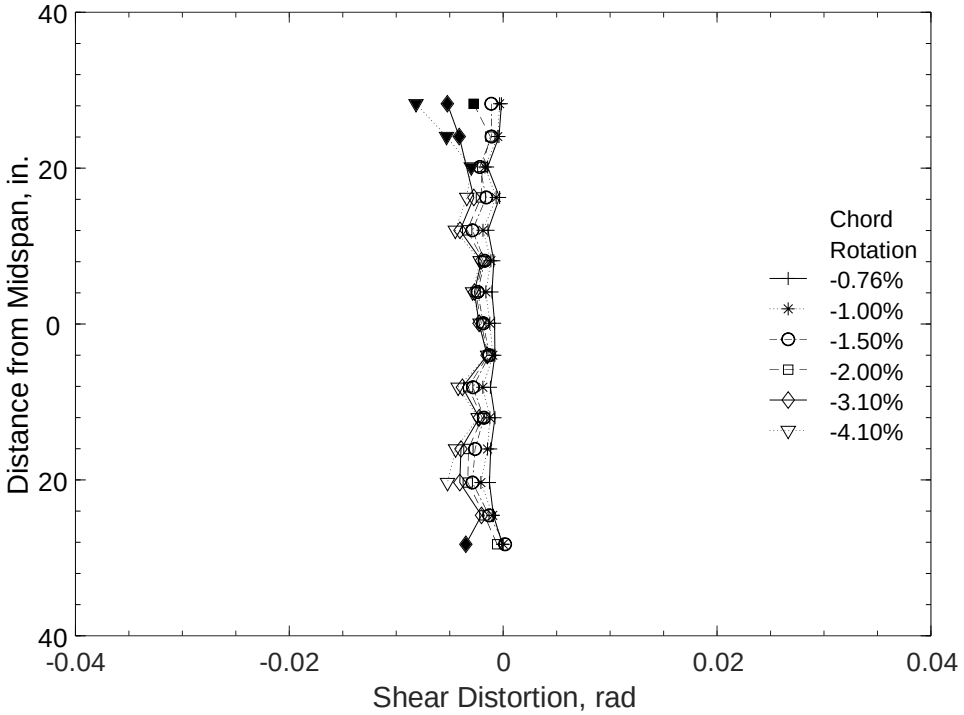

Figure 193 – Calculated shear distortion at negative chord rotations, D80-3.5 (1 in. = 25.4 mm)

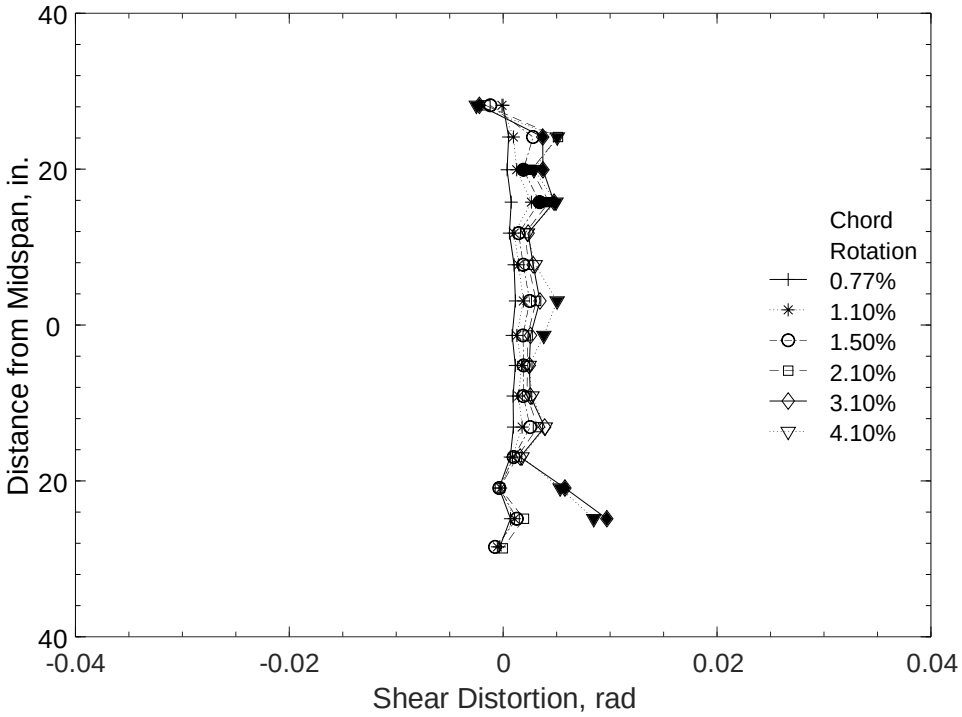

Figure 194 – Calculated shear distortion at positive chord rotations, D100-3.5 (1 in. = 25.4 mm)

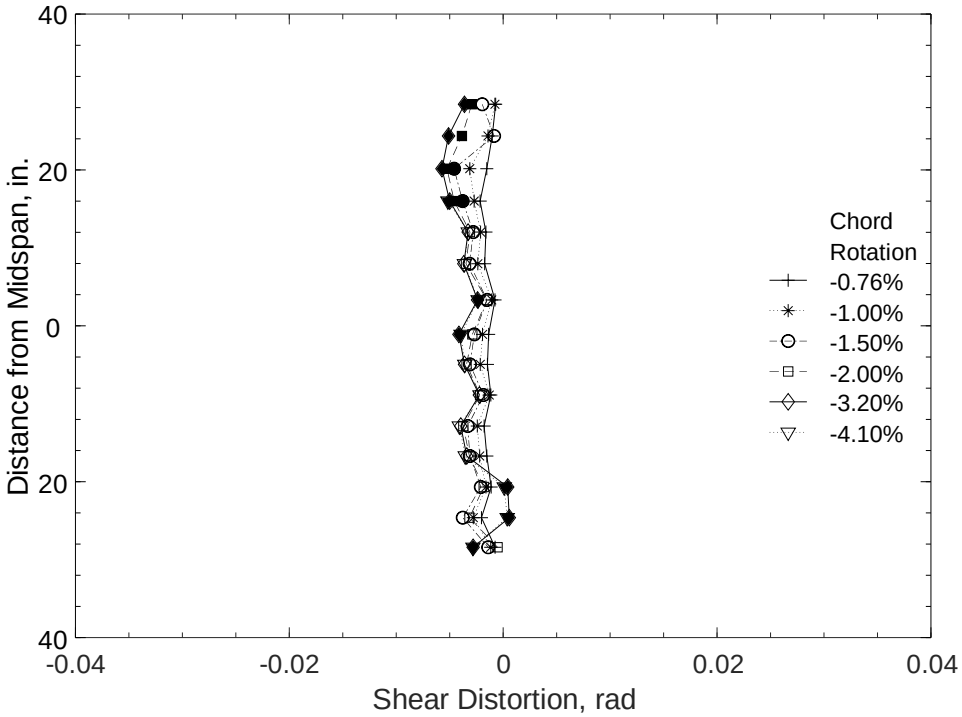

Figure 195 – Calculated shear distortion at negative chord rotations, D100-3.5 (1 in. = 25.4 mm)

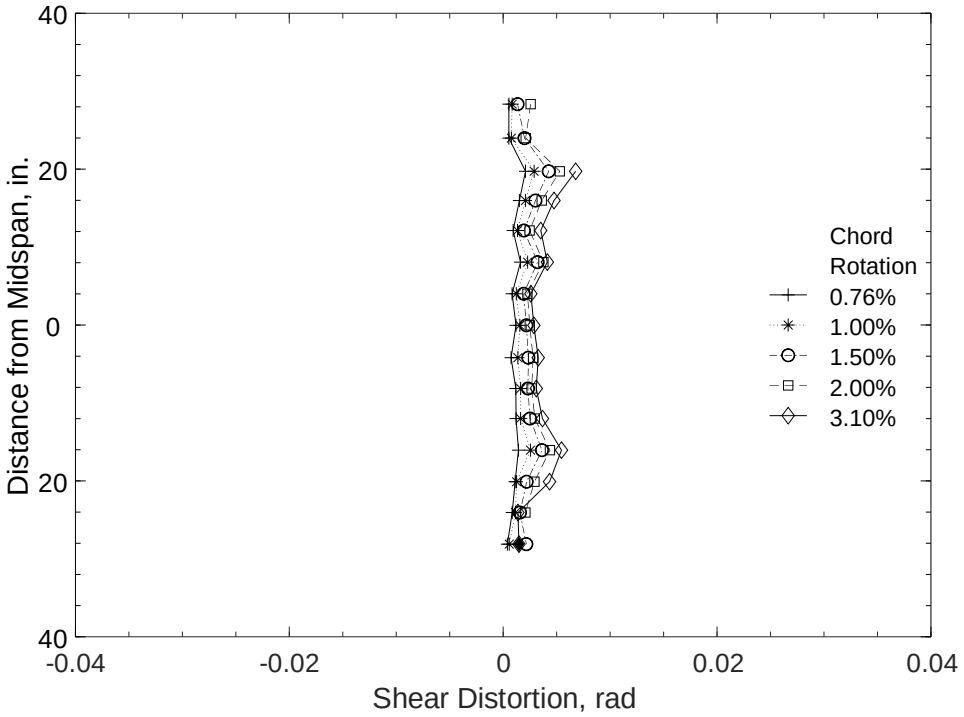

Figure 196 – Calculated shear distortion at positive chord rotations, D120-3.5 (1 in. = 25.4 mm)

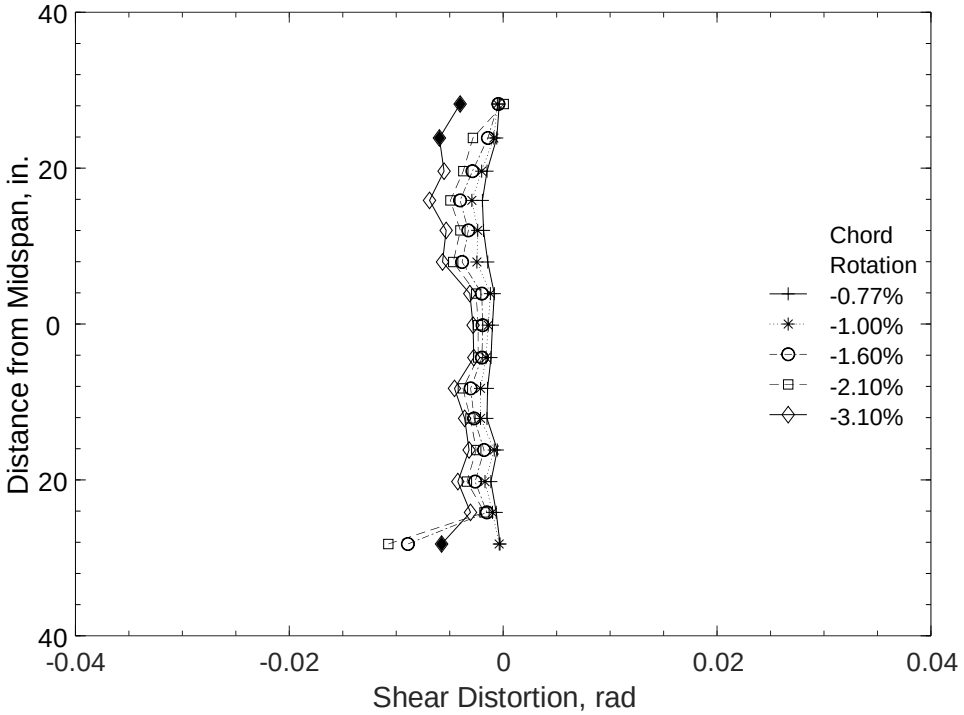

Figure 197 – Calculated shear distortion at negative chord rotations, D120-3.5 (1 in. = 25.4 mm)

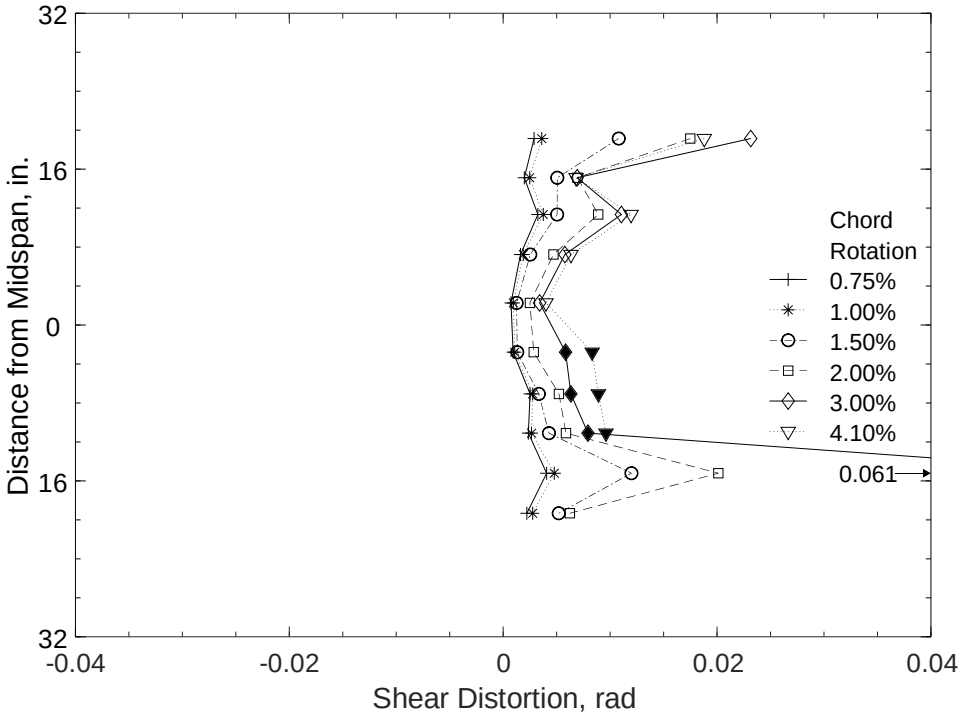

Figure 198 – Calculated shear distortion at positive chord rotations, P80-2.5 (1 in. = 25.4 mm)

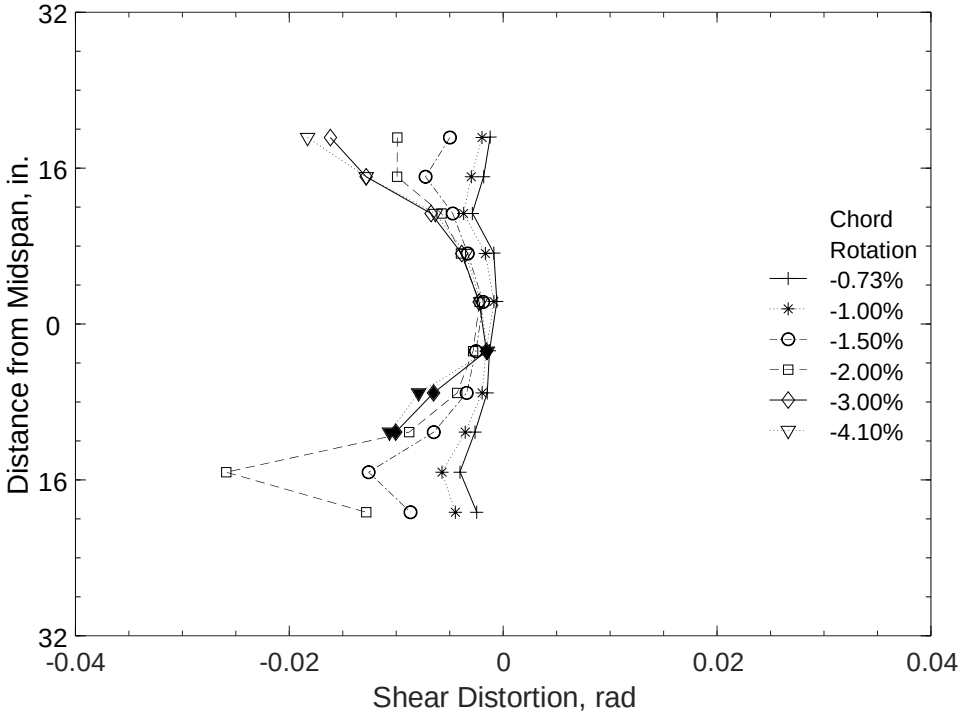

Figure 199 – Calculated shear distortion at negative chord rotations, P80-2.5 (1 in. = 25.4 mm)

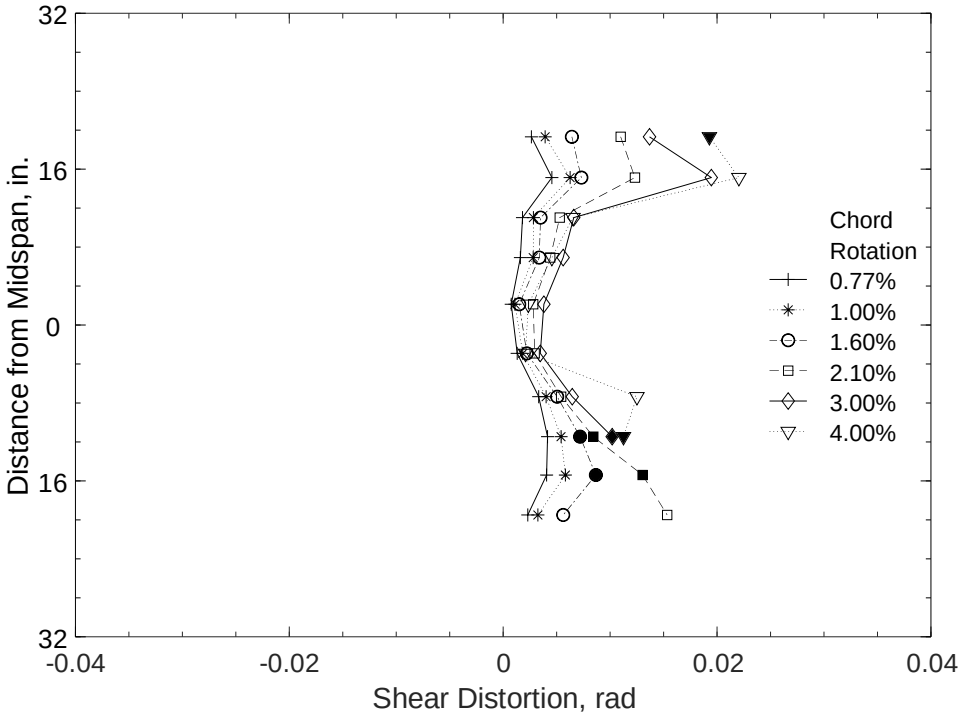

Figure 200 – Calculated shear distortion at positive chord rotations, P100-2.5 (1 in. = 25.4 mm)

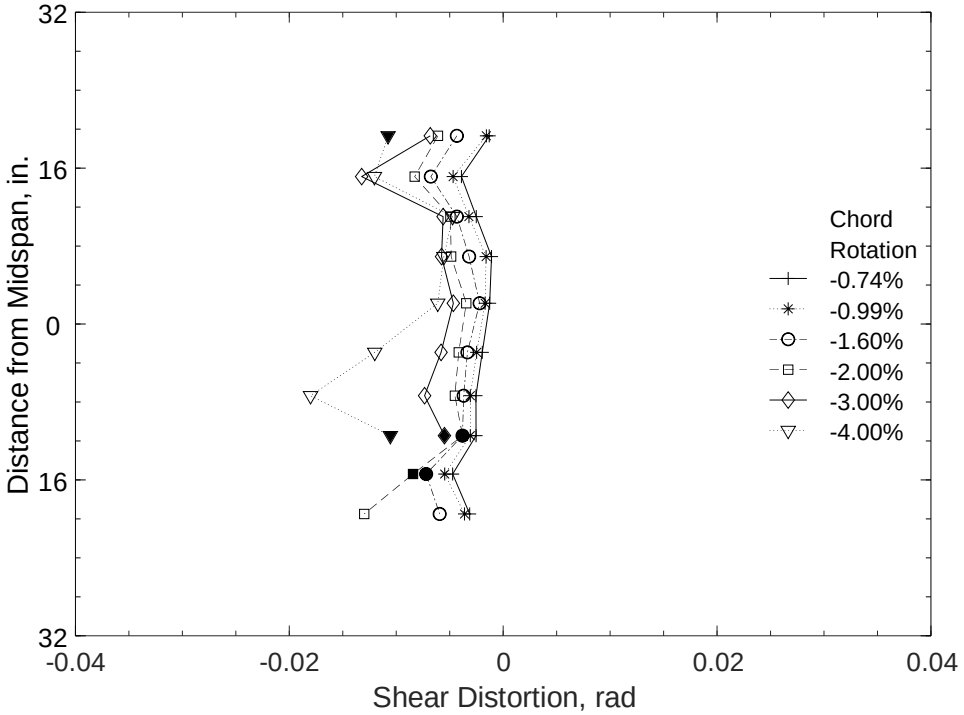

Figure 201 – Calculated shear distortion at negative chord rotations, P100-2.5 (1 in. = 25.4 mm)

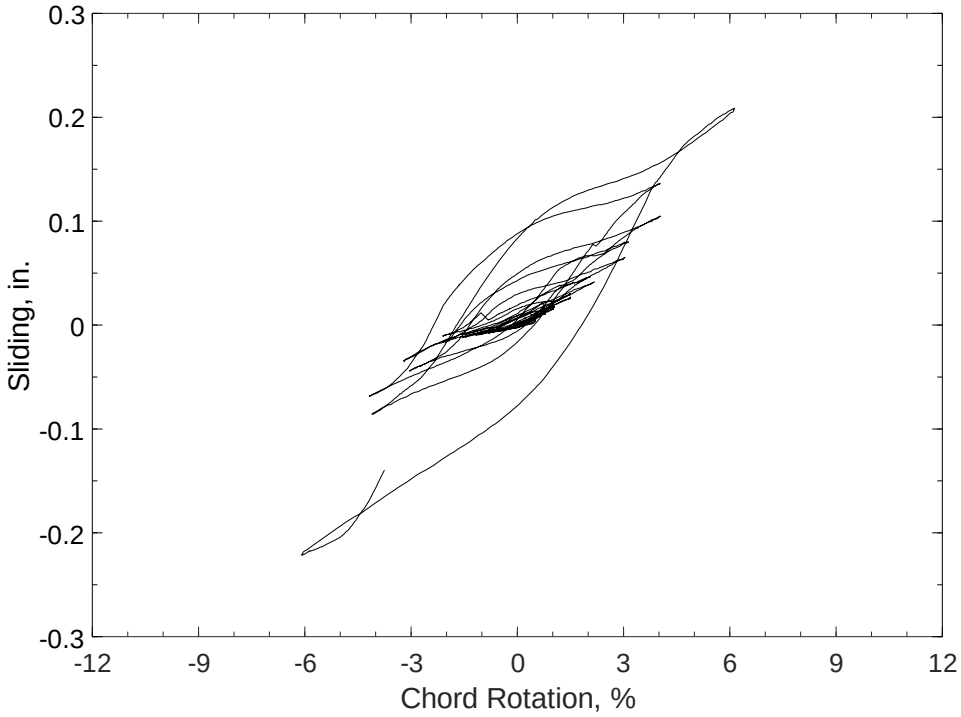

Figure 202 – Calculated sliding at top beam-block interface,
D80-1.5 (1 in. = 25.4 mm)

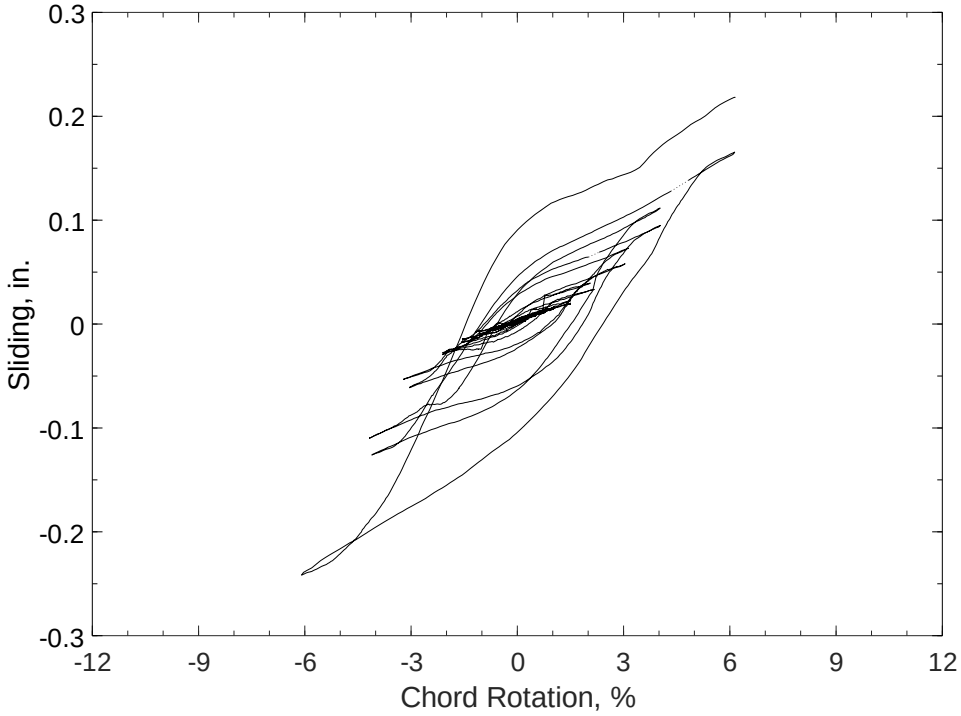

Figure 203 – Calculated sliding at bottom beam-block interface,
D80-1.5 (1 in. = 25.4 mm)

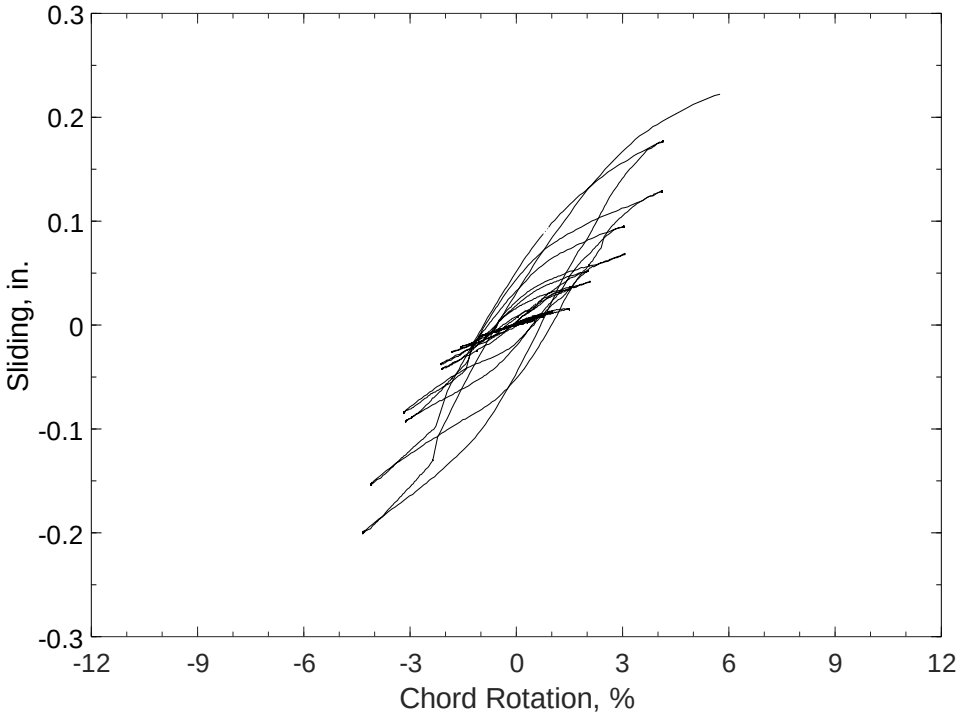

Figure 204 – Calculated sliding at top beam-block interface,
D100-1.5 (1 in. = 25.4 mm)

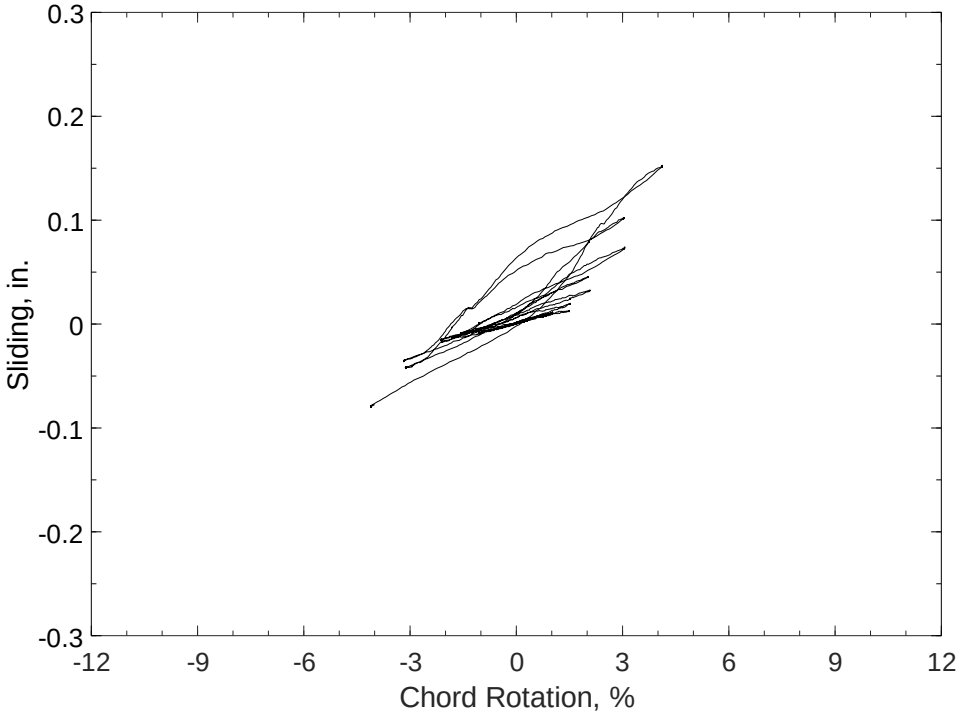

Figure 205 – Calculated sliding at bottom beam-block interface,
D100-1.5 (1 in. = 25.4 mm)

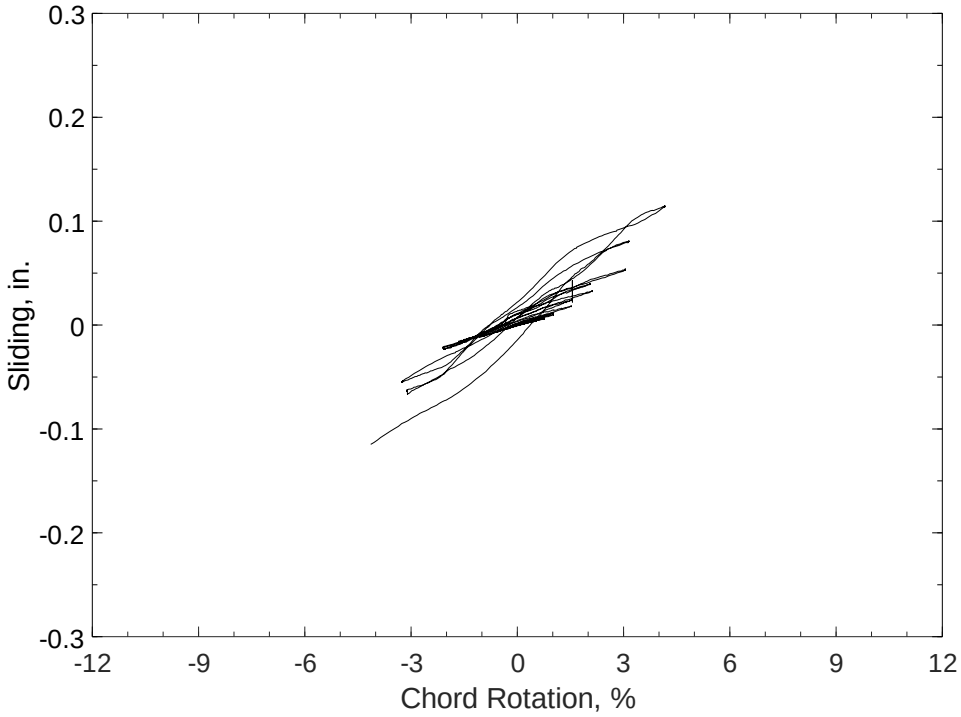

Figure 206 – Calculated sliding at top beam-block interface,
D120-1.5 (1 in. = 25.4 mm)

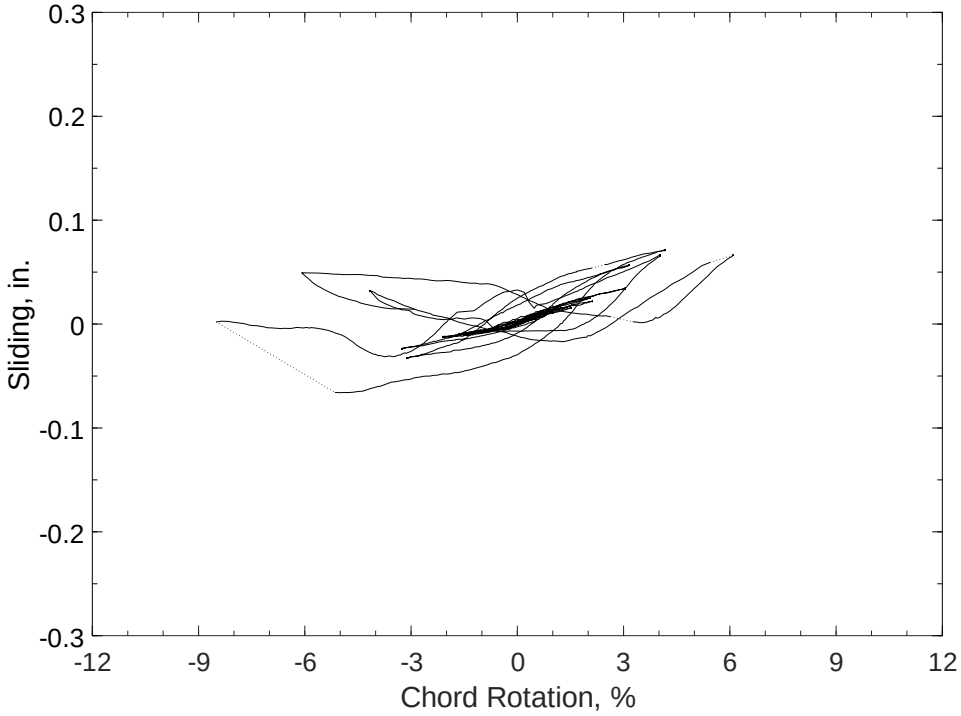

Figure 207 – Calculated sliding at bottom beam-block interface,
D120-1.5 (1 in. = 25.4 mm)

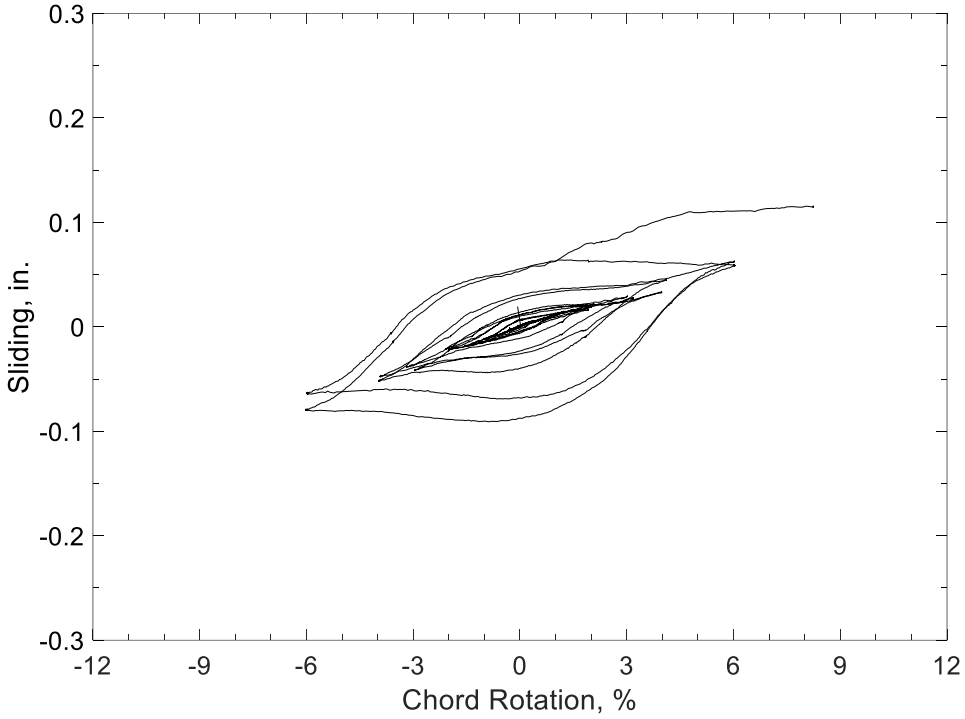

Figure 208 – Calculated sliding at top beam-block interface,
D80-2.5 (1 in. = 25.4 mm)

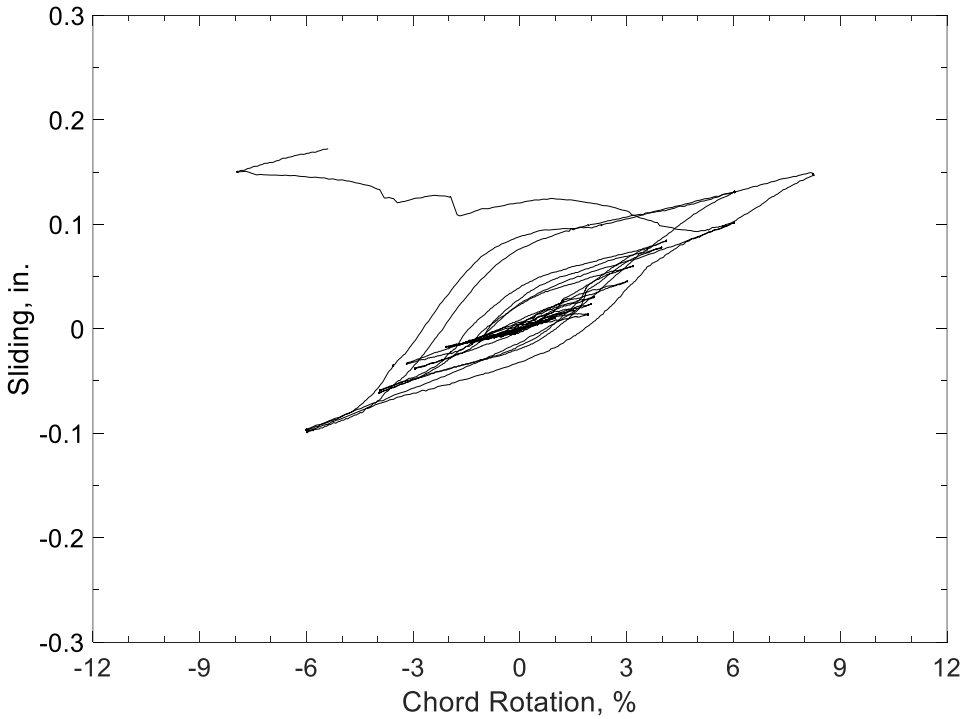

Figure 209 – Calculated sliding at bottom beam-block interface,
D80-2.5 (1 in. = 25.4 mm)

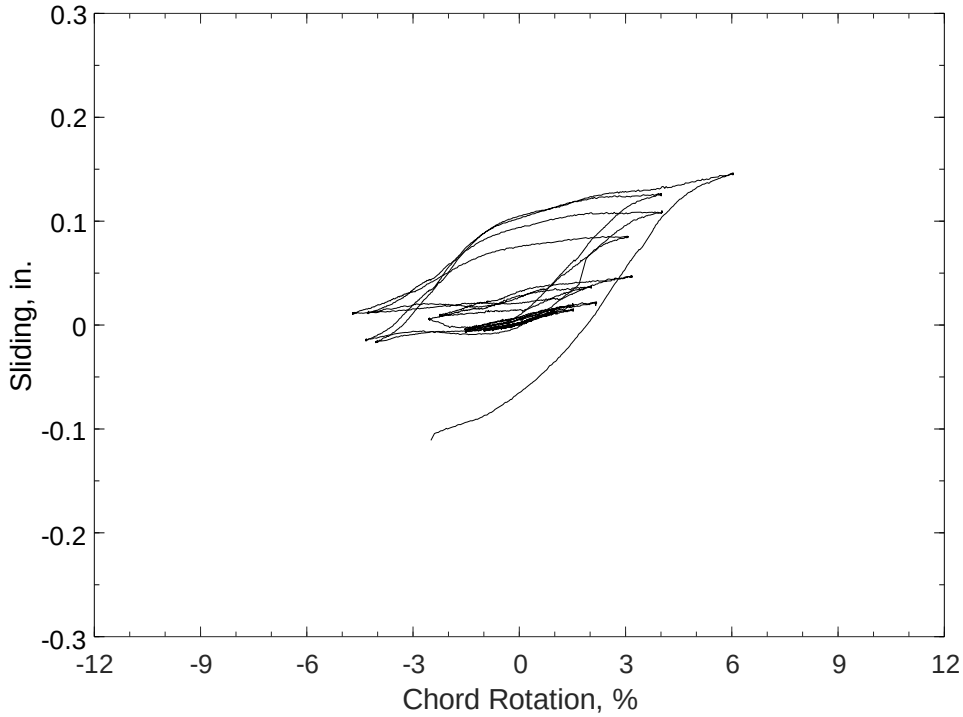

Figure 210 – Calculated sliding at top beam-block interface,
D100-2.5 (1 in. = 25.4 mm)

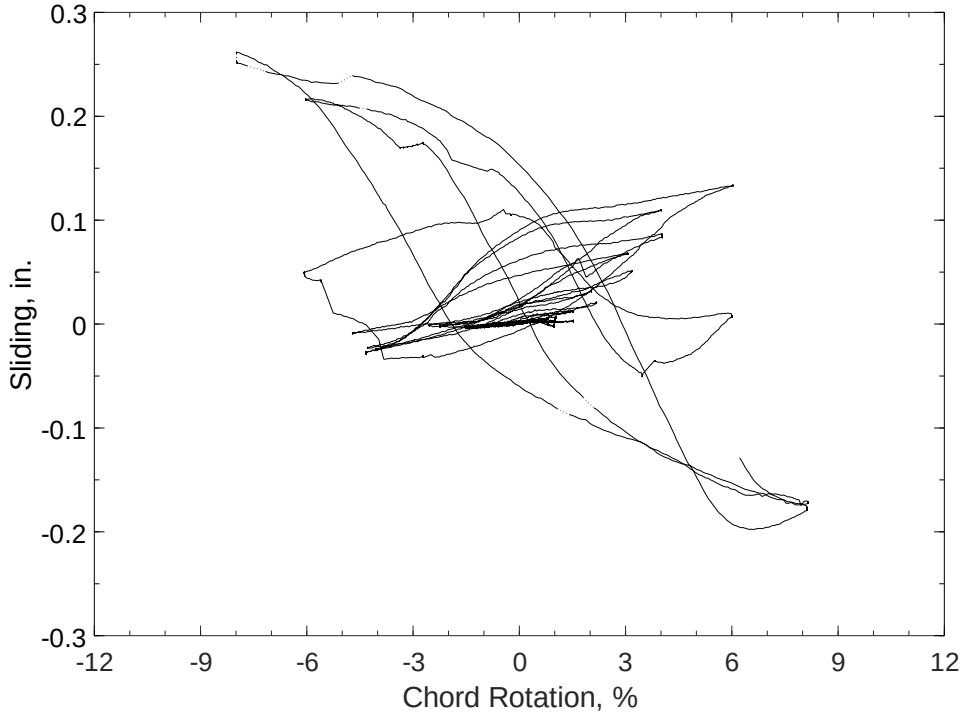

Figure 211 – Calculated sliding at bottom beam-block interface,
D100-2.5 (1 in. = 25.4 mm)

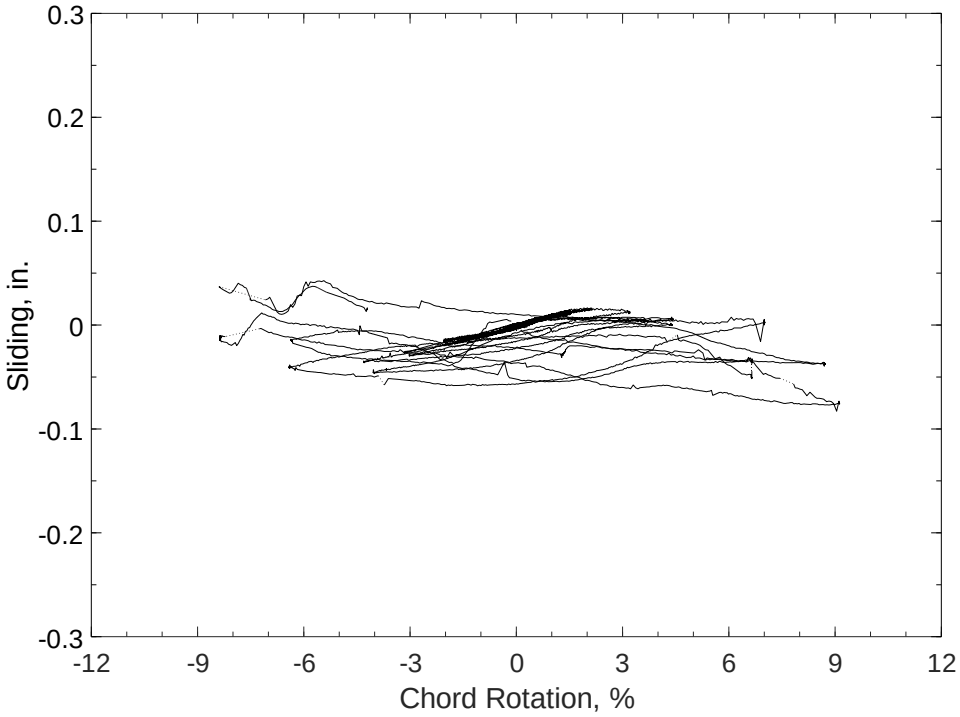

Figure 212 – Calculated sliding at top beam-block interface,
D120-2.5 (1 in. = 25.4 mm)

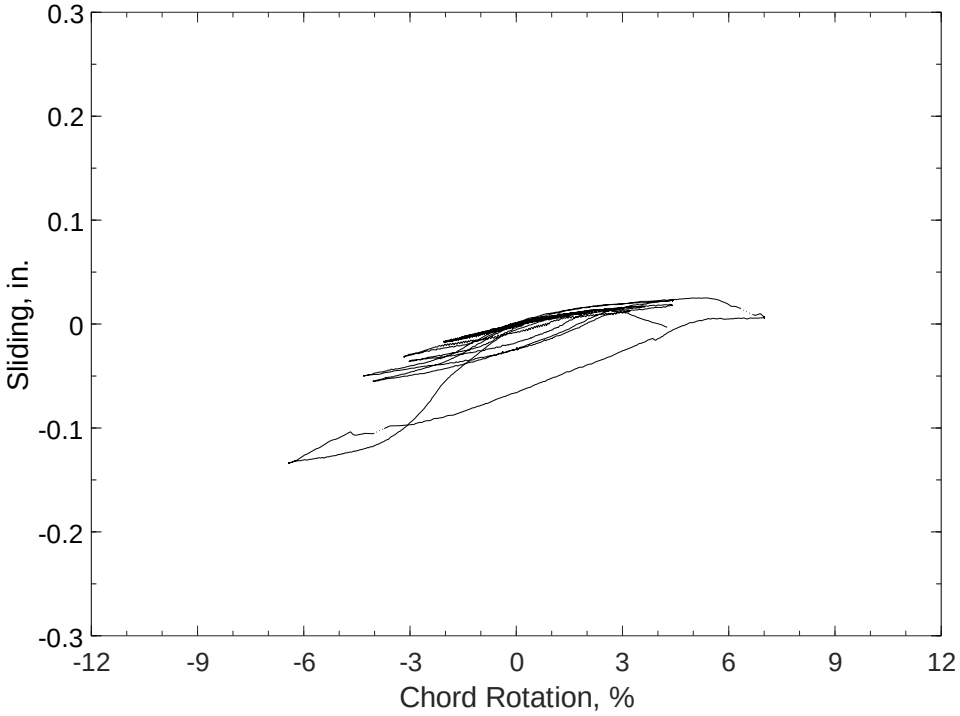

Figure 213 – Calculated sliding at bottom beam-block interface,
D120-2.5 (1 in. = 25.4 mm)

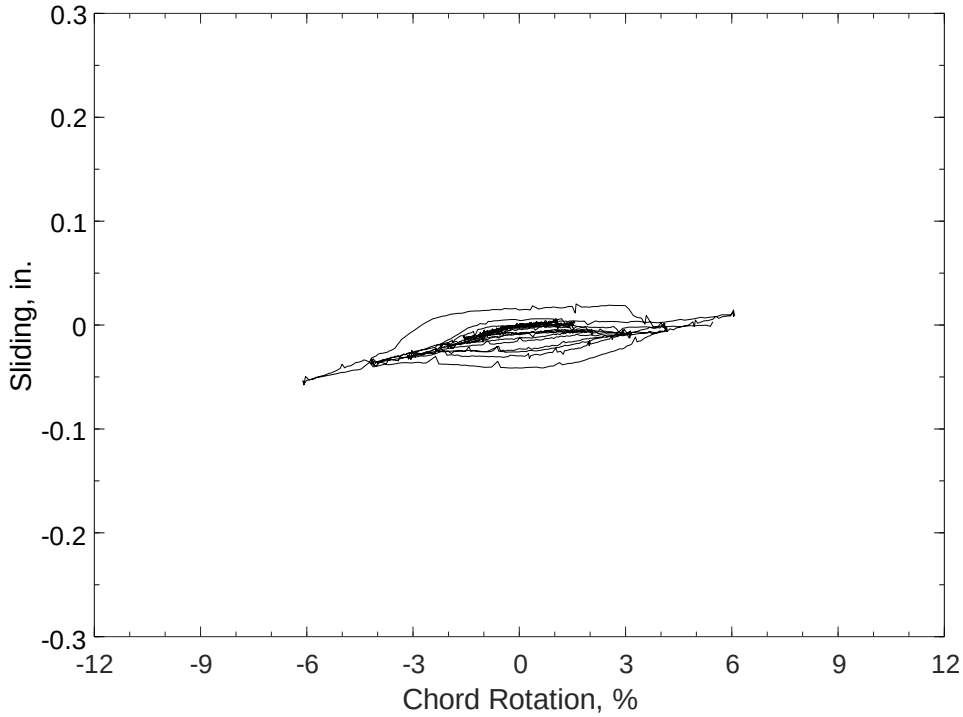

Figure 214 – Calculated sliding at top beam-block interface,
D80-3.5 (1 in. = 25.4 mm)

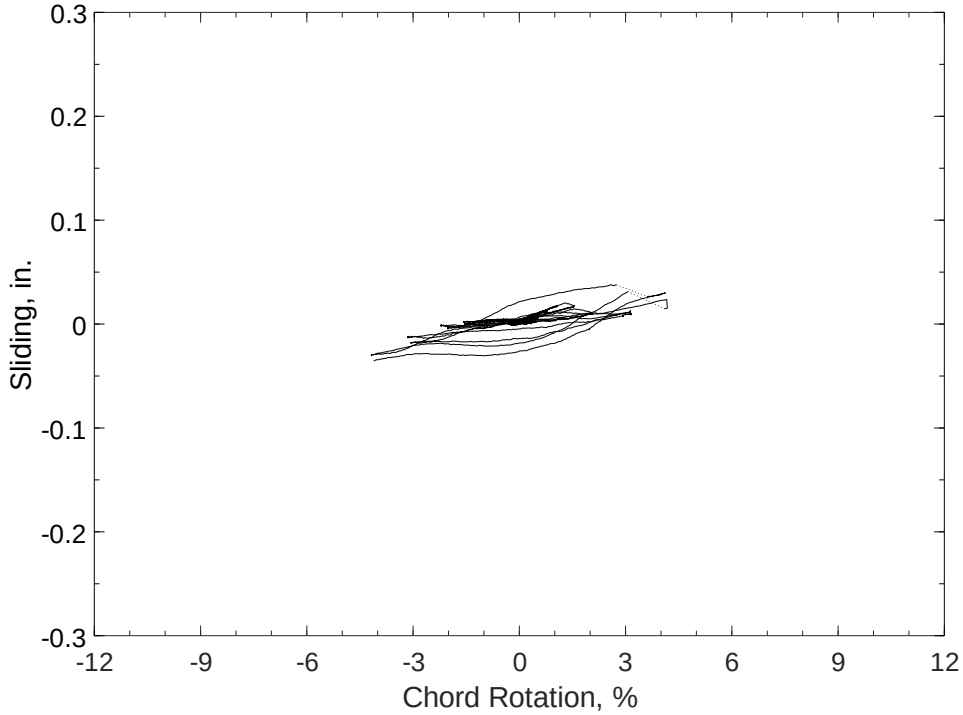

Figure 215 – Calculated sliding at bottom beam-block interface,
D80-3.5 (1 in. = 25.4 mm)

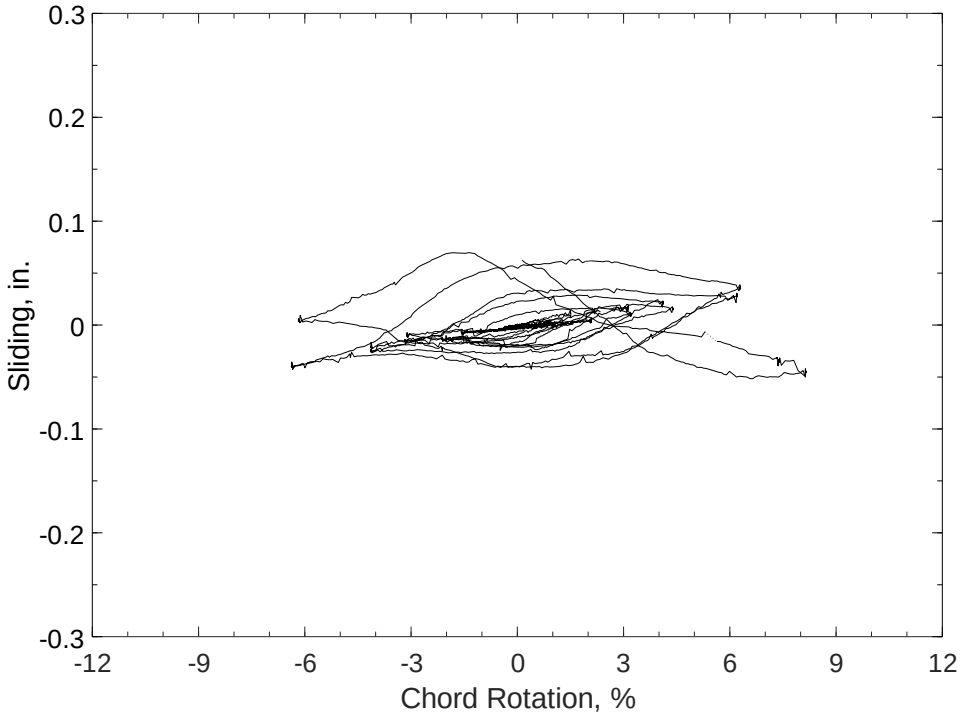

Figure 216 – Calculated sliding at top beam-block interface,
D100-3.5 (1 in. = 25.4 mm)

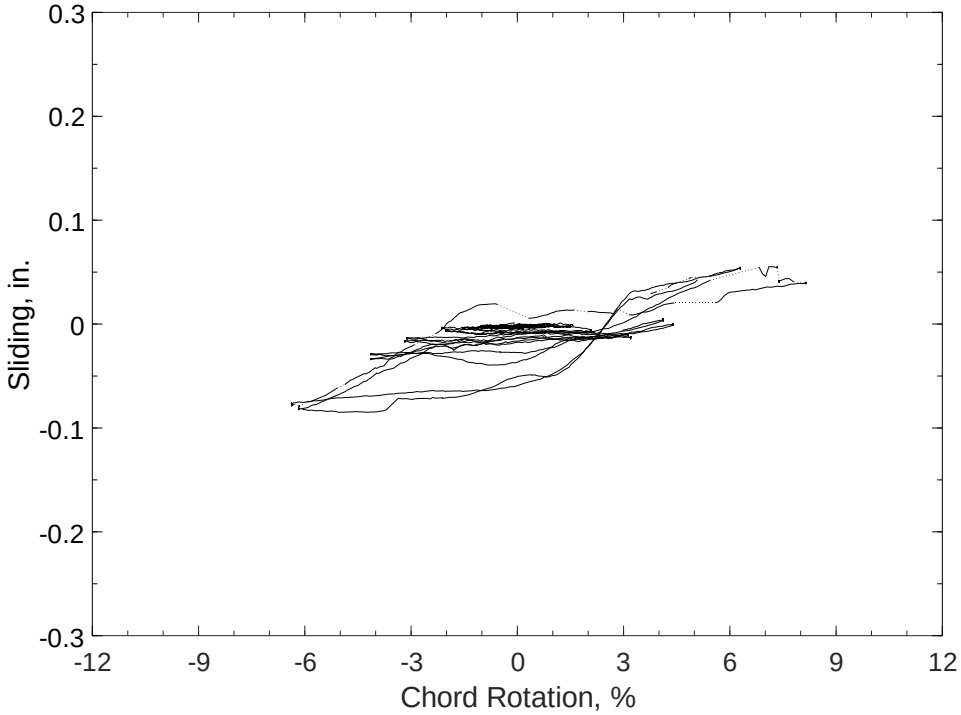

Figure 217 – Calculated sliding at bottom beam-block interface,
D100-3.5 (1 in. = 25.4 mm)

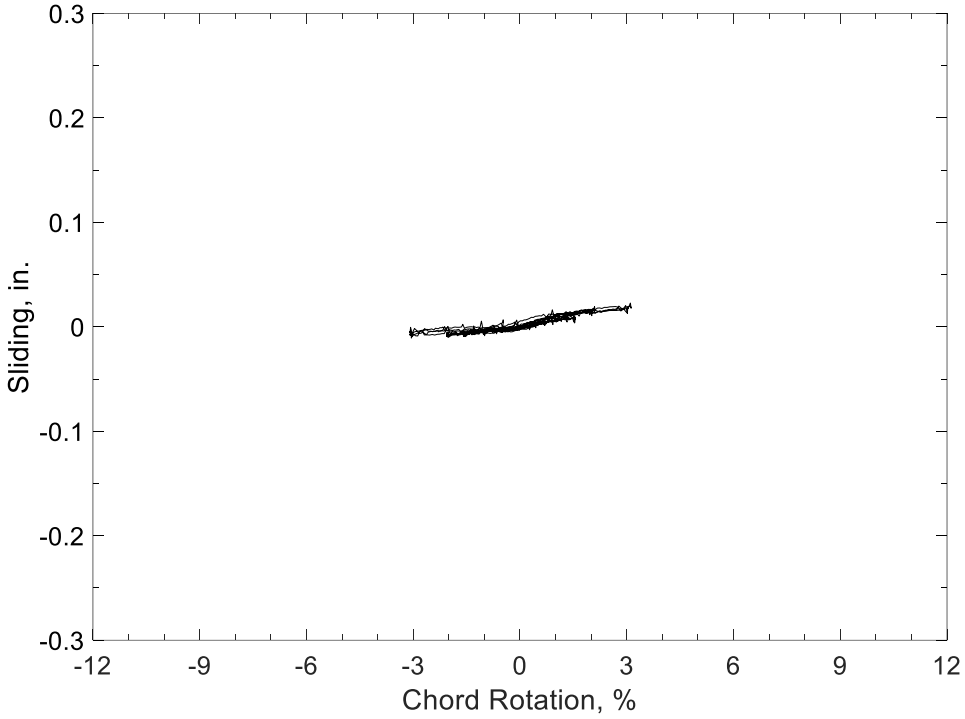

Figure 218 – Calculated sliding at top beam-block interface,
D120-3.5 (1 in. = 25.4 mm)

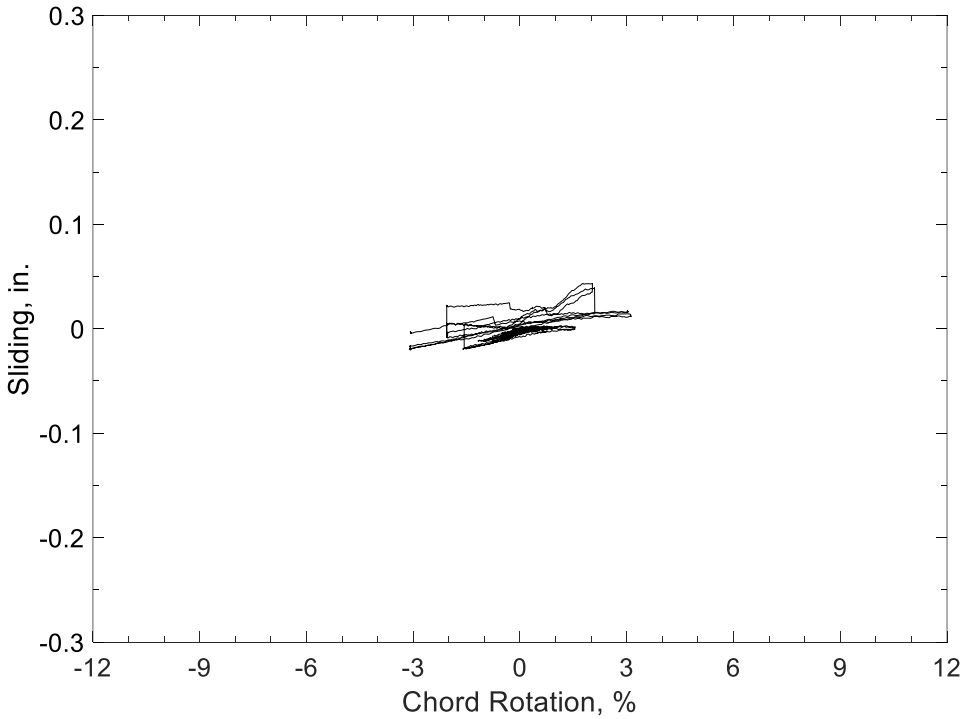

Figure 219 – Calculated sliding at bottom beam-block interface,
D120-3.5 (1 in. = 25.4 mm)

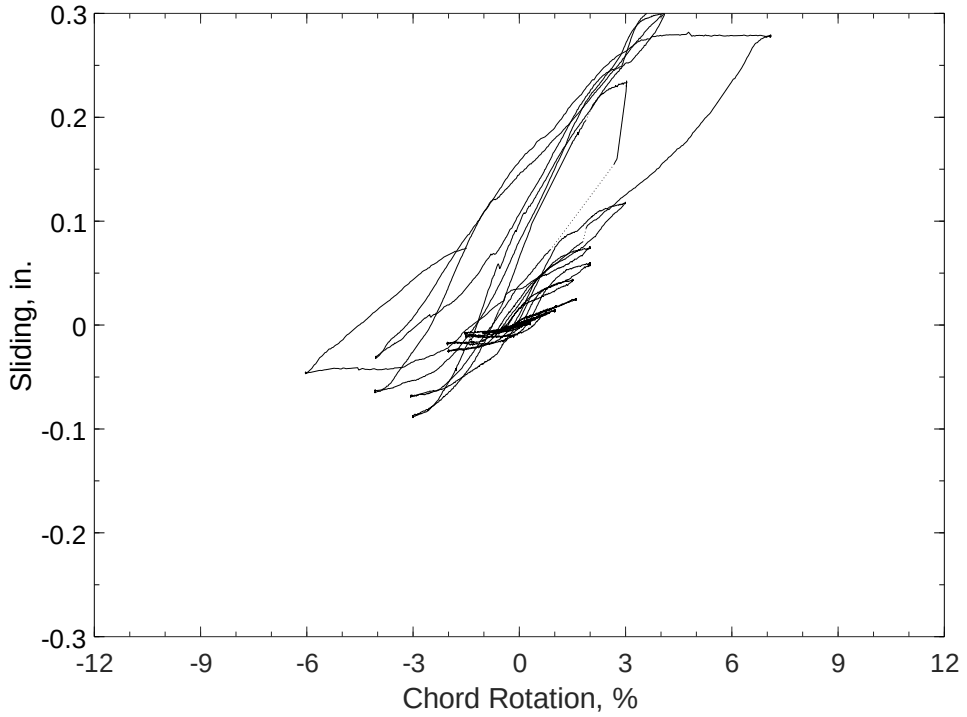

Figure 220 – Calculated sliding at top beam-block interface,
P80-2.5 (1 in. = 25.4 mm)

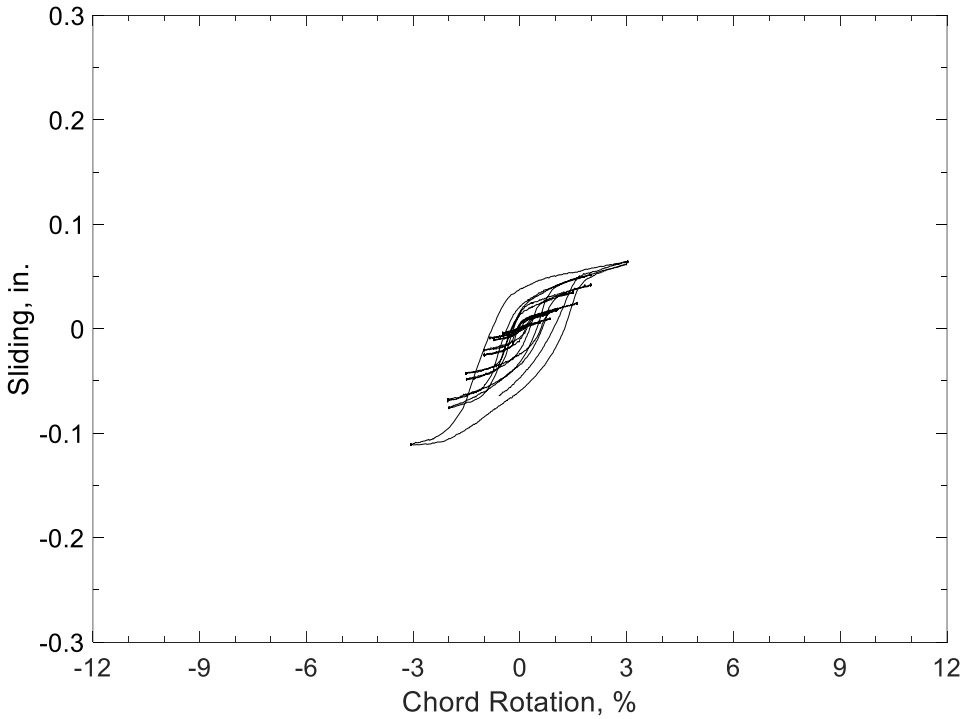

Figure 221 – Calculated sliding at bottom beam-block interface,
P80-2.5 (1 in. = 25.4 mm)

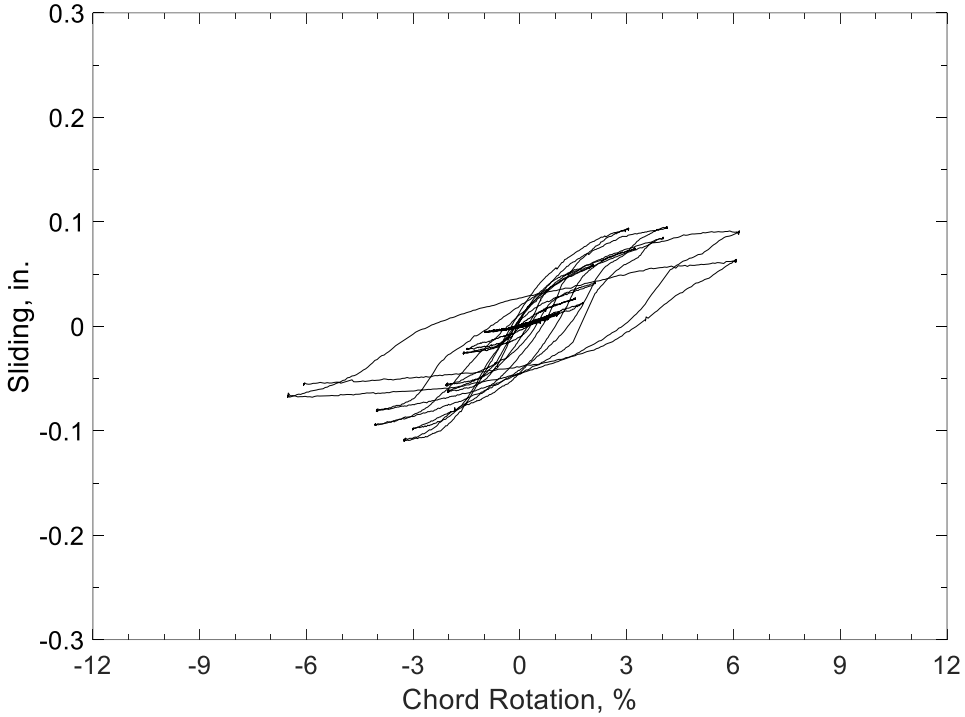

Figure 222 – Calculated sliding at top beam-block interface,
P100-2.5 (1 in. = 25.4 mm)

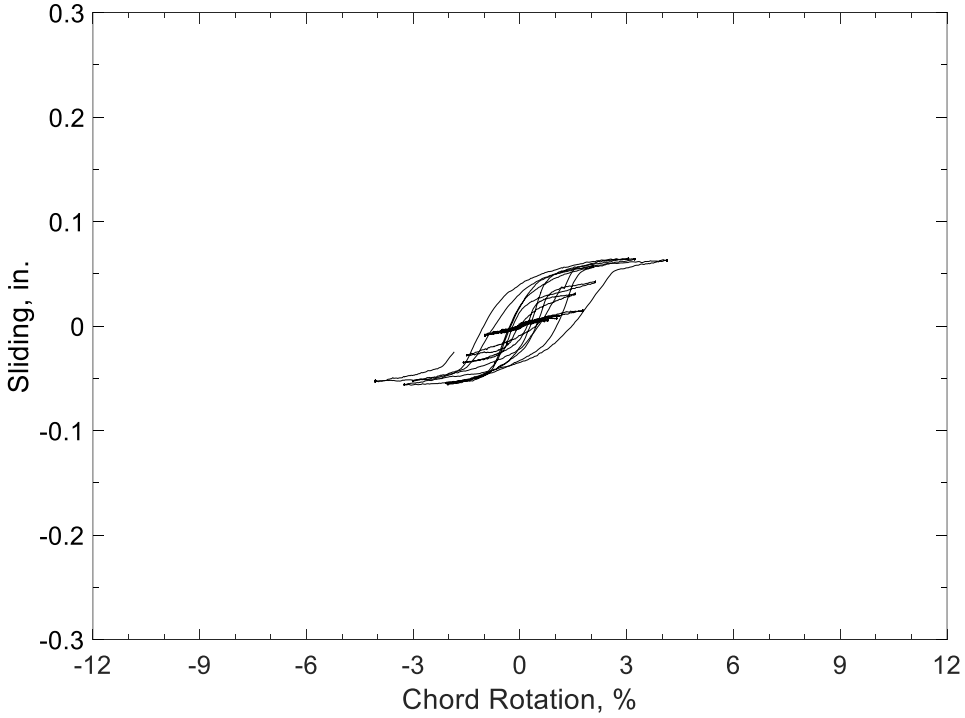

Figure 223 – Calculated sliding at bottom beam-block interface,
P100-2.5 (1 in. = 25.4 mm)

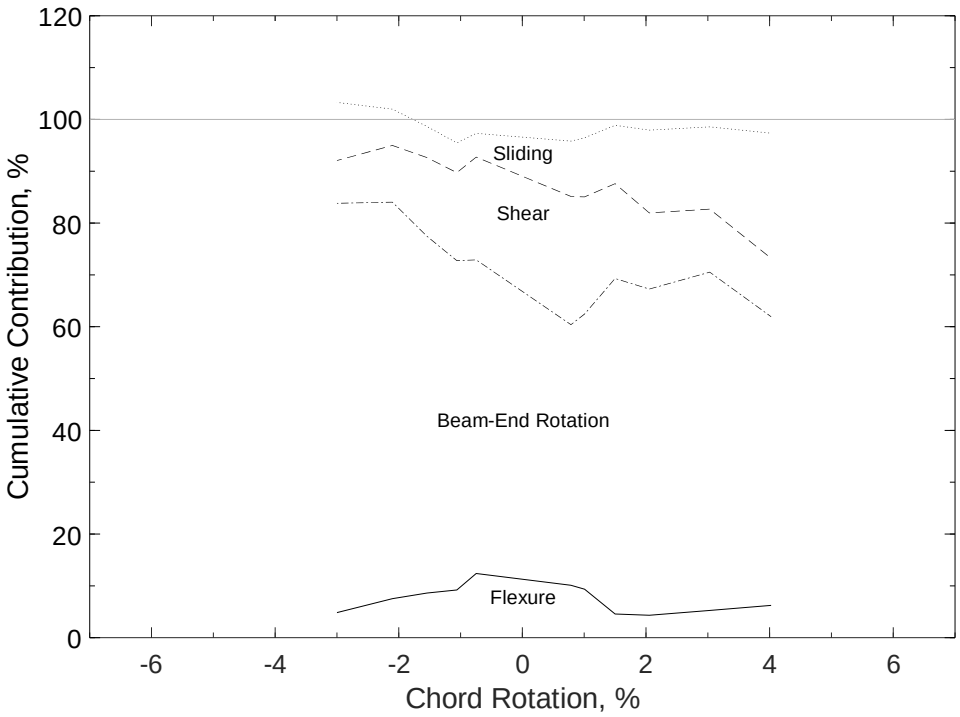

Figure 224 – Cumulative contribution of chord rotation components, D80-1.5

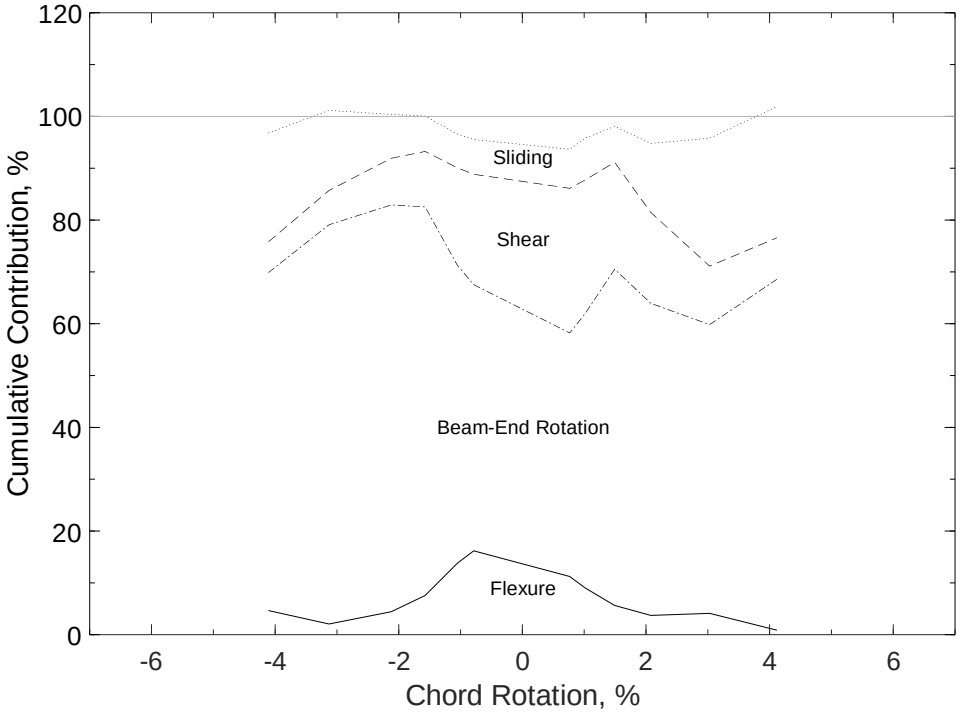

Figure 225 – Cumulative contribution of chord rotation components, D100-1.5

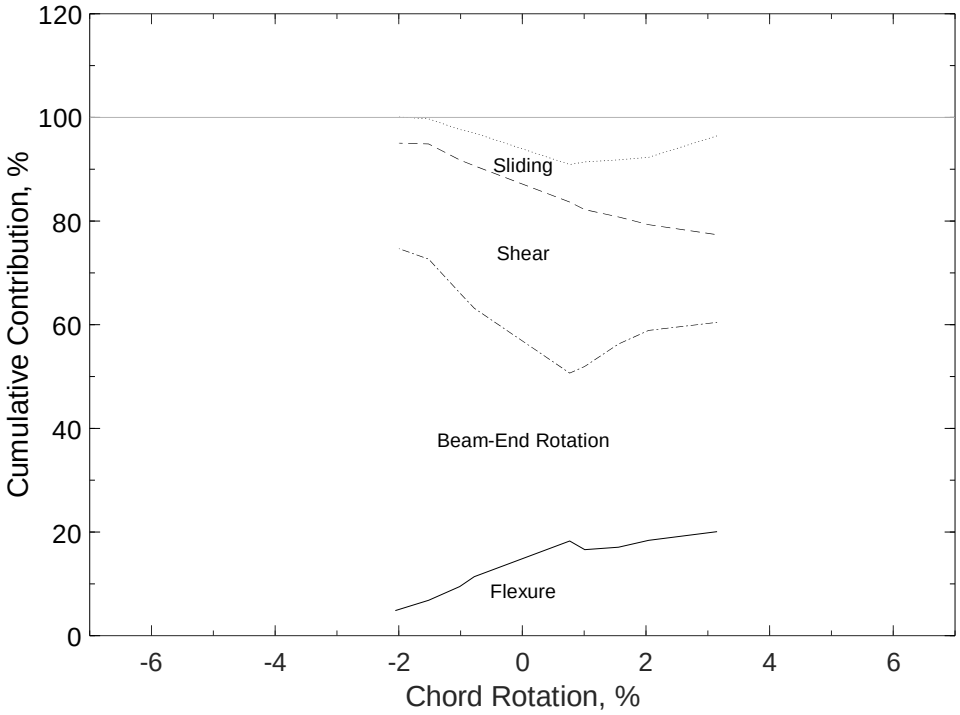

Figure 226 – Cumulative contribution of chord rotation components, D120-1.5

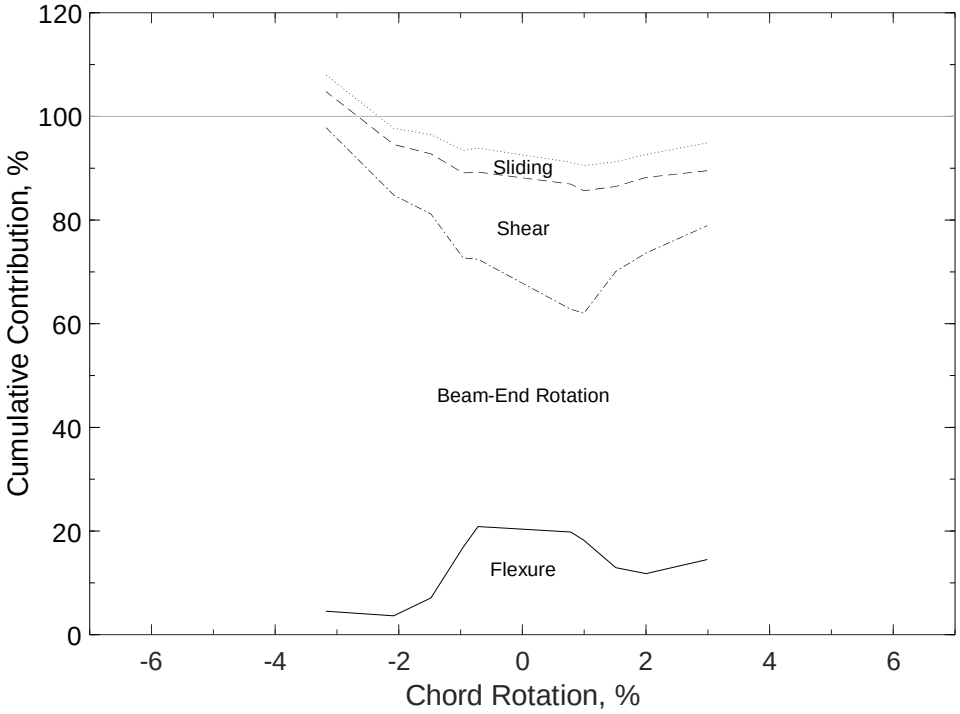

Figure 227 – Cumulative contribution of chord rotation components, D80-2.5

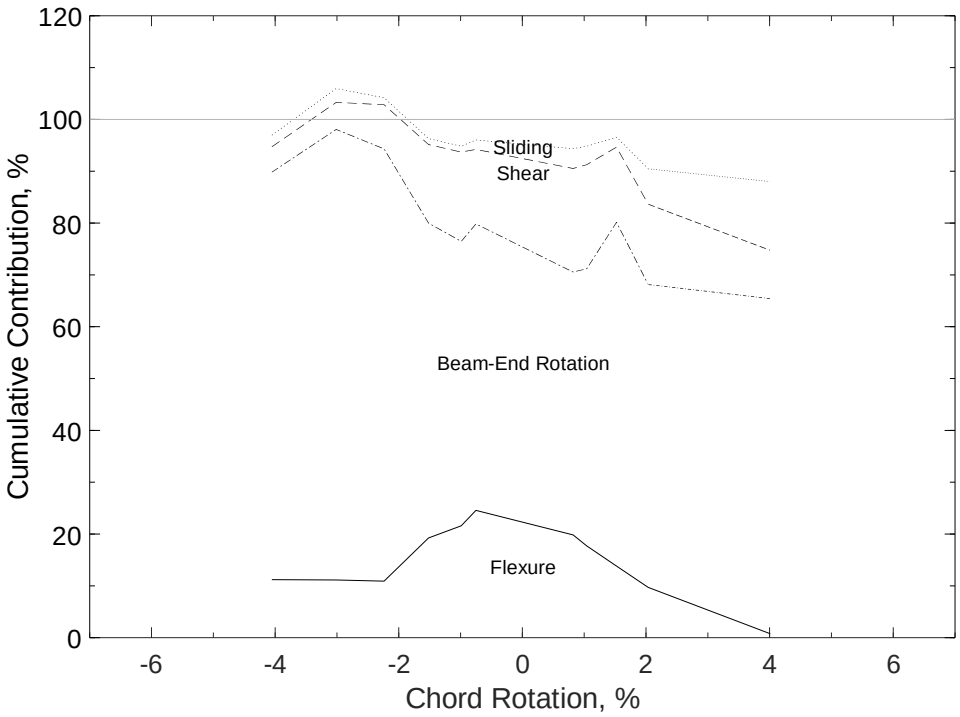

Figure 228 – Cumulative contribution of chord rotation components, D100-2.5

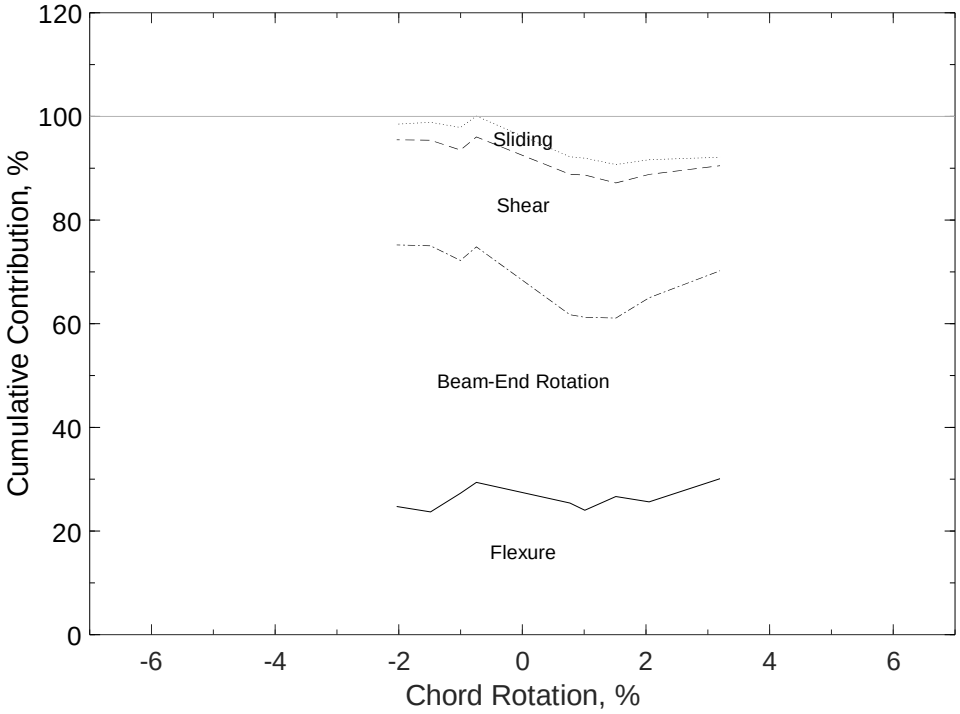

Figure 229 – Cumulative contribution of chord rotation components, D120-2.5

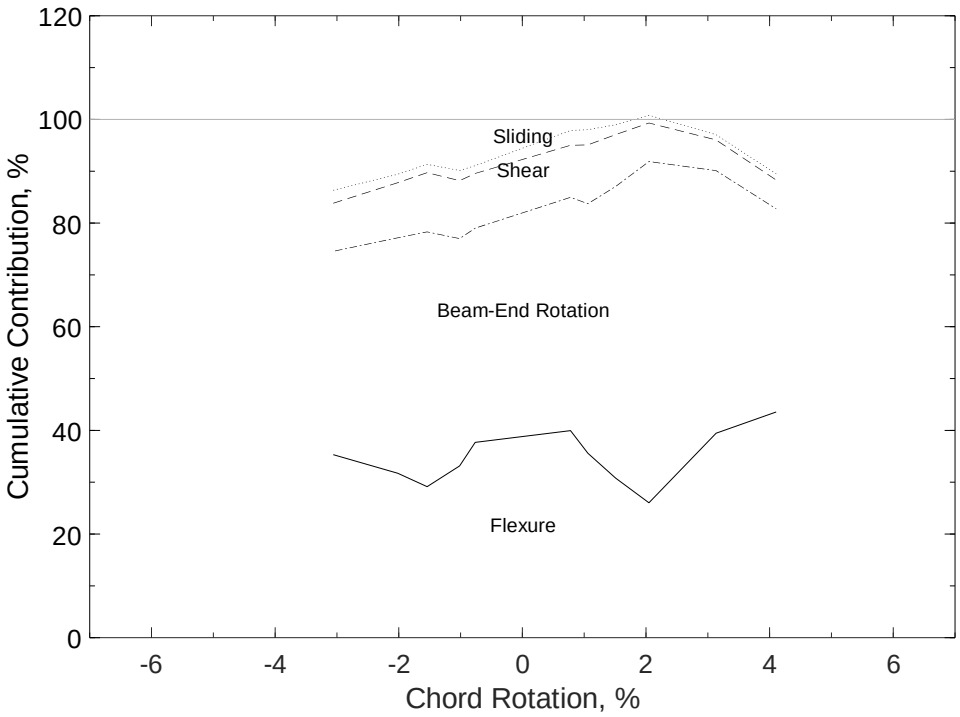

Figure 230 – Cumulative contribution of chord rotation components, D80-3.5

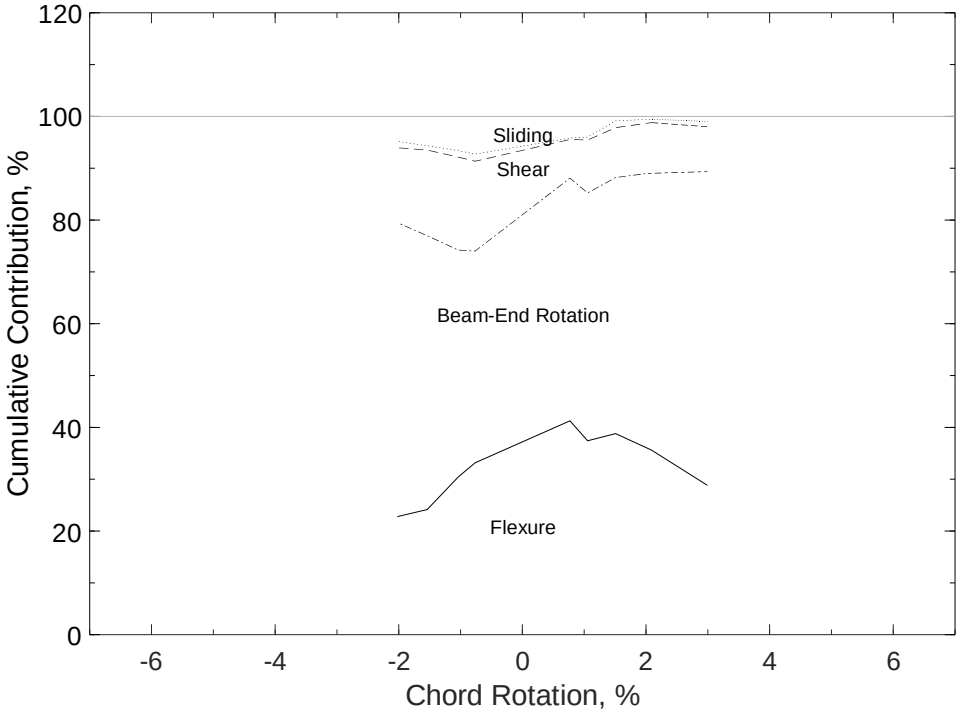

Figure 231 – Cumulative contribution of chord rotation components, D100-3.5

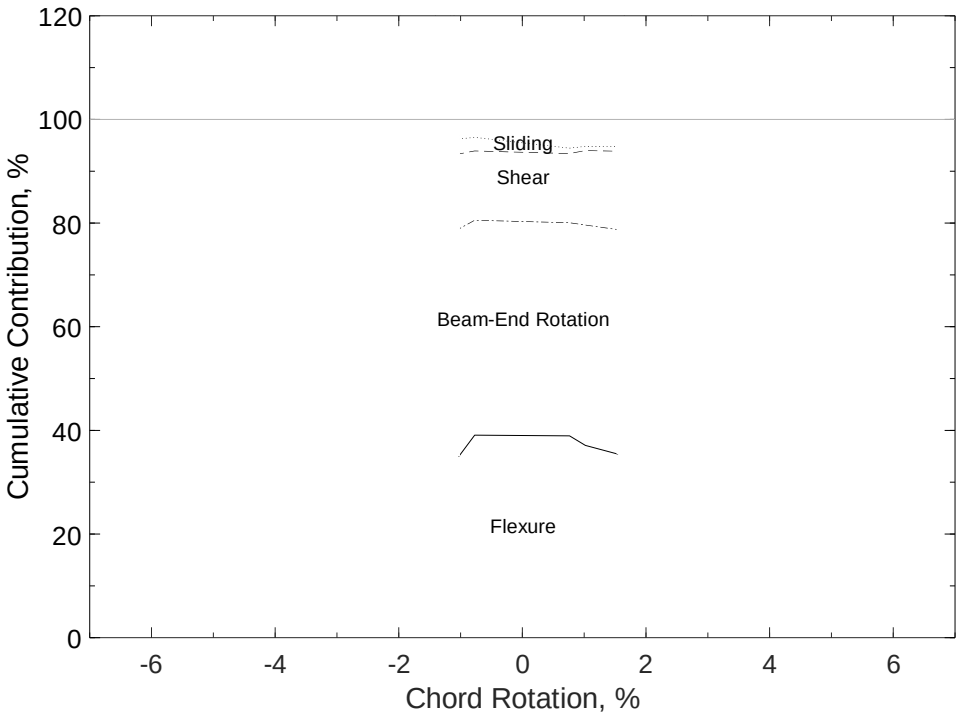

Figure 232 – Cumulative contribution of chord rotation components, D120-3.5

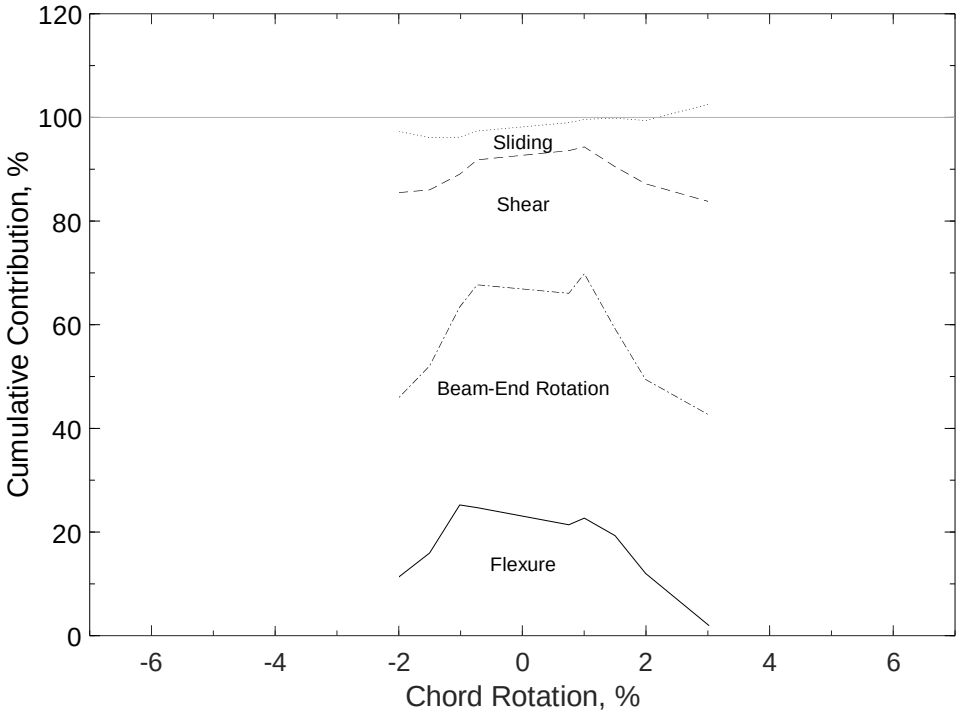

Figure 233 – Cumulative contribution of chord rotation components, P80-2.5

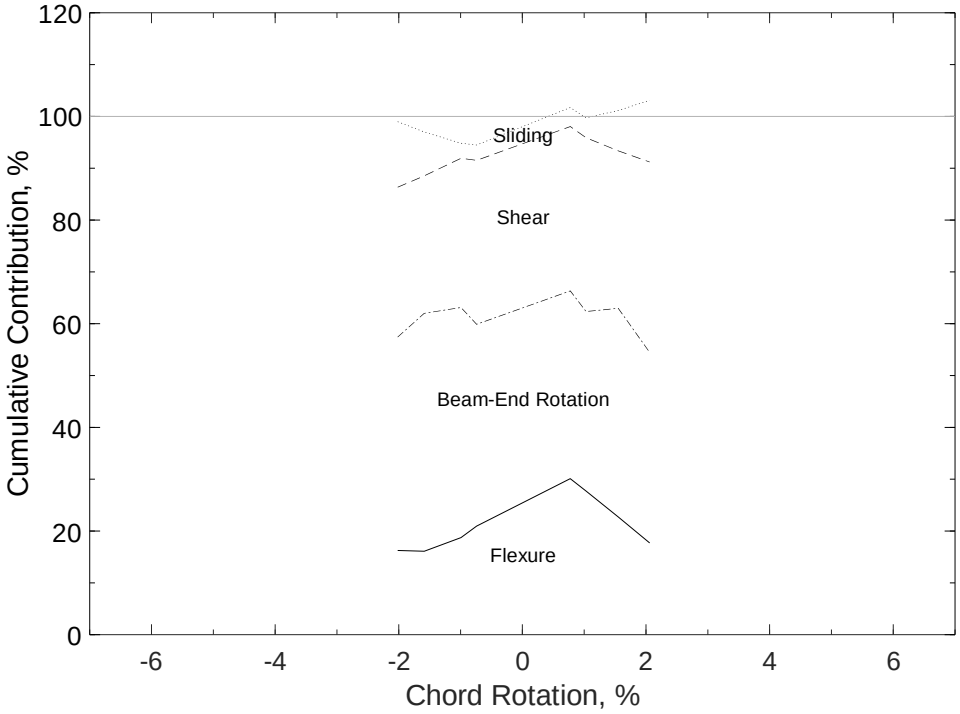

Figure 234 – Cumulative contribution of chord rotation components, P100-2.5

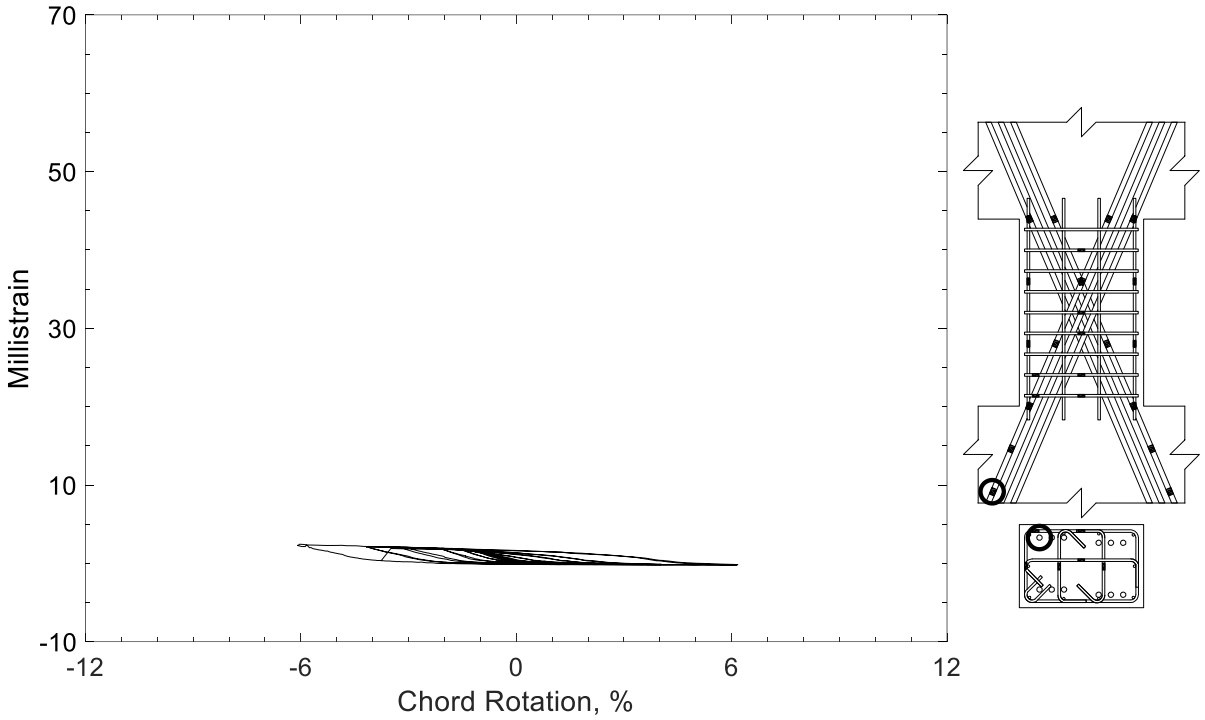

Figure 235 – Measured strain in diagonal bar of D80-1.5, strain gauge D1

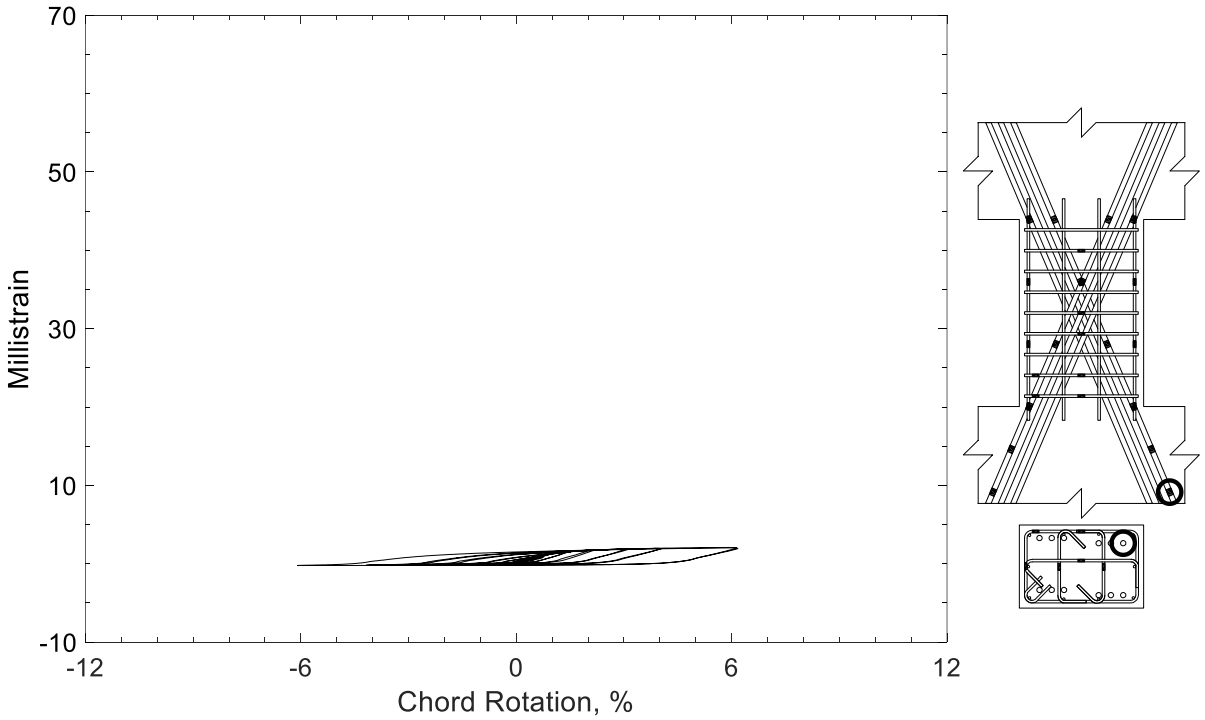

Figure 236 – Measured strain in diagonal bar of D80-1.5, strain gauge D2

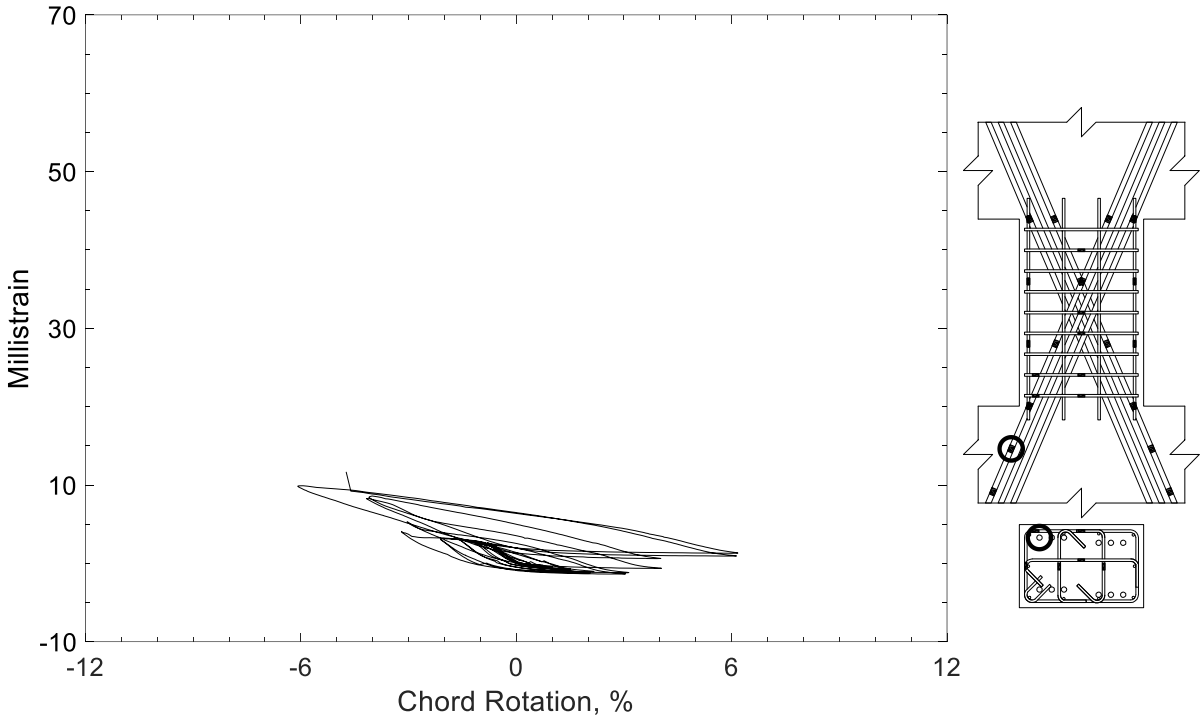

Figure 237 – Measured strain in diagonal bar of D80-1.5, strain gauge D3

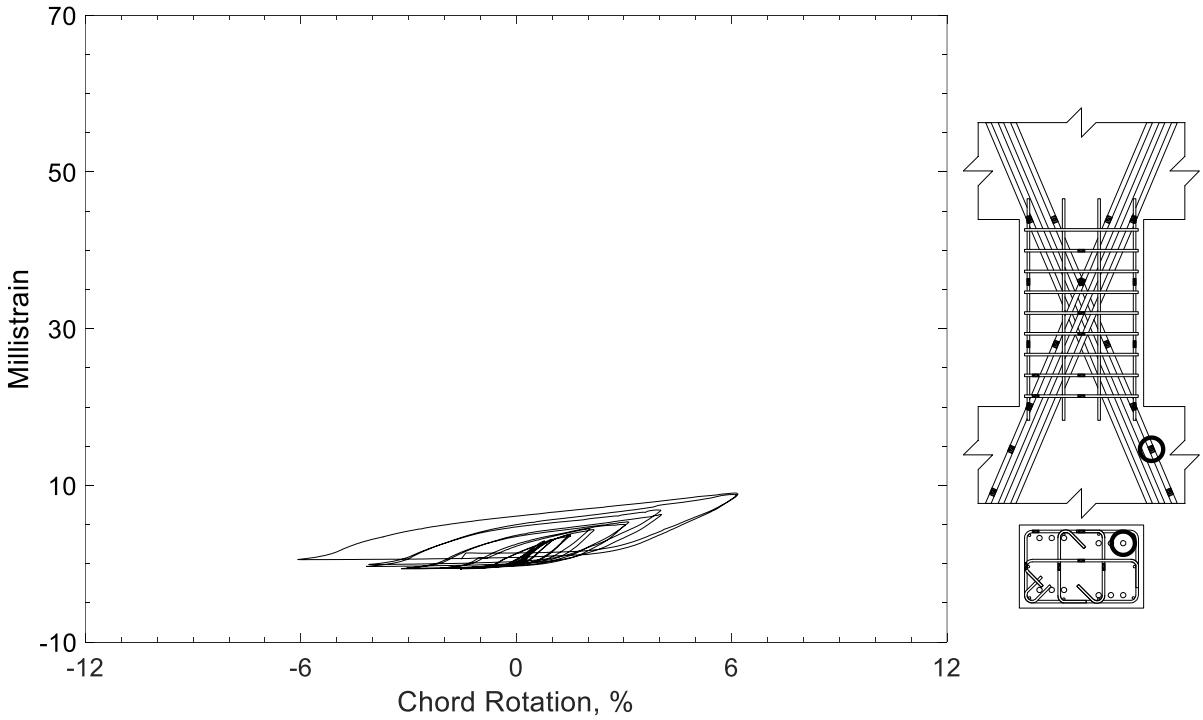

Figure 238 – Measured strain in diagonal bar of D80-1.5, strain gauge D4

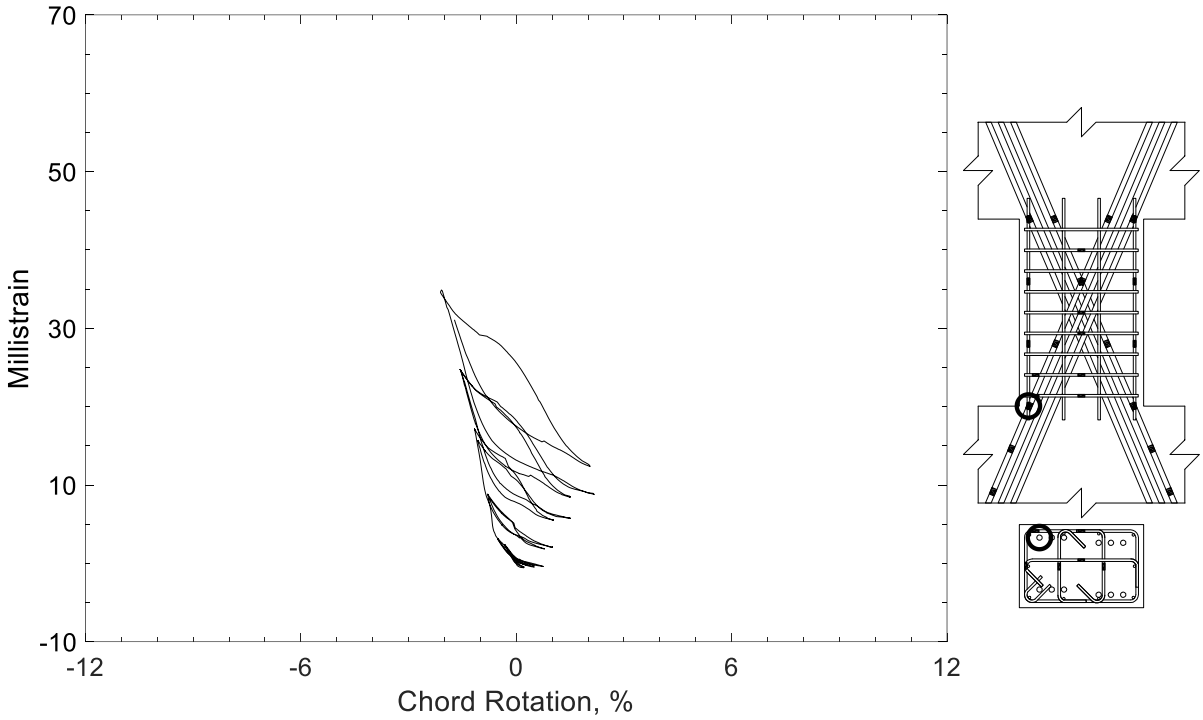

Figure 239 – Measured strain in diagonal bar of D80-1.5, strain gauge D5

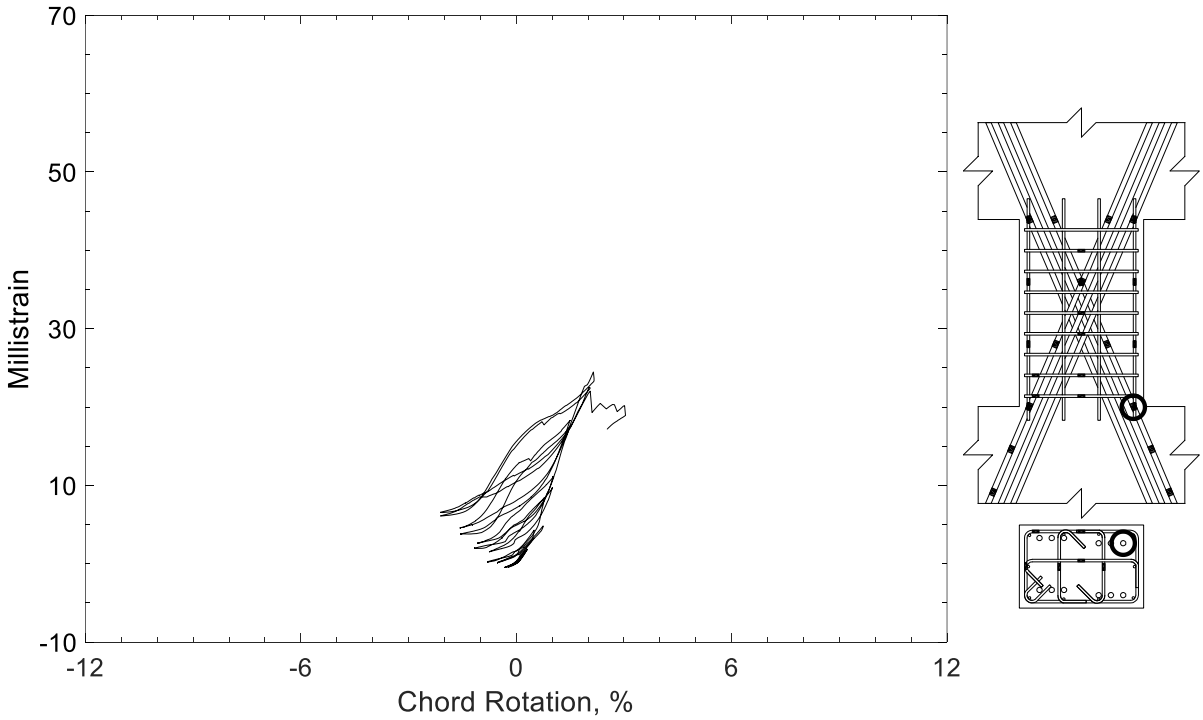

Figure 240 – Measured strain in diagonal bar of D80-1.5, strain gauge D6

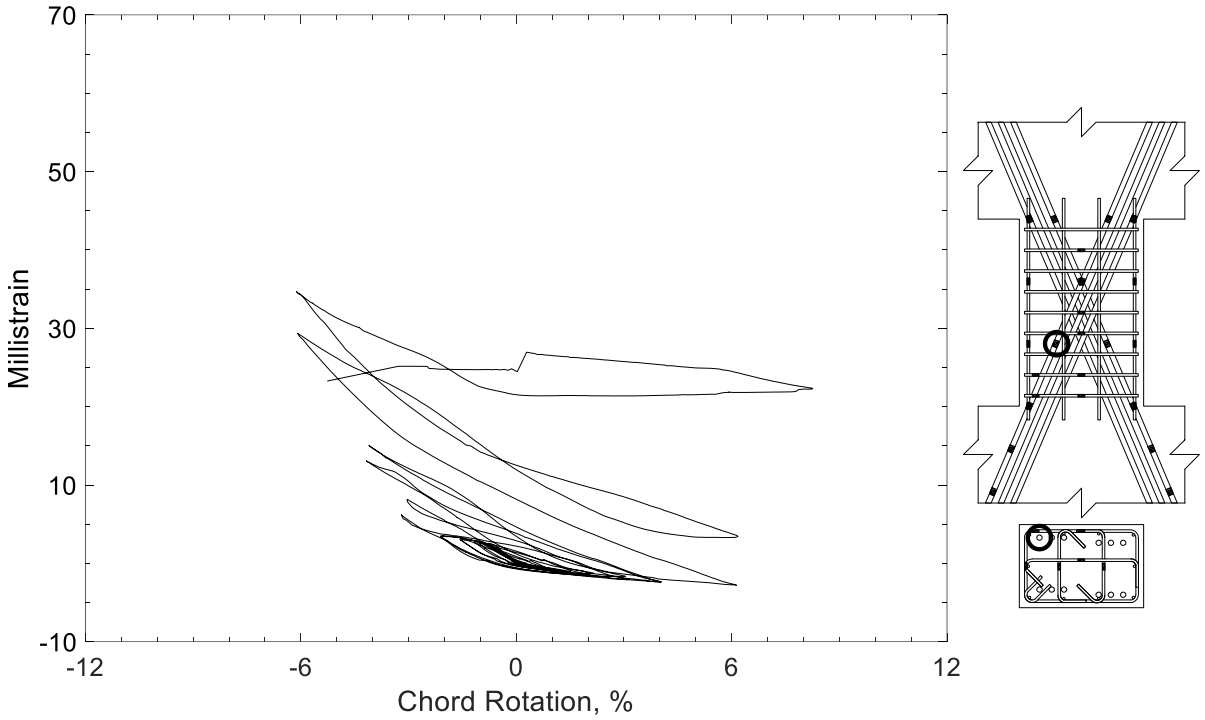

Figure 241 – Measured strain in diagonal bar of D80-1.5, strain gauge D7

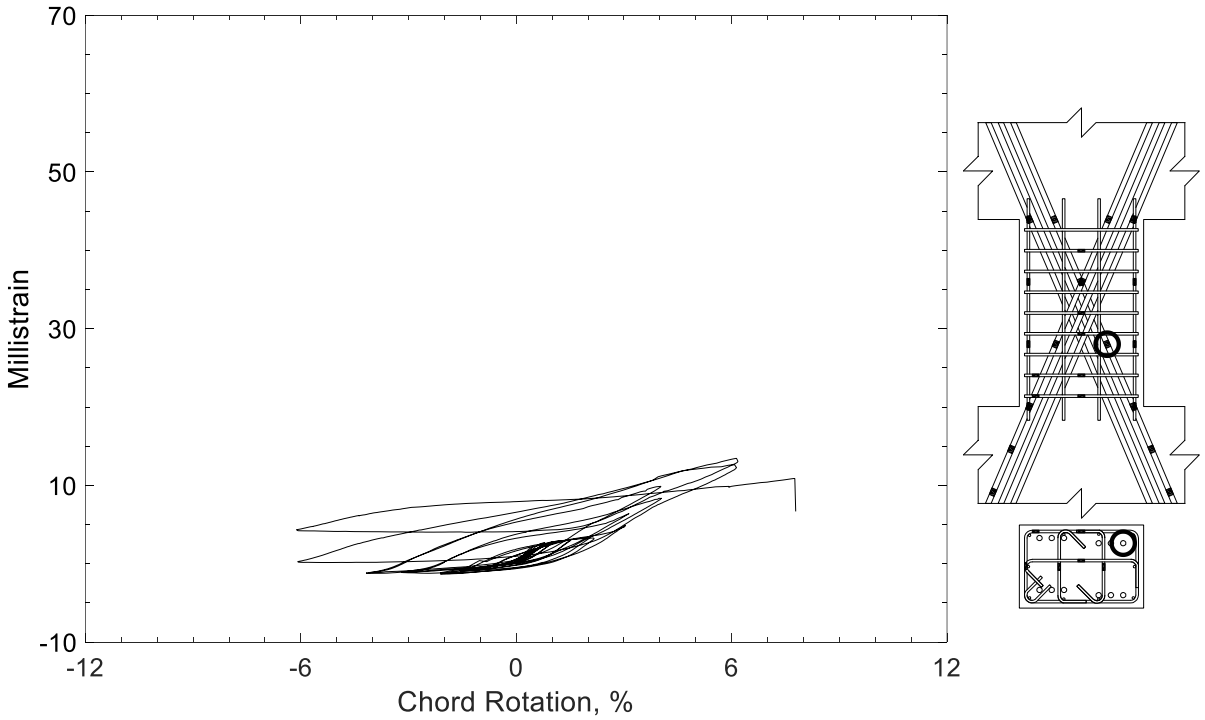

Figure 242 – Measured strain in diagonal bar of D80-1.5, strain gauge D8

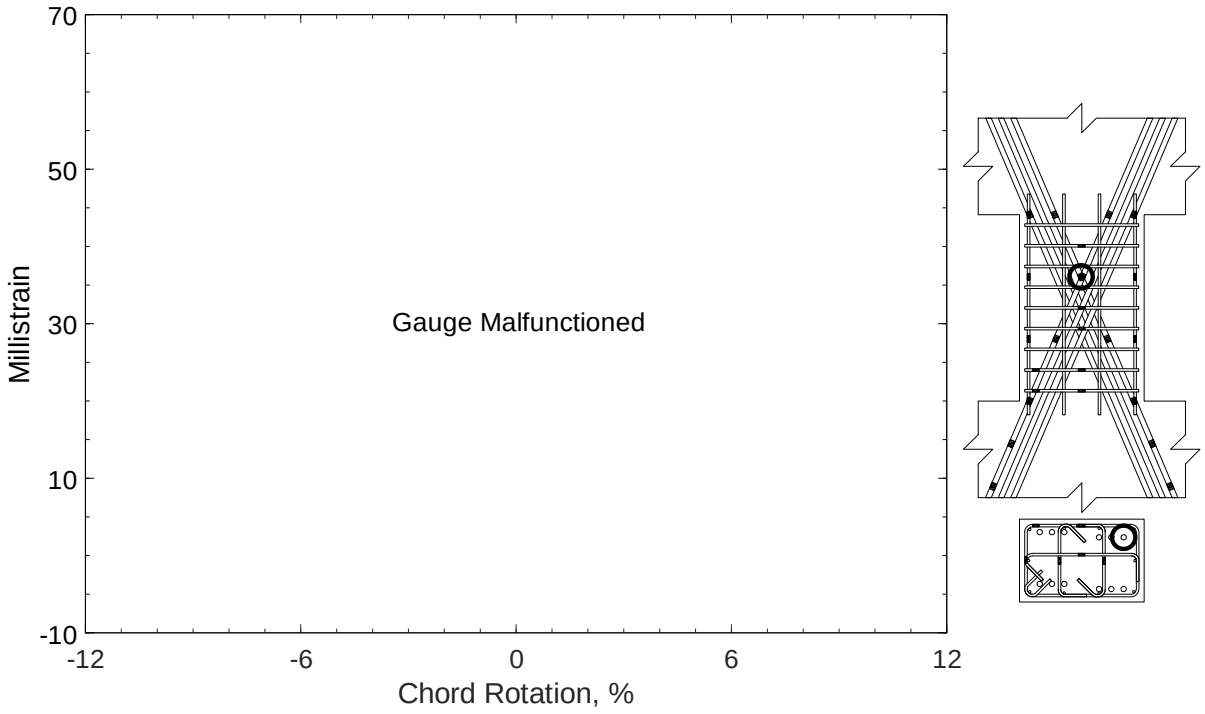

Figure 243 – Measured strain in diagonal bar of D80-1.5, strain gauge D9

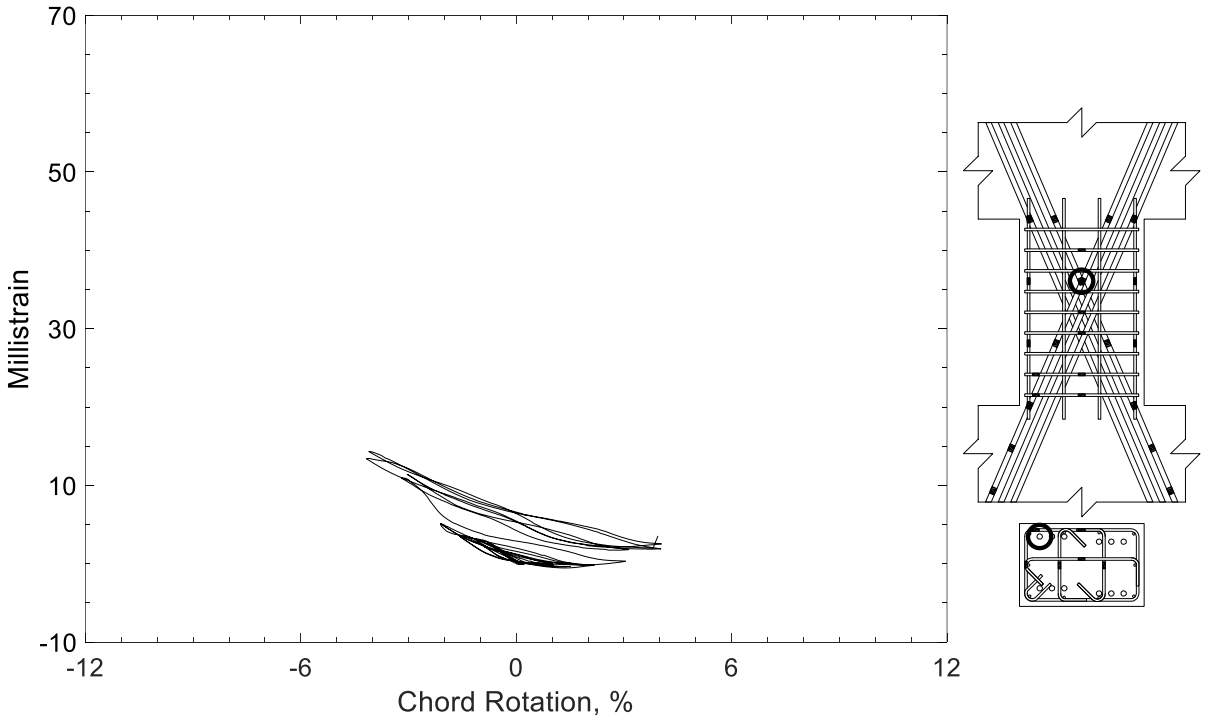

Figure 244 – Measured strain in diagonal bar of D80-1.5, strain gauge D10

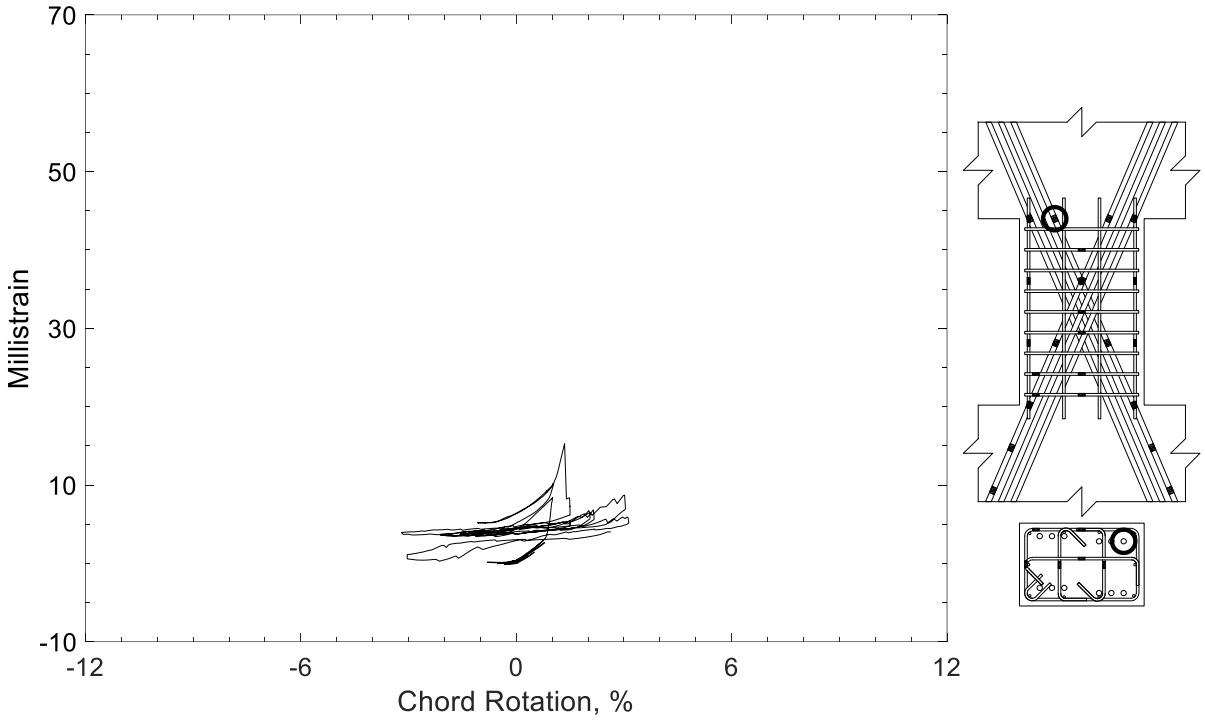

Figure 245 – Measured strain in diagonal bar of D80-1.5, strain gauge D11

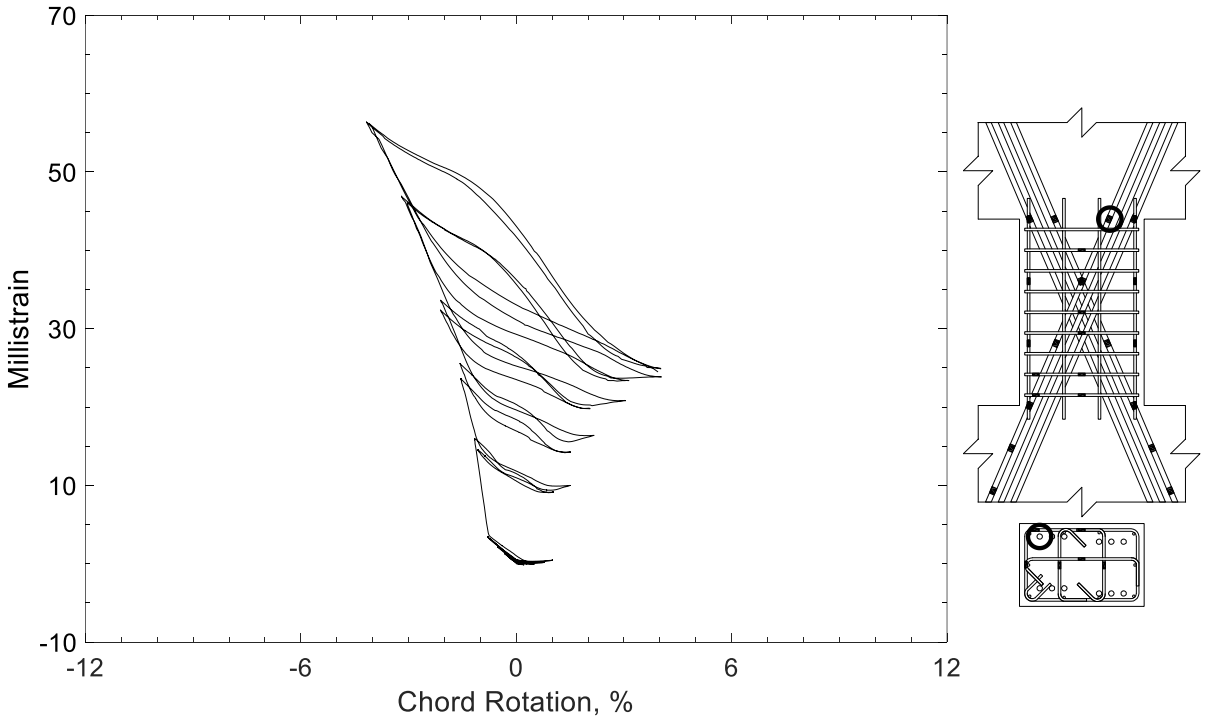

Figure 246 – Measured strain in diagonal bar of D80-1.5, strain gauge D12

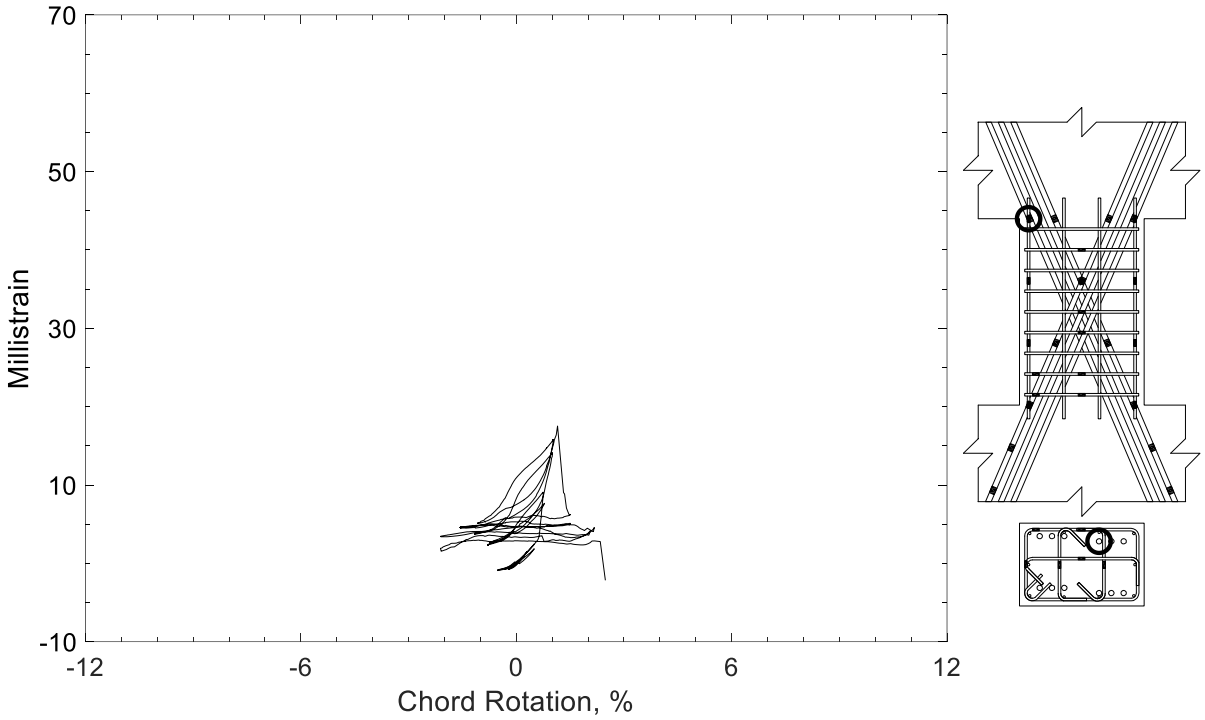

Figure 247 – Measured strain in diagonal bar of D80-1.5, strain gauge D13

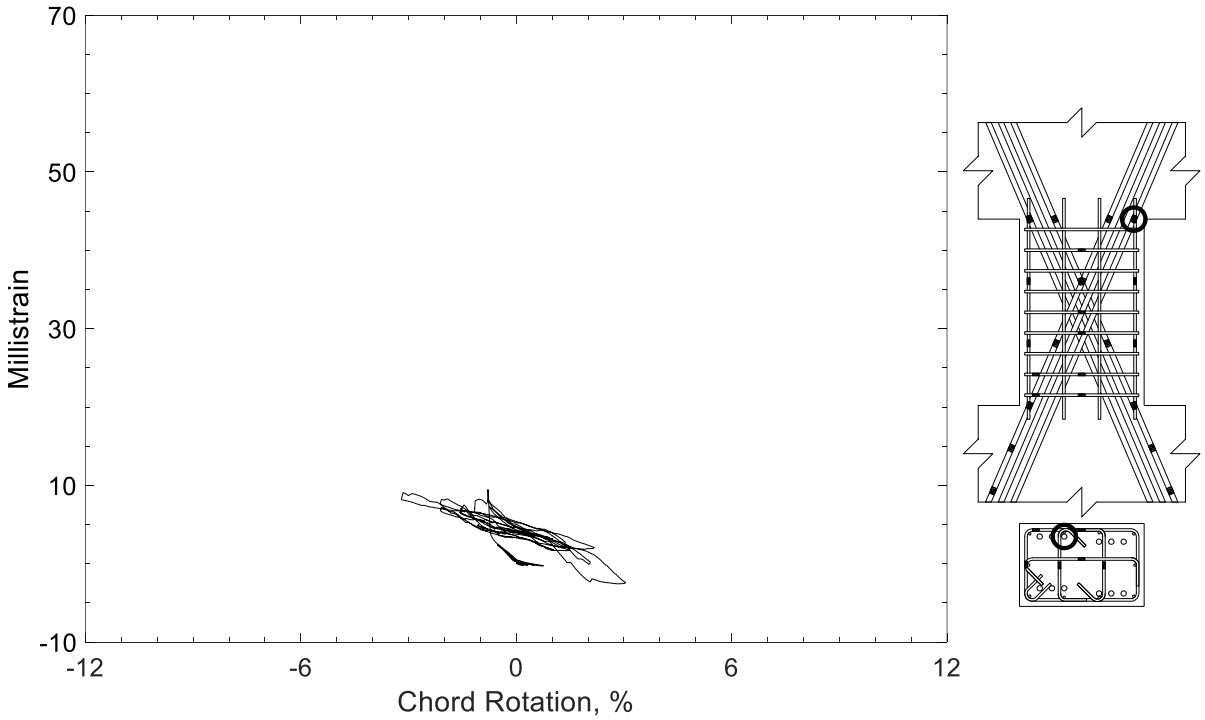

Figure 248 – Measured strain in diagonal bar of D80-1.5, strain gauge D14

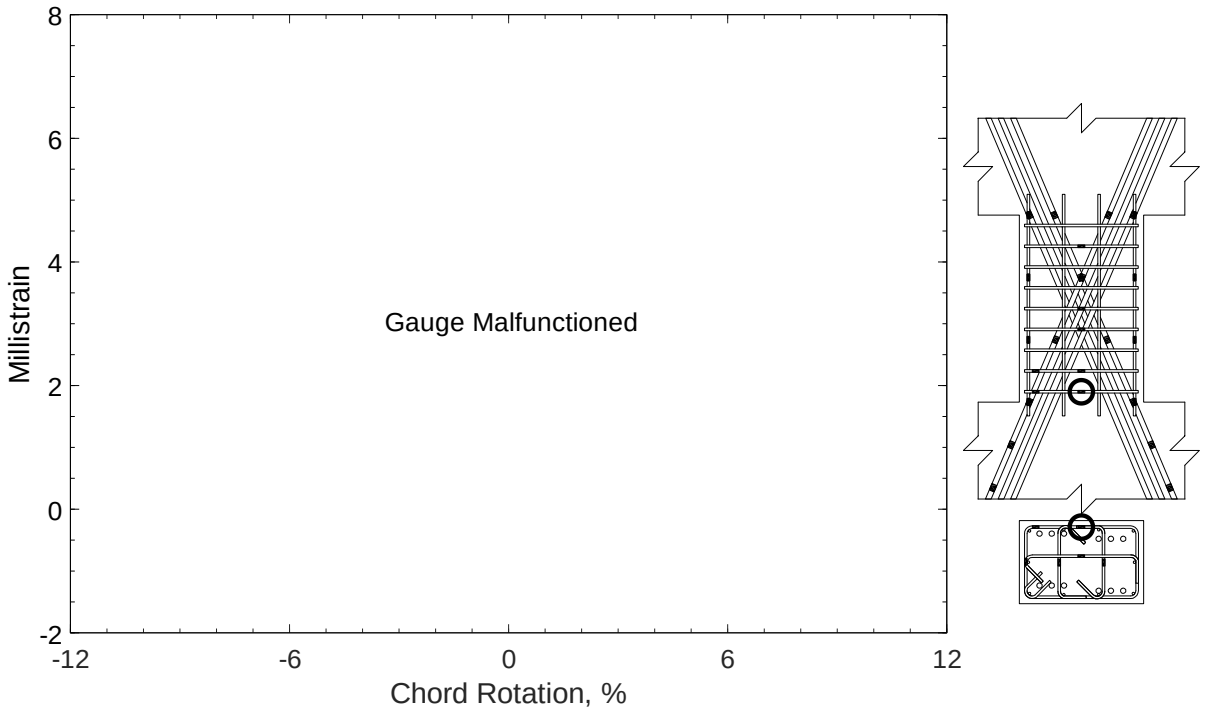

Figure 249 – Measured strain in closed stirrup of D80-1.5, strain gauge S1

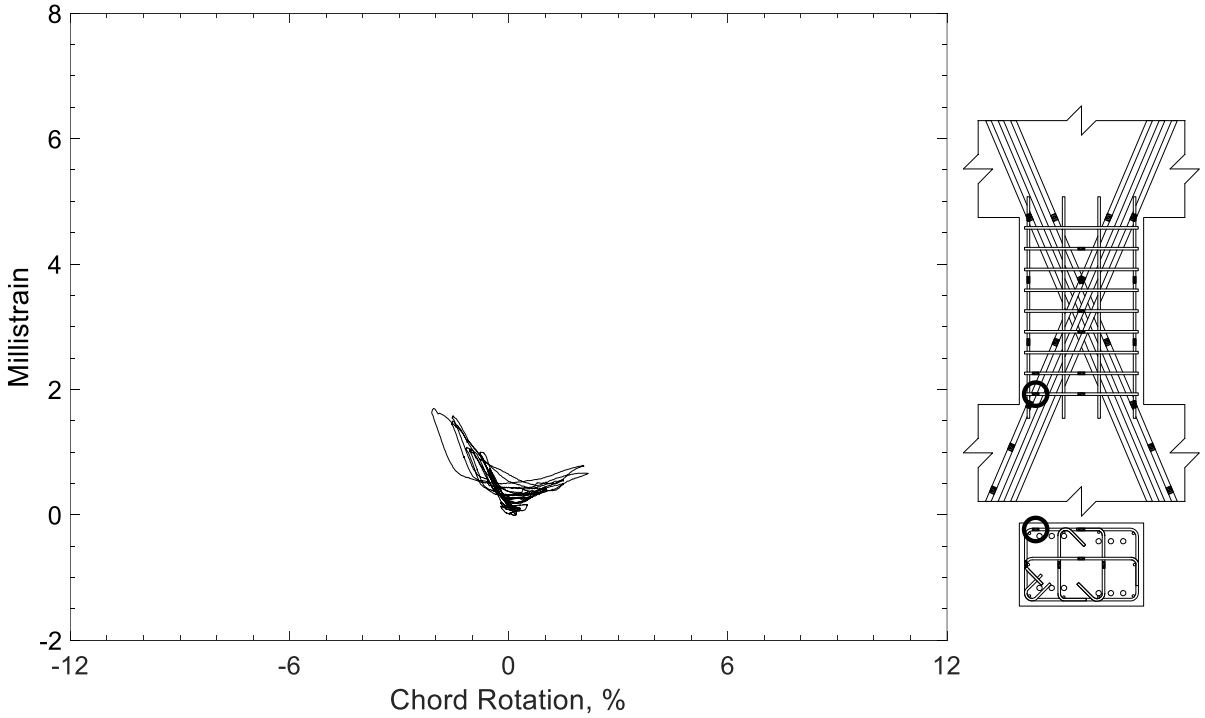

Figure 250 – Measured strain in closed stirrup of D80-1.5, strain gauge S2

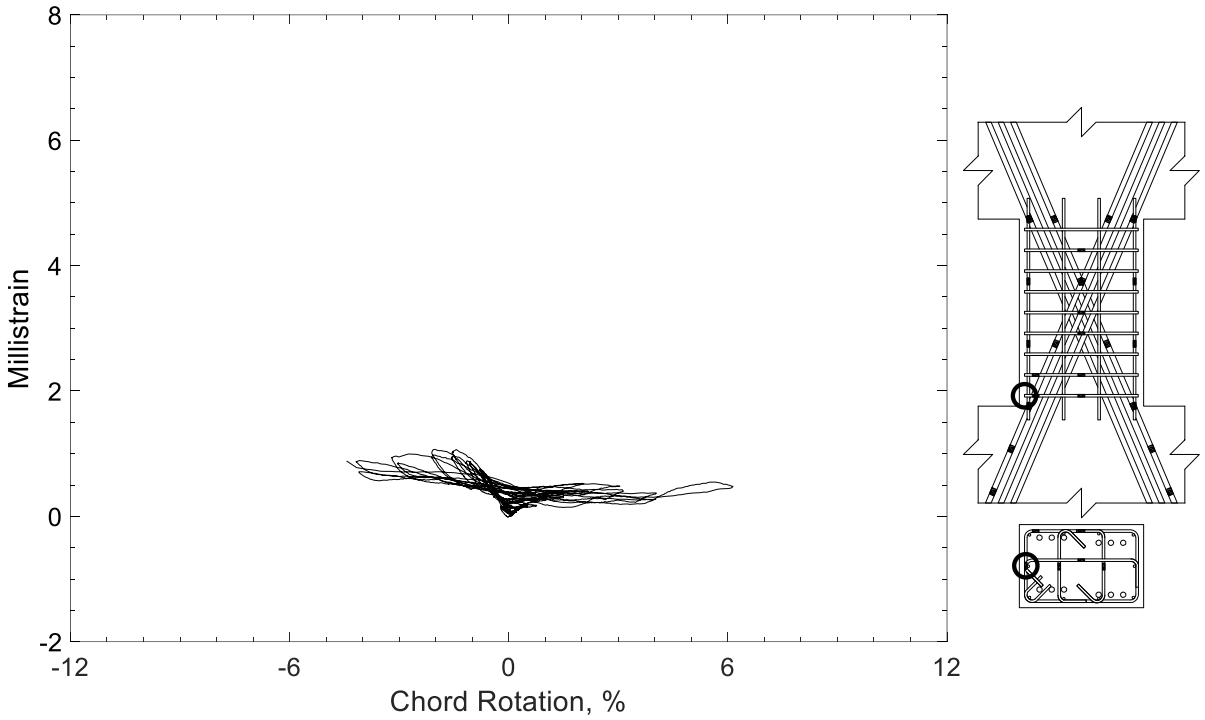

Figure 251 – Measured strain in closed stirrup of D80-1.5, strain gauge S3

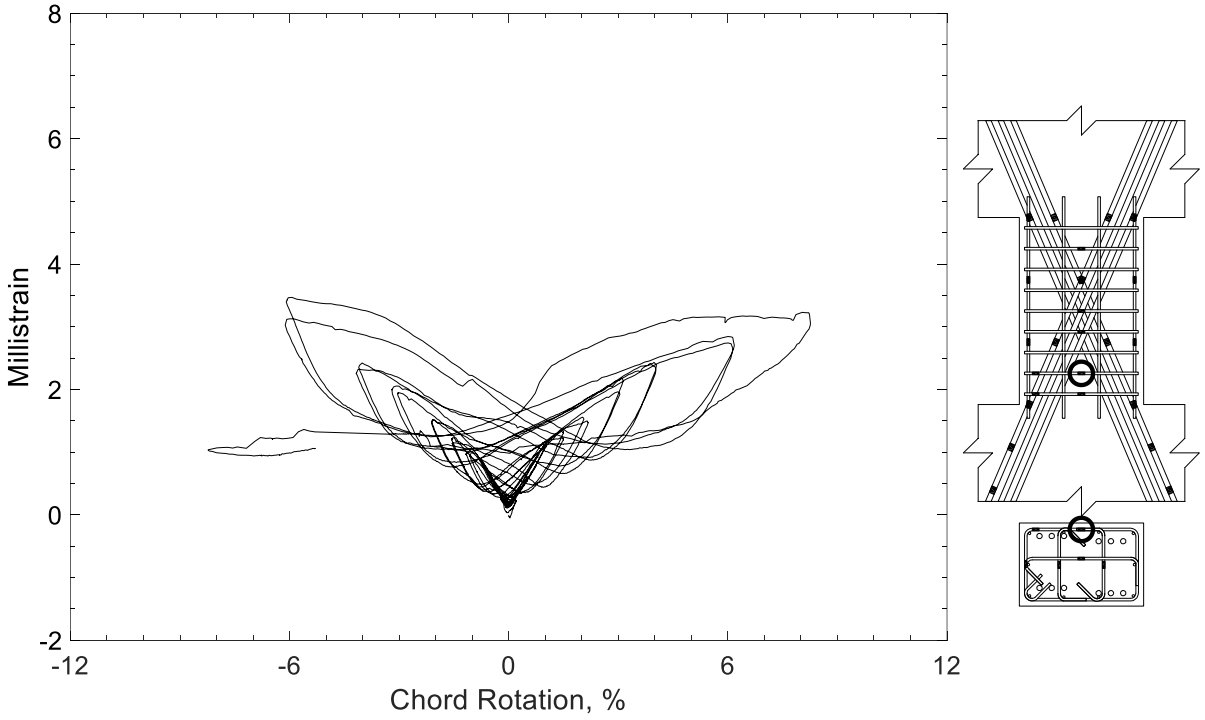

Figure 252 – Measured strain in closed stirrup of D80-1.5, strain gauge S4

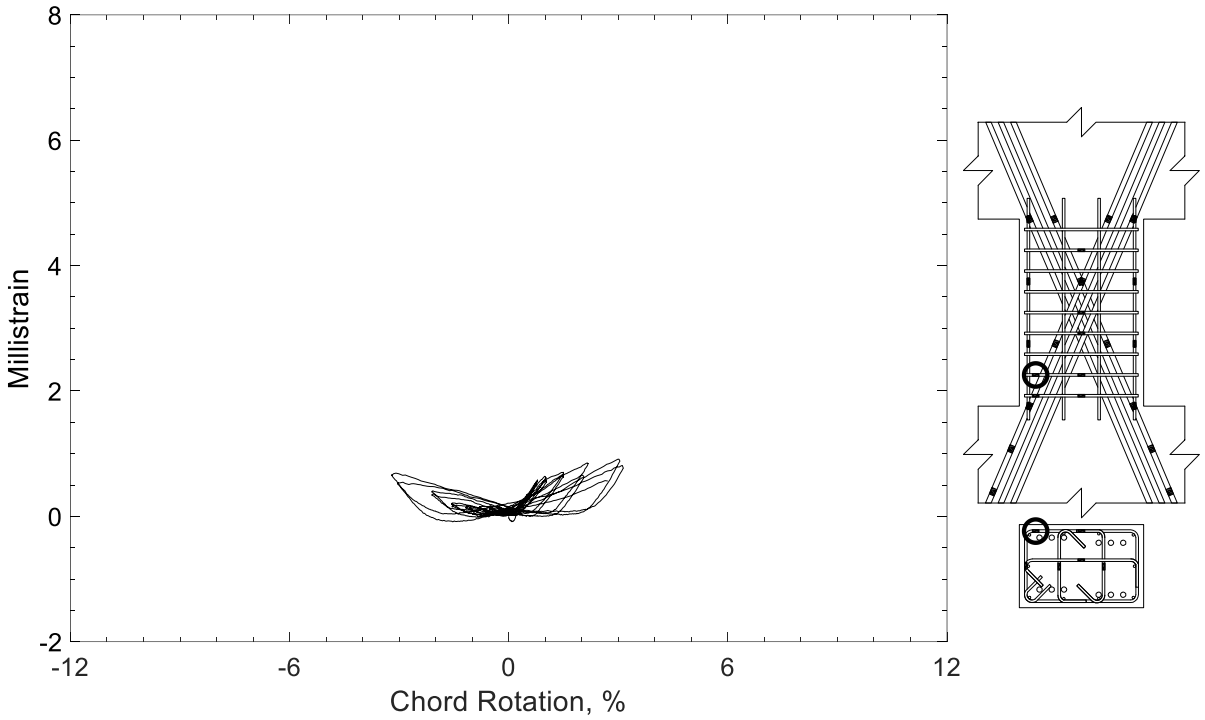

Figure 253 – Measured strain in closed stirrup of D80-1.5, strain gauge S5

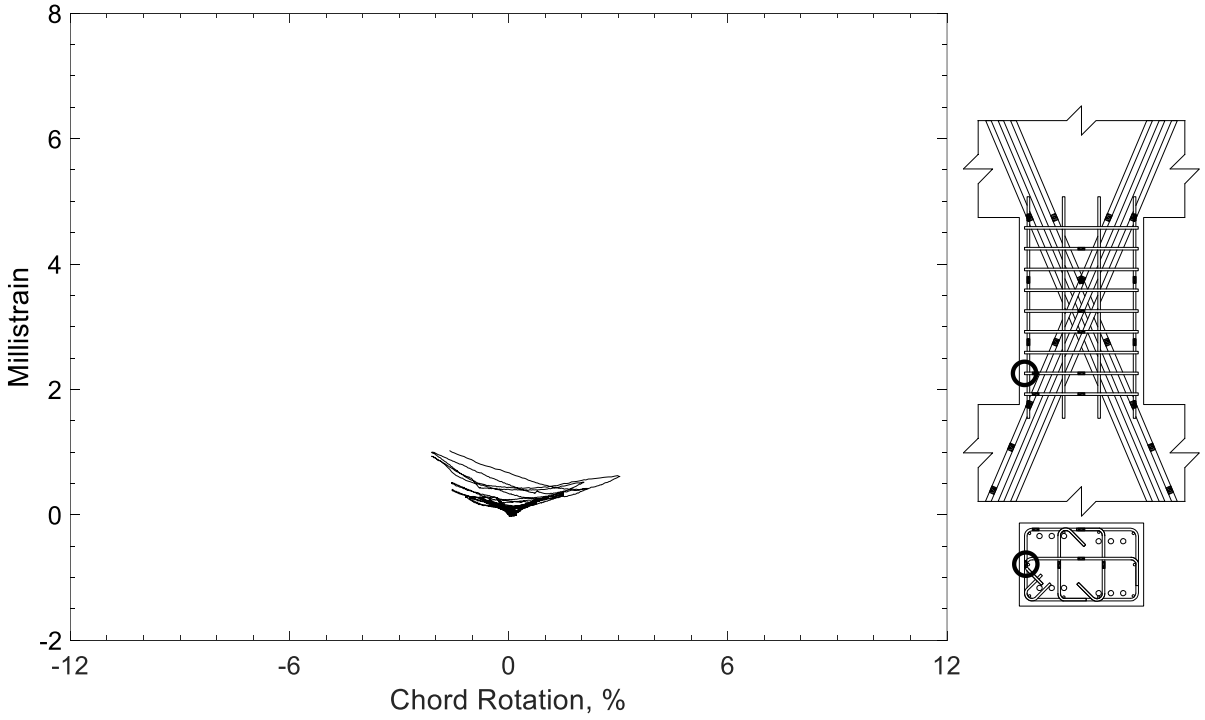

Figure 254 – Measured strain in closed stirrup of D80-1.5, strain gauge S6

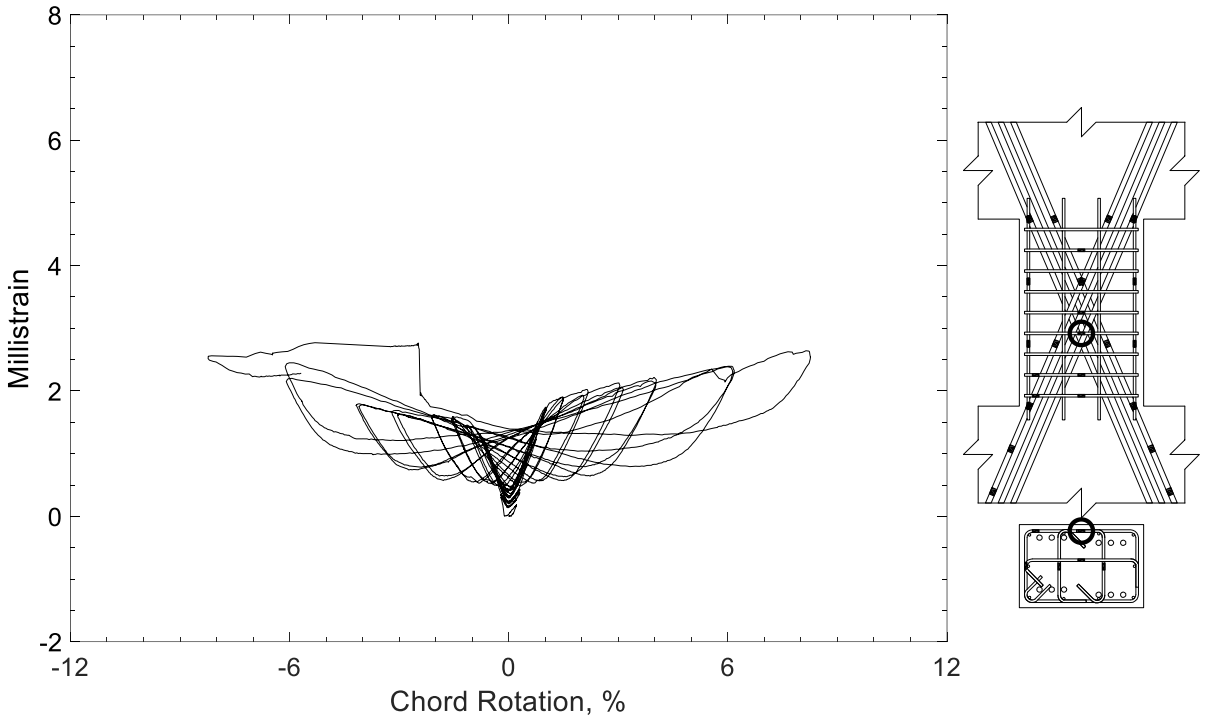

Figure 255 – Measured strain in closed stirrup of D80-1.5, strain gauge S7

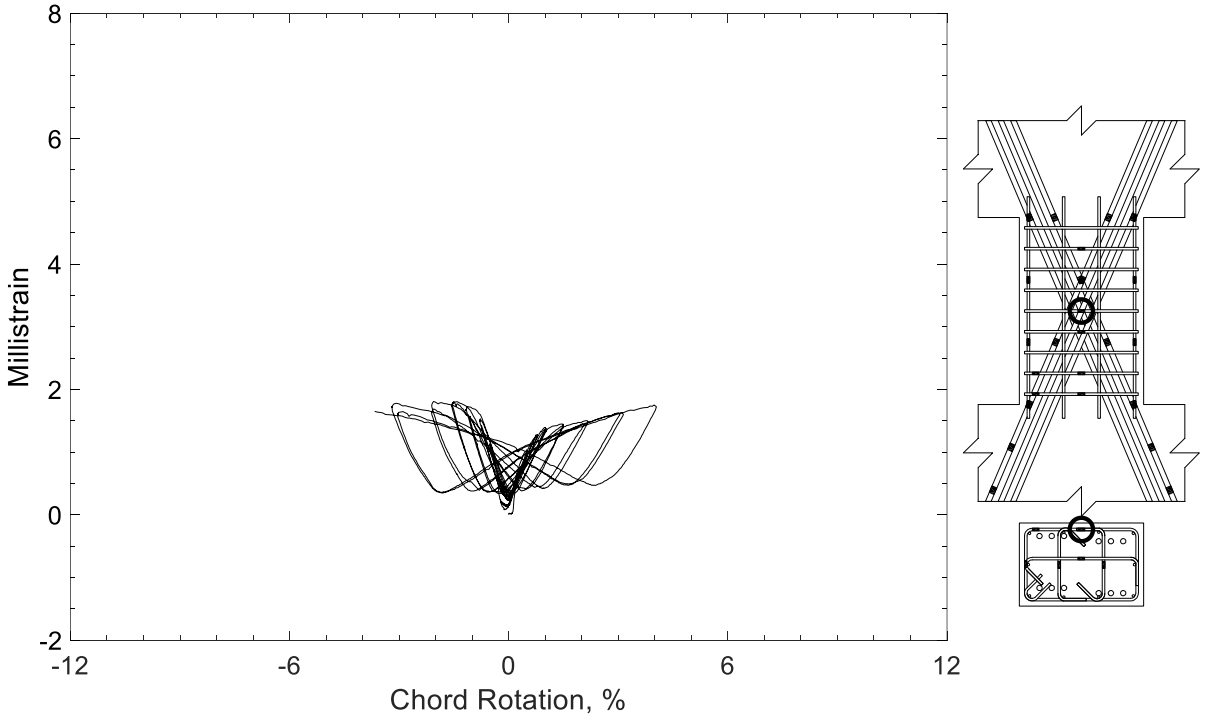

Figure 256 – Measured strain in closed stirrup of D80-1.5, strain gauge S8

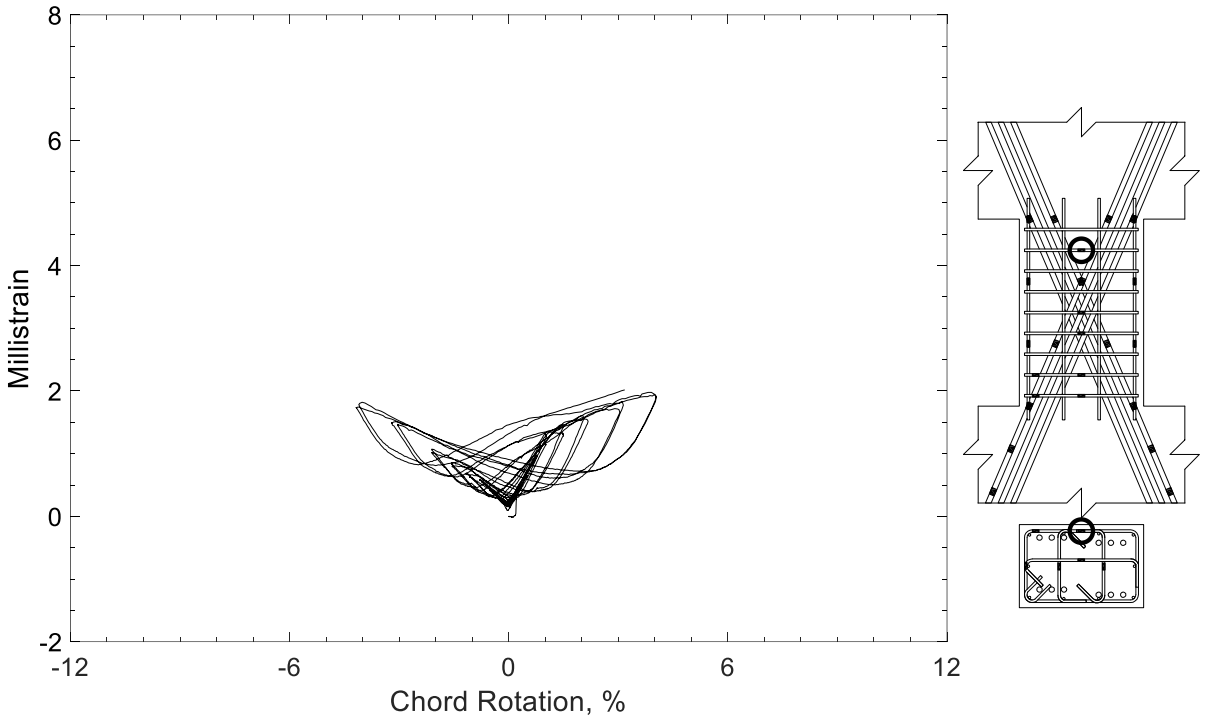

Figure 257 – Measured strain in closed stirrup of D80-1.5, strain gauge S9

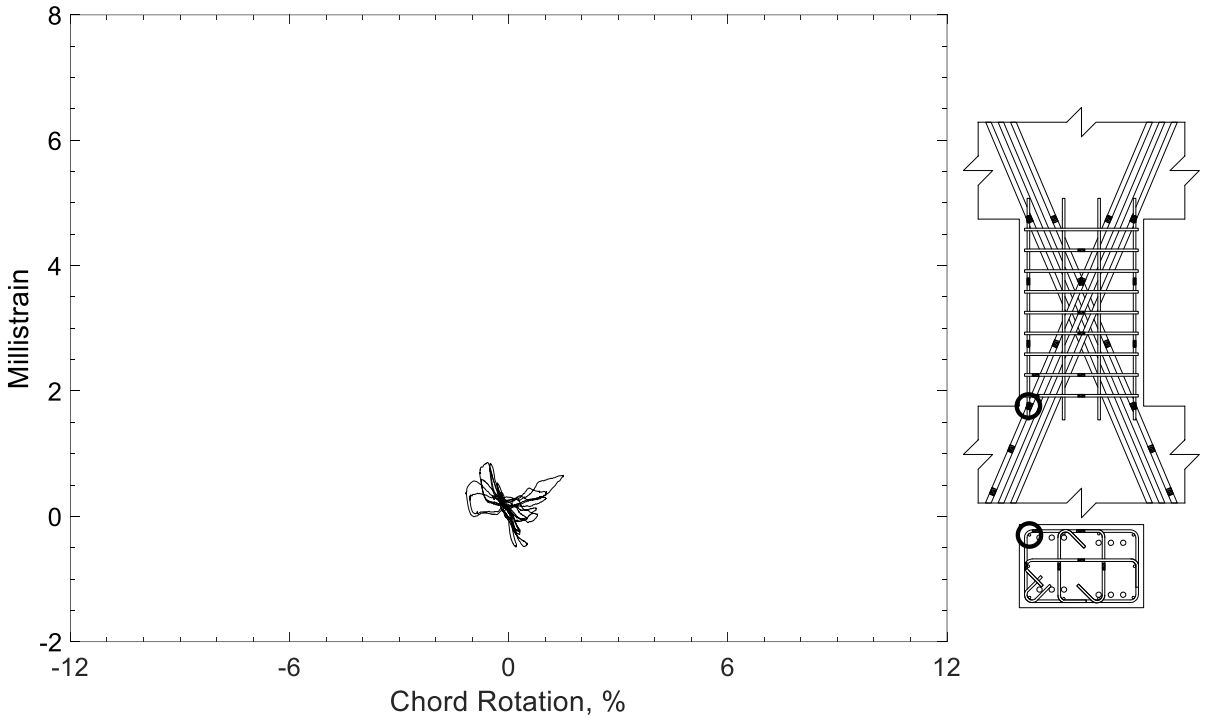

Figure 258 – Measured strain in parallel bar of D80-1.5, strain gauge H1

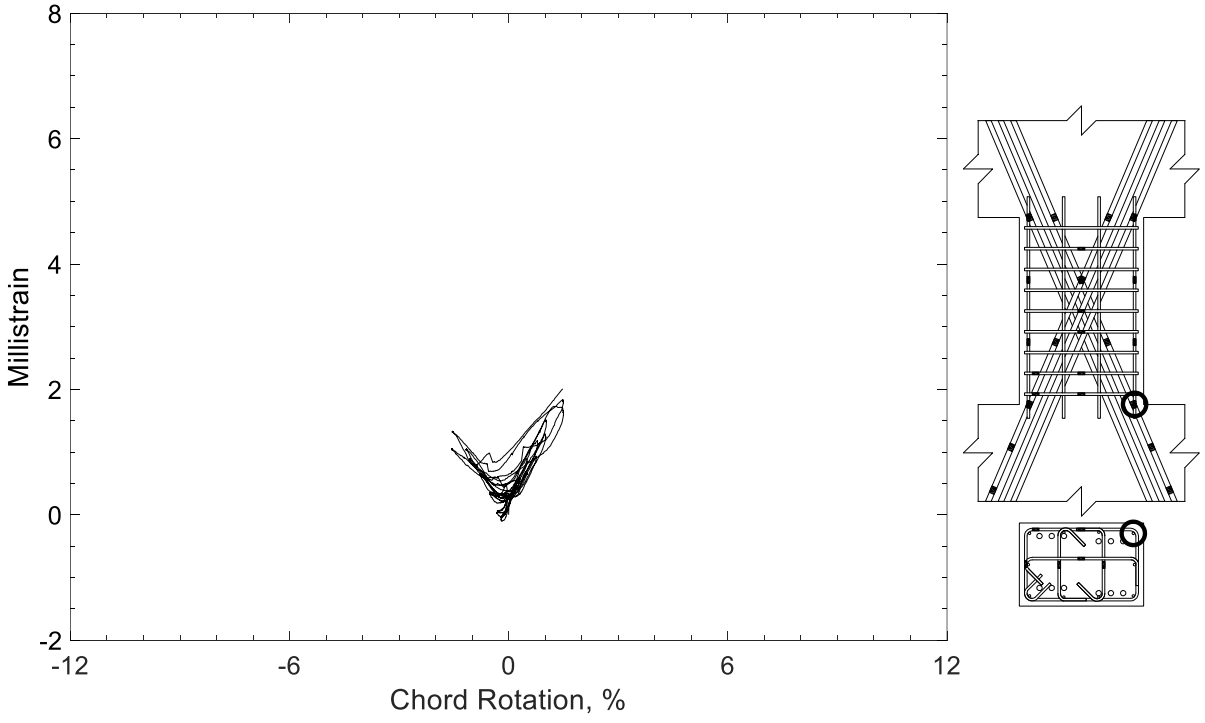

Figure 259 – Measured strain in parallel bar of D80-1.5, strain gauge H2

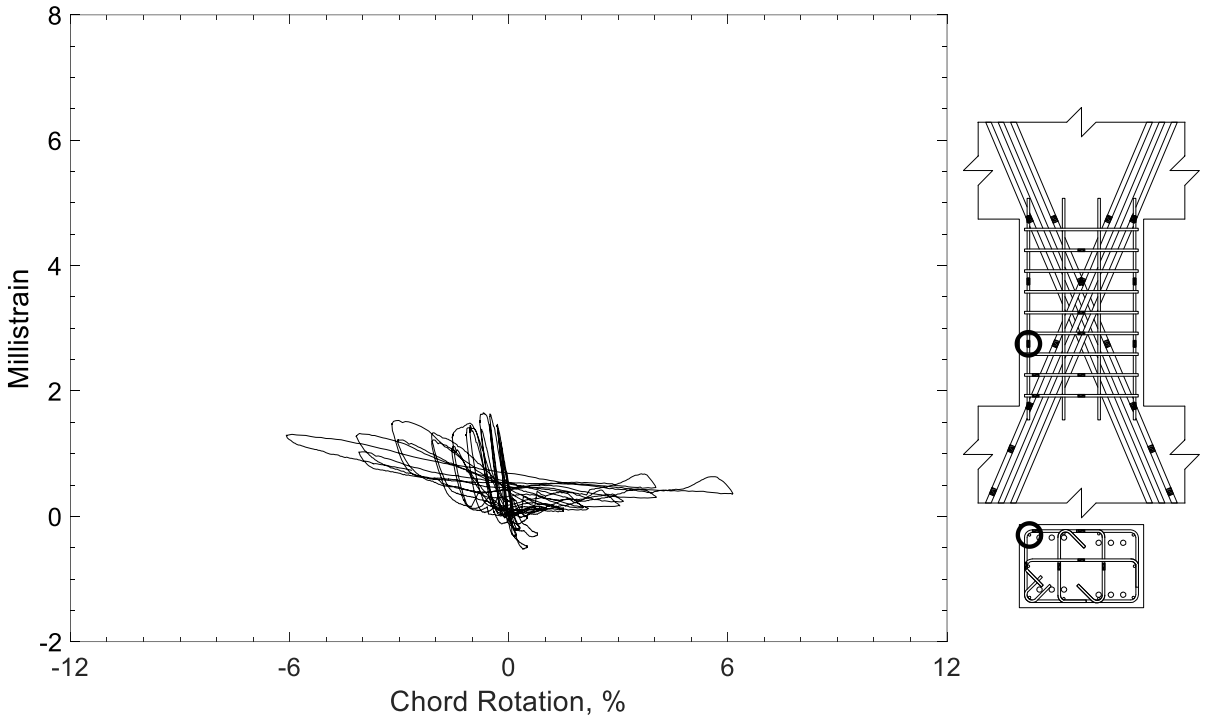

Figure 260 – Measured strain in parallel bar of D80-1.5, strain gauge H3

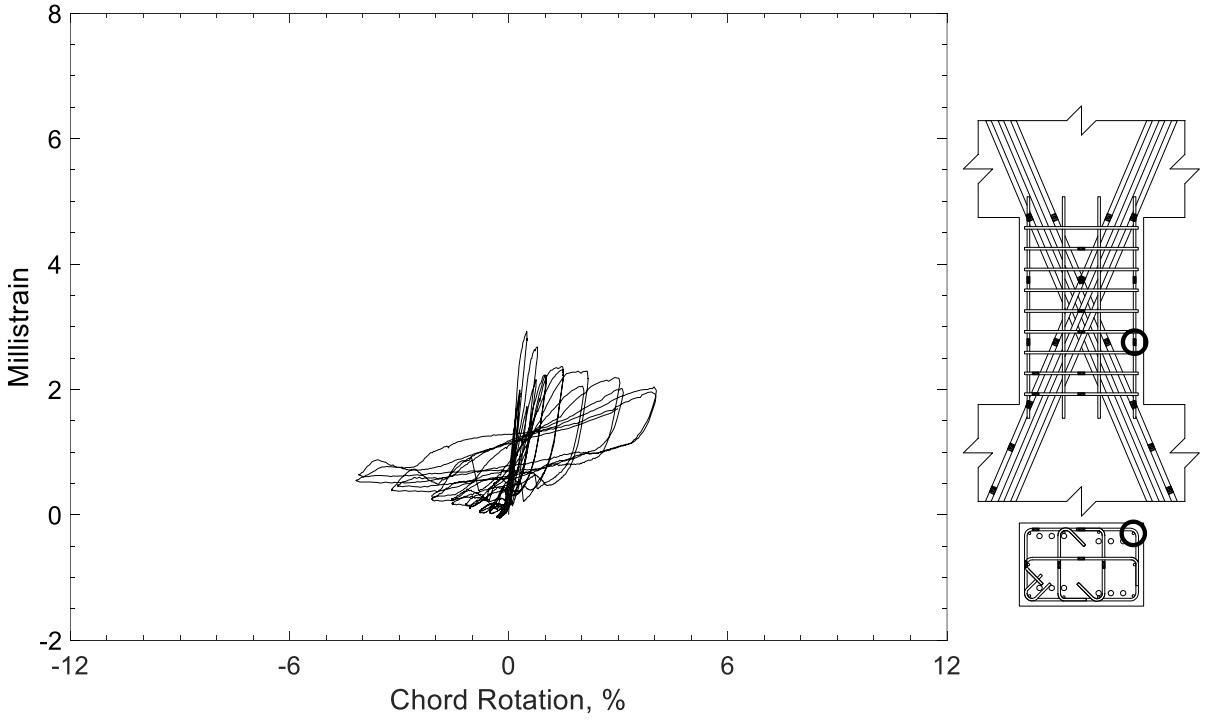

Figure 261 – Measured strain in parallel bar of D80-1.5, strain gauge H4

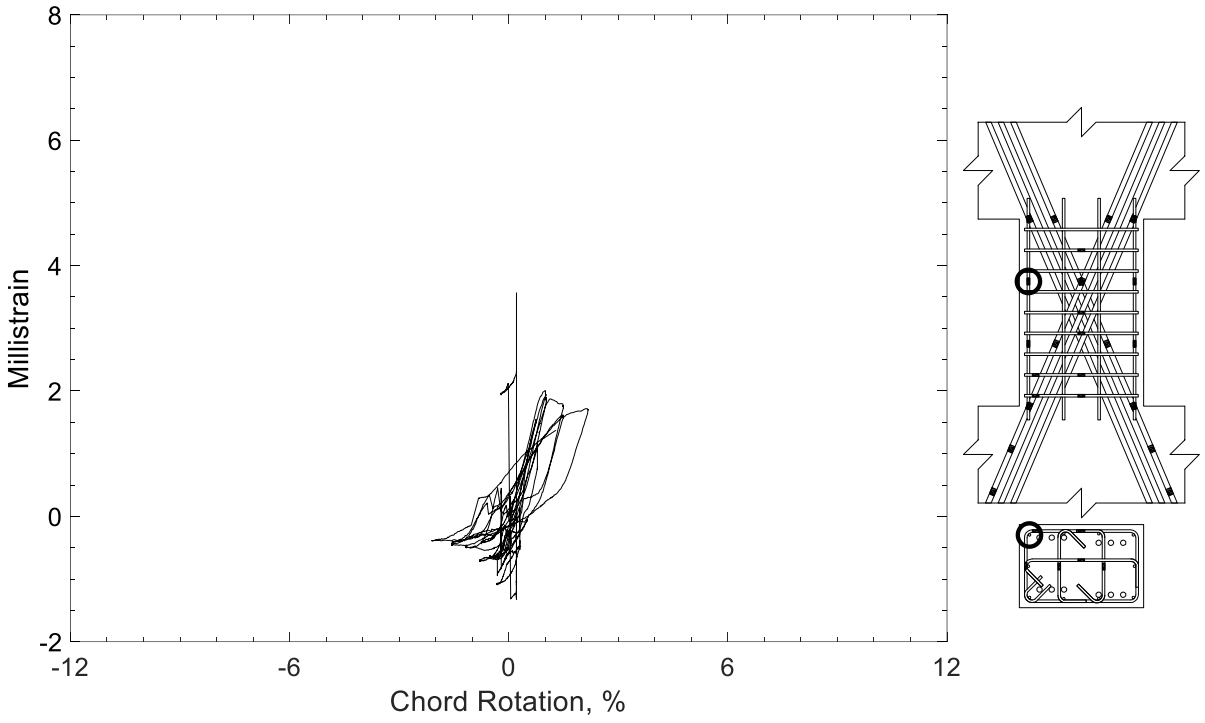

Figure 262 – Measured strain in parallel bar of D80-1.5, strain gauge H5

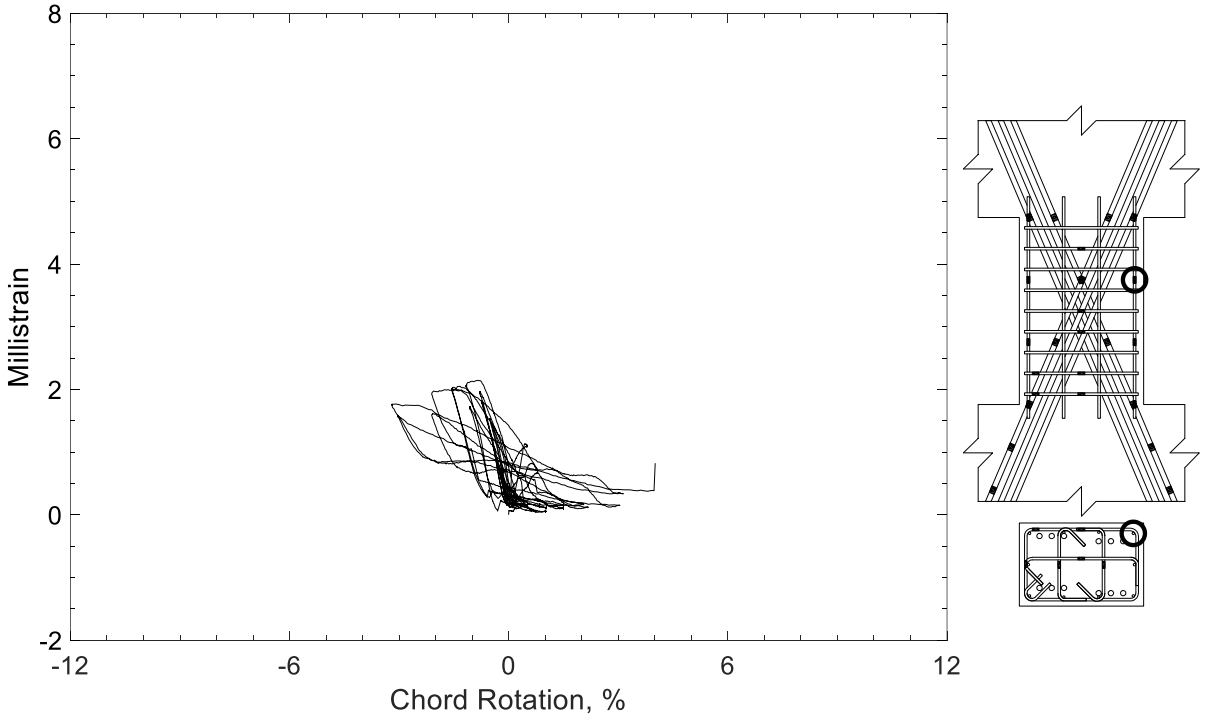

Figure 263 – Measured strain in parallel bar of D80-1.5, strain gauge H6

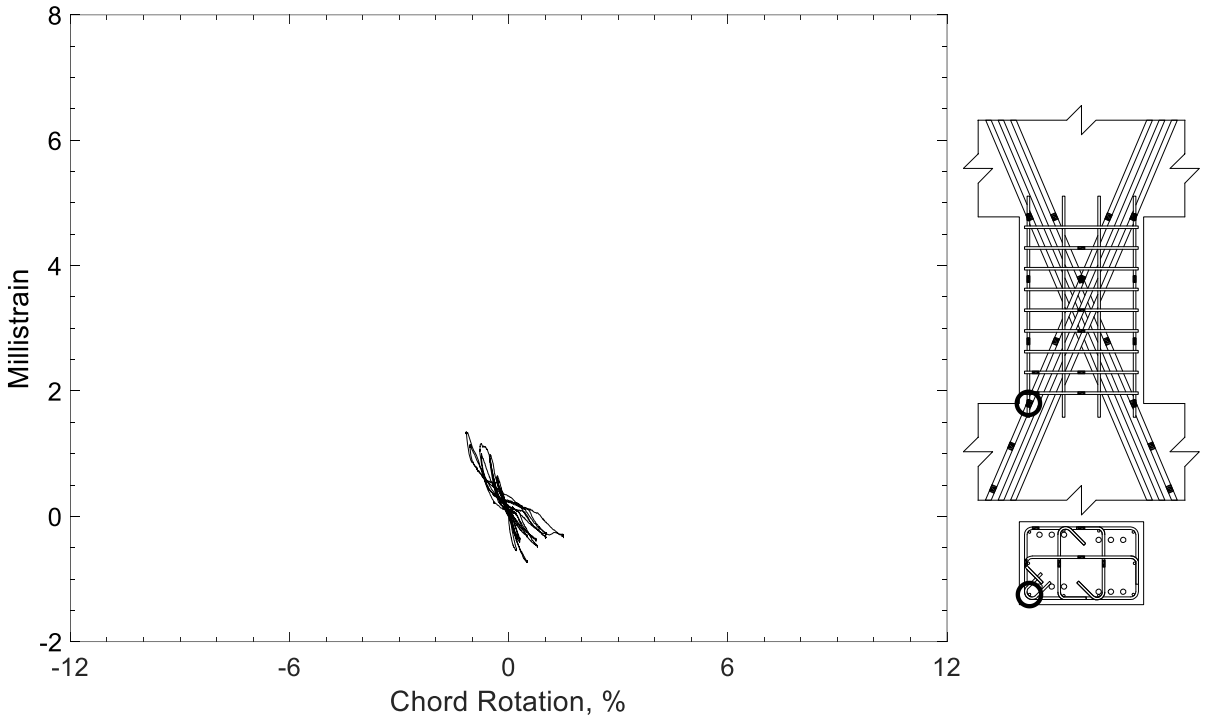

Figure 264 – Measured strain in parallel bar of D80-1.5, strain gauge H9

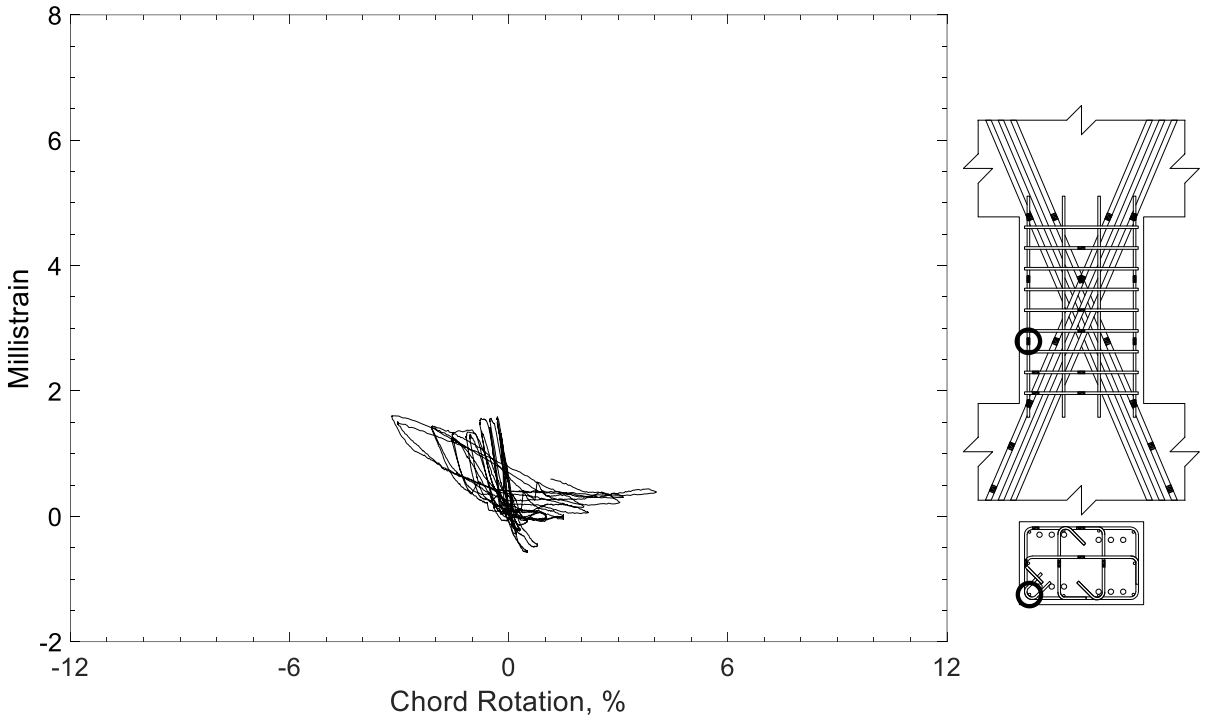

Figure 265 – Measured strain in parallel bar of D80-1.5, strain gauge H11

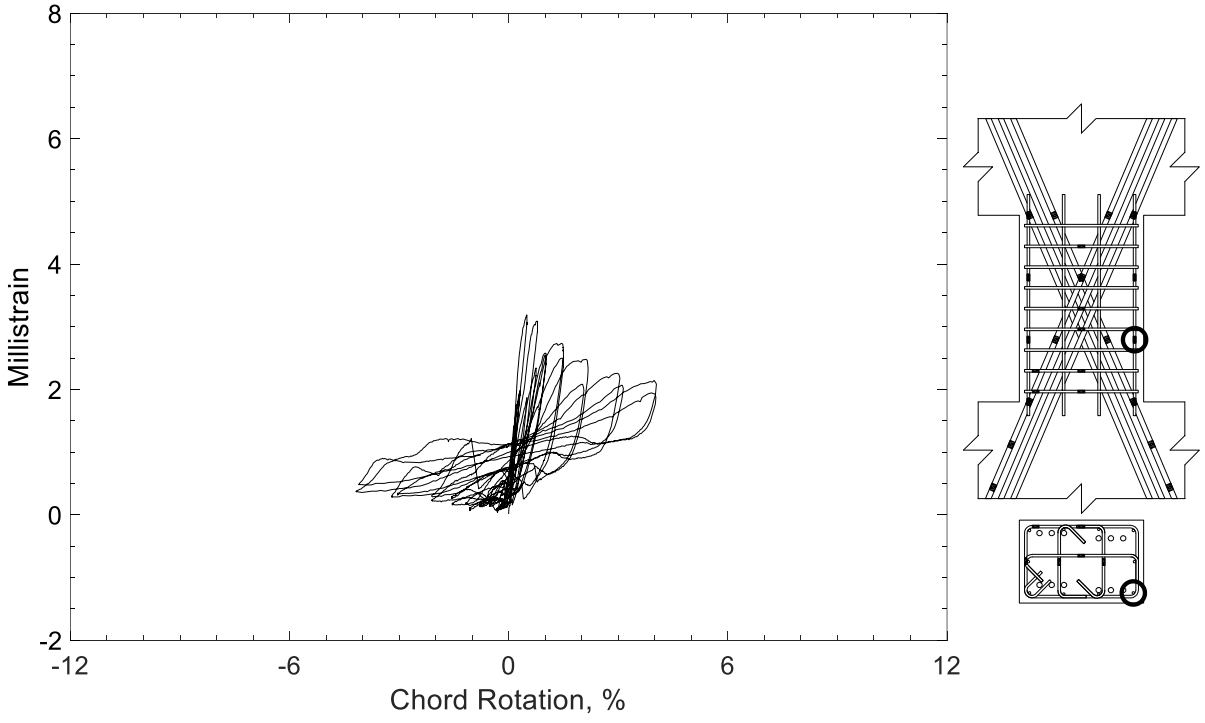

Figure 266 – Measured strain in parallel bar of D80-1.5, strain gauge H12

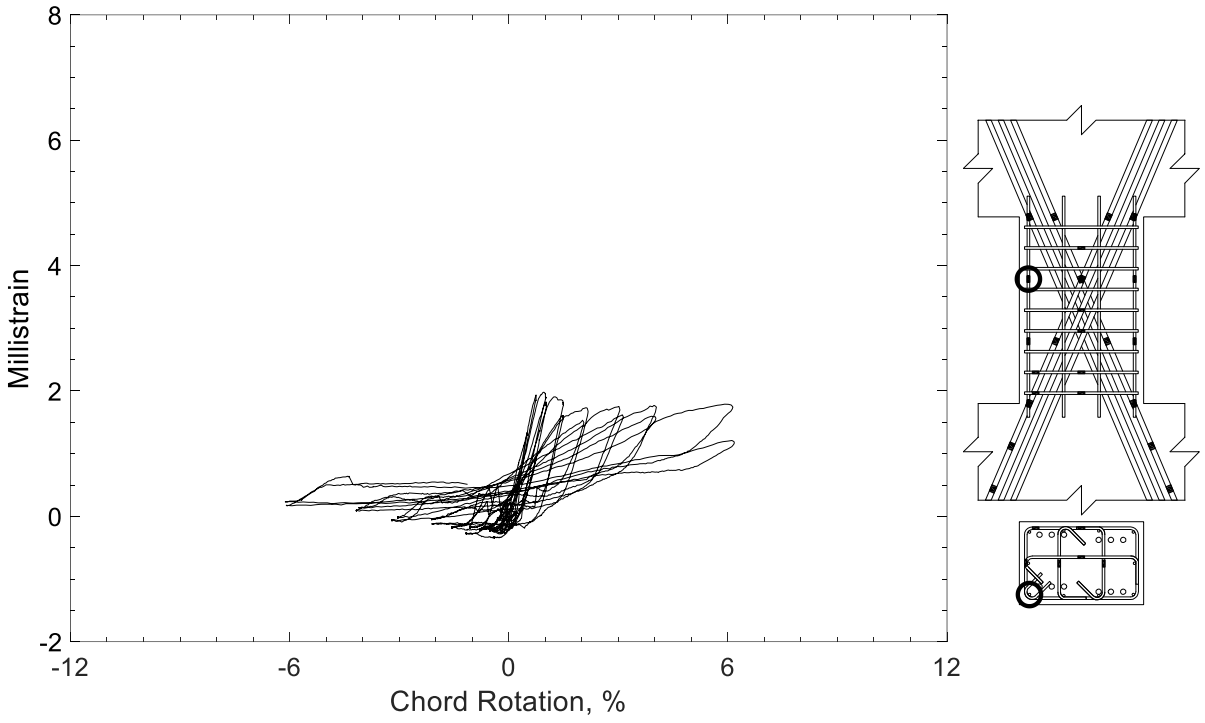

Figure 267 – Measured strain in parallel bar of D80-1.5, strain gauge H13

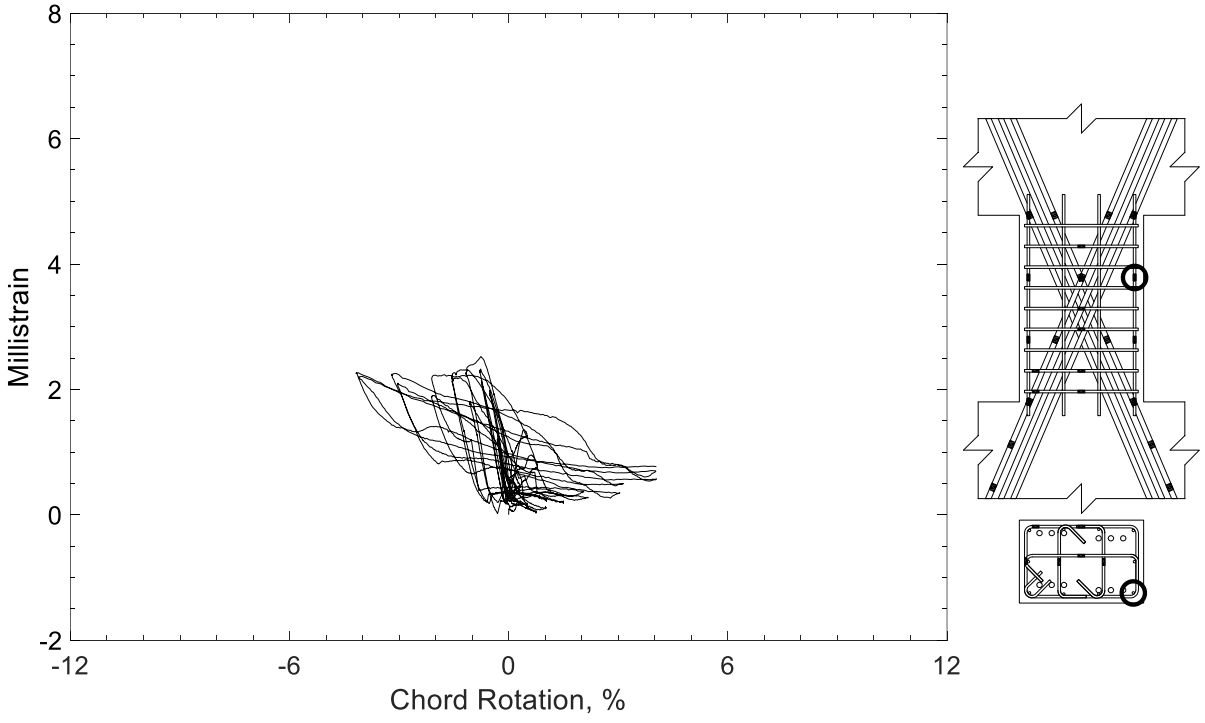

Figure 268 – Measured strain in parallel bar of D80-1.5, strain gauge H14

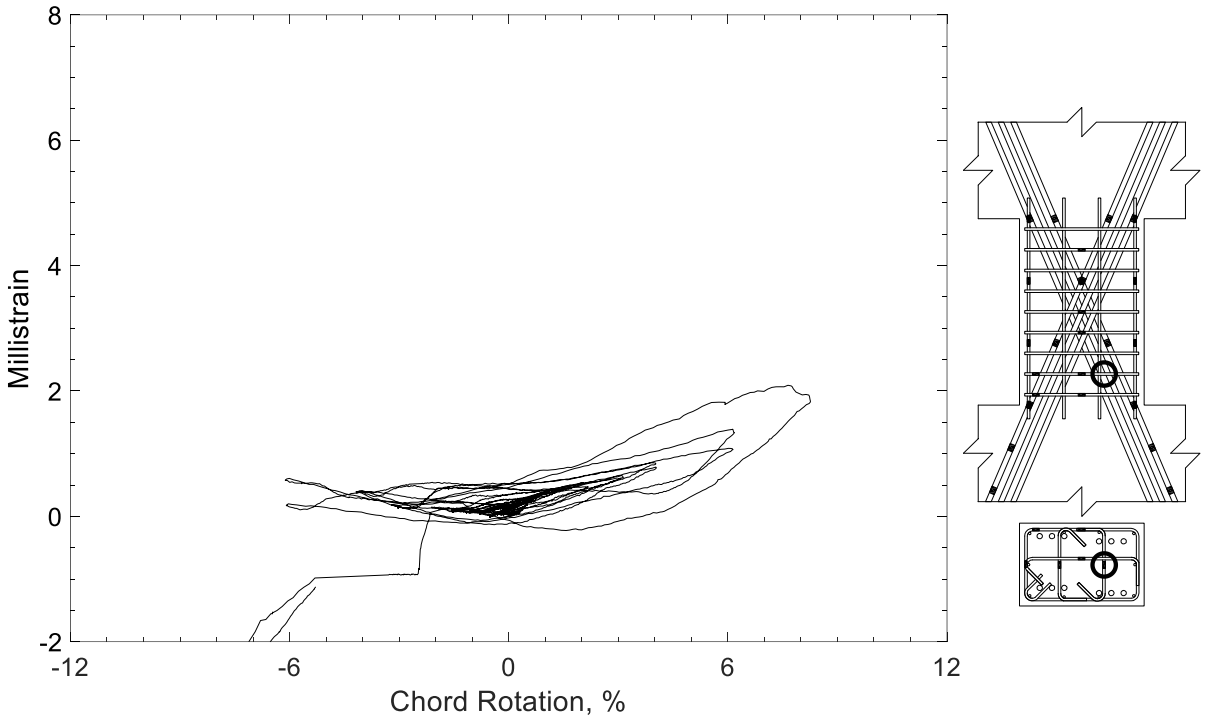

Figure 269 – Measured strain in crosstie of D80-1.5, strain gauge T1

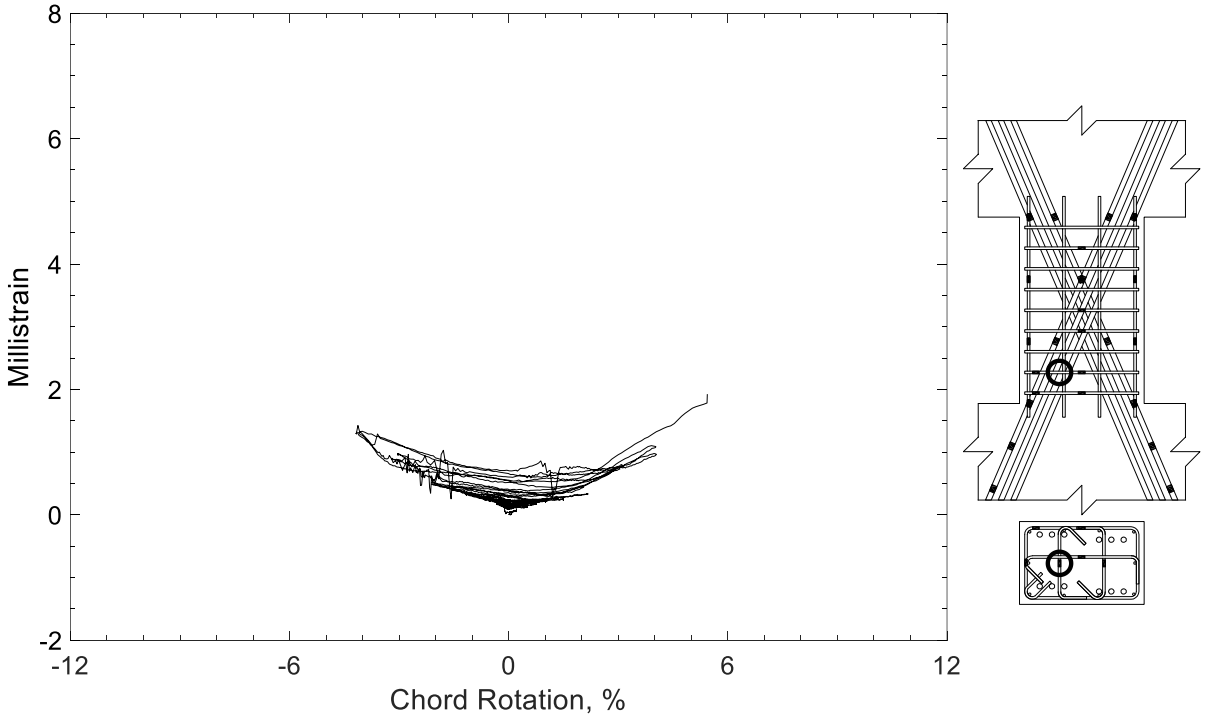

Figure 270 – Measured strain in crosstie of D80-1.5, strain gauge T2

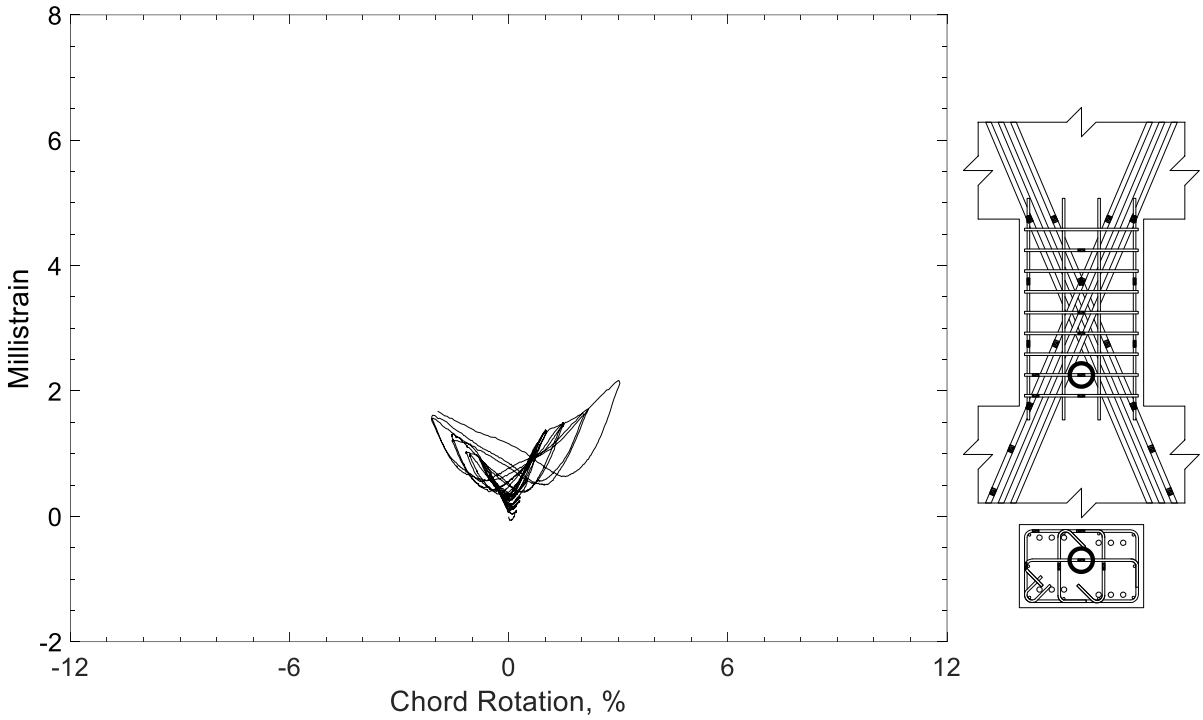

Figure 271 – Measured strain in crosstie of D80-1.5, strain gauge T3

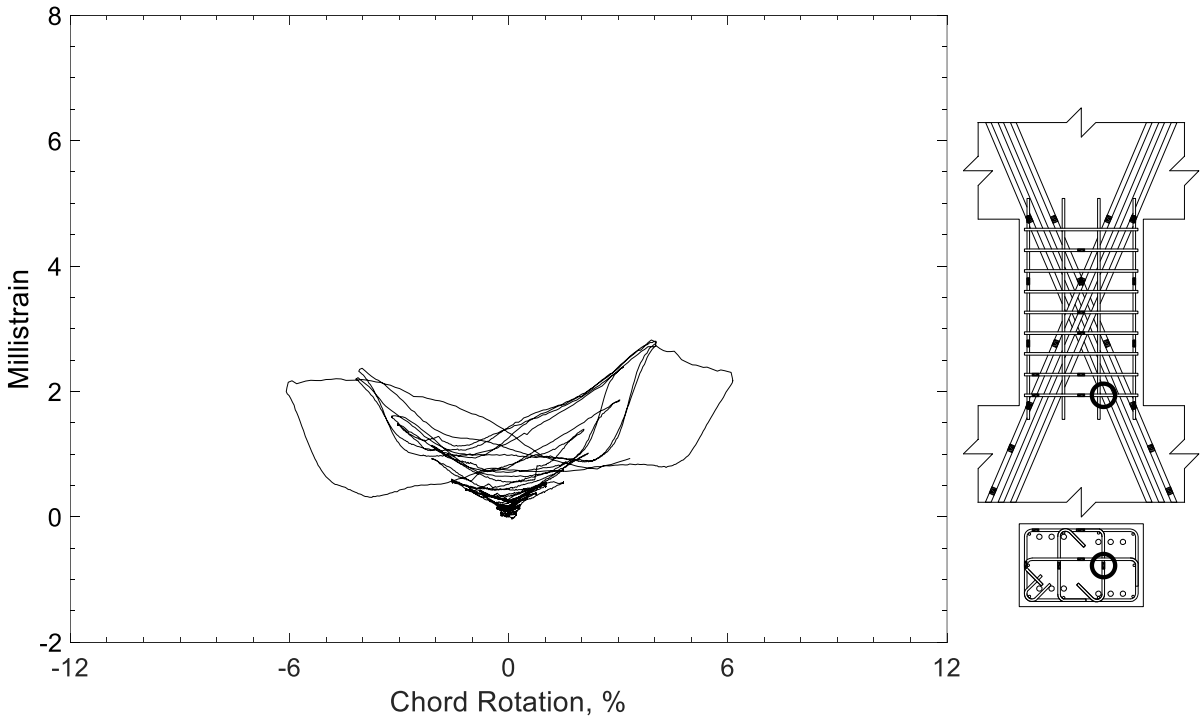

Figure 272 – Measured strain in crosstie of D80-1.5, strain gauge T4

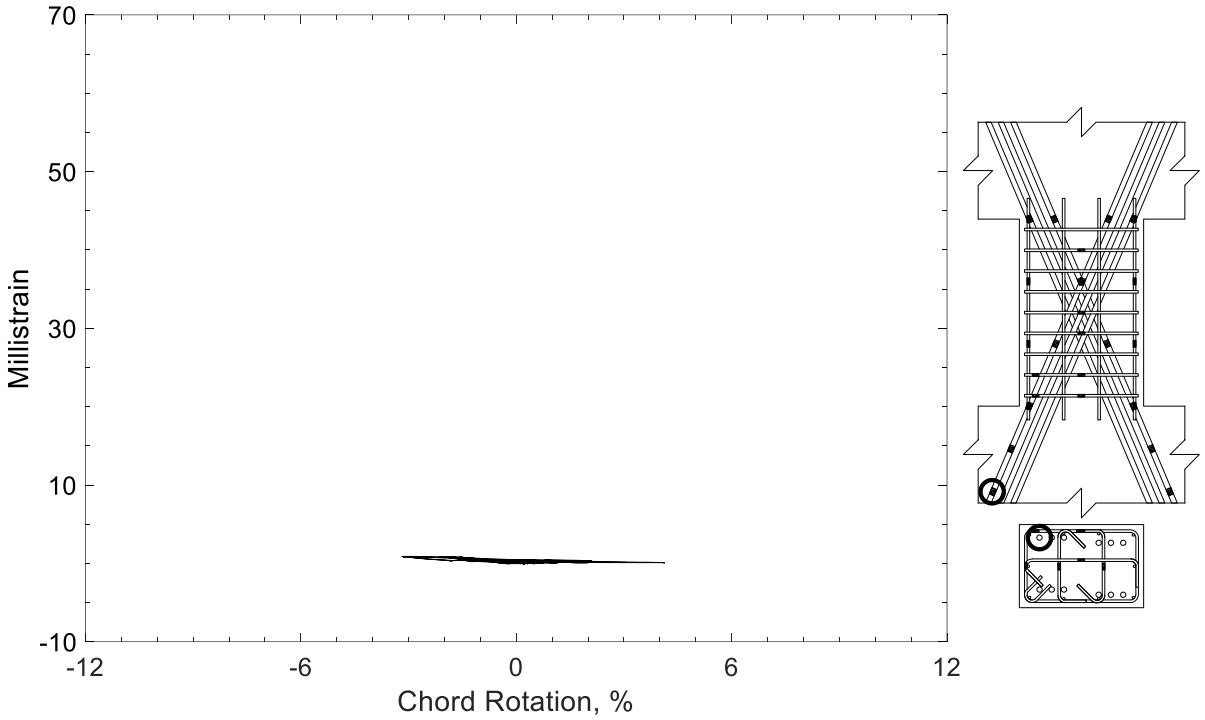

Figure 273 – Measured strain in diagonal bar of D100-1.5, strain gauge D1

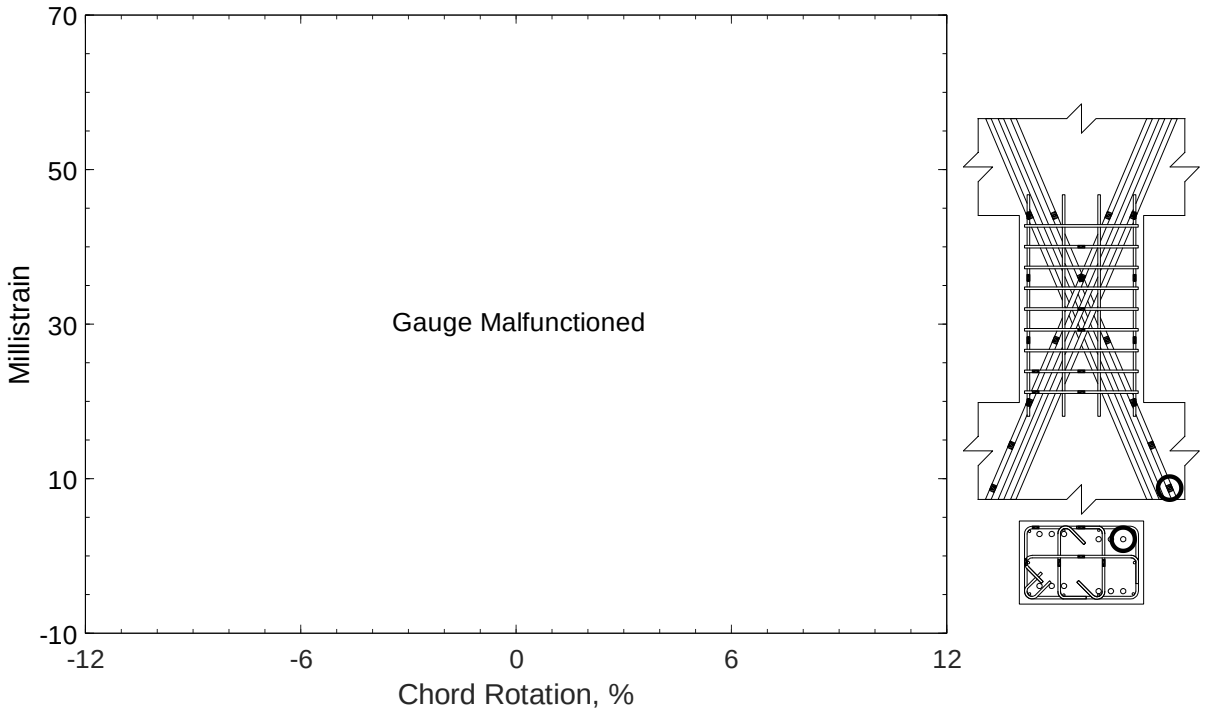

Figure 274 – Measured strain in diagonal bar of D100-1.5, strain gauge D2

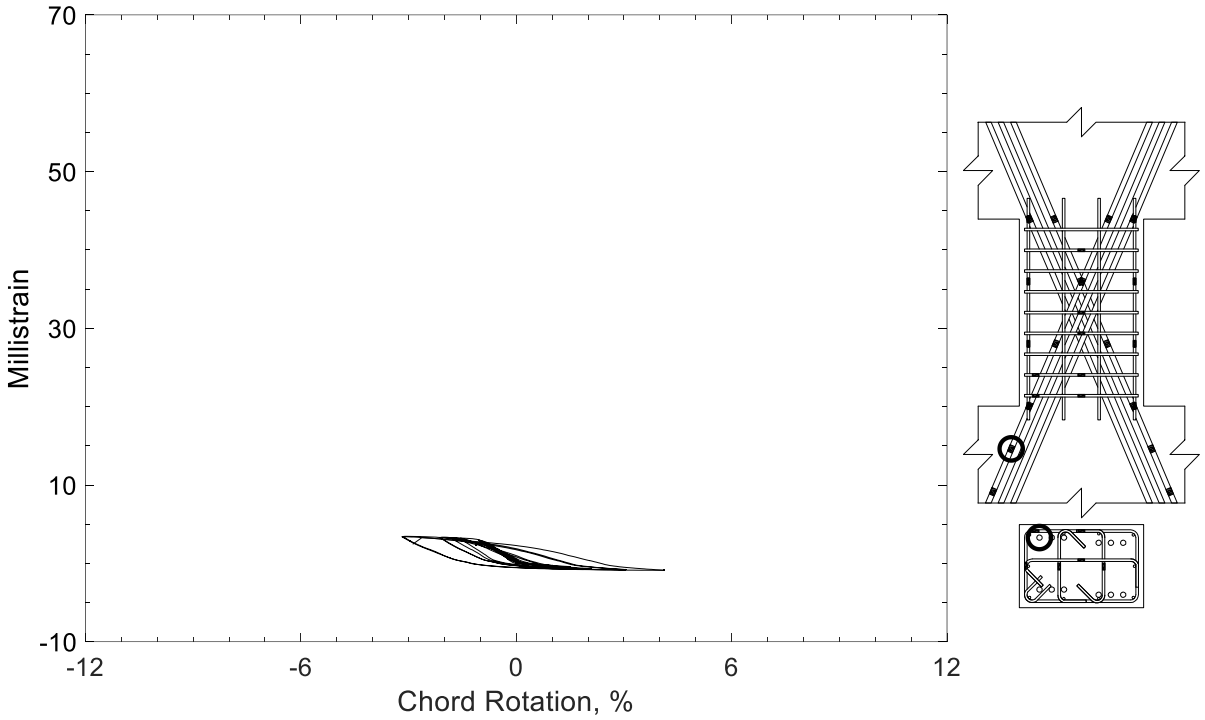

Figure 275 – Measured strain in diagonal bar of D100-1.5, strain gauge D3

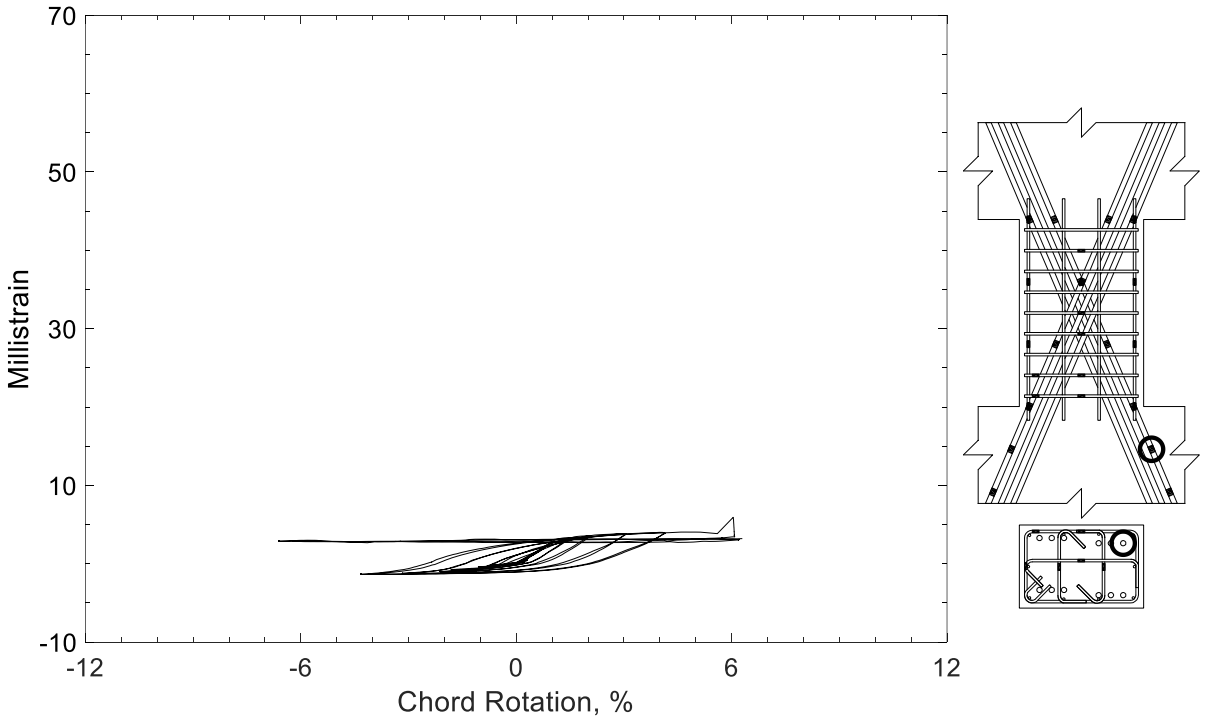

Figure 276 – Measured strain in diagonal bar of D100-1.5, strain gauge D4

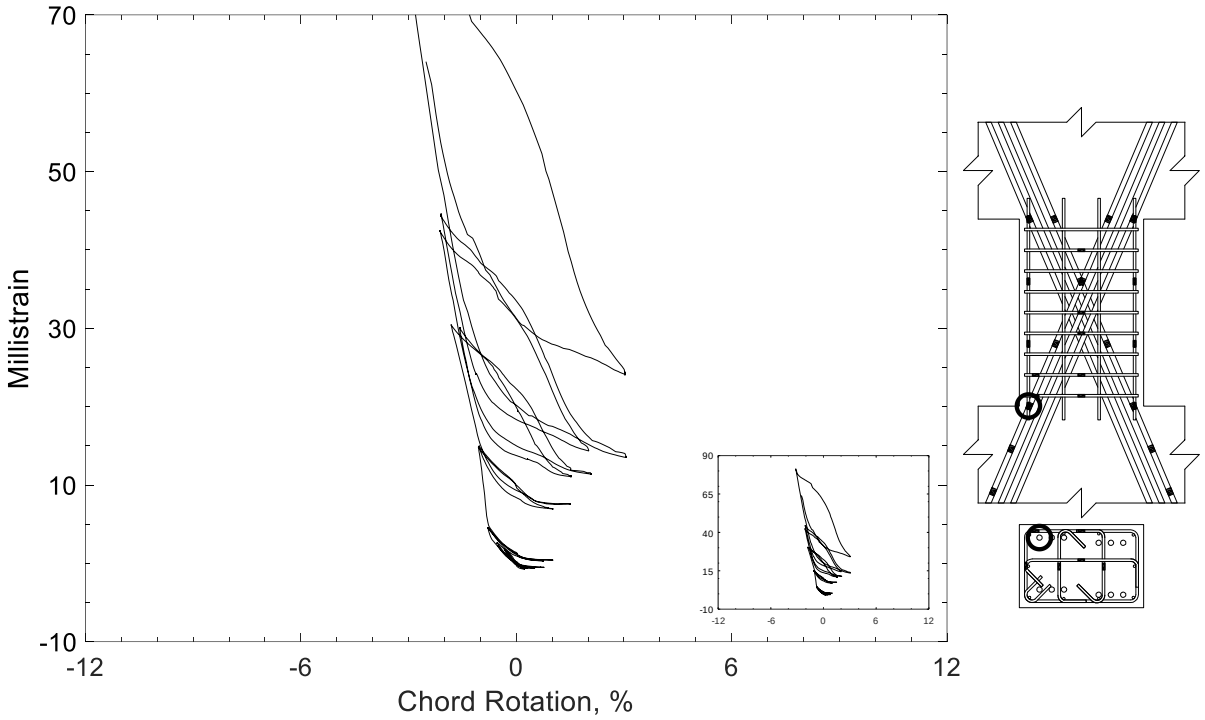

Figure 277 – Measured strain in diagonal bar of D100-1.5, strain gauge D5

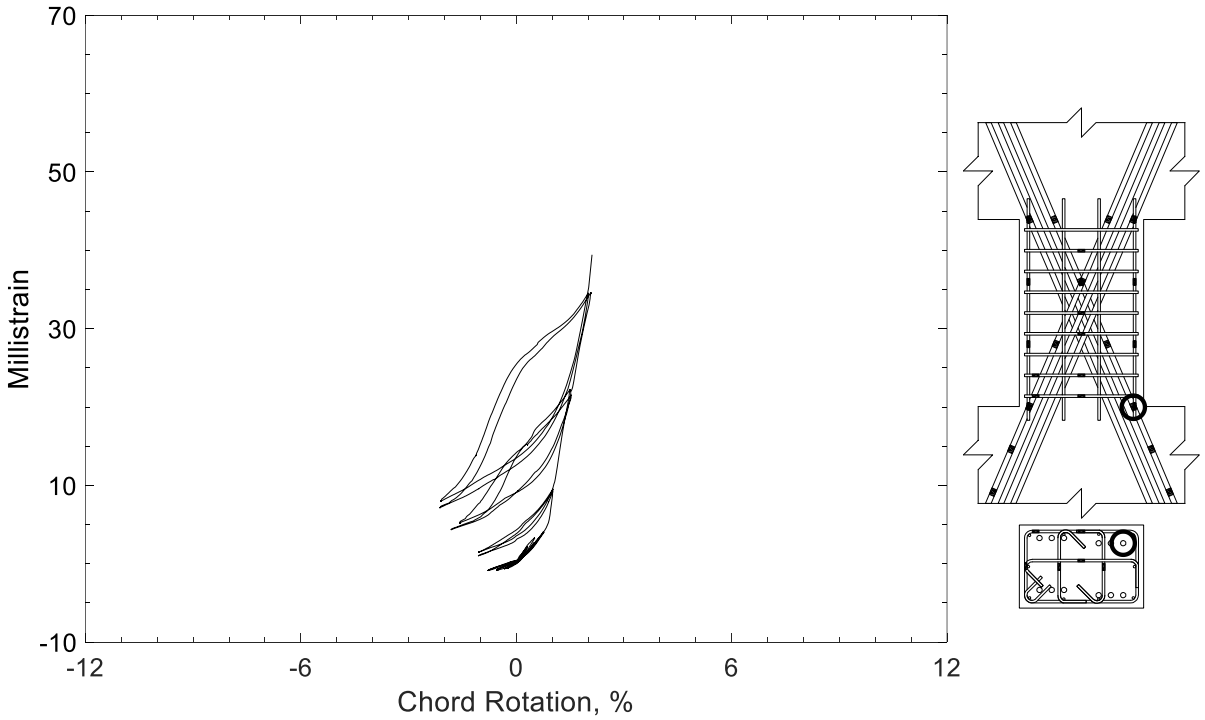

Figure 278 – Measured strain in diagonal bar of D100-1.5, strain gauge D6

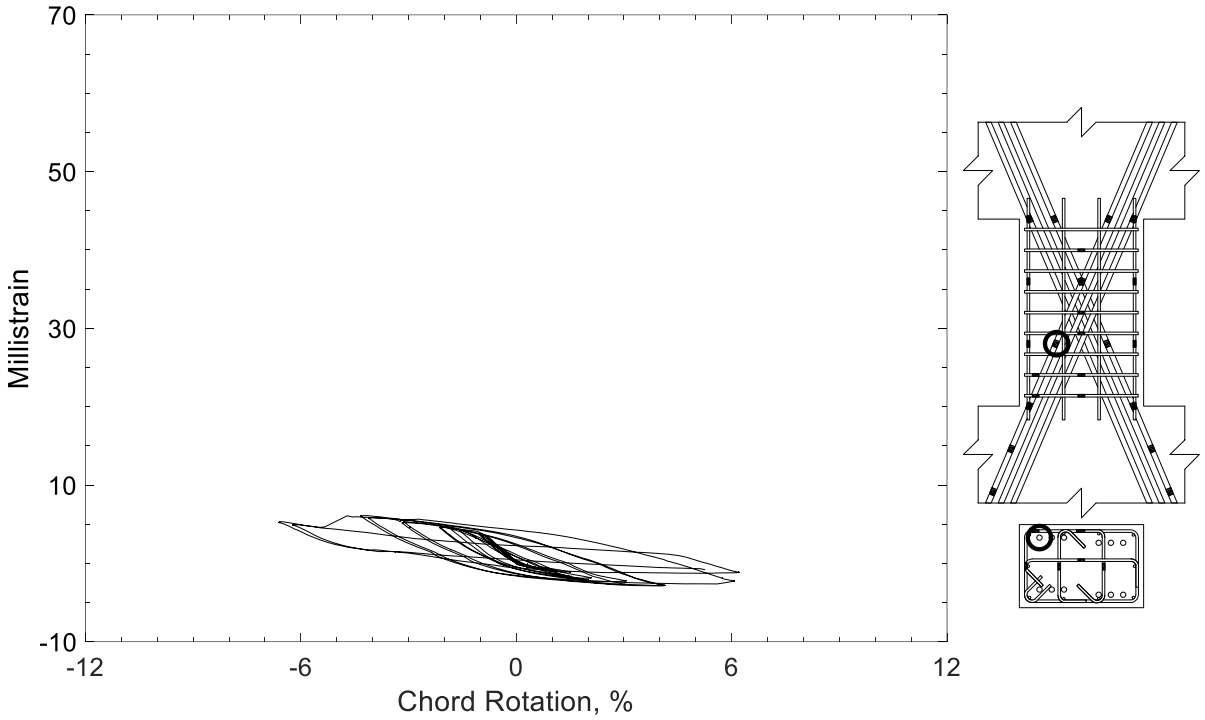

Figure 279 – Measured strain in diagonal bar of D100-1.5, strain gauge D7

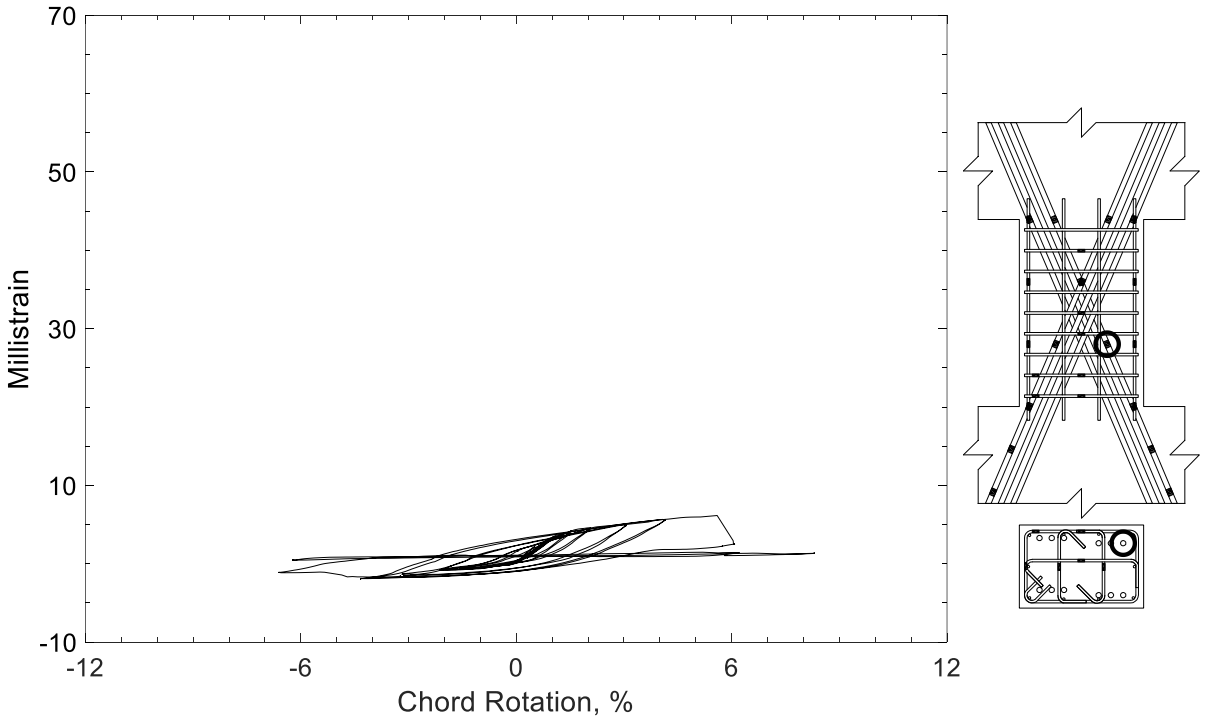

Figure 280 – Measured strain in diagonal bar of D100-1.5, strain gauge D8

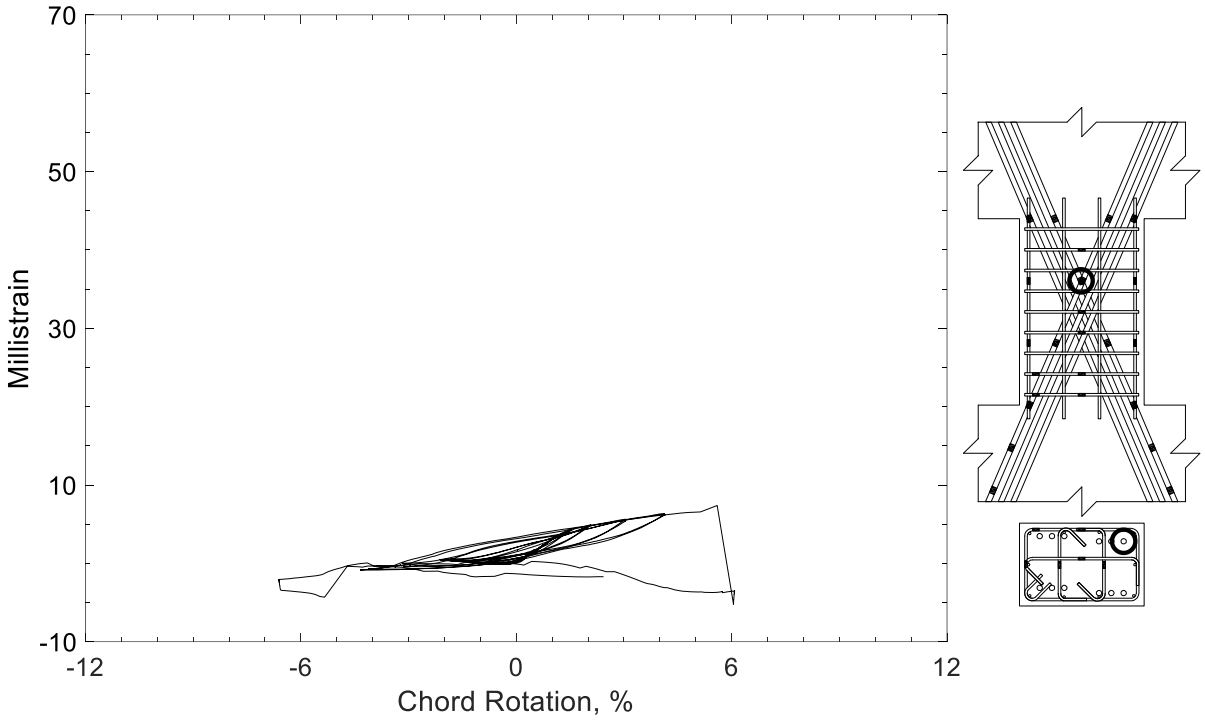

Figure 281 – Measured strain in diagonal bar of D100-1.5, strain gauge D9

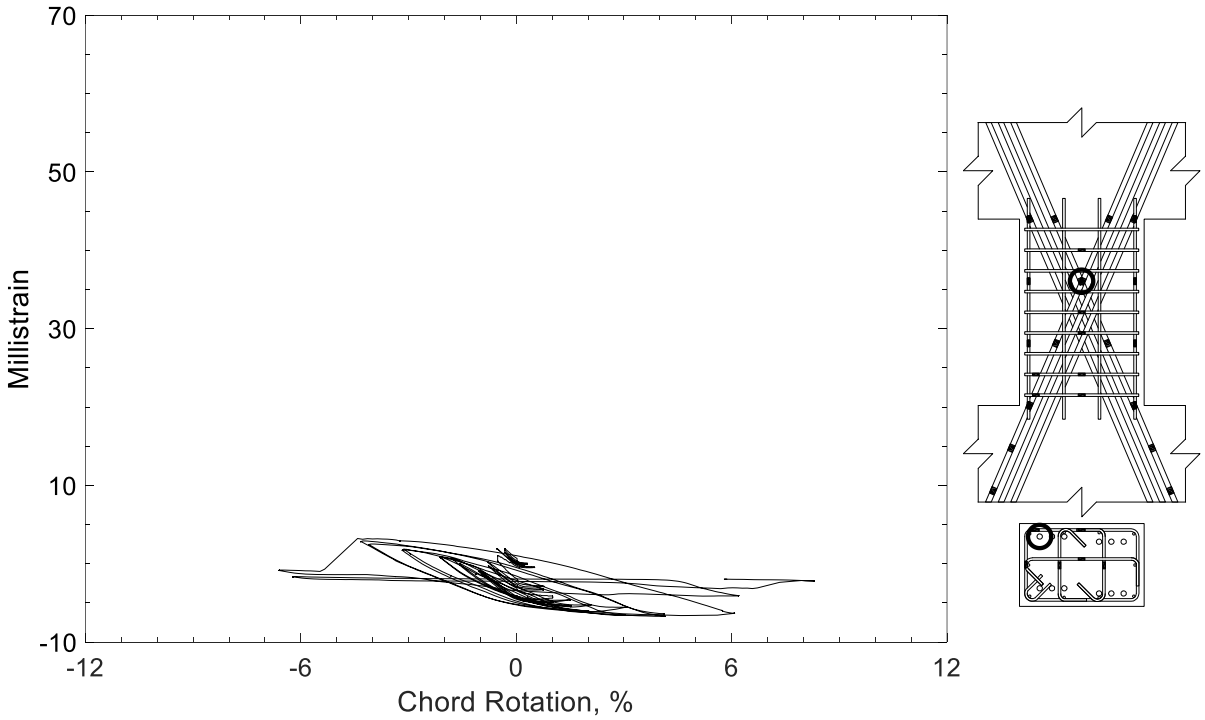

Figure 282 – Measured strain in diagonal bar of D100-1.5, strain gauge D10

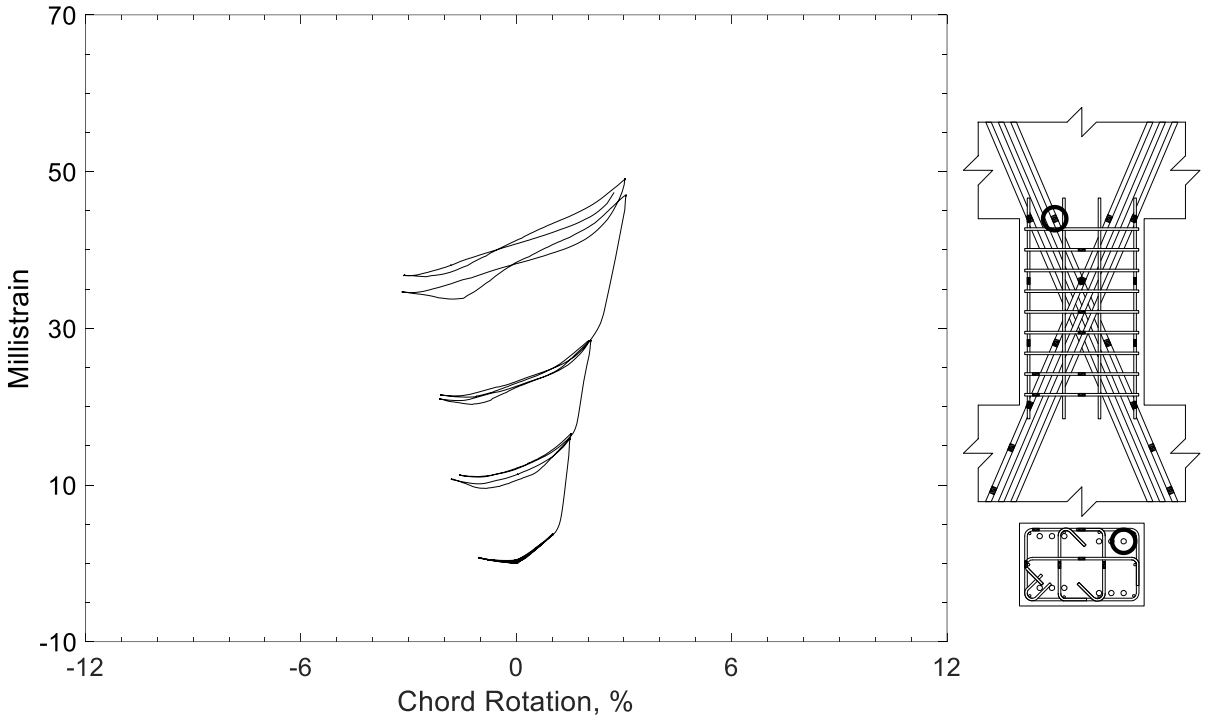

Figure 283 – Measured strain in diagonal bar of D100-1.5, strain gauge D11

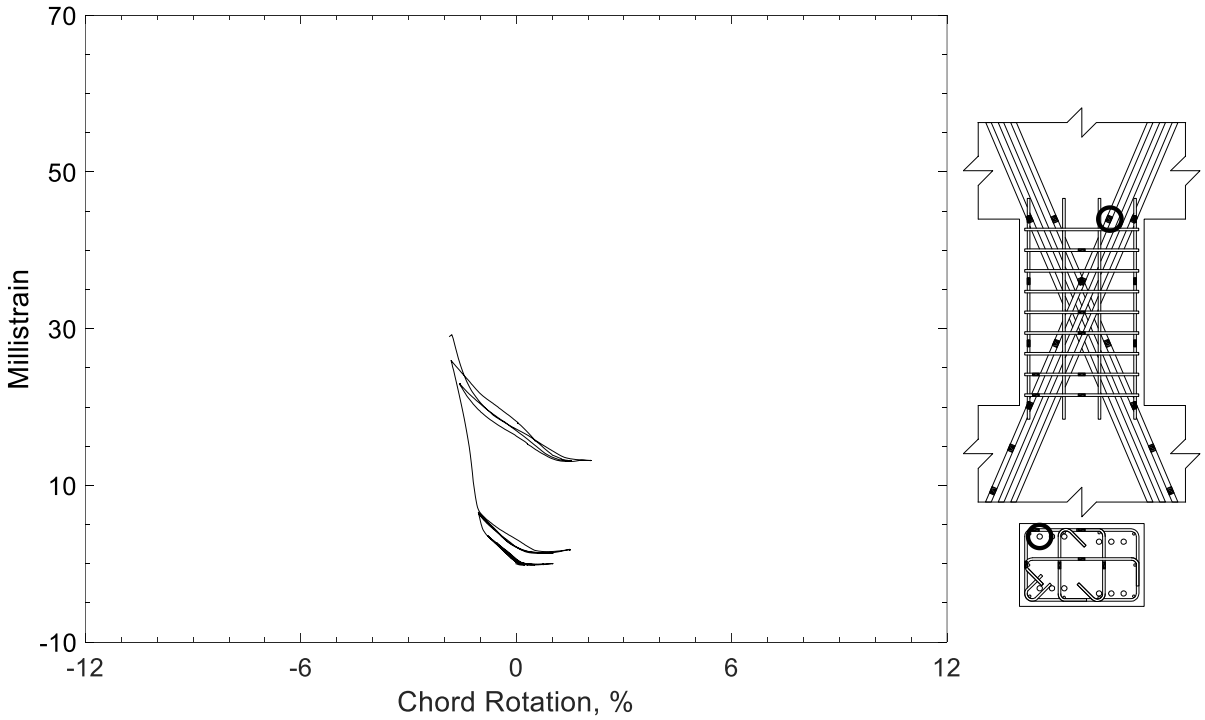

Figure 284 – Measured strain in diagonal bar of D100-1.5, strain gauge D12

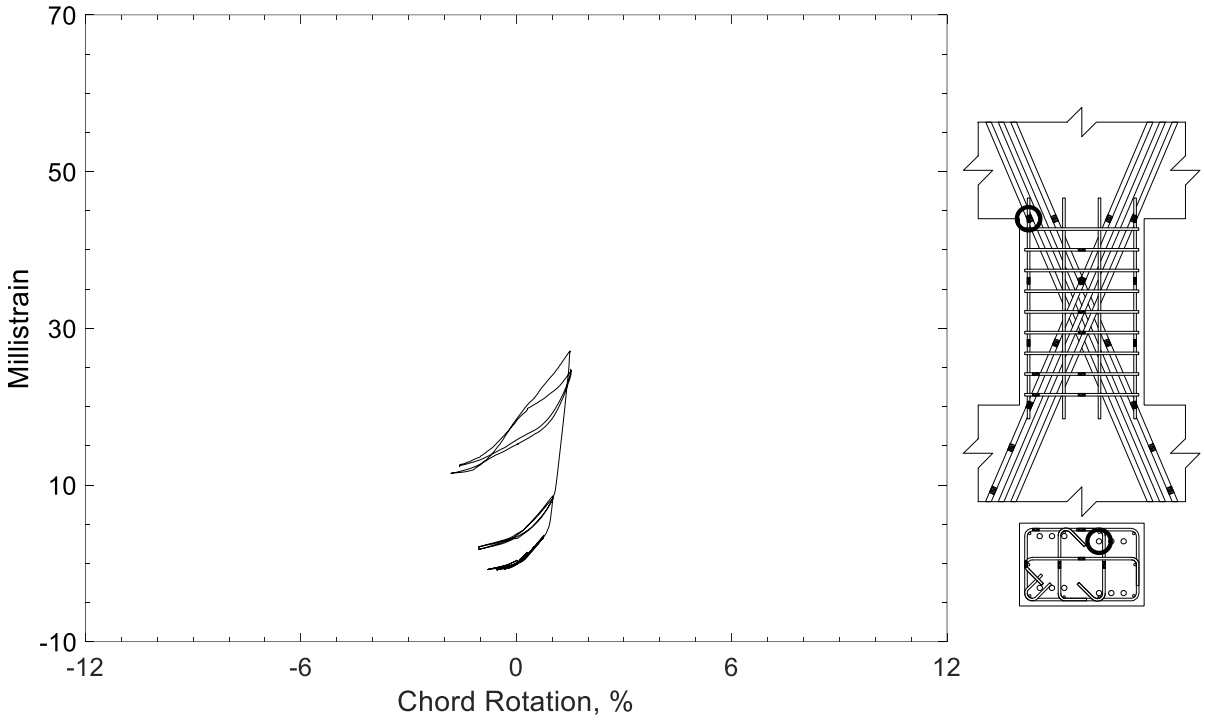

Figure 285 – Measured strain in diagonal bar of D100-1.5, strain gauge D13

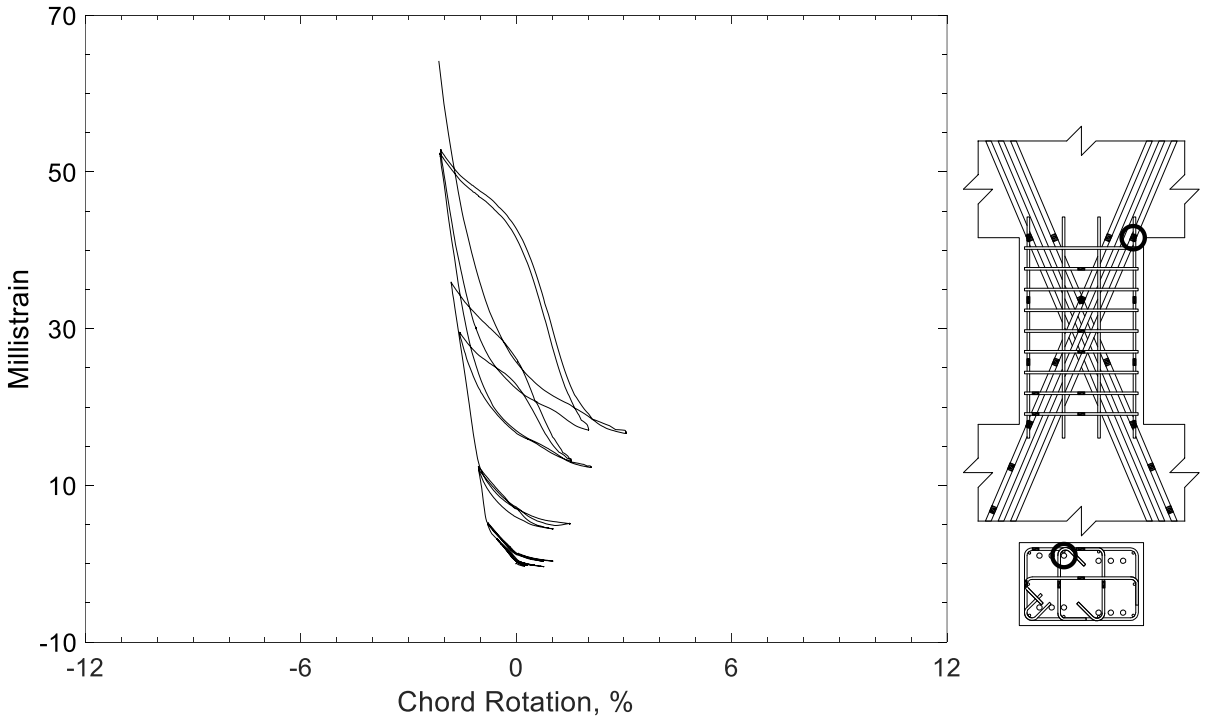

Figure 286 – Measured strain in diagonal bar of D100-1.5, strain gauge D14

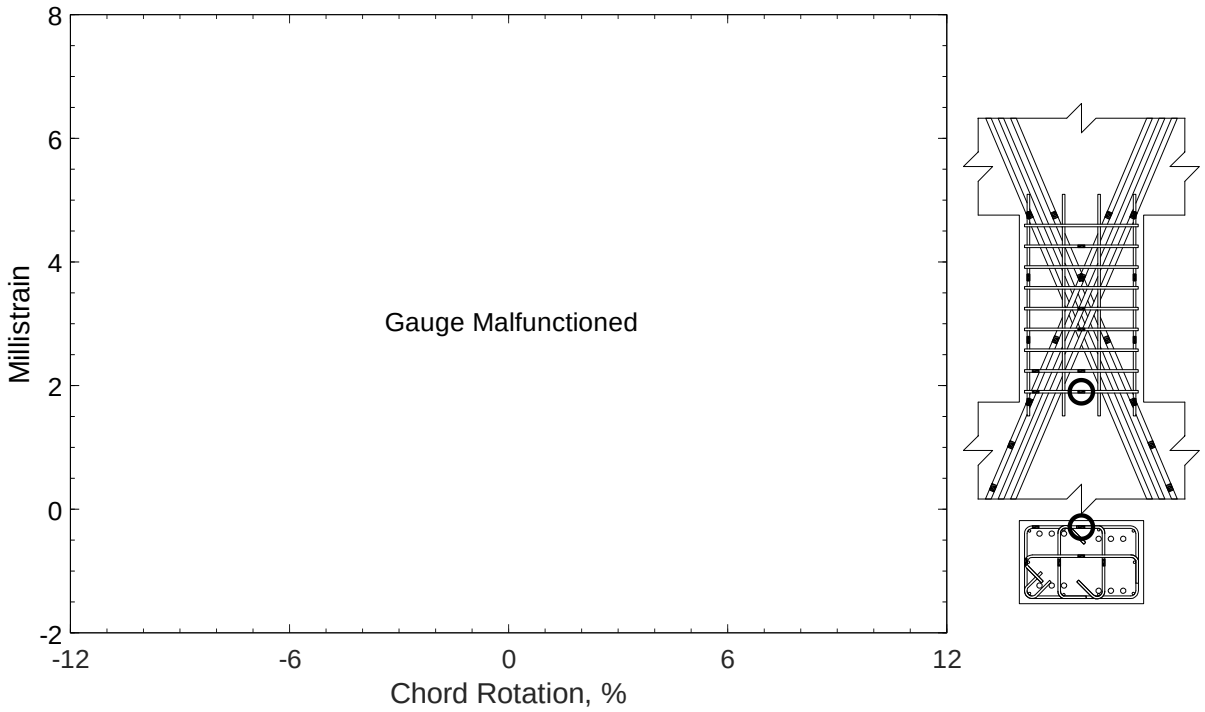

Figure 287 – Measured strain in closed stirrup of D100-1.5, strain gauge S1

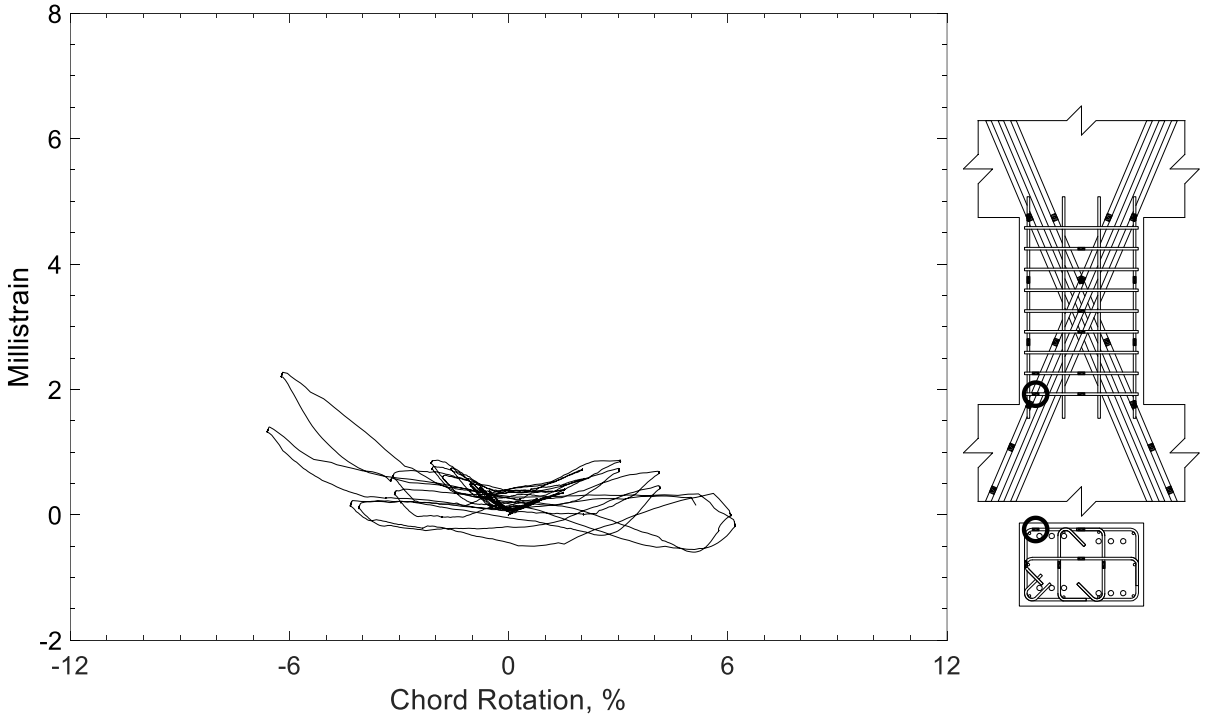

Figure 288 – Measured strain in closed stirrup of D100-1.5, strain gauge S2

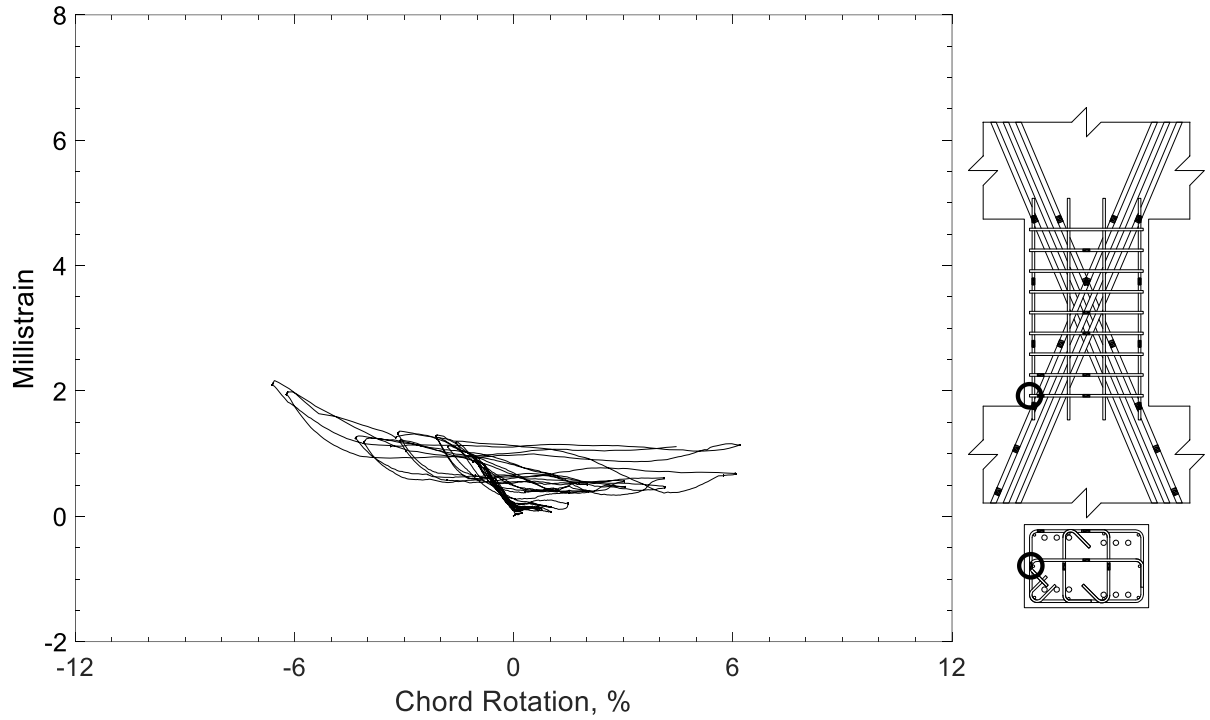

Figure 289 – Measured strain in closed stirrup of D100-1.5, strain gauge S3

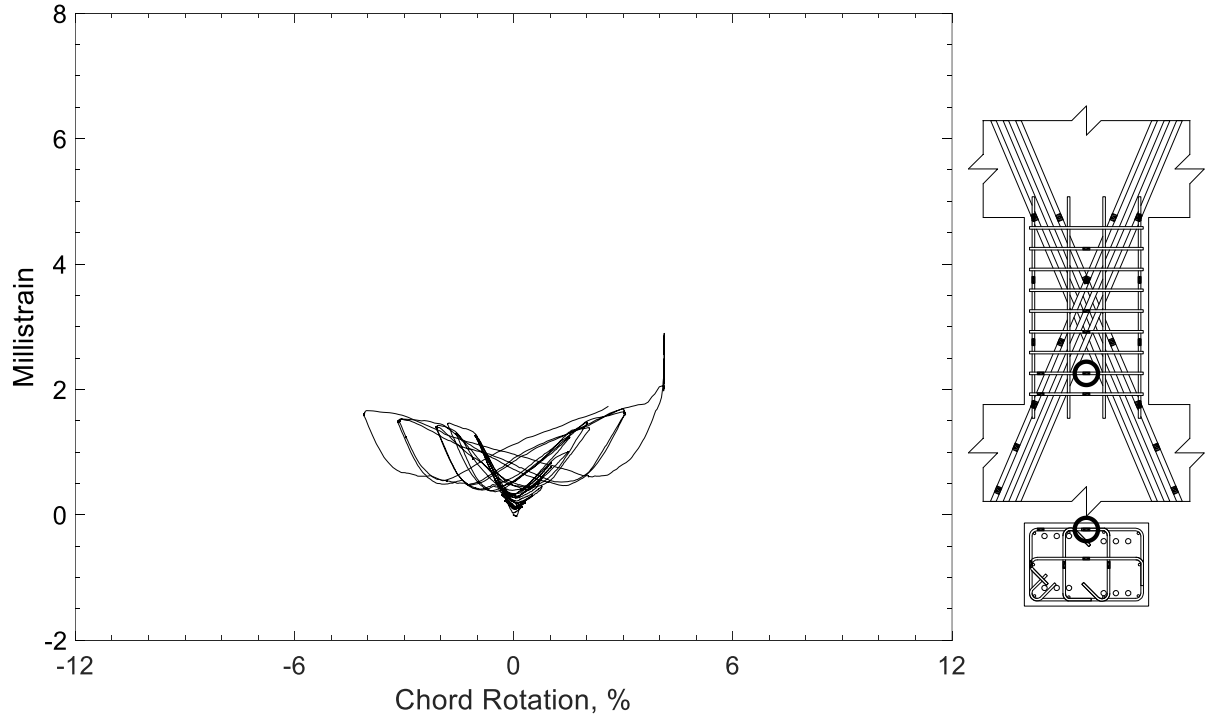

Figure 290 – Measured strain in closed stirrup of D100-1.5, strain gauge S4

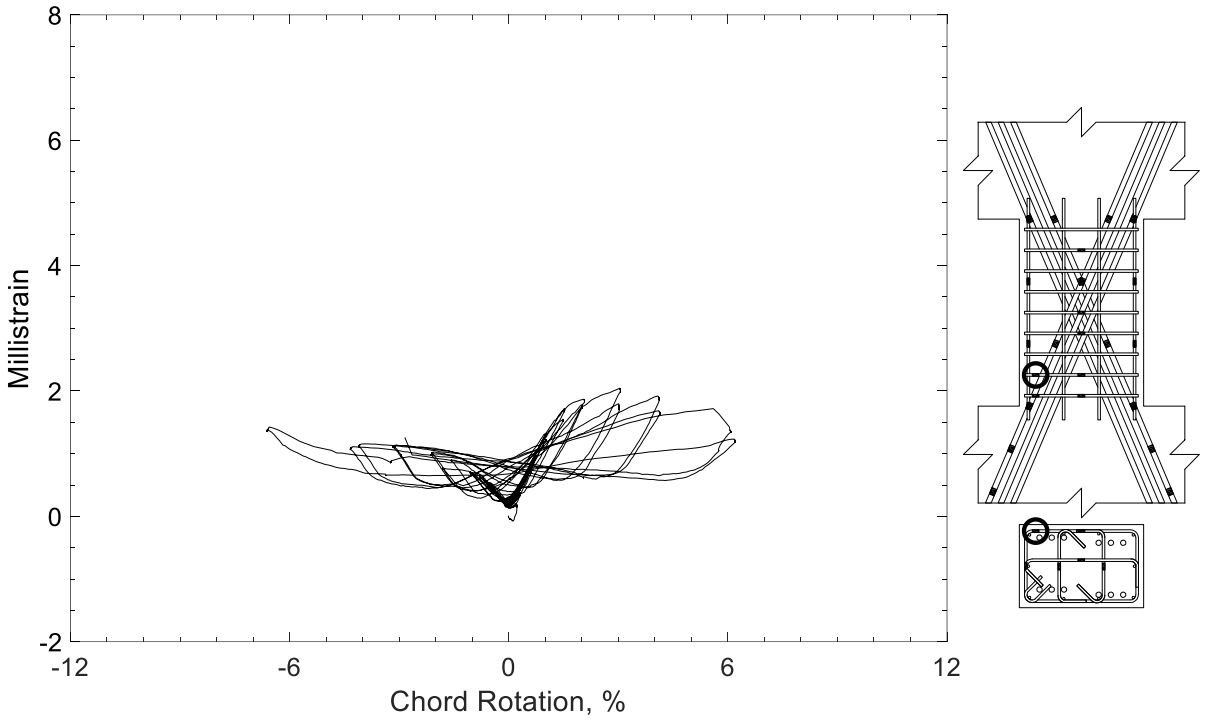

Figure 291 – Measured strain in closed stirrup of D100-1.5, strain gauge S5

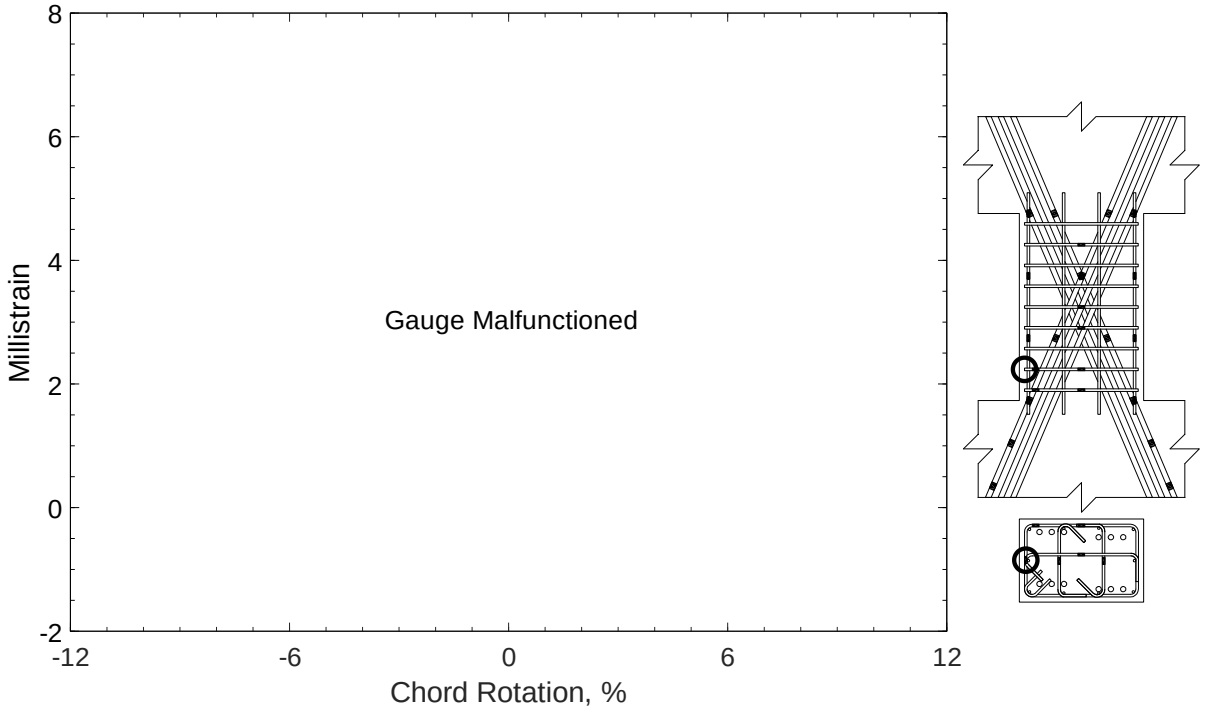

Figure 292 – Measured strain in closed stirrup of D100-1.5, strain gauge S6

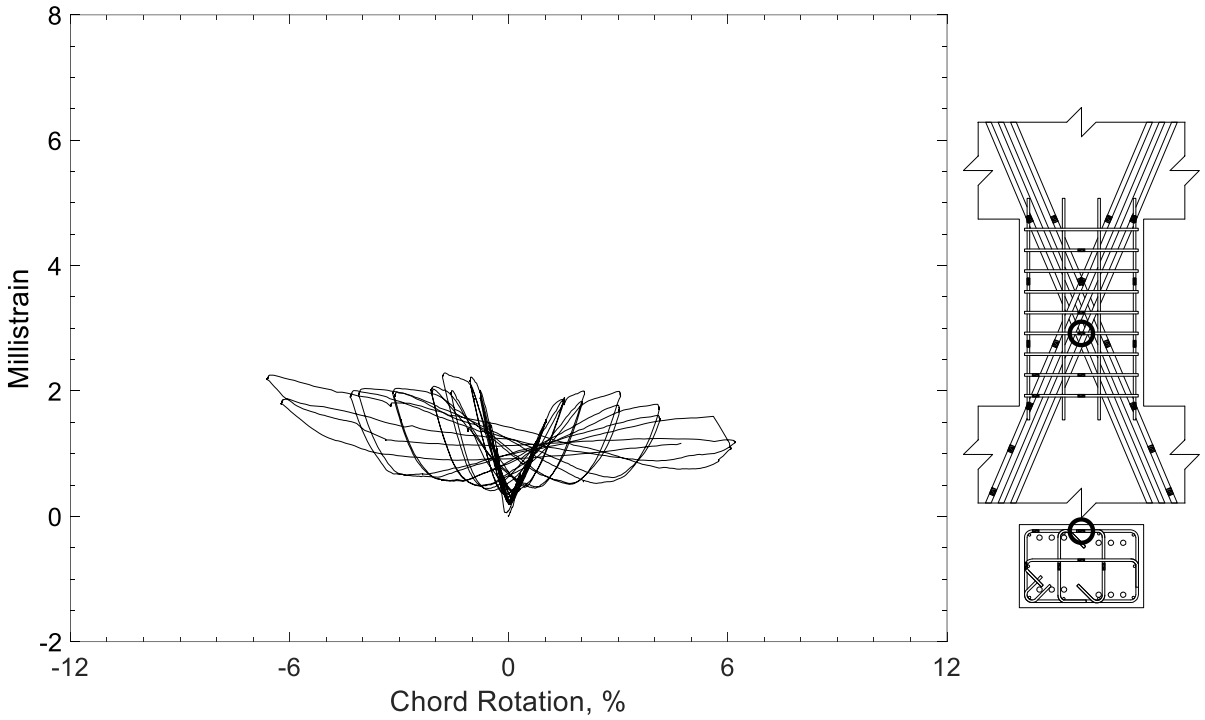

Figure 293 – Measured strain in closed stirrup of D100-1.5, strain gauge S7

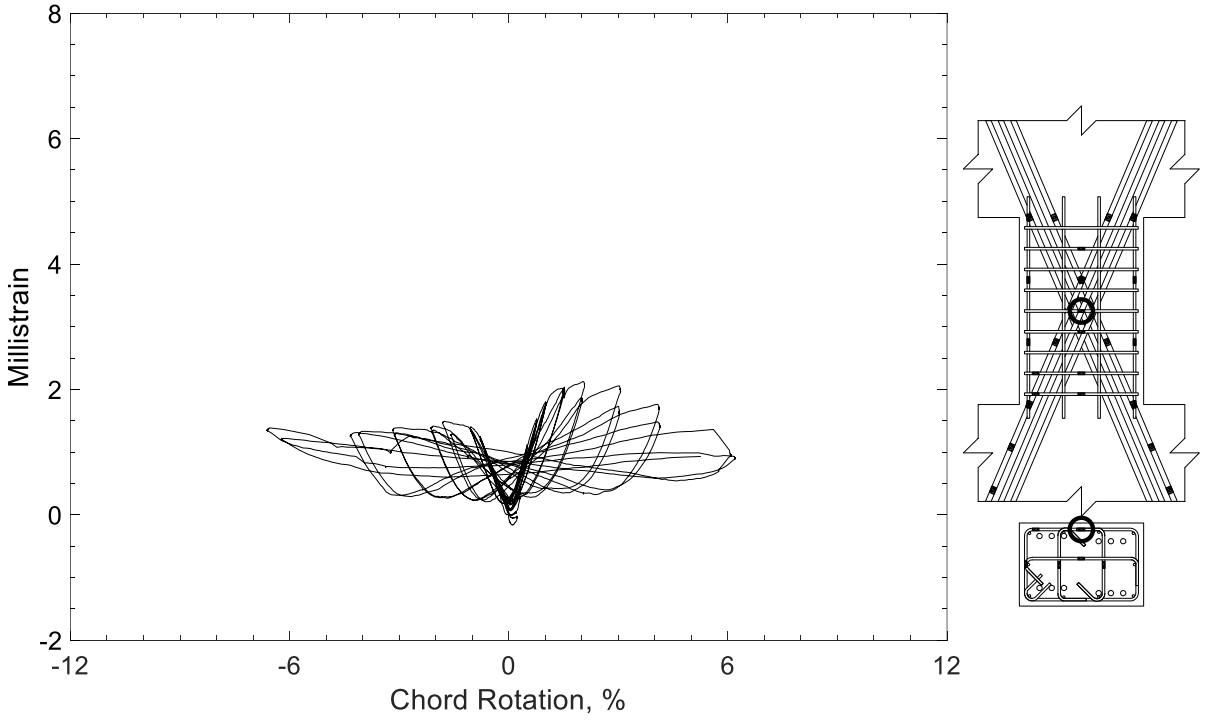

Figure 294 – Measured strain in closed stirrup of D100-1.5, strain gauge S8

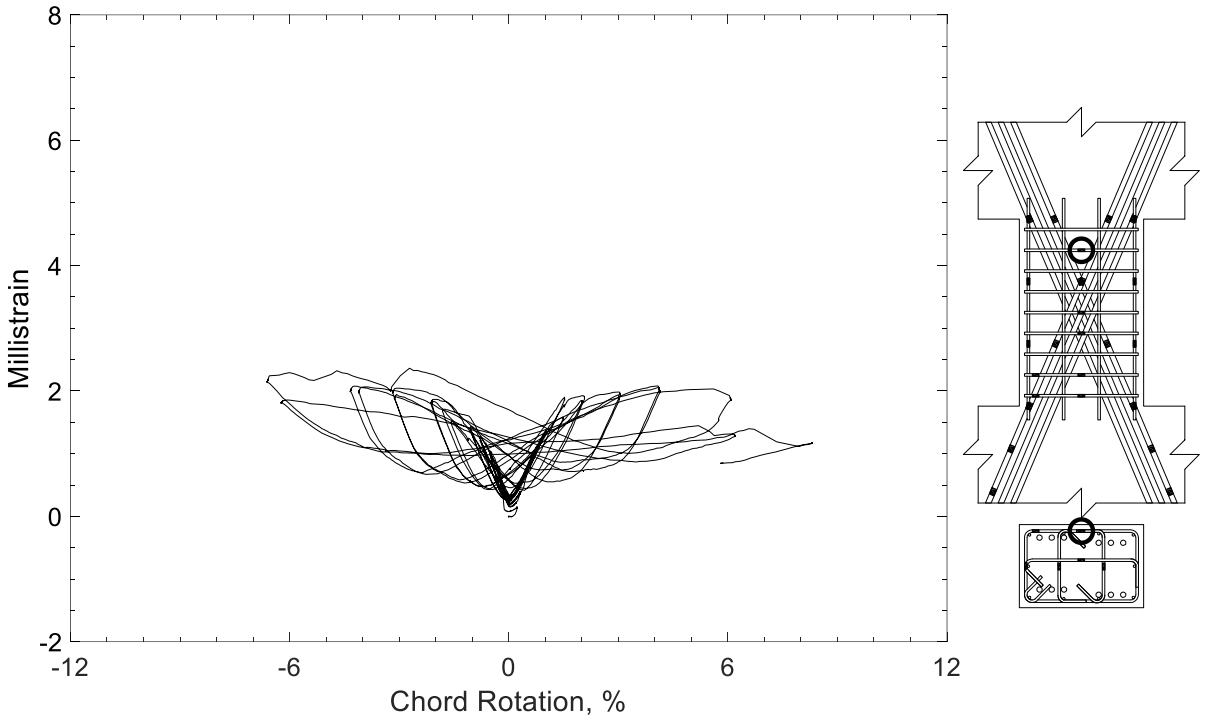

Figure 295 – Measured strain in closed stirrup of D100-1.5, strain gauge S9

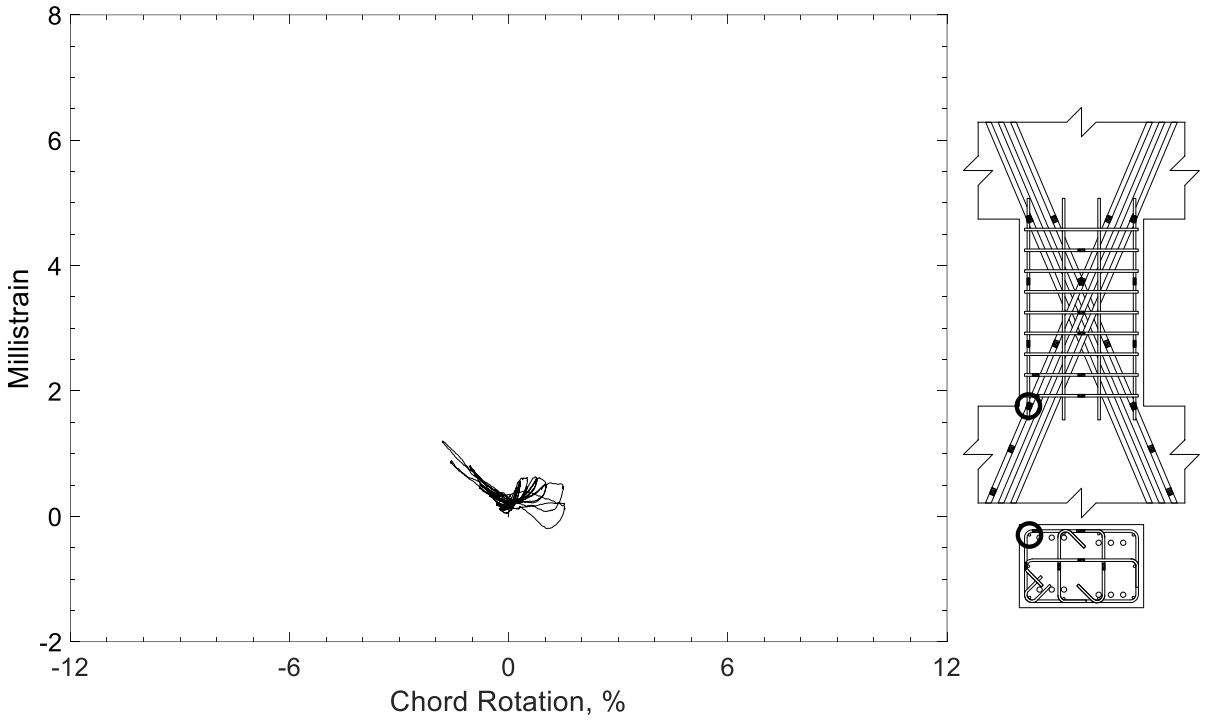

Figure 296 – Measured strain in parallel bar of D100-1.5, strain gauge H1

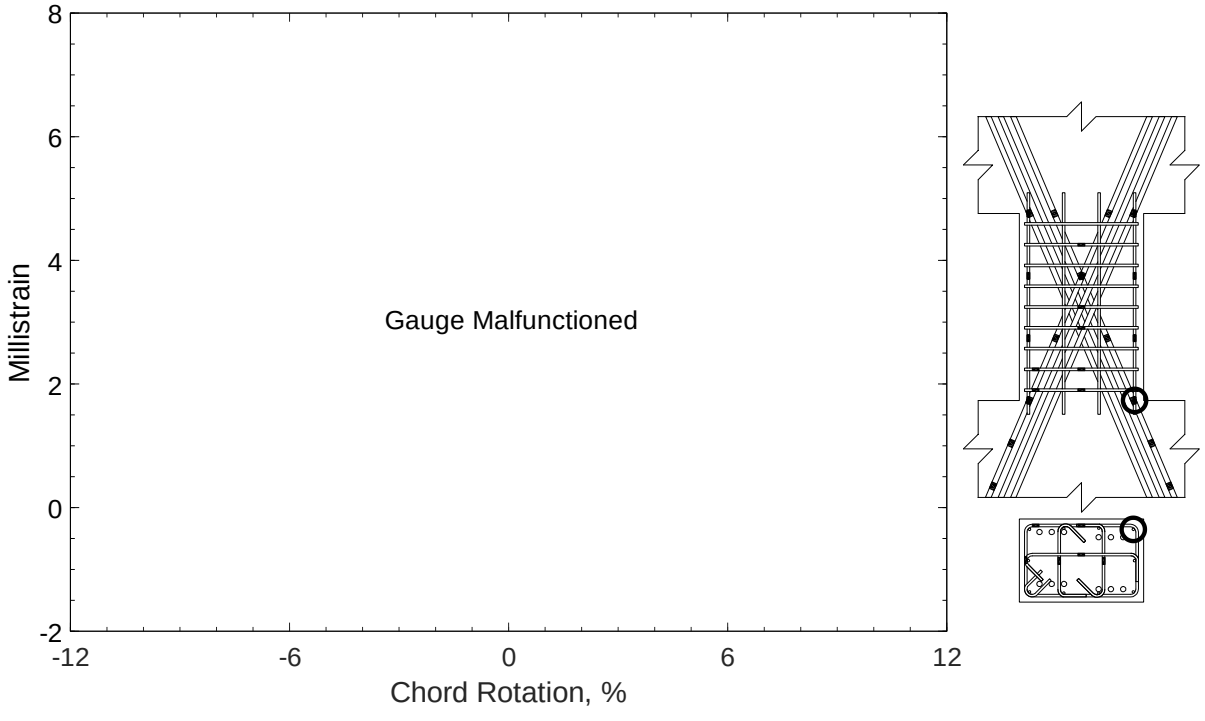

Figure 297 – Measured strain in parallel bar of D100-1.5, strain gauge H2

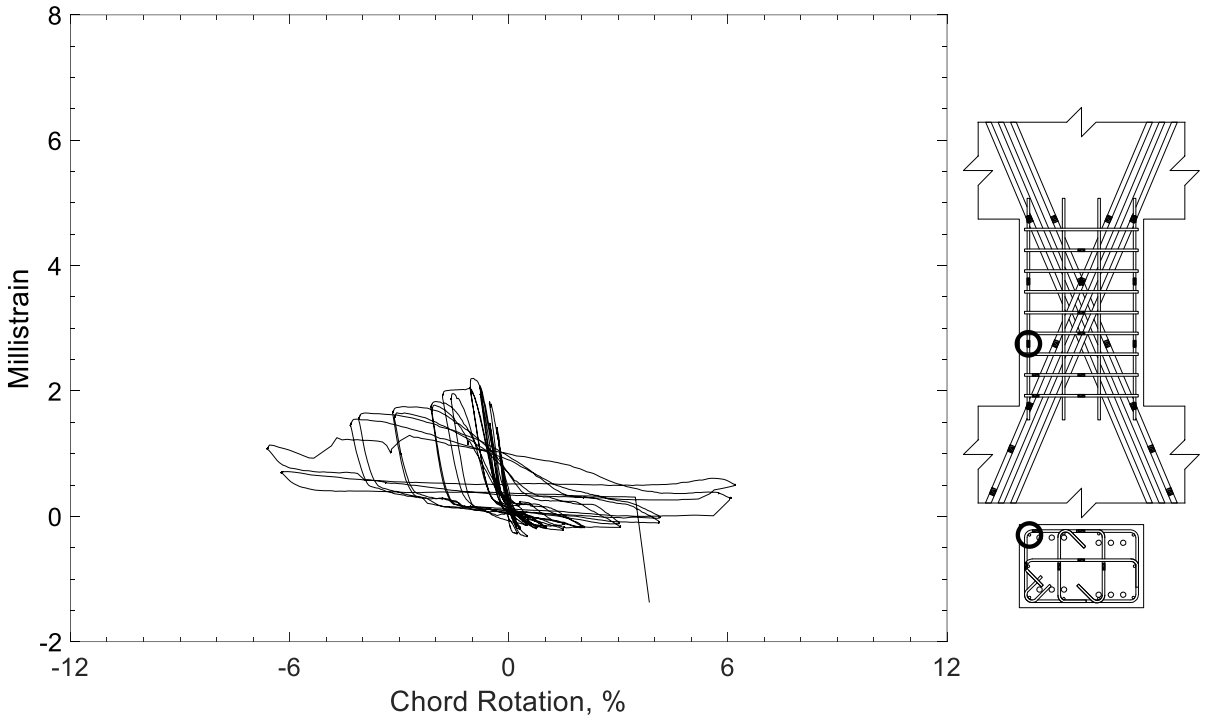

Figure 298 – Measured strain in parallel bar of D100-1.5, strain gauge H3

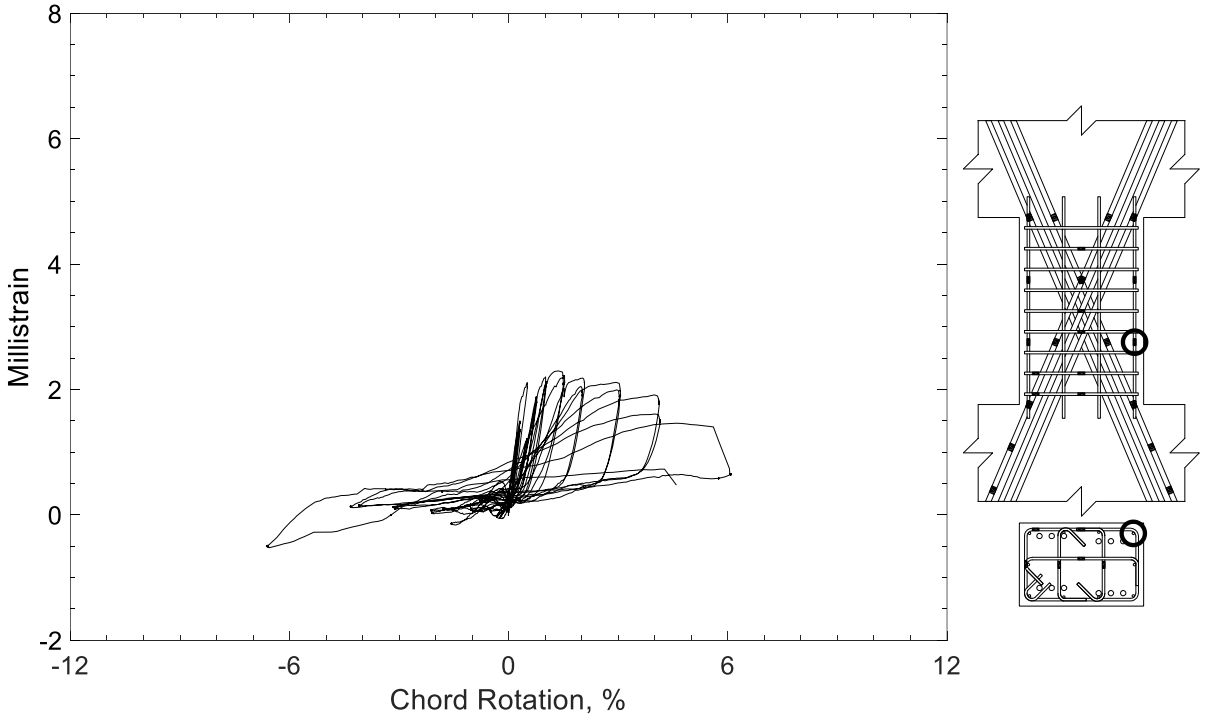

Figure 299 – Measured strain in parallel bar of D100-1.5, strain gauge H4

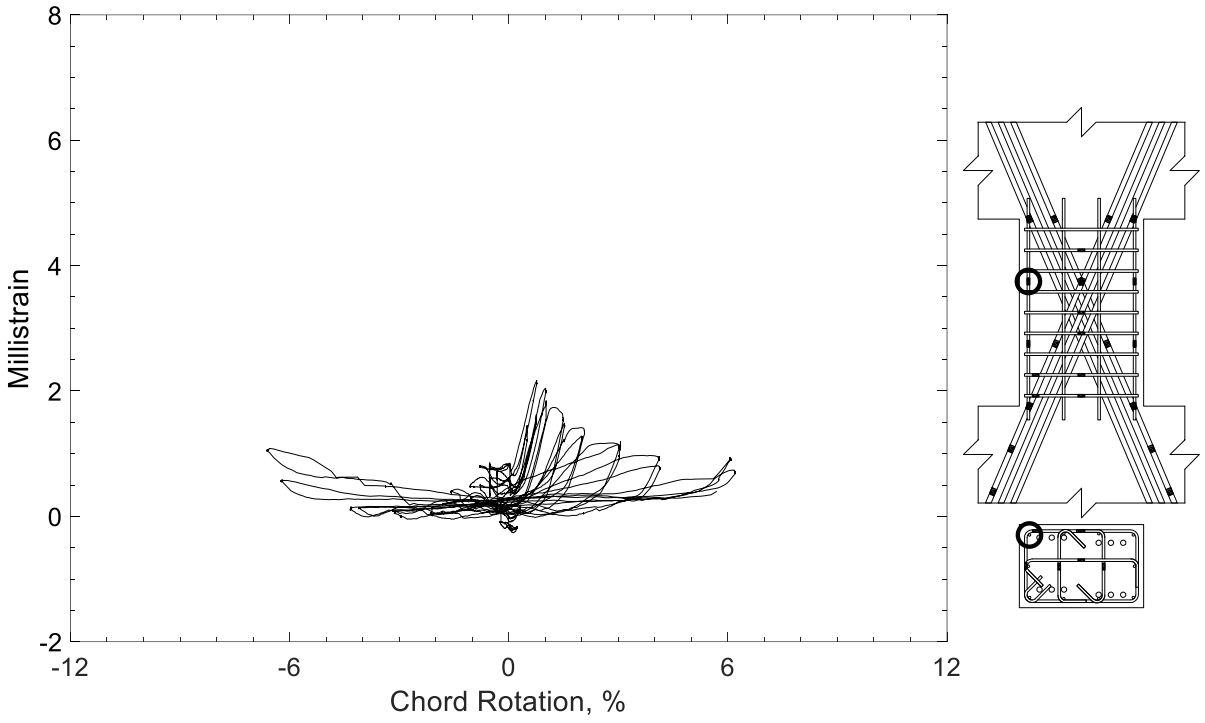

Figure 300 – Measured strain in parallel bar of D100-1.5, strain gauge H5

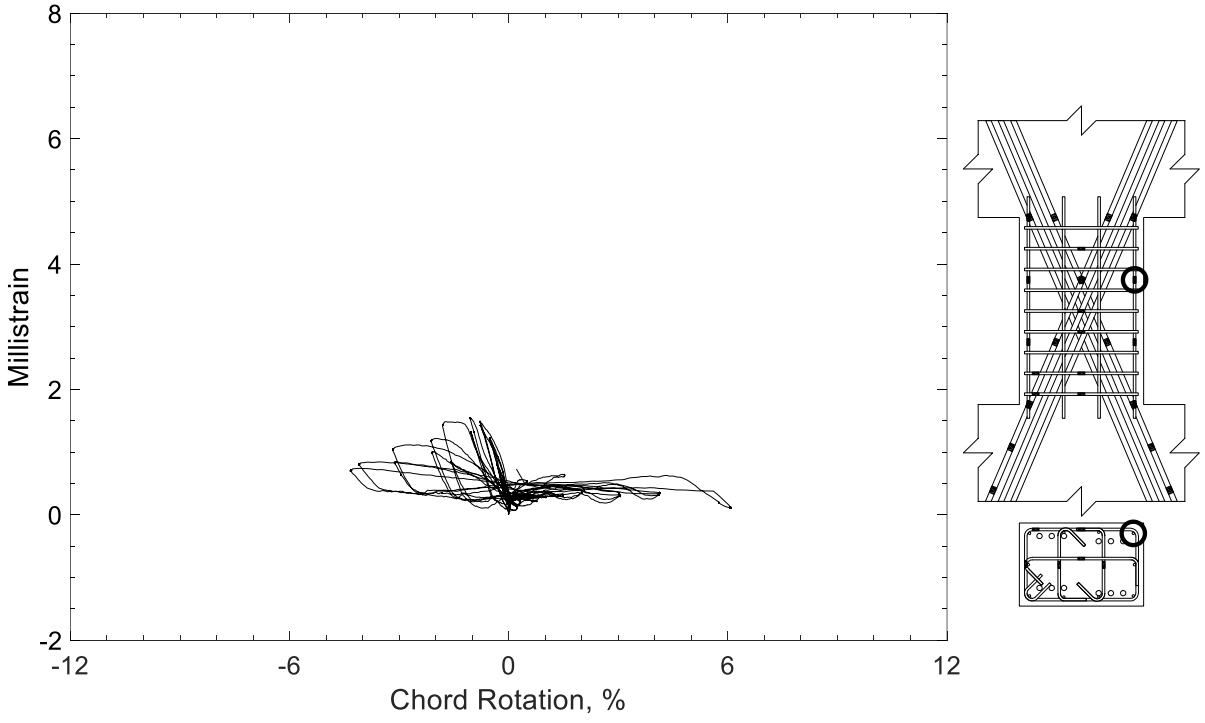

Figure 301 – Measured strain in parallel bar of D100-1.5, strain gauge H6

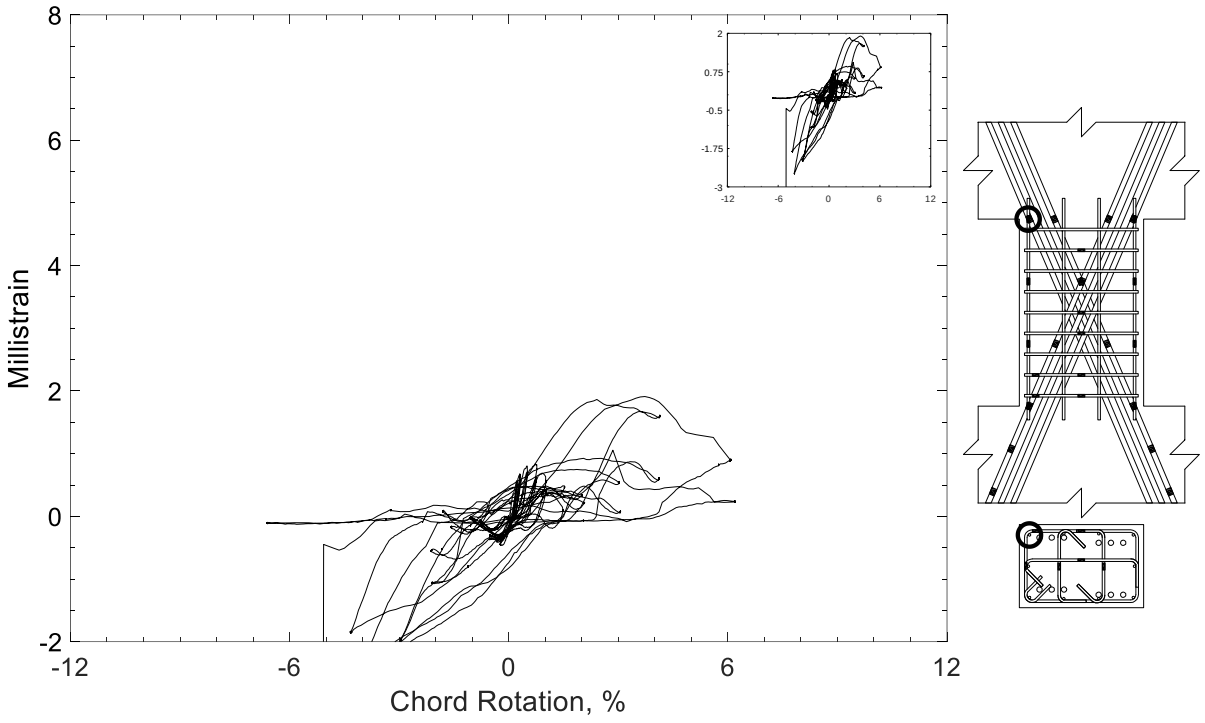

Figure 302 – Measured strain in parallel bar of D100-1.5, strain gauge H7

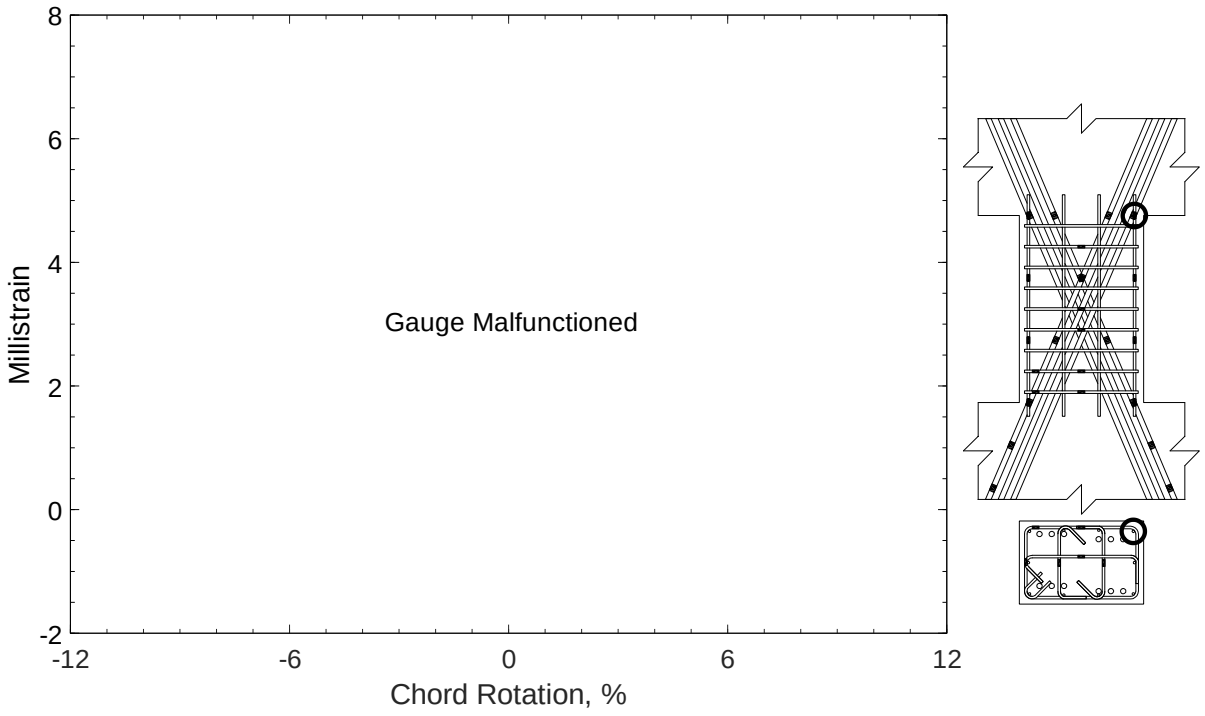

Figure 303 – Measured strain in parallel bar of D100-1.5, strain gauge H8

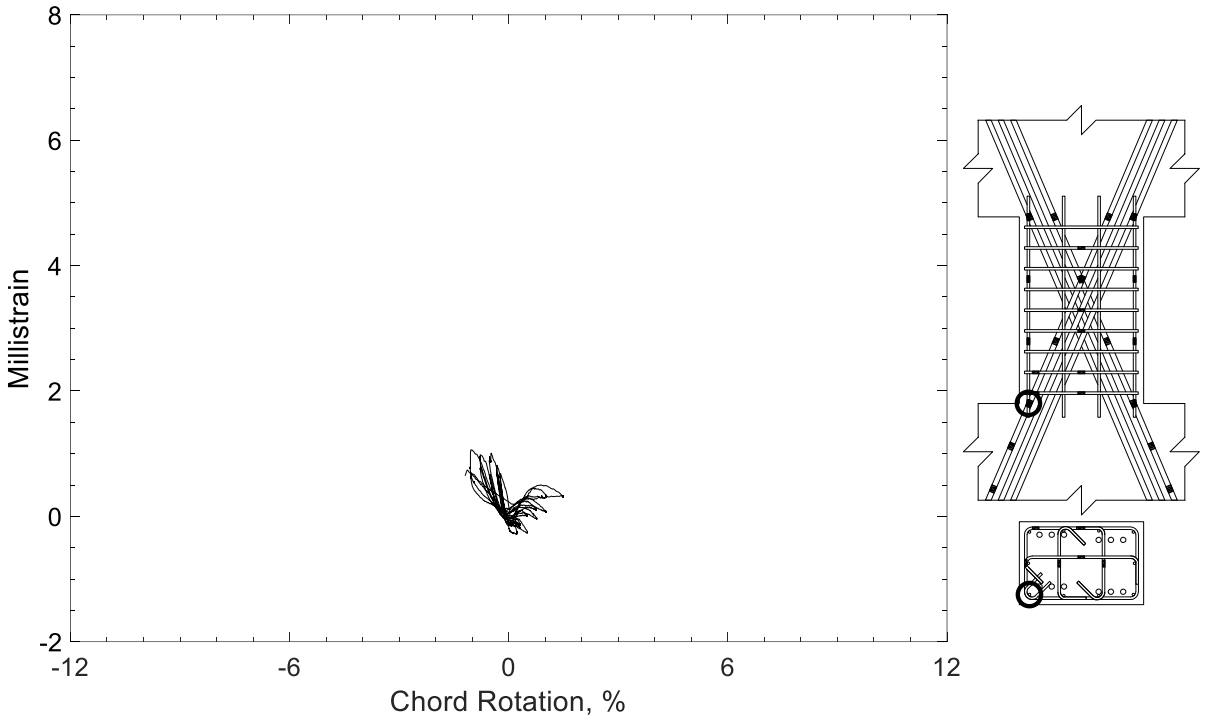

Figure 304 – Measured strain in parallel bar of D100-1.5, strain gauge H9

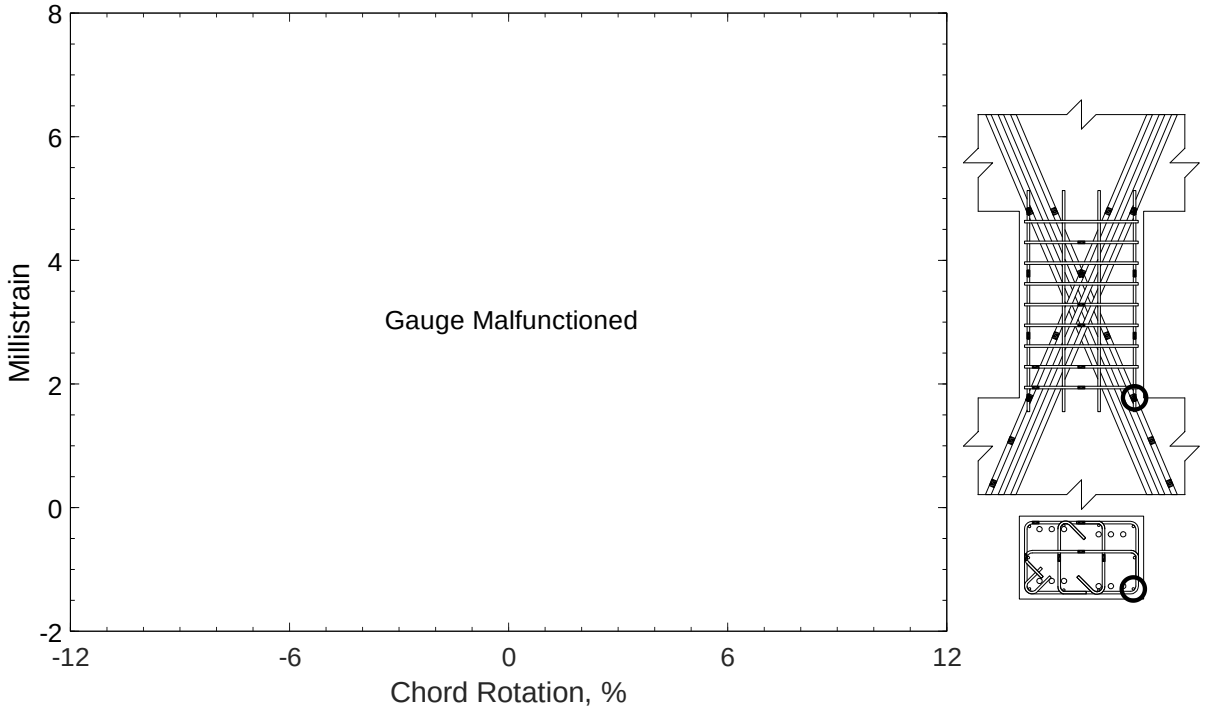

Figure 305 – Measured strain in parallel bar of D100-1.5, strain gauge H10

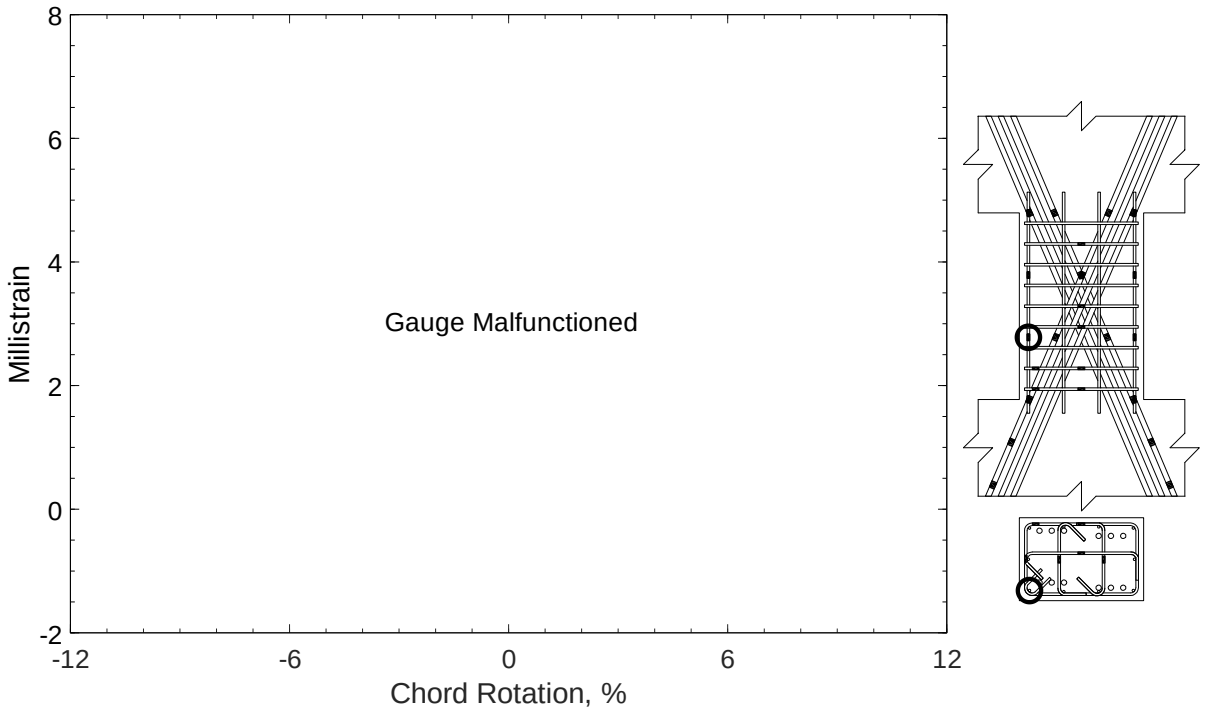

Figure 306 – Measured strain in parallel bar of D100-1.5, strain gauge H11

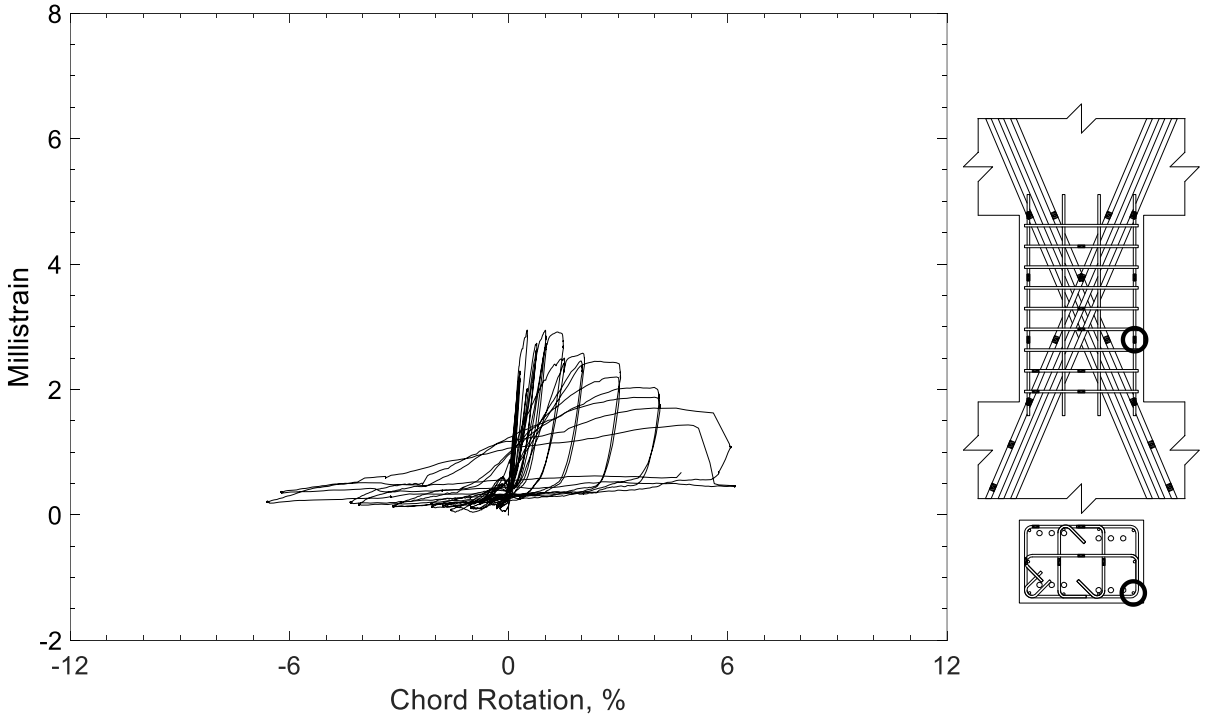

Figure 307 – Measured strain in parallel bar of D100-1.5, strain gauge H12

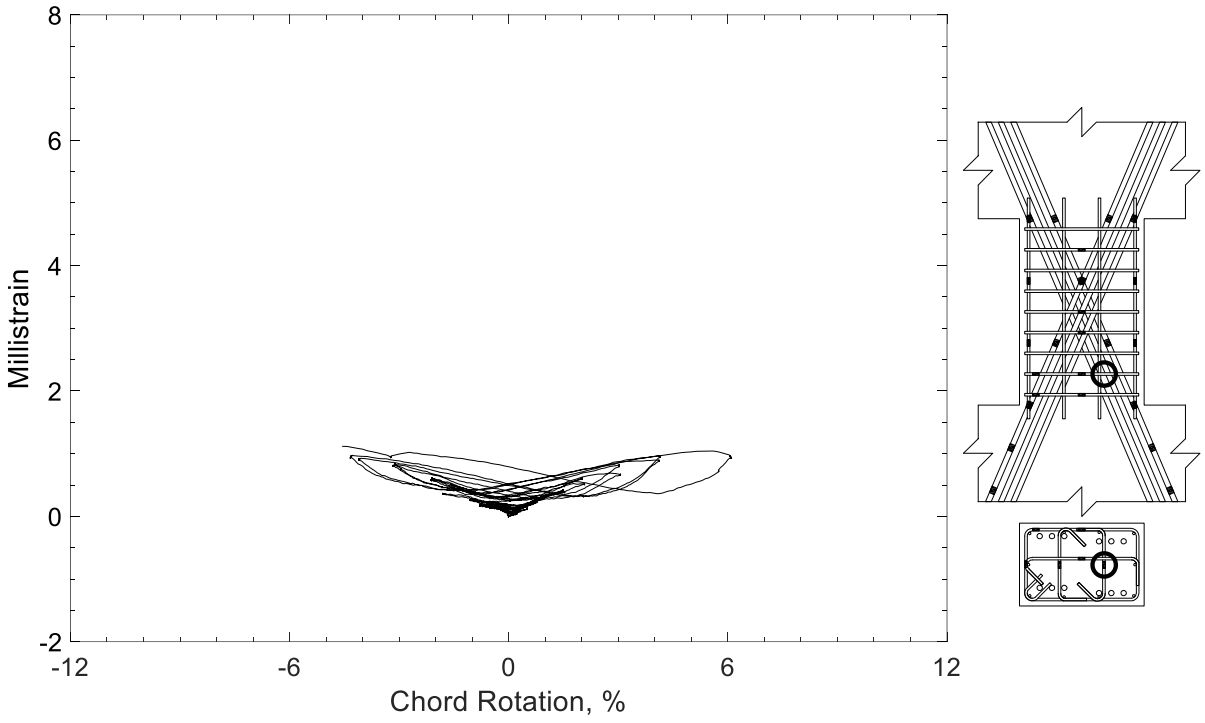

Figure 308 – Measured strain in crosstie of D100-1.5, strain gauge T1

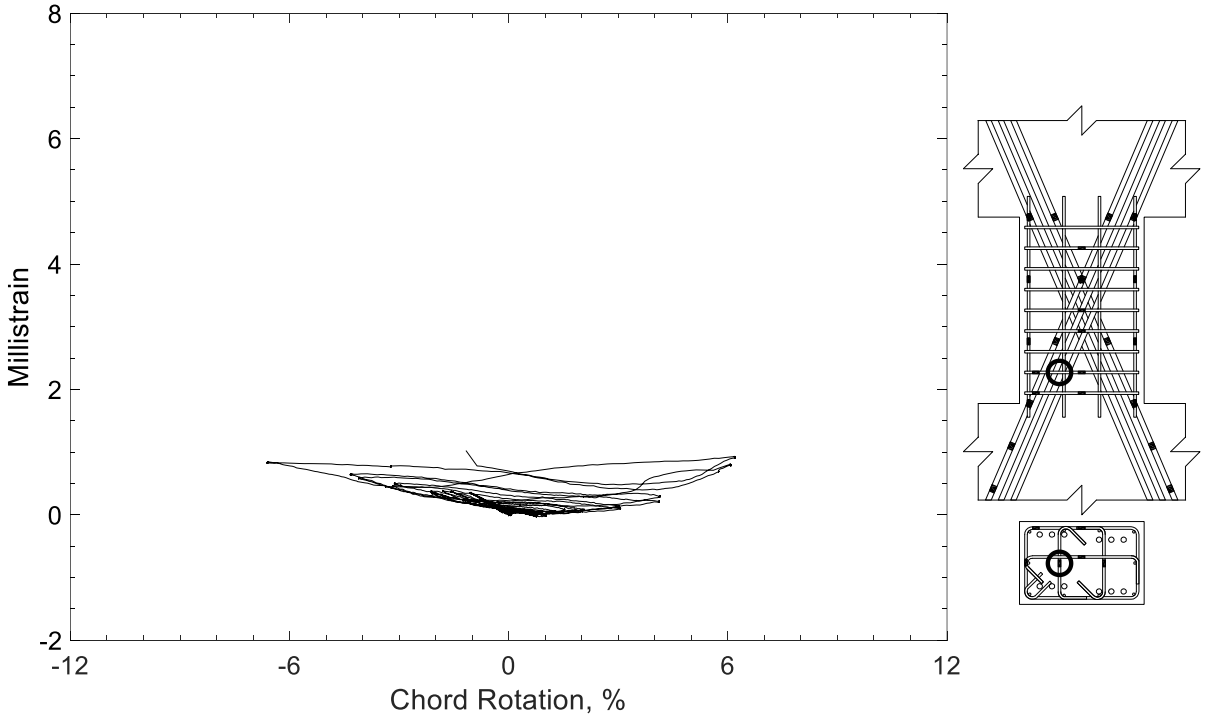

Figure 309 – Measured strain in crosstie of D100-1.5, strain gauge T2

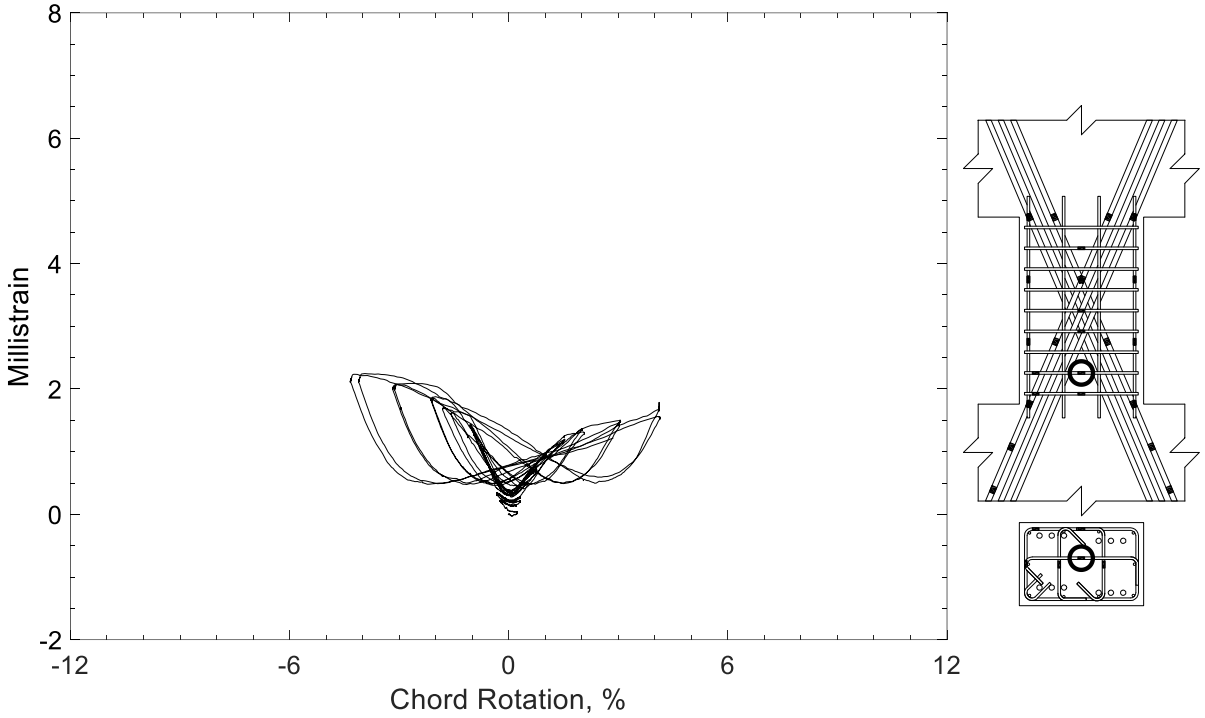

Figure 310 – Measured strain in crosstie of D100-1.5, strain gauge T3

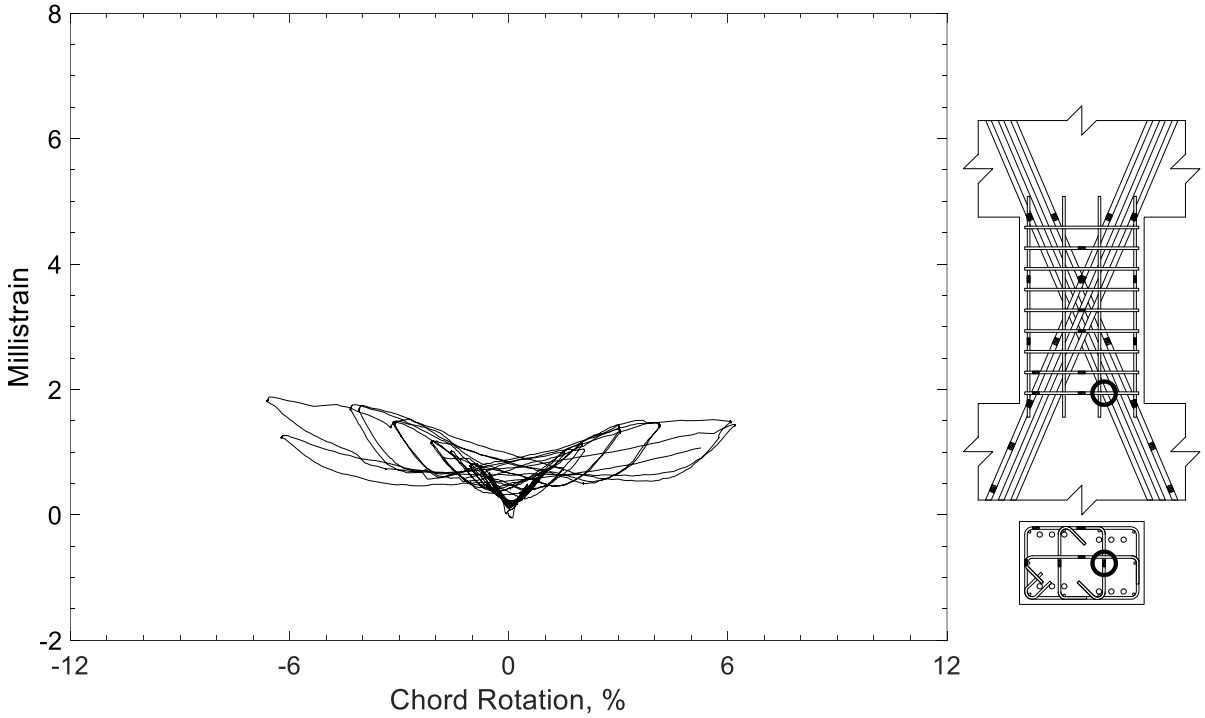

Figure 311 – Measured strain in crosstie of D100-1.5, strain gauge T4

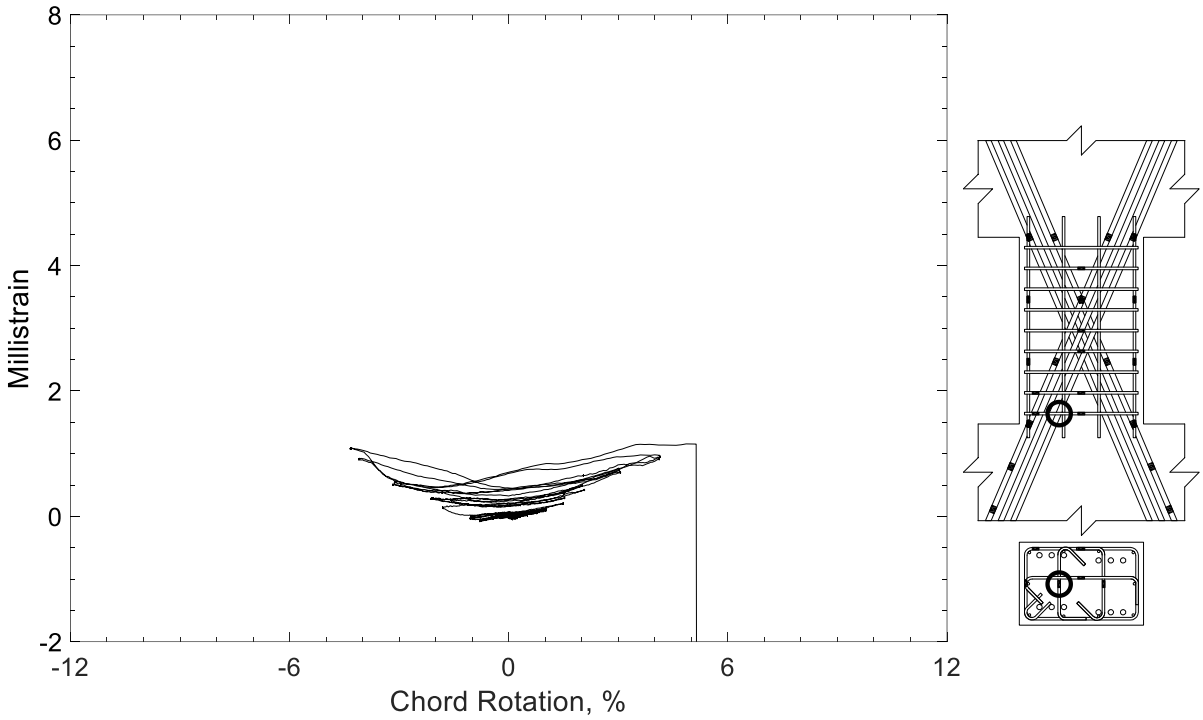

Figure 312 – Measured strain in crosstie of D100-1.5, strain gauge T5

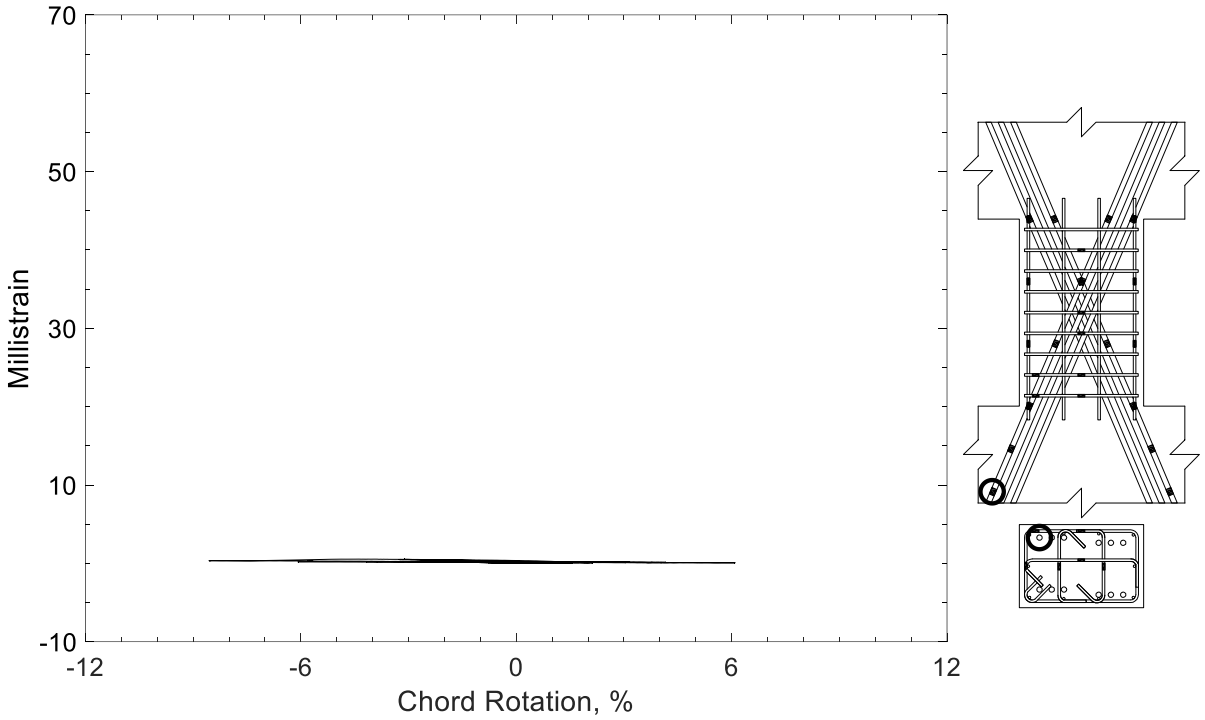

Figure 313 – Measured strain in diagonal bar of D120-1.5, strain gauge D1

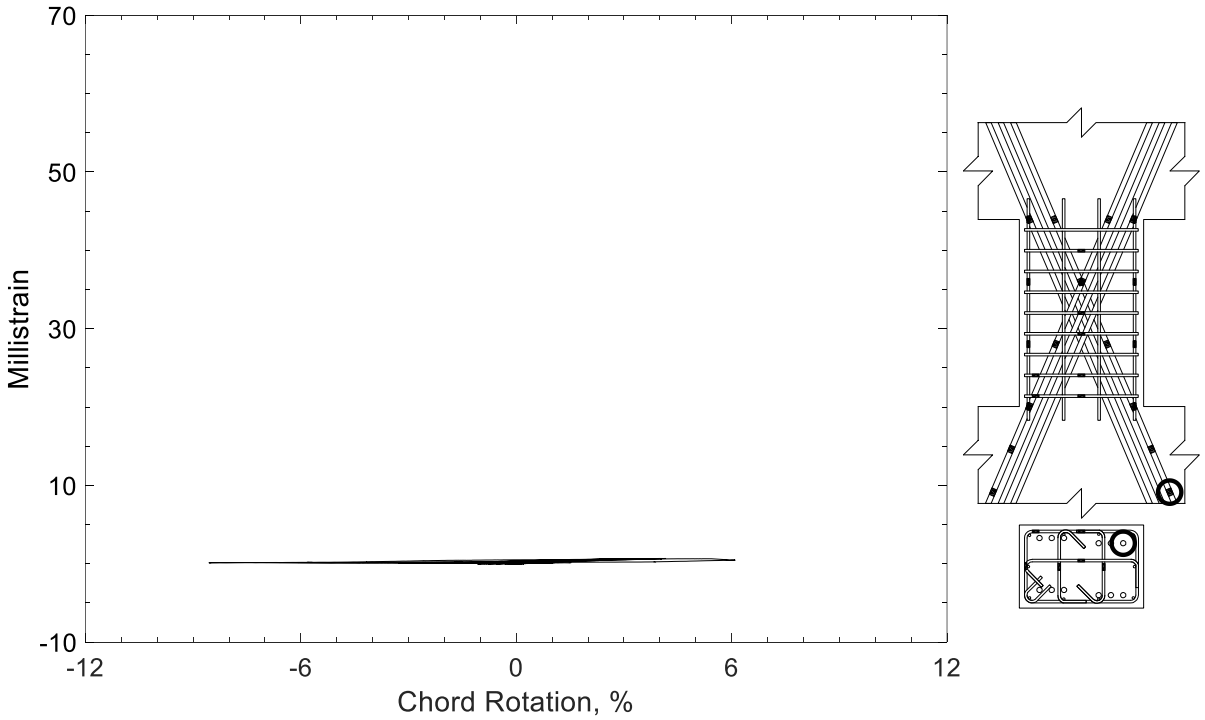

Figure 314 – Measured strain in diagonal bar of D120-1.5, strain gauge D2

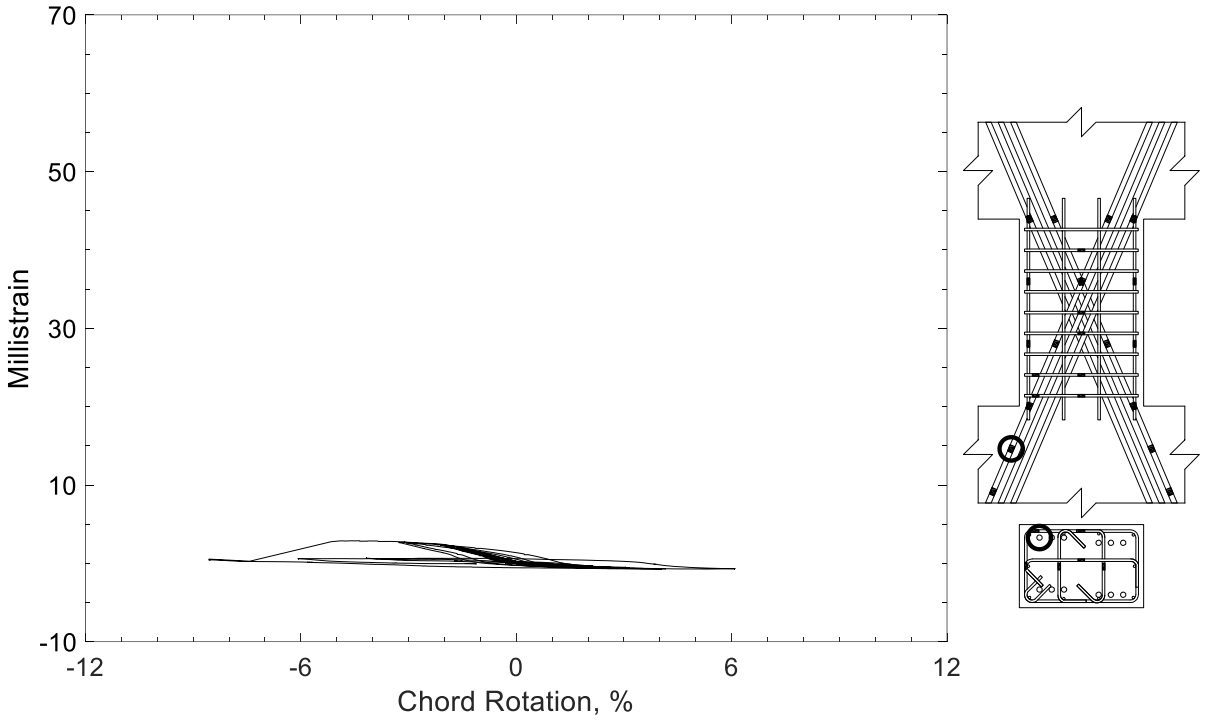

Figure 315 – Measured strain in diagonal bar of D120-1.5, strain gauge D3

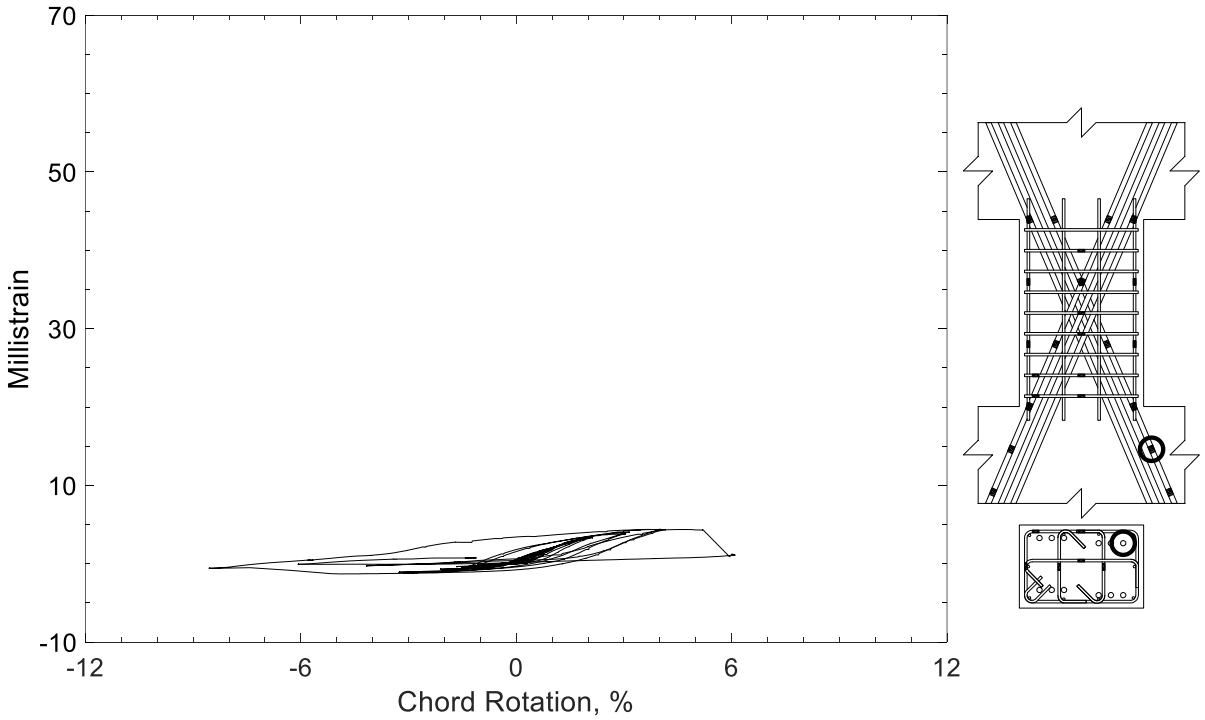

Figure 316 – Measured strain in diagonal bar of D120-1.5, strain gauge D4

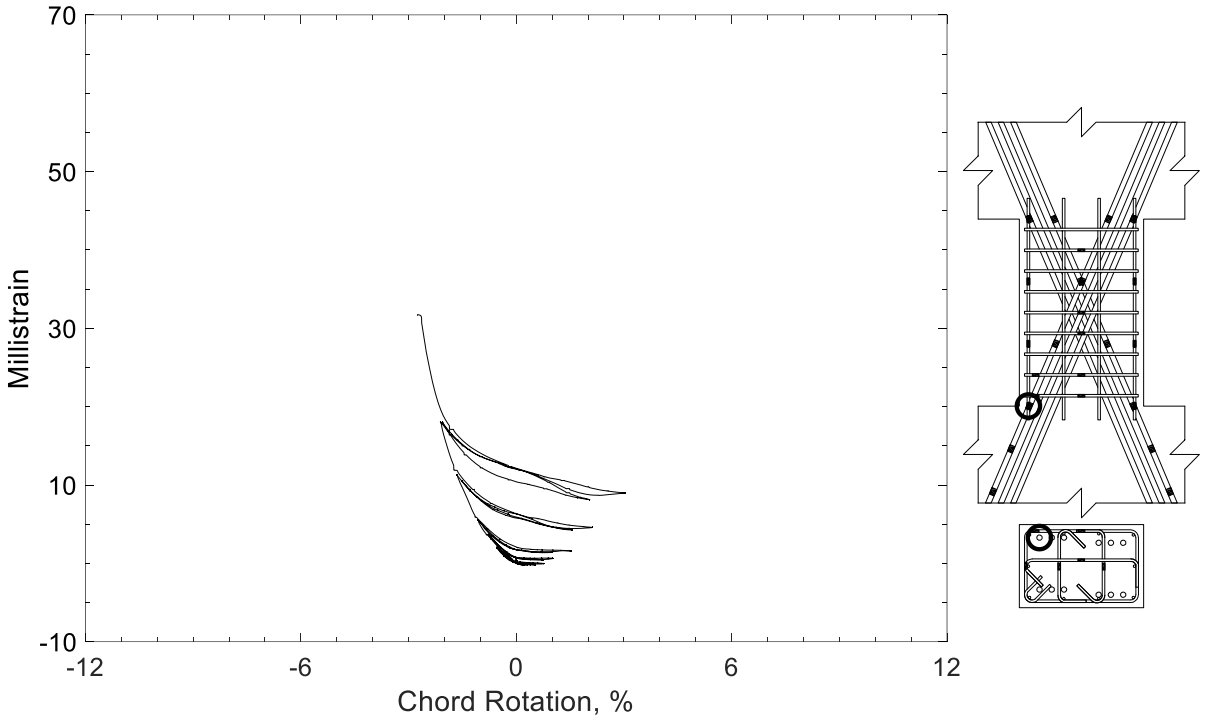

Figure 317 – Measured strain in diagonal bar of D120-1.5, strain gauge D5

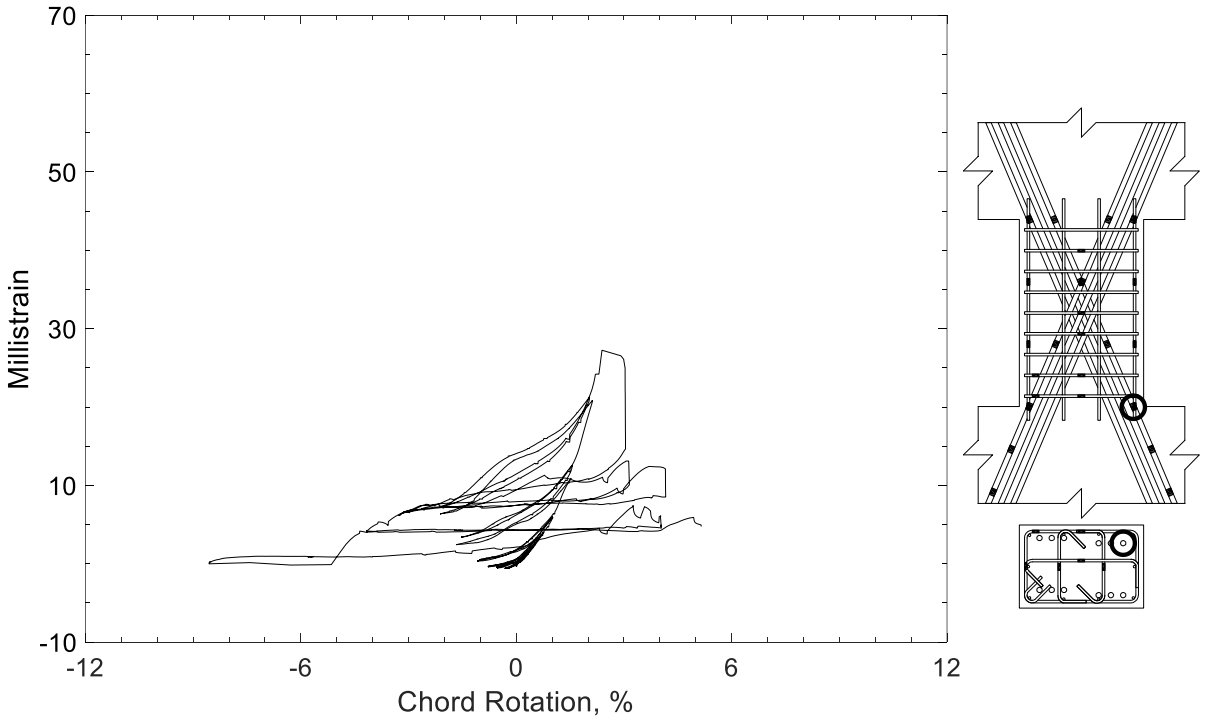

Figure 318 – Measured strain in diagonal bar of D120-1.5, strain gauge D6

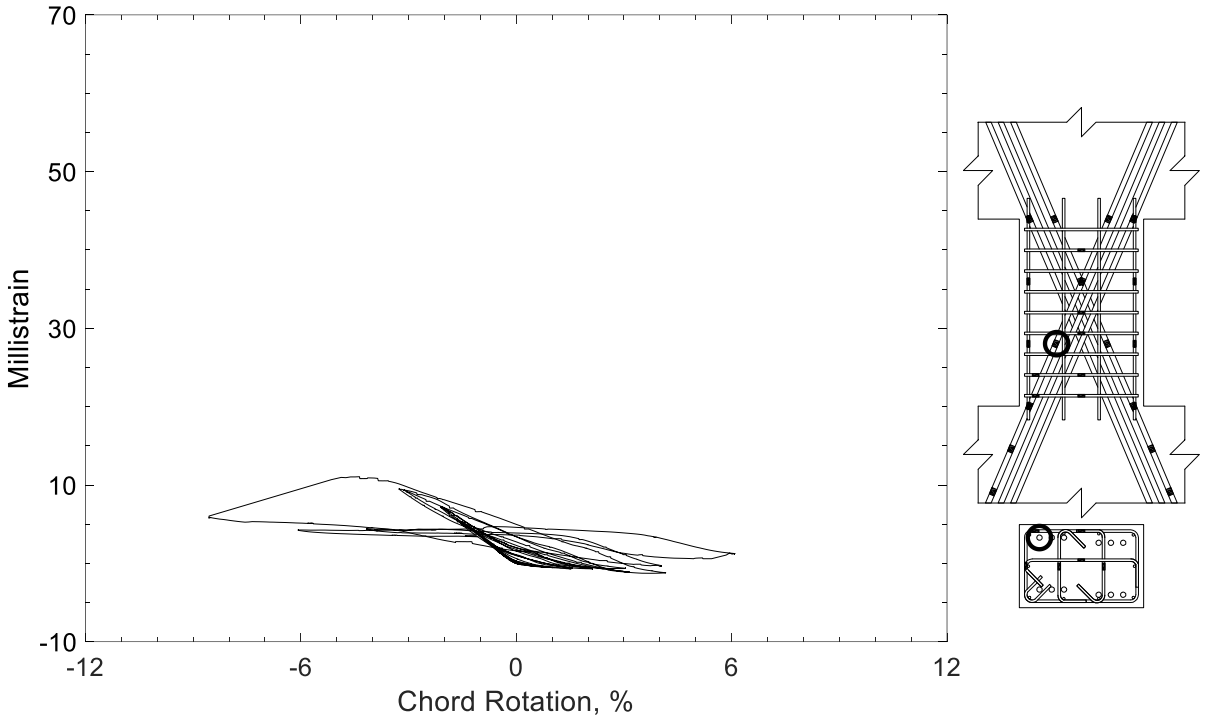

Figure 319 – Measured strain in diagonal bar of D120-1.5, strain gauge D7

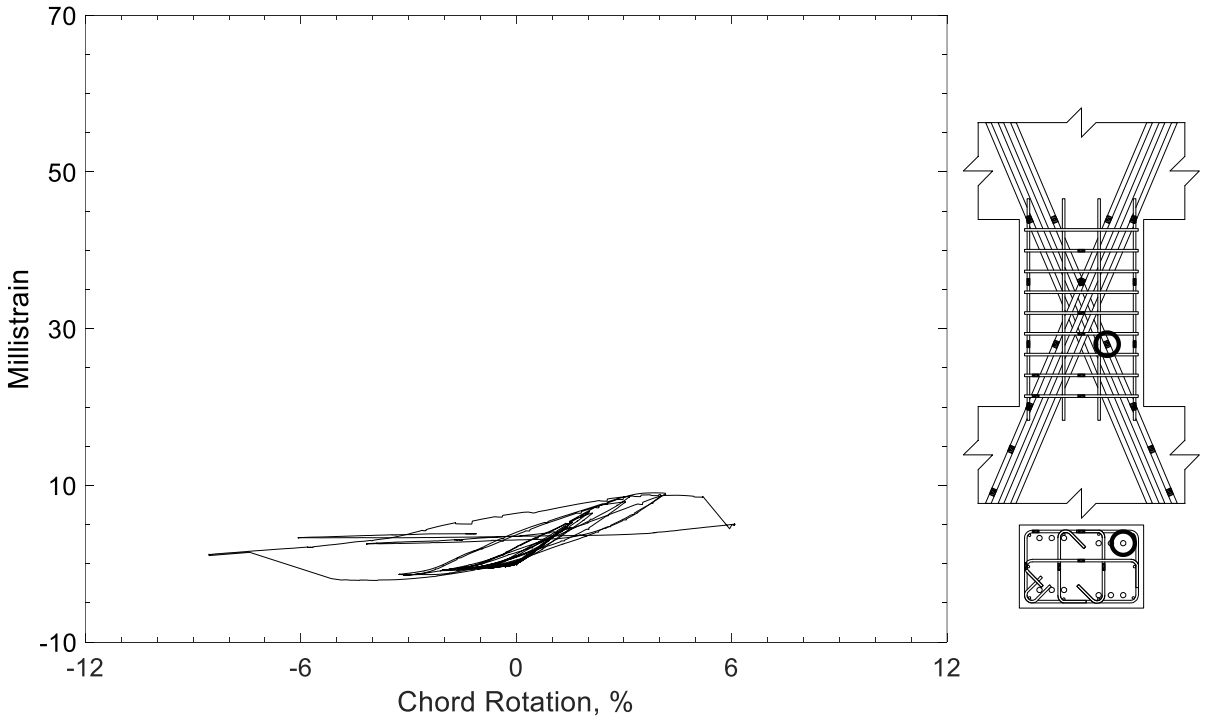

Figure 320 – Measured strain in diagonal bar of D120-1.5, strain gauge D8

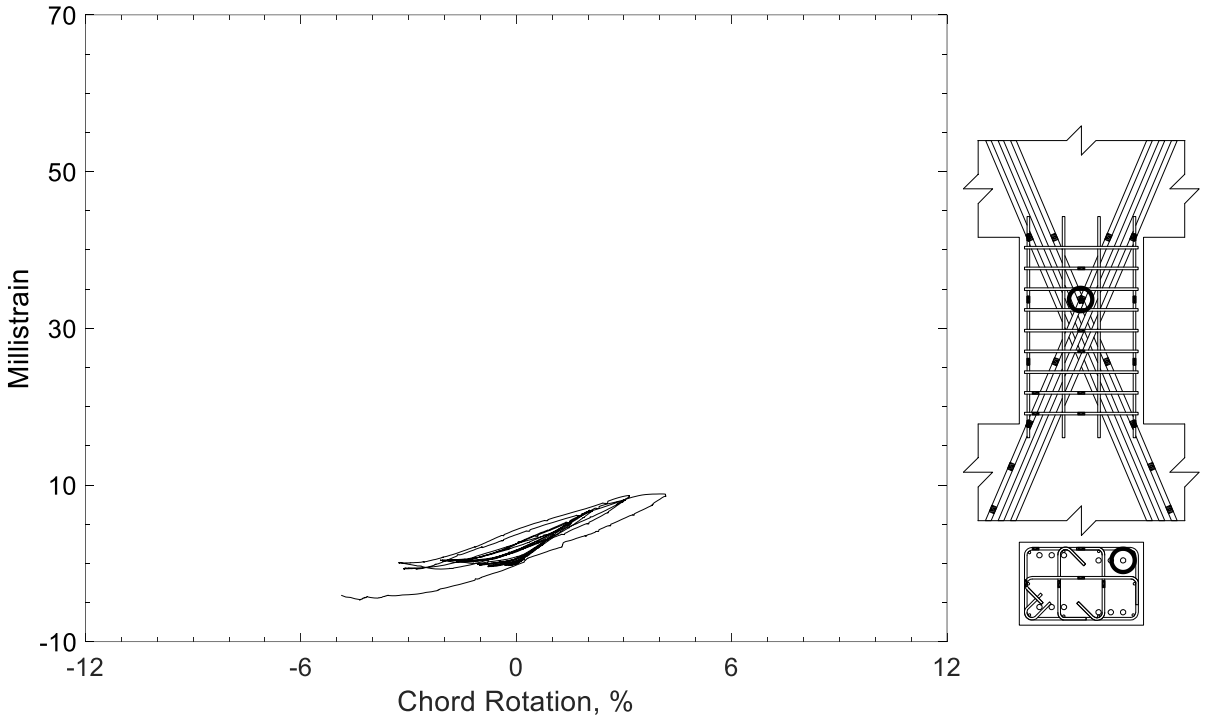

Figure 321 – Measured strain in diagonal bar of D120-1.5, strain gauge D9

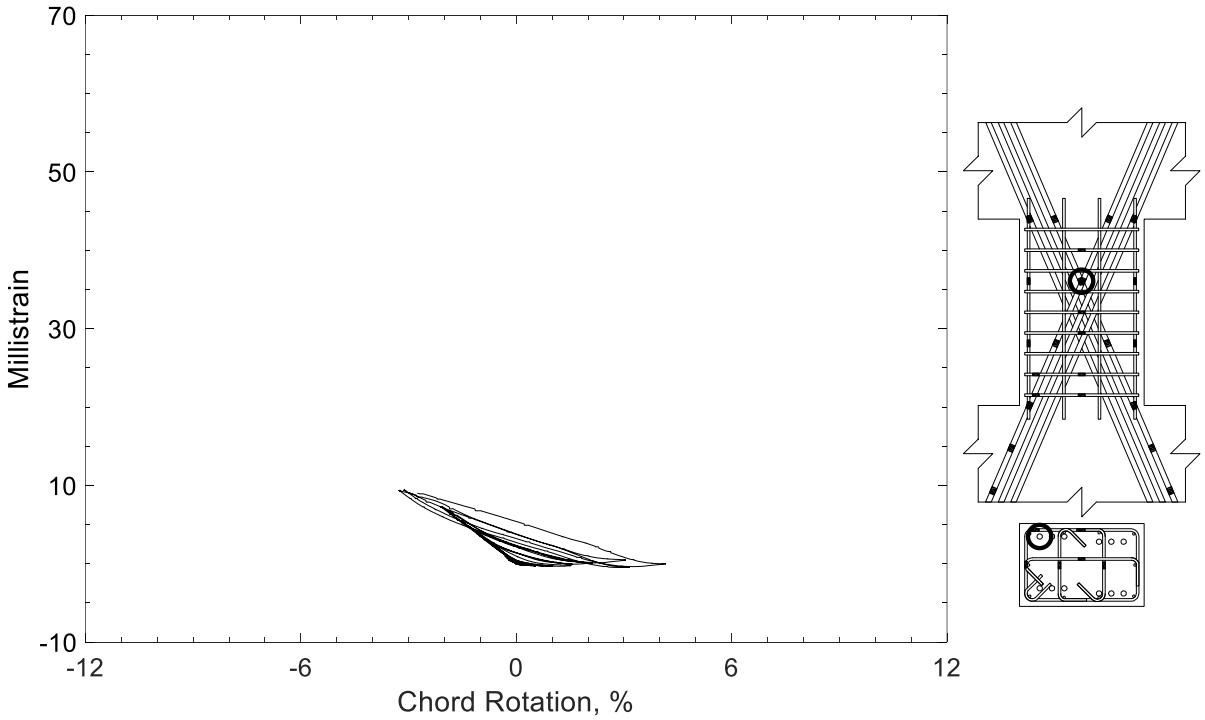

Figure 322 – Measured strain in diagonal bar of D120-1.5, strain gauge D10

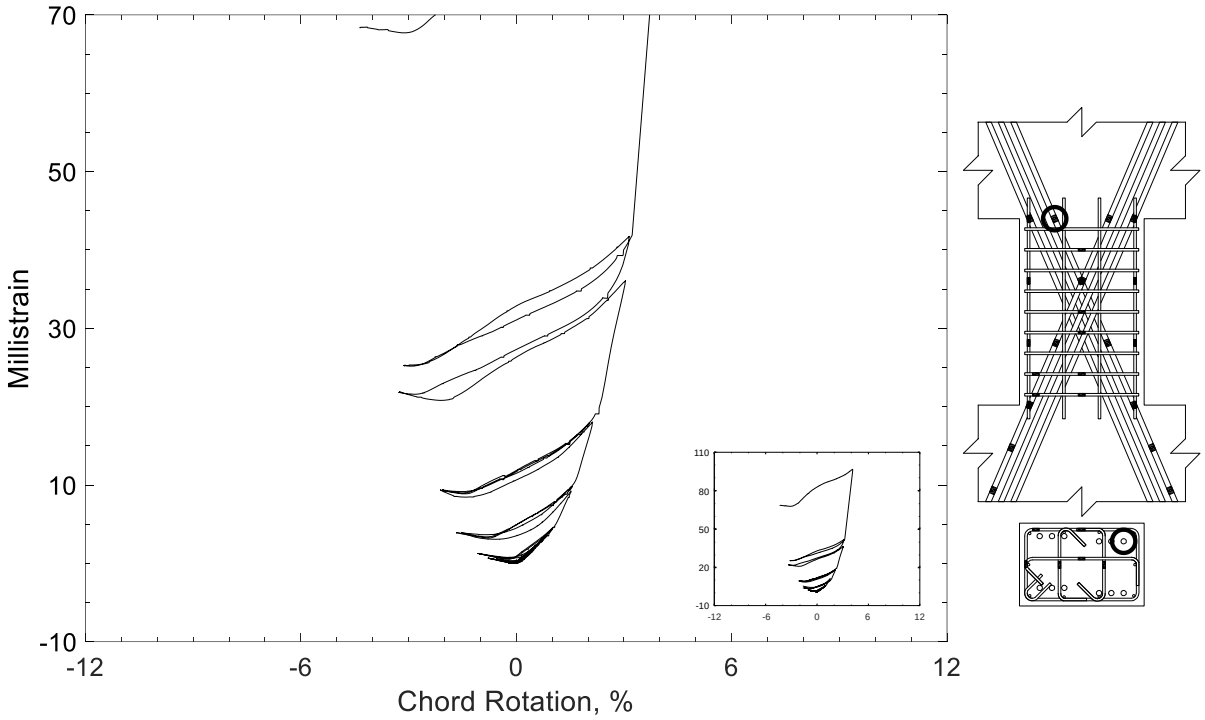

Figure 323 – Measured strain in diagonal bar of D120-1.5, strain gauge D11

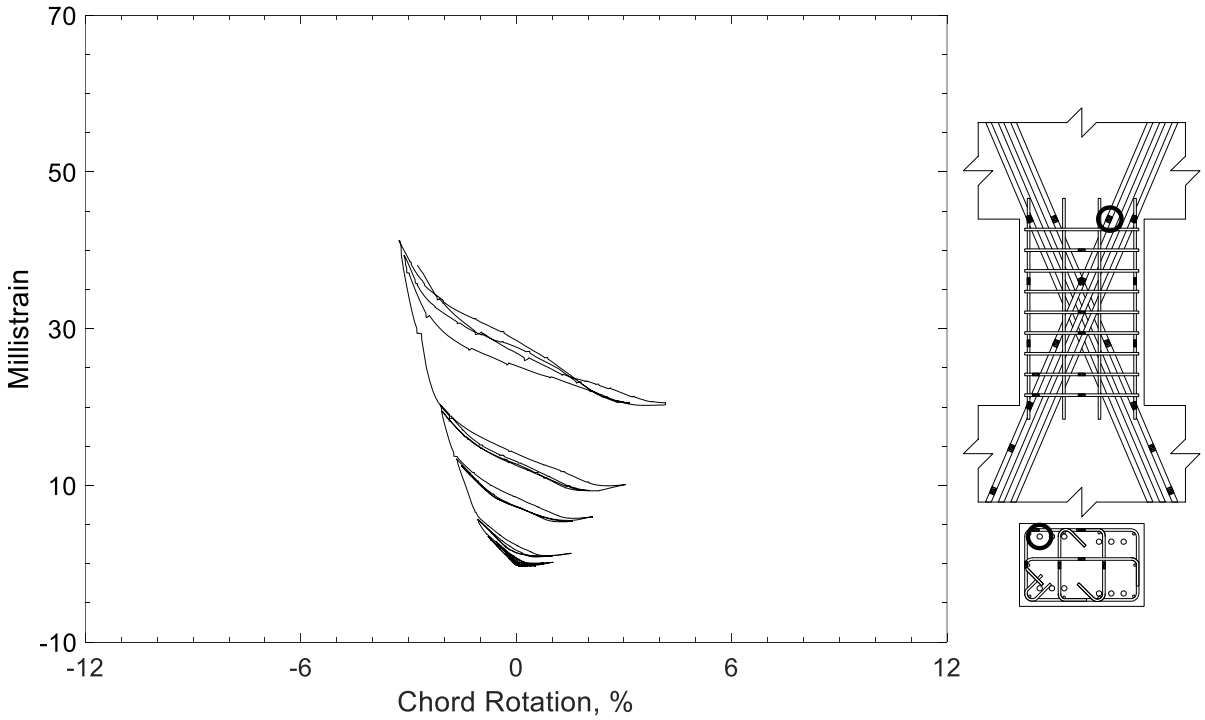

Figure 324 – Measured strain in diagonal bar of D120-1.5, strain gauge D12

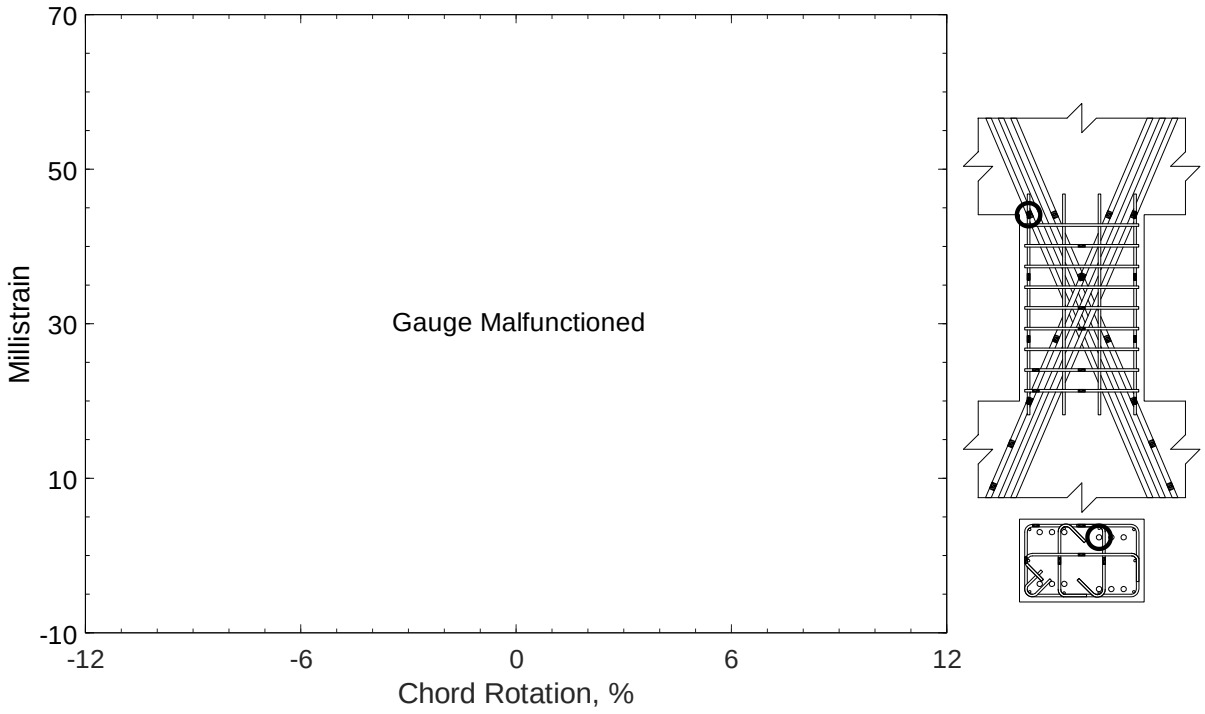

Figure 325 – Measured strain in diagonal bar of D120-1.5, strain gauge D13

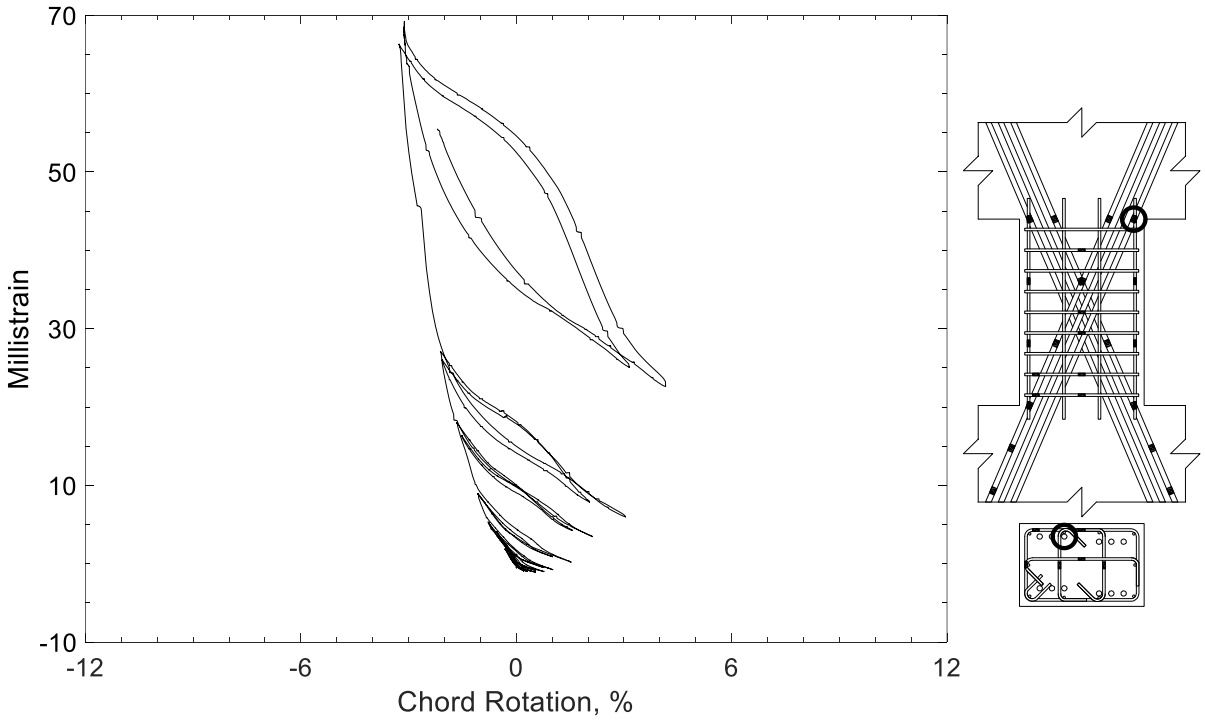

Figure 326 – Measured strain in diagonal bar of D120-1.5, strain gauge D14

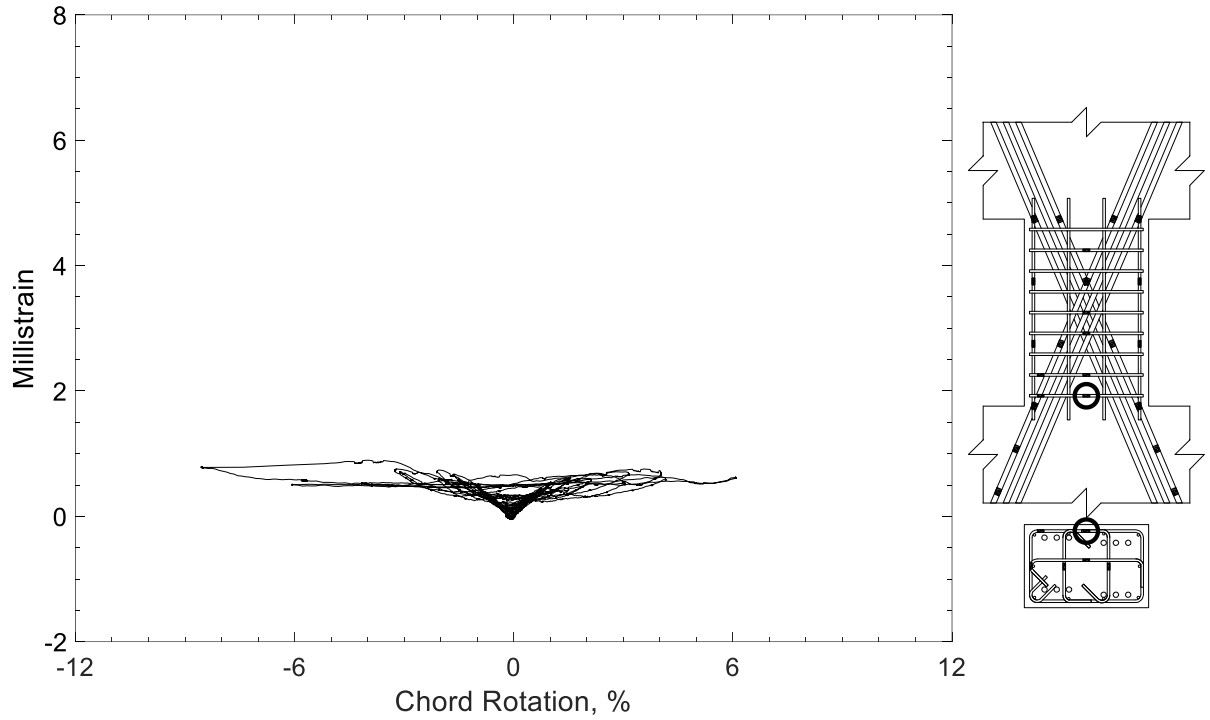

Figure 327 – Measured strain in closed stirrup of D120-1.5, strain gauge S1

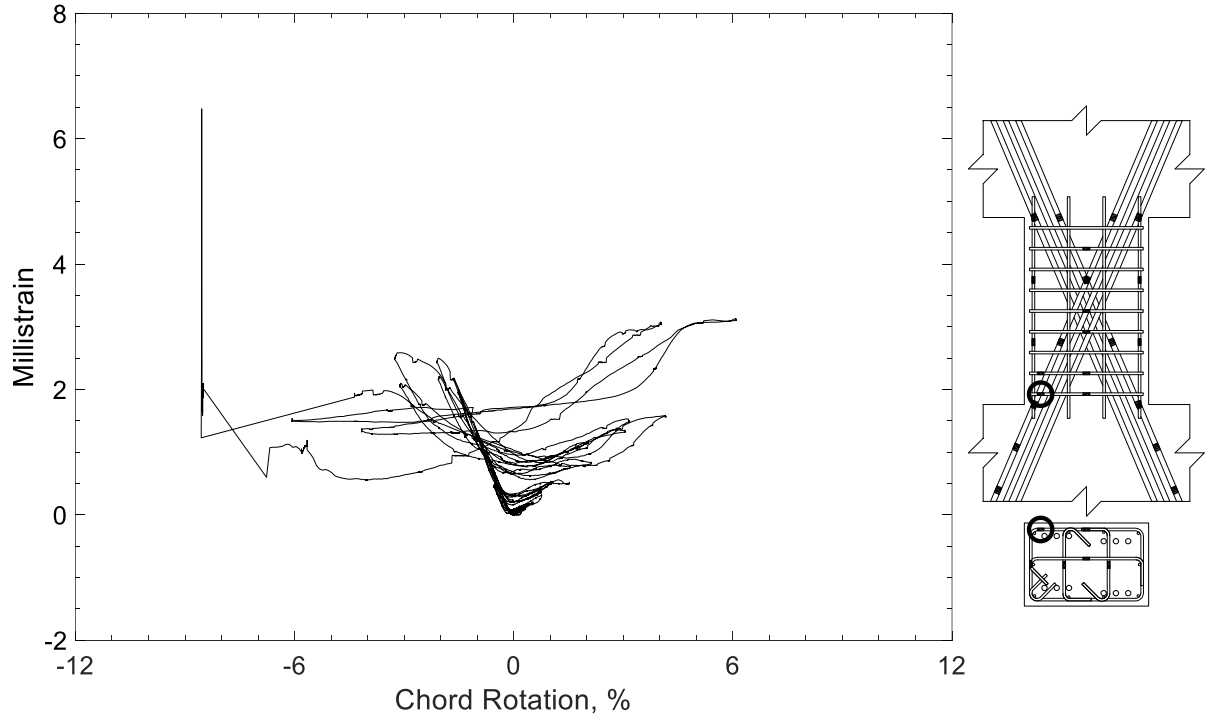

Figure 328 – Measured strain in closed stirrup of D120-1.5, strain gauge S2

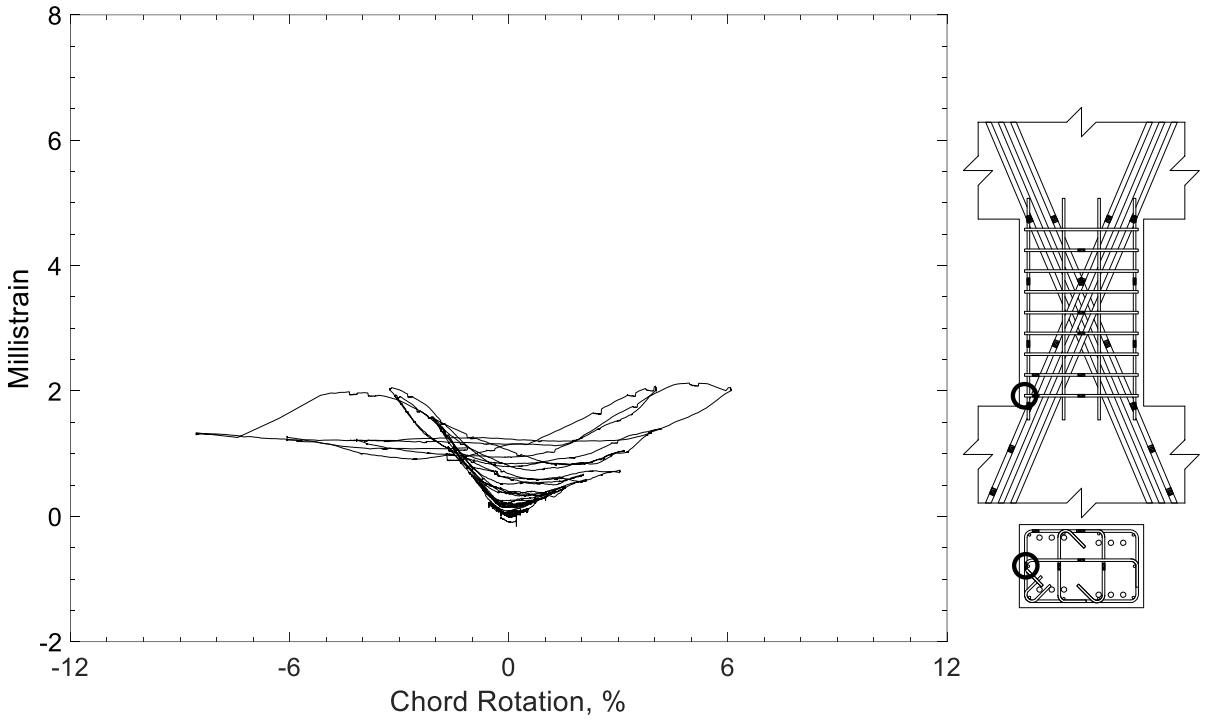

Figure 329 – Measured strain in closed stirrup of D120-1.5, strain gauge S3

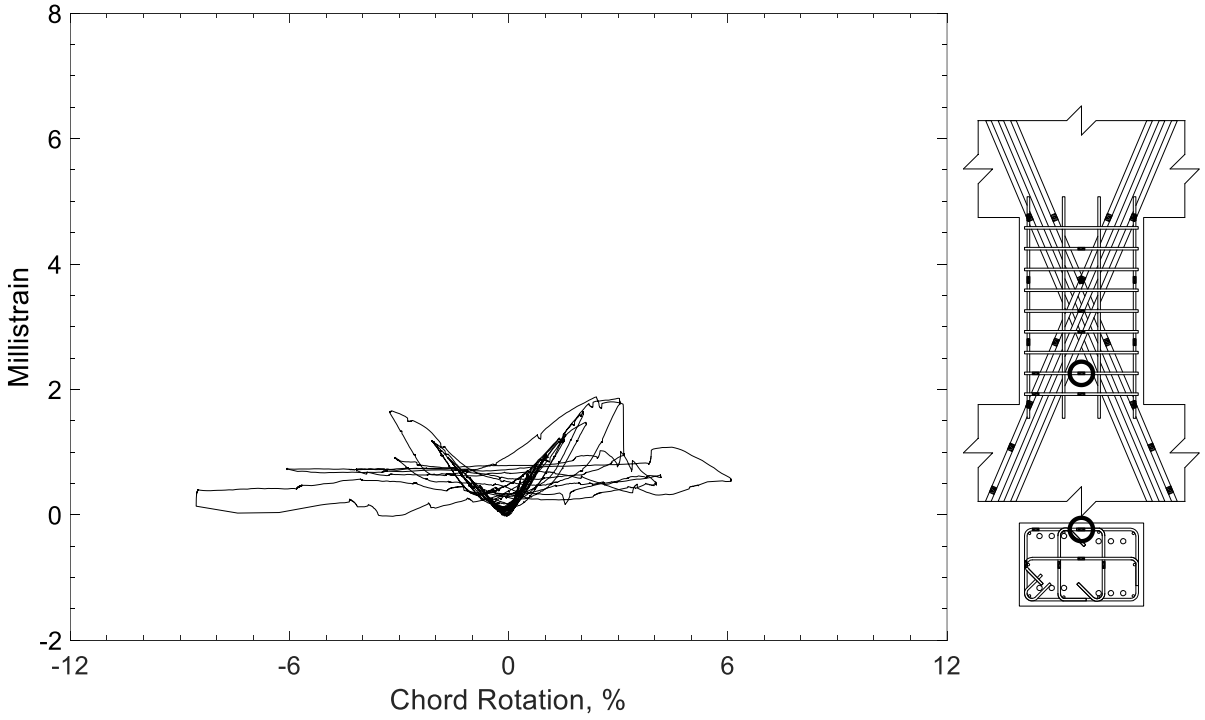

Figure 330 – Measured strain in closed stirrup of D120-1.5, strain gauge S4

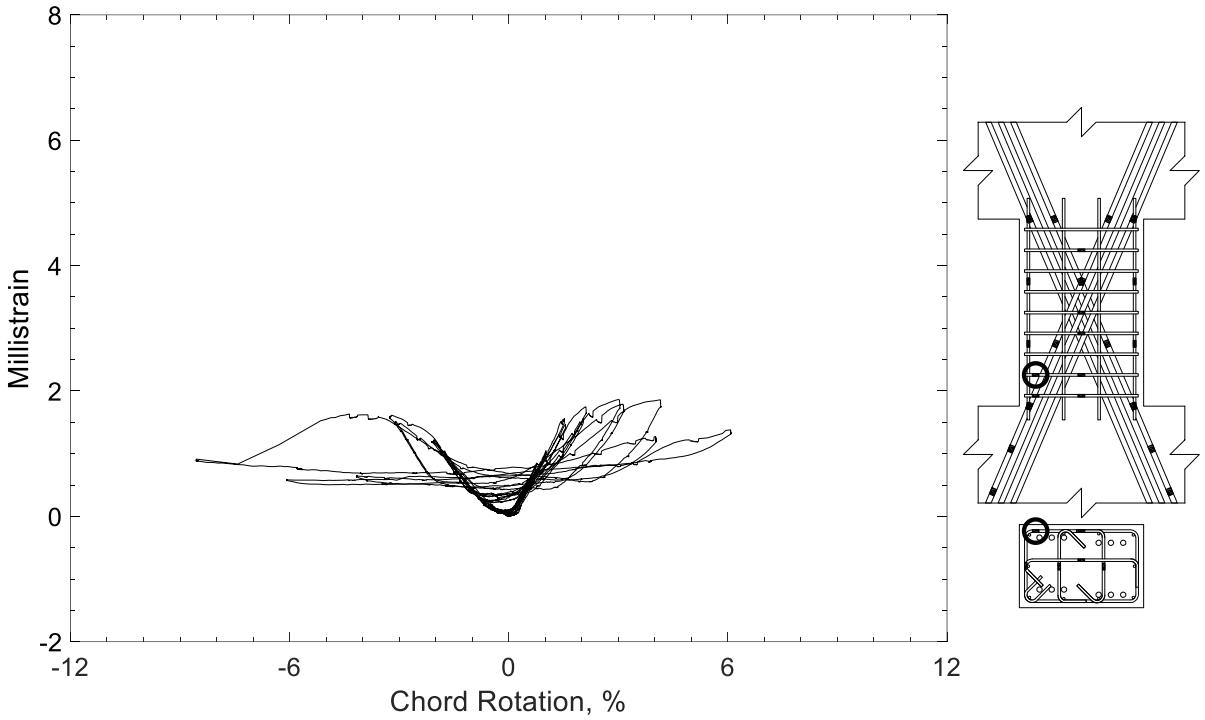

Figure 331 – Measured strain in closed stirrup of D120-1.5, strain gauge S5

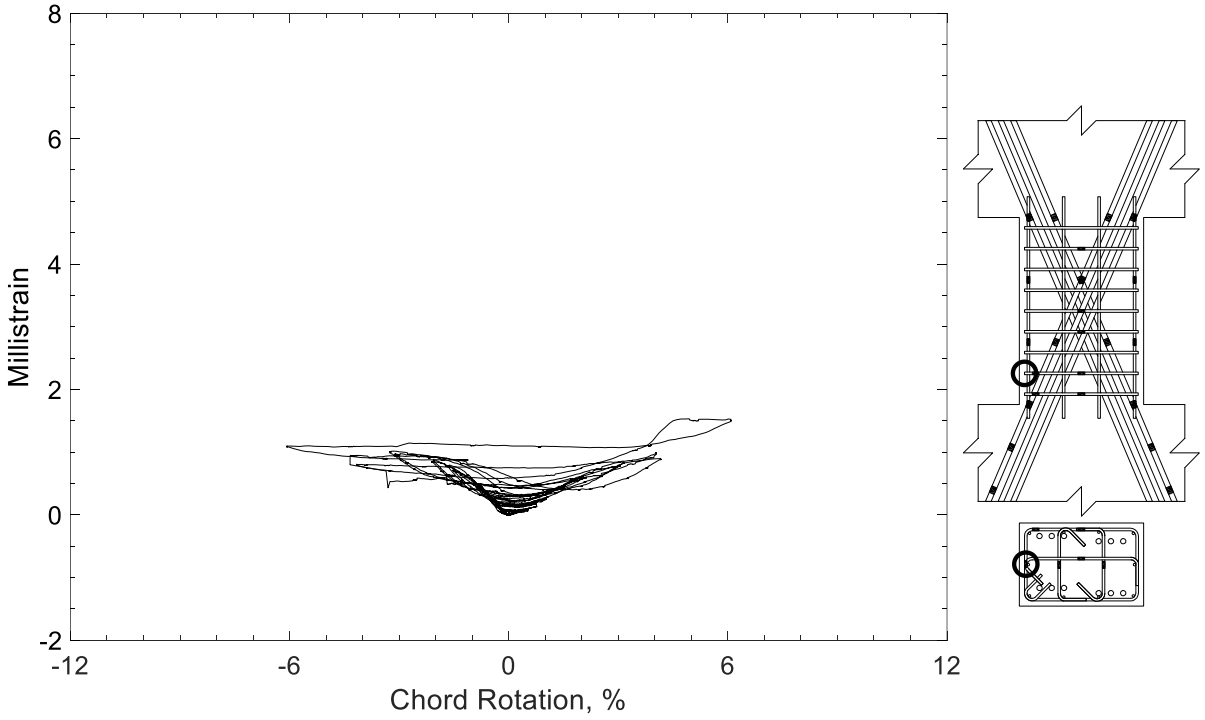

Figure 332 – Measured strain in closed stirrup of D120-1.5, strain gauge S6

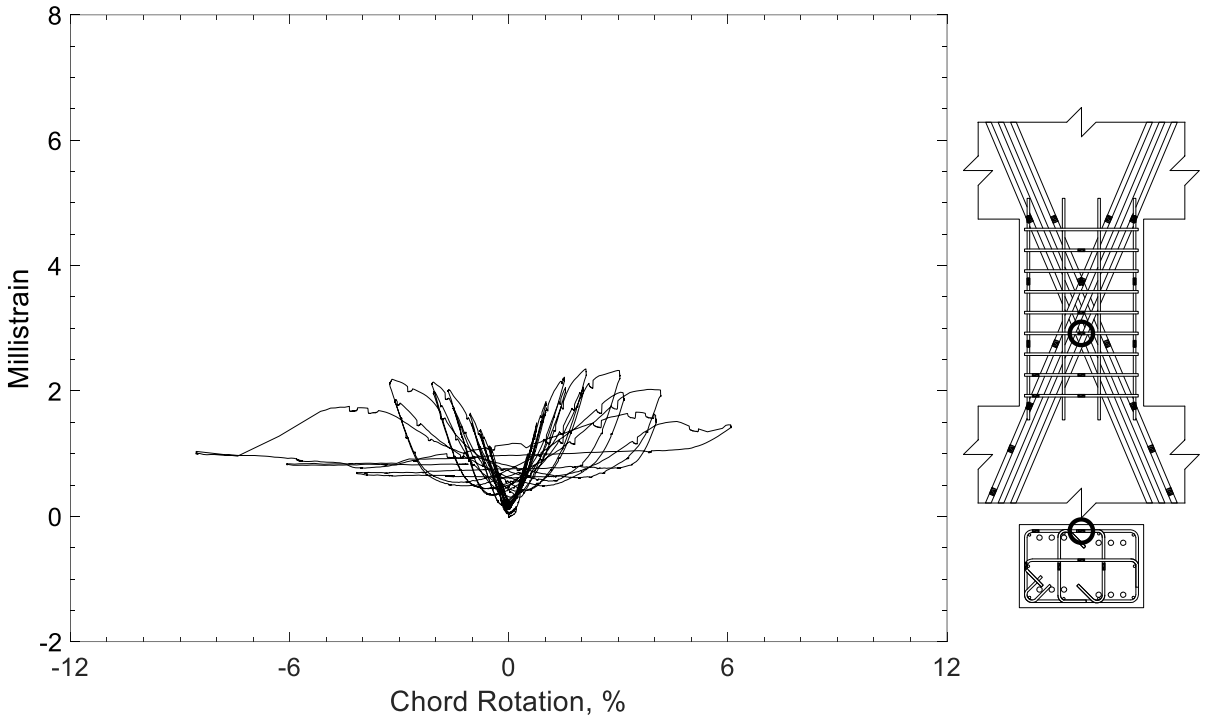

Figure 333 – Measured strain in closed stirrup of D120-1.5, strain gauge S7

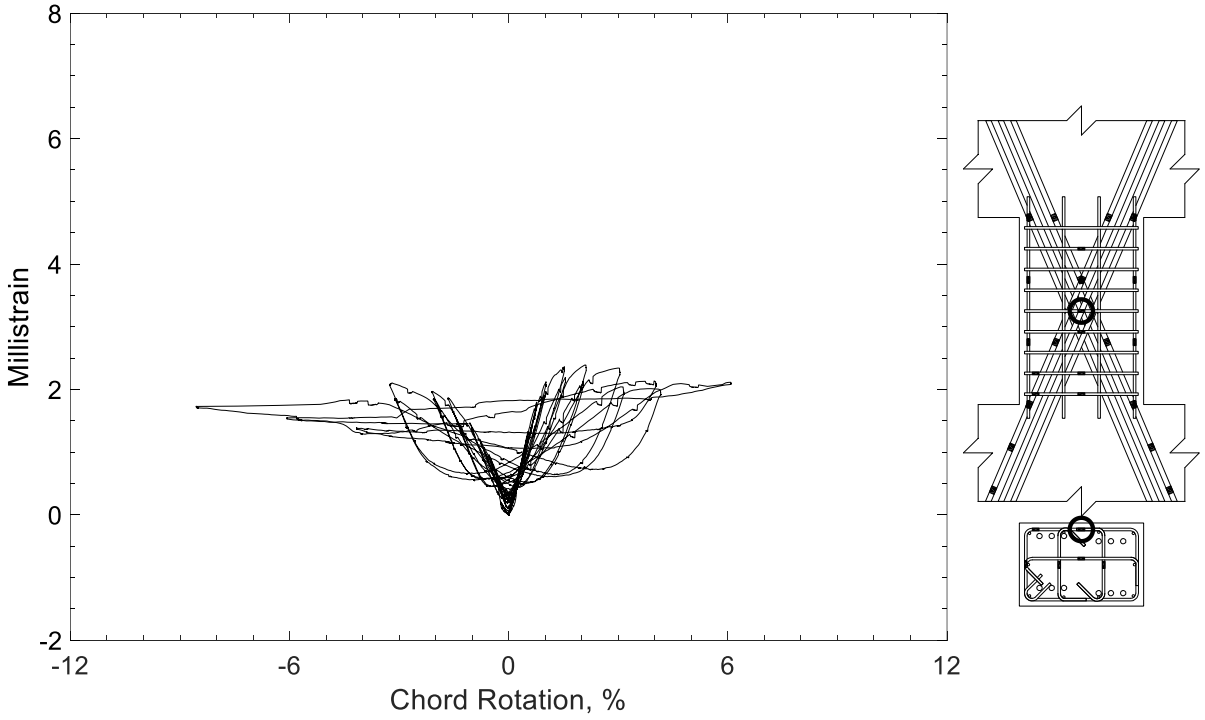

Figure 334 – Measured strain in closed stirrup of D120-1.5, strain gauge S8

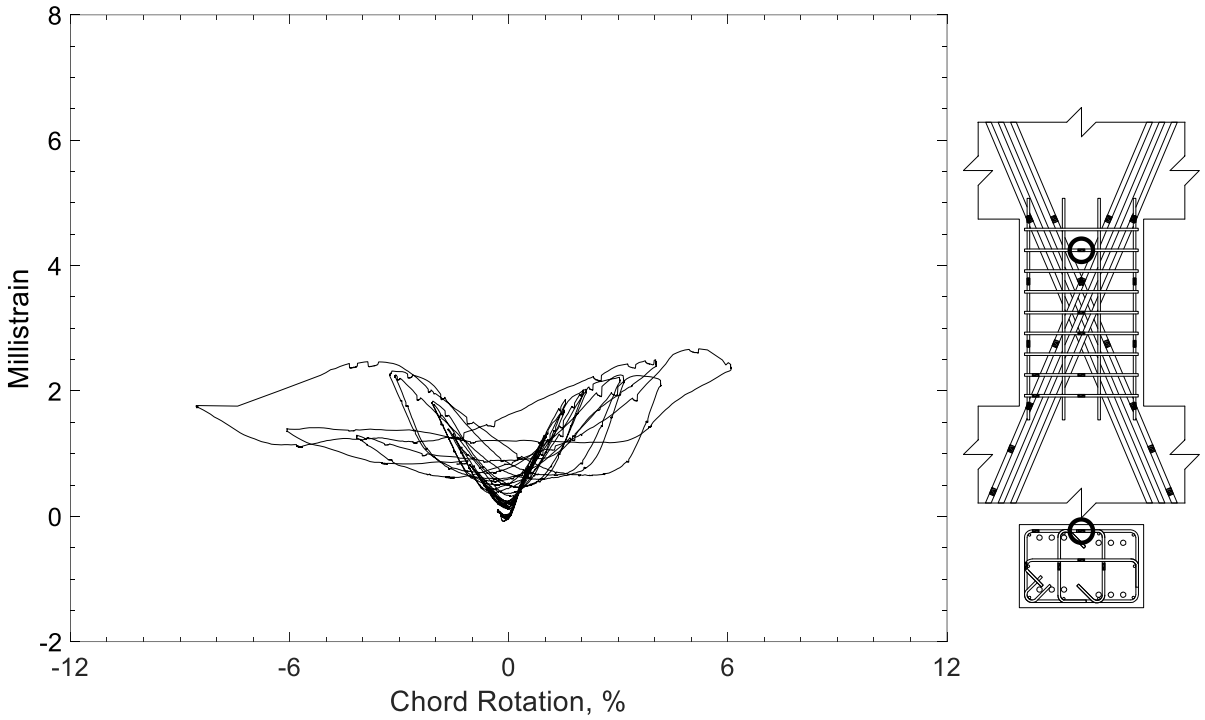

Figure 335 – Measured strain in closed stirrup of D120-1.5, strain gauge S9

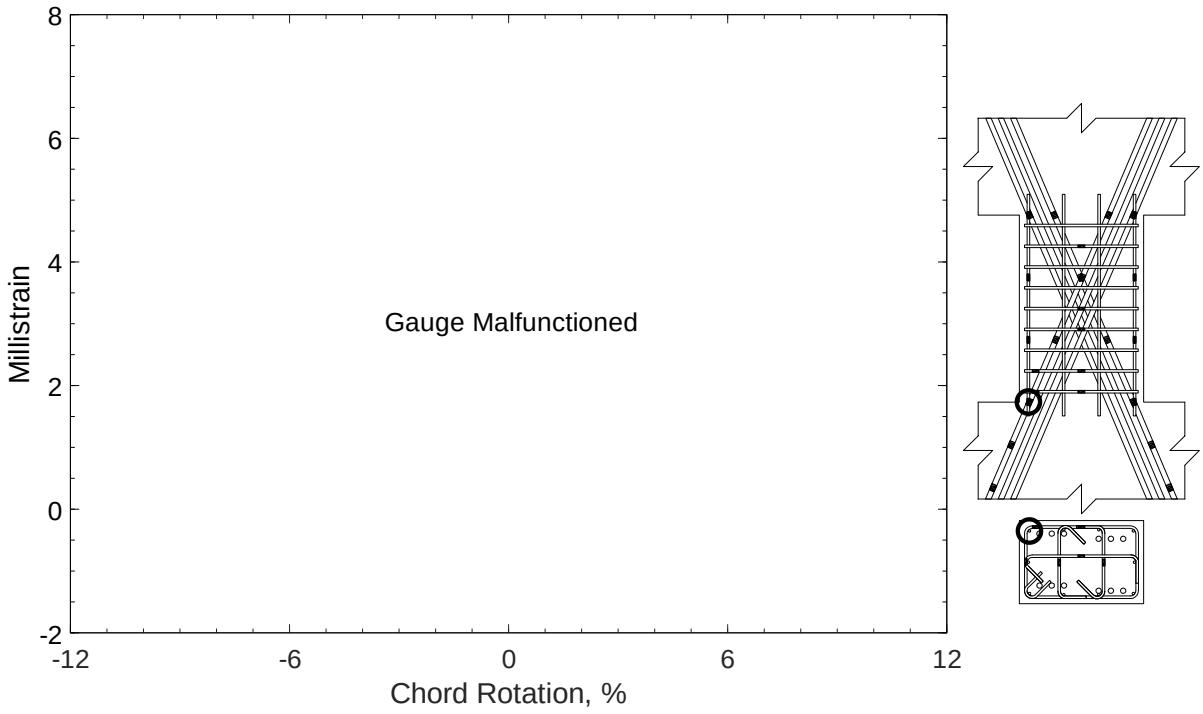

Figure 336 – Measured strain in parallel bar of D120-1.5, strain gauge H1

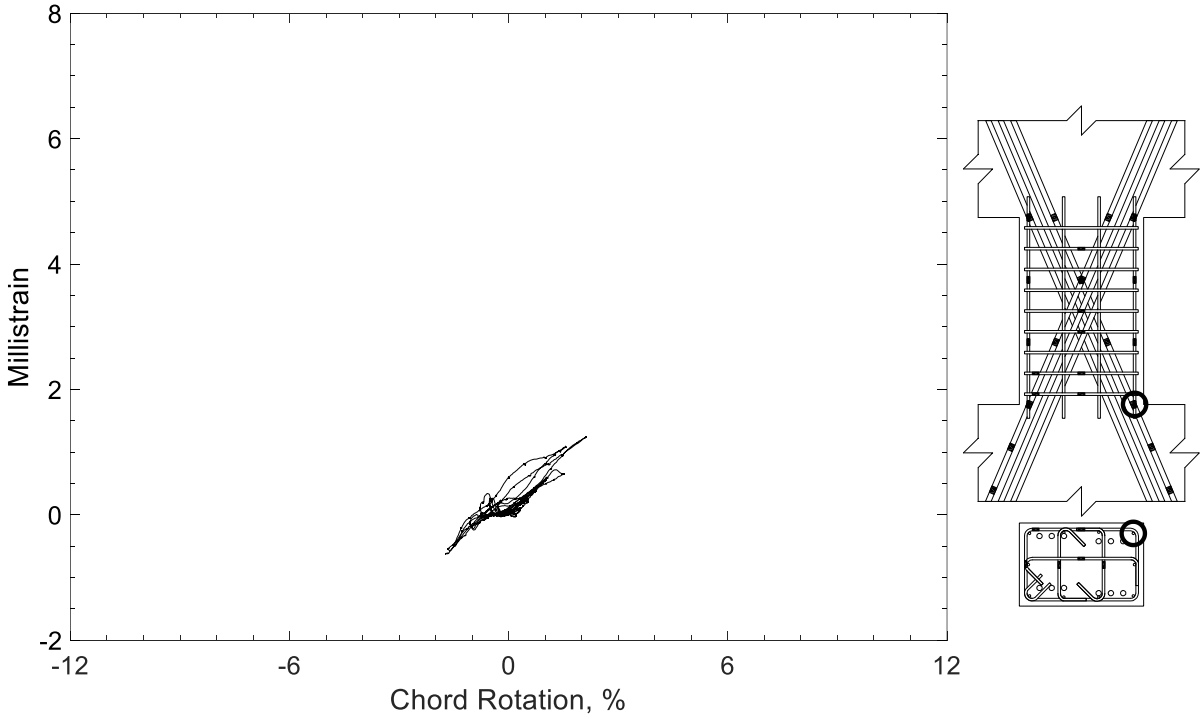

Figure 337 – Measured strain in parallel bar of D120-1.5, strain gauge H2

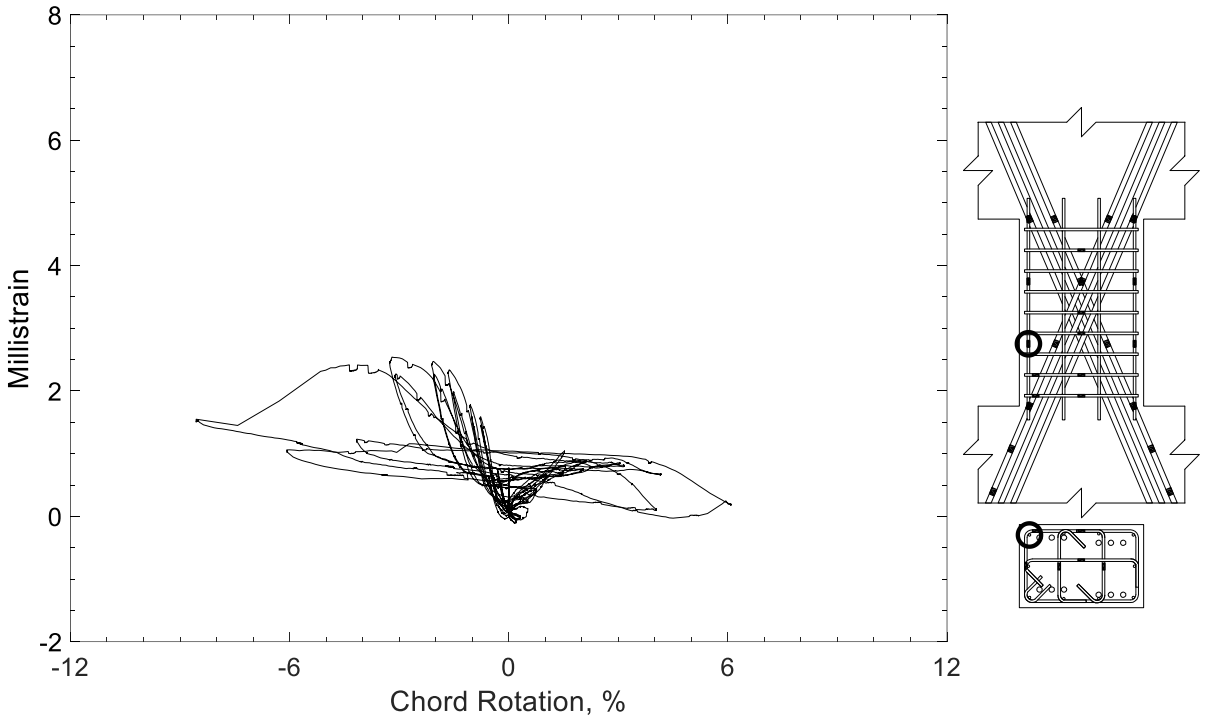

Figure 338 – Measured strain in parallel bar of D120-1.5, strain gauge H3

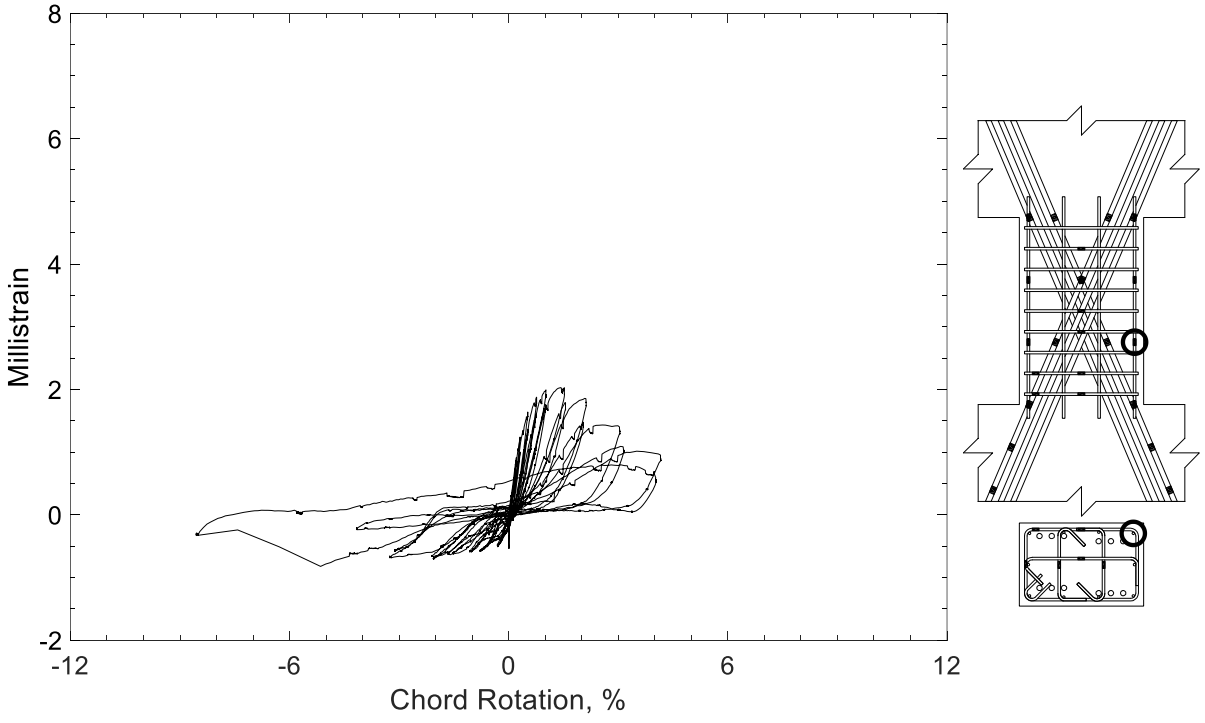

Figure 339 – Measured strain in parallel bar of D120-1.5, strain gauge H4

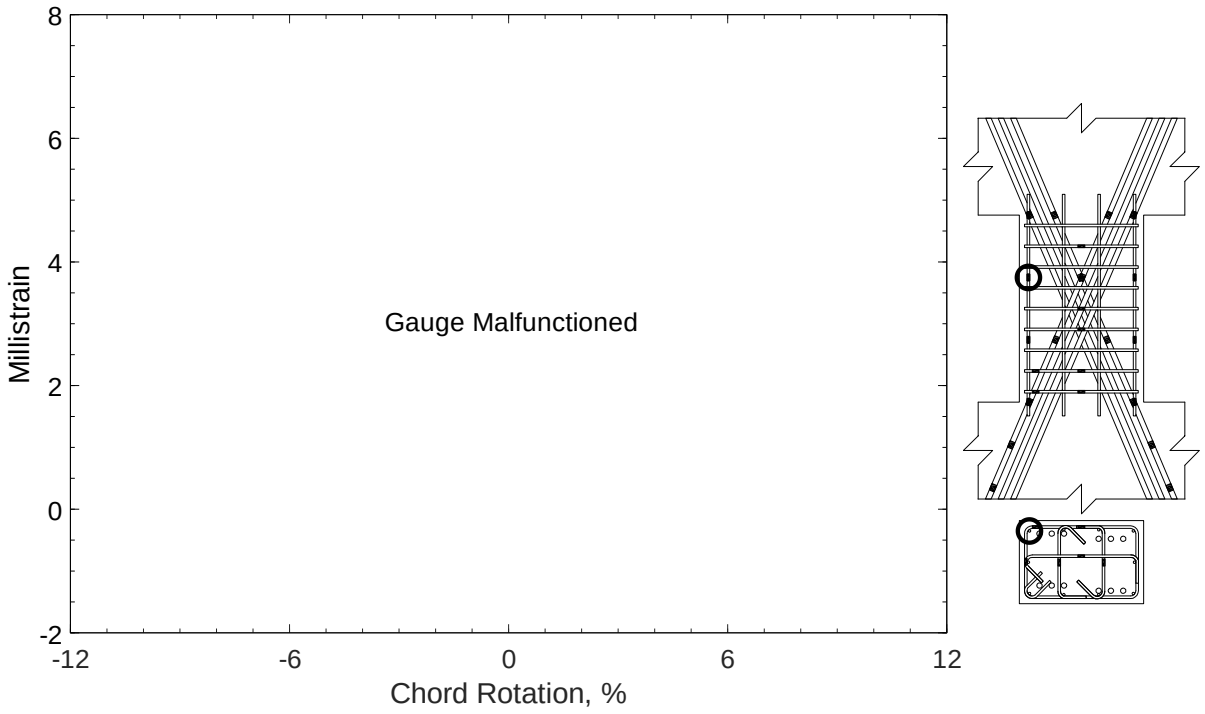

Figure 340 – Measured strain in parallel bar of D120-1.5, strain gauge H5

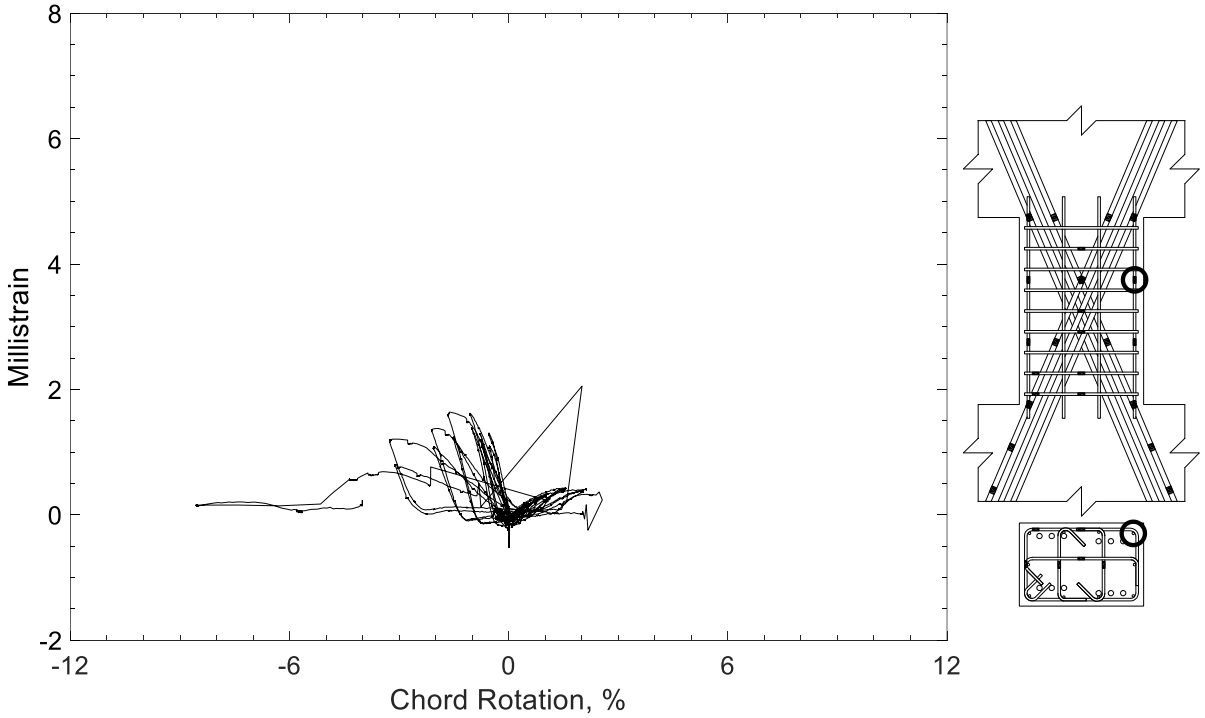

Figure 341 – Measured strain in parallel bar of D120-1.5, strain gauge H6

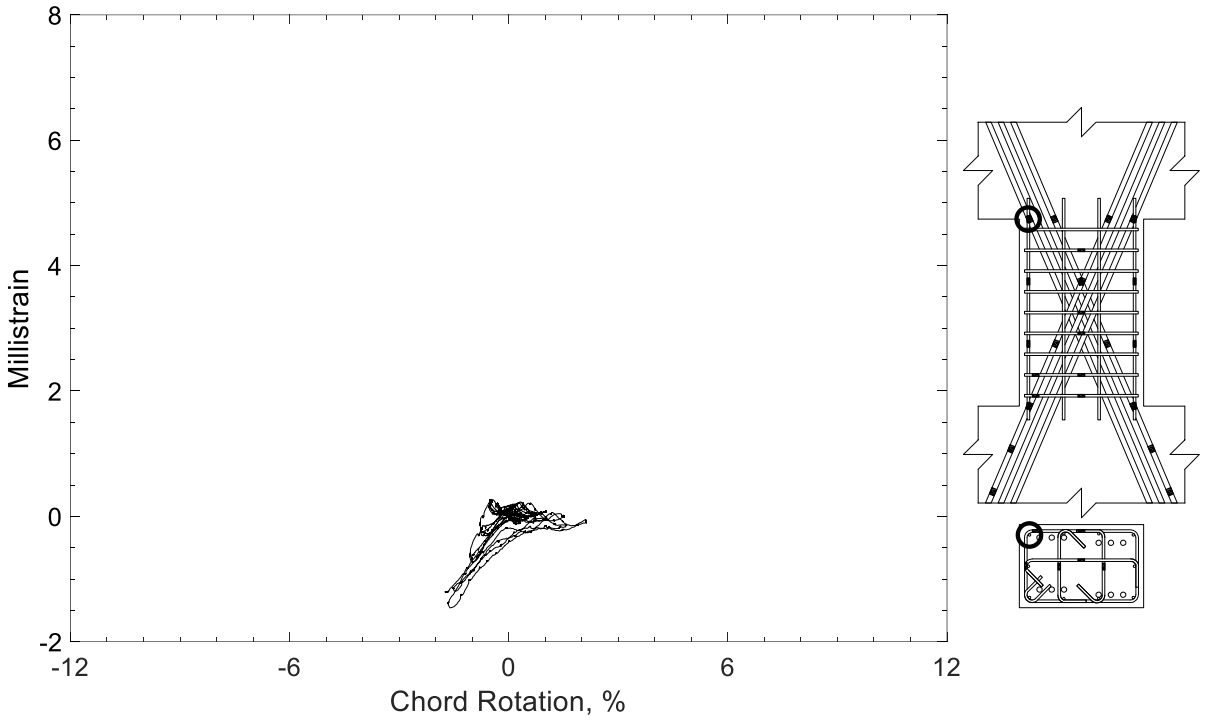

Figure 342 – Measured strain in parallel bar of D120-1.5, strain gauge H7

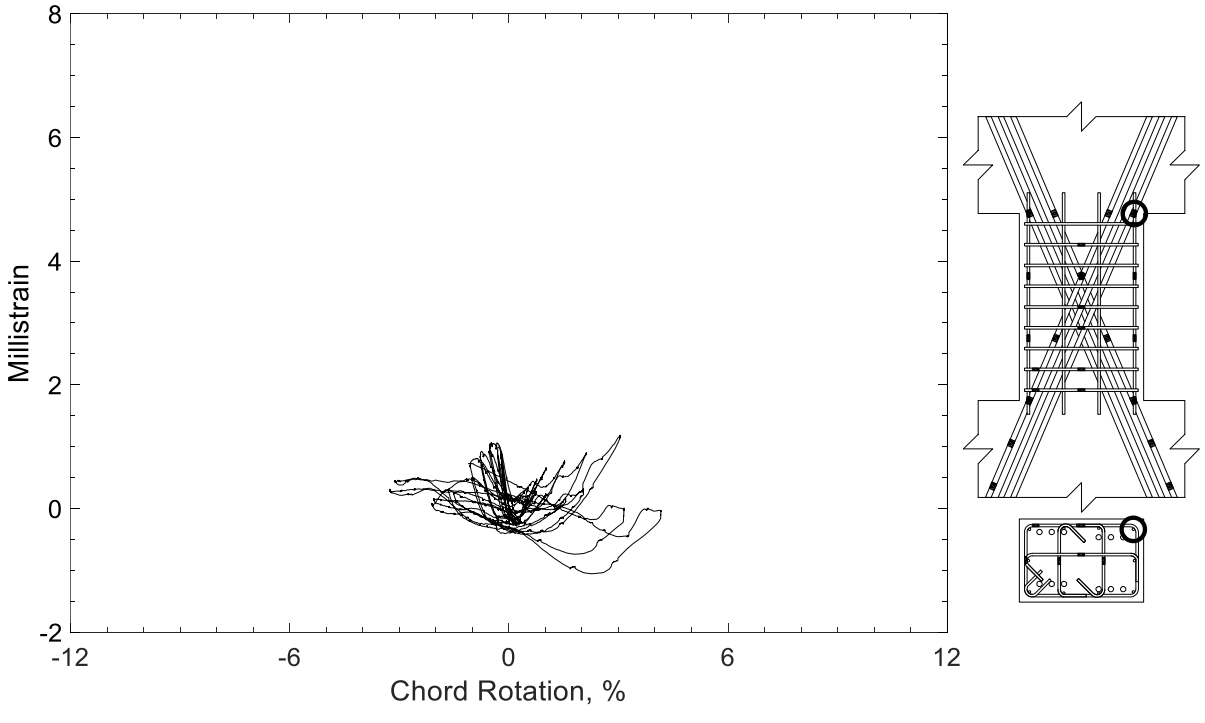

Figure 343 – Measured strain in parallel bar of D120-1.5, strain gauge H8

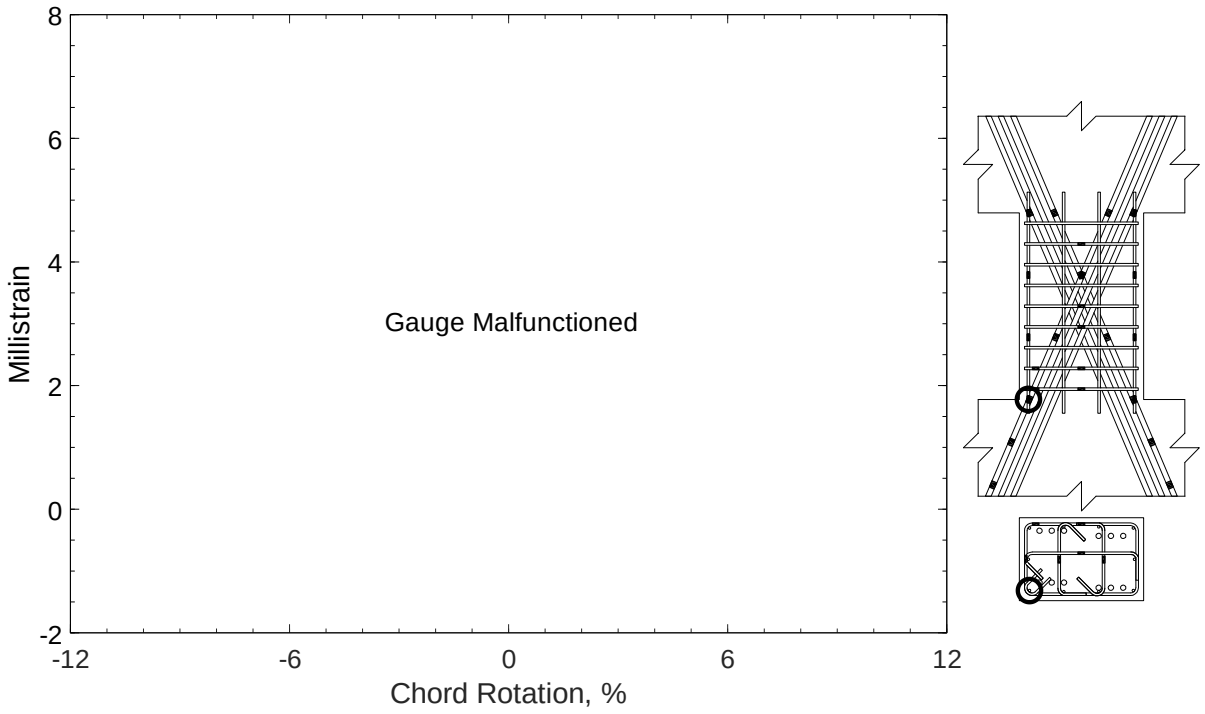

Figure 344 – Measured strain in parallel bar of D120-1.5, strain gauge H9

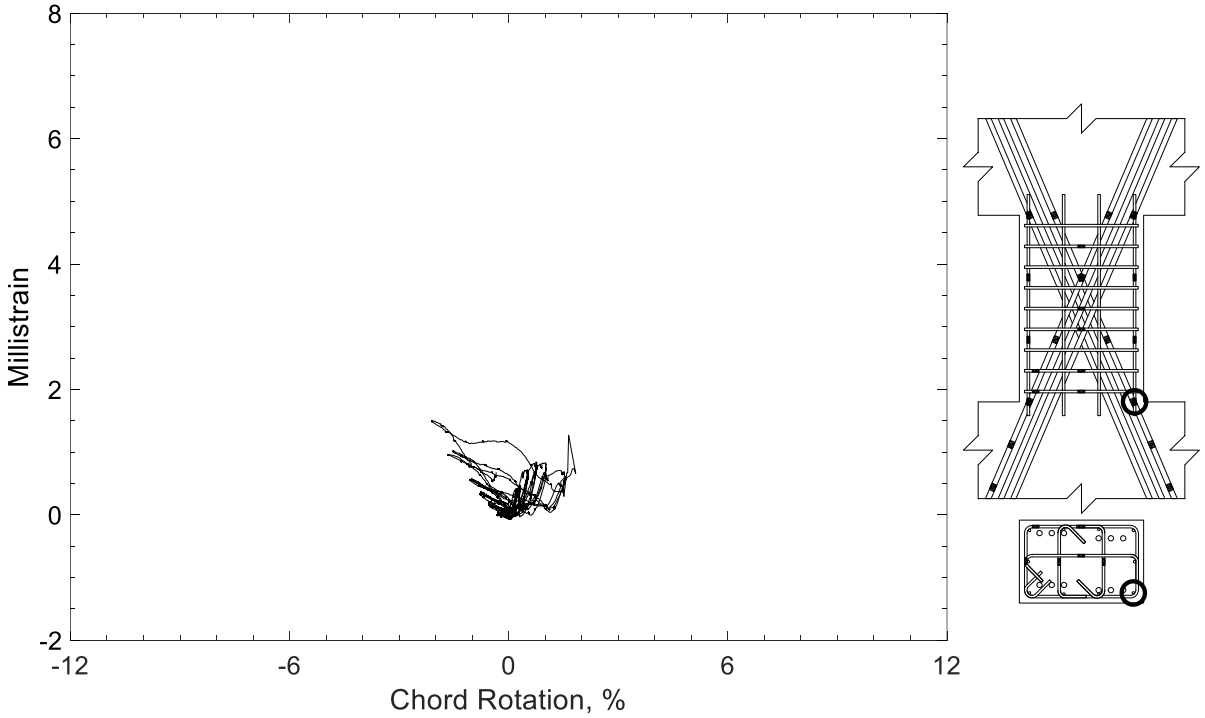

Figure 345 – Measured strain in parallel bar of D120-1.5, strain gauge H10

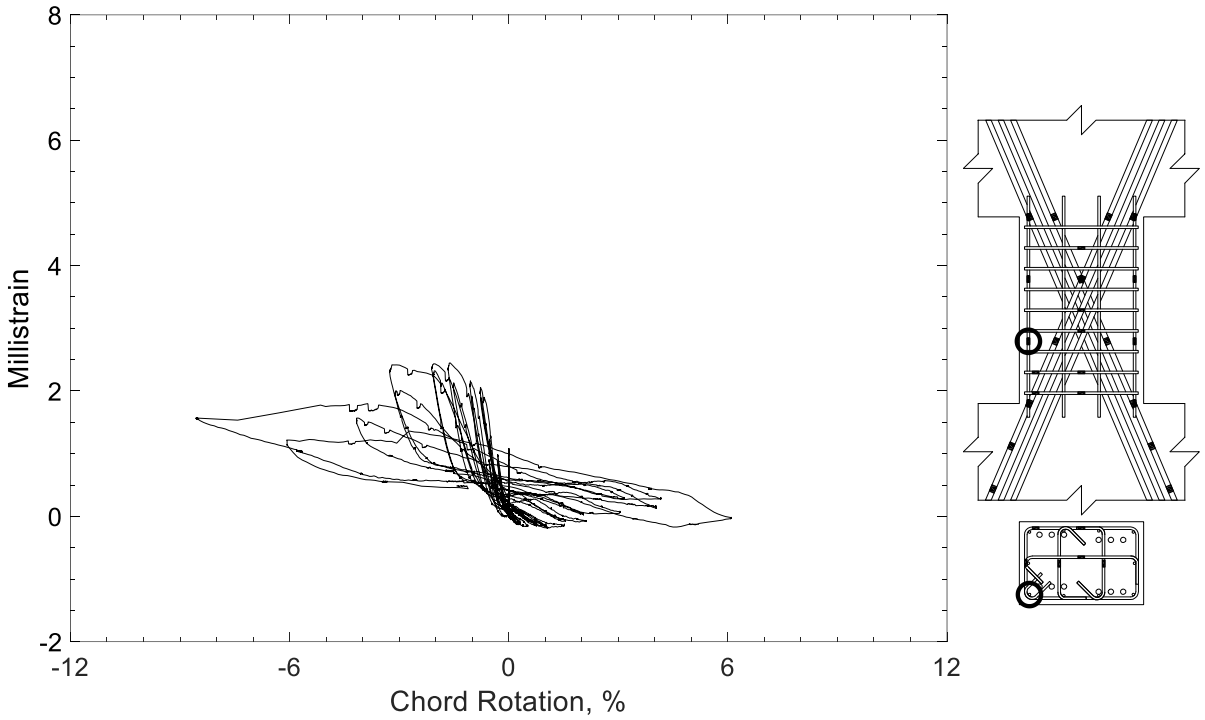

Figure 346 – Measured strain in parallel bar of D120-1.5, strain gauge H11

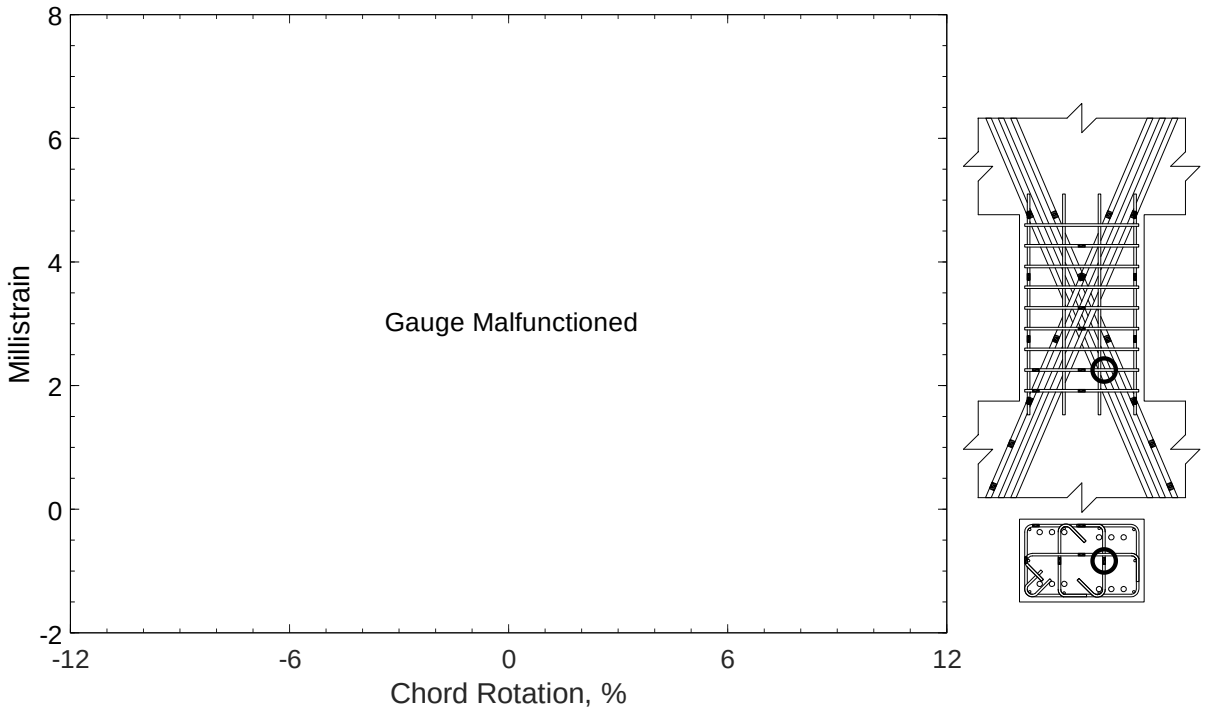

Figure 347 – Measured strain in crosstie of D120-1.5, strain gauge T1

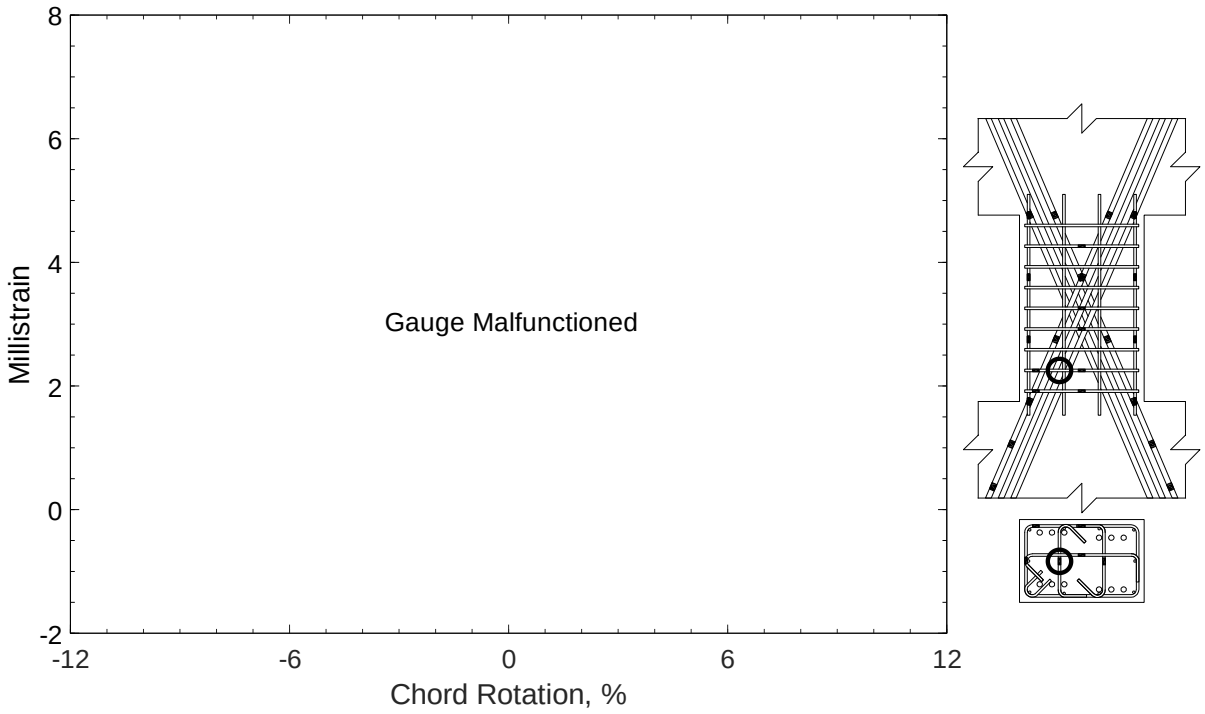

Figure 348 – Measured strain in crosstie of D120-1.5, strain gauge T2

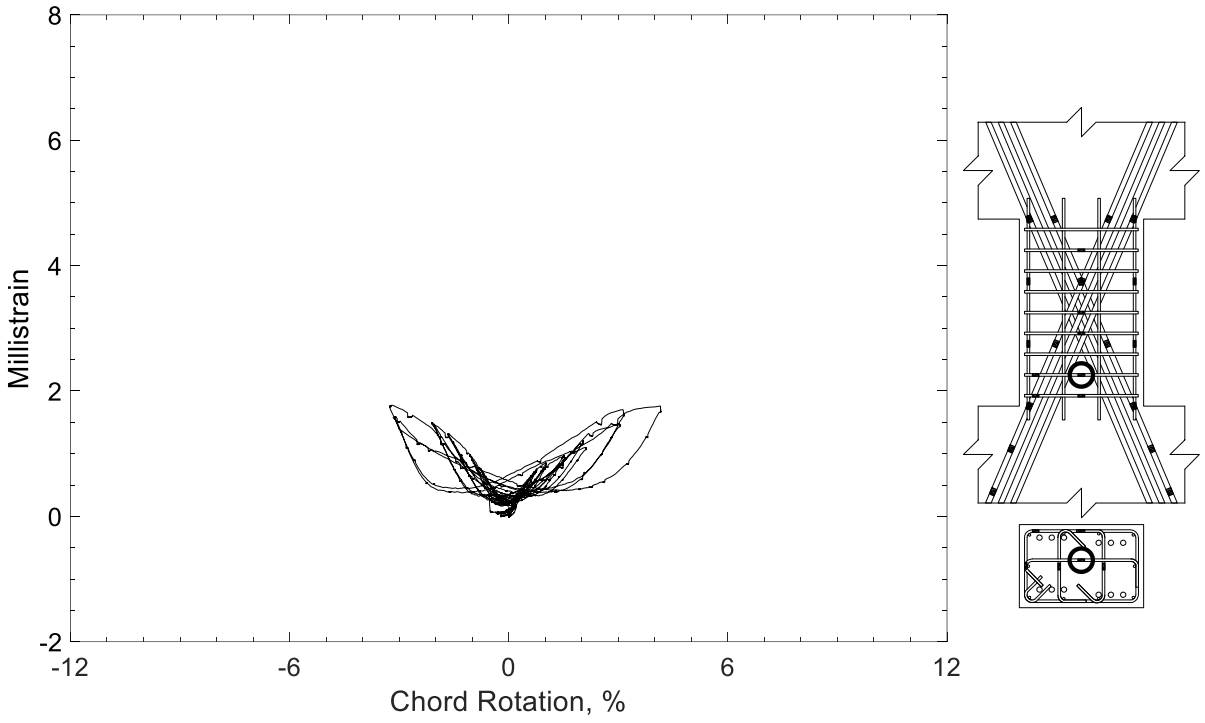

Figure 349 – Measured strain in crosstie of D120-1.5, strain gauge T3

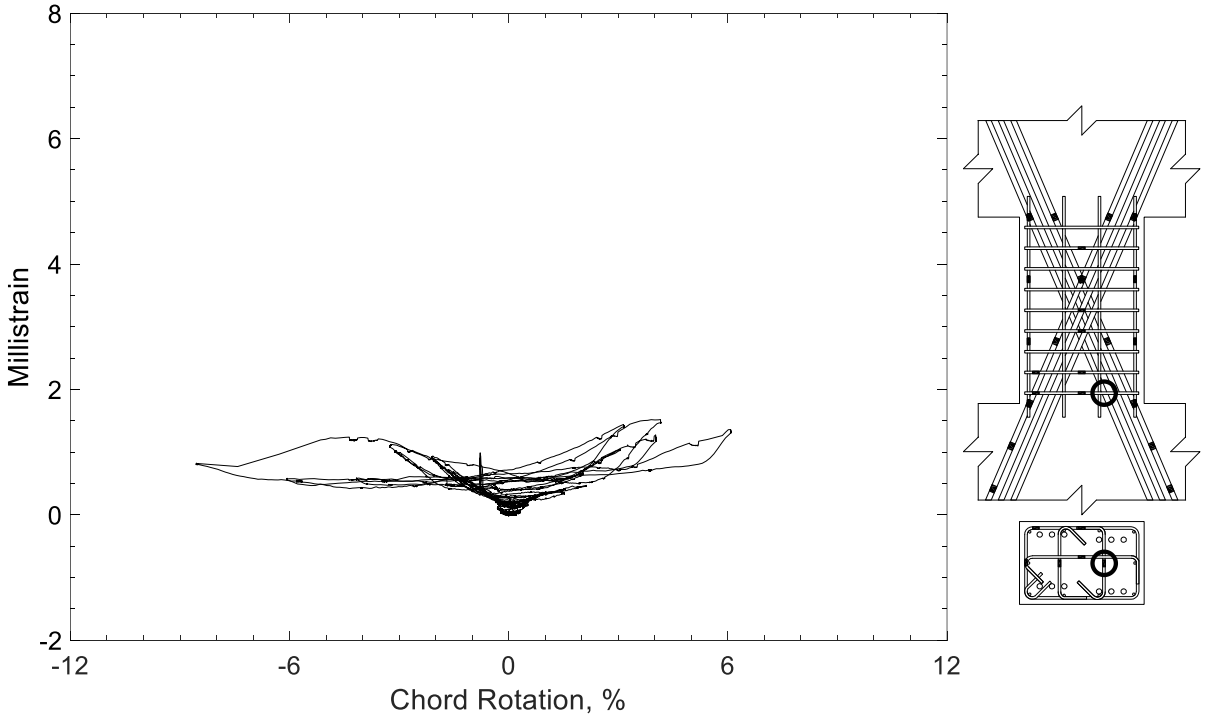

Figure 350 – Measured strain in crosstie of D120-1.5, strain gauge T4

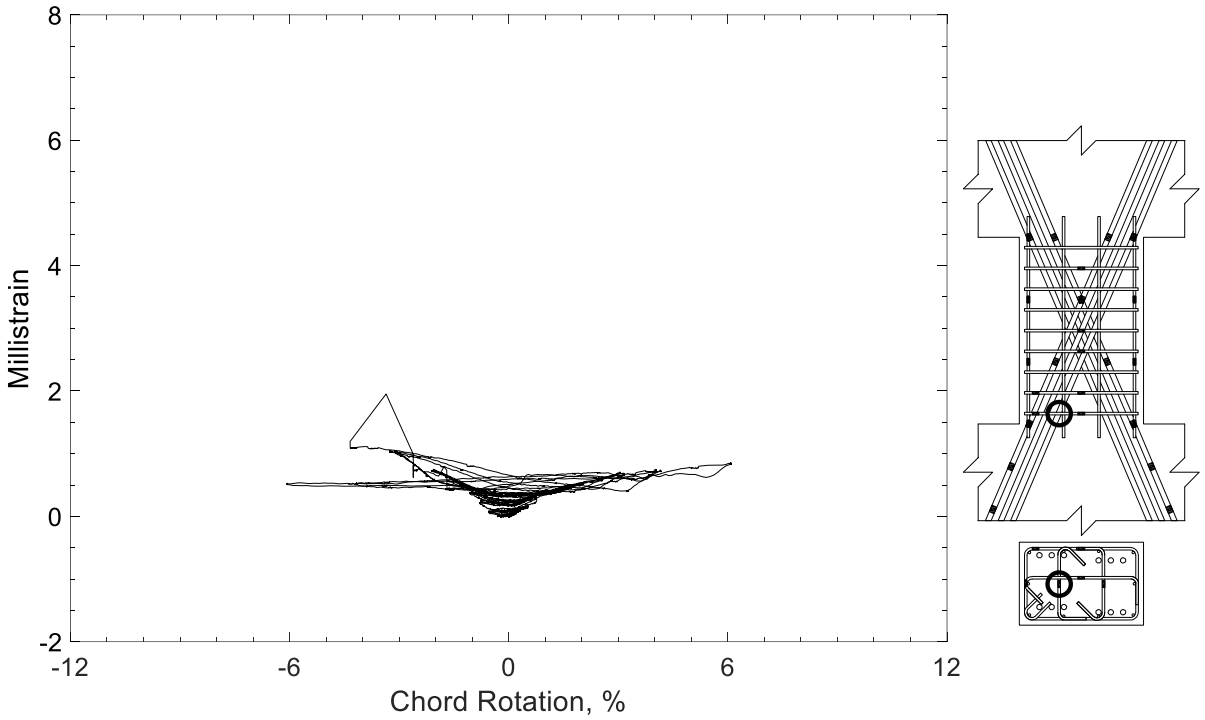

Figure 351 – Measured strain in crosstie of D120-1.5, strain gauge T5

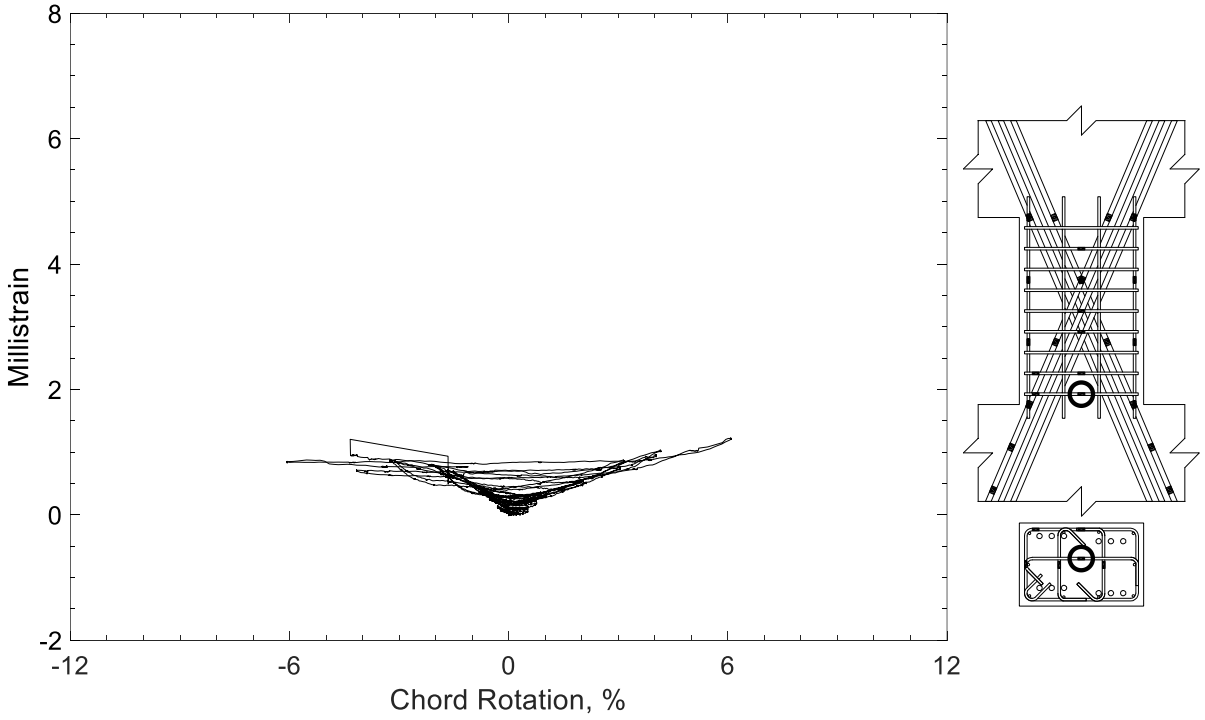

Figure 352 – Measured strain in crosstie of D120-1.5, strain gauge T6

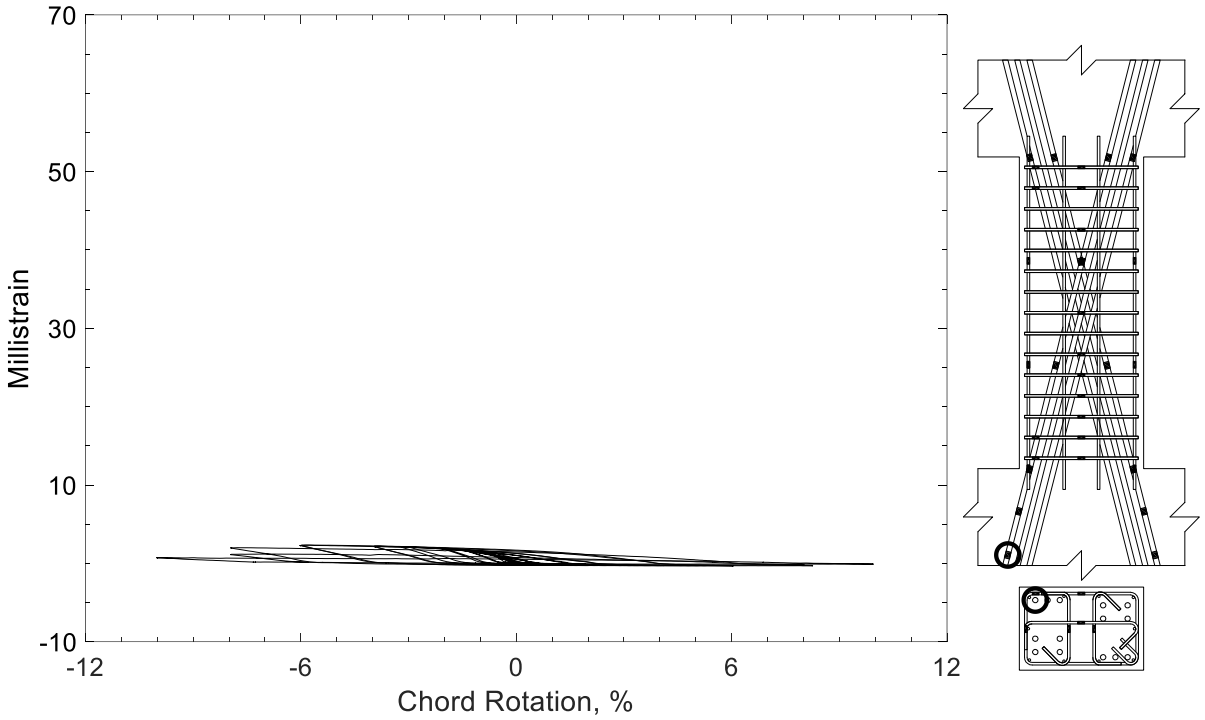

Figure 353 – Measured strain in diagonal bar of D80-2.5, strain gauge D1

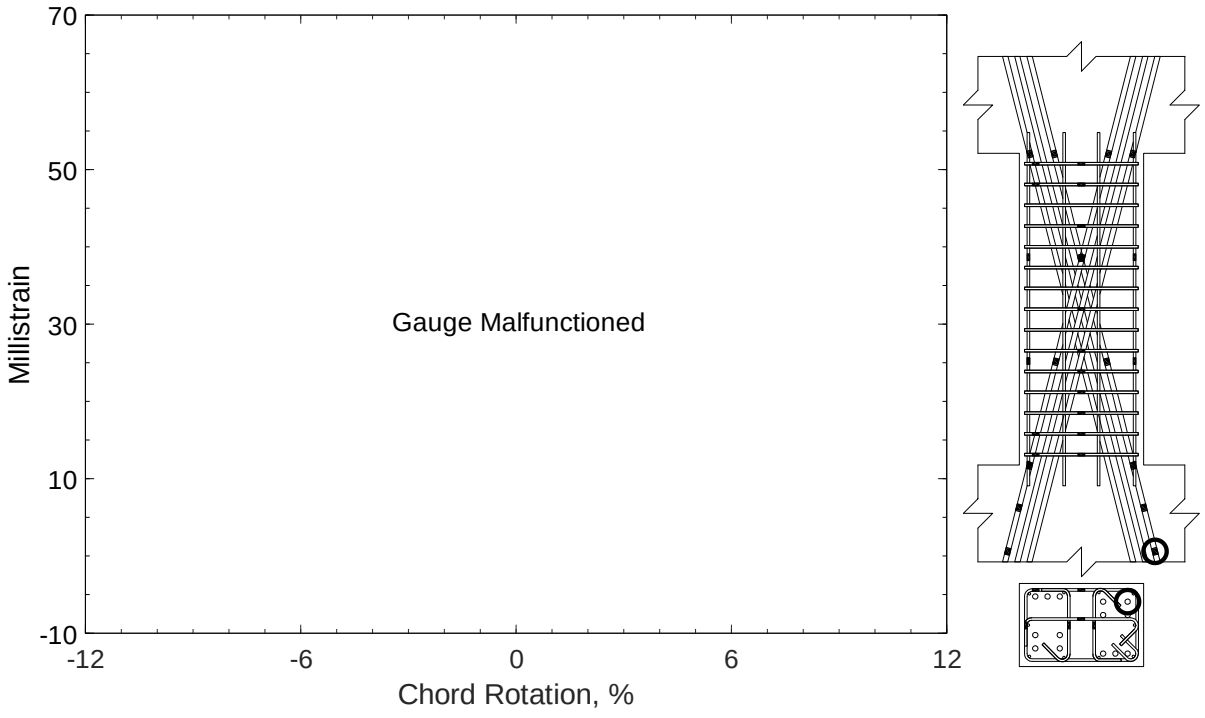

Figure 354 – Measured strain in diagonal bar of D80-2.5, strain gauge D2

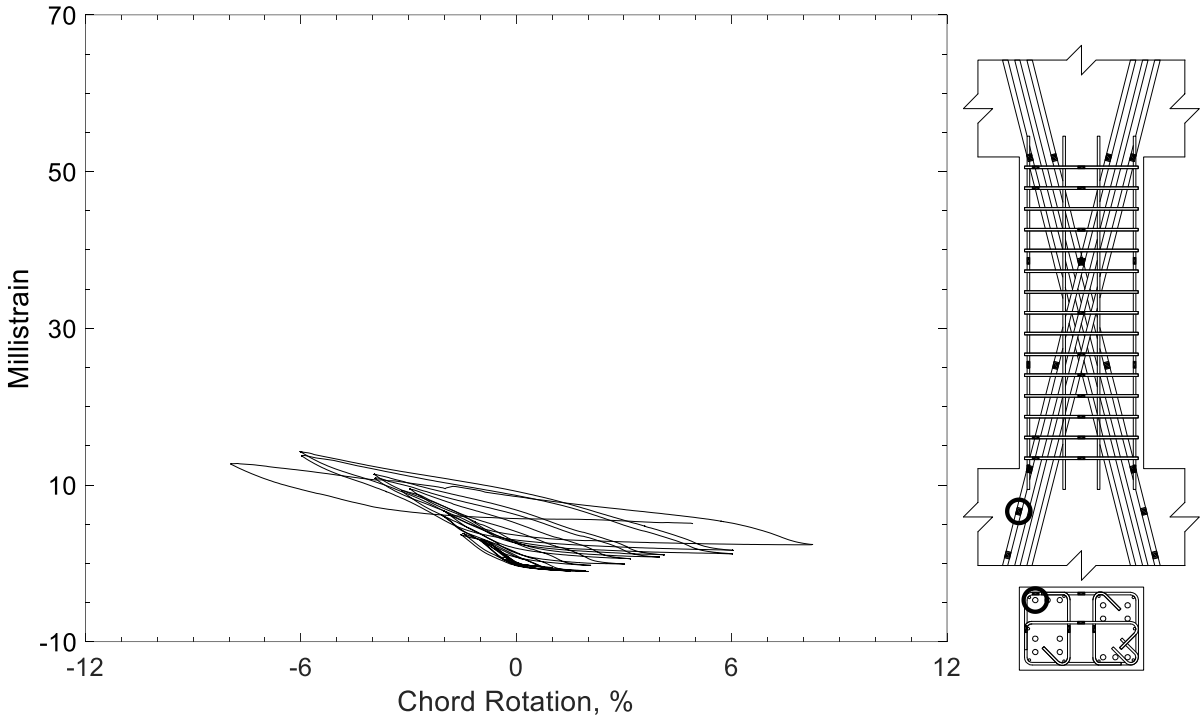

Figure 355 – Measured strain in diagonal bar of D80-2.5, strain gauge D3

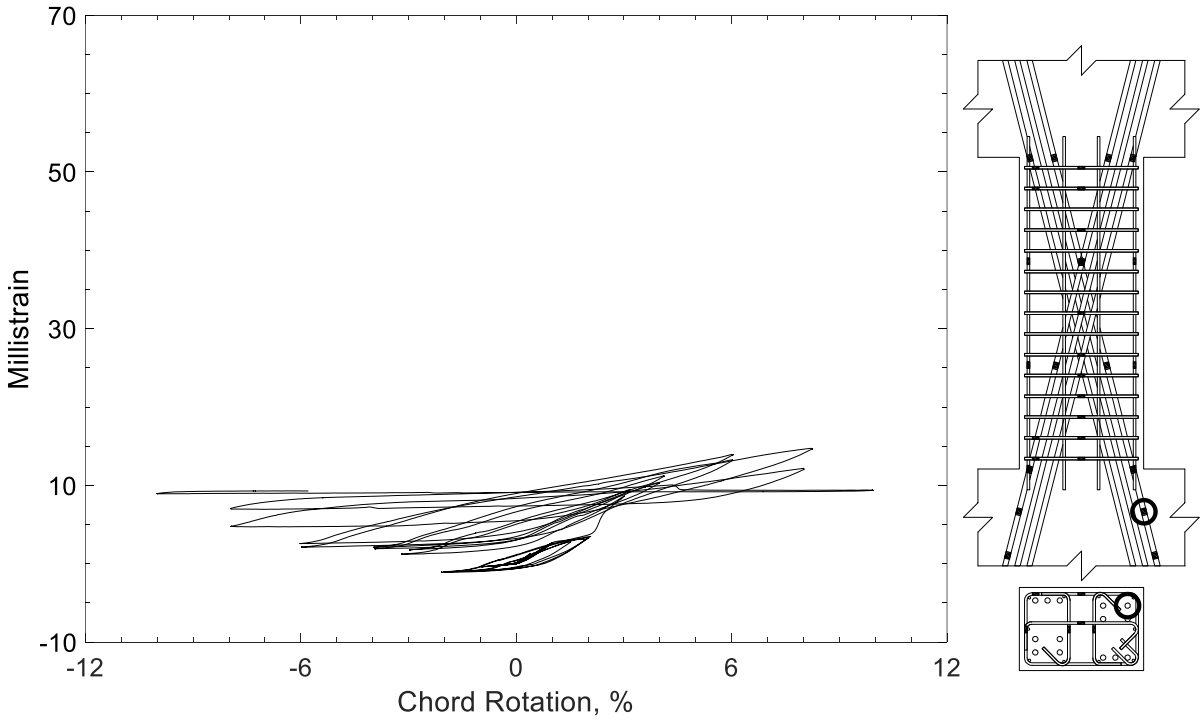

Figure 356 – Measured strain in diagonal bar of D80-2.5, strain gauge D4

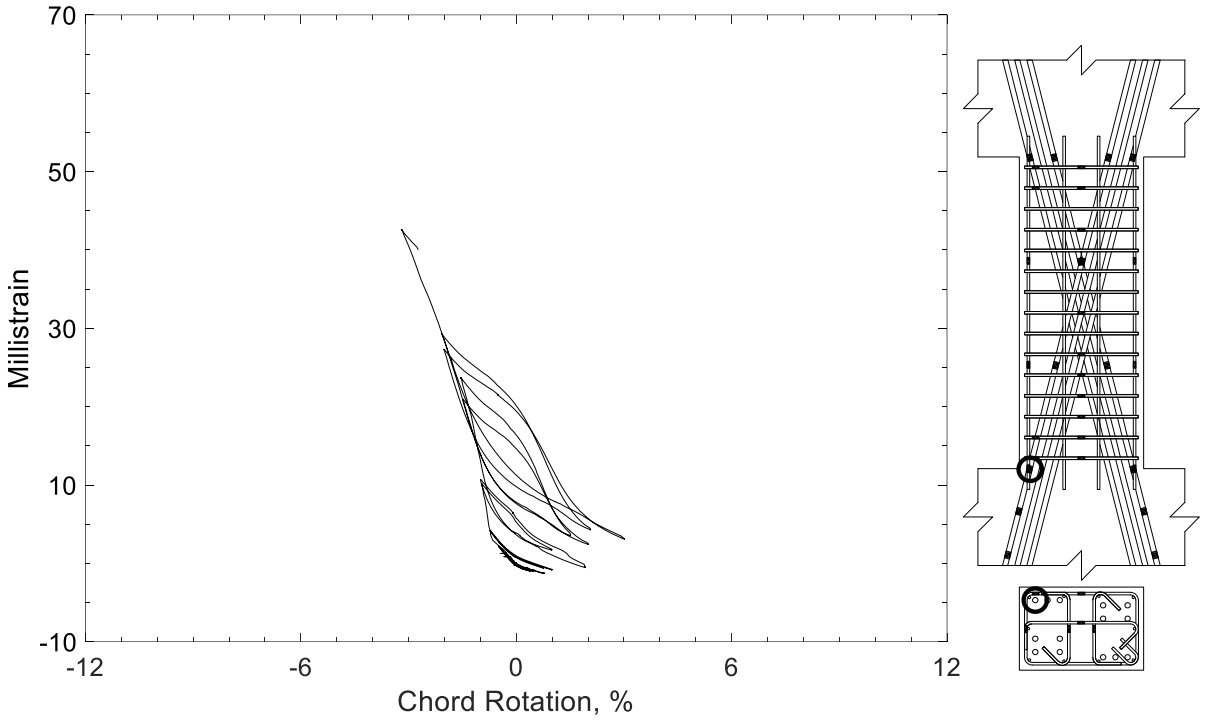

Figure 357 – Measured strain in diagonal bar of D80-2.5, strain gauge D5

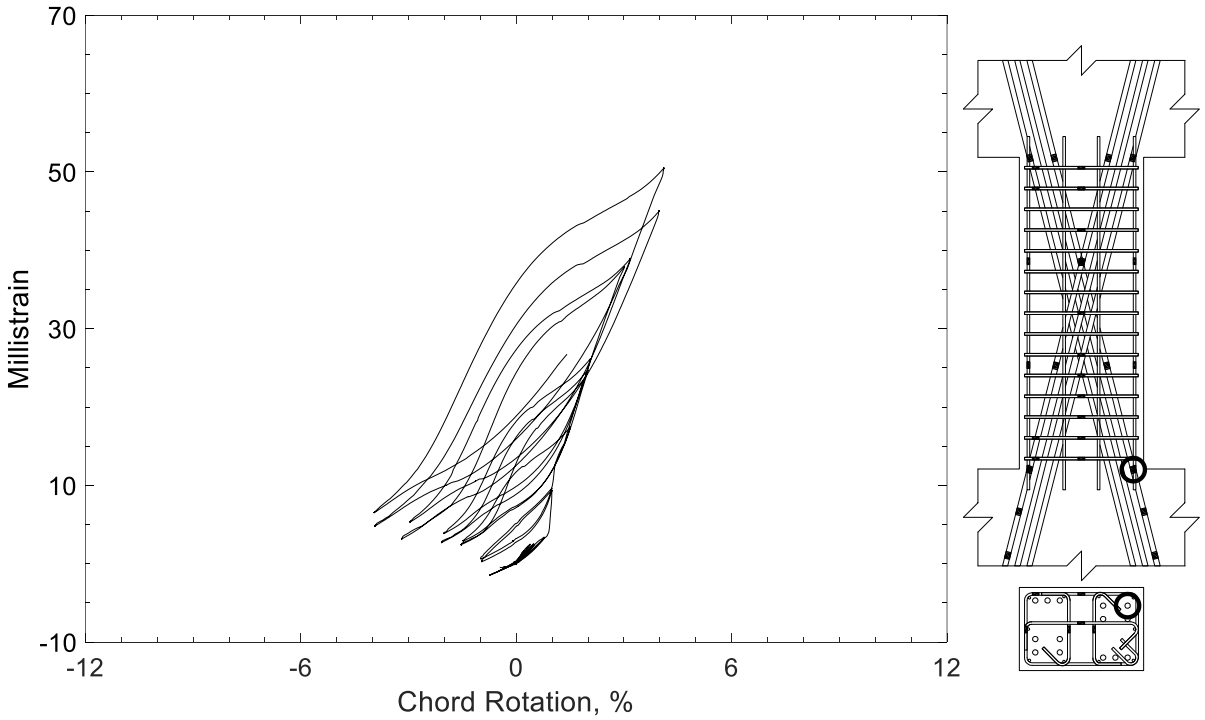

Figure 358 – Measured strain in diagonal bar of D80-2.5, strain gauge D6

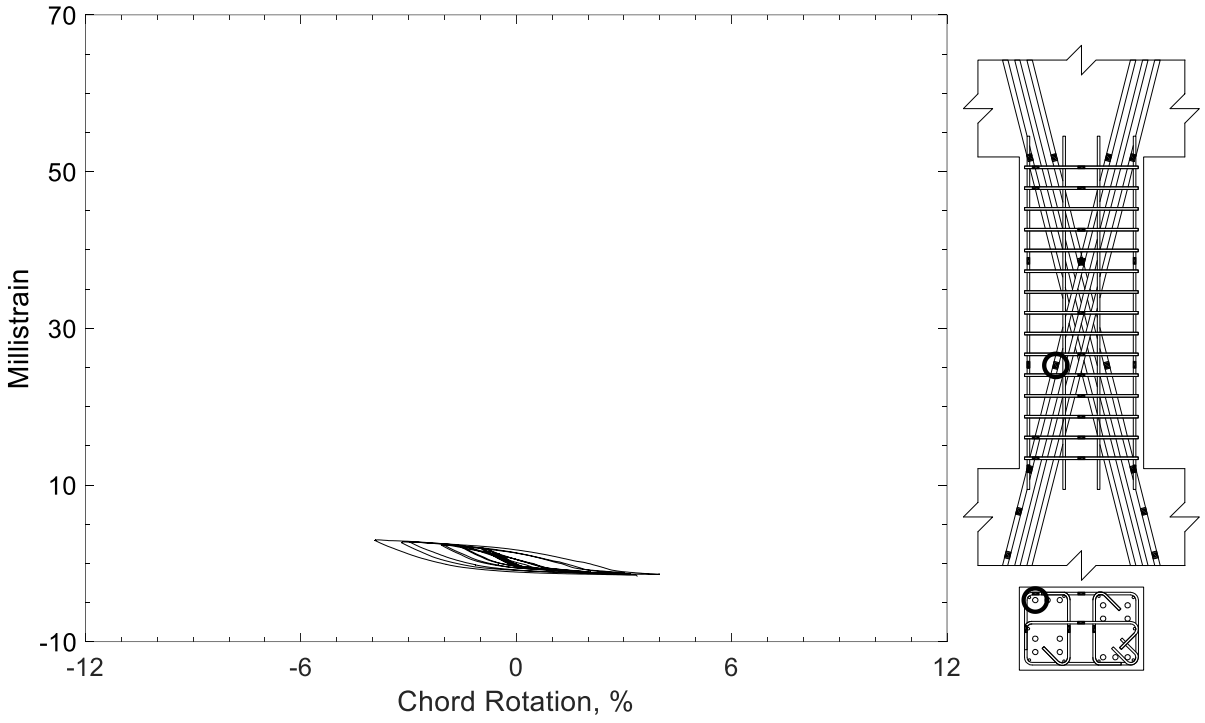

Figure 359 – Measured strain in diagonal bar of D80-2.5, strain gauge D7

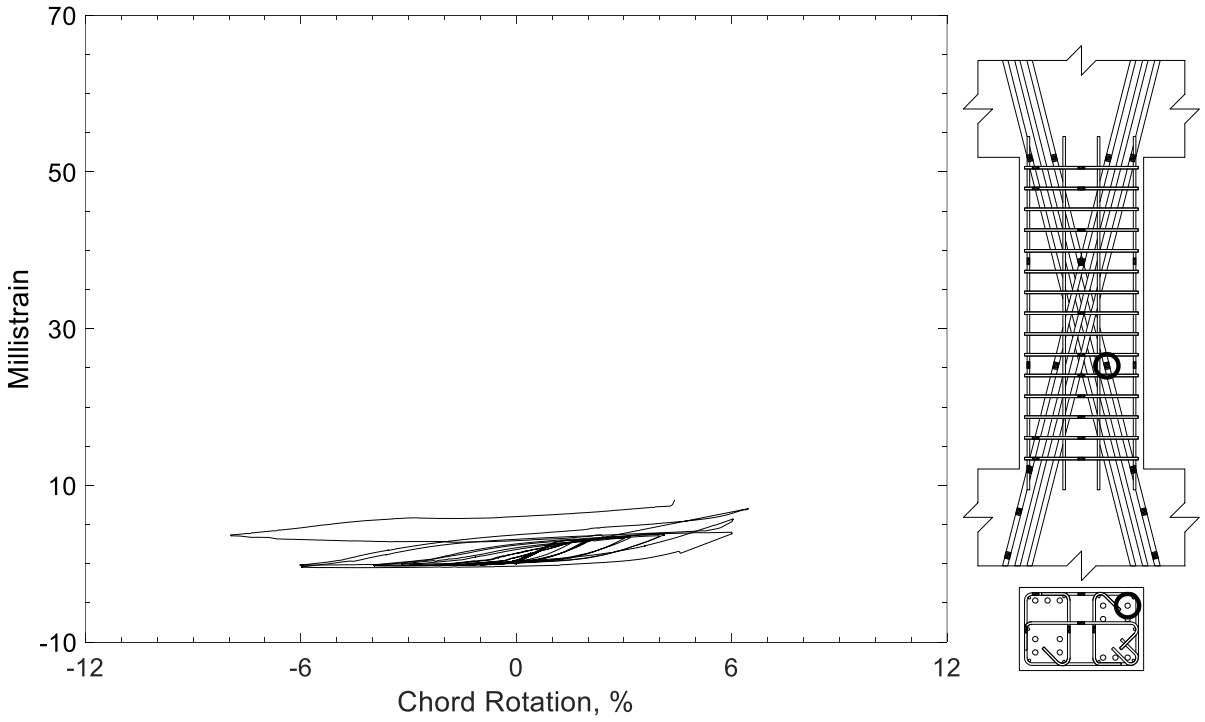

Figure 360 – Measured strain in diagonal bar of D80-2.5, strain gauge D8

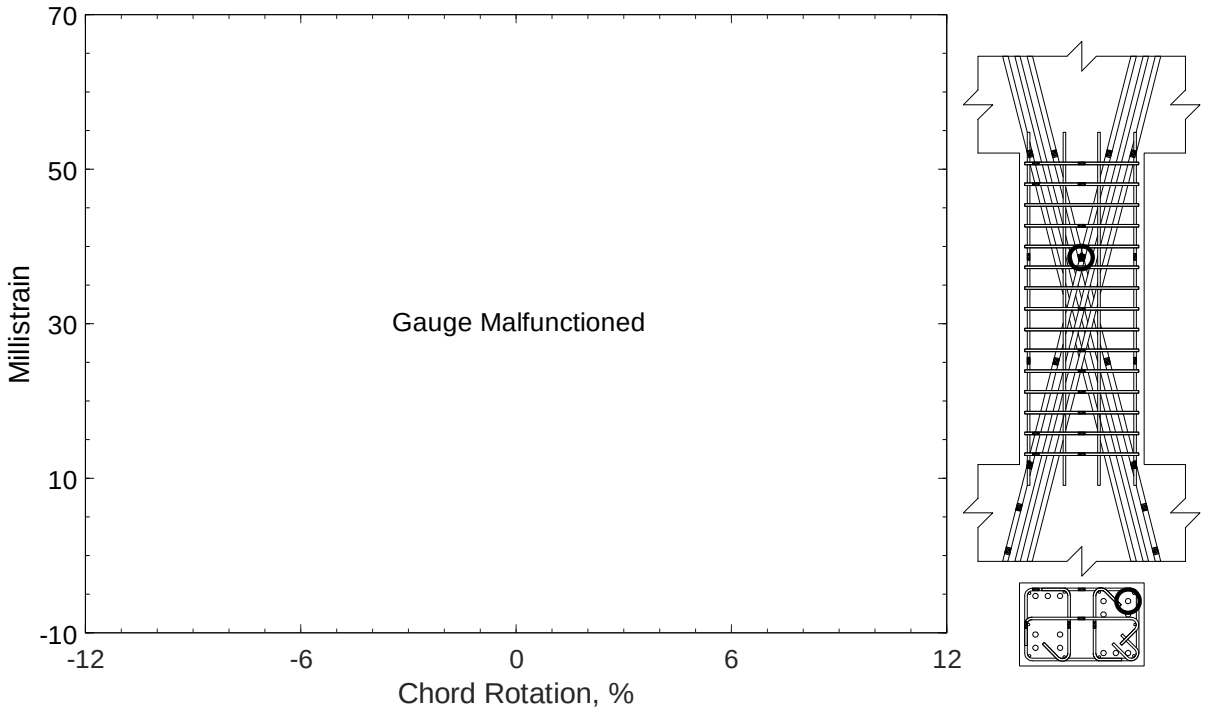

Figure 361 – Measured strain in diagonal bar of D80-2.5, strain gauge D9

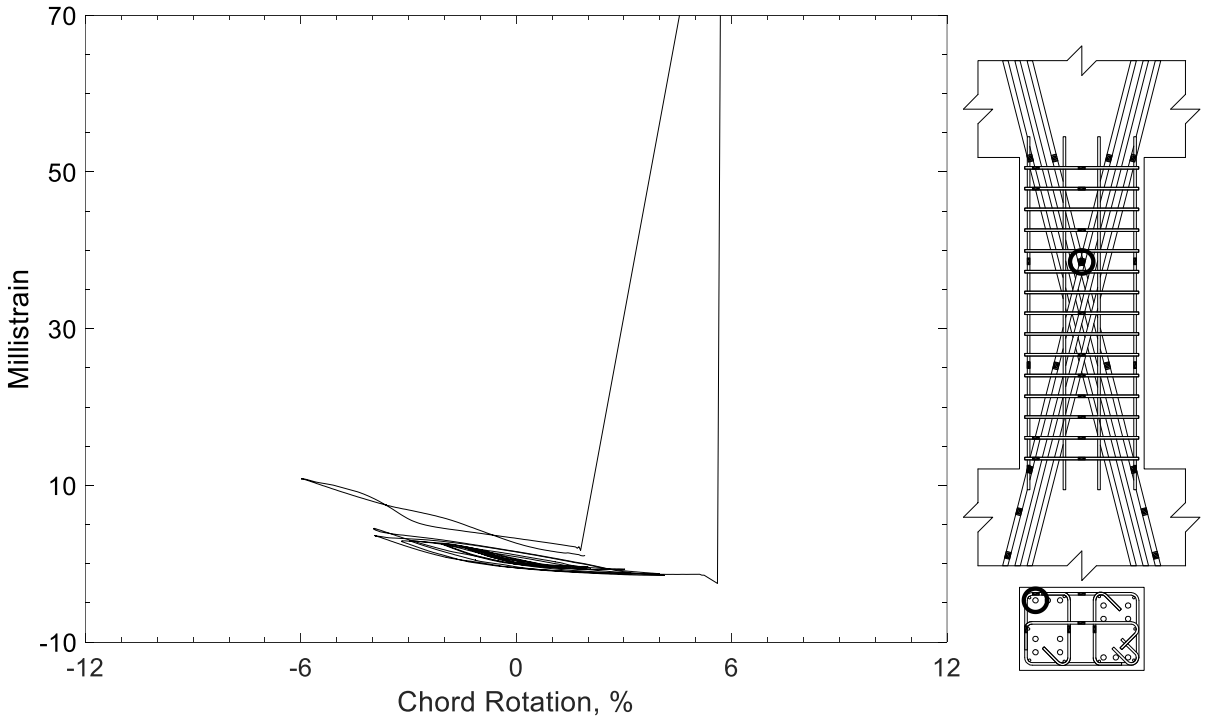

Figure 362 – Measured strain in diagonal bar of D80-2.5, strain gauge D10

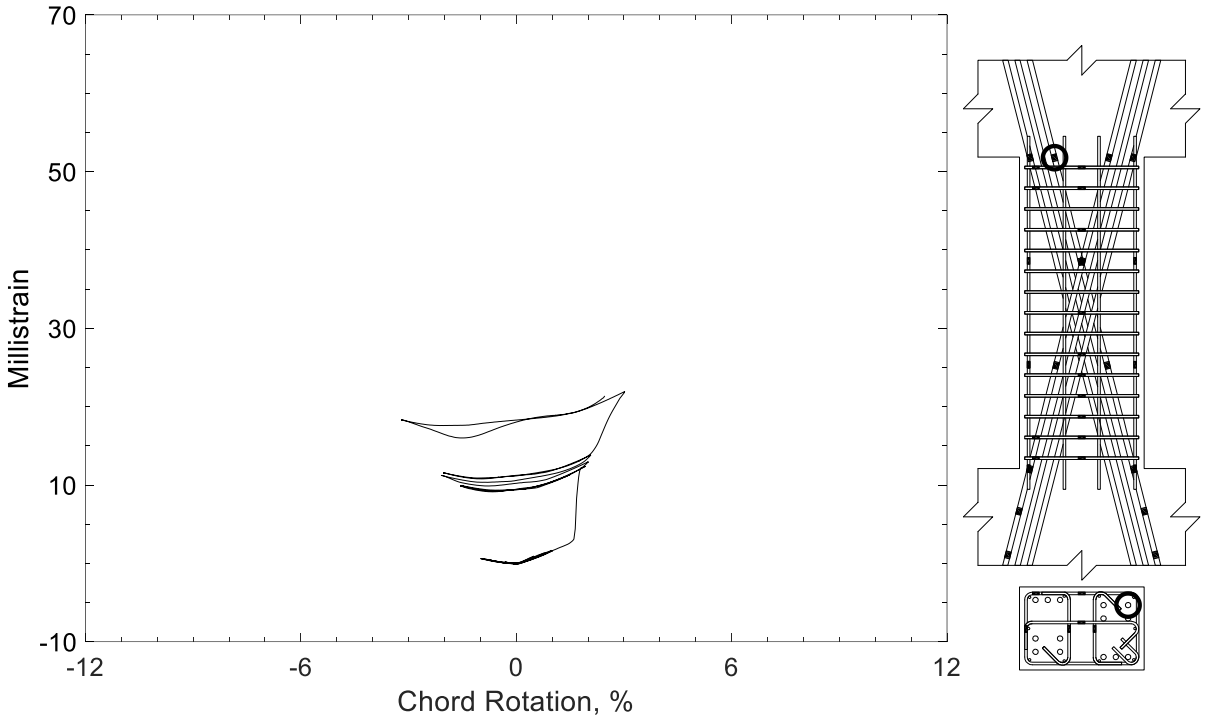

Figure 363 – Measured strain in diagonal bar of D80-2.5, strain gauge D11

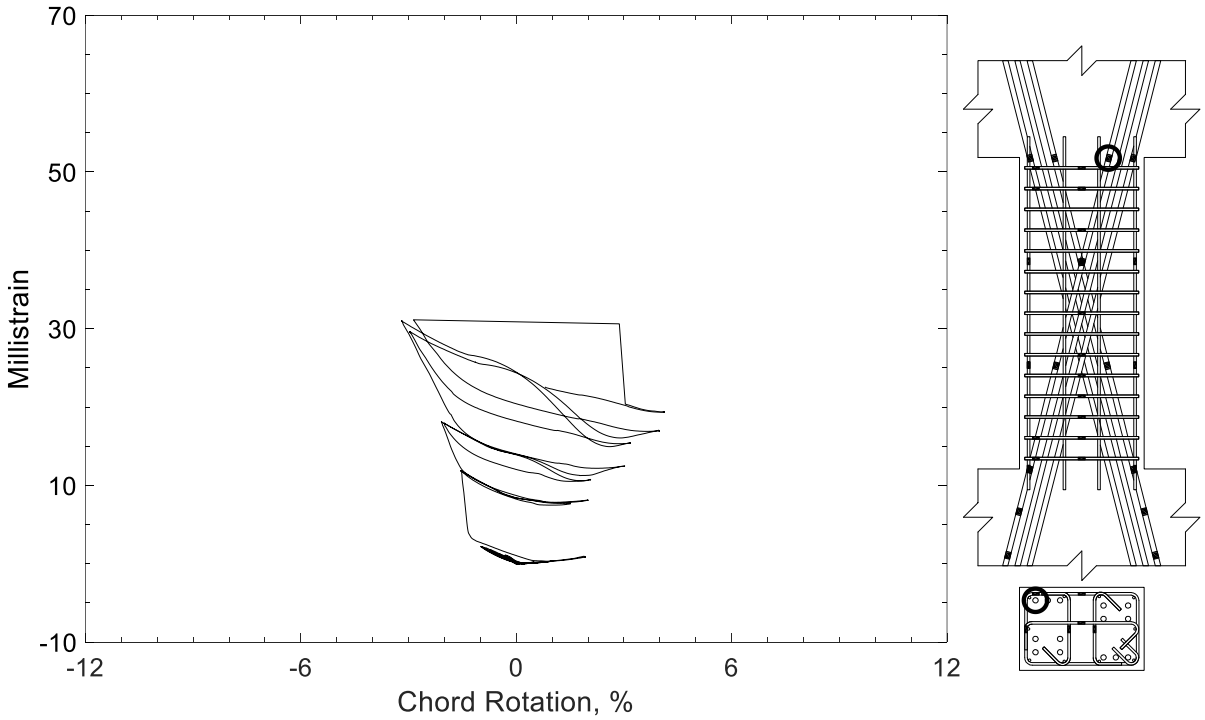

Figure 364 – Measured strain in diagonal bar of D80-2.5, strain gauge D12

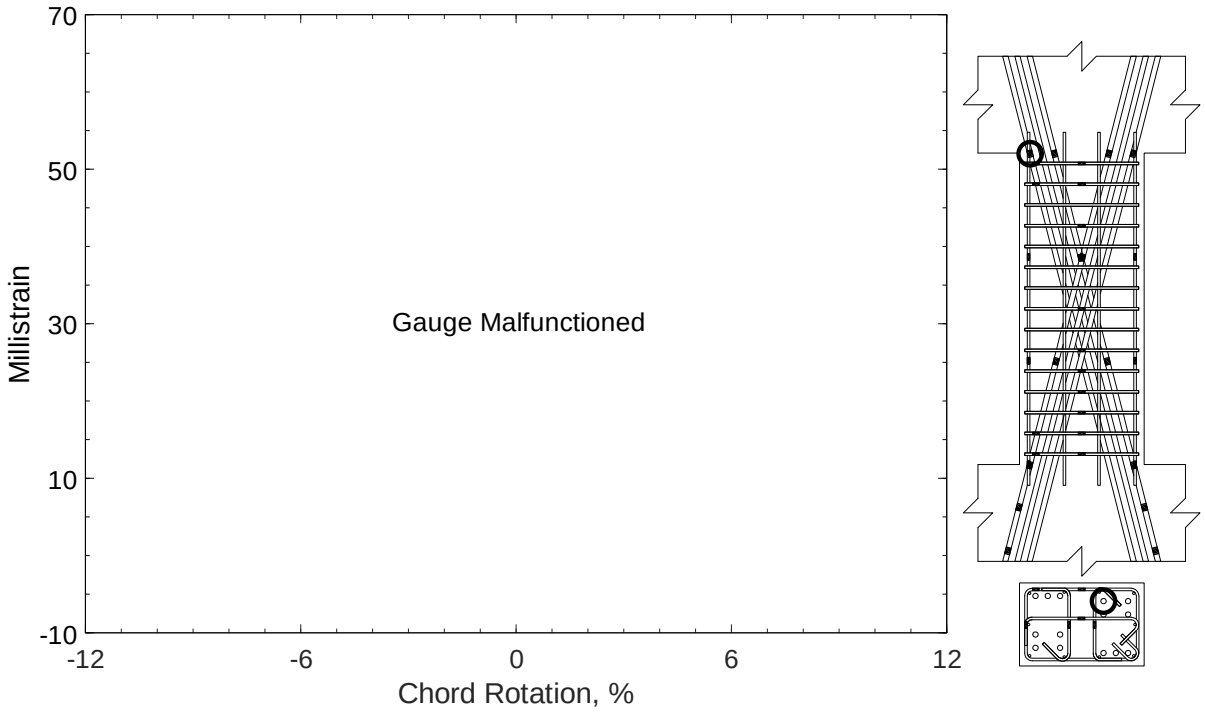

Figure 365 – Measured strain in diagonal bar of D80-2.5, strain gauge D13

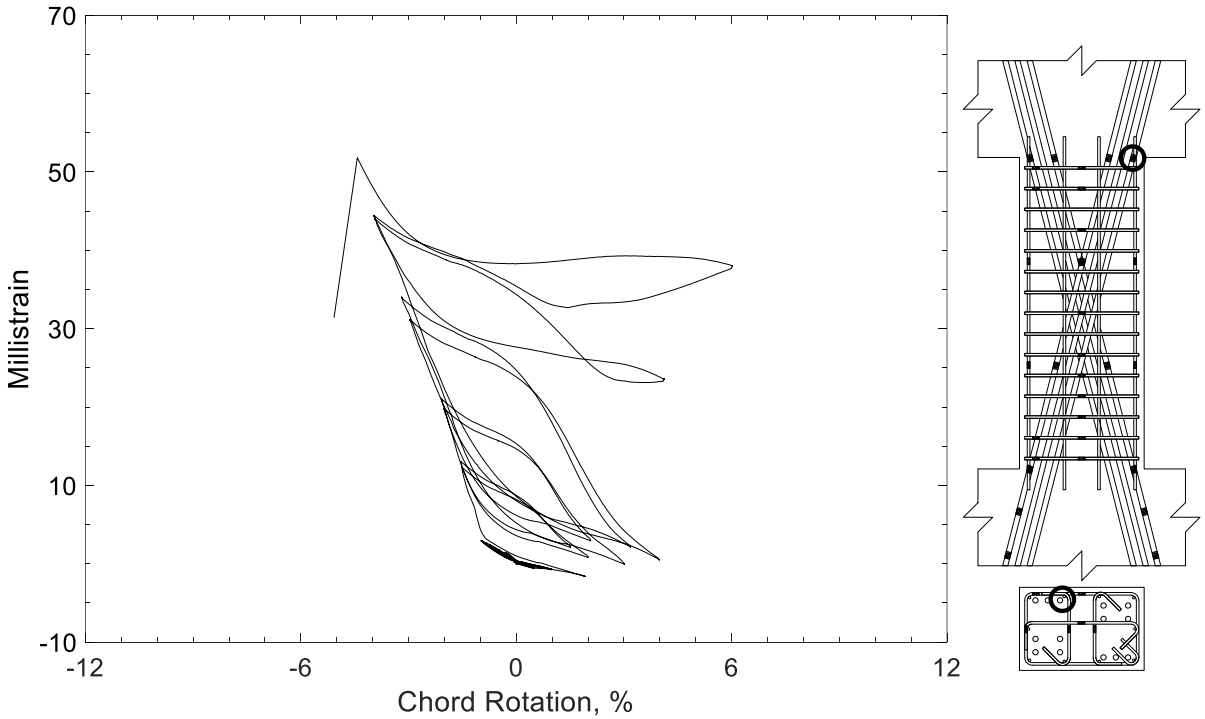

Figure 366 – Measured strain in diagonal bar of D80-2.5, strain gauge D14

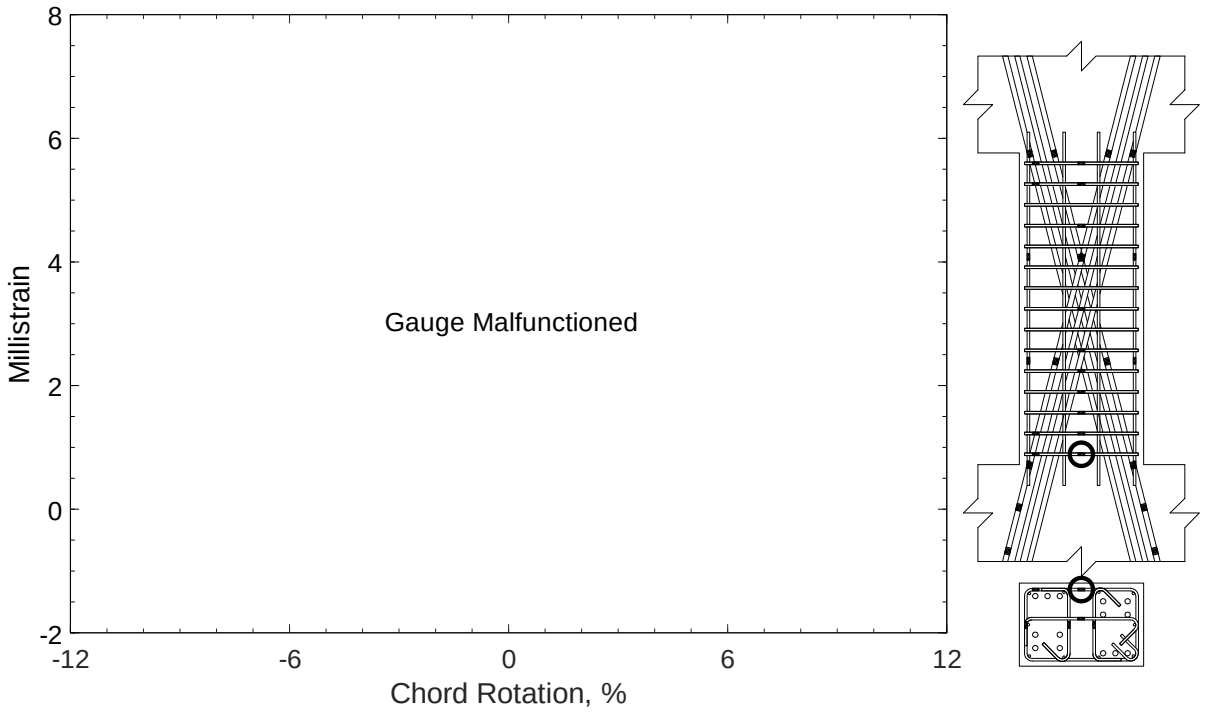

Figure 367 – Measured strain in closed stirrup of D80-2.5, strain gauge S1

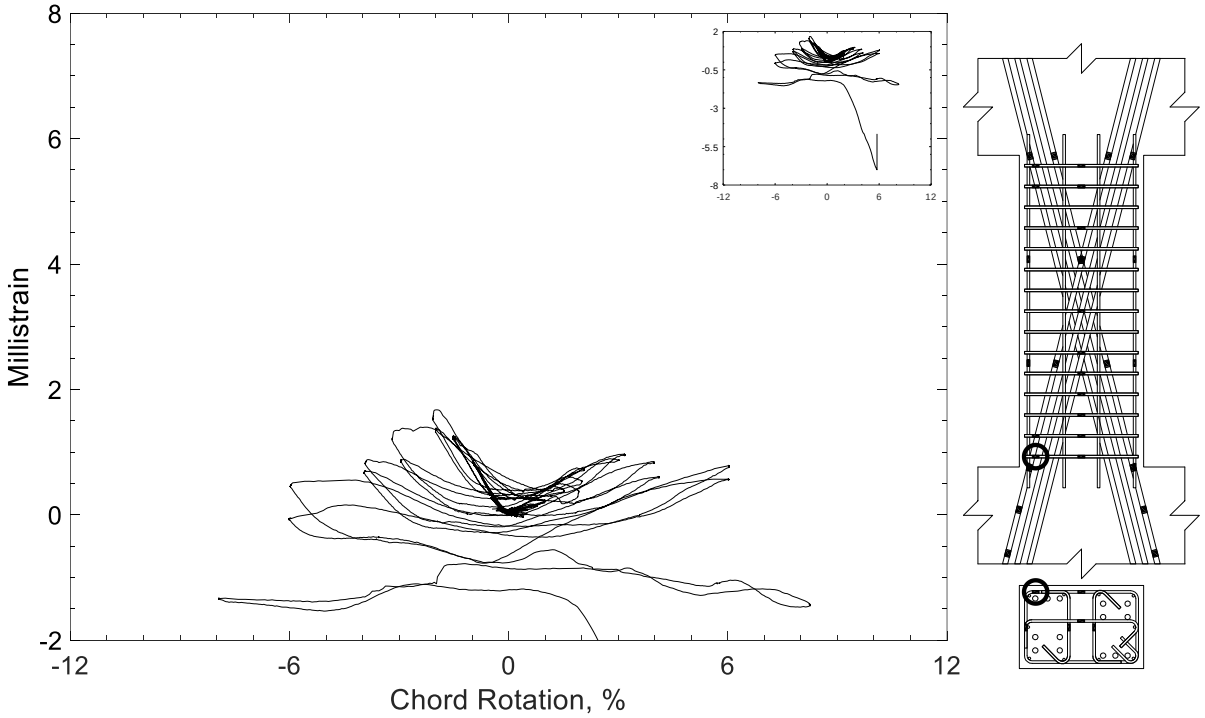

Figure 368 – Measured strain in closed stirrup of D80-2.5, strain gauge S2

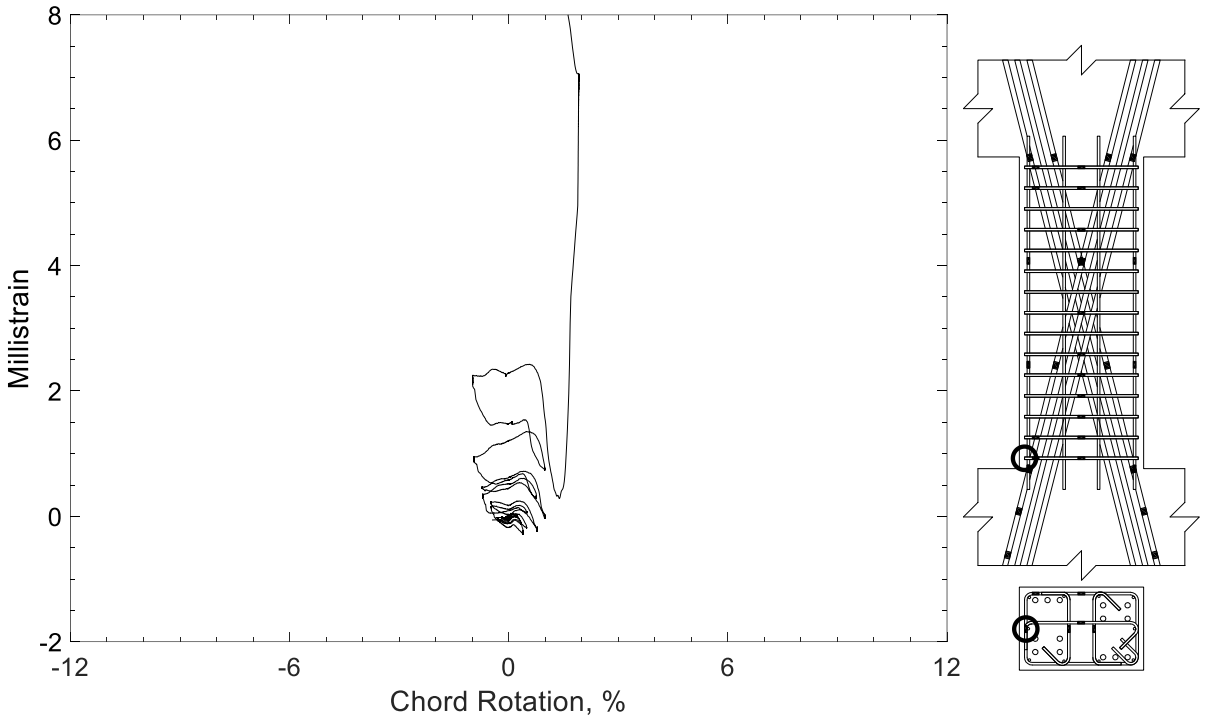

Figure 369 – Measured strain in closed stirrup of D80-2.5, strain gauge S3

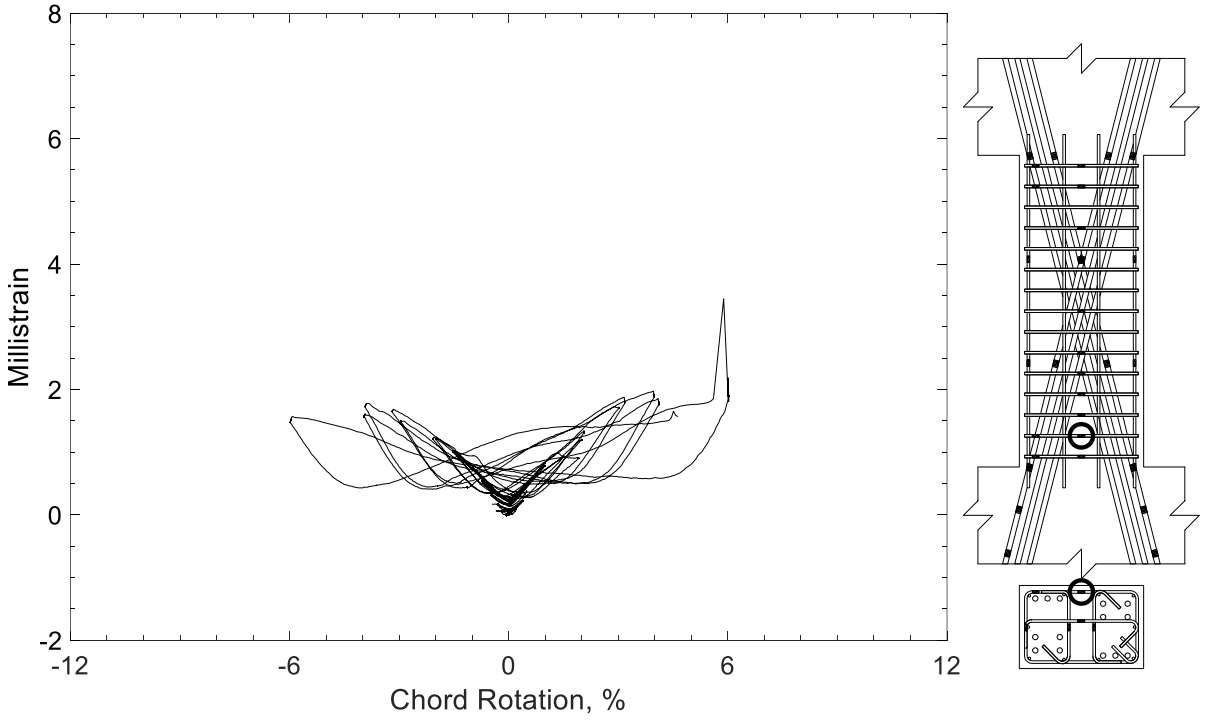

Figure 370 – Measured strain in closed stirrup of D80-2.5, strain gauge S4

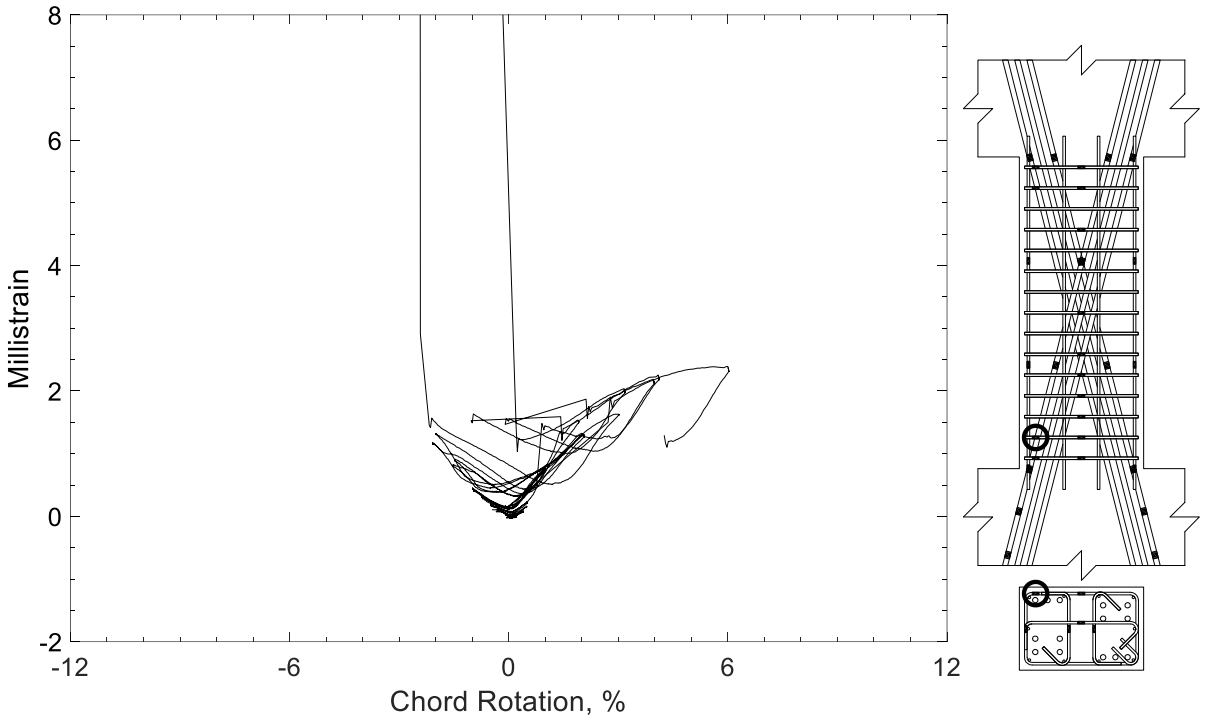

Figure 371 – Measured strain in closed stirrup of D80-2.5, strain gauge S5

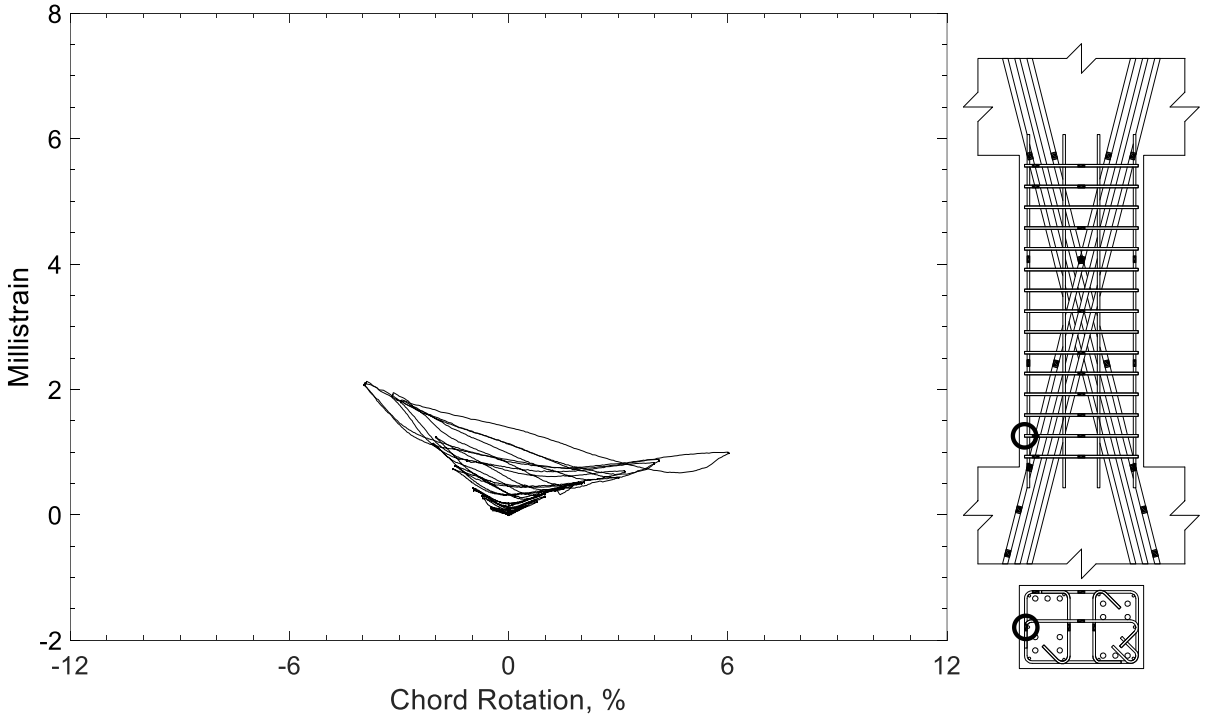

Figure 372 – Measured strain in closed stirrup of D80-2.5, strain gauge S6

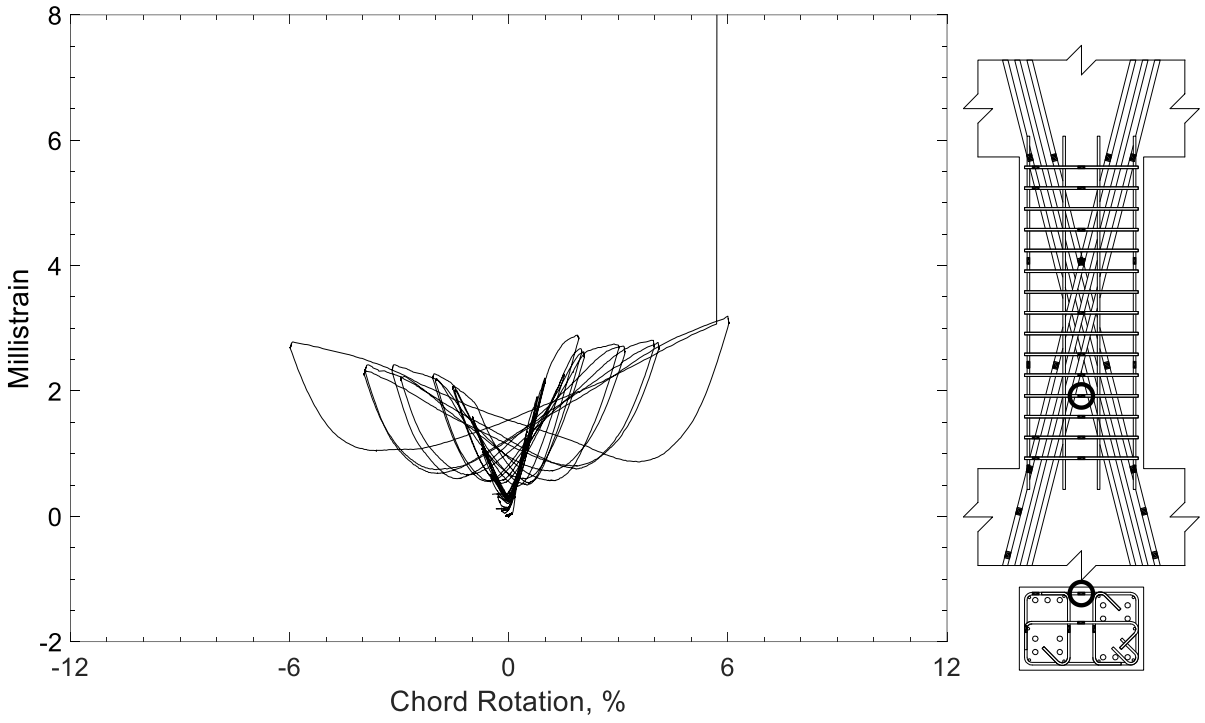

Figure 373 – Measured strain in closed stirrup of D80-2.5, strain gauge S7

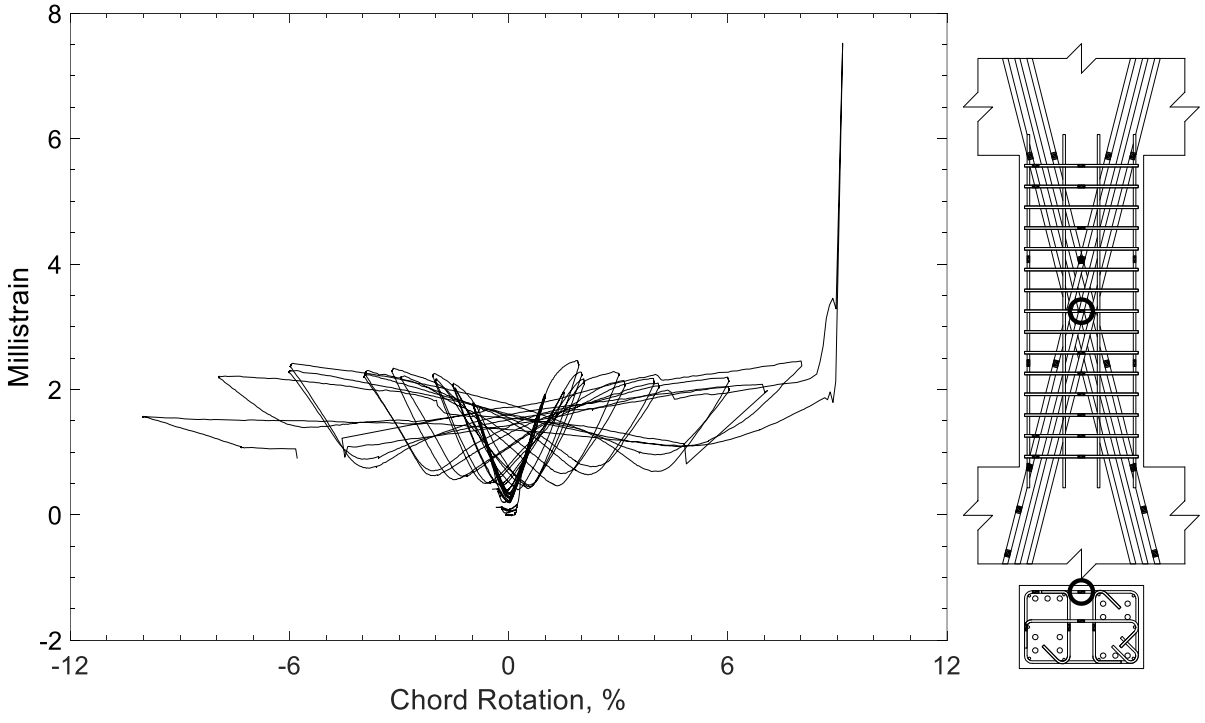

Figure 374 – Measured strain in closed stirrup of D80-2.5, strain gauge S8

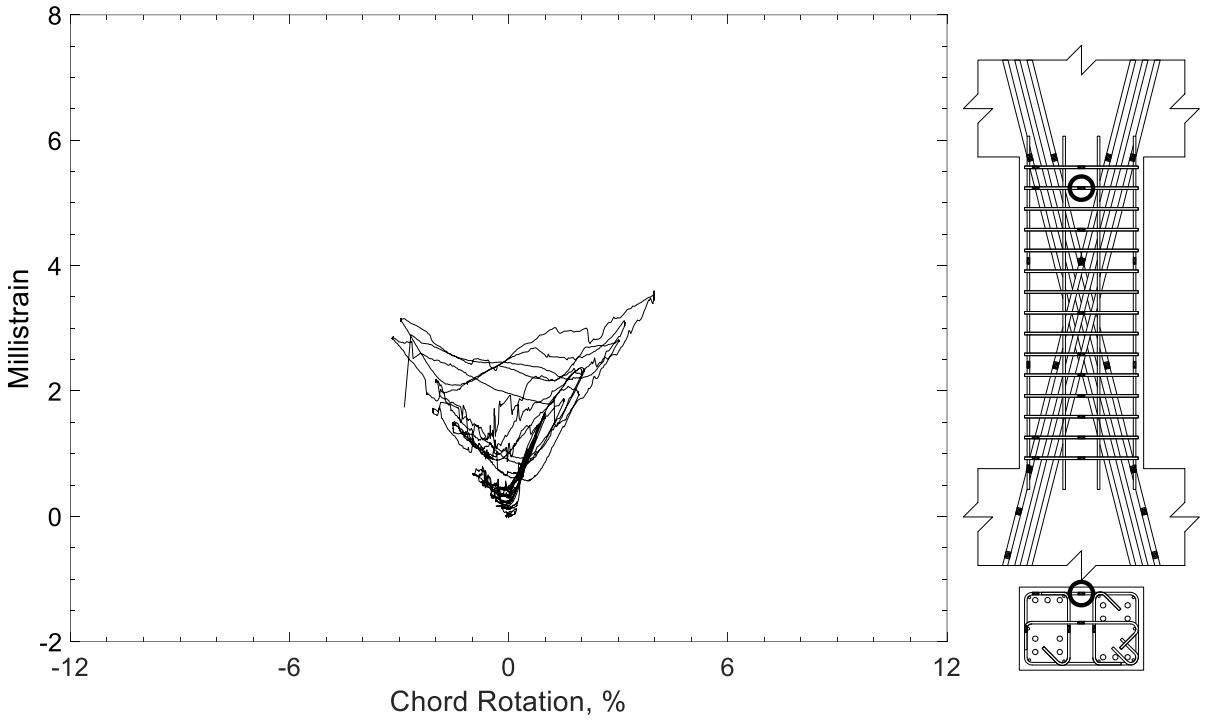

Figure 375 – Measured strain in closed stirrup of D80-2.5, strain gauge S9

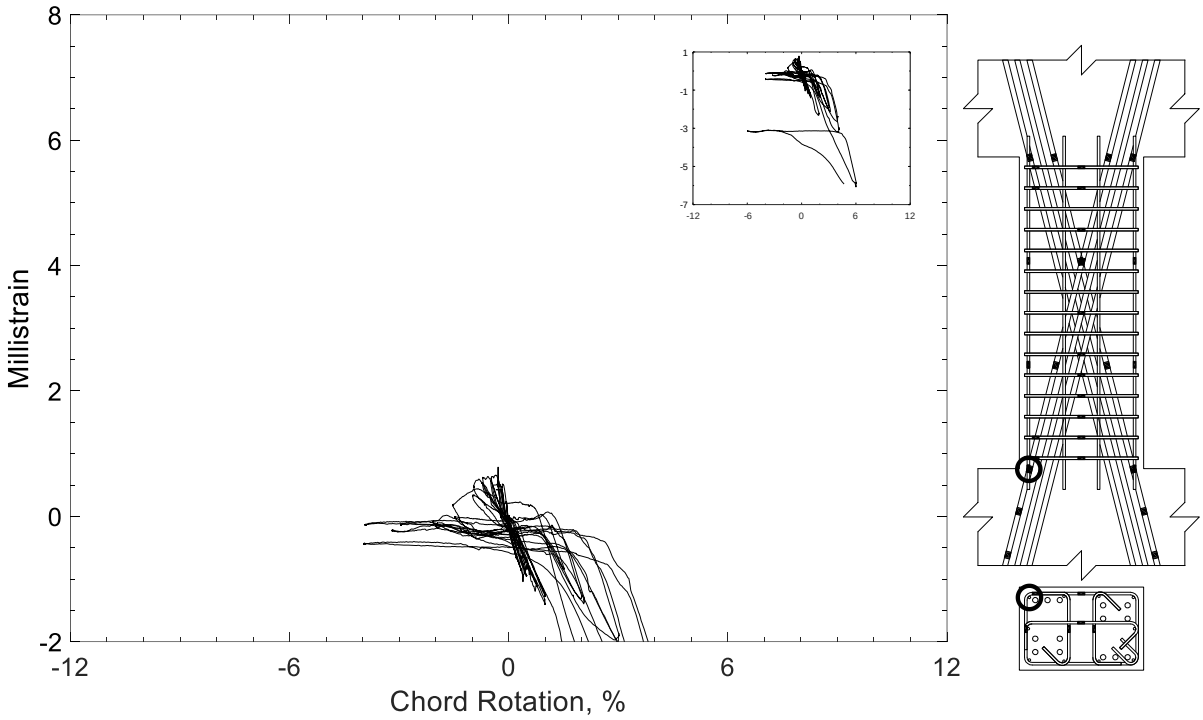

Figure 376 – Measured strain in parallel bar of D80-2.5, strain gauge H1

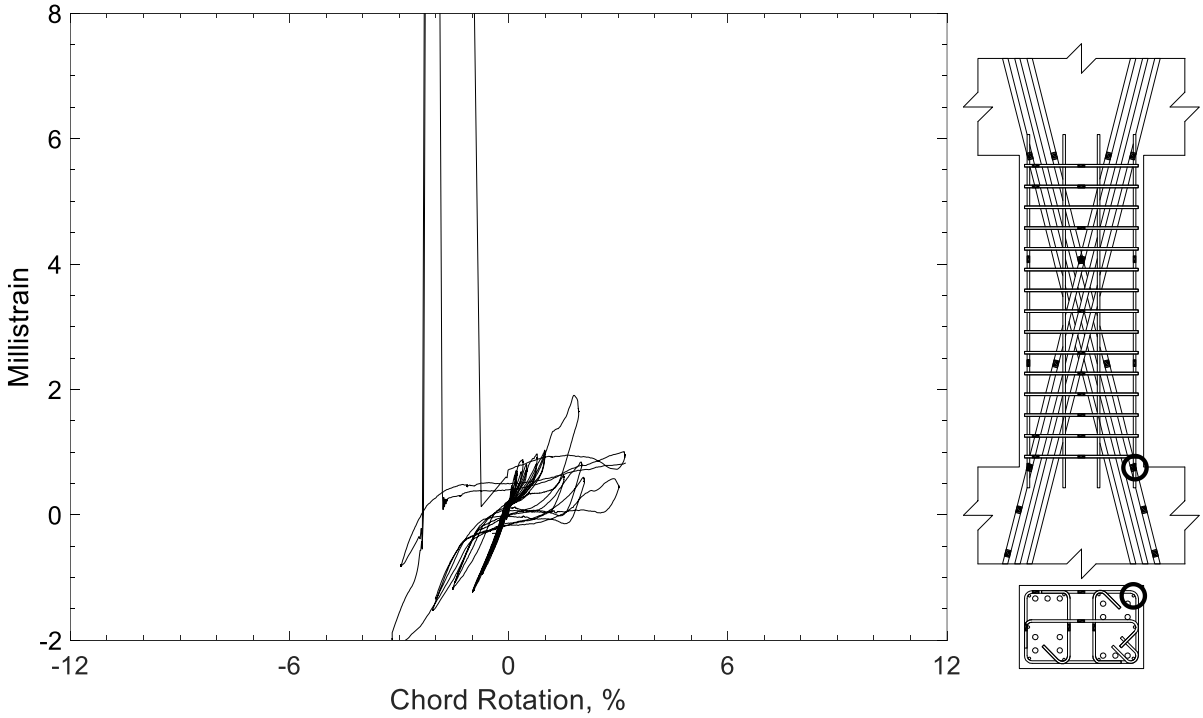

Figure 377 – Measured strain in parallel bar of D80-2.5, strain gauge H2

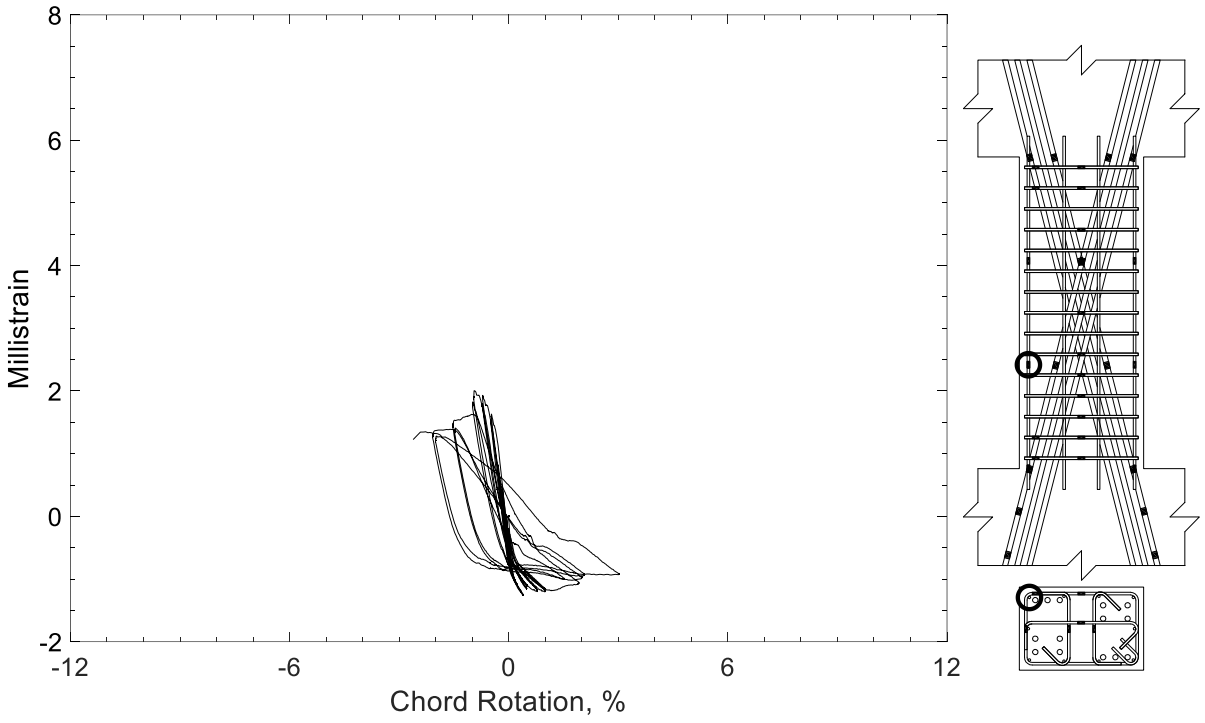

Figure 378 – Measured strain in parallel bar of D80-2.5, strain gauge H3

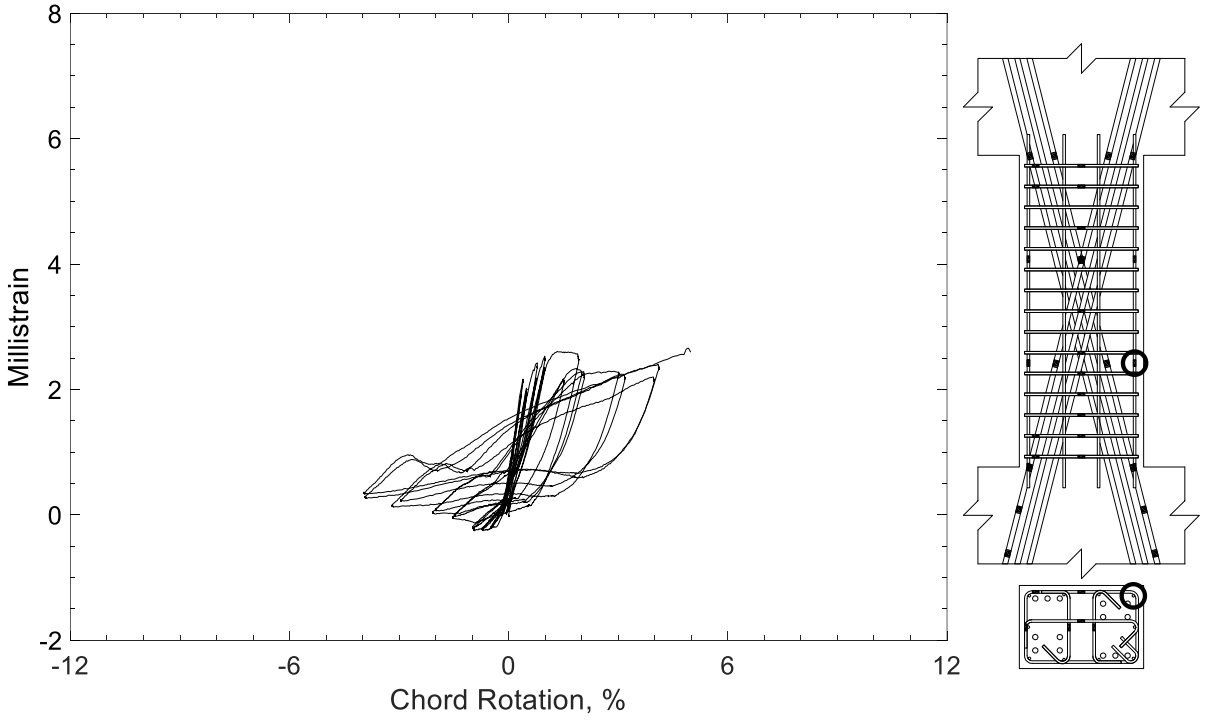

Figure 379 – Measured strain in parallel bar of D80-2.5, strain gauge H4

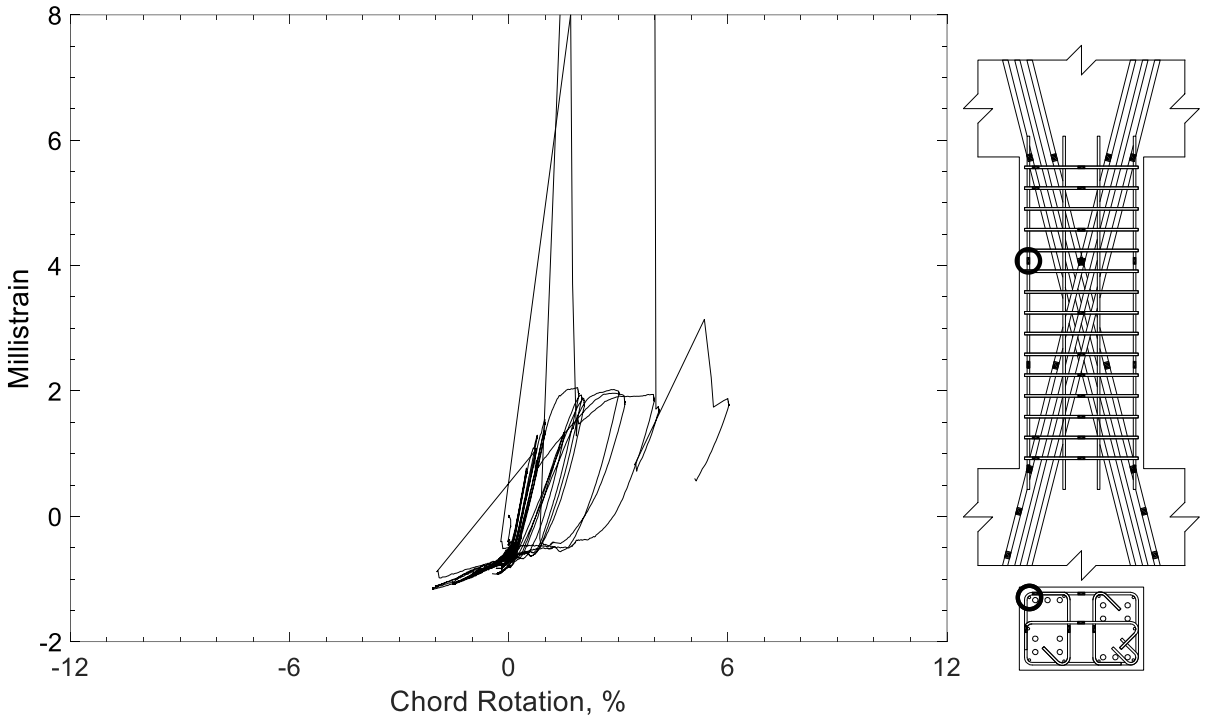

Figure 380 – Measured strain in parallel bar of D80-2.5, strain gauge H5

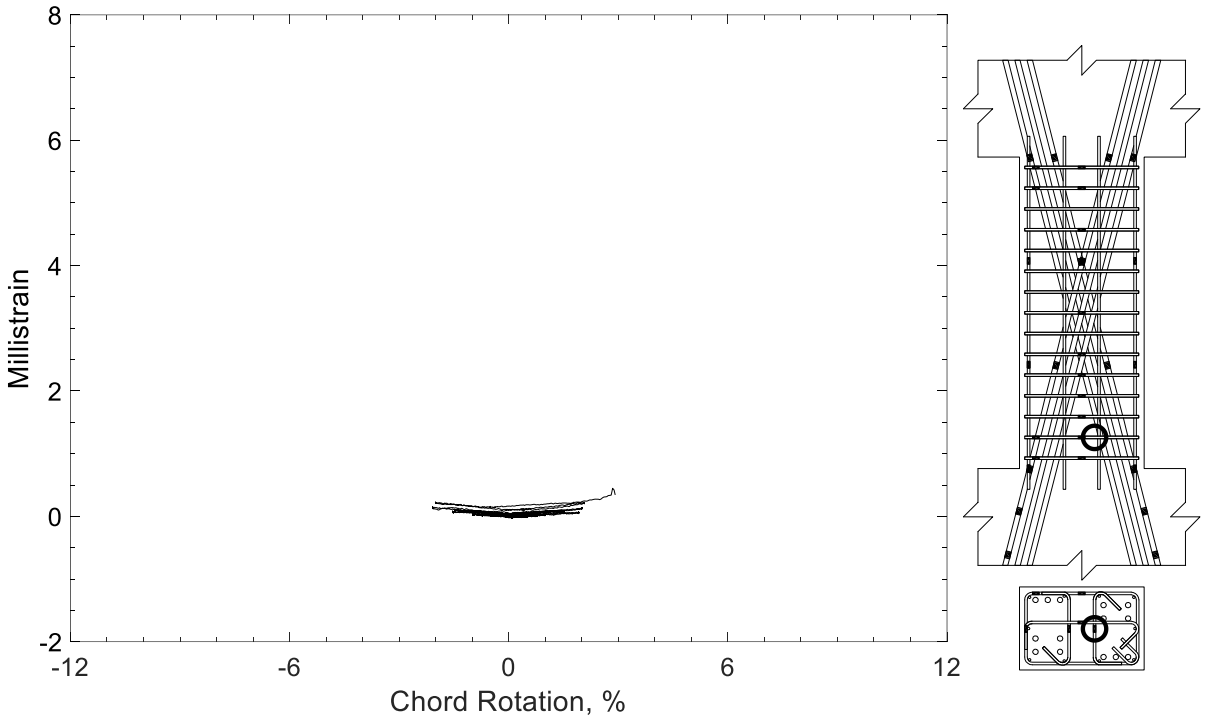

Figure 381 – Measured strain in crosstie of D80-2.5, strain gauge T1

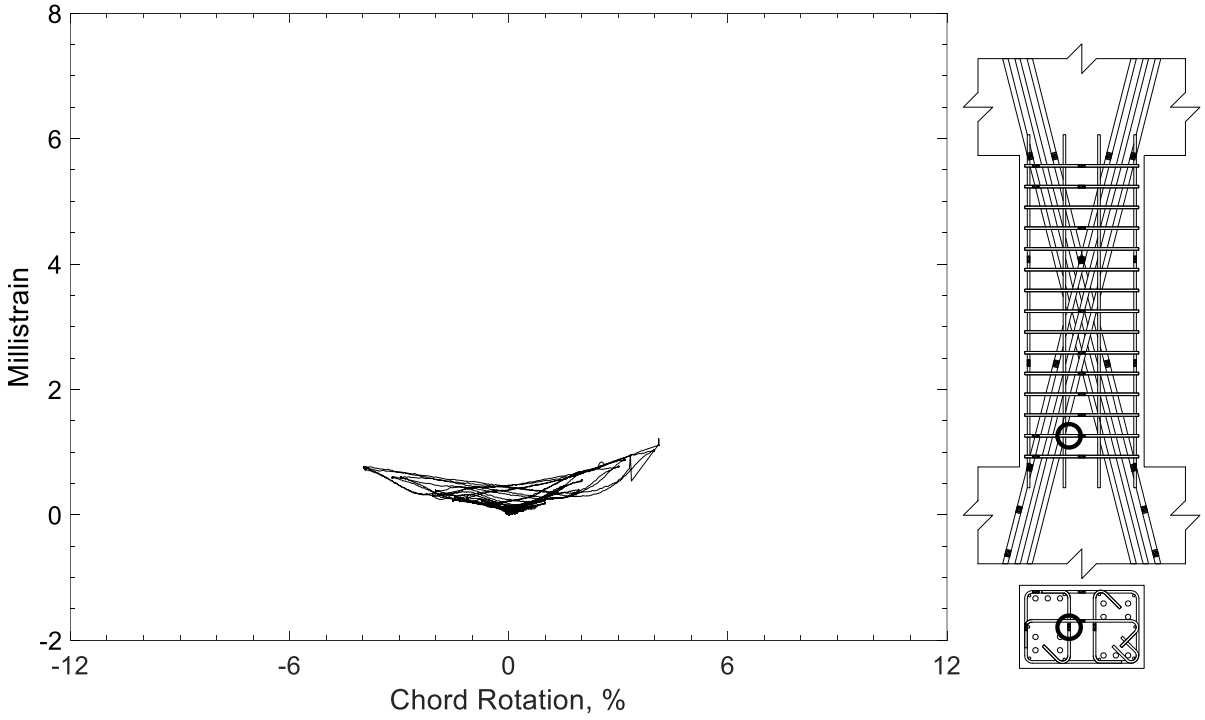

Figure 382 – Measured strain in crosstie of D80-2.5, strain gauge T2

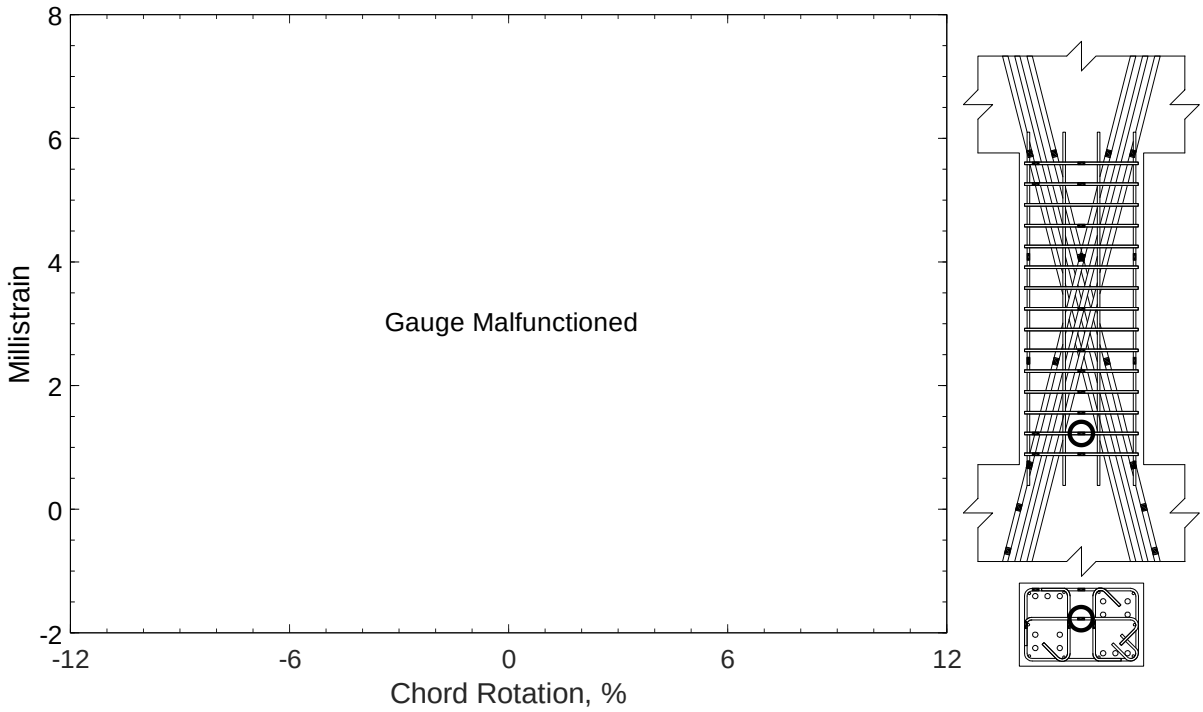

Figure 383 – Measured strain in crosstie of D80-2.5, strain gauge T3

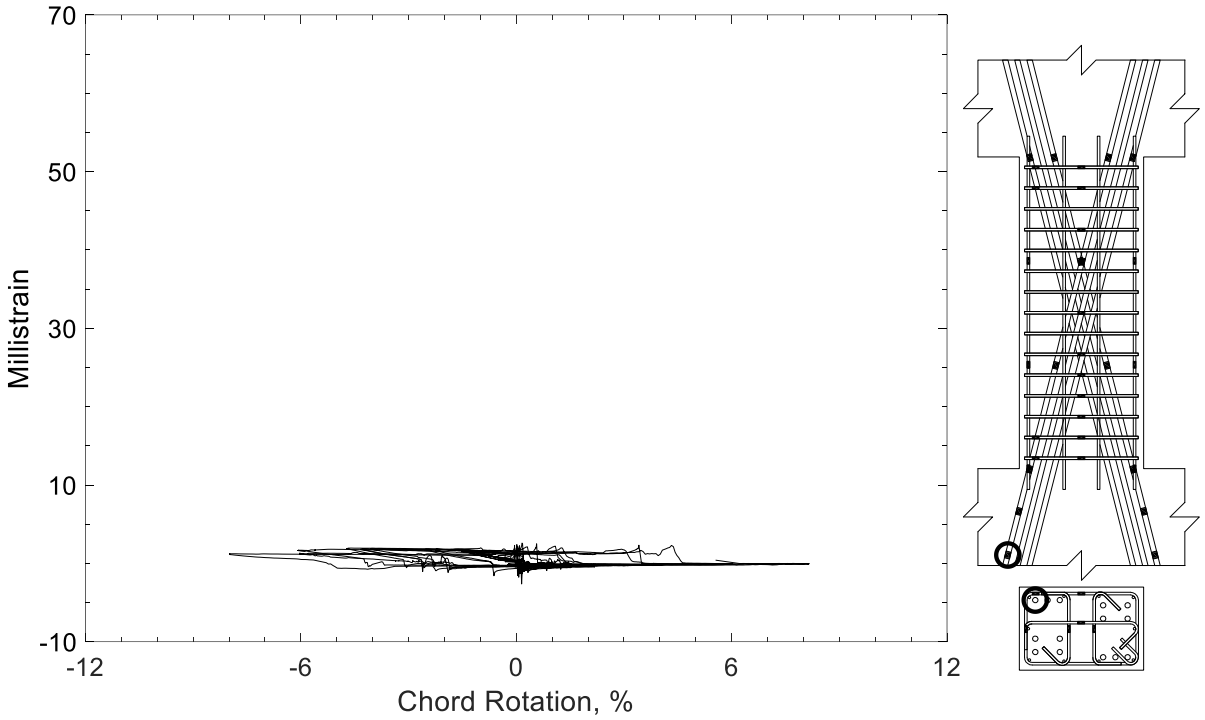

Figure 384 – Measured strain in diagonal bar of D100-2.5, strain gauge D1

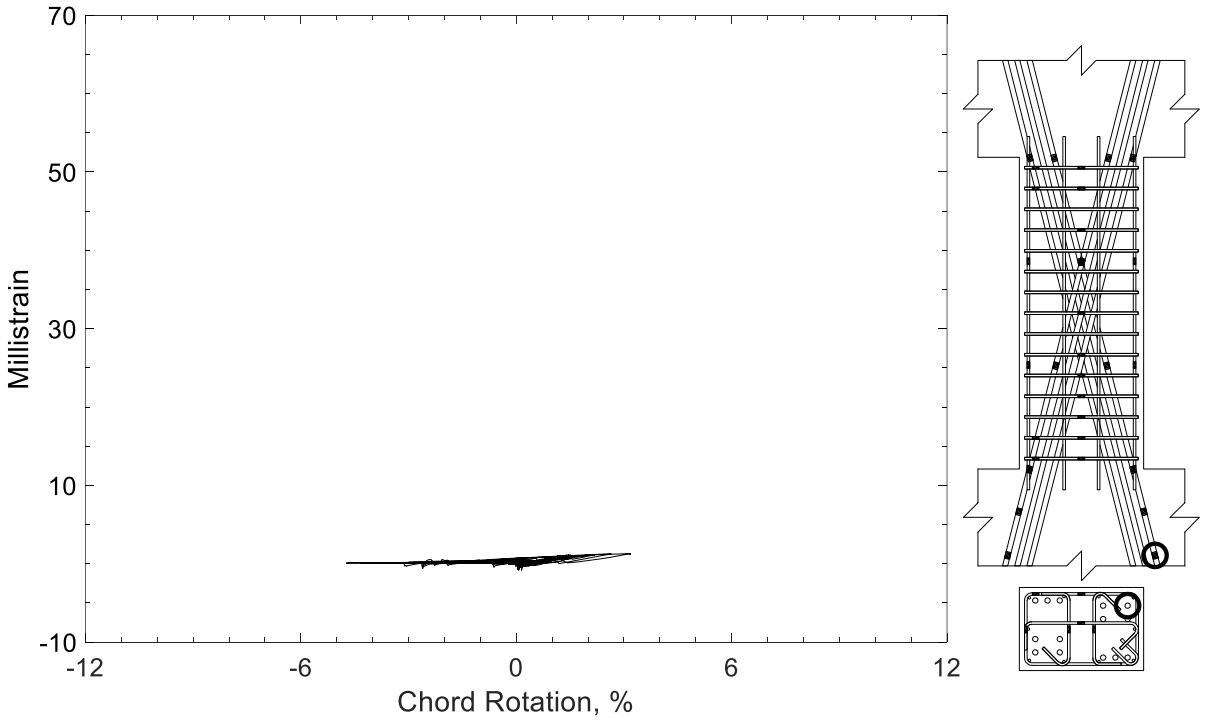

Figure 385 – Measured strain in diagonal bar of D100-2.5, strain gauge D2

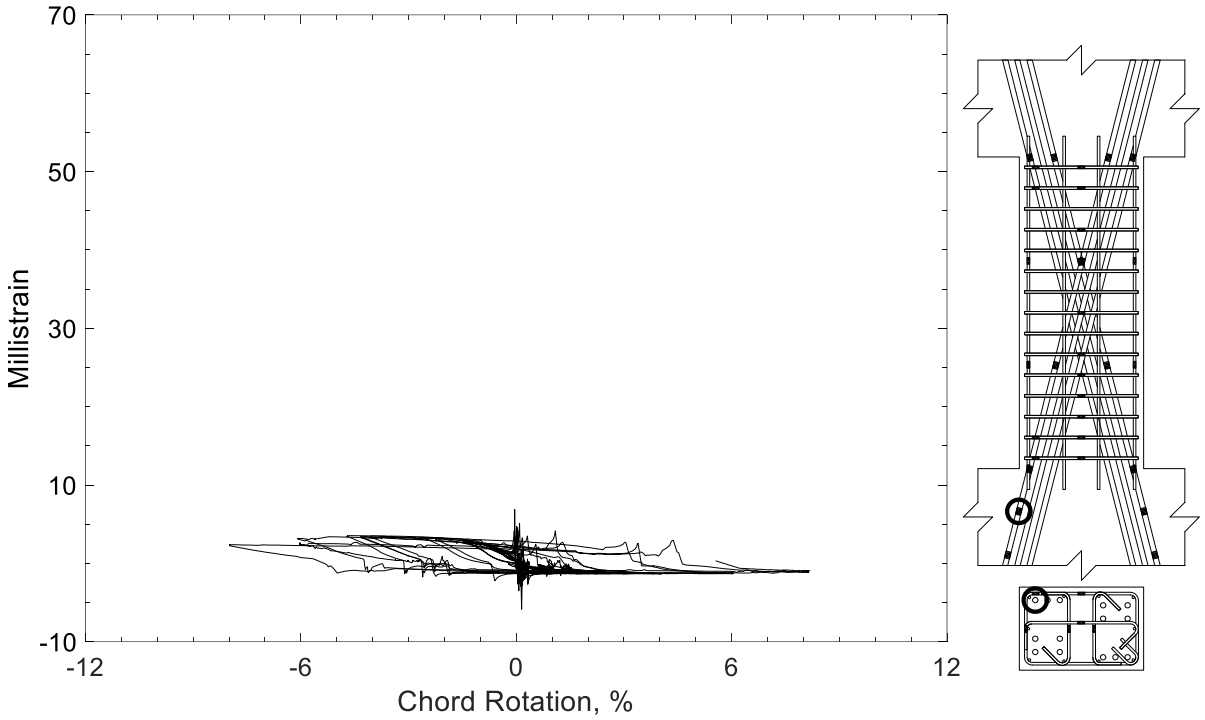

Figure 386 – Measured strain in diagonal bar of D100-2.5, strain gauge D3

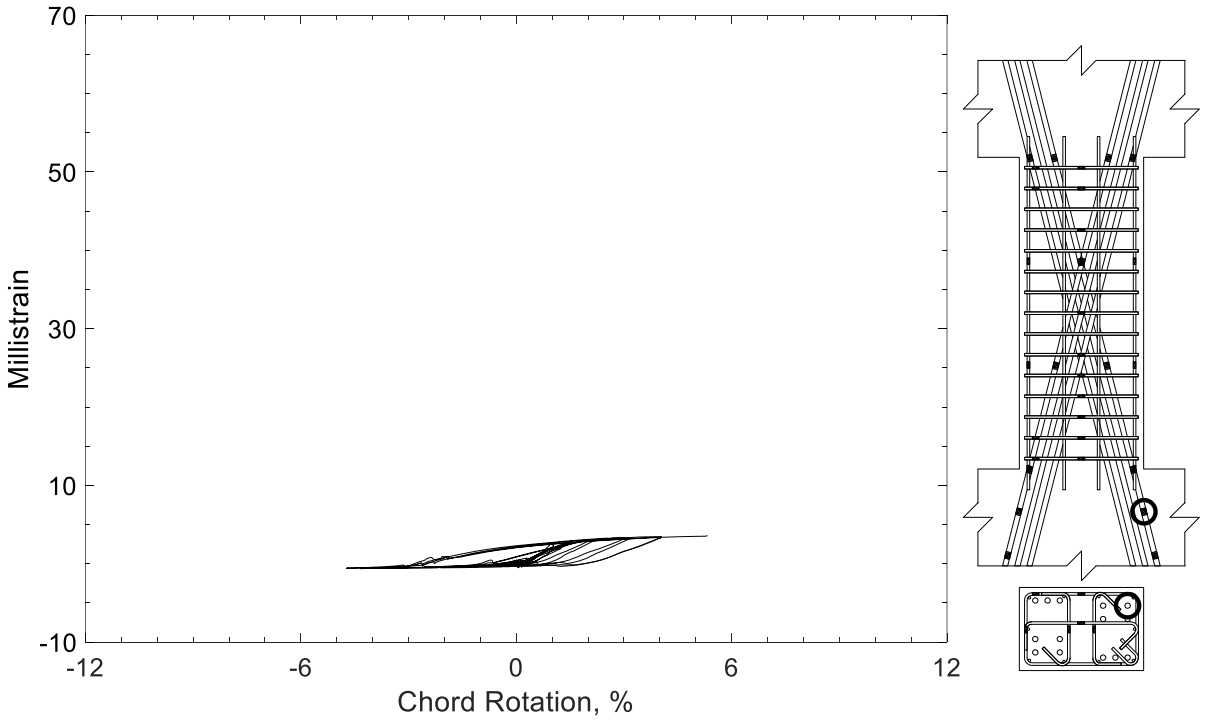

Figure 387 – Measured strain in diagonal bar of D100-2.5, strain gauge D4

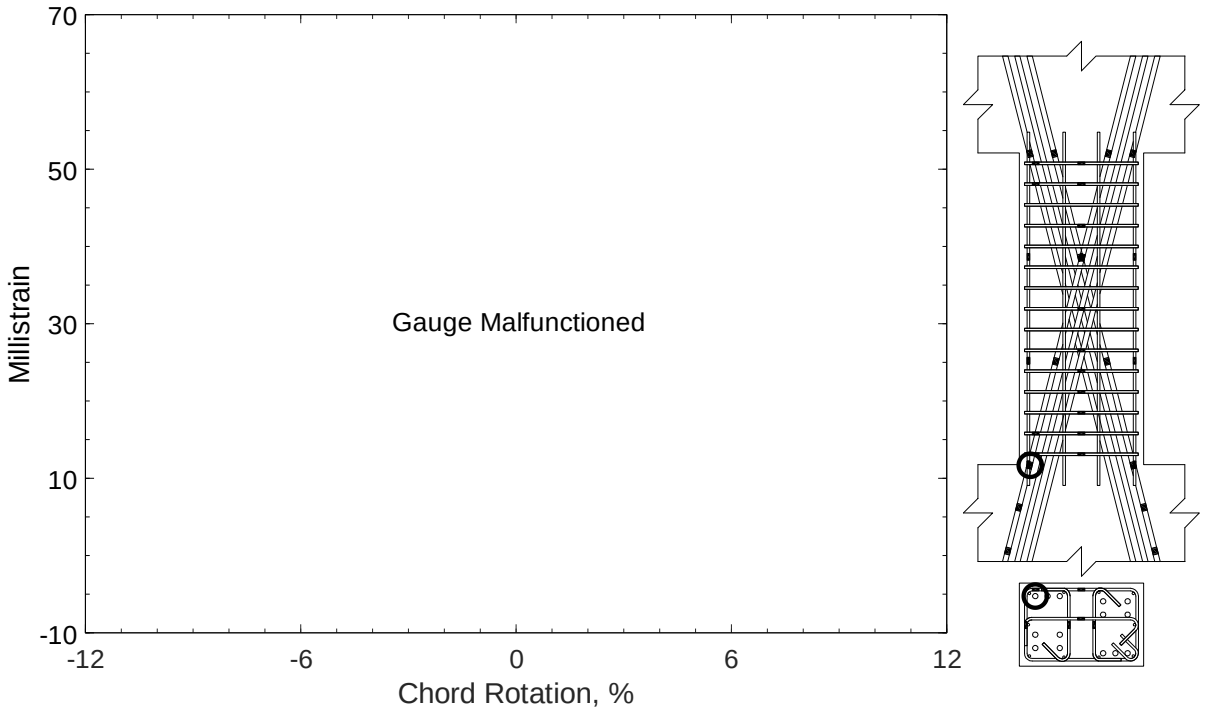

Figure 388 – Measured strain in diagonal bar of D100-2.5, strain gauge D5

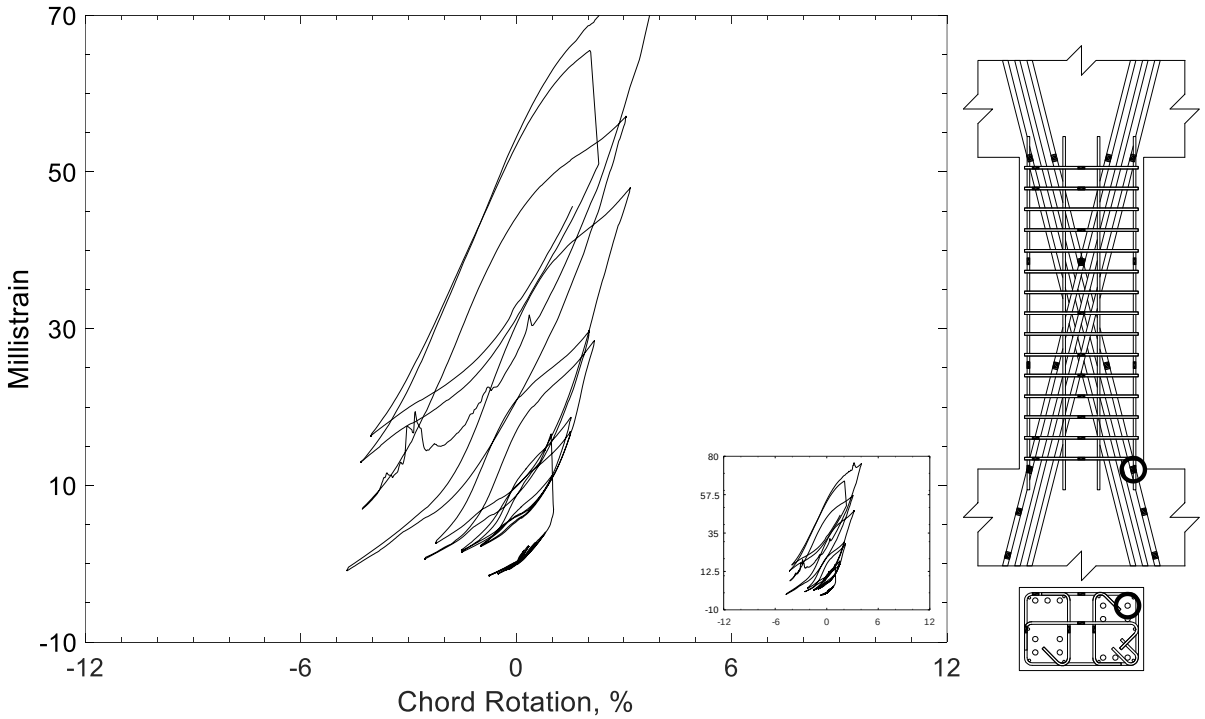

Figure 389 – Measured strain in diagonal bar of D100-2.5, strain gauge D6

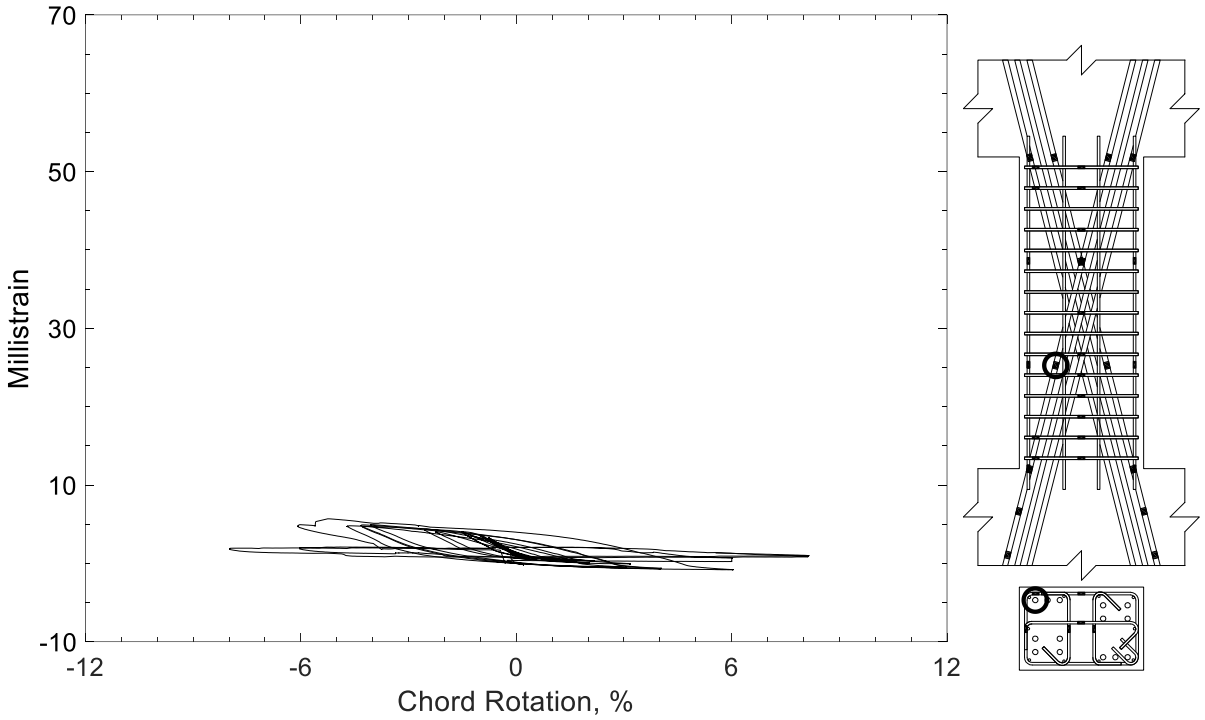

Figure 390 – Measured strain in diagonal bar of D100-2.5, strain gauge D7

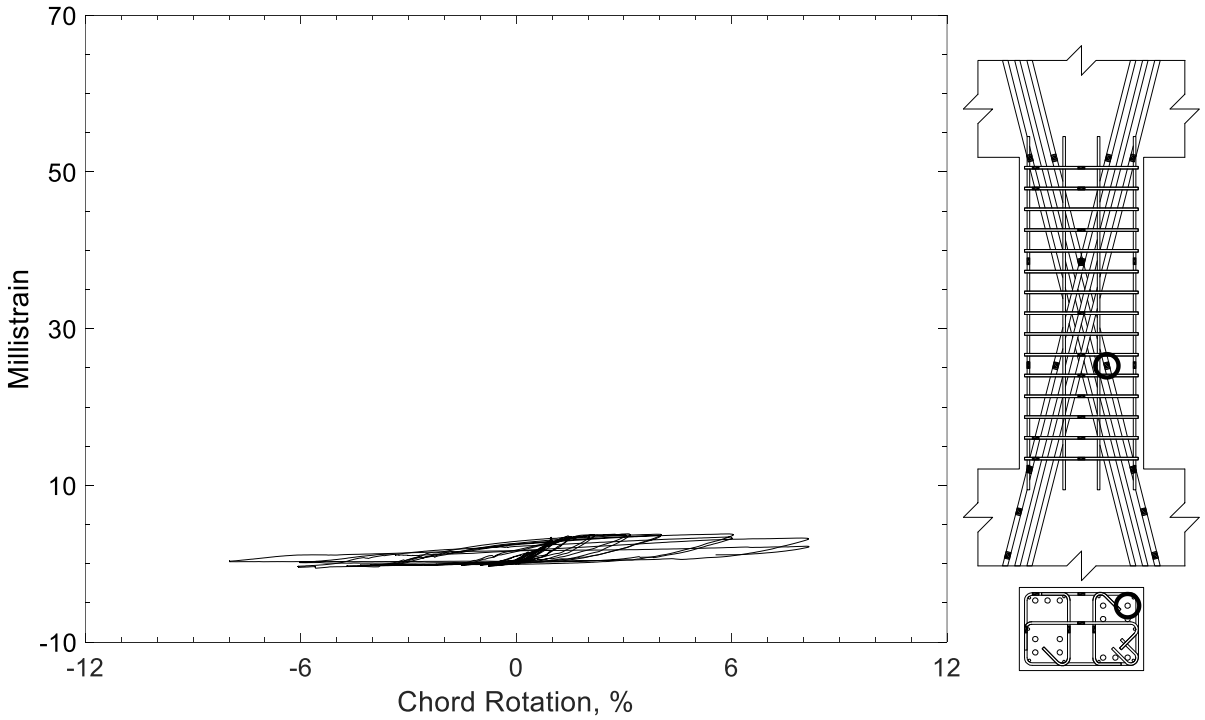

Figure 391 – Measured strain in diagonal bar of D100-2.5, strain gauge D8

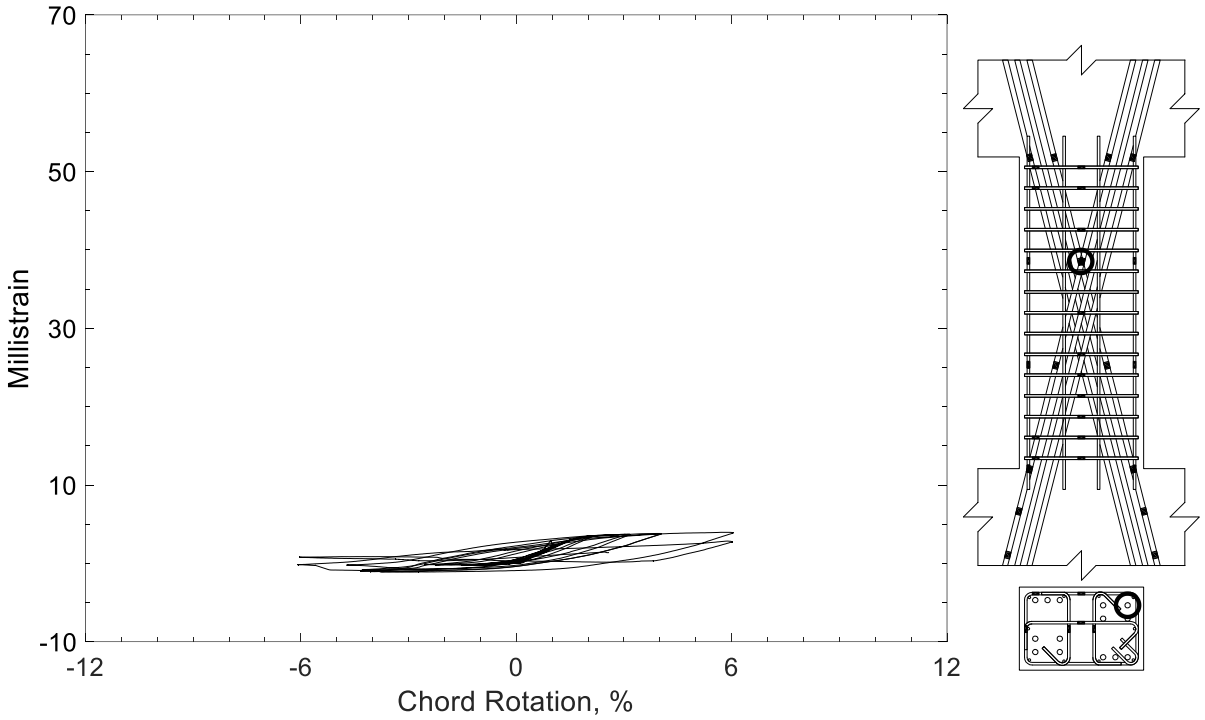

Figure 392 – Measured strain in diagonal bar of D100-2.5, strain gauge D9

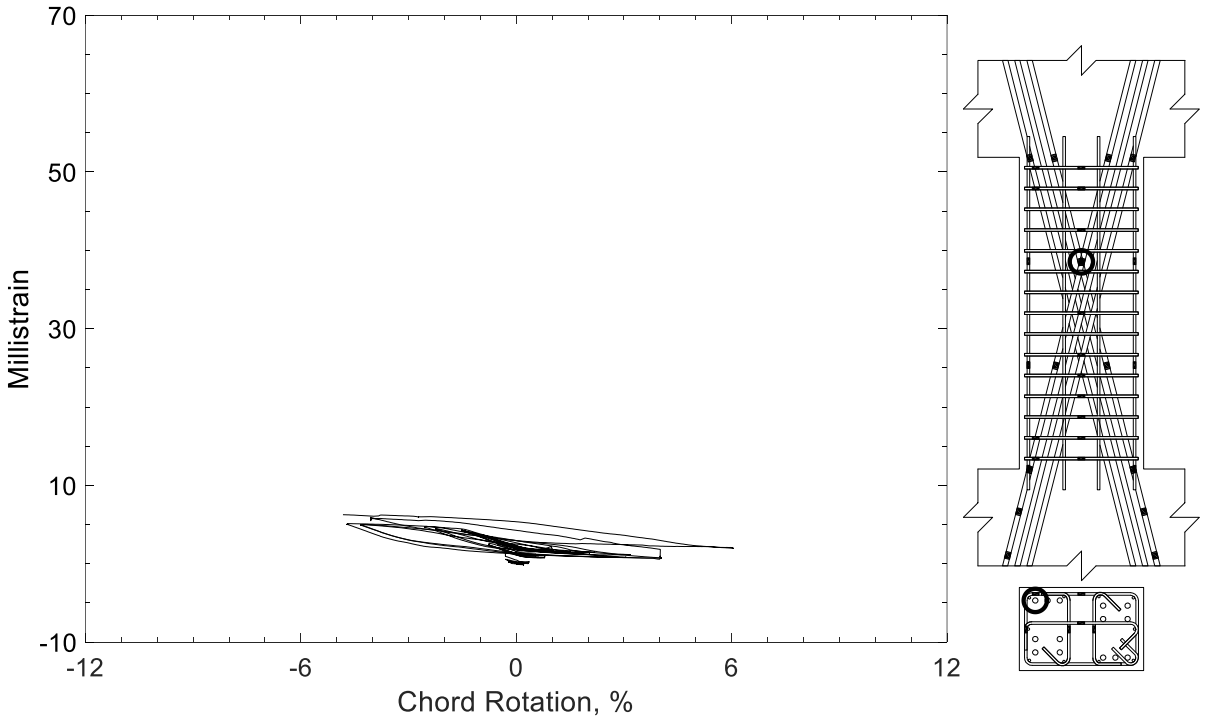

Figure 393 – Measured strain in diagonal bar of D100-2.5, strain gauge D10

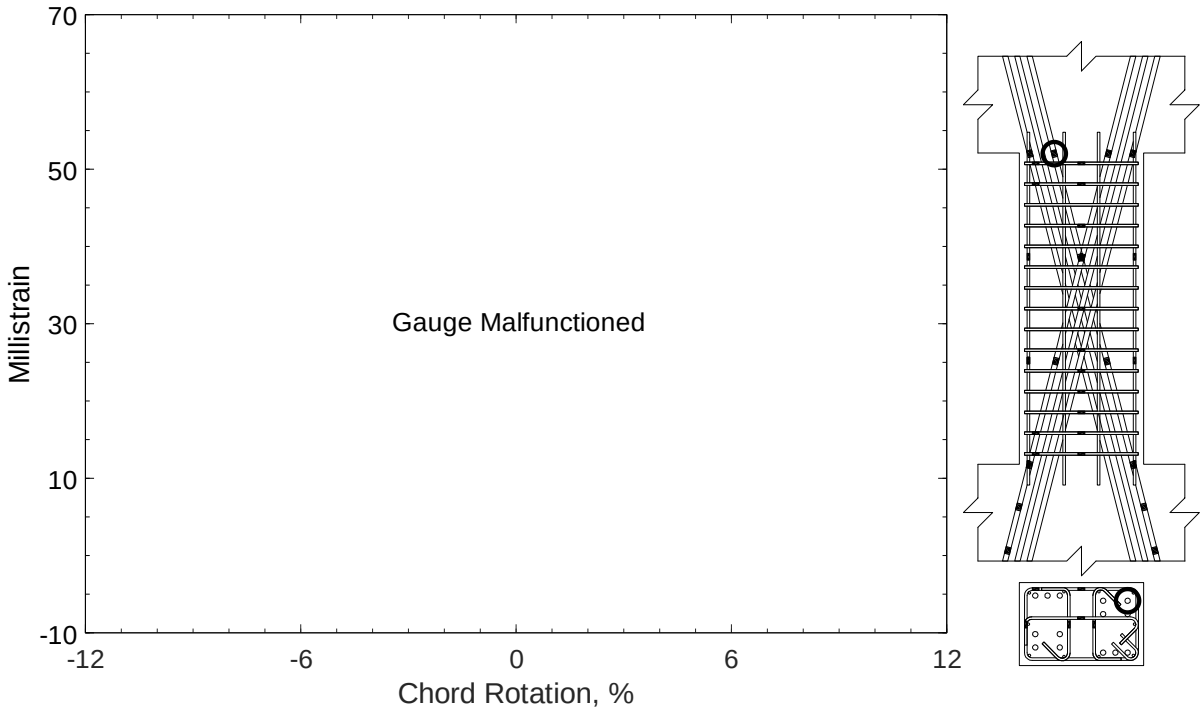

Figure 394 – Measured strain in diagonal bar of D100-2.5, strain gauge D11

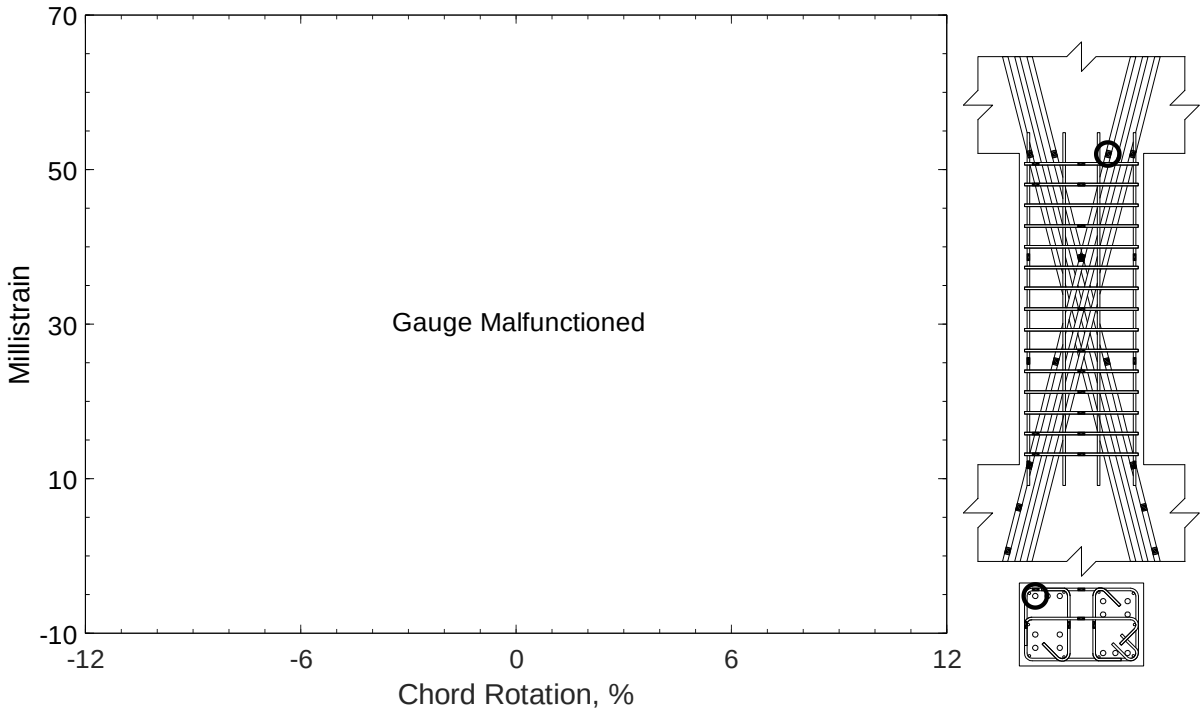

Figure 395 – Measured strain in diagonal bar of D100-2.5, strain gauge D12

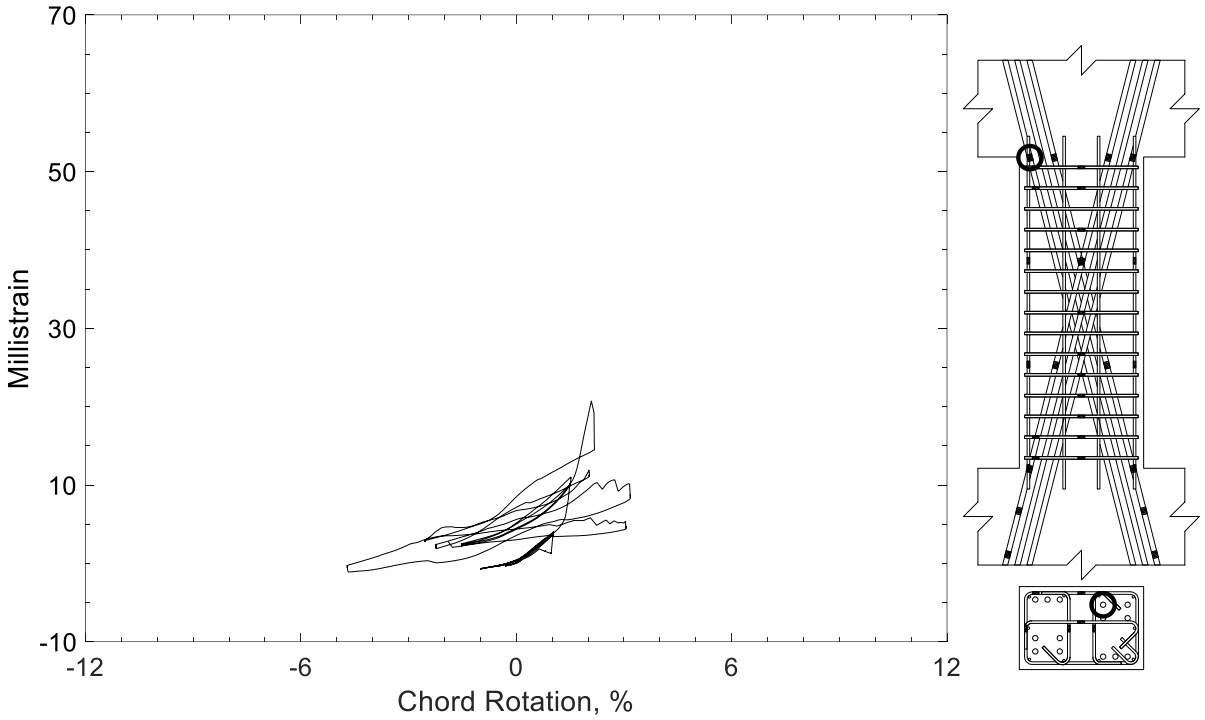

Figure 396 – Measured strain in diagonal bar of D100-2.5, strain gauge D13

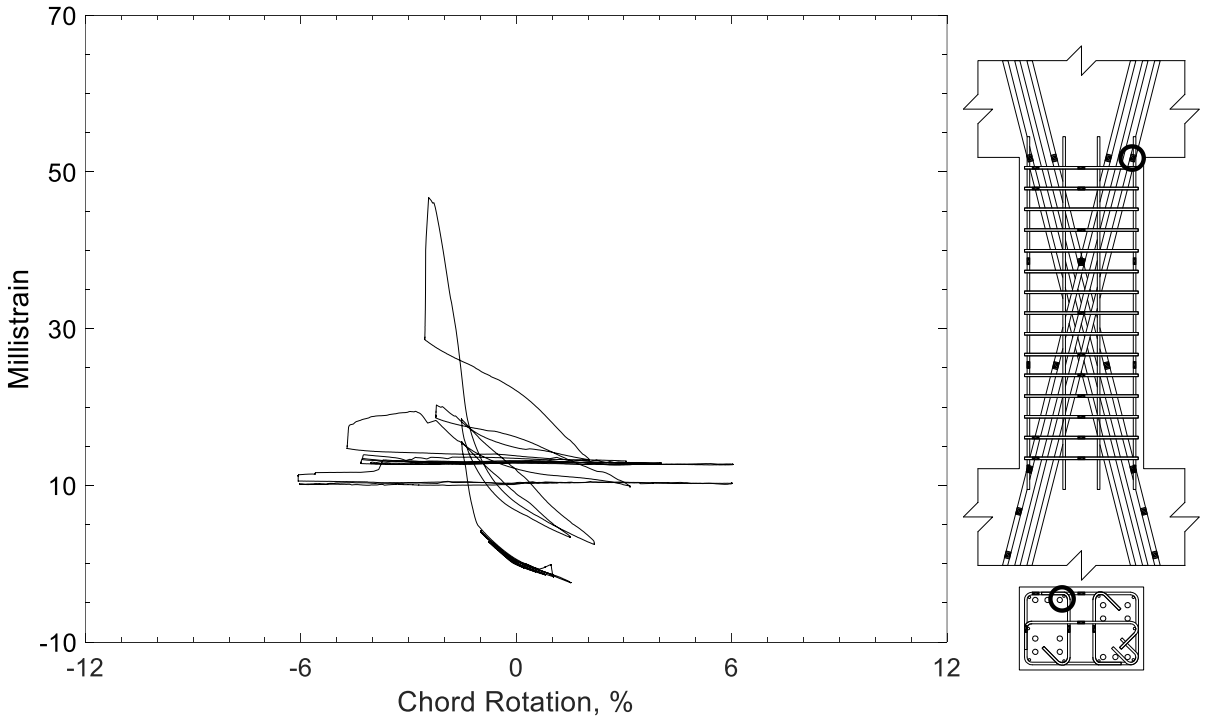

Figure 397 – Measured strain in diagonal bar of D100-2.5, strain gauge D14

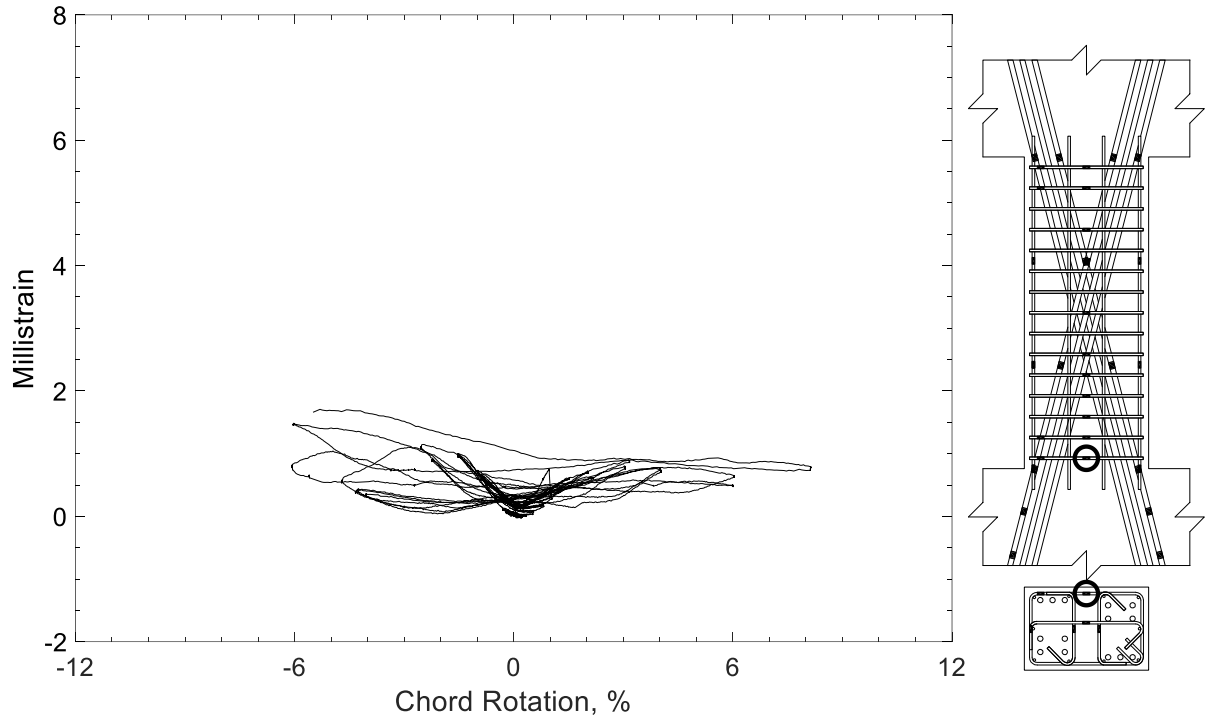

Figure 398 – Measured strain in closed stirrup of D100-2.5, strain gauge S1

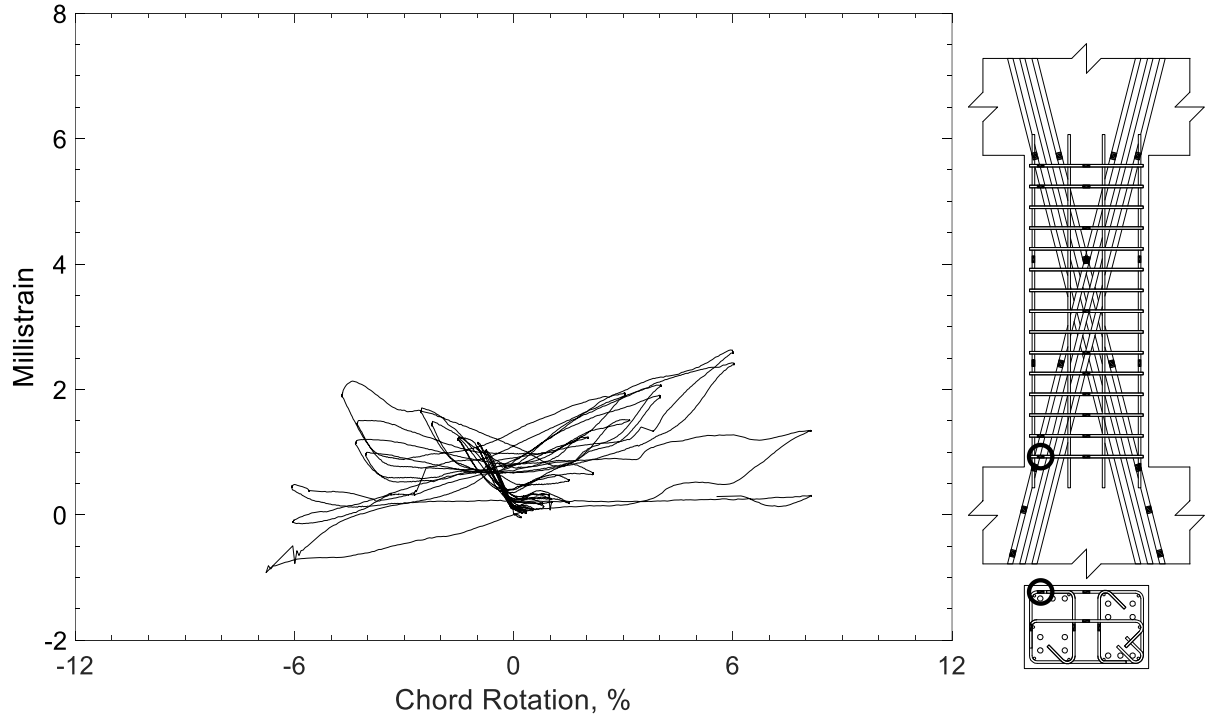

Figure 399 – Measured strain in closed stirrup of D100-2.5, strain gauge S2

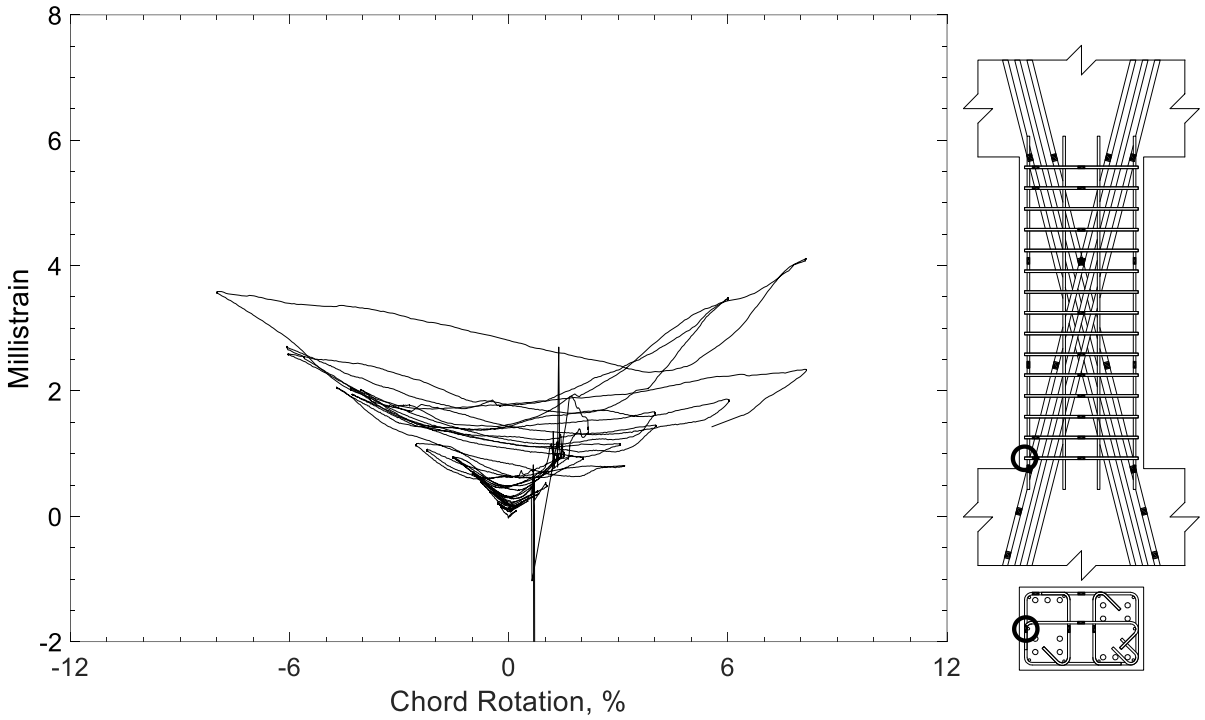

Figure 400 – Measured strain in closed stirrup of D100-2.5, strain gauge S3

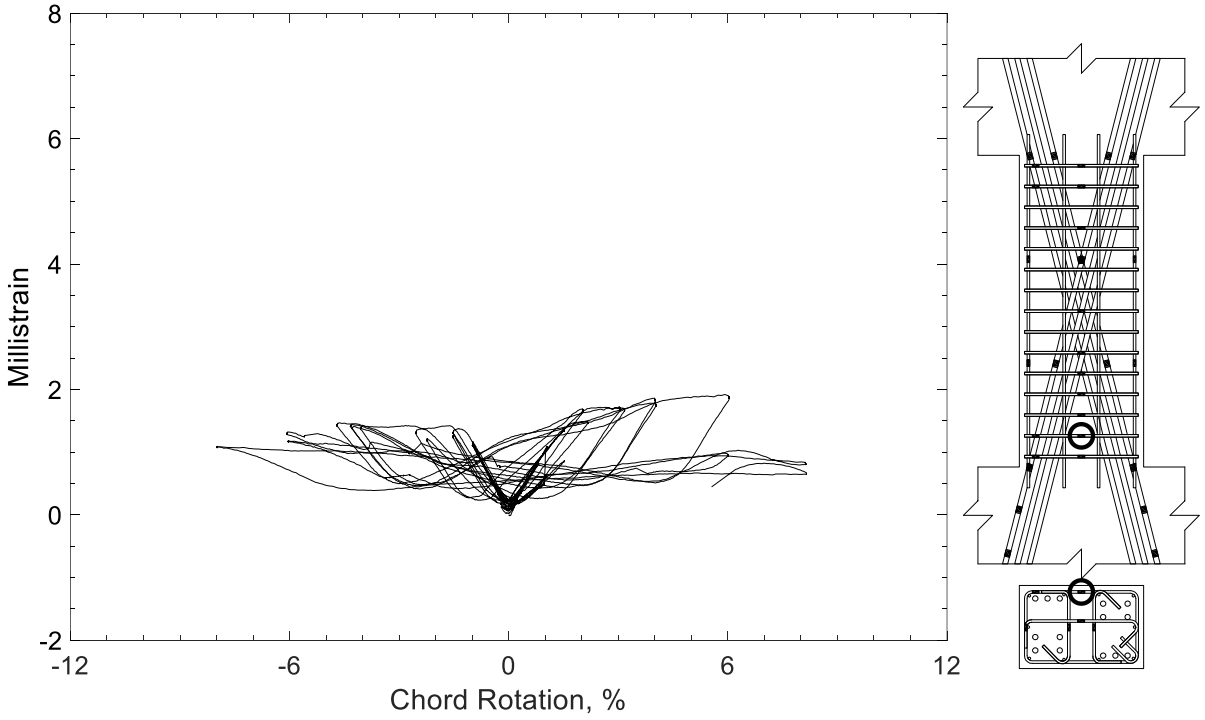

Figure 401 – Measured strain in closed stirrup of D100-2.5, strain gauge S4

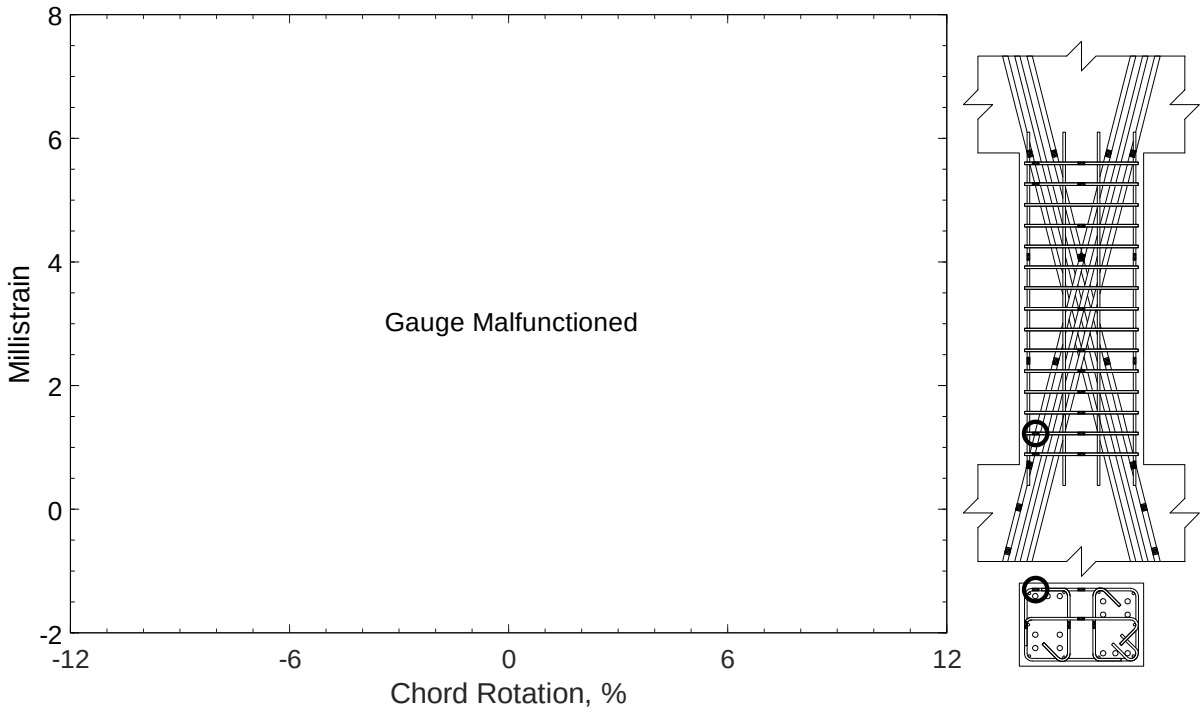

Figure 402 – Measured strain in closed stirrup of D100-2.5, strain gauge S5

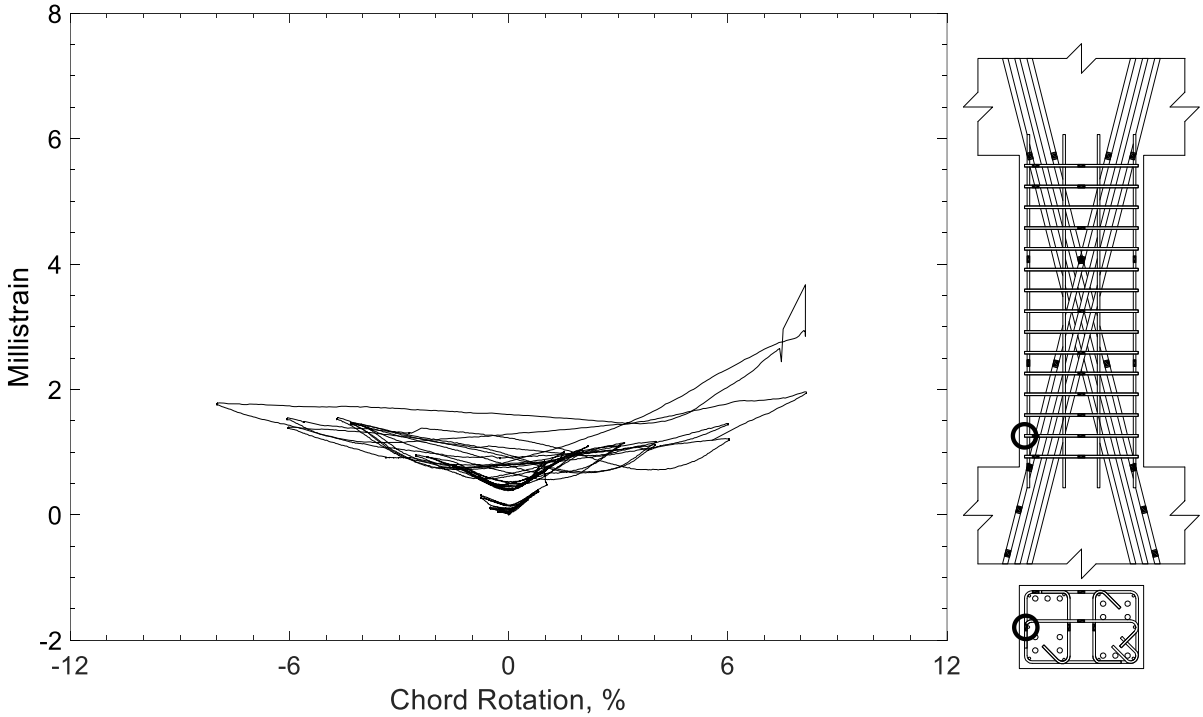

Figure 403 – Measured strain in closed stirrup of D100-2.5, strain gauge S6

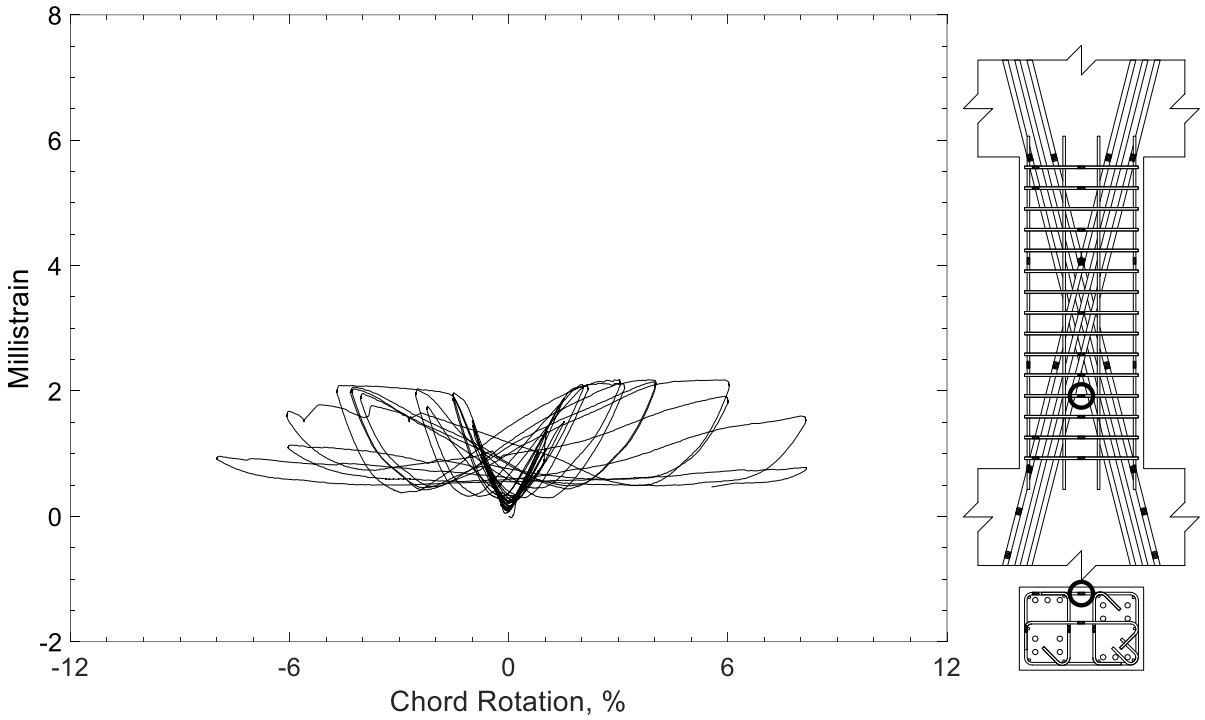

Figure 404 – Measured strain in closed stirrup of D100-2.5, strain gauge S7

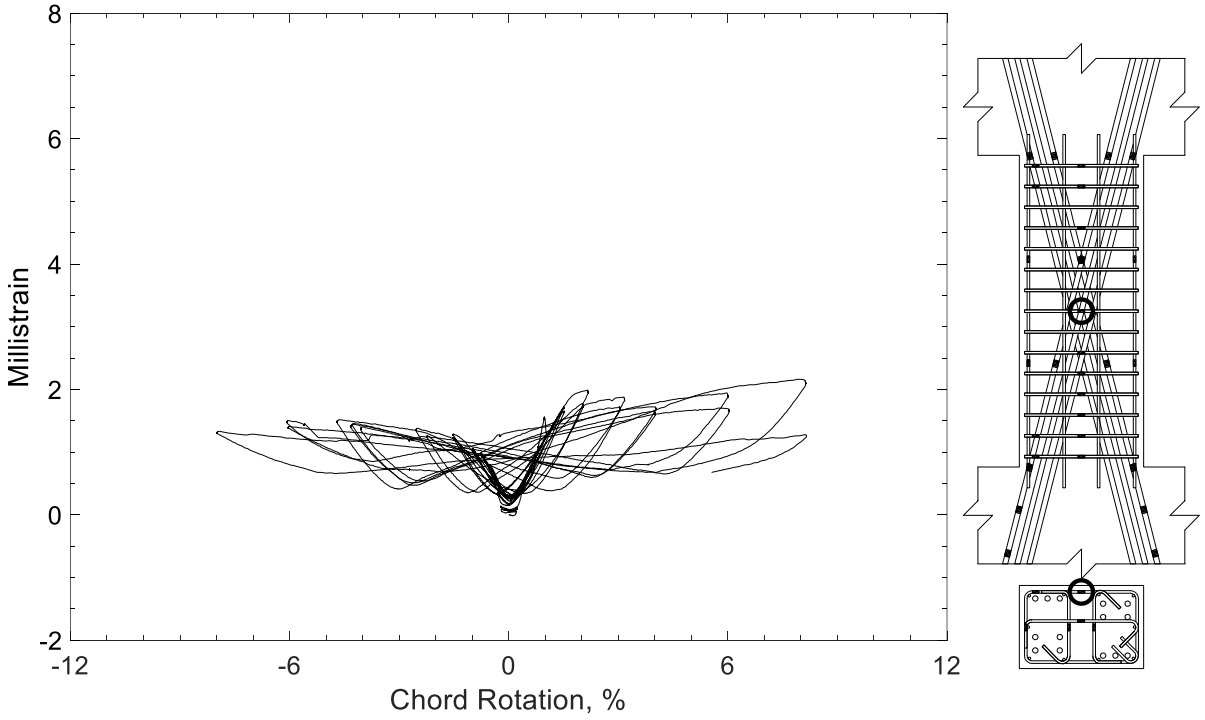

Figure 405 – Measured strain in closed stirrup of D100-2.5, strain gauge S8

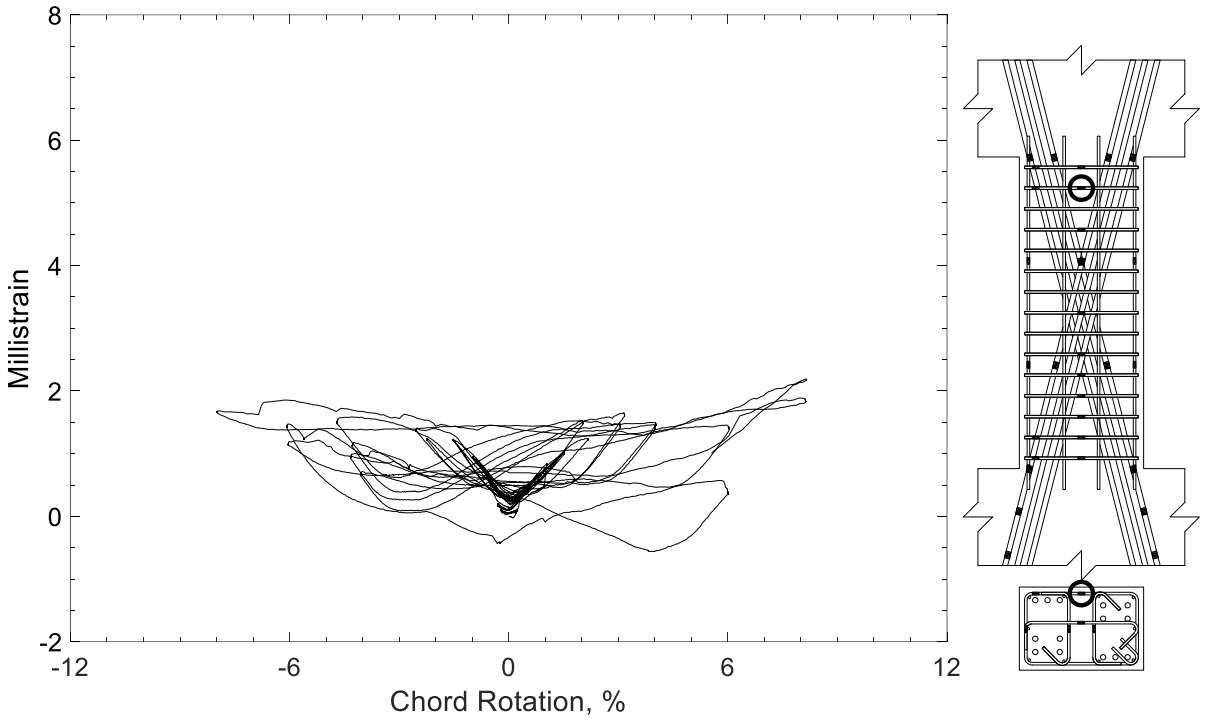

Figure 406 – Measured strain in closed stirrup of D100-2.5, strain gauge S9

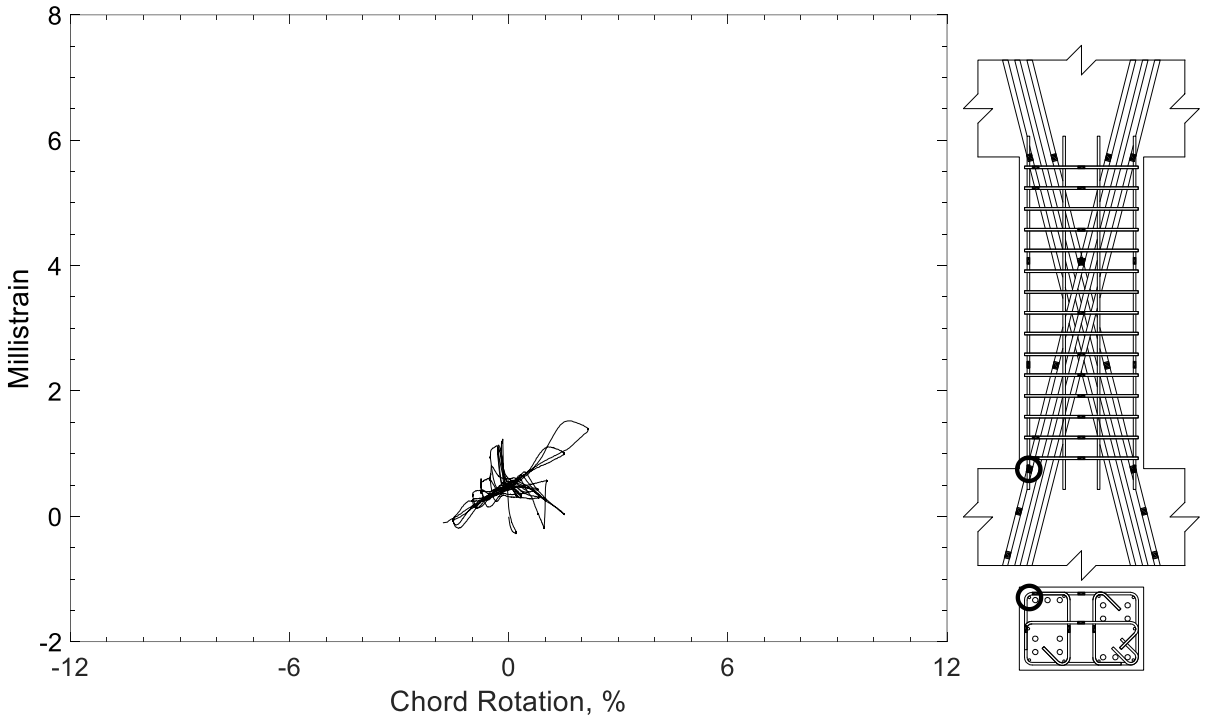

Figure 407 – Measured strain in parallel bar of D100-2.5, strain gauge H1

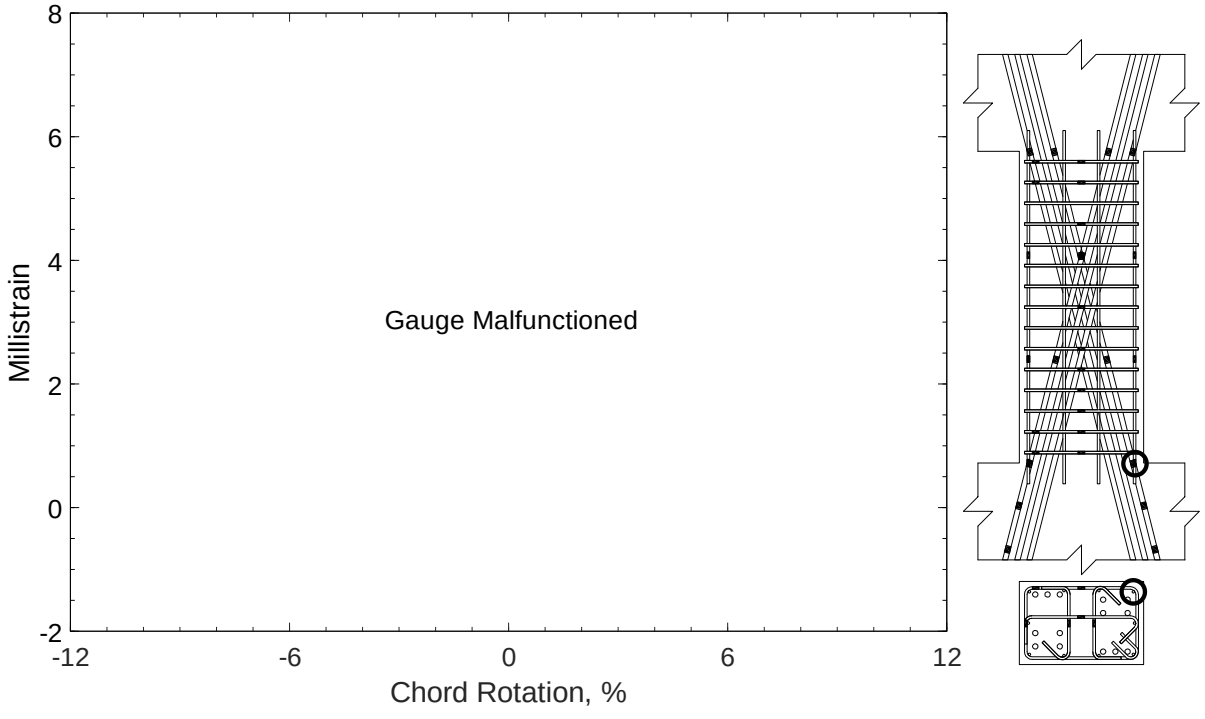

Figure 408 – Measured strain in parallel bar of D100-2.5, strain gauge H2

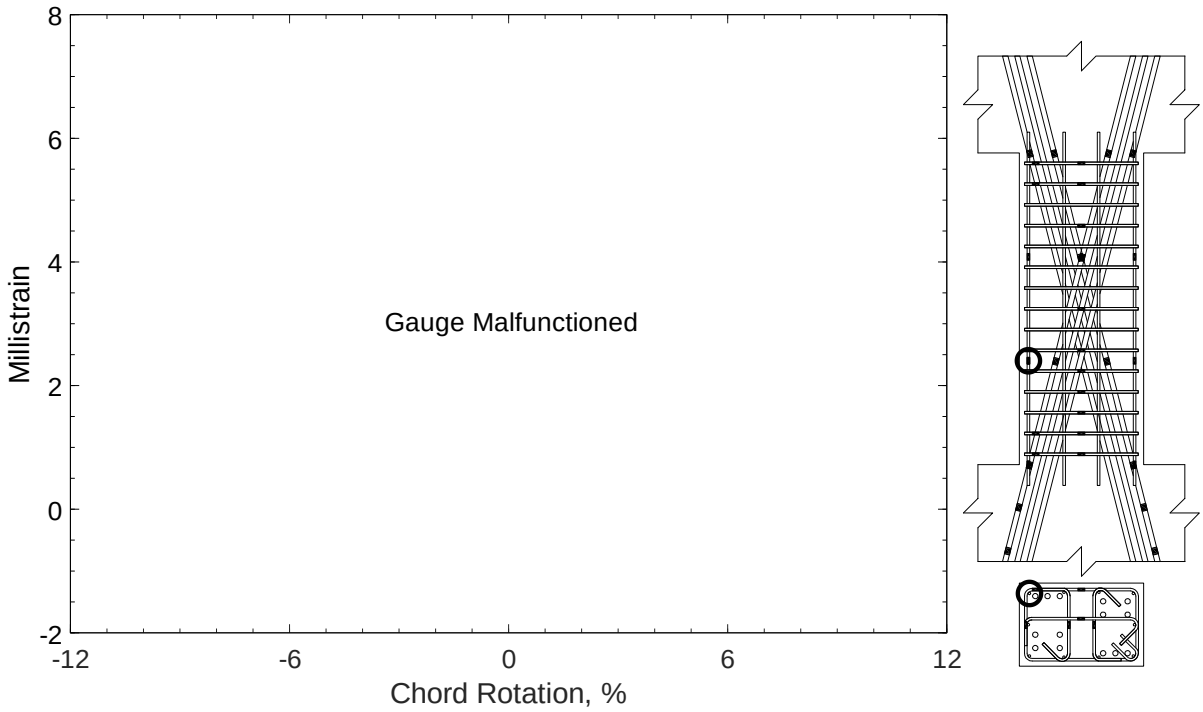

Figure 409 – Measured strain in parallel bar of D100-2.5, strain gauge H3

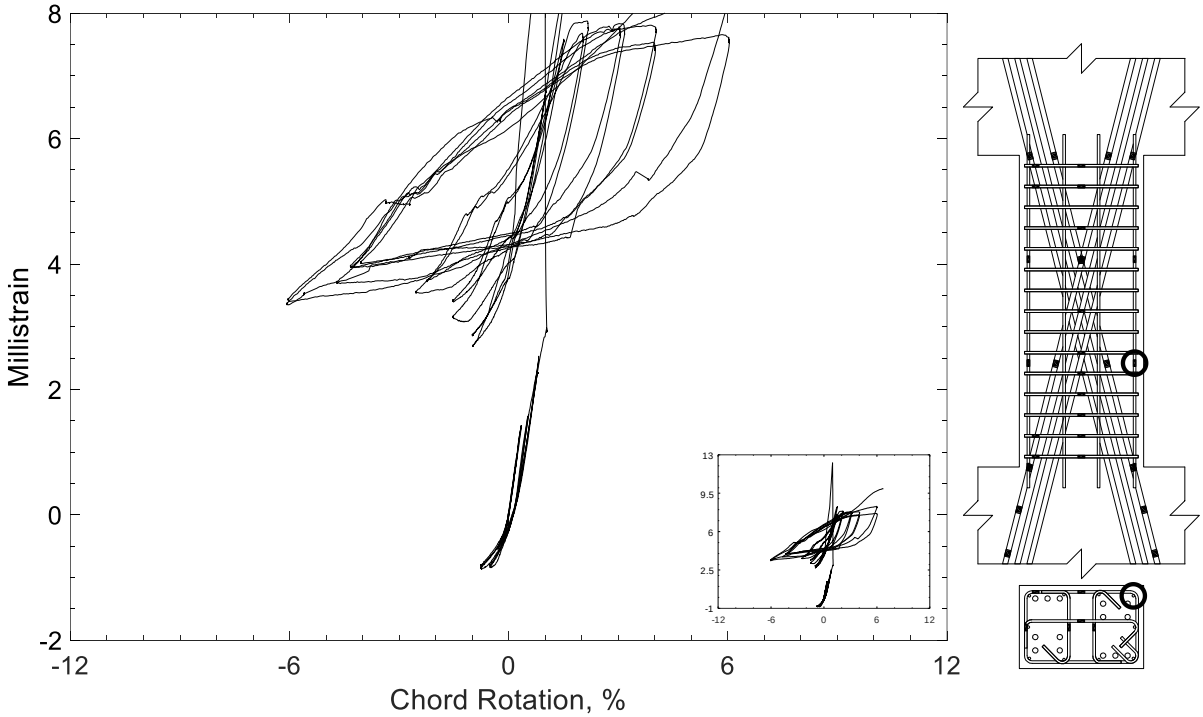

Figure 410 – Measured strain in parallel bar of D100-2.5, strain gauge H4

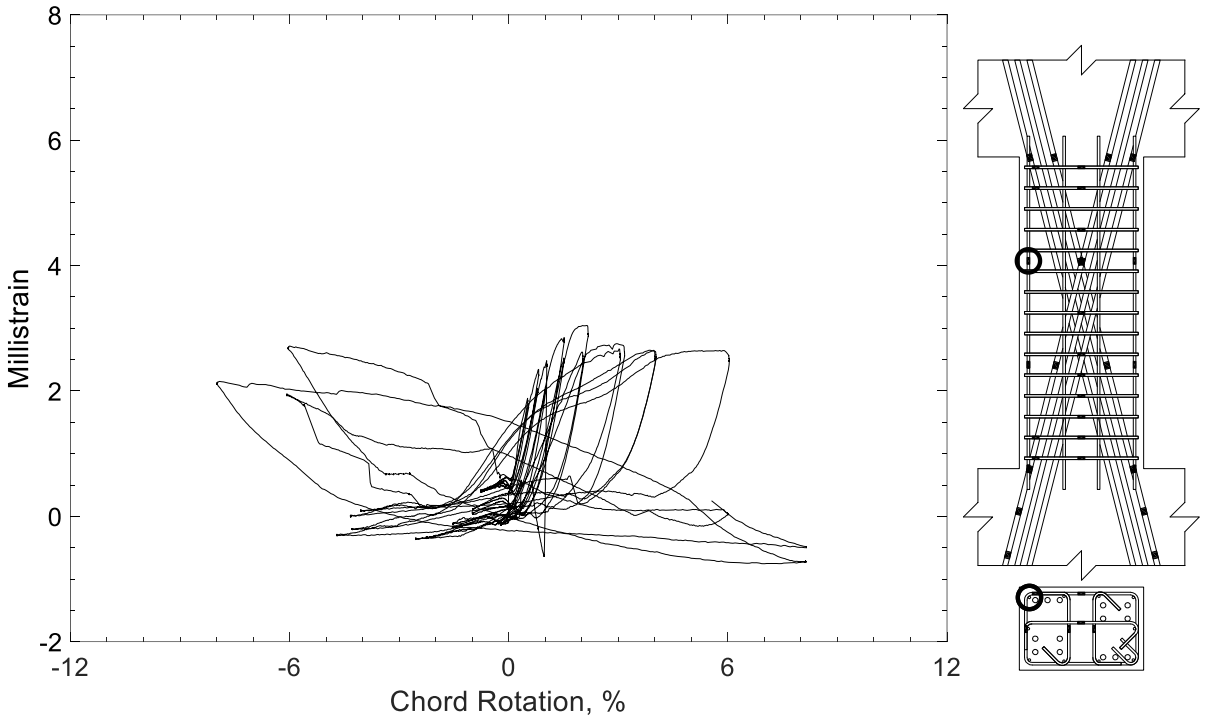

Figure 411 – Measured strain in parallel bar of D100-2.5, strain gauge H5

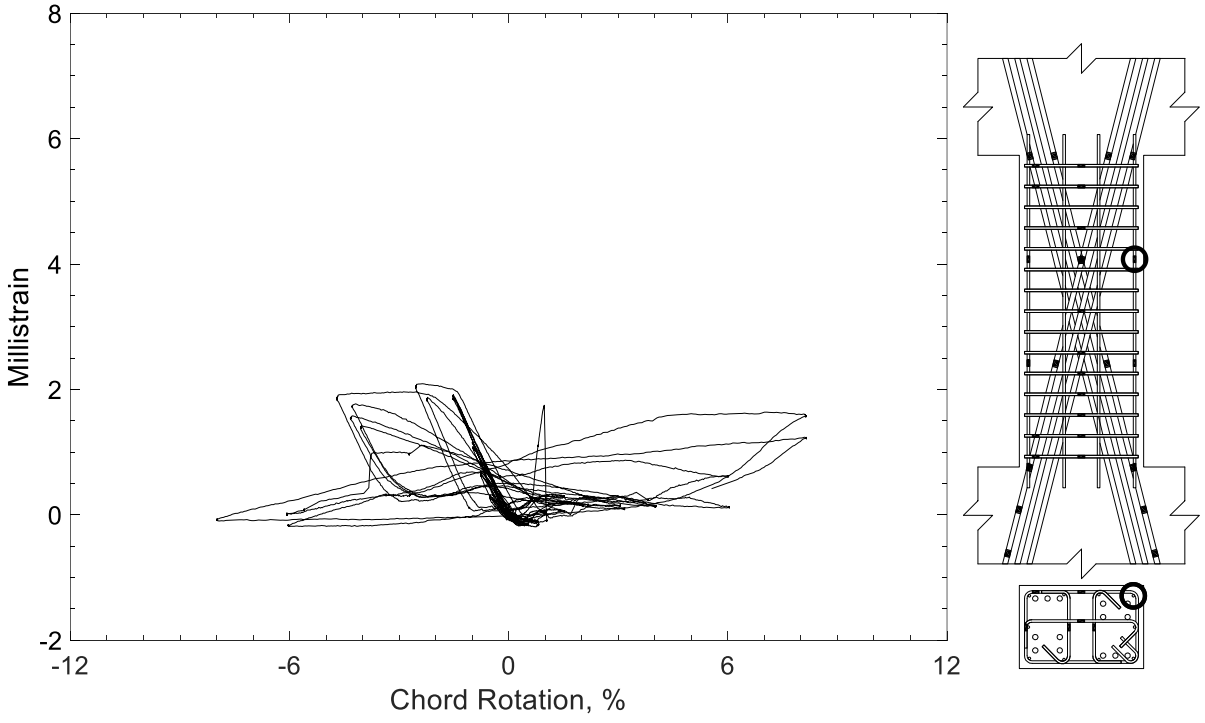

Figure 412 – Measured strain in parallel bar of D100-2.5, strain gauge H6

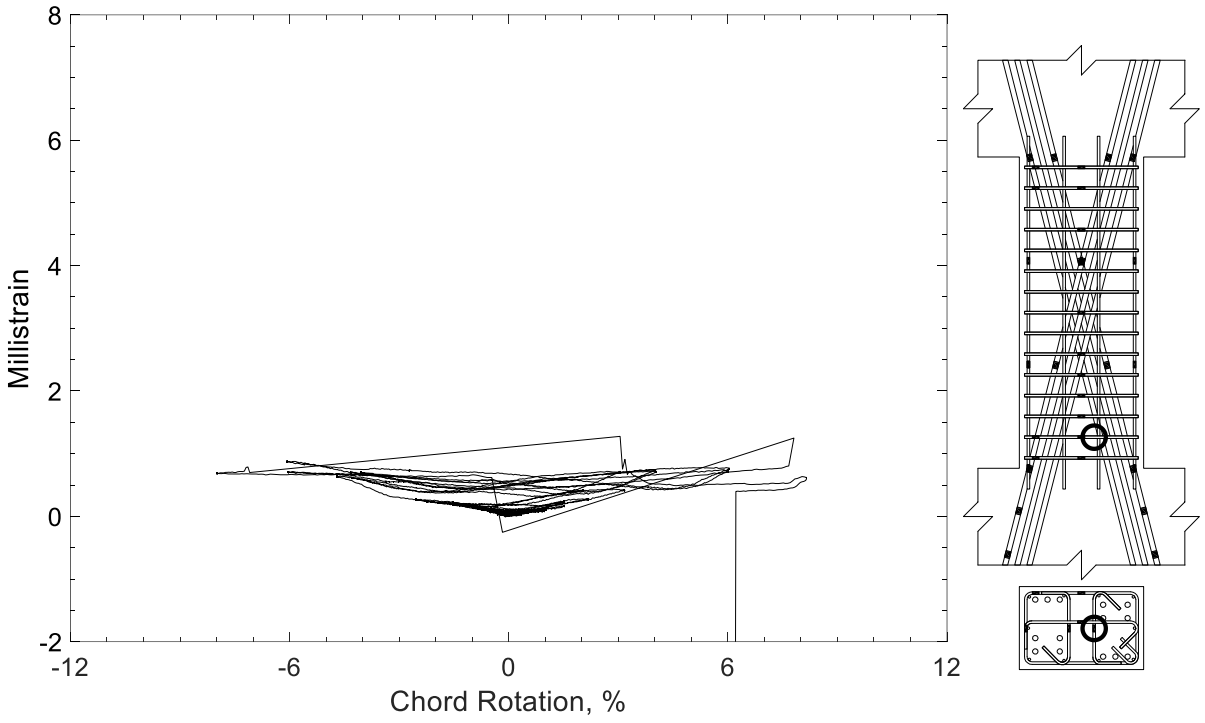

Figure 413 – Measured strain in crosstie of D100-2.5, strain gauge T1

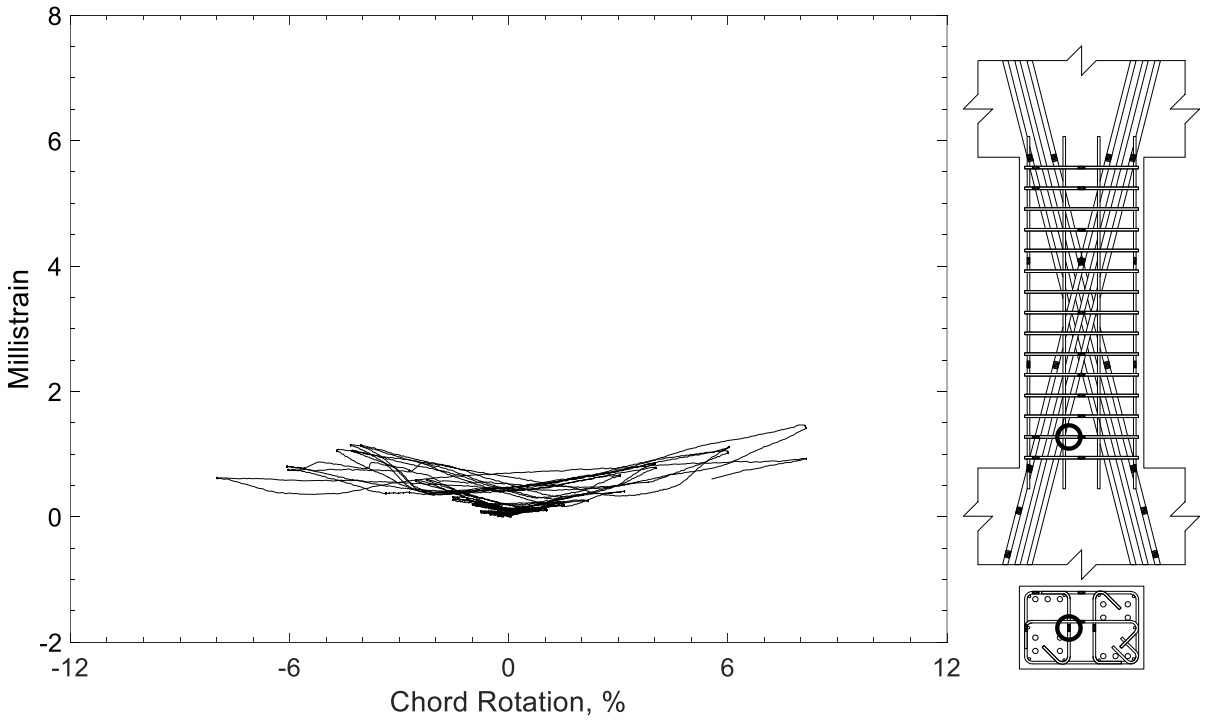

Figure 414 – Measured strain in crosstie of D100-2.5, strain gauge T2

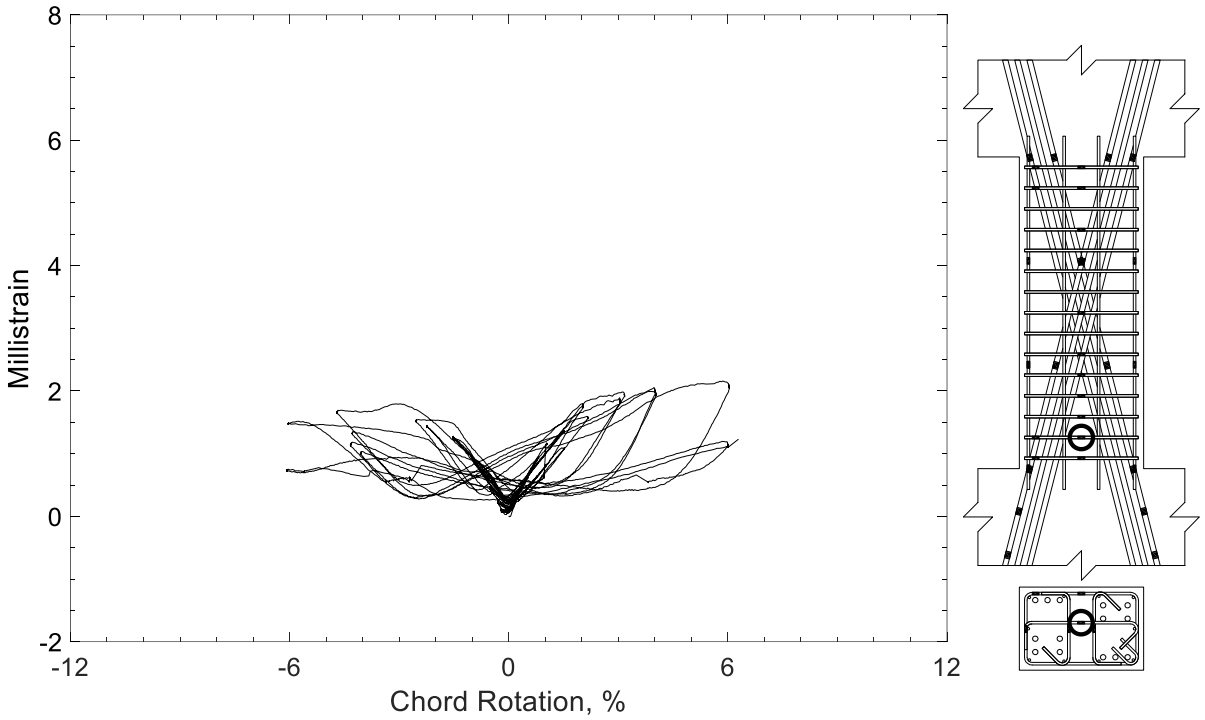

Figure 415 – Measured strain in crosstie of D100-2.5, strain gauge T3

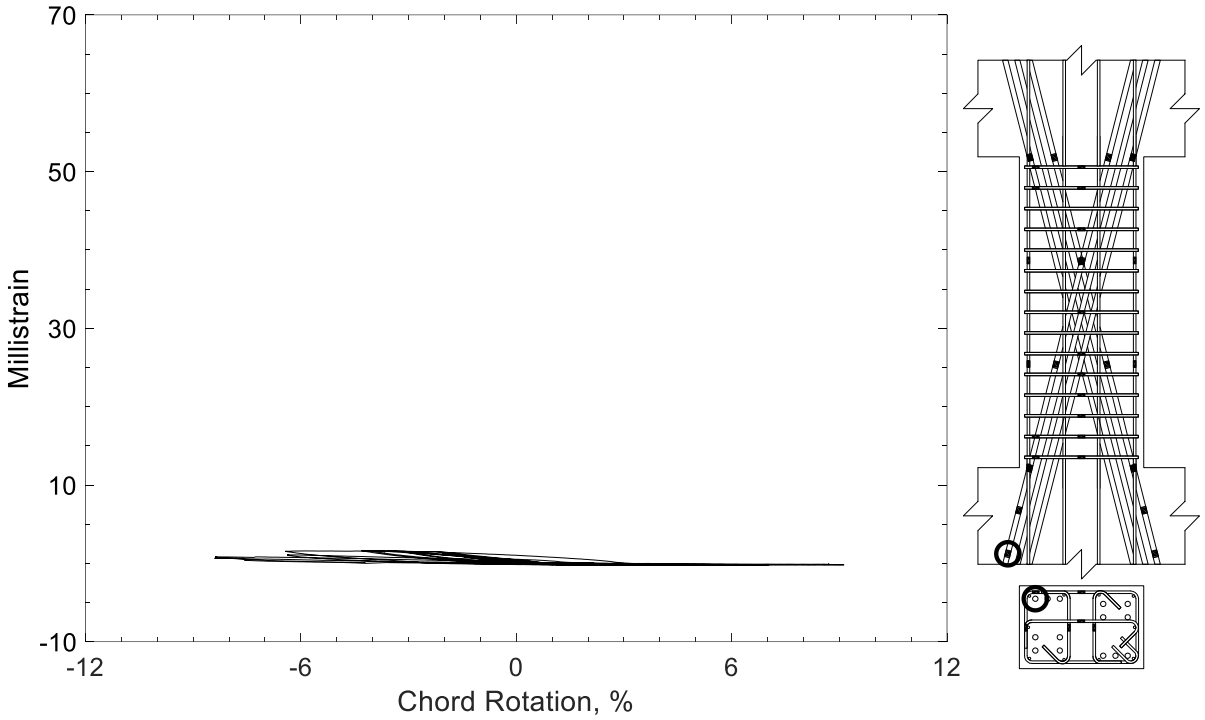

Figure 416 – Measured strain in diagonal bar of D120-2.5, strain gauge D1

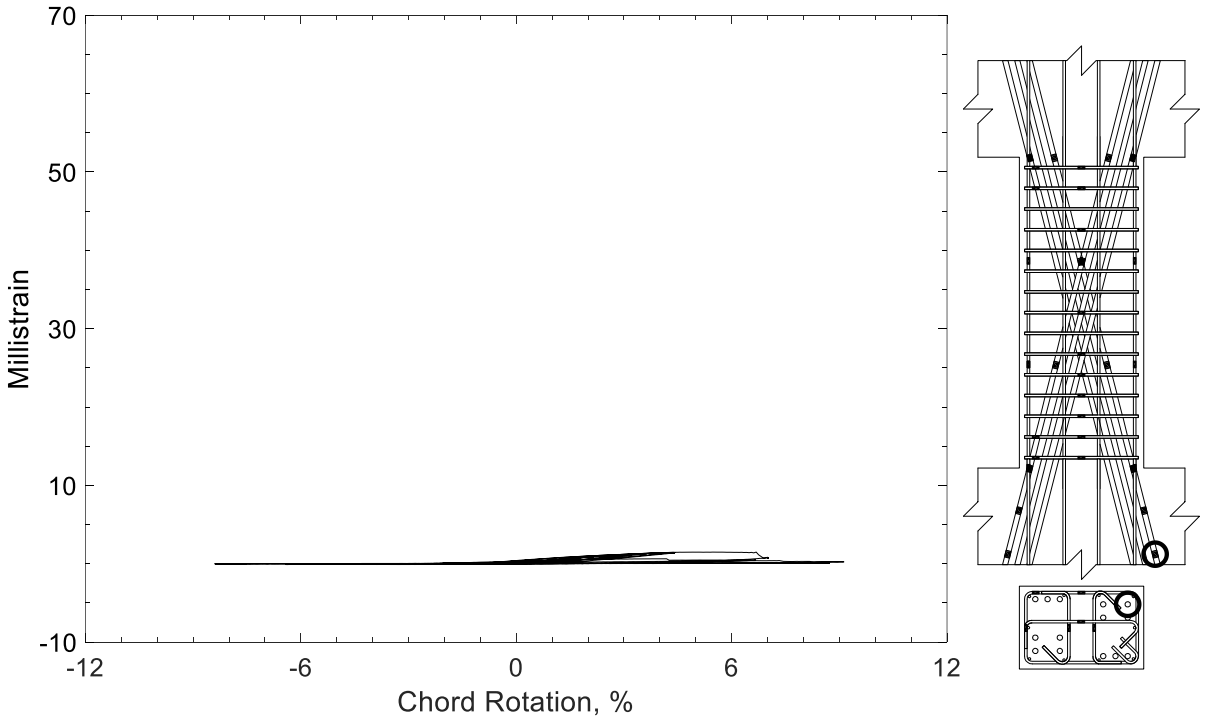

Figure 417 – Measured strain in diagonal bar of D120-2.5, strain gauge D2

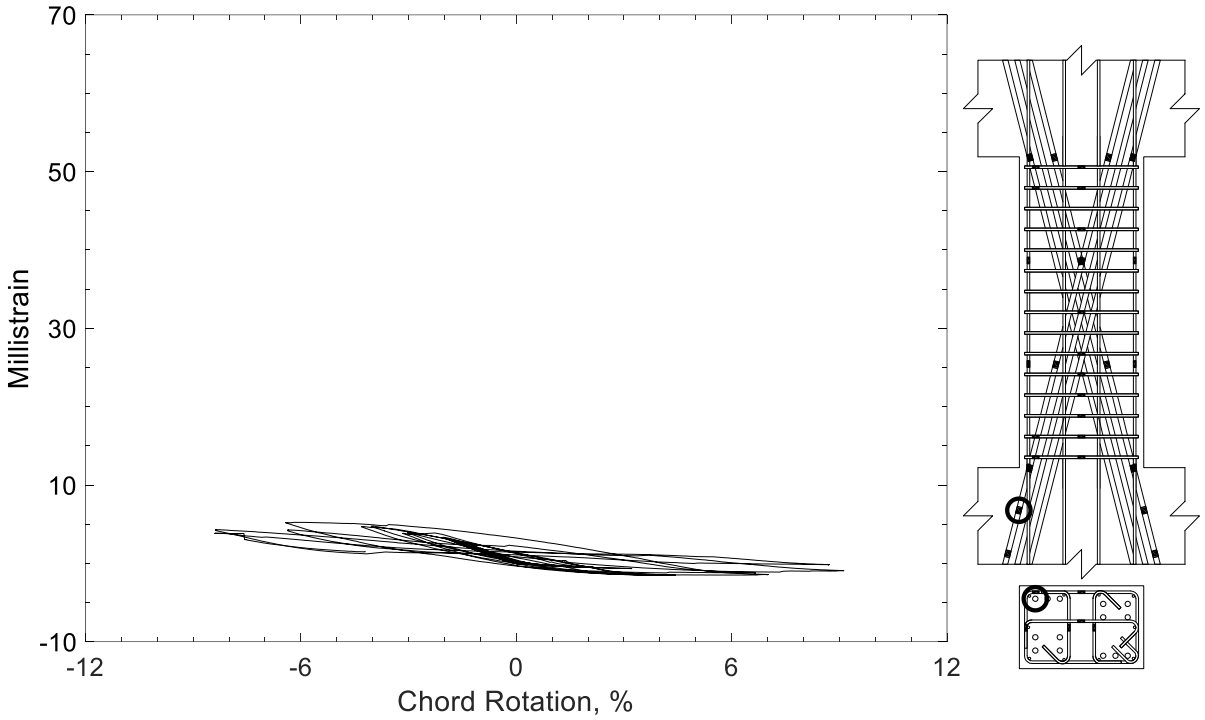

Figure 418 – Measured strain in diagonal bar of D120-2.5, strain gauge D3

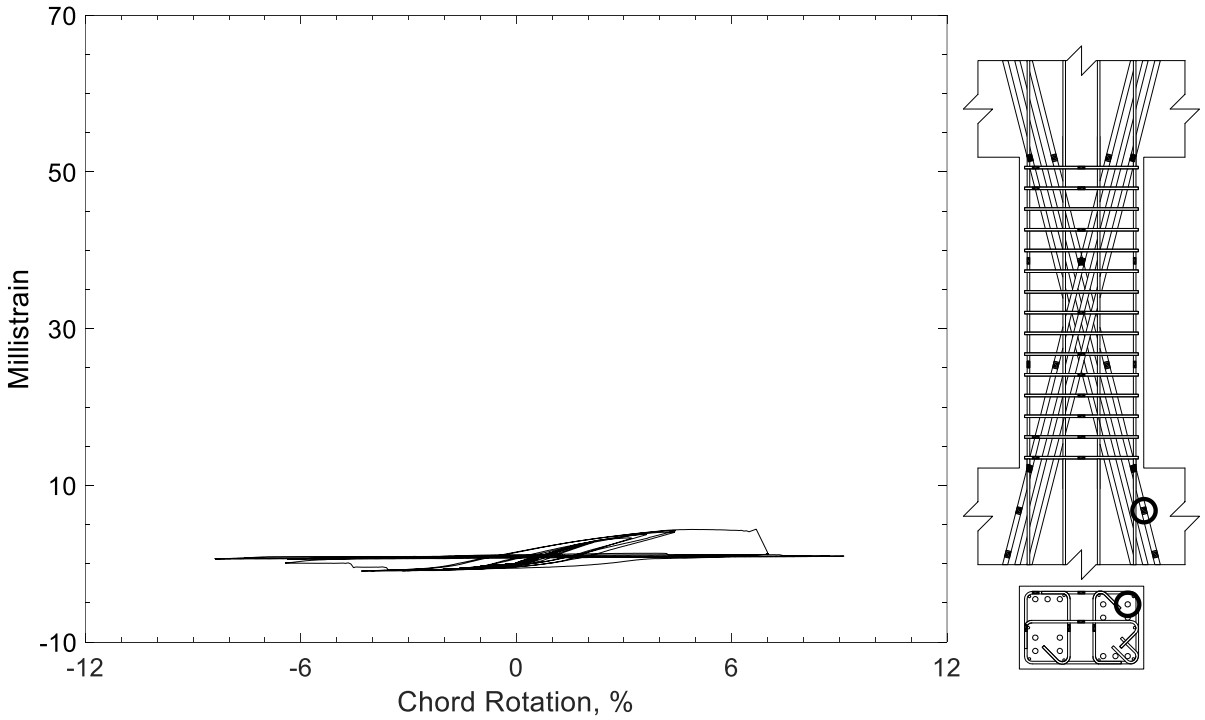

Figure 419 – Measured strain in diagonal bar of D120-2.5, strain gauge D4

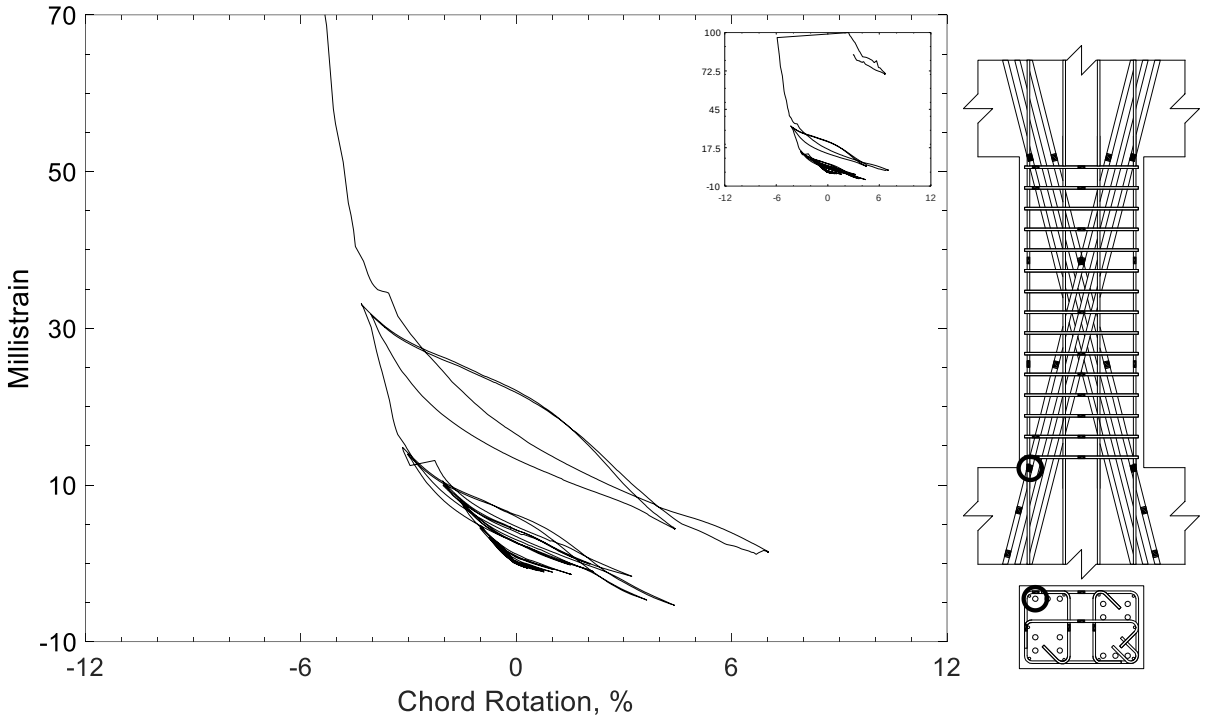

Figure 420 – Measured strain in diagonal bar of D120-2.5, strain gauge D5

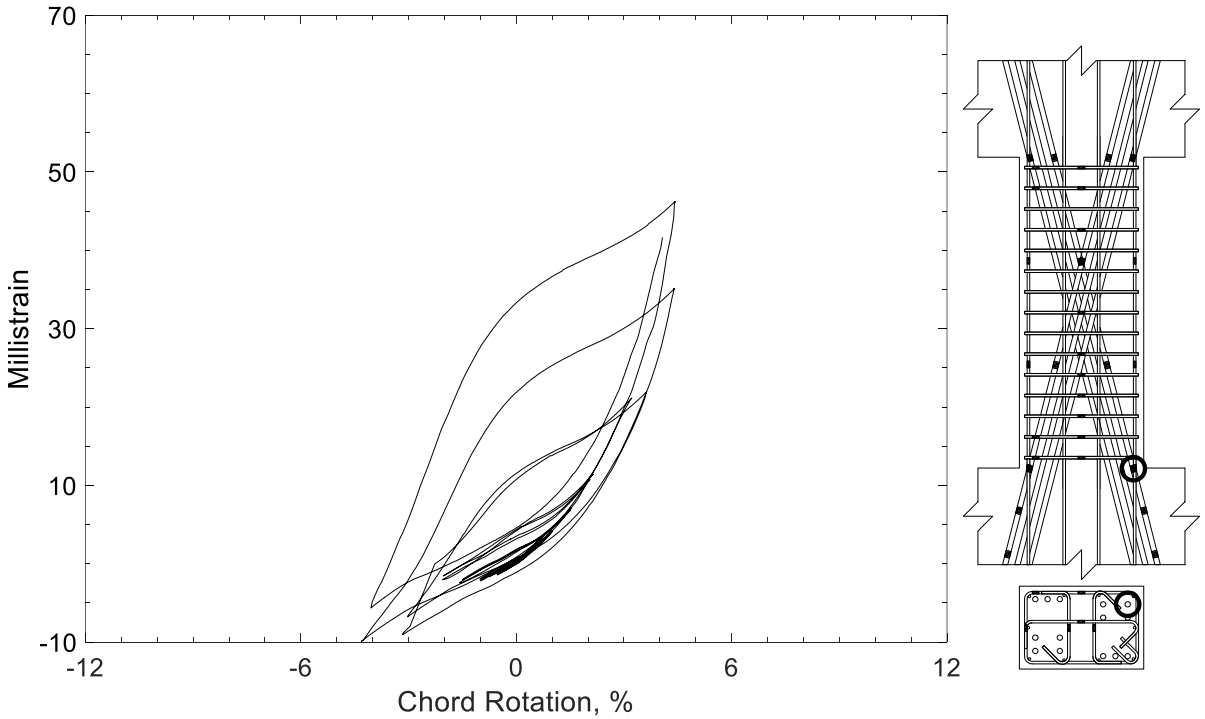

Figure 421 – Measured strain in diagonal bar of D120-2.5, strain gauge D6

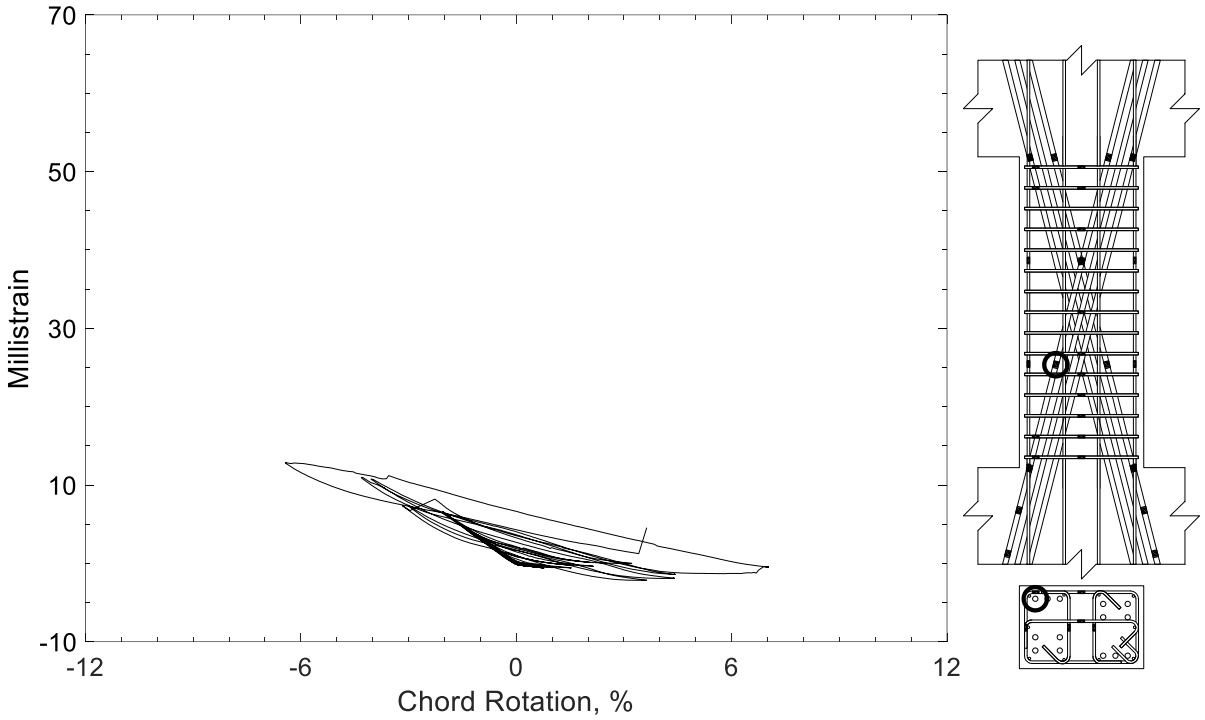

Figure 422 – Measured strain in diagonal bar of D120-2.5, strain gauge D7

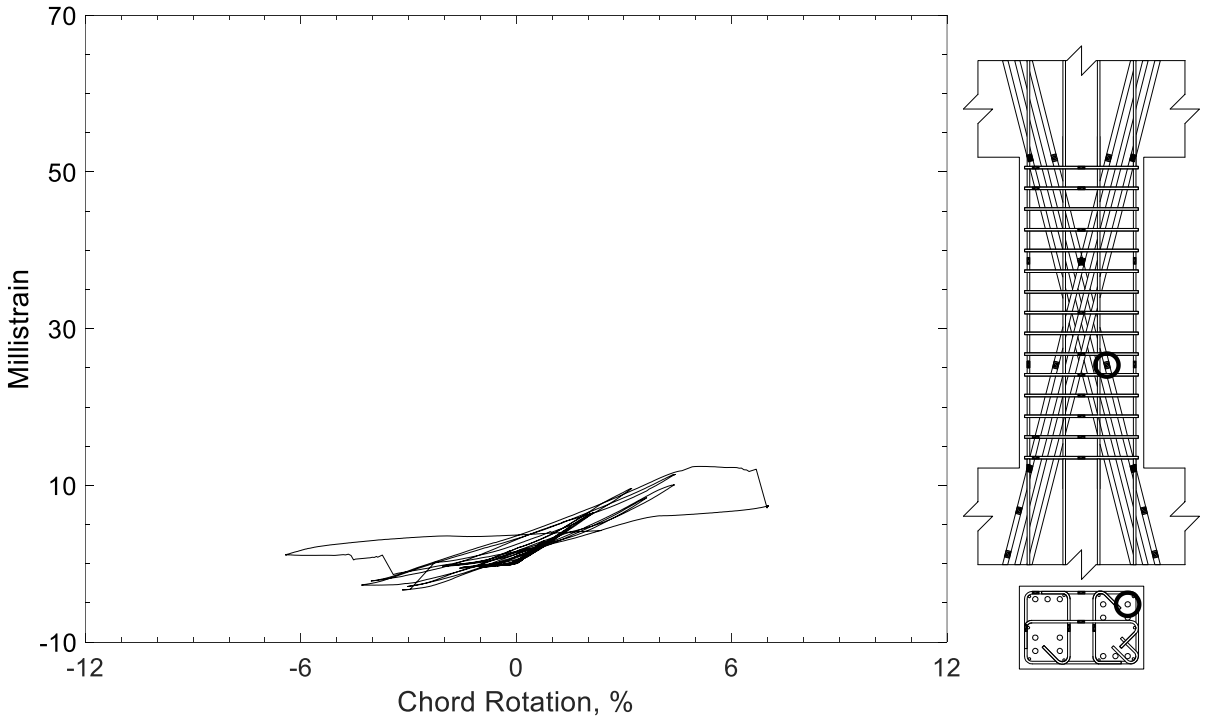

Figure 423 – Measured strain in diagonal bar of D120-2.5, strain gauge D8

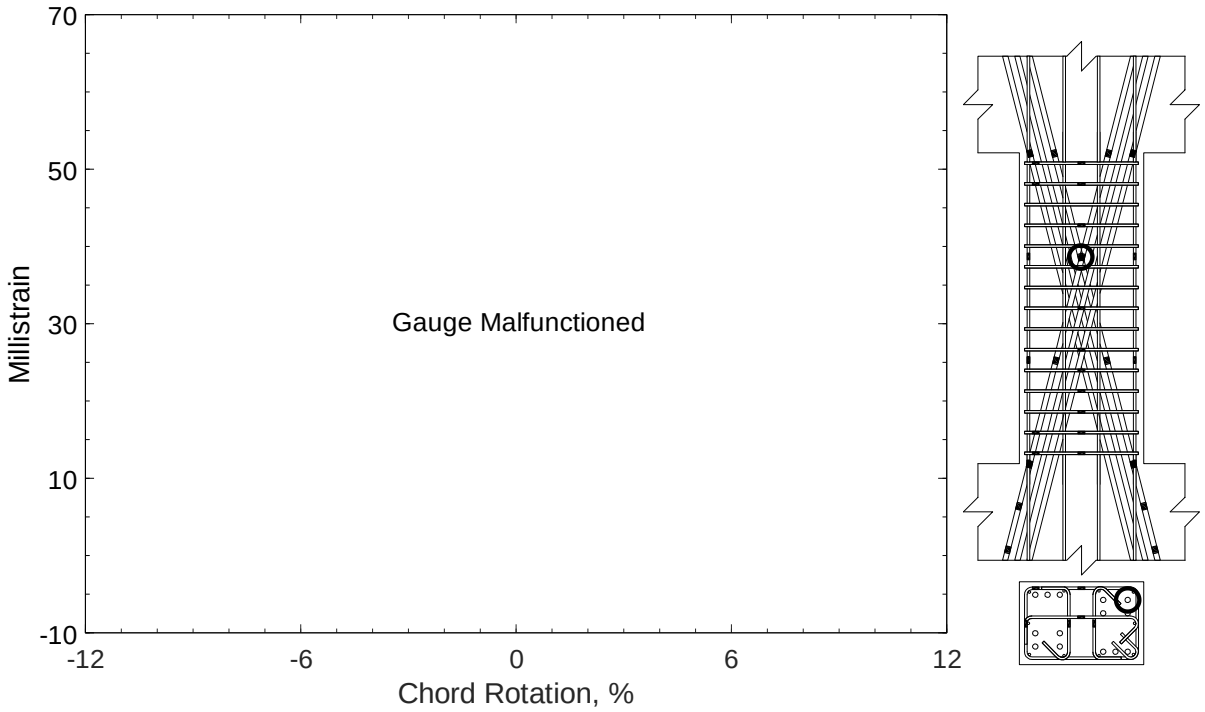

Figure 424 – Measured strain in diagonal bar of D120-2.5, strain gauge D9

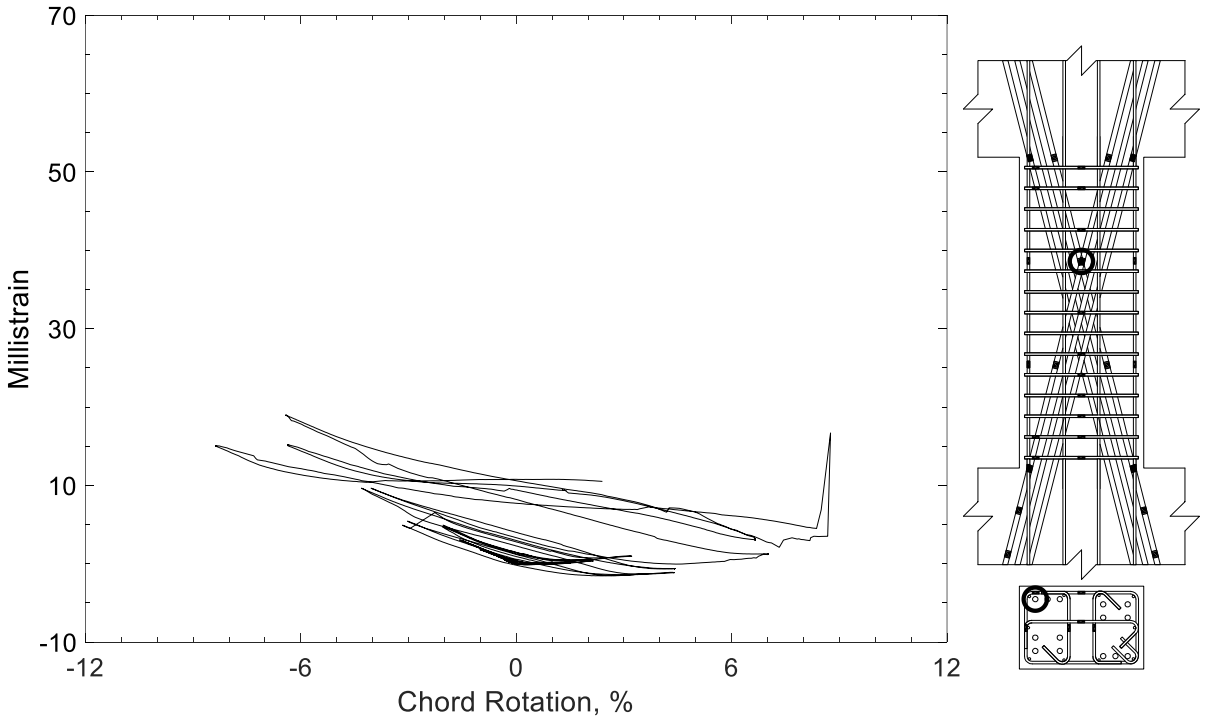

Figure 425 – Measured strain in diagonal bar of D120-2.5, strain gauge D10

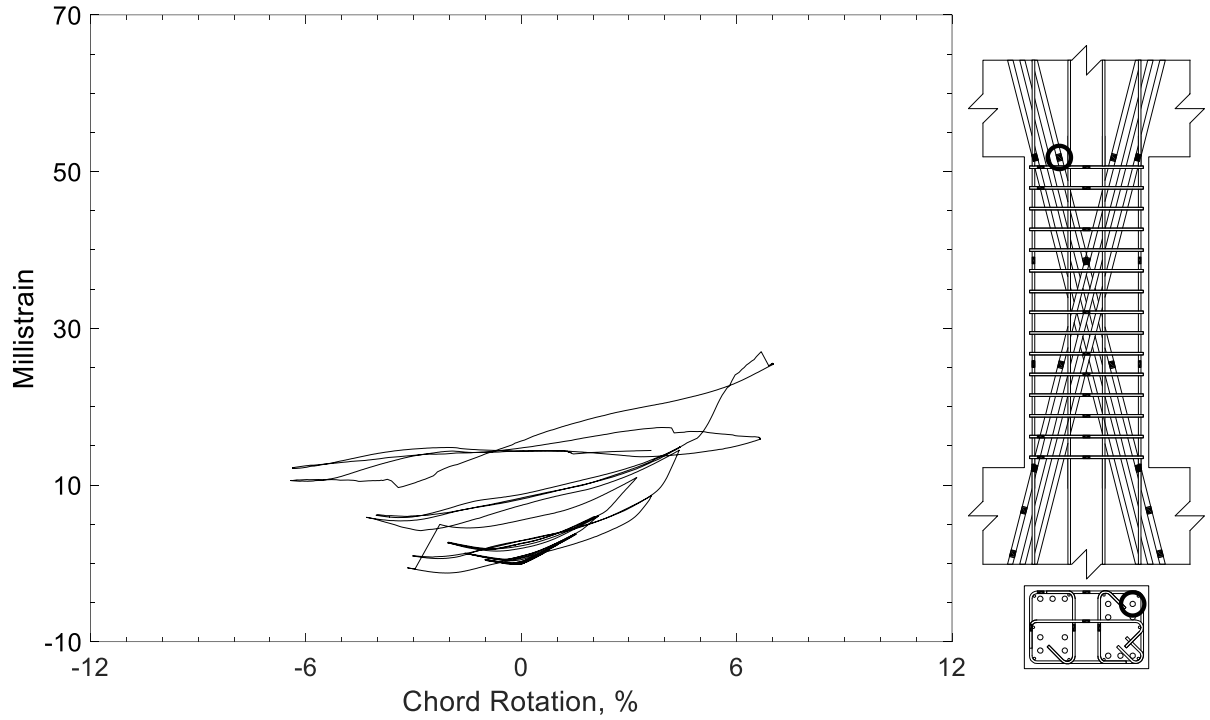

Figure 426 – Measured strain in diagonal bar of D120-2.5, strain gauge D11

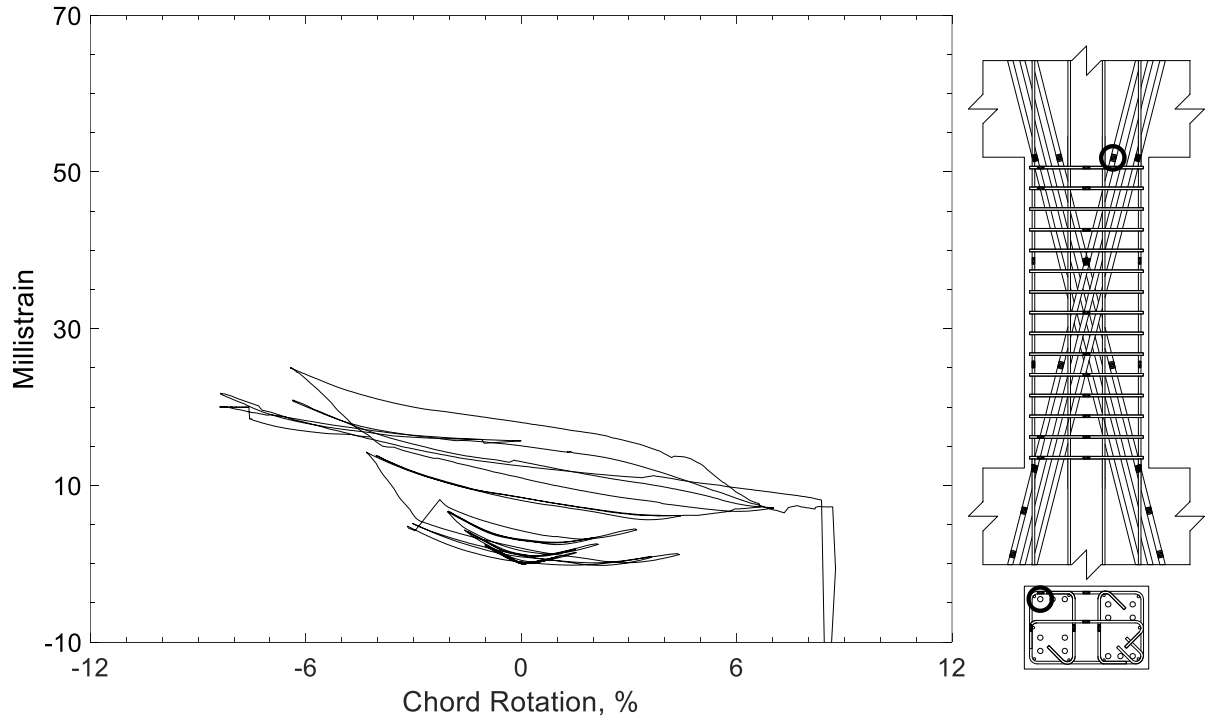

Figure 427 – Measured strain in diagonal bar of D120-2.5, strain gauge D12

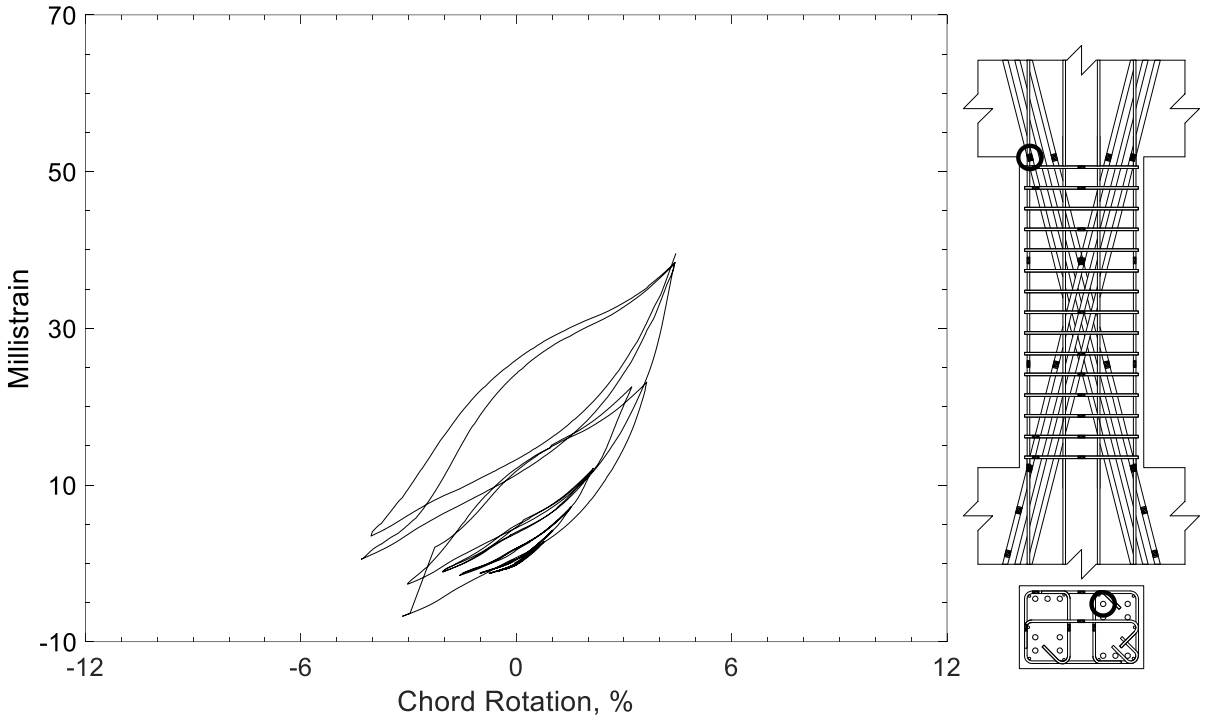

Figure 428 – Measured strain in diagonal bar of D120-2.5, strain gauge D13

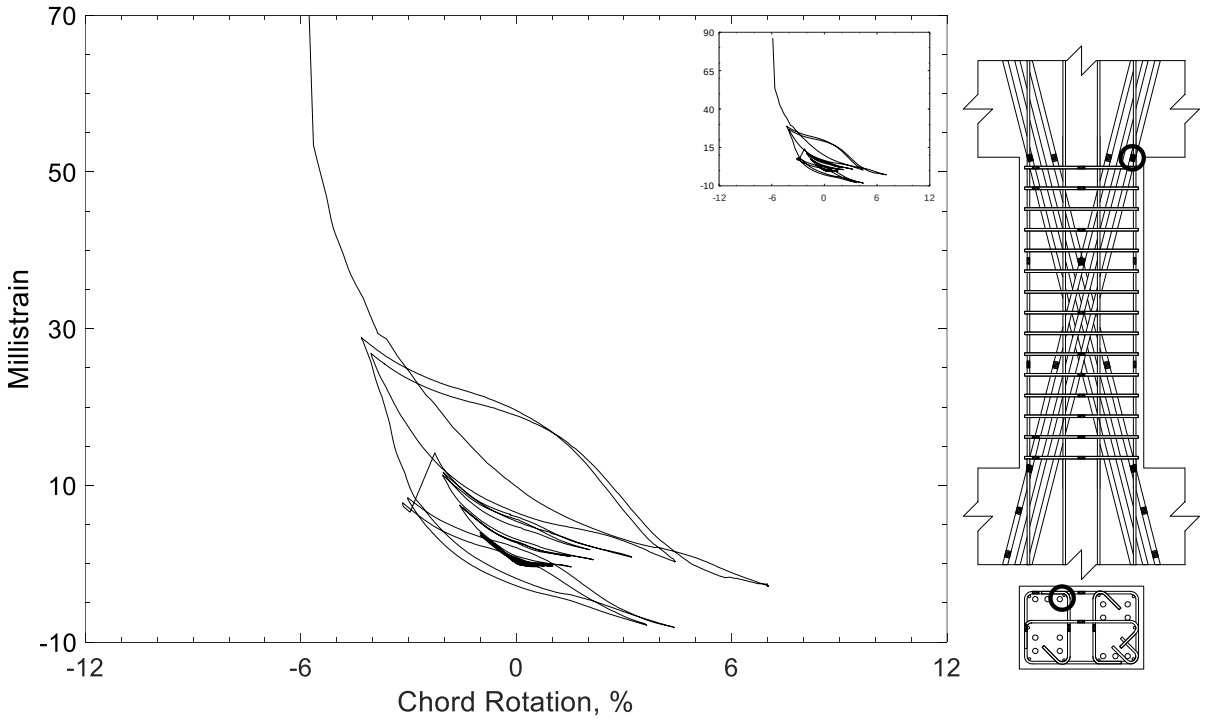

Figure 429 – Measured strain in diagonal bar of D120-2.5, strain gauge D14

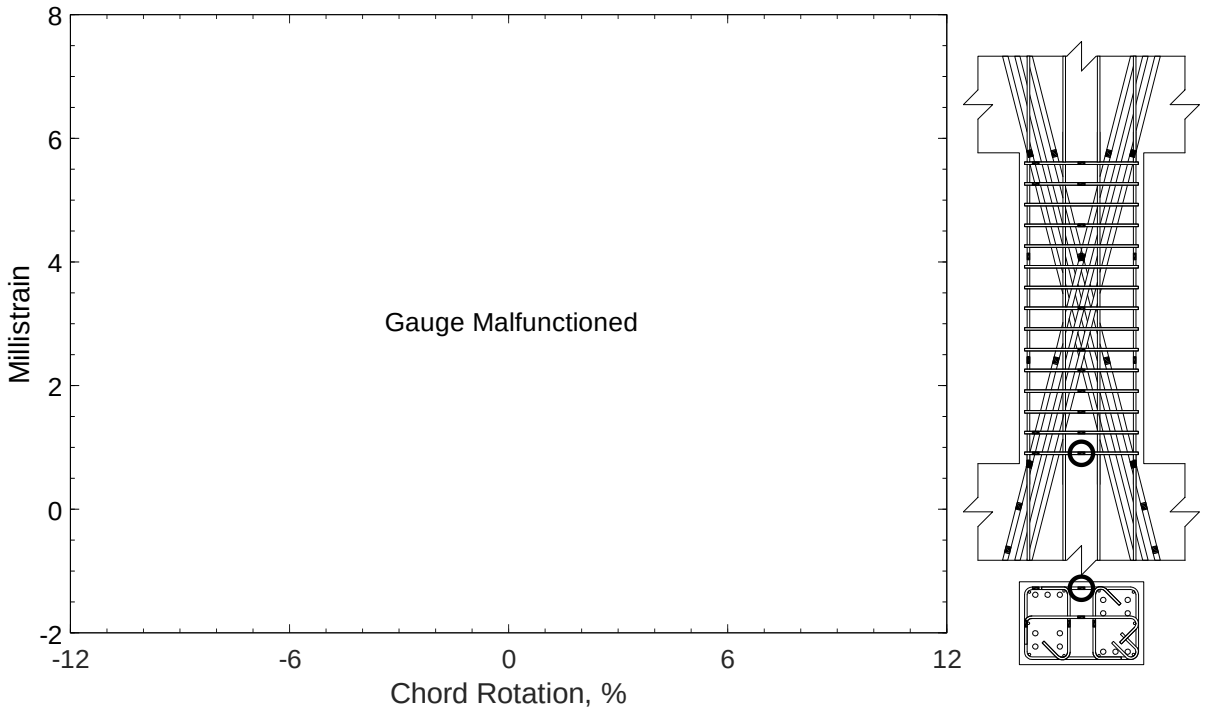

Figure 430 – Measured strain in closed stirrup of D120-2.5, strain gauge S1

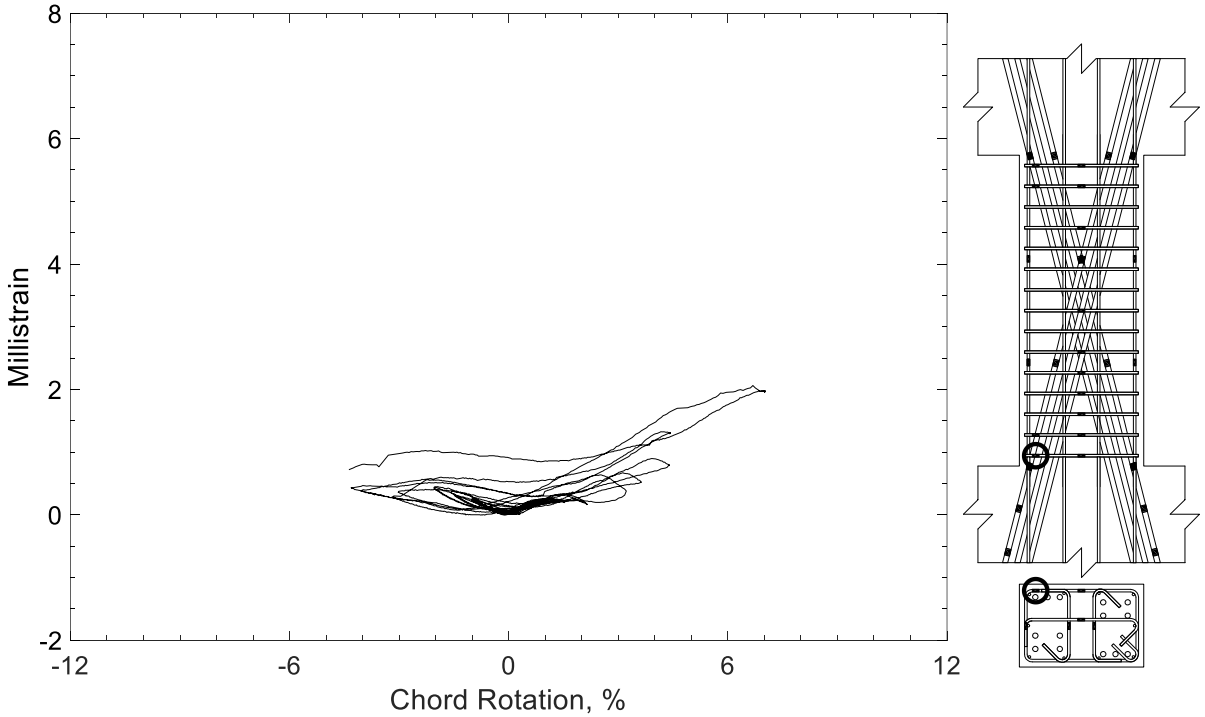

Figure 431 – Measured strain in closed stirrup of D120-2.5, strain gauge S2

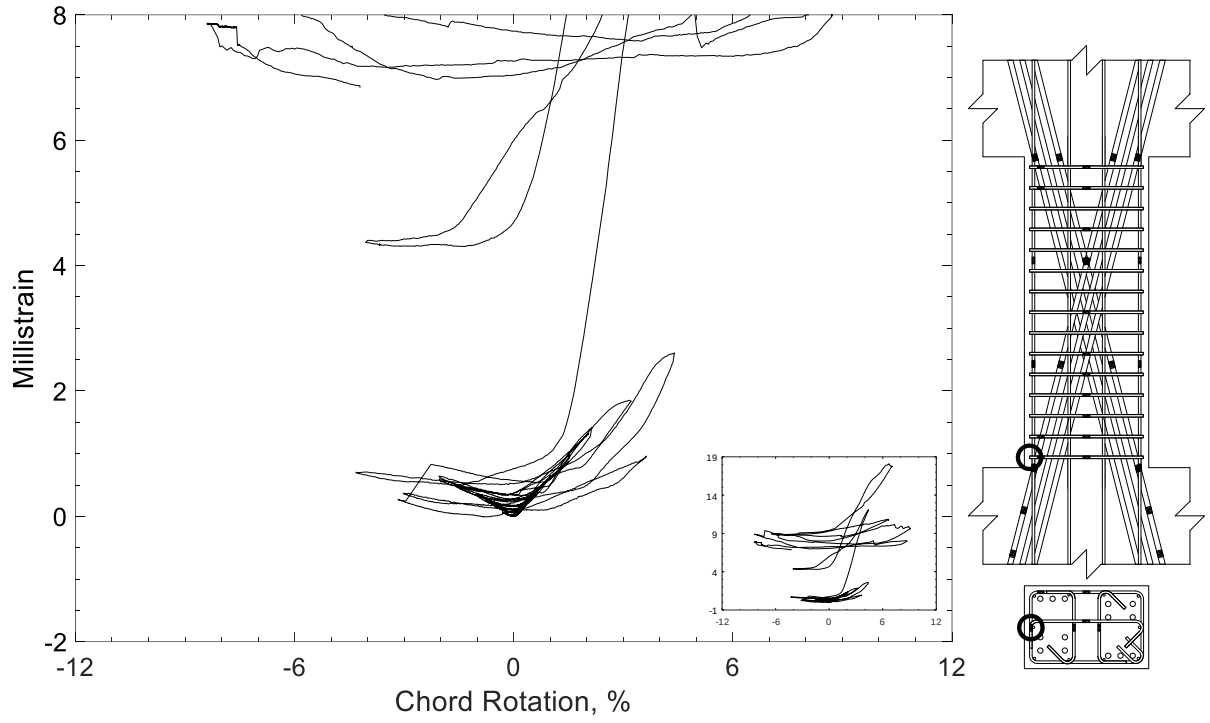

Figure 432 – Measured strain in closed stirrup of D120-2.5, strain gauge S3

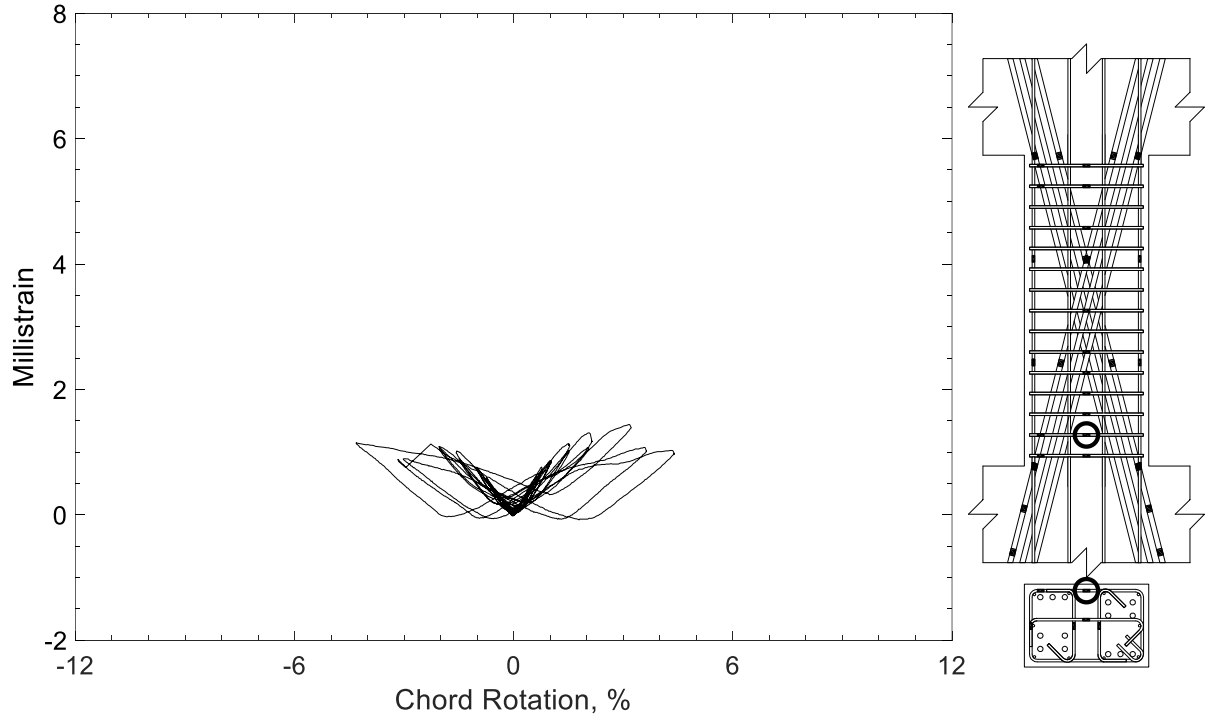

Figure 433 – Measured strain in closed stirrup of D120-2.5, strain gauge S4

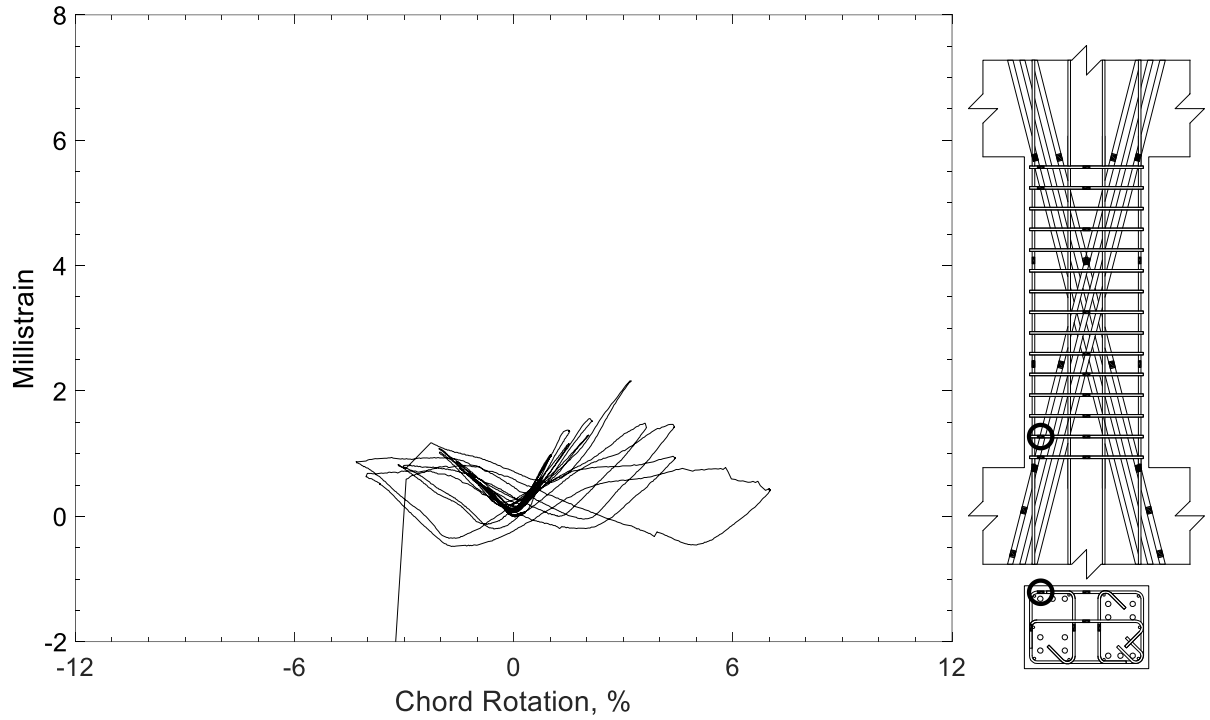

Figure 434 – Measured strain in closed stirrup of D120-2.5, strain gauge S5

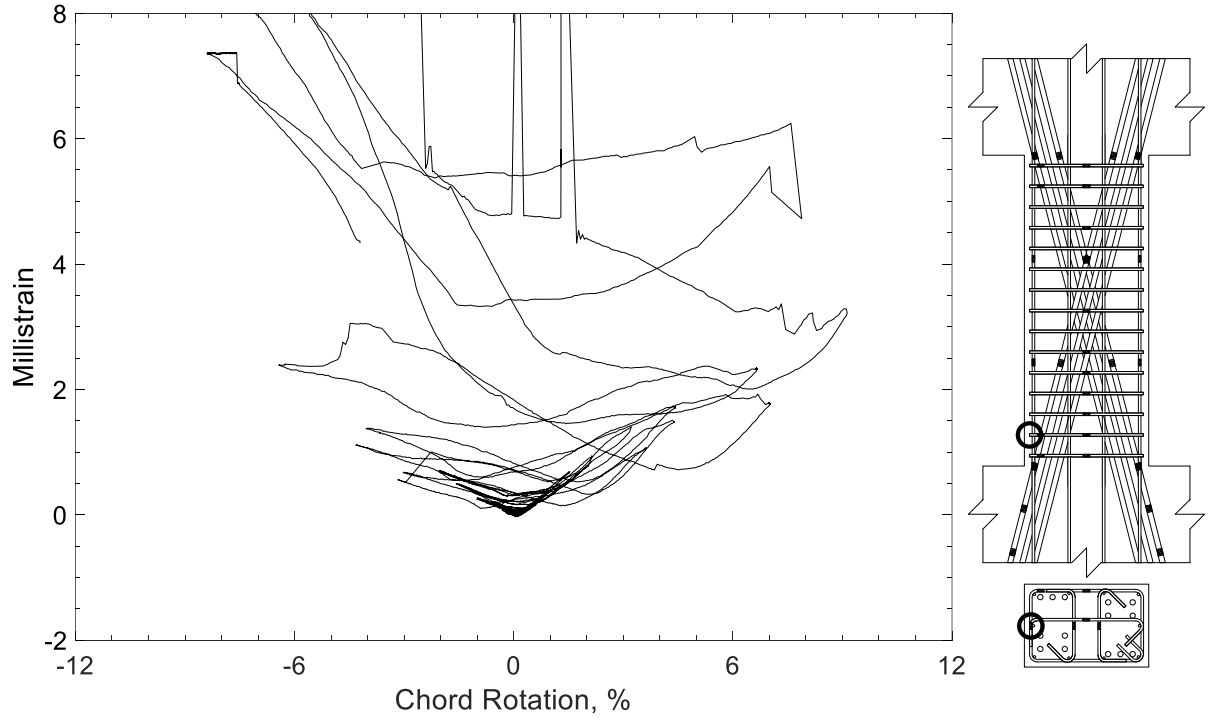

Figure 435 – Measured strain in closed stirrup of D120-2.5, strain gauge S6

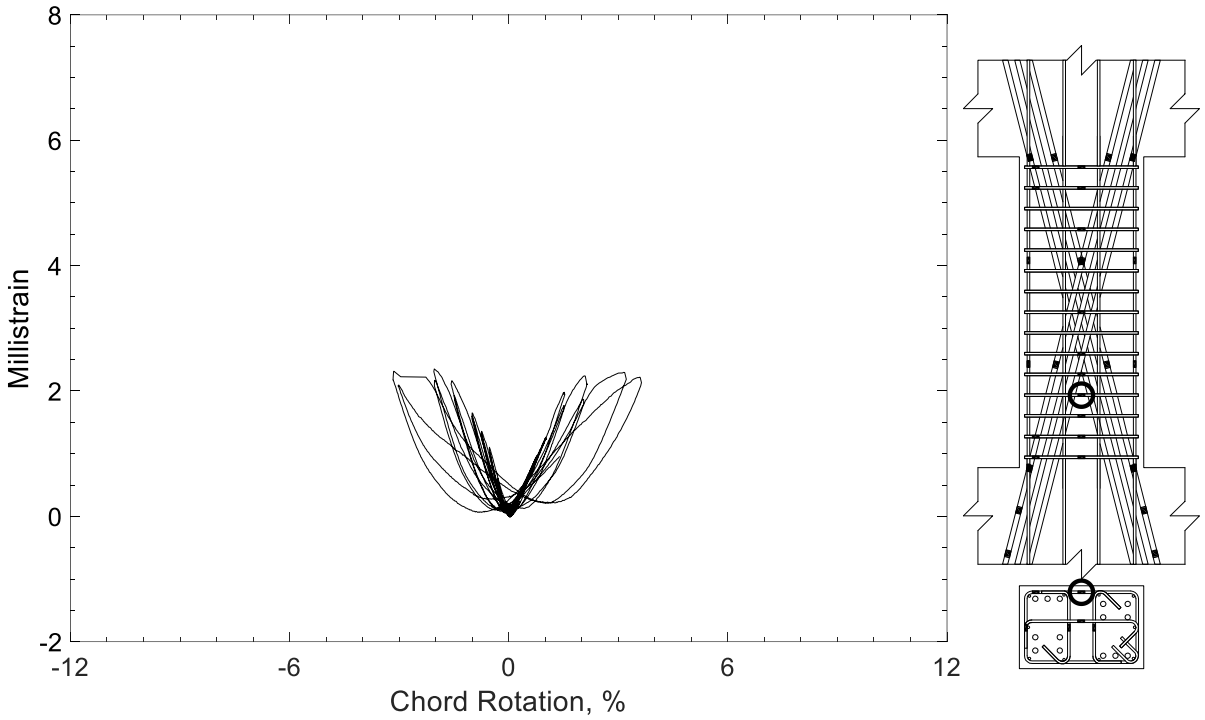

Figure 436 – Measured strain in closed stirrup of D120-2.5, strain gauge S7

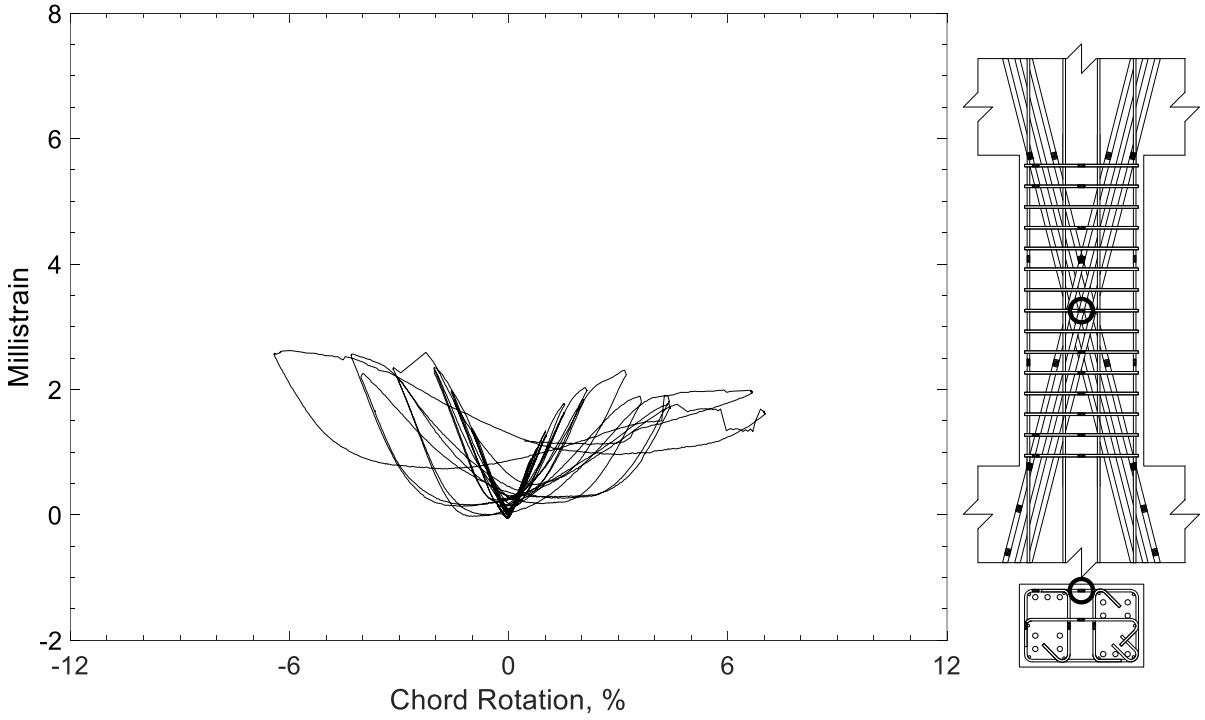

Figure 437 – Measured strain in closed stirrup of D120-2.5, strain gauge S8

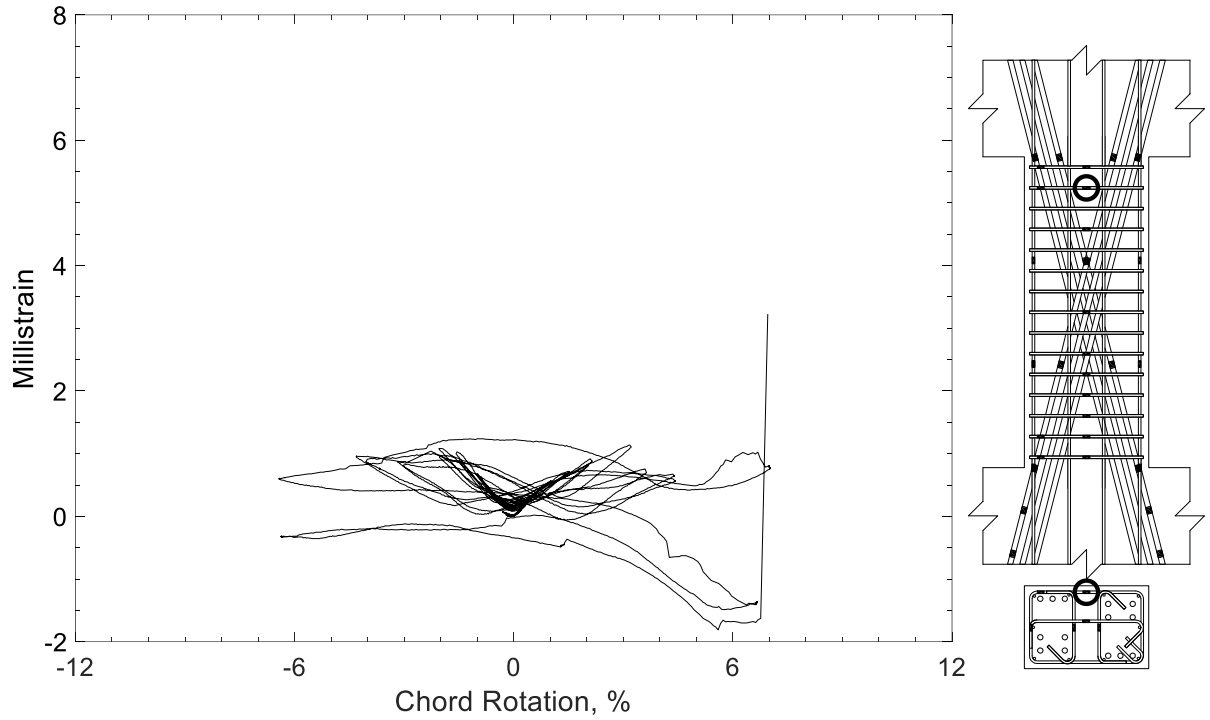

Figure 438 – Measured strain in closed stirrup of D120-2.5, strain gauge S9

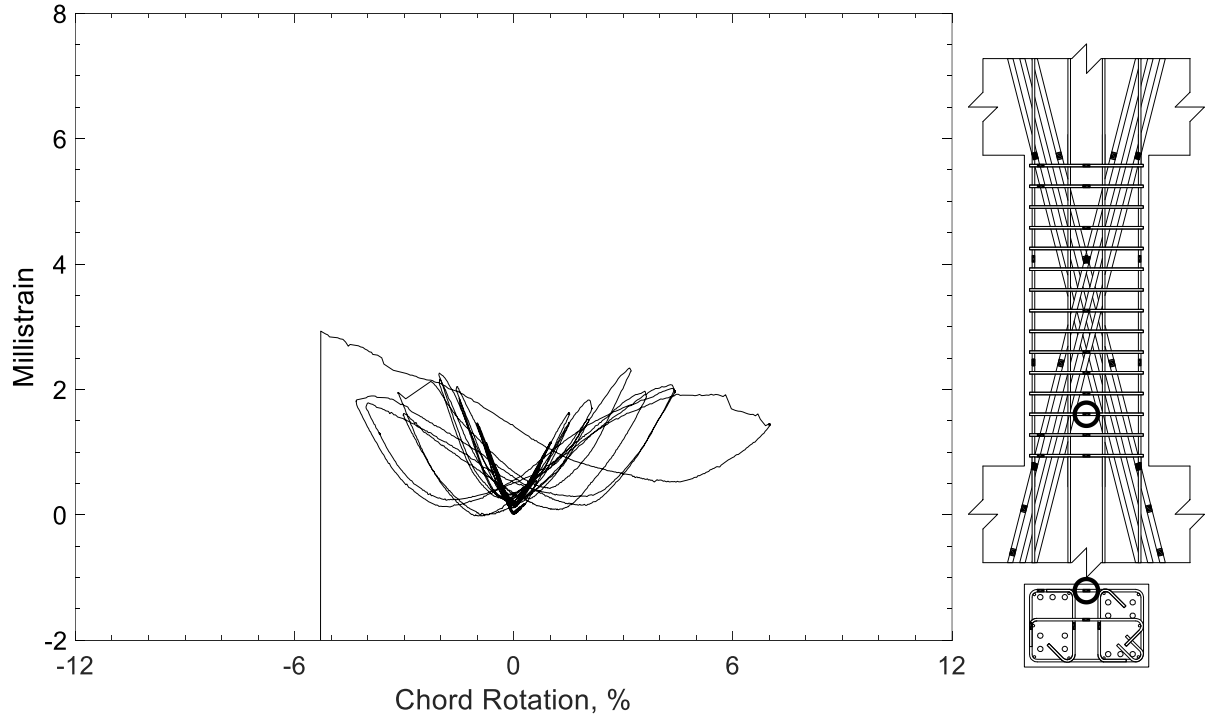

Figure 439 – Measured strain in closed stirrup of D120-2.5, strain gauge S10

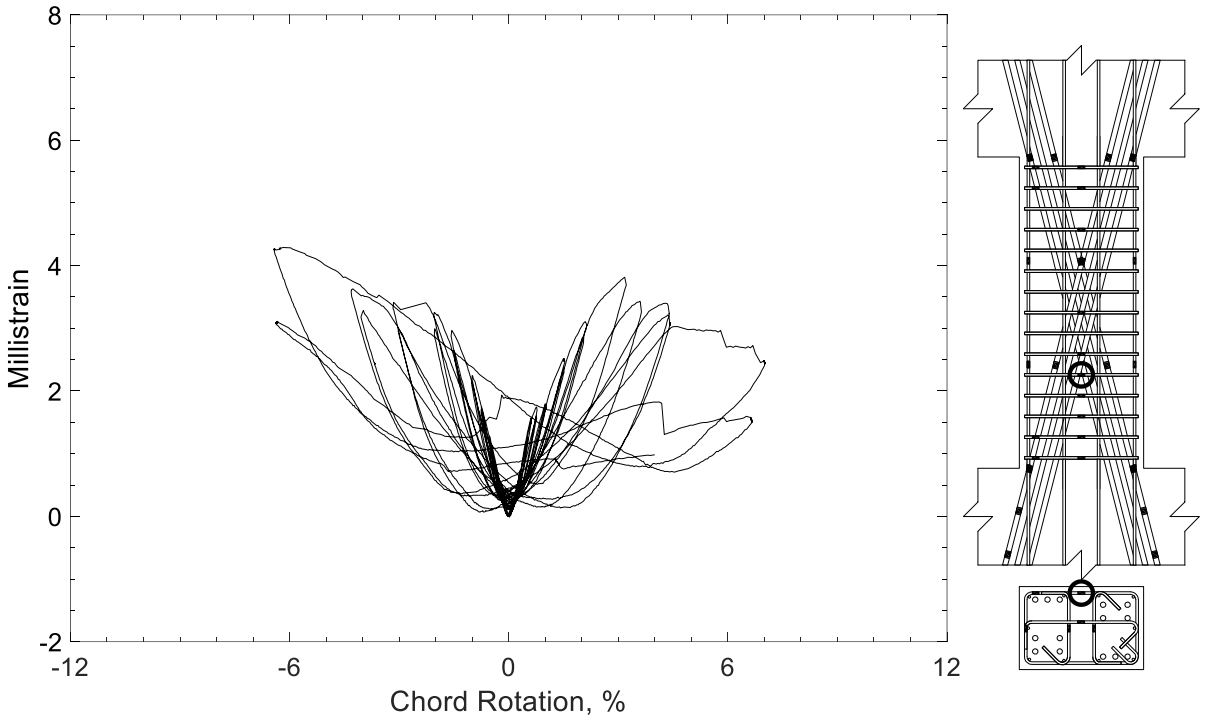

Figure 440 – Measured strain in closed stirrup of D120-2.5, strain gauge S11

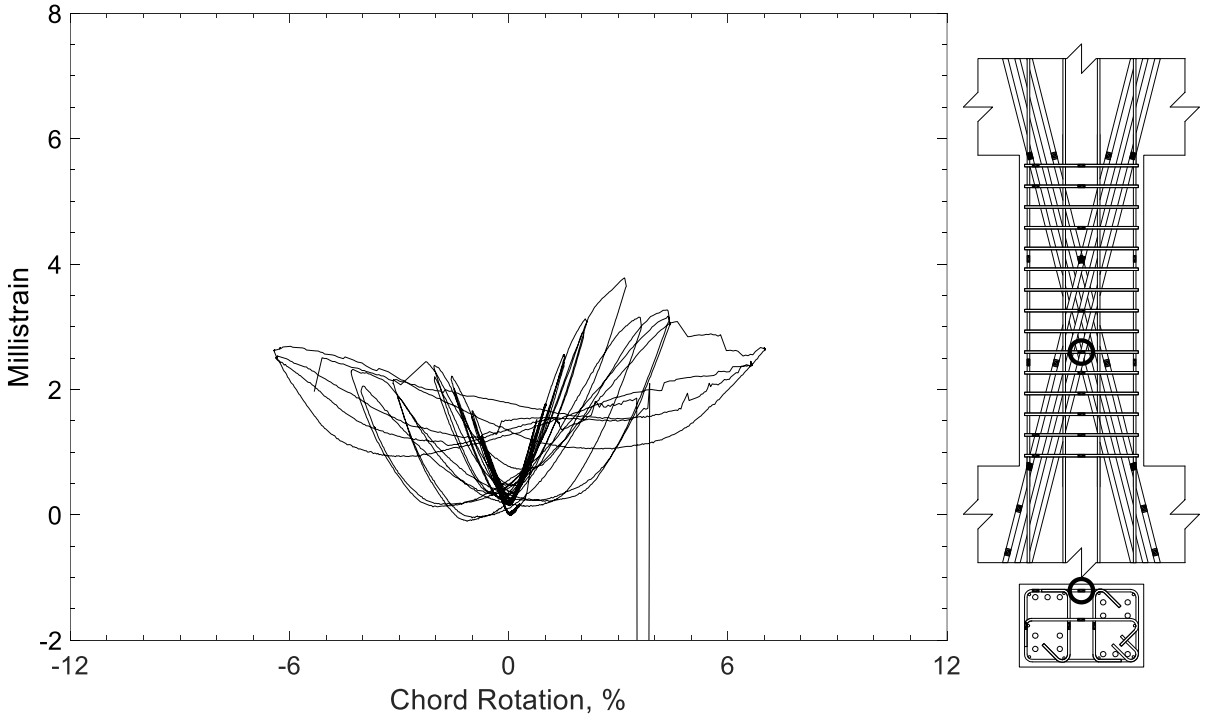

Figure 441 – Measured strain in closed stirrup of D120-2.5, strain gauge S12

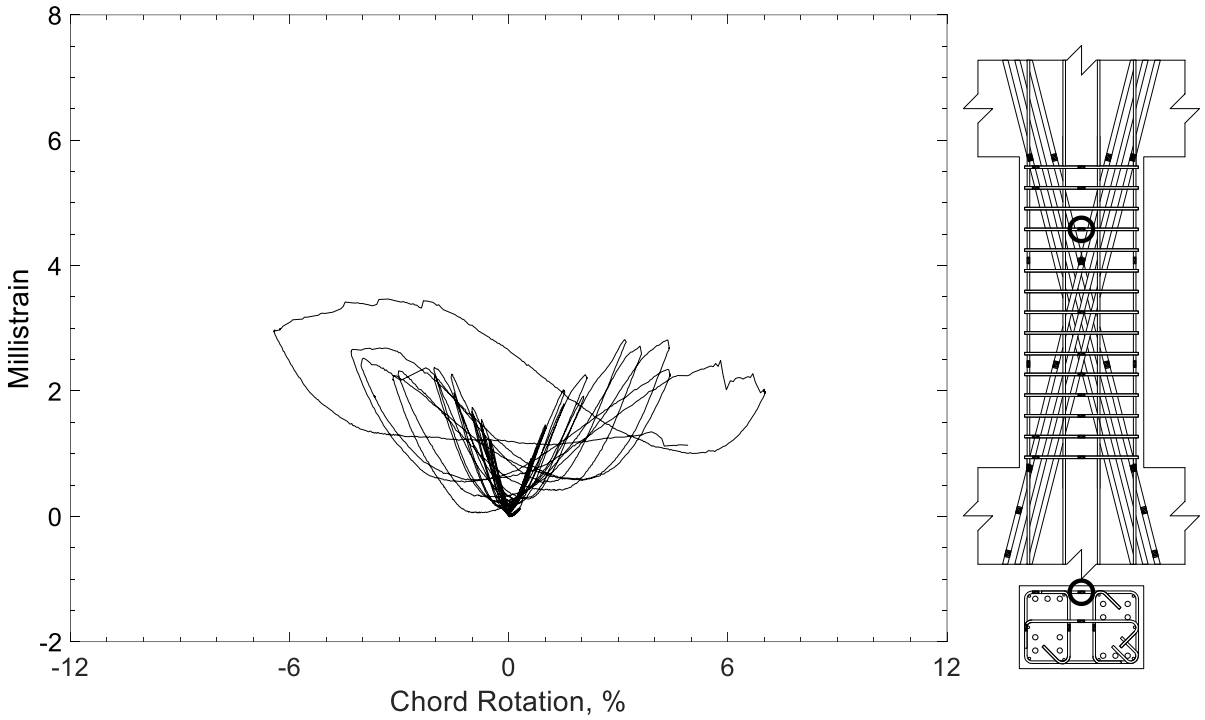

Figure 442 – Measured strain in closed stirrup of D120-2.5, strain gauge S13

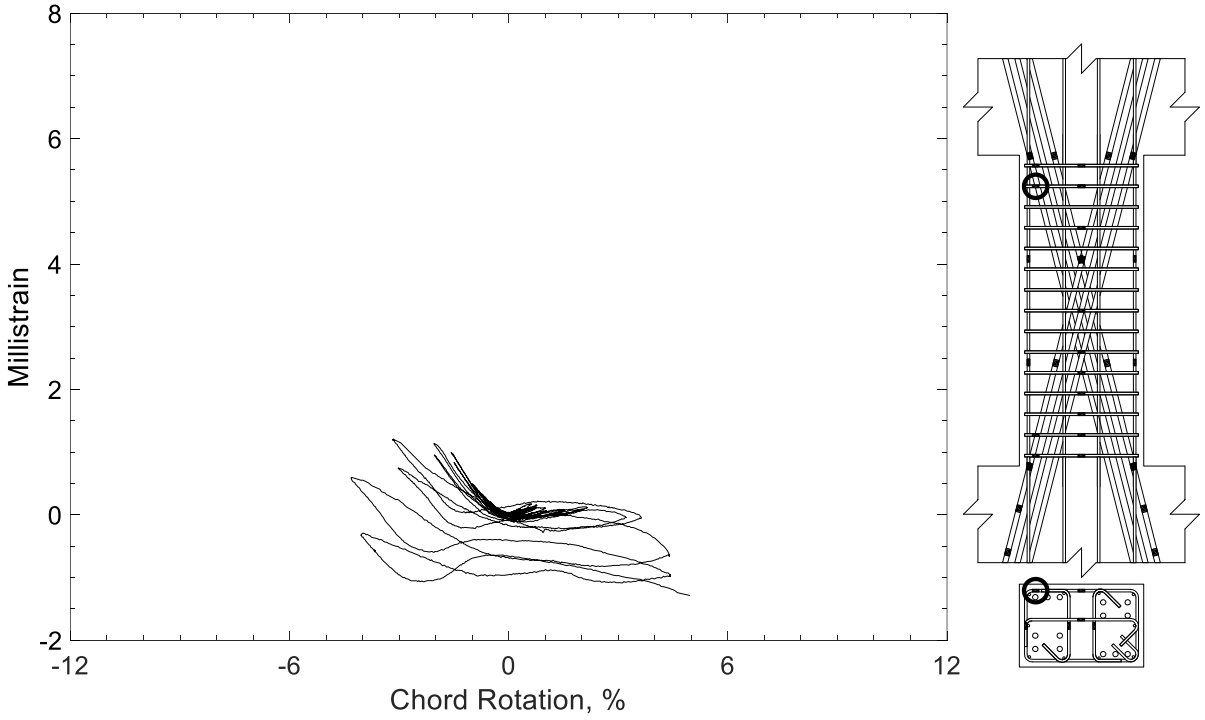

Figure 443 – Measured strain in closed stirrup of D120-2.5, strain gauge S14

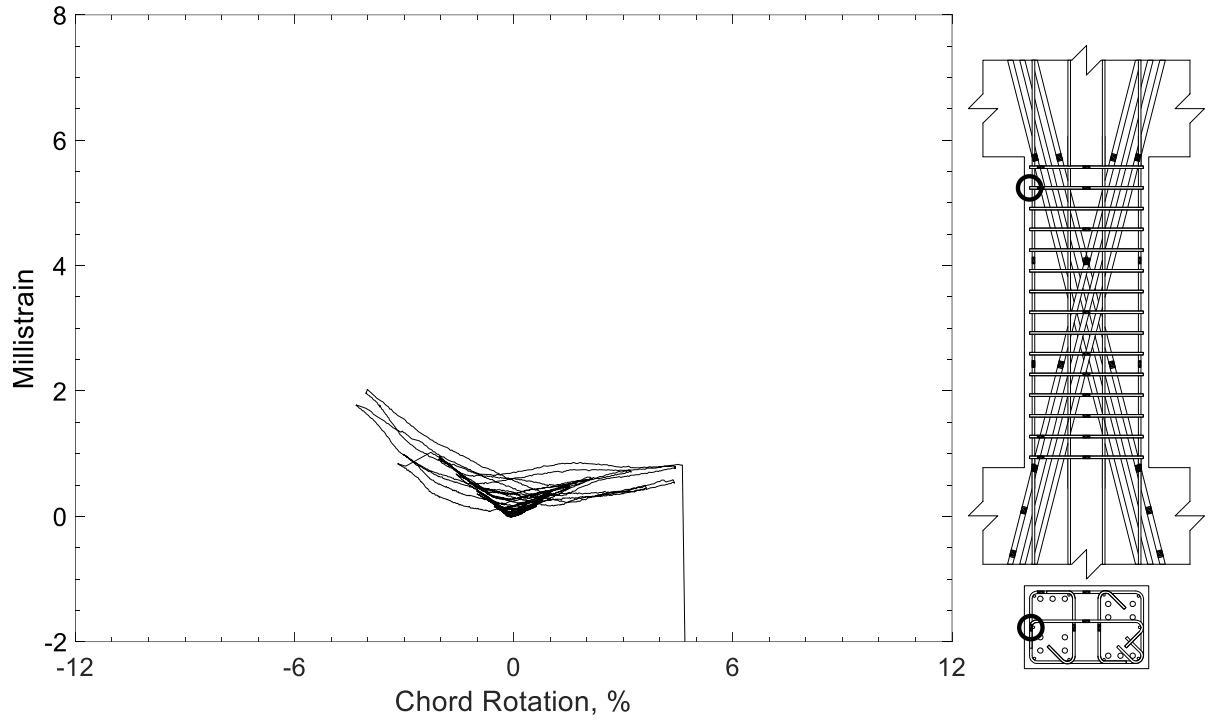

Figure 444 – Measured strain in closed stirrup of D120-2.5, strain gauge S15

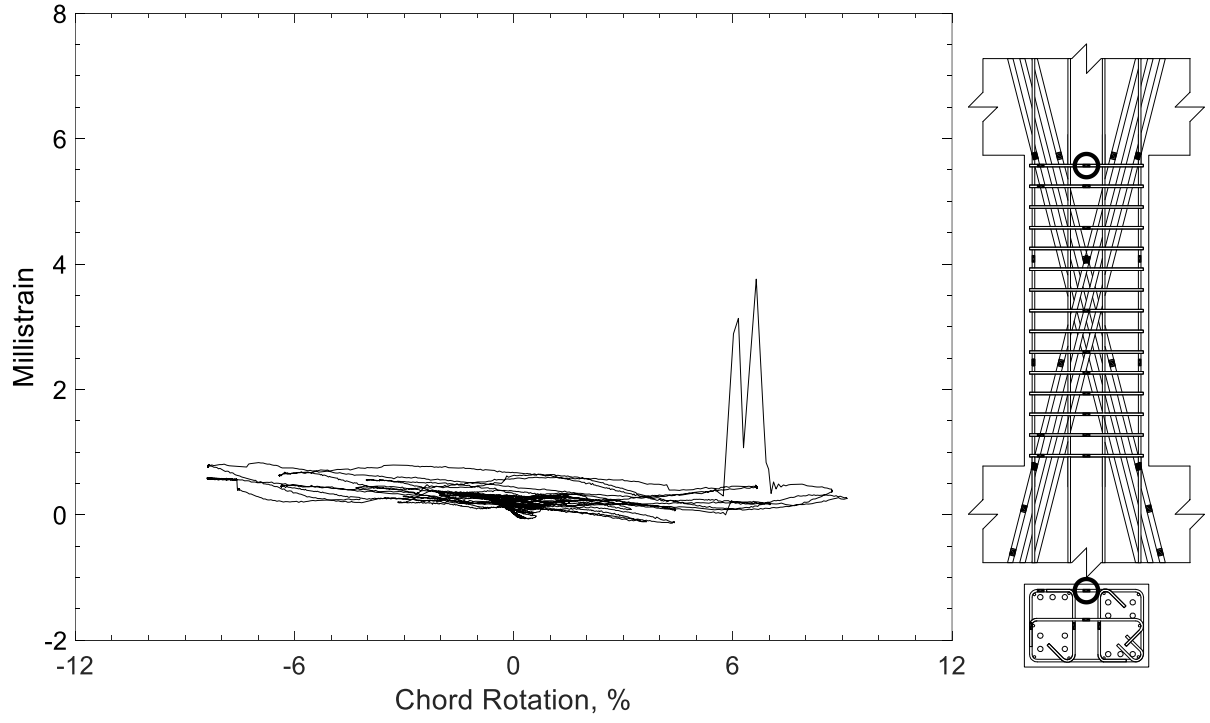

Figure 445 – Measured strain in closed stirrup of D120-2.5, strain gauge S16

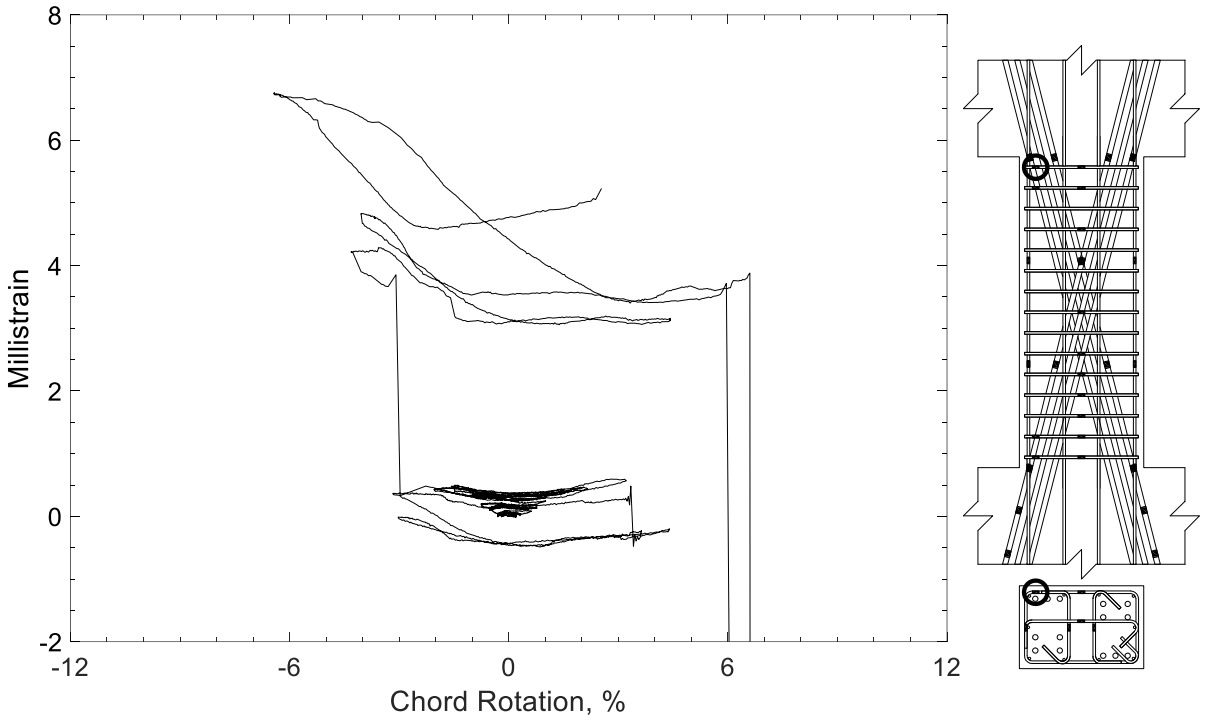

Figure 446 – Measured strain in closed stirrup of D120-2.5, strain gauge S17

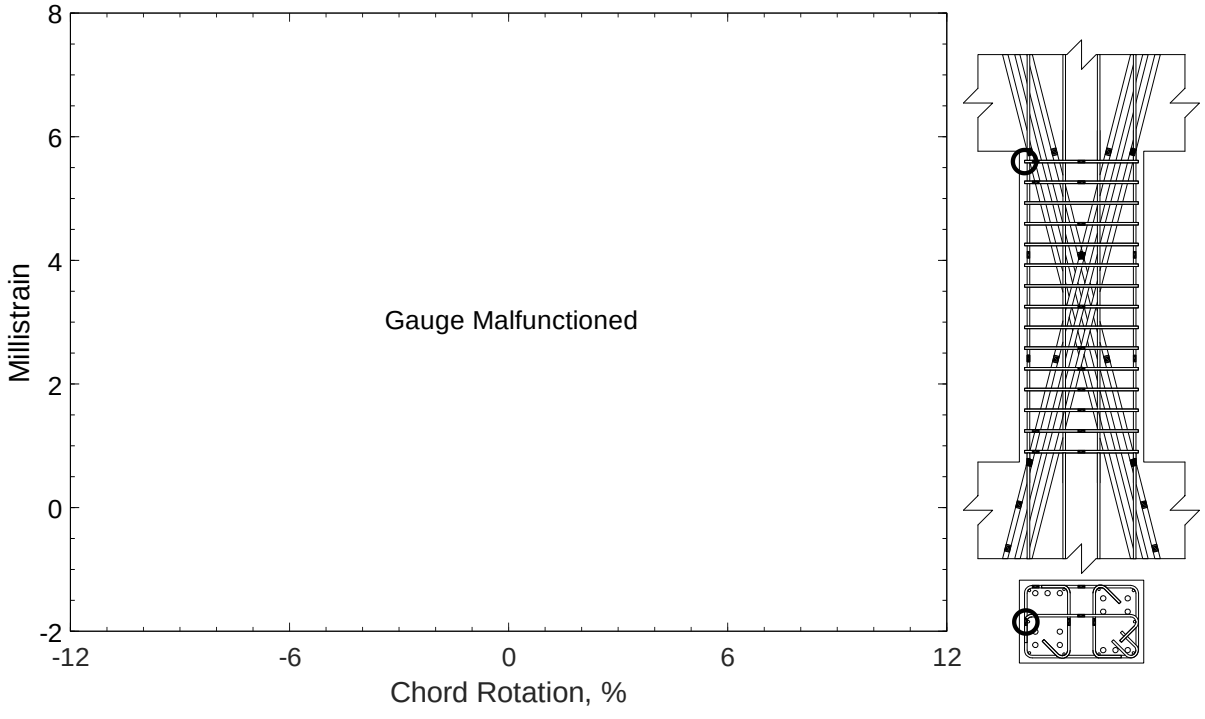

Figure 447 – Measured strain in closed stirrup of D120-2.5, strain gauge S18

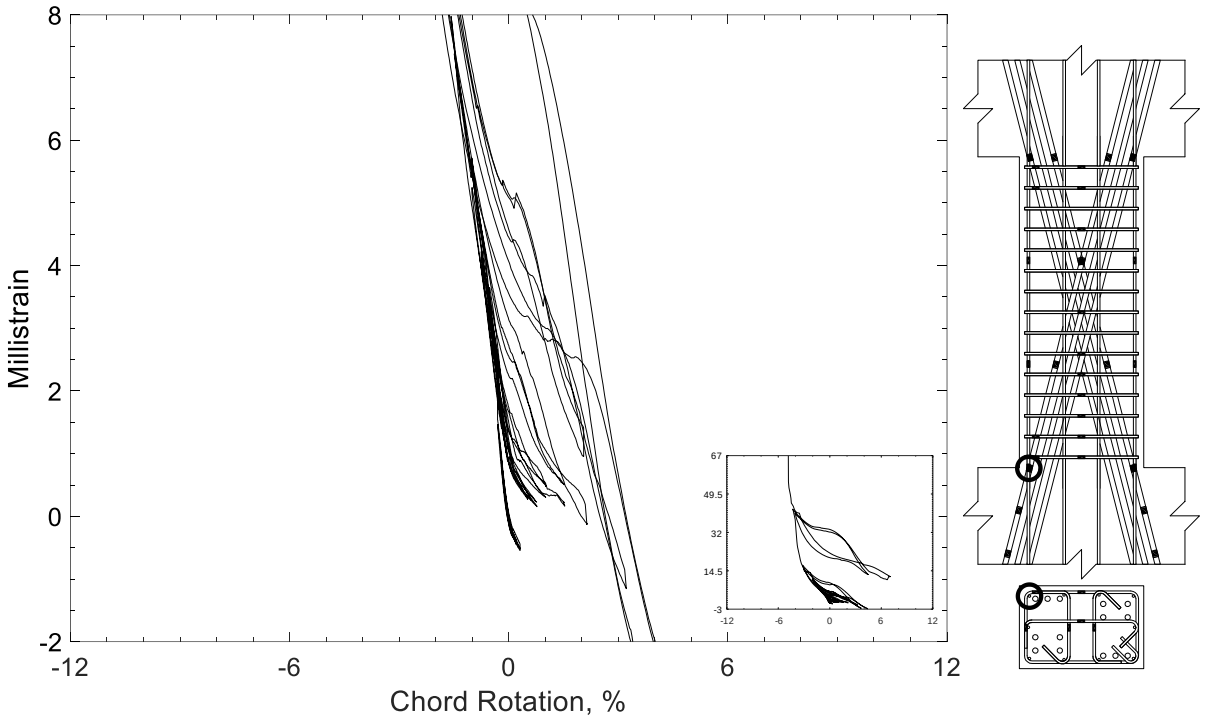

Figure 448 – Measured strain in parallel bar of D120-2.5, strain gauge H1

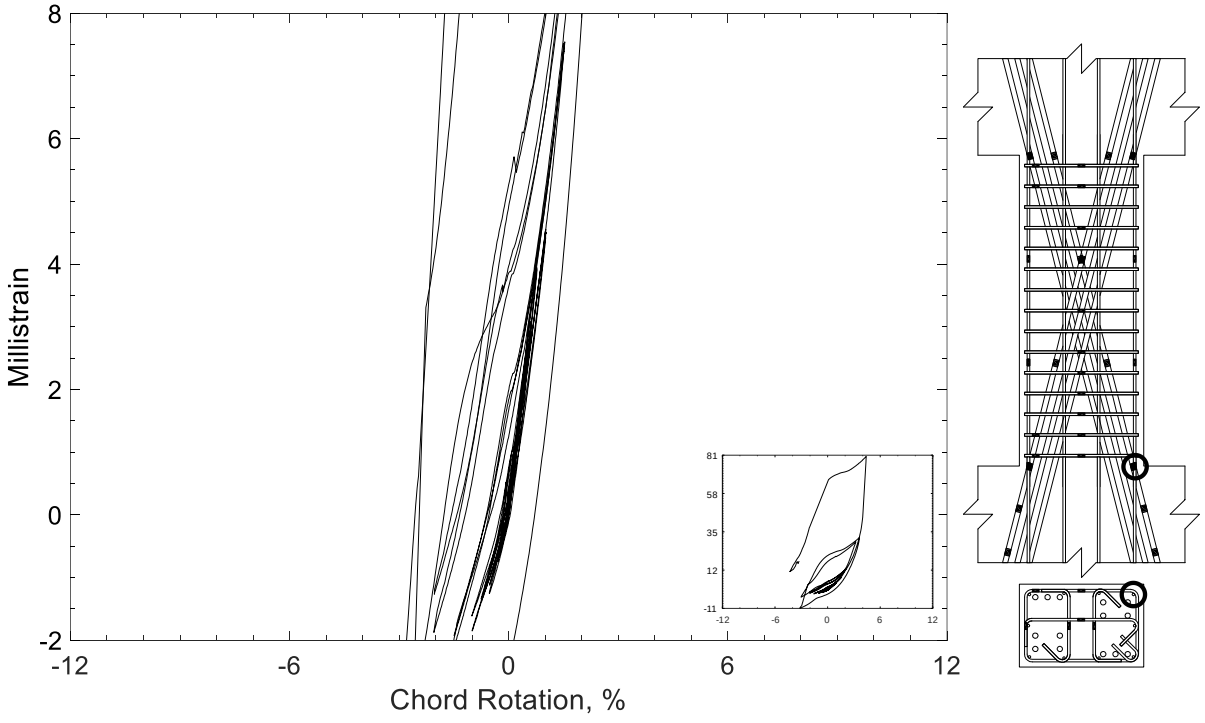

Figure 449 – Measured strain in parallel bar of D120-2.5, strain gauge H2

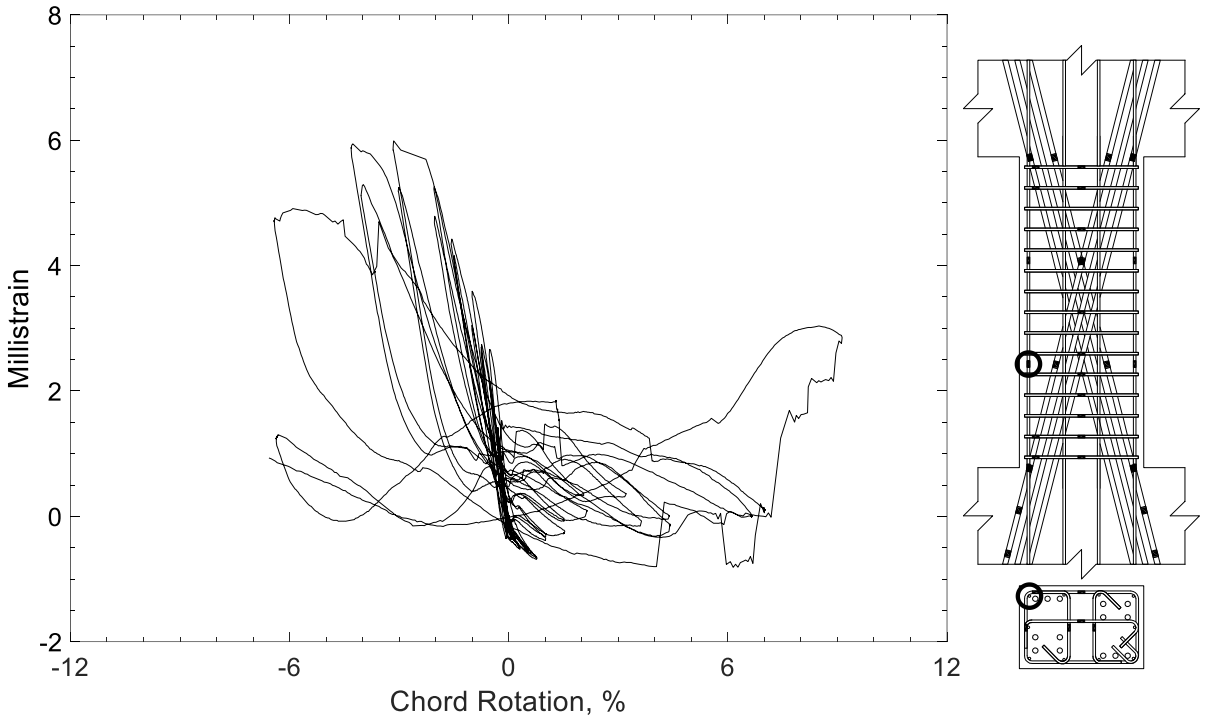

Figure 450 – Measured strain in parallel bar of D120-2.5, strain gauge H3

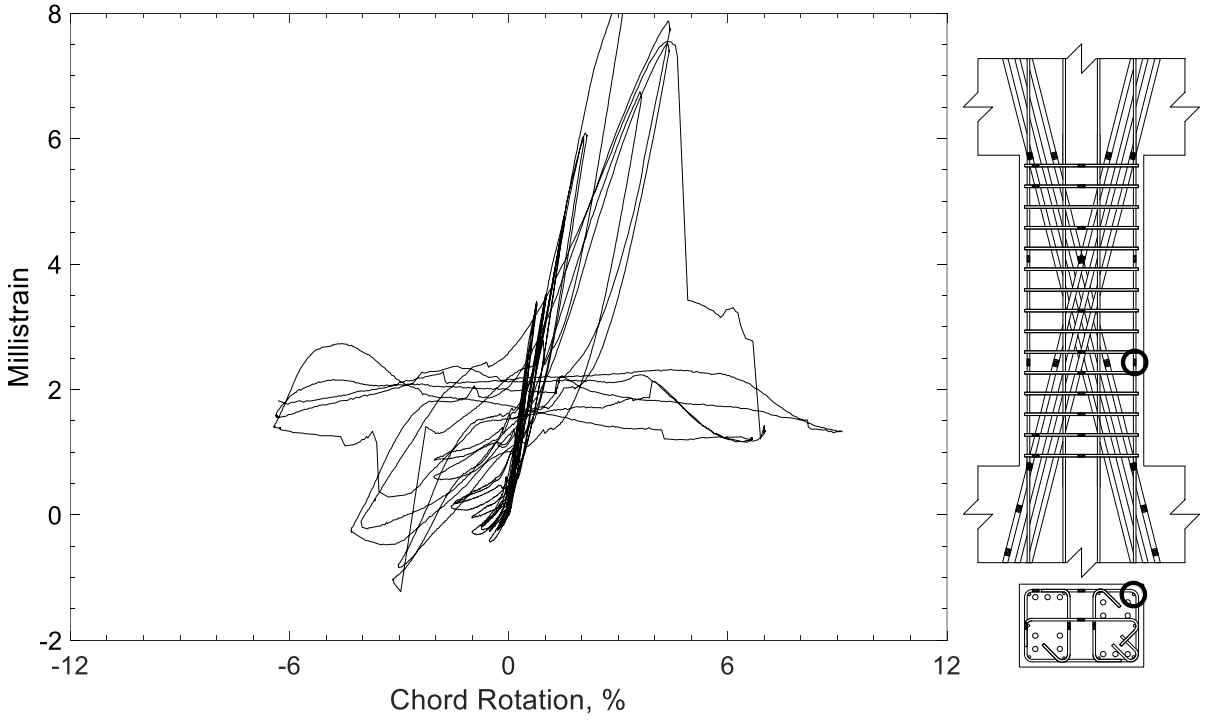

Figure 451 – Measured strain in parallel bar of D120-2.5, strain gauge H4

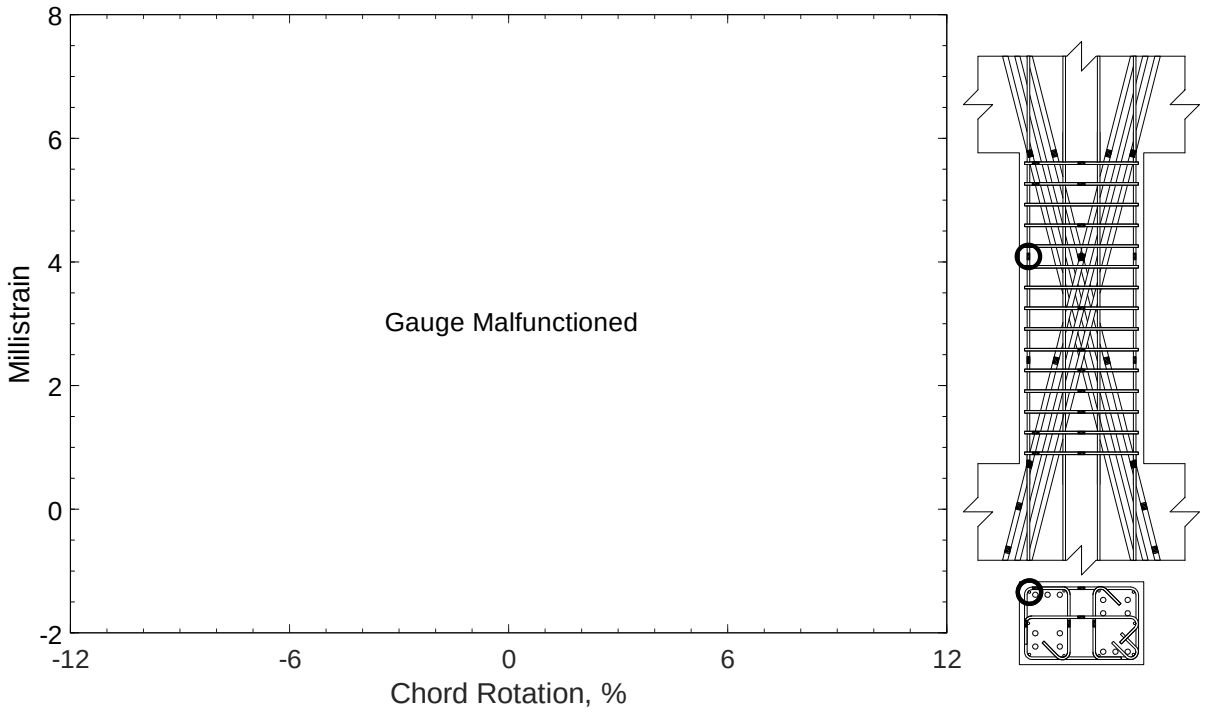

Figure 452 – Measured strain in parallel bar of D120-2.5, strain gauge H5

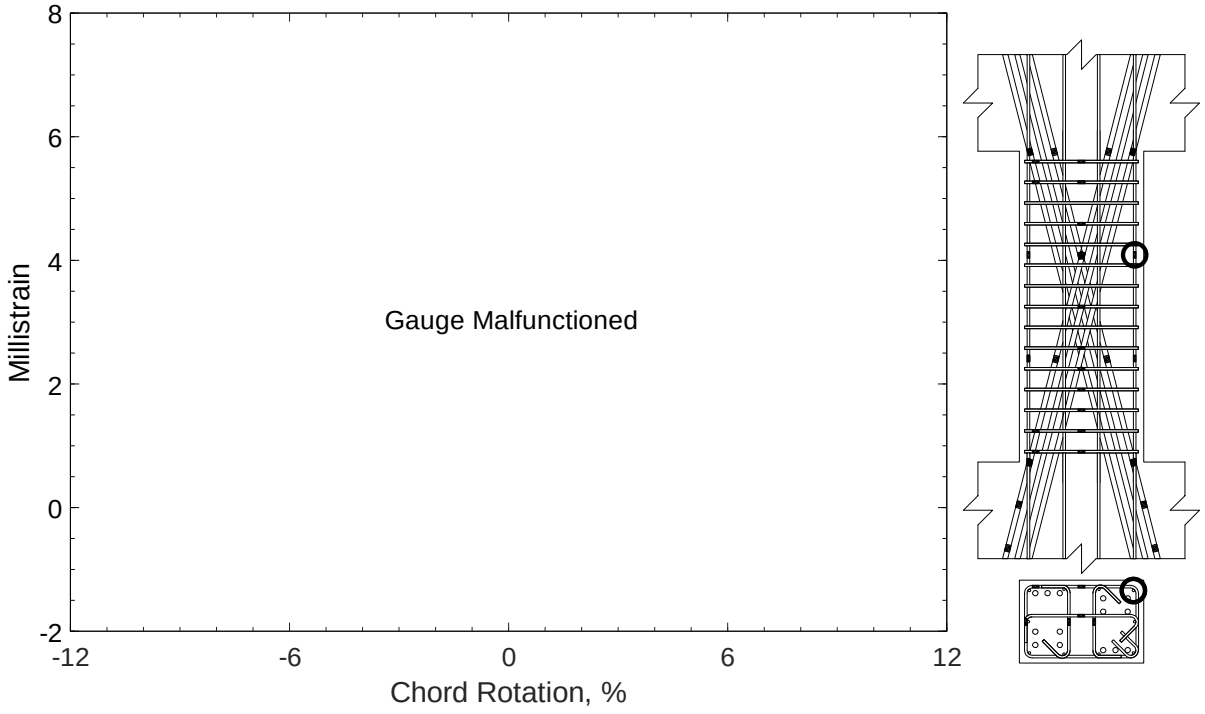

Figure 453 – Measured strain in parallel bar of D120-2.5, strain gauge H6

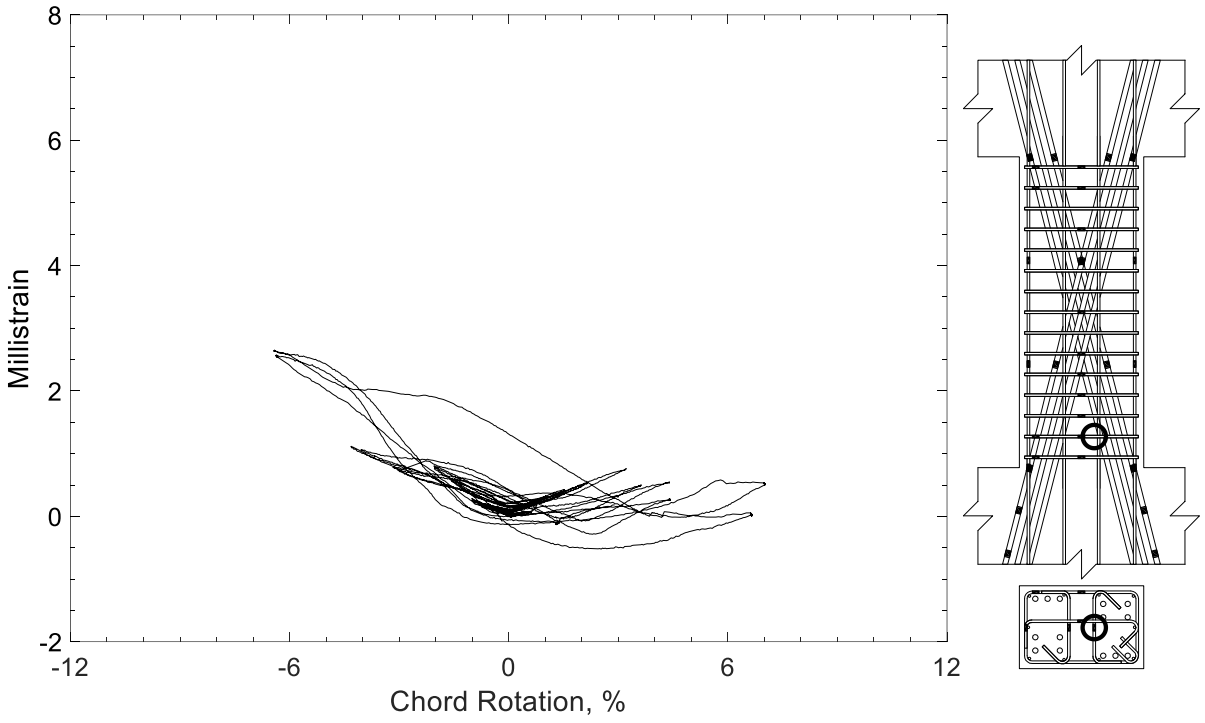

Figure 454 – Measured strain in crosstie of D120-2.5, strain gauge T1

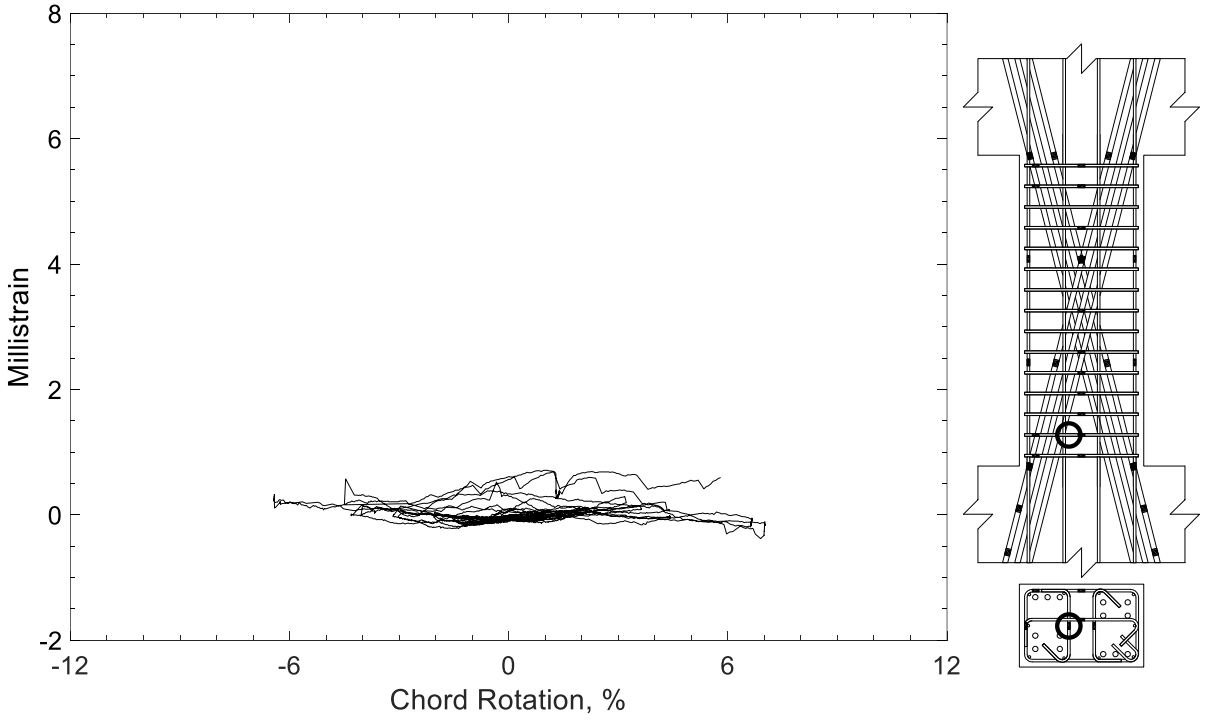

Figure 455 – Measured strain in crosstie of D120-2.5, strain gauge T2

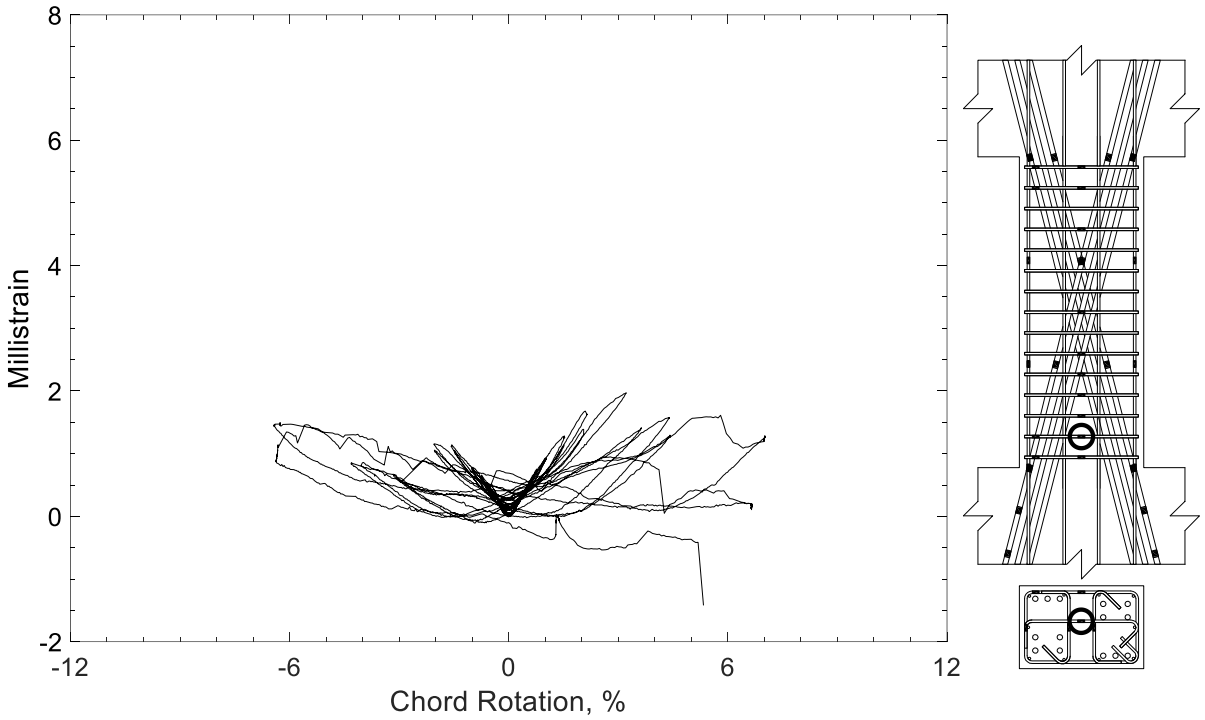

Figure 456 – Measured strain in crosstie of D120-2.5, strain gauge T3

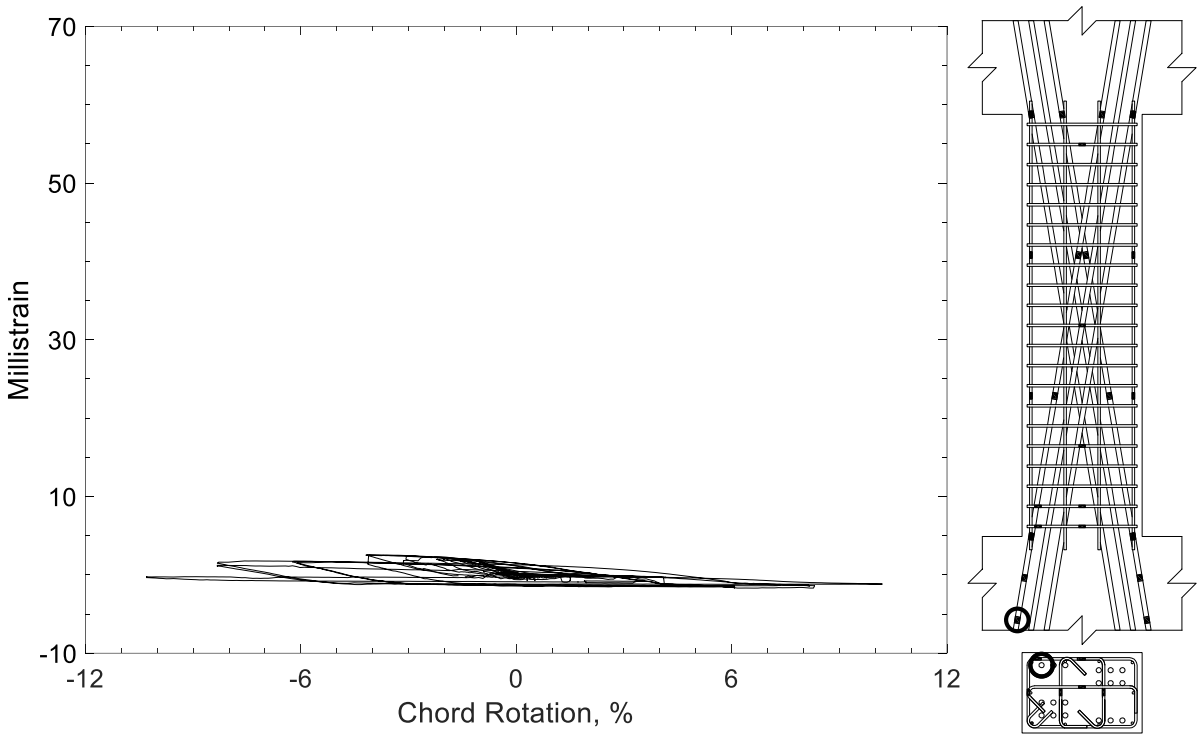

Figure 457 – Measured strain in diagonal bar of D80-3.5, strain gauge D1

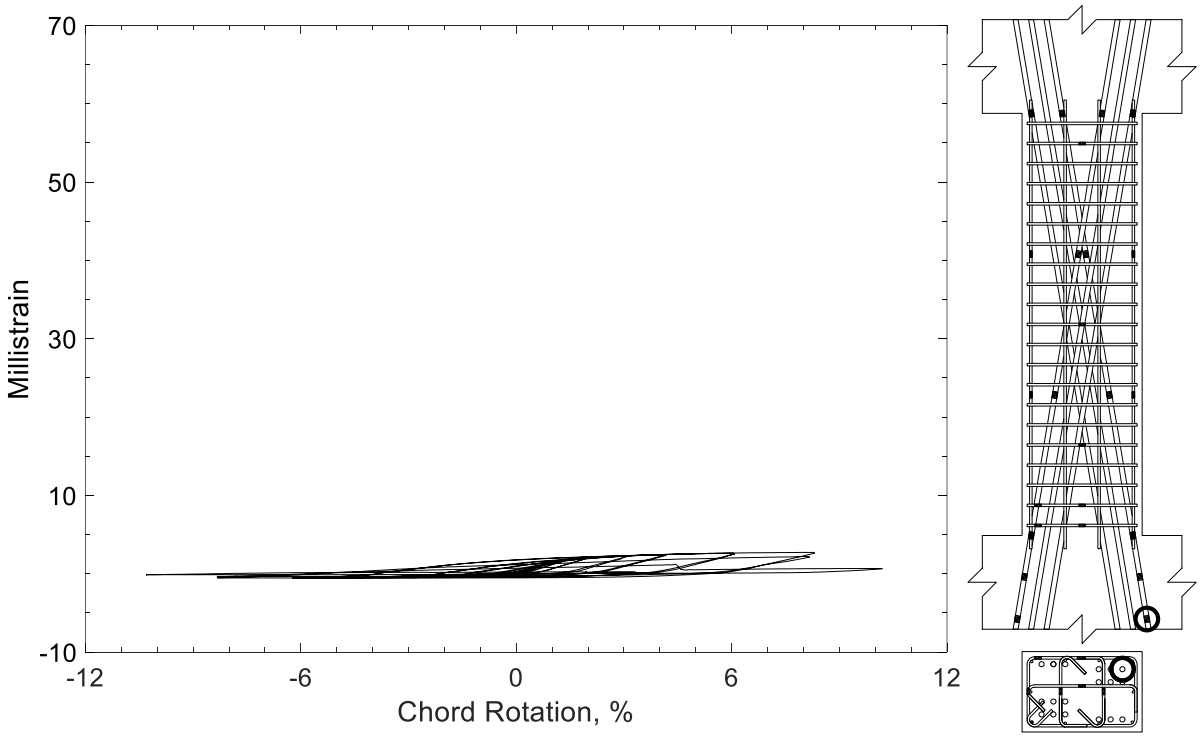

Figure 458 – Measured strain in diagonal bar of D80-3.5, strain gauge D2

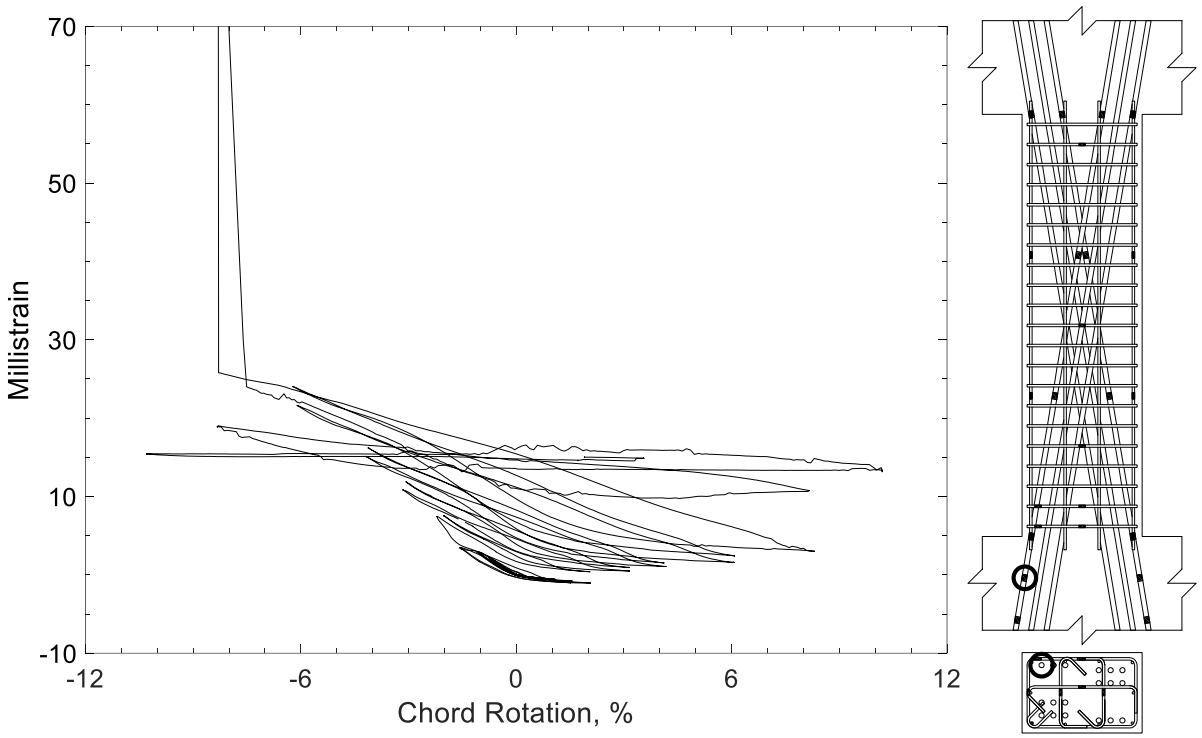

Figure 459 – Measured strain in diagonal bar of D80-3.5, strain gauge D3

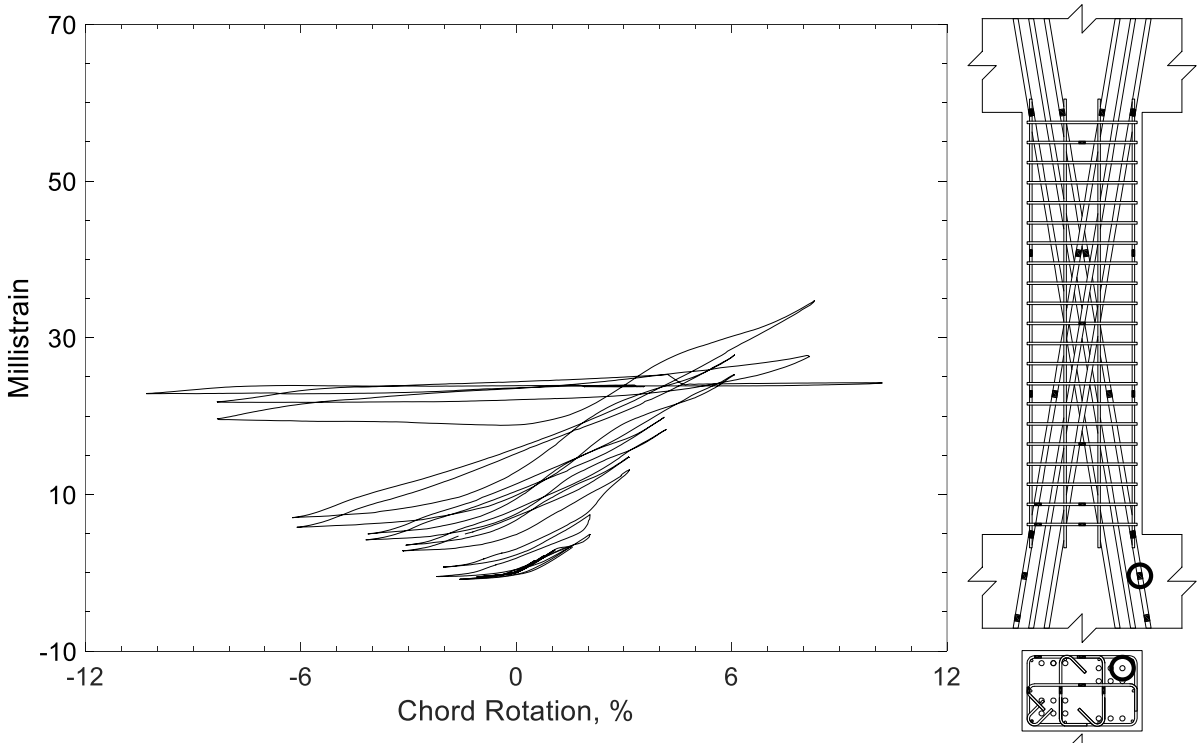

Figure 460 – Measured strain in diagonal bar of D80-3.5, strain gauge D4

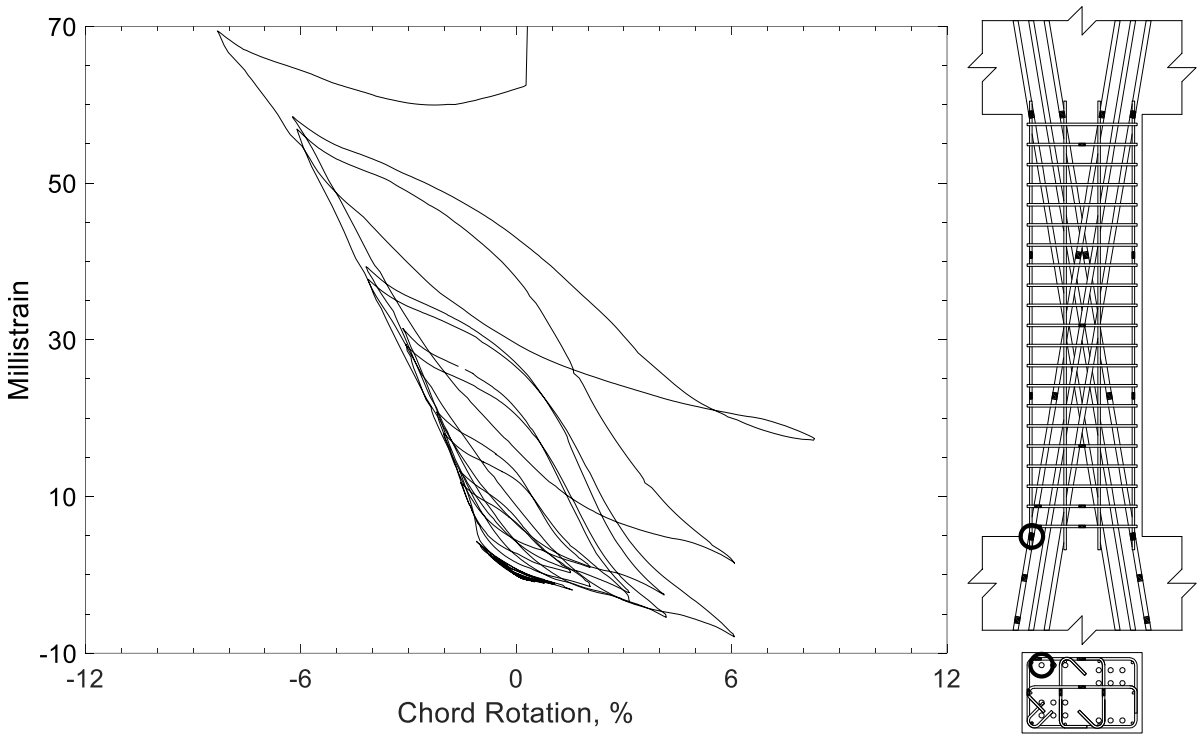

Figure 461 – Measured strain in diagonal bar of D80-3.5, strain gauge D5

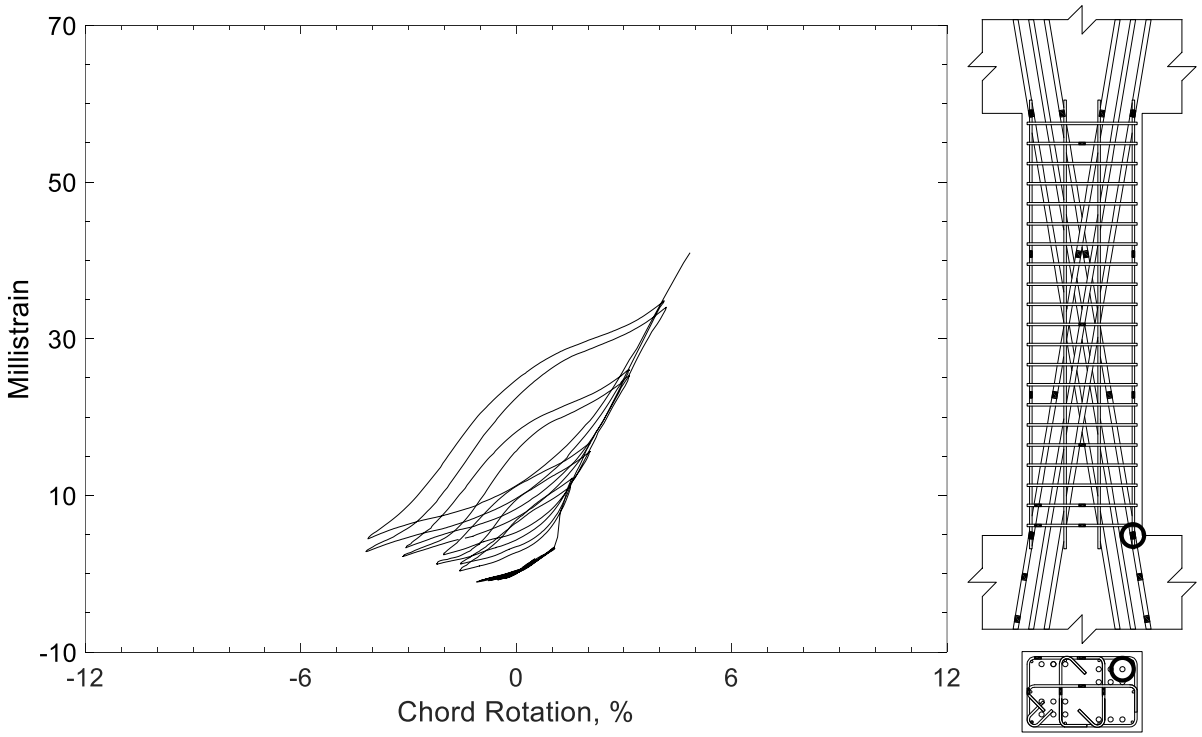

Figure 462 – Measured strain in diagonal bar of D80-3.5, strain gauge D6

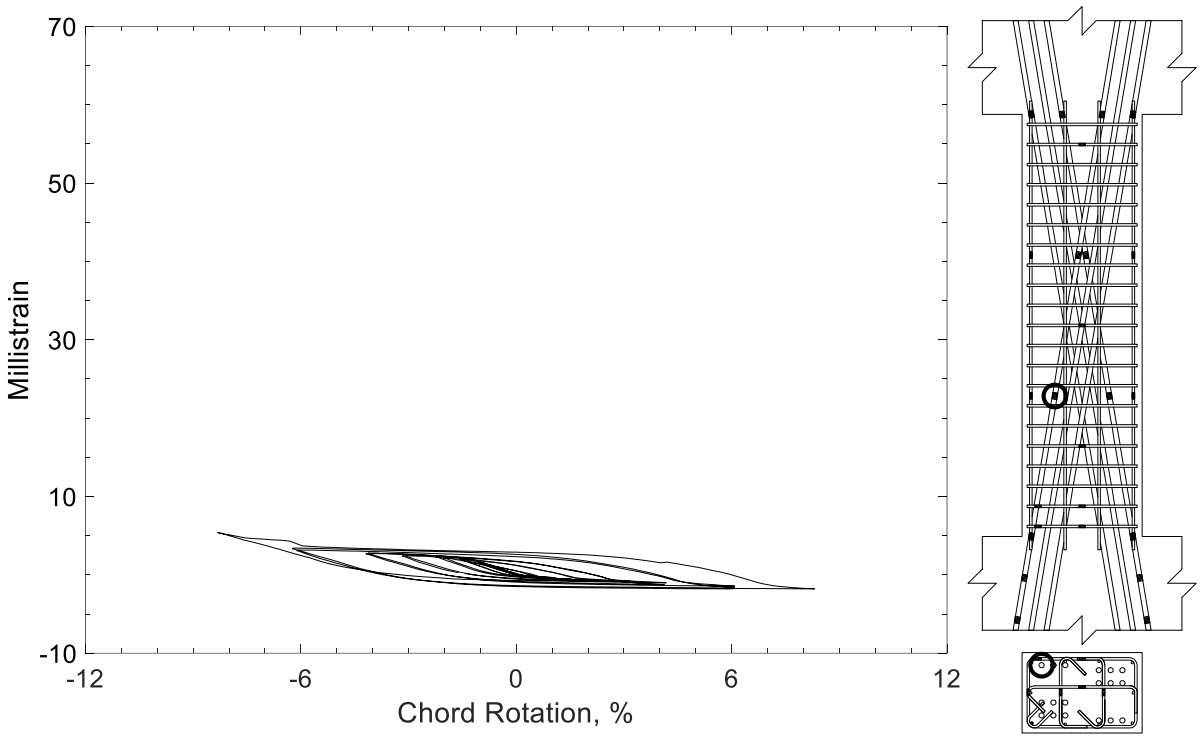

Figure 463 – Measured strain in diagonal bar of D80-3.5, strain gauge D7

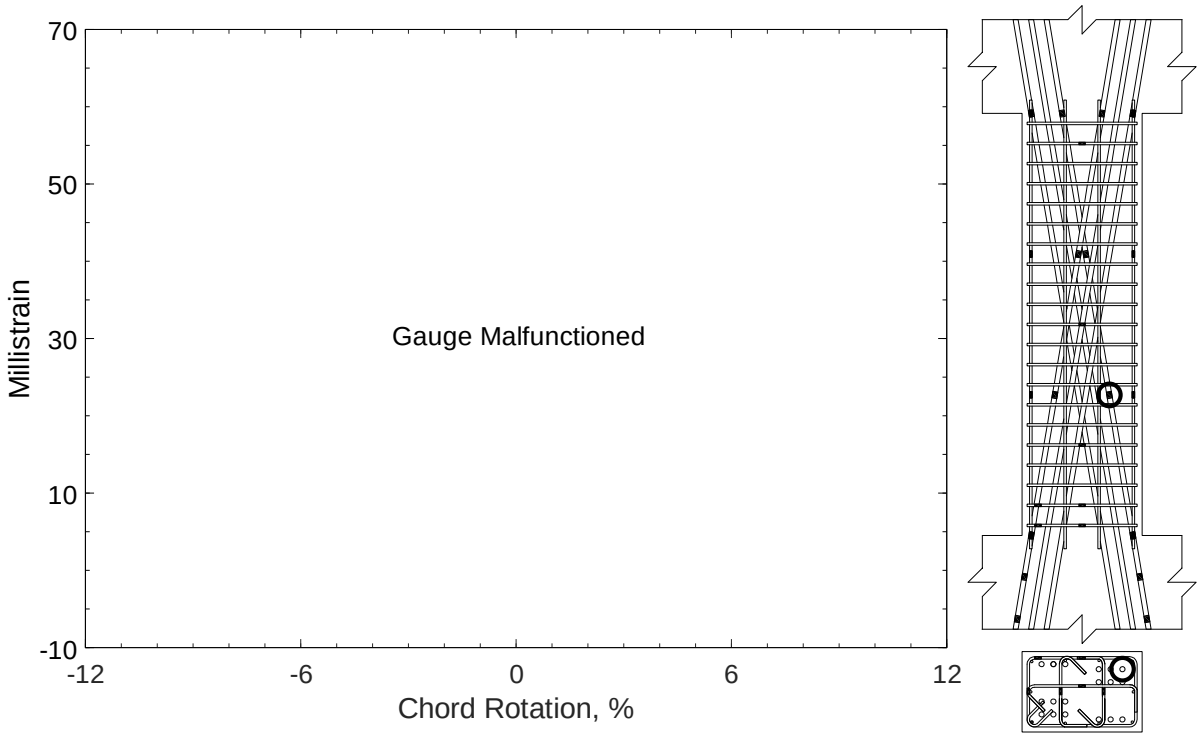

Figure 464 – Measured strain in diagonal bar of D80-3.5, strain gauge D8

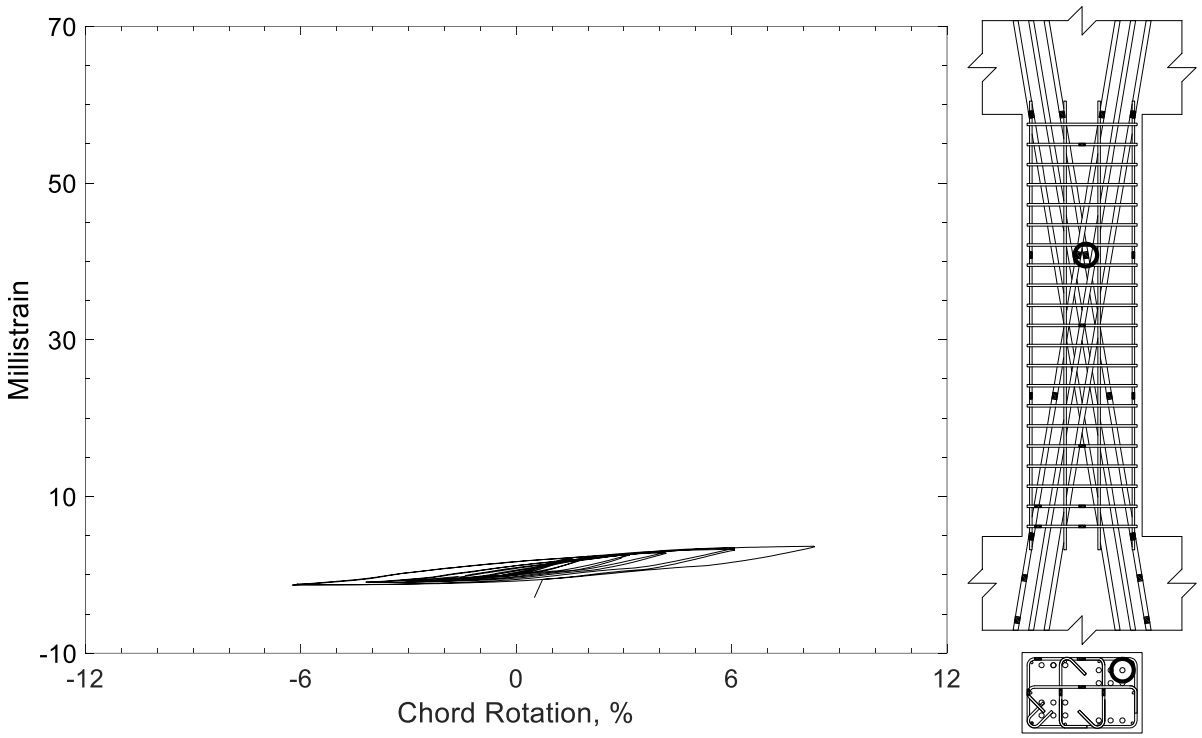

Figure 465 – Measured strain in diagonal bar of D80-3.5, strain gauge D9

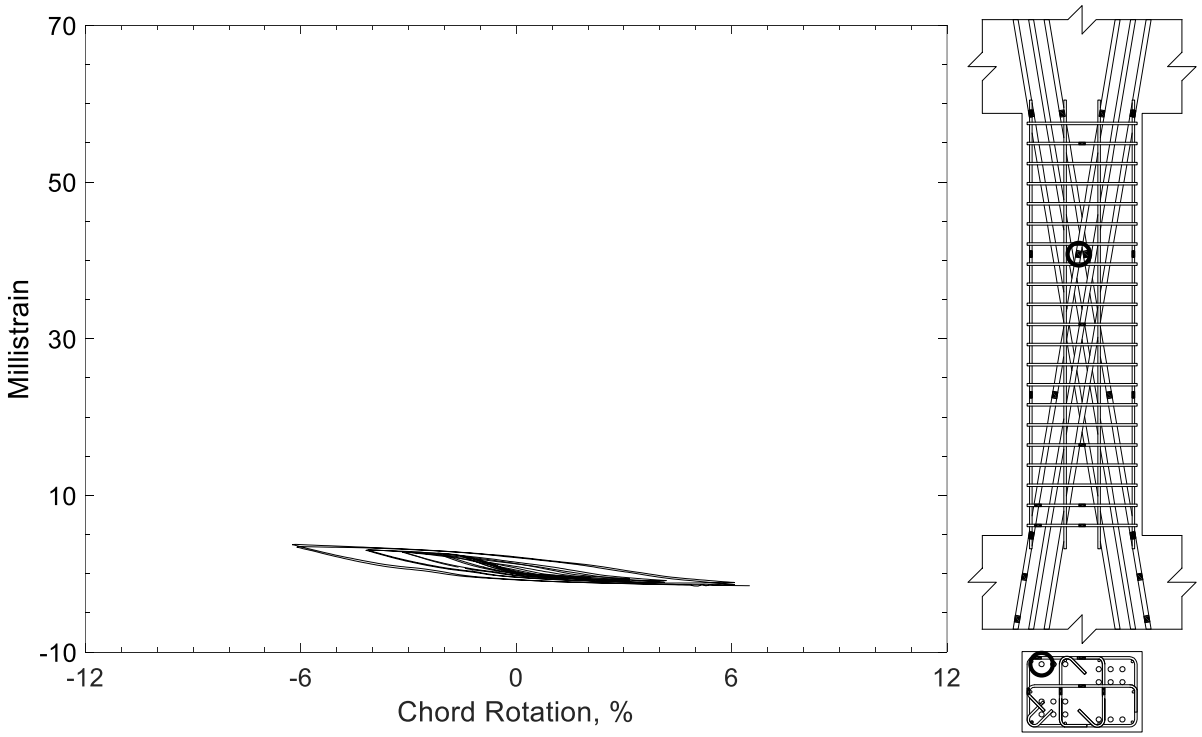

Figure 466 – Measured strain in diagonal bar of D80-3.5, strain gauge D10

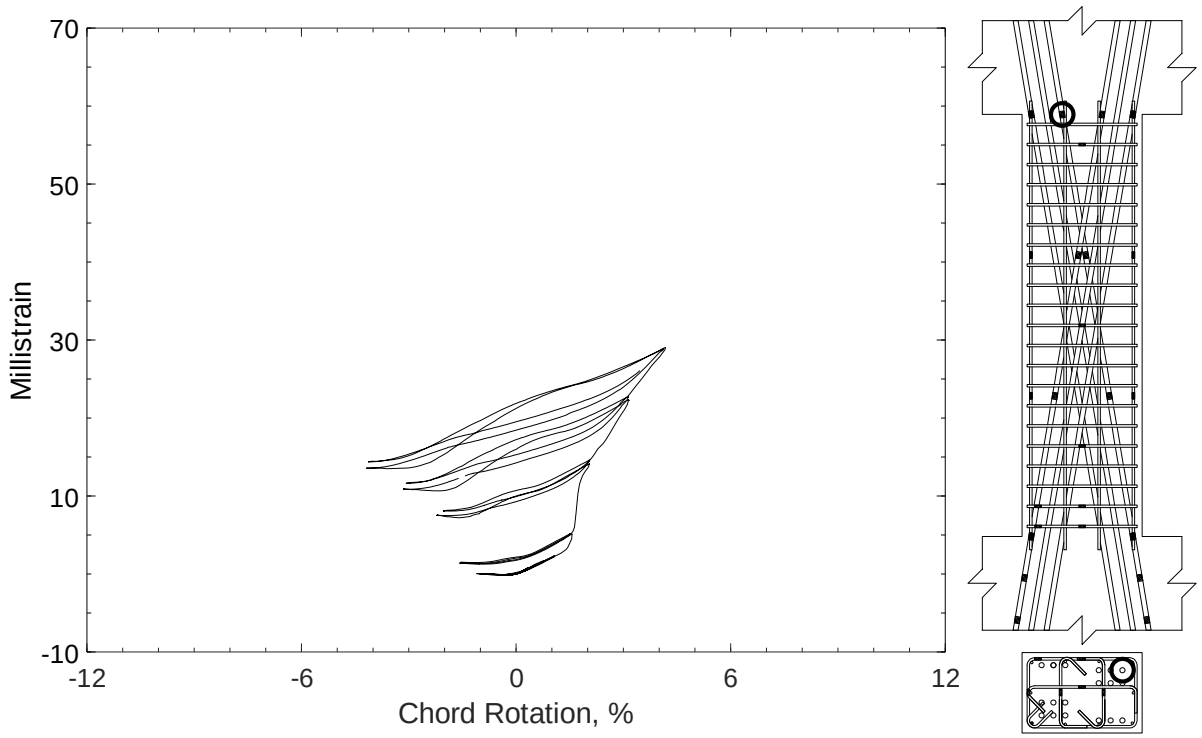

Figure 467 – Measured strain in diagonal bar of D80-3.5, strain gauge D11

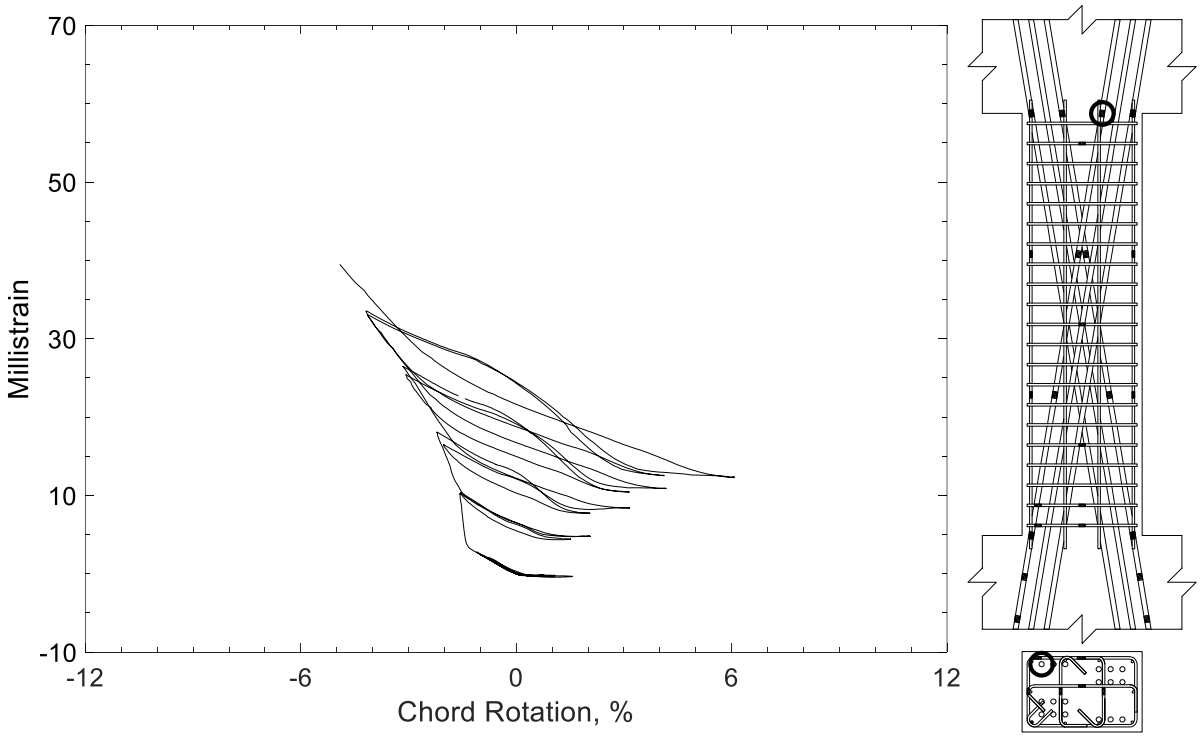

Figure 468 – Measured strain in diagonal bar of D80-3.5, strain gauge D12

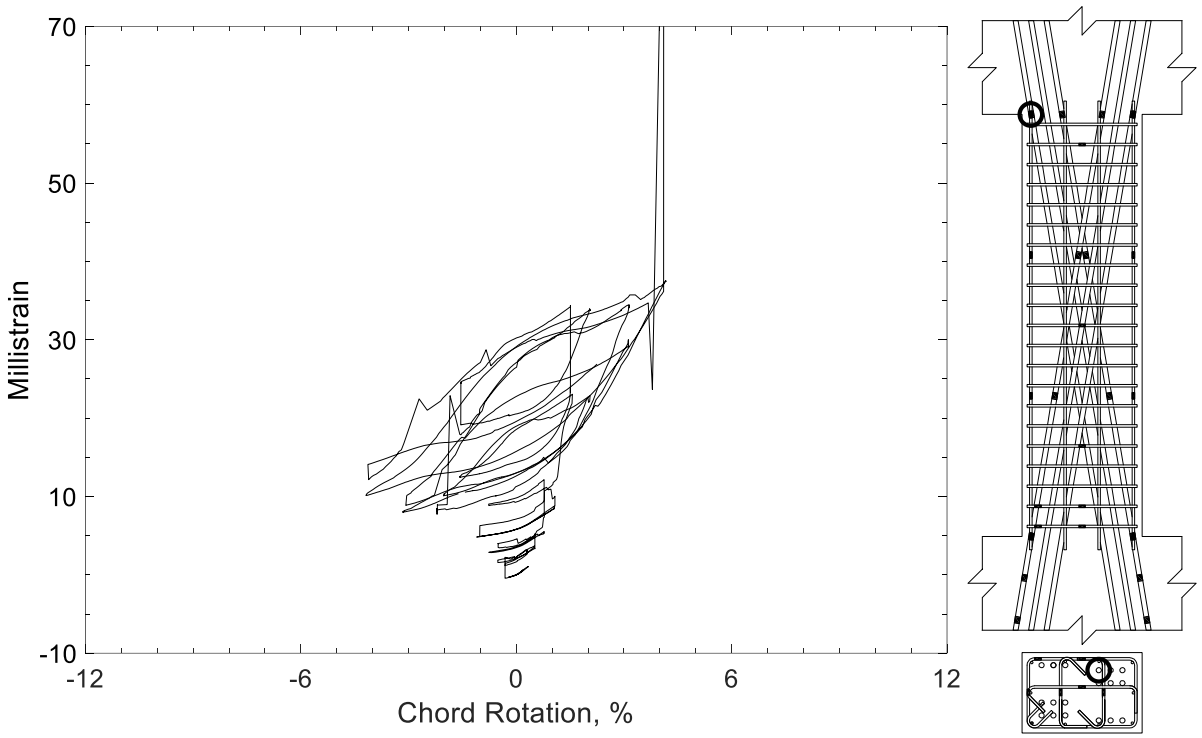

Figure 469 – Measured strain in diagonal bar of D80-3.5, strain gauge D13

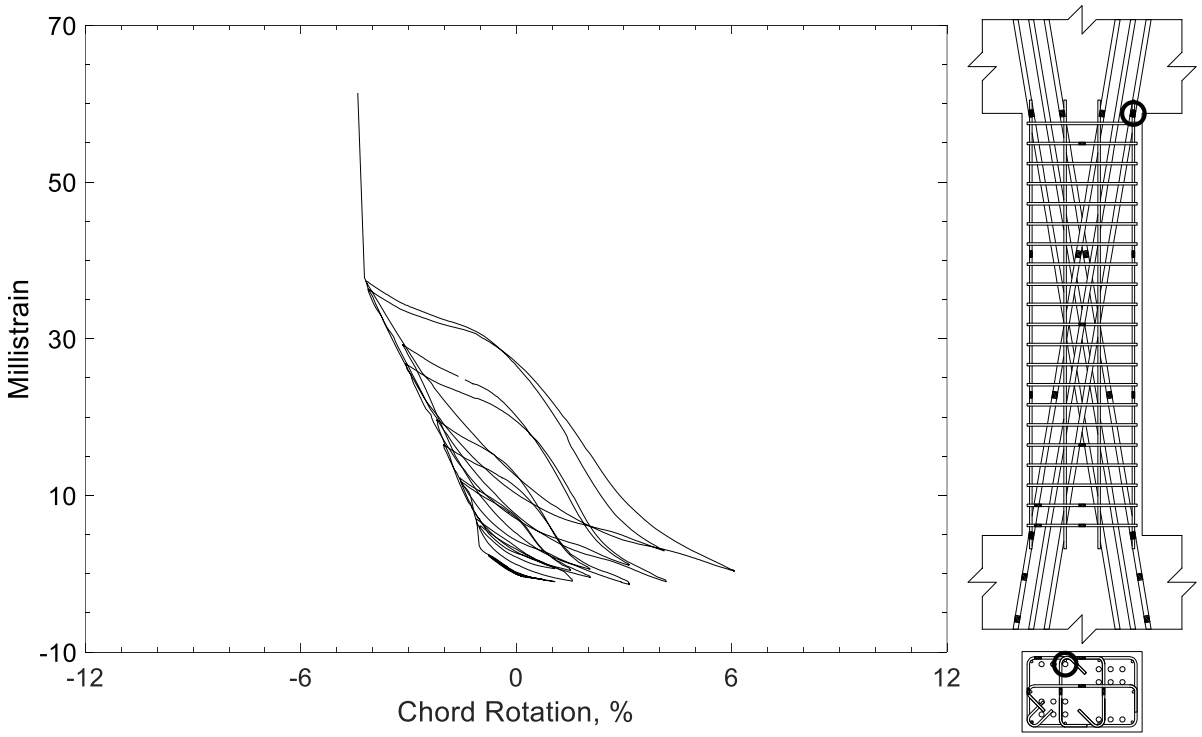

Figure 470 – Measured strain in diagonal bar of D80-3.5, strain gauge D14

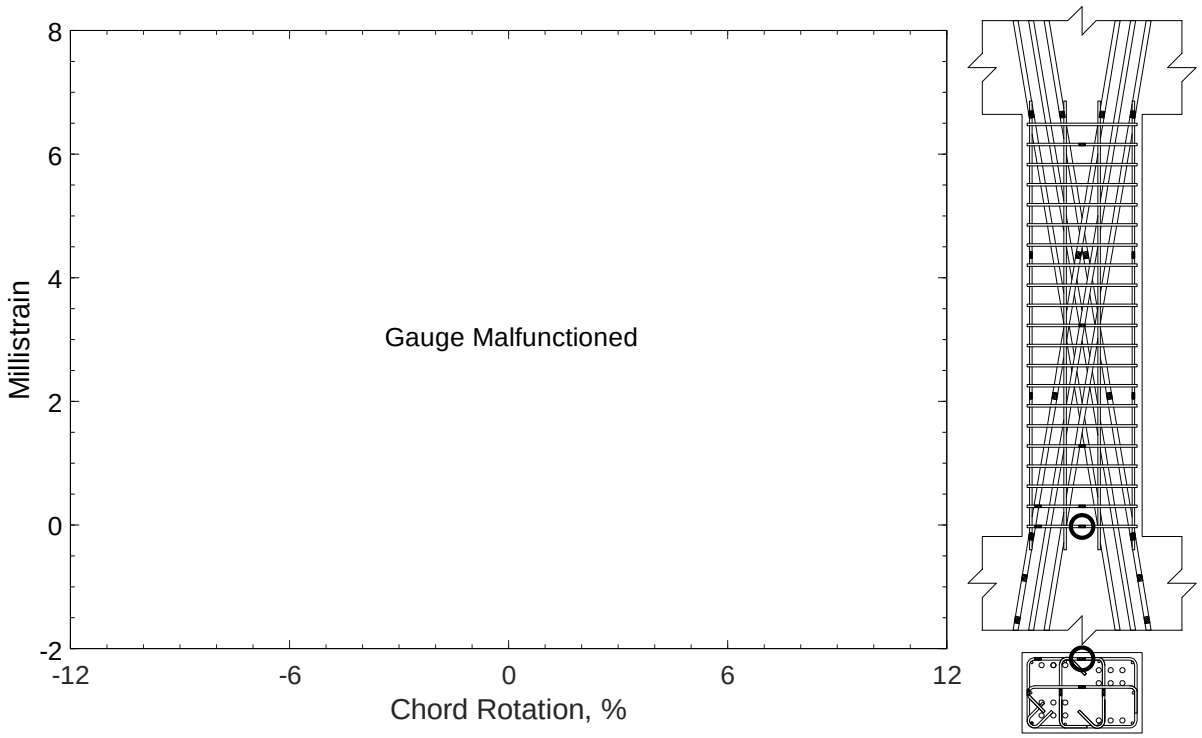

Figure 471 – Measured strain in closed stirrup of D80-3.5, strain gauge S1

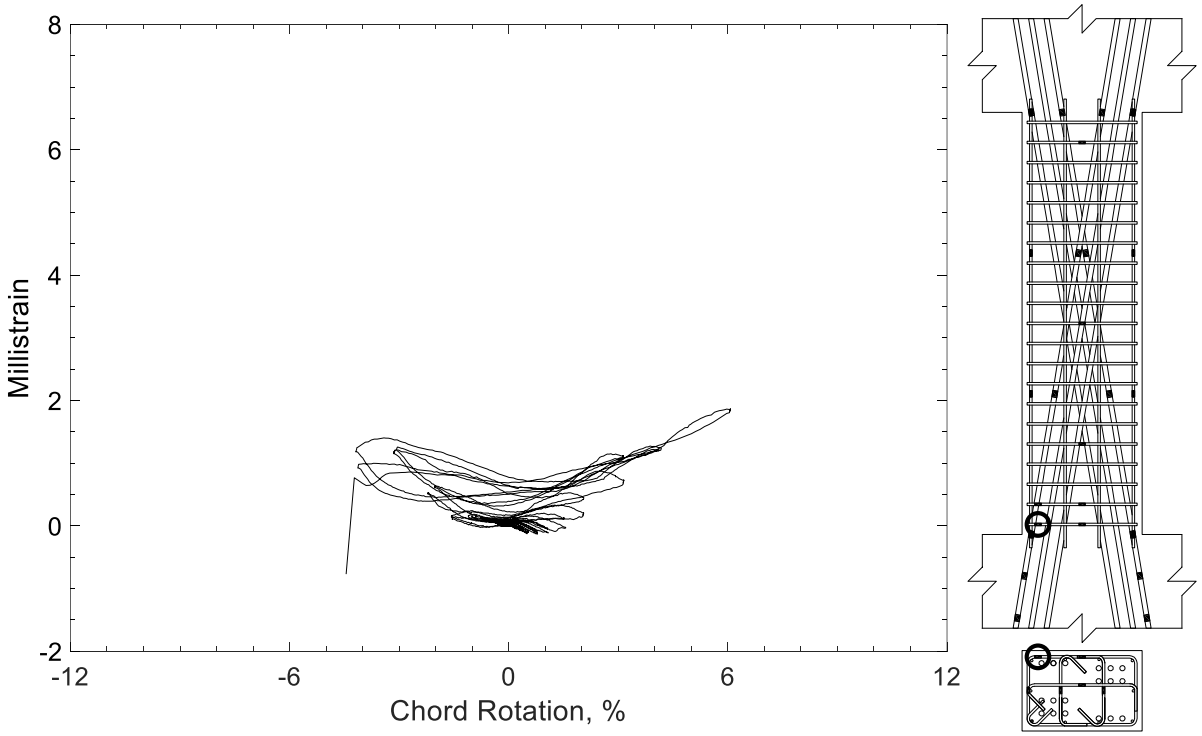

Figure 472 – Measured strain in closed stirrup of D80-3.5, strain gauge S2

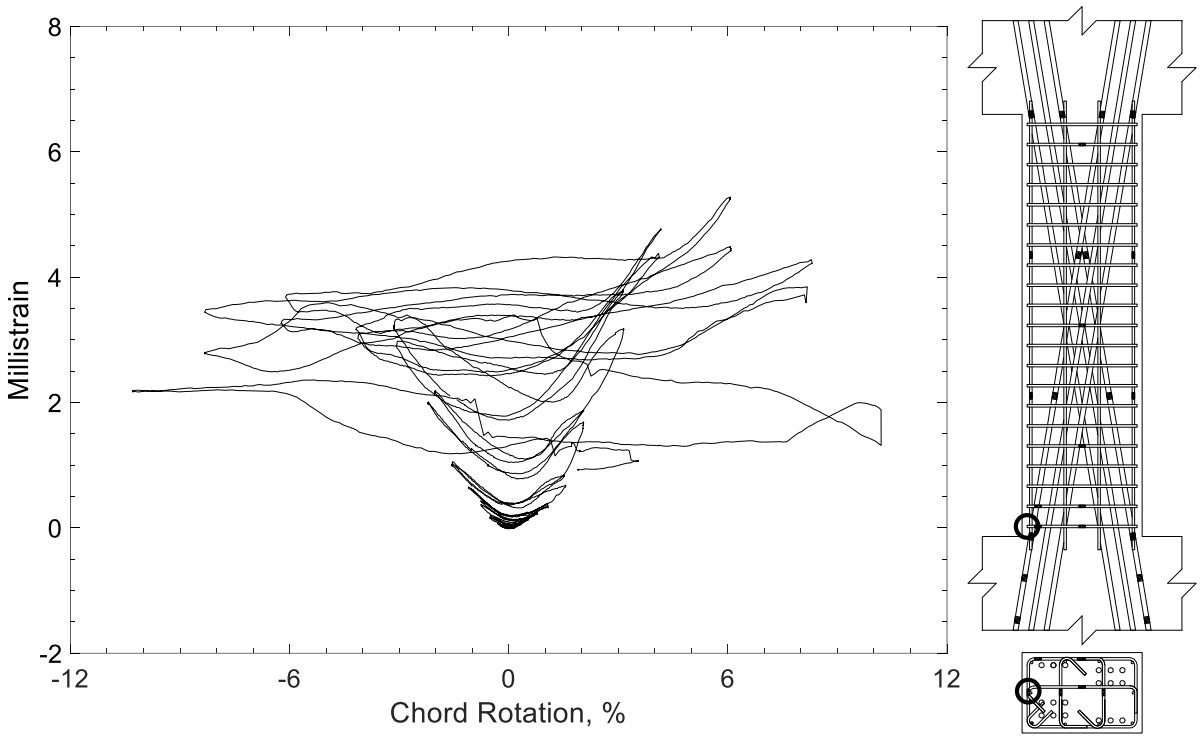

Figure 473 – Measured strain in closed stirrup of D80-3.5, strain gauge S3

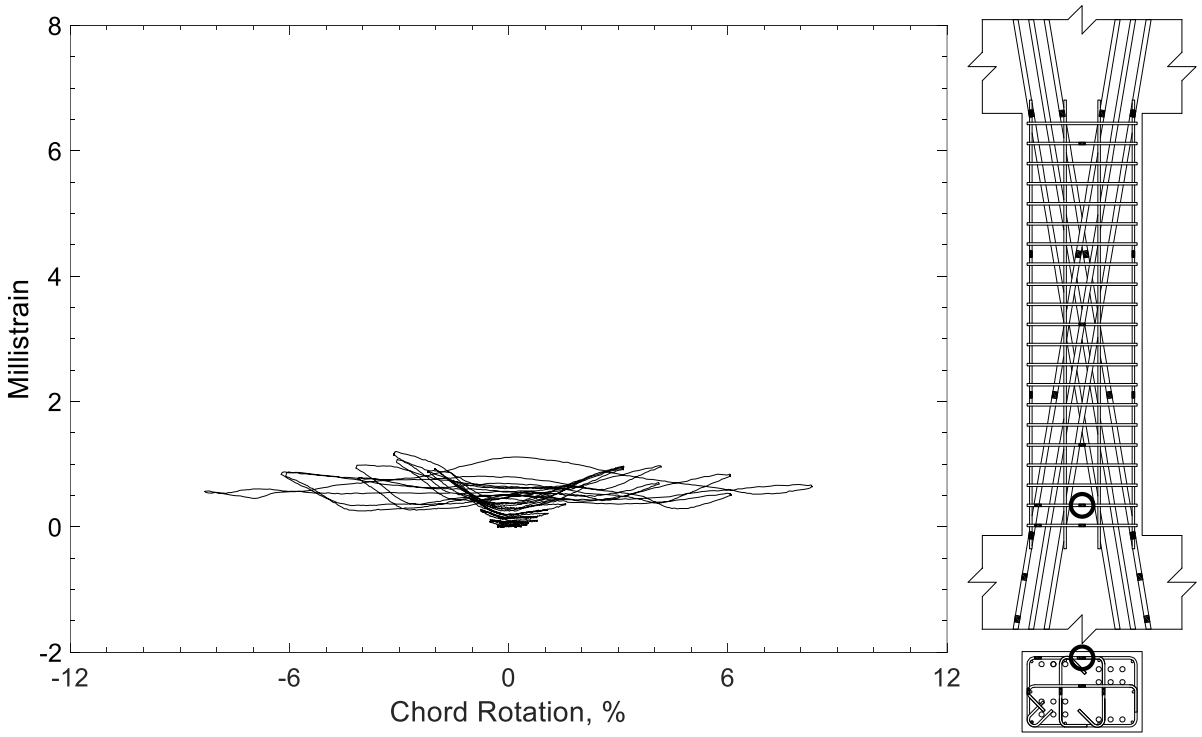

Figure 474 – Measured strain in closed stirrup of D80-3.5, strain gauge S4

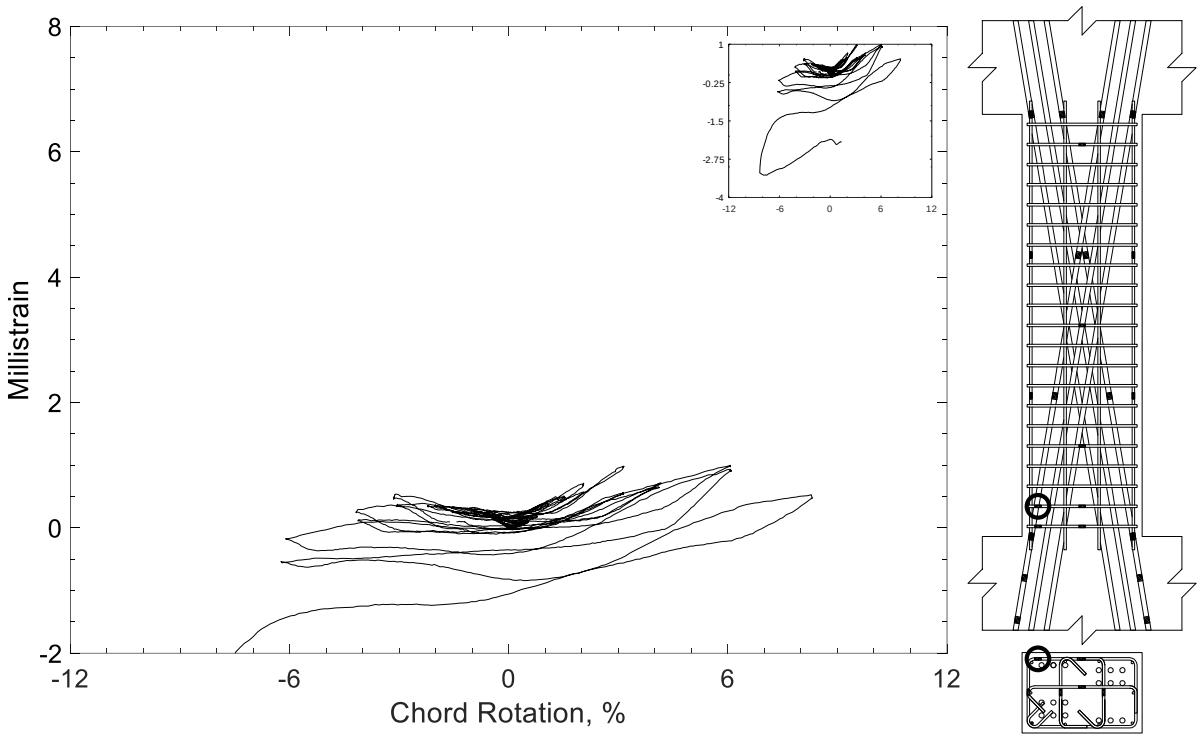

Figure 475 – Measured strain in closed stirrup of D80-3.5, strain gauge S5

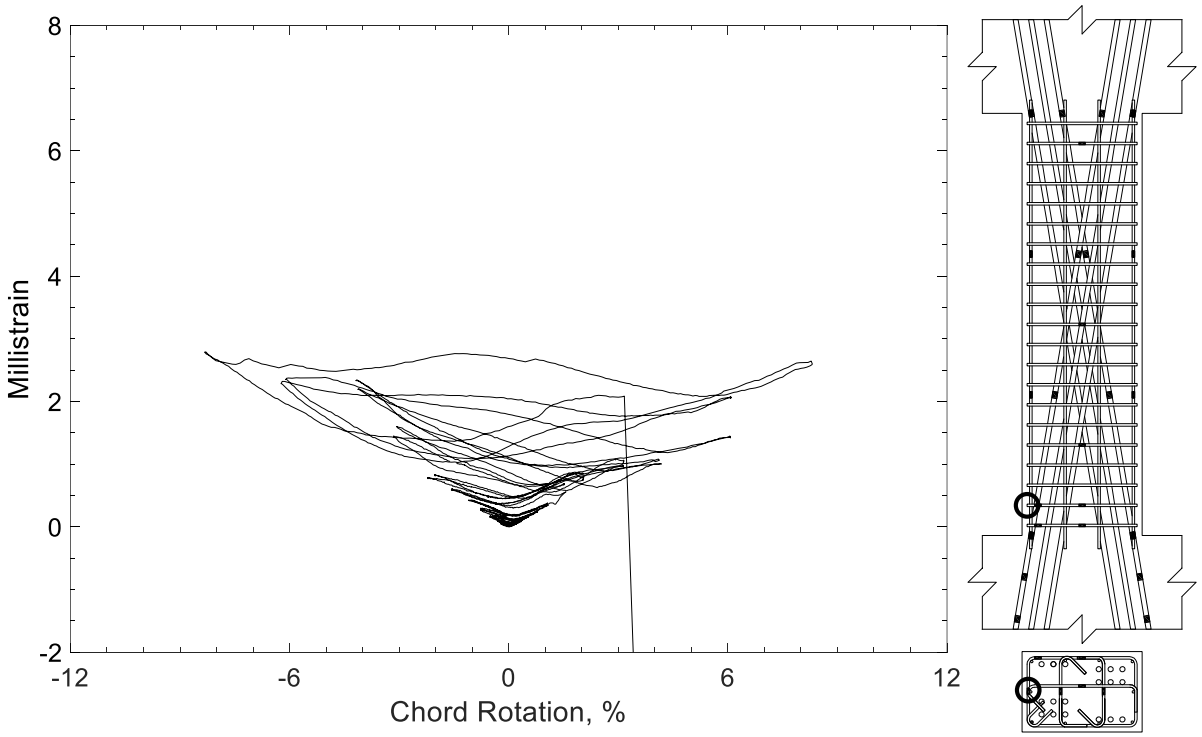

Figure 476 – Measured strain in closed stirrup of D80-3.5, strain gauge S6

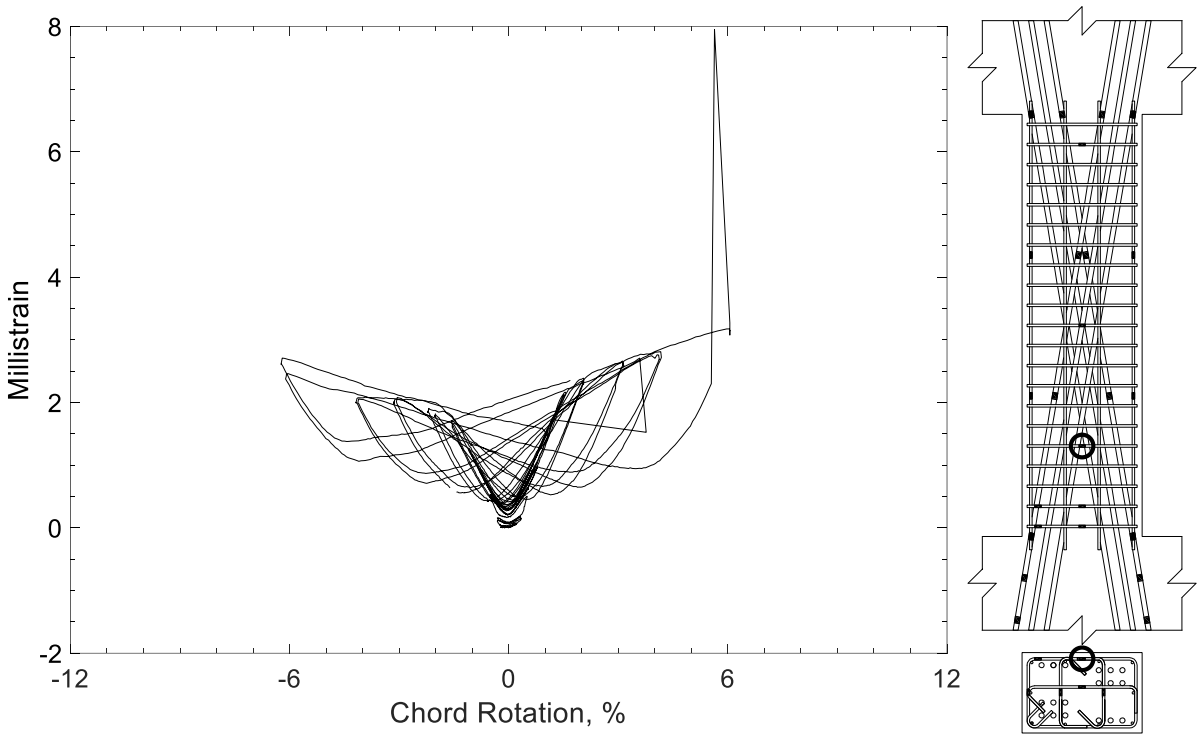

Figure 477 – Measured strain in closed stirrup of D80-3.5, strain gauge S7

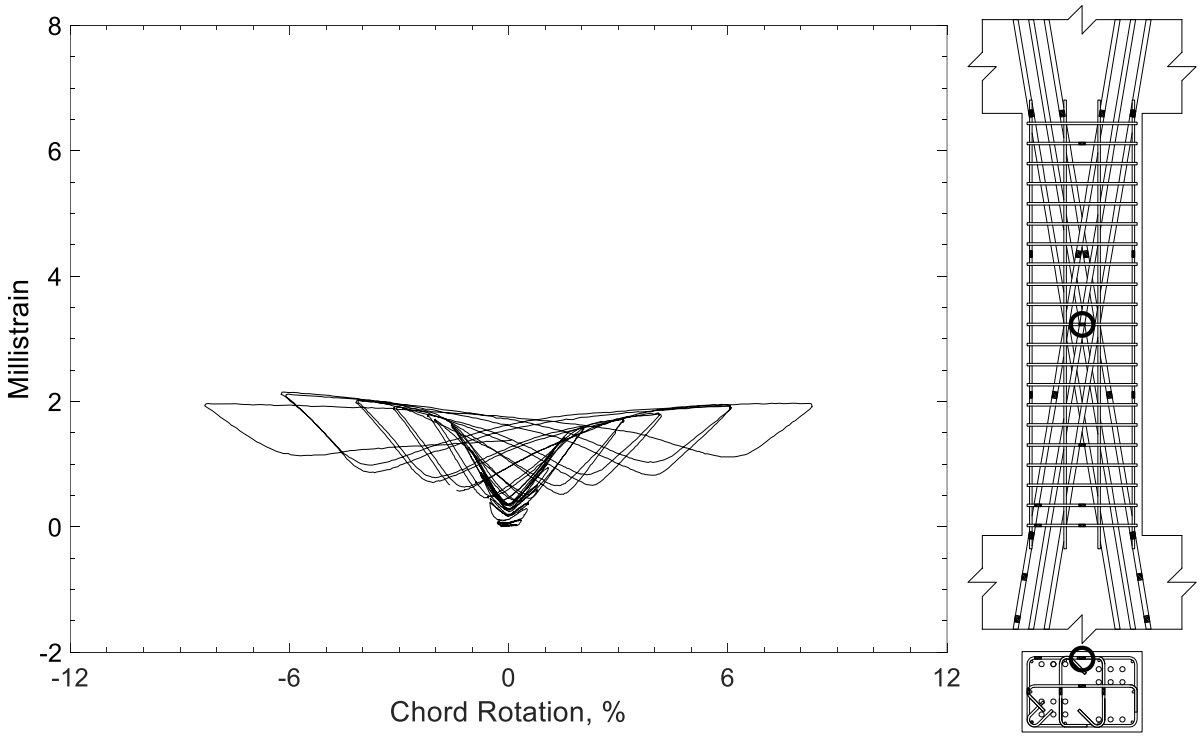

Figure 478 – Measured strain in closed stirrup of D80-3.5, strain gauge S8

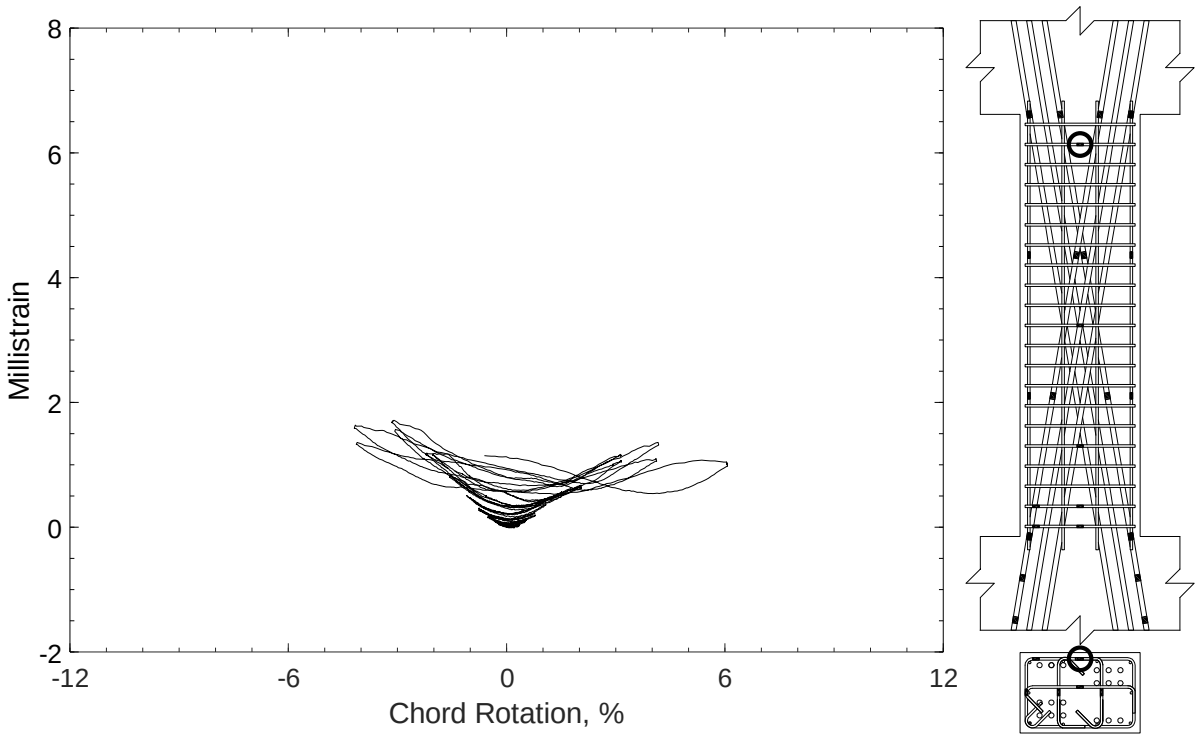

Figure 479 – Measured strain in closed stirrup of D80-3.5, strain gauge S9

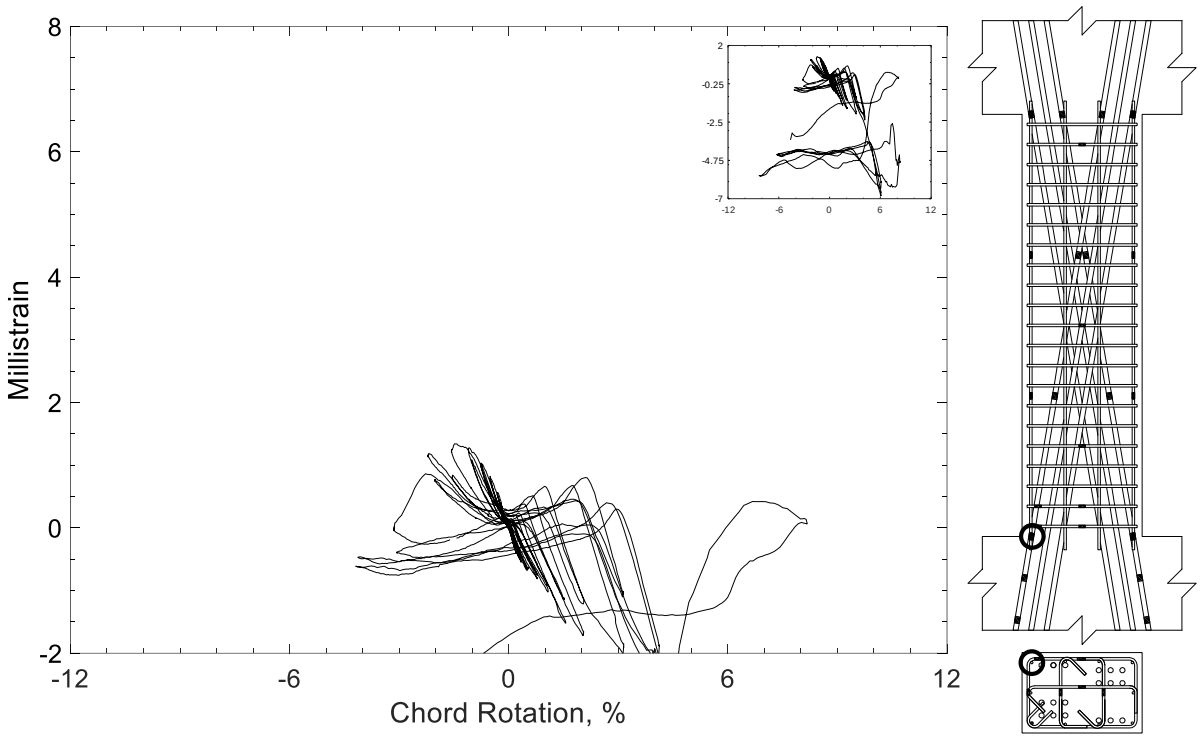

Figure 480 – Measured strain in parallel bar of D80-3.5, strain gauge H1

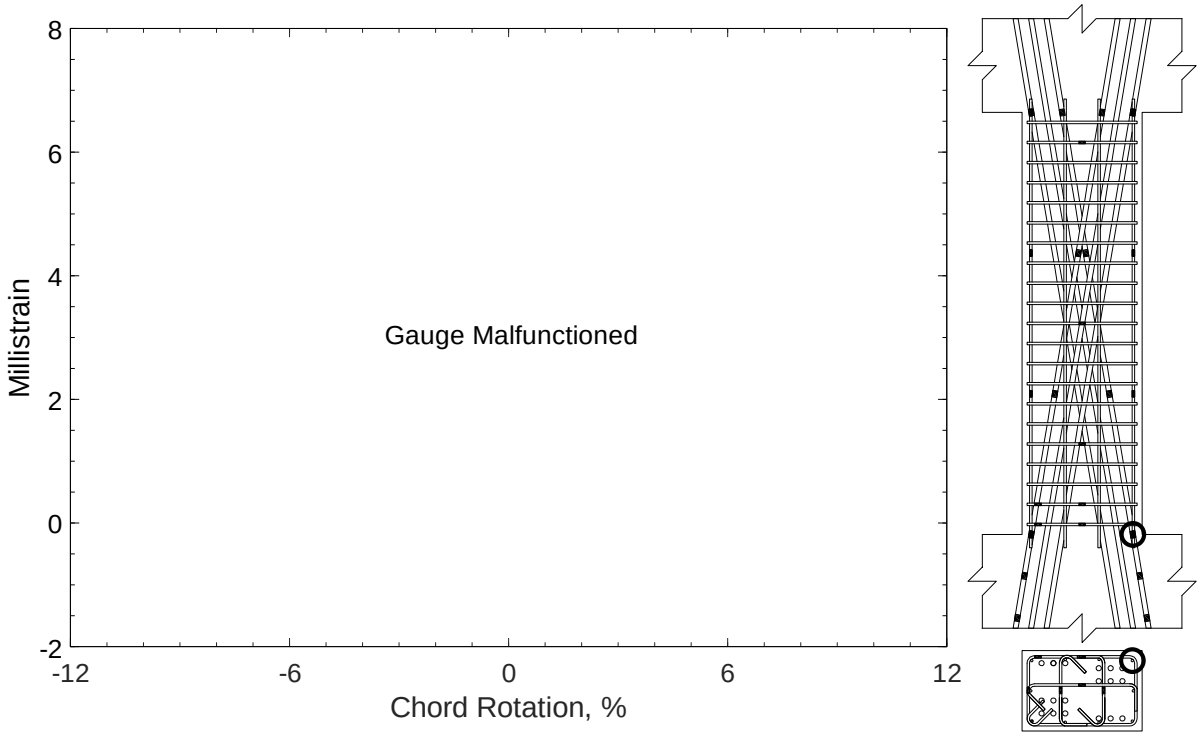

Figure 481 – Measured strain in parallel bar of D80-3.5, strain gauge H2

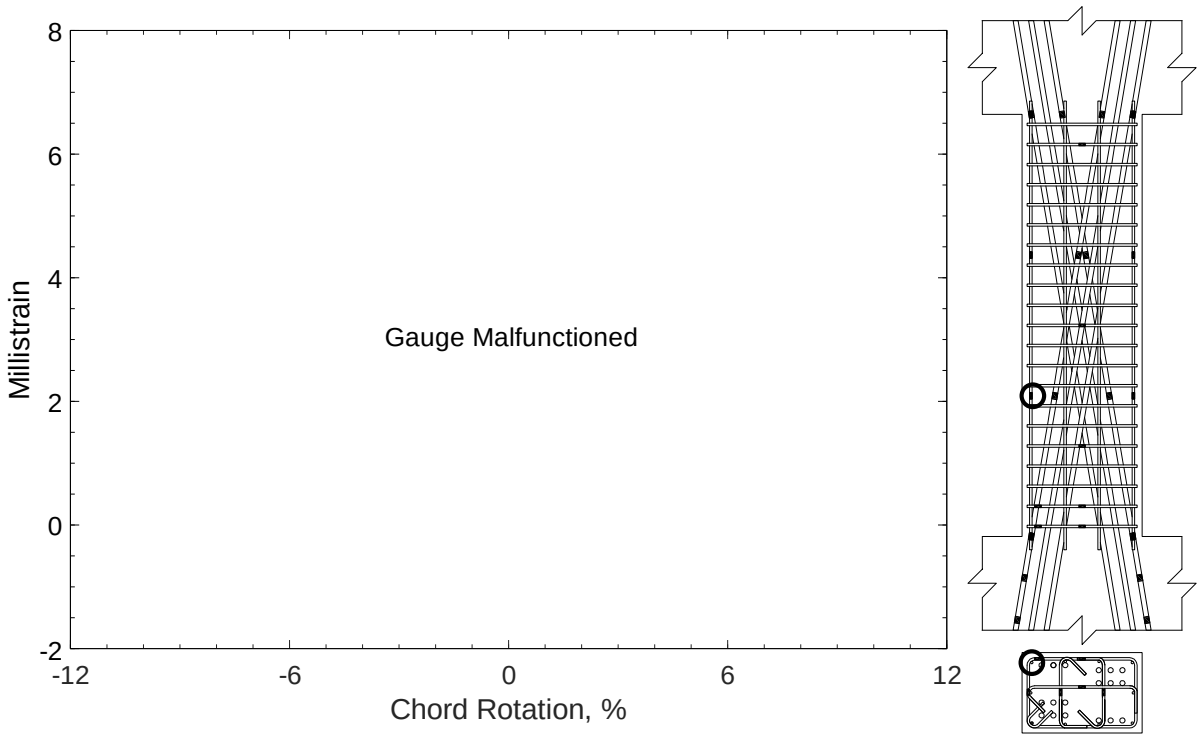

Figure 482 – Measured strain in parallel bar of D80-3.5, strain gauge H3

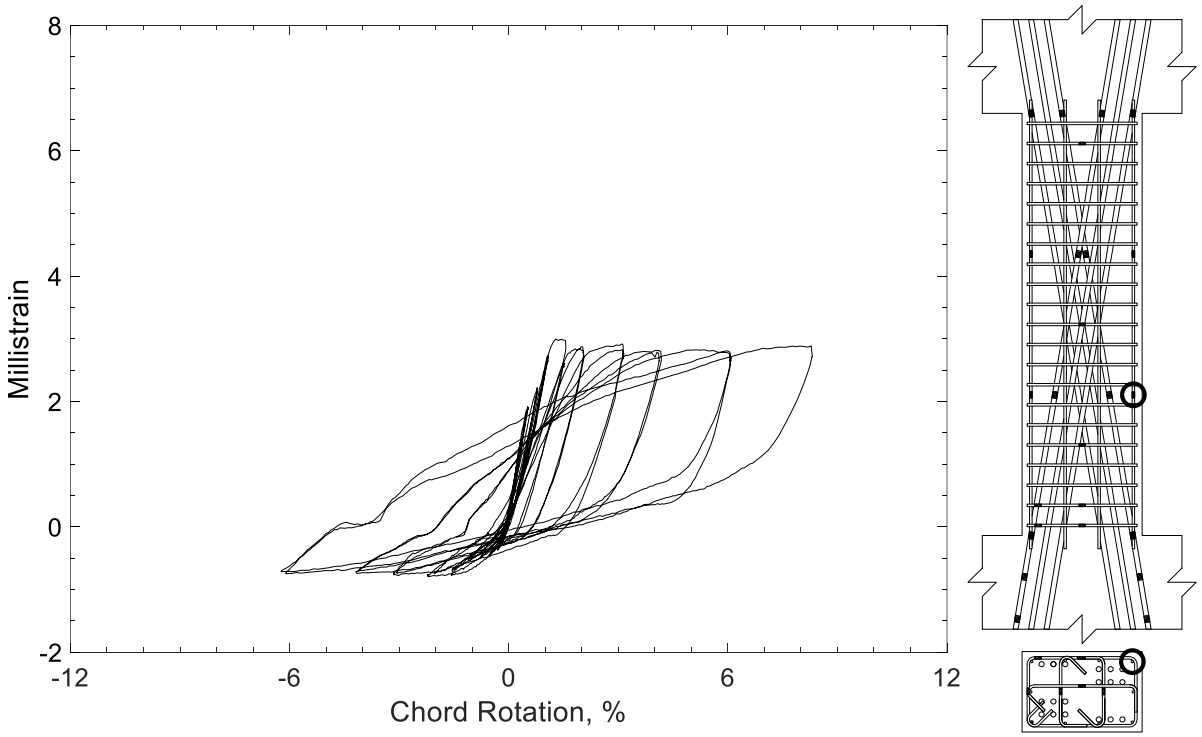

Figure 483 – Measured strain in parallel bar of D80-3.5, strain gauge H4

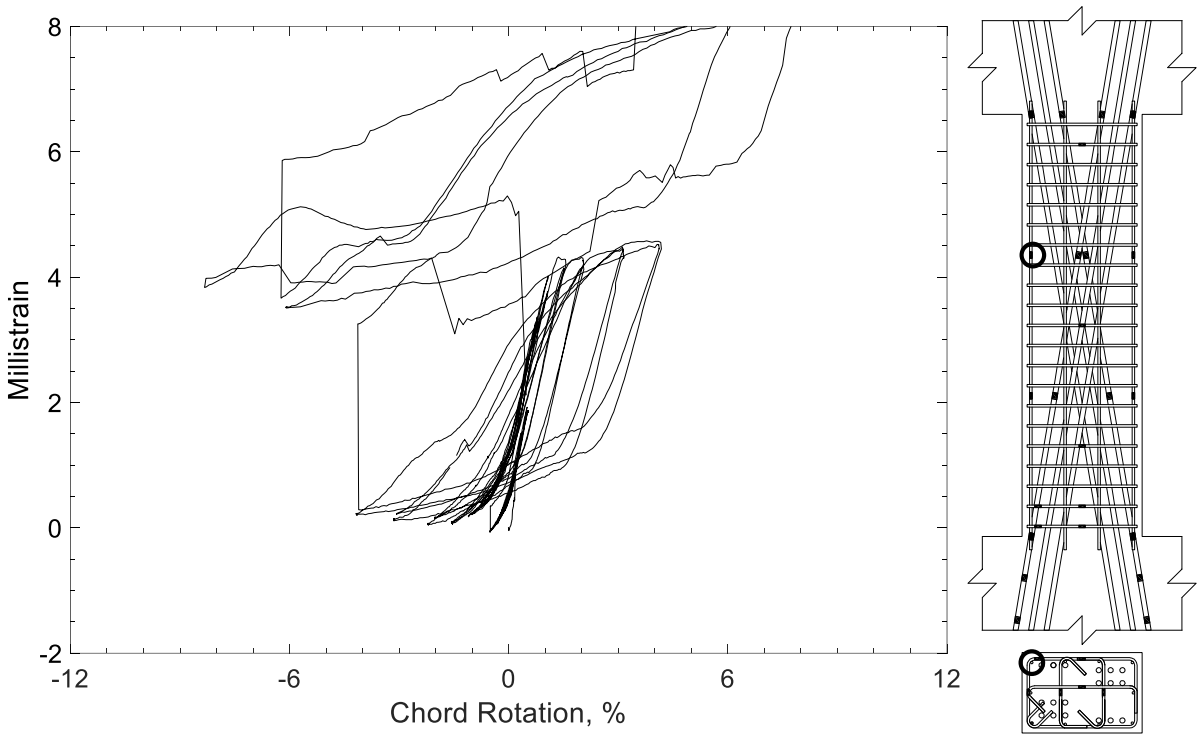

Figure 484 – Measured strain in parallel bar of D80-3.5, strain gauge H5

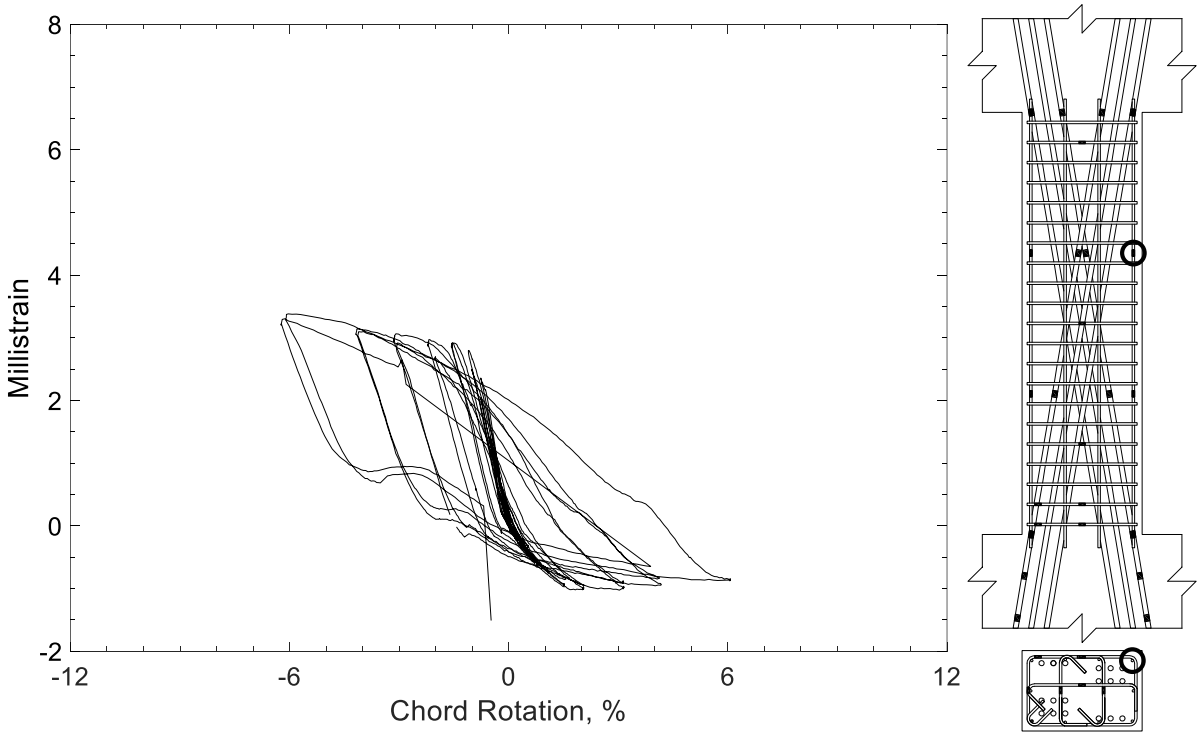

Figure 485 – Measured strain in parallel bar of D80-3.5, strain gauge H6

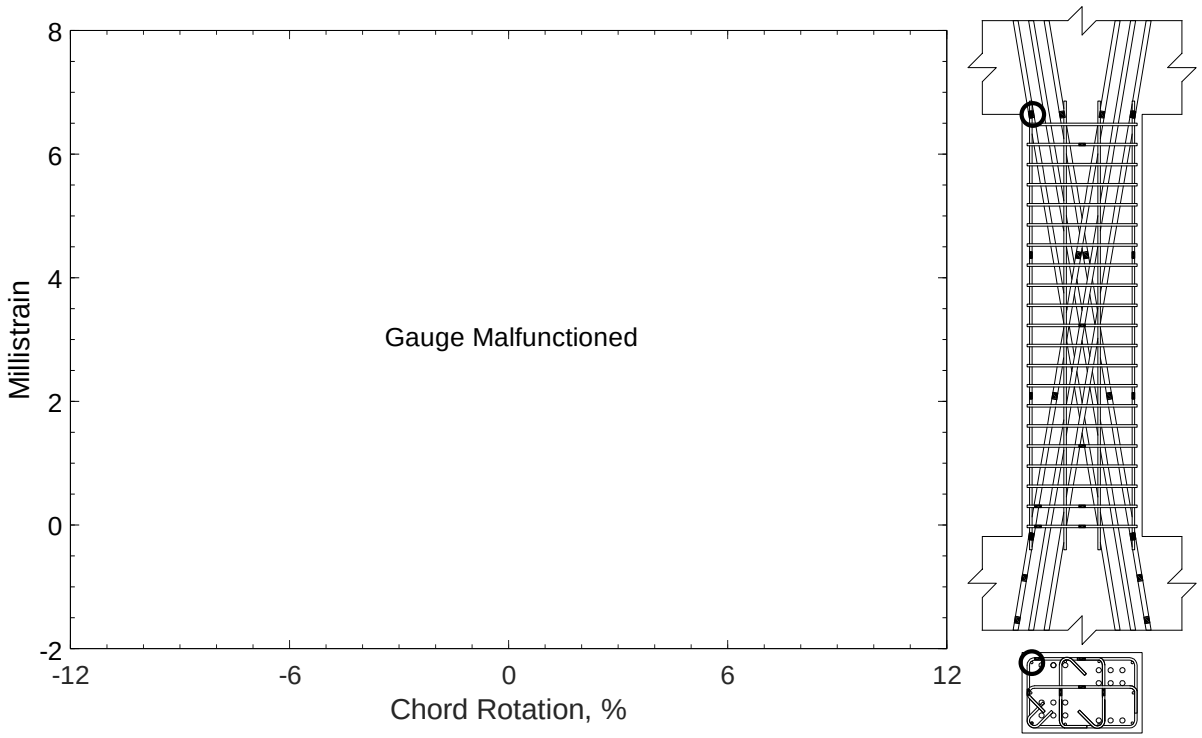

Figure 486 – Measured strain in parallel bar of D80-3.5, strain gauge H7

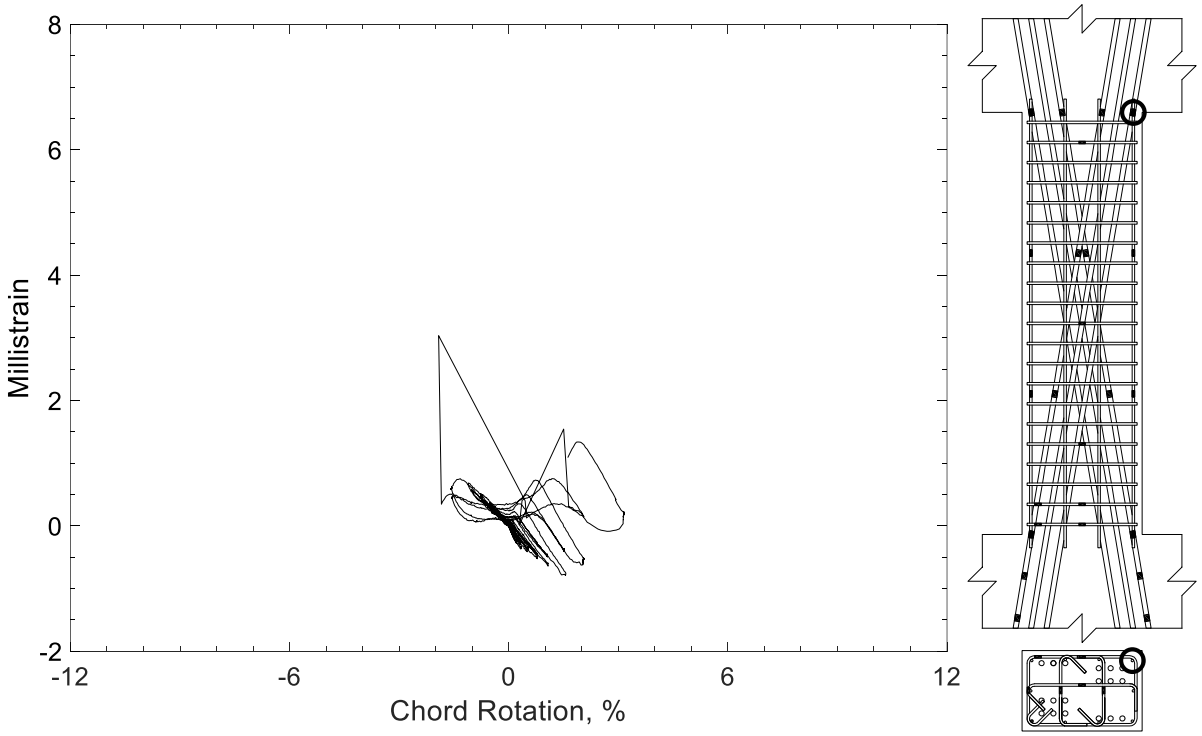

Figure 487 – Measured strain in parallel bar of D80-3.5, strain gauge H8

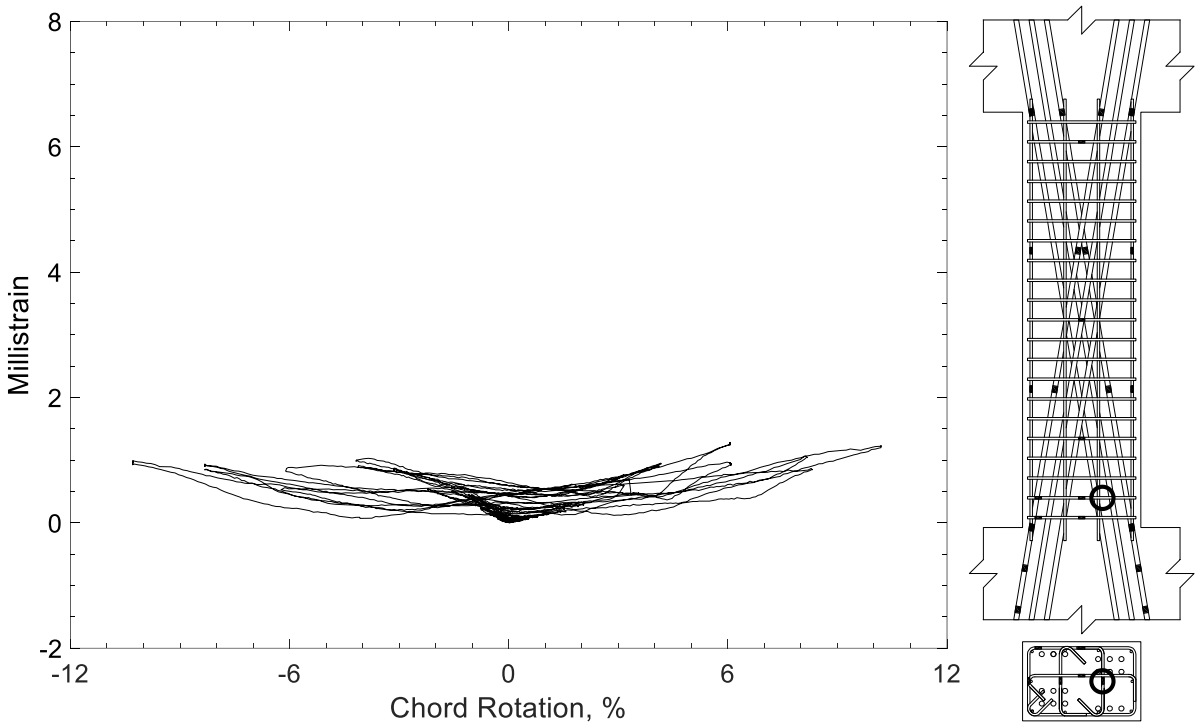

Figure 488 – Measured strain in crosstie of D80-3.5, strain gauge T1

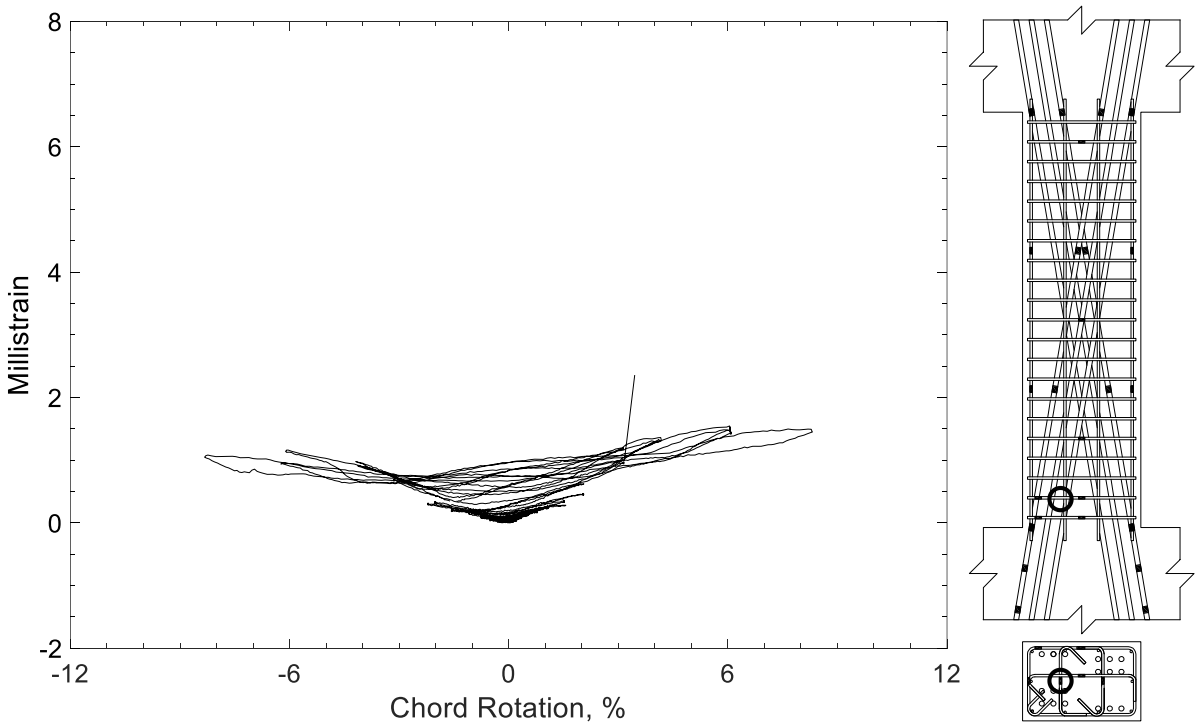

Figure 489 – Measured strain in crosstie of D80-3.5, strain gauge T2

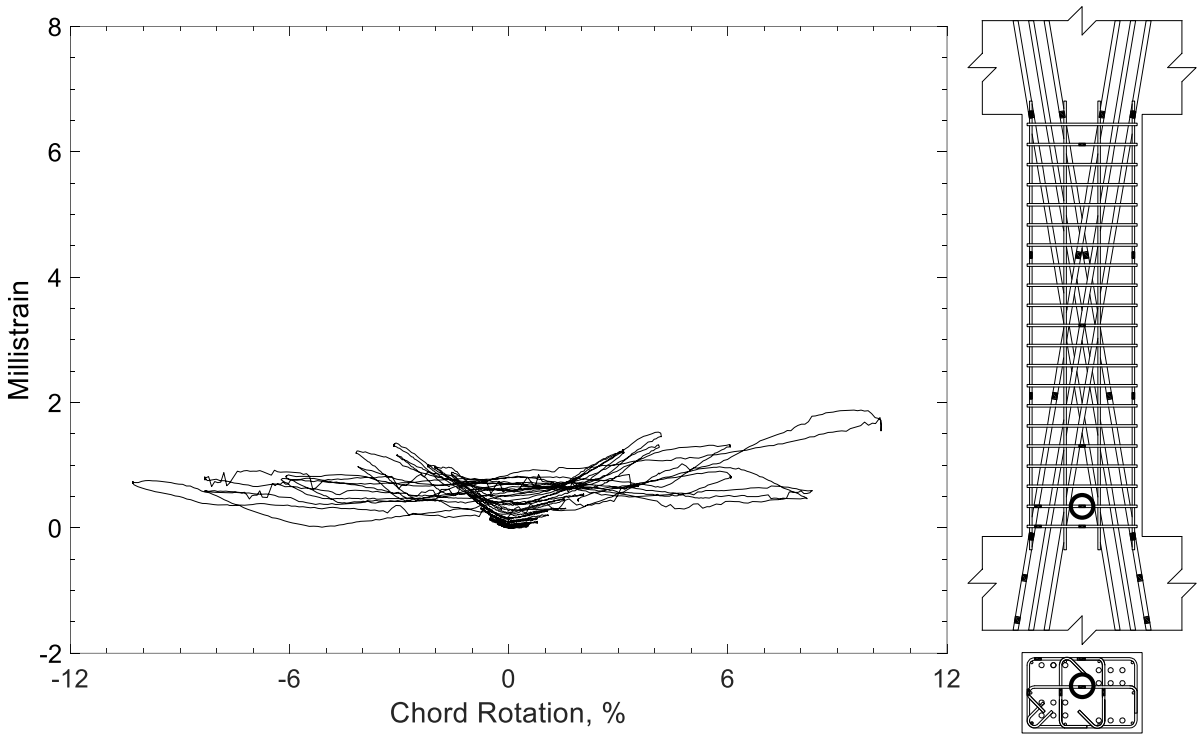

Figure 490 – Measured strain in crosstie of D80-3.5, strain gauge T3

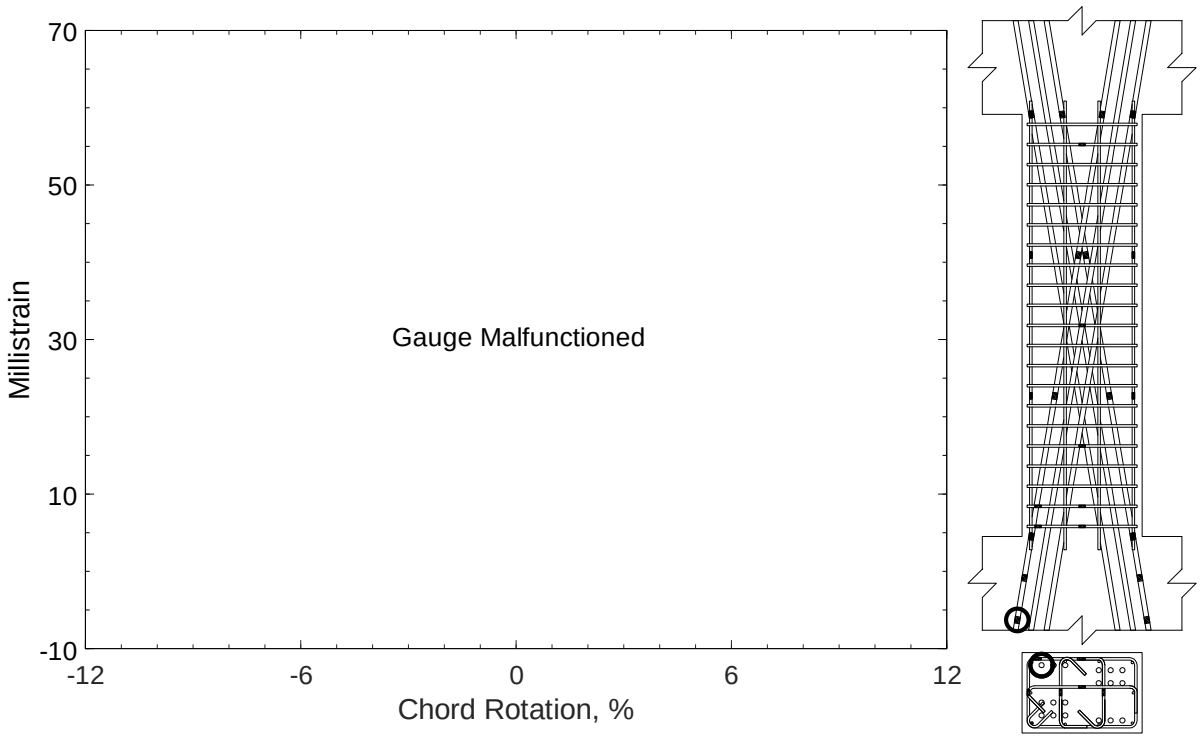

Figure 491 – Measured strain in diagonal bar of D100-3.5, strain gauge D1

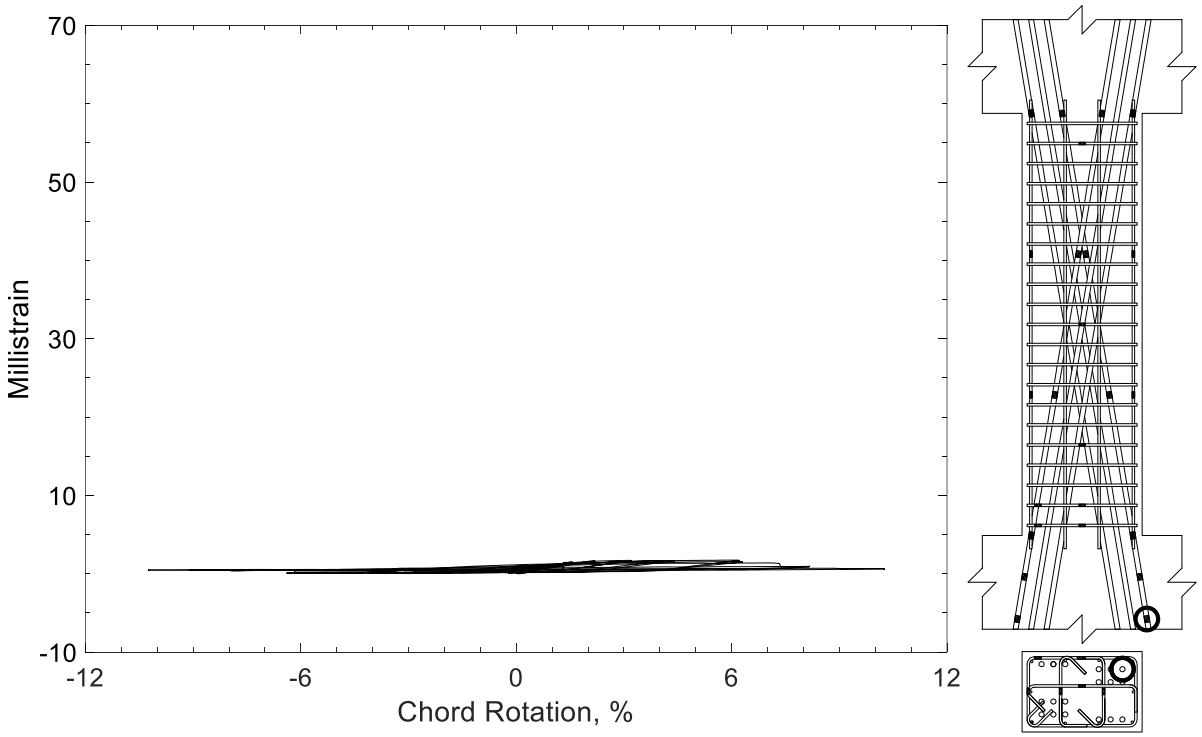

Figure 492 – Measured strain in diagonal bar of D100-3.5, strain gauge D2

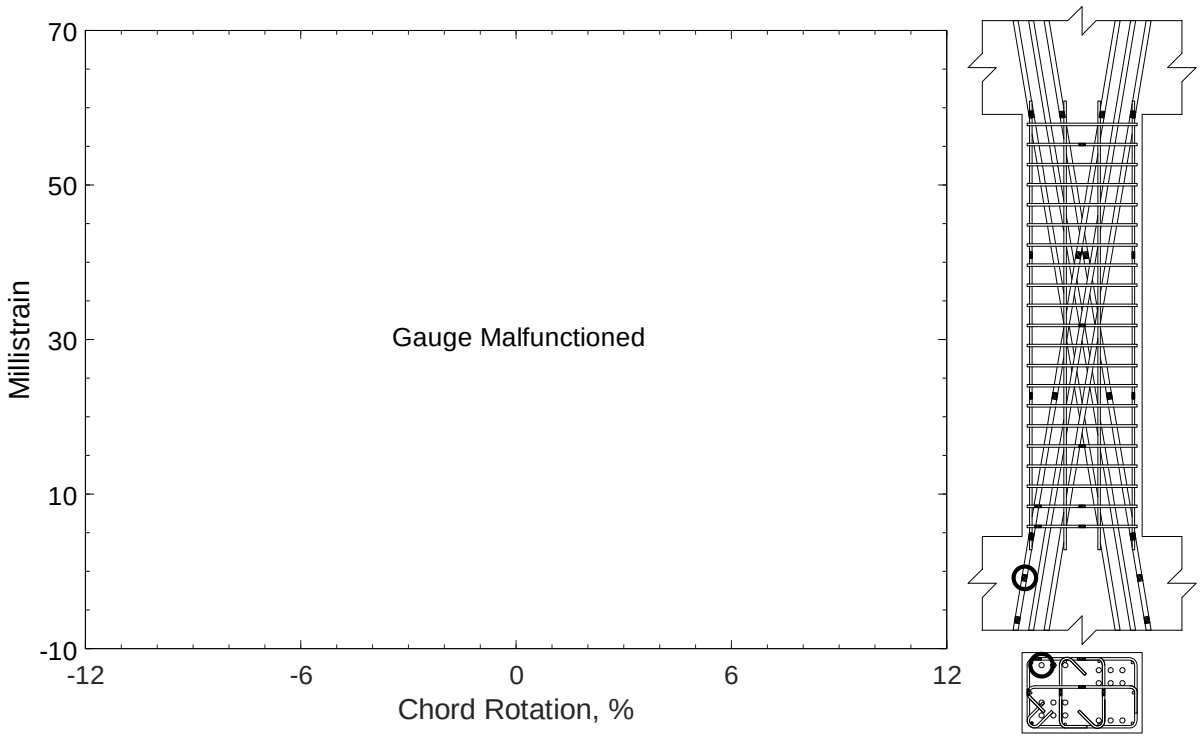

Figure 493 – Measured strain in diagonal bar of D100-3.5, strain gauge D3

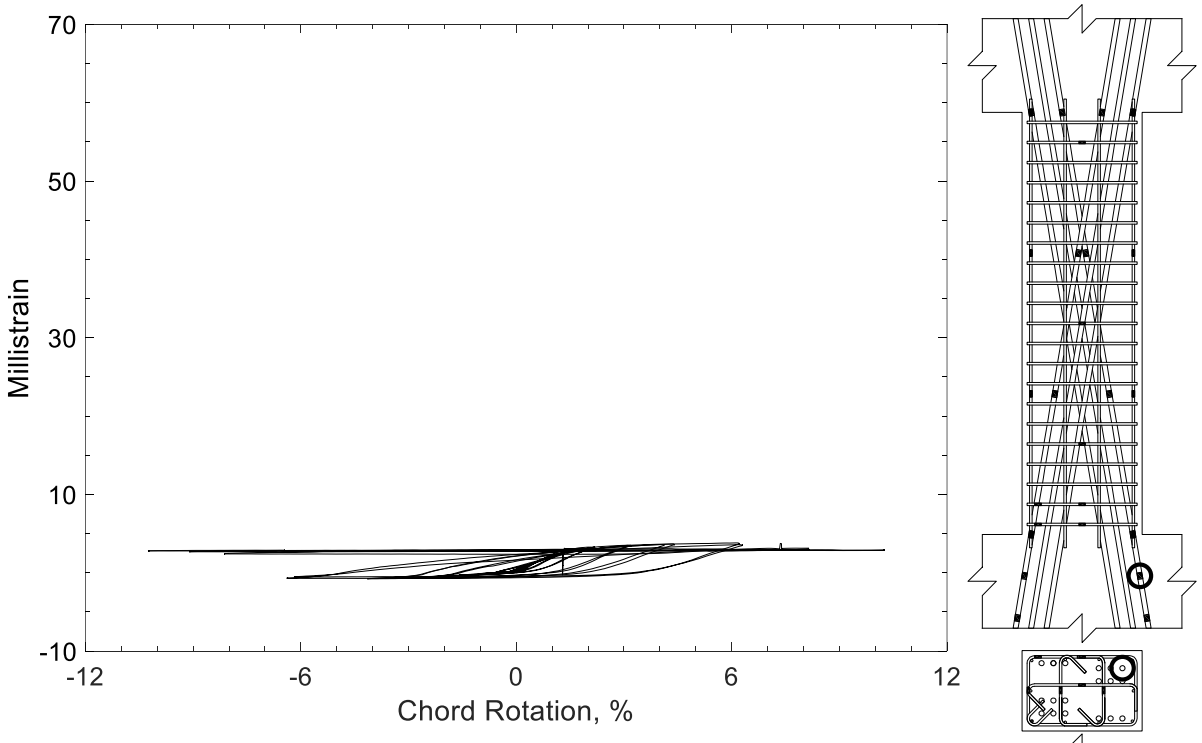

Figure 494 – Measured strain in diagonal bar of D100-3.5, strain gauge D4

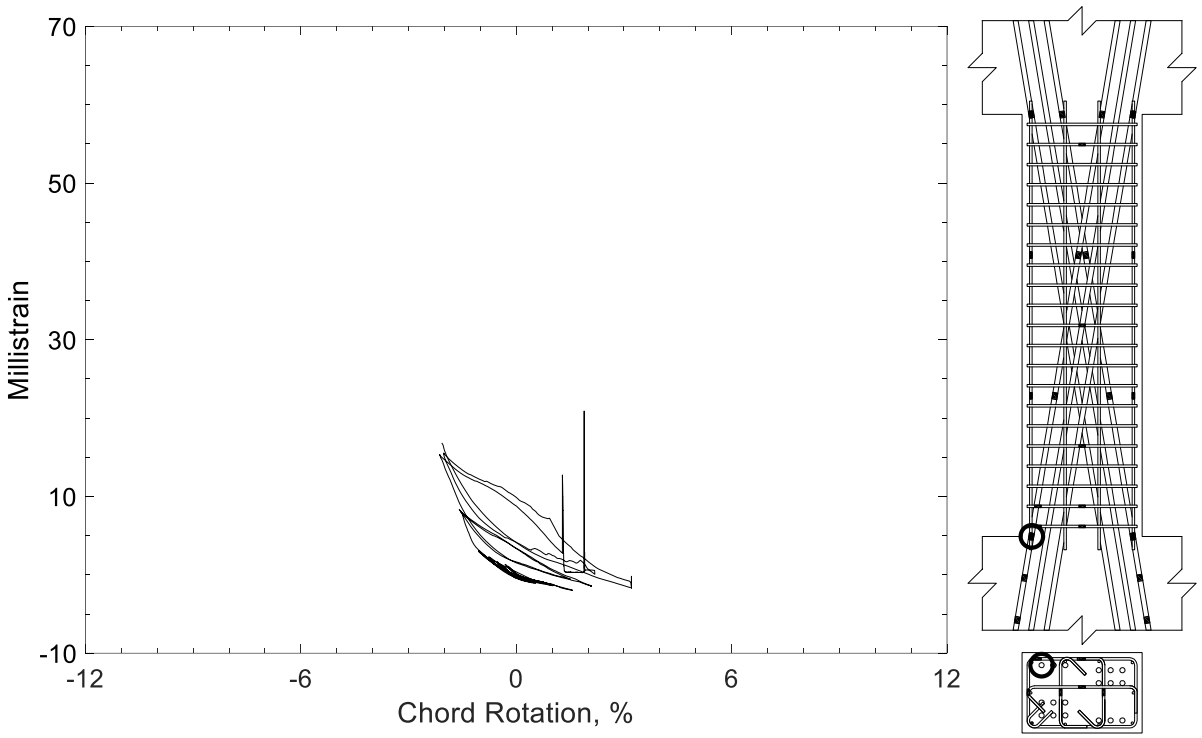

Figure 495 – Measured strain in diagonal bar of D100-3.5, strain gauge D5

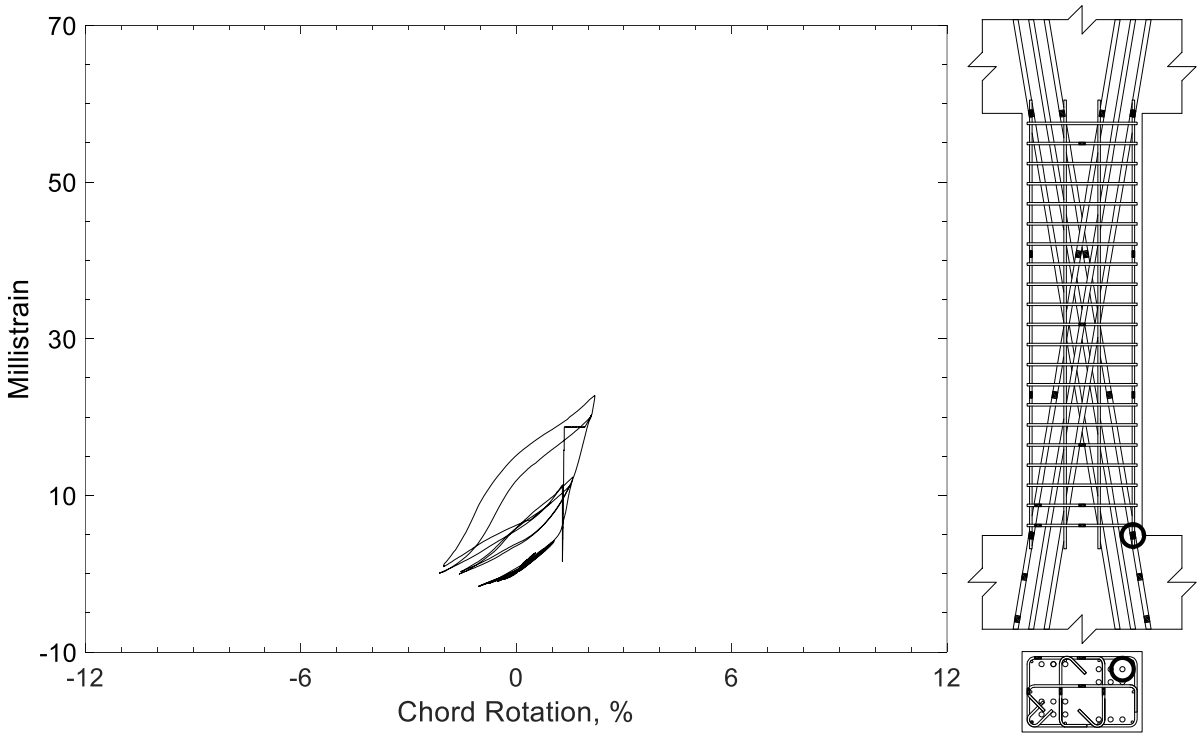

Figure 496 – Measured strain in diagonal bar of D100-3.5, strain gauge D6

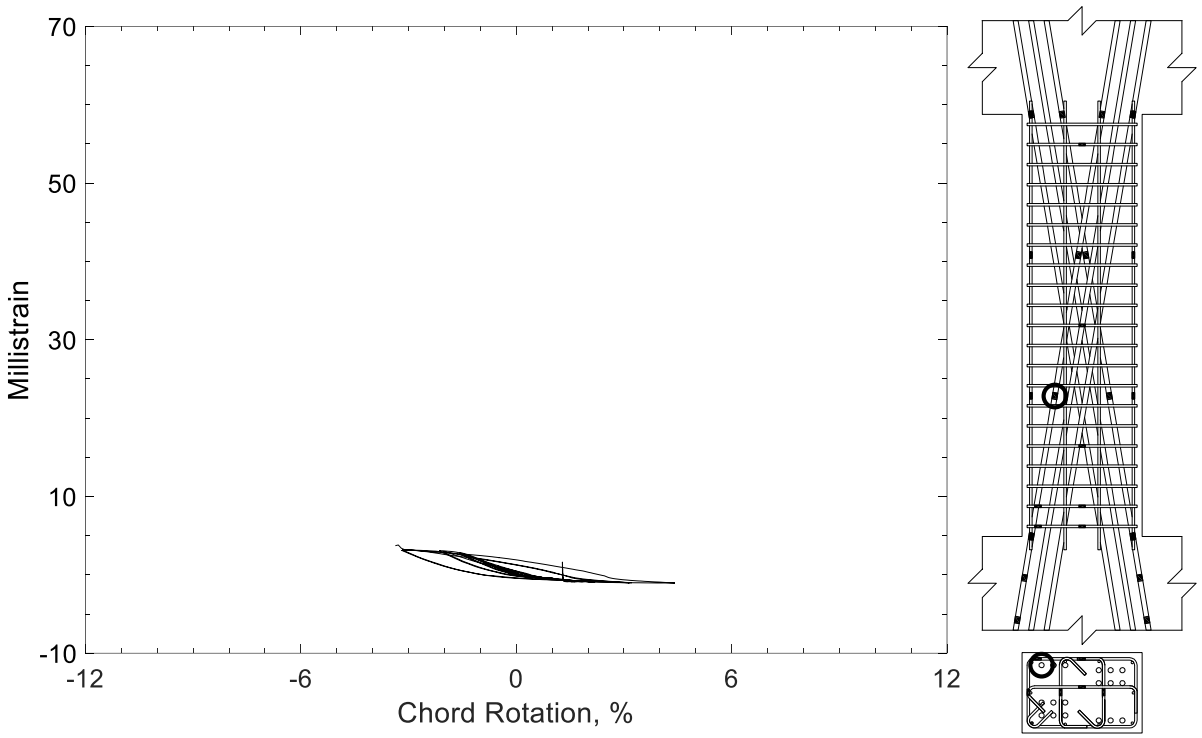

Figure 497 – Measured strain in diagonal bar of D100-3.5, strain gauge D7

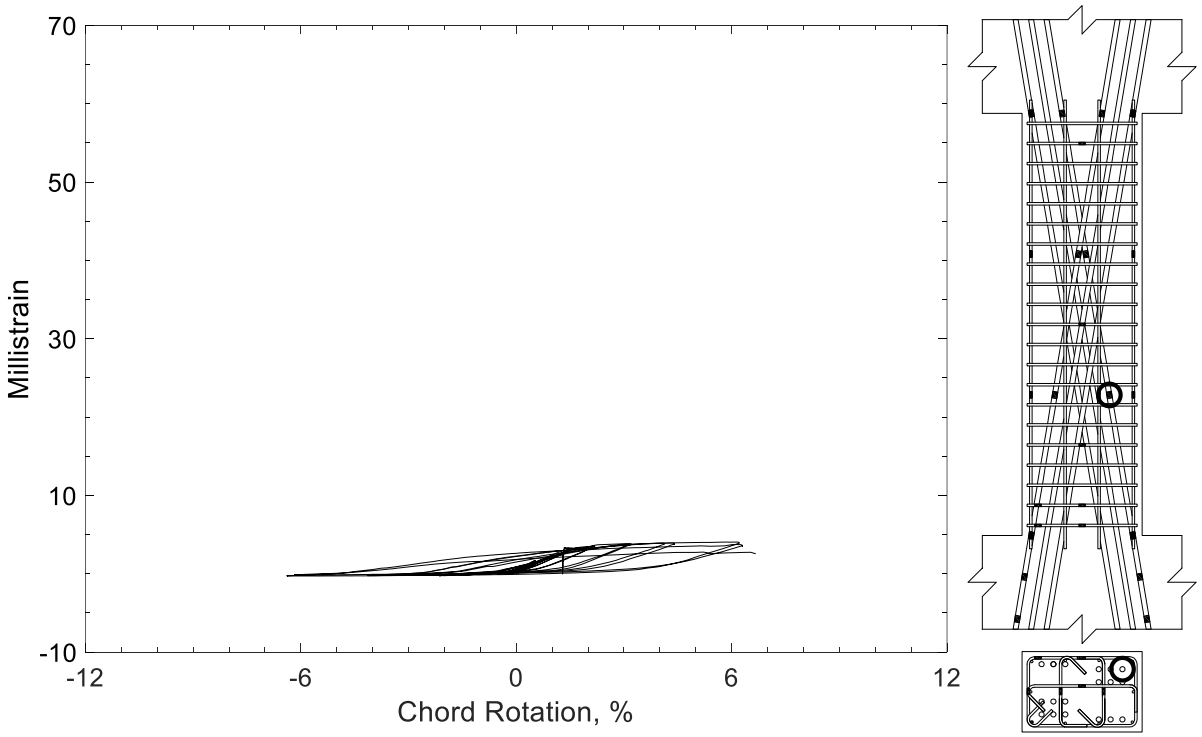

Figure 498 – Measured strain in diagonal bar of D100-3.5, strain gauge D8

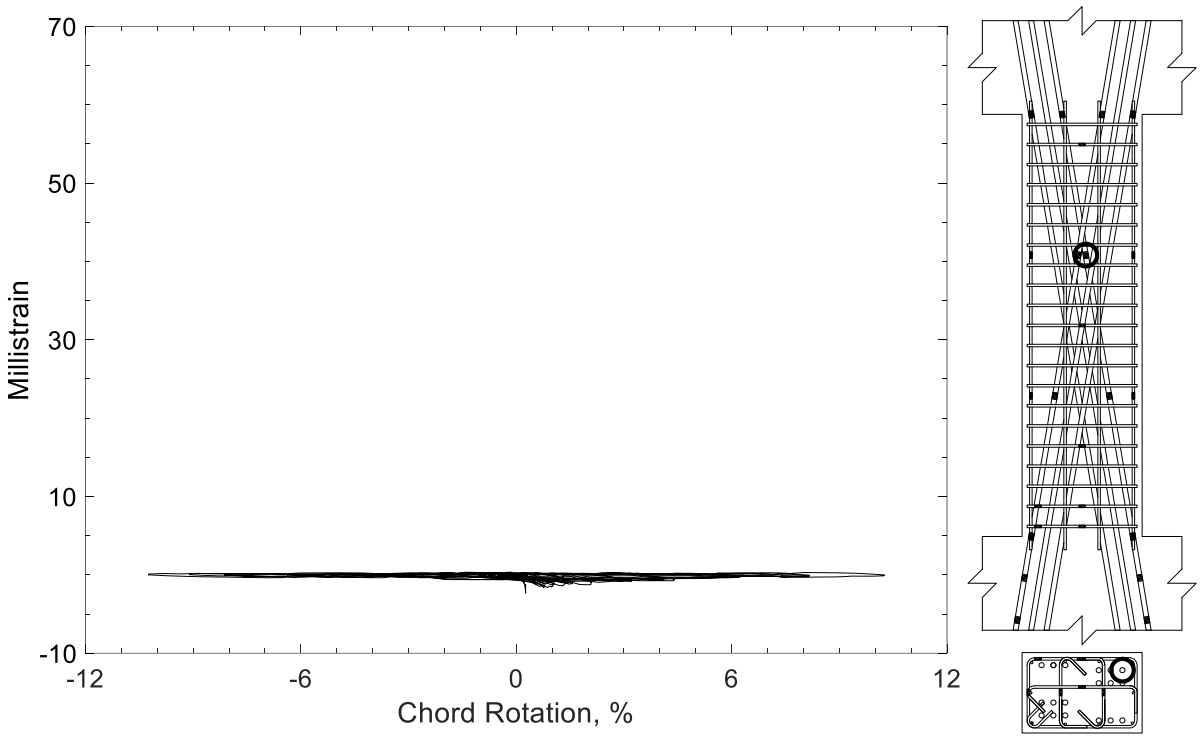

Figure 499 – Measured strain in diagonal bar of D100-3.5, strain gauge D9

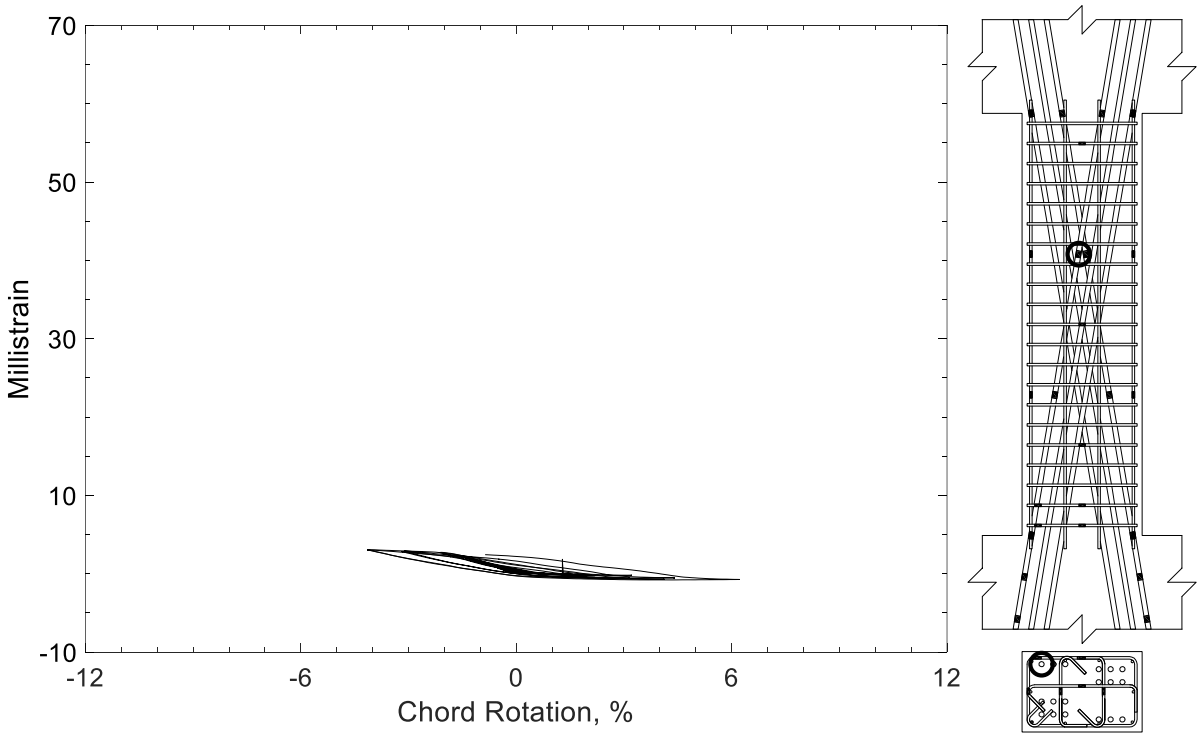

Figure 500 – Measured strain in diagonal bar of D100-3.5, strain gauge D10

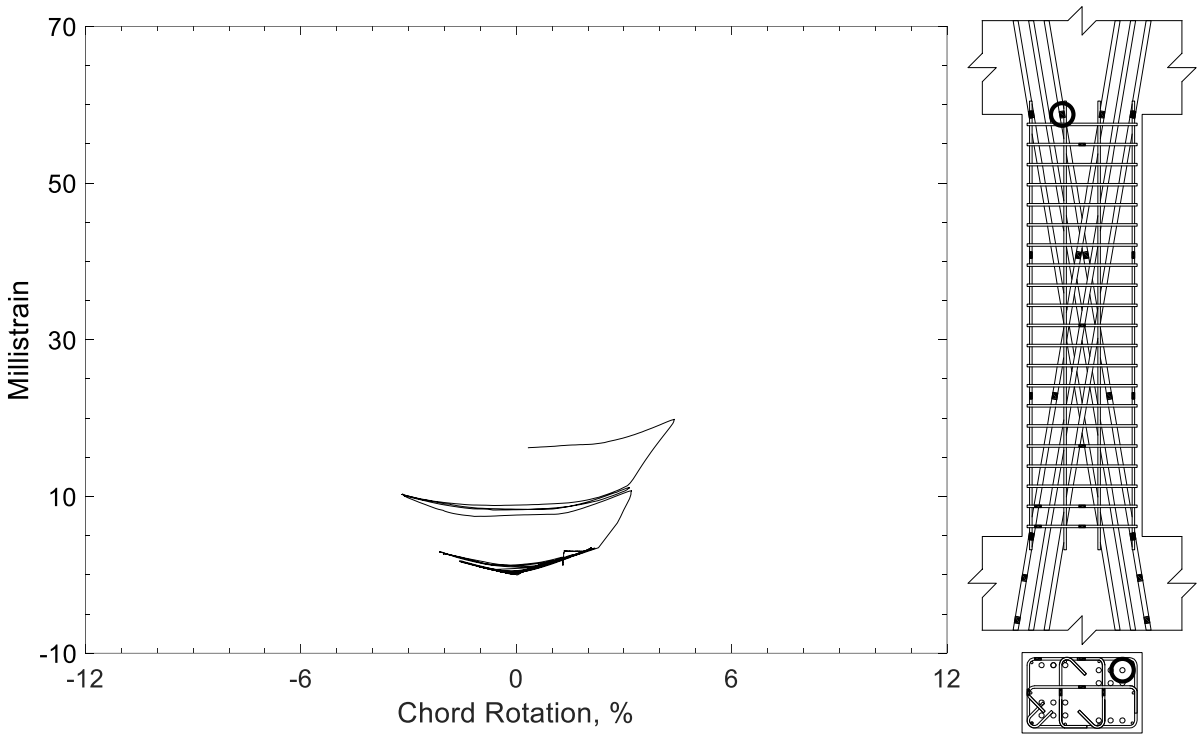

Figure 501 – Measured strain in diagonal bar of D100-3.5, strain gauge D11

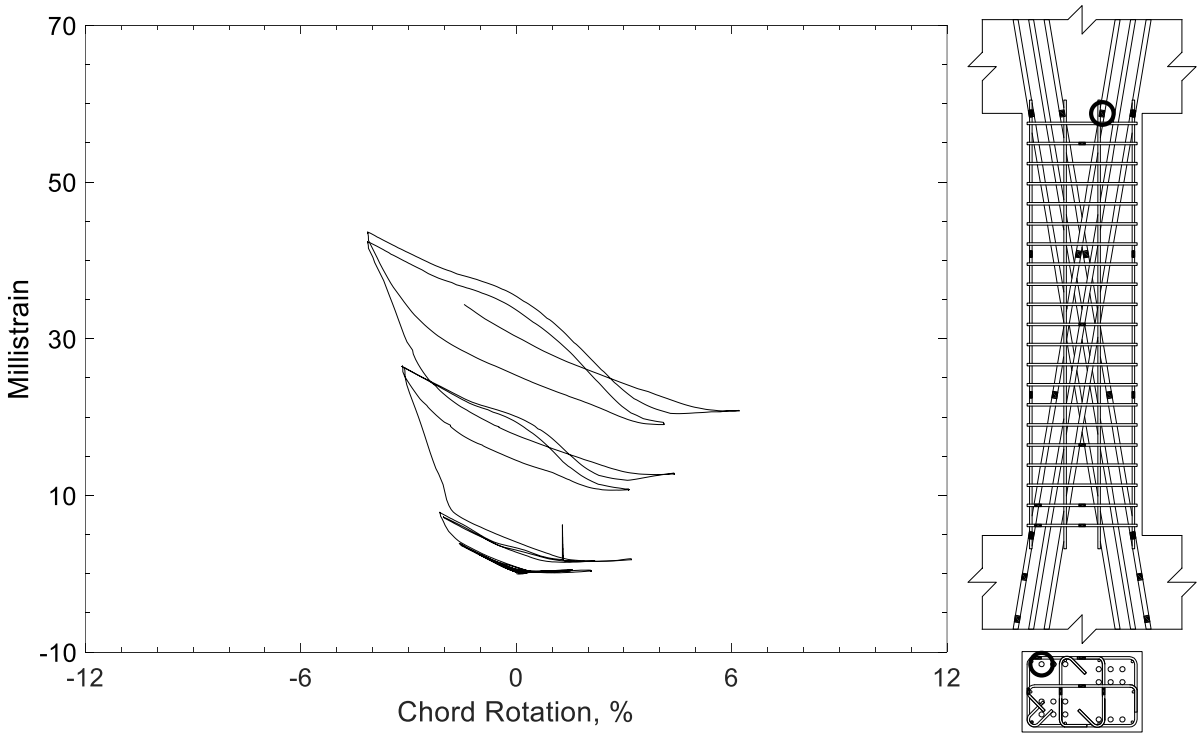

Figure 502 – Measured strain in diagonal bar of D100-3.5, strain gauge D12

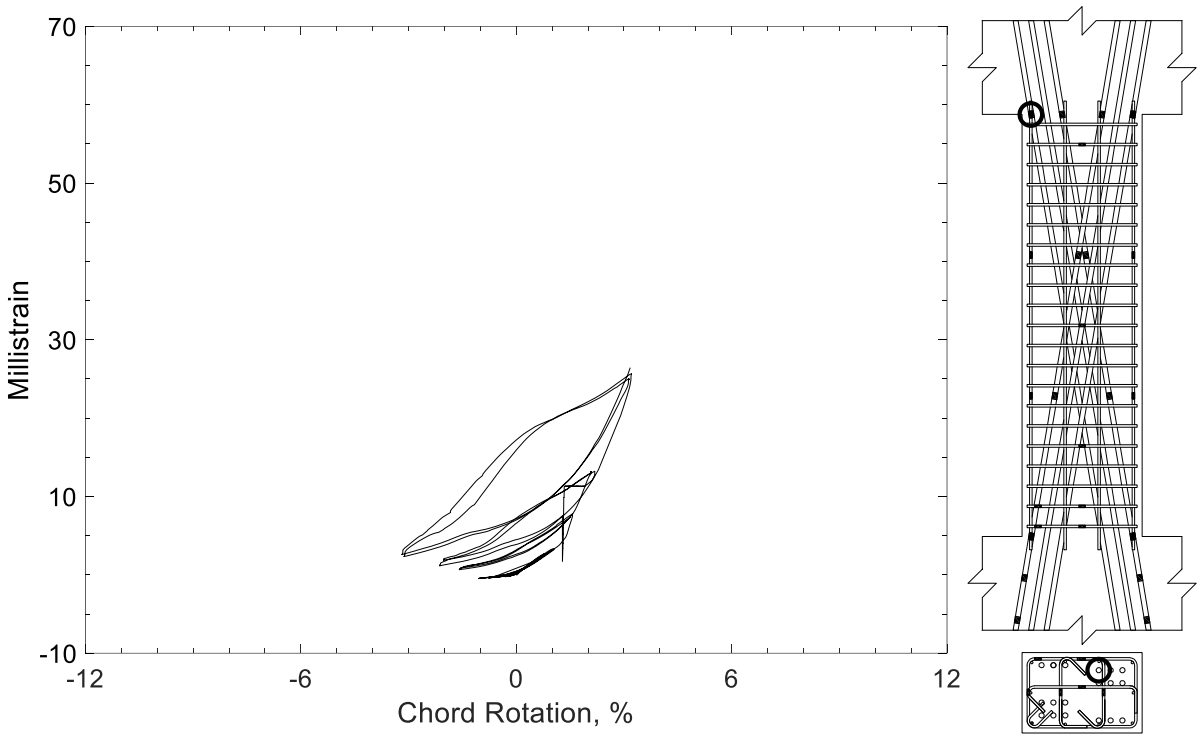

Figure 503 – Measured strain in diagonal bar of D100-3.5, strain gauge D13

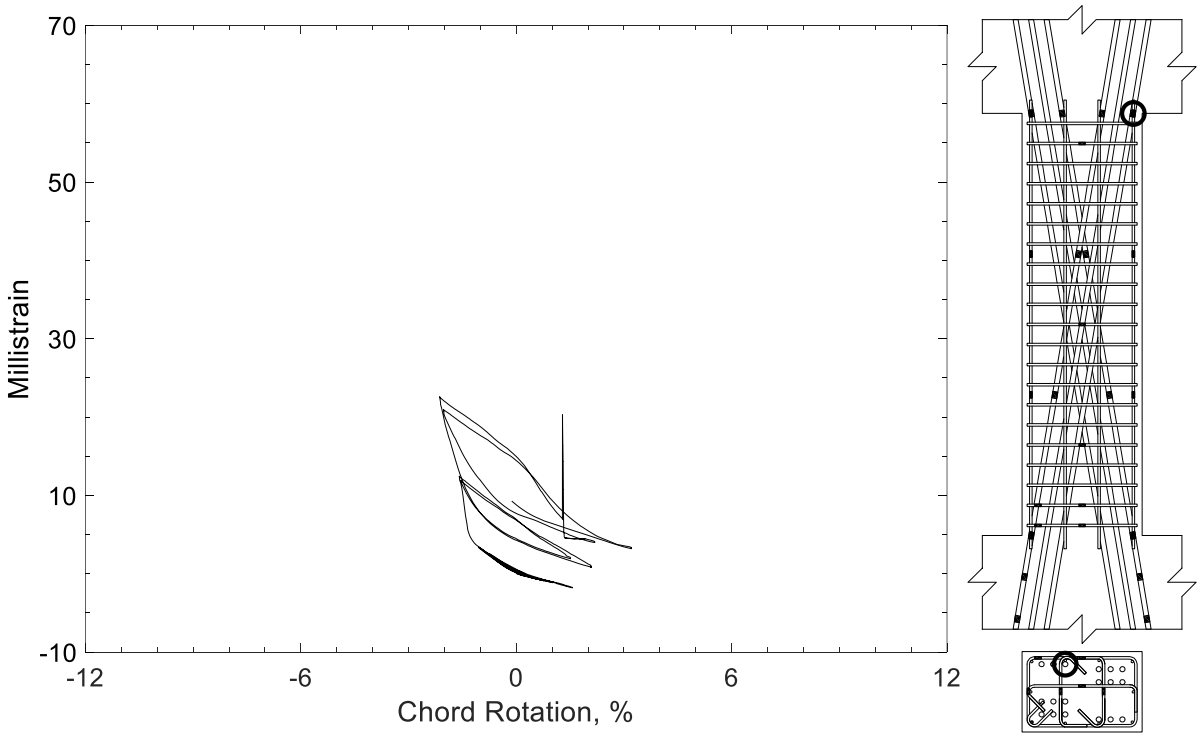

Figure 504 – Measured strain in diagonal bar of D100-3.5, strain gauge D14

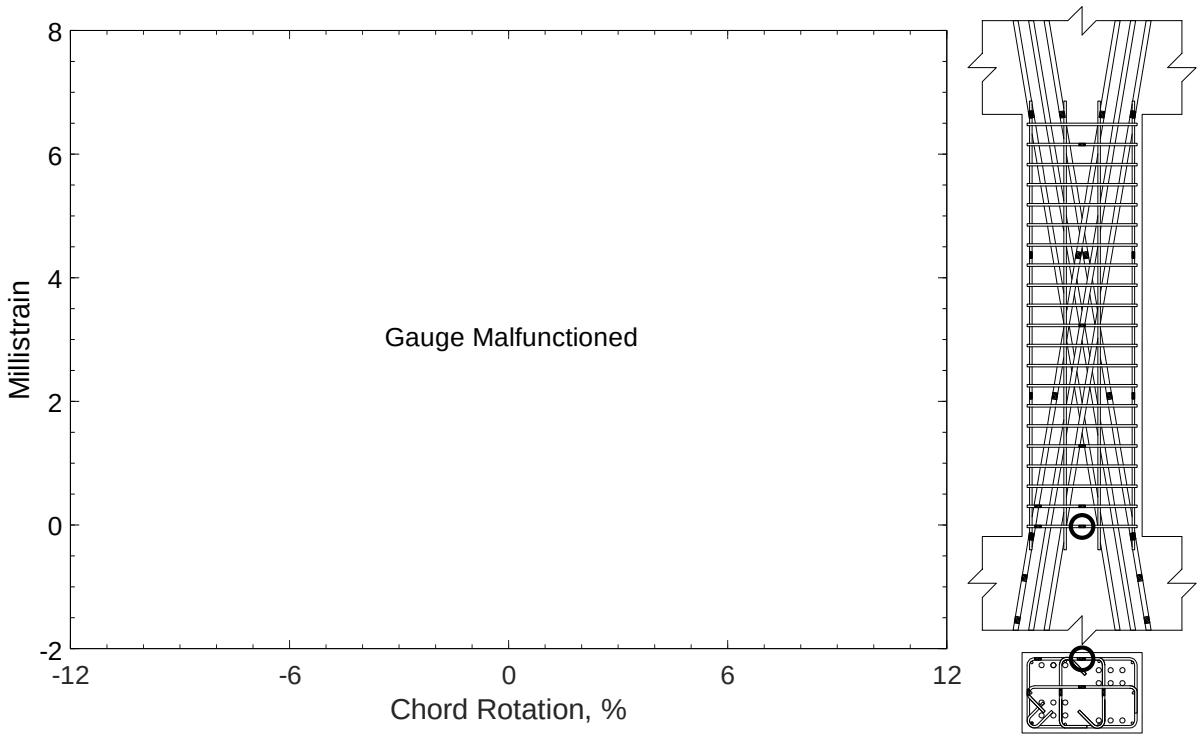

Figure 505 – Measured strain in closed stirrup of D100-3.5, strain gauge S1

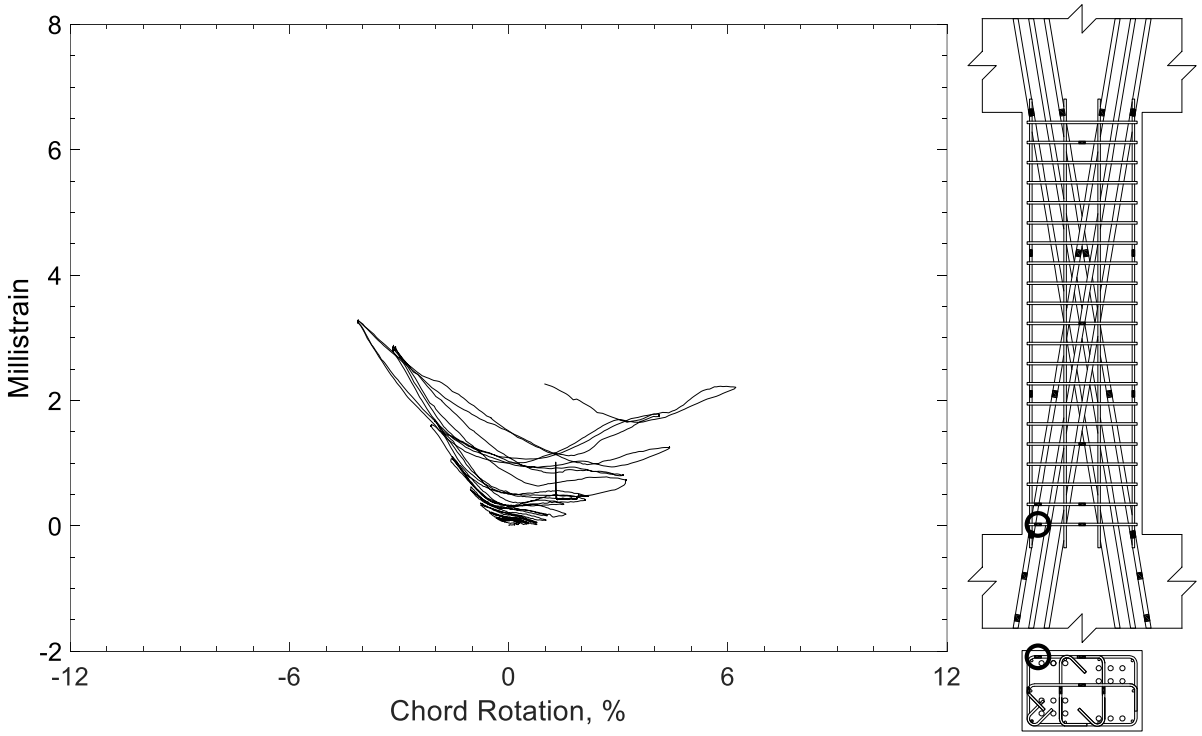

Figure 506 – Measured strain in closed stirrup of D100-3.5, strain gauge S2

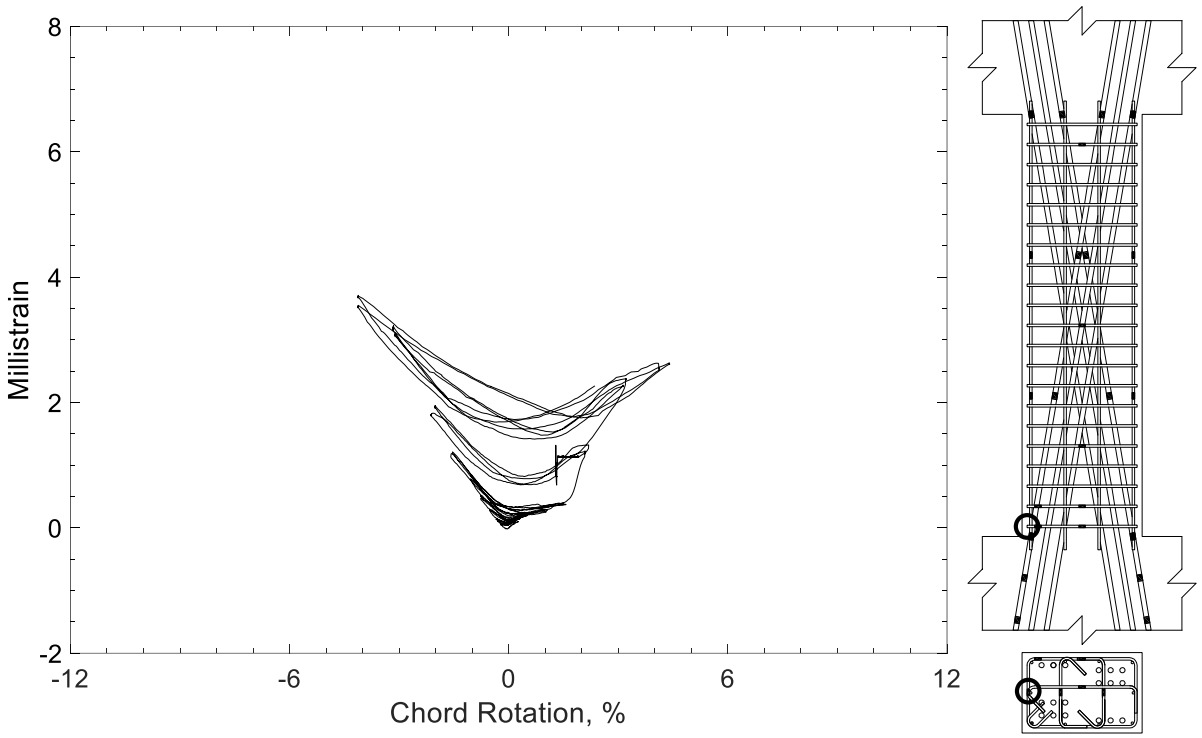

Figure 507 – Measured strain in closed stirrup of D100-3.5, strain gauge S3

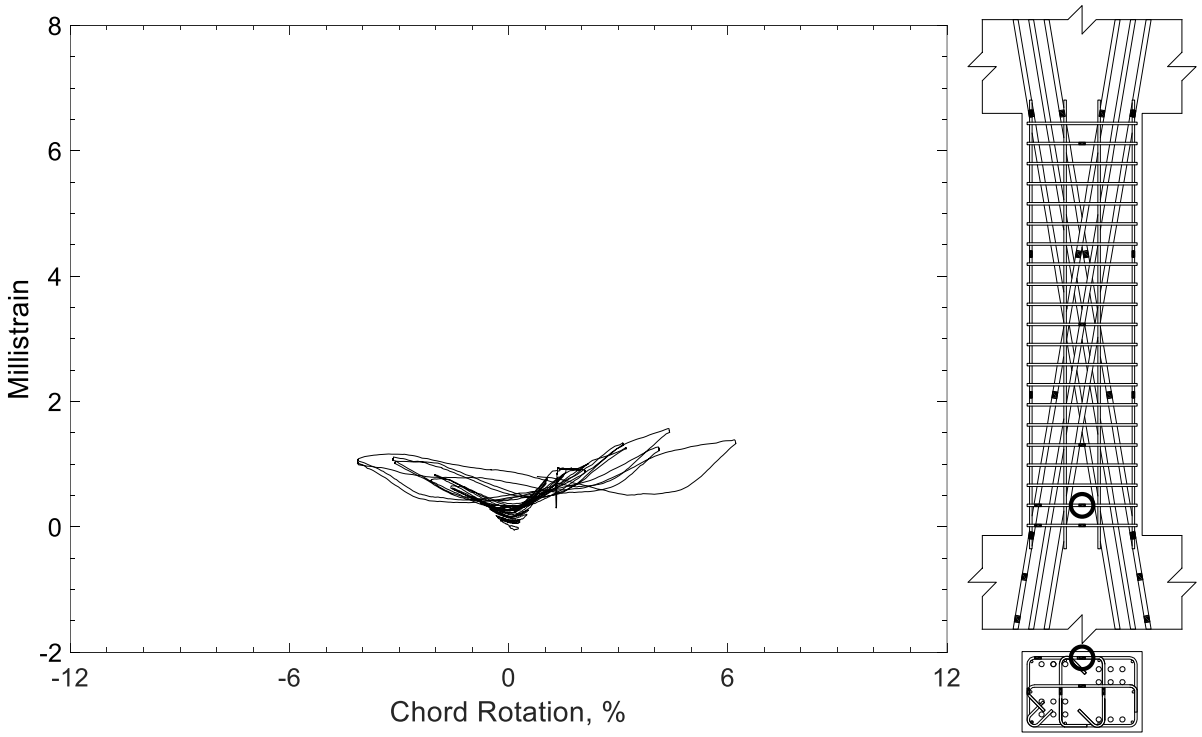

Figure 508 – Measured strain in closed stirrup of D100-3.5, strain gauge S4

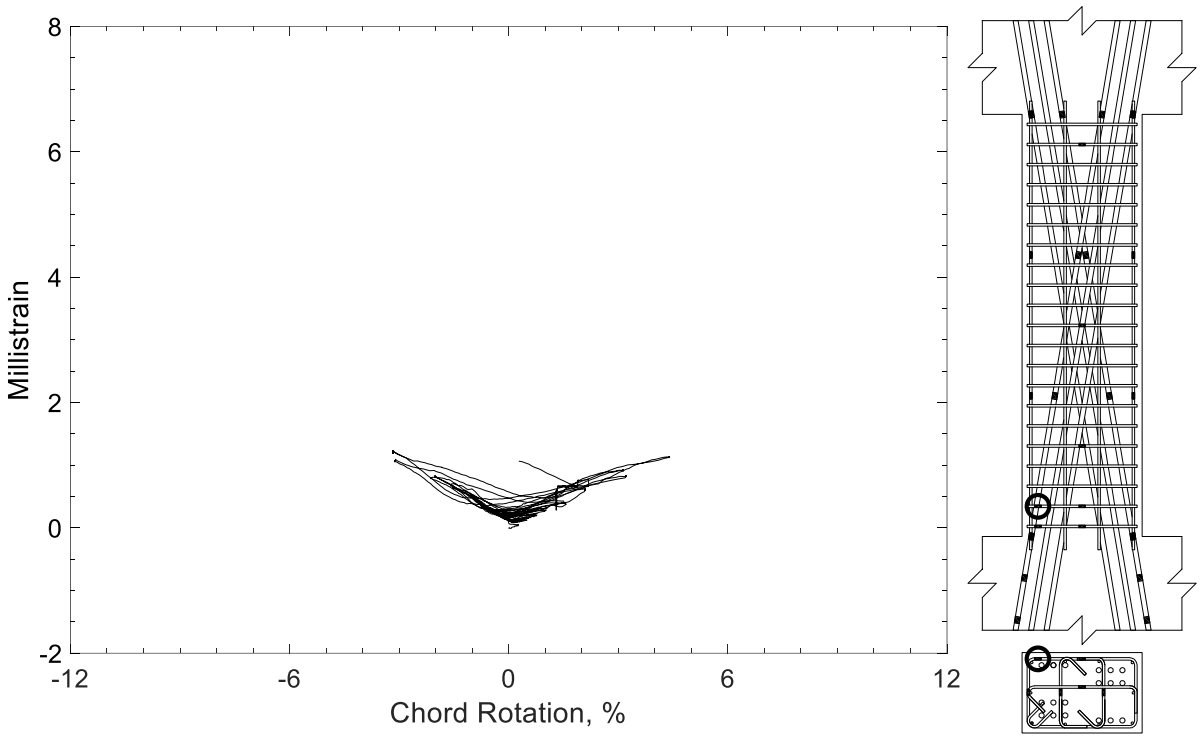

Figure 509 – Measured strain in closed stirrup of D100-3.5, strain gauge S5

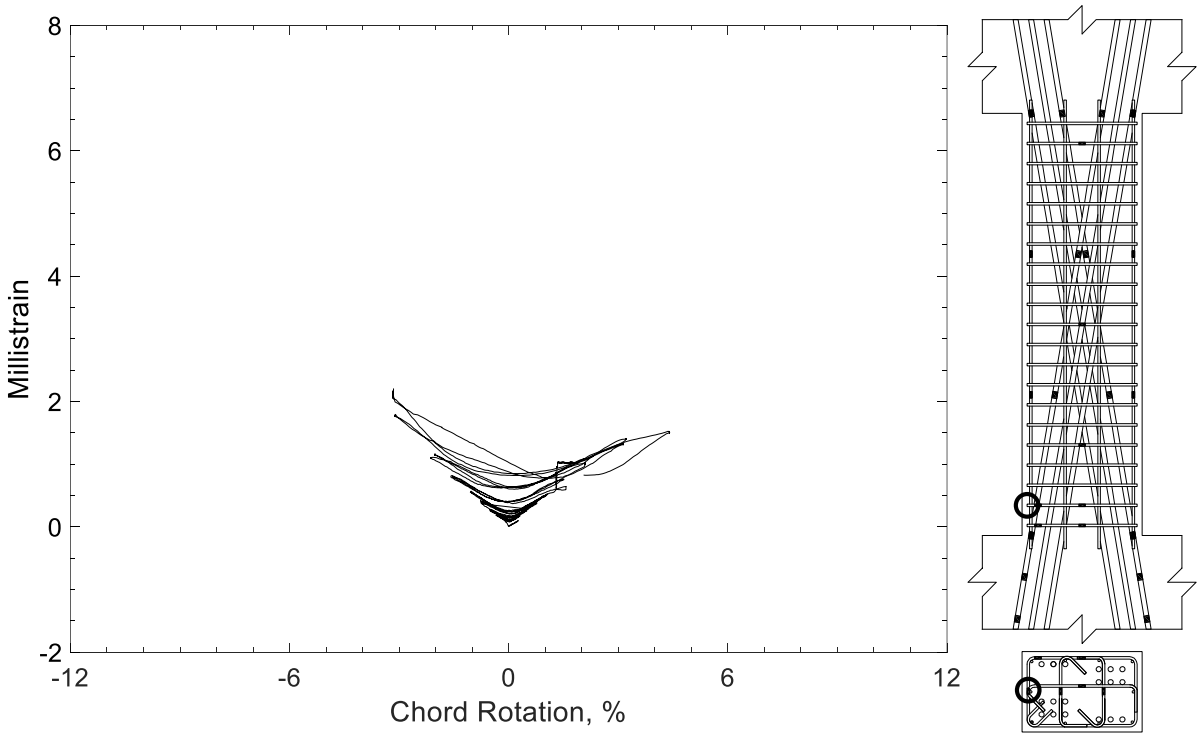

Figure 510 – Measured strain in closed stirrup of D100-3.5, strain gauge S6

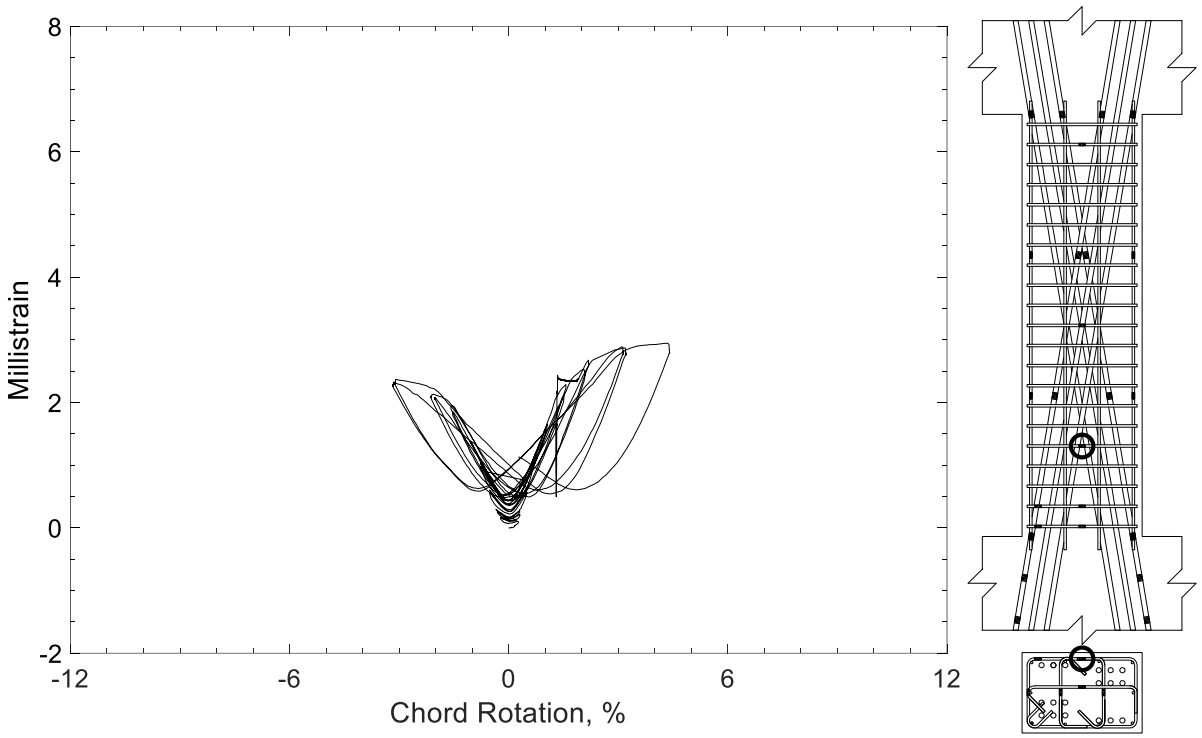

Figure 511 – Measured strain in closed stirrup of D100-3.5, strain gauge S7

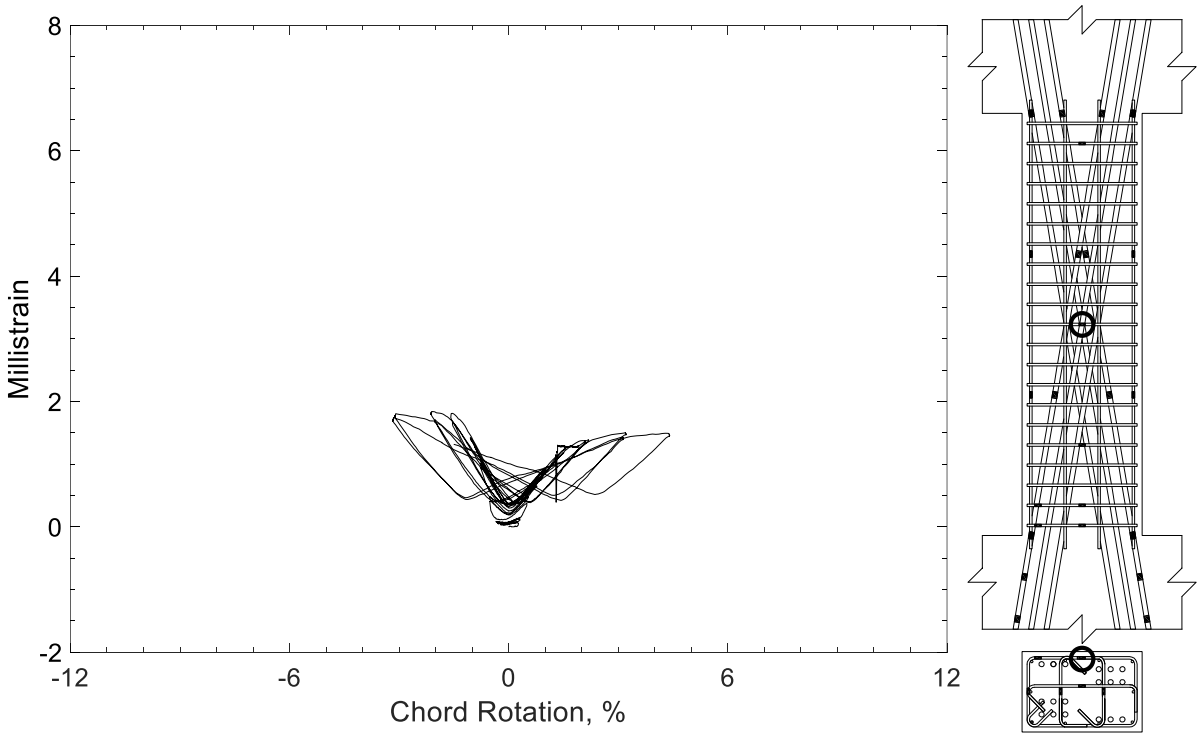

Figure 512 – Measured strain in closed stirrup of D100-3.5, strain gauge S8

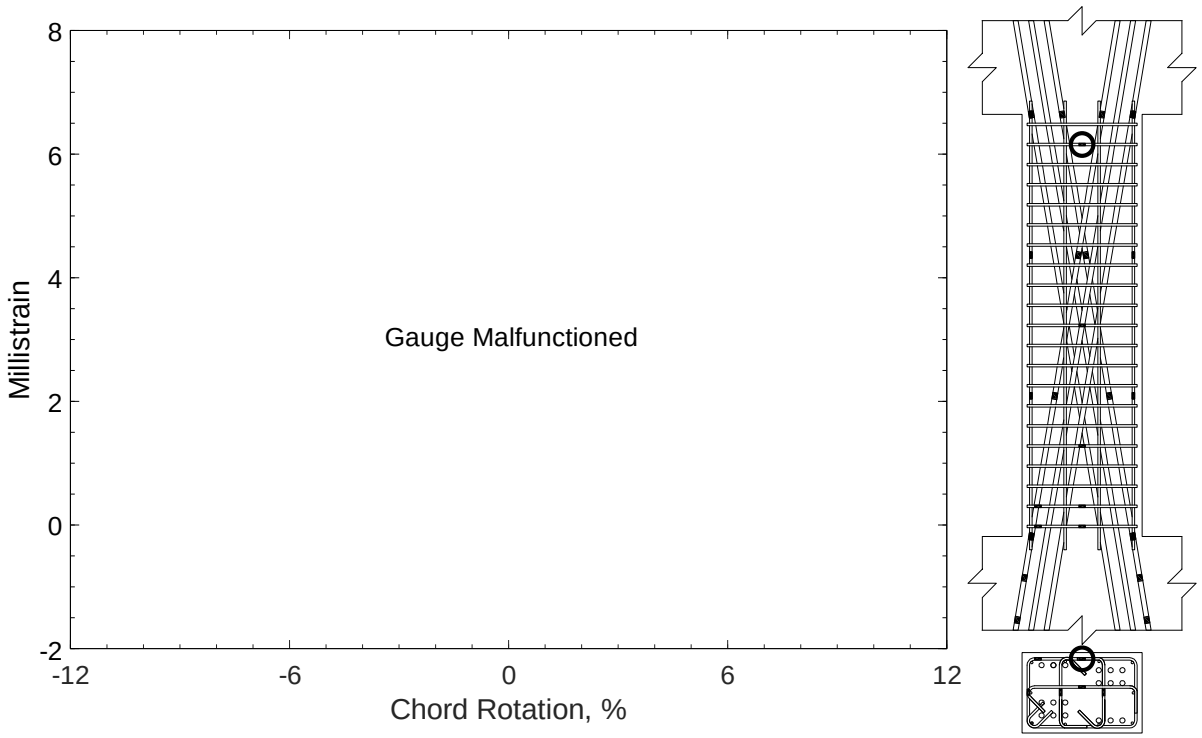

Figure 513 – Measured strain in closed stirrup of D100-3.5, strain gauge S9

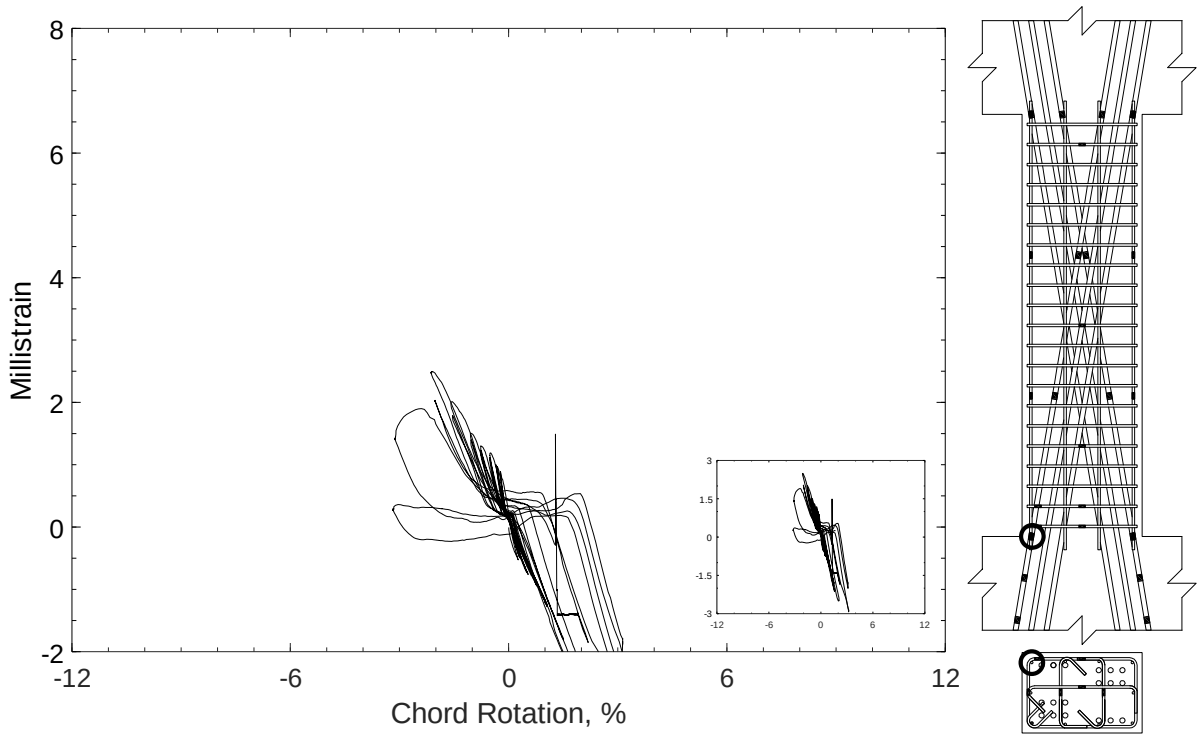

Figure 514 – Measured strain in parallel bar of D100-3.5, strain gauge H1

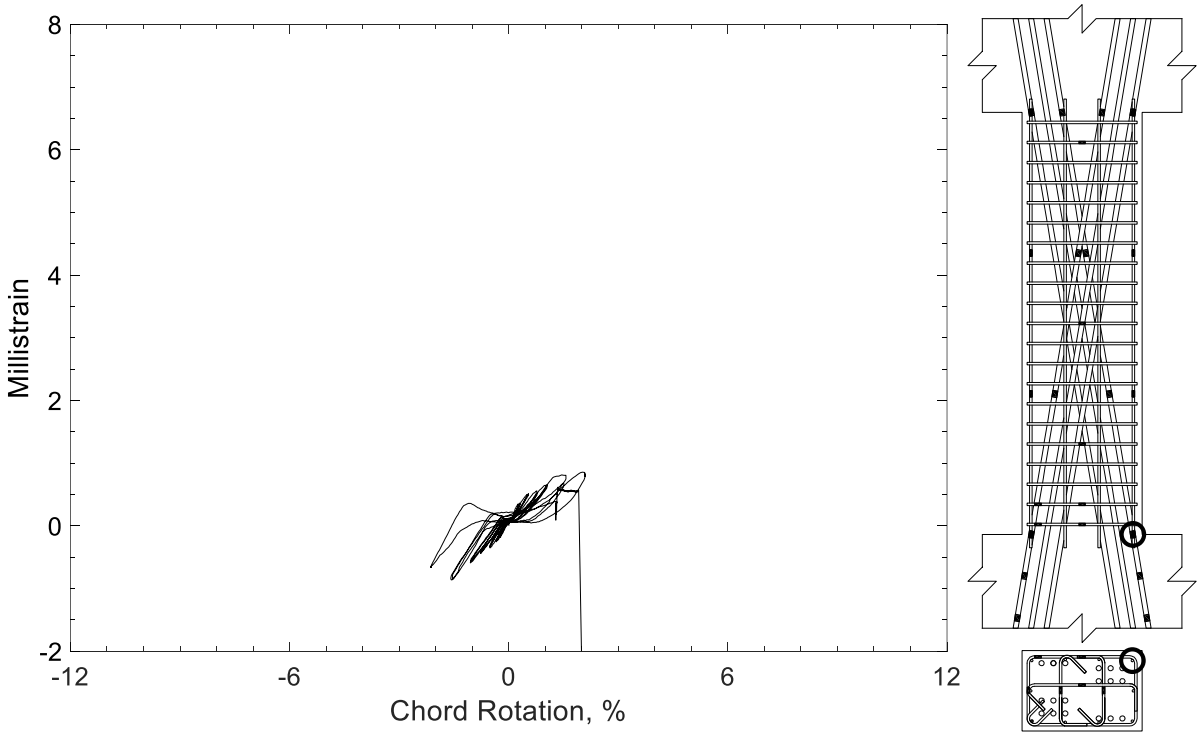

Figure 515 – Measured strain in parallel bar of D100-3.5, strain gauge H2

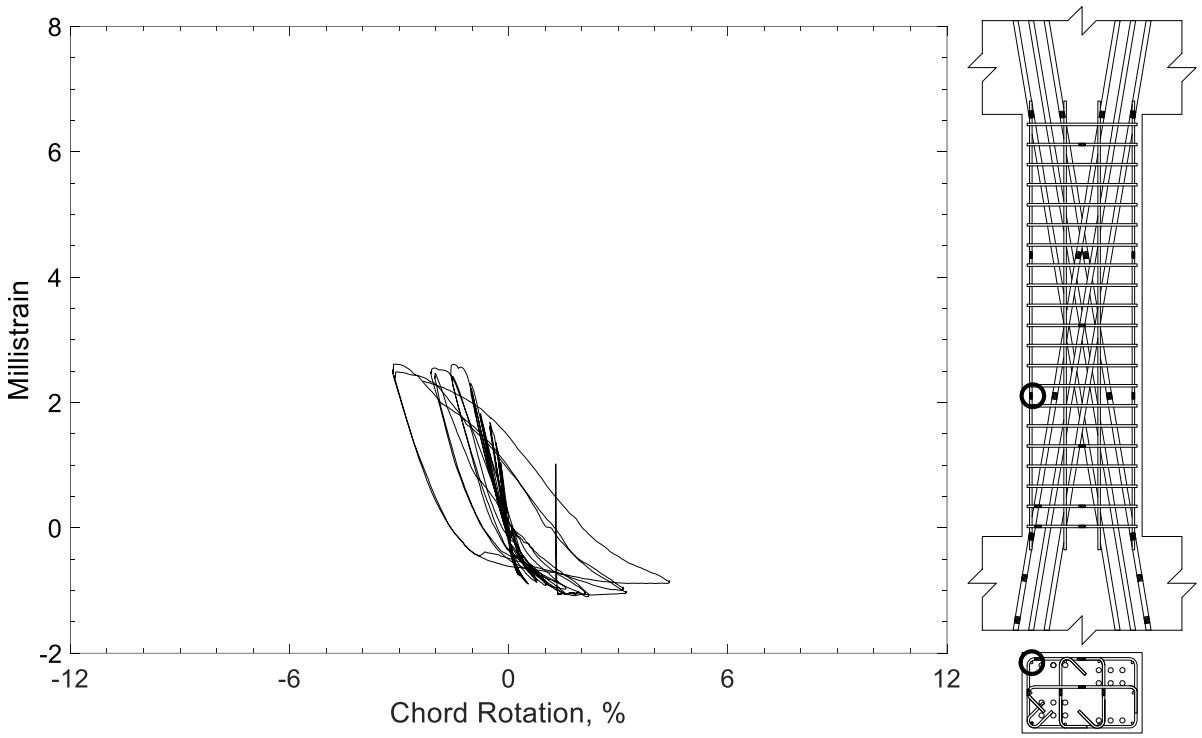

Figure 516 – Measured strain in parallel bar of D100-3.5, strain gauge H3

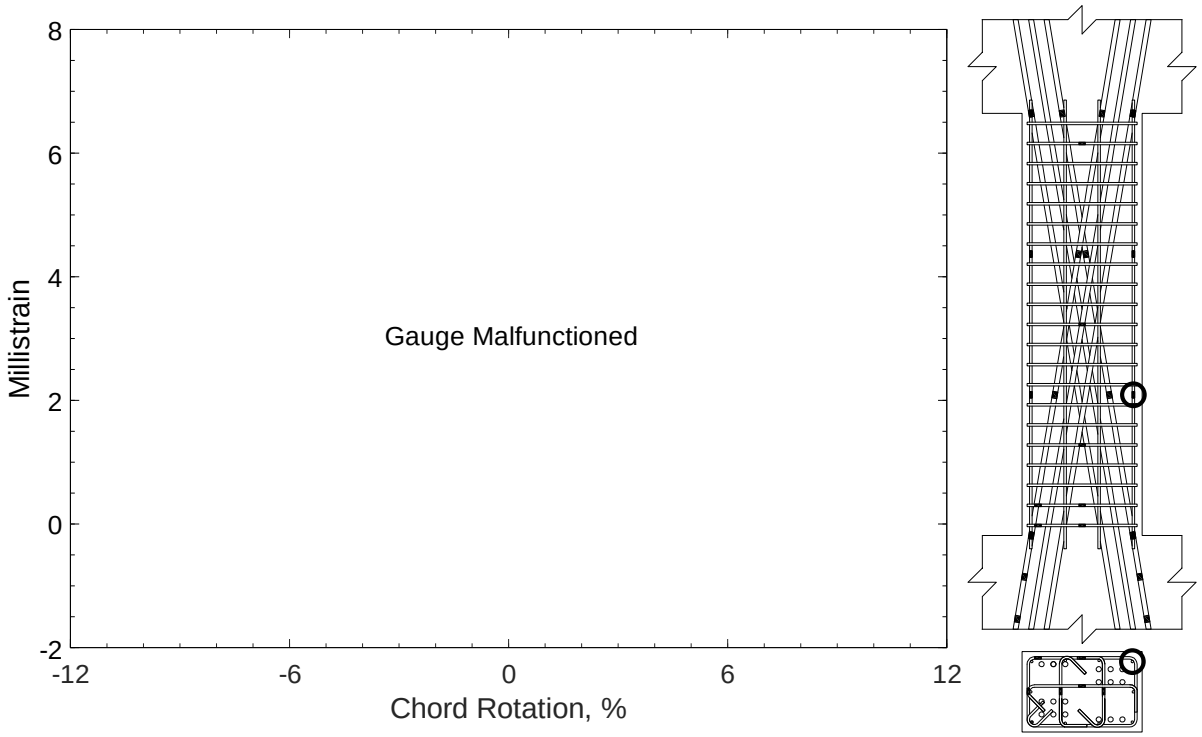

Figure 517 – Measured strain in parallel bar of D100-3.5, strain gauge H4

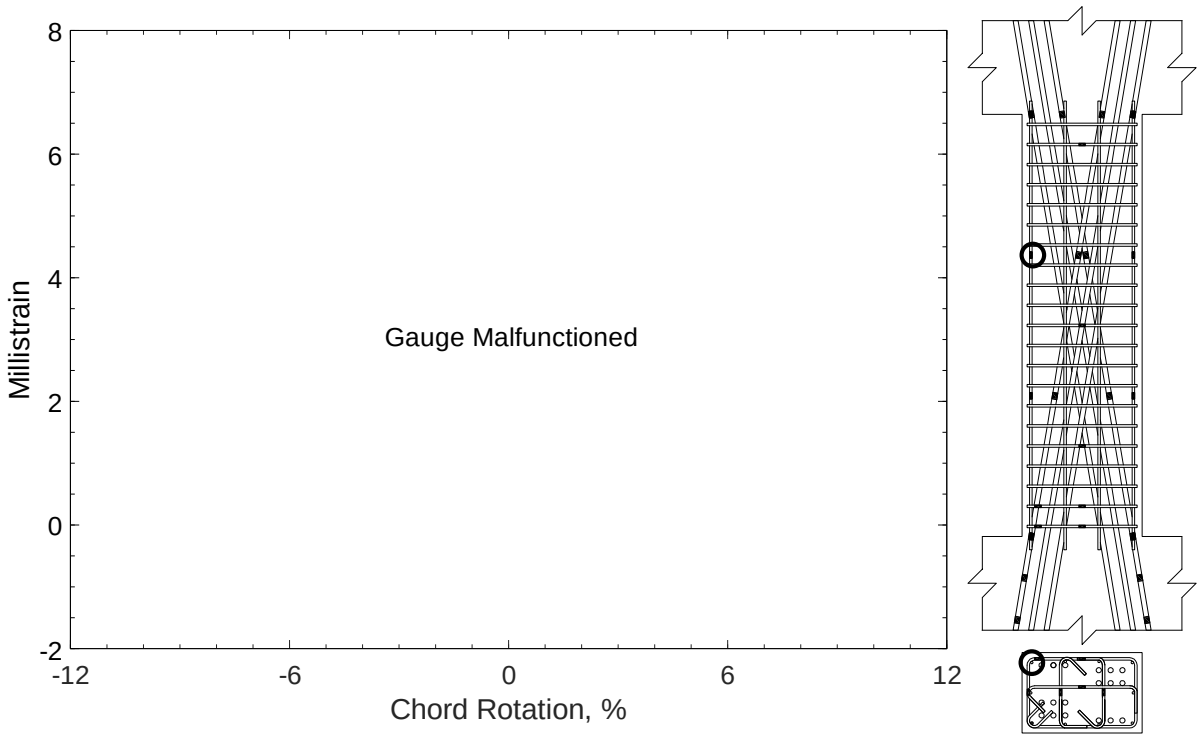

Figure 518 – Measured strain in parallel bar of D100-3.5, strain gauge H5

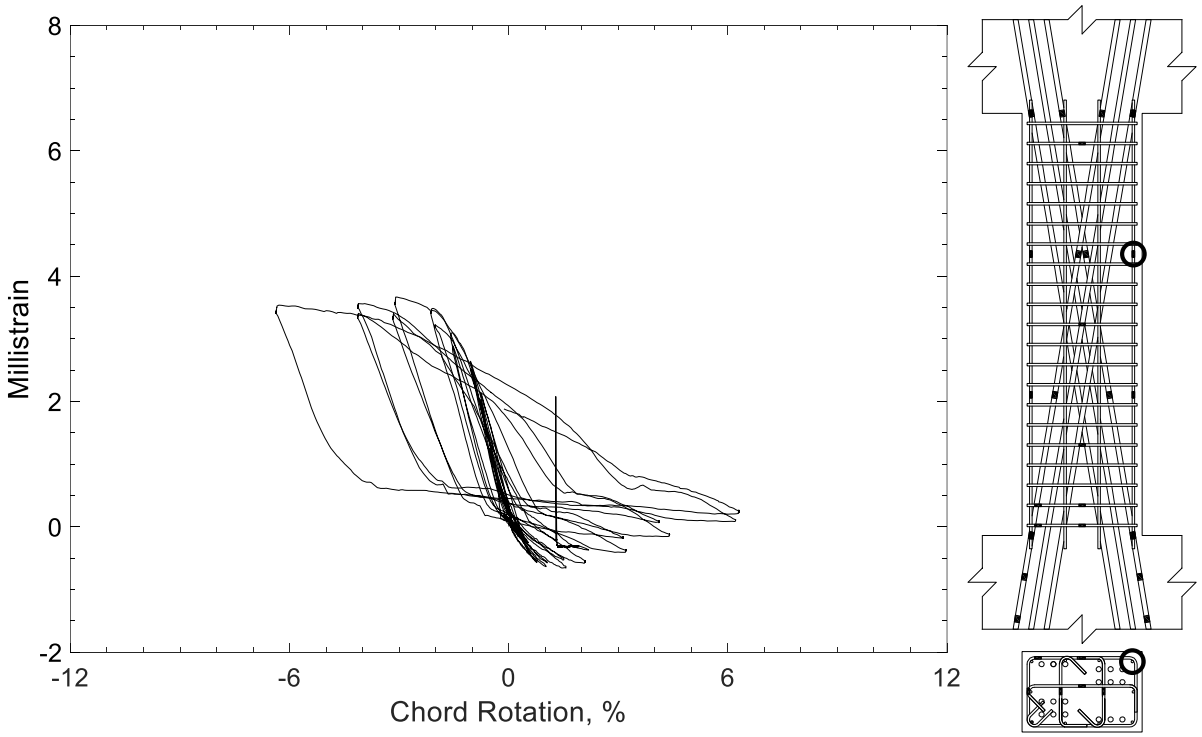

Figure 519 – Measured strain in parallel bar of D100-3.5, strain gauge H6

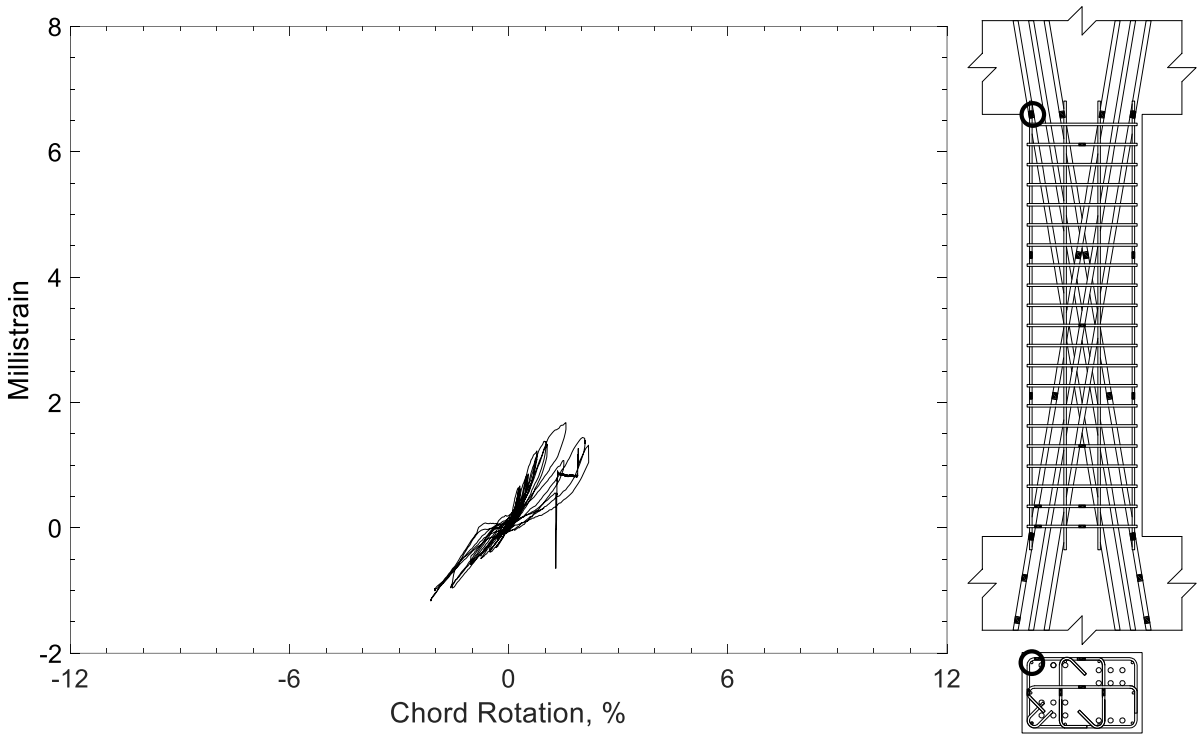

Figure 520 – Measured strain in parallel bar of D100-3.5, strain gauge H7

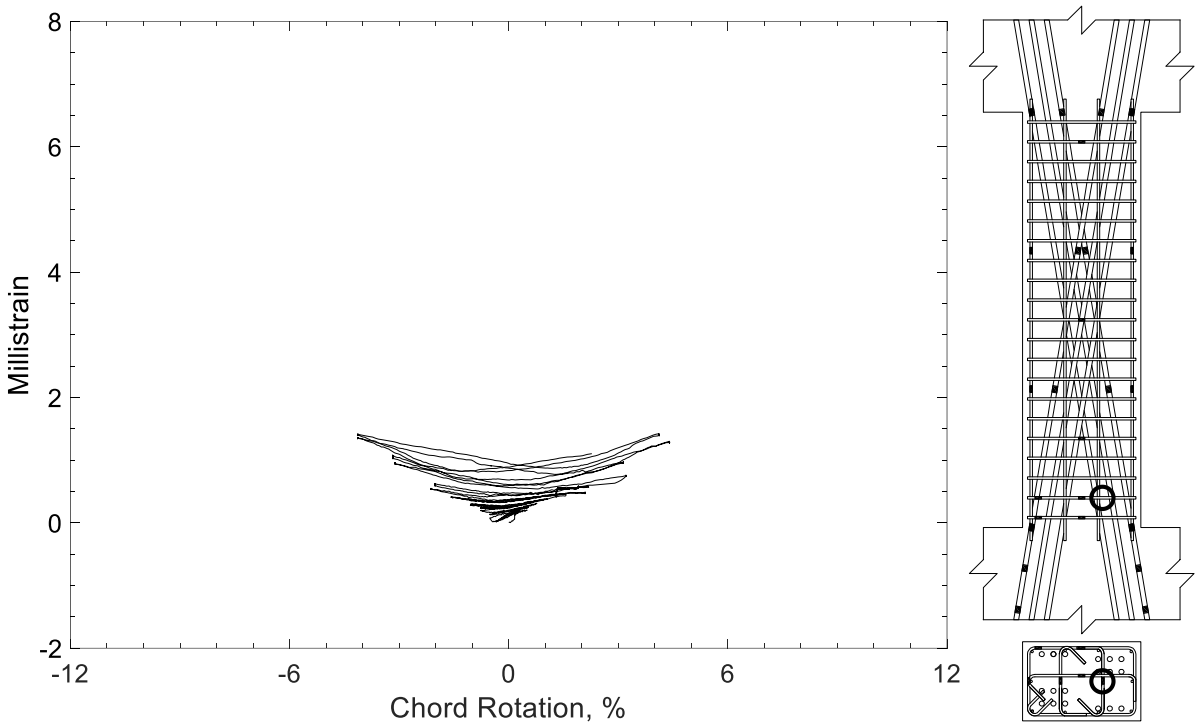

Figure 521 – Measured strain in crosstie of D100-3.5, strain gauge T1

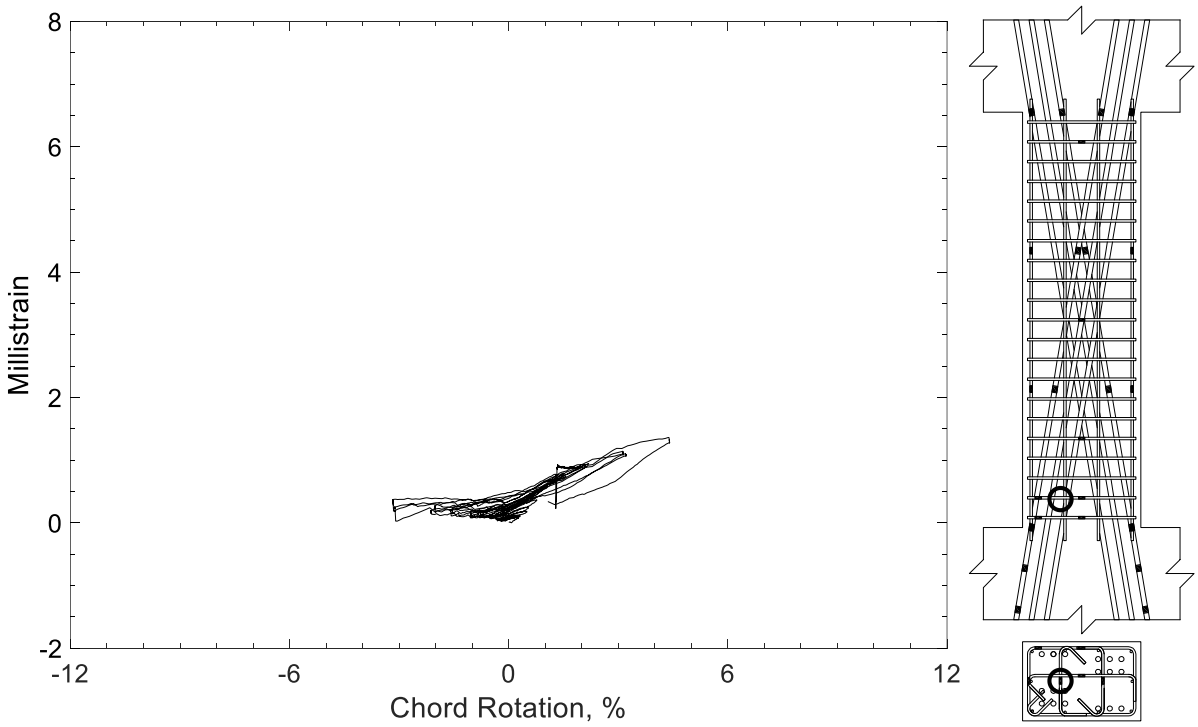

Figure 522 – Measured strain in crosstie of D100-3.5, strain gauge T2

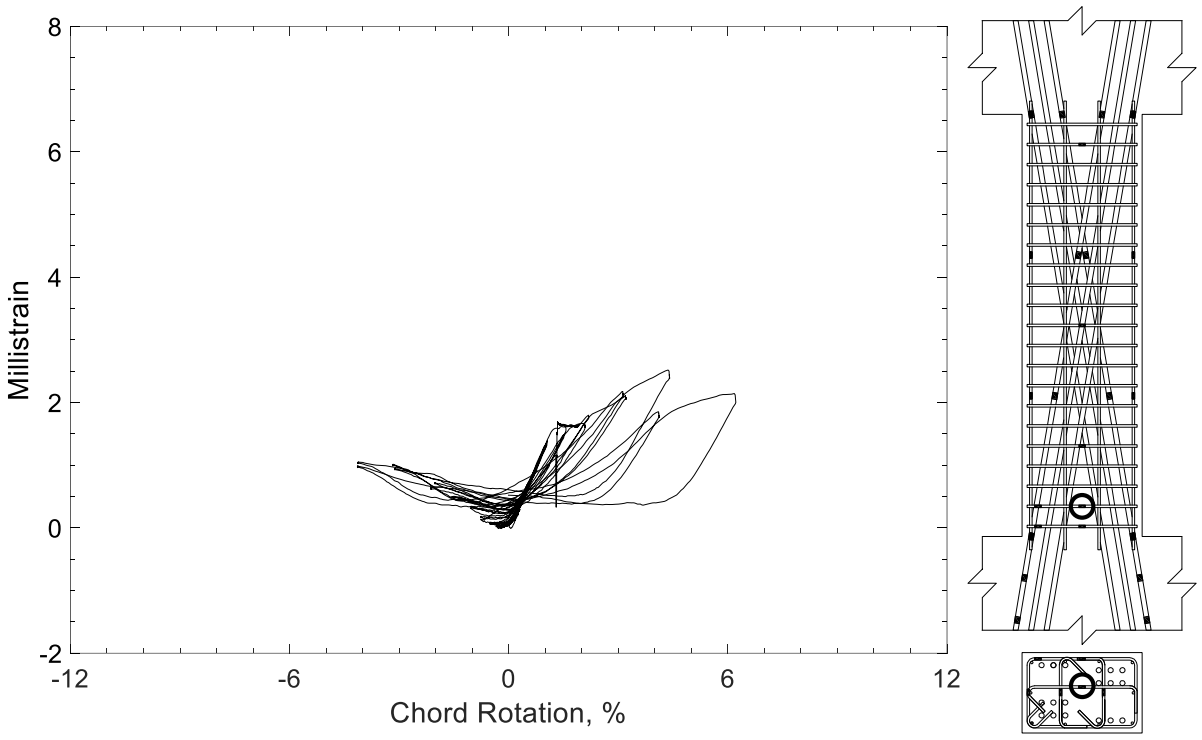

Figure 523 – Measured strain in crosstie of D100-3.5, strain gauge T3

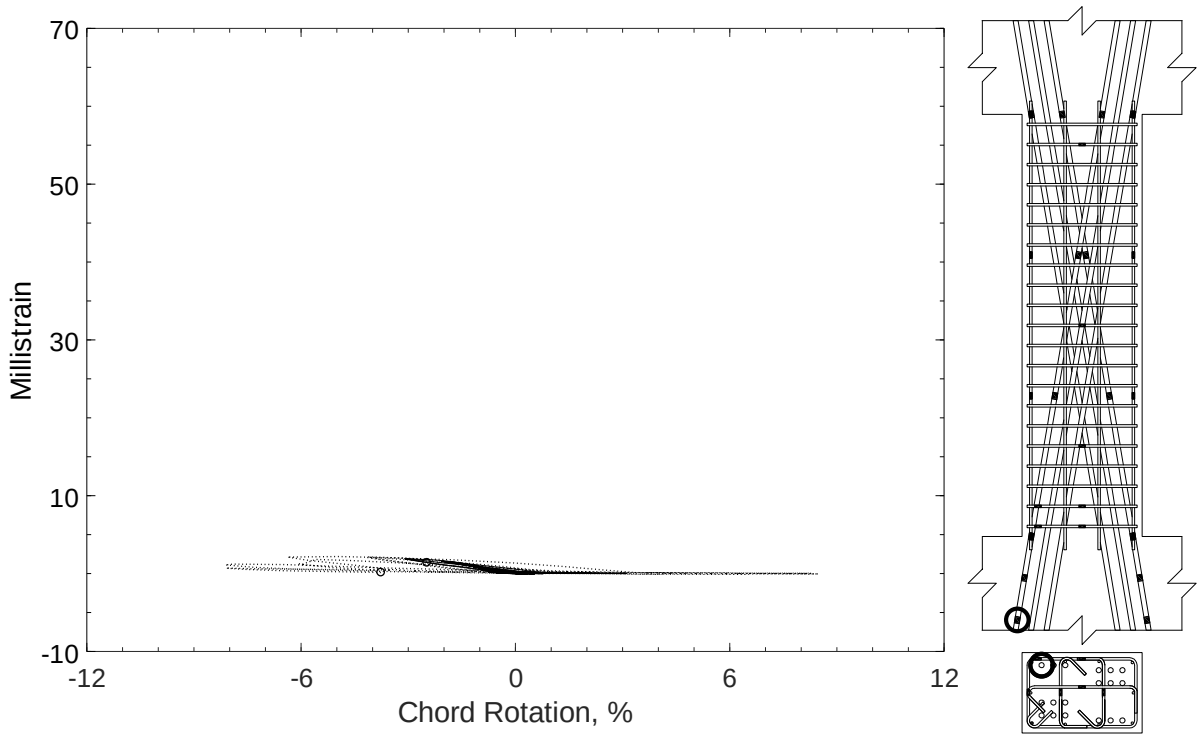

Figure 524 – Measured strain in diagonal bar of D120-3.5, strain gauge D1

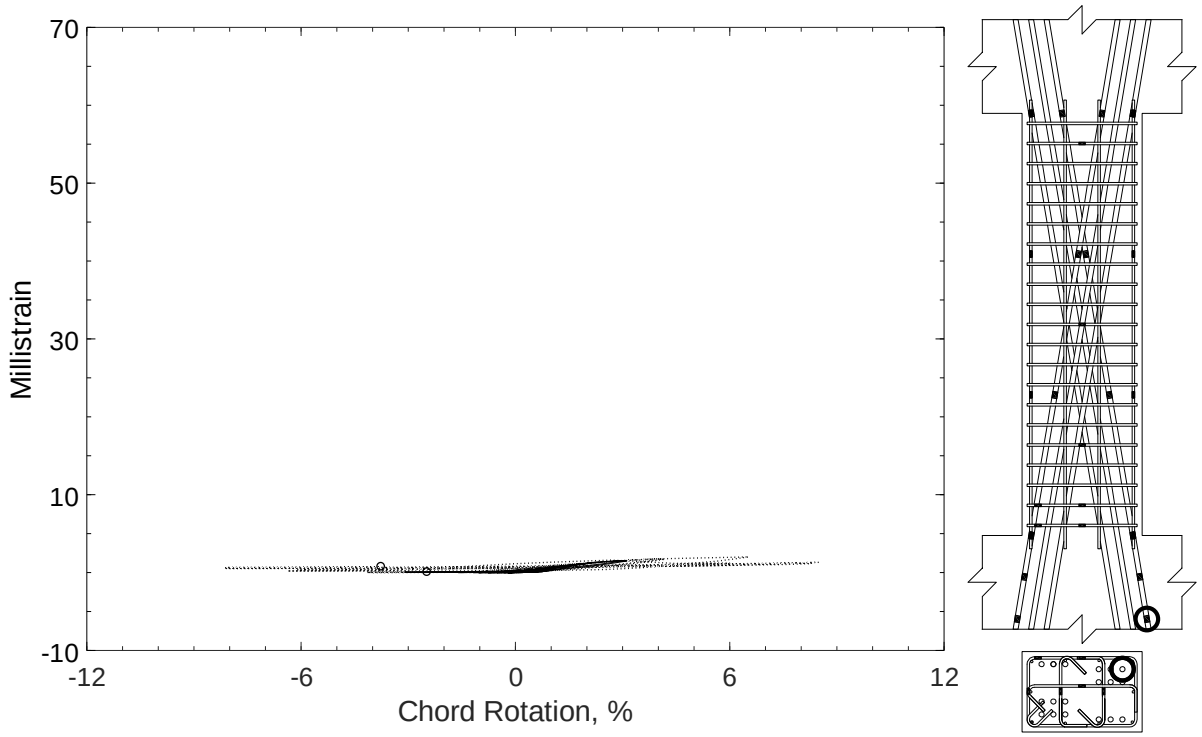

Figure 525 – Measured strain in diagonal bar of D120-3.5, strain gauge D2

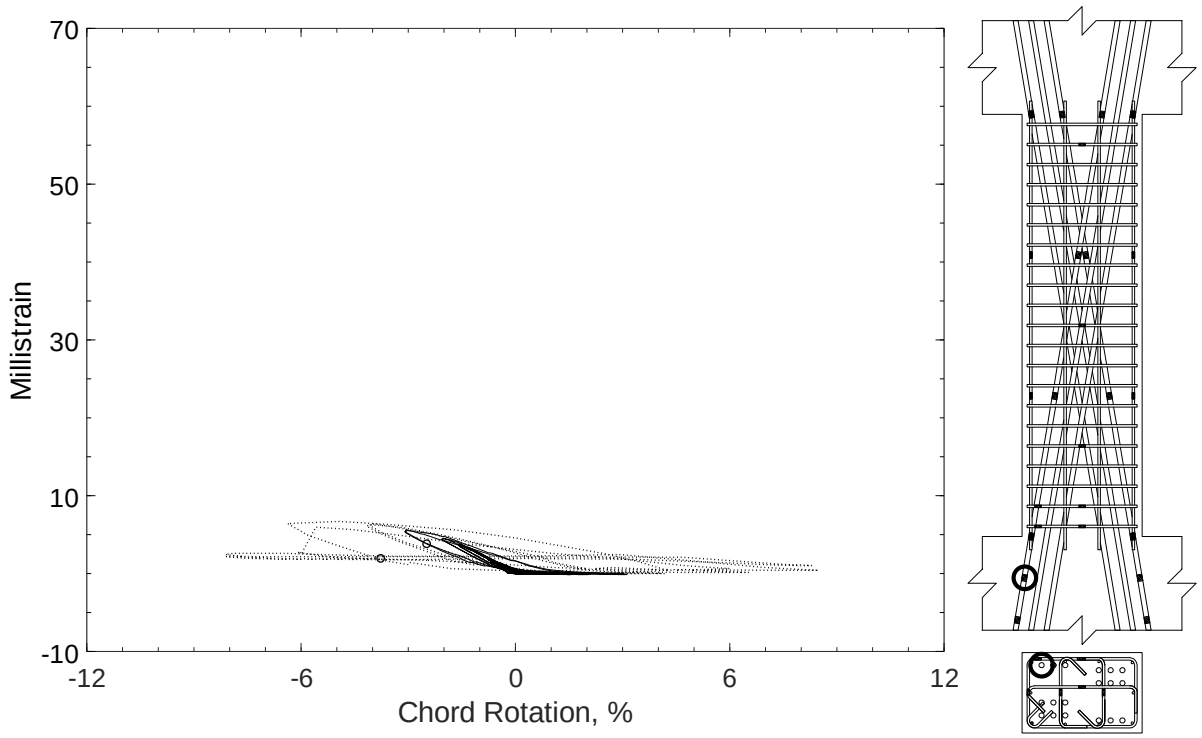

Figure 526 – Measured strain in diagonal bar of D120-3.5, strain gauge D3

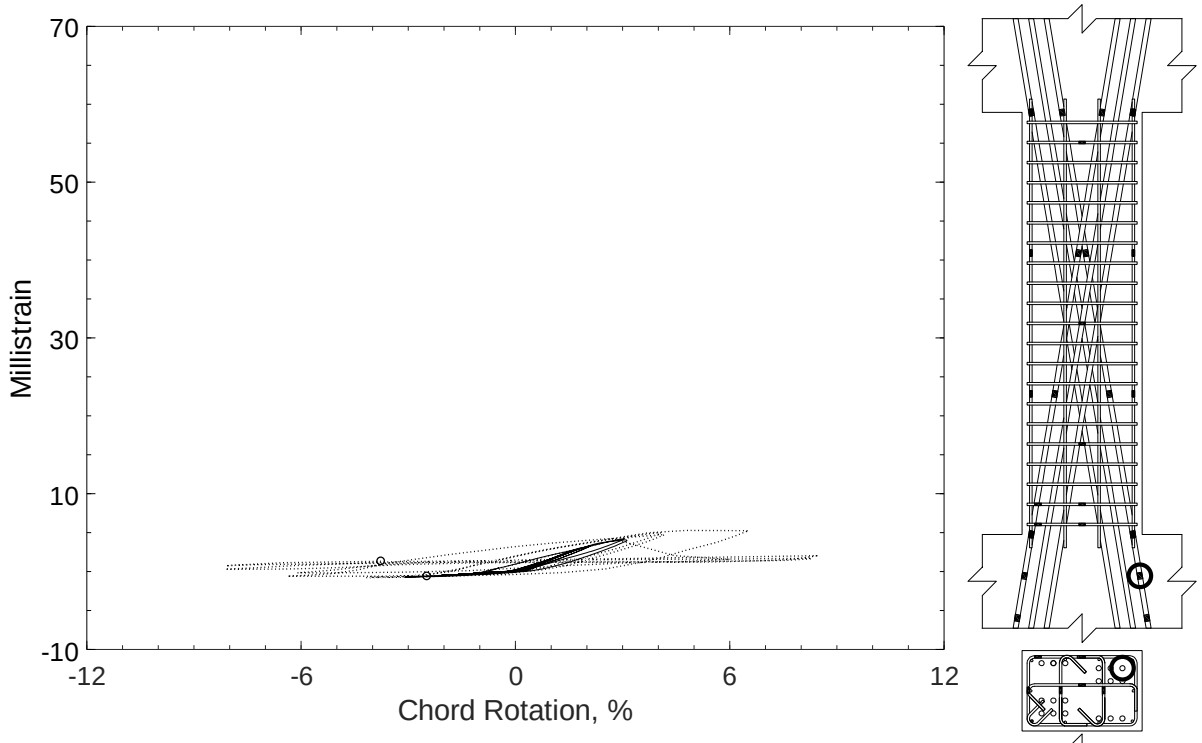

Figure 527 – Measured strain in diagonal bar of D120-3.5, strain gauge D4

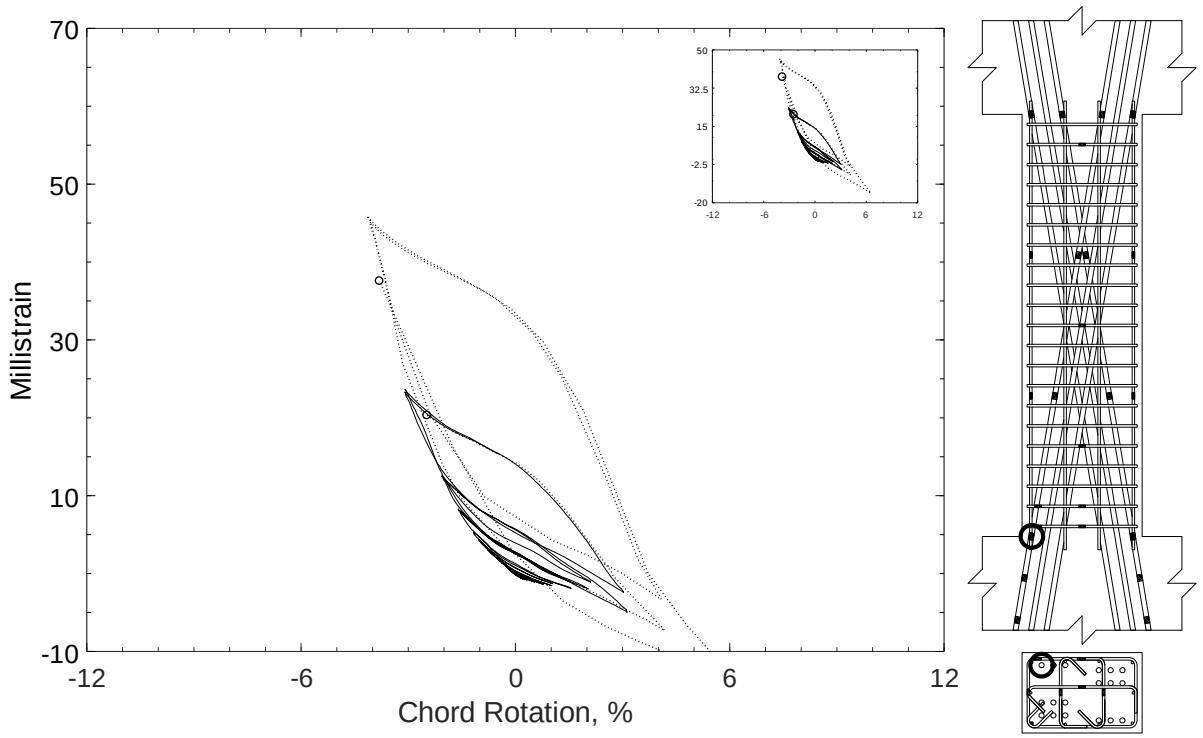

Figure 528 – Measured strain in diagonal bar of D120-3.5, strain gauge D5

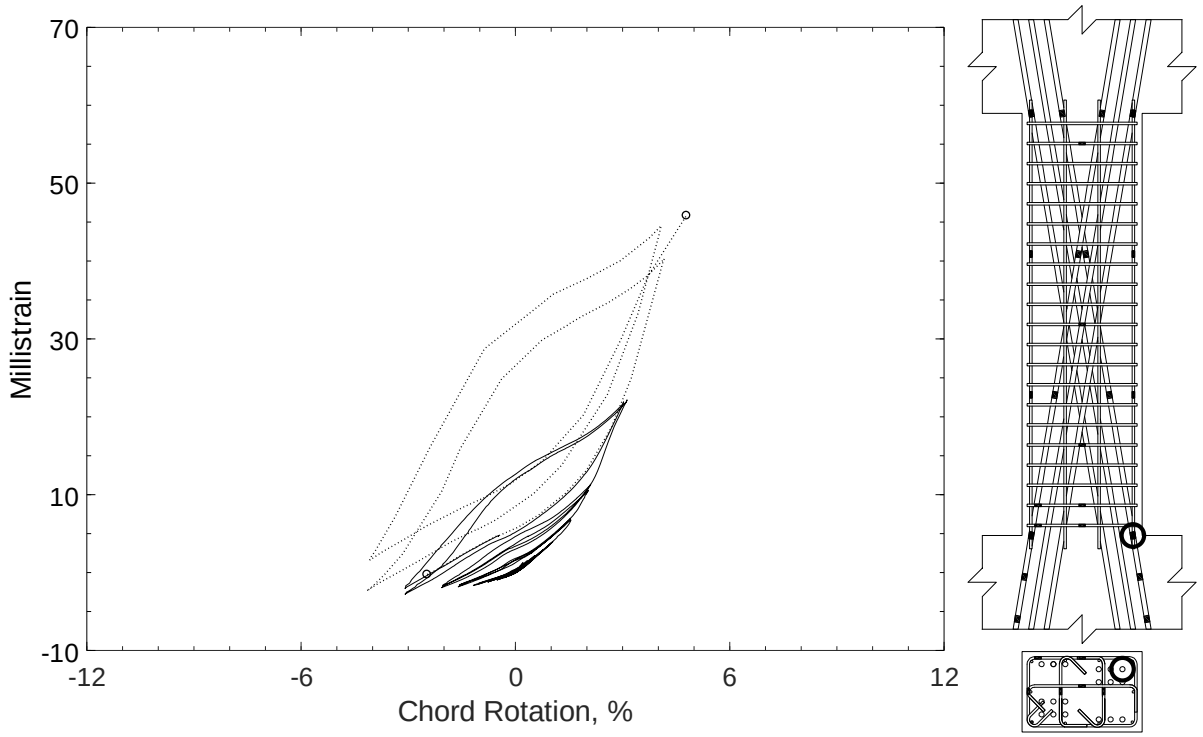

Figure 529 – Measured strain in diagonal bar of D120-3.5, strain gauge D6

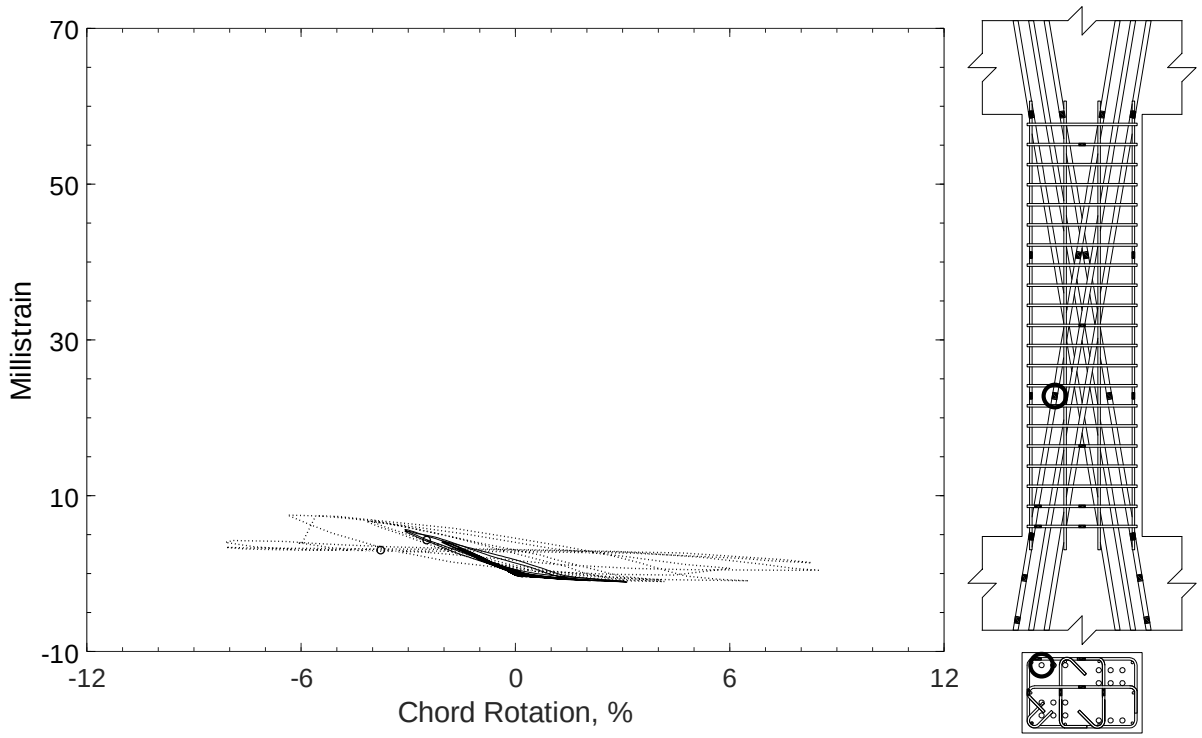

Figure 530 – Measured strain in diagonal bar of D120-3.5, strain gauge D7

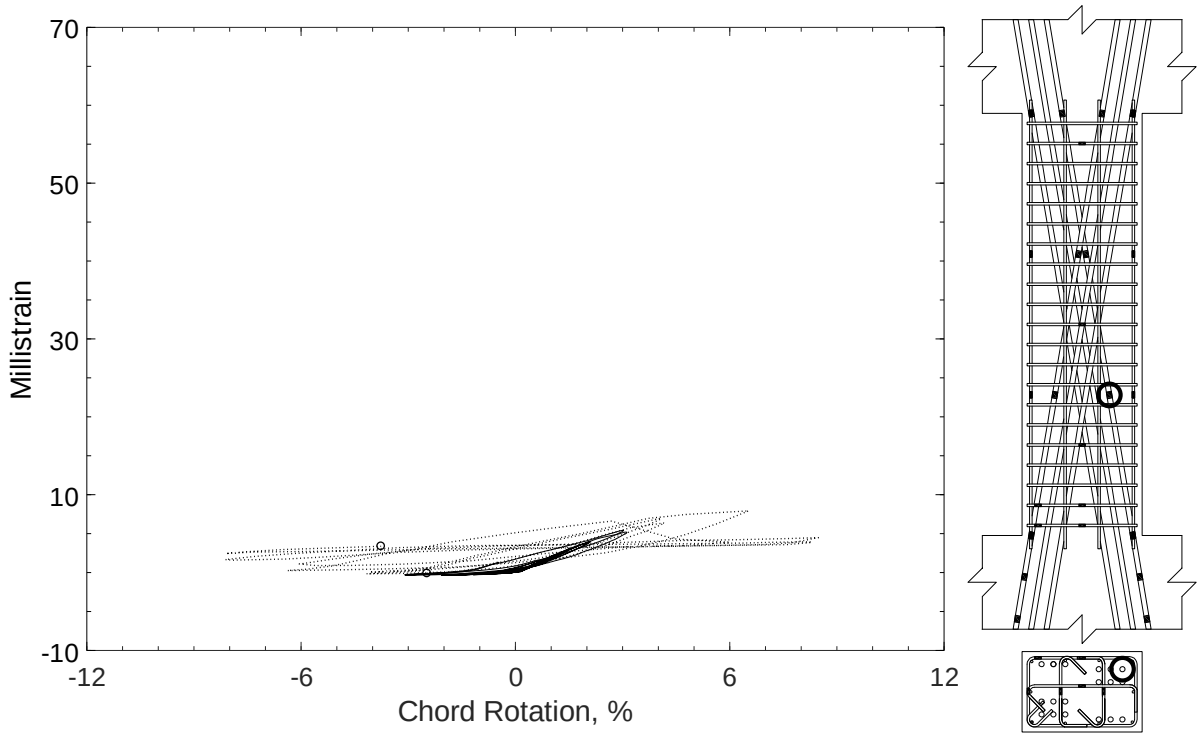

Figure 531 – Measured strain in diagonal bar of D120-3.5, strain gauge D8

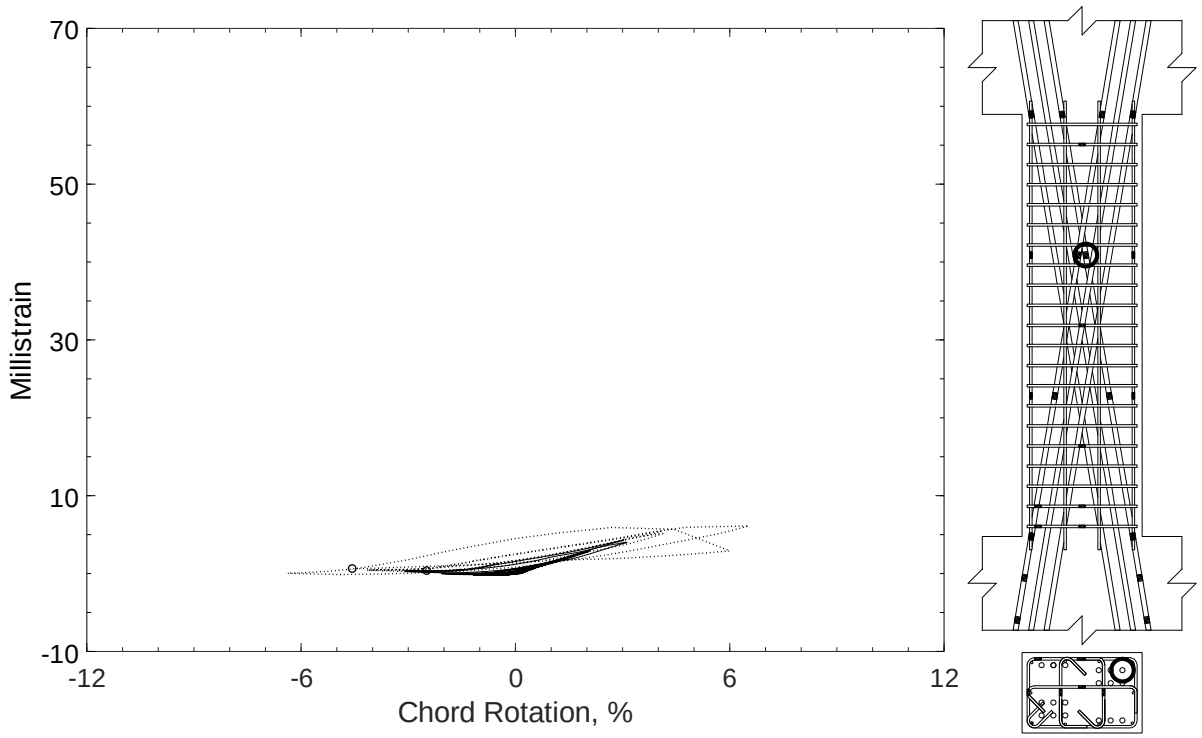

Figure 532 – Measured strain in diagonal bar of D120-3.5, strain gauge D9

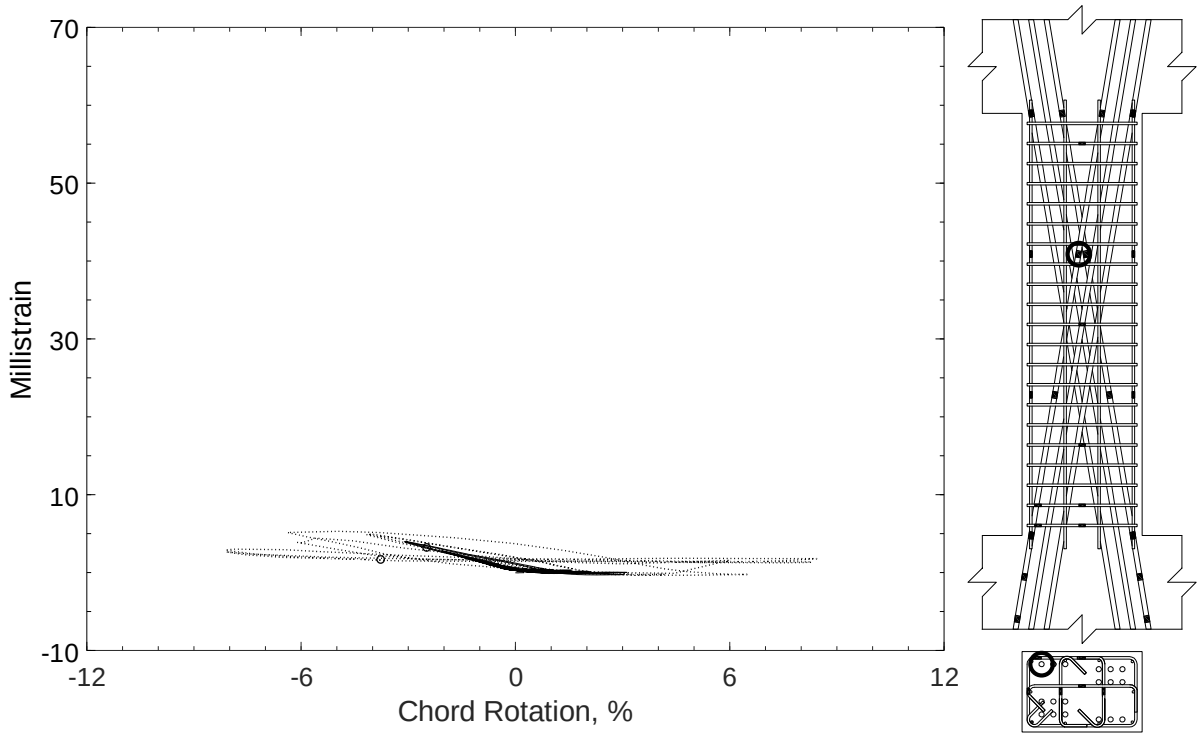

Figure 533 – Measured strain in diagonal bar of D120-3.5, strain gauge D10

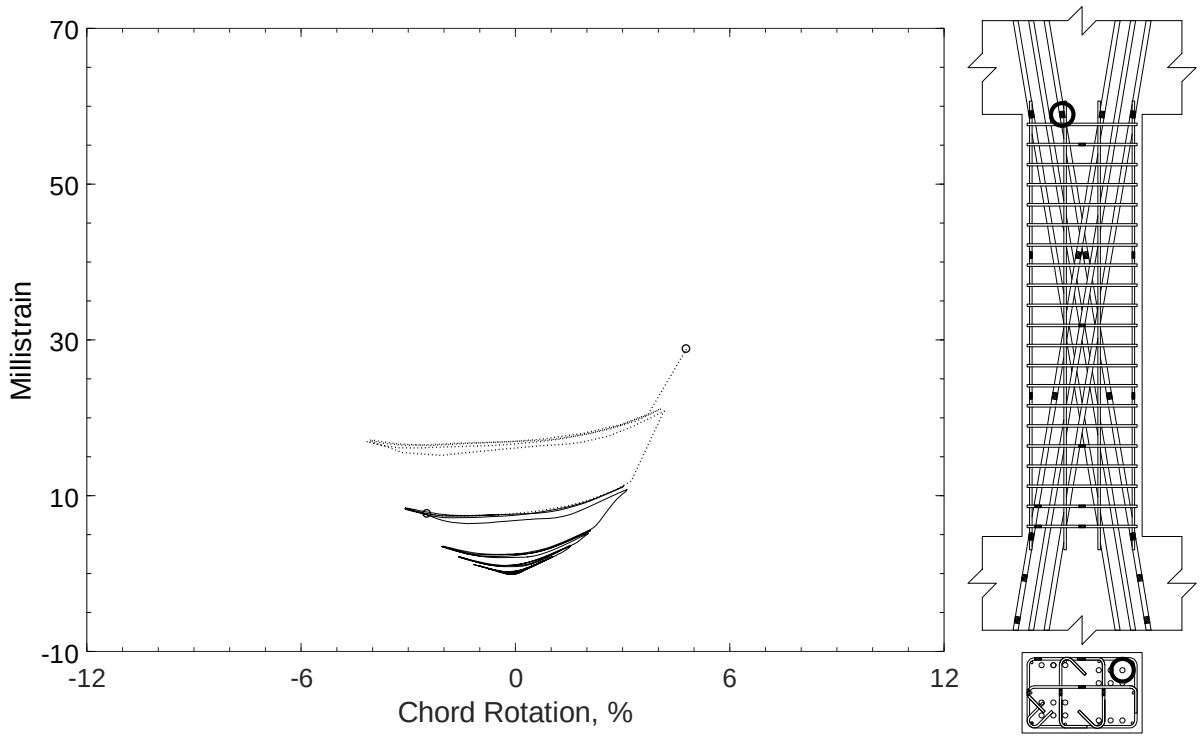

Figure 534 – Measured strain in diagonal bar of D120-3.5, strain gauge D11

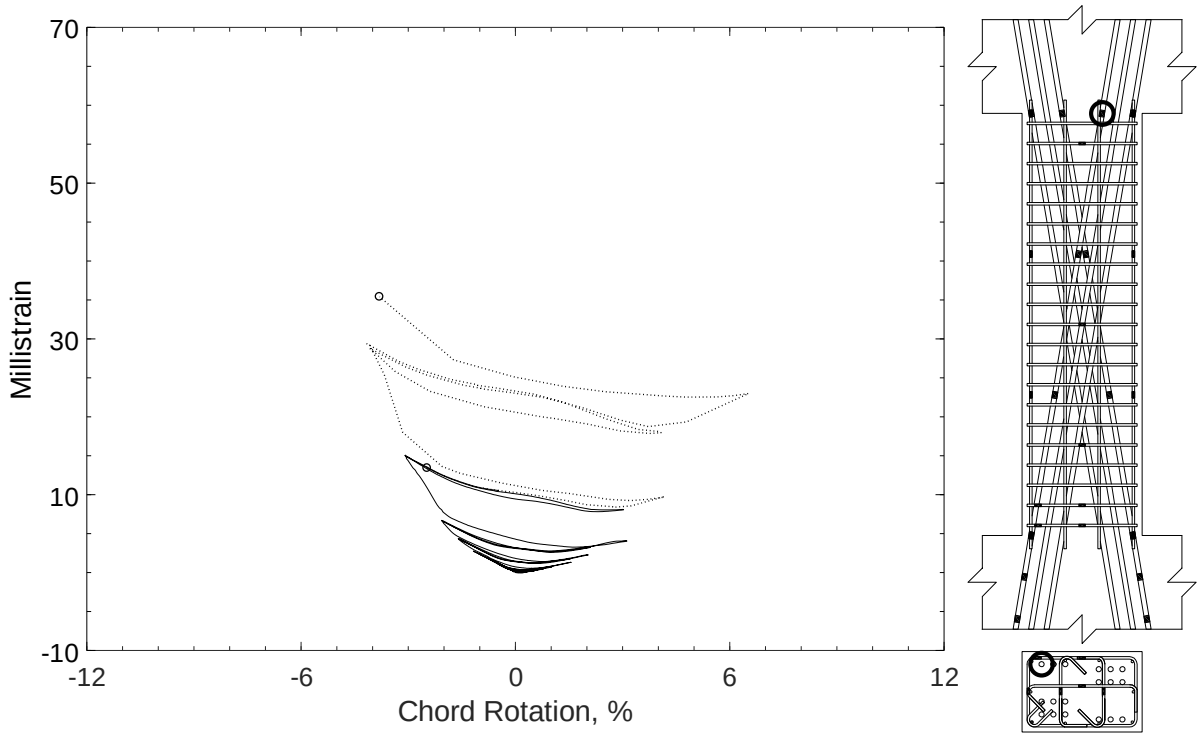

Figure 535 – Measured strain in diagonal bar of D120-3.5, strain gauge D12

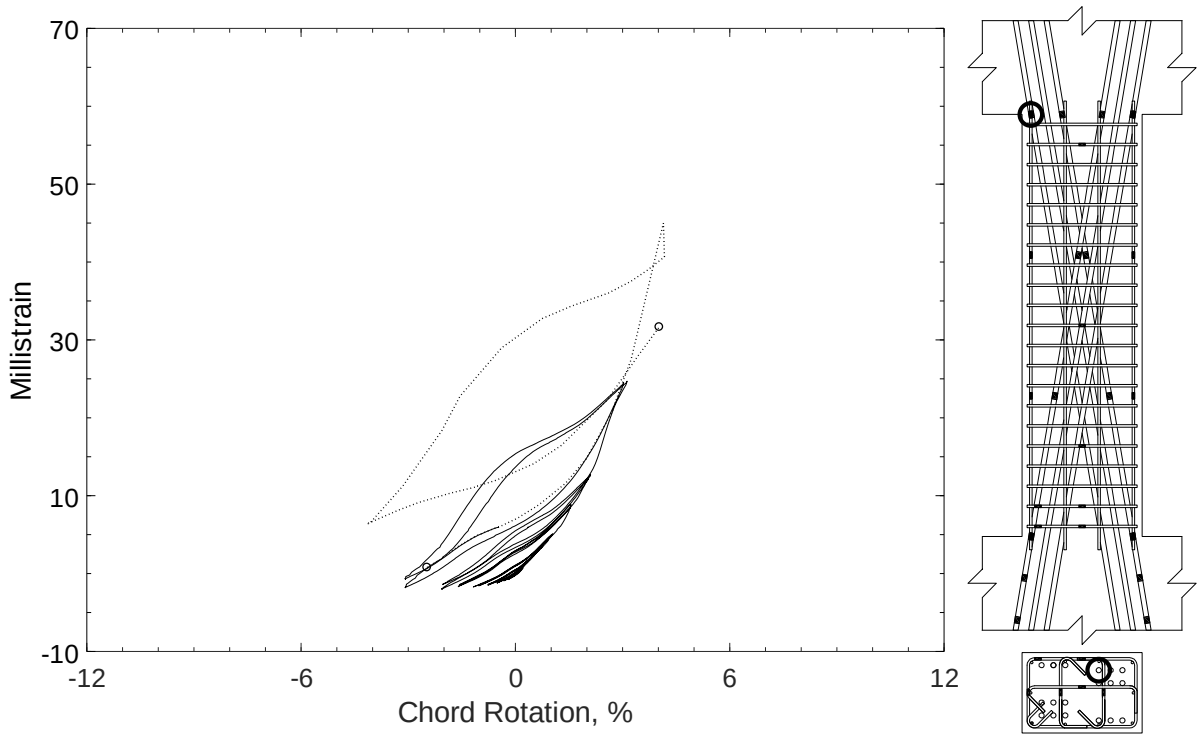

Figure 536 – Measured strain in diagonal bar of D120-3.5, strain gauge D13

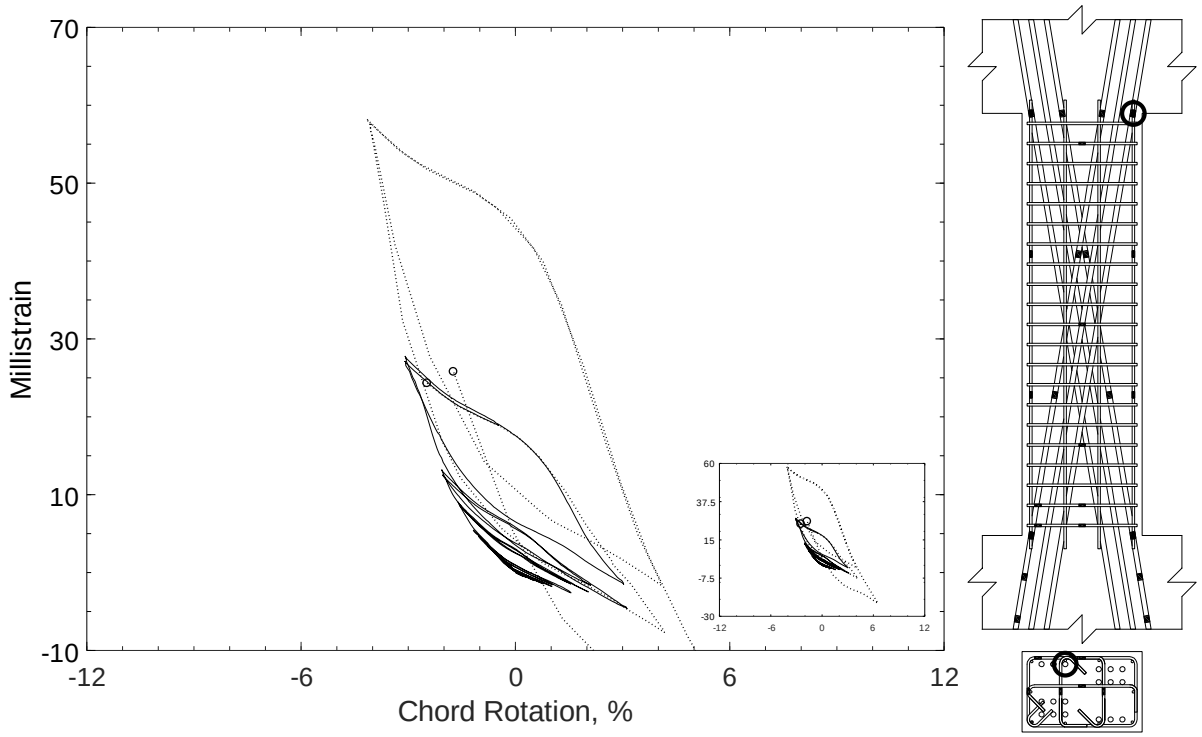

Figure 537 – Measured strain in diagonal bar of D120-3.5, strain gauge D14

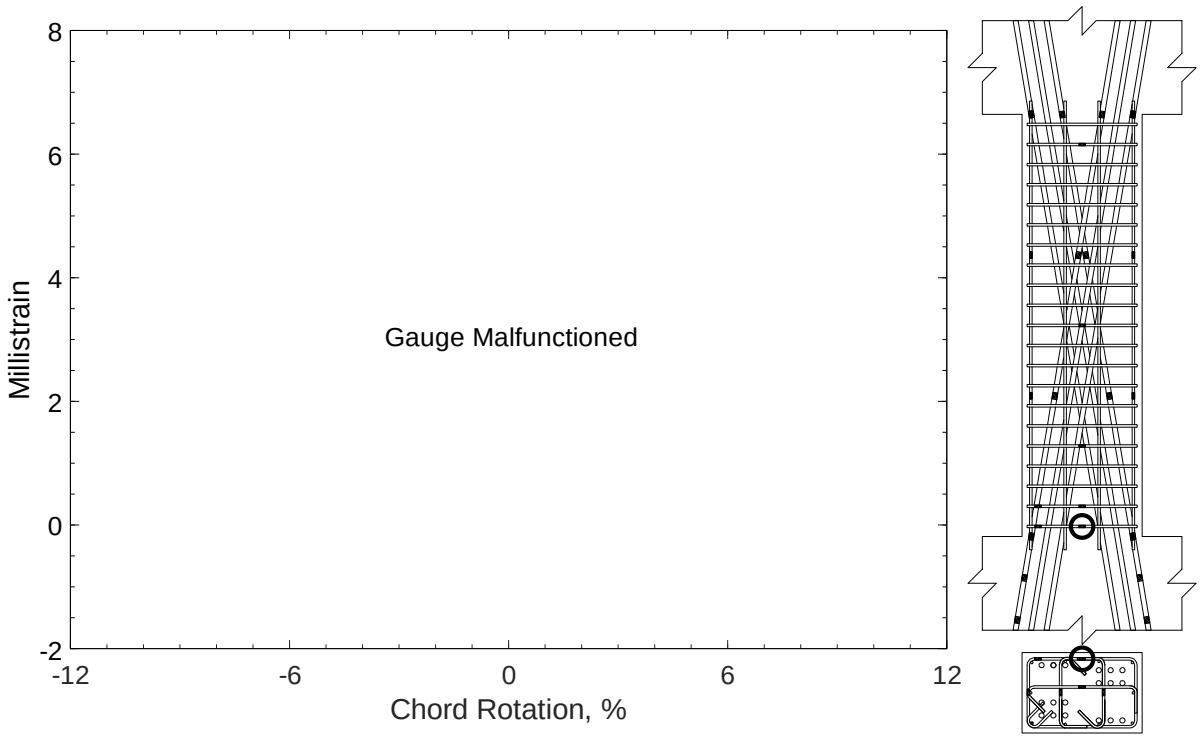

Figure 538 – Measured strain in closed stirrup of D120-3.5, strain gauge S1

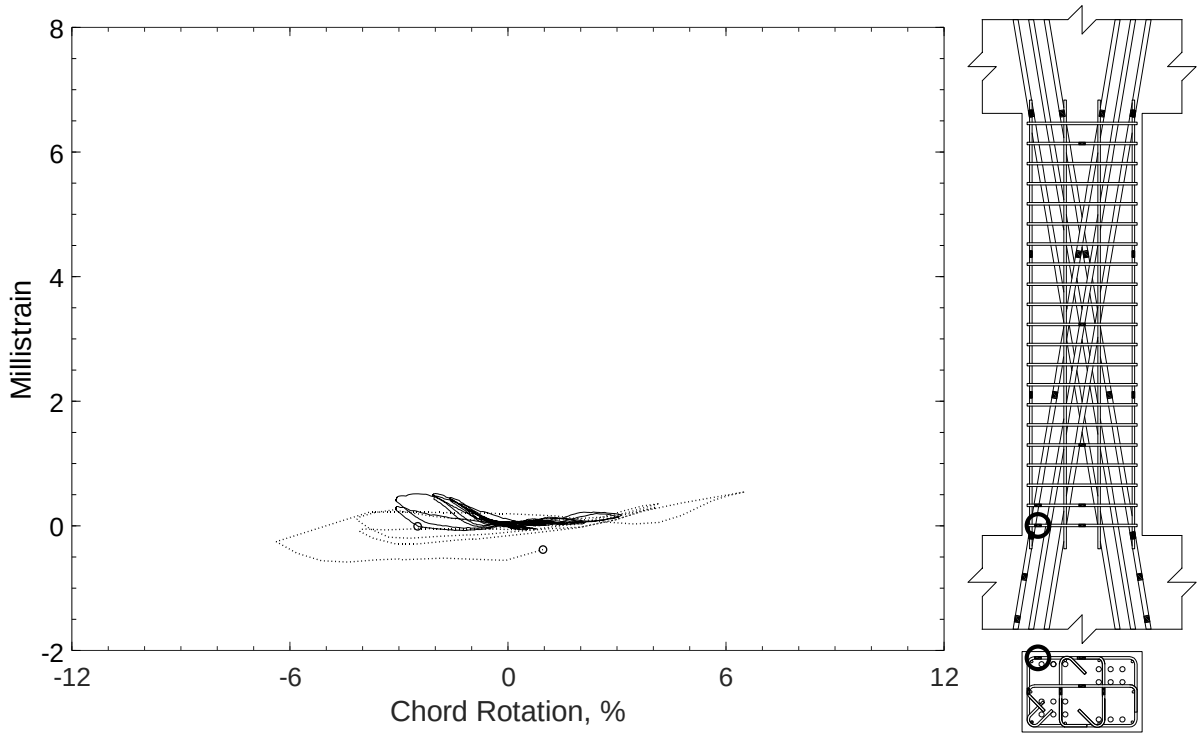

Figure 539 – Measured strain in closed stirrup of D120-3.5, strain gauge S2

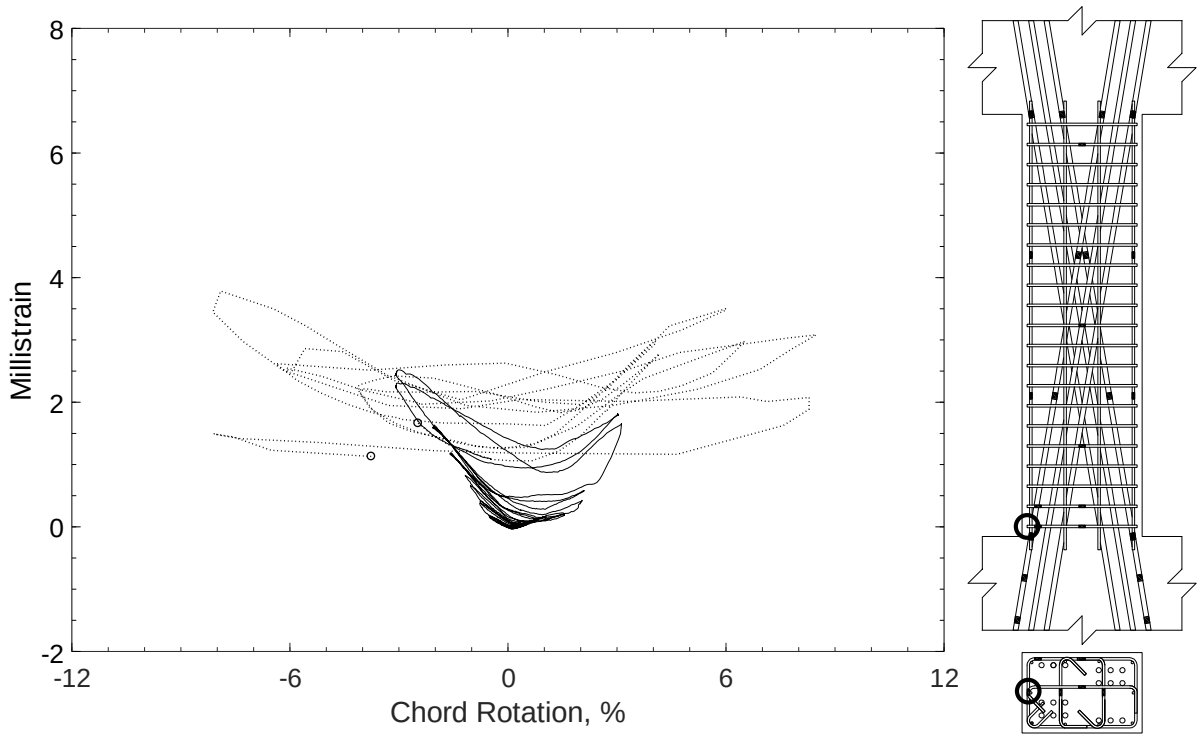

Figure 540 – Measured strain in closed stirrup of D120-3.5, strain gauge S3

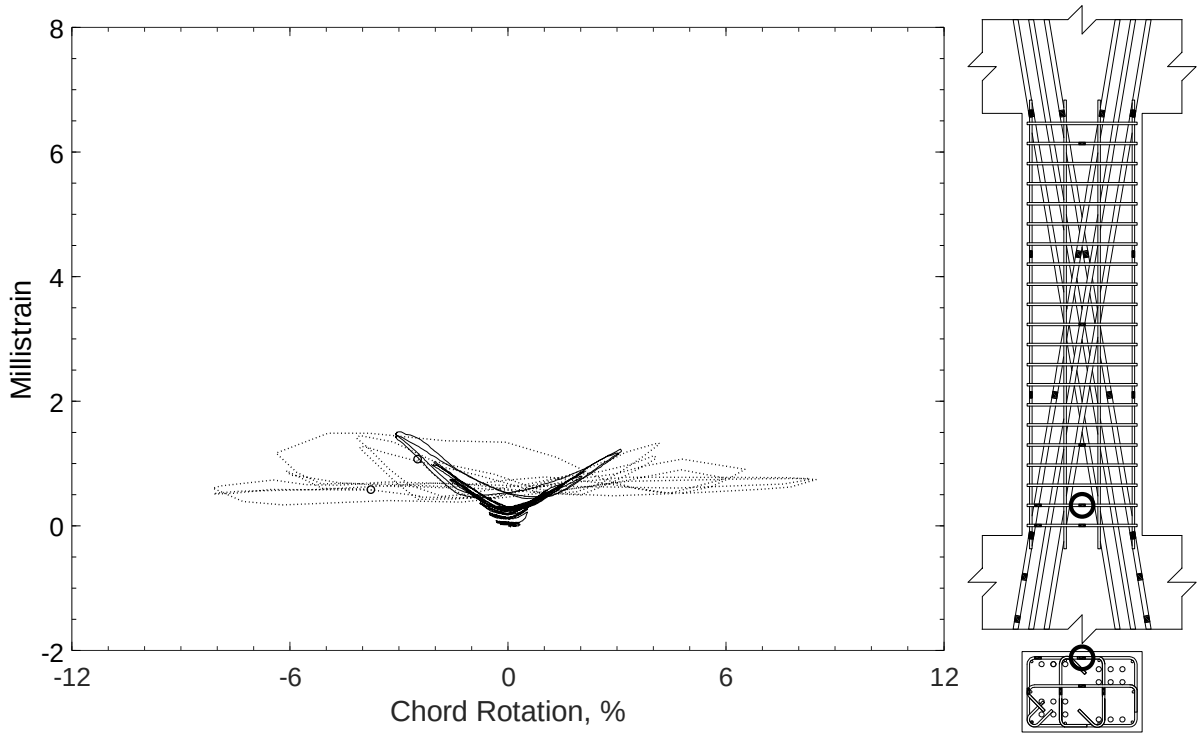

Figure 541 – Measured strain in closed stirrup of D120-3.5, strain gauge S4

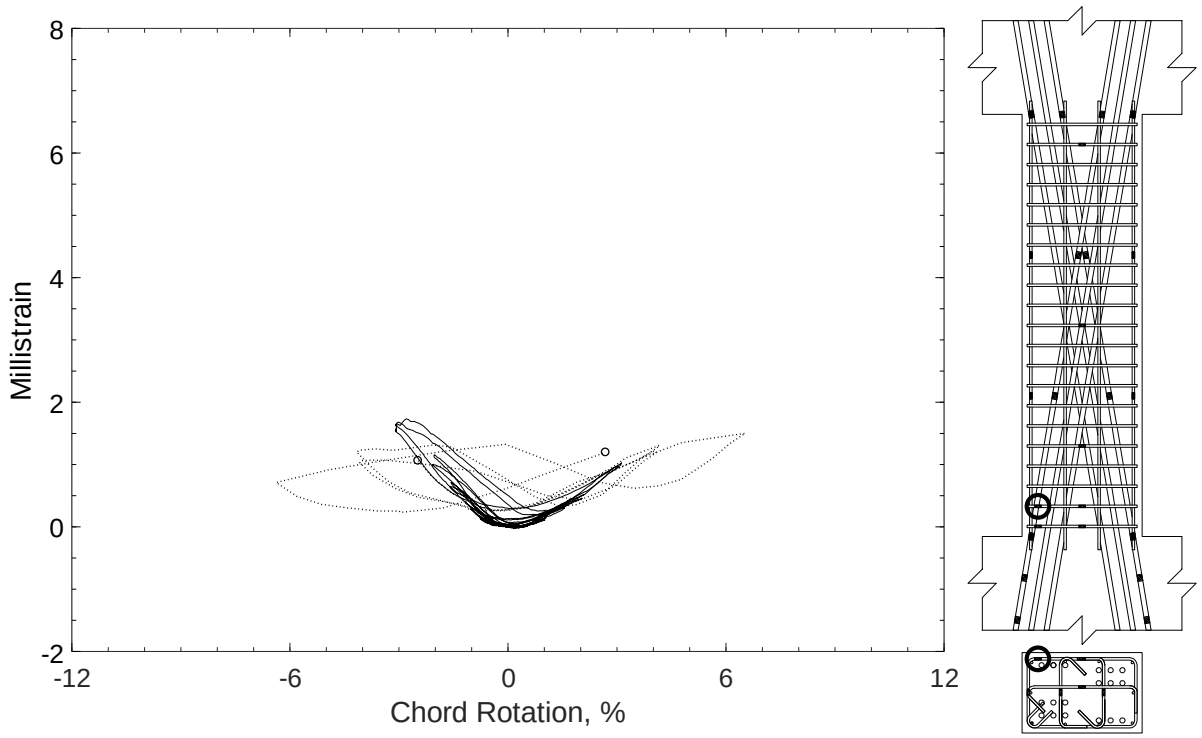

Figure 542 – Measured strain in closed stirrup of D120-3.5, strain gauge S5

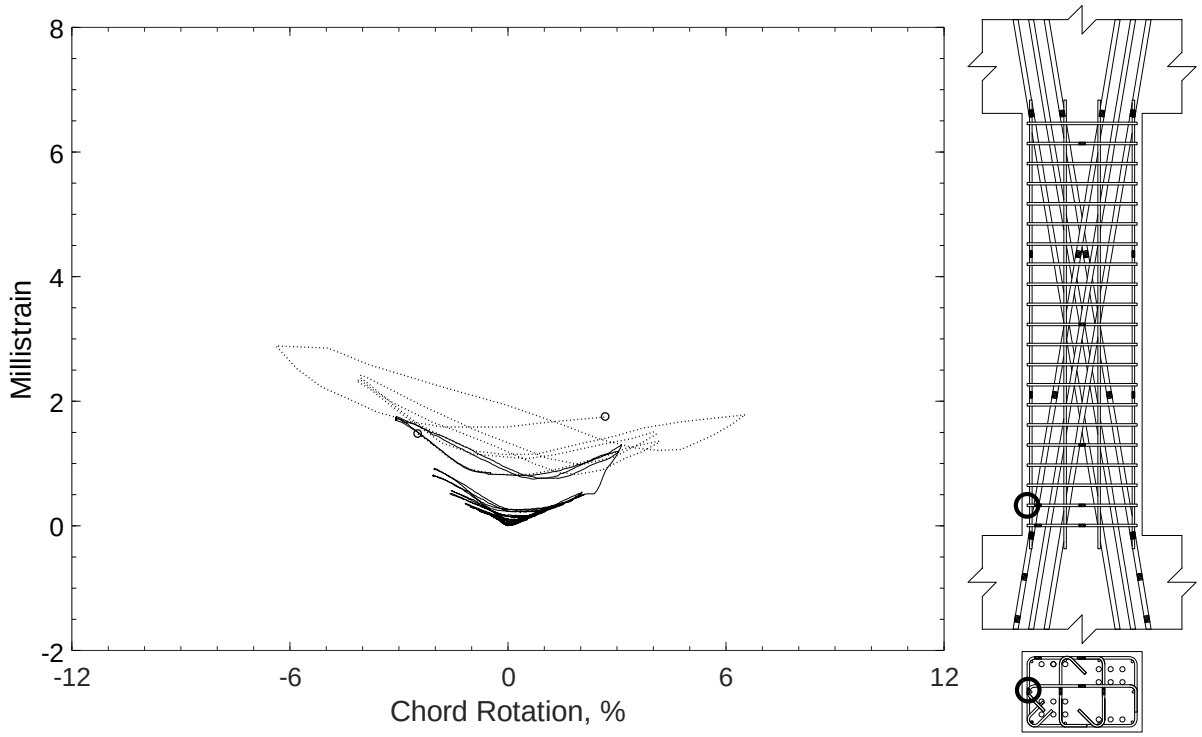

Figure 543 – Measured strain in closed stirrup of D120-3.5, strain gauge S6

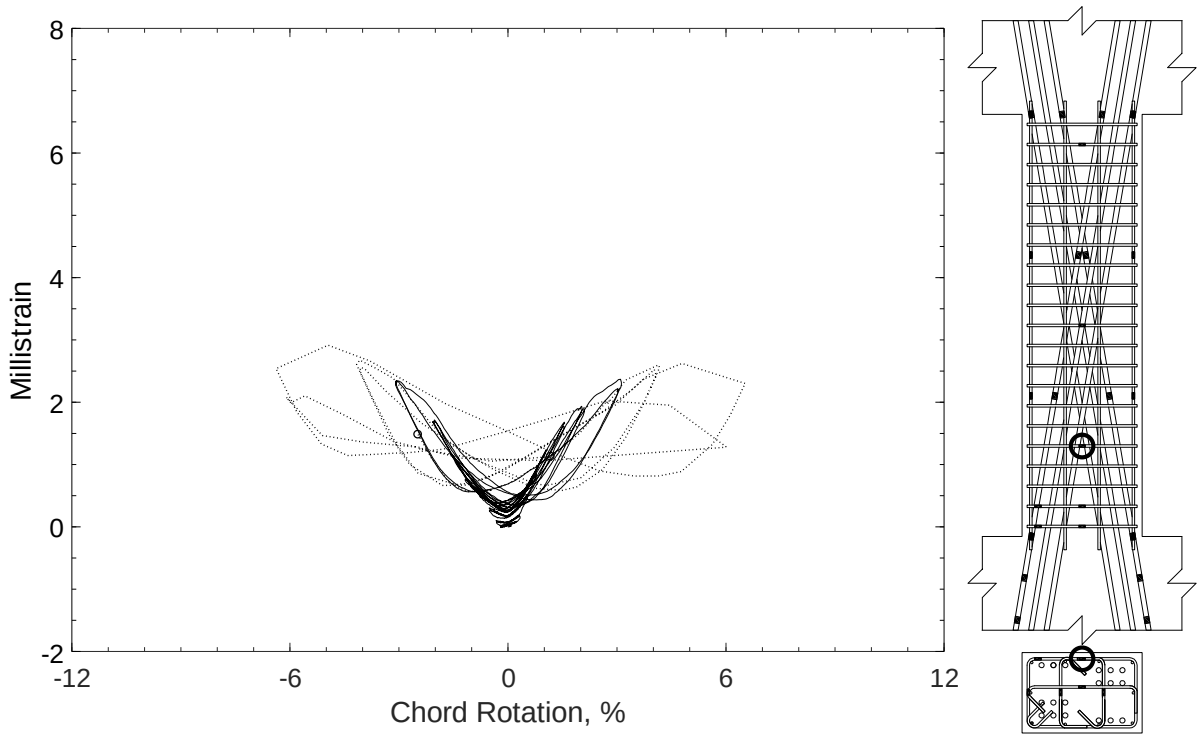

Figure 544 – Measured strain in closed stirrup of D120-3.5, strain gauge S7

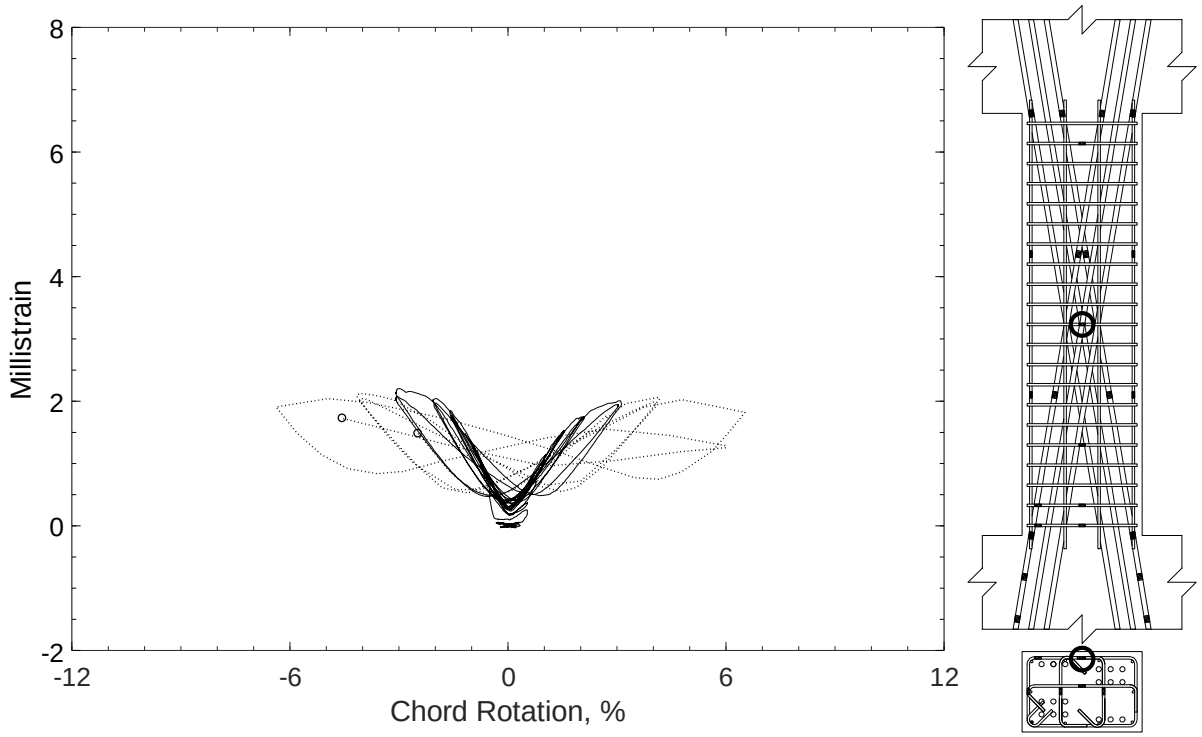

Figure 545 – Measured strain in closed stirrup of D120-3.5, strain gauge S8

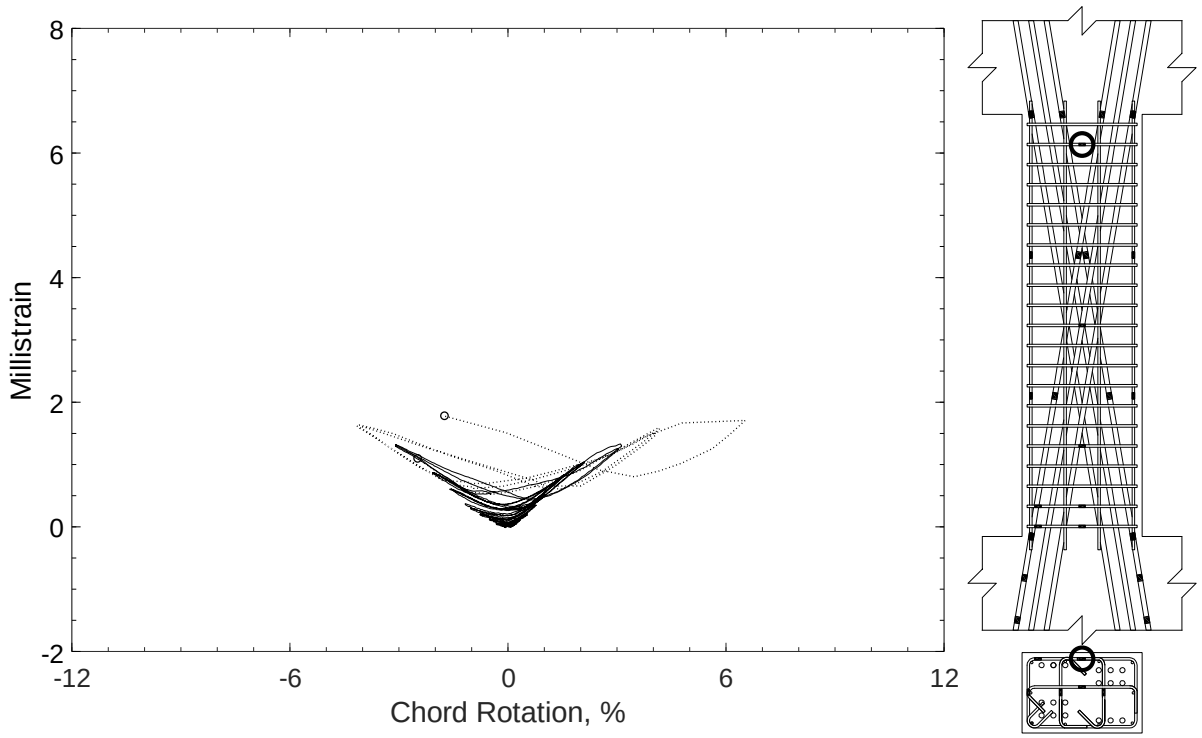

Figure 546 – Measured strain in closed stirrup of D120-3.5, strain gauge S9

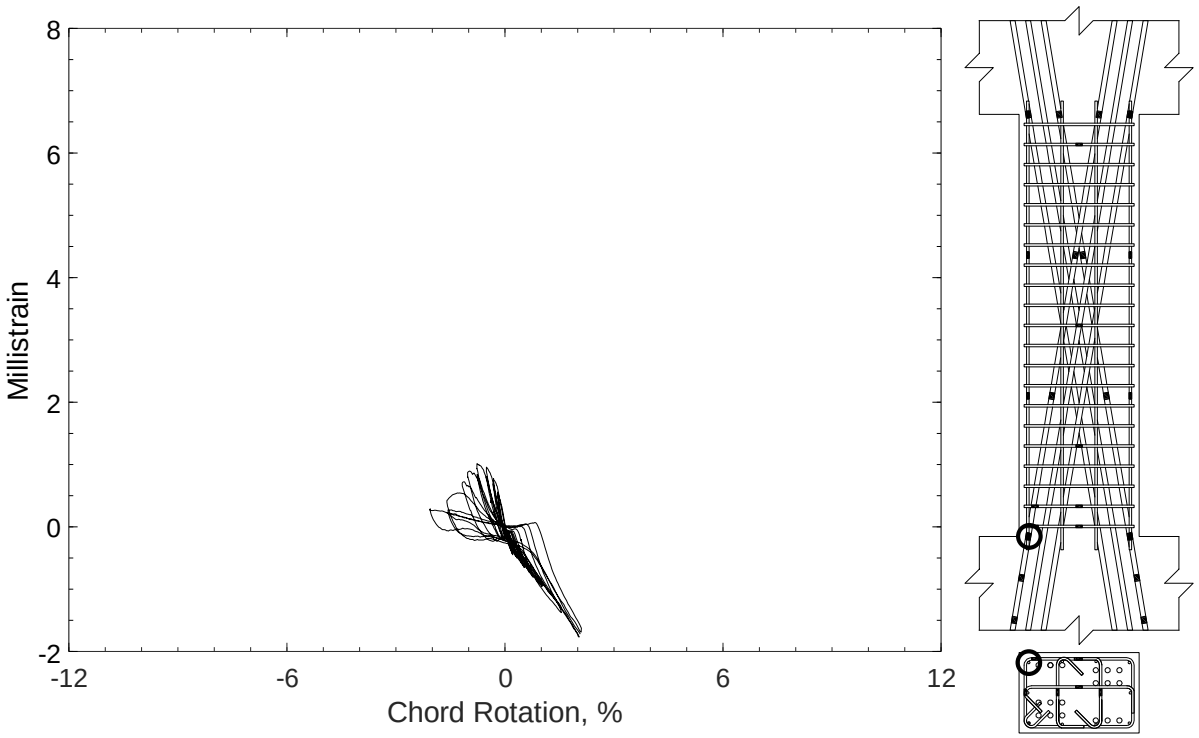

Figure 547 – Measured strain in parallel bar of D120-3.5, strain gauge H1

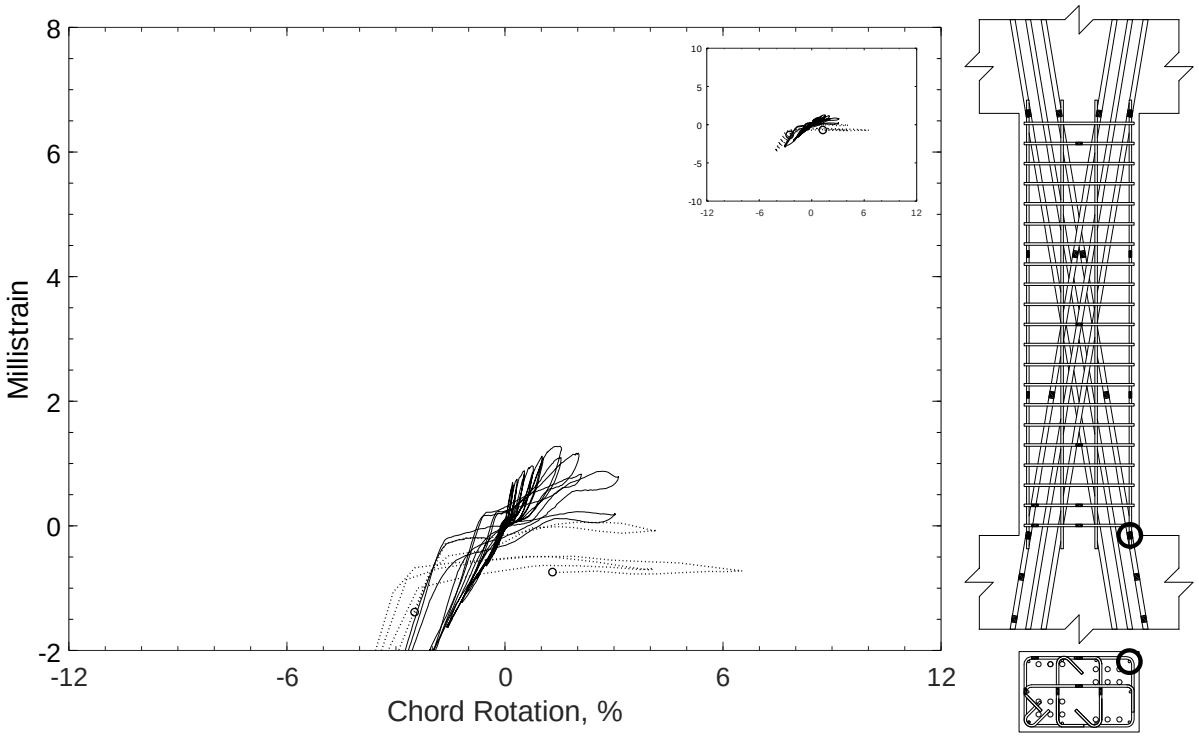

Figure 548 – Measured strain in parallel bar of D120-3.5, strain gauge H2

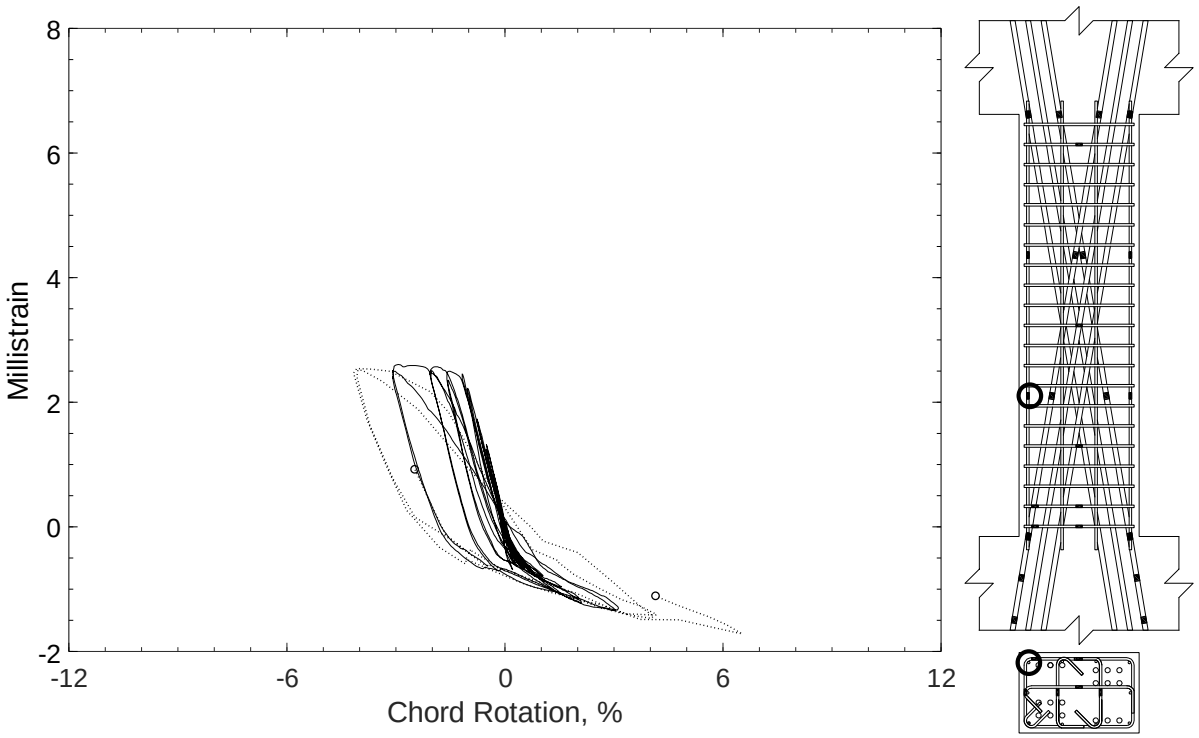

Figure 549 – Measured strain in parallel bar of D120-3.5, strain gauge H3

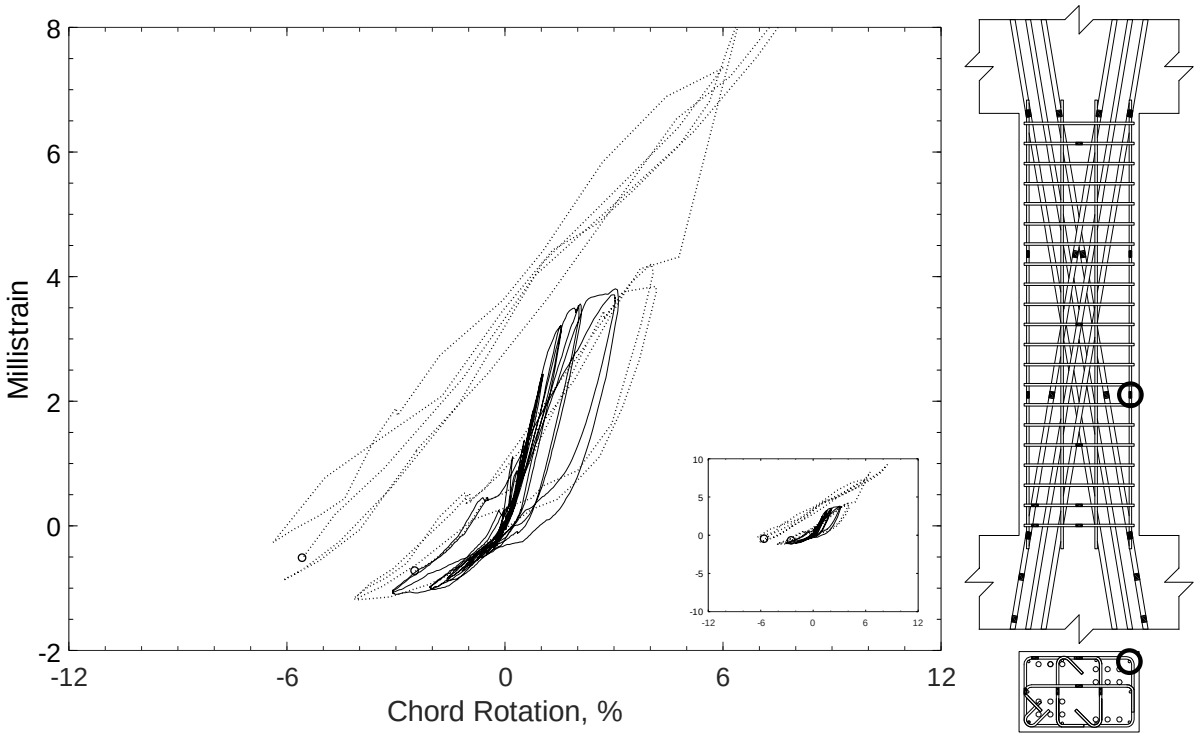

Figure 550 – Measured strain in parallel bar of D120-3.5, strain gauge H4

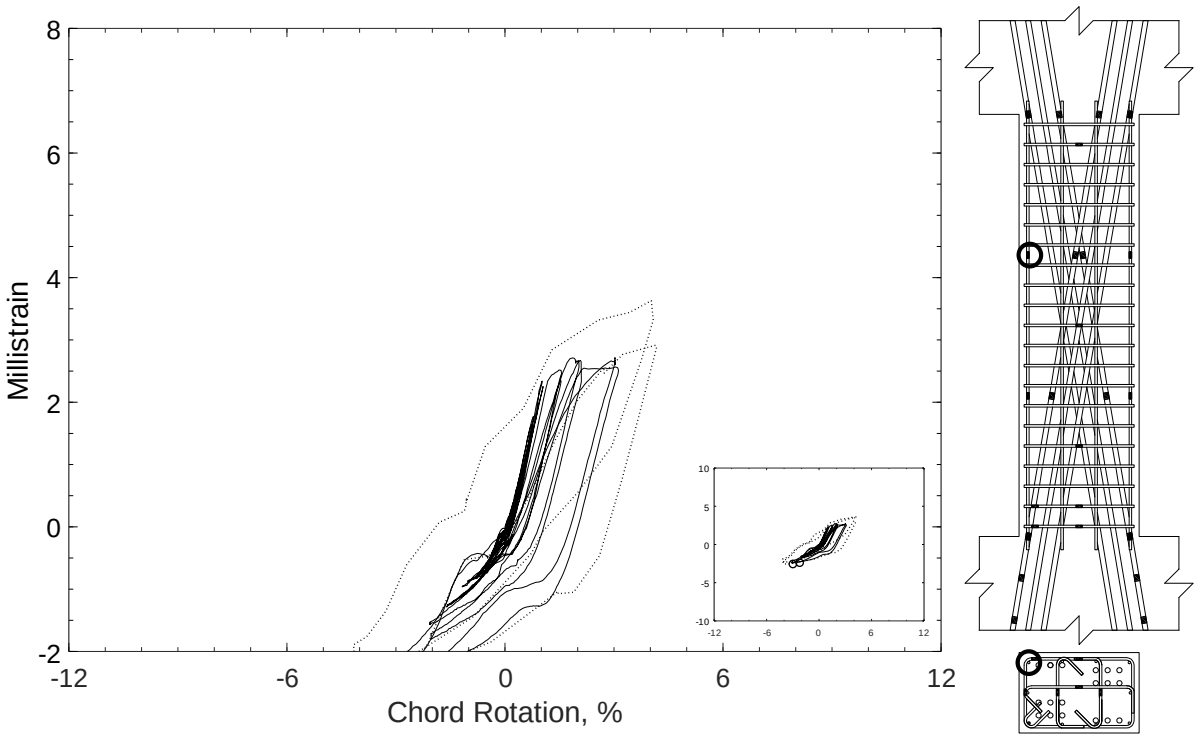

Figure 551 – Measured strain in parallel bar of D120-3.5, strain gauge H5

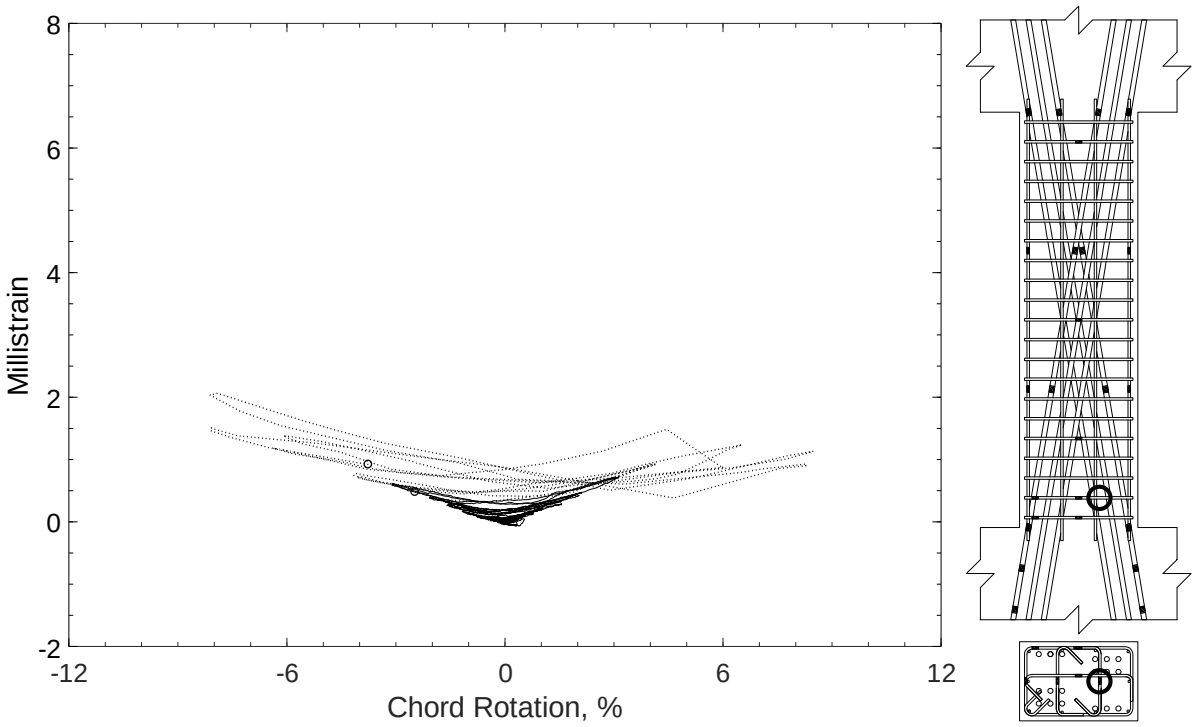

Figure 552 – Measured strain in crosstie of D120-3.5, strain gauge T1

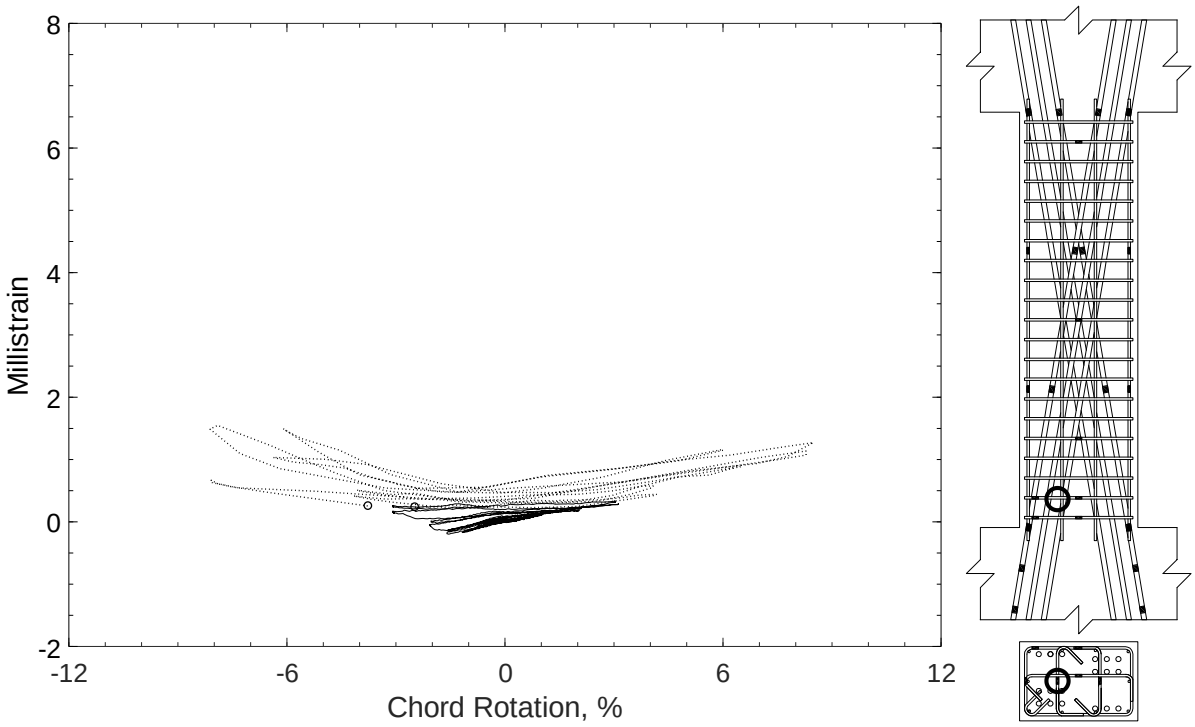

Figure 553 – Measured strain in crosstie of D120-3.5, strain gauge T2

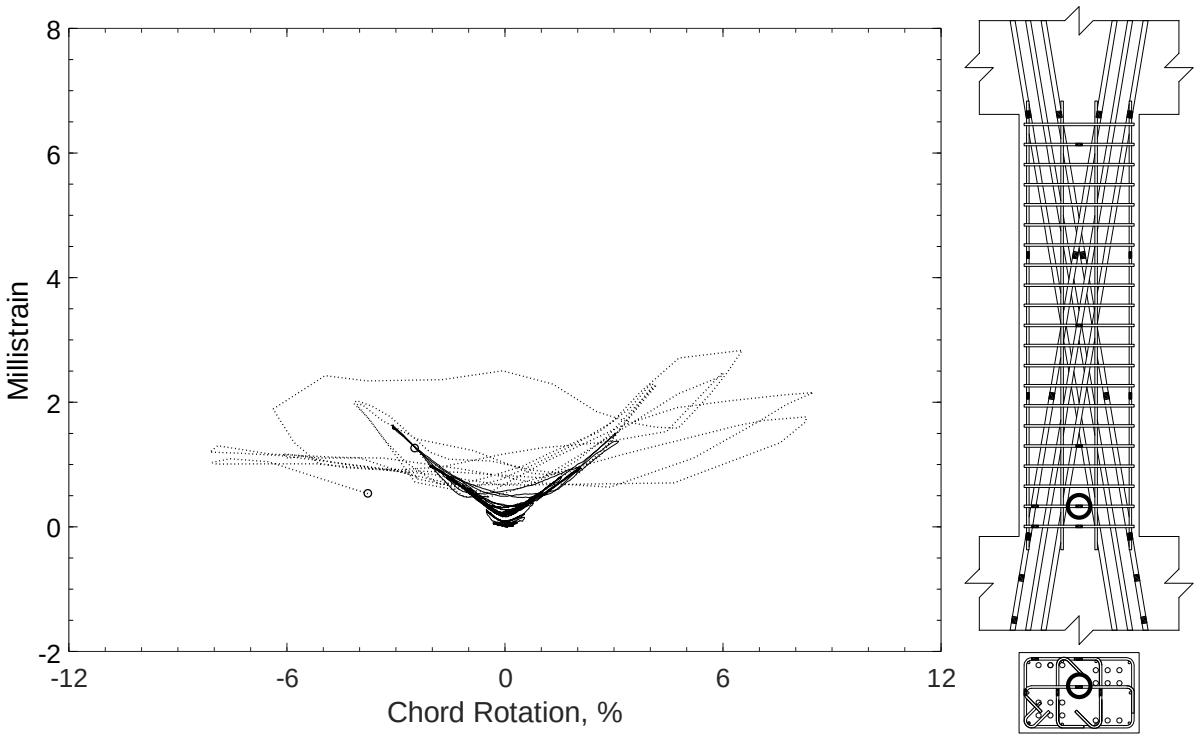

Figure 554 – Measured strain in crosstie of D120-3.5, strain gauge T3

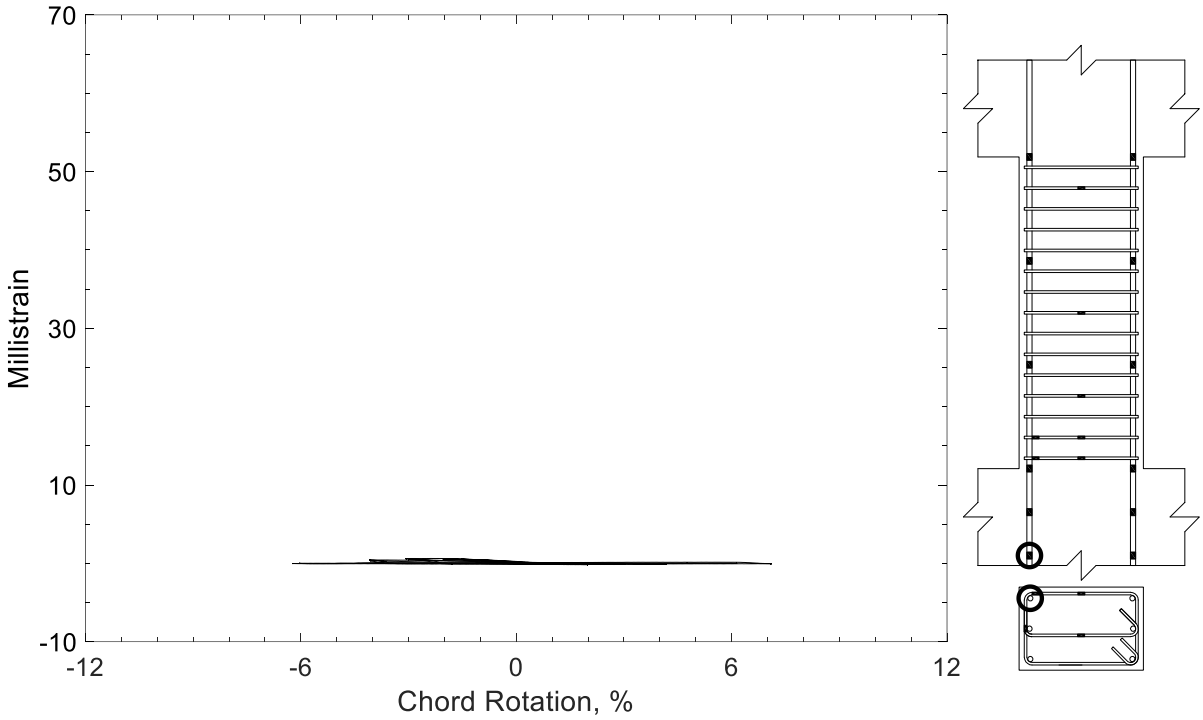

Figure 555 – Measured strain in parallel bar of P80-2.5, strain gauge P1

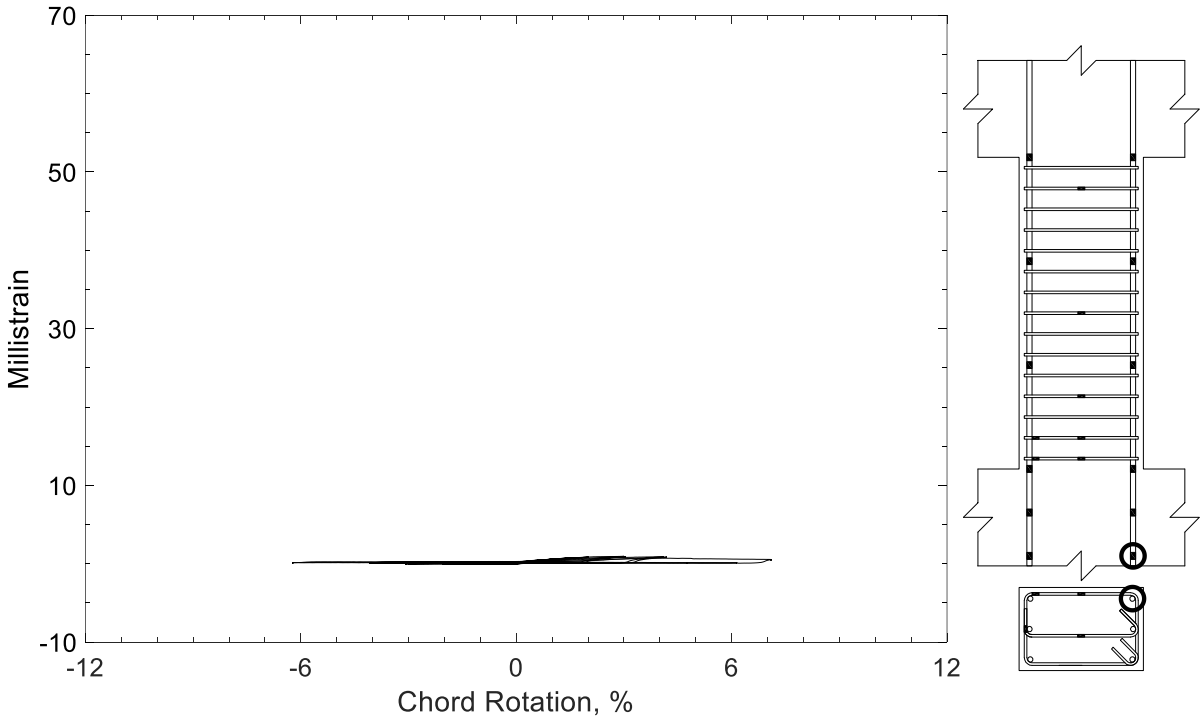

Figure 556 – Measured strain in parallel bar of P80-2.5, strain gauge P2

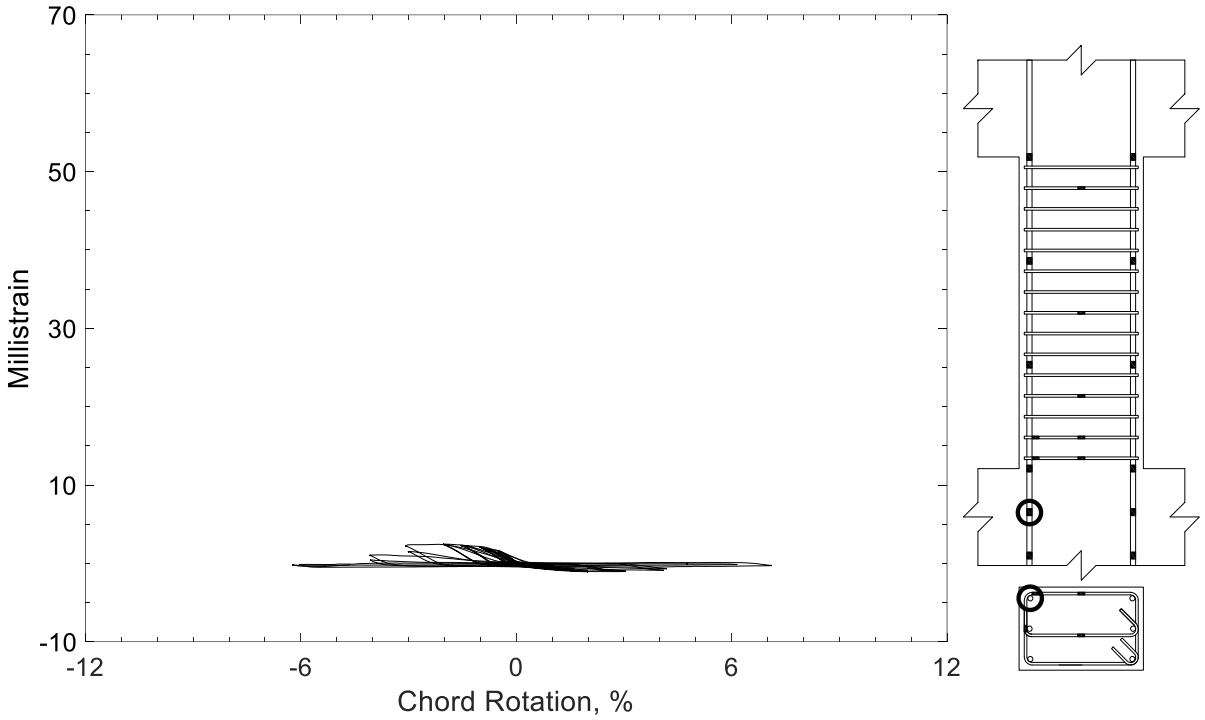

Figure 557 – Measured strain in parallel bar of P80-2.5, strain gauge P3

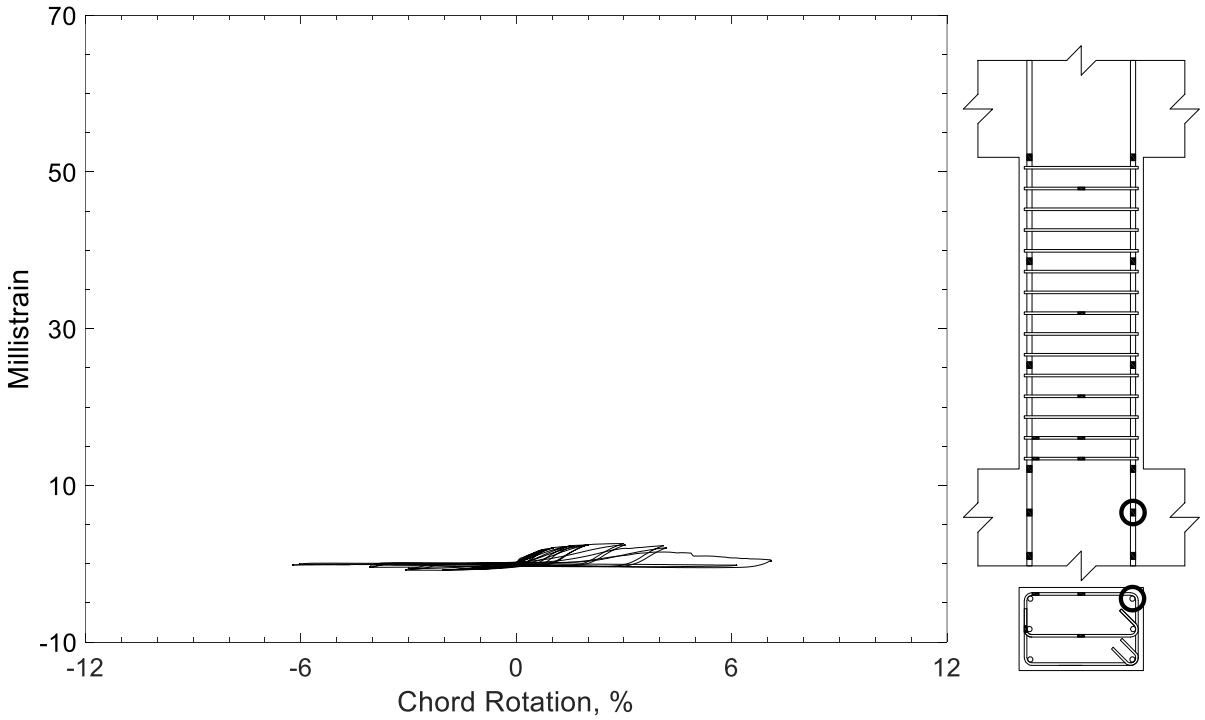

Figure 558 – Measured strain in parallel bar of P80-2.5, strain gauge P4

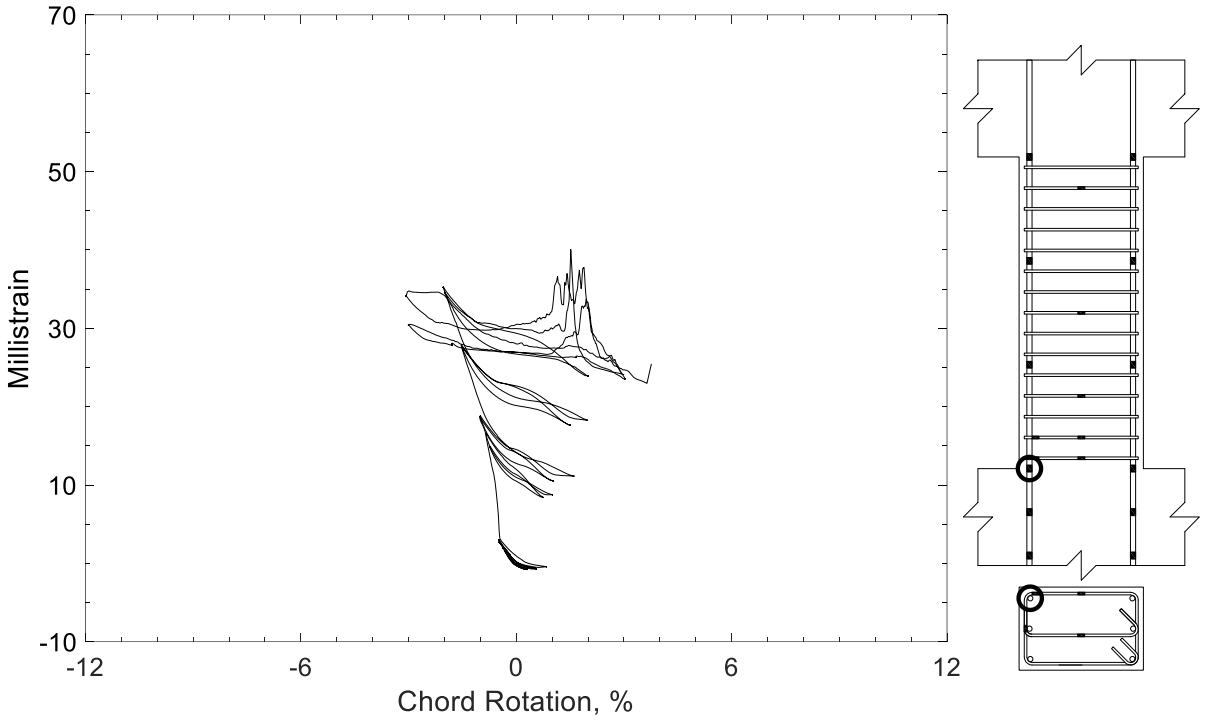

Figure 559 – Measured strain in parallel bar of P80-2.5, strain gauge P5

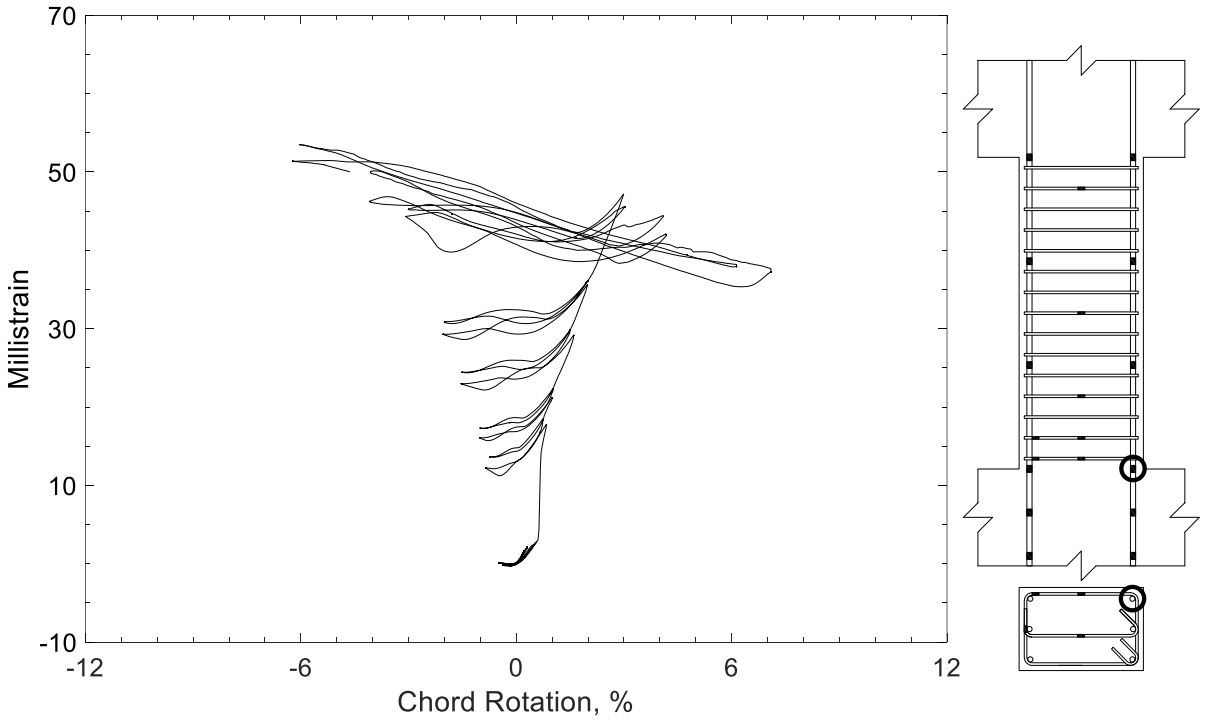

Figure 560 – Measured strain in parallel bar of P80-2.5, strain gauge P6

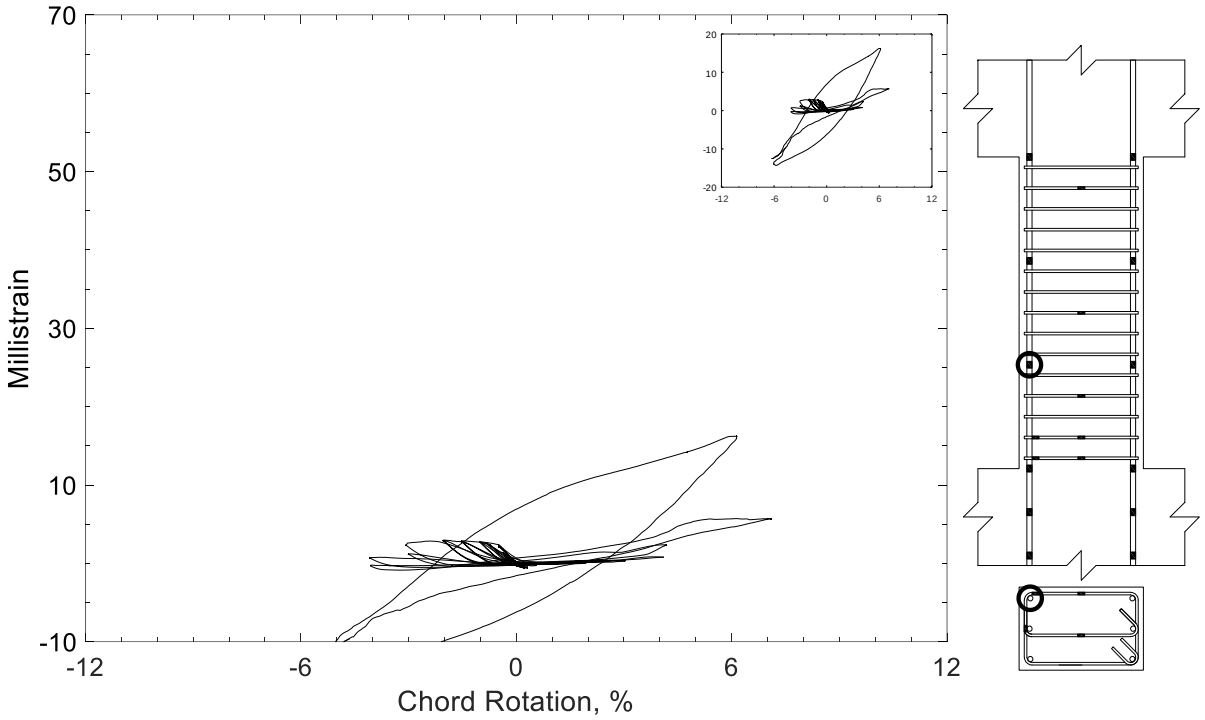

Figure 561 – Measured strain in parallel bar of P80-2.5, strain gauge P7

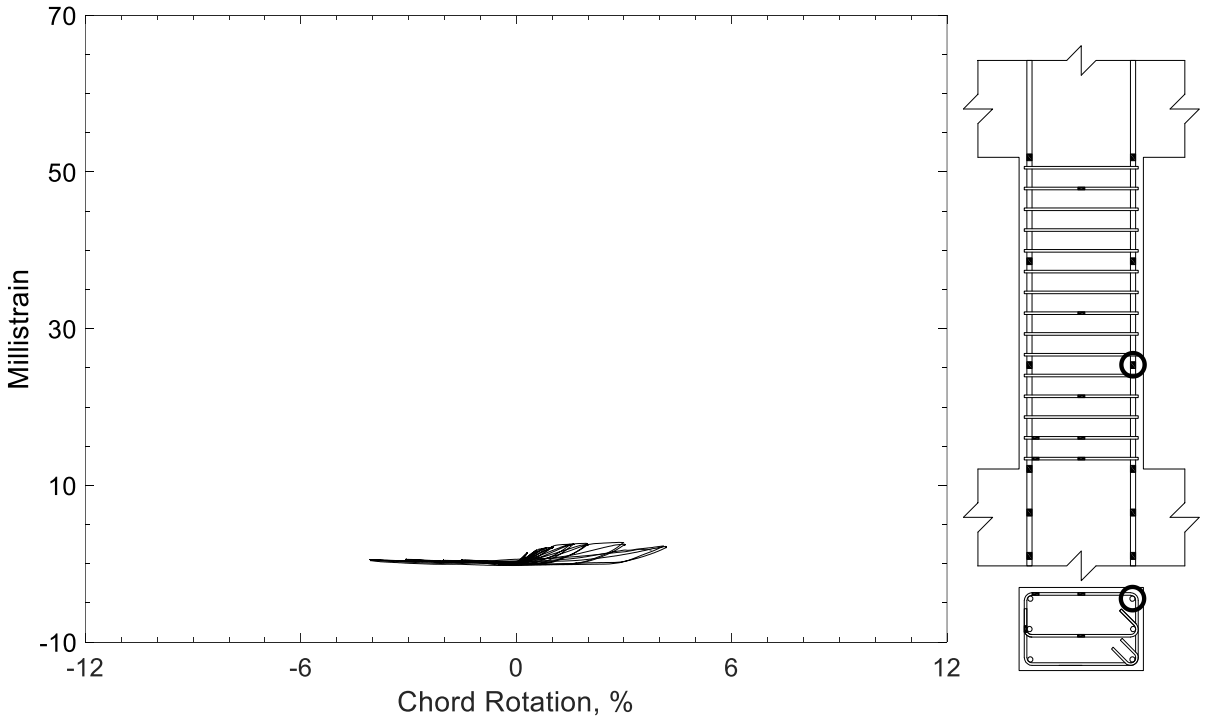

Figure 562 – Measured strain in parallel bar of P80-2.5, strain gauge P8

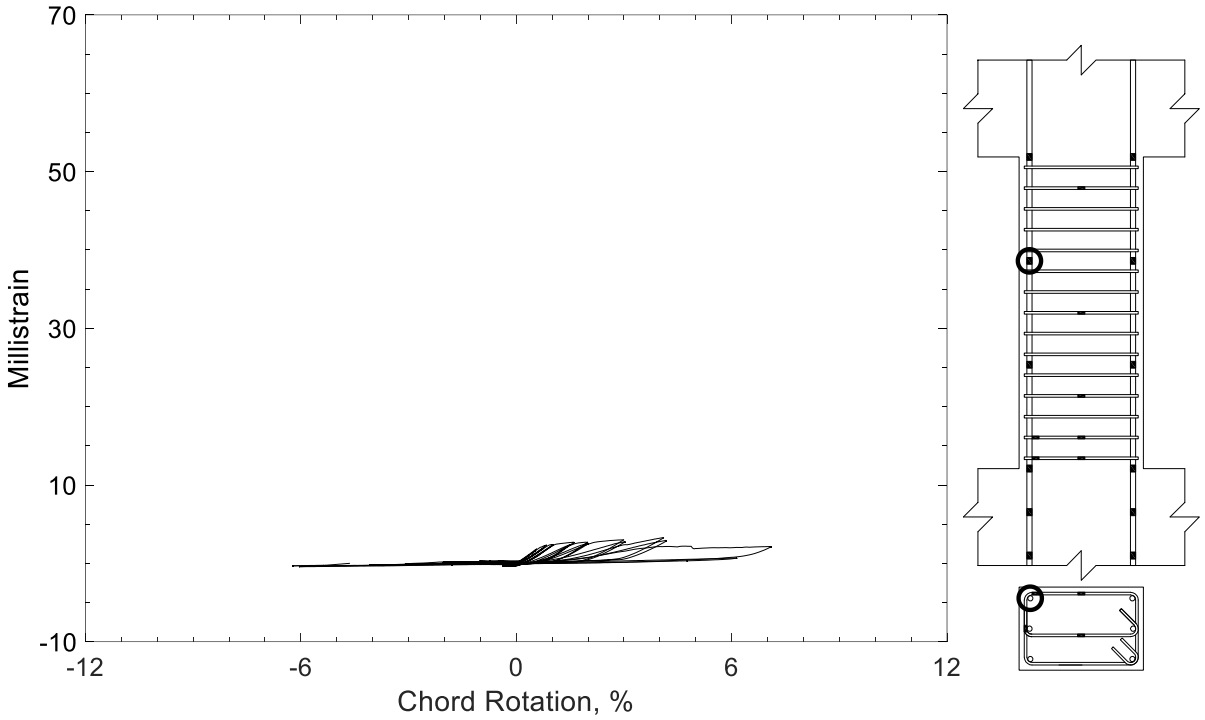

Figure 563 – Measured strain in parallel bar of P80-2.5, strain gauge P9

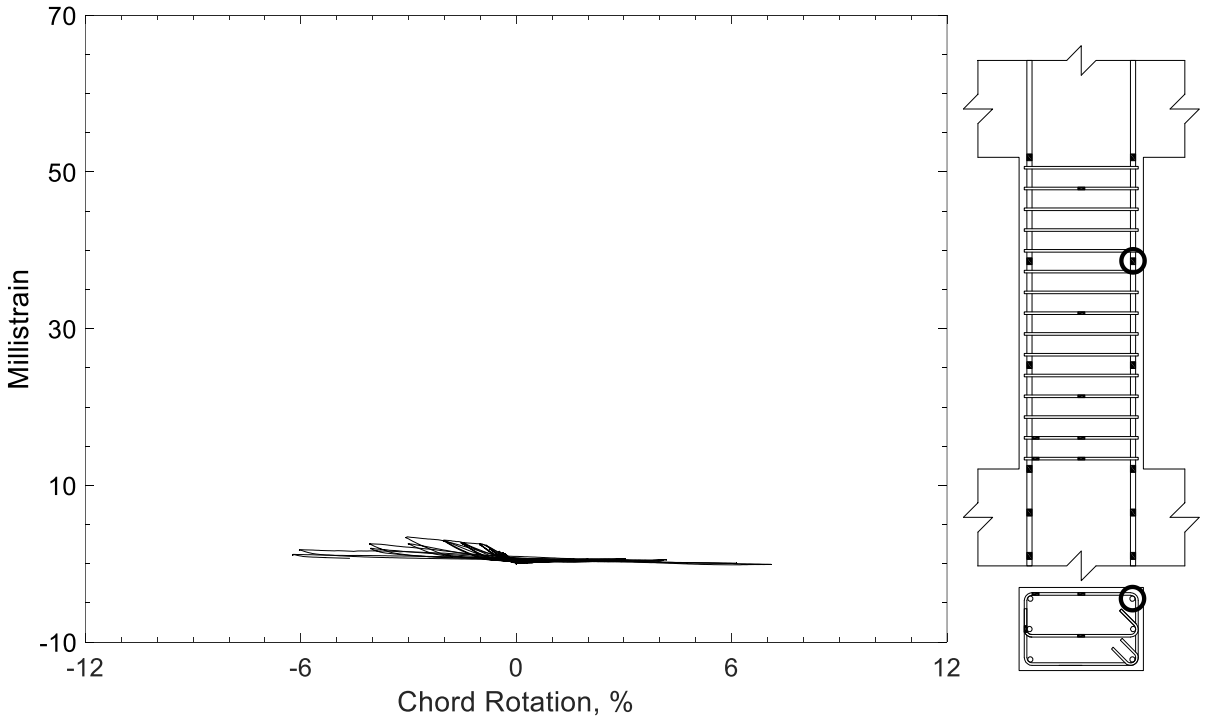

Figure 564 – Measured strain in parallel bar of P80-2.5, strain gauge P10

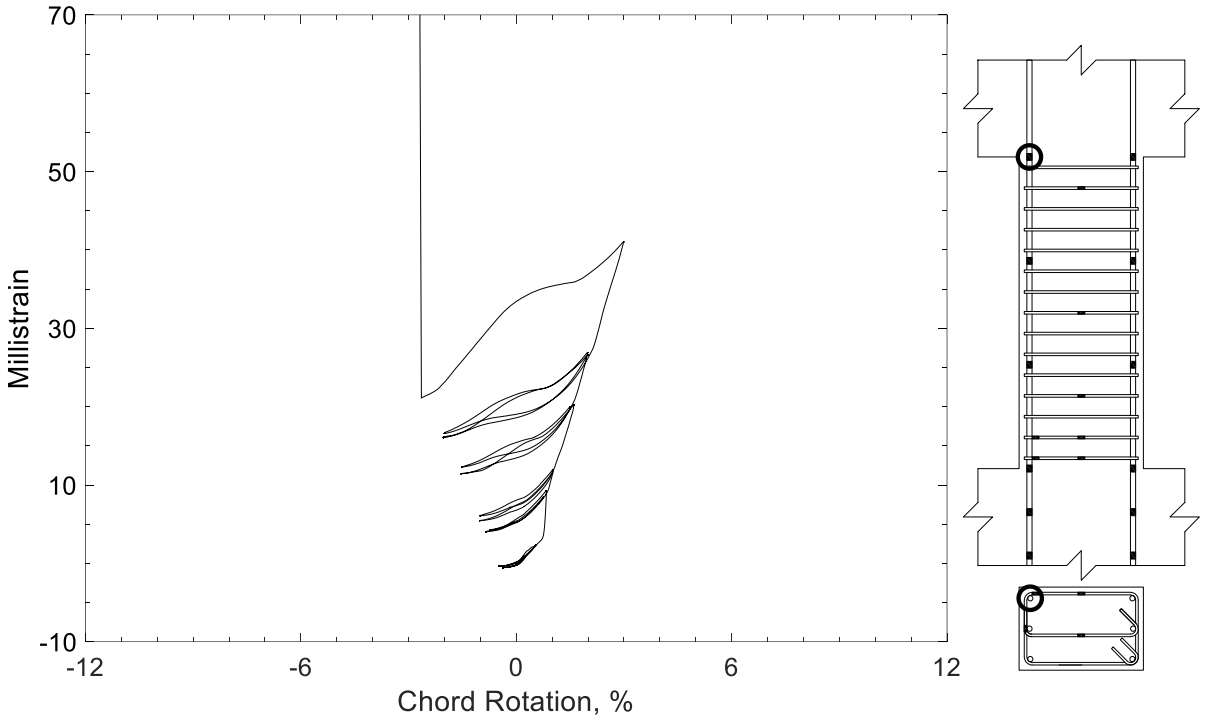

Figure 565 – Measured strain in parallel bar of P80-2.5, strain gauge P11

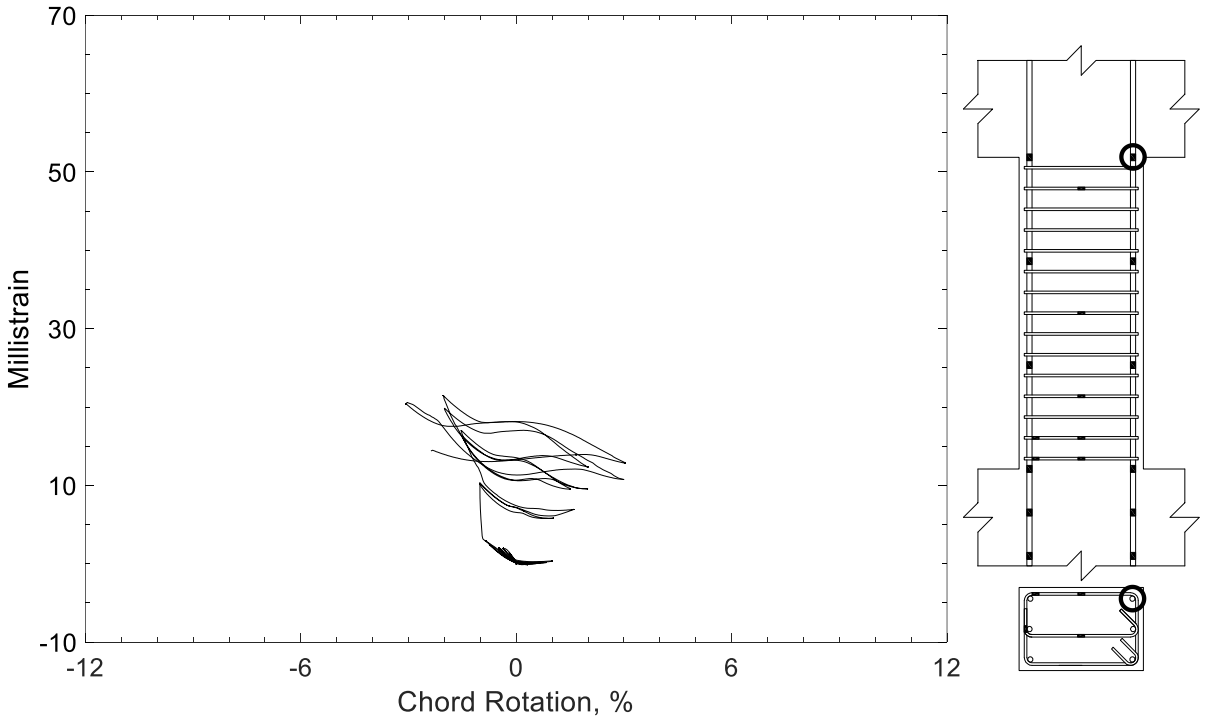

Figure 566 – Measured strain in parallel bar of P80-2.5, strain gauge P12

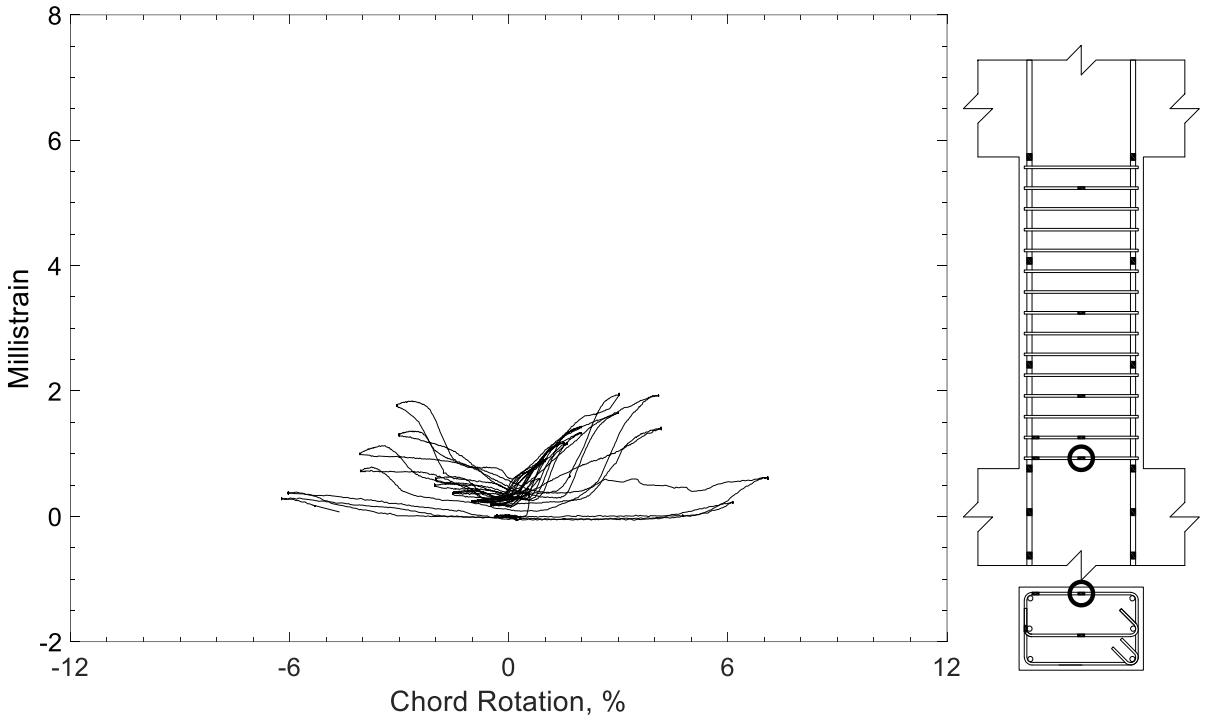

Figure 567 – Measured strain in closed stirrup of P80-2.5, strain gauge S1

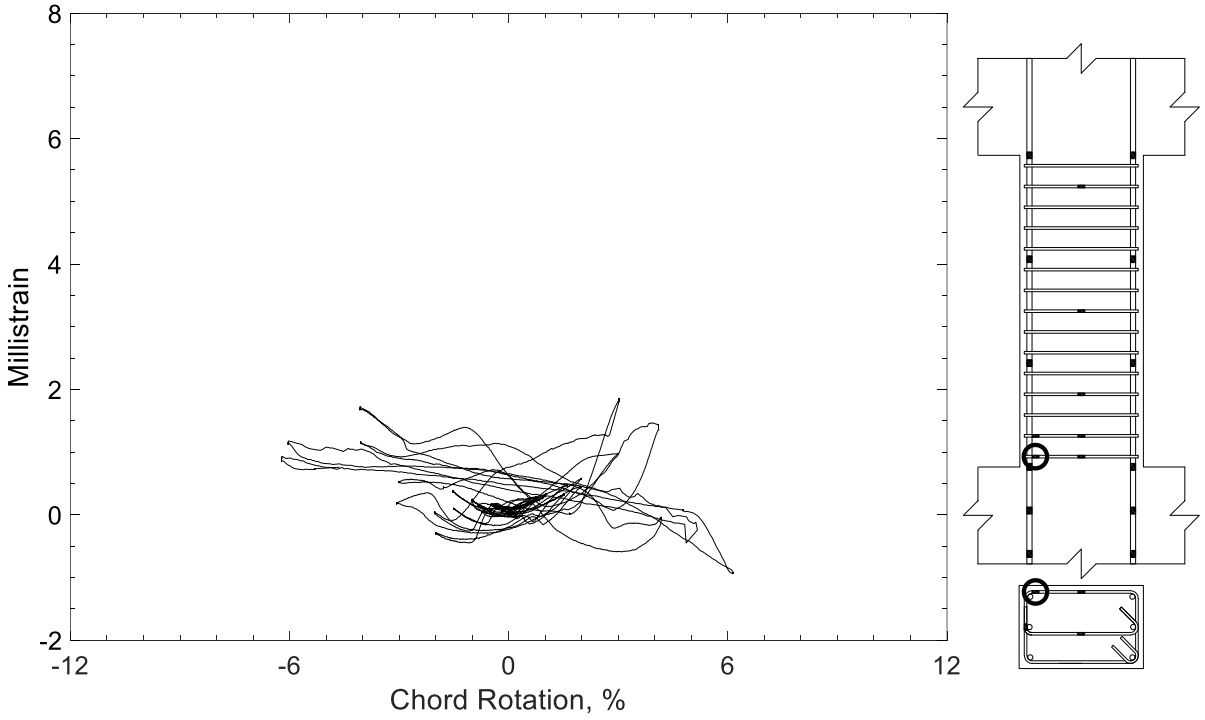

Figure 568 – Measured strain in closed stirrup of P80-2.5, strain gauge S2

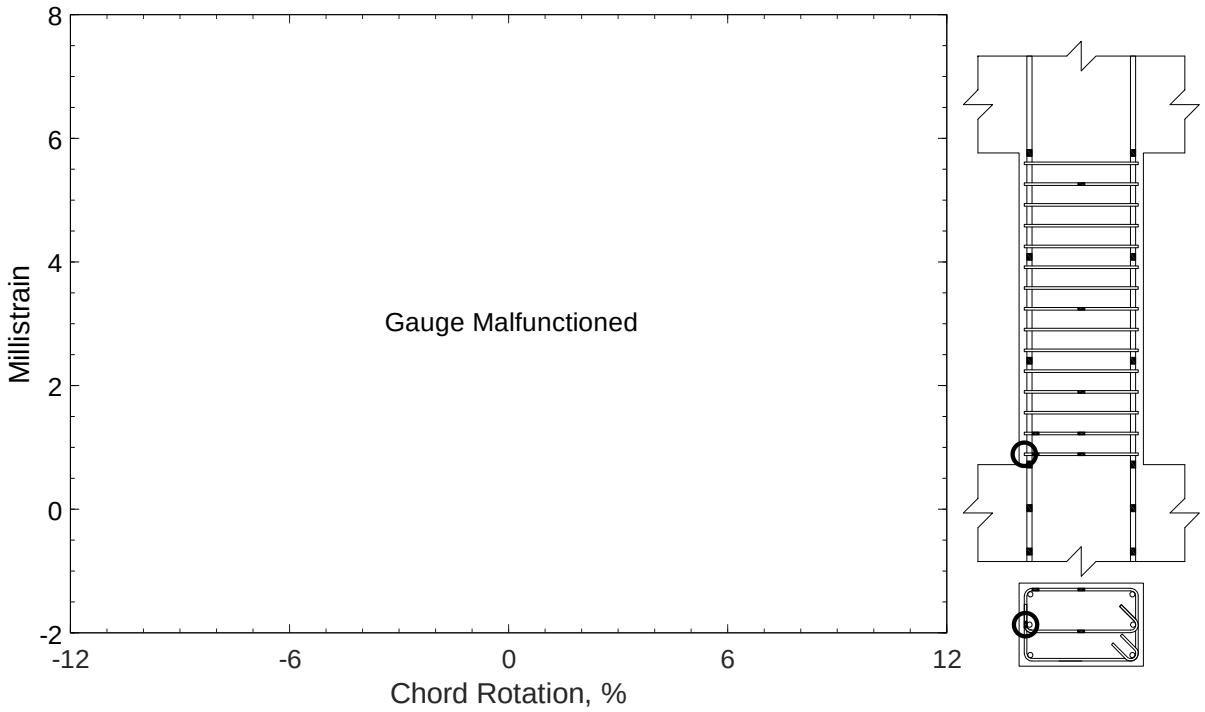

Figure 569 – Measured strain in closed stirrup of P80-2.5, strain gauge S3

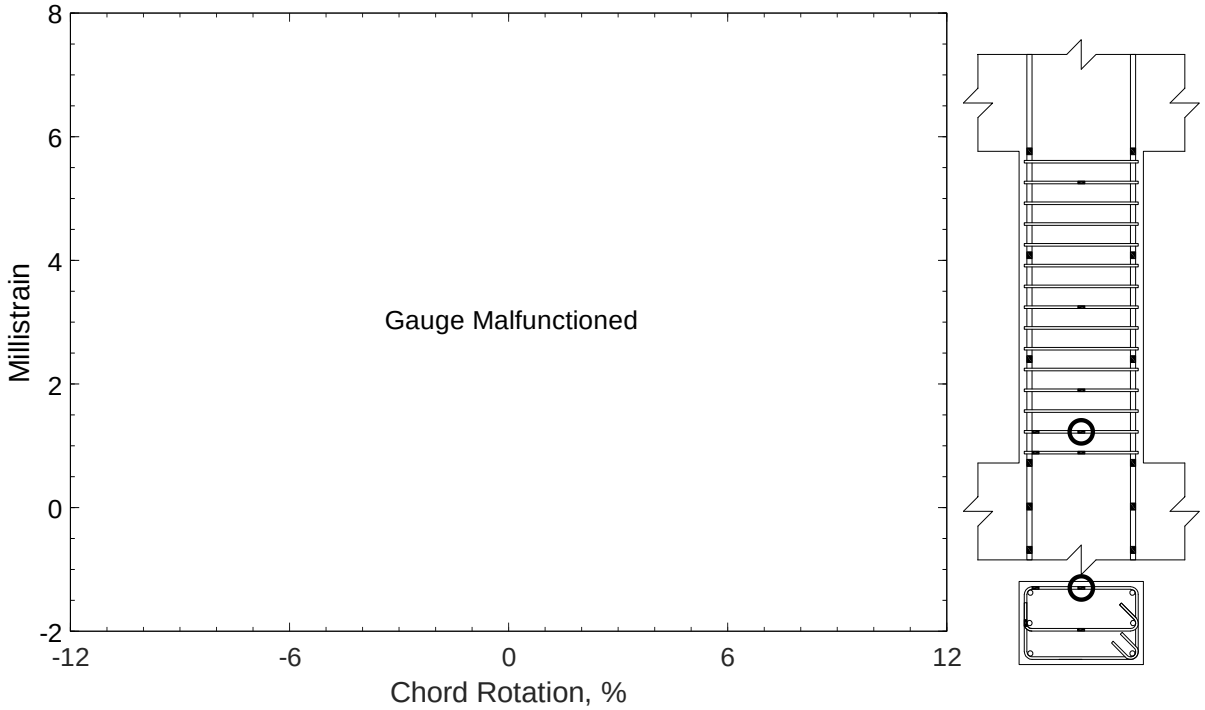

Figure 570 – Measured strain in closed stirrup of P80-2.5, strain gauge S4

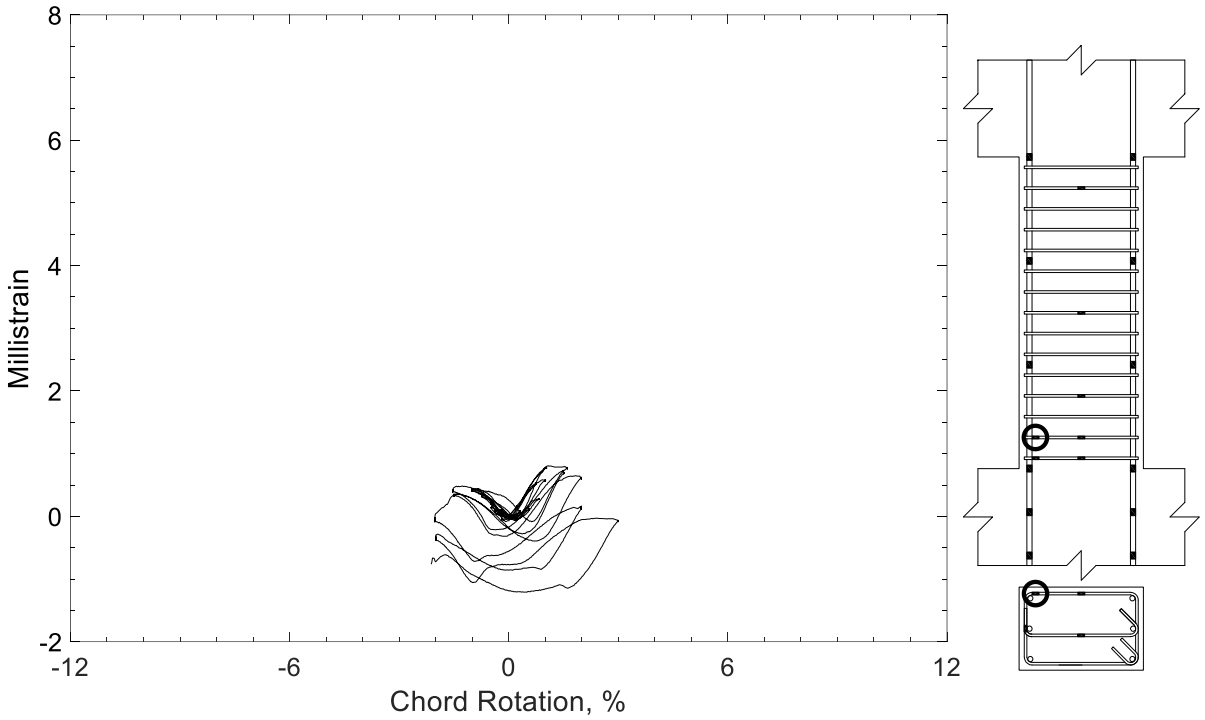

Figure 571 – Measured strain in closed stirrup of P80-2.5, strain gauge S5

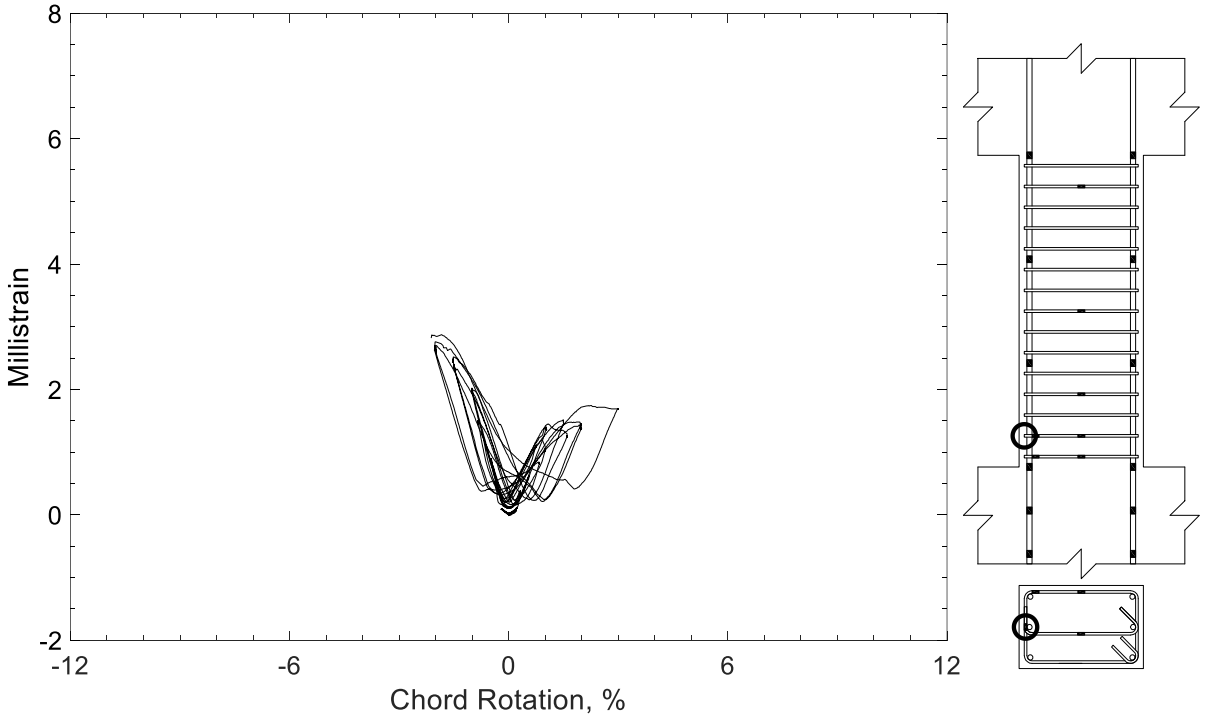

Figure 572 – Measured strain in closed stirrup of P80-2.5, strain gauge S6

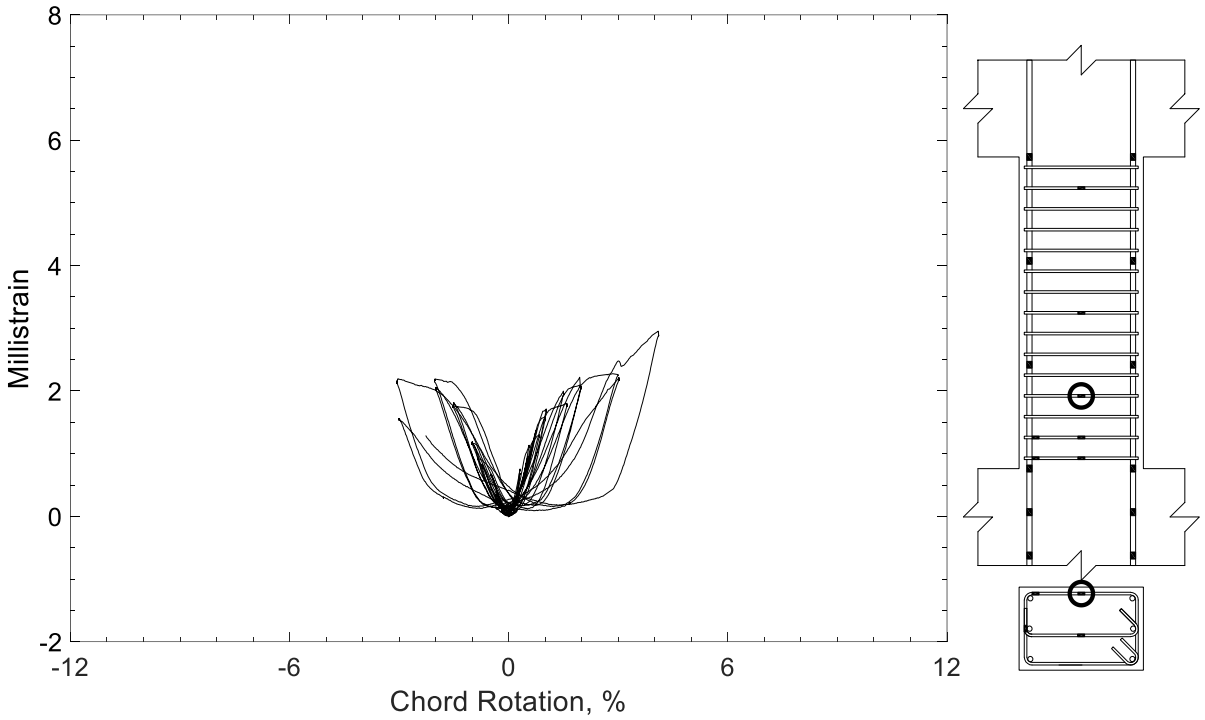

Figure 573 – Measured strain in closed stirrup of P80-2.5, strain gauge S7

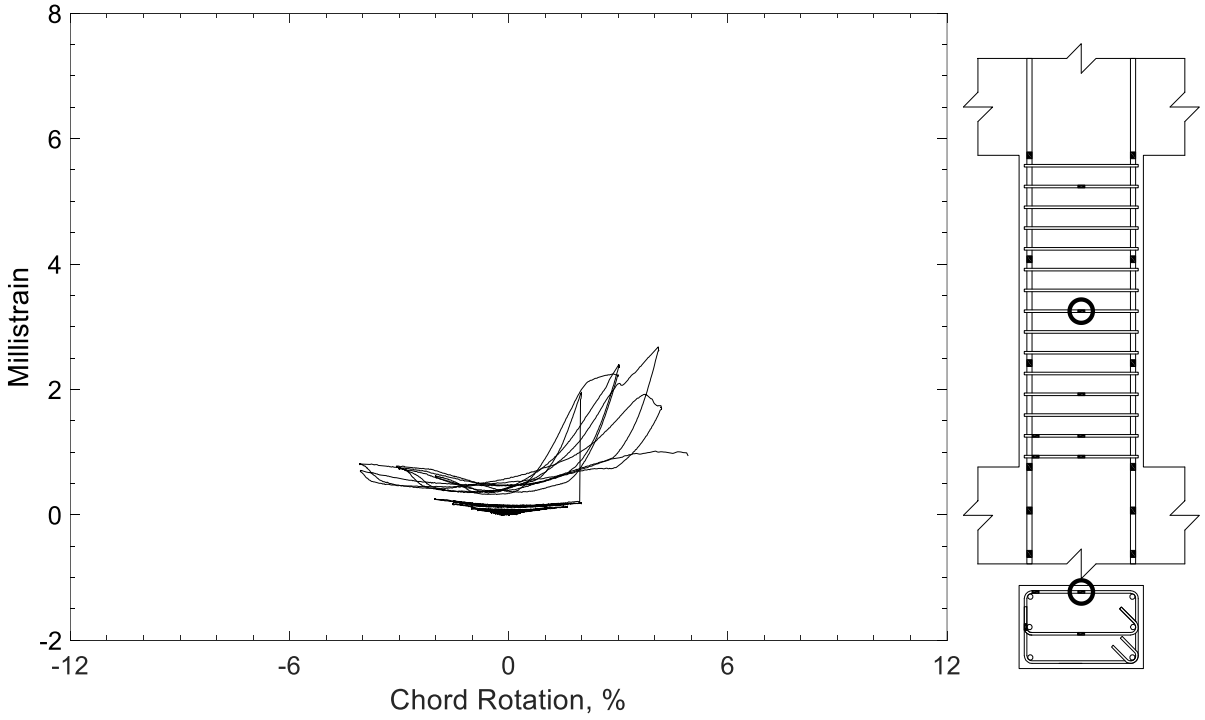

Figure 574 – Measured strain in closed stirrup of P80-2.5, strain gauge S8

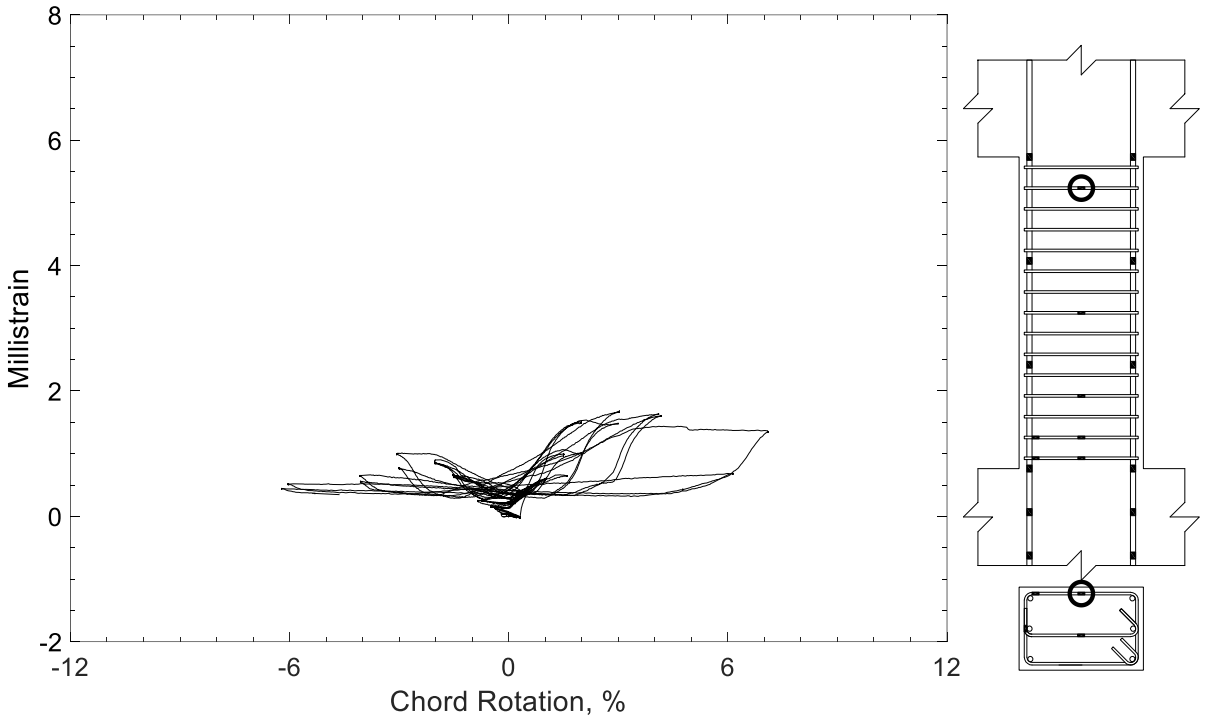

Figure 575 – Measured strain in closed stirrup of P80-2.5, strain gauge S9

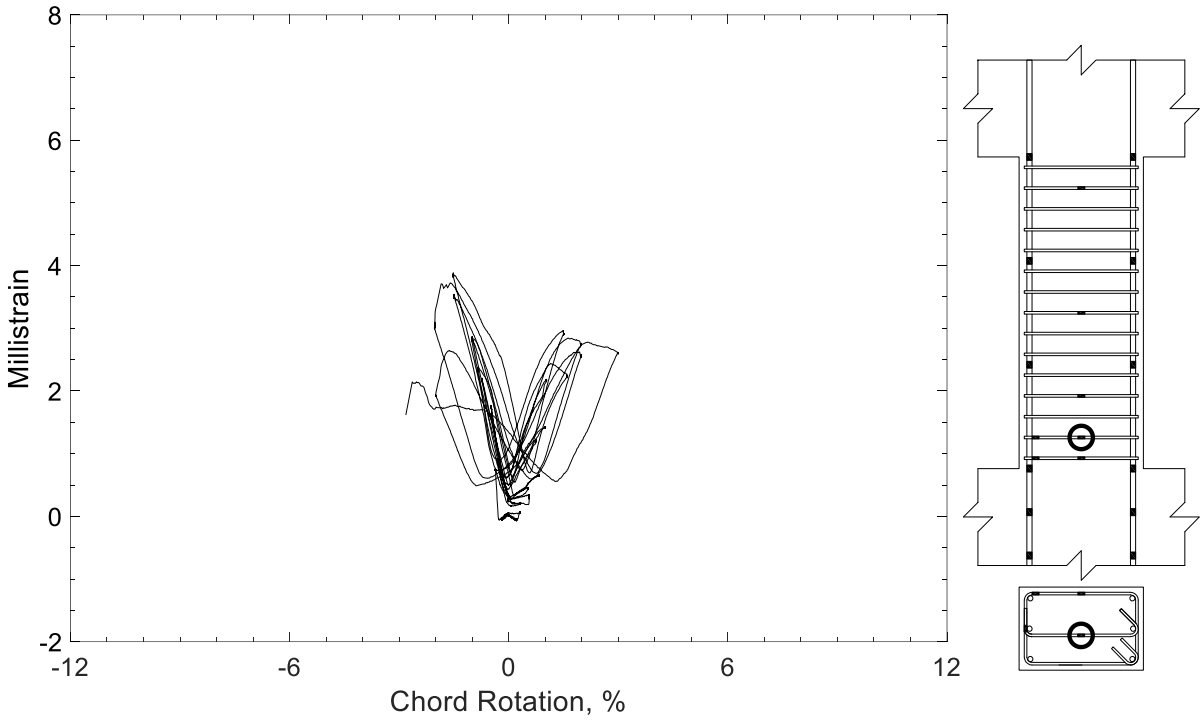

Figure 576 – Measured strain in crosstie of P80-2.5, strain gauge T1

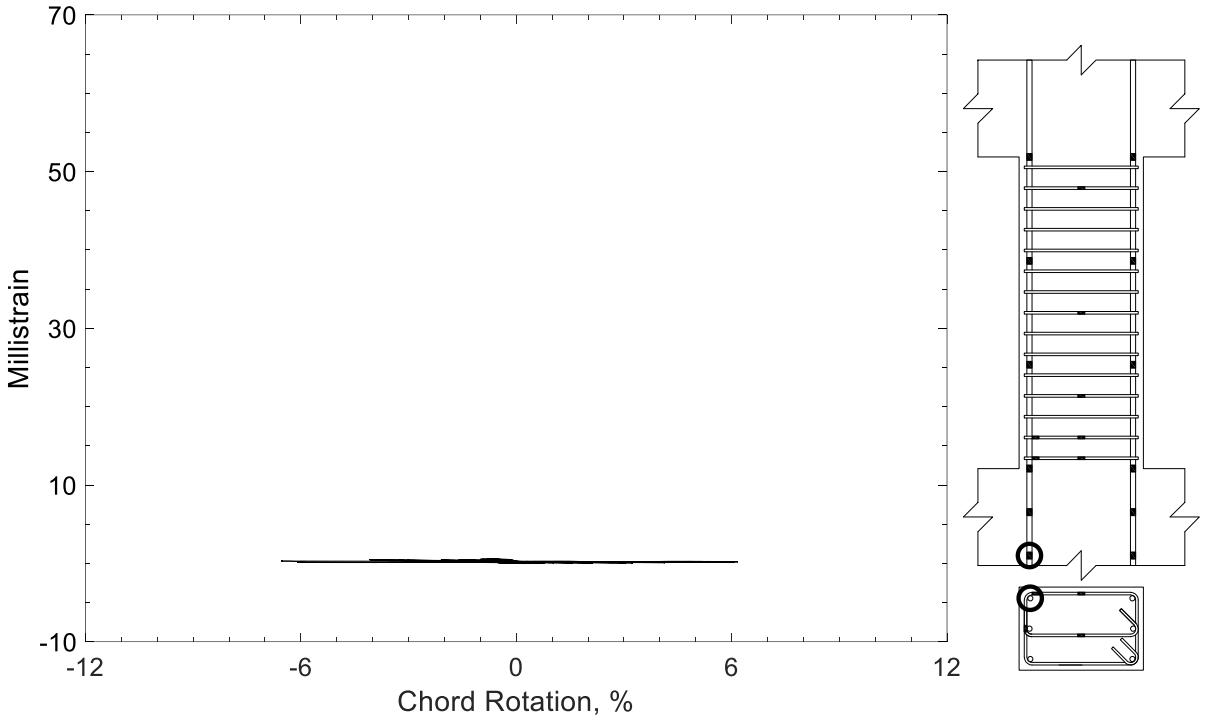

Figure 577 – Measured strain in parallel bar of P100-2.5, strain gauge P1

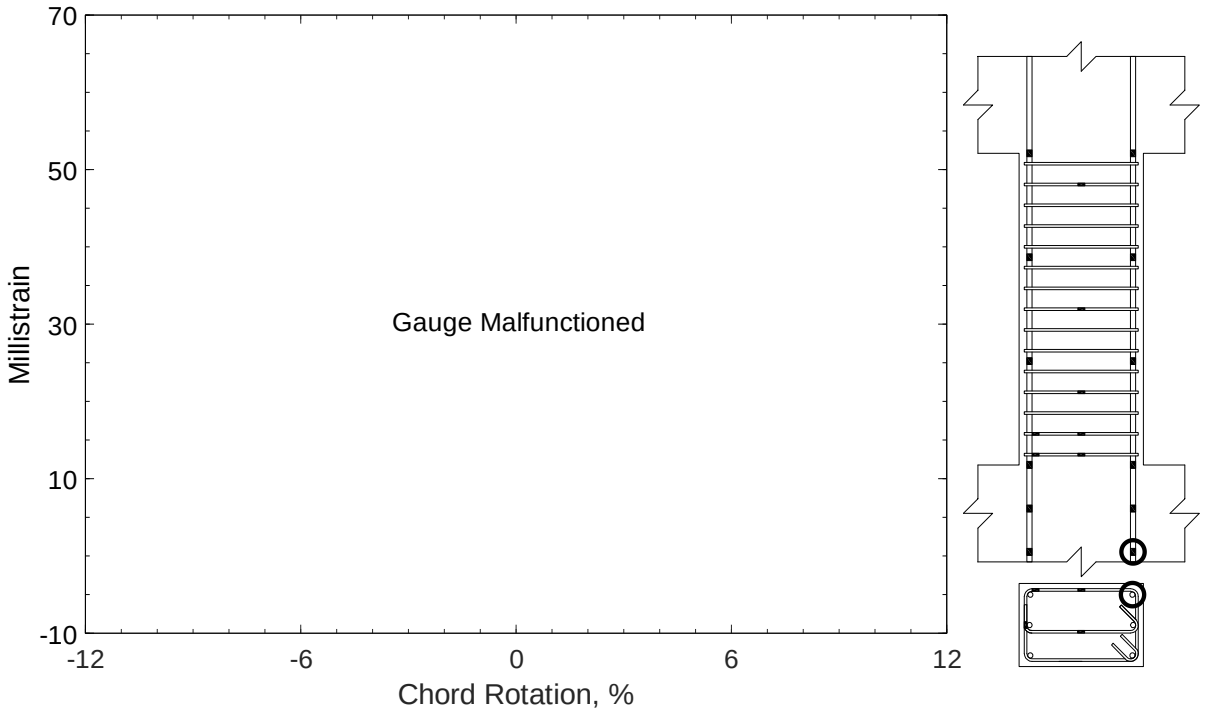

Figure 578 – Measured strain in parallel bar of P100-2.5, strain gauge P2

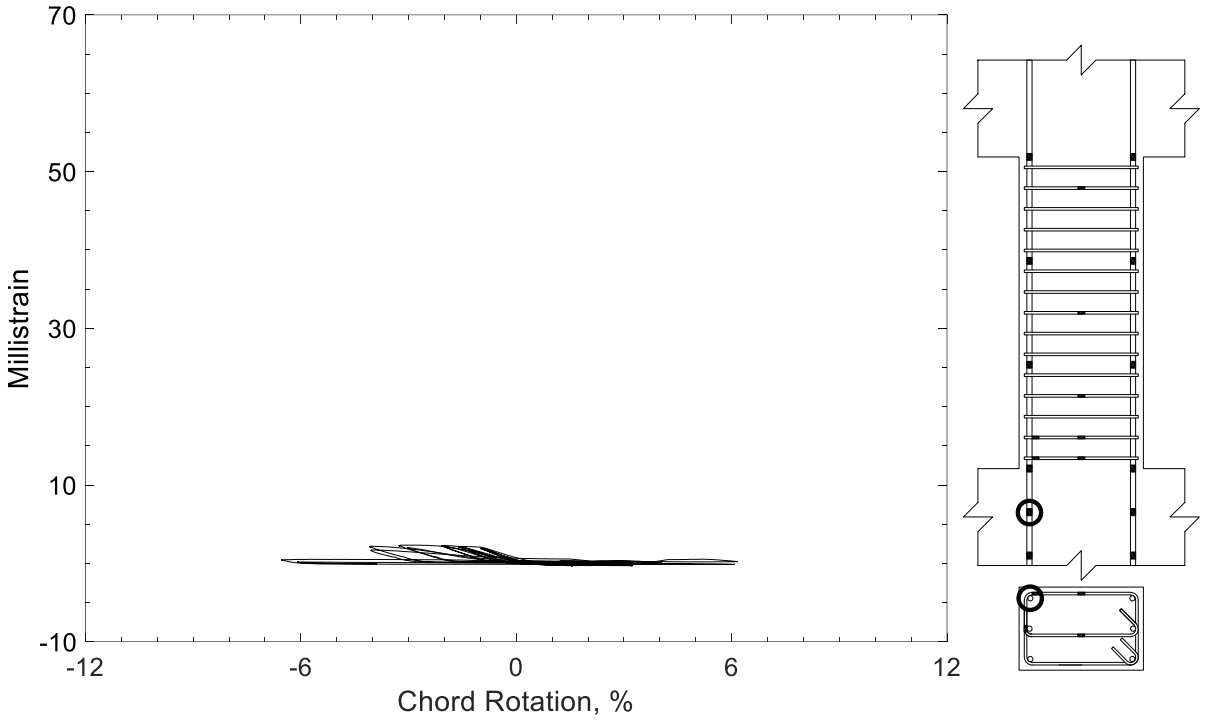

Figure 579 – Measured strain in parallel bar of P100-2.5, strain gauge P3

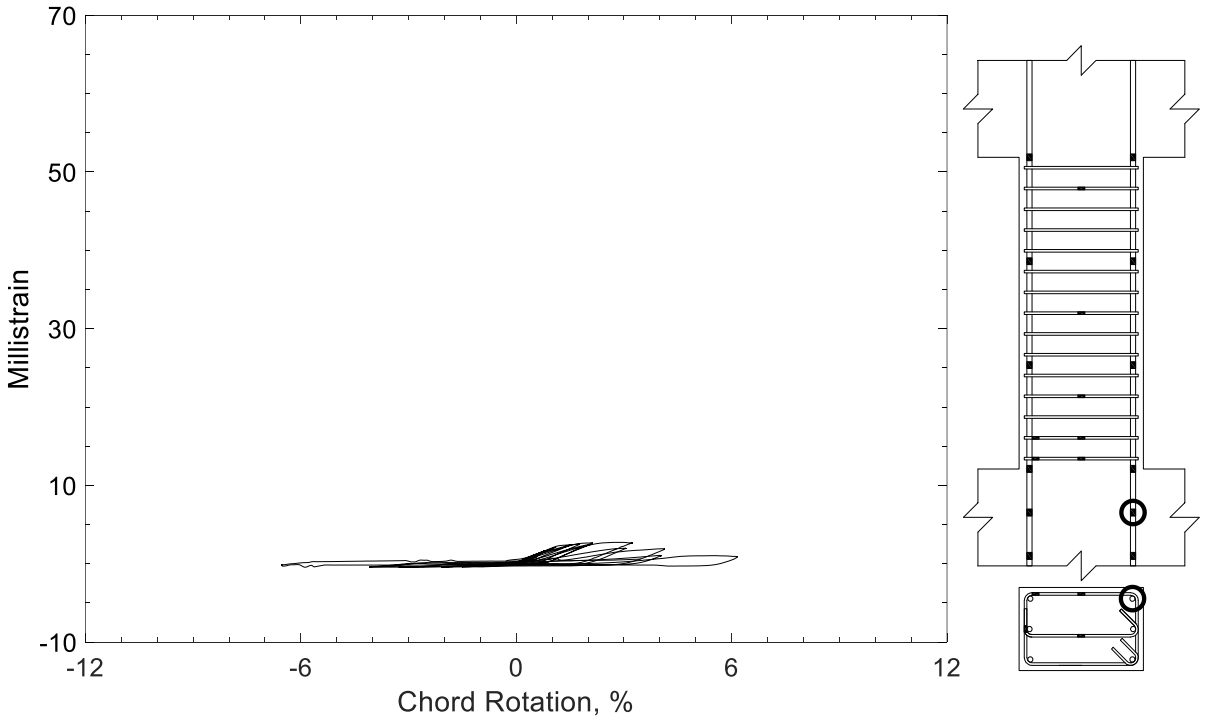

Figure 580 – Measured strain in parallel bar of P100-2.5, strain gauge P4

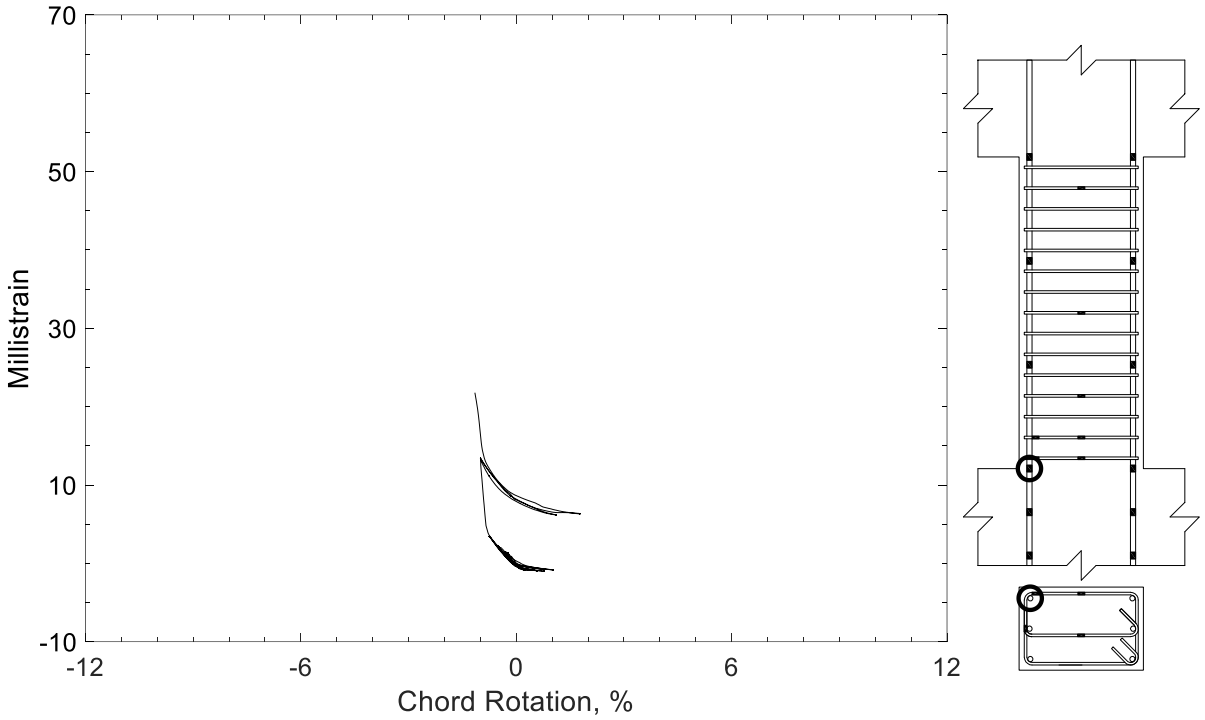

Figure 581 – Measured strain in parallel bar of P100-2.5, strain gauge P5

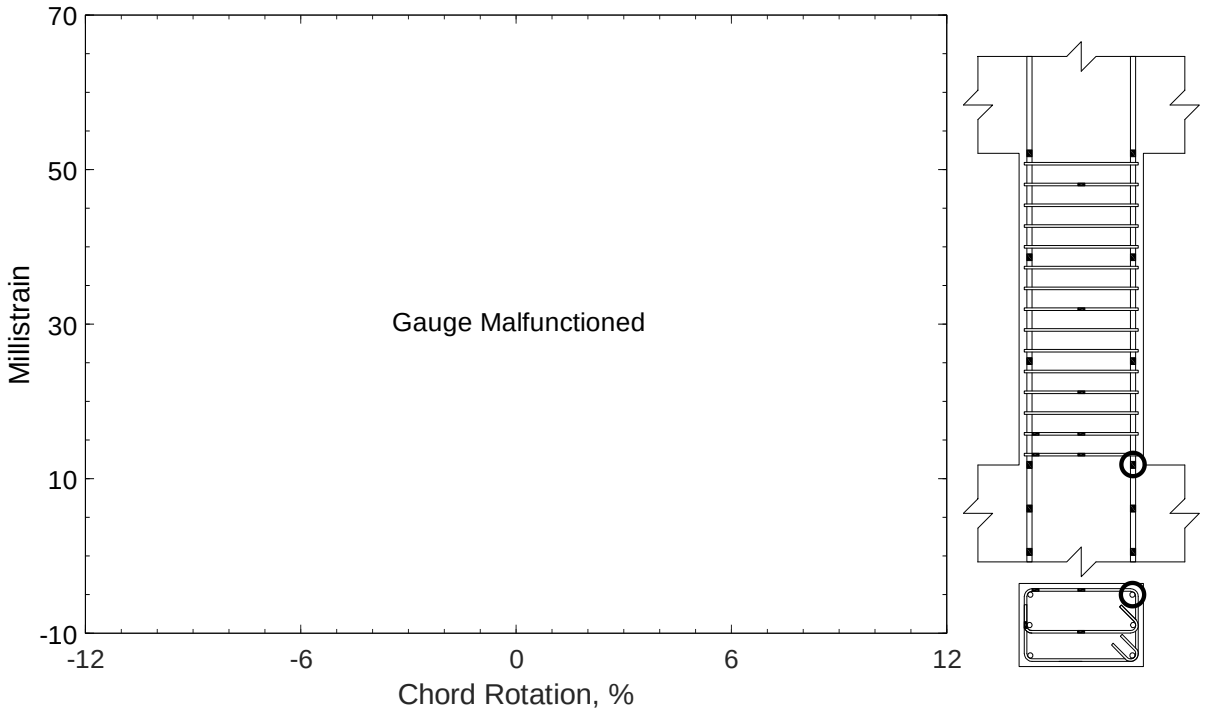

Figure 582 – Measured strain in parallel bar of P100-2.5, strain gauge P6

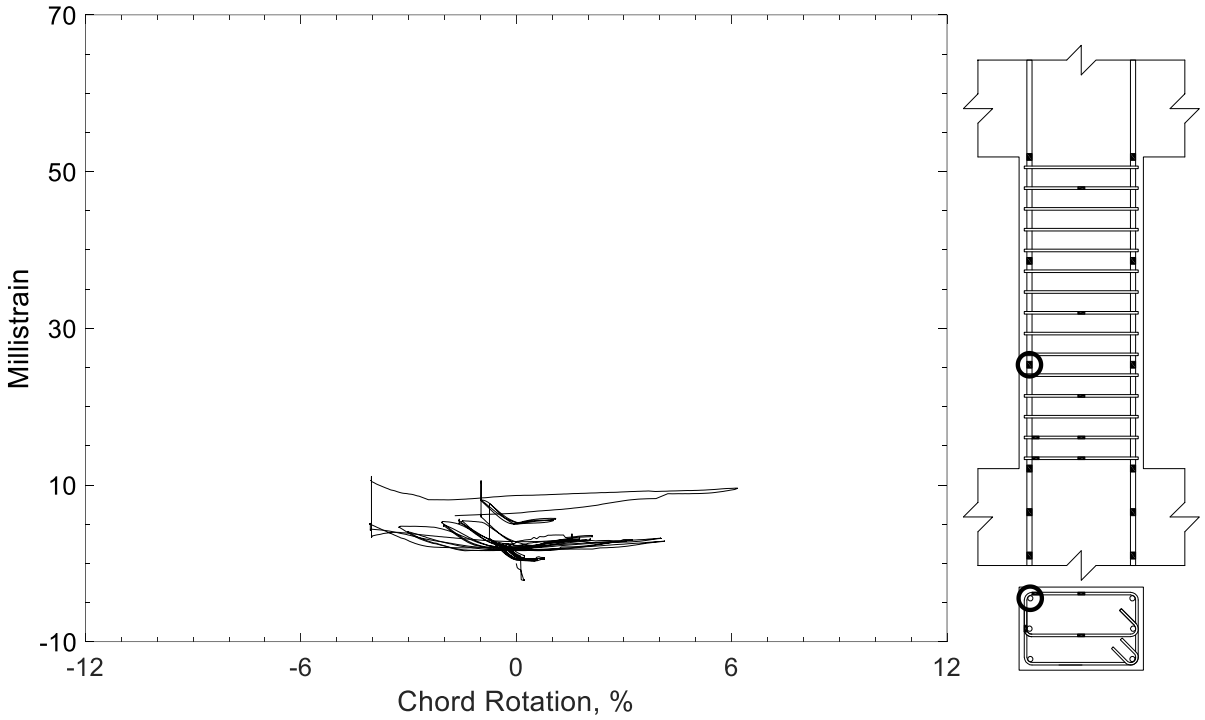

Figure 583 – Measured strain in parallel bar of P100-2.5, strain gauge P7

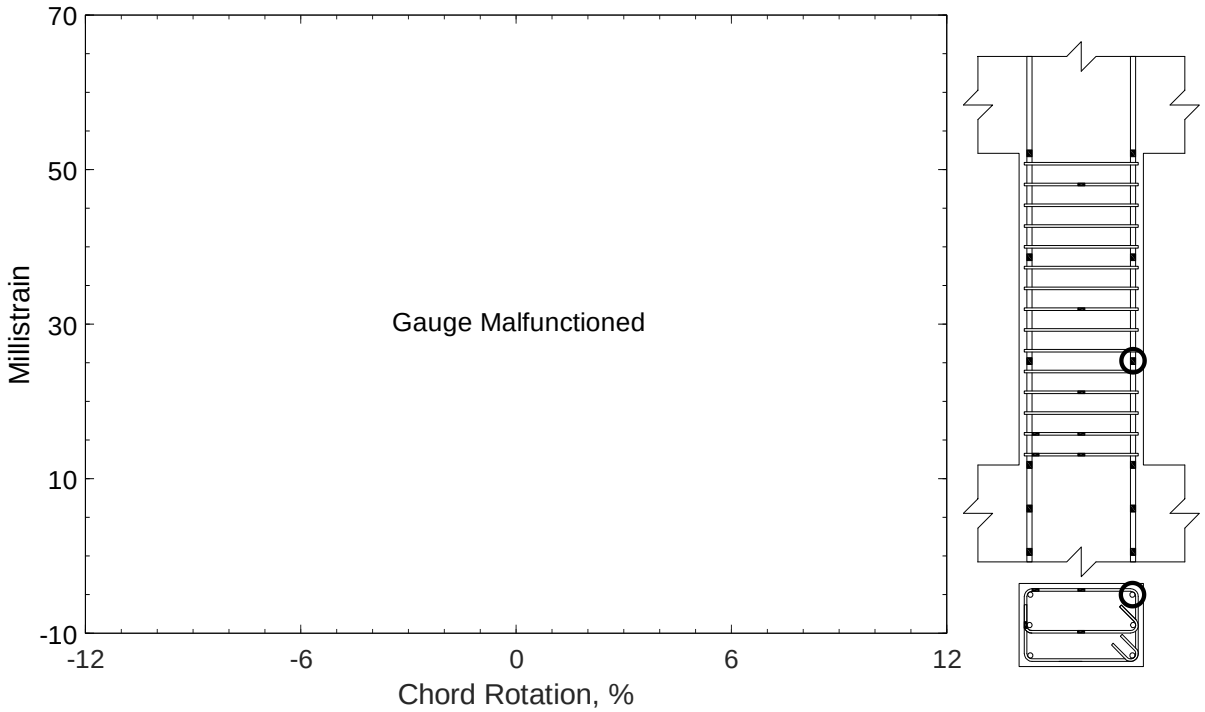

Figure 584 – Measured strain in parallel bar of P100-2.5, strain gauge P8

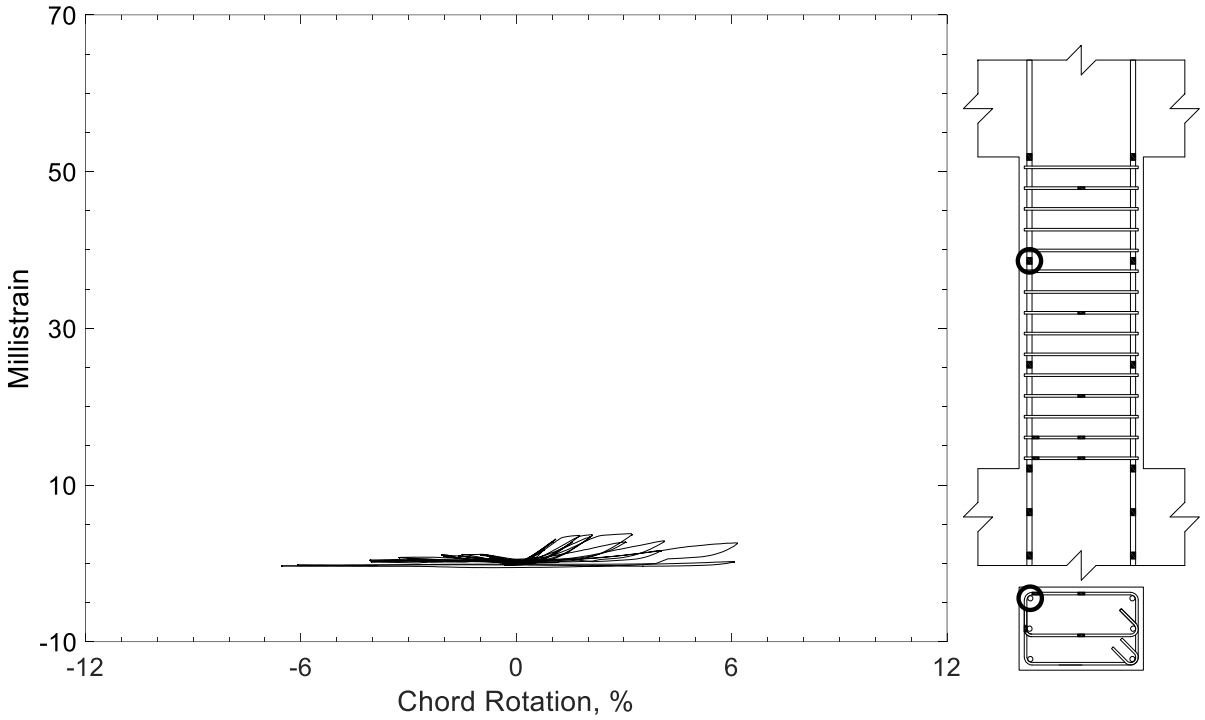

Figure 585 – Measured strain in parallel bar of P100-2.5, strain gauge P9

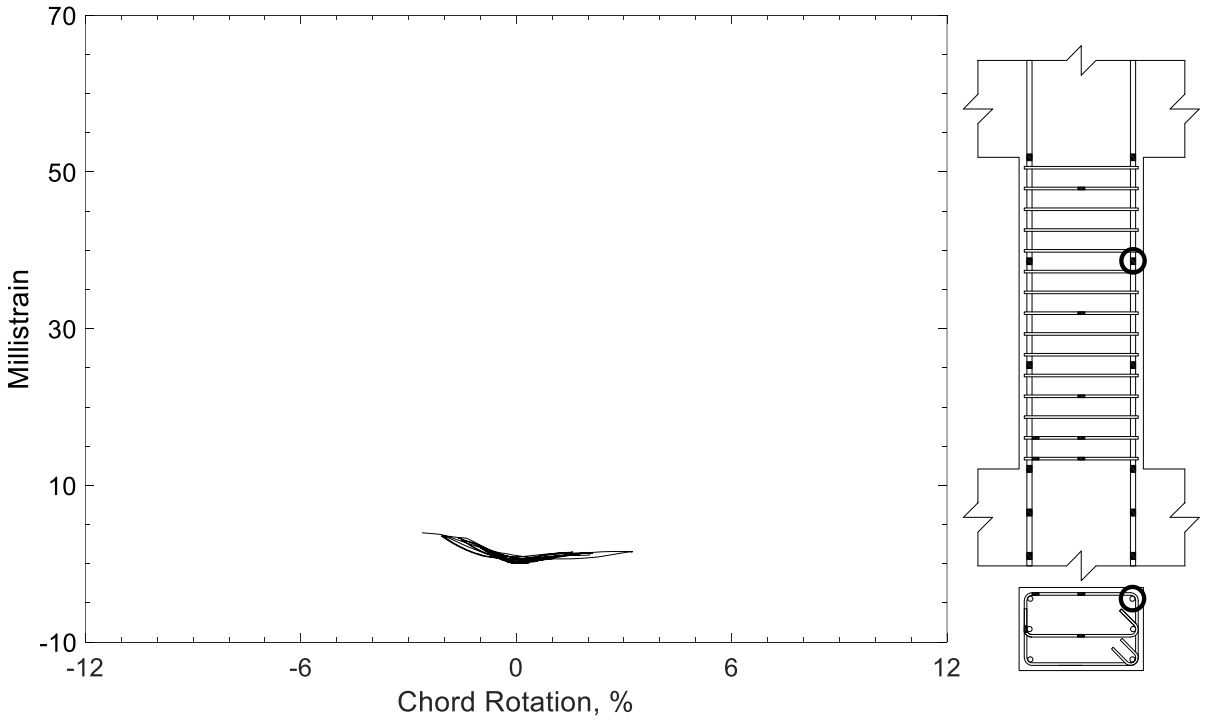

Figure 586 – Measured strain in parallel bar of P100-2.5, strain gauge P10

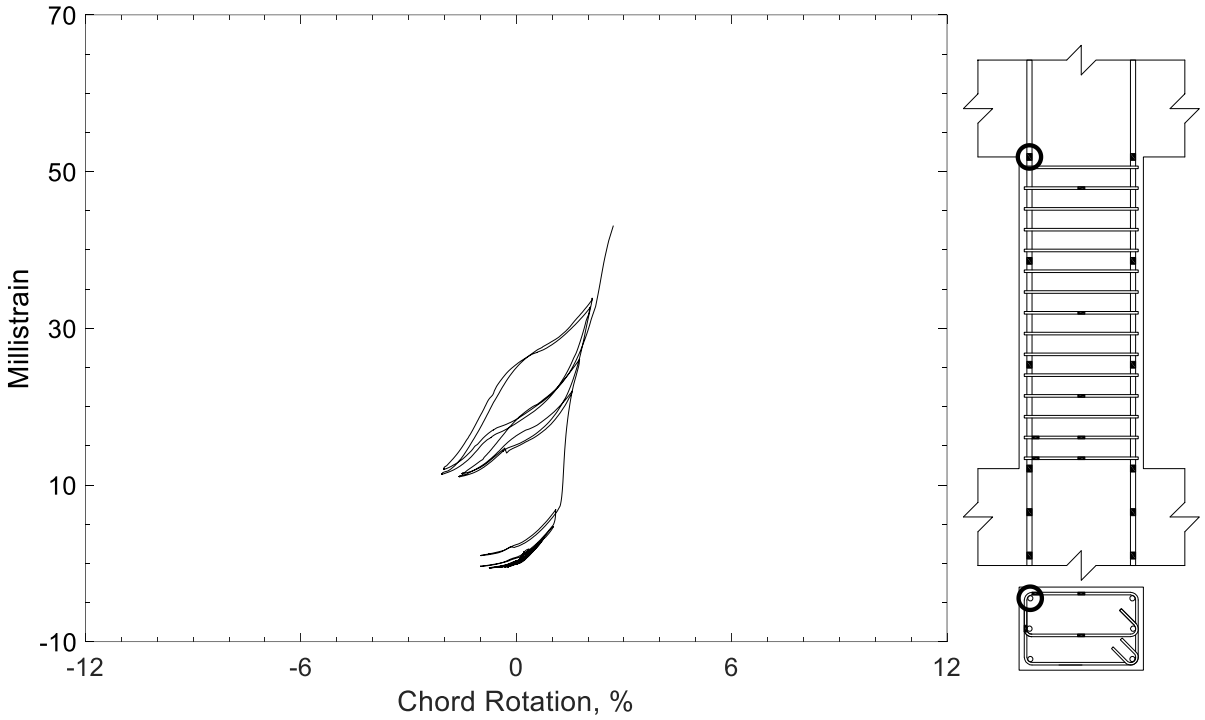

Figure 587 – Measured strain in parallel bar of P100-2.5, strain gauge P11

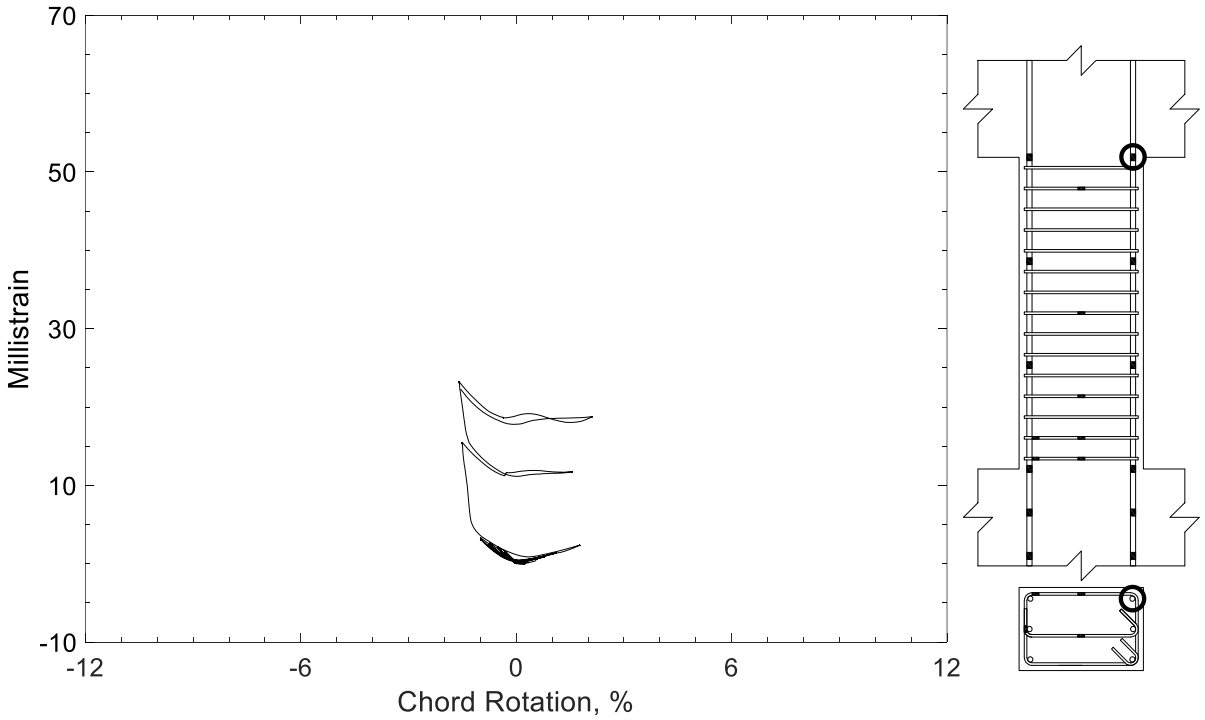

Figure 588 – Measured strain in parallel bar of P100-2.5, strain gauge P12

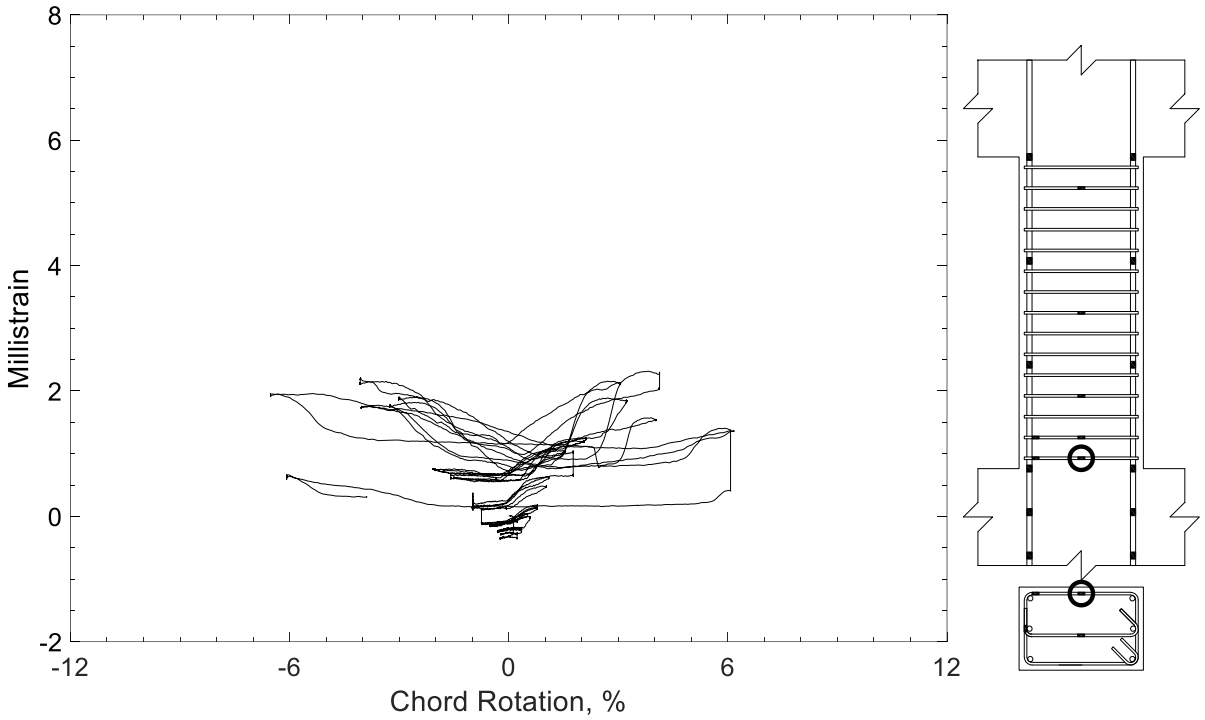

Figure 589 – Measured strain in closed stirrup of P100-2.5, strain gauge S1

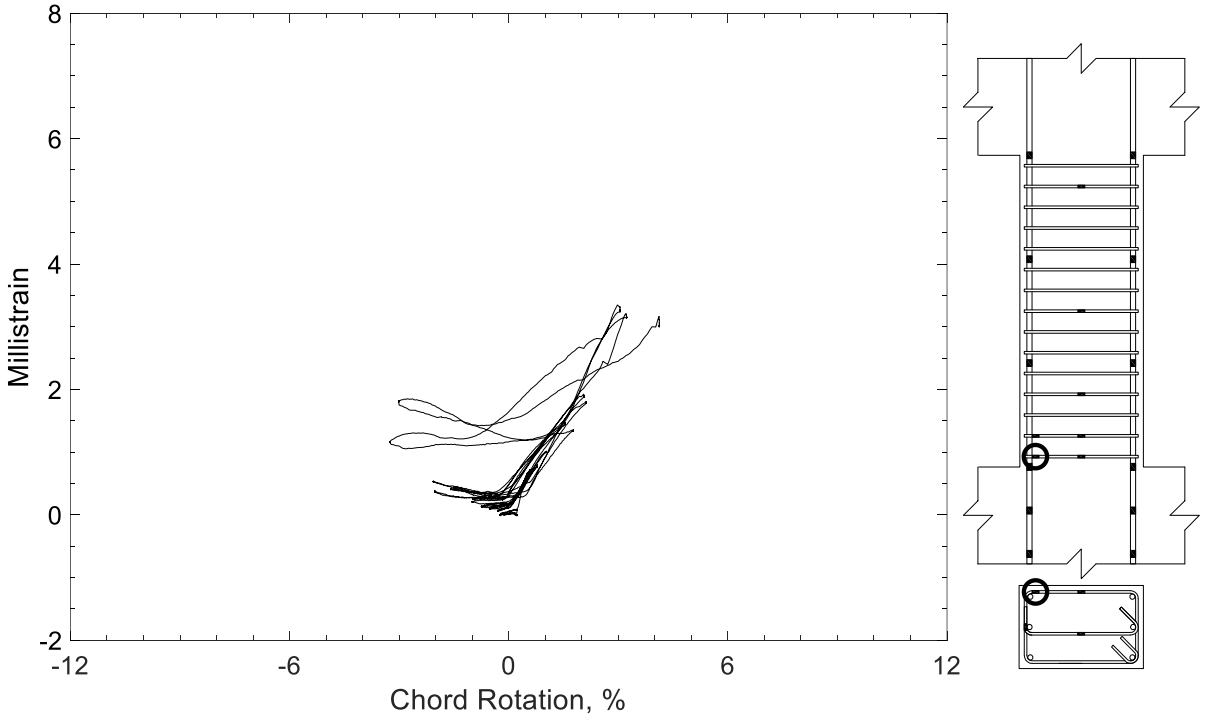

Figure 590 – Measured strain in closed stirrup of P100-2.5, strain gauge S2

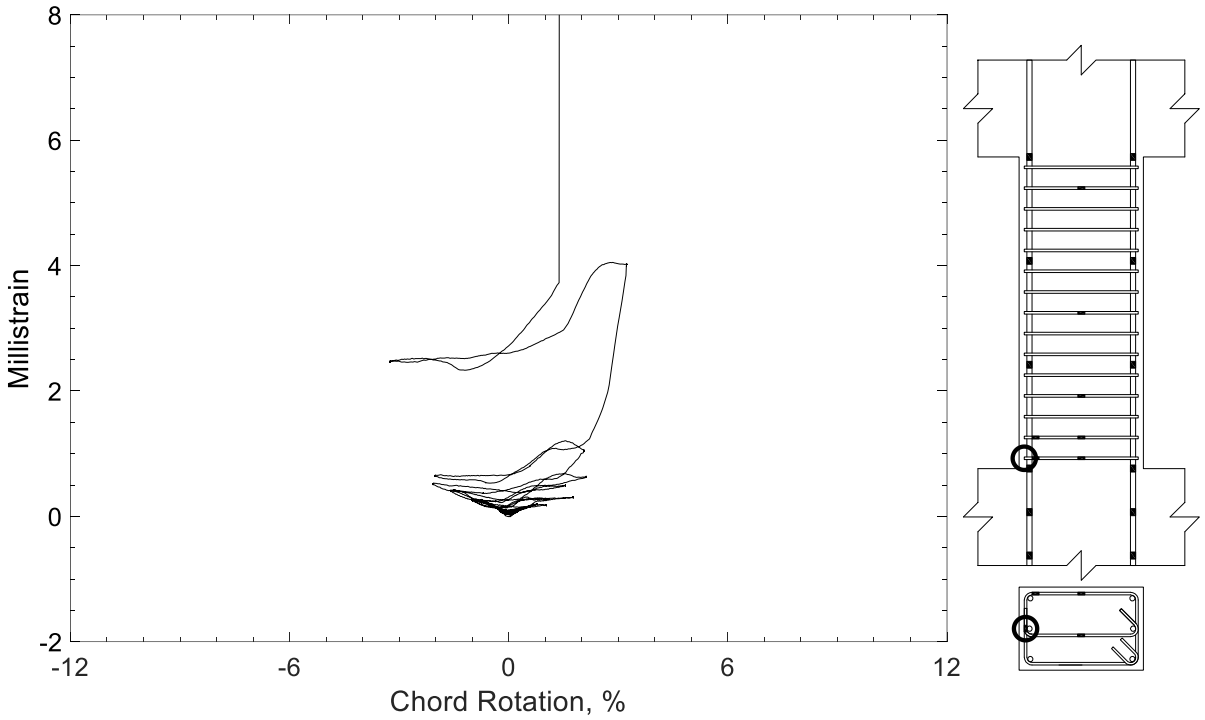

Figure 591 – Measured strain in closed stirrup of P100-2.5, strain gauge S3

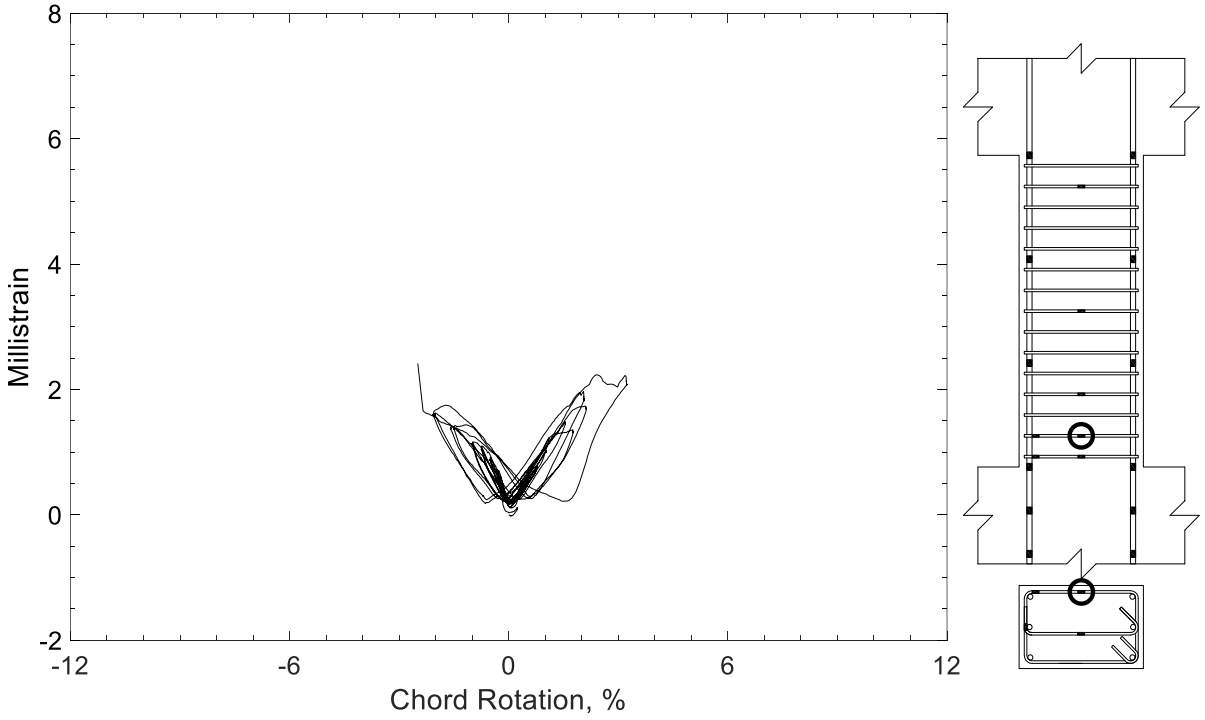

Figure 592 – Measured strain in closed stirrup of P100-2.5, strain gauge S4

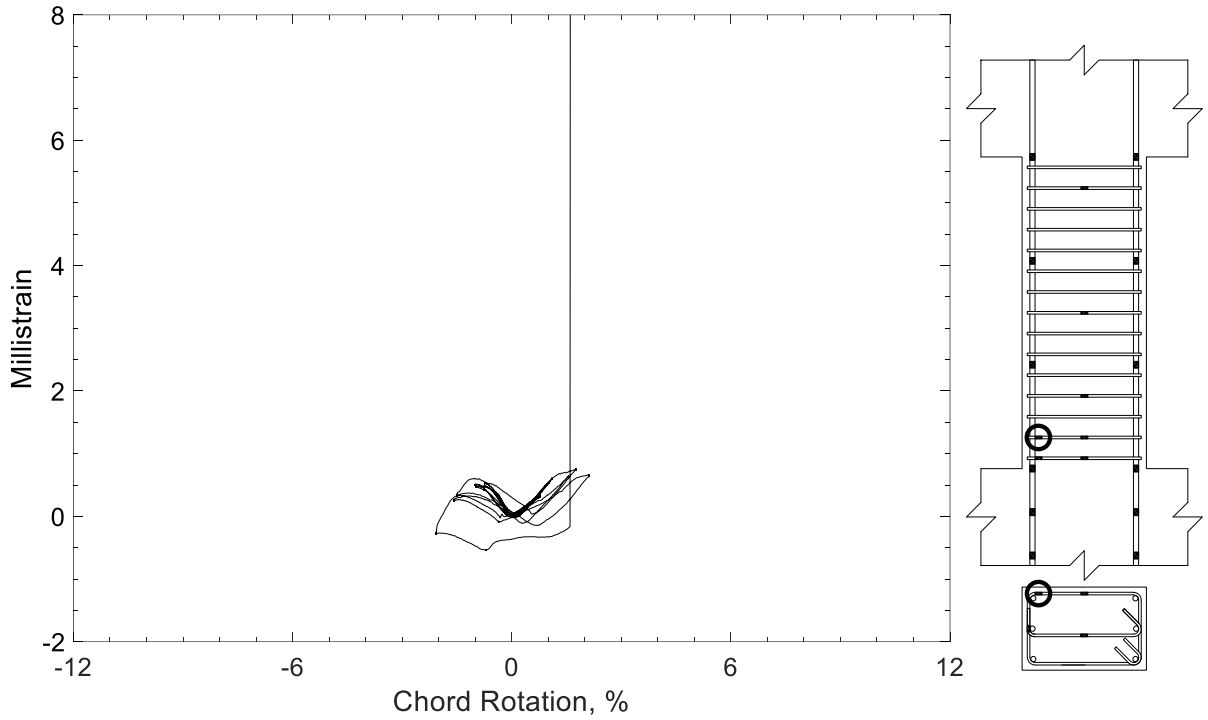

Figure 593 – Measured strain in closed stirrup of P100-2.5, strain gauge S5

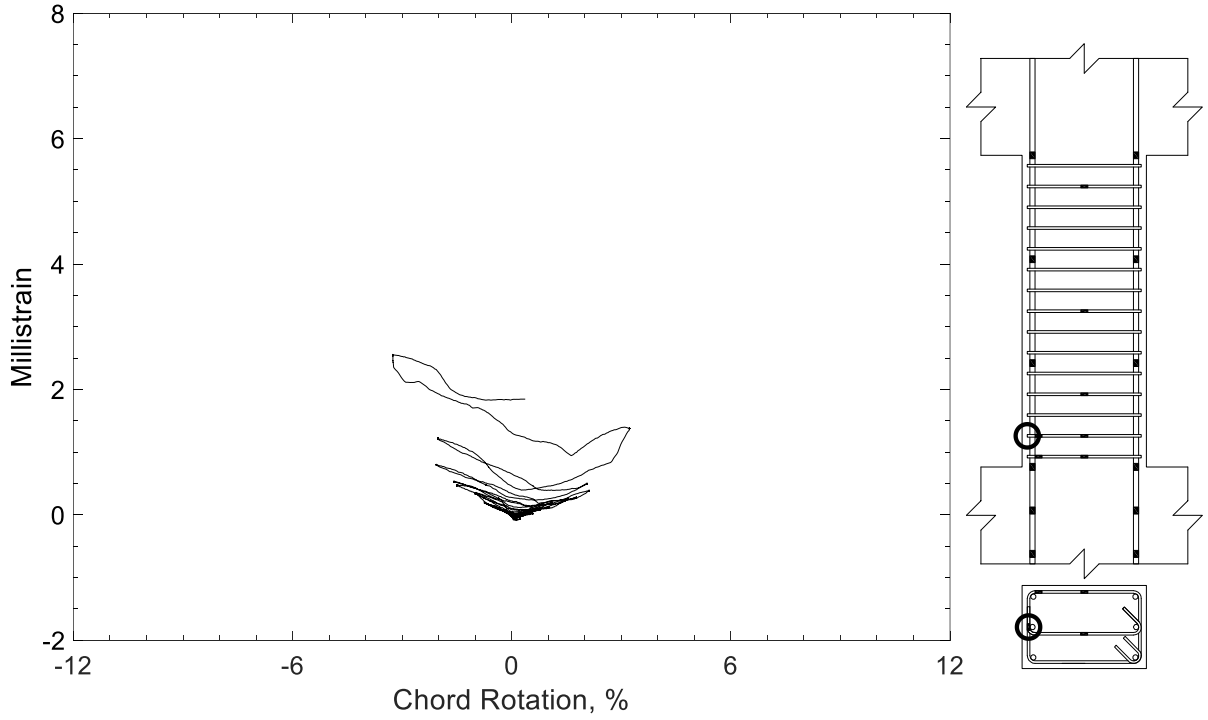

Figure 594 – Measured strain in closed stirrup of P100-2.5, strain gauge S6

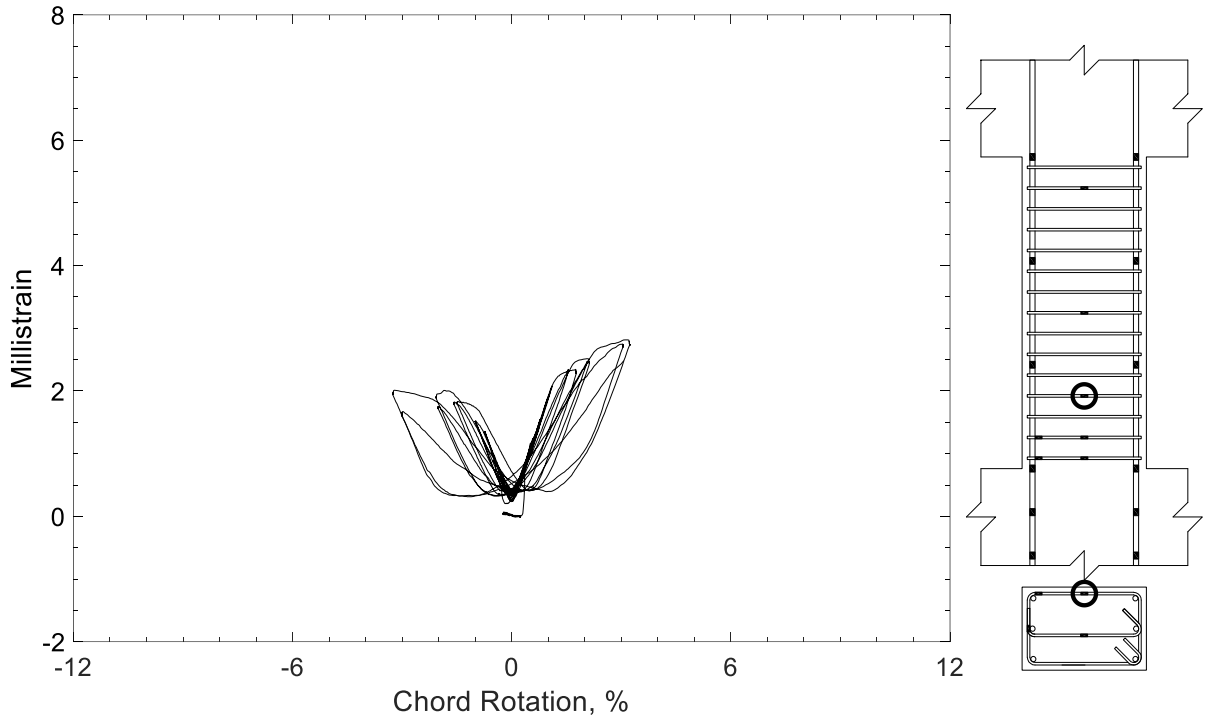

Figure 595 – Measured strain in closed stirrup of P100-2.5, strain gauge S7

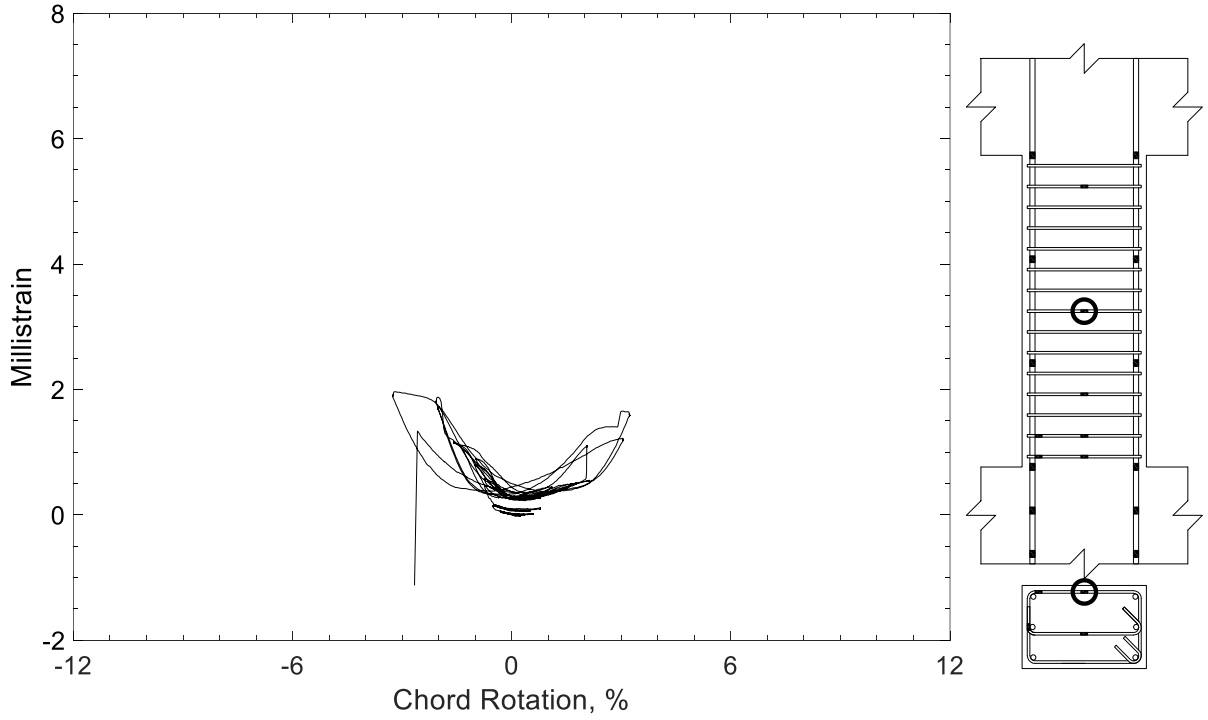

Figure 596 – Measured strain in closed stirrup of P100-2.5, strain gauge S8

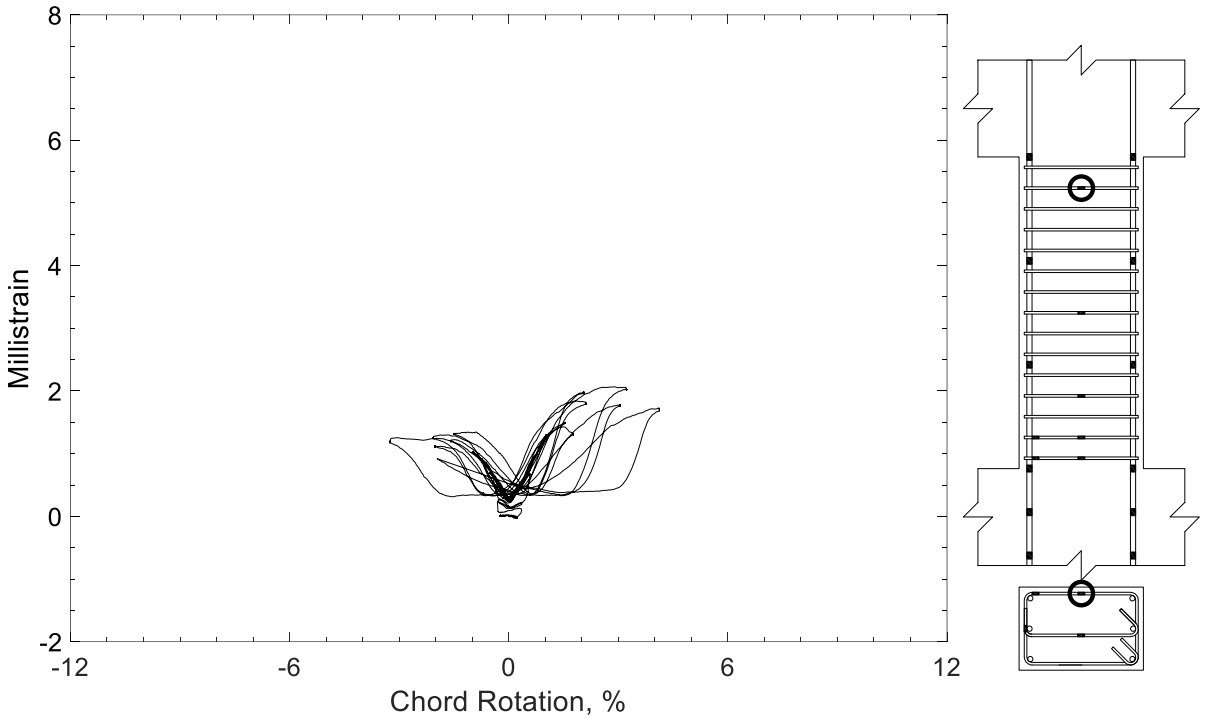

Figure 597 – Measured strain in closed stirrup of P100-2.5, strain gauge S9

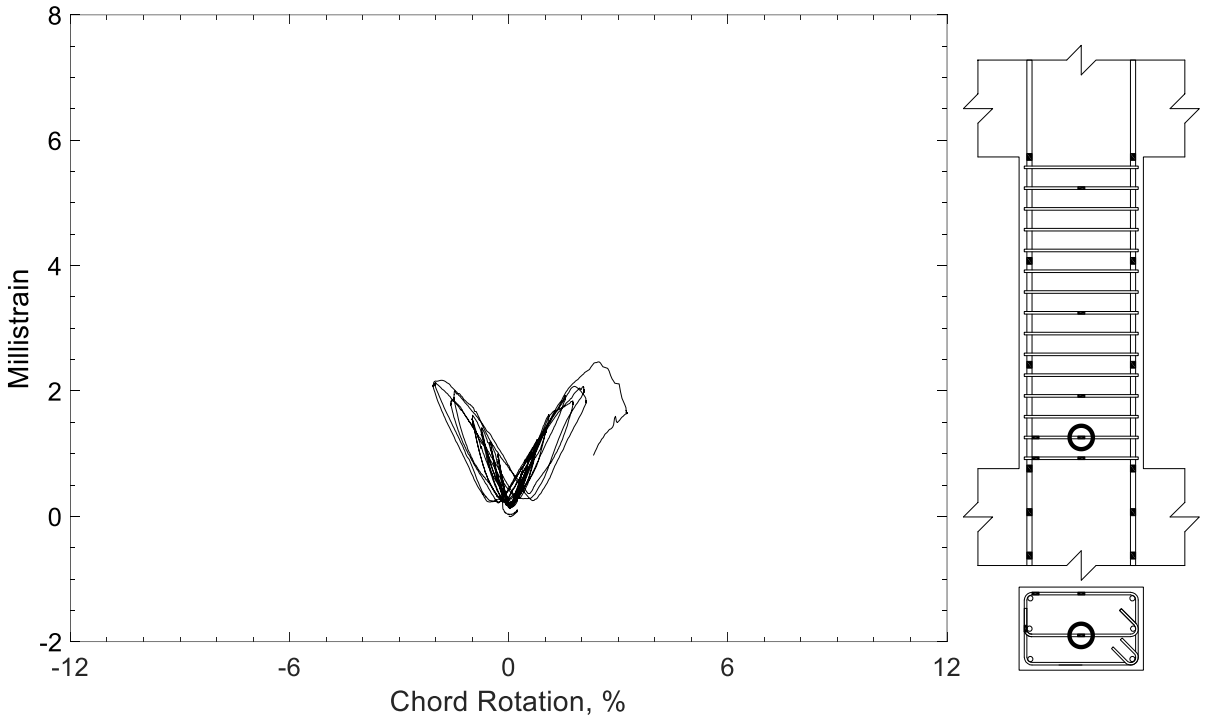

Figure 598 – Measured strain in crosstie of P100-2.5, strain gauge T1

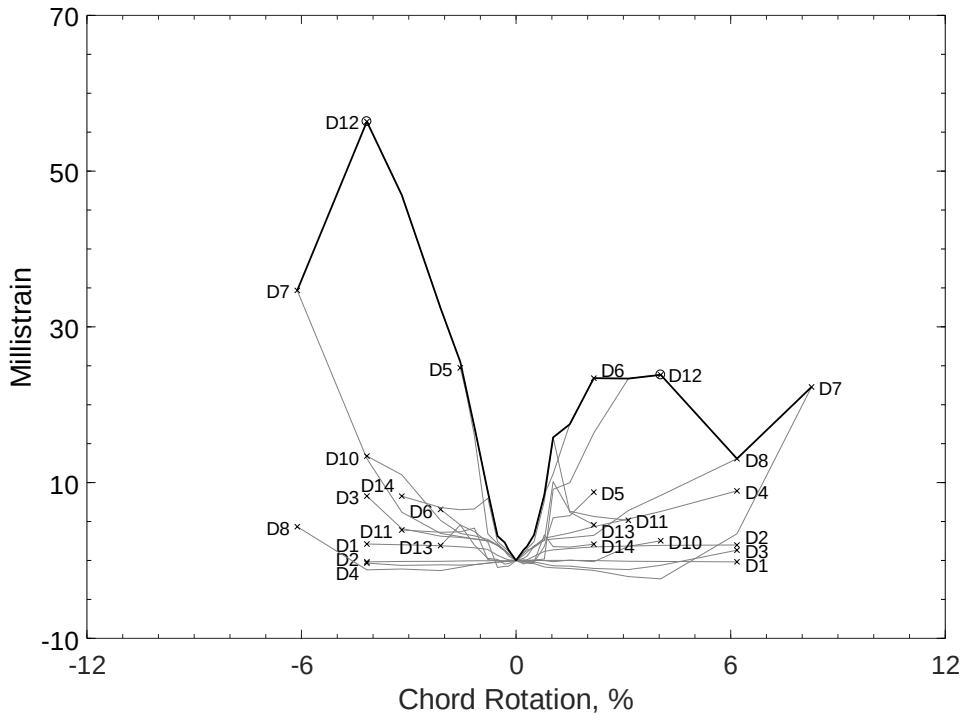

Figure 599 – Envelopes of measured strains in diagonal bars of D80-1.5, D strain gauges

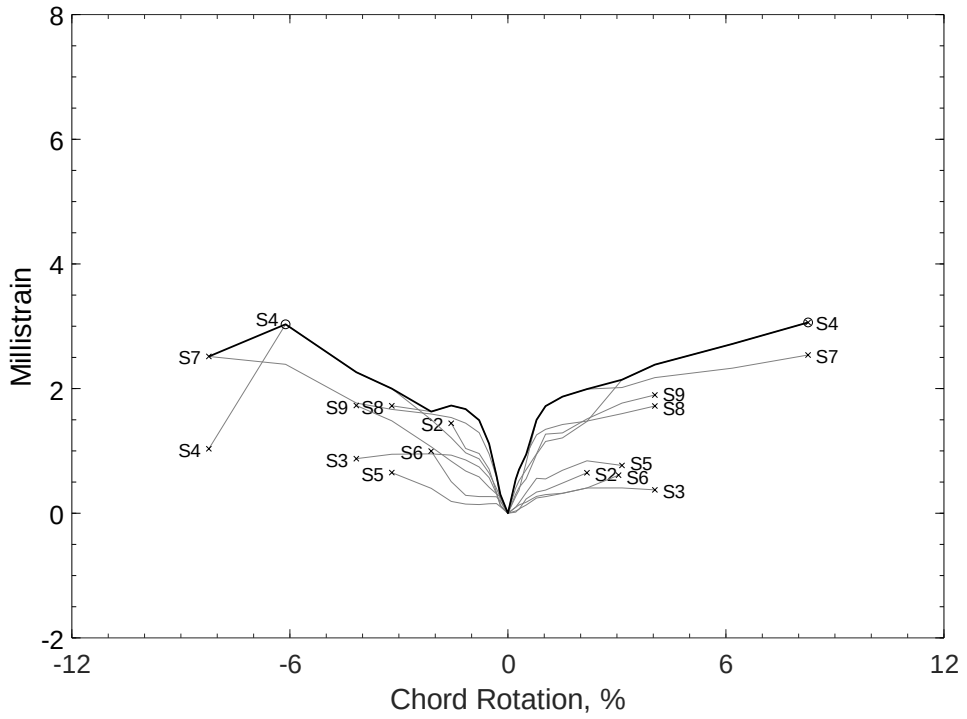

Figure 600 – Envelopes of measured strains in closed stirrups of D80-1.5, S strain gauges

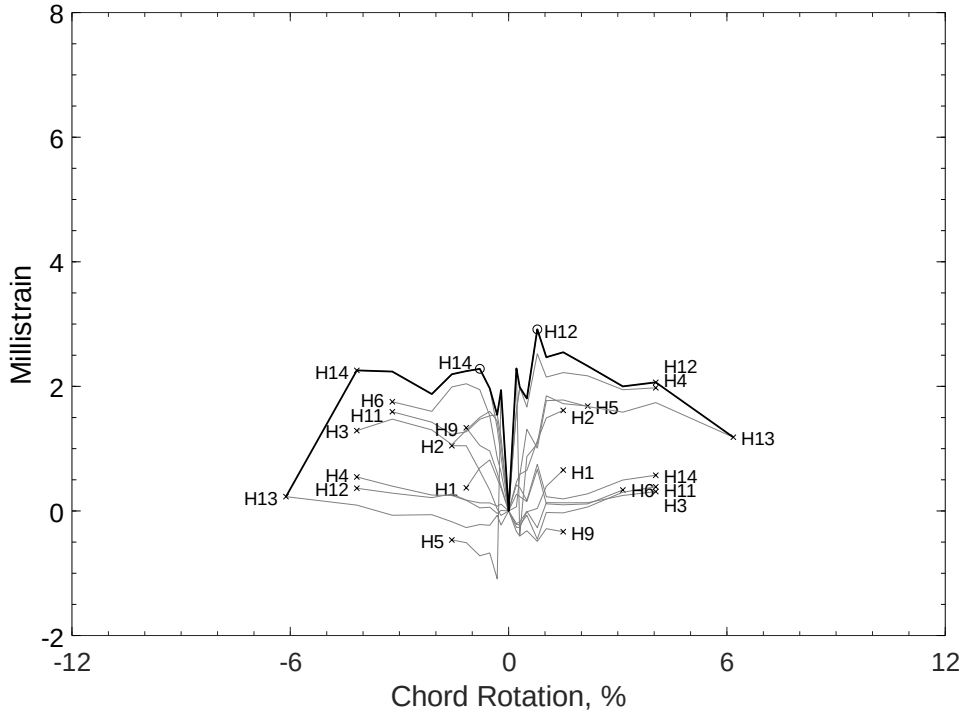

Figure 601 – Envelopes of measured strains in parallel bars of D80-1.5, H strain gauges

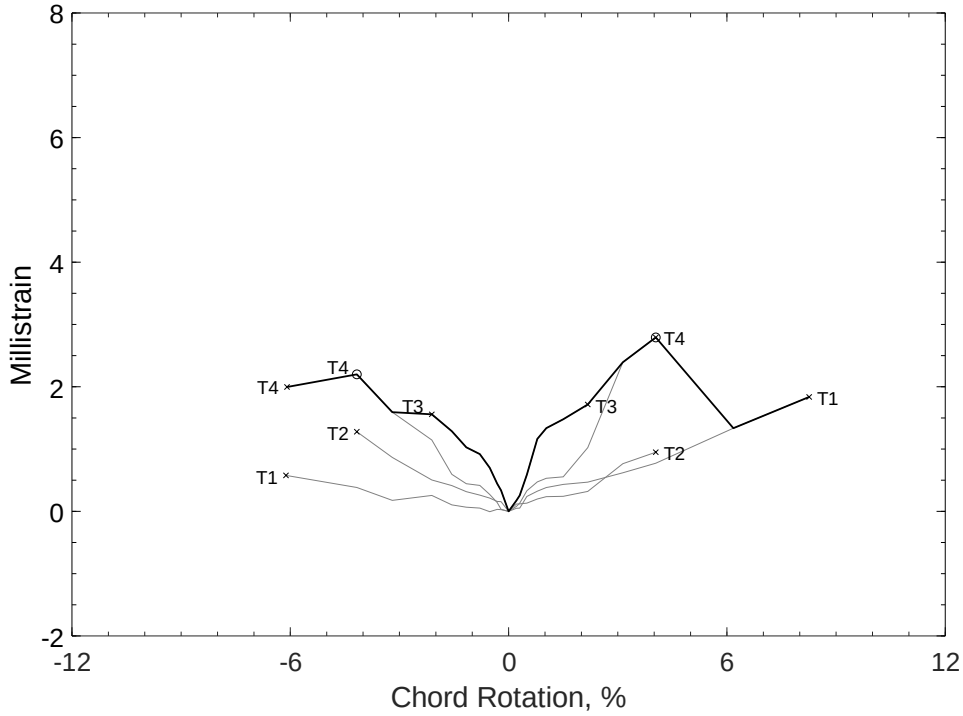

Figure 602 – Envelopes of measured strains in crossties of D80-1.5, T strain gauges

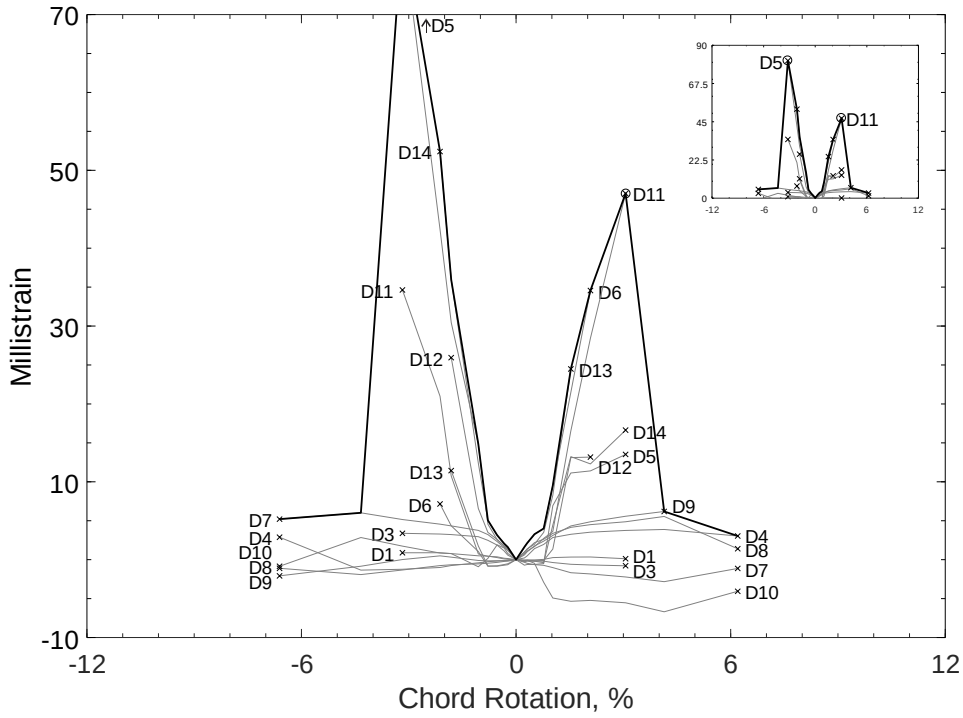

Figure 603 – Envelopes of measured strains in diagonal bars of D100-1.5, D strain gauges

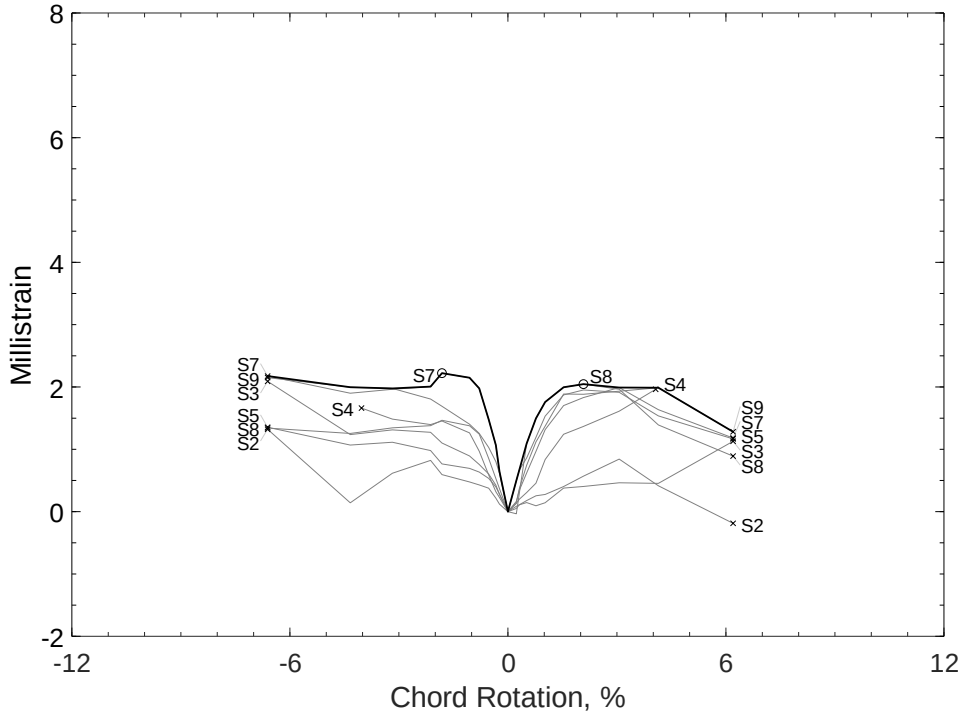

Figure 604 – Envelopes of measured strains in closed stirrups of D100-1.5, S strain gauges

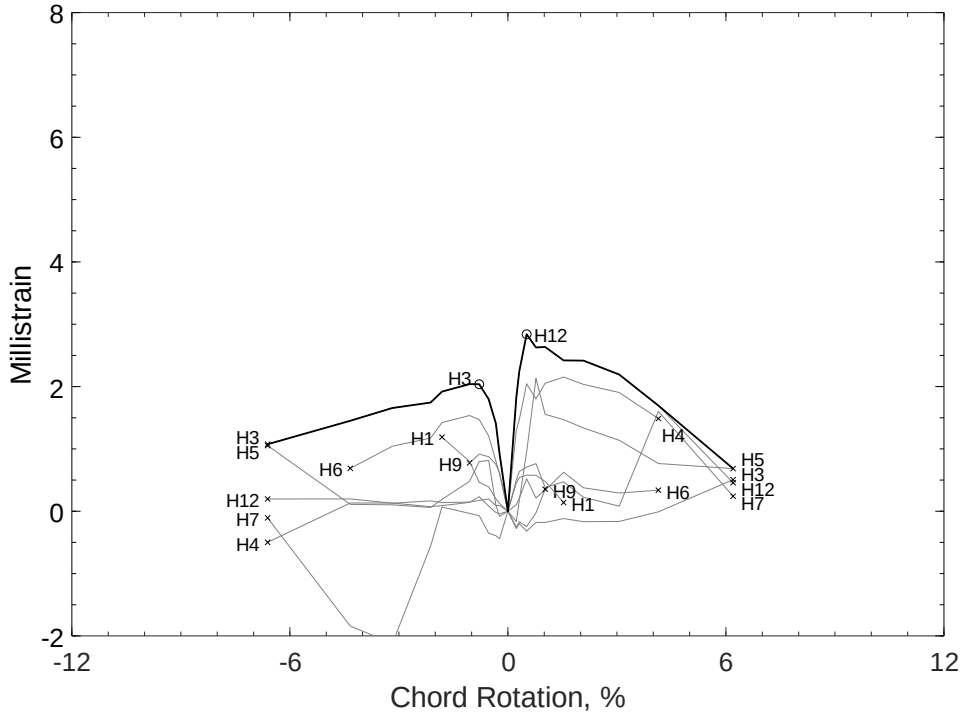

Figure 605 – Envelopes of measured strains in parallel bars of D100-1.5, H strain gauges

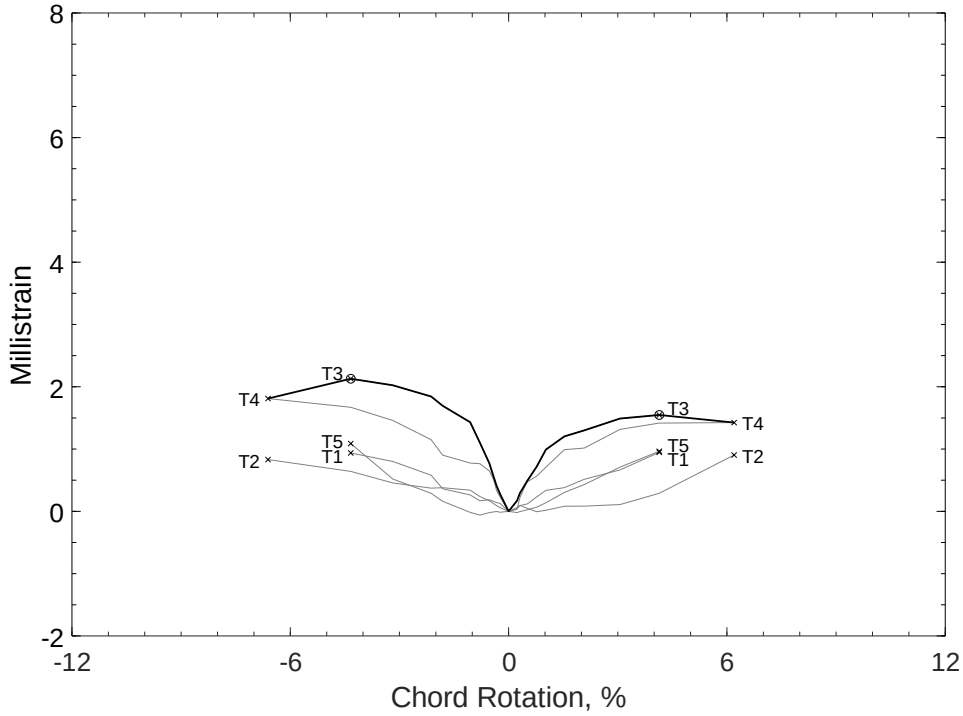

Figure 606 – Envelopes of measured strains in crossties of D100-1.5, T strain gauges

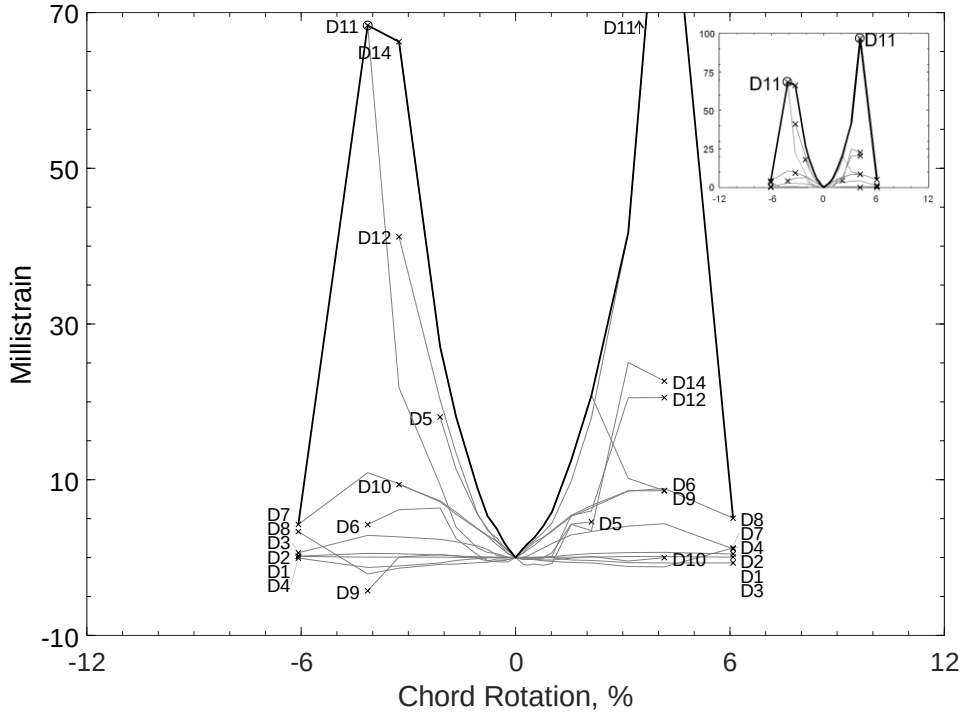

Figure 607 – Envelopes of measured strains in diagonal bars of D120-1.5, D strain gauges

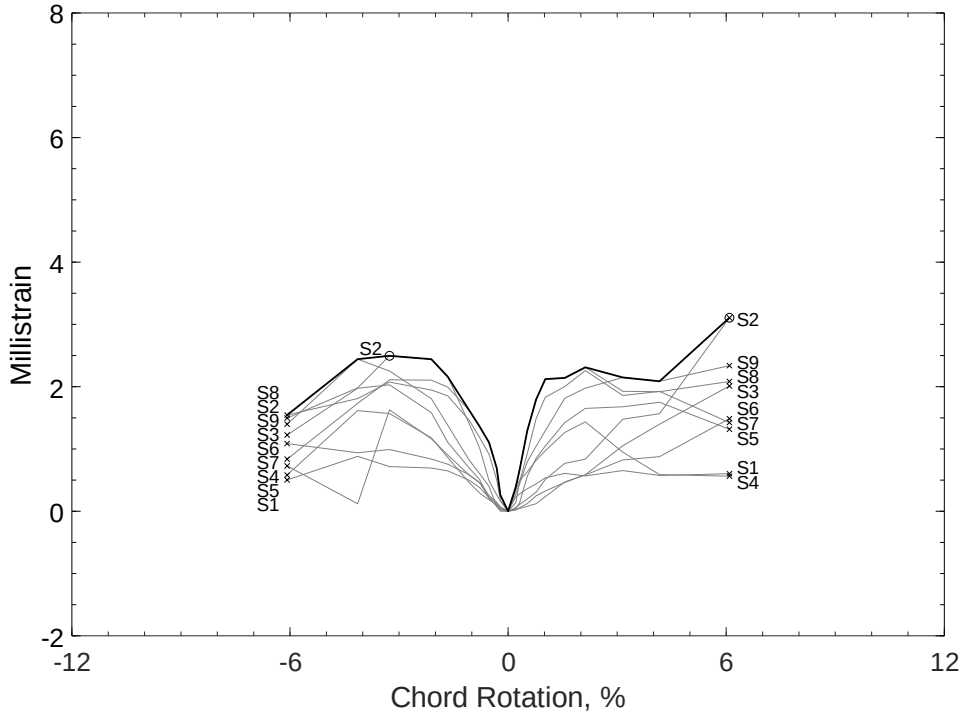

Figure 608 – Envelopes of measured strains in closed stirrups of D120-1.5, S strain gauges

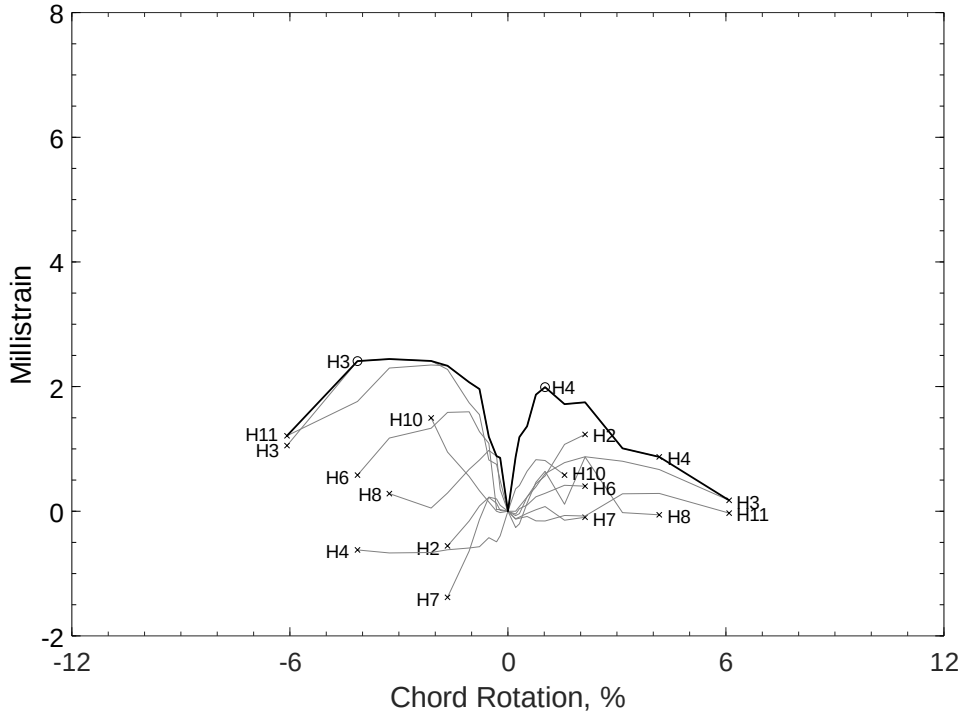

Figure 609 – Envelopes of measured strains in parallel bars of D120-1.5, H strain gauges

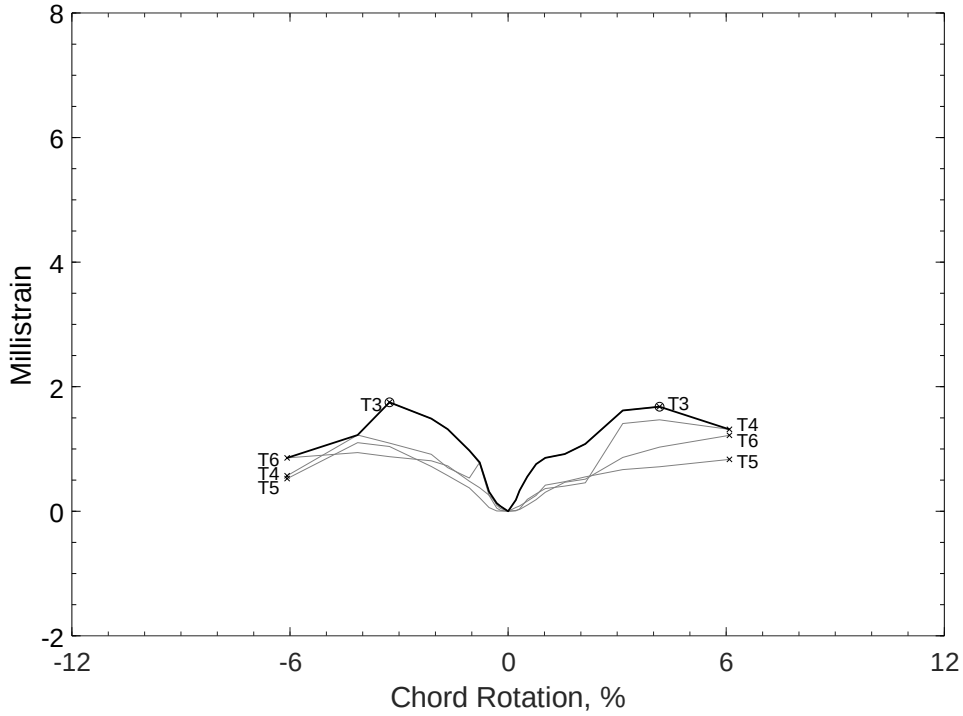

Figure 610 – Envelopes of measured strains in crossties of D120-1.5, T strain gauges

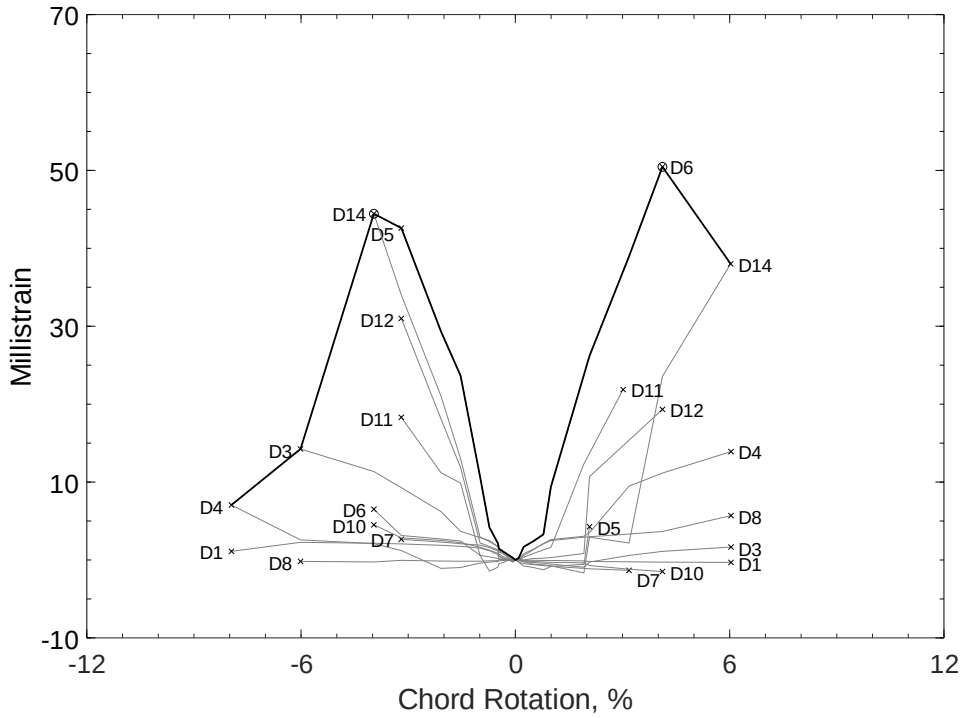

Figure 611 – Envelopes of measured strains in diagonal bars of D80-2.5, D strain gauges

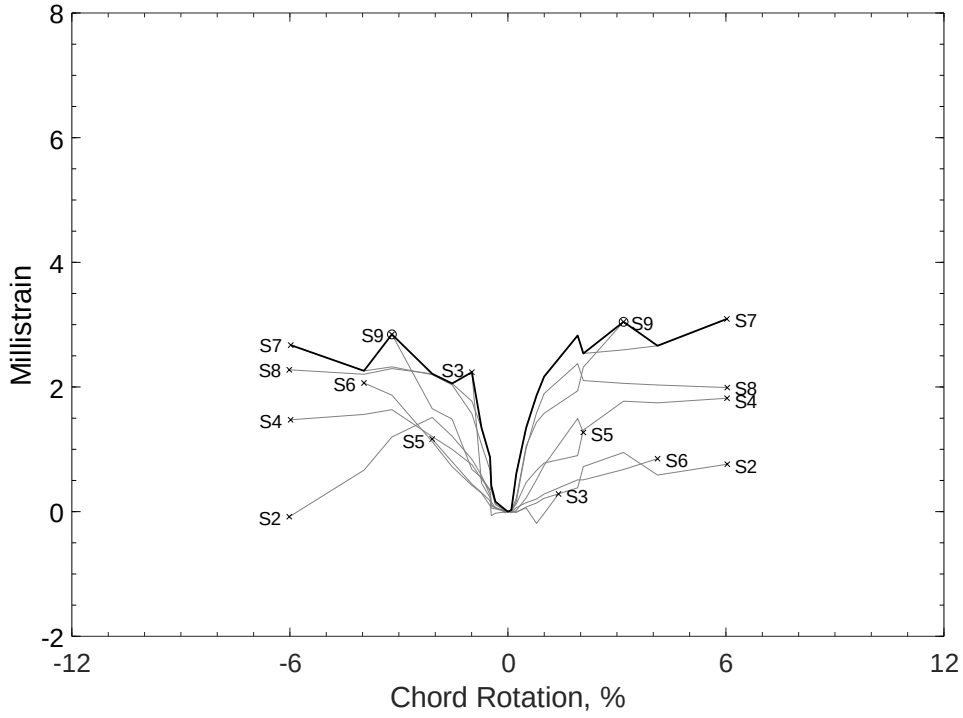

Figure 612 – Envelopes of measured strains in closed stirrups of D80-2.5, S strain gauges

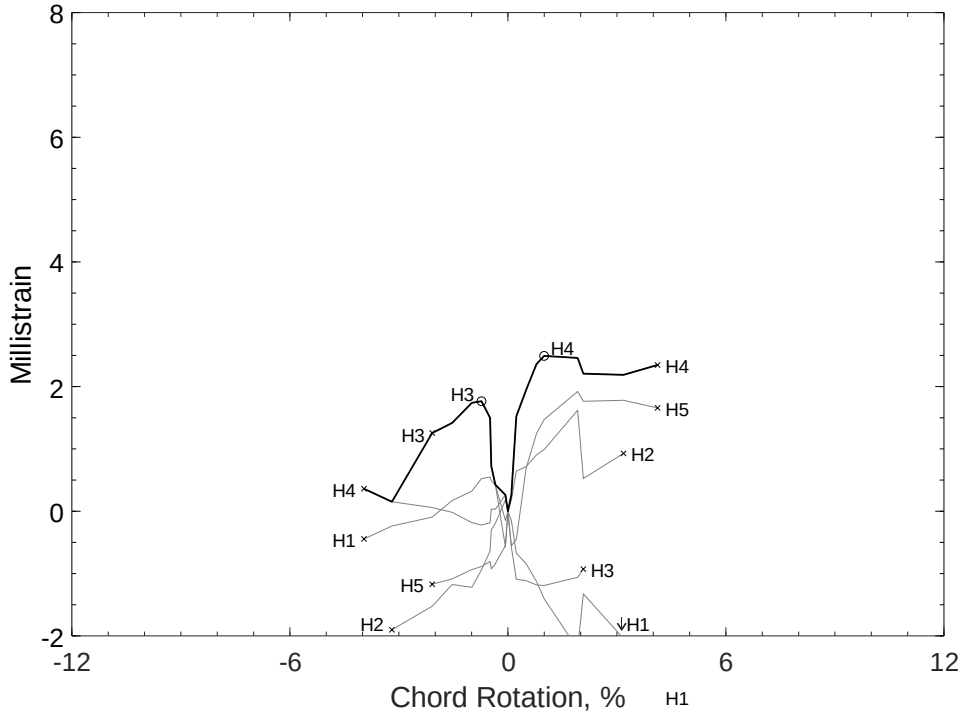

Figure 613 – Envelopes of measured strains in parallel bars of D80-2.5, H strain gauges

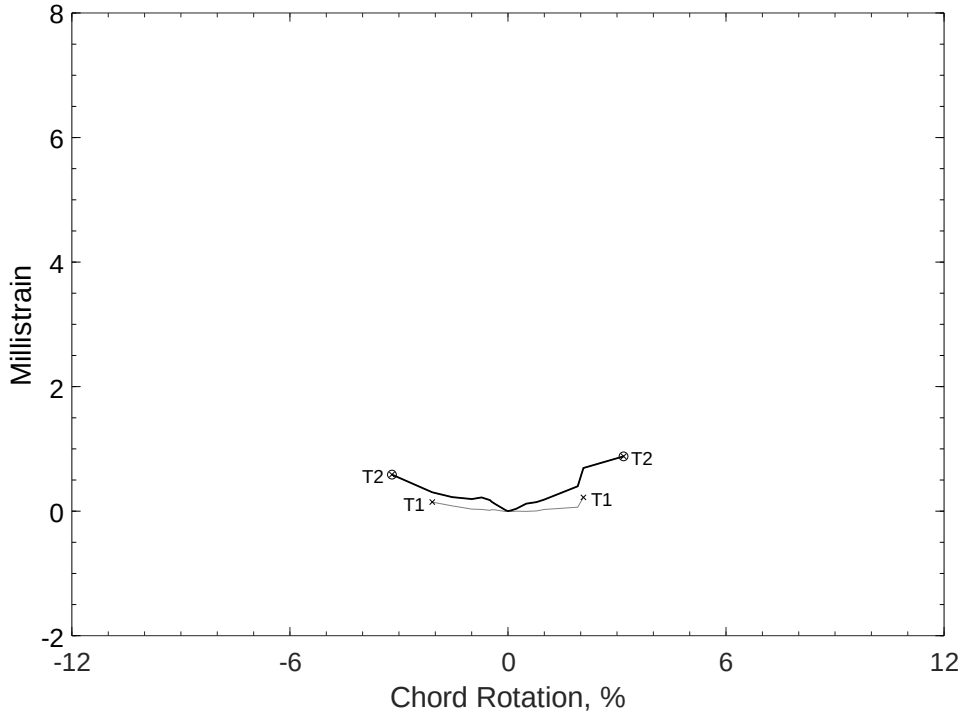

Figure 614 – Envelopes of measured strains in crossties of D80-2.5, T strain gauges

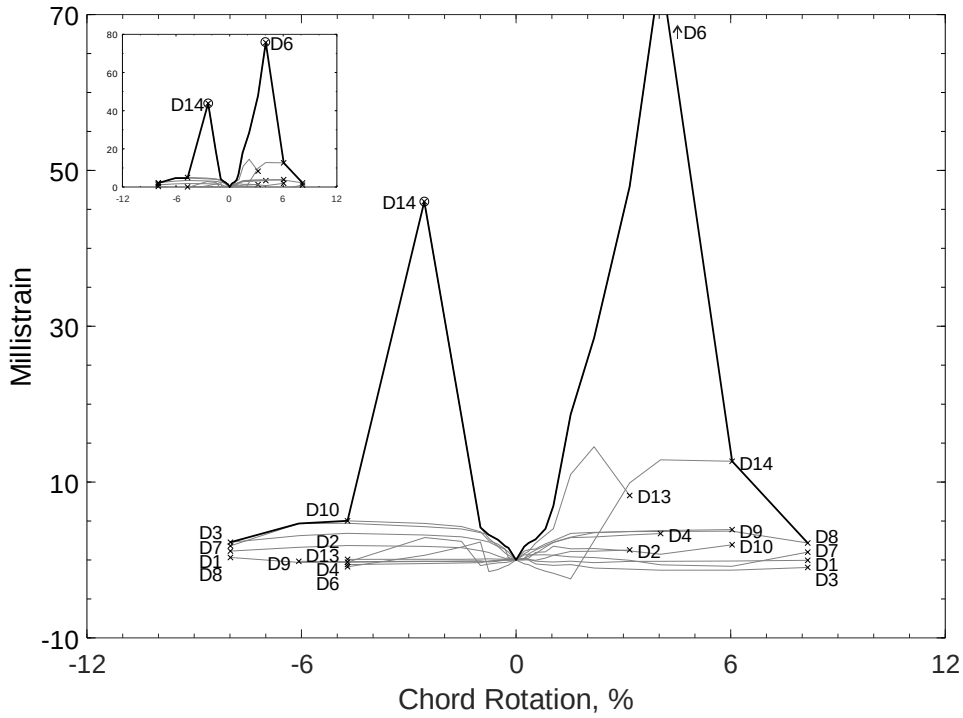

Figure 615 – Envelopes of measured strains in diagonal bars of D100-2.5, D strain gauges

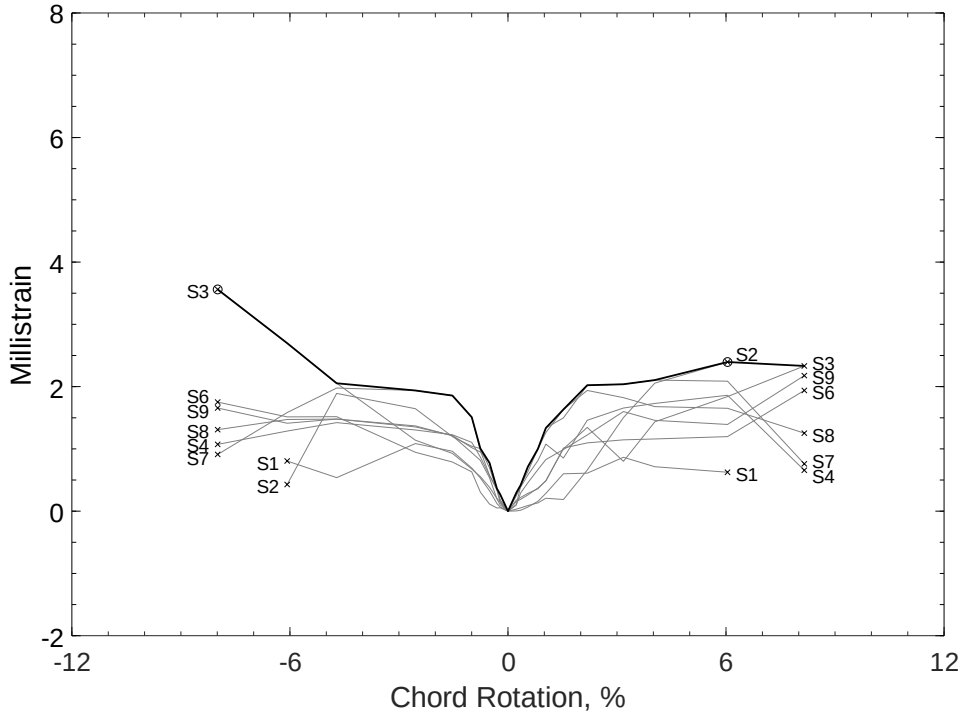

Figure 616 – Envelopes of measured strains in closed stirrups of D100-2.5, S strain gauges

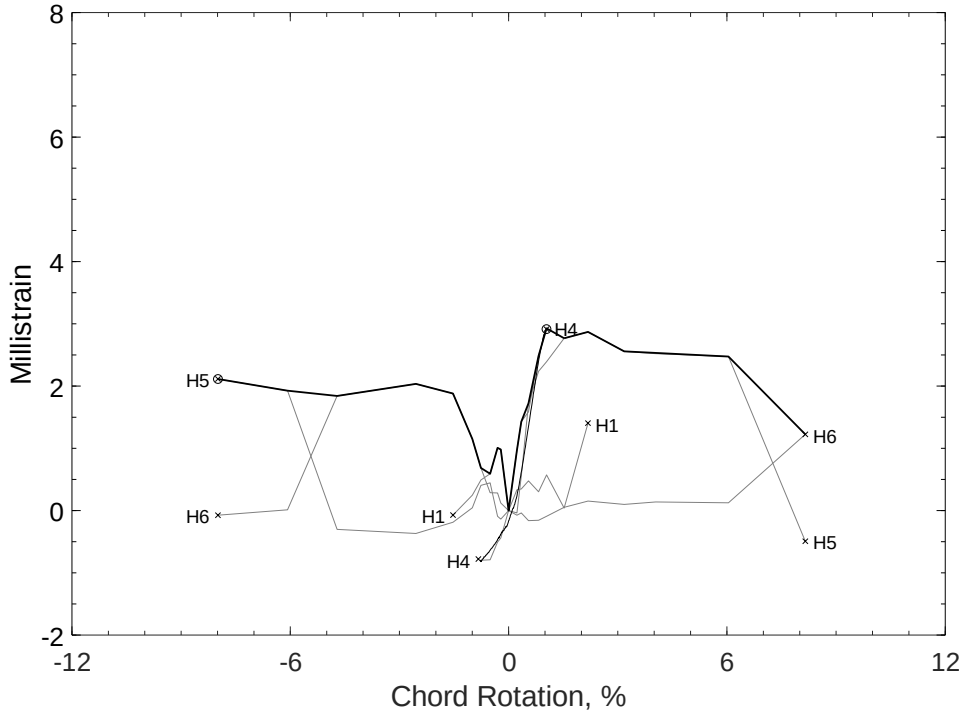

Figure 617 – Envelopes of measured strains in parallel bars of D100-2.5, H strain gauges

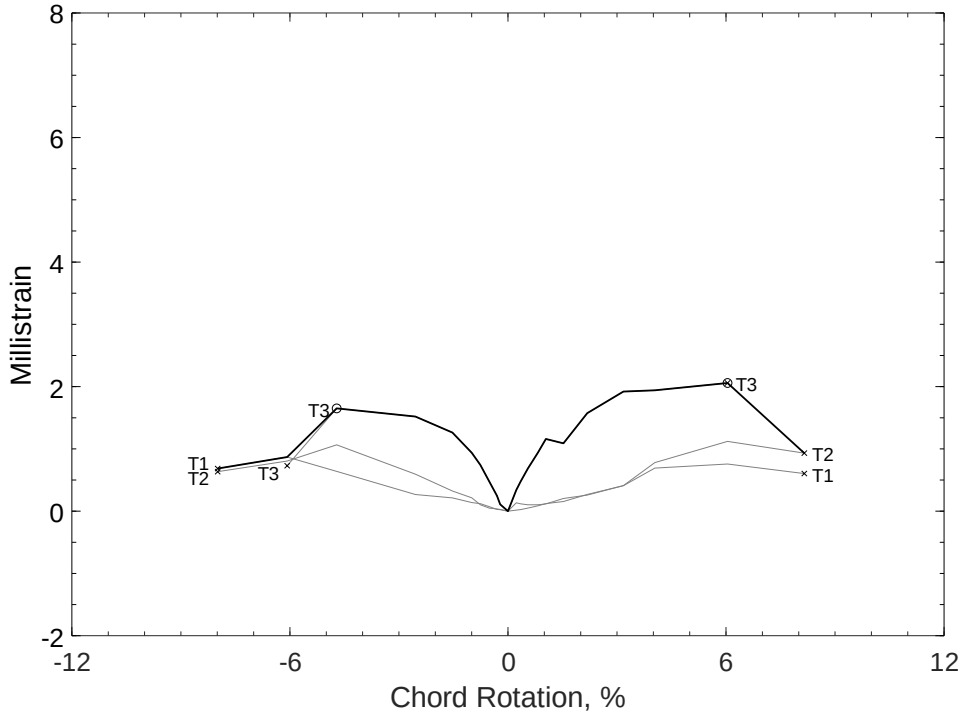

Figure 618 – Envelopes of measured strains in crossties of D100-2.5, T strain gauges

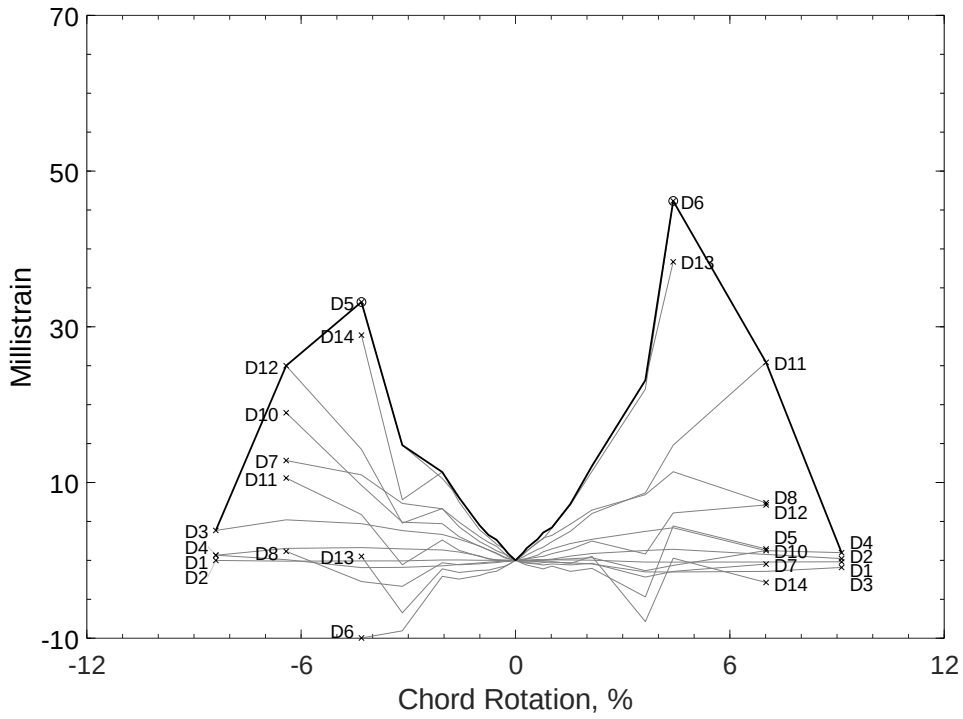

Figure 619 – Envelopes of measured strains in diagonal bars of D120-2.5, D strain gauges

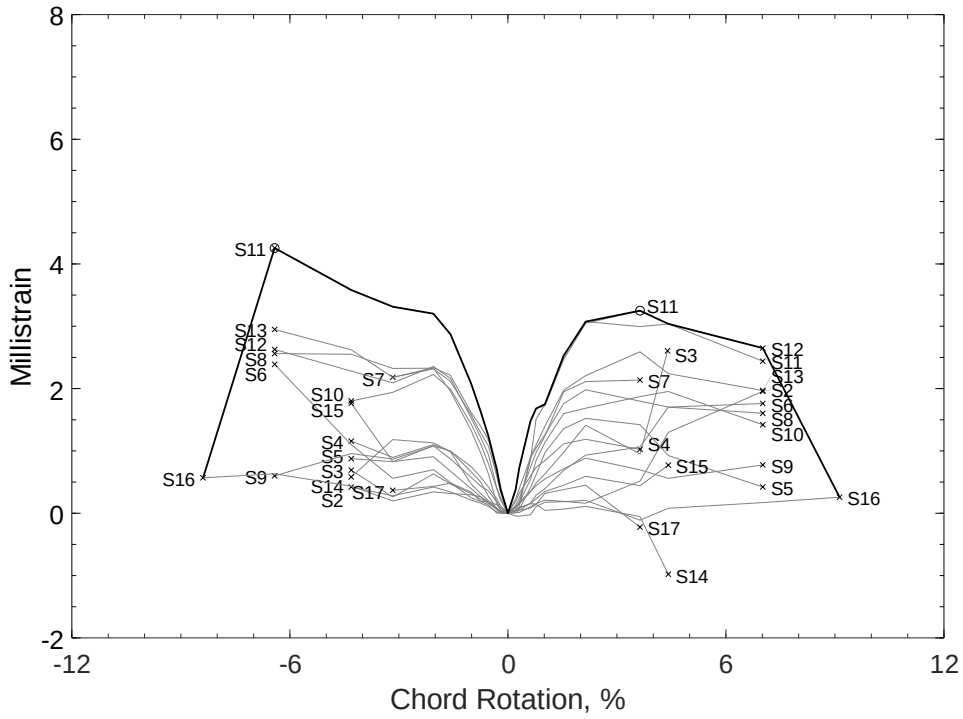

Figure 620 – Envelopes of measured strains in closed stirrups of D120-2.5, S strain gauges

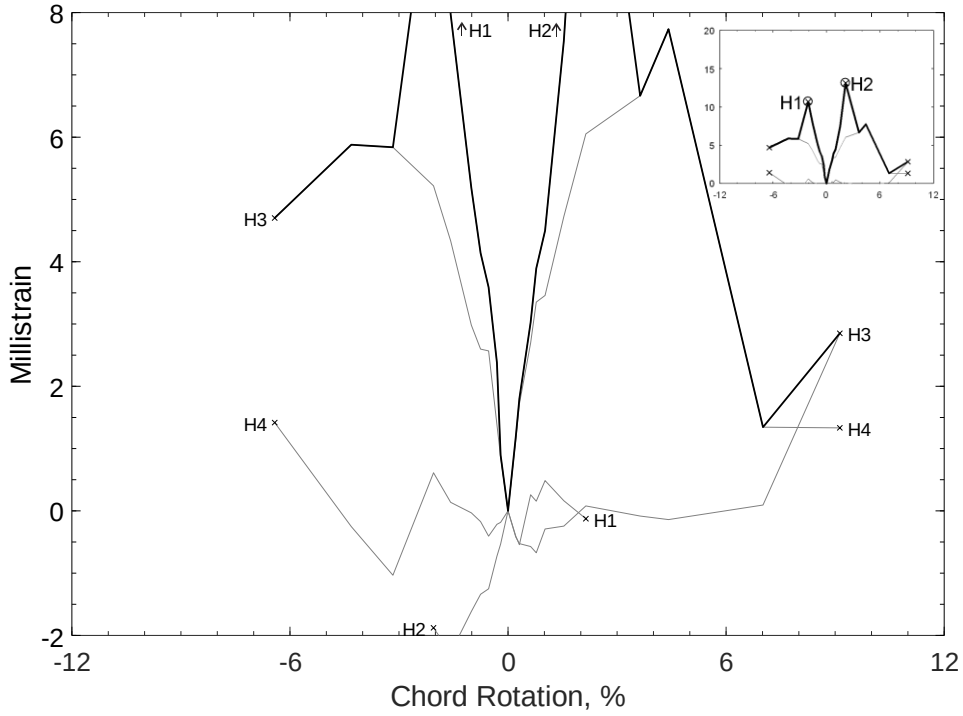

Figure 621 – Envelopes of measured strains in parallel bars of D120-2.5, H strain gauges

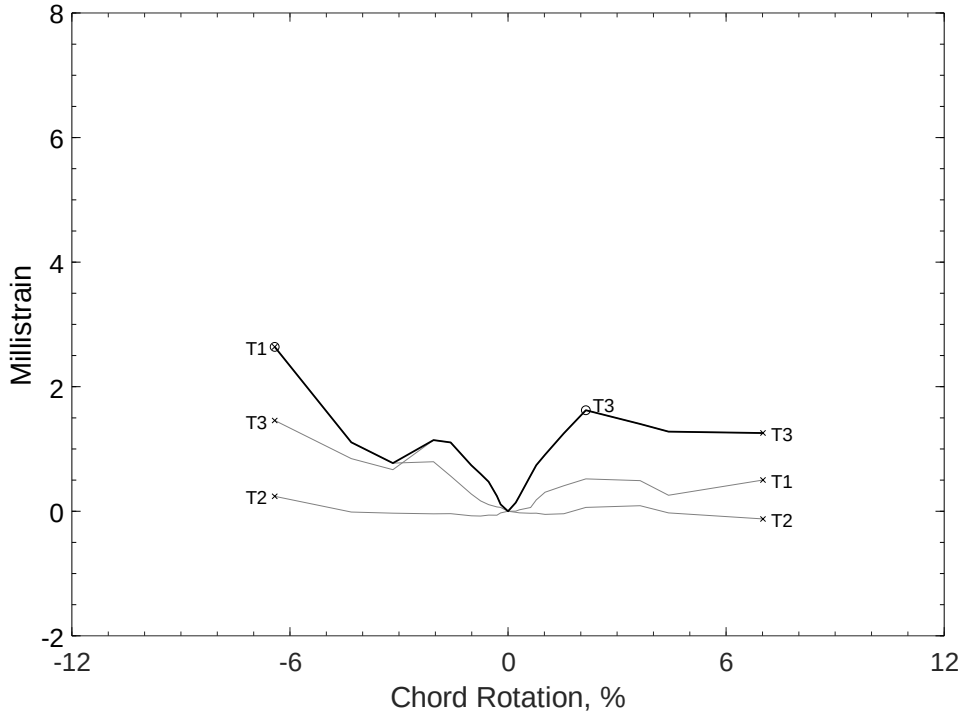

Figure 622 – Envelopes of measured strains in crossties of D120-2.5, T strain gauges

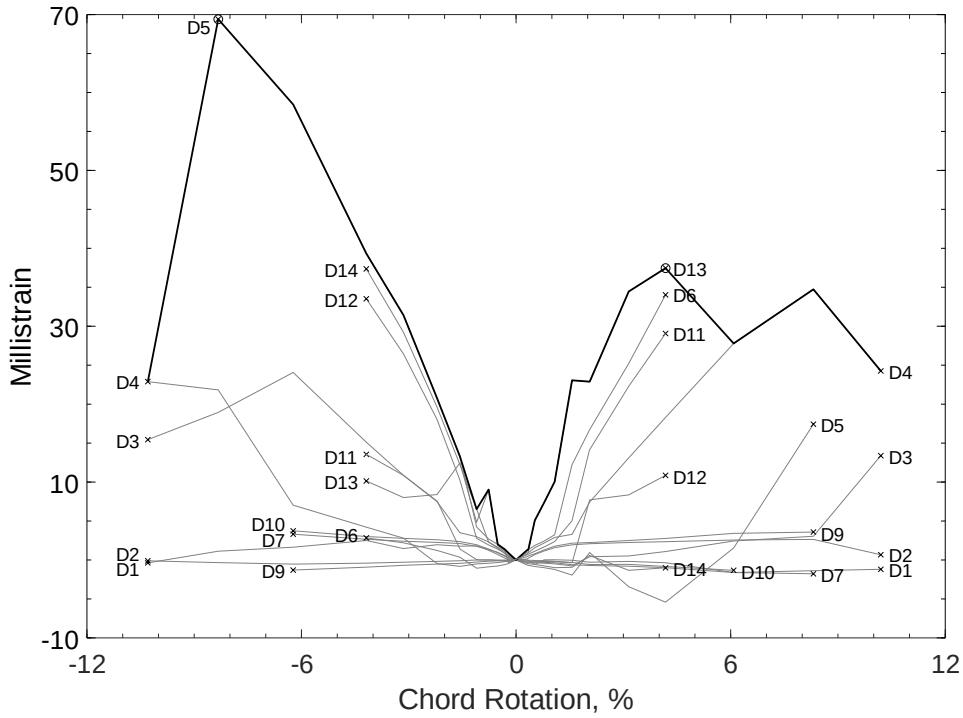

Figure 623 – Envelopes of measured strains in diagonal bars of D80-3.5, D strain gauges

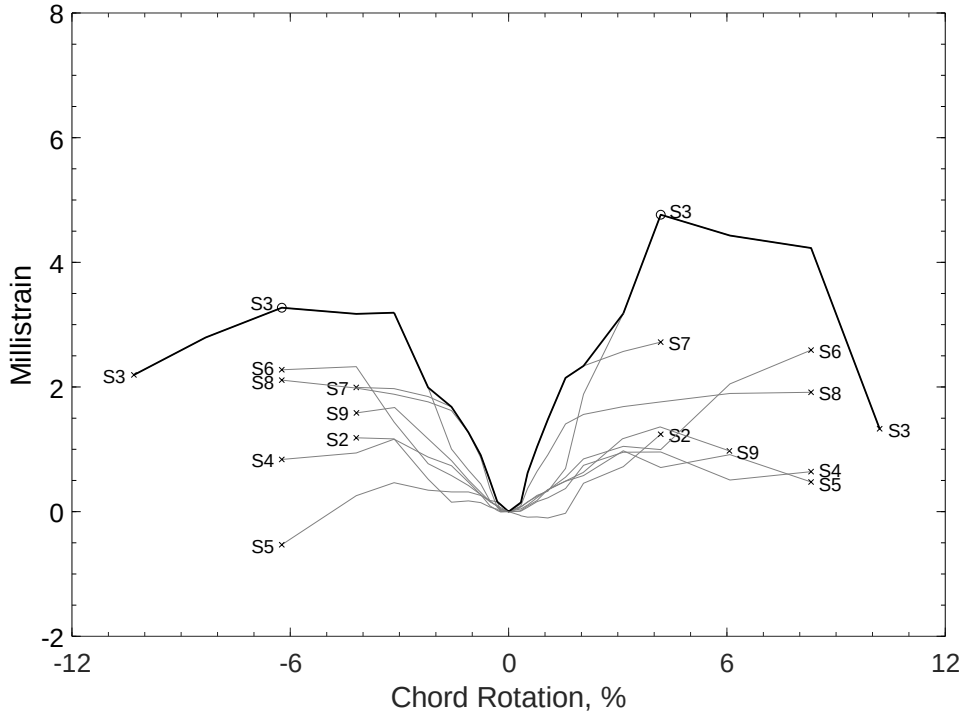

Figure 624 – Envelopes of measured strains in closed stirrups of D80-3.5, S strain gauges

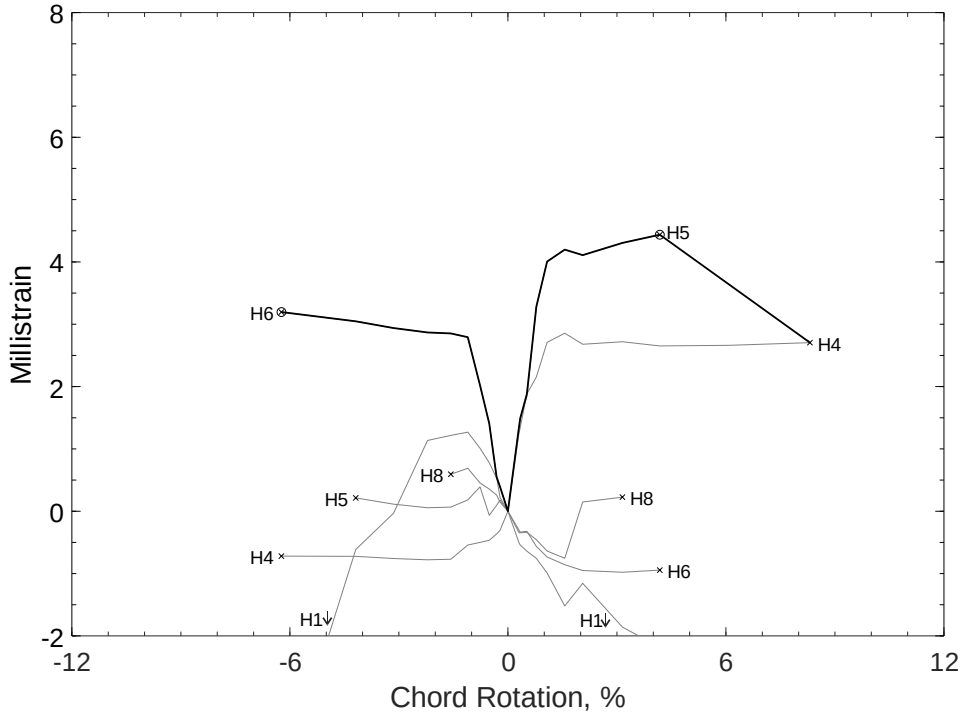

Figure 625 – Envelopes of measured strains in parallel bars of D80-3.5, H strain gauges

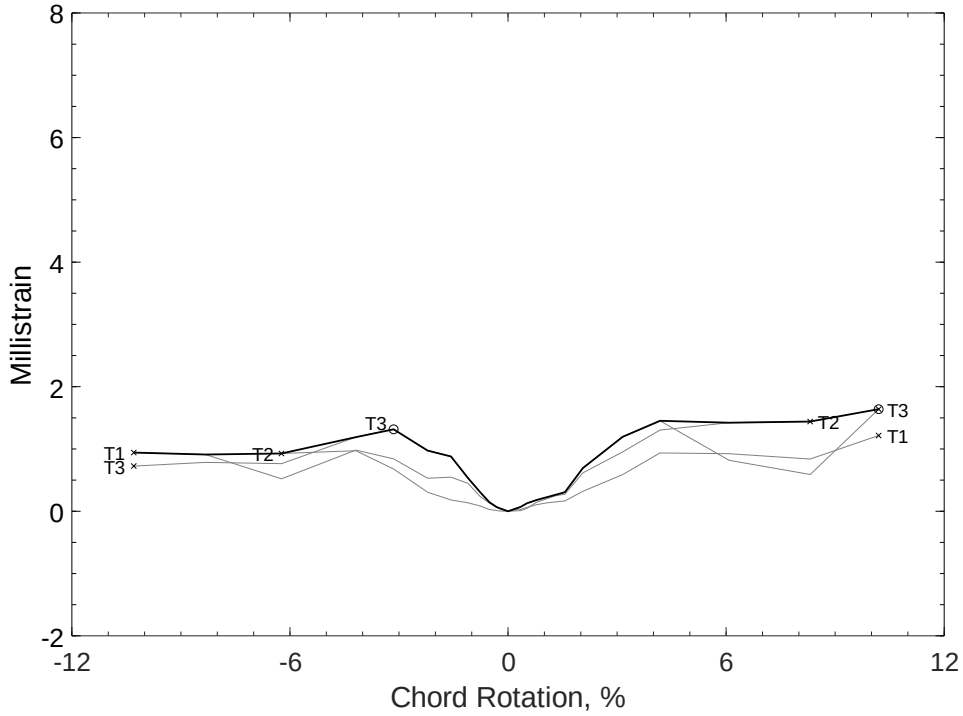

Figure 626 – Envelopes of measured strains in crossties of D80-3.5, T strain gauges

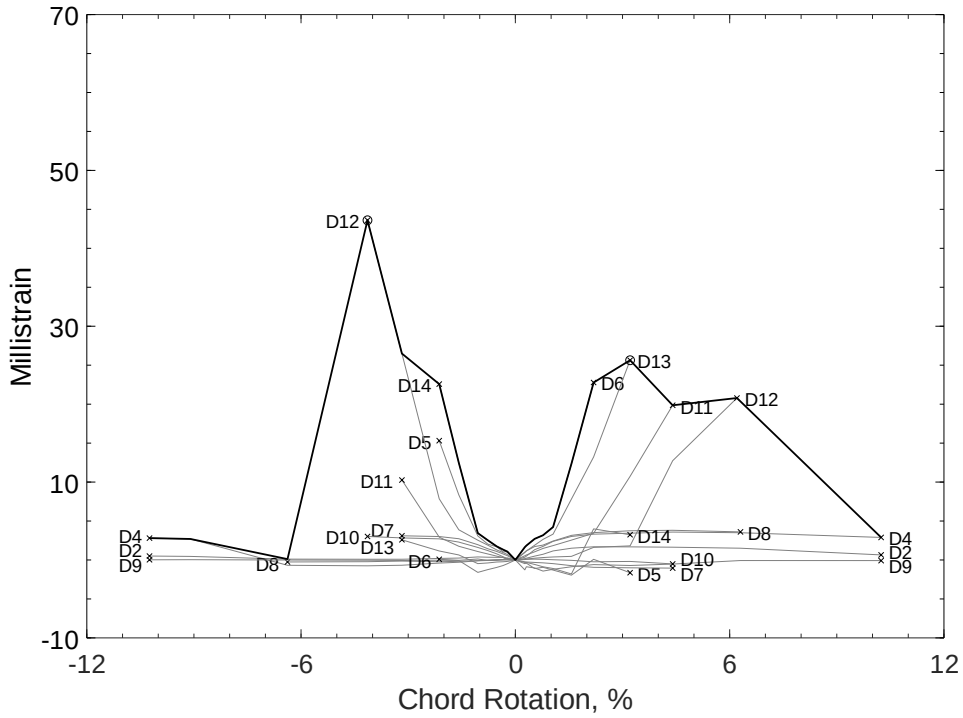

Figure 627 – Envelopes of measured strains in diagonal bars of D100-3.5, D strain gauges

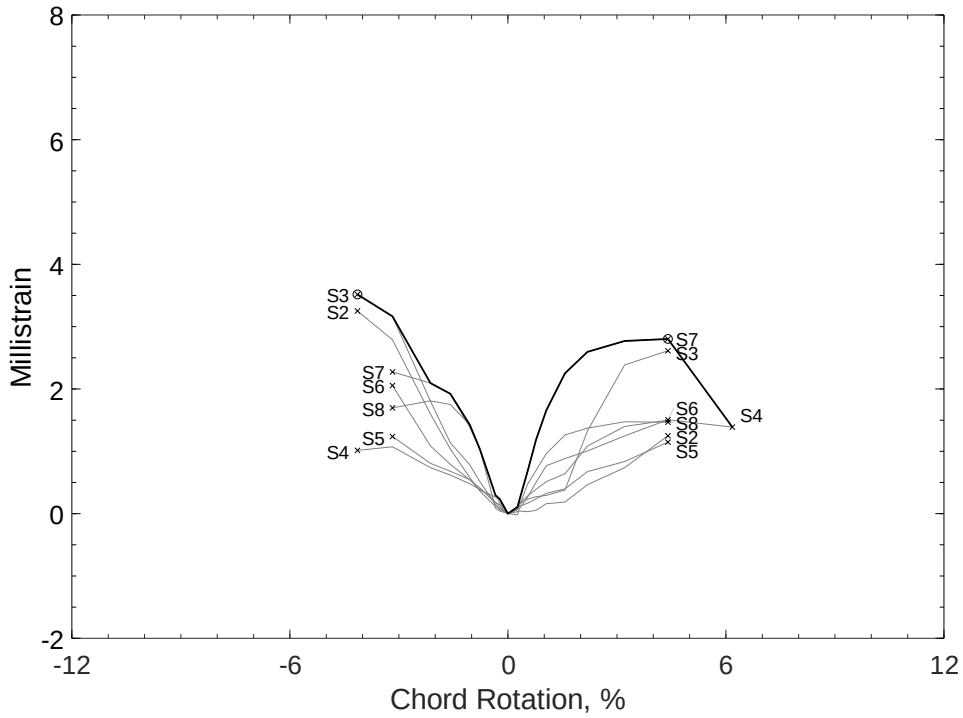

Figure 628 – Envelopes of measured strains in closed stirrups of D100-3.5, S strain gauges

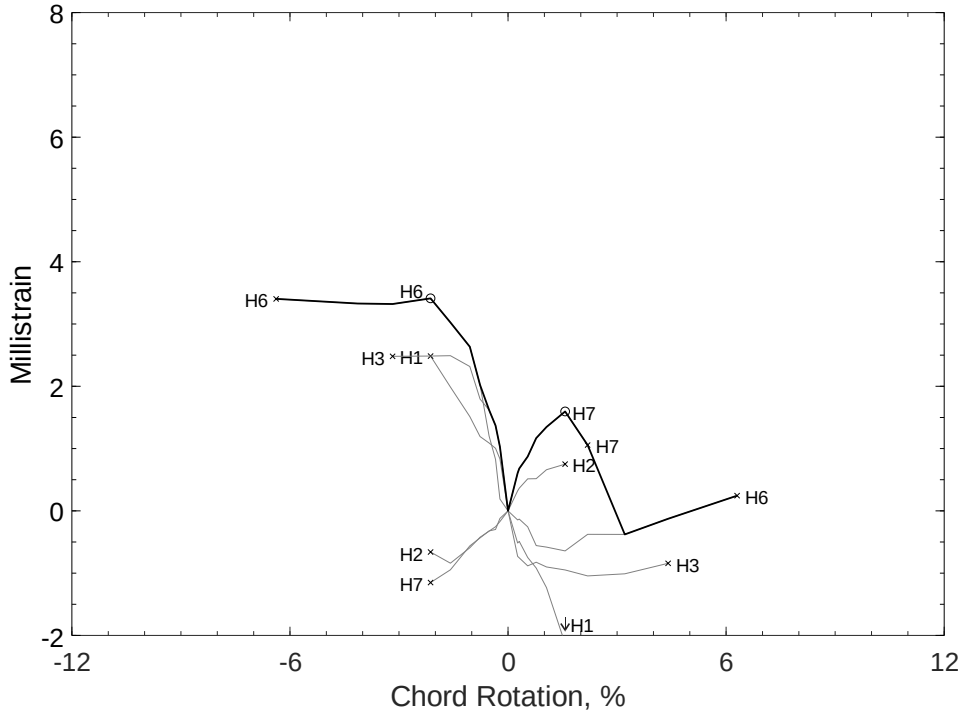

Figure 629 – Envelopes of measured strains in parallel bars of D100-3.5, H strain gauges

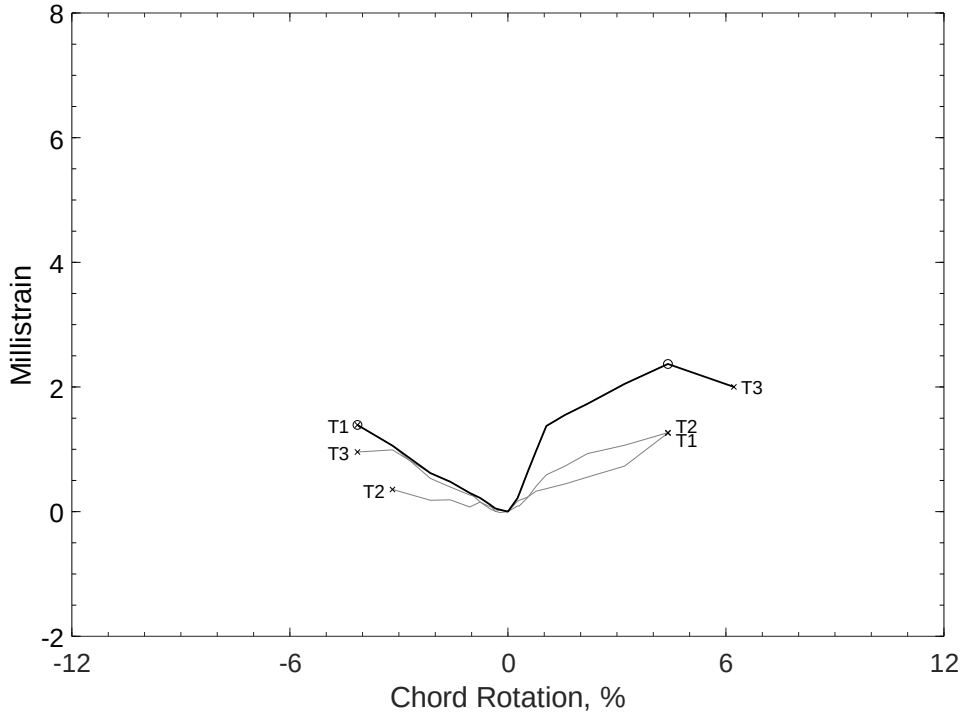

Figure 630 – Envelopes of measured strains in crossties of D100-3.5, T strain gauges

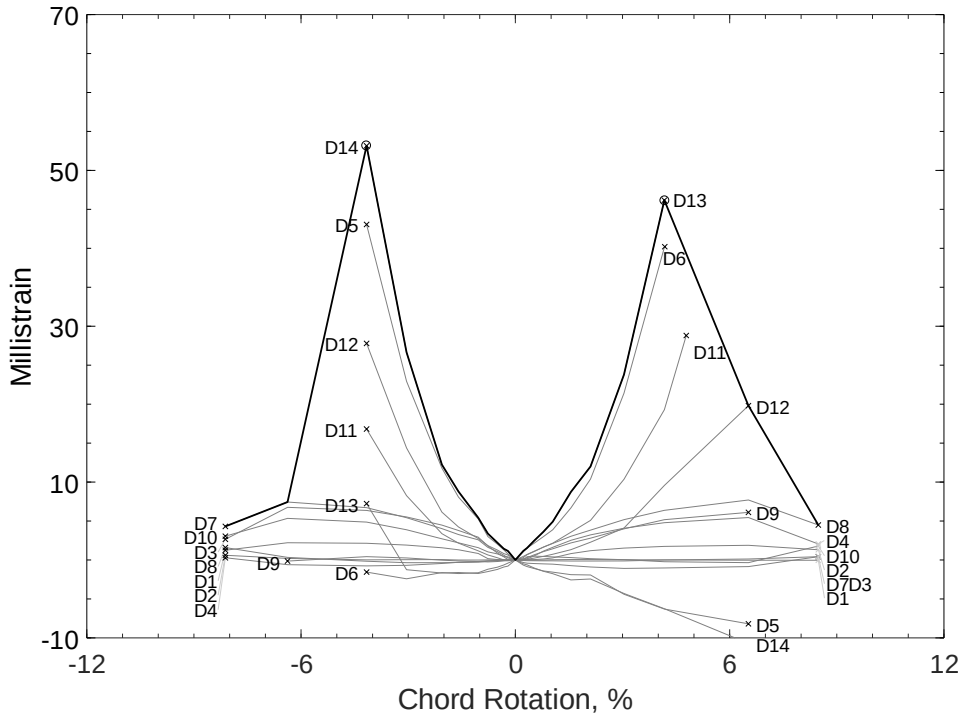

Figure 631 – Envelopes of measured strains in diagonal bars of D120-3.5, D strain gauges

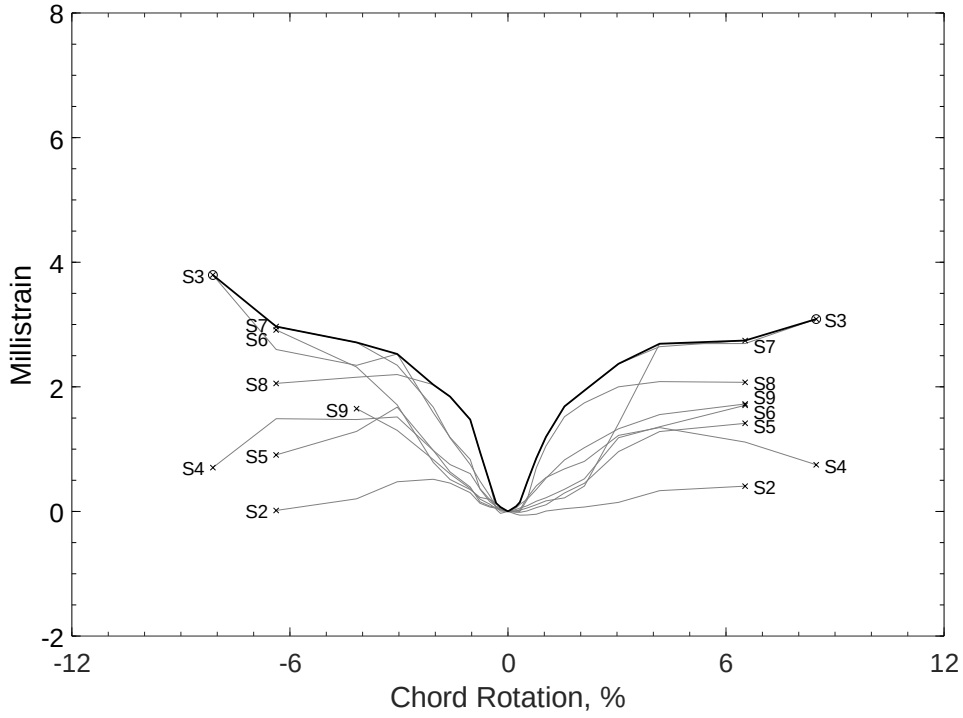

Figure 632 – Envelopes of measured strains in closed stirrups of D120-3.5, S strain gauges

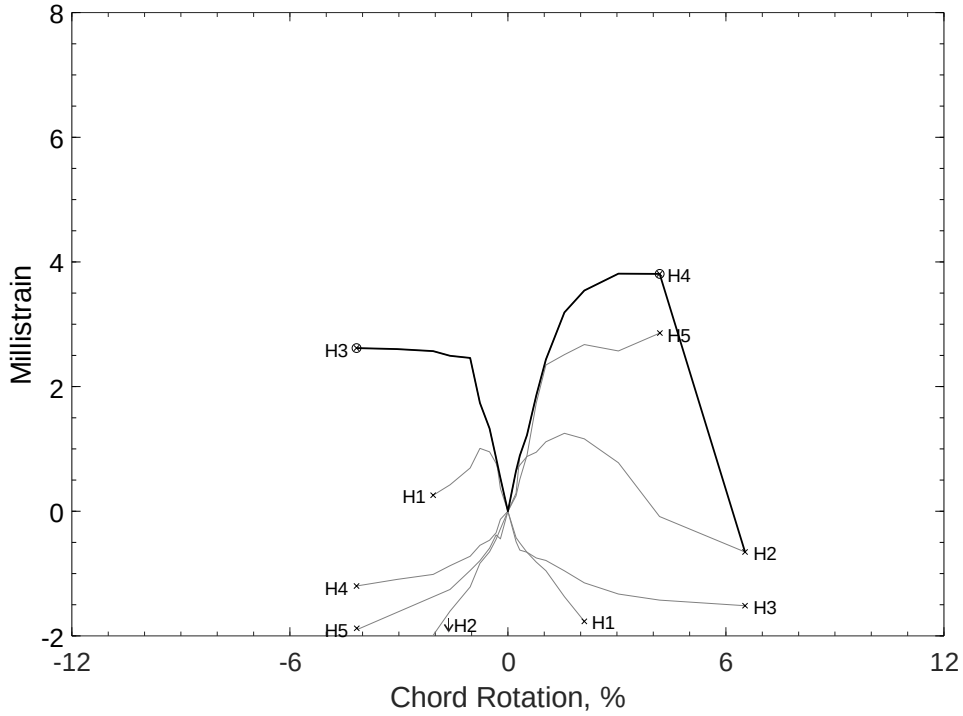

Figure 633 – Envelopes of measured strains in parallel bars of D120-3.5, H strain gauges

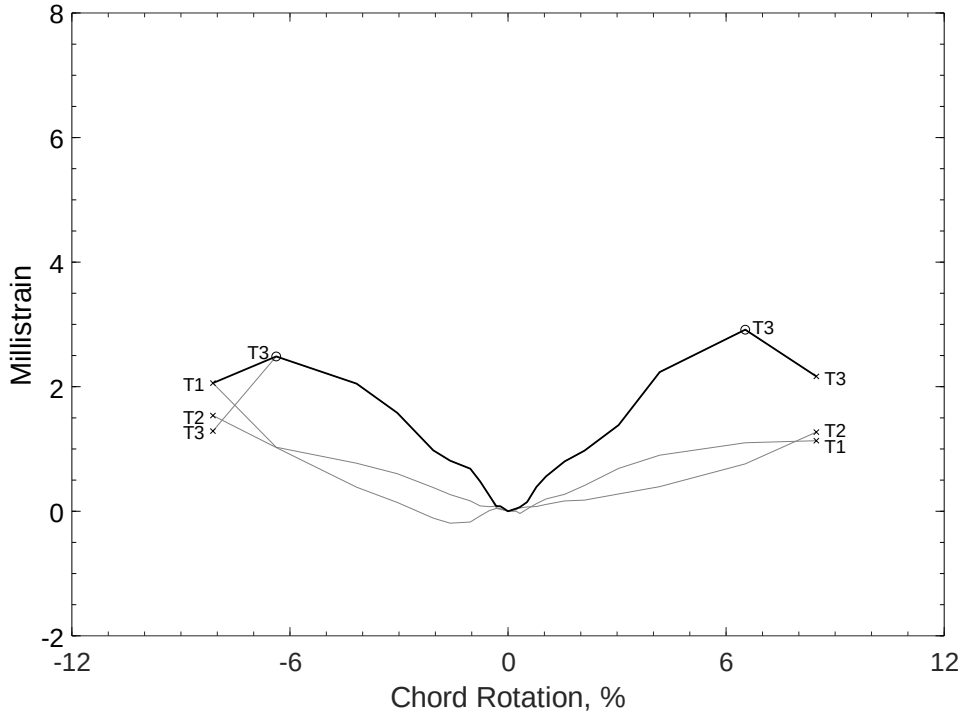

Figure 634 – Envelopes of measured strains in crossties of D120-3.5, T strain gauges

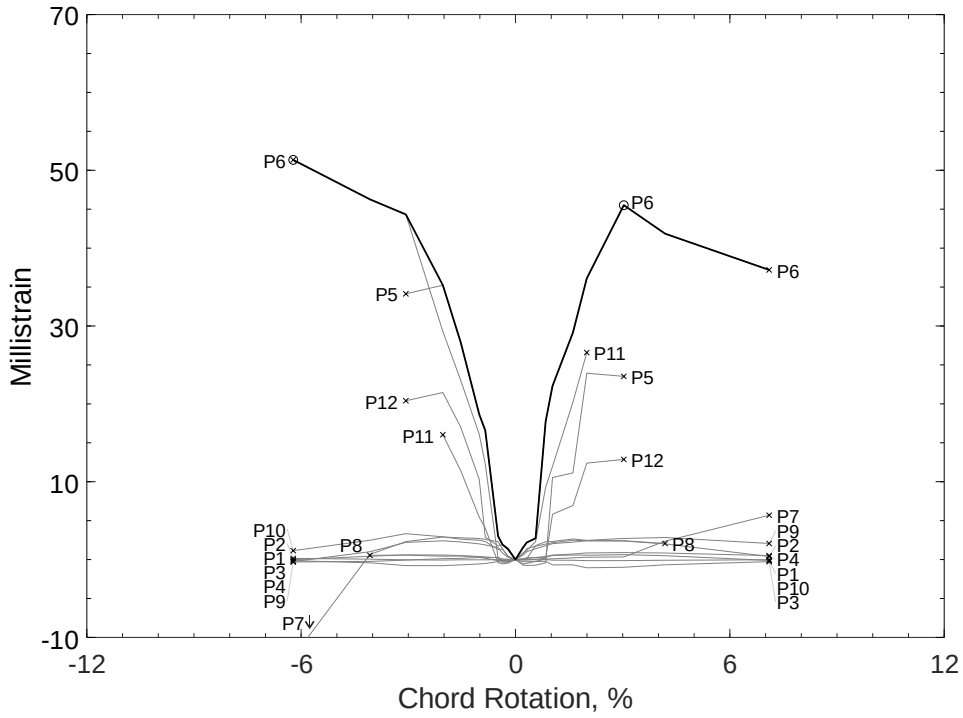

Figure 635 – Envelopes of measured strains in parallel bars of P80-2.5, P strain gauges

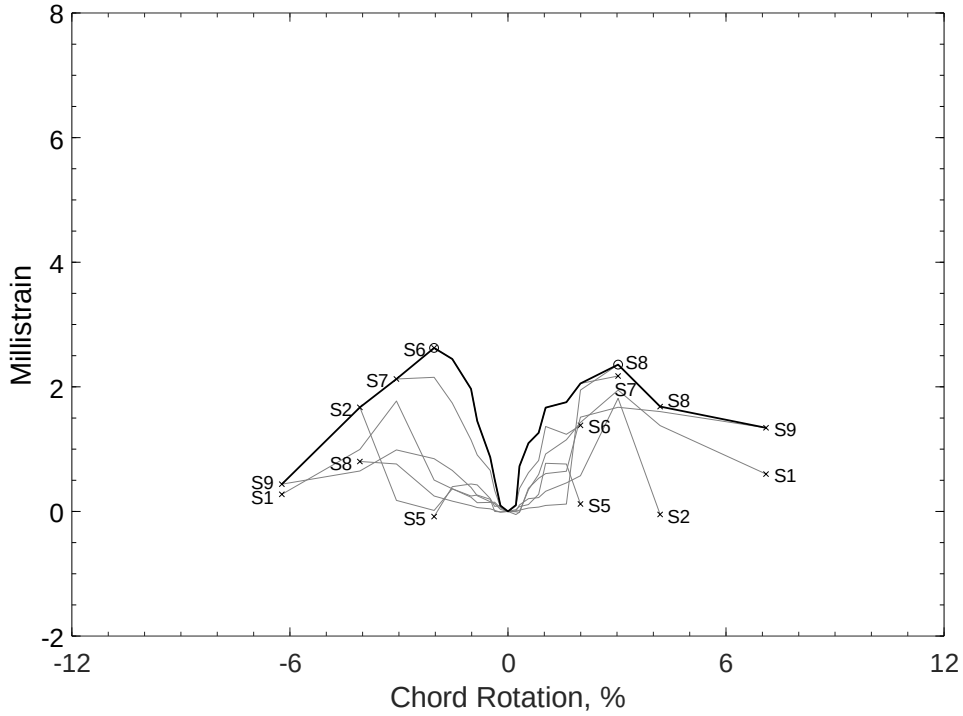

Figure 636 – Envelopes of measured strains in closed stirrups of P80-2.5, S strain gauges

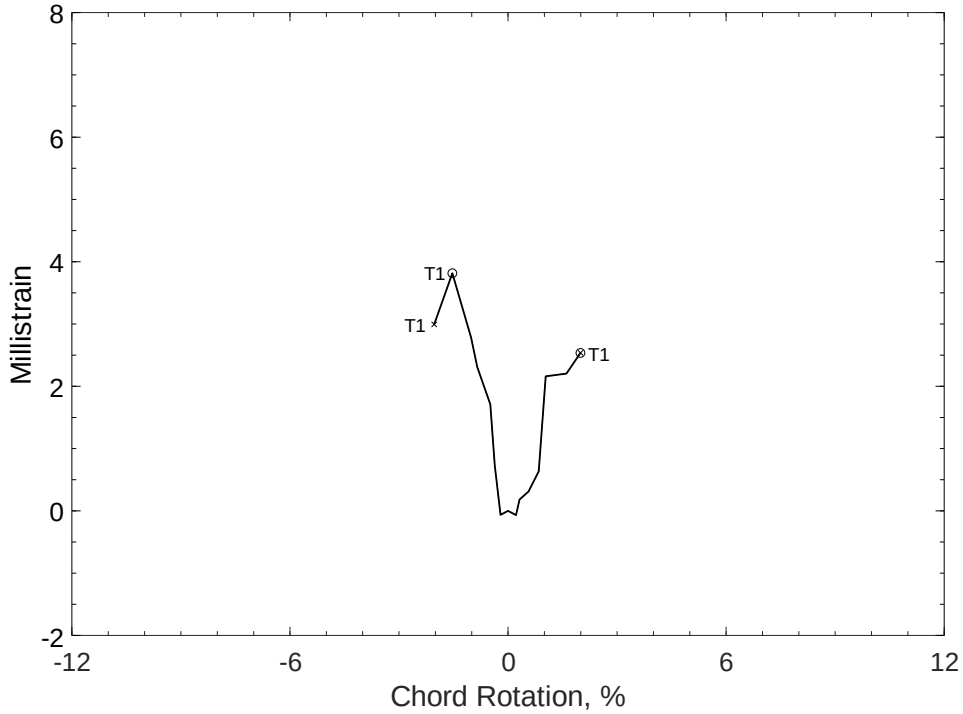

Figure 637 – Envelopes of measured strains in crossties of P80-2.5, T strain gauges

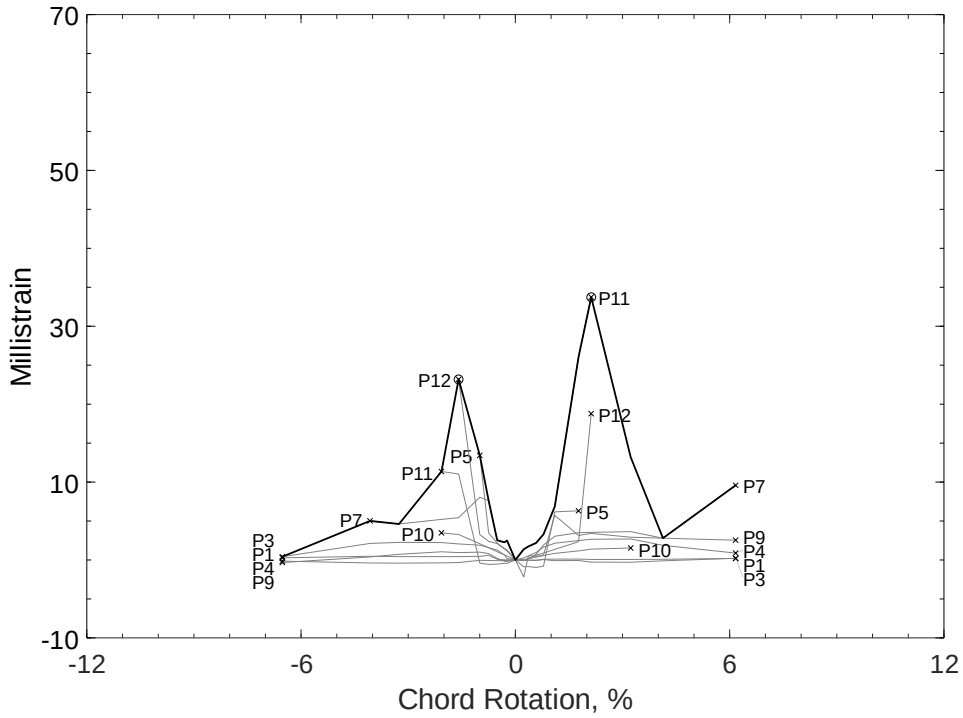

Figure 638 – Envelopes of measured strains in parallel bars of P100-2.5, P strain gauges

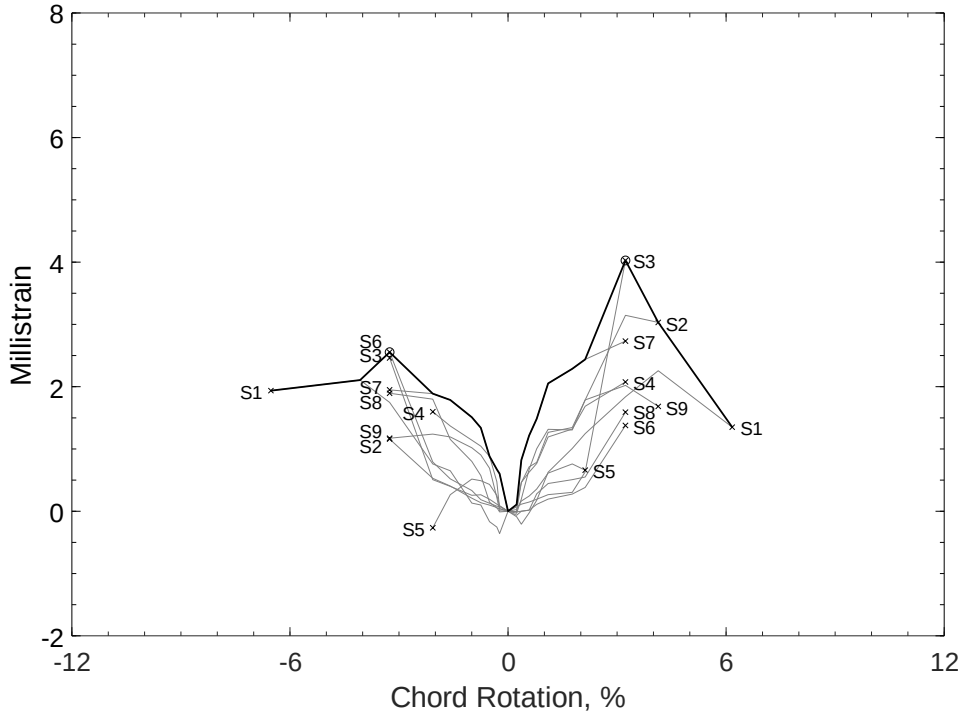

Figure 639 – Envelopes of measured strains in closed stirrups of P100-2.5, S strain gauges

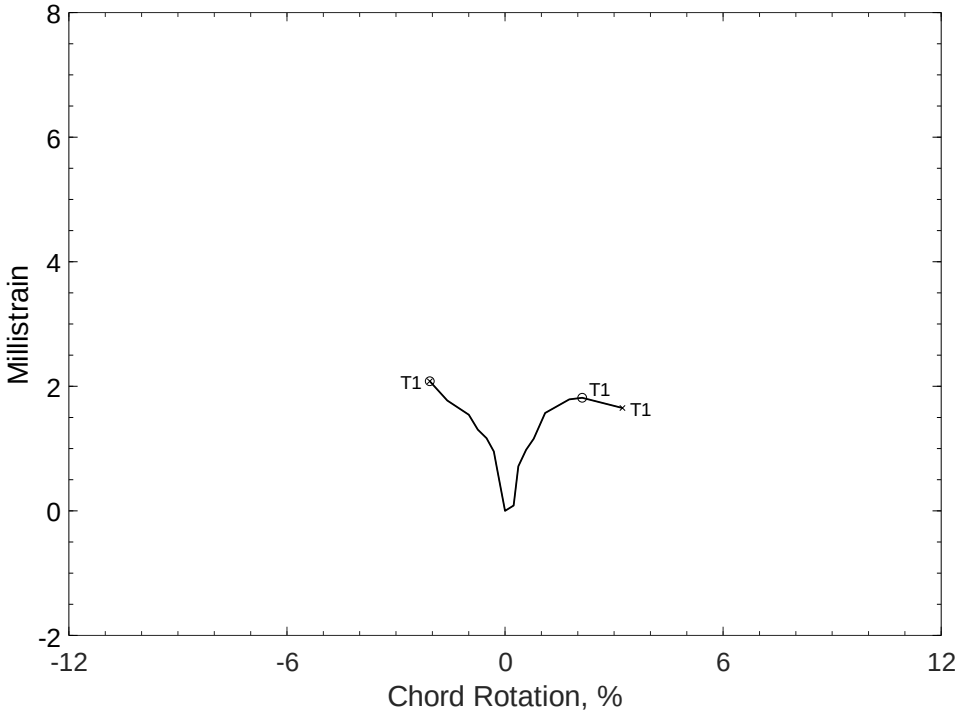

Figure 640 – Envelopes of measured strains in crossties of P100-2.5, T strain gauges

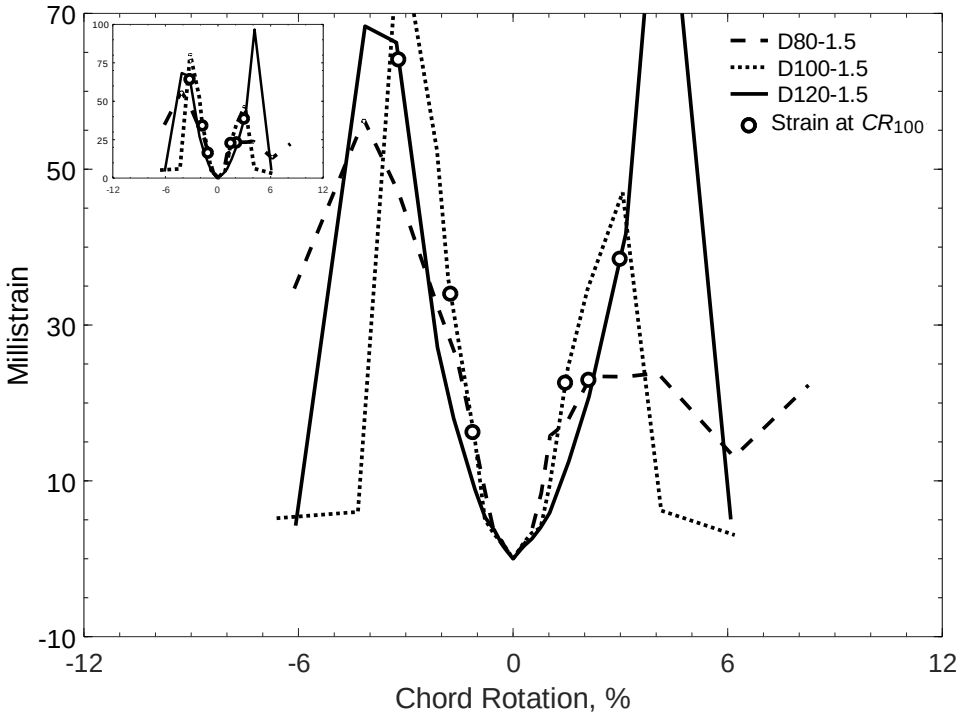

Figure 641 – Envelopes of measured strains in diagonal bars of D-type beams with an aspect ratio of 1.5, D strain gauges

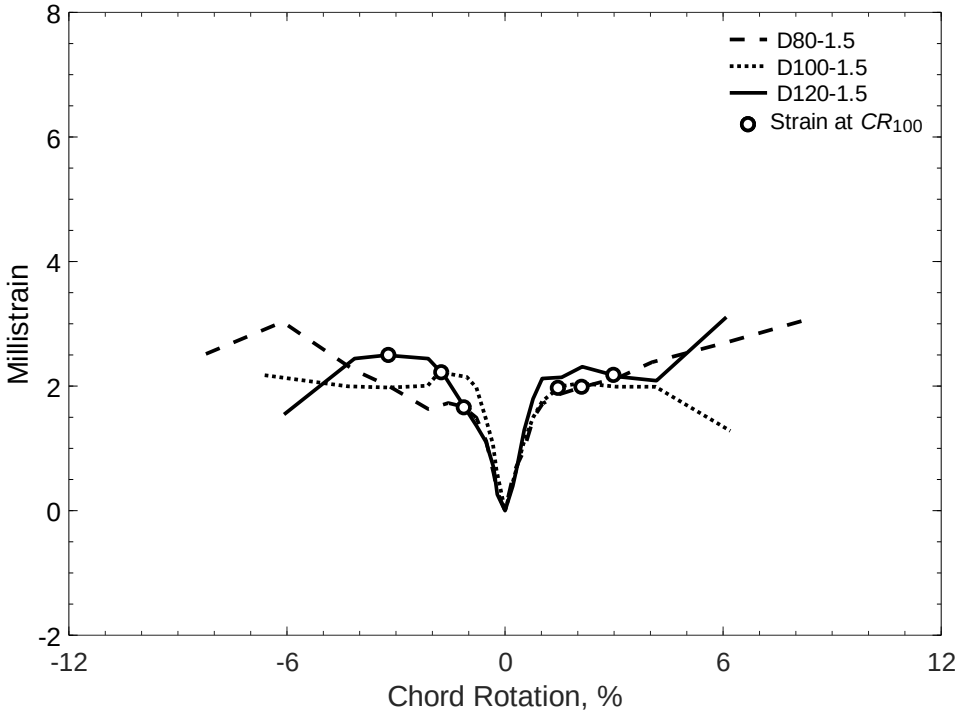

Figure 642 – Envelopes of measured strains in closed stirrups of D-type beams with an aspect ratio of 1.5, S strain gauges

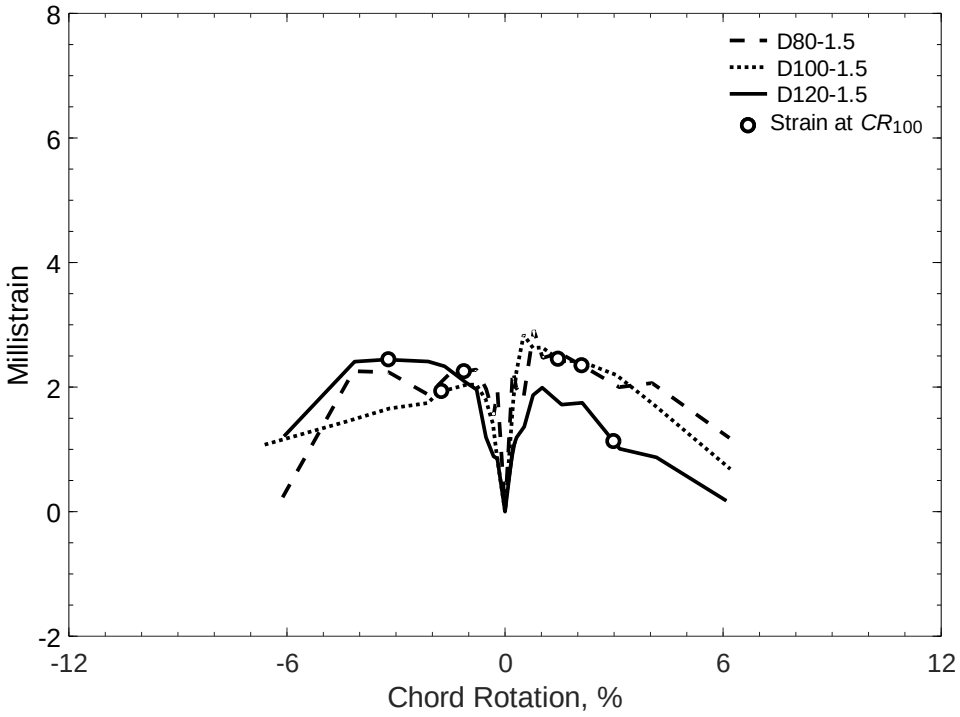

Figure 643 – Envelopes of measured strains in parallel bars
of D-type beams with an aspect ratio of 1.5, H strain gauges

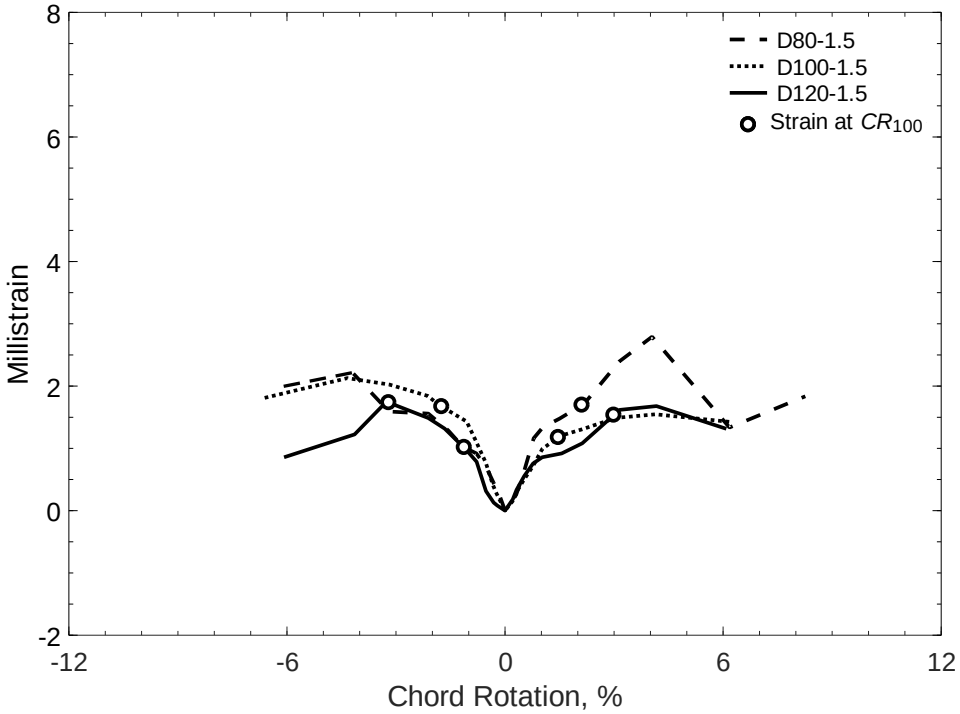

Figure 644 – Envelopes of measured strains in crossties
of D-type beams with an aspect ratio of 1.5, T strain gauges

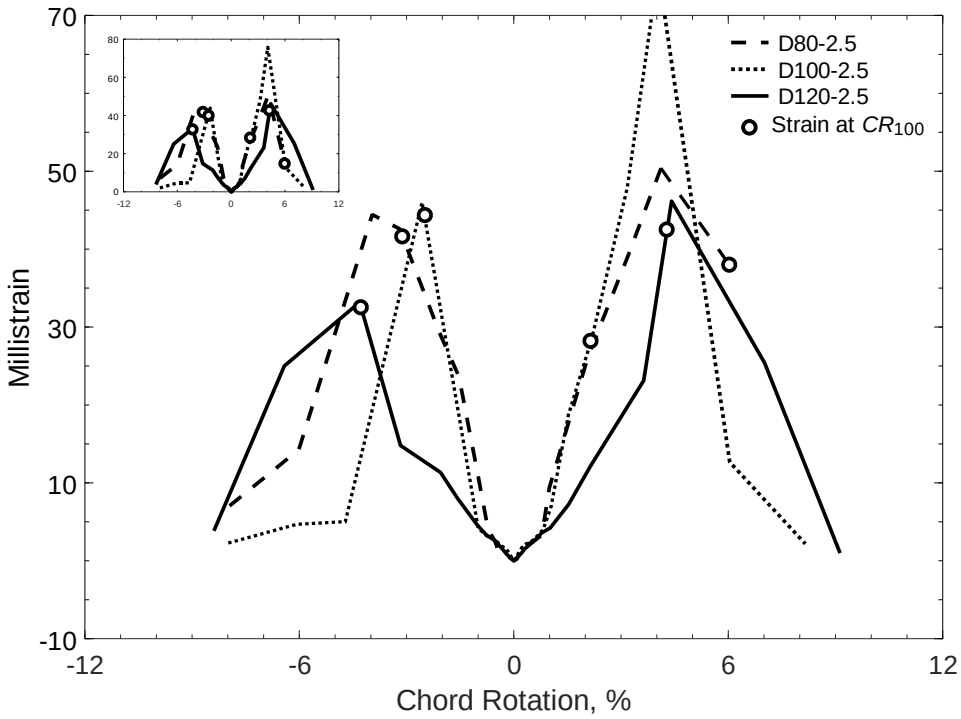

Figure 645 – Envelopes of measured strains in diagonal bars of D-type beams with an aspect ratio of 2.5, D strain gauges

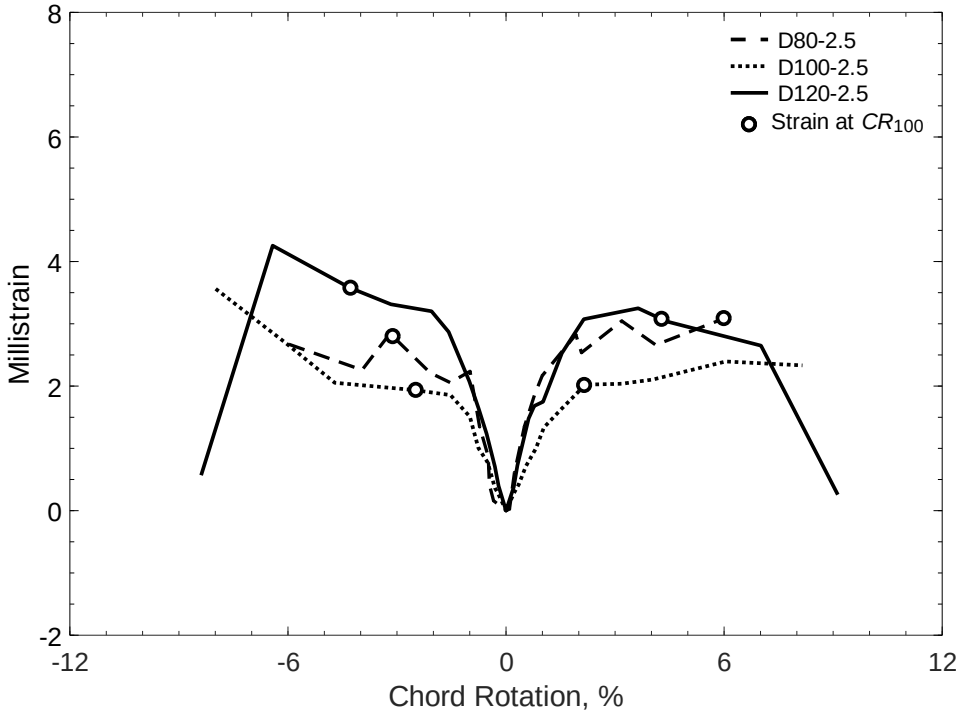

Figure 646 – Envelopes of measured strains in closed stirrups of D-type beams with an aspect ratio of 2.5, S strain gauges

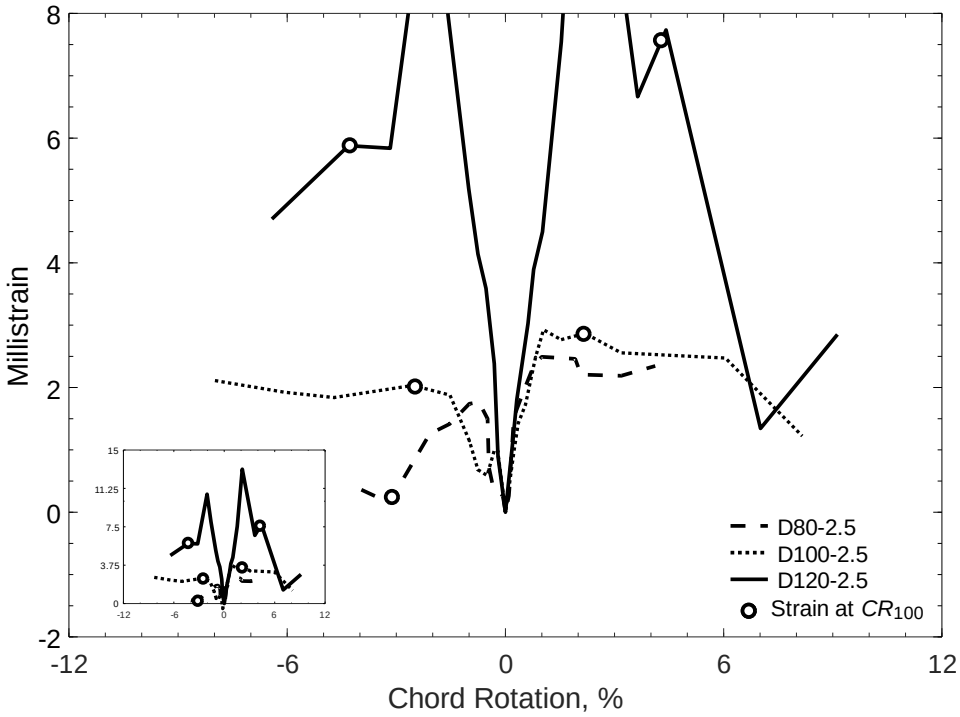

Figure 647 – Envelopes of measured strains in parallel bars
of D-type beams with an aspect ratio of 2.5, H strain gauges

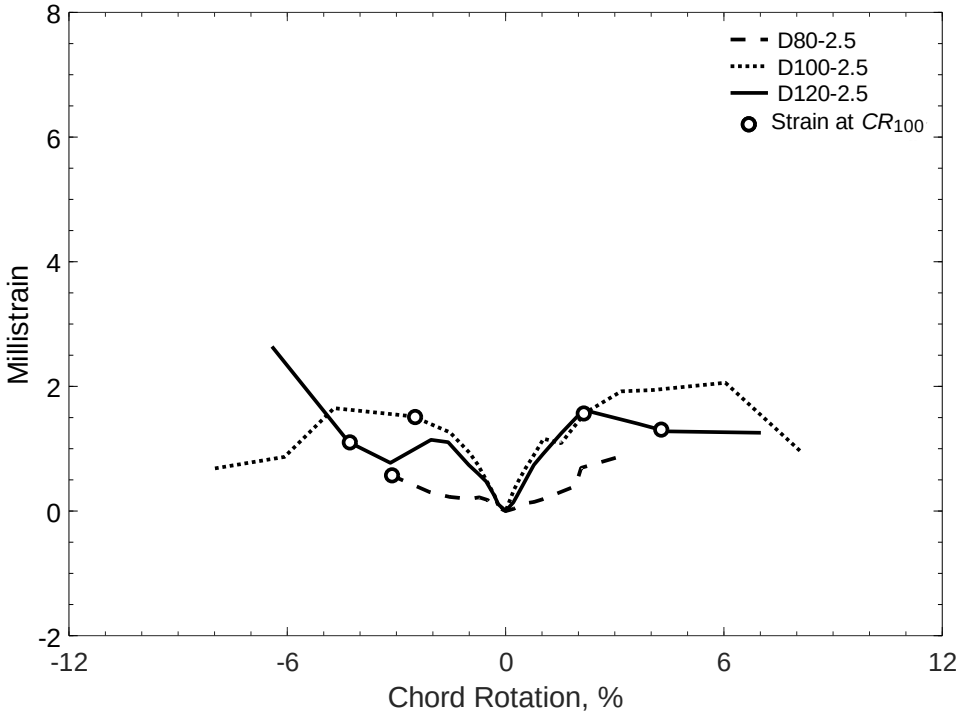

Figure 648 – Envelopes of measured strains in crossties
of D-type beams with an aspect ratio of 2.5, T strain gauges

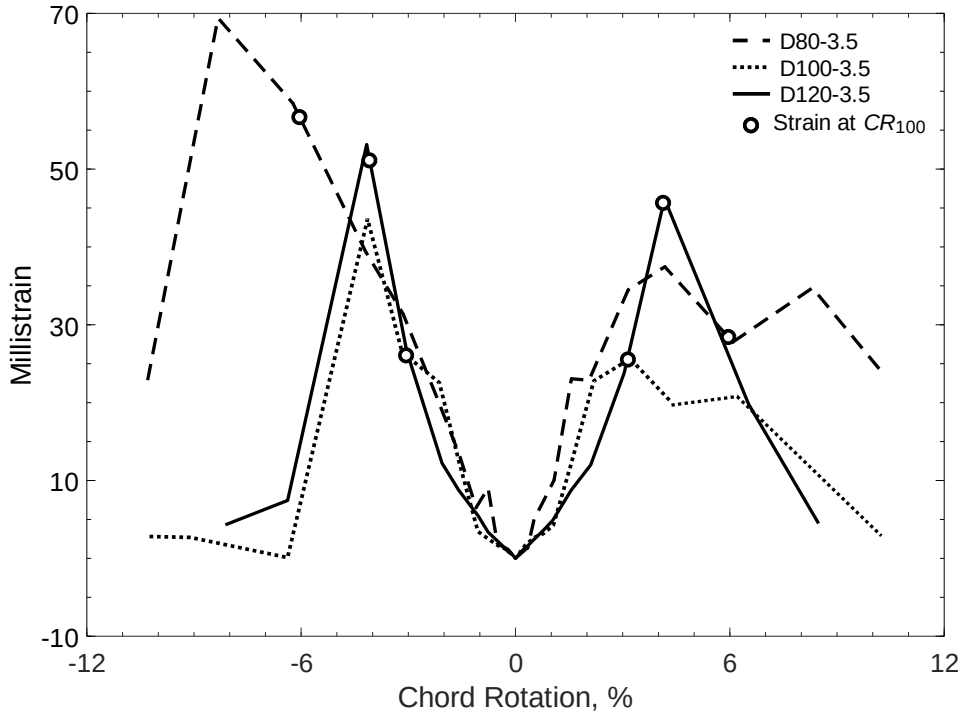

Figure 649 – Envelopes of measured strains in diagonal bars of D-type beams with an aspect ratio of 3.5, D strain gauges

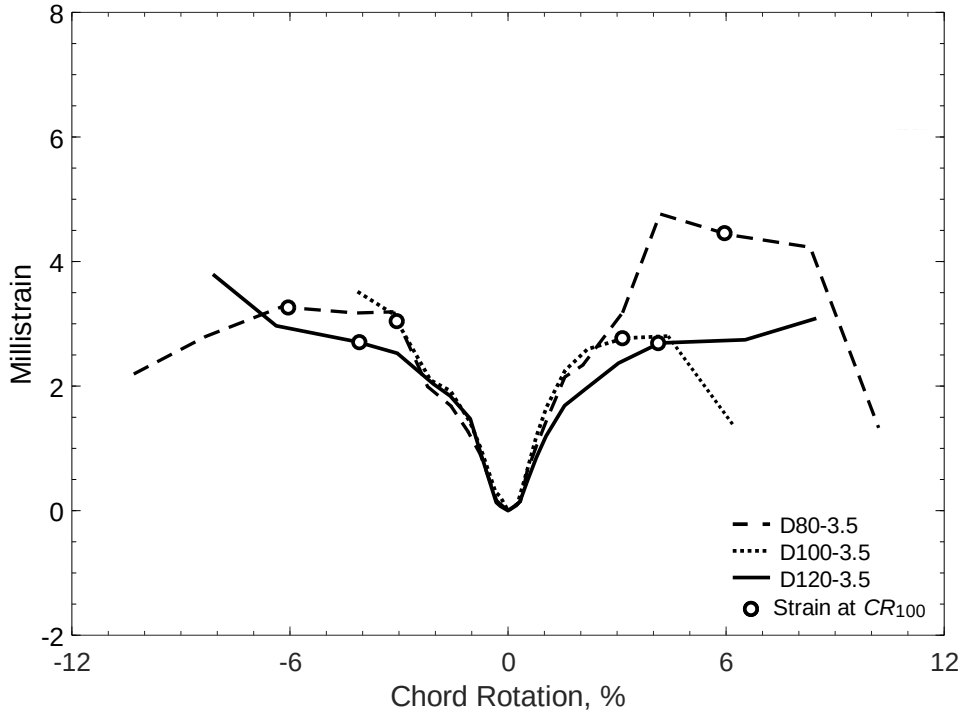

Figure 650 – Envelopes of measured strains in closed stirrups of D-type beams with an aspect ratio of 3.5, S strain gauges

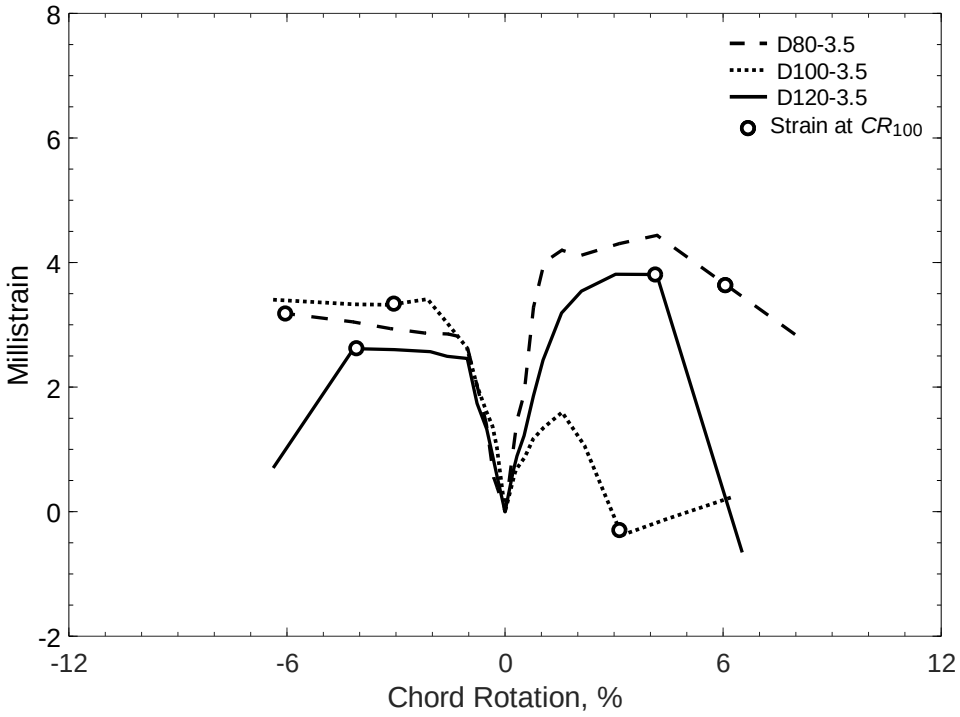

Figure 651 – Envelopes of measured strains in parallel bars
of D-type beams with an aspect ratio of 3.5, H strain gauges

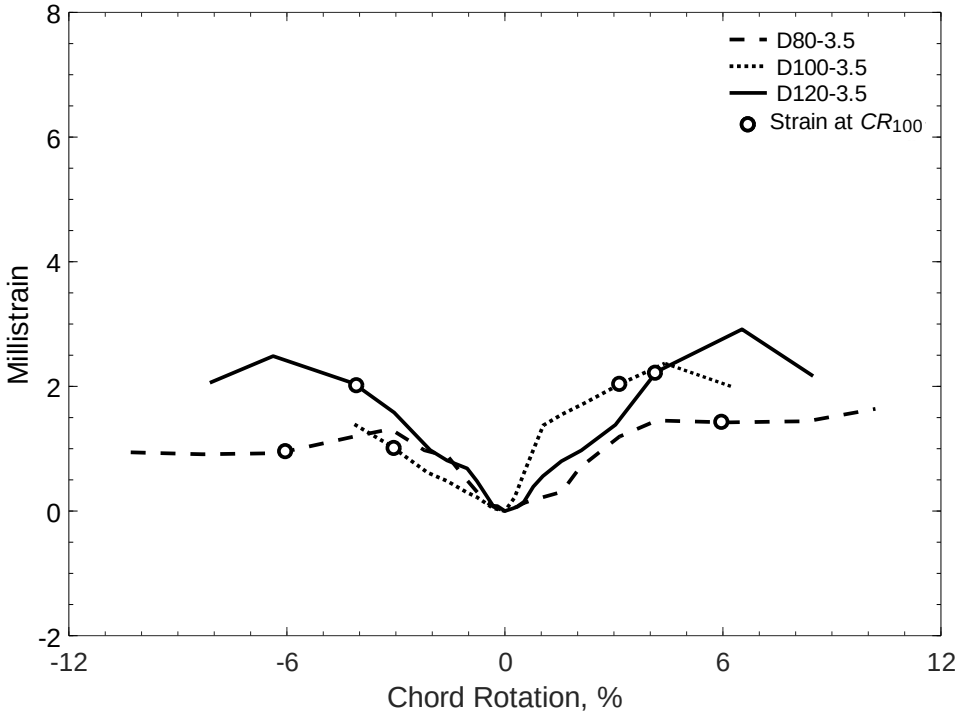

Figure 652 – Envelopes of measured strains in crossties
of D-type beams with an aspect ratio of 3.5, T strain gauges

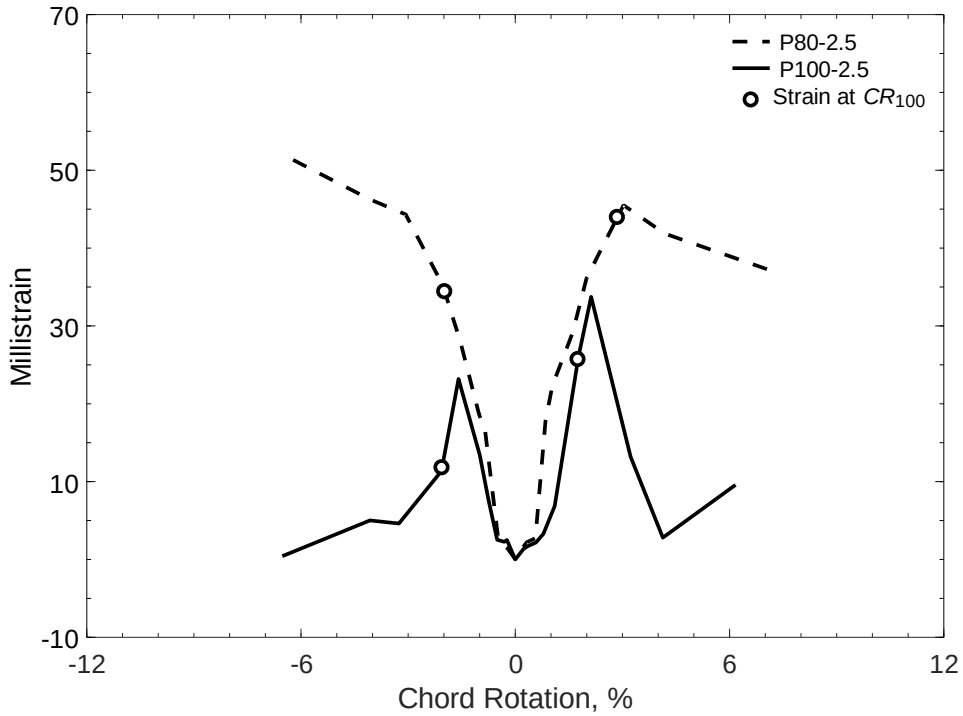

Figure 653 – Envelopes of measured strains in parallel bars of P-type beams with an aspect ratio of 2.5, P strain gauges

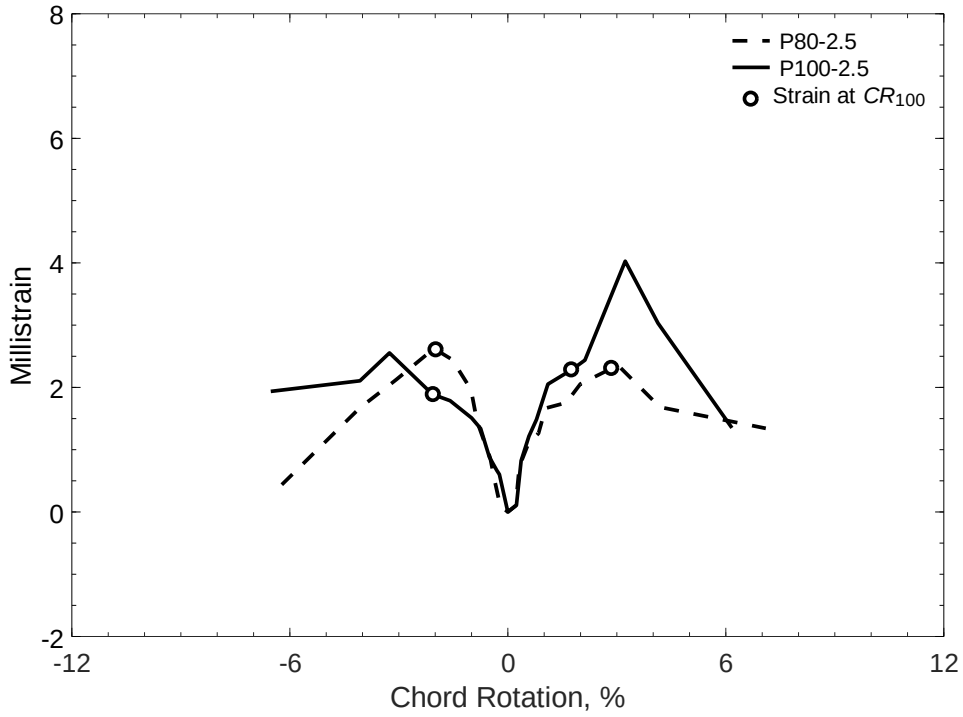

Figure 654 – Envelopes of measured strains in closed stirrups of P-type beams with an aspect ratio of 2.5, S strain gauges

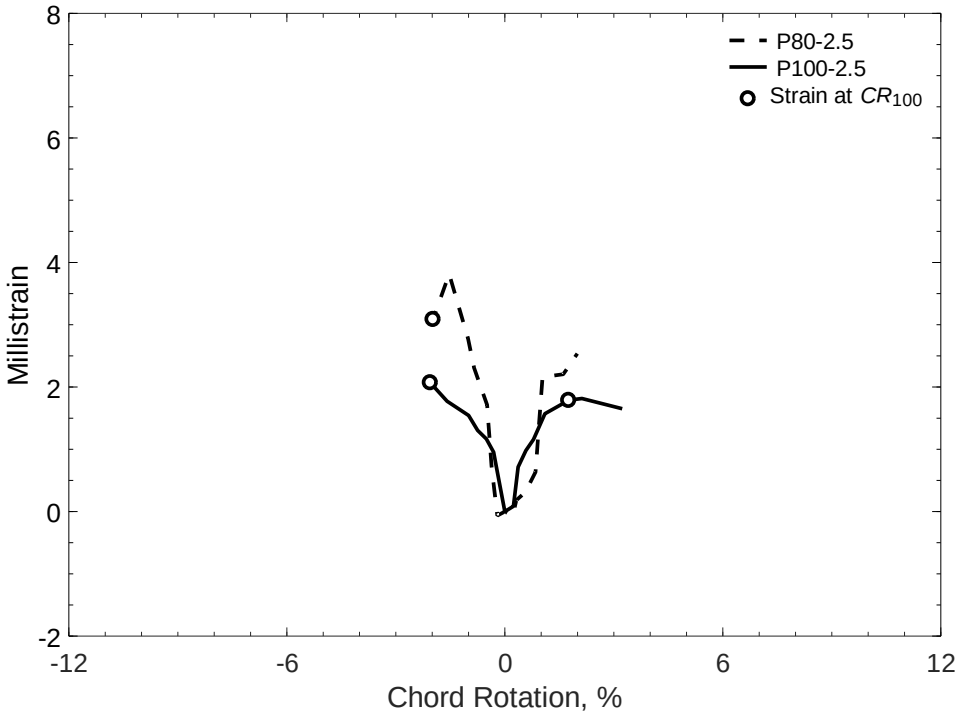

Figure 655 – Envelopes of measured strains in crossties
of P-type beams with aspect ratio of 2.5, T strain gauges

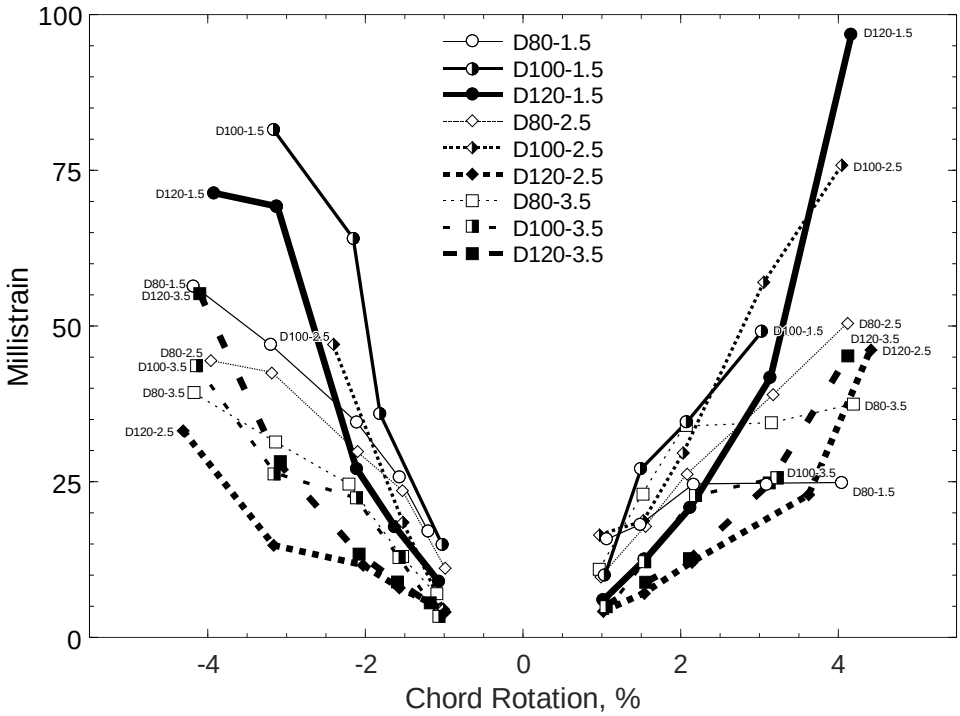

Figure 656 – Maximum strains in D-type beams during
Steps 5 through 9 (1% through 4% chord rotation), D strain gauges

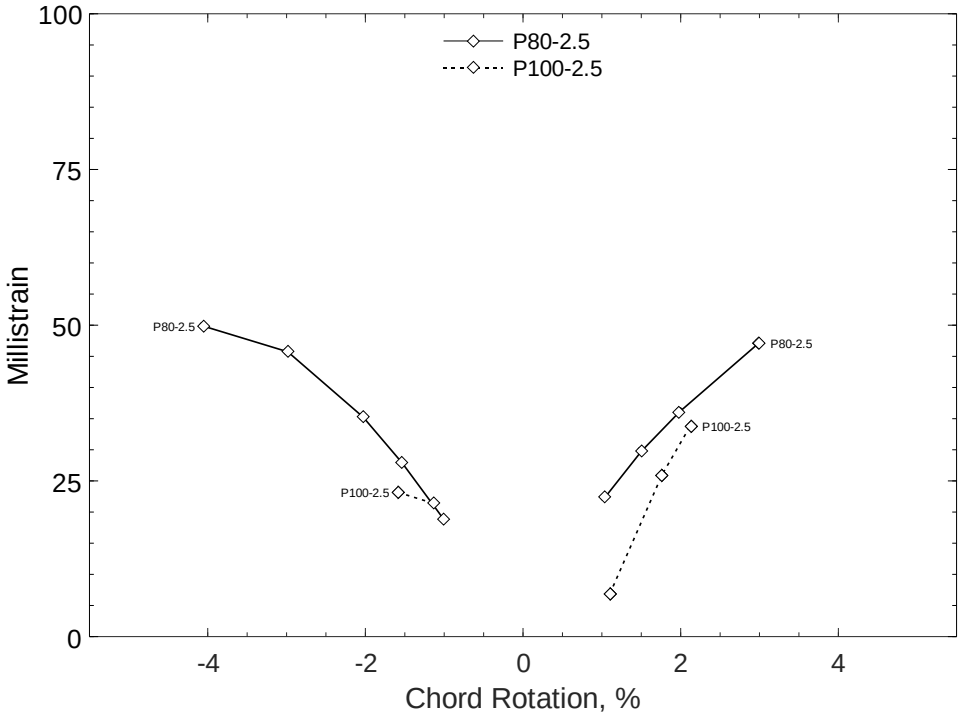

Figure 657 – Maximum strains in P-type beams during
Steps 5 through 9 (1% through 4% chord rotation), P strain gauges

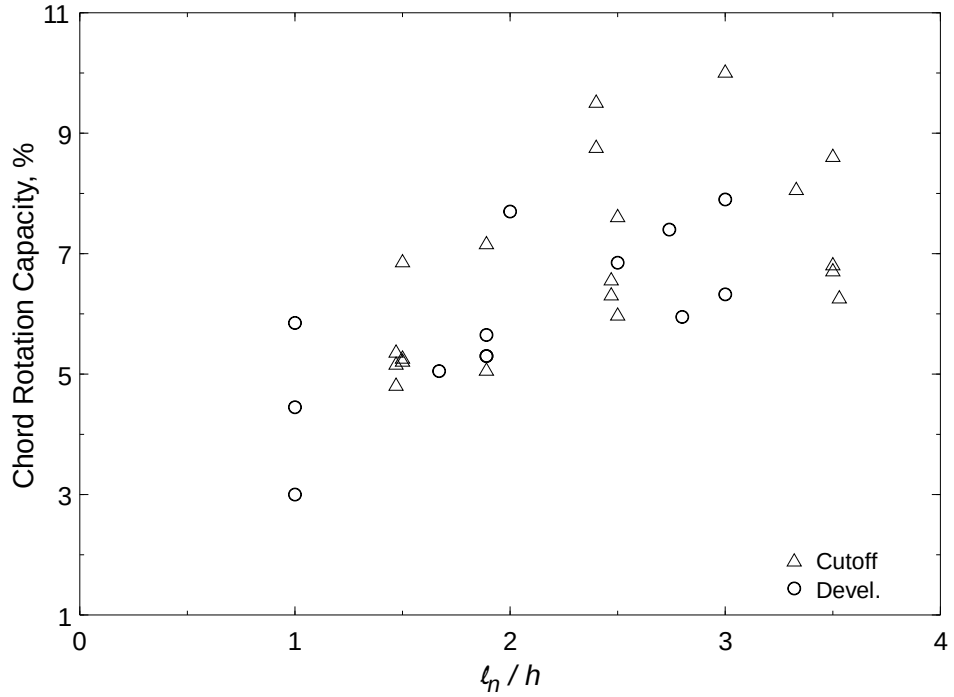

Figure 658 – Chord rotation capacity versus aspect ratio (ℓ_n/h) for specimens in Table 17 [a]

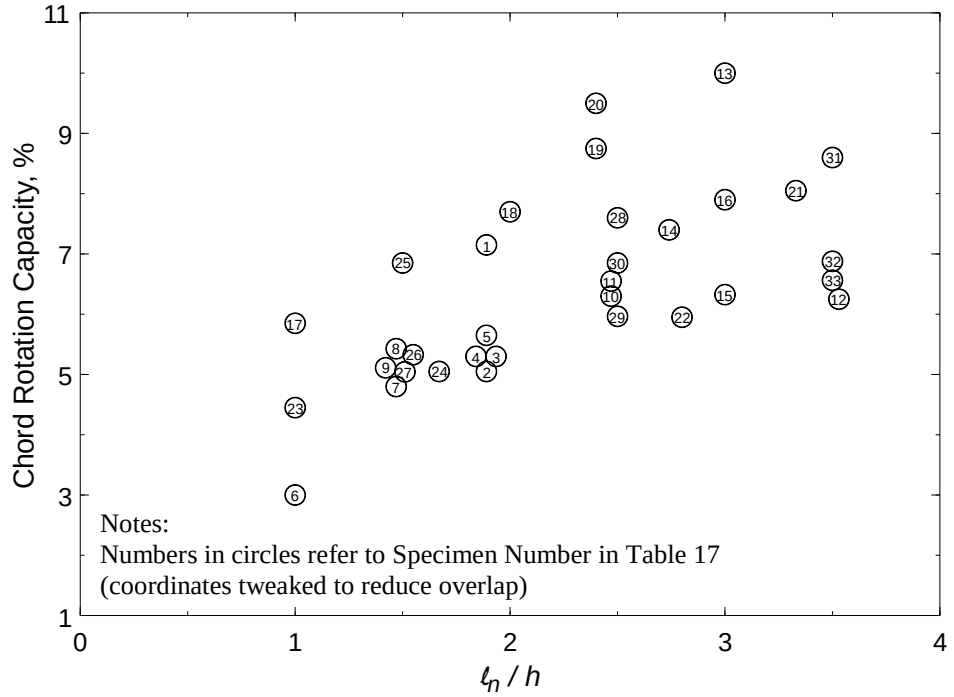

Figure 659 – Chord rotation capacity versus aspect ratio (ℓ_n/h)

[a] "Cutoff" refers to secondary longitudinal bars not developed into the supports; "Devel." refers to secondary longitudinal bars developed into the supports.

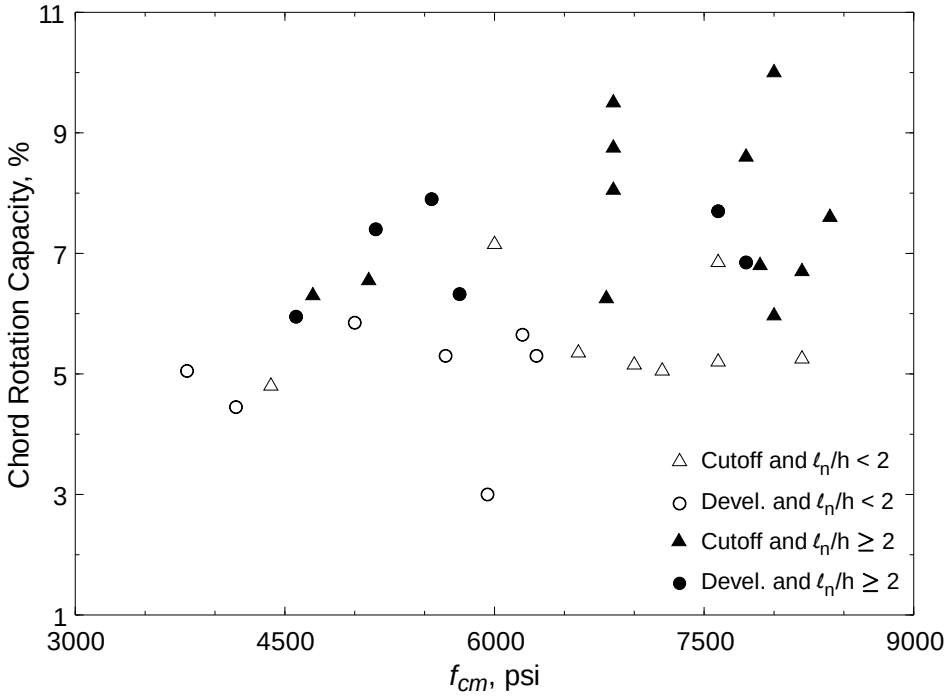

Figure 660 – Chord rotation capacity versus concrete compressive strength (f_{cm}) for specimens in Table 17 [a]

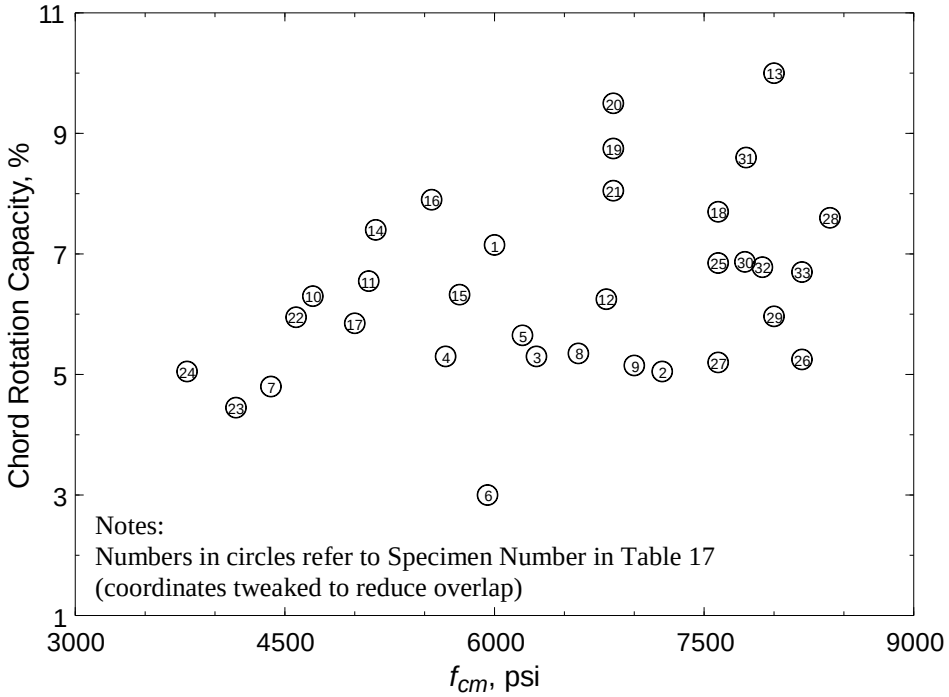

Figure 661 – Chord rotation capacity versus concrete compressive strength (f_{cm})

[a] "Cutoff" refers to secondary longitudinal bars not developed into the supports; "Devel." refers to secondary longitudinal bars developed into the supports.

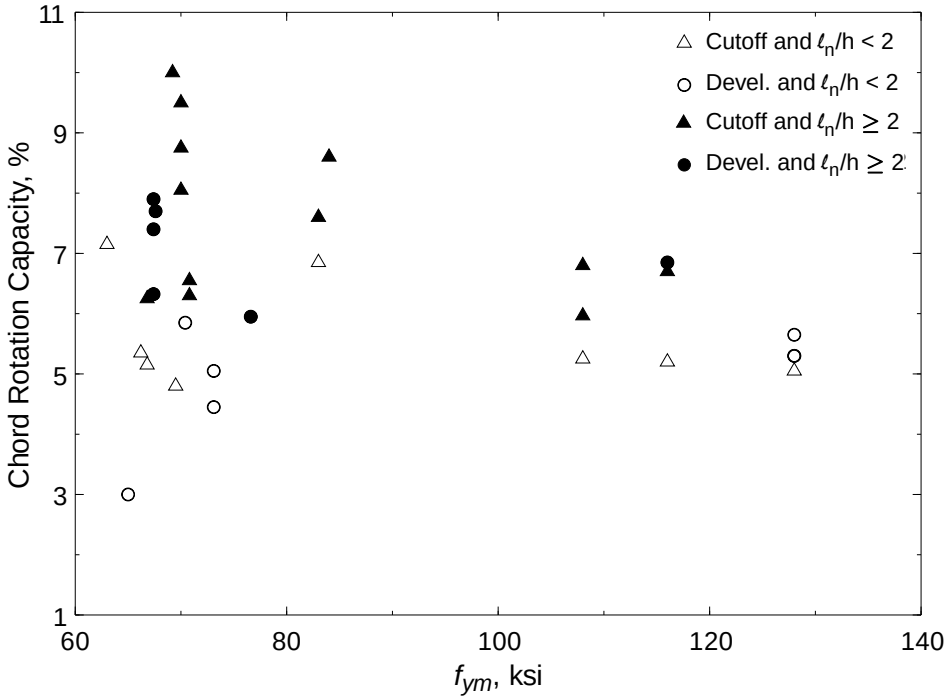

Figure 662 – Chord rotation capacity versus diagonal bar yield strength (f_{ym}) for specimens in Table 17 [a]

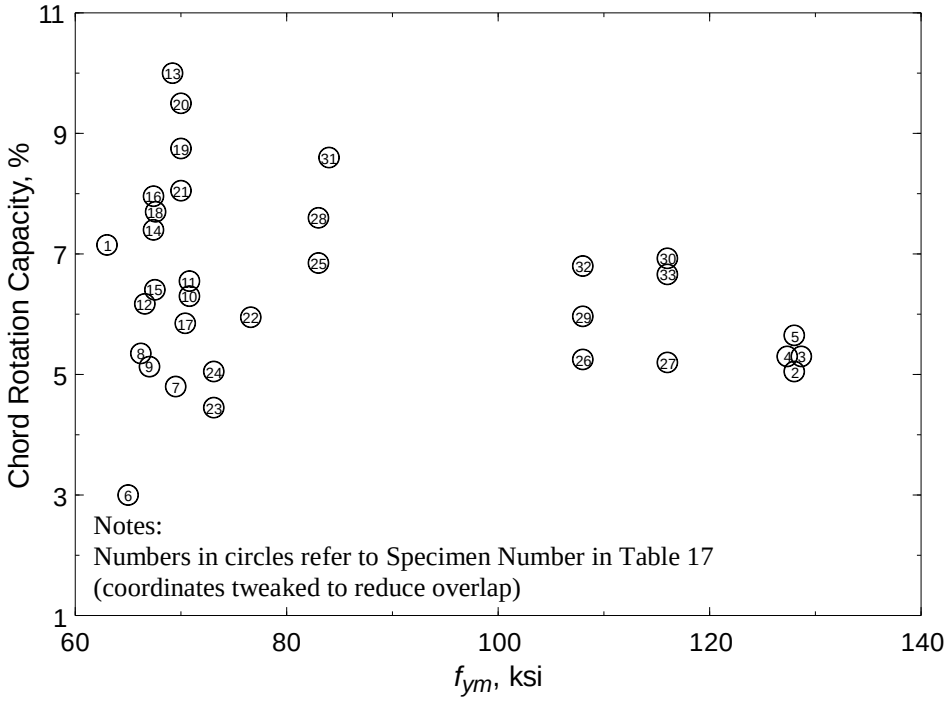

Figure 663 – Chord rotation capacity versus diagonal bar yield strength (f_{ym})

[a] "Cutoff" refers to secondary longitudinal bars not developed into the supports; "Devel." refers to secondary longitudinal bars developed into the supports.

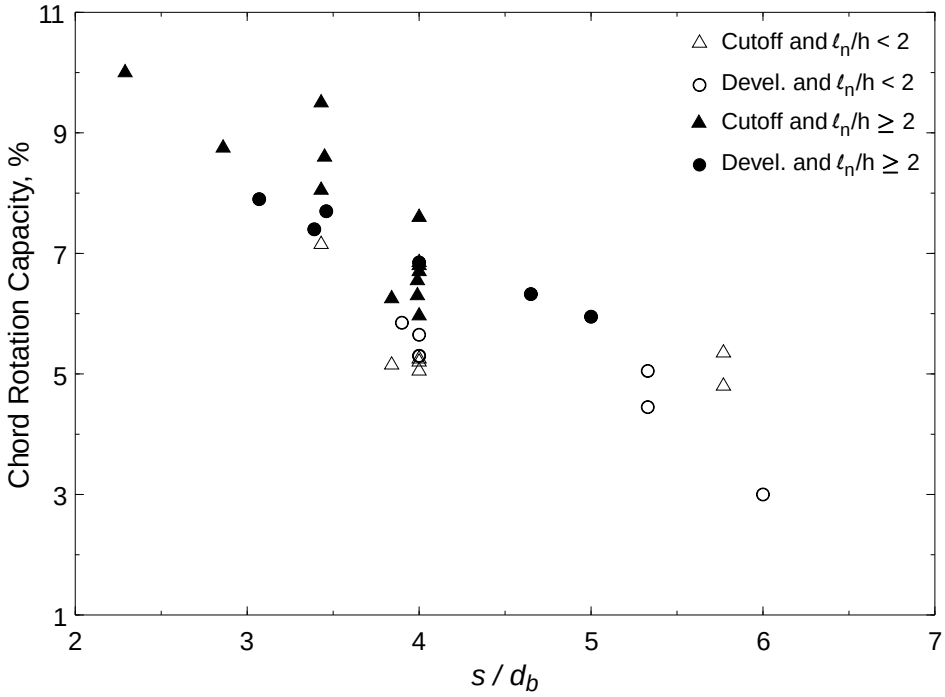

Figure 664 – Chord rotation capacity versus hoop spacing-to-bar diameter ratio (s/d_b) for specimens in Table 17 [a]

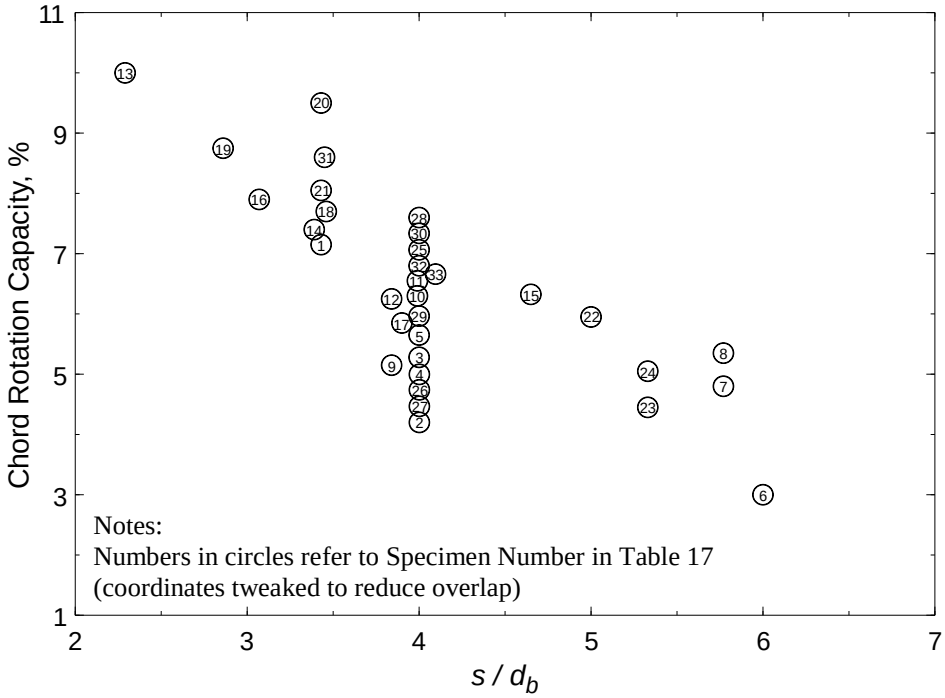

Figure 665 – Chord rotation capacity versus hoop spacing-to-bar diameter ratio (s/d_b)

[a] "Cutoff" refers to secondary longitudinal bars not developed into the supports; "Devel." refers to secondary longitudinal bars developed into the supports.

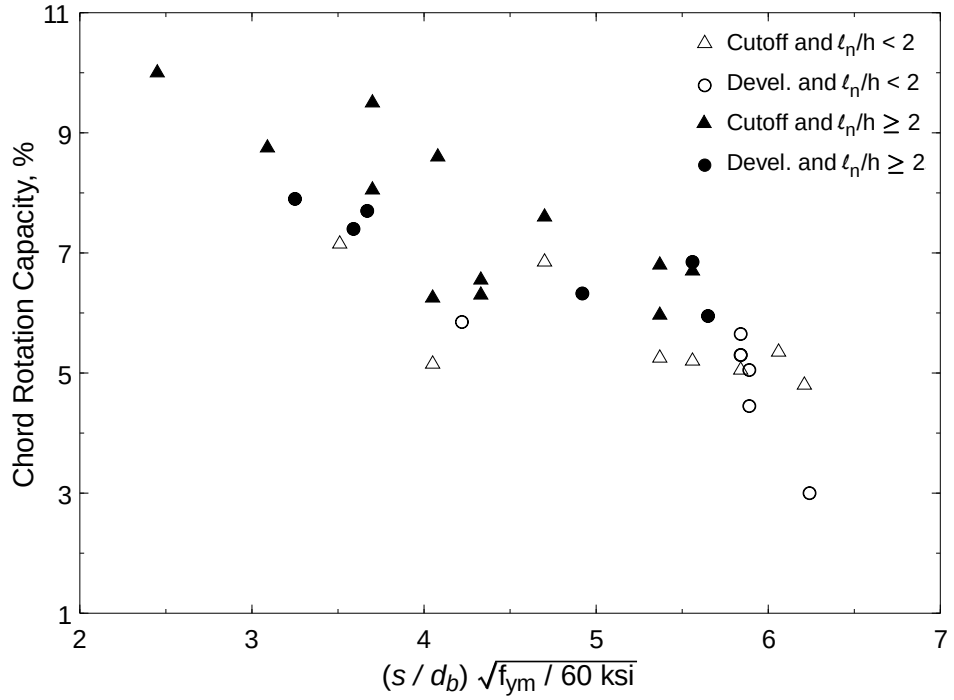

Figure 666 – Chord rotation capacity versus normalized hoop spacing-to-bar diameter ratio for specimens in Table 17 [a]

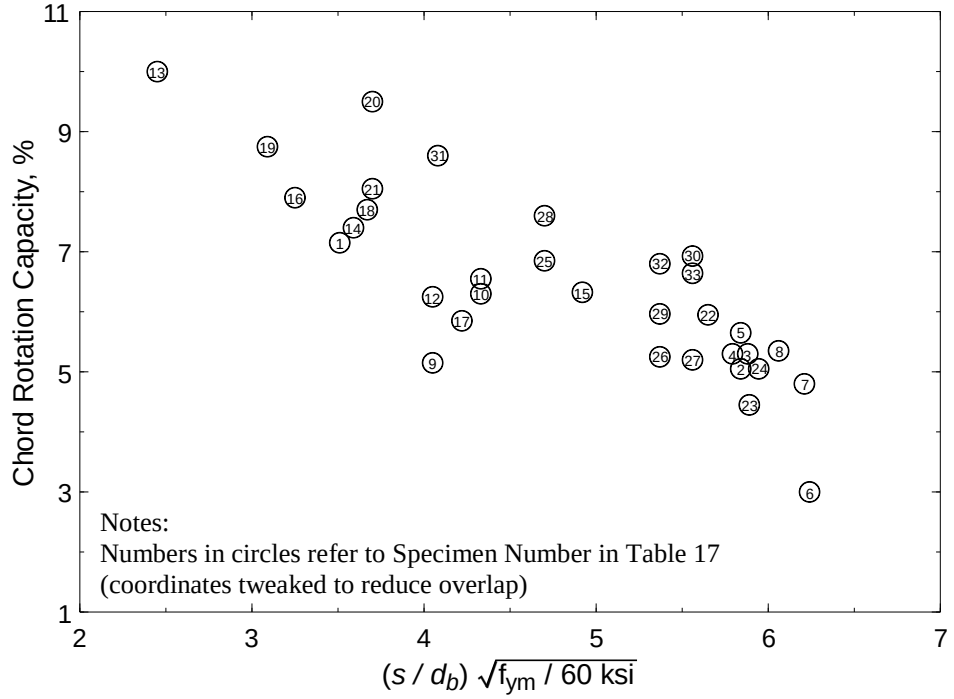

Figure 667 – Chord rotation capacity versus normalized hoop spacing-to-bar diameter ratio

[a] "Cutoff" refers to secondary longitudinal bars not developed into the supports; "Devel." refers to secondary longitudinal bars developed into the supports.

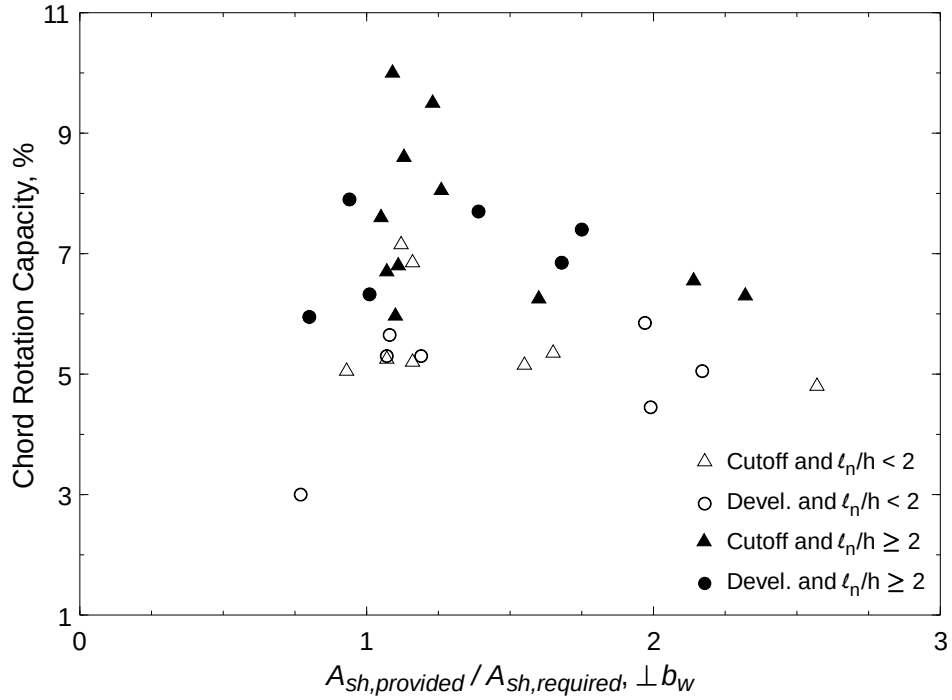

Figure 668 – Chord rotation capacity versus $A_{sh,provided}$-to-$A_{sh,required}$ ratio perpendicular to beam width for specimens in Table 17 [a]

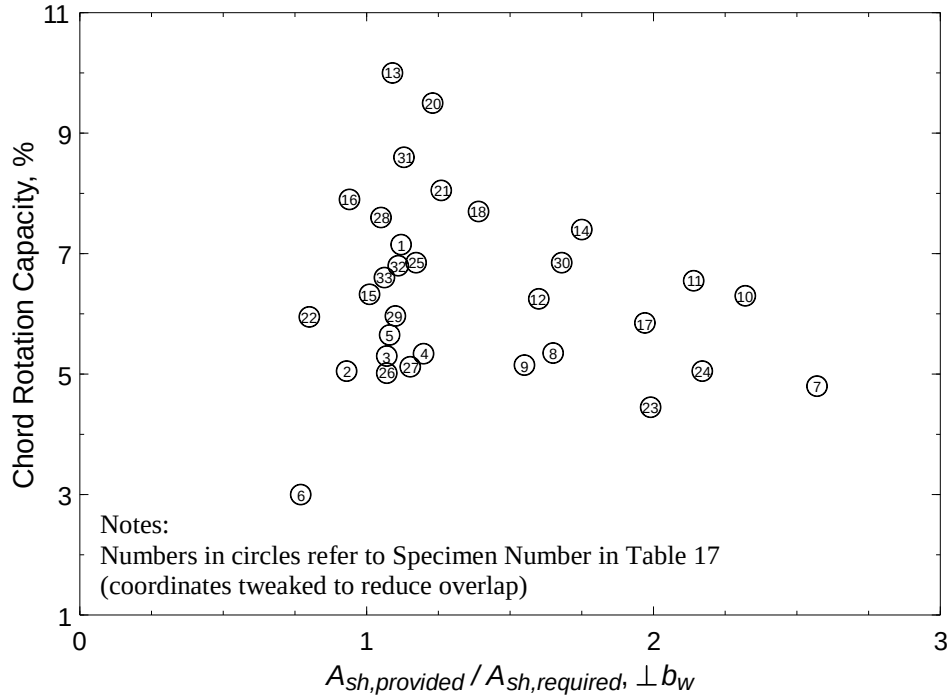

Figure 669 – Chord rotation capacity versus $A_{sh,provided}$-to-$A_{sh,required}$ ratio perpendicular to beam width

[a] "Cutoff" refers to secondary longitudinal bars not developed into the supports; "Devel." refers to secondary longitudinal bars developed into the supports.

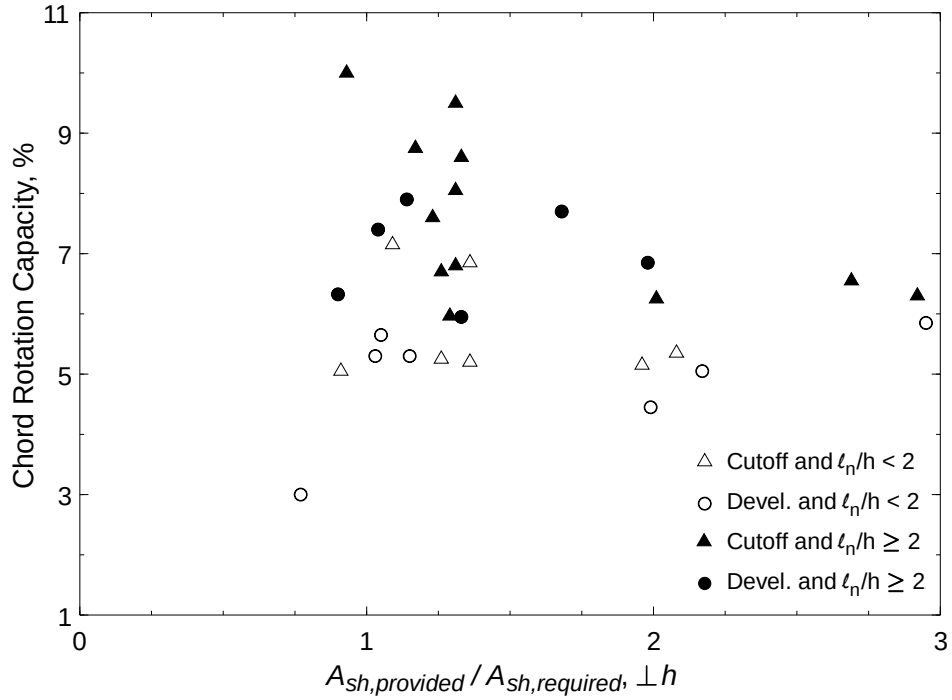

Figure 670 – Chord rotation capacity versus $A_{sh,provided}$-to-$A_{sh,required}$ ratio perpendicular to beam depth for specimens in Table 17 [a]

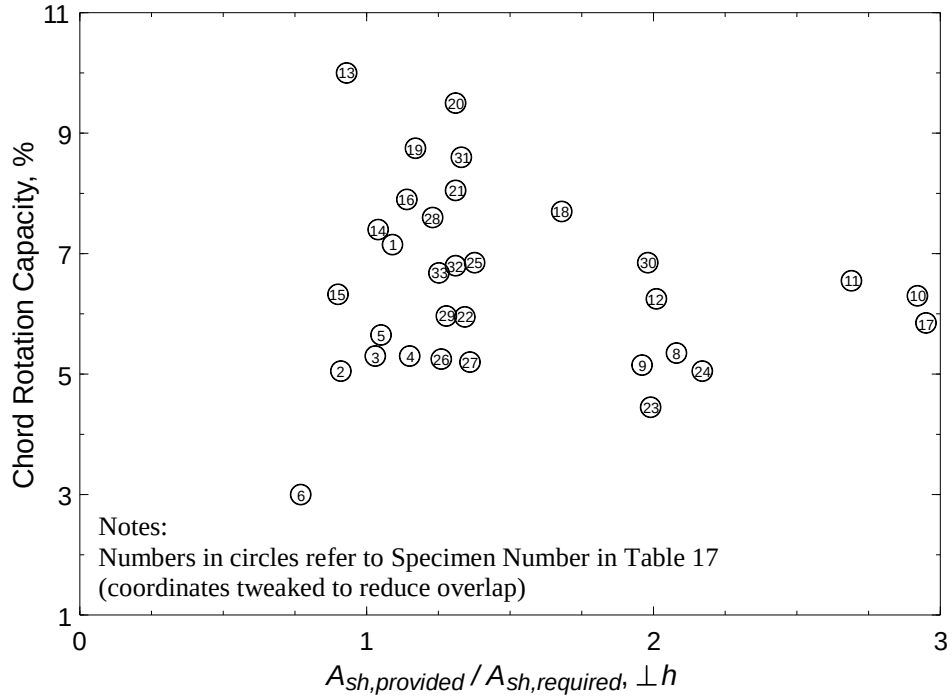

Figure 671 – Chord rotation capacity versus $A_{sh,provided}$-to-$A_{sh,required}$ ratio perpendicular to beam depth

[a] "Cutoff" refers to secondary longitudinal bars not developed into the supports; "Devel." refers to secondary longitudinal bars developed into the supports.

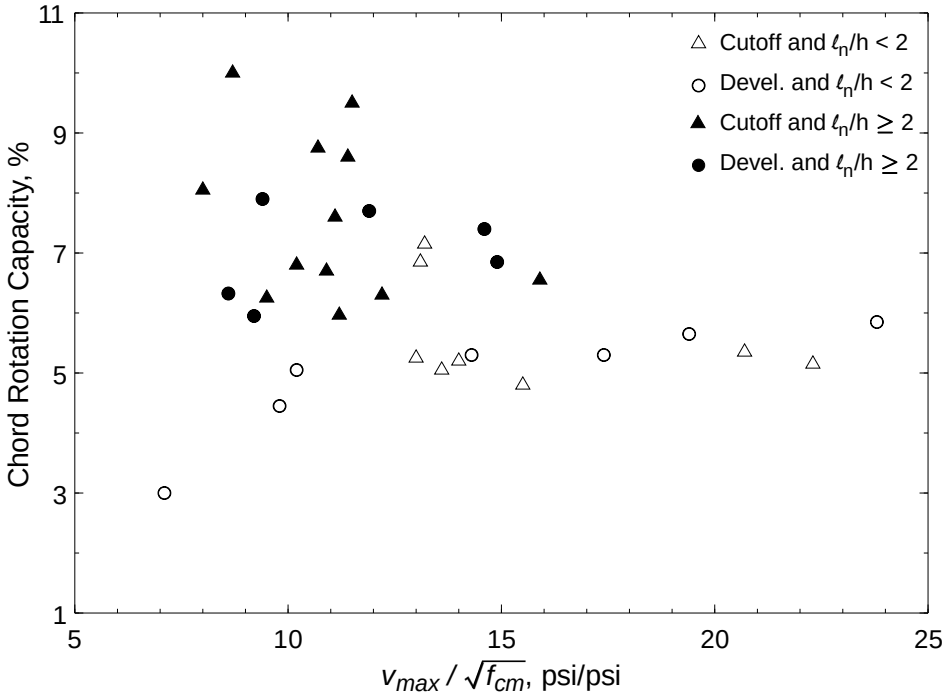

Figure 672 – Chord rotation capacity versus normalized shear stress for specimens in Table 17 [a]

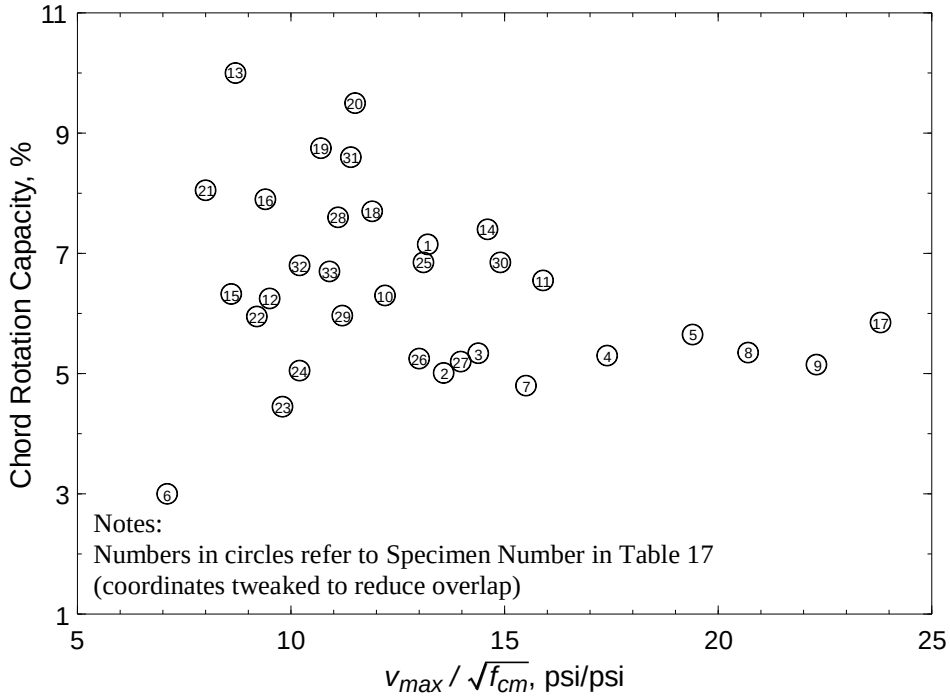

Figure 673 – Chord rotation capacity versus normalized shear stress

[a] "Cutoff" refers to secondary longitudinal bars not developed into the supports; "Devel." refers to secondary longitudinal bars developed into the supports.

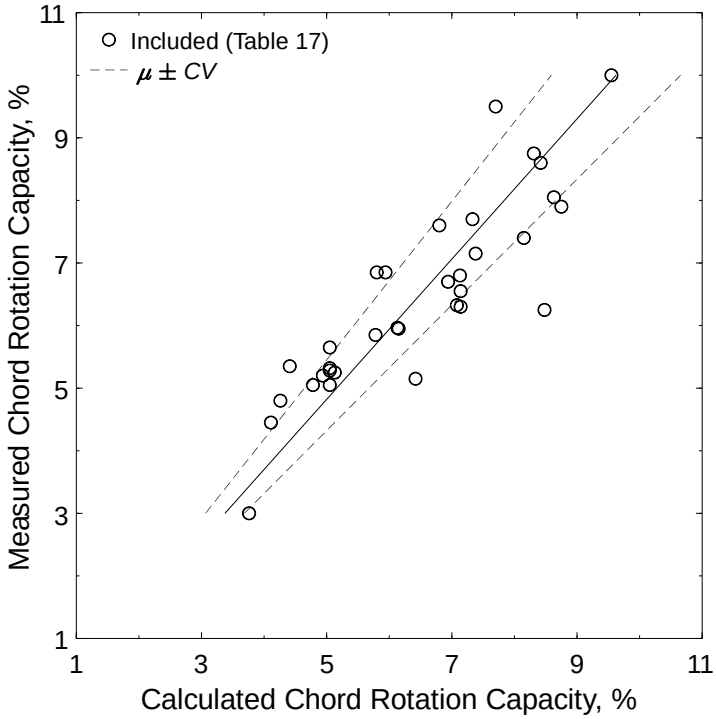

Figure 674 – Measured versus calculated chord rotation capacity for specimens in Table 17

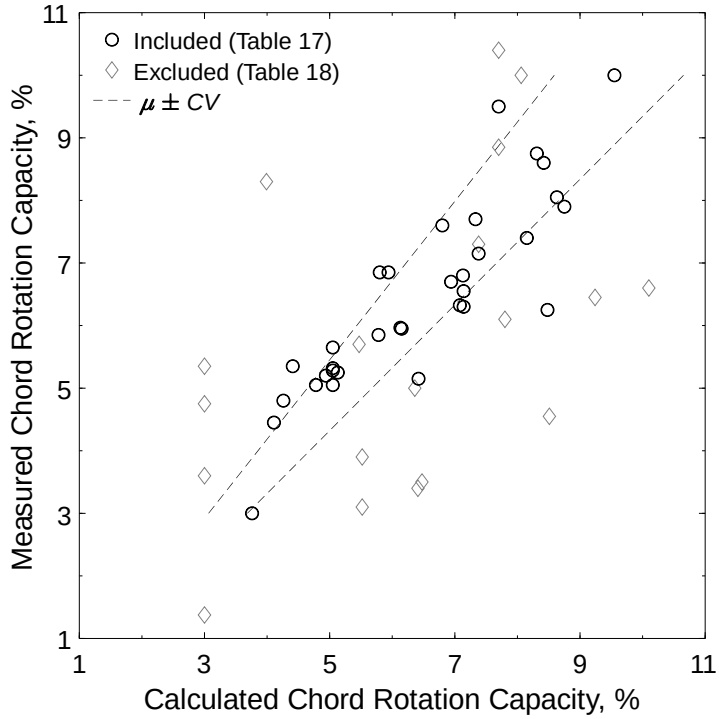

Figure 675 – Measured versus calculated chord rotation capacity for specimens in Table 17 and 18

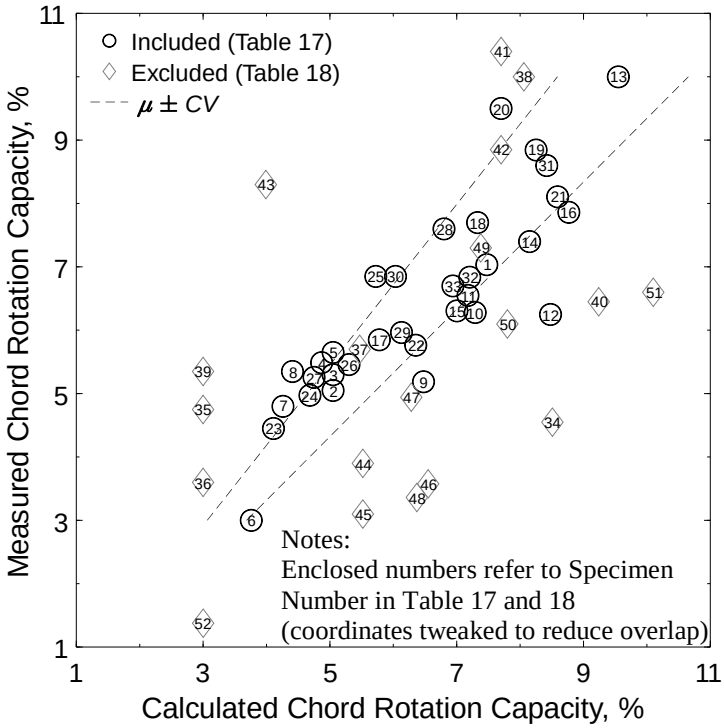

Figure 676 – Measured versus calculated chord rotation capacity

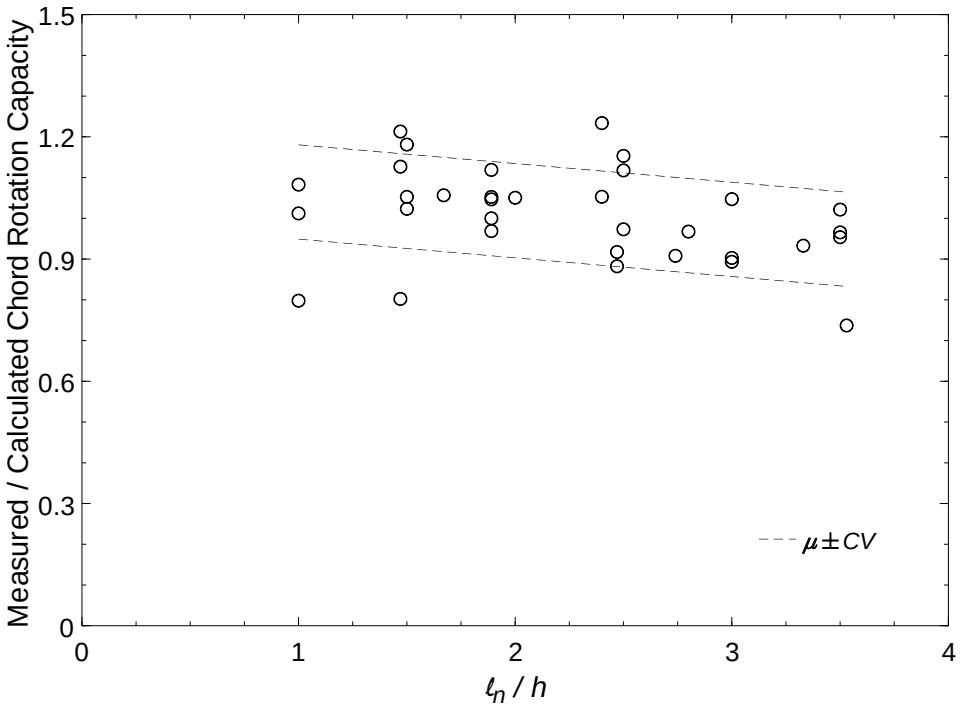

Figure 677 – Measured-to-calculated ratio of chord rotation capacity versus aspect ratio

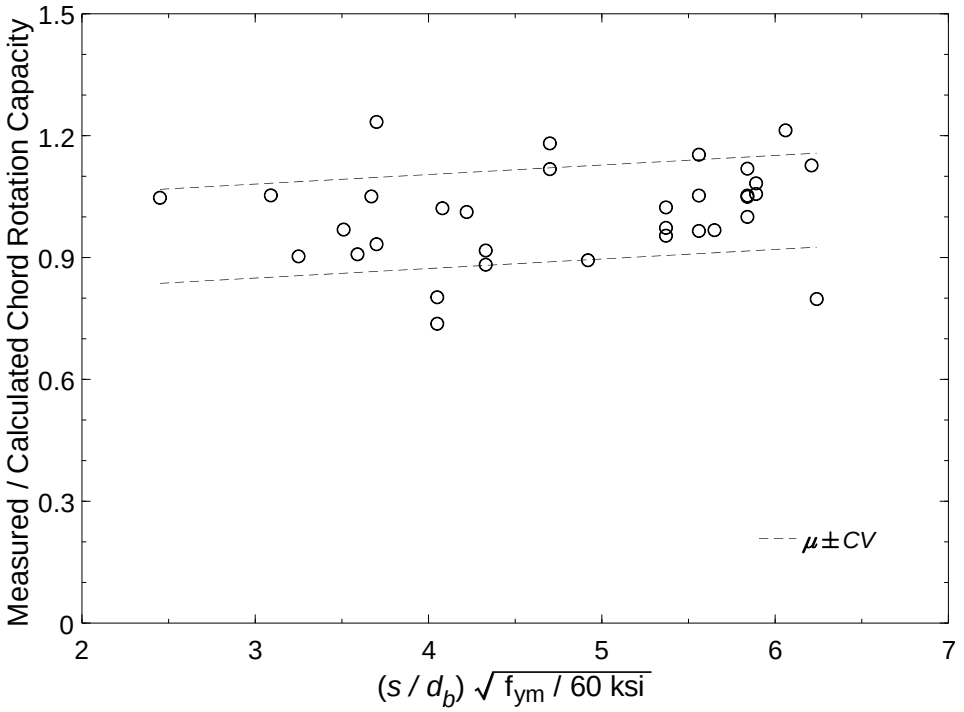

Figure 678 – Measured-to-calculated ratio of chord rotation capacity versus normalized hoop spacing-to-bar diameter ratio

APPENDIX A: NOTATION

A_{ch} = cross-sectional area of a member measured to outside edges of transverse reinforcement, in.^{2}

A_{eff} = effective shear area, taken as a fraction of gross area of concrete section, in.^{2}

A_g = gross area of concrete section, in.^{2}

A_s = total area of primary longitudinal reinforcement along the top or bottom face of a coupling beam with parallel reinforcement layout, in.^{2}

A_{sh} = total cross-sectional area of transverse reinforcement, including crossties, within spacing *s* and perpendicular to dimension b_c, in.^{2}

A_{vd} = total area of reinforcement in each group of diagonal bars in a diagonally-reinforced coupling beam, in.^{2}

A_w = shear area, $A_w = b_w h/1.2$ (for rectangular sections), in.^{2}

b_c = cross-sectional dimension of member core measured to outside edges of the transverse reinforcement composing area A_{sh}, in.

b_w = beam width, in.

c_c = clear cover of reinforcement, in.

CR = chord rotation of the coupling beam, corrected for sliding and relative rotation between the top and bottom blocks, rad

CR_{be} = chord rotation due to beam-end rotation, rad

CR_{cap} = average of the maximum chord rotations in each loading direction where the envelope of the shear versus chord rotation curve (formed by connecting the maximum chord rotation of the first cycle of each loading step) intersects 80% of the maximum applied shear, rad

CR_{est} = estimated chord rotation capacity for a diagonally-reinforced coupling beam, rad

CR_f = chord rotation due to flexural deformation, rad

CR_{sl} = chord rotation due to sliding at the beam-block interface, rad

CR_v = chord rotation due to shear distortion, rad

CR_{75} = chord rotation corresponding to $V = 0.75V_{max}$ on the V versus CR envelope curve (before V_{max} and for a given loading direction), rad

CR_{100} = chord rotation corresponding to V_{max}, rad

CV = coefficient of variation, equal to the ratio of the standard deviation to the mean

d = distance from extreme compression fiber to centroid of longitudinal tension reinforcement, in.

d_b = nominal diameter of the primary longitudinal reinforcing bar, in.

d_i = distance between midspan of the beam and midheight of Layer i (see Figure 33), positive for layers below midspan of the beam, in.

d_1 = distance between the top left and bottom right corners of a station (A to C, as shown in Figure 156), in.

d_2 = distance between the bottom left and top right corners of a station (D to B, as shown in Figure 156), in.

D_m = peak chord rotation during half loading cycle, rad

E_c = modulus of elasticity of concrete, psi

E_h = hysteretic energy dissipation index

E_s = modulus of elasticity of steel reinforcement, 29,000 ksi (200,000 MPa)

f_c' = specified compressive strength of concrete, psi

f_{cm} = measured average compressive strength of concrete, psi

f_{ct} = measured average splitting tensile strength of concrete, psi

f_t = measured peak stress or tensile strength of reinforcement, ksi

f_y = specified yield stress of longitudinal reinforcement, ksi

f_{ym} = measured yield stress of longitudinal reinforcement, ksi

f_{yt} = specified yield stress of transverse reinforcement, ksi

f_{ytm} = measured yield stress of transverse reinforcement, ksi

G_c = shear modulus of concrete, $G_c = 0.4E_c$, ksi

h = beam height, in.

h_b = distance between the bottom corners of a station (C to D, as shown in Figure 156), in.

h_t = distance between the top corners of a station (A to B, as shown in Figure 156), in.

i = index referring to a station, row, column, or layer of markers (Figure 33)

I_{eff} = effective moment of inertia, in.^{4}

I_g = gross moment of inertia, in.^{4}

I_{tr} = uncracked moment of inertia of the transformed section, in.^{4}

j = index referring to a station, row, column, or layer of markers (Figure 33)

K = stiffness calculated using ASCE 41-17 Table 10-19[16], kips/in.

K_e = secant stiffness associated with CR_{75}, kips/in.

K_S = secant stiffness associated with the peak force of a loading step (Tables 11 through 14), kips/in.

ℓ_e = minimum straight embedment length to develop a tension stress of 1.25f_y, in.

ℓ_i = initial horizontal distance between markers in Columns 1 and 5 (Figure 33), in.

ℓ_j = length (along the beam depth) of a station, nominally 4 in. (100 mm), in.

ℓ_n = length of clear span measured face-to-face of supports, in.

M_{nm} = calculated flexural strength corresponding to a stress of f_{ym} in the primary longitudinal reinforcement (per equation in Table 15), in.-kips

M_{pr} = calculated flexural strength corresponding to a stress of 1.25f_y in the primary longitudinal reinforcement, in.-kips

n = total number of primary longitudinal reinforcing bars in a group or layer:
For a D-type beam, number of bars in each group of diagonal reinforcement
For a P-type beam, number of bars in each layer of top or bottom reinforcement

n_r = total number of rows of optical markers within beam clear span

for a beam with an aspect ratio of 1.5, n_r =7

for a beam with an aspect ratio of 2.5, n_r =11

for a beam with an aspect ratio of 3.5, n_r =16

r^2 = coefficient of determination or square of correlation coefficient

s = center-to-center spacing of transverse reinforcement, in.

v_e = calculated shear stress based on specified material properties, psi

for a D-type beam, $v_e = 2A_{vd}\, f_y \sin\alpha\, /(b_w\, h)$ [f_y in lb]

for a P-type beam, $v_e = (2M_{pr}/\ell_n)\, /(b_w\, d)$ [M_{pr} in in.-lb]

v_l = distance between the left corners of a station (A to D, as shown in Figure 156), in.

v_{max} = shear stress associated with V_{max}, psi

for a D-type beam, $v_{max} = V_{max}\, /(b_w\, h)$ [V_{max} in lb]

for a P-type beam, $v_{max} = V_{max}\, /(b_w\, d)$ [V_{max} in lb]

v_{nm} = shear stress associated with V_{nm}, psi

for a D-type beam, $v_{nm} = V_{nm}/(b_w\, h)$ [V_{nm} in lb]

for a P-type beam, $v_{nm} = V_{nm}/(b_w\, d)$ [V_{nm} in lb]

v_r = distance between the right corners of a station (B to C, as shown in Figure 156), in.

V = applied shear, kips

V_m = maximum shear during half loading cycle, kips

V_{max} = maximum applied shear, kips

V_{nm} = calculated shear strength based on measured material properties, kips

for a D-type beam, $V_{nm} = 2A_{vd}\, f_{ym} \sin\alpha$

for a P-type beam, $V_{nm} = 2M_{nm}/\ell_n$

W = amount of hysteretic energy dissipated per one half of a loading cycle, rad-kips

α = angle of inclination of diagonal reinforcement relative to beam longitudinal axis, degrees

γ = distortion due to shear (Figure 157), rad

γ_i = average distortion due to shear for Layer *i* (Figure 33), rad

$\gamma'_{i,j}$ = distortion due to shear for Layer *i* at station *j* (Figure 33), rad

δ_{bot} = displacement of the bottom block top surface, in.

δ_{top} = displacement of the top block bottom surface, in.

$\Delta_{sl,bot}$ = sliding at the bottom beam-block interface, in.

$\Delta_{sl,top}$ = sliding at the top beam-block interface, in.

Δx = the change in horizontal position of a marker from the initial position, in.

Δy = the change in vertical position of a marker from the initial position, in.

ΔA,ΔB,ΔC,ΔD = change in angle A, B, C, or D of a station (as shown in Figure 156) from the initial angle, rad

ε_{max} = maximum reinforcement strain, in./in.

ε_{sf} = fracture elongation of reinforcement, in./in.

ε_{su} = uniform elongation of reinforcement or strain corresponding to f_t, in./in.

θ = rotation due to flexure (Figure 157), rad

$\theta_{be,bot}$ = beam-end rotation at the bottom block, rad

$\theta_{be,top}$ = beam-end rotation at the top block, rad

θ_{bot} = rotation of the bottom block (in the loading plane), rad

θ_i = rotation due to flexural deformation for Layer *i*, rad

θ_{top} = rotation of the top block about the z axis(in the loading plane), rad

θ_y = rotation about the y axis, rad

θ_z = rotation about the z axis, rad

μ = mean of the multivariate linear regression

ρ = ratio of A_s to $b_w d$

ρ_t = ratio of area of distributed transverse reinforcement to gross concrete area perpendicular to that reinforcement

ψ = angular change due to core expansion (Figure 157), rad

APPENDIX B: SELECTED PHOTOS OF SPECIMENS DURING CONSTRUCTION

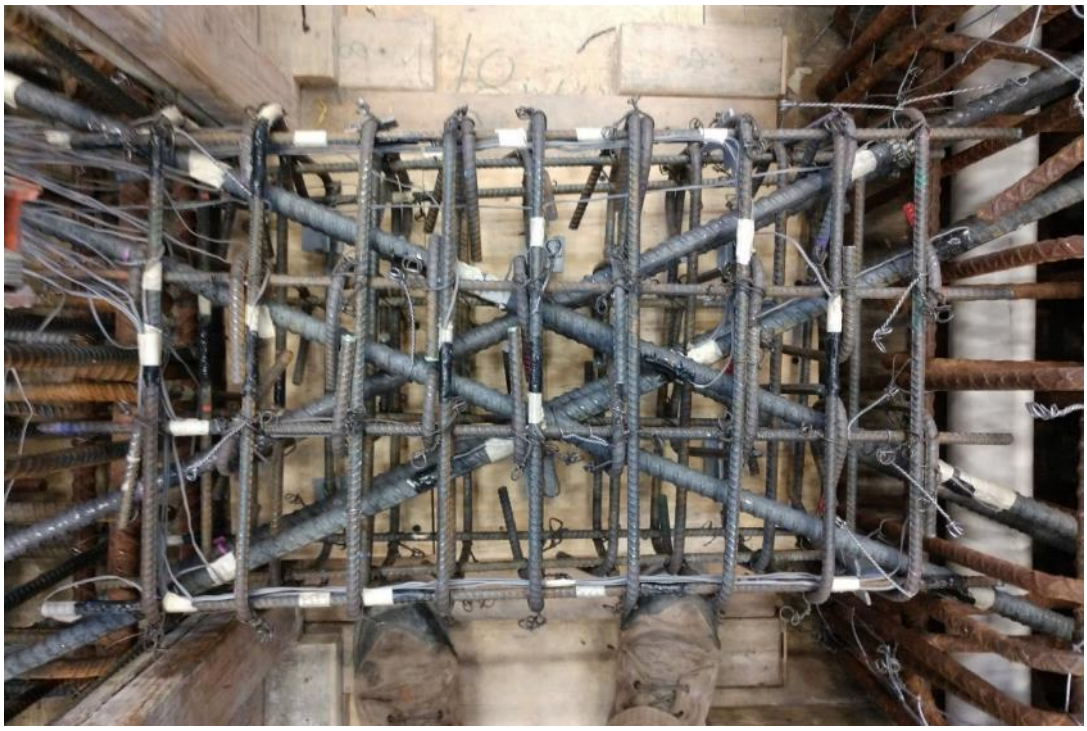

Figure B.1 – Coupling beam reinforcement, D120-1.5

Figure B.2 – Coupling beam reinforcement, D120-2.5

Figure B.3 – Coupling beam reinforcement, D120-3.5

Figure B.4 – Coupling beam reinforcement, P100-2.5

Figure B.5 – Base block reinforcement,
typical of beams with aspect ratios of 2.5 and 3.5

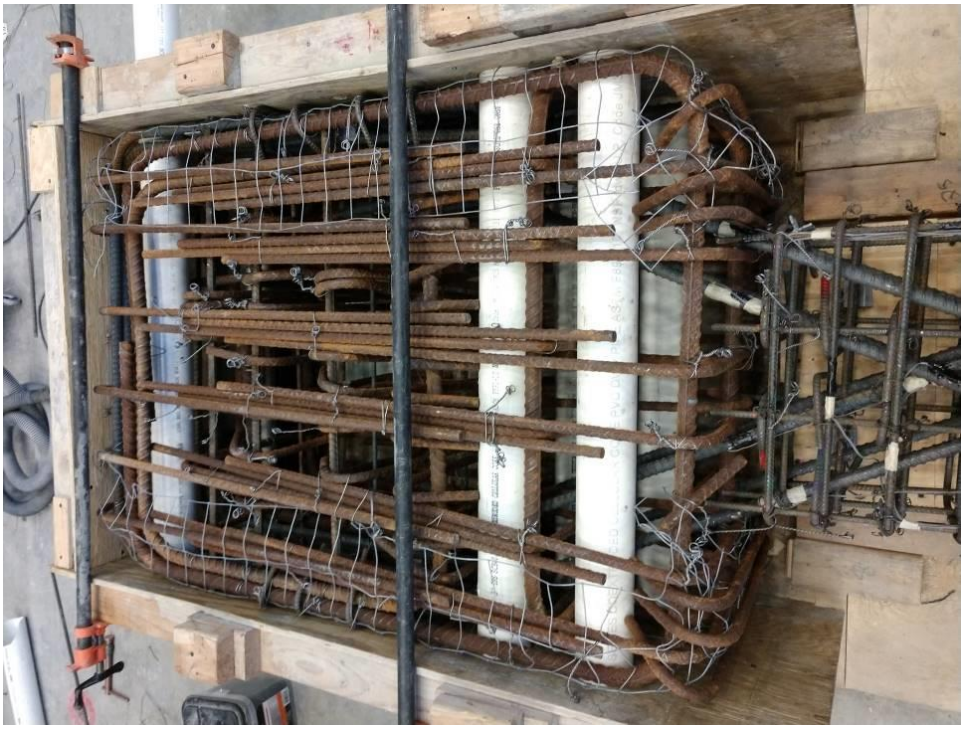

Figure B.6 –Top block reinforcement,
typical of beams with aspect ratios of 2.5 and 3.5

Figure B.7 – Specimens before casting, D80-1.5, D100-1.5, and D120-1.5 (from left to right)

Figure B.8 – Specimens after formwork removal, D100-3.5, D80-3.5, P100-2.5, P80-2.5, D100-2.5, and D80-2.5 (from left to right)

APPENDIX C: SELECTED PHOTOS OF SPECIMENS DURING TESTING

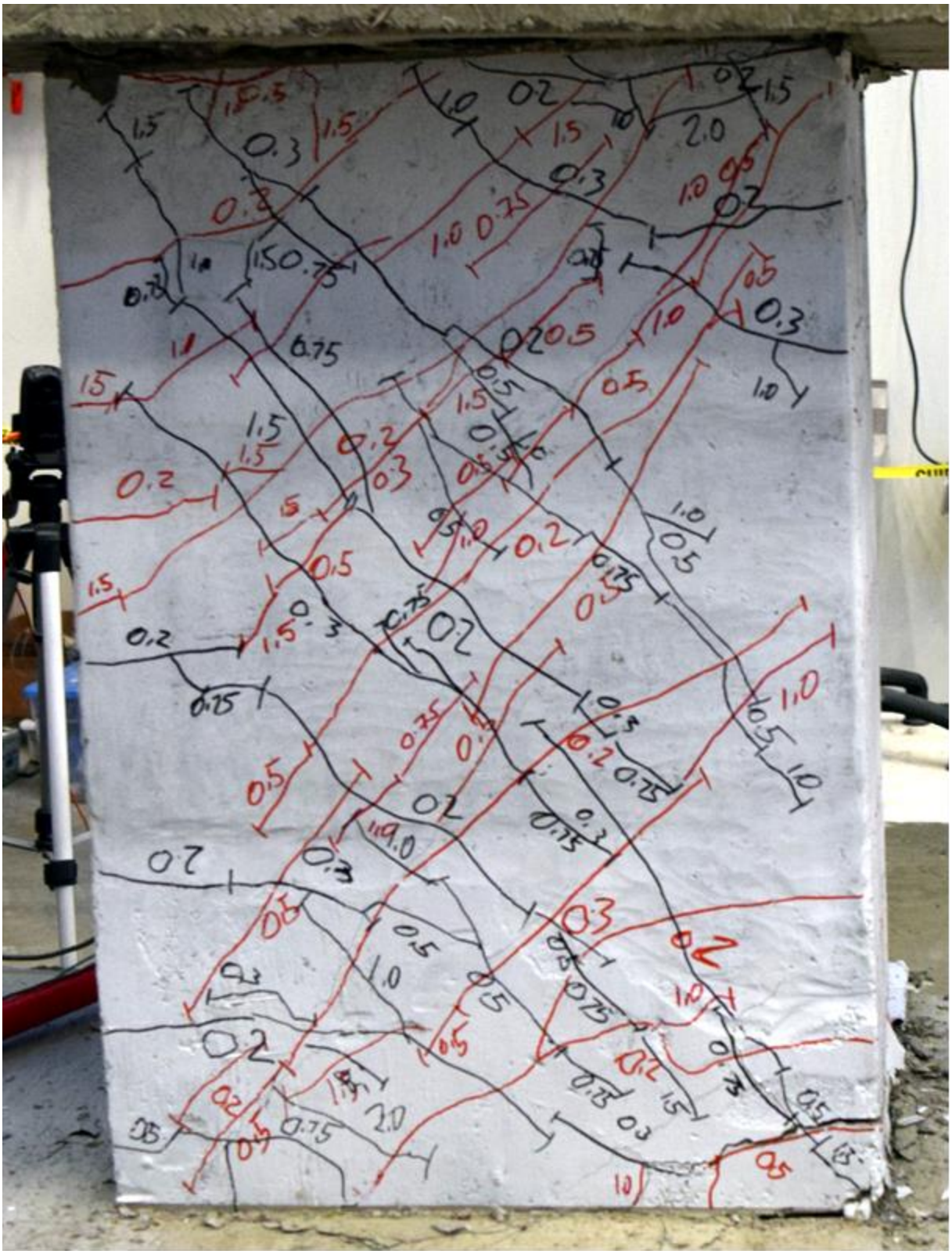

Figure C.1 – D80-1.5 during
second cycle to 2% chord rotation

Figure C.2 – D80-1.5 during
second cycle to 6% chord rotation

Figure C.3 – D80-1.5 at
+2% chord rotation, second cycle

Figure C.4 – D80-1.5 at
-2% chord rotation, second cycle

Figure C.5 – D80-1.5 at
+4% chord rotation, second cycle

Figure C.6 – D80-1.5 at
-4% chord rotation, second cycle

Figure C.7 – D80-1.5 at
+6% chord rotation, second cycle

Figure C.8 – D80-1.5 at
-6% chord rotation, second cycle

Figure C.9 – D80-1.5 at
+8% chord rotation, first cycle

Figure C.10 – D80-1.5 at
-8% chord rotation, first cycle

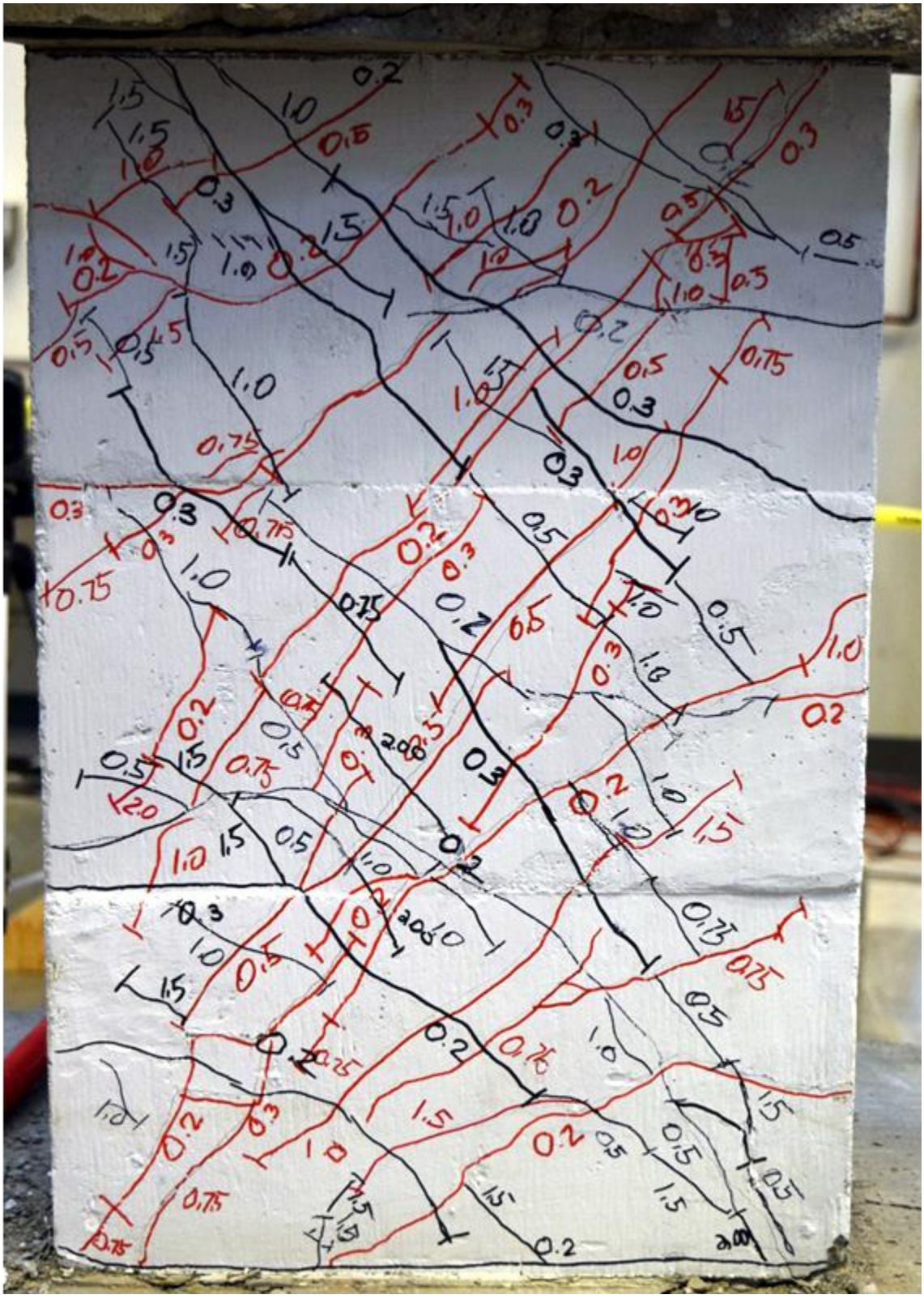

Figure C.11 – D100-1.5 during
second cycle to 2% chord rotation

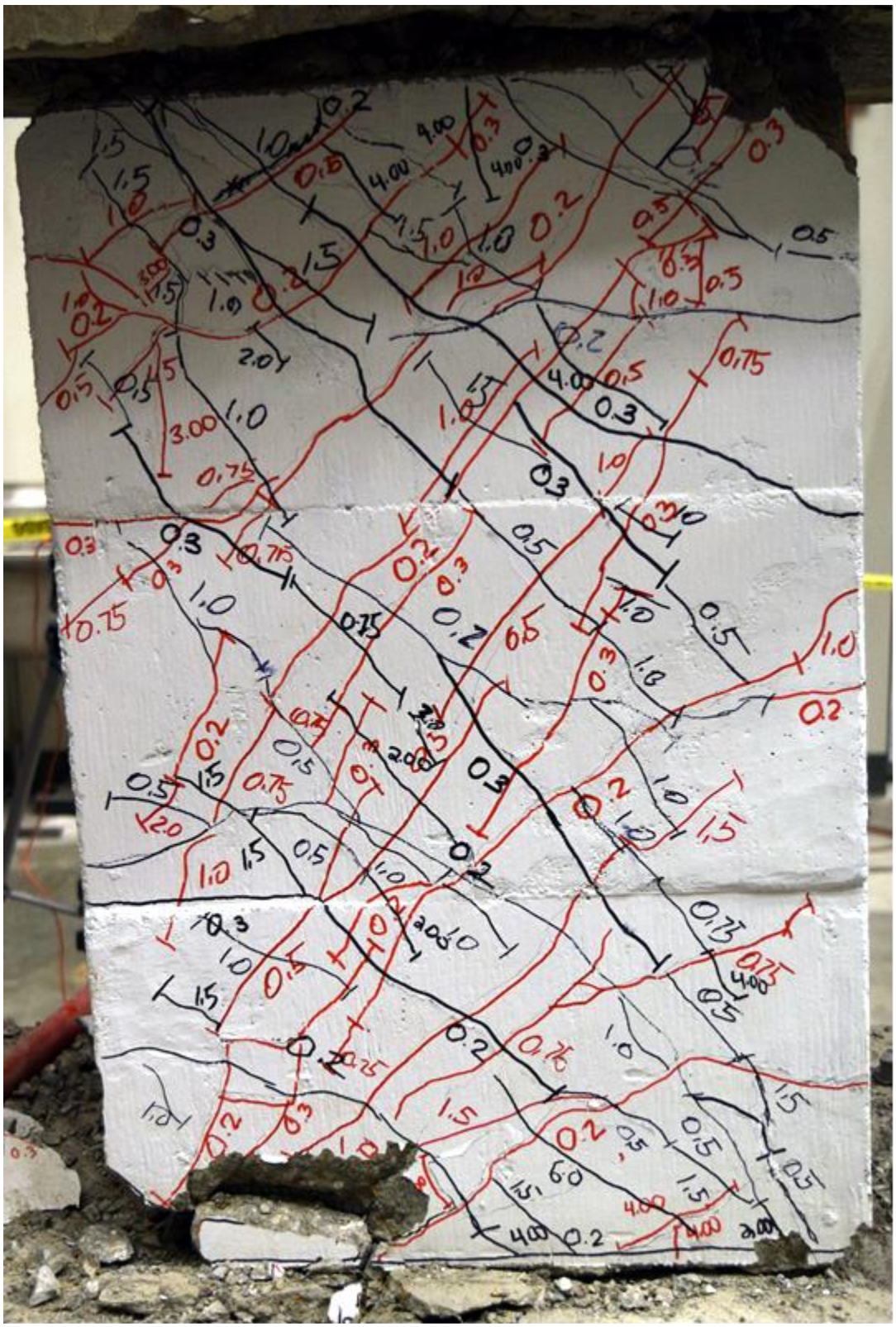

Figure C.12 – D100-1.5 during
second cycle to 6% chord rotation

Figure C.13 – D100-1.5 at
+2% chord rotation, second cycle

Figure C.14 – D100-1.5 at
-2% chord rotation, second cycle

Figure C.15 – D100-1.5 at
+4% chord rotation, second cycle

Figure C.16 – D100-1.5 at
-4% chord rotation, second cycle

Figure C.17 – D100-1.5 at
+6% chord rotation, second cycle

Figure C.18 – D100-1.5 at
-6% chord rotation, second cycle

Figure C.19 – D100-1.5 at
+8% chord rotation, first cycle

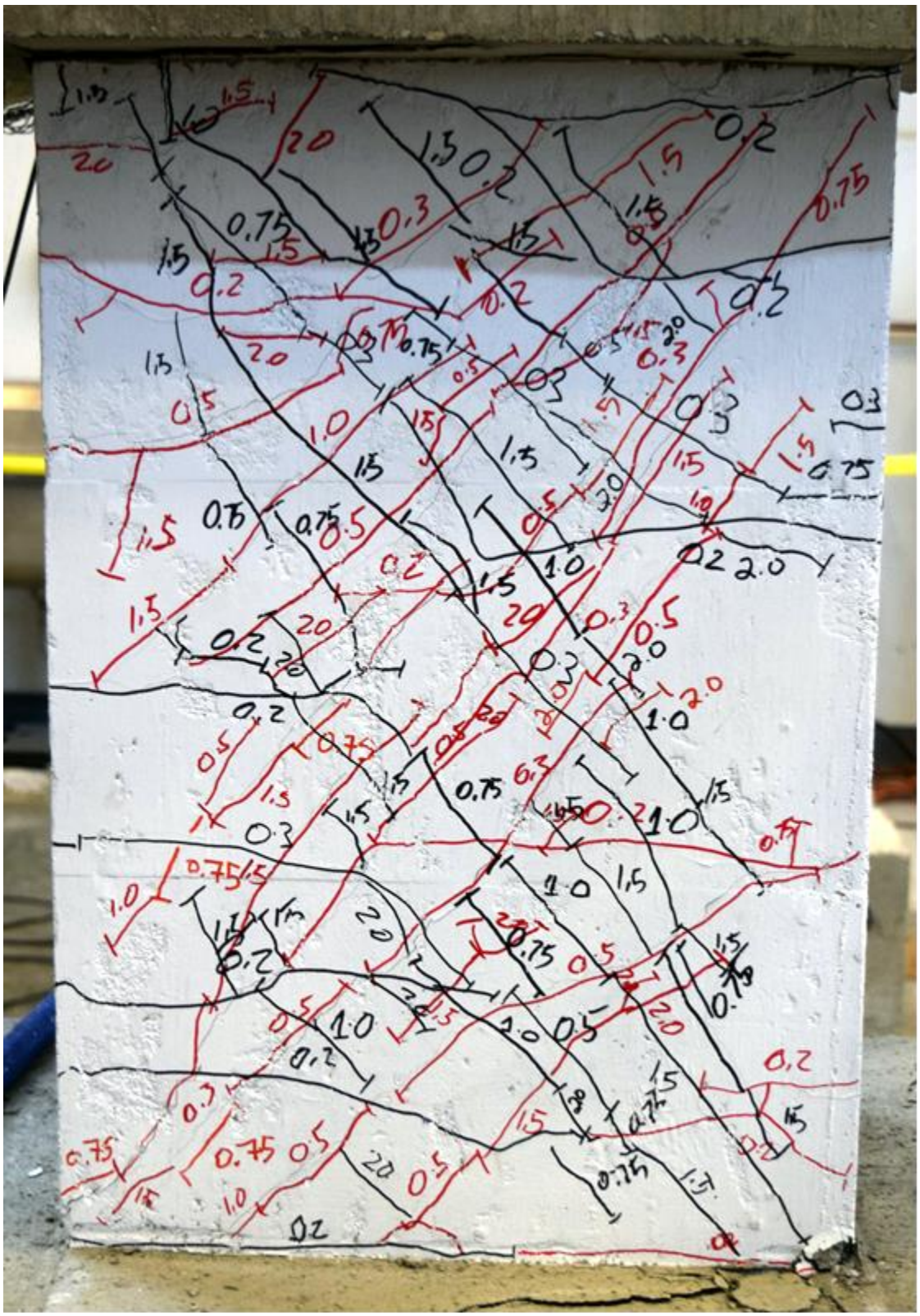

Figure C.20 – D120-1.5 during
second cycle to 2% chord rotation

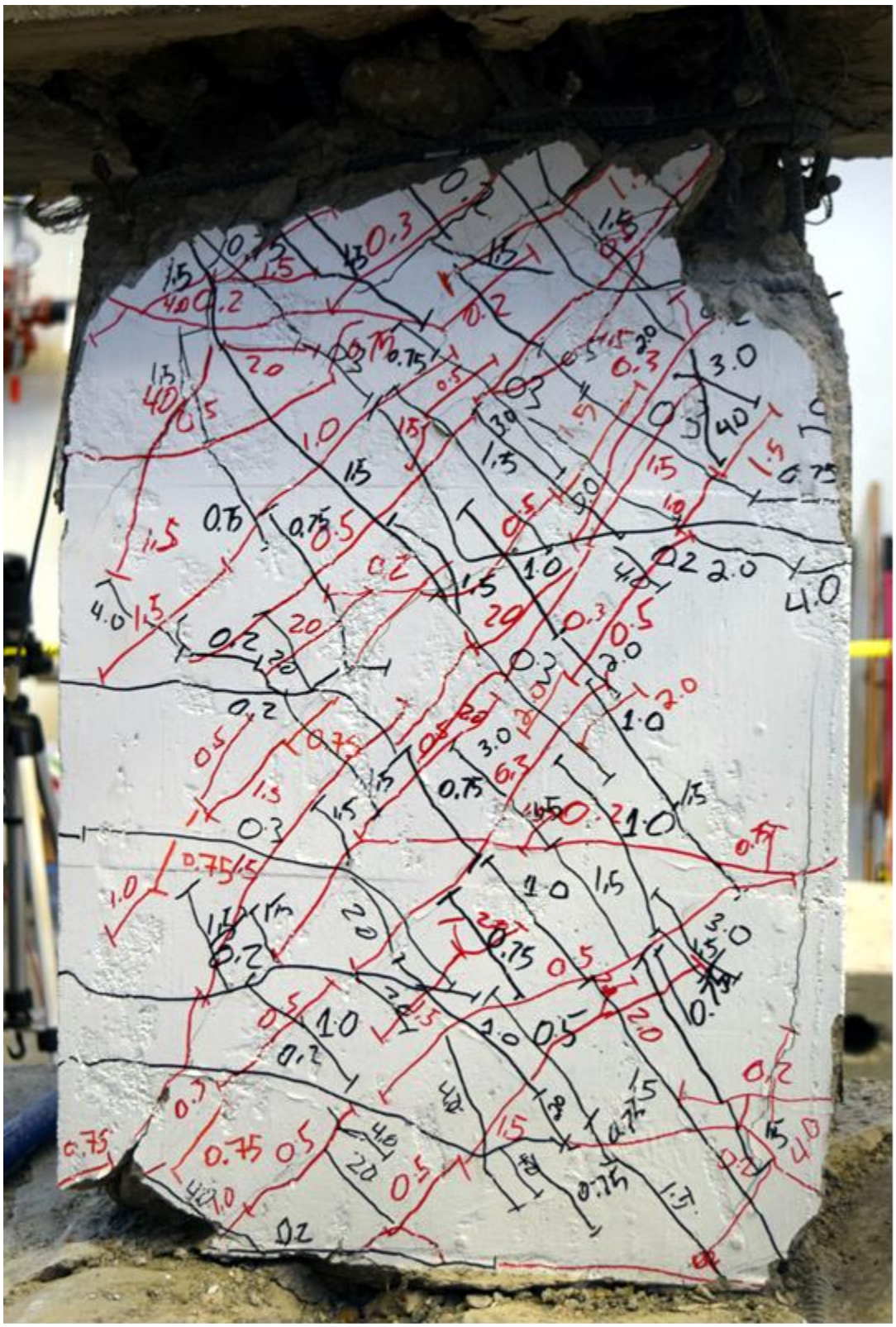

Figure C.21 – D120-1.5 during
first cycle to 6% chord rotation

Figure C.22 – D120-1.5 at
+2% chord rotation, second cycle

Figure C.23 – D120-1.5 at
-2% chord rotation, second cycle

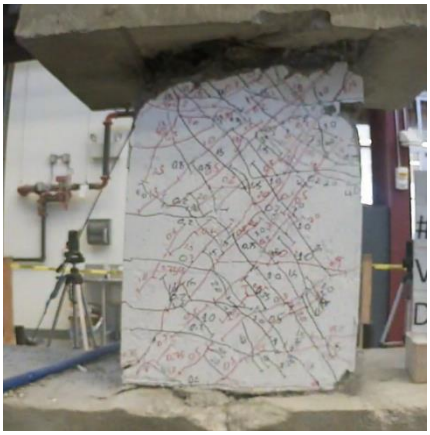

Figure C.24 – D120-1.5 at
+4% chord rotation, second cycle

Figure C.25 – D120-1.5 at
-4% chord rotation, second cycle

Figure C.26 – D120-1.5 at
+6% chord rotation, first cycle

Figure C.27 – D120-1.5 at
-6% chord rotation, first cycle

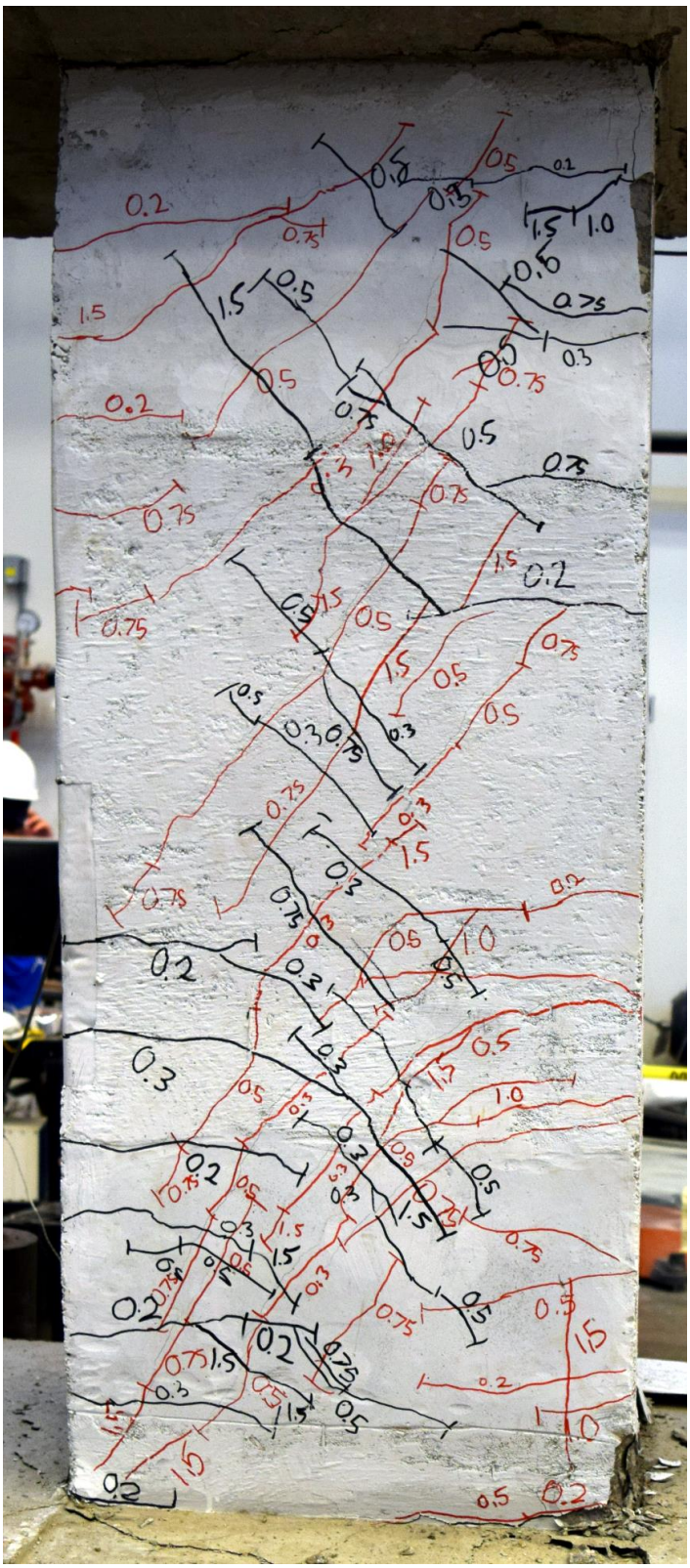

Figure C.28 – D80-2.5 during
second cycle to 2% chord rotation

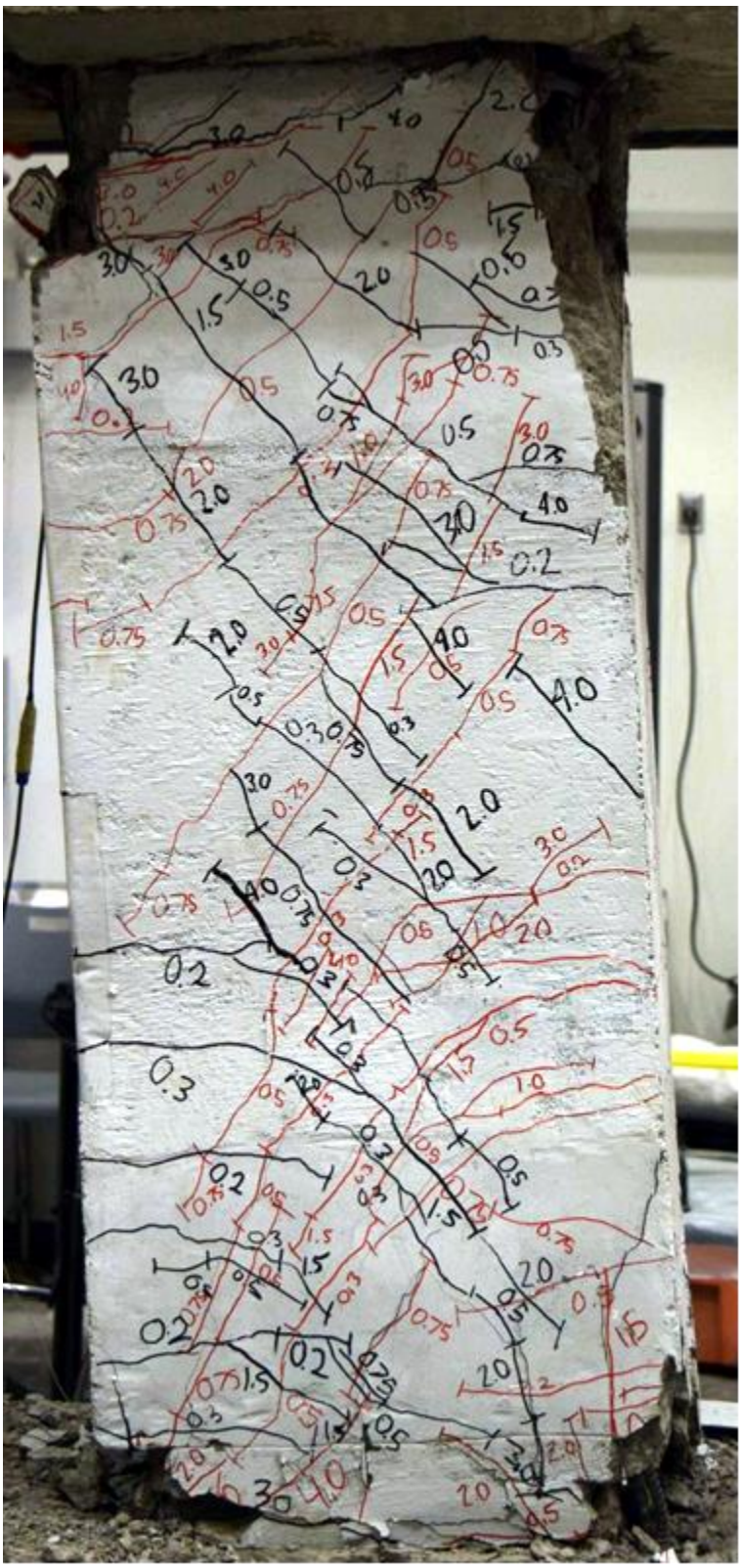

Figure C.29 – D80-2.5 during
second cycle to 6% chord rotation

Figure C.30 – D80-2.5 at
+2% chord rotation, second cycle

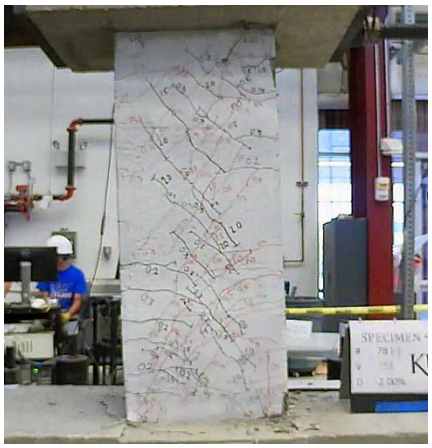

Figure C.31 – D80-2.5 at
-2% chord rotation, second cycle

Figure C.32 – D80-2.5 at
+4% chord rotation, second cycle

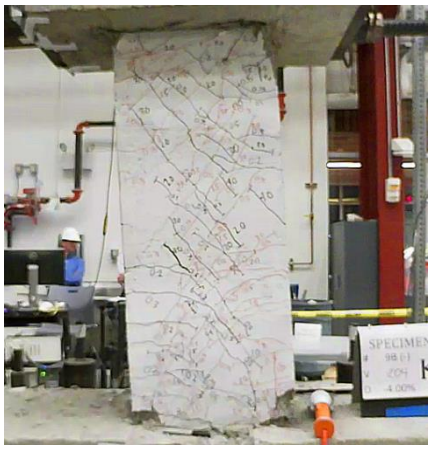

Figure C.33 – D80-2.5 at
-4% chord rotation, second cycle

Figure C.34 – D80-2.5 at
+6% chord rotation, second cycle

Figure C.35 – D80-2.5 at
-6% chord rotation, second cycle

Figure C.36 – D80-2.5 at
+8% chord rotation, second cycle

Figure C.37 – D80-2.5 at
-8% chord rotation, second cycle

Figure C.38 – D80-2.5 at
+10% chord rotation, first cycle

Figure C.39 – D80-2.5 at
-10% chord rotation, first cycle

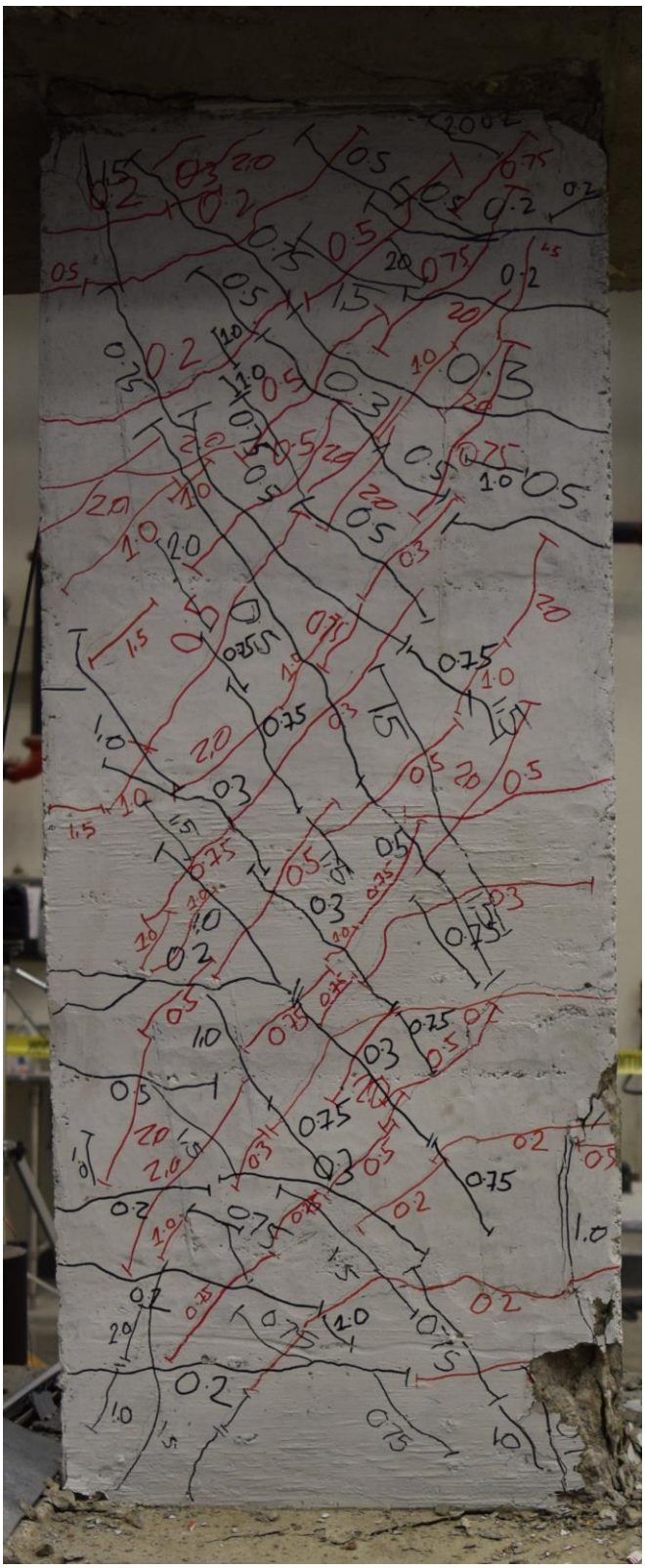

Figure C.40 – D100-2.5 during
second cycle to 2% chord rotation

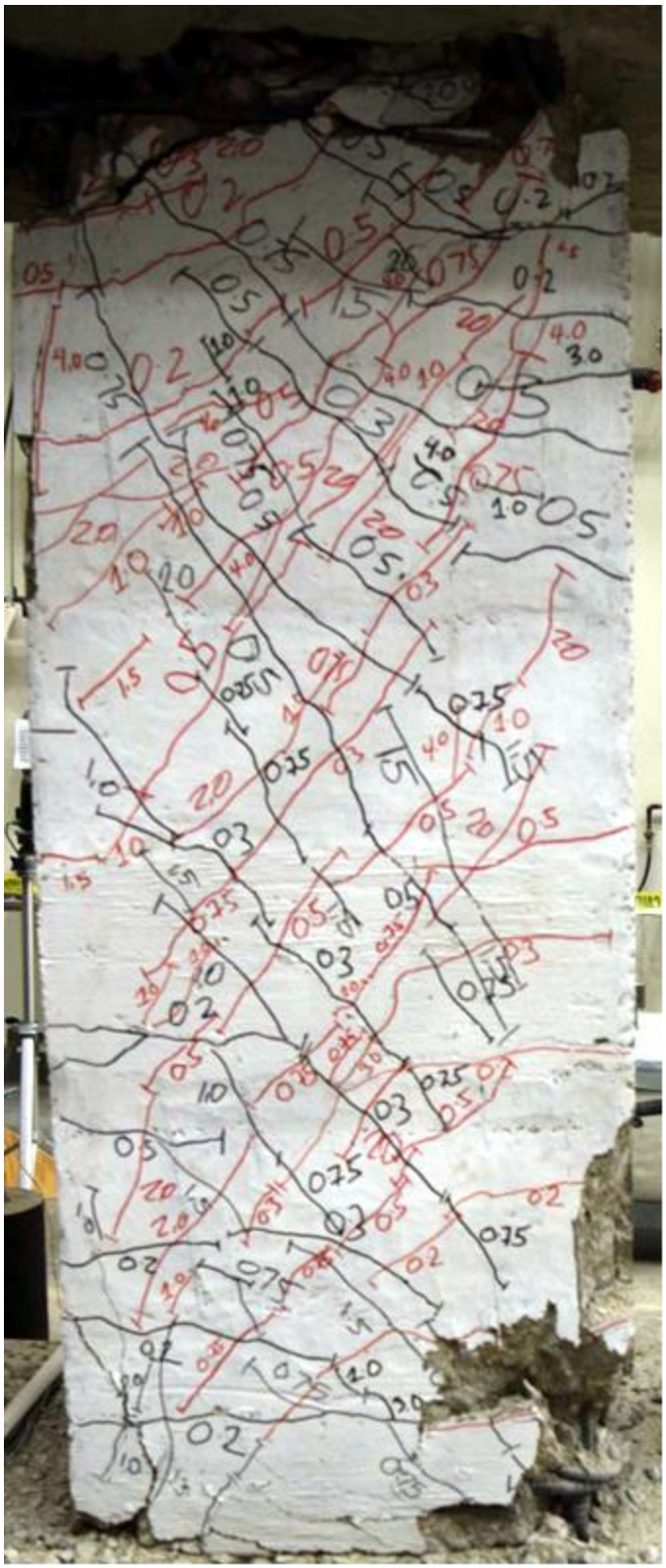

Figure C.41 – D100-2.5 during
second cycle to 6% chord rotation

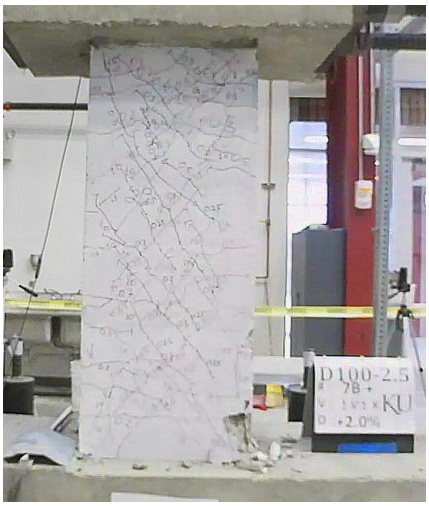

Figure C.42 – D100-2.5
at +2% chord rotation, second cycle

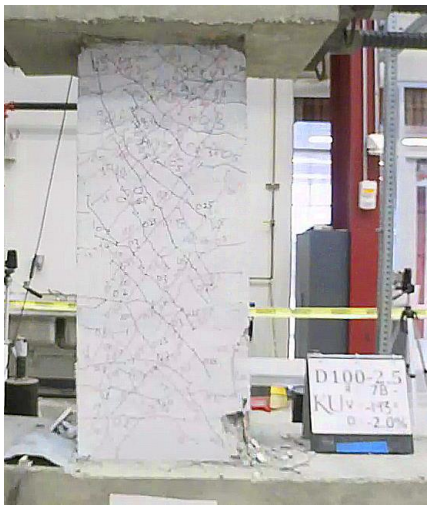

Figure C.43 – D100-2.5 at
-2% chord rotation, second cycle

Figure C.44 – D100-2.5 at
+4% chord rotation, second cycle

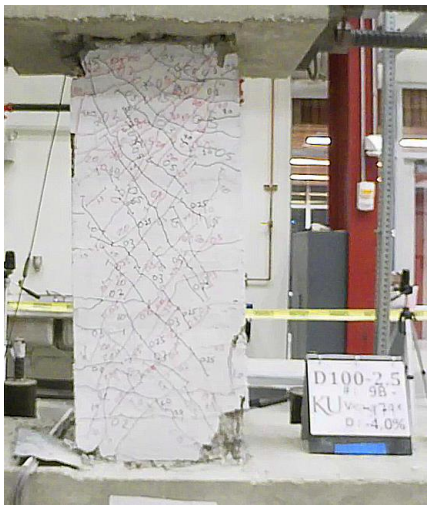

Figure C.45 – D100-2.5 at
-4% chord rotation, second cycle

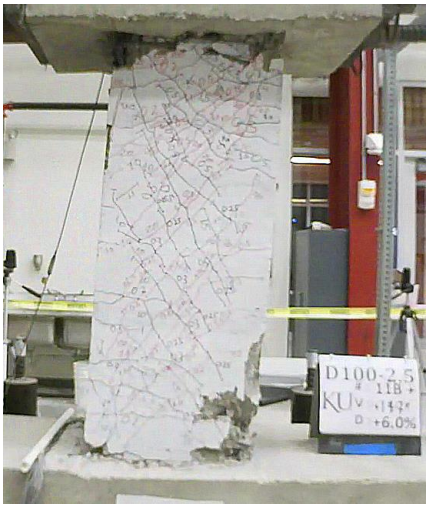

Figure C.46 – D100-2.5 at
+6% chord rotation, second cycle

Figure C.47 – D100-2.5 at
-6% chord rotation, second cycle

Figure C.48 – D100-2.5 at
+8% chord rotation, first cycle

Figure C.49 – D100-2.5 at
-8% chord rotation, first cycle

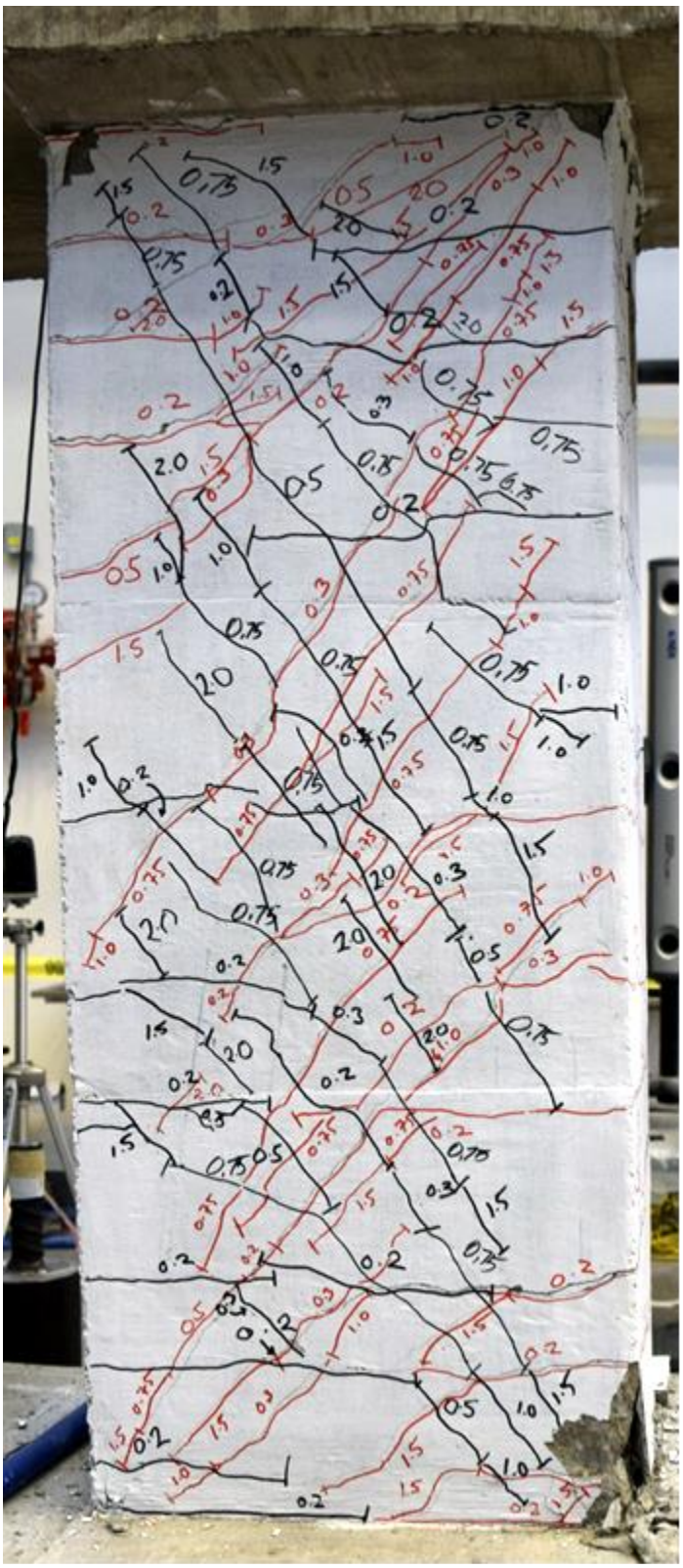

Figure C.50 – D120-2.5 during
second cycle to 2% chord rotation

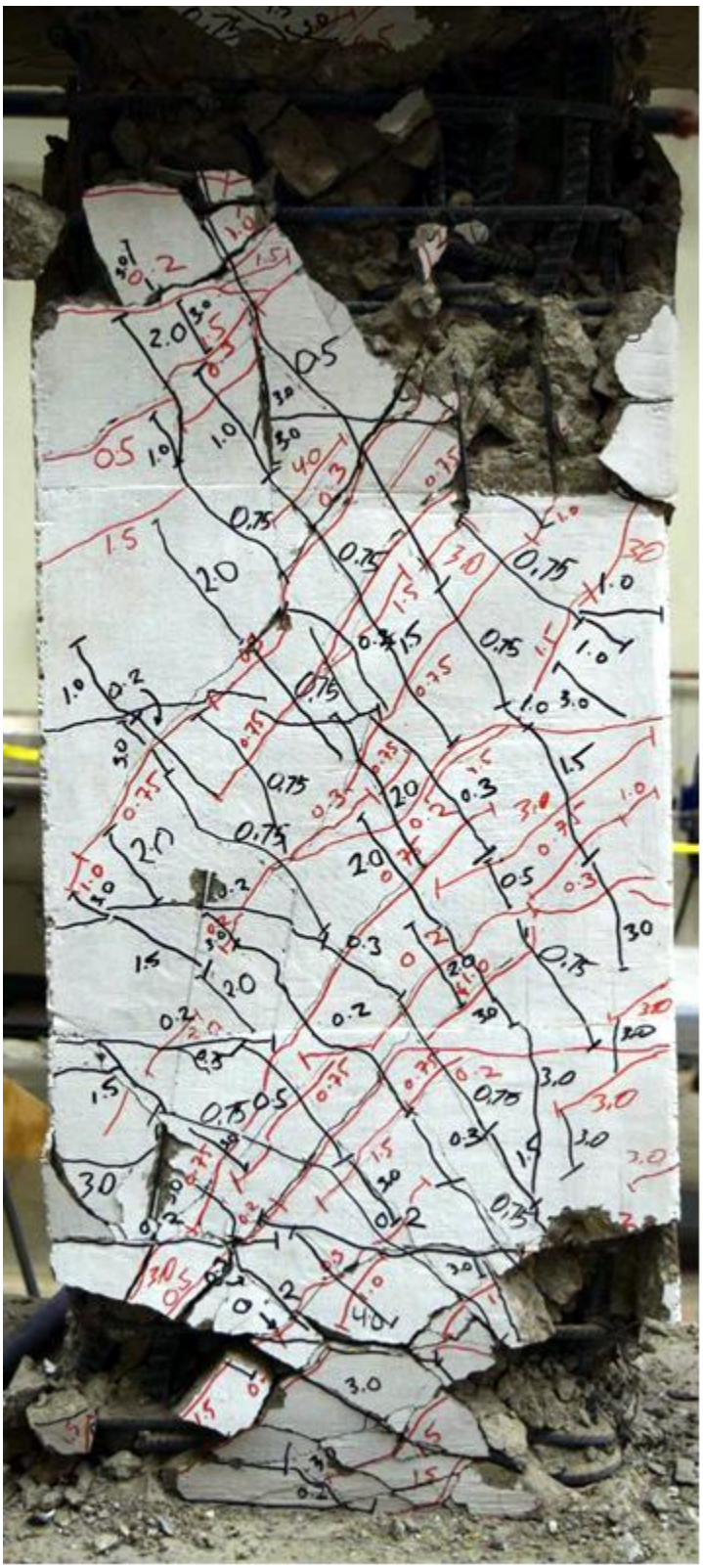

Figure C.51 – D120-2.5 during
second cycle to 6% chord rotation

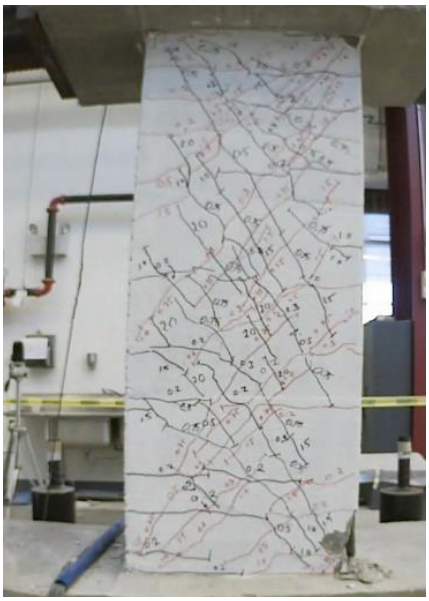

Figure C.52 – D120-2.5 at
+2% chord rotation, second cycle

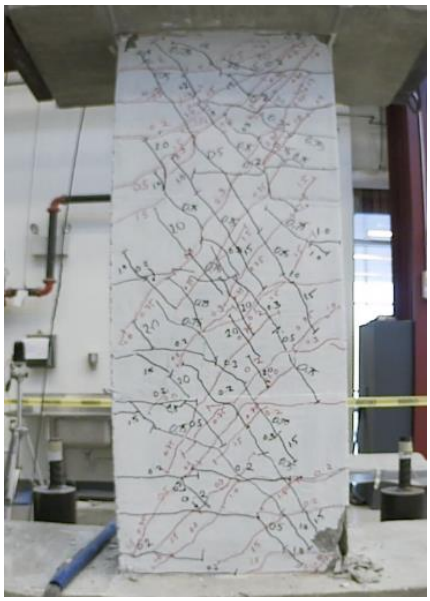

Figure C.53 – D120-2.5 at
-2% chord rotation, second cycle

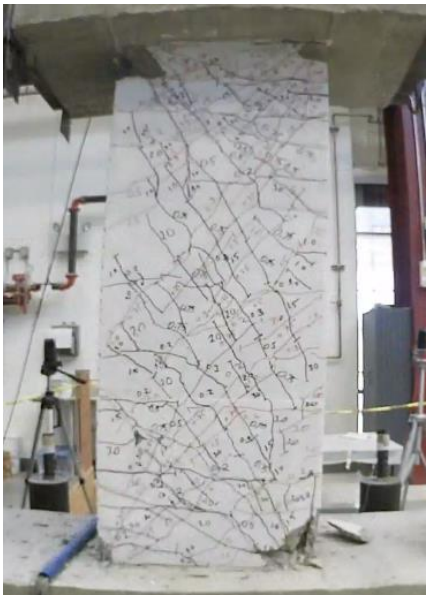

Figure C.54 – D120-2.5 at
+4% chord rotation, second cycle

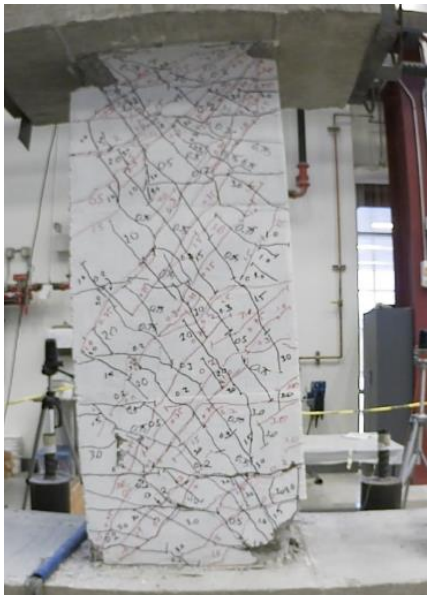

Figure C.55 – D120-2.5 at
-4% chord rotation, second cycle

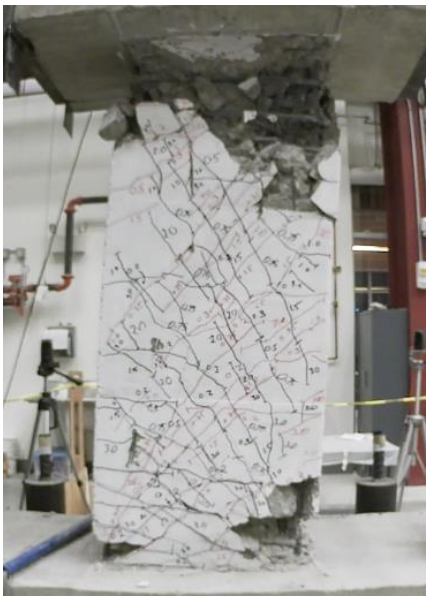

Figure C.56 – D120-2.5 at
+6% chord rotation, second cycle

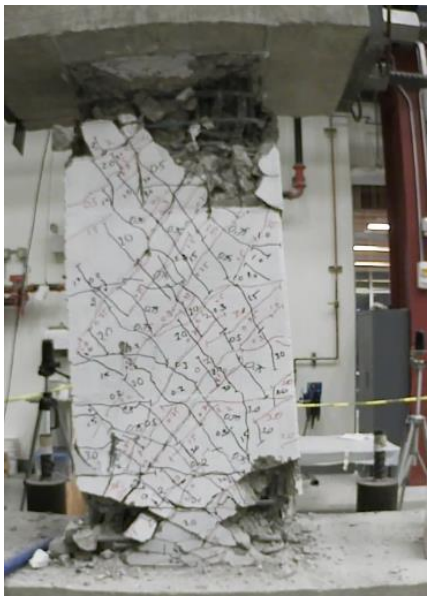

Figure C.57 – D120-2.5 at
-6% chord rotation, second cycle

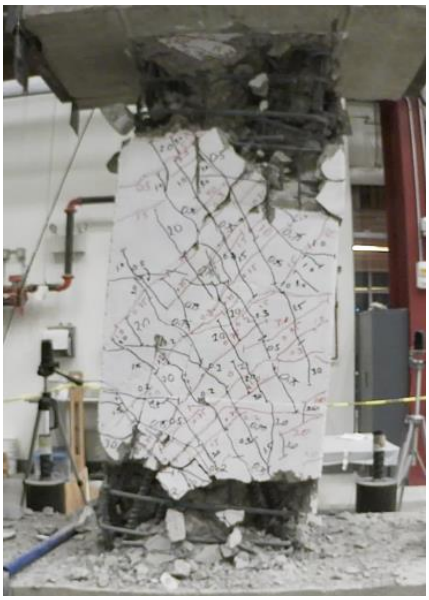

Figure C.58 – D120-2.5 at
+8% chord rotation, second cycle

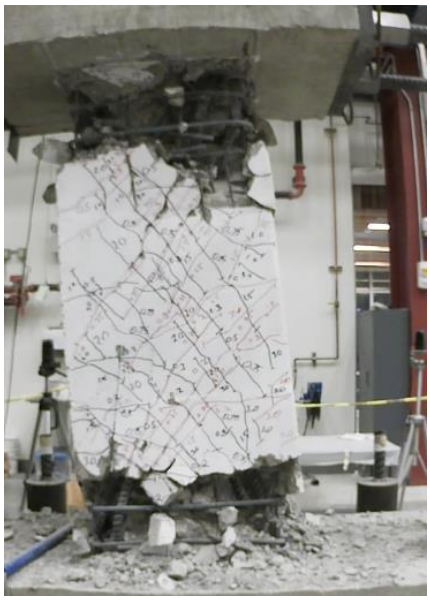

Figure C.59 – D120-2.5 at
-8% chord rotation, second cycle

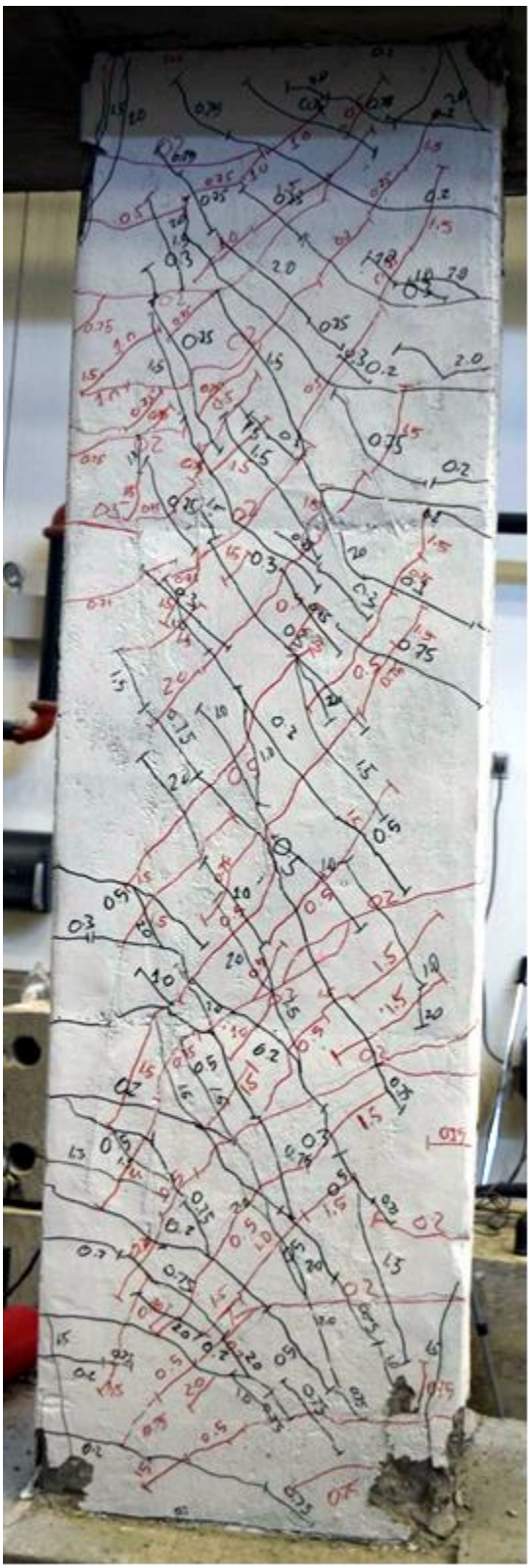

Figure C.60 – D80-3.5 during
second cycle to 2% chord rotation

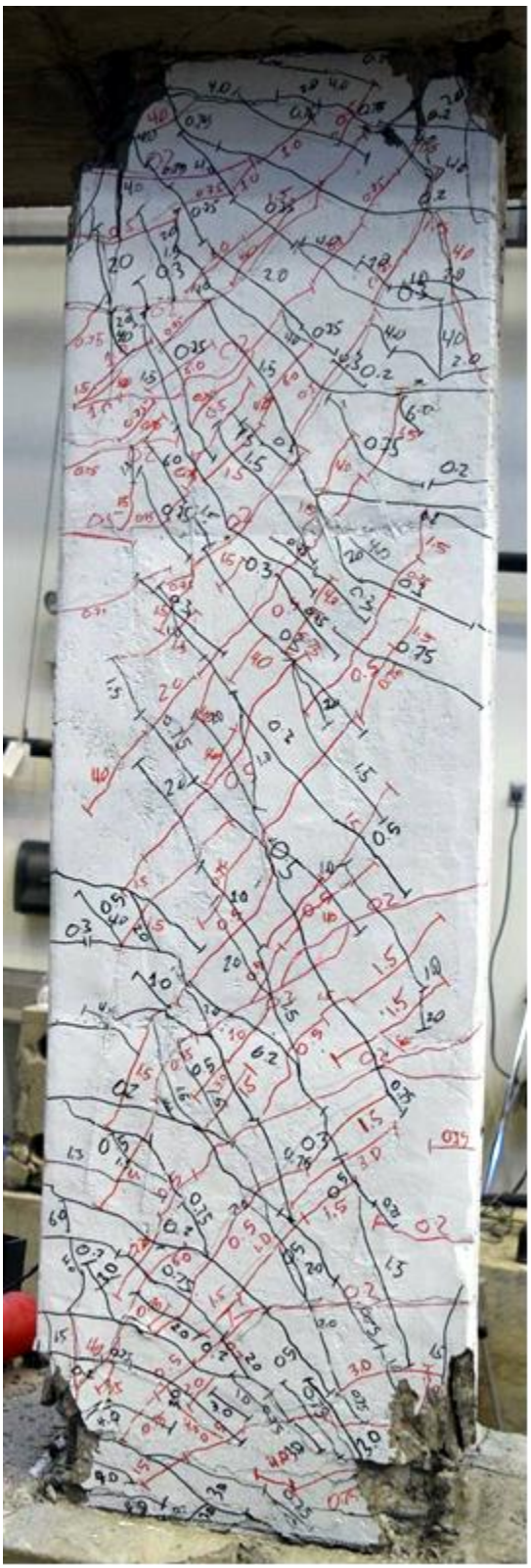

Figure C.61 – D80-3.5 during
second cycle to 6% chord rotation

Figure C.62 – D80-3.5 at
+2% chord rotation, second cycle

Figure C.63 – D80-3.5 at
-2% chord rotation, second cycle

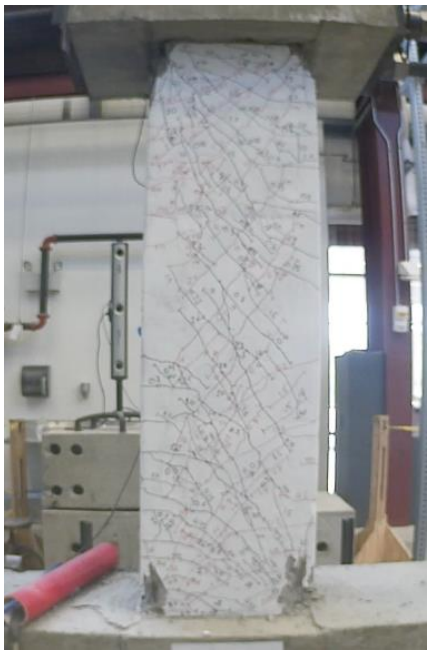

Figure C.64 – D80-3.5 at
+4% chord rotation, second cycle

Figure C.65 – D80-3.5 at
-4% chord rotation, second cycle

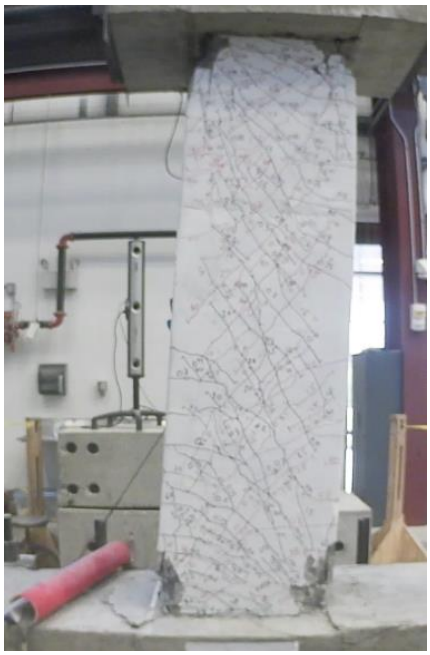

Figure C.66 – D80-3.5 at
+6% chord rotation, second cycle

Figure C.67 – D80-3.5 at
-6% chord rotation, second cycle

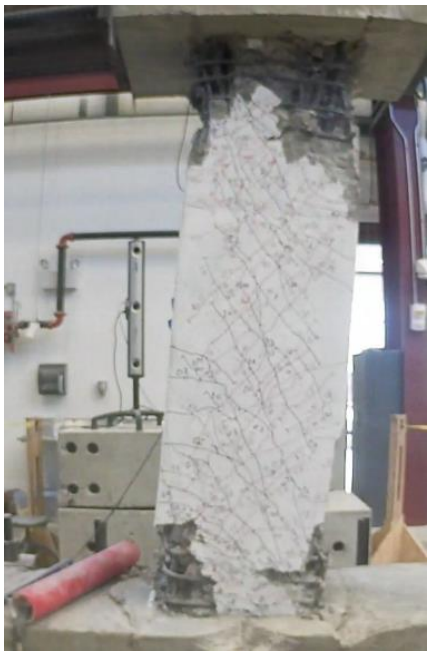

Figure C.68 – D80-3.5 at
+8% chord rotation, second cycle

Figure C.69 – D80-3.5 at
-8% chord rotation, second cycle

Figure C.70 – D80-3.5 at
+10% chord rotation, first cycle

Figure C.71 – D80-3.5 at
-10% chord rotation, first cycle

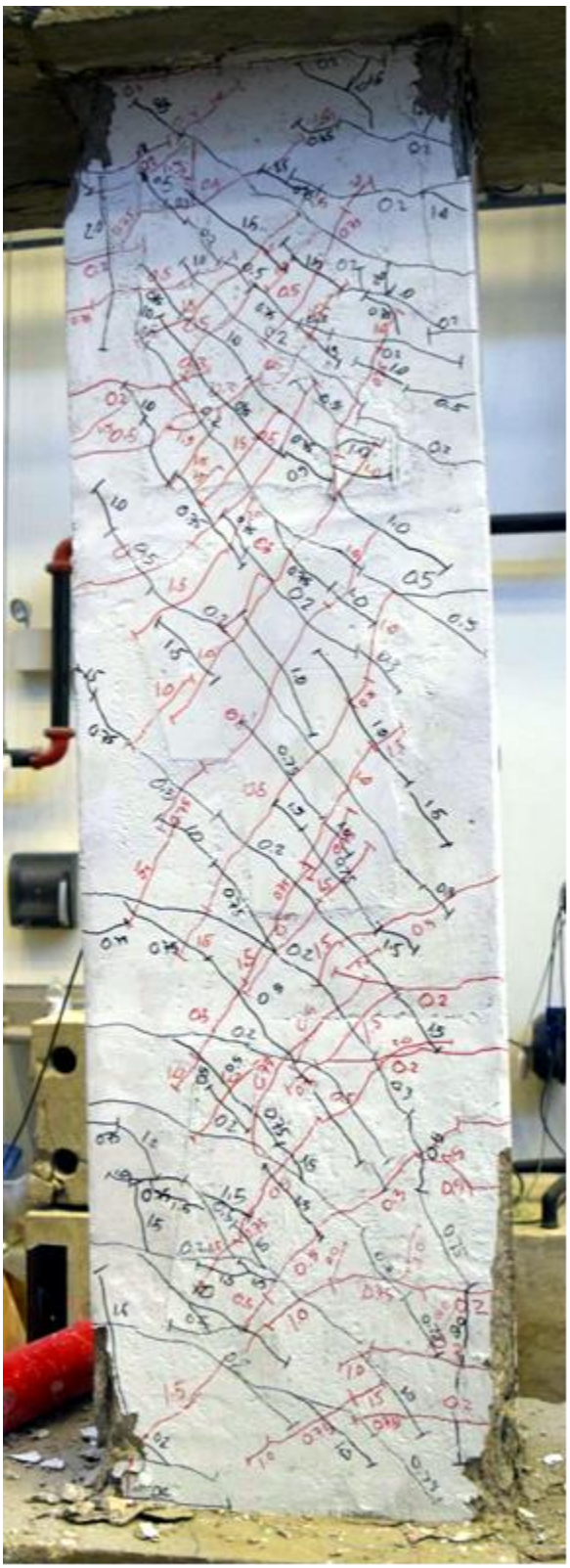

Figure C.72 – D100-3.5 during
second cycle to 2% chord rotation

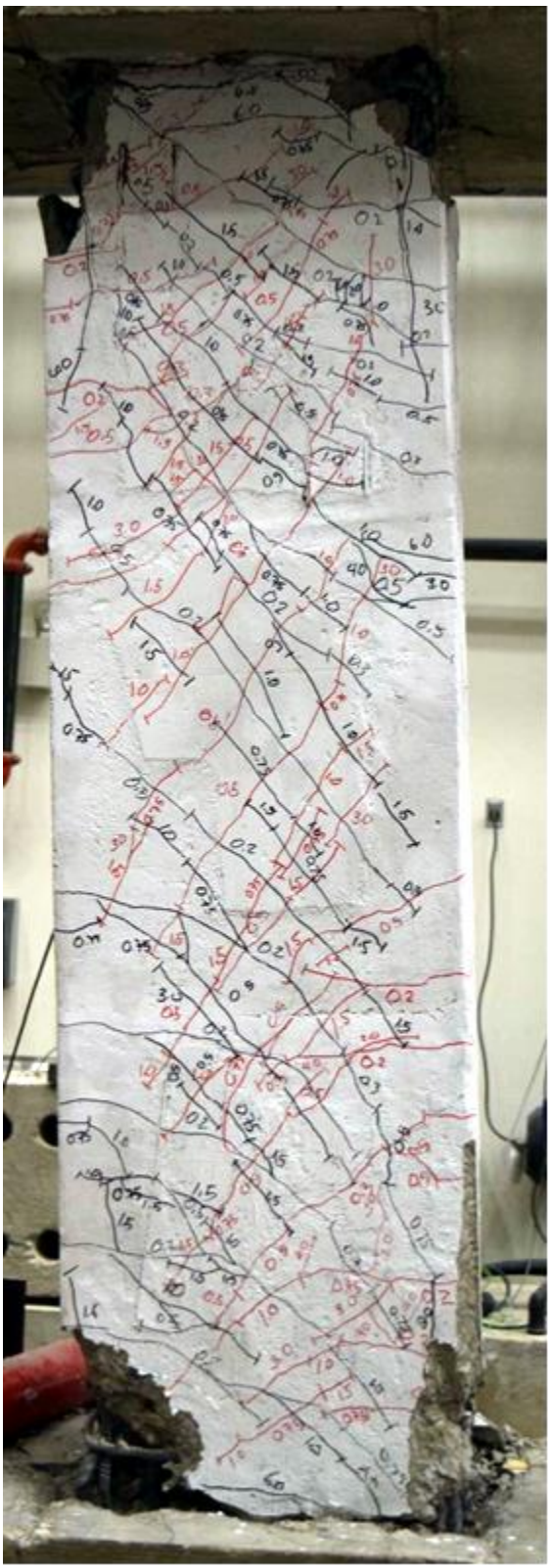

Figure C.73 – D100-3.5 during
second cycle to 6% chord rotation

Figure C.74 – D100-3.5 at
+2% chord rotation, second cycle

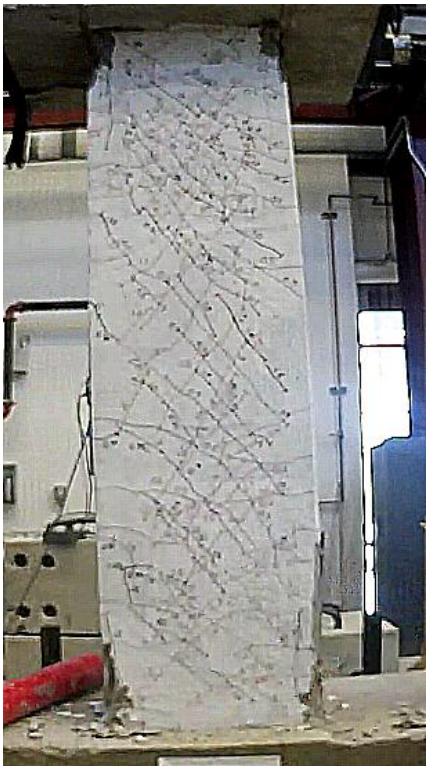

Figure C.75 – D100-3.5 at
-2% chord rotation, second cycle

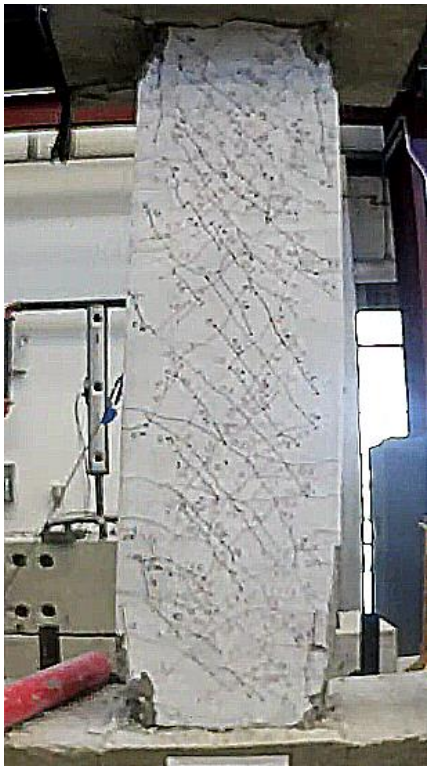

Figure C.76 – D100-3.5 at
+4% chord rotation, second cycle

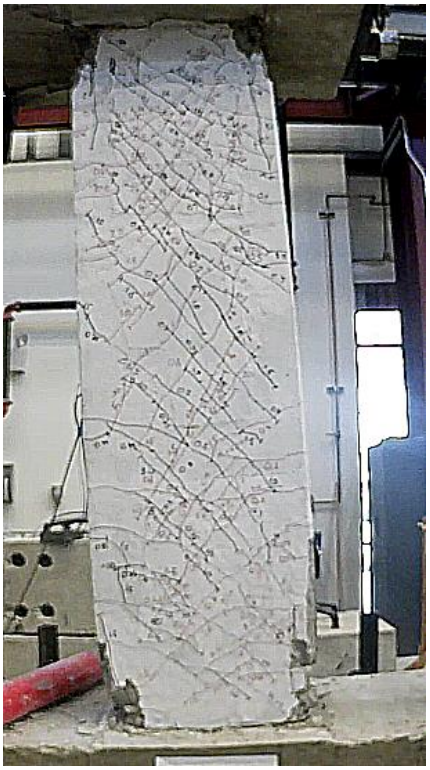

Figure C.77 – D100-3.5 at
-4% chord rotation, second cycle

Figure C.78 – D100-3.5 at
+6% chord rotation, second cycle

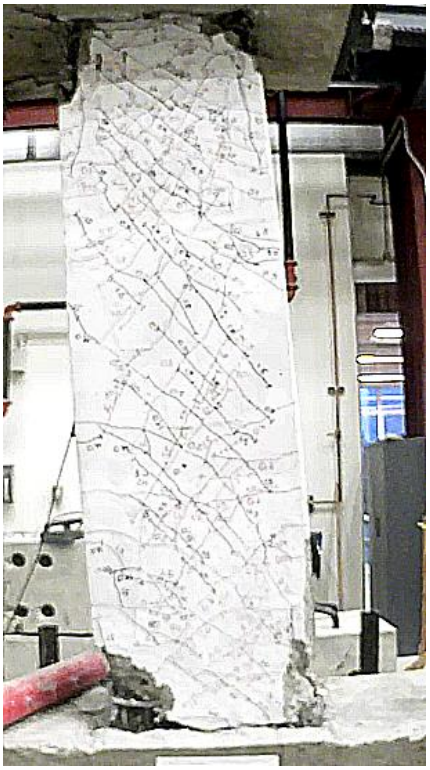

Figure C.79 – D100-3.5 at
-6% chord rotation, second cycle

Figure C.80 – D100-3.5 at
+8% chord rotation, second cycle

Figure C.81 – D100-3.5 at
-8% chord rotation, second cycle

Figure C.82 – D100-3.5 at
+10% chord rotation, first cycle

Figure C.83 – D100-3.5 at
-10% chord rotation, first cycle

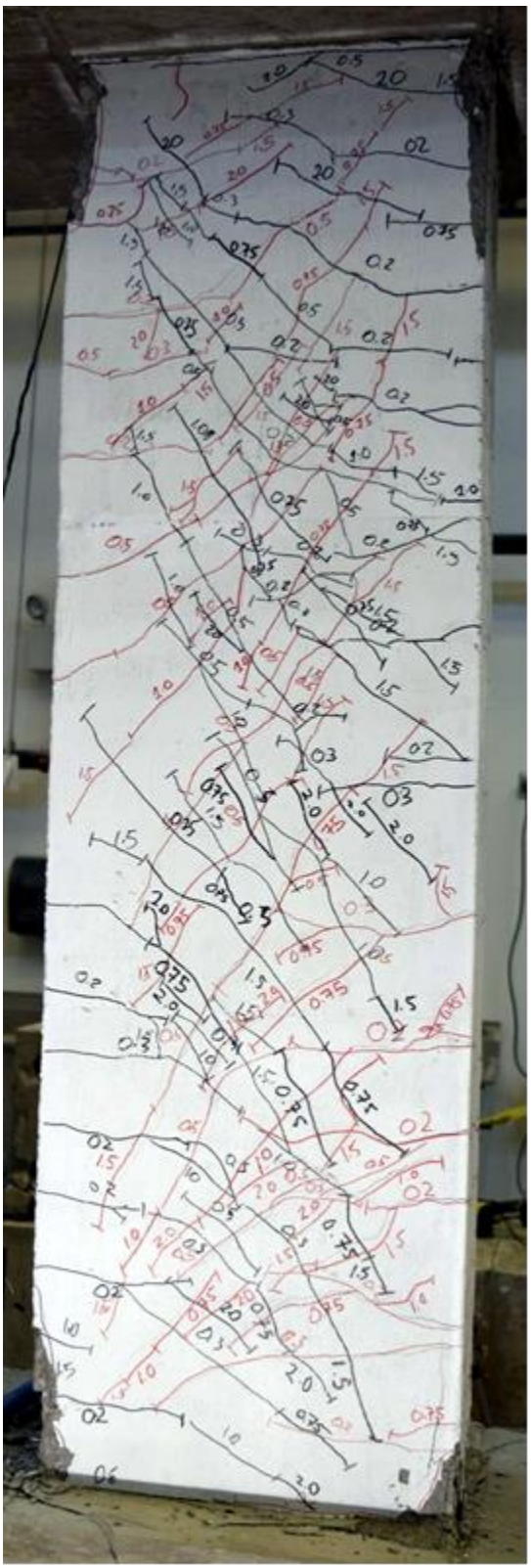

Figure C.84 – D120-3.5 during
second cycle to 2% chord rotation

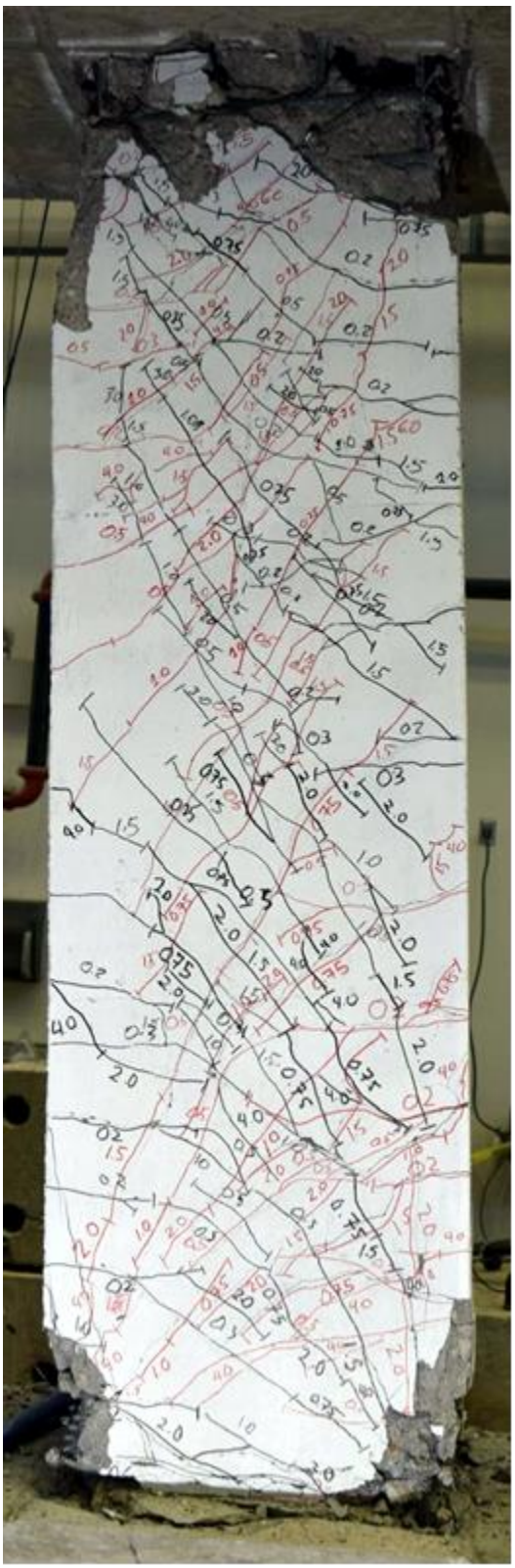

Figure C.85 – D120-3.5 during
second cycle to 6% chord rotation

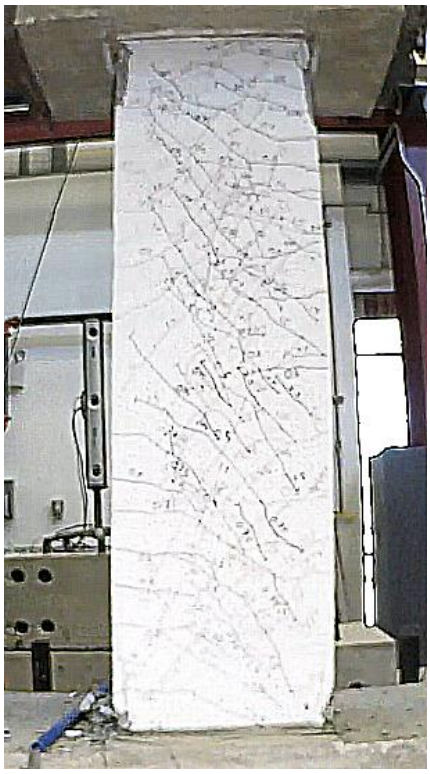

Figure C.86 – D120-3.5 at
+2% chord rotation, second cycle

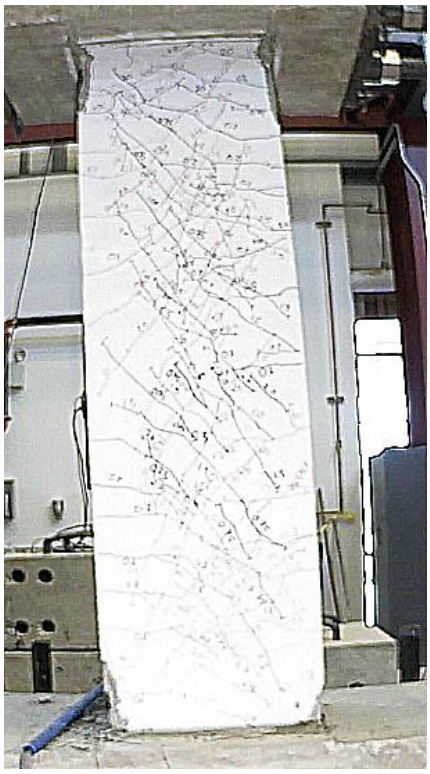

Figure C.87 – D120-3.5 at
-2% chord rotation, second cycle

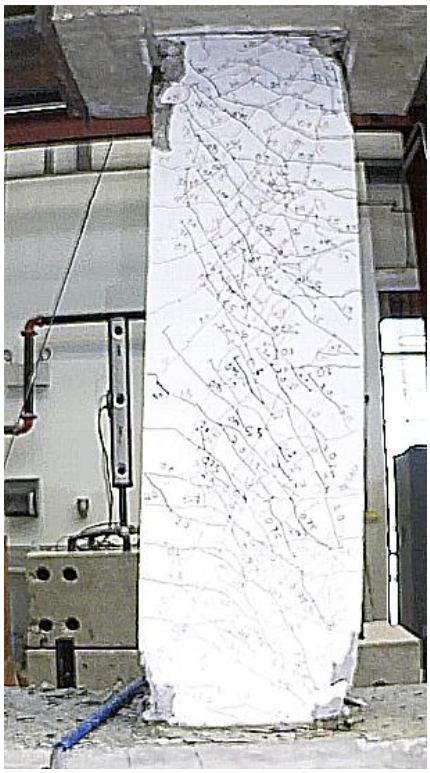

Figure C.88 – D120-3.5 at
+4% chord rotation, second cycle

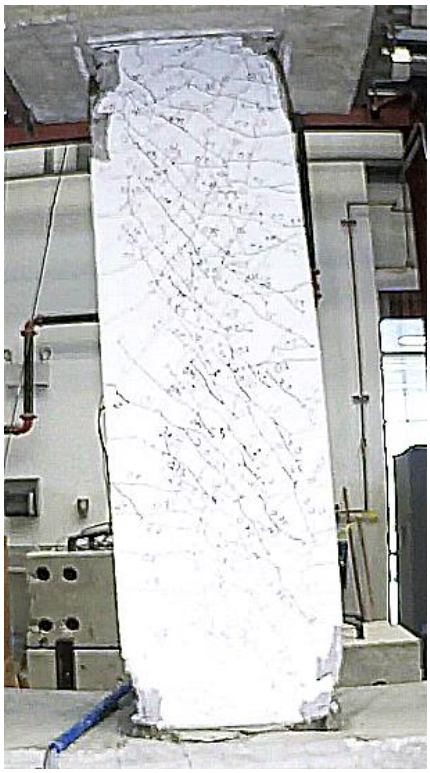

Figure C.89 – D120-3.5 at
-4% chord rotation, second cycle

Figure C.90 – D120-3.5 at
+6% chord rotation, second cycle

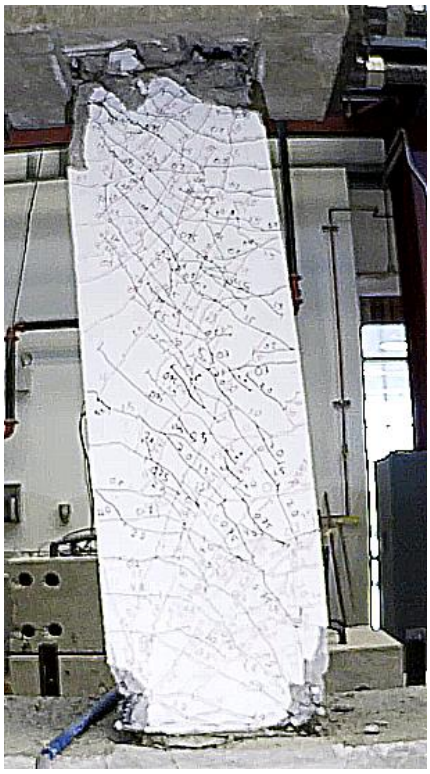

Figure C.91 – D120-3.5 at
-6% chord rotation, second cycle

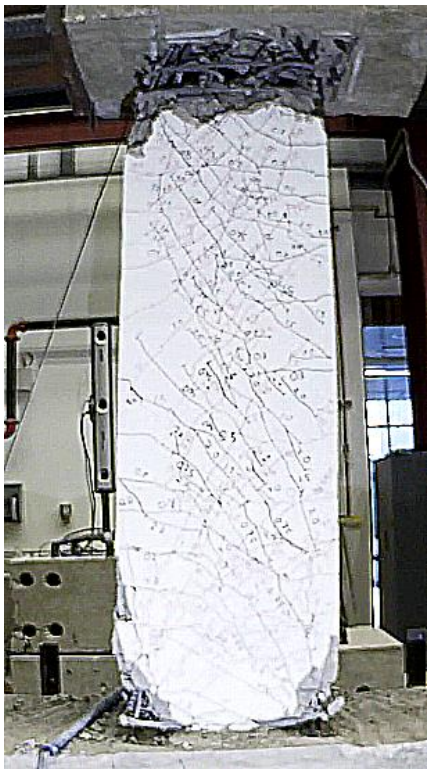

Figure C.92 – D120-3.5 at
+8% chord rotation, second cycle

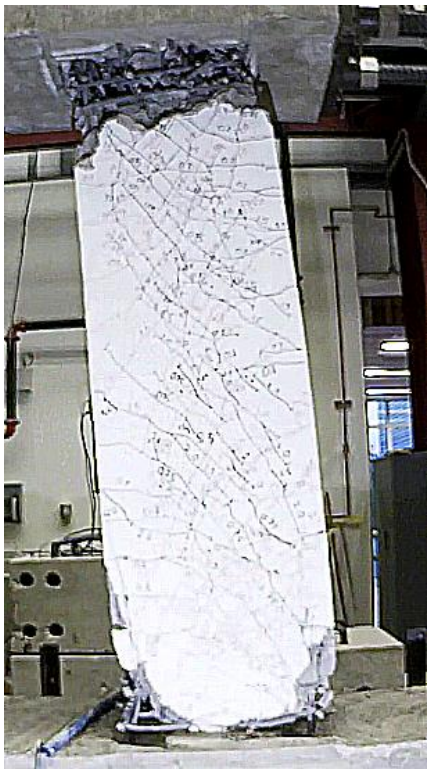

Figure C.93 – D120-3.5 at
-8% chord rotation, second cycle

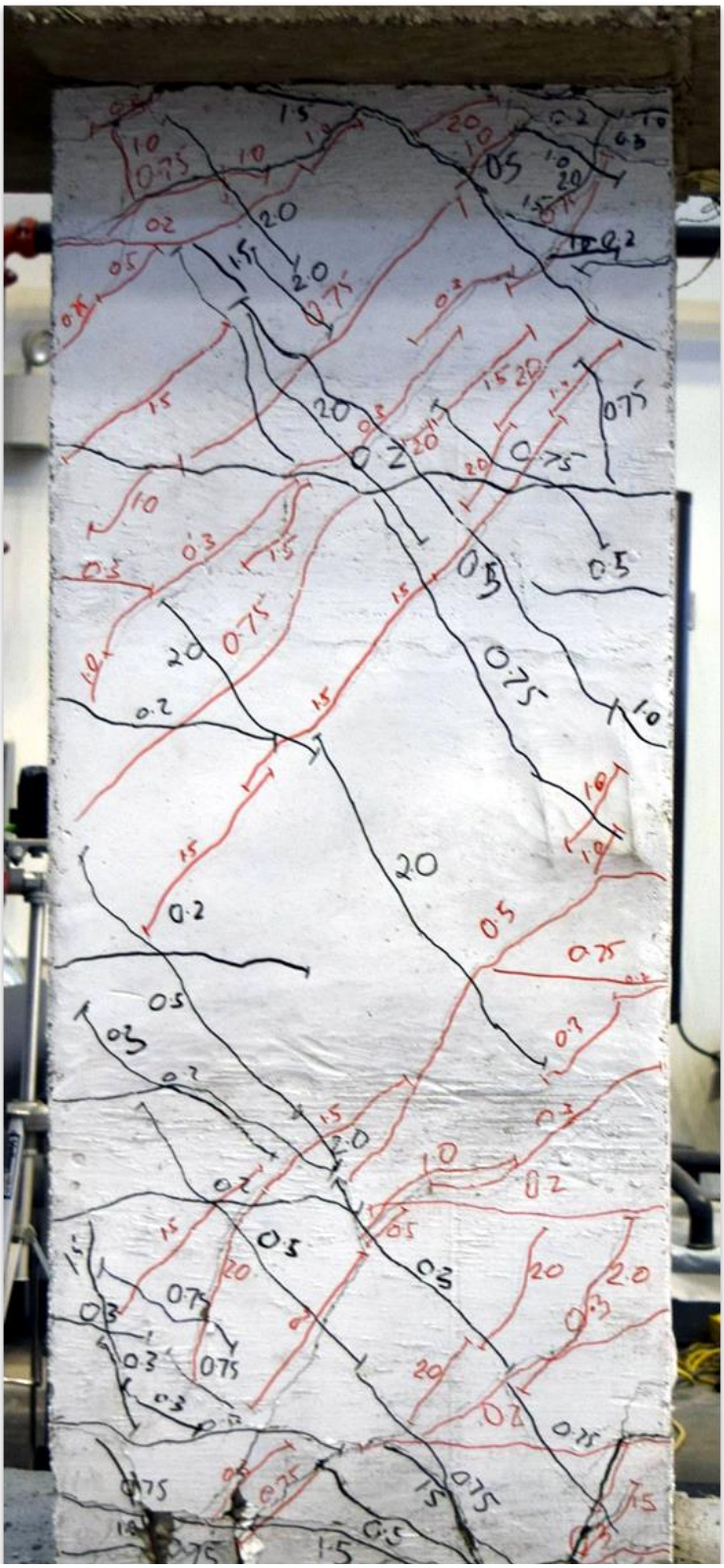

Figure C.94 – P80-2.5 during
second cycle to 2% chord rotation

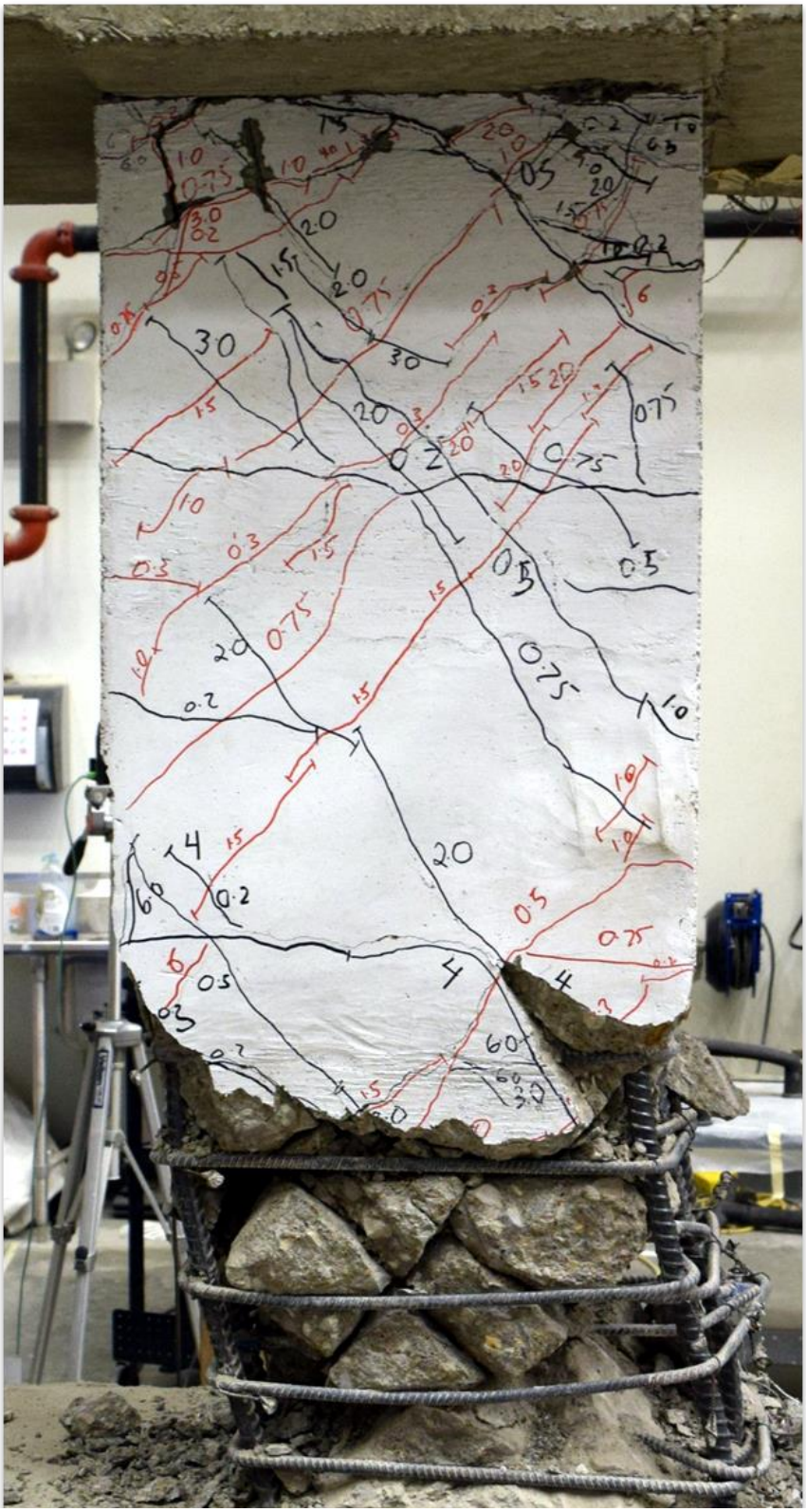

Figure C.95 – P80-2.5 during
second cycle to 6% chord rotation

Figure C.96 – P80-2.5 at
+2% chord rotation, second cycle

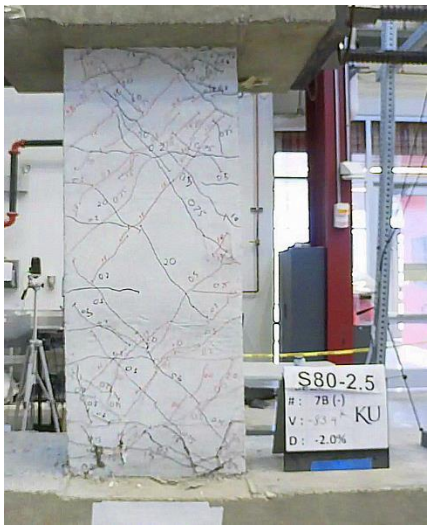

Figure C.97 – P80-2.5 at
-2% chord rotation, second cycle

Figure C.98 – P80-2.5 at
+4% chord rotation, second cycle

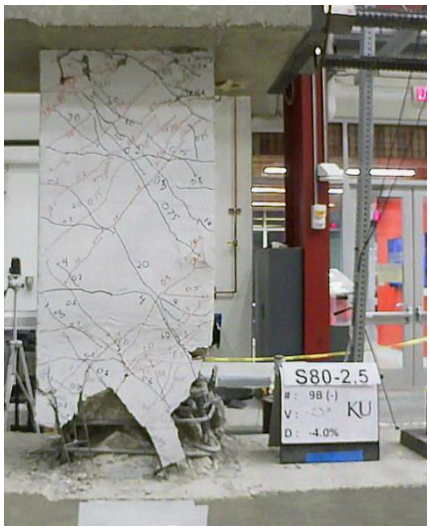

Figure C.99 – P80-2.5 at
-4% chord rotation, second cycle

Figure C.100 – P80-2.5 at
+6% chord rotation, second cycle

Figure C.101 – P80-2.5 at
-6% chord rotation, second cycle

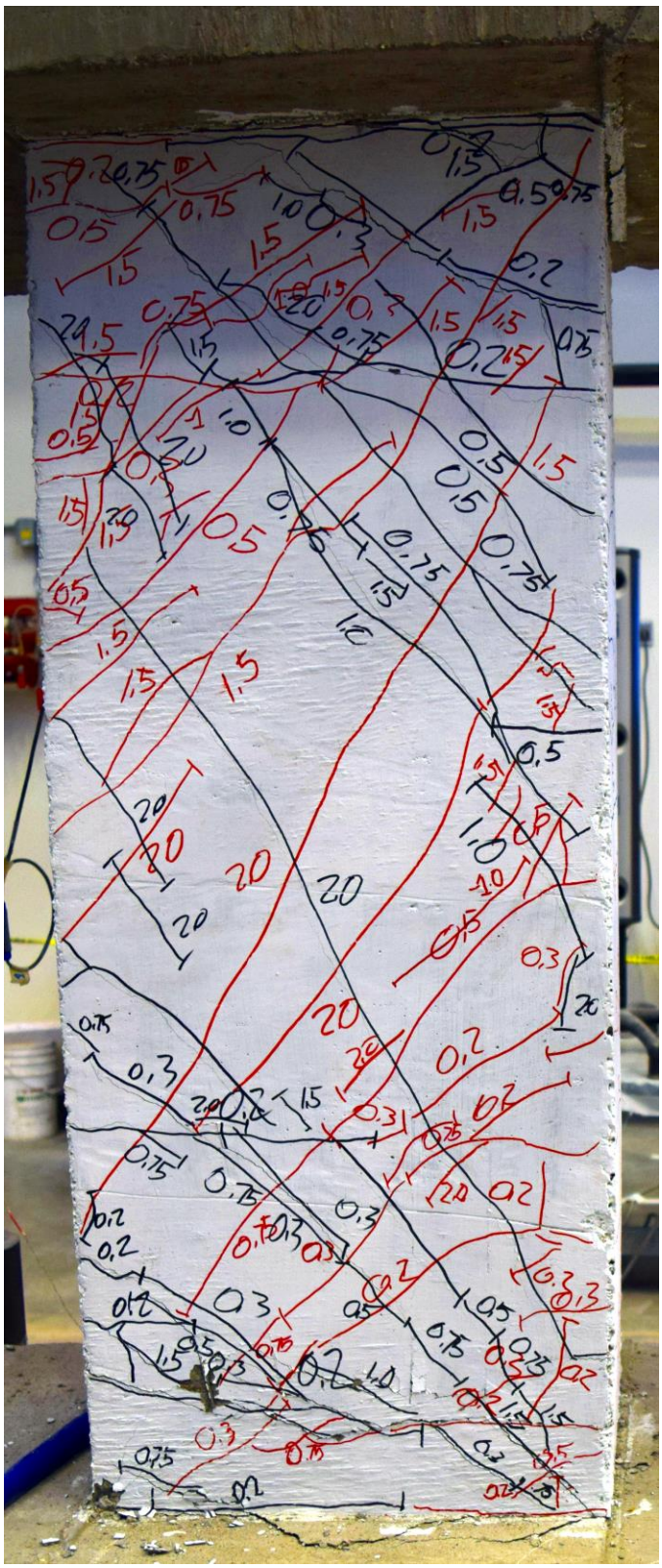

Figure C.102 – P100-2.5 during
second cycle to 2% chord rotation

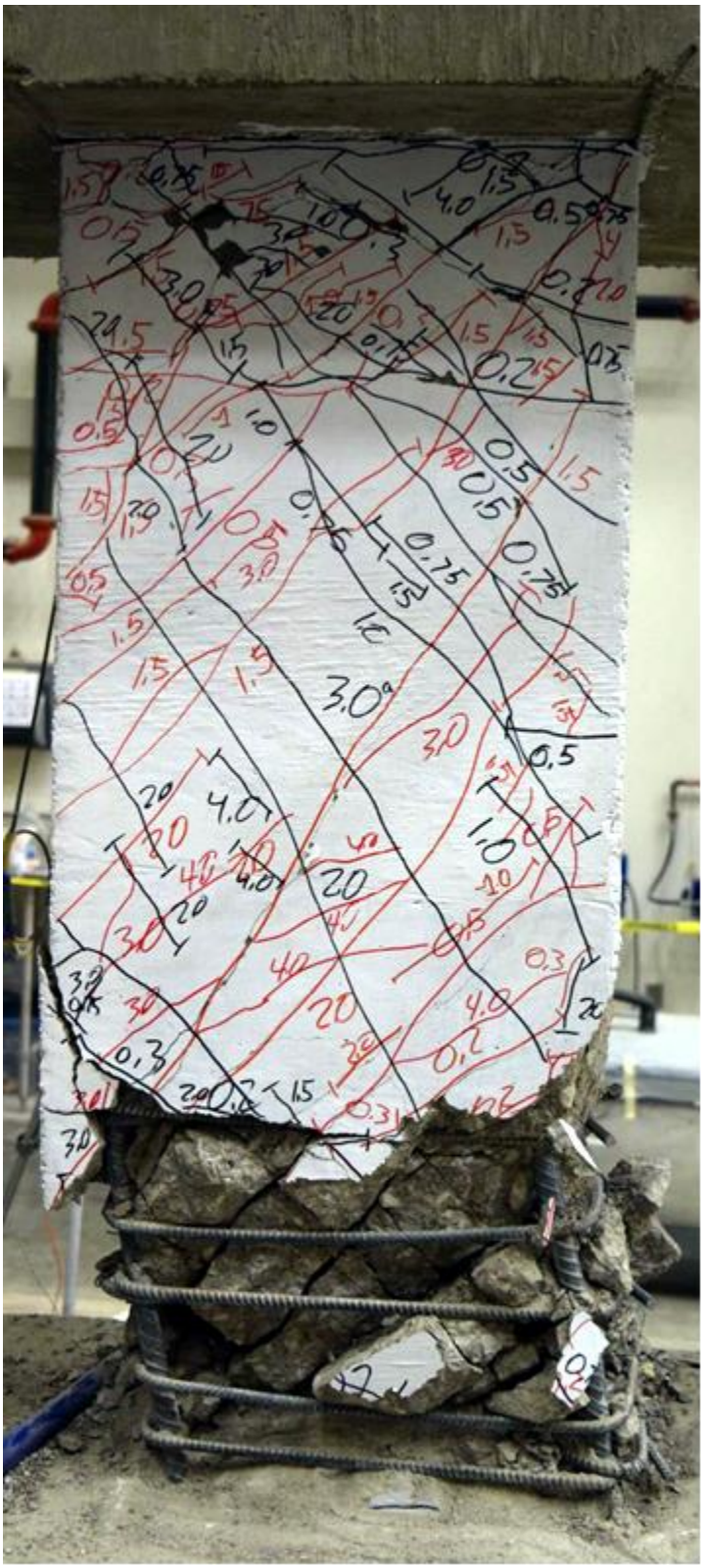

Figure C.103 – P100-2.5 during
second cycle to 6% chord rotation

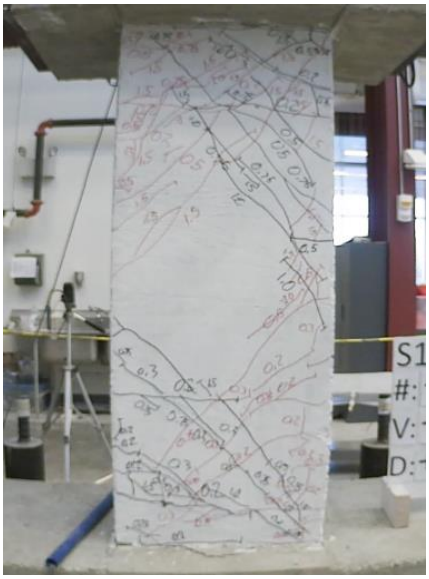

Figure C.104 – P100-2.5 at
+2% chord rotation, second cycle

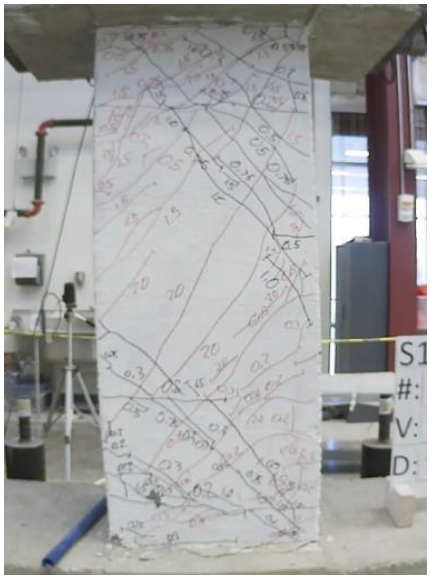

Figure C.105 – P100-2.5 at
-2% chord rotation, second cycle

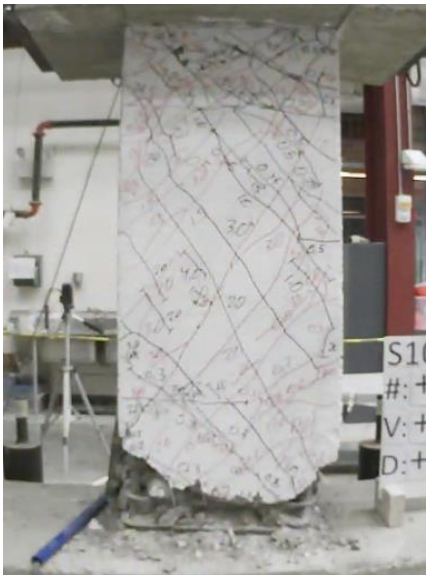

Figure C.106 – P100-2.5 at
+4% chord rotation, second cycle

Figure C.107 – P100-2.5 at
-4% chord rotation, second cycle

Figure C.108 – P100-2.5 at
+6% chord rotation, second cycle

Figure C.109 – P100-2.5 at
-6% chord rotation, second cycle